Spectroscopic Methods in Mineralogy and Material Sciences



Grant S. Henderson
Daniel R. Neuville
Robert T. Downs

Copyright 2015. De Gruyter. All rights reserved. May not be reproduced in any form without permission from the publisher, except fair uses permitted under U.S. or applicable copyright law.

EBSCO Publishing : eBook Collection (EBSCOhost) - printed on 2/13/2023 5:26 AM via
AN: 935620 ; Grant Henderson, Daniel Neuville, Robert Downs.; Spectroscopic Methods in Mineralogy and Material Sciences
Account: ns335141

REVIEWS IN MINERALOGY AND GEOCHEMISTRY

Volume 78 2015

Spectroscopic Methods in Mineralogy and Materials Sciences

EDITORS

Grant S. Henderson
University of Toronto
Toronto, Canada

Daniel R. Neuville
IPGP-CNRS
Paris, France

Robert T. Downs
University of Arizona
Tucson, Arizona

COVER:

The cover image shows a crystal of Fluorite, along with a ball and stick model of the structure overlain by the Raman spectrum. Courtesy of Joel Dyon, IPGP.

Series Editor: ***Jodi J. Rosso***

MINERALOGICAL SOCIETY OF AMERICA
GEOCHEMICAL SOCIETY

DE GRUYTER

EBSCOhost - printed on 2/13/2023 5:26 AM via . All use subject to https://www.ebsco.com/terms-of-use

Reviews in Mineralogy and Geochemistry, Volume 78

Spectroscopic Methods in Mineralogy and Materials Sciences

ISSN 1529-6466
ISBN 978-0-939950-93-5

Copyright 2015

The MINERALOGICAL SOCIETY of AMERICA
3635 Concorde Parkway, Suite 500
Chantilly, Virginia, 20151-1125, U.S.A.
www.degruyter.com

The appearance of the code at the bottom of the first page of each chapter in this volume indicates the copyright owner's consent that copies of the article can be made for personal use or internal use or for the personal use or internal use of specific clients, provided the original publication is cited. The consent is given on the condition, however, that the copier pay the stated per-copy fee through the Copyright Clearance Center, Inc. for copying beyond that permitted by Sections 107 or 108 of the U.S. Copyright Law. This consent does not extend to other types of copying for general distribution, for advertising or promotional purposes, for creating new collective works, or for resale. For permission to reprint entire articles in these cases and the like, consult the Administrator of the Mineralogical Society of America as to the royalty due to the Society.

EBSCOhost - printed on 2/13/2023 5:26 AM via . All use subject to https://www.ebsco.com/terms-of-use

Spectroscopic Methods in Mineralogy and Materials Sciences

78 *Reviews in Mineralogy and Geochemistry* **78**

FROM THE SERIES EDITOR

In 1988, when the RiMG series was called the "Reviews in Mineralogy," Volume 18, *Spectroscopic Methods in Mineralogy and Geology,* edited by Frank Hawthorne, was published. Although there were many texts in the field of spectroscopy at that time, very few had a slant toward geological materials and virtually none stressed the integrated, multitechnique approach necessary for use in geochemical and geophysical problems. Volume 18 provided a timely review of cutting-edge spectroscopic techniques beginning to be used in Earth sciences and became an essential resource to many scientists and educators for the past two decades.

Sixty RiMG volumes later, Grant Henderson, Daniel Neuville, and Bob Downs have taken up the task to provide an up-to-date, 21st century perspective of the spectroscopic and microscopic techniques that are continuing to be developed and used in the Earth and materials sciences. One will find that the now "familiar" techniques introduced in Volume 18 have advanced significantly and are more powerful than ever and that there are many new techniques available for probing the secrets of Earth materials. Considering how rapidly this field continues to grow, it wouldn't be surprising to see another RiMG "Spectroscopic Methods" volume published in 20 years!

All supplemental materials associated with this volume can be found at the MSA website. Errata will be posted there as well.

Jodi J. Rosso, Series Editor
Richland, Washington
February 2014

PREFACE

Spectroscopy is the study of the interaction between matter and radiation and spectroscopic methods measure this interaction by measuring the radiative energy of the interaction in terms of frequency or wavelength or their changes. A variety of spectroscopic methods saw their first applications in mineralogical studies in the early 1960s and 1970s and since then have flourished where today they are routinely employed to probe both the general nature of mineralogical and geochemical processes as well as more atom specific interactions. In 1988, a Reviews in Mineralogy volume (Volume 18) was published on *Spectroscopic Methods in Mineralogy and Geology* by Frank Hawthorne (ed). The volume introduced the reader to a variety of spectroscopic techniques that, up to that time, were relatively unknown to most of the mineralogical and geochemical community. The volume was a great success and resulted

1529-6466/14/0078-0000$00.00 http://dx.doi.org/10.2138/rmg.2014.78.0

EBSCOhost - printed on 2/13/2023 5:26 AM via . All use subject to https://www.ebsco.com/terms-of-use

in many of these techniques becoming main stream research tools. Since 1988, there have been many significant advances in both the technological aspects of these techniques and their applications to problems in Earth Sciences in general while the range and breadth of the techniques currently employed have greatly expanded since those formative years. The current volume compliments the original volume and updates many of the techniques. In addition, new methods such as X-ray Raman and Brillouin spectroscopy have been added, as well as non-spectroscopic chapters such as Transmission Electron Microscopy (TEM) and Atomic Force Microscopy (AFM) for completeness.

The first chapter by Lavina et al. introduces the reader to current X-ray diffraction methods, while those of Newville and Henderson et al. separately cover the widely used techniques of EXAFS and XANES. The new *in situ* high-pressure technique of X-ray Raman is covered in the chapter by Lee et al. There is an emphasis in all these chapters on synchrotron based methods which continues in the Luminescence chapter by Waychunas. Chapters on high resolution TEM and its associated spectroscopies, and X-ray photoelectron spectroscopy are covered by Brydson et al., and Nesbitt and Bancroft, respectively. The study of mineral surfaces by Atomic Force Microscopy has been covered by Jupille. UV/Vis and IR spectroscopies are described in the chapters by Rossman, Clark et al., Della Ventura et al., and Hofmeister. Rossman's chapter covers the basics of UV/Vis while Clark et al. describes the detection of materials in the Solar system utilizing UV and IR methods. Synchrotron-based IR imaging is covered by Della Ventura et al. and errors and uncertainties associated with IR and UV/Vis data are covered in the chapter by Hofmeister. Photon/phonon interactions such as Raman and Brillouin are outlined by Neuville et al. and Speziale et al. The latter technique is relatively new outside the fields of condensed matter and mineral physics but is gaining increasing use as interest in elastic properties and anomalous behaviors at high pressure continues to grow. The chapters by Stebbins and Xue, and Pan and Nilges outline the current status of magnetic resonance methods such as NMR and EPR, respectively. Finally the last three chapters have been included for completeness and cover the basics of the theoretical simulations that are carried out to investigate phases beyond accessible experimental pressure-temperature ranges, as well as aiding in the interpretation of experimental spectra (Jahn and Kowalski), the high pressure methods that are now commonly employed for many spectroscopic studies (Shen and Wang) and finally a chapter on methods used in high-temperature melt and crystallization studies (Neuville et al.).

This volume is the cumulative effort of many people whom we gratefully thank, especially the authors of the chapters for their contributions and the reviewers for their comments and suggestions. We thank the series editor Jodi Rosso for all her work and Joel Dyon for the cover image. GSH especially thanks G. Michael Bancroft for his help as the "go to" reviewer when a quick turnaround was essential. With 20 different groups of authors from all over the world (Canada, England, France, Germany, Italy, Japan, Korea, Netherlands, USA) and with varying abilities to adhere to deadlines, it has been a long process and we thank all the authors for their patience during this time.

Grant S. Henderson
University of Toronto, Canada

Daniel R. Neuville
IPGP-CNRS, France

Robert T. Downs
University of Arizona, U.S.A.

EBSCOhost - printed on 2/13/2023 5:26 AM via . All use subject to https://www.ebsco.com/terms-of-use

Spectroscopic Methods in Mineralogy and Materials Sciences

78 *Reviews in Mineralogy and Geochemistry* **78**

TABLE OF CONTENTS

1 **Modern X-ray Diffraction Methods in Mineralogy and Geosciences**

Barbara Lavina, Przemyslaw Dera, Robert T. Downs

INTRODUCTION 1
GENERAL ASPECTS 2
Brief introduction to X-ray diffraction theory 2
Ideal structures, real structures, liquids 5
Information obtained from X-ray diffraction experiments 6
X-ray: characteristics, sources, choice 7
X-RAY DIFFRACTION TECHNIQUES 10
Single crystal monochromatic diffraction (SXD) 10
Laue method 13
Powder diffraction 15
Peak and whole pattern fitting 21
The atomic pair distribution function technique (PDF) 25
ACKNOWLEDGMENTS 27
REFERENCES 27

2 **Fundamentals of XAFS**

Matthew Newville

INTRODUCTION 33
X-RAY ABSORPTION AND FLUORESCENCE 35
A SIMPLE THEORETICAL DESCRIPTION OF XAFS 40
A rough explanation of the EXAFS equation 42
The EXAFS $\chi(E)$ is proportional to the amplitude of the scattered photoelectron at the absorbing atom 43
$\lambda(\boldsymbol{k})$: The inelastic mean free path 44
S_0^2: intrinsic losses 45
Multiple scattering of the photoelectron 46

EBSCOhost - printed on 2/13/2023 5:26 AM via . All use subject to https://www.ebsco.com/terms-of-use

Disorder terms and $g(R)$ 46
Discussion 48
XAFS MEASUREMENTS: TRANSMISSION AND FLUORESCENCE 49
Transmission XAFS measurements 51
Fluorescence and electron yield XAFS measurements 51
Self-absorption (or over-absorption) of fluorescence XAFS 54
Deadtime corrections for fluorescence XAFS 56
XAFS DATA REDUCTION 57
Pre-edge subtraction and normalization 58
Background subtraction 59
EXAFS Fourier transforms 62
XAFS DATA MODELING 65
Running and using FEFF for EXAFS calculations 65
First-shell fitting 66
Fit statistics and estimated uncertainties 67
Second-shell fitting 70
REFERENCES 73

3 X-ray Absorption Near-Edge Structure (XANES) Spectroscopy

Grant S. Henderson, Frank M.F. de Groot, Benjamin J.A. Moulton

PREFACE 75
INTRODUCTION 76
Interaction of X-rays with matter 76
Binding energy 76
Single electron excitation approximation and selection rules 77
Calculations of XANES spectra 77
EXPERIMENTAL ASPECTS OF XANES 78
Doing a XANES experiment at a beamline 78
Data reduction 79
XANES DETECTION MODES 80
Transmission detection of XANES 80
Electron yield detection of XANES 80
Fluorescence yield detection of XANES 81
Partial Fluorescence Yield detection of XANES 81
Electron energy loss spectroscopy and X-ray Raman 81
XANES microscopy 82
XANES ANALYSIS OF METAL *K*-EDGES 82
Special energy positions of X-ray absorption edges 82
The pre-edge region 83
The edge region and peaks at higher energies in the XANES region 84
XANES analysis of metal *L*-edges 85
Multiplet analysis of *L*-edges 85
QUALITATIVE SPECTRAL ANALYSIS OF THE *L*-EDGES 86
Energy shifts 86

EBSCOhost - printed on 2/13/2023 5:26 AM via . All use subject to https://www.ebsco.com/terms-of-use

Intensities of the *L*-edges 86
The branching ratio 86
Polarization dependence and XMCD 86
XANES ANALYSIS OF LIGAND *K*-EDGES 86
APPLICATIONS OF XANES IN MINERALOGY AND GEOCHEMISTRY 86
Transition metals: *K*-edges 86
Transition metals: *L*-edges 92
Silicon and aluminum *K*- and *L*-edges 94
Alkalis (Li, Na, K, Rb, Cs) 100
Alkaline-Earths (Be, Ca, Mg, Sr, Ba) 102
Ligand edges (C, O, B, S, P) 106
SOME EXAMPLES OF STUDIES UTILIZING XANES 121
Assessing trace element substitution in minerals: Cerium speciation (Ce^{3+}/Ce^{4+}) in Ti-rich minerals 121
Assessing changes in oxidation state of Nb and Ta with varying f_{O_2} at 1.5 GPa as a possible explanation for the negative Nb/Ta anomaly or "arc signature" of melts 122
In situ high-temperature determination of Cr oxidation state in basaltic melts: A novel XANES furnace design 123
The behavior of Br in CO_2-bearing fluids in low-temperature geological settings: A Br K-edge study on synthetic fluid inclusions 124
ACKNOWLEDGMENTS 125
REFERENCES 125

4 Probing of Pressure-Induced Bonding Transitions in Crystalline and Amorphous Earth Materials: Insights from X-ray Raman Scattering at High Pressure

Sung Keun Lee, Peter J. Eng, Ho-kwang Mao

INTRODUCTION 139
BRIEF REMARKS ON THEORETICAL BACKGROUNDS AND XRS EXPERIMENTS AT HIGH PRESSURE 141
Brief theoretical backgrounds 141
Comparison with other core-electron excitation spectroscopy and traditional experimental probes at high pressure 143
XRS experiments 146
PRESSURE-INDUCED STRUCTURAL CHANGES IN CRYSTALLINE AND AMORPHOUS EARTH MATERIALS: INSIGHTS FROM X-RAY RAMAN SCATTERING 147
Application of *K*-edge XRS to materials under high pressure 148
Insights from quantum chemical calculations 161
REMAINING CHALLENGES AND OUTLOOK: APPLICATIONS OF NEW *K*-, *L*-, *M*-EDGE XRS, XRS WITH MOMENTUM TRANSFER, *IN SITU* HIGH-TEMPERATURE AND HIGH-PRESSURE XRS STUDY FOR MULTI-COMPONENTS GLASSES 164

EBSCOhost - printed on 2/13/2023 5:26 AM via . All use subject to https://www.ebsco.com/terms-of-use

Application of *L*- and *M*-edge XRS techniques to oxides and silicates under pressure 166
Application of XRS technique to multi-component oxide glasses under pressure 167
Application of new *K*-edges (elements in the 3rd row of the periodic table) and momentum transfer XRS to crystals under pressure 168
In situ high-temperature and high-pressure XRS studies 168
Outlook and prospects 168
ACKNOWLEDGMENTS 168
REFERENCES 169

5 Luminescence Spectroscopy

Glenn A. Waychunas

INTRODUCTION 175
THE TYPES AND PHYSICAL PROCESSES OF LUMINESCENCE 175
Luminescence 175
Fluorescence 176
Phosphorescence 177
Thermoluminescence 177
Cathodoluminescence 178
X-ray excited optical luminescence 179
Activators, sensitizers, and quenchers 179
Emission and excitation spectra 181
Semiconductor vs. insulator models 182
Luminescence in organic molecules and structures 182
Total Luminescence Spectra 182
SPECIFIC LUMINESCENCE METHODOLOGY AND APPLICATIONS 183
Time-gated laser excitation and emission techniques 183
EXAMPLES OF APPLICATIONS 184
Activator determination 184
Site occupancy and partitioning 188
Organic-derived luminescence 191
Cathodoluminescence techniques 194
Scanning cathodoluminescence microscopy 195
APPLICATIONS 196
Quartz 196
Feldspars 197
Zircon 201
Carbonates 201
Apatite 203
Thermoluminescence techniques 204
Applications 206
Developing areas for luminescence applications 209
ACKNOWLEDGMENTS 211
REFERENCES 211

EBSCOhost - printed on 2/13/2023 5:26 AM via . All use subject to https://www.ebsco.com/terms-of-use

6 Analytical Transmission Electron Microscopy

Rik Brydson, Andy Brown, Liane G. Benning, Ken Livi

INTRODUCTION 219
INTRODUCTION TO ANALYTICAL TRANSMISSION ELECTRON MICROSCOPY (TEM) 219
Basic design of transmission electron microscopes (TEM) 219
Interactions between the electron beam and the specimen 222
The specimen 227
Recent developments in analytical TEM 228
ELEMENTAL QUANTIFICATION – EDX AND EELS 229
EDX 229
Example of the practical application of EDX: clay minerals 232
EELS 236
EEL SPECTROMETRY 239
EEL low-loss spectroscopy 239
EELS core-loss fine structure 242
EDX AND EELS IMAGING 245
EXAMPLE OF THE PRACTICAL APPLICATION OF EELS: EELS OF MANGANESE IN MINERALS AND ENVIRONMENTAL HEALTH 247
Introduction 247
Analytical considerations for EELS determination of manganese valence 247
Near edge structure of Mn $M_{2,3}$-edge 248
Near edge structure of Mn $L_{2,3}$-edge 248
Quantification of valence by $L_{2,3}$-ELNES 249
Beam damage 251
Applications 252
GENERAL APPLICATION OF EELS, SAED AND EDX 253
Use of (S)TEM to assess transport and retardation mechanisms of trace metal contaminants 253
Developments in TEM specimen preparation 255
Developments in analyzing poorly crystalline, beam sensitive materials 261
CONCLUSIONS 263
REFERENCES 265

7 High Resolution Core- and Valence-Level XPS Studies of the Properties (Structural, Chemical and Bonding) of Silicate Minerals and Glasses

H.W. Nesbitt, G.M. Bancroft

INTRODUCTION 271
XPS studies of silicates 271
Technical advances 272
Focus of the review 273

EBSCOhost - printed on 2/13/2023 5:26 AM via . All use subject to https://www.ebsco.com/terms-of-use

FUNDAMENTAL PRINCIPLES OF XPS 273
Photoionization and analysis depths 273
Non-conductors and sample charging 275
Photopeak assignments and intensities 276
Depth of analysis 277
Linewidths 277
Si 2*p* AND O 1*s* LINEWIDTHS: EXPERIMENT AND THEORY 282
Evidence for minimum linewidths for silicates 282
Si 2*p* vibrational contributions 287
O 1*s* vibrational contributions 289
Effects of phonon broadening 289
Experimental and fitting considerations 290
Chemical shifts in silicates 291
Surface core-level shifts in silicates 292
CORE LEVEL BULK APPLICATIONS 294
Crystalline silicates 294
Silicate glasses: general aspects 297
Silicate glasses: O 1*s* spectra, and NBO and BO linewidths 303
Silicate glasses: uncertainties in BO% from O 1*s* spectra 305
Determination of free oxide O^{2-} and its importance 309
CORE LEVEL SURFACE STUDIES OF SILICATES 312
Adsorption on silicate and oxide surfaces 312
Leaching of silicates 314
VALENCE LEVEL BULK APPLICATIONS 317
Nature of the contributions to the valence band 317
ACKNOWLEDGEMENTS 323
REFERENCES 323

8 Analysis of Mineral Surfaces by Atomic Force Microscopy

Jacques Jupille

INTRODUCTION 331
EXPERIMENTAL METHODS 332
AFM set-ups 333
Experimental conditions 337
DISSOLUTION, PRECIPITATION AND GROWTH 338
Determination of reaction rates at crystal surfaces from step velocities 339
Size and shape of clay minerals 343
Limits of the AFM observation 343
AFM rates versus bulk rates 346
FORCE MEASUREMENTS 347
Hydration forces 348
Determination of the point of zero charge (PZC) 349
Kelvin Force Probe Microscopy (KPFM) 351
ATOMICALLY RESOLVED SURFACE STRUCTURES 354
Structures in contact mode 354

EBSCOhost - printed on 2/13/2023 5:26 AM via . All use subject to https://www.ebsco.com/terms-of-use

Surface structures analyzed by AFM in dynamic mode 355
CONCLUSIONS 360
ACKNOWLEDGMENTS 362
REFERENCES 363

9 Optical Spectroscopy

George R. Rossman

INTRODUCTION 371
GENERAL CONCEPTS 372
UNITS 375
Wavelength and energy 375
Intensities 375
THE EXPERIMENT – SAMPLE AND EQUIPMENT CONSIDERATIONS 376
Types of spectrometers 376
NOMENCLATURE OF THE DIFFERENT SPECTRA 377
INTENSITIES AND SELECTION RULES 377
The Laporte selection rule 377
Spin-forbidden transitions 378
QUANTITATIVE CONCENTRATIONS FROM OPTICAL SPECTRA 378
IDENTIFICATION OF THE OXIDATION STATES OF CATIONS 379
A GALLERY OF SPECTRA OF METAL IONS COMMONLY RESPONSIBLE FOR THE OPTICAL SPECTRA OF MINERALS. 379
Titanium 379
Vanadium 379
Chromium 380
Manganese 381
Iron 382
Cobalt 384
Nickel 384
Copper 384
Rare Earth Elements and Uranium 386
INTERVALENCE CHARGE TRANSFER 388
Intervalence charge transfer in low-symmetry crystals 388
BAND GAPS 390
RADIATION-INDUCED COLOR CENTERS 390
VIBRATIONAL OVERTONES AND COMBINATIONS 392
ARTIFACTS 392
Interference fringes 392
Wood's grating anomaly 393
TEMPERATURE AND PRESSURE DEPENDENCE 393
ABSORPTION BAND INTENSIFICATION 394
COMPILATIONS OF MINERAL OPTICAL SPECTRAL DATA 395
CONCLUDING THOUGHTS 396
REFERENCES 397

EBSCOhost - printed on 2/13/2023 5:26 AM via . All use subject to https://www.ebsco.com/terms-of-use

10 Spectroscopy from Space

Roger N. Clark, Gregg A Swayze, Robert Carlson, Will Grundy, Keith Noll

ABSTRACT 399
INTRODUCTION 400
DETECTION OF MINERALS AND THEIR SPECTRAL PROPERTIES 402
MINERAL AND FROZEN VOLATILES SPECTRAL SIGNATURES 406
- H_2O (ice) 406
- SO_2 ice 406
- Nitrogen ice (N_2) 406
- Hydrocarbons and other ices 407
- Methane ice (CH_4) 408

MINERALS AND COMPOUNDS IN THE SOLAR SYSTEM DETECTED WITH SPECTROSCOPY 408
- Terrestrial planets 408
- Asteroids and comets 415
- Jupiter system 416
- Saturn system 422
- Uranus system 427
- The Neptune system and beyond 428

SUMMARY 430
ACKNOWLEDGMENTS 431
REFERENCES 432

11 SR-FTIR Microscopy and FTIR Imaging in the Earth Sciences

Giancarlo Della Ventura, Augusto Marcelli, Fabio Bellatreccia

INTRODUCTION 447
FTIR MICROSCOPY AND IMAGING TECHNIQUES 449
SYNCHROTRON-RADIATION FTIR SPECTROSCOPY IN MINERAL SCIENCES 453
- Introduction 453
- Applications in mineral sciences 455

FTIR IMAGING 464
- Introduction 464
- The distribution of H and C in minerals 465
- Imaging of inclusions in minerals 468
- FTIR imaging of dynamic processes 472

CONCLUSIONS 474
ACKNOWLEDGMENTS 474
REFERENCES 474

EBSCOhost - printed on 2/13/2023 5:26 AM via . All use subject to https://www.ebsco.com/terms-of-use

12 Carryover of Sampling Errors and Other Problems in Far-Infrared to Far-Ultraviolet Spectra to Associated Applications

Anne M. Hofmeister

INTRODUCTION AND PURPOSE 481
EXPERIMENTAL METHODS 482
EXTRACTION OF SPECTRAL PROPERTIES FROM LABORATORY MEASUREMENTS 482
Ideal interactions of light with perfect, single crystals 482
Limitations of real measurements 488
Errors originating in instrumentation 488
Concerns in obtaining quantitative spectra from powders 489
Concerns regarding thin-film spectra obtained in the diamond anvil cell 490
Propagation of errors 491
Errors arising during data processing and extracting spectral parameters 491
Emission spectra 492
EXAMPLES OF SAMPLING PROBLEMS IN THE LABORATORY 497
Overly large grains in absorbing regions 497
Too small of crystals for the near-IR transparent region 497
Information on *d-d* transitions in the UV may pertain to band assignments 499
REMOTELY SENSED SPECTRA AND OBSERVATIONAL DATA 500
Ascertaining surface mineralogy of large bodies 501
Ascertaining the mineralogy of the 10 μm feature in observational data 503
DEDUCING DIFFUSIVE RADIATIVE TRANSFER FROM SPECTRA 504
CONCLUSIONS 505
ACKNOWLEDGMENTS 505
REFERENCES 506

13 Advances in Raman Spectroscopy Applied to Earth and Material Sciences

Daniel R. Neuville, Dominique de Ligny, Grant S. Henderson

BRIEF HISTORICAL PERSPECTIVE AND SIMPLE THEORY 509
Quantum mechanical theory 512
INSTRUMENTATION 513
Excitation line 513
Notch filters, optical spectrometer or grating 514
Optics, monochromators, detectors 515
Different manufacturers and instrument types 515
Confocal system 516
Data acquisition and reduction 517
Baseline correction and normalization 521

EBSCOhost - printed on 2/13/2023 5:26 AM via . All use subject to https://www.ebsco.com/terms-of-use

OTHER TYPES OF RAMAN SPECTROSCOPY 521
Hyper-Raman scattering (HRS) 521
Surface Enhanced Raman Scattering (SERS) 522
APPLICATIONS 523
Crystalline spectra 523
Amorphous materials 524
Silicate glasses 524
Aluminosilicate glasses 528
Borosilicate glasses 529
Titanosilicate glasses 530
Iron silicate glasses 530
Volatiles in glasses 531
Fluid inclusions 532
In situ Raman spectroscopy 533
CONCLUSIONS 536
REFERENCES 536

14 Brillouin Scattering and its Application in Geosciences

Sergio Speziale, Hauke Marquardt, Thomas S. Duffy

INTRODUCTION 543
HISTORICAL BACKGROUND 544
PHYSICAL PRINCIPLES OF THE BRILLOUIN EFFECT 545
Brillouin scattering in fluids 547
Brillouin scattering in solids 549
BRILLOUIN SPECTROSCOPY 551
Basic experimental setup 551
Light source 552
Scattering geometry 552
The spectrometer 553
Detectors 556
Measurements on transparent materials 557
Measurements of surface Brillouin scattering on opaque materials and thin films 558
Brillouin scattering at ambient or near-ambient conditions 562
Determination of Pockel's coefficients 566
Brillouin scattering at extreme conditions 566
ANALYSIS OF THE BRILLOUIN SPECTRA AND RECOVERY OF THE ELASTIC TENSOR 571
Linear elasticity of anisotropic solids 572
Determining the elastic constants 573
What is the information from Brillouin scattering that is relevant to Earth science? 576
APPLICATIONS OF BRILLOUIN SPECTROSCOPY IN GEOSCIENCES 577
Experimental techniques to determine the anisotropic elasticity of Earth materials 577

EBSCOhost - printed on 2/13/2023 5:26 AM via . All use subject to https://www.ebsco.com/terms-of-use

Lithosphere and upper mantle 580
Transition zone 581
Lower mantle 582
FRONTIERS 583
Elasticity under deep mantle conditions 583
Combining Brillouin scattering with other techniques to characterize elastic anisotropy at high pressures 587
Surface Brillouin scattering at extreme conditions 587
ACKNOWLEDGMENTS 588
REFERENCES 588

15 NMR Spectroscopy of Inorganic Earth Materials

Jonathan F. Stebbins, Xianyu Xue

INTRODUCTION 605
THE BASICS 606
Nuclear spins, NMR frequencies and signal intensities 606
How NMR experiments are done 610
Anisotropy, motional averaging, and magic-angle spinning 611
CHEMICAL SHIFT VS. STRUCTURE 612
QUADRUPOLAR INTERACTIONS AND STRUCTURE 615
MAGNETIC DIPOLAR INTERACTIONS AND INDIRECT SPIN-SPIN COUPLINGS 619
MORE ADVANCED NMR METHODS 621
FIRST-PRINCIPLES CALCULATIONS OF NMR PARAMETERS 624
NUCLEAR SPIN RELAXATION 624
APPLICATIONS TO CRYSTALLINE SILICATES, OXIDES AND OTHER INORGANIC MATERIALS 625
Structural order/disorder in minerals 625
^{1}H NMR in minerals 629
NMR crystallography 631
APPLICATIONS TO GLASSES, MELTS AND OTHER AMORPHOUS MATERIALS 631
Volatile-free silicate glasses 631
Volatile-containing glasses 635
Other amorphous materials 636
Silicate and oxide melts 637
DYNAMICS, KINETICS AND TRANSITIONS 638
Phase transitions 638
Interactions of water with minerals and glasses 638
Aqueous solutions: ambient to elevated pressures 639
MINERALS CONTAINING ABUNDANT UNPAIRED ELECTRON SPINS 640
ACKNOWLEDGMENTS 642
REFERENCES 642

EBSCOhost - printed on 2/13/2023 5:26 AM via . All use subject to https://www.ebsco.com/terms-of-use

16 Electron Paramagnetic Resonance Spectroscopy: Basic Principles, Experimental Techniques and Applications to Earth and Planetary Sciences

Yuanming Pan, Mark J. Nilges

INTRODUCTION 655
BASIC PRINCIPLES AND SPIN HAMILTONIAN 656
Electron resonance condition and EPR spectra 656
Spin Hamiltonian 657
GUIDES TO EPR EXPERIMENTS AND SPECTRAL ANALYSES 662
Samples and techniques for generating paramagnetic species 662
Continuous-wave (CW) EPR 663
Pulse ESEEM and ENDOR 667
Ab initio calculations of EPR parameters 672
APPLICATIONS TO EARTH AND PLANETARY SCIENCES 673
EPR as a structural probe of point defects in minerals 673
In situ high-temperature and high-pressure EPR experiments 675
Optically detected magnetic resonance (ODMR) and mineral coloration 680
EPR as structural probe for other Earth and planetary materials 680
Quantitative EPR analysis 682
ACKNOWLEDGMENTS 684
REFERENCES 684

17 Theoretical Approaches to Structure and Spectroscopy of Earth Materials

Sandro Jahn, Piotr M. Kowalski

INTRODUCTION 691
THEORETICAL FRAMEWORK 692
Quantum-chemical methods 693
Density Functional Theory (DFT) 696
Excitation methods 702
Classical force field methods 705
Molecular dynamics 707
STRUCTURE DETERMINATION AND OPTIMIZATION 708
VIBRATIONAL SPECTRA 712
Lattice dynamics in the harmonic approximation 713
Atomic dynamics via time correlation functions 714
Infrared absorption spectroscopy 717
Raman spectra 719
ELECTRONIC EXCITATION SPECTRA 721
UV-vis 721
XAFS and XRS 723
EELS and ELNES 726
XPS 727

EBSCOhost - printed on 2/13/2023 5:26 AM via . All use subject to https://www.ebsco.com/terms-of-use

SPECTROSCOPY RELATED TO NUCLEAR EXCITATIONS....728
NMR....728
Mössbauer spectroscopy....731
CONCLUDING REMARKS....731
ACKNOWLEDGMENTS....732
REFERENCES....732

18 High-pressure Apparatus Integrated with Synchrotron Radiation

Guoyin Shen, Yanbin Wang

INTRODUCTION....745
SYNCHROTRON TECHNIQUES APPLICABLE TO HIGH-PRESSURE RESEARCH....746
Synchrotron radiation....746
High-pressure synchrotron techniques....748
HIGH PRESSURE TECHNIQUES INTEGRATED WITH SYNCHROTRON RADIATION....757
The large volume press (LVP)....757
Diamond anvil cell techniques....763
Dynamic shockwave techniques....766
A BRIEF OUTLOOK....767
Expanding *P-T* range....767
New HP synchrotron techniques....767
ACKNOWLEDGMENTS....768
REFERENCES....768

19 *In situ* High-Temperature Experiments

Daniel R. Neuville, Louis Hennet, Pierre Florian, Dominique de Ligny

PREFACE....779
INTRODUCTION....779
LEVITATION TECHNIQUES....780
Introduction....780
Acoustic levitation....781
Electromagnetic levitation....781
Electrostatic levitation....781
Aerodynamics levitation....782
Experimental techniques....784
APPLICATIONS OF AERODYNAMICS LEVITATION....784
NMR experiments....784
X-ray absorption spectroscopy (XAS)....786
SAXS and SANS....787
X-ray and neutron diffraction....787

EBSCOhost - printed on 2/13/2023 5:26 AM via . All use subject to https://www.ebsco.com/terms-of-use

WIRE OR PLATE HEATING SYSTEM....788
Description, temperature and atmosphere control....788
Raman spectroscopy....790
X-ray diffraction....791
X-ray absorption....794
ADVANTAGES, DIFFERENCES AND CONCLUSIONS....795
ACKNOWLEDGMENTS....797
REFERENCES....797

EBSCOhost - printed on 2/13/2023 5:26 AM via . All use subject to https://www.ebsco.com/terms-of-use

Reviews in Mineralogy & Geochemistry
Vol. 78 pp. 1-31, 2014
Copyright © Mineralogical Society of America

Modern X-ray Diffraction Methods in Mineralogy and Geosciences

Barbara Lavina
High Pressure Science and Engineering Center
and
Department of Physics and Astronomy
University of Nevada
Las Vegas, Nevada 89154, U.S.A.
lavina@physics.unlv.edu

Przemyslaw Dera
Hawaii Institute of Geophysics and Planetology
School of Ocean and Earth Science and Technology
University of Hawaii at Manoa
1680 East West Road, POST Bldg, Office 819E
Honolulu, Hawaii 96822, U.S.A.

Robert T. Downs
Department of Geosciences
University of Arizona
Tucson, Arizona 85721-0077, U.S.A.

INTRODUCTION

A century has passed since the first X-ray diffraction experiment (Friedrich et al. 1912). During this time, X-ray diffraction has become a commonly used technique for the identification and characterization of materials and the field has seen continuous development. Advances in the theory of diffraction, in the generation of X-rays, in techniques and data analysis tools changed the ways X-ray diffraction is performed, the quality of the data analysis, and expanded the range of samples and problems that can be addressed. X-ray diffraction was first applied exclusively to crystalline structures idealized as perfect, rigid, space and time averaged arrangements of atoms, but now has been extended to virtually any material scattering X-rays. Materials of interest in geoscience vary greatly in size from giant crystals (meters in size) to nanoparticles (Hochella et al. 2008; Waychunas 2009), from nearly pure and perfect to heavily substituted and poorly ordered. As a consequence, a diverse range of modern diffraction capabilities is required to properly address the problems posed. The time and space resolution of X-ray diffraction now reaches to nanoseconds and tens of nanometers. Time resolved studies are used to unravel the mechanism and kinetics of mineral formation and transformations. Non-ambient conditions such as extreme pressure and temperature are created in the laboratory to investigate the structure and properties of the Earth's deep interior and the processes that shape the planet.

This chapter is not intended to be comprehensive or detailed, because diffraction is such a vast subject. We will, however, summarize the principles of diffraction theory under the assumption that the reader is familiar with basic concepts of the crystalline state. We will

1529-6466/14/0078-0001$05.00 http://dx.doi.org/10.2138/rmg.2014.78.1

EBSCOhost - printed on 2/13/2023 5:26 AM via . All use subject to https://www.ebsco.com/terms-of-use

briefly review the basics of diffraction techniques, using laboratory and synchrotron X-ray sources and highlight some of their applications in geoscience. For briefness, we will omit the discussion of structure solution as most of experiments in the geosciences are performed on materials of known structure.

General resources for crystallographers include the International Tables for Crystallography (2006), a comprehensive learning and working resource including symmetry and properties of crystals, theory and practice of most techniques as well as tables of symmetry elements and mathematical, physical and chemical parameters. A thorough presentation of the theory of diffraction can be found in Fundamentals of Crystallography (Giacovazzo 2011), while other noteworthy books include Boisen and Gibbs (1985), Stout and Jensen (1989), Warren (1990), Ladd and Palmer (2003), Blake and Clegg (2009), and Glusker and Trueblood (2010). The websites CCP14 and SINCRIS list and link most of the available crystallographic software; useful crystallographic tools can be found at the Bilbao Crystallographic server (Aroyo et al. 2006a,b). Crystal structure databases of minerals include the open access American Mineralogist Crystal Structure Database (Downs and Hall-Wallace 2003), and the Crystallographic and Crystallochemical Database for Minerals and their Structural Analogues of the Russian Academy of Science (MINCRYST, Chichagov et al. 2001). Resources for inorganic crystal structures in general include the Crystallographic Open Database (Gražulis et al. 2012), the Inorganic Crystal Structure Database (ICSD) and the Cambridge Structural Database (CSD).

GENERAL ASPECTS

Brief introduction to X-ray diffraction theory

Most X-ray diffraction techniques rely exclusively on the portion of X-rays elastically scattered by electrons (Thomson scattering). The diffraction event can be visualized as a consequence of the interaction between electromagnetic radiation and electrons. The electromagnetic radiation enters the material with a certain frequency and the electrons in the material "ride the waves", oscillating in the direction of the polarization of the incident light. Since an accelerating electron in turn creates electromagnetic radiation, the oscillating electrons in the material give off light in spherical distributions, all with the frequency of the oscillating electrons. The transfer of energy from the incident light into the oscillation of the electrons takes place by decreasing the intensity of the incident X-rays. In order for X-rays to be diffracted, namely to be spherically scattered and then experience constructive interactions in particular directions, they have to interact with a material showing a periodicity in the distribution of electrons comparable to the X-ray wavelength (λ). The wavelength of X-rays, ranging from 0.1 to 100 Å (equivalent to energies of about 120 to 0.1 keV) is in the range of interatomic distances or unit cell sizes, and therefore diffraction can be produced by the elastic interaction of X-rays with matter having some degree of ordering.

X-rays are scattered by electrons, and as a consequence the scattering power of an atom is correlated to its number of electrons. Due to the interference between scattered waves from different portions of the electronic cloud of an atom, the effective scattering intensity, or scattering factor, decreases with the scattering angle (Fig. 1). Interference effects are greater with increasing distance from the atom center; outer-shell electrons contribution to the scattered wave decreases more rapidly in comparison to inner electrons contribution with increasing scattering angle. For most applications, the distribution of electrons around nuclei is considered spherical, and so is the scattering factor. Tables of the calculated scattering factors for neutral atoms ideally at rest can be found in Brown et al. (2006b). Atoms constantly vibrate about their equilibrium positions. The amplitudes of vibration have two components, there is a quantum effect, known as zero-point motion, due to the uncertainty principle, while

EBSCOhost - printed on 2/13/2023 5:26 AM via . All use subject to https://www.ebsco.com/terms-of-use

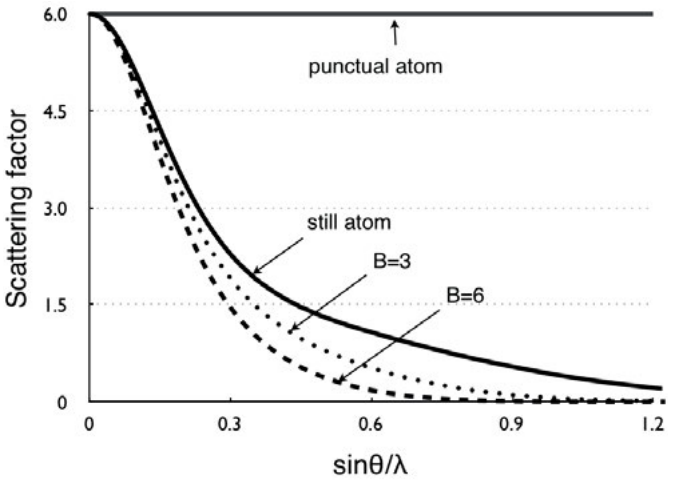


Figure 1. The atomic scattering factor for an ideal point-like atom is constant. The volume of a real atom, however, causes the scattering factor to decrease substantially with the scattering angle (solid curve), an effect that is increased for atoms in motion as shown by dotted curves calculated for two values of the displacement parameter B.

above 0 K atoms undergo thermal vibrations around their average positions (Downs 2000). Furthermore, different atoms, e.g., Si and Al, may occupy a single crystallographic site but in slightly different locations, and this creates a smear in the average electron density known as static displacement. Static and dynamic disorders are represented in the description of a crystal structure with atomic displacement parameters (ADP). The positional disorder of an atom, whether static or dynamic, has the effect of increasing the average volume of the electron cloud and therefore decreases the scattering amplitude (Fig. 1). For practical purposes, the most important facts related to the scattering factors are: i) the Z dependence of the scattering power makes atoms with similar atomic numbers virtually undistinguishable by means of X-ray diffraction; ii) the diffracted signal decreases with the scattering angle, therefore X-ray diffraction peaks at high scattering angles are on average weak; iii) the latter effect is increased by static and dynamic positional disorder.

Bragg's description of diffraction by a crystal, although not physical, is useful to explain X-ray diffraction in an intuitive way and to provide a mathematical method for computing diffraction directions. In Bragg's representation, diffraction is described as the reflection of an X-ray beam by crystallographic planes defined by indices *hkl*. Incident waves reflected by equivalent planes with characteristic separation d_{hkl} are in phase if the difference in their travel (2Δ in Fig. 2) is equal to an integral number of wavelengths, n:

$$2d_{hkl} \sin\theta_{hkl} = n\lambda \tag{1}$$

The d-spacing of the set of planes generating a diffraction peak may be easily calculated from observed diffraction angles, provided the wavelength is known, using the Bragg equation. The minimum d-spacing measured in an experiment defines the resolution. From Bragg equation, it appears that if an experiment imposes small maximum 2θ, as is often the case in non-ambient experiments, the use of incident radiation with short wavelength improves the resolution.

A very useful representation of the translational symmetry of a crystal is given by the reciprocal lattice, which is derived from the direct lattice as the set of vectors with directions normal to lattice planes ($h\ k\ l$) and lengths of $1/d_{hkl}$. The reciprocal lattice allows a simple

EBSCOhost - printed on 2/13/2023 5:26 AM via . All use subject to https://www.ebsco.com/terms-of-use

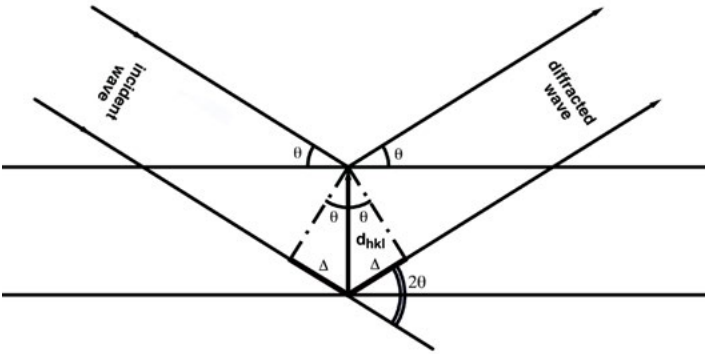


Figure 2. Bragg's representation of the diffraction condition as the reflection of X-rays by lattice planes (*h k l*).

visualization of diffraction conditions by the Ewald construction (Ewald 1921) shown in Figure 3. The origin of the reciprocal lattice (*O*) is set at the intersection of a sphere of radius 1/λ, the Ewald sphere, with the incident beam passing through the center of the sphere (*C*). It is easy to verify that for any reciprocal vector intersecting the Ewald sphere, the angle at the vertex of the isosceles triangle $O\hat{C}R$ in Figure 3 equals 2θ, and therefore Bragg's equation, i.e., the diffraction condition, is satisfied when a reciprocal lattice node intersects the Ewald sphere. Using Ewald's sphere we can readily notice that the wavelength defines the maximum resolution: $d^*_{max} = 1/d_{min} = 2/\lambda$, the sphere of radius 2/λ is indeed called the limiting sphere. The value of $d^*_{max} = 2/\lambda$ is imposed by Equation (1) since the scattering angle cannot exceed $2\theta = 180°$.

The intensity of a diffracted beam is a function of the technique (formulation for powder and single crystal monochromatic techniques will be given later), instrumental parameters (e.g., intensity of the source) and composition and crystal structure of the specimen. As mentioned earlier, the objects scattering X-rays are electrons, and so it follows that the intensity of a diffracted beam depends on the electron density distribution within the crystal. In ordered (in

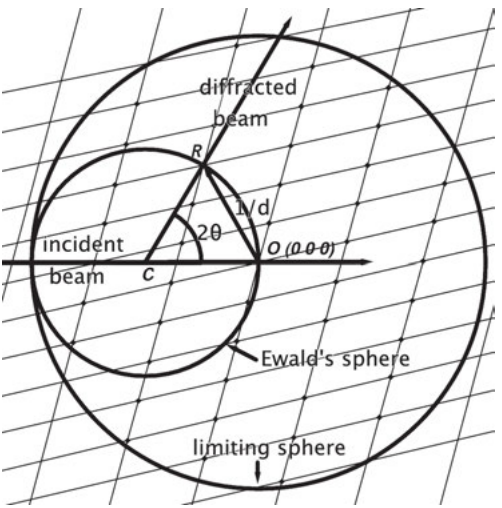


Figure 3. Ewald representation of the diffraction condition. O: origin of the reciprocal lattice, C: center of the Ewald sphere, R: reciprocal node positional vector of length 1/*d*. Only the nodes of the reciprocal space falling within a radius 2/*d* may be placed, upon crystal rotation, on the surface of the Ewald sphere and be measured.

EBSCOhost - printed on 2/13/2023 5:26 AM via . All use subject to https://www.ebsco.com/terms-of-use

a crystalline sense) materials, only the electron density within the asymmetric part of the unit cell needs to be considered and it can be represented with a set of atomic positions, scattering factors and displacement parameters. The scattering power of a crystal in the direction of a diffraction peak is given by the structure factor, $\boldsymbol{F}_{hkl}$:

$$\boldsymbol{F}_{hkl} = \sum_{j=1}^{N} f_j e^{2\pi i(\vec{h}\cdot\vec{r})} = \sum_{j=1}^{N} f_j \exp\left[2\pi i\left(hx_j + ky_j + lz_j\right)\right] \quad (2)$$

where *hkl* are the reflection indices, *j* indicates an atom in the unit cell with scattering factor f_j (which includes thermal vibrations), *i* is the imaginary number, $\vec{h}$ and $\vec{r}$ are the interplanar vector and the positional vectors, and *x, y, z* are the atomic fractional coordinates. The complex term $2\pi i(hx_j + ky_j + lz_j)$ may be viewed as the difference in phase between the atomic position and the origin of the unit cell. The electron density distribution may be calculated from values of the structure factors through Fourier transform. However, because only the amplitude of the scattering factors and not their phase can be measured, the electron density map of an unknown structure cannot be simply calculated from its diffraction pattern (the phase problem in crystallography).

Ideal structures, real structures, liquids

Nature offers many examples of large, nearly pure and perfect gems of astonishing beauty, usually grown in rather unique environments over long time periods. The vast majority of minerals, however, contain a high concentration and variety of defects that appear wonderful to the eye of a geoscientist because of the wealth of information they bear. Defects have an important contribution in a crystal energetics; they are typically strongly affected by the history of a mineral and, as such, are an important part of the geological record (Putnis 1992; Ottonello 1997). Defects strongly affect mineral properties, including color, crystal form, reactivity, diffusion, mechanical strength, thermal conductivity and electronic properties. Some widespread materials, such as clays and hydroxides, rarely grow in grains large enough to produce a "good powder pattern." Furthermore, interstitial water and cations are typically highly variable from particle to particle and within particles, generating variability in site occupancies and layer stacking disorders. In contrast, amorphous materials and liquids usually display short range ordering where interatomic distances show a spherical distribution that rapidly randomizes beyond a few bond lengths. We will show later that these materials can also be explored by means of X-ray diffraction.

Common structural defects in minerals include twinning, vacancies and interstitials, chemical substitutions, chemical disorder among crystallographic sites, dislocations and stacking faults. Recently, natural quasicrystals have been discovered (Bindi et al. 2009; Steinhardt and Bindi 2012). Structural defects may be randomly distributed in a crystal or may be clustered or periodically distributed with very different effects on diffraction patterns. Defects formed in a crystal at high temperature may achieve an ordered distribution upon cooling, eventually forming a modulated structure resulting in "extra" peaks in diffraction patterns compared to random distributions. Defects can be pictured as disruption of the ideal symmetry, therefore, like a distorted or damaged mirror, they cause a reduction in the "phasing power" of a lattice, it is therefore intuitive that they have the effect of decreasing or broadening the Bragg peaks and produce scattering in between Bragg peaks. Structural defects show a different degree of ordering; the lower the degree of ordering, the more diffuse is its associated scattering. Defects generate superstructure and satellite reflections, diffuse lines and planes and more or less isotropic diffuse scattering. Different diffraction methods are employed to investigate defects, which often require high resolution in order to emphasize weak features such as the diffuse scattering. The modeling required for the interpretation of defect structures and their diffraction effects changes with the degree of ordering. Vacancies, interstitials and modulated structures, twins and stacking fault structures can still be described in terms of unit

EBSCOhost - printed on 2/13/2023 5:26 AM via . All use subject to https://www.ebsco.com/terms-of-use

cell parameters and atomic coordinates, in a 4 or higher dimensions space. Consequently, the diffraction effects of such defects can be described with the same theory of diffraction used for perfect crystals. For amorphous and liquid phases or highly disordered materials such as clays, a generalized theory of diffraction is adopted and will be briefly presented later. Among books dedicated to the characterization of defect structures we mention Billinge and Thorpe (1998), Snyder and Bunge (2000) and Frey et al. (2010).

Information obtained from X-ray diffraction experiments

Having reviewed the principles of X-ray diffraction, we now summarize the information that may be derived from diffraction experiments and how it can relate to geoscience problems. If samples of good crystallinity and suitable instruments are available, X-ray diffraction can provide structural information of very high precision and accuracy. We recall that the information is averaged over the volume of the illuminated sample and is not element-selective (with the exception of resonant diffraction techniques). For instance, most X-ray diffraction techniques cannot discriminate between a site occupied entirely by silver and a site occupied by equal amounts of palladium and cadmium because the total number of electrons is the same in both cases. Spectroscopic data, displacement parameters and bond lengths considerations are therefore complementary to X-ray diffraction. In contrast, structural parameters from diffraction analysis are often indispensable information in the interpretation of spectroscopic results.

The combination of diffraction angles and intensities is characteristic of a mineral, and therefore constitute a powerful tool for phase identification through search/match routines using crystallographic databases. It is also possible to perform an estimation of phase abundances through whole profile fitting of powder diffraction data.

From the geometrical distribution of diffraction effects (diffraction angles) the geometry of the crystal lattice, its orientation, and the unit cells parameters *a, b, c*, α, β, γ can be determined. Lattice parameters not only represent a fundamental component in the structural characterization of a material, but from these a wealth of geologically relevant information may be derived. Provided the composition is known, the mineral density may be calculated, a parameter essential to the modeling of the Earth's interior and processes such as the segregation of crystals in magma and planetary differentiation. The determination of lattice parameters as a function of pressure and temperature provides important thermodynamic parameters such as bulk and linear compressibility and thermal expansion. Materials of the Earth may experience immense non-hydrostatic stresses (orogenesis, earthquakes, meteorite impacts etc.), resulting in lattice deformations that depend on pressure, temperature, grain size, orientation and material properties. Strain is measured *in situ* by producing controlled stress and measuring the deformation. Residual strain is measured in natural samples with the purpose of reconstructing the history and value of the stress tensor, estimate the size and velocity of an extraterrestrial object impacted on Earth, or to determine the origin of a mineral. The lattice preferred orientation in a rock (widely studied by electron microscopy except for in situ investigations) usually determines the rock anisotropy.

Diffraction intensities, as mentioned earlier, depend on the atomic arrangement and static or dynamic displacements of atoms. The structural solution is the process of assigning the atomic distribution in the unit cell. Structure refinement produces accurate atomic positions, site occupancies and displacement parameters, typically determined through an iterative process of least-squares minimization of the differences between observed and calculated structure factors. Structure factors are obtained from the intensities of the diffraction peaks, and are mathematically related to the structural model. Results of structural refinement can be used to interpret bulk properties in terms of atomic structure; for instance, the bulk compressibility of a silicate can be understood in terms of differential bond compressibility and bridging Si-O-Si

EBSCOhost - printed on 2/13/2023 5:26 AM via . All use subject to https://www.ebsco.com/terms-of-use

angle bending. The determination of the coordination numbers and bond distances is crucial in understanding isomorphic substitutions and consequently processes such as differentiation, ore formation and so forth. Experimental site occupancies give the intracrystalline atomic distribution of binary solid solutions as long as atomic species differ sufficiently in atomic number. The systematic characterization of mineral structures leads to the development of predictive models of the crystal chemistry of minerals and empirical trends in the behavior of minerals (Hazen and Finger 1982).

Some of the main weaknesses of X-ray diffraction are related to the Z-dependency of atomic diffraction power. Parameters of light (low atomic number) elements can be difficult to determine particularly when the sample also contains heavy elements, because the contribution of the stronger scatterers dominates the signal. Furthermore the information derived from an X-ray experiment is an average over the illuminated volume, it makes no difference in most techniques if substituting elements are clustered in neighbor unit cells or are randomly distributed.

X-ray: characteristics, sources, choice

X-ray sources differ substantially in power, energy (wavelength), beam geometry and tunability. An X-ray source is described by its intensity (photons/sec), collimation (angular divergence), beam size, spectral distributions, and time structure. A quantity commonly used to characterize an X-ray source is the brilliance:

$$brilliance = \frac{intensity}{divergence \times area \times bandwidth} \tag{3}$$

in which the intensity is usually expressed in photons/seconds, the divergence in mrad^2, the area in mm^2, the bandwidth, describing the spectral distribution, is expressed in 0.1%. Several orders of magnitude separate the brilliance of laboratory sources from synchrotrons and these from free-electron lasers (Fig. 4).

Laboratory sources include sealed tubes and rotating anodes. In both devices a metal target is bombarded with a beam of electrons accelerated by a high electrical potential applied between the filament emitting electrons and the target. The interaction between the electron beam and the target's electrons include collision, excitation and de-excitation events that generate X-ray emissions composed of a white radiation spectrum and few strong peaks of characteristic wavelength dependent on the material used. The wavelength (λ) of the characteristic radiation is given by Moseley's Law:

$$\frac{1}{\lambda} = c\left(Z - \sigma\right)^2 \tag{4}$$

where c and σ are constants and Z is the atomic number. In most laboratory instruments, the inner energy level "K_α" characteristic wavelength is selected using a monochromator. Most common target materials are molybdenum and copper with characteristic average K_α wavelengths of 0.7107 and 1.5418 Å respectively; other target metals such as Ag and Au are used for applications requiring higher energy. X-ray laboratory sources are in continuous development; we recommend consulting vendor websites for the latest updates in laboratory sources. The performances of laboratory sources differ considerably in flux, and in the focusing size from about 1 mm to about 0.05 mm. The radiation is unpolarized and spherically divergent.

Large user facilities, storage rings and free electron lasers, provide radiation of very high brilliance and properties tunable over a very wide range. Synchrotron radiation is generated when charged particles traveling at relativistic speed are accelerated. User-dedicated sources of synchrotron radiation are storage rings of diameter up to about 2 km where a small, high

EBSCOhost - printed on 2/13/2023 5:26 AM via . All use subject to https://www.ebsco.com/terms-of-use

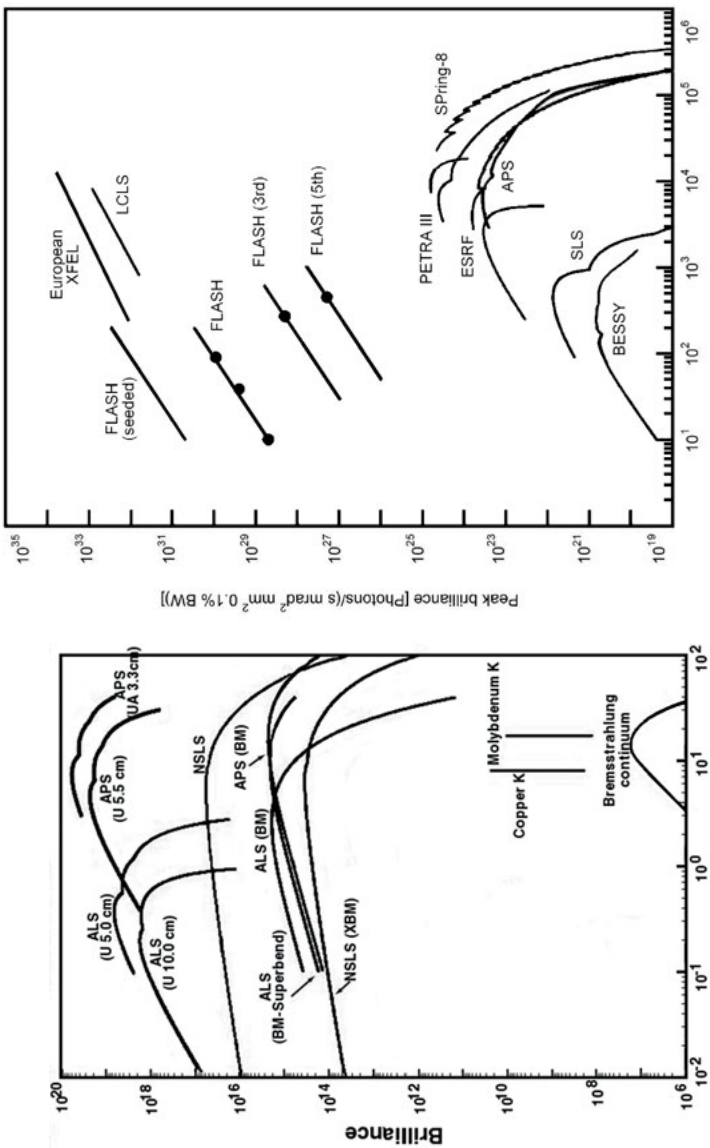


Figure 4. These figures compare the brilliance of storage rings sources with laboratory sources (*left*, Argonne National Laboratory) and storage rings sources with free electron laser sources (*right*) as a function of energy.[Right figure modified and used with permission of IOP Science from Robinson et al. (2010) *New J Phys*, Vol. 12, Fig. 1, p. 2.]

EBSCOhost - printed on 2/13/2023 5:26 AM via . All use subject to https://www.ebsco.com/terms-of-use

energy, pulsed electron beam travels at relativistic speed in a closed path. The energy of a storage ring reaches 8 GeV (Spring-8, Japan) in third generation synchrotrons; the beam size is of the order of tens to hundreds of μm, the bunch length is of the order of tens of ps. Because of relativistic effects, a broad spectrum light is emitted when charged particles traveling at such speed are accelerated, in a synchrotron this happens as a result of the magnets used to curve the beam trajectory (curved sections of the ring) and in insertion devices (straight sections of the ring). Bending magnet sources are characterized by a broad spectrum. Insertion devices contain an array of magnets of alternate fields causing the electron beam to oscillate in the horizontal direction. In wigglers the oscillations are relatively large and the light produced at each oscillation sums up incoherently, the effect is to greatly increase the total power of the beam, which still displays a broad spectral range. Undulators are designed to obtain coherent interactions between the light emitted at each oscillation, this occurs for a particular wavelength and its harmonics only; the emitted beam has reduced angular divergence and is composed of a few intense peaks with a much higher brilliance compared to bending magnets and wigglers. The characteristic wavelength of an undulator can be tuned by changing the intensity of the magnetic field. X-ray optics are used to monochromatize and focus the beam to a wide range of sizes. Monochromatization is achievable down to meV and focusing can be brought down to tens of nm. A synchrotron hosts a large number of beamlines, equipped with different insertion devices and X-ray optics to customize the experimental stations with the radiation most suitable for a given technique and type of experiments.

X-ray free-electron lasers (FEL) generate much brighter and shorter pulsed X-rays compared to synchrotrons (Fig. 4). A few are under construction; the Linac Coherent Light Source (LCLS, Stanford) is the first facility available to the user community. FEL radiation sources have the power to "see" single atoms and to resolve in time processes such as the bond formation: observations fundamental to the nature of materials that may affect science broadly. One of the applications relevant to planetary science is ultrafast diffraction on samples under pressures and temperatures of the interior of giant planets in laser generated shock events. Useful introductions to synchrotron and FEL radiations and their applications include Margaritondo (1988, 2002), Brown et al. (2006a), Sutton (2006), Als-Nielsen and McMorrow (2011), and Lee (2011).

Finally, efforts have been made to develop sources for portable diffractometers for field-work and extraterrestrial exploration (Bochenin 1973; Sarrazin et al. 1998, 2005; Yamashita et al. 2009; Hansford 2011) such as the CheMin instrument installed in the 2012 Mars Rover (Blake et al. 2009).

Selecting the proper X-ray source is critical to the success of an experiment. The choice of the source depends on materials, techniques, and type of experiment. Laboratory sources are routinely used in geoscience for a wide range of experiments, from phase identification to high resolution non-ambient studies. Compared to central research facilities such as synchrotrons, where time allocated for individual experiments is very limited (typically a few hours to a few days), laboratory X-ray diffraction instruments have much less time restrictions, which can be used to tune and optimize the data collection conditions. The high brilliance of synchrotron radiation is essential to perform experiments on very small samples and weak scatterers, for ultra-fast time-resolved studies, where highly focused radiation is required to reduce scattering effects from the environmental cell, for high resolution mapping, or when high energy or specific wavelengths are necessary. The drawbacks of using synchrotron radiation are mostly related to the limited time available, the traveling costs, and less standardized data collection and processing procedures compared to laboratory sources. Accurate planning of an experiment is critical to its success. In general, there is no cost associated with running the experiment, as these costs are usually absorbed by the agency that funds the facility.

EBSCOhost - printed on 2/13/2023 5:26 AM via . All use subject to https://www.ebsco.com/terms-of-use

X-RAY DIFFRACTION TECHNIQUES

Single crystal monochromatic diffraction (SXD)

Single crystal monochromatic diffraction is a very mature technique described in details in several books, including Stout and Jensen (1989), Clegg (2001), Ladd and Palmer (2003), Dauter and Wilson (2007), Glusker and Trueblood (2010). As shown in Figure 3, for an arbitrary orientation of a crystal in a monochromatic X-ray beam, it is highly unlikely that more than a few reciprocal space nodes fall on the Ewald sphere and therefore, satisfy the reflection condition, and generate Bragg peaks. In order to measure a sufficient portion of reciprocal space, a crystal must be rotated to bring more vectors into the diffraction condition. If a large area detector and short wavelengths are used, it might be sufficient to rotate the crystal along a single axis (rotation method). The output of a typical SXD data collection consists of a peak list, including indices, diffraction angles, integrated intensities and their standard deviations. If an area detector is used, then the peak positions (directions of diffracted beams) are represented by detector pixel coordinates, whereas with a point detector, all diffraction events occur in the detector plane (usually horizontal) and the detector angle is sufficient. Angles are used to determine unit cell parameters, while intensities are used to determine the average atomic arrangement in a crystal.

Measurements. The essential parts of a single crystal diffractometer are a monochromatic X-ray source, a goniostat, a detector and computer control. Most laboratory diffractometers use Mo K_α radiation (with two spectral components $K_{\alpha1}$ and $K_{\alpha2}$) which provides sufficient resolution. Rotations are realized with Eulerian cradles or kappa goniostats with a variable number of circles. The greater the number of circles the greater the flexibility in sample and detector positioning, which is particularly useful when environmental cells are used. The precision of goniostats is given by the sphere of confusion (SoC): the minimum spherical volume covering all possible locations of an infinitely small object at all possible goniometer orientations (Davis et al. 1968). High precision goniostats are required when small crystals are studied with beams of comparable size. Point (scintillator-based) and area detectors (CCD, image plate, etc.) are used in SXD. A point detector can be collimated (narrow slits are positioned in front of the detector to block radiation coming from directions other than the sample), which is particularly useful in case of high background. Furthermore a point-detector data collection can be programmed to modify the speed according to peak intensities, improving the statistics of weak reflection measurements by increasing $I/\sigma(I)$. This is an important advantage, considering that the range of intensities of SXD peaks typically exceeds the linear range of most detectors. Area detectors have the advantages of being fast, and allow the whole integrated peak intensity to be recorded in one exposure, while a profile is usually measured in step-scan mode with a point detector. Area detectors record whole portions of reciprocal space, including off-Bragg intensities. In this way, diffuse scattering or satellite peaks, that might be overlooked when point detectors are used, can also be recorded.

Sample choice, peak search and indexing. Sample crystals should be carefully selected using a microscope. Crystals without inclusions, of euhedral shape and with sharp extinction are more likely to be unstrained single crystals. Depending on sample scattering power and source intensity, crystals of roughly 50 to 500 μm in diameter can be measured with laboratory instruments while smaller samples, down to below 1 μm in size, are measured using synchrotron radiation. The crystal is positioned at the instrument center (intersection of the rotation axes) on the beam path. The measurement proceeds with a search for reflections, an operation that might require a few hours with a point detector. A first evaluation of the crystal quality is based on peak shapes. “Good crystals” show narrow, symmetric peak profiles. If the unit cell of the crystal is approximately known, with at least two, but usually not less than 5, non-coplanar reciprocal vectors (peaks) a lattice can be defined, and using mathematical tools the conventional cell may be derived, this allows the calculation of an orientation matrix and

EBSCOhost - printed on 2/13/2023 5:26 AM via . All use subject to https://www.ebsco.com/terms-of-use

indexing of the peaks. The presence of peaks that cannot be indexed is usually an indication of multiple crystals or twins. The initial matrix is used to predict peak positions and define the data collection strategy. This consists of sets of reflections with calculated angular positions if a point detector is used. With area detectors, a set of rotations/step scans that allow the exploration of a large portion of reciprocal space is collected.

Lattice parameters. The accurate determination of lattice parameters is critical in mineralogy. Lattice parameters are determined by least-squares refinements against peak angles or *d*-spacings, imposing symmetry constraints when appropriate. The full list of measured reflections is used in the least-squares refinement when a 2D area detector is used. With point detectors, a short peak list of particularly carefully chosen reflections is used. The "8-position centering method" (King and Finger 1979), described in detail by Angel et al. (2000), consists of measuring one or more reflections at 8 diffractometer positions at opposite diffraction angles to compensate for instrumental and centering errors provides the basis for a very precise lattice parameter determination.

Diffraction intensities and data reduction. Peak intensities are measured by swiping nodes of the reciprocal space through the Ewald sphere (Fig. 3). Unlike the ideal geometric points, nodes of the reciprocal lattice have a volume determined by the crystal shape and mosaicity; in order to collect meaningful intensities the entire volume of the nodes must cross through the Ewald sphere at constant speed. The expression linking experimental integrated intensities with the structure factors assumes the following form in SXD:

$$I(hkl) = I_0 \frac{\lambda^3}{V_{\text{cell}}^2} \left(\frac{e^2}{mc^2} \right) V_{\text{cr}} LPTE \left[F(hkl) \right]^2 \tag{5}$$

where I_0 is the intensity of the incident beam, λ is its wavelength, e, m, c are universal constants, V_{cell} and V_{cr} are the volume of the unit cell and of the crystal, L, P and T are the Lorentz, polarization and transmission factors, E is the extinction coefficient. The process of deriving observed structure factors from experimental intensities by estimating the above terms is called data reduction. The L, P, T and E factors differ from peak to peak in SXD; the proper evaluation of these corrections is essential to obtain high quality structural analysis. The Lorentz factor is a technique-dependent parameter that accounts for the time required for reflections to cross the Ewald's sphere. Algorithms for the calculation of the L factor are given in the literature (Lipson et al. 2006) and are implemented in most commercial diffractometers. The polarization factor is a function of the polarization of the incident beam and the scattering angle. For non-polarized beam, in the case of conventional source, P is given by $P = (1 + \cos^2 2\theta)/2$. The fully polarized synchrotron radiation is slightly modified by the X-ray optics, algorithms for the calculation of P are given by Kahn et al. (1982); the magnitude of the polarization correction at synchrotrons is usually very small.

The transmission factor accounts for the attenuation of the incident and diffracted beam due to crystal absorption. For each reflection the paths of the incident and diffracted beam in the crystal differ, so does the transmission factor. Due to the systematic trends of X-ray attenuation factors with energy and atomic number (Chantler 2000), T is small for light-element samples measured with high energy radiation. It is customary to calculate the "μr" product to gauge the absorption correction, where μ is the X-ray absorption coefficient (Hubbell and Seltzer 2004) and r is the average crystal size. The absorption correction is considered negligible in standard data collections when $\mu r < 0.1$. There are different strategies for calculating the absorption correction: i) if the crystal shape is known (either a euhedral shape defined by face indices and the distance of the facet from the crystal center of gravity) the absorption correction is calculated exactly for every set of diffraction angles; ii) in the semi-empirical correction (North et al. 1968) a measurement of the attenuation is obtained by measuring the intensity of few peaks at different combinations of two angles (called ψ-scan, this azimuthal scan is

EBSCOhost - printed on 2/13/2023 5:26 AM via . All use subject to https://www.ebsco.com/terms-of-use

equivalent to moving the reciprocal space node on the surface of the Ewald sphere). Carefully chosen ψ-scan curves are then used to model the three dimensional absorption correction; iii) if the dataset contains a large number of redundant and symmetry equivalent reflections, an idealized crystal shape can be calculated through the minimization of the discrepancy among equivalent reflections.

Extinction includes the attenuation of the incident beam, as it travels in the crystal due to diffraction, and the effect of multiple diffraction within the crystal. *E* is usually significant only in low mosaicity specimens measured with fairly low energy radiation. The correction is usually performed within the structural refinement.

The quality of observed structure factors $\boldsymbol{F}_{\mathrm{O}}$ is quantified by the ratio between the intensities uncertainties and their values:

$$R_{\mathrm{sigma}} = \frac{\sum \sigma\left(F_{\mathrm{O}}^2\right)}{\sum F_{\mathrm{O}}^2} \tag{6}$$

and, in the case redundant reflections are measured, by the discrepancy among equivalent reflections:

$$R_{\mathrm{int}} = \frac{\sum \left|F_{\mathrm{O}}^2 - \overline{F}_{\mathrm{O}}^2\right|}{\sum F_{\mathrm{O}}^2} \tag{7}$$

where $\overline{F}_{\mathrm{O}}$ is the average intensity of a set of equivalents; the summations are performed over all *i* reflections for which at least one equivalent have been measured.

Structural refinement. Due to instrumental limitations (angular limits determined by movement range, collision limits, detector size) and time constraints, only a portion of reciprocal space within the resolution limit is usually measured in SXD experiments. Because the reciprocal lattice has some degree of symmetry, at least the center of symmetry, it is actually not necessary to measure all peaks within Ewald sphere; nonetheless, collecting redundant reflections greatly enhances the accuracy and precision of the structural analysis.

Observed structure factors are the input information for structural solution and refinement. Popular computer programs include SHELX (Sheldrick 2008) and SIR (Burla et al. 2012). A structural refinement consists of minimization of the differences between observed and calculated structure factors, for instance:

$$\sum w\left(F_{\mathrm{O}}^2 - F_{\mathrm{C}}^2\right)^2 \tag{8}$$

where *w* is a weighting factor, which is related to the confidence of individual measurements. $\boldsymbol{F}_{\mathrm{C}}$ structure factors are calculated based on a structural model defined through atomic parameters (coordinates, occupancies, and displacement parameters) that are the variables in the structural refinement. The figures of merit used to assess the quality of a refinement are:

$$wR_2 = \left\{ \frac{\sum \left[w\left(F_{\mathrm{O}}^2 - F_{\mathrm{C}}^2\right)^2 \right]}{\sum \left[w\left(F_{\mathrm{O}}^2\right)^2 \right]} \right\}^{\frac{1}{2}} \tag{9}$$

$$R_1 = \frac{\sum \left| \left|F_{\mathrm{O}}\right| - \left|F_{\mathrm{C}}\right| \right|}{\sum \left|F_{\mathrm{O}}\right|} \tag{10}$$

EBSCOhost - printed on 2/13/2023 5:26 AM via . All use subject to https://www.ebsco.com/terms-of-use

$$Goof = \left\{ \frac{\sum \left[w\left(F_O^2 - F_C^2\right)^2 \right]}{\left(n-p\right)} \right\}^{\frac{1}{2}} \quad (11)$$

where n is the number of independent reflections observed and p is the number of refined parameters. Detailed discussion of these procedures is beyond the scope of this chapter; nonetheless, it is worth recalling that it is crucial to critically evaluate the output of crystallographic calculations and to understand whether or not the experimental data can constrain structural parameters to the desired accuracy. A rule of thumb is to have five or more independent reflections per refined parameter; a "solid" refinement will have disagreements between observed and calculated parameters that are randomly distributed with respect to different sets of reflections (weak and strong, high and low 2θ); it is important to examine the correlations between parameters (site occupancies and displacement parameters are, in many calculations, highly correlated because similar local electron density distributions can be modeled with different combinations of the two parameters).

Advantages. Commercial instruments and software offer highly automated data collection and reduction procedures. Nonetheless, SXD experiments are cumbersome and time consuming measurements compared to powder diffraction or Laue techniques. SXD has, however, advantages that make the technique irreplaceable in several applications. The advantages include: i) symmetry equivalents reflection and reflections having the same *d*-spacing do not overlap, as in powder measurements, reducing the possibility of incorrect interpretations; ii) subtle features such as weak diffuse scattering can be more easily identified, as will be shown in detail below; iii) high background and broad peaks, while affecting the overall quality of the data, do not correlate with structural parameters in the structural analysis; iv) compared to polychromatic techniques, the data reduction is rather simple. In summary, monochromatic SXD provides the best measurement of reciprocal space; therefore if crystals of suitable size are available, then SXD is the method of choice for structural determination of new minerals or new synthetic phases (e.g., Britvin et al. 2002; Berlepsch et al. 2003; Bindi et al. 2011; Tait et al. 2011; Zelenski et al. 2011), for the study of defect structures, the determination of accurate site occupancies, atomic displacement parameters (e.g., Nakatsuka et al. 1999) and electron density distributions. SXD, however, is not suitable for fast time resolved studies and is particularly challenging at non-ambient conditions.

Laue method

The Laue method is the oldest of the X-ray diffraction techniques and it offers the simplest setting with minimal instrumental requirements. The technique uses polychromatic radiation. The sample, composed of one or few crystals, is stationary and the diffracted pattern is collected with an area detector in transmitted or reflected geometry. In the Laue method, the diffraction condition is realized for all reciprocal nodes that, for the particular orientation of the crystal, fall in the volume included between the Ewald spheres of radii $1/\lambda_{max}$ and $1/\lambda_{min}$ (Fig. 5). Many reflections satisfy the diffraction condition simultaneously; a large, though incomplete, sampling of the reciprocal space is realized in a single exposure from a stationary crystal (Fig. 6). Because most X-ray area detectors do not discriminate amongst the energies of diffracted peaks, for a peak at a given 2θ only the ratio λ/d may be calculated, which makes indexing more challenging compared to monochromatic techniques. Furthermore, lattice parameters may be determined up to a multiplicative constant (relative lattice parameters). This problem can be overcome by collecting also a single monochromatic exposure (at available beamlines) so the absolute value of few *d*-spacing may be measured (Budai et al. 2008). Alternatively, in the quasi-Laue technique, multiple diffraction patterns are collected while scanning the energy of the beam, so the Laue image is obtained as a series of single variable energy images

EBSCOhost - printed on 2/13/2023 5:26 AM via . All use subject to https://www.ebsco.com/terms-of-use

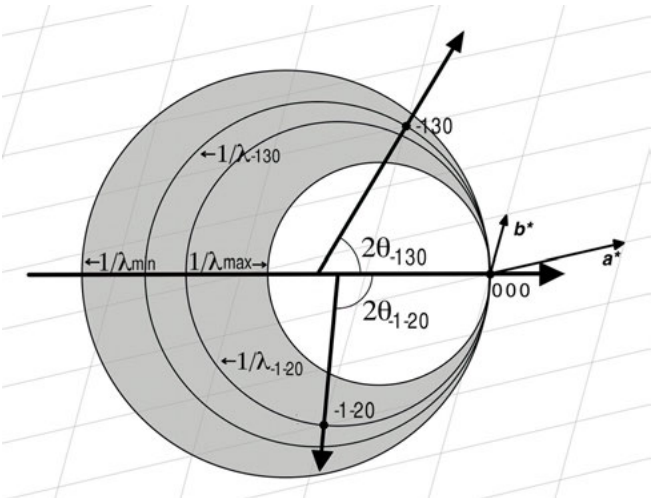


Figure 5. Two dimensional representation of diffraction in the Laue method. The node of the reciprocal lattice for a given crystal orientation that fall in the volume enclosed by the $1/\lambda_{max}$ and $1/\lambda_{min}$ spheres (grey area) diffract intermediate energies.

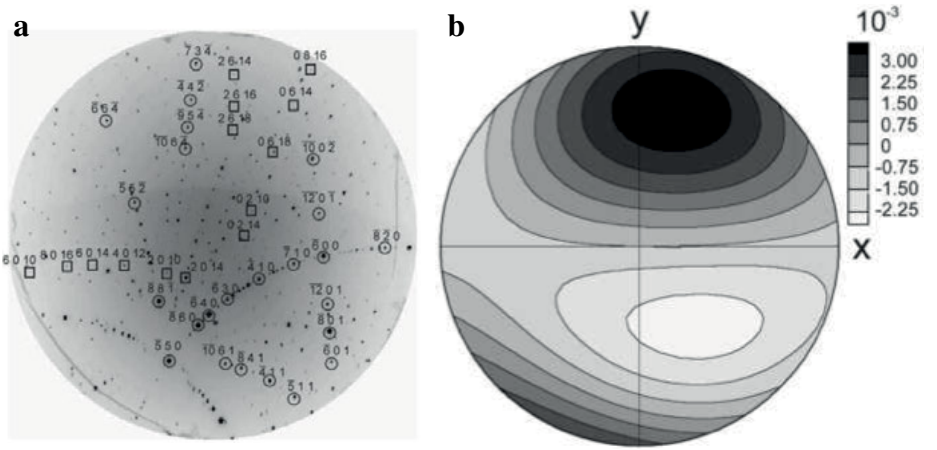


Figure 6. a) Example of a Laue diffraction pattern obtained from a magnetite crystal (squares) embedded in plagioclase (circles) and b) strain tensor in polar coordinates for the same sample of magnetite. Unit of contour are micro-strain (Wenk et al. 2011).

(Wang et al. 2010). If structural refinement is the goal of the experiment, then reciprocal space needs to be sampled with sufficient coverage. In this case, patterns are collected at different angles by rotations perpendicular to the beam. Compared to monochromatic data collection, the data reduction requires additional terms including harmonic deconvolution and intensity normalization to account for the energy dependence of the intensity of the incident spectrum, the diffraction efficiency, the crystal absorption and the detector efficiency (Srajer et al. 2000). For these reasons, Laue diffraction is not commonly the technique of choice for structural determinations but yet a viable option (Ren et al. 1996, 1999; Yang et al. 1998; Srajer et al. 2000). The Laue technique takes advantage of the full energy spectrum of an X-ray source. A remarkable advantage of the technique is that the sample can be stationary, unless collecting

EBSCOhost - printed on 2/13/2023 5:26 AM via . All use subject to https://www.ebsco.com/terms-of-use

intensity data for structural refinement, so there is no need for the sophisticated goniometers required in other micro-crystallography techniques. It follows that data collection may be extremely fast (orders of magnitude faster than monochromatic data collection) and samples may be very small. These two characteristics permit ultrafast time or space resolved studies of single crystals. Many synchrotrons have one or more beamlines dedicated to the Laue method (Lennie et al. 2007; Nozawa et al. 2007; Budai et al. 2008; Tamura et al. 2009).

The Laue method has several interesting applications in geoscience. It is possible to efficiently collect accurate maps of the crystallites size, morphology and mutual orientation of the grain distribution in a rock sample in one, two or three dimensions (Ishida et al. 2003; Courtin-Nomade et al. 2008, 2010; Wenk et al. 2011), or to study the residual stress and orientation of the stress tensor in crystals embedded in rocks (Kunz et al. 2009; Chen et al. 2011a,b). In these studies, the lattice parameters are known beforehand with good approximation simplifying the indexing of the Laue pattern. Compared to electron back scattering techniques, mapping of crystal orientation and lattice strain may be determined with greater accuracy and with depth resolution in a non-destructive fashion. The Laue method is also useful for the characterization of micro-minerals embedded in rocks (Kariuki and Harding 1995), this is particularly valuable for extraterrestrial and rare specimens. Laue maps may be overlapped with compositional or spectroscopic maps. By using a beam of less than 2 μm, Ivanov et al. (2000) characterized the structure of florenskyite, FeTiP, a new phosphide mineral embedded in a meteorite thin section. Shock waves can be used to produce conditions of planetary interiors on small samples for a very short time; the *in situ* characterization of these materials must be ultrafast and if the specimen is a single crystal monochromatic diffraction cannot be performed. Laue exposures have been used to characterize crystals under shock compression with a resolution of nanoseconds in pump-and-probe manner (Ichiyanagia et al. 2007; Suggit et al. 2010).

Powder diffraction

Introduction. X-ray powder diffraction is a crystallographic technique for characterizing structure and phase composition of crystalline samples when the sample is prepared in a polycrystalline form. Powder diffraction is one of the principal research tools of mineralogists, since many minerals are available in polycrystalline form. There is a number of very good books and monographs offering a comprehensive and detailed overview of modern powder diffraction, in particular Bish and Post (1989), Pecharsky and Zavalij (2009) and Dinnebier and Billinge (2008) can be recommended to a reader who would like to develop a more in-depth understanding of the experimental aspects and theory.

The principal condition which needs to be fulfilled to assure sufficient quality of experimental powder diffraction results is satisfactory ***particle statistics***. Powder diffraction experiments typically require as many as 10^6 micrograins of the sample in the X-ray illuminated volume, with random/uniform distribution of grain orientations.

In single crystal experiments with monochromatic radiation, the crystal needs to be re-oriented for each diffraction event. However, in the case of powder diffraction, if the particle statistics conditions are satisfied, then there are grains that are randomly oriented into all the many diffracting conditions, and therefore diffraction from all of the lattice plane families is observed simultaneously. Another consequence of powder particle statistics is the shape of the diffracted signal. In single crystal diffraction, once diffraction condition is met, a directional beam is scattered from the sample along vector $\vec{S}_d^{hkl}$, which can be calculated from the Ewald construction:

$$\vec{S}_d^{hkl} = \vec{S}_0 + \lambda \breve{R} \vec{r}_{hkl} \tag{12}$$

where $\vec{S}_0$ is incident beam vector, $\vec{S}_d^{hkl}$ is diffracted beam vector, $\vec{r}_{hkl}$ is the scattering vector, and $\breve{R}$ is goniometer rotation matrix.

EBSCOhost - printed on 2/13/2023 5:26 AM via . All use subject to https://www.ebsco.com/terms-of-use

With powder samples, the different grains that are aligned for scattering of a specific diffraction peak have many possible azimuthal orientations around the beam, and the diffracted signal assumes a conical shape (*Debye-Scherrer cone*) centered around the incident beam direction.

Powder diffraction performed with a polychromatic incident beam leads to a continuous diffraction signal with smooth intensity variations as a function of angle and no distinct spatially resolved peaks. Such signal can only be interpreted if an energy-resolving detector is used.

Powder diffraction measurement. A goal of the typical powder diffraction experiment is to measure the angles and intensities of observable diffraction peaks. A critical factor determining the quality of diffraction data is the resolution, measured as $\Delta d/d$, where d is the d-spacing, and Δd its uncertainty. For high resolution synchrotron powder instruments $\Delta d/d$ is often in the 10^{-4} range. High resolution (i.e., low value of $\Delta d/d$) means that peak positions are more accurately determined, and peaks at similar d-spacing values can be better resolved.

Depending on the type of incident radiation used, the powder diffraction experiment can be carried out with a polychromatic beam in energy-dispersive mode (EDX) (using a solid state detector with energy resolution) or with monochromatic radiation in angular dispersive mode (ADX).

Energy dispersive method. The EDX experiment has the advantage of a stationary point detector, which does not require much angular access to the sample. The detector is placed at some fixed scattering angle (typically near 10°). This feature is particularly useful in experiments with sophisticated sample enclosures such as Large Volume Presses, or Diamond Anvil Cells, which significantly obscure access to the sample (Baublitz et al. 1981). The signal in the solid state detector is acquired as intensity vs. energy of the diffracted photons. The simultaneous accumulation of the signal over a wide range of energies (usually 5-100 keV) makes the EDX data acquisition quite fast. The energy scale of the detector is usually calibrated using a set of radioactive sources with known values of emission energies. Accurate calibration of the detector angle is performed with a diffraction standard. The main disadvantage of the polychromatic approach is the limited-energy resolution of the available detectors. Typical Ge-based solid state detectors have a resolution of about 25 eV. The uncertainty in the diffraction peak energy measurement translates into uncertainty in the d-spacing determination as follows:

$$\frac{\Delta d}{d} = \frac{1}{d}\left|\frac{\partial d}{\partial \lambda}\right|\Delta\lambda + \frac{1}{d}\left|\frac{\partial d}{\partial \theta}\right|\Delta\theta = \frac{\Delta E}{E} + \left|\cot\theta\right|\Delta\theta \tag{13}$$

As a consequence of the limited energy resolution, EDX diffraction peaks are typically quite broad and for more complex or lower symmetry crystal structures resolving peak overlaps at higher energies becomes a significant problem. The EDX method was widely used in the 1980s and 1990s but has become much less popular with the introduction of area detectors for monochromatic experiments. In principle, it is possible to use peak intensities recorded in the EDX experiment for structure refinement, however, complicated energy-dependent corrections (e.g., incident intensity, detector quantum efficiency, sample and sample environment absorption, etc.) need to be applied (Yamanaka and Ogata 1991; Neuling et al. 1992). Recently, an interesting hybrid modification of the EDX method, named Combined Angle- and Energy-dispersive Structural Analysis and Refinement (CAESAR) has been proposed (Wang et al. 2004), which greatly enhances the resolution of the diffraction data while still taking advantage of the energy-dispersive detector. However, the data collection process in CAESAR is several orders of magnitude more time consuming, compared to the classical EDX.

Monochromatic method. Two principal ways to detect the diffraction signal scattered from the sample in the ADX experiment are either to use a scanning point-detector (e.g.,

EBSCOhost - printed on 2/13/2023 5:26 AM via . All use subject to https://www.ebsco.com/terms-of-use

scintillator-based), which measures scattered intensity as a function of scattering angle along a single direction at a time, or to use an imaging area detector which can be placed in the diffracted signal path and intersects the diffraction cones. Each of these two approaches has its benefits and disadvantages and we will briefly review specific applications for which one is recommended over the other.

High resolution powder instruments. When using monochromatic incident X-rays in the ADX experiment, the spectral purity of both the incident, as well as scattered radiation contributes to the error in the *d*-spacing determination through the ΔE term in Equation (13). High resolution instruments feature sophisticated monochromators composed of several highest-quality single crystals (typically Si), which remove most of the unwanted energy-components of the incident beam. The diffraction signal often contains additional energy contributions that arise from Compton scattering, X-ray fluorescence, thermal diffuse scattering, *etc.* To filter out these contributions, high resolution instruments are often equipped with an additional detector-path monochromator (analyzer) which provides energy-filtering.

The most popular instrument geometry for high resolution powder diffraction is Bragg-Brentano design, shown in Figure 7, in which the incident beam, defined by a set of slits, diverges from a small source towards the sample, and then the diffraction signal, scattered from the sample, converges (again defined by a set of slits) towards the point detector. To keep the incident and diffracted beam path symmetric, a $\theta/2\theta$ rotation is typically used, in which during the scanning process the sample is rotated by θ, while the detector moves by 2θ with each step. Modern synchrotron-based high resolution instruments are equipped with multiple analyzer-detector banks which permit simultaneous data collection in several 2θ ranges at the same time and significantly shorten the data collection time (Wang et al. 2008). Figure 8 shows a comparison of instrumental function (angle-dependence of peak width for a peak profile standard) for a high resolution instrument and an instrument employing an area detector.

Powder experiments with area detectors. The two most common types of area detectors used for X-ray diffraction include charge coupled devices (CCDs) and image plate (IP)

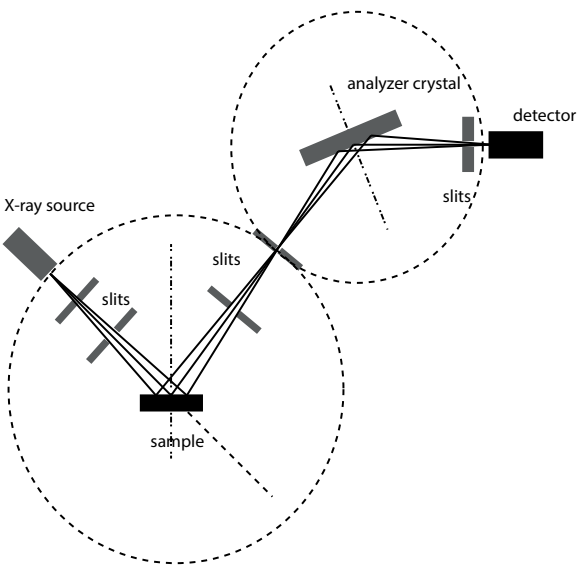


Figure 7. Bragg-Brentano high resolution diffractometer with analyzer crystal.

EBSCOhost - printed on 2/13/2023 5:26 AM via . All use subject to https://www.ebsco.com/terms-of-use

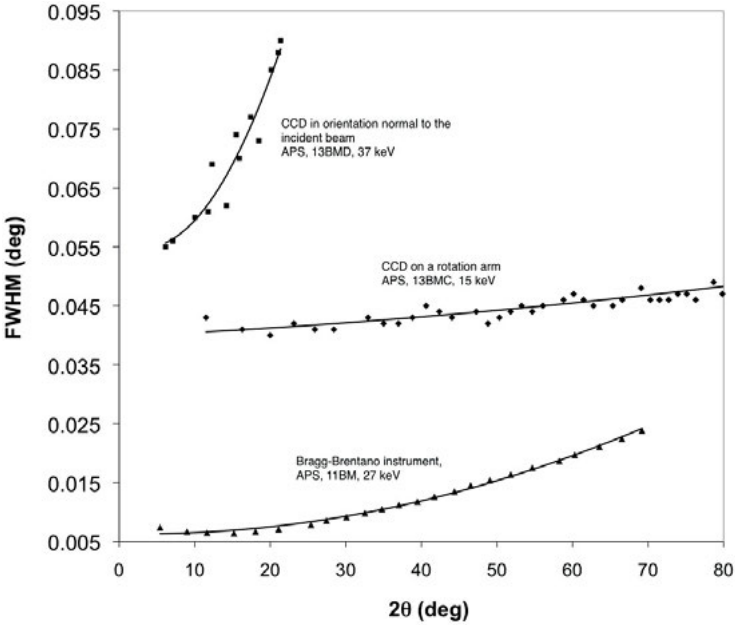


Figure 8. Comparison of instrumental function for a high-resolution instrument and an instrument employing an area detector.

detectors. Burns (1998) presented an overview of many applications of CCD detectors in the X-ray diffraction analysis of minerals. CCDs utilize a phosphor screen which converts diffracted X-rays into visible light and then use electronic chip of the type used in digital photographic cameras to detect the visible light image. IP detectors store the diffraction information by utilizing the activation of Eu^{2+} centers present on the surface of the plate. The signal can then be read with the use of photo-stimulated luminescence in a scanner. CCD detectors are characterized by much shorter readout time (few seconds) than IPs with on-line scanners (few minutes), but have higher background noise and smaller dynamic range.

From the point of view of imperfect particle statistics, the area detector has the advantage of sampling multiple points of intersection of the diffraction cone with the detector surface. If significant non-uniformity of the intensity of diffracted signal occurs as a function of azimuth (along the ring of intersection of Debye-Scherrer cone with the detector surface), then area detectors can be used to average the intensity and better model the intensity distribution. A scanning point-detector, on the other hand, intersects the Debye-Scherrer cone only at one point, and therefore is highly susceptible to the effects of preferred orientation, which may result in peak intensity measurement significantly departing from the theoretical structure factor amplitudes. These effects can be accounted for by including a preferred orientation model in the refinement of the structure, but this always significantly reduces the reliability of the structure determination.

Because of the relatively small size of the CCD chips, CCD detectors often use optical taper, which de-magnifies the image created on the phosphor to match the size of the chip. This permits a large active area of detection and increases angular coverage for single exposure. The taper, however, may introduce an optical distortion to the image and a special distortion correction is typically required, which can be calibrated. Most modern CCD detectors apply spatial correction immediately after the diffraction pattern is taken, and the bitmap image that

EBSCOhost - printed on 2/13/2023 5:26 AM via . All use subject to https://www.ebsco.com/terms-of-use

is saved is already spatially corrected. Another correction needed for CCD detectors is a dark current correction, which accounts for the electronic noise contribution.

Area detectors need to be calibrated prior to use for powder data collection. The calibration procedure determines the sample-to-detector distance, point of intersection of the incident beam with the detector surface, as well as the detector orientation with respect to the incident beam. The incident energy is usually calibrated independently of the detector calibration, e.g., using an absorption edge of a metal foil. The detector calibration is carried out with a diffraction standard such as LaB_6, CeO_2 or Si powder. Once a detector calibration is constrained, it can be used to integrate a diffraction image into a one-dimensional pattern of $I(2\theta)$.

Popular computer programs that can be used to calibrate detector geometry and integrate diffraction images include Fit2d (Hammersley et al. 1996), Two2One (Vogel et al. 2002; Vogel and Knorr 2005), Powder3d and Powder3d_IP (Hinrichsen et al. 2006) and Datasqueeze (Heiney 2005).

A very comprehensive review of all aspects of the use of area detector for X-ray diffraction applications can be found in He (2009).

Peak intensity. In the powder diffraction technique, the peak intensity is derived from the crystal structure through the structure factor equation in much the same way as in single-crystal diffraction. The formula for the calculation of the overall intensity contribution of one phase p to the diffraction pattern has the following form:

$$I_p^i = S_F \frac{\lambda^3 f_p}{V_p^2} \sum_{hkl} \left(m_{hkl} L_{hkl} P_{hkl} A_{hkl} S_{hkl}^i(\theta) \left| F_{hkl} \right|^2 \right)_p + bkg^i \tag{14}$$

where S_F is the global scale factor (applicable to all phases present in the sample, reflecting the volume of the illuminated sample, incident intensity, etc.), f_p is the volume fraction of phase p, V_p is the unit cell volume of phase p, L_{hkl} is the combined Lorenz and polarization correction, m_{hkl} is the peak multiplicity, F_{hkl} is the structure factor, $S_{hkl}^i(\theta)$ is the peak profile function, P_{hkl} is the preferred orientation correction, A_{hkl} is the absorption correction, and bkg^i is the background term.

The main difference between peak intensity in powder (Eqn. 14) and single crystal diffraction (Eqn. 5) is the peak multiplicity, m_{hkl}. In single crystal diffraction experiments, the symmetry-dependent peaks, which have exactly the same d-spacing, are observed independently, and should all have identical intensities. In powder diffraction these peaks overlap with each other and their intensities sum together. Depending on the number of symmetry equivalent peaks, different numbers of peak intensities are summed, and therefore, in order to compare powder and single-crystal peak intensities, the former have to be divided by the peak multiplicity factor.

The types of intensity corrections that have to be applied to powder diffraction data prior to structure analysis (L_{hkl}, P_{hkl}, and A_{hkl}) are analogous to corrections used in single crystal diffraction.

Peak overlap. One of the principal challenges of powder diffraction is the one-dimensional character of the diffraction data and resulting peak overlap. Since all of the Debye-Scherrer cones are simultaneously observed and all have the same geometric shape, the cones corresponding to reciprocal vectors with the same, or very close, d-spacings overlap with each other. If two or more peaks are too close to each other it becomes difficult to reliably fit their positions and relative intensities (both of which are necessary for unit cell and crystal structure refinement). The peak width and the "density" of peaks increase at higher scattering angles, and the problem becomes much more pronounced in this region. Peak overlap is particularly dramatic for low symmetry structures, in which many closely spaced peaks occur throughout

EBSCOhost - printed on 2/13/2023 5:26 AM via . All use subject to https://www.ebsco.com/terms-of-use

the whole powder pattern. Problems with excessive peak overlap can be at least partially resolved with the use of high resolution powder diffraction instruments, which contribute very little instrument-related broadening to the experimental data. For experiments with broader peaks and significant peak overlap, refinement methods which constrain the peak positions from the unit cell (LeBail, Pawley and Rietveld methods) provide some help, as peak positions and intensities are not individually and independently refined, however, the problem with reliably constraining the intensity partitioning remains.

Peak width. In powder diffraction experiments the observed peak width is a convolution of sample-related effects and instrument-related effects. Decoupling these two classes of effects from each other permits the understanding of potentially important sample characteristics.

Typical instrument-related factors, which affect observed peak width, include divergence of the incident beam, spectral purity (energy-width) for monochromatic beams, detector acceptance angle (for point detectors) and diffracted signal incidence angle on the detector (for area detectors). In general, peak width effects of the instrument vary as a function of scattering angle in a regular way. One of the possible equations to account for this factor, which was originally derived for neutron diffraction and Gaussian peak shapes, is known as the Caglioti law (Caglioti et al. 1958):

$$H_{hkl}^2 = U\tan^2\theta_{hkl} + V\tan\theta_{hkl} + W \tag{15}$$

where H_{hkl} is full width at half maximum of the given peak, and U, V and W parameters can be calculated according to specification of a particular instrument and source, but are usually refined. Caglioti's law was later generalized for application to synchrotron and laboratory X-ray instruments (Sabine 1987; Gozzo et al. 2006).

Scherrer (1918) first observed an empirical rule that the integral breadth of the diffraction peak, β_{hkl} defined as the ratio of peak area to peak maximum, is proportional to the average particle size of the sample D:

$$\beta_{hkl} = \frac{\lambda K_\beta}{D\cos\theta_{hkl}} \tag{16}$$

where K_β is a dimensionless particle shape factor, with a typical value of about 0.9, which varies with the actual shape of the crystallites. The Scherrer formula is useful for characterizing statistical distributions of grain sizes in nanoparticle materials. It has to be emphasized that the Scherrer formula is not applicable to grains larger than about 0.1 μm, which precludes those observed in most metallographic and ceramic microstructures.

Besides the particle size, the diffraction peak width is also affected by the statistical distribution of the unit cell parameters (strain) of individual micrograins. Real materials often exhibit defects, which affect the micrograin unit cell parameters. Fluctuations of these individual unit cell parameters, in turn, affect position, size and shape of powder peak profiles. In general, two types of strain are considered in relation to powders: macrostrain (macroscopic homogeneous strain affecting all grains equally), and microstrain (non-homogenous strain field - on the length scale of individual crystallites, which can significantly vary from grain to grain). Macrostrain affects mainly peak positions, while microstrain results in peak width changes. Stokes and Wilson proposed a simple relation for the estimation of the effect of strain on peak profiles:

$$\beta = 2\left\langle \varepsilon^2 \right\rangle^{\frac{1}{2}} \tan\theta \tag{17}$$

where ε is the lattice strain. By combining the size and strain contributions, the following relation, originally proposed by Williamson and Hall (1953) is obtained:

EBSCOhost - printed on 2/13/2023 5:26 AM via . All use subject to https://www.ebsco.com/terms-of-use

$$\cos\theta_{hkl} = \frac{\lambda K_\beta}{\beta_{hkl} D} + \frac{2\left\langle \varepsilon^2 \right\rangle^{\frac{1}{2}}}{\beta_{hkl}} \sin\theta \tag{18}$$

If peak breadths are plotted in $y = \beta\cos\theta$, $x = \sin\theta$ coordinate system, then a linear regression can approximate the average grain size from the line intercept, and the average microstrain from the line slope. It should be noted that Equation (18) does not account for instrumental broadening, therefore instrumental function should be calibrated with a line profile standard (e.g., LaB_6 supplied by the National Institutes for Standards in Technology) and subtracted from the observed peak breadths prior to the Williamson-Hall analysis.

While very useful for semi-quantitative interpretation of grain size and strain effects, the Williamson-Hall method is very approximate. Methods based on Fourier analysis and convolution decomposition are recommended when more quantitative results are required (e.g., Warren-Averbach method; Warren 1969).

Preferred orientation. With perfect particle statistics the distribution of scattered intensity around the diffraction cone should be uniform, except for the incident radiation polarization effects. In many real cases, however, the requirement for random distribution of micrograins in the powder sample cannot be satisfied e.g., because of highly anisotropic grain shapes, or stress-history. Departure from a uniform distribution of grain orientations is known as ***preferred orientation***. For example metallurgical samples are essentially polycrystalline powders with frozen grain orientations. The processes involved in fabrication of the metal (e.g., rolling, drawing, casting) leave a specific record of preferred orientation pattern, which can often be traced back to the manufacturing methods using diffraction data. Extensive review of all aspects of texture and preferred orientation can be found in Kocks et al. (1998).

The two most popular methods for the inclusion of the effect of preferred orientation in structure refinement from powder data are the Dollawse-March model (March 1932; Dollase 1986) and the spherical harmonics approach (Bunge 1965; Roe 1965). In the Dollase-March method, the P_{hkl} correction in Equation (14) is calculated according to the following formula:

$$P = \frac{1}{m} \sum_n \left(P_{MD}^2 \cos^2 \alpha_n + \frac{\sin^2 \alpha_n}{P_{MD}} \right)^{-\frac{3}{2}} \tag{19}$$

where summation is over the equivalent peaks occurring at the same *d*-spacing, *m* is the multiplicity factor, α_n is the angle between the reciprocal vector corresponding to the n-*th* peak and the vector of preferred orientation, and P_{MD} is the additional parameter included in the refinement which accounts for the degree of preferred orientation.

Results of preferred orientation modeling are often represented in a form of graphs, known as ***pole figures*****,** showing the probability of finding certain crystallographic directions of polycrystalline grains along different directions in the sample.

Peak and whole pattern fitting

Individual peak fitting. The simplest approach to retrieving diffraction peak position and intensity information from experimental powder pattern is to perform peak fitting with appropriate peak shape function for each peak individually. Typical profile functions used in powder diffraction analysis include:

Gaussian:

$$S_{hkl}(2\theta) = G(2\theta) = I_h \exp\left(-0.6931K\left(2\theta - 2\theta_{hkl}\right)^2\right) \tag{20}$$

EBSCOhost - printed on 2/13/2023 5:26 AM via . All use subject to https://www.ebsco.com/terms-of-use

Lorenzian:

$$S_{hkl}(2\theta) = L(2\theta) = I_{\mathrm{h}}\left[1 + K\left(2\theta - 2\theta_{hkl}\right)^2\right]^{-1} \quad (21)$$

Pseudo-Voigt

$$S_{hkl}(2\theta) = I_{\mathrm{h}}\left[aL(2\theta) + (1-a)G(2\theta)\right] \quad (22)$$

and Pearson-VII:

$$S_{hkl}(2\theta) = I_{\mathrm{h}}\left[1 + 2^{1/M}K(2\theta - 2\theta_{hkl})^2\right]^{-M} \quad (23)$$

where $K = 4(1 + S)/H^2$, I_{h} is peak height, H is FWHM, S is the asymmetry parameter, and M is additional exponent parameter used in the Pearson-VII function. In individual peak refinement, the peak position θ_{hkl} is usually one of the directly refined parameters, and integrated peak intensity is calculated from other refined parameters (intensity at peak maximum, peak width, peak asymmetry parameters, etc.) using analytical formulas for the particular peak shape function used. In this approach, peak positions are not constrained in any way and the unit cell is calculated using least squares optimization, after assigning each of the fitted peaks appropriate Miller indices. Integrated peak intensities obtained from individual peak fitting can, in principle, be used for structure refinement in the same way as single crystal intensities. A free computer program that can be used to perform individual peak fitting is CrystalSleuth (Laetsch and Downs 2006).

A popular computer program which can be used to refine unit cell parameters from fitted peak positions with assigned indices is Unitcell (Holland and Redfern 1997). Unitcell implements several possible statistical weight models that can be assigned to each peak, as well as an algorithm which identifies outliers that do not follow general statistical trends (e.g., because of errors in fitting closely overlapping peaks).

Individual peak fitting is an acceptable approach for very simple crystal structures with high symmetry, in which peak overlap is not significant. For more complex crystal structures and lower symmetry cases peak overlap, particularly at high scattering angles, makes fitting of individual profiles for groups of closely spaced peaks problematic.

One case in which individual peak fitting may have advantages over other fitting approaches are experiments with significant nonhydrostatic stress. In such cases, the individual powder peaks may move at a different rate as a function of stress, depending on the linear modulus along the appropriate lattice direction. The fact that the peak positions are not constrained in any way during the refinement accounts for this effect. It should be noted that it is possible to implement a microstrain model into Rietveld refinement (Daymond et al. 1997, 1999), however this approach introduces additional fitting parameters and is quite sophisticated and, as a result, not used very often.

Rietveld refinement. The ultimate tool for structure refinement from powder diffraction data is Rietveld refinement (Rietveld 1967, 1969). Conceptually, the idea of Rietveld refinement is very simple. The observed diffraction pattern I_i^{obs} (index i corresponds numbers all measured spectral points) is assumed to be a sum of background function bkg_i and contributions from all individual diffraction peaks $I_{i,k}^{obs}$

$$I_i^{obs} = bkg_i + \sum_k I_{i,k}^{obs} \quad (24)$$

where index k refers to individual diffraction peaks. $I_{i,k}^{obs}$ includes appropriate peak profile functions. Once individual observed peak intensities $I_{i,k}^{obs}$ are extracted, they can be compared with calculated peak intensities $I_{i,k}^{calc}$, obtained from the approximate crystal structure model. The refinement involves minimization of a weighted sum of squares WSS, defined as follows:

EBSCOhost - printed on 2/13/2023 5:26 AM via . All use subject to https://www.ebsco.com/terms-of-use

$$WSS = \sum_k w_k \left(I_k^{obs} - I_k^{calc} \right)^2 \tag{25}$$

$$w_k = \frac{1}{I_k^{obs}}$$

while varying the structural parameters (unit cell parameters, fractional atomic coordinates, atomic displacement parameters, site occupancy factors) as well as the peak profile and background functions to achieve the best match between the observed and calculated pattern. In the original papers (Rietveld 1967, 1969) which introduced the method, the background was modeled prior to structure refinement, so that the minimization was done with a background-subtracted pattern, and the statistical weights were uniform. In the modern implementation of the method, the background is fit at the same time as the structure is determined.

The main difference between the Rietveld approach and single-crystal refinement is that all the additional parameters need to be refined at the same time as the structural parameters, while the number of independent observations is typically much lower than in single-crystal case. Due of this deficiency, optimization of all of the refinable parameters at the same time can lead to divergence and unrealistic values of the parameters. As a consequence, Rietveld refinement is usually carried out in stages in which different classes of parameters are included in the optimization individually, while other parameters are fixed. Since Rietveld and Le Bail refinement include the same definition of peak profile functions and their angular dependence, it is a common practice to first carry out a Le Bail refinement to optimize unit cell parameters, peak profiles, and background function independent of the structure, and then use these as starting values for a Rietveld refinement in which peak intensities are derived from the structure. Because of the overparametrization problem Rietveld refinement is usually carried out with isotropic atomic displacement parameters, and often includes constraints or restraints based on crystallochemical assumptions.

A review of the principles and examples of Rietveld analysis is presented by Von Dreele in Dinnebier and Billinge (2008). For a more in-depth introduction to the method, Bish and Post (1989) as well as Young (1993) are recommended.

Most popular computer programs which can be used to carry out Rietveld refinement include GSAS (Larson and Von Dreele 2000; Toby 2001), Fullprof (Rodriguez-Carvajal 1990), Rietan (Young 1993) and MAUD (Lutterotti et al. 1999).

Pawley and Le Bail whole pattern refinement. Because of the problems with individual fitting of closely overlapping peak it is difficult to use that approach to extract reliable peak intensities that could be used for solution of unknown crystal structures. To resolve this situation, in the 1980's, a new whole pattern refinement method, which constrains peak positions to values determined by unit cell parameters, while allowing individual peak intensities to be refined independently, was introduced (LeBail et al. 1988; Pawley 1981). This new approach dramatically reduces the number of refined parameters (for N observed peaks instead of refining N peak position one uses 6 or less cell parameters) and aids in more reliable refinement of intensity partitioning between closely overlapping peaks. In the Pawley method (Pawley 1981) peak profile width is constrained by the Caglioti law with the three refinable parameters U, V, W as defined in Equation (15).

Constraints are introduced to help provide stability of the refinement of closely overlapped peaks. The Pawley method also calculates a co-variance matrix describing how the extracted peak intensities correlate with each other and provides reasonable estimates of peak intensity standard deviations. The disadvantage of the Pawley method is that the inclusion of all the peak intensities as independent parameters in the optimization creates a challenging numerical

EBSCOhost - printed on 2/13/2023 5:26 AM via . All use subject to https://www.ebsco.com/terms-of-use

problem for computer software (very large matrix that has to be inverted) and results in long computation times.

To solve this numerical challenge a different approach for determining peak intensities, but still taking advantage of constrained peak positions from unit cell parameters was introduced by Le Bail et al. (1998). The Le Bail method uses a two-step iterative process in which peak intensities are no longer treated as refinable parameters. As a consequence, the least-squares matrix is much smaller and the optimization significantly faster than in the Pawley approach. In Rietveld refinement, the partitioning of calculated intensity I_i^{calc} between overlapping peaks $I_{i,k}^{calc}$ is determined by the structure model. In order to obtain observed intensities for the same peaks, it is then assumed that the I_i^{obs} partitions in the same way as I_i^{calc}. The caveat of this approach is that for overlapping peaks, an inaccurate or wrong model will lead to improper estimation of I_i^{obs}. Le Bail peak intensity extraction starts from a uniform partitioning of all calculated intensities $I_{i,k}^{calc} = 1$. The Rietveld algorithm is then used to extract I_i^{obs}, after which the $I_{i,k}^{calc}$ are reset from the extracted $I_{i,k}^{obs}$. This approach assures optimal estimates of peak intensities in which the intensities of completely overlapped peaks is apportioned according to peak multiplicity.

Le Bail refinement is often used to retrieve unit cell parameters and confirm the correctness of indexing in cases when the quality of peak intensities is insufficient for structure refinement or if the structure of the sample is not known.

Parametric Rietveld refinement. While Rietveld refinement is a very valuable tool for retrieving information about the atomic arrangements of the crystalline sample, the reliability of the structure models derived from Rietveld analysis often suffers from insufficient number of independent observations. In some extreme cases is has even been demonstrated that a refinement with a wrong unit cell and essentially wrong structure can yield figures of merit that look satisfactory (Buchsbaum and Schmidt 2007). This problem is particularly dramatic for experiments at nonambient conditions (e.g., high pressure or high temperature), in which the sample environment is complicated by the presence of heaters, high pressure cells, etc. that contribute unwanted signal and intensity-affecting effects to the observed pattern. On the other hand, when investigating systematic trends, a time, temperature or pressure series of diffraction patterns, all collected within the same phase stability field are not completely independent from each other (because the structure changes in a continuous way). Based on this assumption, Stinton and Evans (2007) proposed an approach to fitting all of these serial diffraction patterns at the same time while tying the refined parameters together by means of polynomial equations. This method has been demonstrated to yield much more reliable and physically reasonable structure models than individual Rietveld refinements (Bish and Howard 1988; Agostini et al. 2010; Halasz et al. 2010; Müller et al. 2011). Additional benefit of the parametric Rietveld refinement is the fact that it produces a model of the structural evolution accompanying the studied process, which can be much easier understood than a series of individual models.

Quantitative analysis of phase mixtures. The powder pattern of a crystalline substance is like its fingerprint, and, as can be seen from Equation (14), its overall intensity is dependent on the illuminated volume of the sample. For samples composed from multiple crystalline phases, each phase contribution is scaled by the volume fraction of the given phase. Powder diffraction-based quantitative analysis (QA) provides for the determination of the composition of phase mixtures by carrying out a refinement that includes phase volume fractions. The most popular type of QA analysis with powder data is carried out using multi-phase Rietveld refinement (Bish and Howard 1988).

In principle, it is possible to carry out powder diffraction based QA even if the structure of some or all of the phase mixture components are not known (e.g., in case of poorly crystalline

EBSCOhost - printed on 2/13/2023 5:26 AM via . All use subject to https://www.ebsco.com/terms-of-use

or amorphous phases) (Scarlett and Madsen 2006). In such cases, it is necessary to obtain pure-phase samples of each of the components and measure calibration patterns from mixtures of these pure components with an internal diffraction standard (a common internal standard is Al_2O_3 corundum), which yields information about relative total scattering power of each component. Chipera and Bish (2002) introduced software called FULLPAT for QA if a full set of such calibration data is available for all components.

The atomic pair distribution function technique (PDF)

The atomic pair distribution function technique, introduced in the 1930s for the experimental investigation of liquid and crystalline materials (Debye and Menke 1930; Warren 1934; Warren and Gingrich 1934), has found renewed interest and has been extended to materials with a wide range of ordering, from completely amorphous to nanocrystalline. The technique is useful for producing an estimate of the probability distribution of interatomic separations. A comprehensive description of the technique can be found in Egami and Billinge (2003); and summarized in several review papers (Proffen et al. 2003; Billinge 2004; Billinge and Kanatzidis 2004; Page et al. 2004; Proffen 2006). Bragg peaks and diffuse scattered radiation are treated as a whole in the PDF analysis. The formalism of the PDF technique is general; no assumptions are made on the atomic structure of materials, instead it is concerned with the frequency of occurrence of atoms as a function of interatomic distances. The data collection procedure is basically the same as for collecting a powder diffraction pattern to high Q values ($Q = 4\pi\sin\theta/\lambda$ is the magnitude of the scattering vector or momentum transfer), usually obtained using high energy synchrotron radiation (the real space resolution is inversely related to the wavelength), but also polychromatic laboratory sources (e.g., Di Marco et al. 2009). The data collection time varies from several hours to seconds depending on the detector type and the sample characteristics. Measurements are carried out to high-Q values in order to avoid artificial ripples from the Fourier transformation termination. Particular care must be taken in the measurement of the background which is subtracted from the sample data; inaccurate background subtraction can produce severe artifacts in the analysis because the full pattern is used to constrain structural parameters. From the experimental coherent intensities I(Q), expressed as a function of the momentum transfer Q, the total scattering structure function is calculated:

$$S(Q) = \frac{I(Q) - \sum c_i \left| f_i(Q) \right|^2}{\left| \sum c_i f_i(Q) \right|^2} \tag{26}$$

where c_i and f_i are the respective atom concentrations and atomic scattering factors of the i^{th} atoms, summed over the scattering volume. The experimental PDF is denoted with the function $G(r)$, calculated as the Fourier transform of the total scattering:

$$G(r) = 4\pi r\left[\rho(r) - \rho_0\right] = \frac{2}{\pi}\int_0^{Q\max} Q\left[S(Q) - 1\right]\sin(Qr)dQ \tag{27}$$

where ρ_0 is the average atomic number density and $\rho(r)$ is the atomic pair density. Peculiar to the PDF technique is that a plot of the $G(r)$ function is a rather intuitive pattern showing real space maxima corresponding to interatomic distances "weighted" by the scattering factor of the pairs of atoms and the frequency with which they occur. Highly ordered and symmetric materials have well defined interatomic distances for many coordination shells and therefore show sharp peaks in the $G(r)$ plots, while disordered materials have a greater spread of interatomic distances and therefore they will show broad peaks, particularly at high r. Liquids, where the ordering vanishes quickly with distance and so interatomic distance randomize rapidly beyond the first coordination shell (short range ordering), show peaks confined to a fairly low-r range. The interpretation of a PDF pattern is not necessarily unique. The technique

EBSCOhost - printed on 2/13/2023 5:26 AM via . All use subject to https://www.ebsco.com/terms-of-use

is especially suitable for the analysis of elusive structures of complex minerals such as clays and weathering products (Gualtieri et al. 2008; Di Marco et al. 2009; Fernandez-Martinez et al. 2010; White et al. 2010) where Bragg and diffuse components are equally important. The analysis of PDF patterns is a challenging task, but can yield satisfactory results when coupled with other experiments (Krayzman et al. 2009) and first principle calculations (White et al. 2010; Fernandez- Martinez et al. 2010). The PDF technique is also a useful tool in the structural analysis of materials with long range ordering, Billinge and Kanatzidis (2004) discuss examples where incorrect structural solutions from single crystal analysis are readily verified by means of PDF analysis. Toby and Billinge (2004) present an important analysis of the statistics of structural determinations with the PDF technique. In a novel application of the technique, Li et al. (2011), studied the effect of arsenate doping in γ-alumina by analyzing the differential PDF of untreated and treated samples.

The Fernandez-Martinez et al. (2010) study of the structure of schwertmannite, $(Fe_8O_8(OH)_{8-x}(SO_4)_x$, an important scavenger of As and Se contaminants, offers an instructive example of the application of the PDF techniques. Occurring as poorly crystallized nanosize material, schwertmannite achieved the status of mineral only recently (Bigham et al. 1994) due to the difficulty in defining both its composition and structure. The modeling of the PDF pattern is performed starting from the structure of the sulfate-free akaganeite (Post et al. 2003), a mineral with an arrangement of FeO_6 octahedra similar to schwertmannite. Figure 9, with simulated partial and total PDFs of sulfate doped akaganeite, shows how single atomic pairs sum to give the total $G(r)$. Fe-Fe and Fe-O pairs provide a strong contribution to the total scattering and therefore are better resolved. Nonetheless, the short S-O bond results in a distinct feature in the simulated and experimental PDFs (Fig. 9). The authors used the intensity of the S-O and Fe-O correlations and their weighting factors to estimate the amount of sulfate in the sample. The fitting of the PDF data provides evidence of a triclinic distortion of the unit

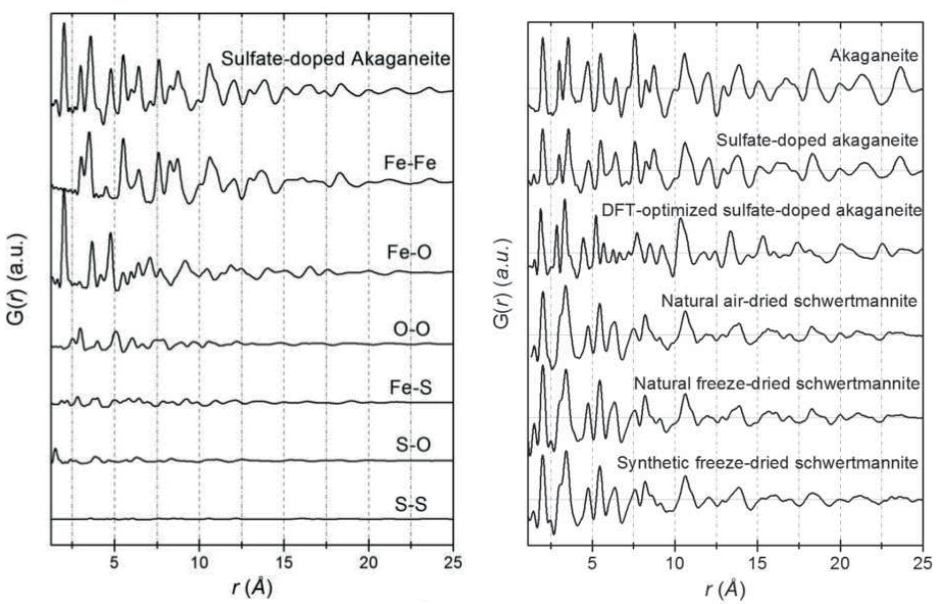


Figure 9. Simulated partial and total PDFs of sulfate-doped akaganeite (*left*) and comparison between calculated (upper three) and experimental (bottom three) PDFs of the oxyhydroxysulfates (*right*) by Fernandez-Martinez et al. (2010).

EBSCOhost - printed on 2/13/2023 5:26 AM via . All use subject to https://www.ebsco.com/terms-of-use

cell of schwertmannite from the monoclinic akaganeite, however it could not discriminate two different models for the arrangement of the FeO_6 octahedra.

ACKNOWLEDGMENTS

The UNLV High Pressure Science and Engineering Center (HiPSEC) is supported by DOE-NNSA Cooperative Agreement DE-FC52-06NA262740. GeoSoilEnviroCARS is supported by the National Science Foundation - Earth Sciences (EAR-0622171) and Department of Energy - Geosciences (DE-FG02-94ER14466). The APS is supported by DOE-BES, under Contract No. DE-AC02-06CH11357.

REFERENCES

Agostini G, Lamberti C, Palin L, Milanesio M, Danilina N, Xu B, Janousch M, van Bokhoven JA (2010) *In situ* XAS and XRPD parametric Rietveld refinement to understand dealumination of Y zeolite catalyst. J Am Chem Soc 132:667-678

Als-Nielsen J, McMorrow D (2011) Elements of Modern X-ray Physics. Wiley, Hoboken

Angel RJ, Downs RT, Finger LW (2000) High-temperature – high-pressure diffractometry. Rev Mineral Geochem 41:559-597

Aroyo MI, Kirov A, Capillas C, Perez-Mato JM, Wondratschek H (2006a) Bilbao crystallographic server. II. Representations of crystallographic point groups and space groups. Acta Crystallogr A 62:115-128

Aroyo MI, Perez-Mato JM, Capillas C, Kroumova E, Ivantchev S, Madariaga G, Kirov A, Wondratschek H. (2006b) Bilbao crystallographic server: I. Databases and crystallographic computing programs. Z Kristallogr 221:15-27

Baublitz MA, Arnold V, Ruoff AL (1981) Energy dispersive-X-ray diffraction from high-pressure polycrystalline specimens using synchrotron radiation. Rev Sci Instrum 52:1616-1624

Berlepsch P, Armbruster T, Brugger J, Criddle AJ, Graeser S (2003) Tripuhyite, $FeSbO_4$, revisited. Mineral Mag 67:31-46

Bigham JM, Carlson L, Murad E. Schwertmannite, a new iron oxyhydroxysulphate from Pyhasalmi, Finland, and other localities (1994) Mineral Mag 58:641-648

Billinge SJL (2004) The atomic pair distribution function: past and present. Z Kristallogr 219:117-121

Billinge SJL, Kanatzidis MG (2004) Beyond crystallography: the study of disorder, nanocrystallinity and crystallographically challenged materials with pair distribution functions. Chem Comm 7:749-760

Billinge SJL, Thorpe MF (1998) Local Structure from Diffraction. Plenum Press, New York

Bindi L, Carbone C, Cabella R, Lucchetti G (2011) Bassoite, $SrV_3O_7 \cdot 4H_2O$, a new mineral from Molinello mine, Val Graveglia, eastern Liguria, Italy. Mineral Mag 75:2677-2686

Bindi L, Steinhardt PJ, Yao N, Lu PJ (2009) Natural quasicrystals. Science 324:1306-1309

Bish DL, Howard SA (1988) Quantitative phase-analysis using the Rietveld method. J Appl Crystallogr 21:86-91

Bish DL, Post JE (eds) (1989) Modern Powder Diffraction. Reviews in Mineralogy, Volume 20. Mineralogical Society of America

Blake AJ, Clegg W (2009) Crystal structure analysis: principles and practice. Vol. 13 International Union of Crystallography book series. 2nd ed. Oxford University Press. Oxford,

Blake DF, Vaniman D, Anderson R, Bish D, Chipera S, Chemtob S, Crisp J, DesMais DJ, Downs RT, Farmer J, Gailhanou M, Ming D, Morris D, Stolper E, Sarrazin P, Treiman A, Yen A (2009) The CHEMIN mineralogical instrument on the Mars science laboratory mission. Proceedings of the 40th Lunar and Planetary Science Conference, 1484

Bochenin VI (1973) Portable X-ray diffractometer for phase analysis of materials with a radiation source on ^{55}Fe basis. Prib Tekh Eksp 5:228-230

Boisen MB Jr, Gibbs GV (1985) Mathematical Crystallography. Reviews in Mineralogy, Volume 15. Mineralogical Society of America

Britvin SN, Rudashevsky NS, Krivovichev SV, Burns PC, Polekhovsky YS (2002) Allabogdanite, $(Fe,Ni)_2P$, a new mineral from the Onello meteorite: The occurrence and crystal structure. Am Mineral 87:1245-1249

Brown GE Jr, Sutton SR, Calas G (2006a) User facilities around the world. Elements 2:9-14

Brown PJ, Fox AG, Maslen EN, O'Keefe MA, Willis BTM (2006b) Intensity of diffracted intensities. *In*: International Tables for Crystallography. Volume C. Prince E (ed) John Wiley & Sons, Ltd, p 554-595

Buchsbaum C, Schmidt MU (2007) Rietveld refinement of a wrong crystal structure. Acta Crystallogr B 63:926-932

EBSCOhost - printed on 2/13/2023 5:26 AM via . All use subject to https://www.ebsco.com/terms-of-use

Budai JD, Liu W, Tischler JZ, Pan ZW, Norton DP, Larson BC, Yang W, Ice GE (2008) Polychromatic X-ray micro- and nanodiffraction for spatially-resolved structural studies. Thin Solid Films 516:8013-8021

Bunge HJ (1965) Zur darstellung allgemeiner texturen. Z Metallkd 56:872-874

Burla MC, Caliandro R, Camalli M, B Carrozzini B, GL Cascarano GL, Giacovazzo C, Mallamo M, Mazzone A, Polidori G, Spagna R (2012) SIR2011: a new package for crystal structure determination and refinement. J Appl Crystallogr 45:357-361

Burns PC (1998) CCD area detectors of X-rays applied to the analysis of mineral structures. Can Mineral 36:847-853

Caglioti G, Paoletti A, Ricci FP (1958) Choice of collimators for a crystal spectrometer for neutron diffraction. Nucl Instrum Methods 3:223-228

Chantler CT (2000) Detailed tabulation of atomic form factors, photoelectric absorption and scattering cross section, and mass attenuation coefficients in the vicinity of absorption edges in the soft X-ray (Z=30-36, Z=60-89, E=0.1 keV-10 kev), addressing convergence issues of earlier work. J Phys Chem Ref Data 29:597-1048

Chen K, Kunz M, Tamura N, Wenk H-R (2011a) Evidence for high stress in quartz from the impact site of Vredefort, South Africa. Eur J Mineral 23:169-178

Chen K, Kunz M, Tamura N, Wenk H-R (2011b) Deformation twinning and residual stress in calcite studied with synchrotron polychromatic X-ray microdiffraction. Phys Chem Mineral 38:491-500

Chichagov AV, Varlamov DA, Dilanyan RA, Dokina TN, Drozhzhina NA, Samokhvalova OL, Ushakovskaya TV (2001) MINCRYST: a crystallographic database for minerals, local and network (www) versions. Crystallogr Rep+ 46:876-879

Chipera SJ, Bish DL (2002) FULLPAT: a full-pattern quantitative analysis program for X-ray powder diffraction using measured and calculated patterns. J Appl Crystallogr 35:744-749

Clegg W (2001) Crystal Structure Analysis: Principles and Practice. Volume 6. International Union of Crystallography

Courtin-Nomade A, Vanaecker M, Kunz M, Tamura N (2008) Coupling micro-Raman and microscanning X-ray diffraction to characterize heterogeneous material. Geochim Cosmochim Acta 72:A185-A185

Courtin-Nomade A, Bril H, Beny J-M, Kunz M, Tamura N (2010) Sulfide oxidation observed using micro-Raman spectroscopy and micro-X-ray diffraction: The importance of water/rock ratios and pH conditions. Am Mineral 95:582-591

Dauter Z, Wilson KS (2007) Principles of monochromatic data collection. *In:* International Tables for Crystallography, Volume F. International Union of Crystallography, p 177-195

Davis MF, Groter C, Kay HF (1968) On choosing off-line automatic X-ray diffractometers. J Appl Crystallogr 1:209-217

Daymond MR, Bourke MAM, Von Dreele RB, Clausen B, Lorentzen T (1997) Use of Rietveld refinement for elastic macrostrain determination and for evaluation of plastic strain history from diffraction spectra. J Appl Phys 82:1554-1562

Daymond MR, Bourke MAM, Von Dreele RB (1999) Use of Rietveld refinement to fit a hexagonal crystal structure in the presence of elastic and plastic anisotropy. J Appl Phys 85:739-747

Debye P, Menke H (1930) The determination of the inner structure of liquids by X-ray means. Phys Z 31:797-798

Di Marco M, Ballirano P, Port M, Piscopiello E, Couvreur P, Dubernet C, and Sadun C (2009). Atomic pair distribution function (PDF) study of iron oxide nanoparticles in aqueous suspension. J Mat Chem 19:6354-6360

Dinnebier RE, Billinge SJL (2008) Powder Diffraction: Theory and Practice. Royal Society of Chemistry, Cambridge

Dollase WA (1986) Correction of intensities for preferred orientation in powder diffractometry - application of the March model. J Appl Crystallogr 19:267-272

Downs RT (2000) Analysis of harmonic displacement factors. Rev Mineral Geochem 41:61-87

Downs RT, Hall-Wallace M (2003) The American Mineralogist crystal structure database. Am Mineral 88:247-250

Egami T, Billinge SJL (2003) Underneath the Bragg-peaks: Structural Analysis of Complex Material. Elsevier Sci LTD, New York

Ewald PP (1921) The "reciprocal lattice" in structure theory. Z Kristallogr 56:129-156

Fernandez-Martinez A, Timon V, Roman-Ross G, Cuello GJ, Daniels JE, Ayora C (2010) The structure of schwertmannite, a nanocrystalline iron oxyhydroxysulfate. Am Mineral 95:1312-1322

Frey F, Boysen H, Jagodzinski H (2010) Disorder diffuse scattering of X-rays and neutrons. *In*: International Tables for Crystallography B. John Wiley & Sons, Ltd, p 492-539

Friedrich W, Knipping P, Laue M (1912). Sitzungsberichte der mathematisch-physikalischen klasse der koeniglich bayerischen akademie der wissenschaften zu muenchen. Proc Bavarian Acad Sci 303-322

Giacovazzo C (2011) Fundamentals of Crystallography. Oxford University Press, Oxford

Glusker JP, Trueblood KN (2010) Crystal Structure Analysis: A Primer. Oxford University Press, Oxford

EBSCOhost - printed on 2/13/2023 5:26 AM via . All use subject to https://www.ebsco.com/terms-of-use

Gozzo F, De Caro L, Giannini C, Guagliardi A, Schmitt B, Prodi A (2006) The instrumental resolution function of synchrotron radiation powder diffractometers in the presence of focusing optics. J Appl Crystallogr 39:347-357

Gražulis S, Daškevič A, Merkys A, Chateigner D, Lutterotti L, Quirós M, Serebryanaya NR, Moeck P, Downs RT, Le Bail A (2012) Crystallography Open Database (COD): an open-access collection of crystal structures and platforms for world-wide collaboration. Nucleic Acids Res 40:D420-D427

Gualtieri AF, Ferrari S, Leoni M, Grathoff G, Hugo R, Shatnawi M, Paglia G, Billinge S (2008) Structural characterization of the clay mineral illite-1M. J Appl Crystallogr 41:402-415

Halasz I, Dinnebier RE, Angel R (2010) Parametric Rietveld refinement for the evaluation of powder diffraction patterns collected as a function of pressure. J Appl Crystallogr 43:504-510

Hammersley AP, Svensson SO, Hanfland M, Fitch AN, Hausermann D (1996) Two-dimensional detector software: From real detector to idealised image or two-theta scan. High Pressure Res 14:235-248

Hansford GM (2011) Optimization of a simple X-ray diffraction instrument for portable and planetary applications. Nucl Instrum Meth 632:81-88

Hazen RM, Finger LW (1982) Comparative Crystal Chemistry: Temperature, Pressure, Composition, and the Variation of Crystal Structure. Wiley, New York

He BB (2009) Two-Dimensional X-ray Diffraction. Wiley, Hoboken, N.J.

Heiney PA (2005) Datasqueeze: A software tool for powder and small-angle X-ray diffraction analysis. Newsletter of the IUCr Commission on Powder Diffraction 32:9-11

Hinrichsen B, Dinnebier RE, Jansen M (2006) Powder3D: An easy to use program for data reduction and graphical presentation of large numbers of powder diffraction patterns. Z Kristallogr Suppl 23:231-236

Hochella MF Jr, Lower SK, Maurice PA, Penn RL, Sahai N, Sparks, DL Twining BS (2008) Nanominerals, mineral nanoparticles, and Earth systems. Science 319:1631-1635

Holland TJB, Redfern SAT (1997) UNITCELL: A nonlinear least-squares program for cell-parameter refinement and implementing regression and deletion diagnostics. J Appl Crystallogr 30:84

Hubbell JH, Seltzer SM (2004) Tables of X-ray mass attenuation coefficients and mass energy- absorption coefficients (version 1.4). National Institute of Standards and Technology, Gaithersburg, MD, http://physics.nist.gov/xaamdi

Ichiyanagia K, Adachi S-I, Nozawa S, Hironaka Y, Nakamura KG, Sato T, Tomita A, Koshihara S-Y (2007) Shock-induced lattice deformation of CdS single crystal by nanosecond time-resolved Laue diffraction. Appl Phys Lett 91:231918

International Tables for Crystallography (2006) 1st online ed. International Union of Crystallography. http://onlinelibrary.wiley.com/book/10.1107/97809553602060000001

Ishida H, Ogasawara Y, K Ohsumi K, Saito A (2003) Two stage growth of microdiamond in UHP dolomite marble from Kokchetav massif, Kazakhstan. J Metamorphic Geol 21:515-522

Ivanov AV, Zolensky ME, Saito A, Ohsumi K, Yang SV, Kononkova NN, Mikouchi T (2000) Florenskyite FeTiP, a new phosphide from the Kaidun meteorite. Am Mineral 85:1082-1086

Kahn R, Fourme R, Gadet A, Janin J, Dumas C, AndreE D (1982) Macromolecular crystallography with synchrotron radiation - photographic data-collection and polarization correction. J Appl Crystallogr 15:330-337

Kariuki BM, Harding MM (1995) Application of synchrotron-radiation Laue diffraction to small single-crystals of a mineral - structure determination and identification. J Synchrotron Radiat 2:185-189

King HE, Finger LW (1979) Diffracted beam crystal centering and its application to high-pressure crystallography. J Appl Crystallogr 12:374-378

Kocks UF, Tomé CN, Wenk H-R (1998) Texture and Anisotropy: Preferred Orientations in Polycrystals and Their Effect on Materials Properties. Cambridge University Press, Cambridge, UK

Krayzman V, Levin I, Woicik JC, Proffen T, Vanderah TA, Tucker MG (2009). A combined fit of total scattering and extended X-ray absorption fine structure data for local-structure determination in crystalline materials. J Appl Crystallogr 42:867-877

Kunz M, Chen K, Tamura N, Wenk H-R (2009) Evidence for residual elastic strain in deformed natural quartz. Am Mineral 94:1059-1062

Ladd MFC, Palmer RA (2003) Structure Determination by X-ray Crystallography. Kluwer Academic/Plenum Publishers, New York, 4th edition

Laetsch T, Downs RT (2006) Software for identification and refinement of cell parameters from powder diffraction data of minerals using the RRUFF project and American Mineralogist crystal structure databases. IMA General Meeting

Larson AC, Von Dreele RB (2000) General structure analysis system (GSAS). LANL Report LAUR 86-748

Le Bail A, Duroy H, Fourquet JL (1988) Ab-initio structure determination of $LiSbWO_6$ by X-ray-powder diffraction. Mater Res Bull 23:447-452

Lee J (2011) X-ray Lasers 2010. Springer, New York

Lennie AR, Laundy D, Roberts MA, Bushnell-Wye G (2007) A novel facility using a Laue focusing monochromator for high-pressure diffraction at the SRS, Daresbury, UK. J Synchrotron Radiat 14:433-438

EBSCOhost - printed on 2/13/2023 5:26 AM via . All use subject to https://www.ebsco.com/terms-of-use

Li W, Harrington R, Tang Y, Kubicki JD, Aryanpour M, Reeder RJ, Parise JB, Phillips BL (2011) Differential pair distribution function study of the structure of arsenate adsorbed on nanocrystalline γ-alumina. Environ Sci Technol 45:9687-9692

Lipson H, Langford JI, Hu HC (2006) Trigonometric intensity factors. International Tables for Crystallography, Vol C, p 596-598

Lutterotti L, Matthies S, Wenk H-R (1999) MAUD (Material Analysis Using Diffraction): a user friendly java program for Rietveld texture analysis and more. Proceeding of the Twelfth International Conference on Textures of Materials (ICOTOM-12), Vol. 1, 1599

March A (1932) Mathematical theory on regulation according to the particle shape and affine deformation. Z Kristallogr 81:285-297

Margaritondo G (1988) Introduction to Synchrotron Radiation. Oxford University Press, New York

Margaritondo G (2002) Elements of Synchrotron Light: for Biology, Chemistry, and Medical Research. Oxford University Press, Oxford

Müller M, Dinnebier RE, Schorr S (2011) A case study of parameterized Rietveld refinement: the structural phase transition of $CuInSe_2$ (2011) Z Kristallogr 226:956-962

Nakatsuka A, Yoshiasa A, Yamanaka T, Ohtaka O, Katsura T, Ito E (1999) Symmetry change of majorite solid-solution in the system $Mg_3Al_2Si_3O_{12}$-$MgSiO_3$. Am Mineral 84:1135-1143

Neuling HW, Schulte O, Kruger T, Holzapfel WB (1992) Texture-sensitive energy dispersive- X-ray diffraction on powders at high-pressure with synchrotron radiation. Meas Sci Technol 3:170-173

North ACT, Phillips DC, Mathews FS (1968) A semi-empirical method of absorption correction. Acta Crystallogr A 24:351-359

Nozawa S, Adachi S, Takahashi J, Tazaki R, Guerin L, Daimon M, Tomita A, Sato T, Chollet M, Collet E, Cailleau H, Yamamoto S, Tsuchiya K, Shioya T, Sasaki H, Mori T, Ichiyanagi K, Sawa H, Kawata H, Koshihara S (2007) Developing 100 ps-resolved X-ray structural analysis capabilities on beamline NW14A at the photon factory advanced ring. J Synchrotron Radiat 14:313-319

Ottonello G (1997) Principles of Geochemistry. Columbia University Press, New York

Page KL, Proffen T, McLain SE, Darling TW, TenCate JA (2004) Local atomic structure of Fontainebleau sandstone: Evidence for an amorphous phase? Geophys Res Lett 31:L24606

Pawley GS (1981) Unit-cell refinement from powder diffraction scans. J Appl Crystallogr 14:357-361

Pecharsky VK, Zavalij PY (2009) Fundamentals of Powder Diffraction and Structural Characterization of Materials. Springer, New York, 2nd edition

Post JE, Heaney PJ, Von Dreele RB, and Hanson JC (2003) Neutron and temperature-resolved synchrotron X-ray powder diffraction study of akaganeite. Am Mineral 88:782-788

Proffen T (2006) Analysis of disordered materials using total scattering and the atomic pair distribution function. Rev Mineral Geochem 63:255-274

Proffen T, Billinge SJL, Egami T, Louca D (2003) Structural analysis of complex materials using the atomic pair distribution function - a practical guide. Z Kristallogr 218:132-143

Putnis A (1992) Introduction to Mineral Sciences. Cambridge University Press, Cambridge

Ren Z, Bourgeois D, Helliwell JR, Moffat K, Srajer V, Stoddard BL (1999) Laue crystallography: coming of age. J Synchrotron Radiat 6:891-917

Ren Z, Ng K, Borgstahl GEO, Getzoff ED, Moffat K (1996) Quantitative analysis of time-resolved Laue diffraction patterns. J Appl Crystallogr 29:246-260

Rietveld HM (1967) Line profiles of neutron powder-diffraction peaks for structure refinement. Acta Crystallogr 22:151-152

Rietveld HM (1969) A profile refinement method for nuclear and magnetic structures. J Appl Crystallogr 2:65-71

Robinson I, Gruebel G, Mochrie S (2010) X-ray beams with high coherence. New J Phys 12:035002

Rodriguez-Carvajal J (1990) FULLPROF: A program for Rietveld refinement and pattern matching analysis. Abstracts of the Satellite Meeting on Powder Diffraction of the XV Congress of the IUCr, p 127

Roe RJ (1965) Description of crystallite orientation in polycrystalline materials. 3. General solution to pole figure inversion. J Appl Phys 36:2024-2031

Sabine TM (1987) A powder diffractometer for a synchrotron source. J Appl Crystallogr 20:173-178

Sarrazin P, Blake D, Bish D, Vaniman D, Collins S (1998) A miniature XRD/XRF instrument for in-situ characterization of Martian soils and rocks. J Phys IV 8:465-470

Sarrazin P, Blake D, Feldman S, Chipera S, Vaniman D, Bish D (2005) Field deployment of a portable X-ray diffraction/X-ray flourescence instrument on Mars analog terrain. Powder Diffr 20:128-133

Scarlett NVY, Madsen IC (2006) Quantification of phases with partial or no known crystal structures. Powder Diffr 21:278-284

Scherrer P (1918) Bestimmung der größe und der inneren struktur von kolloidteilchen mittels röntgenstrahlen. Nachrichten von der gesellschaft der wissenschaften zu Göttingen. Mathematisch- Physikalische Klasse 2:98

EBSCOhost - printed on 2/13/2023 5:26 AM via . All use subject to https://www.ebsco.com/terms-of-use

Sheldrick GM (2008) A short history of SHELX. Acta Crystallogr A 64:112-122
Snyder RL, Bunge HJ (2000) Defect and Microstructure Analysis by Diffraction. Oxford University Press
Srajer V, Crosson S, Schmidt M, Key J, Schotte F, Anderson S, Perman B, Ren Z, Teng TY, Bourgeois D, Wulff M, Moffat K (2000) Extraction of accurate structure-factor amplitudes from Laue data: wavelength normalization with wiggler and undulator X-ray sources. J Synchrotron Radiat 7:236-244
Steinhardt PJ, Bindi L (2012) In search of natural quasicrystals. Rep Prog Phys 75:092601
Stinton GW, Evans JSO (2007). Parametric Rietveld refinement. J Appl Crystallogr 40:87-95
Stout GH, Jensen LH (1989) X-ray Structure Determination: A Practical Guide. Wiley, New York
Suggit M, Kimminau G, Hawreliak J, Remington B, Park N, Wark J (2010) Nanosecond X-ray Laue diffraction apparatus suitable for laser shock compression experiments. Rev Sci Instrum 81:083902
Sutton SR (2006) User research facilities in the earth sciences. Elements 2:7-8
Tait KT, Barkley MC, Thompson RM, Origlieri MJ, Evans SH, Prewitt CT, Yang H (2011) Bobdownsite, a new mineral species from Big Fish river, Yukon, Canada, and its structural relationship with whitlockite-type compounds. Can Mineral 49:1065-1078
Tamura N, Kunz M, Chen K, Celestre RS, MacDowell AA, Warwick T (2009) A superbend X-ray microdiffraction beamline at the advanced light source. Mater Sci Eng A Struct 524:28-32
Toby BH (2001) EXPGUI, a graphical user interface for GSAS. J Appl Crystallogr 34:210-213
Toby BH, Billinge SJL (2004) Determination of standard uncertainties in fits to pair distribution functions. Acta Crystallogr A 60:315-317
Vogel S, Ehm L, Knorr K, Braun G (2002) Automated processing of 2D powder diffraction data. Adv X-ray Anal 45:31-33
Vogel SC, Knorr K (2005) Two2One - Software for the analysis of two dimensional diffraction data. Newsletter of the IUCr Commission on Powder Diffraction 32:23-25
Wang J, Toby BH, Lee PL, Ribaud L, Antao SM, Kurtz C, Ramanathan M, Von Dreele RB, Beno MA (2008). A dedicated powder diffraction beamline at the advanced photon source: Commissioning and early operational results. Rev Sci Instrum 79:085105
Wang Y, Hilairet N, Dera P (2010) Recent advances in high pressure and temperature rheological studies. J Earth Sci 21:495-516
Wang Y, Uchida T, Von Dreele R, Rivers ML, Nishiyama N, Funakoshi K, Nozawa A, Kaneko H (2004) A new technique for angle-dispersive powder diffraction using an energy-dispersive setup and synchrotron radiation. J Appl Crystallogr 37:947-956
Warren BE (1934) X-ray determination of the structure of glass. J Am Ceram Soc 17:249-254
Warren BE (1969) X-ray Diffraction Reading, MS: Addison-Wesley
Warren BE (1990) X-ray diffraction. Dover Publications, New York
Warren BE, Gingrich NS (1934) Fourier integral analysis of X-ray powder patterns. Phys Rev 46:0368-0372
Waychunas GA (2009) Natural nanoparticle structure, properties and reactivity from X-ray studies. Powder Diffraction 24:89-93
Wenk H-R, Chen K, Smith R (2011) Morphology and microstructure of magnetite and ilmenite inclusions in plagioclase from Adirondack anorthositic gneiss. Am Mineral 96:1316-1324
White CE, Provis JL, Proffen T, Riley DP, van Deventer JSJ (2010) Combining density functional theory (DFT) and pair distribution function (PDF) analysis to solve the structure of metastable materials: the case of metakaolin. Phys Chem Chem Phys 12:3239-3245
Williamson GK, Hall WH (1953) X-ray line broadening from filed aluminium and wolfram. Acta Metall 1:22-31
Yamanaka T, Ogata K (1991) Structure refinement of GeO_2 polymorphs at high-pressures and temperatures by energy-dispersive spectra of powder diffraction. J Appl Crystallogr 24:111-118
Yamashita D, Ishizaki A, Uda M (2009) Development of portable X-ray diffractometer equipped with X-ray fluorescence spectrometer and its application to archaeology. Bunseki Kagaku 58:347-355
Yang XJ, Ren Z, Moffat K (1998) Structure refinement against synchrotron Laue data: Strategies for data collection and reduction. Acta Crystallogr D 54:367-377
Young RA (1993) The Rietveld Method. International Union of Crystallography
Zelenski ME, Zubkova N, Pekov IV, Boldyreva MM, Pushcharovsky DY, Nekrasov AN (2011) Pseudolyonsite, $Cu_3(VO_4)_2$, a new mineral species from the Tolbachik volcano, Kamchatka peninsula, Russia. Eur J Mineral 23:475-481

EBSCOhost - printed on 2/13/2023 5:26 AM via . All use subject to https://www.ebsco.com/terms-of-use

EBSCOhost - printed on 2/13/2023 5:26 AM via . All use subject to https://www.ebsco.com/terms-of-use

Reviews in Mineralogy & Geochemistry
Vol. 78 pp. 33-74, 2014
Copyright © Mineralogical Society of America

Fundamentals of XAFS

Matthew Newville

Center for Advanced Radiation Sources
University of Chicago
Chicago, Illinois 60637, U.S.A.

newville@cars.uchicago.edu

The basic physical principles of X-ray Absorption Fine-Structure (XAFS) are presented. XAFS is an element-specific spectroscopy in which measurements are made by tuning the X-ray energy at and above a selected core-level binding energy of a specified element. Although XAFS is a well-established technique providing reliable and useful information about the chemical and physical environment of the probe atom, its requirement of an energy-tunable X-ray source means it is primarily done with synchrotron radiation sources and so is somewhat less common than other spectroscopic analytical methods. XAFS spectra are especially sensitive to the oxidation state and coordination chemistry of the selected element. In addition, the extended oscillations of the XAFS spectra are sensitive to the distances, coordination number and species of the atoms immediately surrounding the selected element. This Extended X-ray Absorption Fine-Structure (EXAFS) is the main focus of this chapter. As it is element-specific, XAFS places few restrictions on the form of the sample, and can be used in a variety of systems and bulk physical environments, including crystals, glasses, liquids, and heterogeneous mixtures. Additionally, XAFS can often be done on low-concentration elements (typically down to a few ppm), and so has applications in a wide range of scientific fields, including chemistry, biology, catalysis research, material science, environmental science, and geology. Special attention in this chapter is given to the basic concepts used in analysis and modeling of EXAFS spectra.

INTRODUCTION

X-ray absorption fine structure (XAFS) is the modulation of an atom's X-ray absorption probability at energies near and above the binding energy of a core-level electron of the atom. The XAFS is due to the chemical and physical state of the absorbing atom. XAFS spectra are especially sensitive to the formal oxidation state, coordination chemistry, and the distances, coordination number and species of the atoms immediately surrounding the selected element. Because of this sensitivity, XAFS provides a practical and relatively simple way to determine the chemical state and local atomic structure for a selected atomic species, and is used routinely in a wide range of scientific fields, including biology, environmental science, catalysts research, and material science. Since XAFS is an atomic probe, there are few constraints on the form of the samples that can be studied, and it can be used in a variety of systems and sample environments.

All atoms have core level electrons, and XAFS spectra can be measured for essentially every element on the periodic table. Importantly, crystallinity is not required for XAFS measurements, making it one of the few structural probes available for noncrystalline and highly disordered materials, including ions dissolved in solutions. Because X-rays are fairly penetrating in matter, XAFS is not inherently surface-sensitive, though special measurement techniques can be applied to enhance its surface sensitivity. Intense X-ray sources can make

1529-6466/14/0078-0002$05.00 http://dx.doi.org/10.2138/rmg.2014.78.2

EBSCOhost - printed on 2/13/2023 5:26 AM via . All use subject to https://www.ebsco.com/terms-of-use

very small beams, allowing XAFS to be done on samples as small as a few square microns. In addition, many variations on experimental techniques and sample conditions are available for XAFS, including *in situ* chemical processes and extreme conditions of temperature and pressure. XAFS measurements can be made on elements of minority and even trace abundance in many systems, giving a unique and direct measurement of chemical and physical state of dilute species in a variety of systems.

X-ray absorption measurements are relatively straightforward, provided one has an intense and energy-tunable source of X-rays. In practice, this usually means the use of synchrotron radiation, and the history and development of XAFS closely parallels that of synchrotron sources. Since the characteristics of synchrotron sources and experimental station dictate what energy ranges, beam sizes, and intensities are available, this often puts practical experimental limits on the XAFS measurements that can be done at a particular station, even if there are few inherent limits on the XAFS technique itself.

Though XAFS measurements can be straightforward, a complete understanding of XAFS involves a wonderful mixture of modern physics and chemistry and a complete mastery of the data analysis can be somewhat challenging. Though the basic phenomena is well-understood, an accurate theoretical treatment is fairly involved and, in some respects still an area of active research. The interpretation and analysis of XAFS is not always straightforward, though significant progress has been made in both the theoretical and analytical tools for XAFS in the past few decades. Accurate and precise interpretation of XAFS spectra is routine, if not always trivial for novice experimentalists.

The X-ray absorption spectrum is typically divided into two regimes: X-ray absorption near-edge spectroscopy (XANES) and extended X-ray absorption fine-structure spectroscopy (EXAFS). Though the two have the same physical origin, this distinction is convenient for the interpretation. XANES is strongly sensitive to formal oxidation state and coordination chemistry (e.g., octahedral, tetrahedral coordination) of the absorbing atom, while the EXAFS can be used to determine the distances, coordination number, and species of the neighbors of the absorbing atom.

XAFS is a mature technique, with a literature spanning many decades and many disciplines. As a result, several books (Teo 1986; Koningsberger and Prins 1988; Bunker 2010; Calvin 2013) have been written specifically about XAFS, and one book on X-ray physics (Als-Nielsen and McMorrow 2001) covers XAFS in some detail. There have been many chapters and review articles written about XAFS, including early reviews of the fledgling technique (Stern and Heald 1983), complete theoretical treatments (Rehr and Albers 2000), and reviews focusing on applications in a variety of fields, including mineralogy (Brown et al. 1988) and soil science (Kelly et al. 2008). Earlier review articles on applications of synchrotron techniques in geochemistry and environmental science (Manceau et al. 2002; Sutton et al. 2002) also contain considerable information about XAFS. In addition, several on-line resources (XAFS.ORG 2003; IXAS 2012) have lengthy tutorials and links to software packages and documentation for XAFS. It is not possible or particularly useful to give a full review of the XAFS literature, even restricting to a single field such as geochemistry or mineralogy.

In this work, the origins and interpretations of XAFS will be introduced, with a hope of aiding the reader to be able to make high-quality XAFS measurements as well as process and analyze the data. The emphasis here is particularly on the processing and analysis of the extended oscillations of the XAFS spectra, as the near-edge portion of the spectra is covered in more detail elsewhere. This chapter will not make one an expert in XAFS, but it should provide a firm foundation for a new practitioner of XAFS. The above citations are all strongly recommended reading for further insights and different perspectives and emphasis. The reader is not expected to have previous experience with XAFS or X-ray measurements, but some

EBSCOhost - printed on 2/13/2023 5:26 AM via . All use subject to https://www.ebsco.com/terms-of-use

familiarity with advanced undergraduate-level chemistry or physics and a knowledge of experimental practices and data interpretation will be helpful.

X-RAY ABSORPTION AND FLUORESCENCE

X-rays are light with energies ranging from about 500 eV to 500 keV, or wavelengths from about 25 Å to 0.25 Å. In this energy regime, light is absorbed by all matter through the *photoelectric effect*, in which an X-ray photon is absorbed by an electron in a tightly bound quantum core level (such as the 1*s* or 2*p* level) of an atom, as shown in Figure 1.

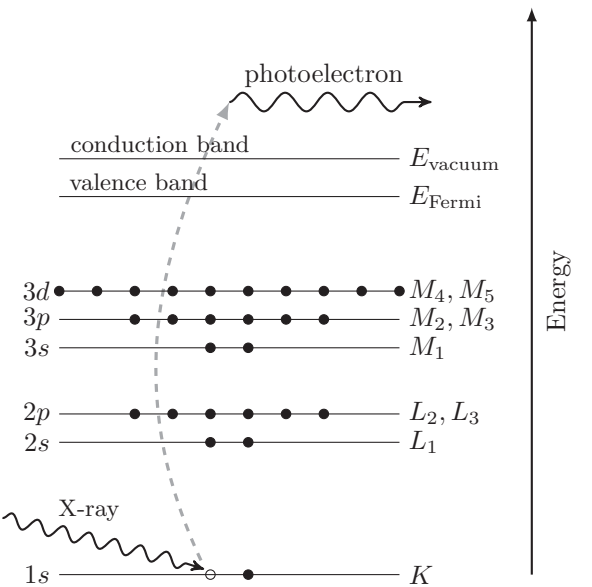


Figure 1. The photoelectric effect, in which an X-ray is absorbed by an atom and a core-level electron is promoted out of the atom, creating a photoelectron and leaving behind a hole in the core electron level.

In order for a particular electronic core level to absorb the X-ray, its binding energy must be less than the energy of the incident X-ray. If the binding energy is greater than the energy of the X-ray, the bound electron will not be perturbed from the well-defined quantum state and will not absorb the X-ray. If the binding energy of the electron is less than that of the X-ray, the electron may be removed from its quantum level. In this case, the X-ray is destroyed (that is, absorbed) and any energy in excess of the electronic binding energy is given to a photoelectron that is ejected from the atom. This process has been well understood for more than a century (Einstein received the Nobel Prize for describing this effect). As we will see, the full implications of this process when applied to molecules, liquids, and solids will give rise to XAFS.

When discussing X-ray absorption, we are primarily concerned with the *absorption coefficient*, μ which gives the probability that X-rays will be absorbed according to the Beer-Lambert Law:

$$I = I_0 e^{-\mu t} \tag{1}$$

where I_0 is the X-ray intensity incident on a sample, t is the sample thickness, and I is the

EBSCOhost - printed on 2/13/2023 5:26 AM via . All use subject to https://www.ebsco.com/terms-of-use

intensity transmitted through the sample, as shown in Figure 2. For X-rays of sufficiently low intensity, the X-ray intensity is proportional to the number of X-ray photons—we will ignore any non-linear or strong field effects here, and consider only the case of absorption by an otherwise unperturbed atom.

At most X-ray energies, the absorption coefficient μ is a smooth function of energy, with a value that depends on the sample density ρ, the atomic number Z, atomic mass A, and the X-ray energy E roughly as

$$\mu \approx \frac{\rho Z^4}{AE^3} \tag{2}$$

The strong dependence of μ on both Z and E is a fundamental property of X-rays, and is the key to why X-ray absorption is useful for medical and other imaging techniques such as X-ray computed tomography. Figure 3 shows the energy-dependence of μ/ρ described in Equation (2) for O, Fe, Cd, and Pb in the normal X-ray regime of 1 to 100 keV. The values span several orders of magnitude, so that good contrast between different materials can be achieved for nearly any sample thickness and concentrations by adjusting the X-ray energy.

When the incident X-ray has an energy equal to that of the binding energy of a core-level electron, there is a sharp rise in absorption: an *absorption edge* corresponding to the promotion of the core level to the continuum. For XAFS, we are concerned with the energy dependence of μ at energies near and just above these absorption edges. An XAFS measurement is then simply a measure of the energy dependence of μat and above the binding energy of a known core level of a known atomic species. Since every atom has core-level electrons with well-defined binding energies, we can select the element to probe by tuning the X-ray energy to an appropriate absorption edge. These absorption edge energies are well-known (usually to within a tenth of percent),

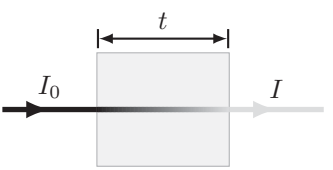


Figure 2. X-ray absorption and the Beer-Lambert law: An incident beam of monochromatic X-rays of intensity I_0 passes through a sample of thickness t, and the transmitted beam has intensity I. The absorption coefficient μ is given by the Beer-Lambert law, $I = I_0 e^{-\mu t}$.

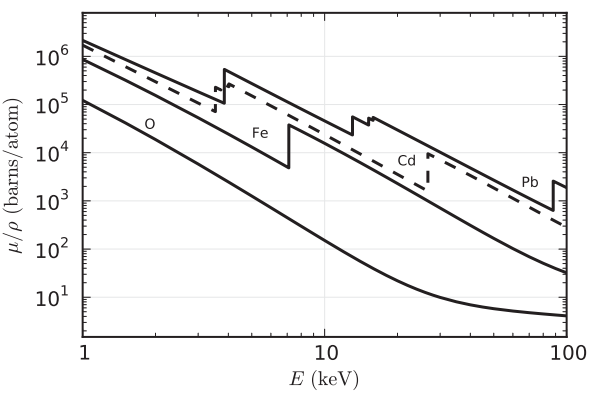


Figure 3. The absorption cross-section μ/ρ for several elements over the X-ray energy range of 1 to 100 keV. Notice that there are at least 5 orders of magnitude in variation in μ/ρ, and that in addition to the strong energy dependence, there are also sharp jumps in cross-section corresponding to the core-level binding energies of the atoms.

EBSCOhost - printed on 2/13/2023 5:26 AM via . All use subject to https://www.ebsco.com/terms-of-use

and tabulated. The edge energies vary with atomic number approximately as Z^2, and both *K* and *L* levels can be used in the hard X-ray regime (in addition, *M* edges can be used for heavy elements in the soft X-ray regime), which allows most elements to be probed by XAFS with X-ray energies between 4 and 35 keV, as shown in Figure 4. Because a particular absorption edge of the element of interest is chosen in the experiment, XAFS is *element-specific*.

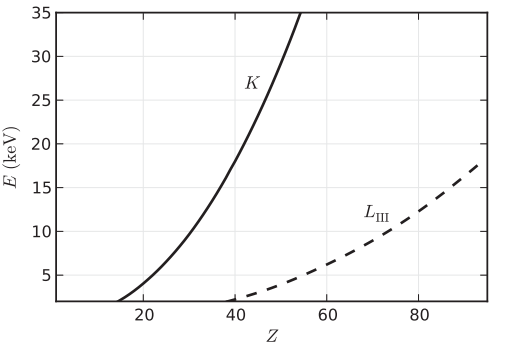


Figure 4. The energies for the X-ray *K* and L_{III} absorption edges as a function of atomic number *Z*. The energies follow $E \sim Z^2$, and all elements with $Z > 20$ have an X-ray edge above 4 keV.

Following an absorption event, the atom is said to be in an *excited state*, with one of the core electron levels left empty (a so-called *core hole*), and a *photoelectron* emitted from the atom. The excited state will eventually decay (typically within a few femtoseconds) of the absorption event. Though this decay does not affect the X-ray absorption process, it is important for the discussion below.

There are two main mechanisms for the decay of the excited atomic state following an X-ray absorption event, as shown in Figure 5. The first of these is X-ray fluorescence, in which a higher energy electron core-level electron fills the deeper core hole, ejecting an X-ray of well-defined energy. The fluorescence energies emitted in this way are characteristic of the atom, and can be used to identify the atoms in a system, and to quantify their concentrations. For example, an *L* shell electron dropping into the *K* level gives the K_α fluorescence line.

The second process for de-excitation of the core hole is the Auger effect, in which an electron drops from a higher electron level and a second electron is emitted into the continuum

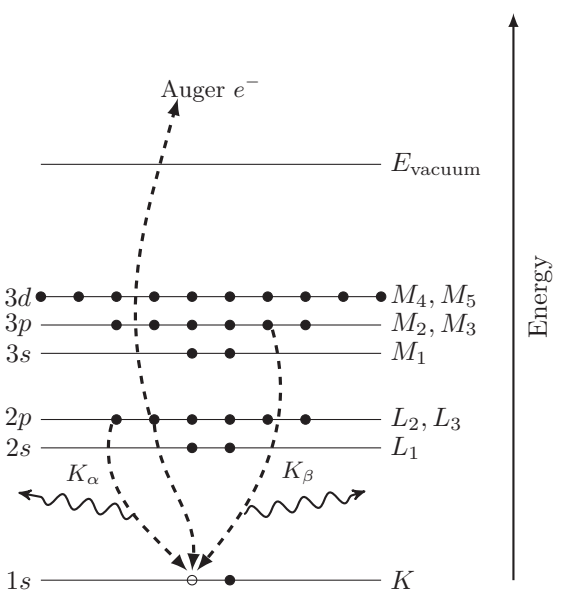


Figure 5. The excited atomic state will decay by either X-ray fluorescence or the Auger effect. In either case, an electron is moved from a less tightly bound orbital to the empty core level, and the energy difference between these levels is given to the emitted particle (X-ray or electron). The emission energies have precise values that are characteristic for each atom, and can be used to identify the absorbing atom. Though the probability of whether the decay occurs by fluorescence or Auger emission depends on the atomic number *Z* and energy-level, the probability of emission is directly proportional to the absorption probability, and so can be used to measure EXAFS and XANES.

EBSCOhost - printed on 2/13/2023 5:26 AM via . All use subject to https://www.ebsco.com/terms-of-use

(and possibly even out of the sample). In either case, a cascade of subsequent emissions will fill the newly formed, less tightly bound hole until the atom is fully relaxed. Either of these processes can be used to measure the absorption coefficient μ, though the use of fluorescence is somewhat more common. In the hard X-ray regime (> 10 keV), X-ray fluorescence is more likely to occur than Auger emission, but for lower energies Auger emission dominates.

XAFS can be measured in two different modes. In transmission mode, the intensity of an X-ray beam is sampled before and after being transmitted through a sample, as shown in Figure 2. In fluorescence mode, a secondary emission resulting from the absorption of the X-ray is measured, such as X-ray fluorescence or Auger electrons just mentioned, or in some cases even by monitoring visible light emitted by a sample as part of the cascade of decay events. We will return to the details of the measurements later, but for now it is enough to say that we can measure the energy dependence of the X-ray absorption coefficient μ(*E*) either in transmission mode as

$$\mu(E) = \ln\left(\frac{I_0}{I}\right)$$

or in fluorescence (or emission) mode as

$$\mu(E) \propto \frac{I_f}{I_0}$$

where I_f is the monitored intensity of a fluorescence line (or electron emission) associated with the absorption process.

A typical XAFS spectrum (measured in the transmission geometry for a powder of FeO) is shown in Figure 6. The sharp rise in μ(*E*) due to the Fe 1s electron level (near 7112 eV) is clearly visible in the spectrum, as are the oscillations in μ(*E*) that continue well past the edge. As mentioned in the introduction, the XAFS is generally thought of in two distinct portions: the near-edge spectra (XANES)—typically within 30 eV of the main absorption edge, and the extended fine-structure (EXAFS), which can continue for a few keV past the edge. As we shall see, the basic physical description of these two regimes is the same, but some important approximations and limits allow us to interpret the extended portion of the spectrum in a simpler and more quantitative way than is currently possible for the near-edge spectra.

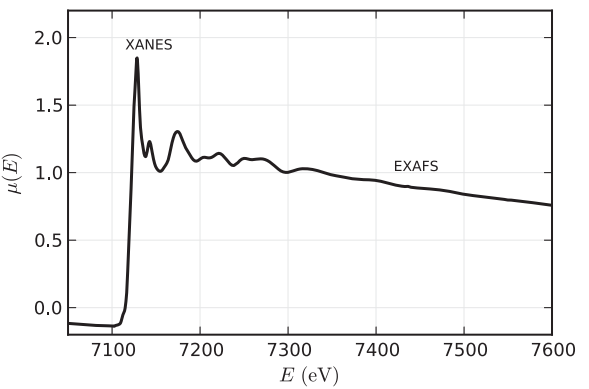


Figure 6. XAFS μ(E) for the Fe K edge of FeO, showing the near-edge (XANES) region and the extended fine structure (EXAFS).

EBSCOhost - printed on 2/13/2023 5:26 AM via . All use subject to https://www.ebsco.com/terms-of-use

For the EXAFS, we are interested in the oscillations well above the absorption edge, and define the EXAFS fine-structure function $\chi(E)$ as a change to $\mu(E)$, as

$$\mu(E) = \mu_0(E)\left[1 + \chi(E)\right] \tag{3}$$

where $\mu(E)$ is the measured absorption coefficient, $\mu_0(E)$ is a smooth background function representing the absorption of an isolated atom. The isolated XAFS is usually written as

$$\chi(E) = \frac{\mu(E) - \mu_0(E)}{\Delta\mu} \tag{4}$$

where $\Delta\mu$ is the measured jump in the absorption $\mu(E)$ at the threshold energy. Note that, due primarily to experimental considerations, XAFS is generally normalized by the energy-independent edge jump rather than an energy-dependent $\mu_0(E)$.

As we will see, EXAFS is best understood in terms of the wave behavior of the photoelectron created in the absorption process. Because of this, it is common to convert the X-ray energy to k, the wave number of the photoelectron, which has dimensions of 1/distance and is defined as

$$k = \sqrt{\frac{2m(E - E_0)}{\hbar^2}} \tag{5}$$

where E_0 is the absorption edge energy, m is the electron mass, and $\hbar$ is Planck's constant. The primary quantity for EXAFS is then $\chi(k)$, the isolated variation in absorption coefficient as a function of photoelectron wave number, and $\chi(k)$ is often referred to simply as "the EXAFS." The EXAFS extracted from the Fe *K*-edge for FeO is shown in Figure 7 (left). The EXAFS is clearly oscillatory, and also decays quickly with k. To emphasize the oscillations, $\chi(k)$ is often multiplied by a power of k typically k^2 or k^3 for display, as is done for the plot in Figure 7.

The different frequencies apparent in the oscillations in $\chi(k)$ correspond to different near-neighbor coordination shells. This can be seen most clearly by applying a Fourier transform to the data, converting the data from depending on wavenumber k to depending on distance R. As seen in the right panel of Figure 7, the oscillations present in the EXAFS $\chi(k)$ give rather well-defined peaks as a function of R. Though these peaks are not at the exact distances from the absorbing atom to its near neighbors, they are due to the neighboring atoms being at particular distances, and the values for the near neighbor distances can be accurately determined from the EXAFS oscillations.

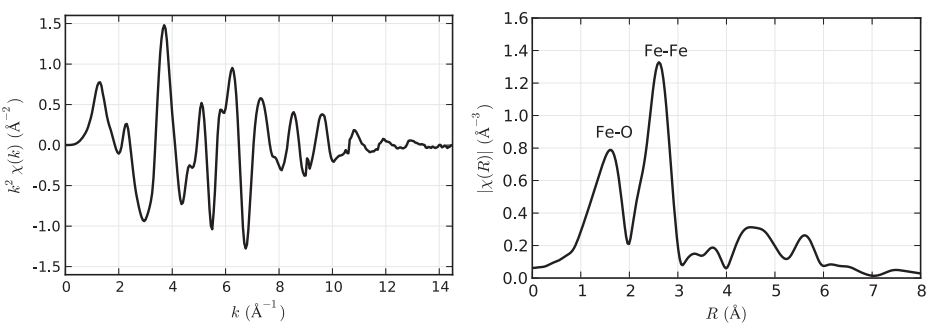


Figure 7. Isolated EXAFS for the Fe K edge of FeO, shown weighted by k^2 (*left*) to emphasize the high-k portion of the spectrum, and the Fourier transform of the k-weighted XAFS, $\chi(R)$ (*right*), showing the contribution from Fe-O and Fe-Fe neighbors.

EBSCOhost - printed on 2/13/2023 5:26 AM via . All use subject to https://www.ebsco.com/terms-of-use

A remarkable feature of EXAFS is that the contributions to the EXAFS from scattering from different neighboring atoms can be described by a relatively straightforward *EXAFS Equation*, a simplified form of which is

$$\chi(k) = \sum_j \frac{N_j f_j(k) e^{-2k^2\sigma_j^2}}{kR_j^{\,2}} \sin\left[2kR_j + \delta_j(k)\right]$$

Here $f(k)$ and $\delta(k)$ are scattering properties of the photoelectron emitted in the absorption process by the atoms neighboring the excited atom, N is the number of neighboring atoms, R is the distance to the neighboring atom, and σ^2 is the disorder in the neighbor distance. Though slightly complicated, the EXAFS equation is simple enough to enable us to model EXAFS data reliably, and so determine N, R, and σ^2 once we know the scattering amplitude $f(k)$ and phase-shifts $\delta(k)$. Furthermore, because these scattering factors depend on the Z of the neighboring atom, EXAFS is also sensitive to the atomic species of the neighboring atom.

A SIMPLE THEORETICAL DESCRIPTION OF XAFS

In this section, a simple physical description of the XAFS process and the origin of the EXAFS Equation will be given. Other useful treatments on a similar level can be found in other places (Stern 1988; Rehr and Albers 2000) as well. As in the previous section, we start with the photoelectric effect, now shown in Figure 8, in which an X-ray of energy E is absorbed by a core-level electron of a particular atom with binding energy E_0. Any energy from the X-ray in excess of this binding energy is given to a photoelectron that propagates away from the absorbing atom. We will treat the photoelectron as a wave, noting that its wavelength is proportional to $1/\sqrt{E-E_0}$. It is most common to describe the photoelectron by its *wavenumber*, $k = 2\pi/\lambda$, given in Equation (5).

The absorption of the X-ray by the particular core electron level requires there to be an *available quantum state* for the ejected photoelectron to go to. If no suitable state is available, there will be no absorption from that core level. At X-ray energies below the 1*s* binding energy (for example, below 7.1 keV for iron) the 1*s* electron could only be promoted to a valence electron level below the Fermi level—there is simply not enough energy to put the electron into the conduction band. Since all the valence levels are filled, there is no state for the 1*s* electron to fill, and so there is no absorption from that core-level. Of course, a sample is not transparent to X-rays with energies below the 1s binding level, as the higher level electrons can be promoted into the continuum, but there is a sharp jump in the probability of absorption as the X-ray energy is increased above a core level binding energy. In fact, these binding levels are often referred to as absorption edges due to this strong increase in absorption probability.

It should be noted that the quantum state that the photoelectron occupies has not only the right energy, but also the right angular momentum. For photo-electric absorption, the angular momentum number must change by 1, so that an *s* core-level is excited into a *p* state, while a *p* core-level can be excited into either an *s* or *d* level. This is important for a detailed, quantitative description of the XAFS, but is not crucial to basic discussion of XAFS here, as we are generally dealing with energies far above the continuum which have large density of states. On the other hand, the momentum state can be extremely important when considering XANES, the near-edge portion of the spectra, as the available energy states of the unfilled anti-bonding orbitals still have well-defined and specific angular momentum states above the continuum level.

The picture above described absorption for an isolated atom. When a neighboring atom is included (Fig. 9), the photoelectron can scatter from the electrons of this neighboring atom, and some part of the scattered photoelectron can return to the absorbing atom. Of course, the

EBSCOhost - printed on 2/13/2023 5:26 AM via . All use subject to https://www.ebsco.com/terms-of-use

simple one-dimensional picture shown above suggests that the probability of scattering the photoelectron by the neighboring atom is quite large. In a real, three dimensional sample, the photoelectron wavefunction spreads radially out and has a lower probability of scattering from the electrons in the neighboring atoms. The important point is that some portion of the photoelectron wavefunction is scattered from the neighboring atom, and returns to the absorbing atom, all in a single coherent quantum state. Since the absorption coefficient depends on whether there is an available, unfilled electronic state at the location of the atom and at the

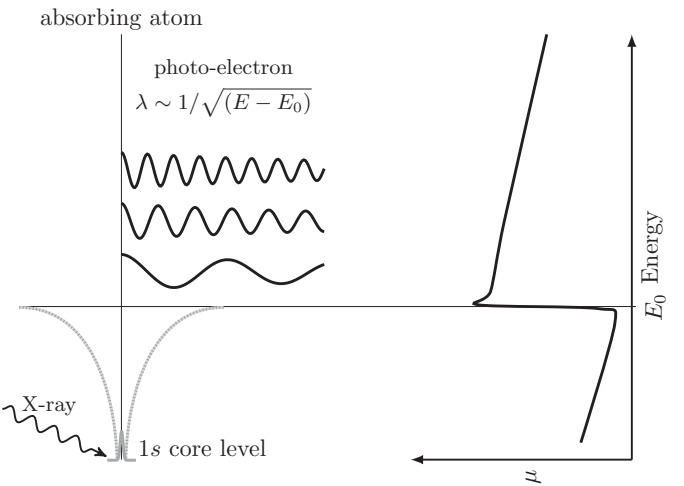


Figure 8. Cartoon of X-ray absorption through the photoelectric process. As the energy of the X-rays is increased to just above the energy of a tightly bound core electron level, E_0, the probability of absorption has a sharp rise—an edge jump. In the absorption process, the tightly bound core-level is destroyed, and a photoelectron is created. The photoelectron travels as a wave with wavelength proportional to $1/(E-E_0)^{1/2}$.

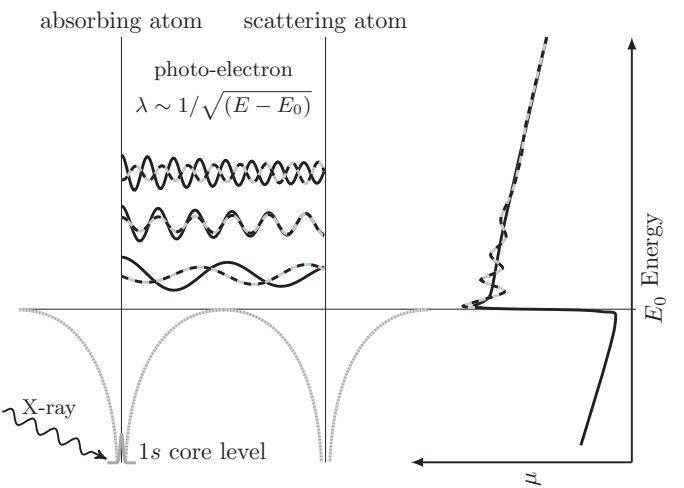


Figure 9. XAFS occurs because the photoelectron can scatter from a neighboring atom. The scattered photoelectron can return to the absorbing atom, modulating the amplitude of the photoelectron wave-function at the absorbing atom. This in turn modulates the absorption coefficient $\mu(E)$, causing the EXAFS.

EBSCOhost - printed on 2/13/2023 5:26 AM via . All use subject to https://www.ebsco.com/terms-of-use

appropriate energy (and momentum), the presence of the photoelectron scattered back from the neighboring atom will alter the absorption coefficient: This is the origin of XAFS.

A rough explanation of the EXAFS equation

We'll now spend some effort developing the standard EXAFS equation using a slightly more formal description of this simple physical picture above, but still somewhat less rigorous than a full-blown quantum mechanical description. The goal here is to describe enough of the basic physics to identify where the different components of the EXAFS equation arise from, and so what they mean for use in the analysis of spectra.

Since X-ray absorption is a *transition* between two quantum states (from an initial state with an X-ray, a core electron, and no photoelectron to a final state with no X-ray, a core hole, and a photoelectron), we describe $\mu(E)$ with Fermi's Golden Rule:

$$\mu(E) \propto \left|\langle i|H|f\rangle\right|^2 \tag{6}$$

where $\langle i|$ represents the initial state (an X-ray, a core electron, and no photoelectron), $|f\rangle$ is the final state (no X-ray, a core hole, and a photoelectron), and H is the interaction term, which we'll come back to shortly. Since the core-level electron is very tightly bound to the absorbing atom, the initial state will not be altered by the presence of the neighboring atom, at least to first approximation. The final state, on the other hand, will be affected by the neighboring atom because the photoelectron will be able to scatter from it. If we expand $|f\rangle$ into two pieces, one that is the "bare atom" portion ($|f_0\rangle$), and one that is the effect of the neighboring atom ($|f\rangle$) as

$$|f\rangle = |f_0\rangle + |\Delta f\rangle$$

We can then expand Equation (6) to

$$\mu(E) \propto \left|\langle i|H|f_0\rangle\right|^2 \left[1 + \langle i|H|\Delta f\rangle \frac{\langle f_0|H|i\rangle^*}{\left|\langle i|H|f_0\rangle\right|^2} + C.C.\right]$$

where C.C. means complex conjugate. We've arranged the terms here so that this expression resembles Equation (3),

$$\mu(E) = \mu_0(E)\left[1 + \chi(E)\right]$$

We can now assign $\mu_0 = \left|\langle i|H|f_0\rangle\right|^2$ as the "bare atom absorption," which depends only on the absorbing atom—as if the neighboring atom wasn't even there. We can also see that the fine-structure χ will be proportional to the term with $|f\rangle$:

$$\chi(E) \propto \langle i|H|\Delta f\rangle$$

which indicates that the EXAFS is due to the interaction of the scattered portion of the photoelectron and the initial absorbing atom.

We can work out this term for χ as an integral equation fairly easily, if approximately. The interaction term H represents the process of changing between two states of given energy and momentum. In quantum radiation theory, the interaction term needed is the $p{\cdot}A$ term, where A is the quantized vector potential (there is also an $A{\cdot}A$ term, but this does not contribute to absorption). For the purposes here, this reduces to a term that is proportional to e^{ikr}. The initial state is a tightly bound core-level, which we can approximate by a delta function (a 1s level for atomic number Z extends to around a_0/Z, where a_0 is the Bohr radius of ≈ 0.529 Å, so this is a good approximation for heavy elements, but less good for very light elements). The change in final state is just the wave-function of the scattered photoelectron, $\psi_{scatter}(r)$. Putting these terms together gives a simple expression for the EXAFS:

EBSCOhost - printed on 2/13/2023 5:26 AM via . All use subject to https://www.ebsco.com/terms-of-use

$$\chi(E) \propto \int dr \delta(r) e^{ikr} \psi_{\text{scatter}}(r) = \psi_{\text{scatter}}(0) \tag{7}$$

In words, this simply states the physical picture shown in Figure 9:

The EXAFS χ(*E*) is proportional to the amplitude of the scattered photoelectron at the absorbing atom.

We can now evaluate the amplitude of the scattered photoelectron at the absorbing atom to get the EXAFS equation. Using the simple physical picture from Figure 9, we can describe the outgoing photoelectron wave-function (*k*, *r*) traveling as a spherical wave,

$$\psi(k,r) = \frac{e^{ikr}}{kr} \tag{8}$$

traveling a distance *R* to the neighboring atom, then scattering from a neighbor atom, and traveling as a spherical wave a distance *R* back to the absorbing atom. We simply multiply all these factors together to get

$$\chi(k) \propto \psi_{\text{scatter}}(k, r=0) = \frac{e^{ikR}}{kR}\left[2kf(k)e^{i\delta(k)}\right]\frac{e^{ikR}}{kR} + C.C.$$

where $f(k)$ and $\delta(k)$ are scattering properties of the neighboring atom, and C.C. means complex conjugate. As mentioned before, these scattering factors depend on the *Z* of the neighboring atom, as illustrated in Figure 10 for a few elements. Combining these terms in and using the complex conjugate to make sure we end up with a real function, we get

$$\chi(k) = \frac{f(k)}{kR^2}\sin\left[2kR + \delta(k)\right] \tag{9}$$

which looks much like the standard EXAFS equation. For mathematical convenience, the EXAFS Equation is sometimes written with the sin term replaced with the imaginary part of an exponential:

$$\chi(k) = \frac{f(k)}{kR^2}\text{Im}\left\{e^{i\left[2kR+\delta(k)\right]}\right\}$$

We'll use this form on occasion.

The treatment to get to Equation (9) was for one pair of absorbing atom and scattering atom, but for a real measurement we'll average over billions of X-ray absorption events and so atom pairs. Even for neighboring atoms of the same type, the thermal and static disorder in the bond distances will give a range of distances that will affect the XAFS. As a first approximation, the bonding environment and disorder will change the XAFS equation from Equation (9) to

$$\chi(k) = \frac{Nf(k)e^{-2k^2\sigma^2}}{kR^2}\sin\left[2kR + \delta(k)\right]$$

where *N* is the coordination number and σ^2 is the mean-square-displacement in the bond distance *R*. We'll return to this topic later.

Of course, real systems usually have more than one type of neighboring atom around a particular absorbing atom. This is easily accommodated in the XAFS formalism, as the measured XAFS will simply be a sum of the contributions from each scattering atom type or *coordination shell*:

$$\chi(k) = \sum_j \frac{N_j f_j(k) e^{-2k^2\sigma_j^2}}{kR_j^{\,2}}\sin\left[2kR_j + \delta_j(k)\right]$$

EBSCOhost - printed on 2/13/2023 5:26 AM via . All use subject to https://www.ebsco.com/terms-of-use

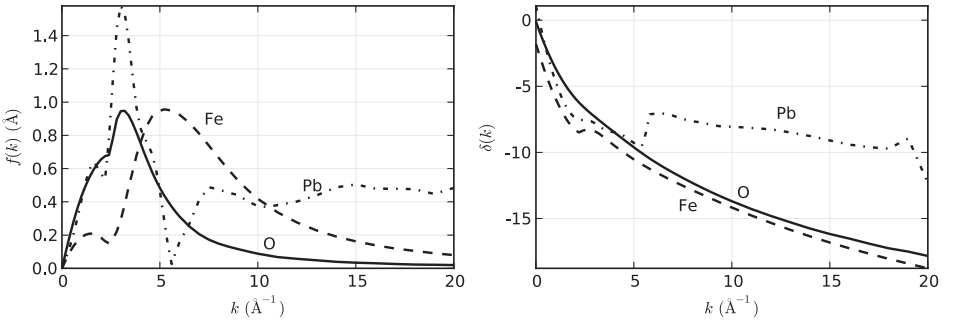


Figure 10. Functional forms for $f(k)$ (left) and $\delta(k)$ (right) for O, Fe, and Pb showing the dependence of these terms on atomic number Z. The variations in functional form allow Z to be determined (±5 or so) from analysis of the EXAFS.

where j represents the individual coordination shell of identical atoms at approximately the same distance from the central atom. In principle there can be many such shells, but as shells of similar Z become close enough (say, within a 0.05 Å of each other), they become difficult to distinguish from one another.

The explanation so far of what goes into the EXAFS equation gives the most salient features of the physical picture for EXAFS but ignores many nuances. In order to be able to quantitatively analyze EXAFS in real systems, we'll need to cover some of these subtleties, giving four main points to discuss. These are 1) the finite photoelectron mean free path, 2) the relaxation due to the passive (non-core) electrons of the excited atom, 3) multiple-scattering of the photoelectron, and 4) a more detailed treatment of structural and thermal disorder.

λ(*k*): The inelastic mean free path

The most significant approximation we made above was to assert that the outgoing photoelectron went out as a spherical wave, as given in Equation (8). In doing so, we neglected the fact that the photoelectron can also scatter *inelastically* from other sources—other conduction electrons, phonons, and so on. In order to participate in the XAFS, the photoelectron has to scatter from the neighboring atom and return to the absorbing atom *elastically* (that is, at the same energy) as the outgoing photoelectron. In addition, the scattered portion of the photoelectron has to make it back to the absorbing atom before the excited state decays (that is, before the core hole is filled through the Auger or fluorescence process). To account for both the inelastic scattering and the finite *core-hole lifetime*, we can use a damped spherical wave:

$$\psi(k,r) = \frac{e^{ikr}e^{-r/\lambda(k)}}{kr}$$

for the photoelectron wave-function in place of the spherical wave of Equation (8). Here, λ is the *mean free path* of the photoelectron, representing how far it can typically travel before scattering inelastically or before the core hole is filled. The core-hole lifetime is on the order of 10^{-15} s, depending somewhat on the energy of the core-level. The mean free path is typically 5 to 30 Å and varies with k with a fairly universal dependence on k, shown in Figure 11. Including this $\lambda(k)$, the EXAFS equation becomes

$$\chi(k) = \sum_j \frac{N_j f_j(k) e^{-2R_j/\lambda(k)} e^{-2k^2\sigma_j^2}}{kR_j^{\,2}} \sin\left[2kR_j + \delta_j(k)\right]$$

It is the finite size of λ, as well as the $1/R^2$ term (which also originates from the wavefunction

EBSCOhost - printed on 2/13/2023 5:26 AM via . All use subject to https://www.ebsco.com/terms-of-use

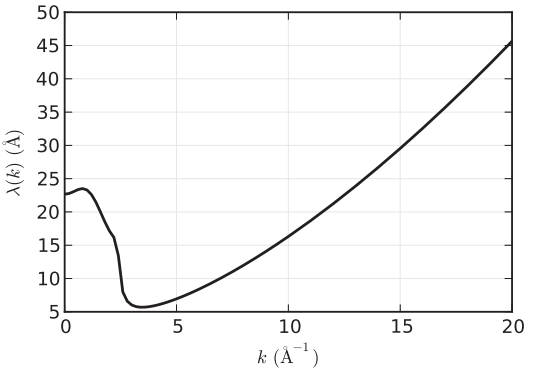


Figure 11. The photoelectron mean free path for XAFS, $\lambda(k)$, representing how far the photoelectron can travel and still participate in the XAFS. This term accounts for both the inelastic scattering of the photoelectron, and the finite lifetime of the core-hole.

of the outgoing photoelectron) in the EXAFS equation that shows EXAFS to be a local probe, insensitive to atomic structure beyond 10 Å or so.

As an aside, we note that it is possible to treat the losses that are described by $\lambda(k)$ as a complex wavenumber, so that k becomes $p = k + i/\lambda$, and the EXAFS Equation can be written with p instead of k. This reflects the common usage in the theoretical condensed matter physics literature that the photoelectron energy is complex, and so includes the effects of the mean free path not only in a $e^{-2R/\lambda}$ term, but also in the disorder terms, which can be important in some analyses. This can be incorporated into quantitative analysis tools, but is beyond the scope of the present work, so we will continue to use the form of the EXAFS Equation above, with the explicit λ term.

S_0^2: intrinsic losses

A second approximation we made in the description above was to ignore the relaxation due to the other electrons in the excited atom. That is, our "initial state" and "final state" above should have been for the entire atom, but we considered only a single core-level electron. Writing $\left|\Phi_0^{Z-1}\right\rangle$ for the remaining $Z-1$ electrons in unexcited atom, and $\left\langle\Phi_f^{Z-1}\right|$ for the $Z-1$ electrons in the excited atoms, we end up with a factor of

$$S_0^2 = \left|\left\langle\Phi_f^{Z-1}\middle|\Phi_0^{Z-1}\right\rangle\right|^2$$

that can be placed in front of the EXAFS equation. Though recent research has suggested that S_0^2 may have some k dependence, especially at low k, it is usually interpreted simply as a constant value, so that the EXAFS equation becomes

$$\chi(k) = \sum_j \frac{S_0^2 N_j f_j(k) e^{-2R_j/\lambda(k)} e^{-2k^2\sigma_j^2}}{kR_j^{\,2}} \sin\left[2kR_j + \delta_j(k)\right] \tag{10}$$

which is the final form of the EXAFS equation that we will use for analysis.

S_0^2 is assumed to be constant, and is generally found to be $0.7 < S_0^2 < 1.0$. By far the biggest consequence of this is that this factor is *completely correlated with N* in the EXAFS equation. This fact, along with the data reduction complication discussed later that the edge step $\Delta\mu$ in Equation (4) is challenging to determine experimentally, makes absolute values for the coordination number N difficult to determine with high accuracy.

EBSCOhost - printed on 2/13/2023 5:26 AM via . All use subject to https://www.ebsco.com/terms-of-use

Multiple scattering of the photoelectron

So far the treatment of EXAFS has implied that the photoelectron always scatters from one neighboring atom and returns to the absorber. In fact, the photoelectron can scatter from more than one neighboring atom, making a more convoluted *scattering path* than simply to one scattering atom and back. Examples of the more important types of multiple scattering paths are illustrated in Figure 12.

Multiple scattering paths can give important contributions for EXAFS, especially beyond the first coordination shell, and are often important for XANES. In general, most first-shell analysis of EXAFS is not strongly affected by multiple scattering, but second-shell analysis can be, and shells beyond the second are almost always complicated by multiple-scattering paths. For highly-ordered crystalline materials, focused linear multiple scattering paths, as shown Figure 12 can be particularly important, and neglecting them in an analysis can give erroneous results.

Though the details of the calculations are beyond the scope of this work (Rehr and Albers 2000), accounting for multiple scattering formally in the EXAFS equation is conceptually quite easy. We can simply change the meaning of the sum in Equation (10) to be a sum over *scattering paths*, including multiple scattering paths, instead of being a sum over coordination shells. We also have to change our interpretation of R from "interatomic distance" to "half path length." In addition, our scattering amplitudes $f(k)$ and phase-shifts $\delta(k)$ now need to include the contribution from each scattering atom in the path, so that the term in the EXAFS equation can be said to be *effective* scattering amplitudes and phase-shifts. Unfortunately, the existence of multiple scattering means that the number of paths needed to properly account for an EXAFS spectra grows quickly (exponentially) with path distance. This puts a practical limit on our ability to fully interpret EXAFS spectra from completely unknown systems.

Disorder terms and $g(R)$

We gave a simple description of disorder above, using $Ne^{-2k^2\sigma^2}$ in the EXAFS equation, where N is the coordination number and σ^2 is the mean-square displacement of the set of

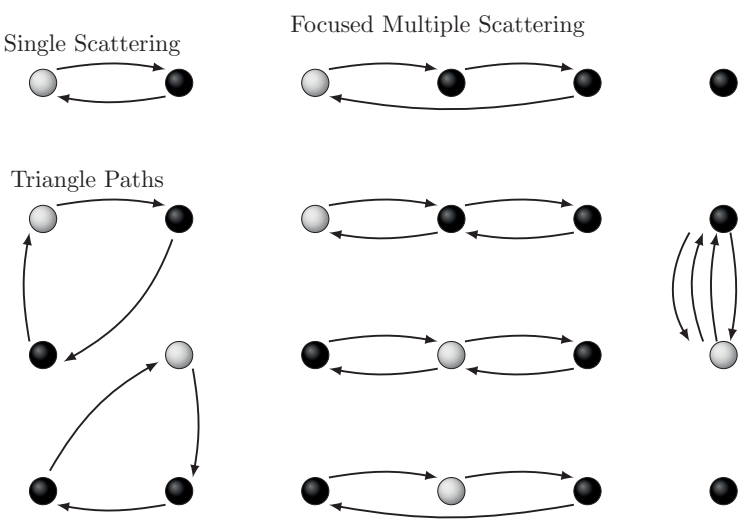


Figure 12. Multiple scattering paths for the photoelectron. While single-scattering paths generally dominate most EXAFS spectra, multiple scattering paths can give important contributions, especially in well-ordered crystalline materials. Fortunately, these terms can easily be included into the standard EXAFS formalism.

EBSCOhost - printed on 2/13/2023 5:26 AM via . All use subject to https://www.ebsco.com/terms-of-use

interatomic distances R sampled by an EXAFS measurement. As noted above, the core-hole lifetime is typically in the femtosecond range. Since thermal vibrations are on the picosecond time-scale, each X-ray absorbed in an EXAFS measurement gives a "snapshot" of the structure around 1 randomly selected absorbing atom in the sample, and the neighboring atoms will be essentially frozen in some configuration. Building up a full spectrum will result in a "blurry picture" due to the addition of many (often billions) of these snapshots. This has the important consequence that a single EXAFS measurement cannot distinguish thermal disorder due to atomic vibrations from static disorder.

An EXAFS measurement is then a *sampling* of the configuration of atoms around the average absorbing atom. Ignoring the contributions from multiple-scattering just discussed, the configuration of pairs of atoms is given by the Partial Pair Distribution function, $g(R)$, which gives the probability that an atom is found a distance R away from an atom of the selected type. Pair distribution functions are found from many structural probes (notably scattering techniques), but the Partial aspect is unique to EXAFS and other element-specific probes. EXAFS is sensitive only to the pairs of atoms that include the absorbing atom. Thus while scattering can give very accurate measures of the total pair distribution function, EXAFS is particularly useful for looking at low concentration elements in complex systems.

To better account for the sampling of $g(R)$ of any particular single-scattering shell of atoms, we should replace our σ^2 term with an integral over *all* absorbing atoms, as with (using a simplified form of the EXAFS Equation in exponential notation and recalling that k might be replaced by p, the complex wavenumber to account for the mean free path $\lambda(k)$):

$$\chi(k) = \left\langle \sum_j \frac{f_j(k) e^{i2kR_j + i\delta_j(k)}}{kR_j^2} \right\rangle$$

where the angle brackets mean averaging over the distribution function:

$$\langle x \rangle = \frac{\int dR\ x\ g(R)}{\int dR\ g(R)}$$

There are a few different approaches that can be used for modeling $g(R)$ in EXAFS. First, one can ask what the principal moments of $g(R)$ might be. Recognizing that e^{i2kR} term (or $\sin(2kR)$ term) is the most sensitive part to small changes in R, and pulling out the other terms, we have

$$\chi(k) = \sum_j f_j(k) \frac{e^{i\delta_j(k)}}{kR_j^2} \left\langle e^{i2kR_j} \right\rangle$$

This average of an exponential term can be described by the *cumulants* of the distribution $g(R)$, as

$$\left\langle e^{i2kR} \right\rangle = \exp\left[\sum_{n=1}^{\infty} \frac{(2ik)^n}{n!} C_n \right]$$

where the coefficients C_n are the cumulants. The cumulants of a distribution can be related to the more familiar moments of the distribution. The lowest order cumulants are

$$\begin{aligned}
C_1 &= \langle r \rangle \\
C_2 &= \langle r^2 \rangle - \langle r \rangle^2 \\
C_3 &= \langle r^3 \rangle - 3\langle r^2 \rangle \langle r \rangle + 2\langle r \rangle^3 \\
C_4 &= \langle r^4 \rangle - 3\langle r^2 \rangle^2 - 4\langle r^3 \rangle \langle r \rangle + 12\langle r^2 \rangle \langle r \rangle^2 - 6\langle r \rangle^4
\end{aligned}$$

EBSCOhost - printed on 2/13/2023 5:26 AM via . All use subject to https://www.ebsco.com/terms-of-use

where $r = R - R_0$ and R_0 is the mean R value of the distribution, and $\langle r^n \rangle$ is the n^{th} moment of the distribution. C_1 is then simply a shift in centroid, and C_2 is the mean-square-displacement, σ^2. C_3 and C_4 measure the skewness and kurtosis for the distribution, respectively, and are 0 for a Gaussian distribution. Because the low order terms in the cumulant expansion represent a small modification to the Gaussian approximation and can be readily applied to any spectrum, they are included in many analyses codes and discussed widely in the EXAFS literature. In particular, the skewness term, C_3, is sometimes found to be important in analysis of moderately disordered systems.

Another approach to modeling complex disorder is to parameterize $g(R)$ by some functional form and use this parameterization in the EXAFS Equation. This can be done either analytically by putting in a functional form for $g(R)$ (Filipponi et al. 1995), or by building a histogram with weights given by the parameterized $g(R)$. The latter approach can be readily done with many existing analysis tools, and can give noticeably better results than the cumulant expansion for very high disorder. For some problems, a more sophisticated analysis using a *Monte Carlo* approach of calculating the EXAFS for a large set of atomic clusters can be useful. For example, atomic configurations from a series of molecular dynamics simulations may be used to predict EXAFS spectra including complex configurations and disorder. Such work can be computationally intensive, but can also give additional insight into the interactions between atoms and molecules in complex systems. We'll continue to use N and σ^2 as the normal form of the EXAFS Equation, but will remember that these more complex descriptions of the distribution of atoms are possible and that we are not limited to studying well-behaved systems with Gaussian distributions.

Discussion

We've used a simple physical picture of photoelectron scattering to develop the EXAFS equation (Eqn. 10) that we can use in the quantitative analysis of EXAFS spectra. From Equation (10), we can draw a few physical conclusions about XAFS. First, because of the $\lambda(k)$ term and the R^{-2} term, XAFS is seen to be an inherently *local probe*, not able to see much further than 5 Å or so from the absorbing atom. Second, the XAFS oscillations consist of different frequencies that correspond to the different distances of atomic shells. This will lead us to use Fourier transforms in the analysis. Finally, in order to extract the distances and coordination numbers, we need to have accurate values for the scattering amplitude and phase-shifts $f(k)$ and $\delta(k)$ from the neighboring atoms.

This last point here—the need for accurate scattering amplitude and phase-shifts—has been a crucial issue in the field of EXAFS. Though early attempts to calculate the terms were qualitatively successful and instructive, they were generally not accurate enough to be used in analysis. In the earliest EXAFS analyses, these factors were most often determined from experimental spectra in which the near-neighbor distances and species were known. Such experimental standards can be quite accurate, but are generally restricted to first neighbor shell and to single-scattering. Since the 1990s, calculations of $f(k)$ and $\delta(k)$ have become more accurate and readily available, and use of experimental standards in EXAFS analysis is now somewhat rare, and restricted to studies of small changes in distances of fairly well-characterized systems. Calculated scattering factors are not without problems, but they have been shown numerous times to be accurate enough to be used in real analysis, and in some cases are more accurate than experimentally derived scattering factors. The calculated factors are not restricted to the first shell, and can easily account for multiple-scattering of the photoelectron. We'll use calculations of $f(k)$ and $\delta(k)$ from FEFF to model real data.

EBSCOhost - printed on 2/13/2023 5:26 AM via . All use subject to https://www.ebsco.com/terms-of-use

XAFS MEASUREMENTS: TRANSMISSION AND FLUORESCENCE

XAFS requires a very good measure of $\mu(E)$. Since the XAFS is a fairly small modulation of the total absorption, a fairly precise and accurate measurement of $\mu(E)$—typically to 10^{-3}—is required. Statistical errors in $\mu(E)$ due to insufficient count rates in intensities are rarely the limiting factor for most XAFS measurements, and can generally be overcome by counting longer. On the other hand, systematic errors in $\mu(E)$ can degrade or even destroy the XAFS, and are more difficult to eliminate. Fortunately, if care is taken in sample preparation, setting up the measurement system, and alignment of the sample in the beam, it is usually not too difficult to get good XAFS measurements.

A sketch of the basic experimental layout is given in Figure 13, showing a monochromatic beam of X-rays striking a sample and the intensities of the incident, transmitted, and emitted X-ray beams being measured. From this, it can be seen that the main experimental challenges are getting an X-ray source that can be reliably and precisely tuned to select a single X-ray energy, and 2) high-quality detectors of X-ray intensity. For most modern experiments, the X-ray source is a synchrotron radiation source, which provides a highly collimated beam of X-rays with a broad range of energies. A particular energy is selected with a double crystal monochromator, which consists of two parallel and nearly perfect crystals, typically silicon. The first crystal is centered in the incident X-ray beam from the source and rotated to a particular angle so as to reflect a particular energy by X-ray diffraction following Bragg's law. By using near-perfect crystals, the diffracted beam is very sharply defined in angle and so also has a very narrow energy range, and the reflectivity is near unity. The second crystal, with the same lattice spacing as the first, is rotated together with the first crystal, and positioned to intercept the diffracted beam and re-diffract so that it is parallel to the original X-ray beam, though typically offset vertically from it. Such a monochromator allows a wide energy range of monochromatic X-rays to be selected simply by rotating a single axis, and is widely used at synchrotron beamlines, and especially at beamlines designed for XAFS measurements.

The principle characteristics of a monochromator that are important for XAFS are *the energy resolution*, the reproducibility, and the stability of the monochromator. Energy resolutions of ≈ 1 eV at 10 keV are readily achieved with silicon monochromators using the Si(111) reflection, and are sufficient for most XAFS measurements. Higher resolution can be achieved by using a higher order reflection, such as Si(220) or Si(311), but this often comes at a significant loss of intensity. In addition, the angular spread of the incident X-ray beam from the source can contribute to the energy resolution, and many beamlines employ a reflective mirror that can be curved slightly to collimate the beam before the monochromator to improve resolution. While poor energy resolution can be detrimental to XAFS measurements, and

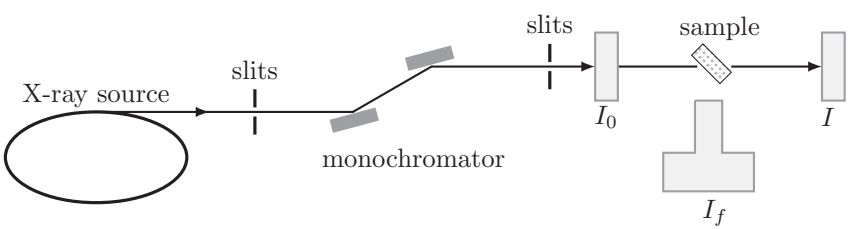


Figure 13. Sketch of an XAFS Experiment. An X-ray source, typically using synchrotron radiation, produces a collimated beam of X-rays with a broad energy spectrum. These X-rays are energy-selected by a slit and monochromator. The incident X-ray intensity, I_0, is sampled. XAFS can be recorded by measuring the intensity transmitted through the sample or by measuring the intensity of a secondary emission—typically X-ray fluorescence or Auger electrons resulting from the X-ray absorption. The X-ray energy is swept through and above the electron binding energy for a particular energy level of the element of interest.

EBSCOhost - printed on 2/13/2023 5:26 AM via . All use subject to https://www.ebsco.com/terms-of-use

especially for XANES measurements, most existing beamlines have resolution sufficient for good XAFS measurements.

Stability and reproducibility of monochromators is sometimes challenging, as the angular precisions of monochromators needed for XAFS are typically on the order of 10^{-4} degrees, so that a very small change in Bragg angle corresponds to a substantial energy shift. Very high quality rotation stages can essentially eliminate such drifts, but may not be installed at all beamlines. In addition, small temperature drifts of the monochromator can cause energy drifts, as the lattice constant of the crystal changes. Stabilizing the temperature of the monochromator is very important, but can be challenging as the power in the white X-ray beam from a modern synchrotron source can easily exceed 1 kW in a few square millimeters. For the most part, these issues are ones of beamline and monochromator design and operation, generally solved by the beamline, and are not a significant problem at modern beamlines designed for XAFS measurements. Still, these issues are worth keeping in mind when assessing XAFS data.

Despite their name, monochromators based on Bragg diffraction do not select only one energy (or color) of light, but also certain *harmonics* (integer multiples) of that energy. While these higher energies will be far above the absorption edge, and so not be absorbed efficiently by the sample, they can cause subtle problems with the data that can be hard to diagnose or correct afterward. These include sharp changes or *glitches* in intensity at particular energies, and unexpectedly large noise in the data. There are two main strategies for removing harmonics. The first is to slightly misalign or "de-tune" the two crystals of the monochromator. This will reduce the transmitted intensity of the higher-energy harmonics much more than it reduces the intensity of the fundamental beam. De-tuning in this way can be done dynamically, often by putting a small piezo-electric crystal on the second monochromator crystal to allow fine motions to slightly misalign the two crystals. The second method for removing harmonics is to put a reflective X-ray mirror in the beam so that it reflects the fundamental beam but not the higher energy harmonics. Such a harmonic-rejection mirror is generally more efficient at removing the higher harmonics than de-tuning the monochromator crystals. Ideally, both of these strategies can be used, but it is generally necessary to use at least one of these methods.

Having linear detectors to measure I_0 and I for transmission measurements is important for good XAFS measurements, and not especially difficult. A simple ion chamber (a parallel plate capacitor filled with an inert gas such nitrogen or argon, and with a high voltage across it through which the X-ray beam passes) is generally more than adequate, as these detectors themselves are generally very linear over a wide range of X-ray intensities. The currents generated from the detectors are quite low (often in the picoampere range, and rarely above a few microampere) and so need to be amplified and transmitted to a counting system. Noise in transmission lines and linearity of the amplification systems used for ion chambers (and other detectors) can cause signal degradation, so keeping cables short and well-grounded is important. Typical current amplifiers can have substantial non-linearities at the low and high ends of their amplification range, and so have a range of linearity limited to a few decades. For this reason, significant dark currents are often set and one must be careful to check for saturation of the amplifiers. In addition, one should ensure that the voltage applied across the ion chamber plates is sufficiently high so that all the current is collected—simply turning up the voltage until the intensity measured for an incident beam of constant intensity is itself constant and independent of voltage is generally sufficient. Such checks for detector linearity can be particularly important if glitches are detected in a spectrum. For fluorescence measurements, several kinds of detectors can be used in addition to ion chambers, and linearity can become an important issue and depend on details of the detector.

With a good source of monochromatic X-rays and a good detection system, accurate and precise transmission measurements on uniform samples of appropriate thickness, are generally easy. Some care is required to make sure the beam is well-aligned on the sample and that

EBSCOhost - printed on 2/13/2023 5:26 AM via . All use subject to https://www.ebsco.com/terms-of-use

harmonics are not contaminating the beam, but obtaining a noise level of 10^{-3} of the signal is generally easy for transmission measurements. Such a noise level is achievable for fluorescence measurements but can be somewhat more challenging, especially for very low concentration samples.

Transmission XAFS measurements

For concentrated samples, in which the element of interest is a major component—10% by weight or higher is a good rule of thumb—XAFS should be measured in transmission. To do this, one needs enough transmission through the sample to get a substantial signal for I. With $\mu t = \ln(I/I_0)$, we typically adjust the sample thickness t so that $\mu t \approx 2.5$ above the absorption edge and/or the edge step $\Delta\mu(E)t \approx 1$. For Fe metal, this gives $t = 7$ μm, while for many solid metal-oxides and pure mineral phases, t is typically in the range of 10 to 25 μm. For concentrated solutions, sample thickness may be several millimeter thick, but this can vary substantially. If both $\mu t \approx 2.5$ for the total absorption and an edge step $\Delta\mu(E)t \approx 1$ cannot be achieved, it is generally better to have a smaller edge step, and to keep the total absorption below $\mu t \approx 4$, so that enough X-rays are transmitted through the sample to measure. Tabulated values for $\mu(E)$ for the elements are widely available, and software such as HEPHAESTUS (Ravel and Newville 2005) can assist in these calculations.

In addition to being the appropriate thickness for transmission measurements, the sample must be of uniform thickness and free of pinholes. Non-uniformity (that is, variations in thickness of 50% or so) and pinholes in the sample can be quite damaging, as μ is logarithmic in I. Since the portion of the beam going through a small hole in the sample will transmit with very high intensity, it will disproportionately contribute to I compared to the parts of the beam that actually goes through the sample. For powdered material, the grain size cannot be much bigger than an absorption length, or the thickness variation across the particle will lead to non-linear variations in the beam transmitted through the sample. If these challenging conditions can be met, a transmission measurement is very easy to perform and gives excellent data. This method is usually appropriate for pure mineral and chemical phases, or for other systems in which the absorbing element has a concentrations > 10%.

A few standard methods for making uniform samples for transmission XAFS exist. If one can use a solution or has a thin, single slab of the pure material (say, a metal foil, or a sample grown in a vacuum chamber), these can make ideal samples. For many cases, however, a powder of a reagent grade chemical or mineral phase is the starting material. Because the required total thickness is so small, and uniformity is important, grinding and sifting the powder to select the finest grains can be very helpful. Using a solvent or other material in the grinding process can be useful. In some case, suspending a powder in a solvent to skim off the smallest particles held up by surface tension can also be used. Spreading or painting the grains onto sticky tape and shaking off any particles that don't stick can also be used to select the finest particles, and can make a fairly uniform sample, with the appropriate thickness built up by stacking multiple layers. Ideally, several of these techniques can be used in combination.

Fluorescence and electron yield XAFS measurements

For samples that cannot be made thin enough for transmission or with the element of interest at lower concentrations (down to a few ppm level in some cases), monitoring the X-ray fluorescence is the preferred technique for measuring the XAFS. In a fluorescence XAFS measurement, the X-rays emitted from the sample will include the fluorescence line of interest, fluorescence lines from other elements in the sample, and both elastically and inelastically (Compton) scattered X-rays. An example fluorescence spectrum is shown in Figure 14. This shows Fe K_α and K_β fluorescence lines along with the elastically scattered peak (unresolvable from the Compton scatter), as well as fluorescence lines from Ca, Ti, and V. In many cases the scatter or fluorescence lines from other elements will dominate the fluorescence spectrum.

EBSCOhost - printed on 2/13/2023 5:26 AM via . All use subject to https://www.ebsco.com/terms-of-use

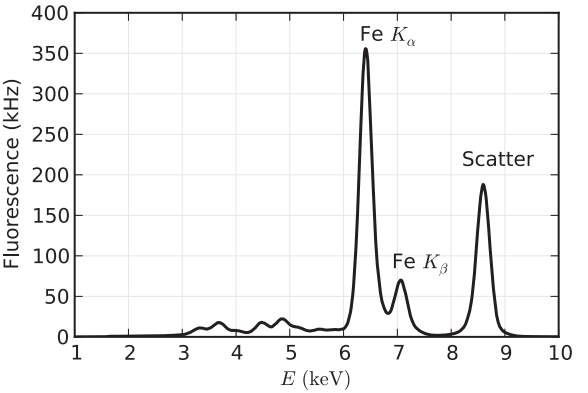


Figure 14. X-ray fluorescence spectrum from an Fe-rich mineral (a feldspar), showing the Fe K_α and K_β emission lines around 6.4 and 7.0 keV, and the elastically (and nearly-elastically) scattered peak near 8.5 keV. At lower energies, peaks for Ca, Ti, and V can be seen.

There are two main considerations for making good fluorescence XAFS measurements: the solid angle collected by the detector, and the energy resolution of the detector for distinguishing the fluorescence lines. The need for solid angle is easy to understand. The fluorescence is emitted isotropically, and we'd like to collect as much of the available signal as possible. X-rays that are elastically and inelastically scattered (for example, by the Compton scattering process) by the sample are not emitted isotropically because the X-rays from a synchrotron are *polarized* in the plane of the synchrotron, (a fact we've neglected up to this point). This polarization means that elastic scatter is greatly suppressed at 90° to the incident beam, in the horizontal plane. Therefore, fluorescence detectors are normally placed perpendicular to the incident beam, and in the horizontal plane.

Energy resolution for a fluorescence detector can be important as it allows discrimination of signals based on energy, so that scattered X-rays and fluorescence lines from other elements can be suppressed relative to the intensity of the fluorescence lines of interest. This lowers the background intensity, and increases the signal-to-noise level. Energy discrimination can be accomplished either physically, by filtering out unwanted emission before it gets to the detector, or electronically after it is detected, or both.

An example of a commonly used physical filter is to place a Mn-rich material between an Fe-bearing sample and the fluorescence detector. Due to the Mn K absorption edge, the filter will preferentially absorb the elastic and inelastic scatter peak and pass the Fe K_α line, as shown in Figure 15. For most K edges, the element with $Z-1$ of the element of interest can be used to make an appropriate filter, and suitable filters can be found for most of the L-edges. A simple filter like this can be used with a detector without any intrinsic energy resolution, such as an ion chamber or large PIN diode. To avoid re-radiation from the filter itself, Soller slits, as shown in Figure 16, can be used to preferentially collect emission from the sample and block most of the signal generated away from the sample from getting into the fluorescence detector, including emission from the filter itself. Such an arrangement can be very effective especially when the signal is dominated by scatter, as when the concentration of the element of interest is in the range of hundreds of ppm or lower, and the matrix is dominated by light elements, with few other heavy elements that have fluorescence lines excited by the incident beam.

Energy discrimination can also be done electronically on the measured X-ray emission spectrum after it has been collected in the detector. A common example of this approach uses a solid-state Si or Ge detector, which can achieve energy resolution of ≈ 200 eV or better

EBSCOhost - printed on 2/13/2023 5:26 AM via . All use subject to https://www.ebsco.com/terms-of-use

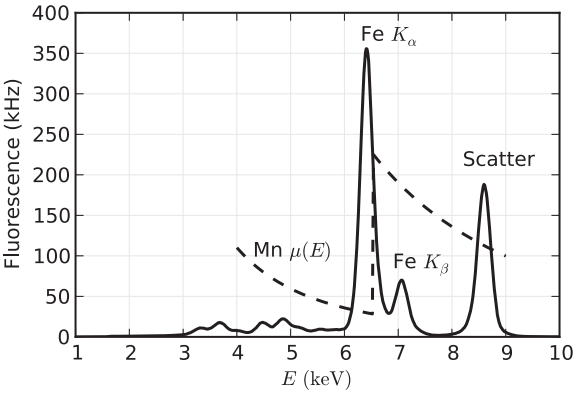


Figure 15. The effect of a "Z–1" filter on a measured fluorescence spectrum. A filter containing Mn placed between sample and detector will absorb most of the scatter peak, while transmitting most of the Fe K_α emission. For samples dominated by the scatter peak, such a filter can dramatically improve the signal-to-noise level.

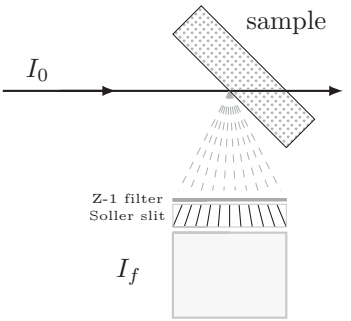


Figure 16. The practical use of "Z–1" filter for energy discrimination of a fluorescence spectrum. The filter placed between sample and detector will absorb most of the scatter peak. Because the filter can itself re-radiate, a set of metal Soller slits pointing at the sample will preferentially absorb the emission from the filter and prevent it from entering the detector.

(approaching 130 eV for modern silicon detectors). The spectrum shown in Figure 14 was collected with such a Ge solid-state detector. These detectors have an impressive advantage of being able to measure the full X-ray fluorescence spectrum, which is useful in its own right for being able to identify and quantify the concentrations of other elements in the sample. Because unwanted portions of the fluorescence spectrum can be completely rejected electronically, these detectors can have excellent signal-to-background ratios and be used for XAFS measurements with concentrations down to ppm levels. Though solid-state detectors have many advantages, they have a few drawbacks:

1. The electronic energy discrimination takes a finite amount of time, which limits the total amount of signal that can be processed. These detectors typically saturate at $\approx 10^5$ Hz of *total* count rate or so. When these rates are exceeded, the detector is effectively unable to count all the fluorescence, and is said to be "dead" for some fraction of the time. It is common to use ten or more such detectors in parallel. Even then, the limit on total intensity incident for these detectors can limit the quality of the measured XAFS.

2. Maintaining, setting up, and using one of these is much more work than using an ion chamber. For example, germanium solid-state detectors must be kept at liquid nitrogen temperatures. The electronics needed for energy discrimination can be complicated, expensive, and delicate.

EBSCOhost - printed on 2/13/2023 5:26 AM via . All use subject to https://www.ebsco.com/terms-of-use

Despite these drawbacks, the use of solid-state detectors is now fairly common practice for XAFS, especially for dilute and heterogeneous samples, and the detectors and electronics themselves are continually being improved.

Before we leave this section, there are two import effects to discuss for XAFS measurements made in fluorescence mode. These are *self-absorption* or *over-absorption* from the sample, and a more detailed explanation of deadtime effects for measurements made with solid-state detectors. If not dealt with properly, these effects can substantially comprise otherwise good fluorescence XAFS data, and so it is worth some attention to understand these in more detail.

Self-absorption (or over-absorption) of fluorescence XAFS

The term *self-absorption,* when referred to fluorescence XAFS, can be somewhat confusing. Certainly, the sample itself can absorb many of the fluoresced X-rays. For example, for a dilute element (say, Ca) in a relatively dense matrix (say, iron oxide), the Ca fluorescence will be severely attenuated by the sample and the measured fluorescence signal for Ca will be dictated by the escape depth of the emitted X-ray in the matrix. Although this type of absorbtion is an important consideration, this is not what is usually meant by the term *self-absorption* in EXAFS. Rather, the term self-absorption for EXAFS usually refers to the situation in which the penetration depth into the sample is dominated by the element of interest, and so is one special case of the term as used in X-ray fluorescence analysis. In the worst case for self-absorption (a very thick sample of a pure element), the XAFS simply changes the penetration depth into the sample, but essentially all the X-rays are absorbed by the element of interest. The escape depth for the fluoresced X-ray is generally much longer than the penetration depth (as the fluoresced X-ray is below the edge energy), so that most absorbed X-rays will generate a fluoresced X-ray that will escape from the sample. This severely dampens the XAFS oscillations, and for a very concentrated sample, there may be no XAFS oscillations at all. With this understanding of the effect, the term *over-absorption* (Manceau et al. 2002) is probably a better description, and should be preferred to *self-absorption* even though the latter is in more common usage.

Earlier we said that for XAFS measured in fluorescence goes as

$$\mu(E) \propto \frac{I_f}{I_0}$$

This is a slight oversimplification. The probability of fluorescence is proportional to the absorption probability but the fluorescence intensity that we measure has to travel back through the sample to get to the detector. Since all matter attenuates X-rays, the fluorescence intensity, and therefore the XAFS oscillations, can be damped. More correctly, the measured fluorescence intensity goes as (see Fig. 17)

$$I_f = I_0 \frac{\varepsilon \Delta\Omega}{4\pi} \frac{\mu_\chi(E)\left\{1 - e^{-\left[\frac{\mu_{tot}(E)}{\sin\theta} + \frac{\mu_{tot}(E_f)}{\sin\phi}\right]t}\right\}}{\frac{\mu_{tot}(E)}{\sin\theta} + \frac{\mu_{tot}(E_f)}{\sin\phi}} \tag{11}$$

where ε is the fluorescence efficiency, $\Delta\Omega$ is the solid angle of the detector, E_f is the energy of the fluorescence X-ray, θ is the incident angle (between incident X-ray and sample surface), ϕ is the exit angle (between fluoresced X-ray and sample surface), $\mu_\chi(E)$ is the absorption from the element of interest, and $\mu_{tot}(E)$ is the *total* absorption in the sample,

$$\mu_{tot}(E) = \mu_\chi(E) + \mu_{other}(E)$$

EBSCOhost - printed on 2/13/2023 5:26 AM via . All use subject to https://www.ebsco.com/terms-of-use

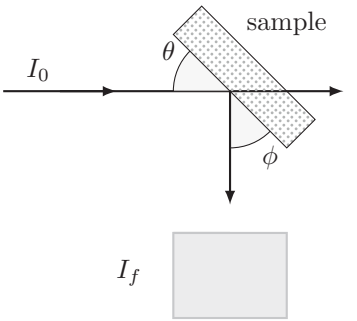


Figure 17. Fluorescence XAFS measurements, showing incident angle θ and exit angle φ.

and $\mu_{other}(E)$ is the absorption due to lower energy edges of the element of interest and other elements in the sample. Equation (11) has several interesting limits that are common for real XAFS measurements. First, there is the thin sample limit, in which $\mu_{tot}t << 1$. The $1 - e^{-\mu t}$ term then becomes (by a Taylor series expansion)

$$1 - e^{-\mu t} \approx \left[\frac{\mu_{tot}(E)}{\sin\theta} + \frac{\mu_{tot}(E_f)}{\sin\phi} \right] t$$

which cancels the denominator, so that

$$I_f \approx I_0 \frac{\varepsilon \Delta\Omega}{4\pi} \mu_\chi(E) t$$

Alternatively, there is the *thick, dilute sample limit*, for which $\mu t >> 1$ and $\mu_\chi << \mu_{other}$. Now the exponential term goes to 0, so that

$$I_f = I_0 \frac{\varepsilon \Delta\Omega}{4\pi} \frac{\mu_\chi(E)}{\frac{\mu_{tot}(E)}{\sin\theta} + \frac{\mu_{tot}(E_f)}{\sin\phi}}$$

In this case we can also ignore the energy dependence of μ_{tot}, leaving

$$I_f \propto I_0 \mu_\chi(E)$$

These two limits (very thin or thick, dilute samples) are the best cases for fluorescence measurements.

For relatively thick and concentrated samples, for which $\mu_\chi \approx \mu_{other}$, we cannot ignore the energy dependence of μ_{tot}, and must correct for the oscillations in $\mu_{tot}(E)$ in Equation (11). As said above, for very concentrated samples, $\mu_{tot}(E) \approx \mu_\chi(E)$, and the XAFS can be completely lost. On the other hand, if the self-absorption is not too severe, it can be corrected using the above equations (Pfalzer et al. 1999; Booth and Bridges 2005).

Finally, these self-absorption effects can be reduced for thick, concentrated samples by rotating the sample so that it is nearly normal to the incident beam. With $\phi \to 0$ or the *grazing exit limit*, $\mu_{tot}(E_f)/\sin\phi >> \mu_{tot}(E)/\sin\theta$, which gives

$$I_f \approx I_0 \frac{\varepsilon \Delta\Omega}{4\pi} \frac{\mu_\chi(E)}{\mu_{tot}(E_f)/\sin\phi}$$

and gets rid of the energy dependence of the denominator.

EBSCOhost - printed on 2/13/2023 5:26 AM via . All use subject to https://www.ebsco.com/terms-of-use

In certain situations, monitoring the intensity of emitted electrons (which includes both Auger electrons and lower-energy secondary electrons) can be used to measure the XAFS. The escape depth for electrons from materials is generally much less than a micron, making these measurements more surface-sensitive than X-ray fluorescence measurements, and essentially immune to over-absorption. Because the relative probability for emitting an electron instead of an X-ray is higher for low energy edges and electron levels, electron yield measurements are much more common and efficient for lower energy edges. Electron yield measurements are generally most appropriate for samples that are metallic or semiconducting (that is, electrically conducting enough so that the emitted electrons can be replenished from a connection to ground, without the sample becoming charged). In order to collect the electron yield signal, a voltage-biased collector needs to be placed very close to the sample surface, typically with a helium atmosphere or vacuum between sample and collector. While electron yield measurements can give very good data, for the reasons mentioned here, measuring XAFS in electron yield is not very common for X-ray energies above 5 keV, and further details of these measurements will be left for further reading.

Deadtime corrections for fluorescence XAFS

For fluorescence XAFS data measured with an energy discriminating fluorescence detector, such as a solid-state Ge or Si detector, it is often necessary to correct for the so-called *deadtime effect*. This accounts for the fact that a finite amount of time is needed to measure the energy of each X-ray detected, and the electronics used to make this measurement can only process one X-ray at a time. At high enough incident count rates, the detector electronics cannot process any more counts and is said to be *saturated*. The incident count rate is due to all the X-rays in the detector, not just from the fluorescence line used in the XAFS measurements. Saturation effects are particularly important when the absorbing atom is of relatively high concentration (above a few percent by weight), because the intensity of the monitored fluorescence line is negligible below the edge, and grows dramatically at the absorption edge. Such an increase in intensity can cause a non-linear reduction of the fluorescence intensity, giving a non-linear artifact to the XAFS.

Fortunately, most energy discriminating detector and electronics systems can be characterized with a simple parameter τ that relates the incident count rate with the output count rate actually processed as

$$I_{\text{out}} = I_{\text{inp}} e^{-I_{\text{inp}}\tau}$$

where I_{inp} is the incident count rate to the detector, I_{out} is the output count rate, giving the intensity reported by the detector, and τ is the deadtime, characteristic of the detector and electronics system. For a realistic value of $\tau = 2$ μs, the relation of input count rate and output count rate is shown in Figure 18. For many detector systems, there is some ability to adjust τ and the maximum output count rate, that can be achieved, but at the expense of energy resolution of the fluorescence spectra. In order to make this correction, one wants to get I_{inp} given I_{out} which can be complicated near the saturation value for I_{inp}, as a particular value recorded for I_{out} could come from one of two values for I_{inp}. For some detector systems, one can simply record I_{inp} and I_{out} for each measurement as an output of the detector and electronics system. Alternatively, one can separately measure τ so that the corrections can be applied easily. Otherwise, a good rule of thumb is that spectra can be corrected up to a rate for which I_{out} is half of I_{inp} (I_{inp} around 350 kHz for the curve shown in Fig. 18). Importantly, for multi-element detector systems, each detector element will have its own deadtime, and corrections should be made for each detector before summing the signals from multiple detectors.

EBSCOhost - printed on 2/13/2023 5:26 AM via . All use subject to https://www.ebsco.com/terms-of-use

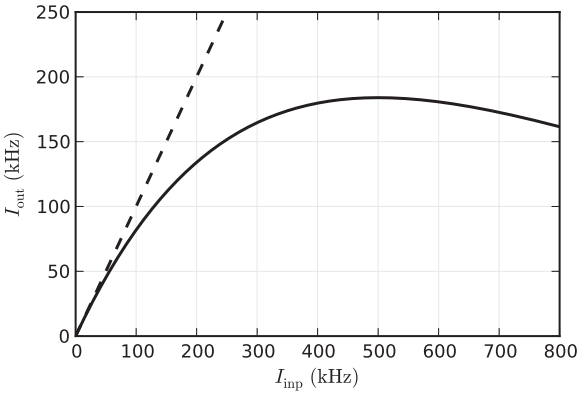


Figure 18. Typical deadtime curve for a pulse-counting, energy-discriminating detector with a deadtime τ of 2 μs. At low input count rates, the output count rate—the rate of successfully processed data—rises linearly. As the count rate increases, some of the pulses cannot be processed, so that the output count rate is lower than the input count rate. At *saturation*, the output count rate cannot go any higher, and increasing the input count rate will decrease the output rate. The dashed line shows a line with unity slope, for a detector with no deadtime.

XAFS DATA REDUCTION

For all XAFS data, whether measured in transmission or fluorescence (or electron emission), the data reduction and analysis are essentially the same. First, the measured intensity signals are converted to $\mu(E)$, and then reduced to $\chi(k)$. After this data reduction, $\chi(k)$ can be analyzed and modeled using the XAFS equation. In this section, we'll go through the steps of data reduction, from measured intensities to $\chi(k)$, which generally proceeds as:

1. Convert measured intensities to $\mu(E)$, possibly correcting systematic measurement errors such as self-absorption effects and detector deadtime.
2. Identify the threshold energy E_0, typically as the energy of the maximum derivative of $\mu(E)$.
3. Subtract a smooth pre-edge function from $\mu(E)$ to get rid of any instrumental background and absorption from other edges.
4. Determine the edge jump, $\Delta\mu$, at the threshold energy, and normalize $\mu(E)$, so that the pre-edge subtracted and normalized $\mu(E)$ goes from approximately 0 below the threshold energy to 1 well above the threshold energy. This represents the absorption of a single X-ray, and is useful for XANES analysis.
5. Remove a smooth post-edge background function approximating $\mu_0(E)$, thereby isolating the XAFS $\chi = (\mu - \mu_0)/\Delta\mu$.
6. Convert χ from energy E to photoelectron wavenumber $k = \sqrt{2m(E - E_0)/\hbar^2}$.
7. k-weight the XAFS $\chi(k)$ and Fourier transform into R-space.

We'll go through each of these steps in slightly more detail, and show them graphically using real XAFS data.

As with many things, the first step is often the most challenging. Here, the differences between measurements made in transmission and fluorescence mode are most pronounced. For transmission measurements, we rearrange Equation (1), and ignore the sample thickness, so that

EBSCOhost - printed on 2/13/2023 5:26 AM via . All use subject to https://www.ebsco.com/terms-of-use

$$\mu(E) = \ln\left(\frac{I_0}{I}\right)$$

where now I_0 and I are the signals measured from the ion chambers. Typically, the signals measured as I_0 and I are actually integrated voltages over some predefined time where the voltages are taken from the output of current amplifiers with input currents from ion chambers as input. Thus the measurements are not the incident flux in photons per second. Rather, they are scaled measures of the flux *absorbed* in the ion chamber. For the most part, the difference between what we think of as I_0 (incident X-ray flux, in photons/second) and what we actually measure for I_0 (scaled, integrated current generated from X-rays absorbed in the ion chamber) is not very significant. When we take the ratio between the two ion chamber signals most of the factors that distinguish the conceptual intensity from the measured signal will either cancel out, give an arbitrary offset, or give a slowly varying monotonic drift with energy. Thus, it is common to see experimental values reported for "raw" $\mu(E)$ in the literature that do not have dimensions of inverse length, and which might even have values that are negative. For real values of $\mu(E)$ in inverse length, these measurements would be nonsensical, but for XAFS work this is of no importance, as we'll subtract off a slowly varying background anyway.

For fluorescence or Auger measurements, the situation is similar, except that one uses

$$\mu(E) = \frac{I_f}{I}$$

where I_f is the integrated fluorescence signal of interest. As with the transmission measurements, there is generally no need to worry about getting absolute intensities, and one can simply use the ratio of measured intensities. Because the instrumental drifts for a solid-state, energy-discriminating fluorescence detector may be different than for a gas-filled ion chamber, it is not unusual for $\mu(E)$ for fluorescence XAFS measurements to have an overall upward drift with energy, where transmission XAFS tends to drift down with energy.

In addition to the corrections for over-absorption and deadtime effects discussed in the previous section, other corrections may need to be made to the measured $\mu(E)$ data. For example, sometimes bad glitches appear in the data that are not normalized away by dividing by I_0. This is often an indication of insufficient voltage in ion chambers, of too much harmonic content in the X-ray beam, poorly uniform samples, incomplete deadtime correction, or a combination of these. If possible, it is preferred to address these problems during the measurement, but this is not always possible. For such glitches, the best approach is simply to remove them from the data—asserting that they were not valid measurements of $\mu(E)$.

Another example of a correction that can be made in the data reduction step is for cases where another absorption edge occurs in the spectrum. This could be from the same element (as is over the case for measurements made at the L_{III} edge, where the L_{II} edge will eventually be excited, or from a different element in a complex sample. As with a glitch, the appearance of another edge means that $\mu(E)$ is no longer from the edge and element of interest, and it is best to simply truncate the data at the other edge.

Pre-edge subtraction and normalization

Once the measurement is converted to $\mu(E)$, the next step is usually to identify the edge energy. Since XANES features can easily move the edge by several eV, and because calibrations vary between monochromators and beamlines, it is helpful to be able to do this in an automated way that is independent of the spectra. Though clearly a crude approximation, the most common approach is to take the maximum of the first derivative of $\mu(E)$. Though it has little theoretical justification, it is easily reproduced, and so can readily be checked and verified.

EBSCOhost - printed on 2/13/2023 5:26 AM via . All use subject to https://www.ebsco.com/terms-of-use

Instrumental drifts from detector systems can be crudely approximated by a simple linear dependence in energy. That is, a linear fit to the pre-edge range of the measured spectrum is found, and subtracted. In some cases, a so-called Victoreen pre-edge function (in which one fits a line to $E^n\mu(E)$ for some value of n, typically 1, 2 or 3) can do a slightly better job at approximating the instrumental drifts for most XAFS spectra. This is especially useful for dilute data measured in fluorescence with a solid-state detector, where the contribution from elastic and Compton-scattered intensity into the energy window of the peak of interest will decrease substantially with energy, as the elastic peak moves up in energy.

The next step in the process is to adjust the scale of $\mu(E)$ to account for the absorption of 1 photoelectron. By convention, we *normalize* the spectrum to go from approximately 0 below the edge to approximately 1 above the edge. To do this, we find the edge step, $\Delta\mu$, and divide $\mu(E)$ by this value. Typically, a low-order polynomial is fitted to $\mu(E)$ well above the edge (away from the XANES region), and the value of this polynomial is extrapolated to E_0 to give the edge step. It should be emphasized that this convention is fairly crude and can introduce systematic biases in the result for $\Delta\mu$.

Examples of these processing steps (location of E_0, subtraction of pre-edge, and normalization to an edge jump of 1) for transmission XAFS data at the Fe *K*-edge of FeO are shown in Figures 19 and 20. For XANES analysis, this amount of data reduction is generally all that is needed. For both XANES and EXAFS analysis, the most important part of these steps is the normalization to the edge step. For XANES analysis, spectra are generally compared by amplitude, so an error in the edge step for any spectra will directly affect the weight given to that spectra. For EXAFS, the edge step is used to scale $\chi(k)$, and so is directly proportional to coordination number. Errors in the edge step will translate directly to errors in coordination number. Getting good normalization (such that $\mu(E)$ goes to 1 above the edge) is generally not hard, but requires some care, and it is important to assess how well and how consistently this normalization process actually works for a particular data set. Most existing analysis packages do these steps reasonably well, especially in making spectra be normalized consistently, but it is not at all unusual for such automated, initial estimates of the edge step to need an adjustment of 10%.

Background subtraction

Perhaps the most confusing and error-prone step in XAFS data reduction is the determination and removal of the post-edge background function that approximates $\mu_0(E)$. This is

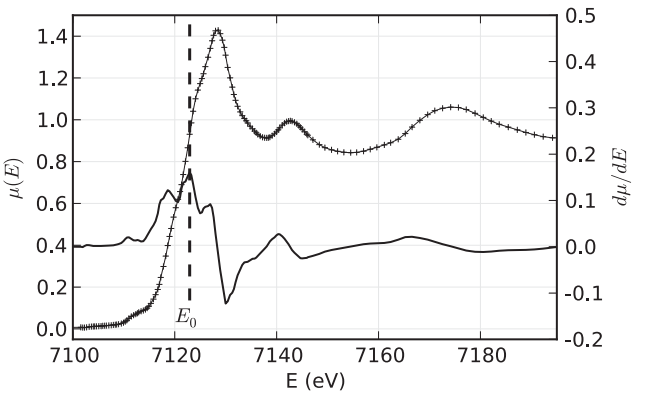


Figure 19. The XANES portion of the XAFS spectrum (solid with +), and the identification of E_0 from the maximum of the derivative $d\mu/dE$ (solid). This selection of E_0 is easily reproduced but somewhat arbitrary, so we may need to refine this value later in the analysis.

EBSCOhost - printed on 2/13/2023 5:26 AM via . All use subject to https://www.ebsco.com/terms-of-use

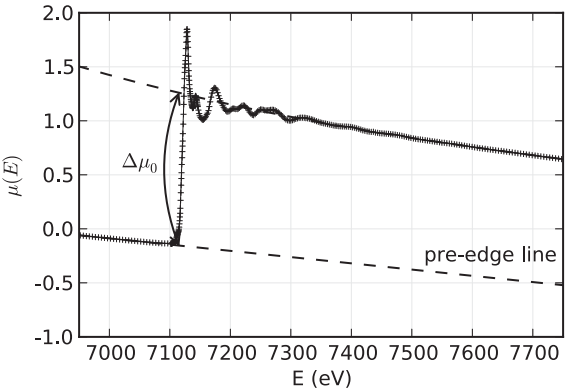


Figure 20. XAFS pre-edge subtraction and normalization. A line (or simple, low-order polynomial) is fit to the spectrum below the edge, and a separate low-order polynomial is fit to the spectrum well above the edge. The edge jump, $\Delta\mu_0$, is approximated as the difference between these two curves at E_0. Subtracting the pre-edge polynomial from the full spectrum and dividing by the edge jump gives a normalized spectrum.

somewhat unfortunate, as it does not need to be especially difficult. Since $\mu_0(E)$ represents the absorption coefficient from the absorbing atom without the presence of the neighboring atoms, we cannot actually measure this function separately from the EXAFS. In fact, even if possible, measuring $\mu(E)$ for an element in the gas phases would not really be correct, as $\mu_0(E)$ represents the absorbing atom embedded in the molecular or solid environment, just without the scattering from the core electrons of the neighboring atoms. Instead of even trying to measure an idealized $\mu_0(E)$, we determine it empirically by fitting a *spline* function to $\mu(E)$. A spline is a piece-polynomial function that is designed to be adjustable enough to smoothly approximate an arbitrary waveform, while maintaining convenient mathematical properties such as continuous first and second derivatives. This is certainly an *ad hoc* approach, without any real physical justification. Still, it is widely used for EXAFS analysis, and has the advantage of being able to account for those systematic drifts in our measurement of $\mu(E)$ that make it differ from the true $\mu(E)$, as long as those drifts vary slowly with energy. The main challenge with using an arbitrary mathematical spline to approximate $\mu_0(E)$ is to decide how flexible to allow it to be, so as to ensure that it does not follow $\mu(E)$ closely enough to remove the EXAFS. That is, we want $\mu_0(E)$ to remove the slowly varying parts of $\mu(E)$ while not changing $\chi(k)$, the part of $\mu(E)$ that varies more quickly with E.

A simple approach for determining $\mu_0(E)$ that works well for most cases relies on the Fourier transform to mathematically express the idea that $\mu_0(E)$ should match the slowly varying parts of $\mu(E)$ while leaving the more quickly varying parts of $\mu(E)$ to give the EXAFS χ. The Fourier transform is critical to EXAFS analysis, and we'll discuss it in more detail shortly, but for now the most important thing to know is that it gives a weight for each frequency making up a waveform. For EXAFS, the Fourier transform converts χ from wavenumber k to distance R.

For determining the background $\mu_0(E)$, we want a smoothly varying spline function that removes the low-R components of χ, while retaining the high-R components. Conveniently, we have a physically meaningful measure of what distinguishes "low-R" from "high-R," in that we can usually guess the distance to the nearest neighboring atom, and therefore assert that there should be no signal in the EXAFS originating from atoms at shorter R. As a realistic rule of thumb, it is rare for atoms to be closer together than about 1.5 Å—this is especially true for the heavier elements for which EXAFS is usually applied. Thus, we can assert that a

EBSCOhost - printed on 2/13/2023 5:26 AM via . All use subject to https://www.ebsco.com/terms-of-use

spline should be chosen for $\mu_0(E)$ that makes the resulting χ have as little weight as possible below some distance R_{bkg}, while ignoring the higher R components of χ. This approach and the use of R_{bkg}, with a typical value around 1 Å, as the cutoff value for R (Newville et al. 1993), is not always perfect, but can be applied easily to any spectra to give a spline function that reasonably approximates $\mu_0(E)$ for most spectra with at least some physically meaningful basis. Figure 21 shows a typical background spline found for FeO, using a high-R cutoff R_{bkg} of 1.0 Å. The resulting $\chi(k)$ is shown in Figure 22.

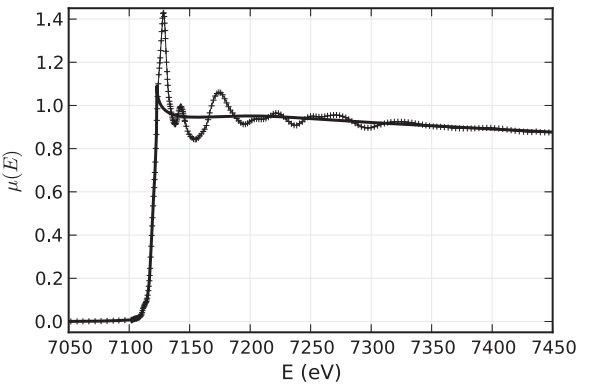


Figure 21. Post-edge background subtraction of FeO EXAFS. The background $\mu_0(E)$ is a smooth spline function that matches the low-R components of $\mu(E)$, in this case using 1 Å for R_{bkg}.

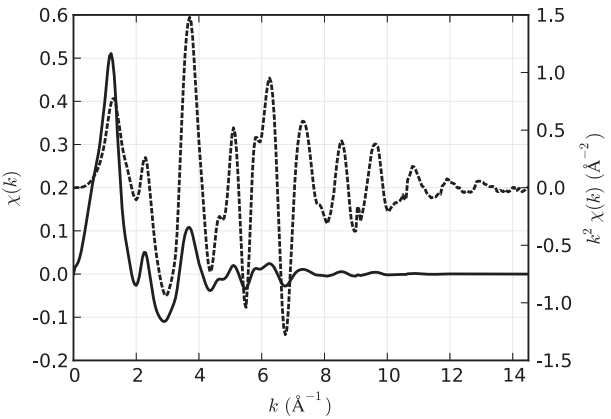


Figure 22. The EXAFS $\chi(k)$ (solid) isolated after background subtraction. The EXAFS decays quickly with k, and weighting by (dashed) amplifies the oscillations at high k.

The effect of varying R_{bkg} on the resulting spline for $\mu_0(E)$ and χ in both k- and R-space can be seen in Figure 23. Here, $\mu_0(E)$ spectra are shown for the same FeO $\mu(E)$ using values for R_{bkg} of 0.2, 1.0, and 4.0 Å. A value for R_{bkg} that is too small (shown with a solid line) results in $\mu_0(E)$ that does not vary enough, giving a slow oscillation in $\chi(k)$, and spurious peak below 0.5 Å in $|\chi(R)|$. On the other hand, setting R_{bkg} too high (shown with a dashed line) may result in a $\mu_0(E)$ that matches all the EXAFS oscillations of interest. Indeed, with R_{bkg} = 4 Å, both the first and second shells of the FeO EXAFS are entirely removed, leaving only the highest R components. This is clearly undesirable. In general, it is not too difficult to find a suitable value for R_{bkg}, with 1 Å or half the near-neighbor distance being fine default choices. As we can see from Figure 23, having R_{bkg} too small is not always a significant problem—the low R peak can simply be ignored in the modeling of the spectra, and there is little effect on the spectrum at higher R.

EBSCOhost - printed on 2/13/2023 5:26 AM via . All use subject to https://www.ebsco.com/terms-of-use

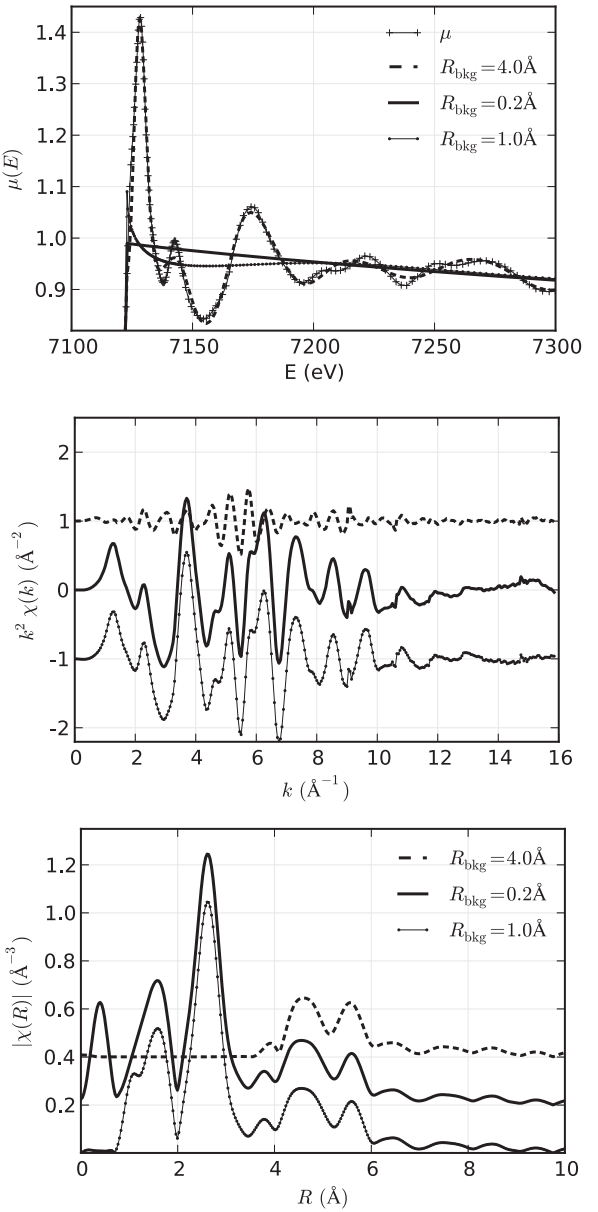


Figure 23. The effect of changing R_{bkg} on $\mu_0(E)$ and χ. A typical value for R_{bkg} of 1.0 Å (dots) results in a spline for (E) that can follow the low-R variations in $\mu(E)$ while not removing the EXAFS. A value too small (R_{bkg} = 0.2 Å, solid) gives a spline that is not flexible enough, leaving a low-R artifact, but one that will not greatly impact further analysis. On the other hand, too large a value (R_{bkg} = 4.0 Å, dashed) will give a spline flexible enough to completely remove the first and second shells of the EXAFS.

EXAFS Fourier transforms

As mentioned above, the Fourier transform is central for the understanding and modeling of EXAFS data. Indeed, the initial understanding of the phenomena was aided greatly by the

EBSCOhost - printed on 2/13/2023 5:26 AM via . All use subject to https://www.ebsco.com/terms-of-use

ability to perform Fourier transforms on measured EXAFS spectra. While there are certainly ample resources describing Fourier transforms and their properties, a few important points about the use of Fourier transforms for EXAFS will be made here.

The first thing to notice from Figure 24 is that two peaks are clearly visible—these correspond to the Fe-O and Fe-Fe distances in FeO. Thus the Fourier transformed XAFS can be used to isolate and identify different coordination spheres around the absorbing Fe atom. Indeed, $|\chi(R)|$ almost looks like a radial distribution function, $g(R)$. While EXAFS does depend on the partial pair distribution—the probability of finding an atom at a distance R from an atom of the absorbing species—$\chi(R)$ is certainly not just a pair distribution function. This can be seen from the additional parts to the EXAFS Equation, including the non-smooth k dependence of the scattering factor $f(k)$ and phase-shift $\delta(k)$.

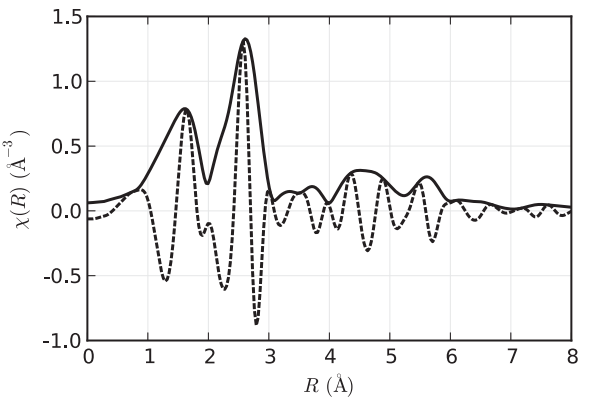


Figure 24. The Fourier Transformed XAFS, $\chi(R)$. The magnitude $|\chi(R)|$ (solid) is the most common way to view the data, but the Fourier transform makes $\chi(R)$ a complex function, with both a real (dashed) and imaginary part, and the magnitude hides the important oscillations in the complex $\chi(R)$.

A very important thing to notice about $\chi(R)$ is that the R positions of the peaks are shifted to lower R from what $g(R)$ would give. For FeO, the first main peak occurs at 1.6 Å, while the FeO distance in FeO is more like 2.1 Å. This is not an error, but is due to the scattering phase-shift—recall that the EXAFS goes as $\sin[2kR + \delta(k)]$. As can be seen from the phase shifts shown in Figure 10, $\delta(k) \sim -k$ is a decent approximation of a typical phase-shift, which gives an apparent shift to the peaks in $\chi(R)$ of −0.5 Å or so.

The Fourier Transform results in a complex function for $\chi(R)$ even though $\chi(k)$ is a strictly real function. It is common to display only the magnitude of $\chi(R)$ as shown in solid in Figure 24, but the real (dashed) and imaginary components contain important information that cannot be ignored. When we get to the modeling the XAFS, it will be important to keep in mind that $\chi(R)$ has real and imaginary components, and we will model these, not just the magnitude.

The standard definition for a Fourier transform of a signal $f(t)$ can be written as

$$\tilde{f}(\omega) = \frac{1}{\sqrt{2\pi}} \int_{-\infty}^{\infty} f(t) e^{-i\omega t} dt$$

$$f(t) = \frac{1}{\sqrt{2\pi}} \int_{-\infty}^{\infty} \tilde{f}(\omega) e^{i\omega t} d\omega$$

where the symmetric normalization is one of the more common conventions. This gives Fourier

EBSCOhost - printed on 2/13/2023 5:26 AM via . All use subject to https://www.ebsco.com/terms-of-use

conjugate variables of ω and t, typically representing frequency and time, respectively. Because the XAFS equation (Eqn. 10) has $\chi(k) \propto \sin[2kR + \delta(k)]$, the conjugate variables in XAFS are generally taken to be k and $2R$. While the normalization for $\chi(R)$ and $\chi(k)$ is a matter of convention, we follow the symmetric case above (with t replaced by k and ω replaced by $2R$).

There are a few important modifications to mention for the typical use of Fourier transforms in XAFS analysis. First, an XAFS Fourier transform multiplies $\chi(k)$ by a power of k, typically k^2 or k^3, as shown in Figure 22. This weighting helps compensate for the strong decay with k of $\chi(k)$, and allows either emphasizing different portions of the spectra, or giving a fairly uniform intensity to the oscillations over the k range of the data. In addition, $\chi(k)$ is multiplied by a window function $\Omega(k)$ which acts to smooth the resulting Fourier transform and remove ripple and ringing that would result from a sudden truncation of $\chi(k)$ at the ends of the data range.

The second important issue is that the continuous Fourier transform described above is replaced by a discrete transform. This better matches the discrete sampling of energy and k values of the data, and allows Fast Fourier Transform techniques to be used, which greatly improves computational performance. Using a discrete transform does change the definitions of the transforms used somewhat. First, the $\chi(k)$ data must be interpolated onto a *uniformly spaced* set of k values. Typically, a spacing of $\delta k = 0.05$ Å^{-1} is used. Second, the array size for $\chi(k)$ used in the Fourier transform should be a power of 2, or at least a product of powers of 2, 3, and 5. Typically, $N_{\rm fft} = 2048$ points are used. With the default spacing between k points, this would accommodate $\chi(k)$ up to $k = 102.4$ Å^{-1}. Of course, real experimental data doesn't extend that far, so the array to be transformed is *zero-padded* to the end of the range.

The spacing of points in R is given as $\delta R = \pi/(N_{\rm fft}\delta k)$. The zero-padding of the extended k range will increase the density of points in $\chi(R)$ and result in smoothly interpolating the values. For $N_{\rm fft} = 2048$ and $\delta k = 0.05$ Å^{-1}, the spacing in R is approximately $\delta R \approx 0.0307$ Å. For the discrete Fourier transforms with samples of $\chi(k)$ at the points $k_n = n\delta k$, and samples of $\chi(R)$ at the points $R_m = m\delta R$, the definitions for the XAFS Fourier transforms become:

$$\tilde{\chi}(R_m) = \frac{i\delta k}{\sqrt{\pi N_{\rm fft}}} \sum_{n=1}^{N_{\rm fft}} \chi(k_n)\Omega(k_n) k_n^w e^{2i\pi nm/N_{\rm fft}}$$

$$\tilde{\chi}(k_n) = \frac{2i\delta R}{\sqrt{\pi N_{\rm fft}}} \sum_{m=1}^{N_{\rm fft}} \tilde{\chi}(R_m)\Omega(R_m) e^{-2i\pi nm/N_{\rm fft}}$$

This normalization convention preserves the symmetry properties of the Fourier Transforms with conjugate variables k and $2R$.

As mentioned above, the window function $\Omega(k)$ will smooth the resulting Fourier transform and reduce the amount of ripple that would arise from a sharp cut-off $\chi(k)$ at the ends of the data range. Since Fourier transforms are used widely in many fields of engineering and science, there is an extensive literature on such window functions, and a lot of choices and parameters available for constructing windows. In general terms, $\Omega(k)$ will gradually increases from 0 to 1 over the low-k region, and decrease from 1 to 0 over the high-k region, and may stay with a value 1 over some central portion. Several functional forms and parameters for these windows can be used, and are available in most EXAFS analysis software. Many good examples of the shapes, parameters, and effects of these on the resulting $\chi(R)$ are available in program documentation, and other on-line tutorials.

In many analyses, the inverse Fourier transform is used to select a particular R range and transform this back to k space, in effect *filtering* out most of the spectrum, and leaving only a narrow band of R values in the resulting filtered $\chi(k)$. Such filtering has the potential advantage of being able to isolate the EXAFS signal for a single shell of physical atoms around the

EBSCOhost - printed on 2/13/2023 5:26 AM via . All use subject to https://www.ebsco.com/terms-of-use

absorbing atom, and was how many of the earliest EXAFS analyses were done. This approach should be used with caution since, for all but the simplest of systems, it can be surprisingly difficult to effectively isolate the EXAFS contribution from an individual scattering atom this way. It is almost never possible to isolate a second neighbor coordination sphere in this way. For this reason, many modern analyses of EXAFS will use a Fourier transform to convert $\chi(k)$ to $\chi(R)$, and use $\chi(R)$ for data modeling, not bothering to try to use a filter to isolate shells of atoms.

XAFS DATA MODELING

In this section, we'll work through an example of a structural refinement of EXAFS. The FeO data shown and reduced in the previous section will be analyzed here. Of course, we know the expected results for this system, but it will serve to demonstrate the principles of XAFS modeling and allow us to comment on a number of subtleties in data modeling.

FeO has a simple rock salt structure, with Fe surrounded by 6 O, with octahedral symmetry, and then 12 Fe atoms in the next shell. Starting with this simple structure, we can calculate scattering amplitudes $f(k)$ and phase-shifts, $\delta(k)$ theoretically. A complete description of this calculation is beyond the scope of this treatment, but a few details will be given below. Once we have these theoretical scattering factors, we can use them in the EXAFS equation to refine structural parameters from our data. That is, we'll use the calculated functions $f(k)$ and $\delta(k)$ (and also $\lambda(k)$) in the EXAFS equation to predict the $\chi(k)$ and modify the structural parameters R, N, and σ^2 from Equation (10), and also allow E_0 (that is, the energy for which $k = 0$) to change until we get the best-fit to the $\chi(k)$ of the data. Because of the availability of the Fourier transform, we actually have a choice of doing the refinement with the measured $\chi(k)$ or with the Fourier transformed data. Working in R-space allows us to selectively ignore higher coordination shells, and we will use this approach in the examples here. When analyzing the data this way, the full complex XAFS $\chi(R)$, not just the magnitude $|\chi(R)|$, must be used.

The examples shown here are done with the FEFF (Rehr et al. 1991) program to construct the theoretical factors, and the IFEFFIT (Newville 2001a) package to do the analysis. Some aspects of the analysis shown here may depend on details of these particular programs, but similar results would be obtained with any of several other EXAFS analysis tools.

Running and using FEFF for EXAFS calculations

In order to calculate the $f(k)$ and $\delta(k)$ needed for the analysis, the FEFF program (Rehr et al. 1991) starts with a cluster of atoms, builds atomic potentials from this, and simulates a photoelectron with a particular energy being emitted by a particular absorbing atom and propagating along a set of scattering paths (Newville 2001b). FEFF represents a substantial work of modern theoretical condensed matter physics, and includes many effects that are conceptually subtle but quantitatively important, including the finite size of the scattering atoms, and many-body effects due to the fact that electrons are indistinguishable particles that must satisfy Pauli's exclusion principle (Rehr and Albers 2000). The details of these effects are beyond the scope of this work.

We do not, as may have been inferred from some of the earlier discussion, use FEFF to calculate $f(k)$ and $\delta(k)$ for the scattering of, say, an oxygen atom, and use that for all scattering of oxygen. Instead, we use FEFF to calculate the EXAFS for a particular path, say Fe-O-Fe taken from a realistic cluster of atoms. This includes the rather complex propagation of the photoelectron out of the Fe atom, through the sea of electrons in an iron oxide material, scattering from an oxygen atom with finite size, and propagating back to the absorbing Fe atom. As a result of this, we use FEFF to calculate the EXAFS for a particular set of paths so that we may then *refine* the path lengths and coordination numbers for those paths.

EBSCOhost - printed on 2/13/2023 5:26 AM via . All use subject to https://www.ebsco.com/terms-of-use

Starting with a cluster of atoms (which does not need to be crystalline, but this is often easy to use), FEFF determines the important scattering paths, and writes out a separate file for the scattering contributions for the EXAFS from each scattering path. Conveniently (and though it does not calculate these factors individually), it breaks up the results in a way that can be put into the standard form of the EXAFS equation (Eqn. 10), even for multiple-scattering paths. This allows analysis procedures to easily refine distances, apply multiplicative factors for coordination numbers and S_0^2, and apply disorder terms. Because the outputs are of a uniform format, we can readily mix outputs from different runs of the programs, which is important for modeling complex structures with multiple coordination environments for the absorbing atom.

First-shell fitting

For an example of modeling EXAFS, we start with FeO, a transition metal oxide with the particularly simple rock-salt structure, while still being representative of many systems found in nature and studied by EXAFS, in that the first shell is oxygen, and the second shell is a heavier metal element. We begin with modeling the first Fe-O shell of FeO, take a brief diversion into the meaning and interpretation of the statistical results of the modeling, and then continue on to analyze the second shell.

We start with the crystal structure, generate the input format for FEFF, run FEFF, and gather the outputs. For the rock-salt structure of FeO with six Fe-O near-neighbors in octahedral coordination, and twelve Fe-Fe second neighbors, there will be one file for the six Fe-O scattering paths, and one file for the twelve Fe-Fe scattering paths. To model the first shell EXAFS, we use the simulation for the Fe-O scattering path, and refine the values for NS_0^2, R, and σ^2. We set S_0^2 to 0.75. We will also refine a value for E_0, the threshold defining where k is 0. This is usually necessary because the choice of E_0 from the maximum of the first derivative of the spectra is *ad hoc*, and because the choice of energy threshold in the calculation is somewhat crude. Even if the refined value for E_0 does not change very much, it is strongly correlated with R, so that getting both its value and uncertainty from the fit is important.

The results of the initial refinement is shown in Figure 25, with best values and estimated uncertainties for the refined parameters given in Table 1. These values are not perfect for crystalline FeO, especially in that the distance is contracted from the expected value of 2.14 Å, but they are reasonably close for a first analysis.

It is instructive to look at this refinement more closely, and discuss a few of the details. The refinement was done on the data in R-space, after a Fourier transform of $k^2\chi(k)\Omega(k)$, where $\Omega(k)$ represents a Hanning window with a range between k = [2.5,13.5] Å^{-1}, and with a dk parameter of 2 Å^{-1}. The refinement used the real and imaginary components of $\chi(R)$ between R = [0.9, 2.0] Å. $k^2\chi(k)$ for the data and best-fit model, as well as $\Omega(k)$ are shown on the left side of Figure 26.

From Figures 25 and 26, it is evident that the higher frequency components (that is, from the second shell of Fe-Fe) dominate $k^2\chi(k)$. This is a useful reminder of the power of the Fourier transform in XAFS analysis: it allows us to concentrate on one shell at a time and ignore the others, even if they have larger overall amplitude.

Table 1. Best values and uncertainties (in parentheses) for the refined first shell parameters for FeO. The refinement fit the components of $\chi(R)$ between R = [0.9,2.0] Å after a Fourier transform using k = [2.5,13.5] Å^{-1}, a k-weight of 2, and a Hanning window function. S_0^2 was fixed to 0.75.

Shell	N	R (Å)	σ^2 (Å^2)	ΔE_0 (eV)
Fe-O	5.5(0.5)	2.10(0.01)	0.015(.002)	−3.2(1.0)

EBSCOhost - printed on 2/13/2023 5:26 AM via . All use subject to https://www.ebsco.com/terms-of-use

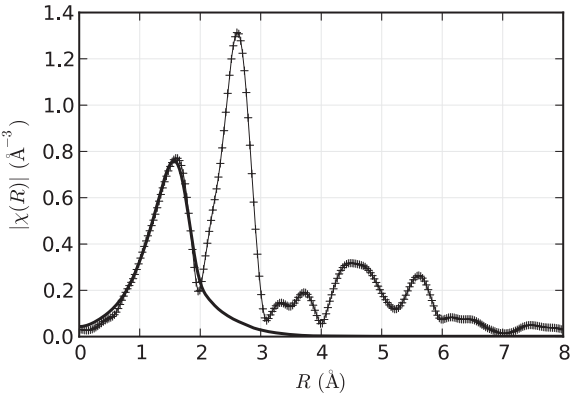


Figure 25. First shell fit to the EXAFS of FeO, showing the magnitude of the Fourier transform of the EXAFS, $|\chi(R)|$, for data (+) and best fit model (solid).

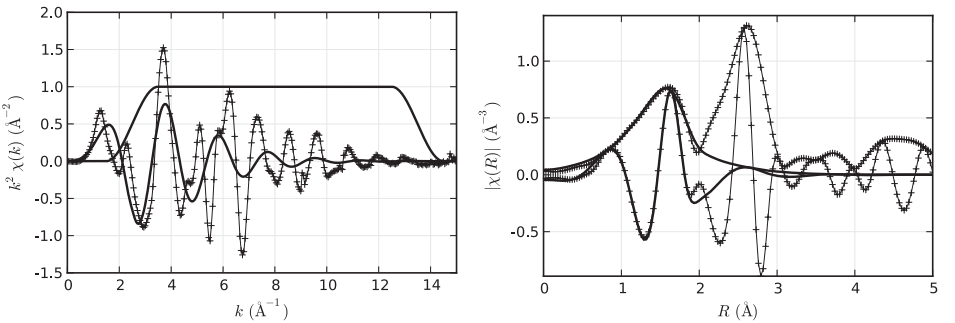


Figure 26. EXAFS $k^2\chi(k)$ (left) for data (+) and best-fit model (solid) for the first shell of FeO, and the window function, $\Omega(k)$, used for the Fourier transform to $\chi(R)$. While the solid curve shows the best-fit to the 1st shell of the EXAFS, this is not obvious from $k^2\chi(k)$. On the right, the real and magnitude components of $\chi(R)$ for the data (+) and best-fit model (solid) show that the model matches the data for the first shell very well.

Fit statistics and estimated uncertainties

At this point, we should pause to discuss further details of the fit, including the fit statistics and how the best-fit values and uncertainties are determined in the refinement. Because the EXAFS equation is complex, and non-linear in the parameters we wish to refine, the refinement is done with a non-linear least-squares fit. Such a fit uses the standard statistical definitions for chi-square and least-squares to determine the best values for the set of parameters varied as those values that give the smallest possible sum of squares of the difference in the model and data. The standard definition of the chi-square or χ^2 statistic (note the use of χ^2 from standard statistical treatments—don't confuse with the EXAFS χ!) that is minimized in a least-squares fit is defined as

$$\chi^2 = \sum_i^{N_{\text{data}}} \frac{[y_i^{\text{data}} - y_i^{\text{model}}(x)]^2}{\varepsilon^2}$$

where y_i^{data} is our experimental data, $y_i^{\text{model}}(x)$ is the model which depends on the variable fitting parameters x, N_{data} is the number of points being fit, and ε is uncertainty in the data. Each of these terms deserves more discussion.

EBSCOhost - printed on 2/13/2023 5:26 AM via . All use subject to https://www.ebsco.com/terms-of-use

The set of variable parameters x are the values actually changed in the fit. If we had fixed a value (say, for N), it would not be a variable. Below, we will impose relationships between parameters in the EXAFS equation, for example, using a single variable to give the value for E_0 for multiple paths. This counts as one variable in the fit, even though it may influence the value of several physical parameters for multiple paths in the model function.

Importantly, the χ^2 definition does not actually specify what is meant by the data y. In the fit above, we used the real and imaginary components of $\chi(R)$, after Fourier transforming the data with a particular window function and k-weight. Using different parameters for the transform would result in different data (and model) to be fit, and could change the results. We could have tried to fit the $k^2\chi(k)$ data without Fourier transforming, but as can be seen from Figure 26, the fit would likely have been substantially worse. But, as we are at liberty to decide what is meant by "the data" to be modeled, we can select the portion of the spectra we're most interested in, including changing the weighting parameters and windows. We can also use multiple spectra that we wish to model with one set of parameters x as "the data." Of course, any transformation or extensions we make to the data must be applied equally to the model for the data. In general, we find that fitting EXAFS data in R-space strikes a good balance between not changing the data substantially, and allowing us to select the k and R ranges we wish to and are able to model.

The uncertainty in the data is represented by ε in the above definition for χ^2. Of course, this too must match what we mean by "the data," and will generally mean the uncertainty in $\chi(R)$ in the range of the data we're modeling. There are many general strategies for estimating uncertainties in data, usually based on involved statistical treatment of many measurements. Such efforts are very useful, but tend to be challenging to apply for every EXAFS spectra. A convenient if crude approach is to rely on the fact that EXAFS decays rapidly with R and to assert that the data at very high R (say, above 15 Å) reflects the noise level. Applying this to the R range of our data assumes that the noise is independent of R (white noise), which is surely an approximation. The advantage of the approach is that it can be applied automatically for any set of data. Tests have shown that it gives a reasonable estimate for data of low to normal quality, and underestimates the noise level for very good data. A simple relationship based on Parseval's theorem and Fourier analysis can be used to relate ε_R, the noise estimate in $\chi(R)$ to ε_k, the noise in $\chi(k)$ (Newville et al. 1999).

There are two additional statistics that are particularly useful (Lytle et al. 1989). One of these is the reduced chi-square, defined as $\chi^2_\nu = \chi^2/(N_{\rm data} - N_{\rm varys})$ where $N_{\rm varys}$ is the number of variable parameters in the fit. This has the feature of being a measure of goodness-of-fit that is takes into account the number of variables used. In principle, for a good fit and data with well-characterized uncertainties, ε, this value should approach 1. χ^2_ν is especially useful when comparing whether one fit is better than another. In simplest terms, a fit with a lower value for χ^2 is said to be better than one with a higher value, even if the two fits have different number of variables. Of course, there is some statistical uncertainty in this assertion, and confidence intervals and F tests can be applied to do a more rigorous analysis. For EXAFS analysis, a principle difficulty is that the values of χ^2_ν are often several orders of magnitude worse than 1, far worse than can be ascribed to a poor estimate of ε. Partly because of this, another statistic is $\mathcal{R}$, or R-factor, defined as

$$\mathcal{R} = \frac{\sum_i^{N_{\rm data}} [y_i^{\rm data} - y_i^{\rm model}(x)]^2}{\sum_i^{N_{\rm data}} [y_i^{\rm data}]^2}$$

which gives the size of the misfit relative to the norm of the data. This value is typically found to below 0.05 or so for good fits, and is often found to be much better than that.

EBSCOhost - printed on 2/13/2023 5:26 AM via . All use subject to https://www.ebsco.com/terms-of-use

Last, and possibly most surprising for the discussion of the pieces in the definition of χ^2, we come to the problem of identifying N_{data}. When measuring $\mu(E)$ we are free to sample as many energy points as we wish, but increasing the number of points in $\mu(E)$ over a particular energy range doesn't necessarily mean we have a better measure of the first shell EXAFS. That is, the EXAFS oscillations are relatively slow in energy, and sampling $\mu(E)$ at 0.1 eV steps over the EXAFS range does not give a better measurement of the first shell EXAFS than acquiring for the same total time but sampling at 1 eV steps. In the previous chapter, we mentioned that the zero-padding and fine spacing of k data sets the spacing of data in R. We should be clear that this can (and usually does) greatly over-sample the data in R space. Oversampling is not bad—it generally improves stability—but it must be understood that it is not adding new, independent data.

For any waveform or signal, the Nyquist-Shannon sampling theorem tells us that the maximum R that can be measured is related to the spacing of sampled data points in k, according to (for EXAFS, with conjugate Fourier variables of k and $2R$):

$$R_{max} = \frac{\pi}{2\delta k}$$

where R_{max} is the maximum R value we can detect, and δk is the spacing for the $\chi(k)$ data. Using $\delta k = 0.05$ Å^{-1} is common in EXAFS, which means we cannot detect EXAFS contributions beyond 31.4 Å. As the converse of this, the resolution for an EXAFS spectrum – the separation in R below which two peaks can be independently measured—is given as

$$\delta R = \frac{\pi}{2k_{max}}$$

where k_{max} is the maximum measured value of k. In short, what matters most for determining how well $\chi(R)$ is measured for any particular value of R is how many periods of oscillations there are in $\chi(k)$.

Related to both R_{max} and the resolution δR, and also resulting from basic signal processing theory and Fourier analysis, the number of independent measurements in a band-limited waveform is

$$N_{ind} \approx \frac{2\Delta k \Delta R}{\pi} + 1 \tag{12}$$

where Δk and ΔR are the range of useful data in k and R. For completeness, the above equation is often given with a "+2" instead of a "+1"(Stern 1993) in the EXAFS literature, though we will follow the more conservative estimate, and note that it would give an upper limit on the number of variables that could be determined from a set of noise-free data. No matter whether "+1" or "+2" is used, the main point is that number of data points available over a particular range of R is given by range of data in k. Making measurements with extremely fine steps in k (or energy) will allow data at higher R to be reliably modeled, but it does allow more parameters to be determined over a particular range of R below R_{max}. In order to be able to fit more parameters over a particular range of R, data needs to be collected to higher k.

Thus, we should modify the definition of χ^2 (and χ^2_ν) used to reflect the number of truly independent data points in the data, as

$$\chi^2 = \frac{N_{ind}}{N_{data}} \sum_{i}^{N_{data}} \frac{[y_i^{data} - y_i^{model}(x)]^2}{\varepsilon^2} \tag{13}$$

where N_{ind} is given by Equation (12) and N_{data} is the number of samples used for the data, even if this far exceeds N_{ind}. Values of N_{ind} for real EXAFS data are not very large. In the first

EBSCOhost - printed on 2/13/2023 5:26 AM via . All use subject to https://www.ebsco.com/terms-of-use

shell fit to FeO, we used k = [2.5,13.5] Å^{-1} and R = [0.9,2.0] Å which gives $N_{ind} \approx 8.7$, and we used 4 variables in the fit—roughly half the maximum. For higher shells and more complicated structures, we will have to come up with ways to limit the number of variables in fits in order to stay below the number of independent measurements for any particular R range that the data actually can support.

Estimates of the uncertainties for variables and correlations between pairs of variables can be made by measuring how χ^2 changes as variables are moved away from their best-fit values. Standard statistical arguments indicate that 1σ error bars (that indicate a 68% confidence in the value) should increase χ^2 by 1 from its best-fit value. This assumes that $\chi^2_\nu \approx 1$, which is usually not true for EXAFS data. As a consequence, it is common in the EXAFS literature to report uncertainties for values that increase χ^2 by χ^2_ν. This is equivalent to asserting that a fit is actually good, and scaling ε so that χ^2_ν is 1.

The estimation of uncertainties and correlations between variables can be very fast, as the computational algorithms used for minimization compute intermediate values related to the correlations between variables (in the form of the covariance matrix) in order to find the best values. Uncertainties determined this way include the effect of correlations (that is, moving the value for one variable away from its best value may change what the best value for another variable would be), but also make some assumptions about how the values of the variable interact. More sophisticated approaches, including brute-force exploration of values by stepping a variable through a set of values and repeatedly refining the rest of the variables, can give better measures of uncertainties, but are more computationally expensive.

Though the aim of a fit is to find the best values for the fitting parameters x, the computational techniques used do not guarantee that the "global" minimum of χ^2 is found, only that a "local" minima is found based on the starting values. This, of course, can cause considerable concern. Care should be taken to check that the results found are not too sensitive to the starting values for the variables or data manipulation parameters including Fourier transform ranges and weights, and background subtraction parameters. Checking for false global minima is somewhat more involved. Fortunately, for EXAFS analysis with reasonably well-defined shells, false minima usually give obviously non-physical results, such as negative or huge coordination numbers or negative values for σ^2. Another warning sign for a poor model is an E_0 shift away from the maximum of the first derivative by 10 eV or more. This can sometimes happen, but it might also indicate that the model $\chi(k)$ may have "jumped" a half or whole period away from its correct position, and that the amplitude parameters may be very far off, as if the Z for the scatterer is wrong.

Our diversion into fitting statistics is complete, and we can return to our first shell fit to Fe-O before continuing on. The data was estimated to have $\varepsilon_R \approx 5 \times 10^{-3}$ and $\varepsilon_k \approx 2 \times 10^{-4}$, which is a typical noise level for experimental $\chi(k)$ data. With a standard k grid of 0.05 Å^{-1}, and an R grid of ≈ 0.0307 Å, the fit had 72 data points, but $N_{ind} \approx 8.7$. Scaled to N_{ind} as in Equation (13), the fit has $\chi^2 \approx 243$ and $\chi^2_\nu \approx 51.7$ (again with 4 variables), and $\mathcal{R} \approx 0.005$.

Second-shell fitting

We are now ready to include the second shell in the model for the FeO EXAFS. To do this, we simply add the path for Fe-Fe scattering to the sum in the EXAFS equation. We will add variables for R, N, and σ^2 for the Fe-Fe shell to those for the Fe-O scattering path. We'll use the same value for E_0 for both the Fe-O and Fe-Fe path, and keep all parameters the same as for the fit above, except that we'll extend the R range to be R = [0.9,3.1] Å. This will increase N_{ind} to ≈ 15.7, while we've increased the number of variables to 7.

The fit is shown in Figure 27 and values and uncertainties for the fitted variables are given in Table 2. The fit gave statistics of $\chi^2 \approx 837$, $\chi^2_\nu \approx 96$, and $\mathcal{R} \approx 0.0059$. The structural

EBSCOhost - printed on 2/13/2023 5:26 AM via . All use subject to https://www.ebsco.com/terms-of-use

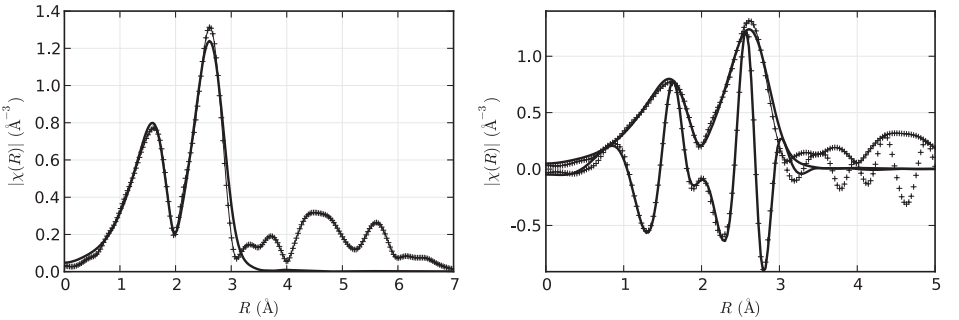


Figure 27. EXAFS $|\chi(R)|$ (left) and $Re[\chi(R)]$ (right) for FeO data (+) and best-fit model (solid) for the first two shells around Fe, including Fe-O and Fe-Fe scattering paths.

Table 2. Best values and uncertainties (in parentheses) for the refined first (Fe-O) and second (Fe-Fe) shells for FeO. The refinement fit the components of $\chi(R)$ between R = [0.9,3.0] Å with all other parameters as in Table 1.

Shell	***N***	***R*** **(Å)**	σ^2 **(Å^2)**	ΔE_0 **(eV)**
Fe-O	5.3(0.5)	2.11(0.01)	0.013(.002)	−1.2(0.5)
Fe-Fe	13.4(1.3)	3.08(0.01)	0.015(.001)	−1.2(0.5)

values for distances and coordination number are consistent with the known crystal structure of FeO, though the Fe-O distance is a bit shorter than expected, and the Fe-Fe is a bit longer than expected, both suggesting that there may be some contamination of a ferric iron phase in the sample. The fits are shown in Figure 27, and individual contributions to the total best-fit spectrum are shown in both *k*- and *R*-space in Figure 28.

An important aspect of using fitting techniques to model experimental data is the ability to compare different fits to decide which of two different models is better. We will illustrate this by questioning the assumption in the above the model that the E_0 parameter should be exactly the same for the Fe-O and Fe-Fe scattering path. Changing this model to allow another variable parameter and re-running the fit is straightforward. For this data set, the fit results are close enough to the previous fit that the graphs of $\chi(k)$ and $\chi(R)$ are nearly unchanged. The newly refined values for the parameter are given in Table 3. Compared to the values in Table 2, the results are very similar except for the values of E_0 and a slight increase in uncertainties.

The fit statistics for this refinement are $\chi^2 \approx 811$, $\chi^2_\nu \approx 105$, and $\mathcal{R} \approx 0.0057$. Since both χ^2 and $\mathcal{R}$ have decreased, the model with 2 independent E_0 values is clearly a closer match to the data. However, we added a variable to the model, so it is reasonable to expect that the fit should be better. But is the fit sufficient to justify the additional variable? The simplest approach to answering this question is to ask if χ^2_ν has improved. In this case, it has not—it went from roughly 96 to 105. Since these statistics all have uncertainties associated with them, a slightly more subtle question is: what is the probability that the second fit is better than the first? A standard statistical *F*-test can be used to give this probability, which turns out to be about 32% for these two fits (that is, with $N_{\rm ind} = 15.7$, $\chi^2 \approx 837$ for 8 variables and $\chi^2 \approx 811$ for 7 variables).

Another way to look at this is to ask if the added variable (E_0 for the Fe-Fe shell) found a value that was significantly different from the value it would have otherwise had. The two values for E_0 in the "2 E_0 model" are noticeably different from one another—approximately at the limits of their uncertainties—but both are consistent with the value found in the "1 E_0 model."

EBSCOhost - printed on 2/13/2023 5:26 AM via . All use subject to https://www.ebsco.com/terms-of-use

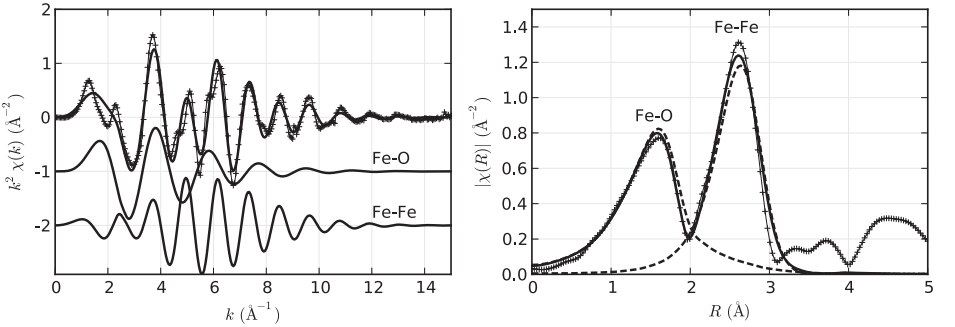


Figure 28. Contributions of the first and second shell to the total model fit to the FeO EXAFS. On the left, the fit (solid) matches the data (+) much better than in Figure 26. Note that, compared to the Fe-O contribution the Fe-Fe contribution has a shorter period corresponding to longer interatomic distance, and has magnitude centered at higher k, as predicted by the $f(k)$ function shown in Figure 10. On the right, the $|\chi(R)|$ of the contributions from the two shells are shown. Though there is a sharp dip at 2 Å between peaks for the two shells, there is substantial leakage from one shell to another.

Table 3. Best values and uncertainties (in parentheses) for the refined first (Fe-O) and second (Fe-Fe) shells for FeO for a model just like that shown in Table 2 except that the 2 values for E_0 are allowed to vary independently.

Shell	***N***	***R*** **(Å)**	σ^2 **(Å^2)**	ΔE_0 **(eV)**
Fe-O	5.3(0.6)	2.12(0.01)	0.013(.002)	−0.7(1.2)
Fe-Fe	13.3(1.3)	3.08(0.01)	0.015(.001)	−1.5(0.8)

This also leads us to the conclusion that the additional variable E_0 is not actually necessary for modeling this data.

We've seen that structural refinement of EXAFS data can be somewhat complicated, even for a relatively straightforward system such as FeO. Many real systems can be much more challenging, but the fundamental principles described here remain the same. The ability to alter which of the physical parameters describing the different paths in the EXAFS sum are independently varied in the refinement, and test the robustness of these, can be especially important for more sophisticated analysis. One way to think about this is that in the first version of the above example, we used the value of one variable for two different path variables—E_0 for the Fe-O and Fe-Fe paths, and then demonstrated that using one value for these two physical parameters was robust. This is the simplest type of constraint that can be applied in an EXAFS analysis. In this case, it has the noticeable advantage of improving the fit because it uses fewer independent variables. For a mixed coordination shell, perhaps a mixture of Fe-O and Fe-S, one may want to include paths for Fe-O and Fe-S and ask the model not to simply refine the weight of each of these independently but rather to ask what fraction of the Fe atoms are coordinated by oxygen. To do this, one would vary the fraction x_{FeO} as a pre-factor to the amplitude term for the Fe-O path and constrain the coordination number for the Fe-S path to use $1 - x_{\mathrm{FeO}}$. More complex constraints can be imposed when simultaneously refining data from different edges or different temperatures measured on the same sample. In a sense, the use of multiple paths for different parts of the R range for $\chi(R)$ in the fit above is merely the starting point for thinking about how different contributions can be put together to make a model for a set of data.

The basic formalism for modeling EXAFS data has been given, based on the Path expansion, theoretical calculations of the contributions for these paths, the Fourier transform,

EBSCOhost - printed on 2/13/2023 5:26 AM via . All use subject to https://www.ebsco.com/terms-of-use

and a statistical understanding of the information present in a real EXAFS spectrum. We have illustrated a simple approach to refining a structural model using EXAFS data, and used statistical methods to compare two different candidate models. Finally we have outlined the route forward to building models for more complex EXAFS data.

Two distinct and essential challenges exist for EXAFS analysis. First, the complexity of the theoretical calculations for photoelectron scattering make it difficult to get scattering factors $f(k)$ and $\delta(k)$ that can match the accuracy of measured EXAFS data. By itself, this has proven to not be a serious problem, as the EXAFS literature is full of examples showing the accuracy of the results from EXAFS despite the imperfect theoretical calculations. Second, the limited information contained in a finite EXAFS spectrum coupled with the number of scattering paths needed to model real systems makes building and testing realistic models for complex systems challenging. Progress in analysis tools for EXAFS continues to make the building and testing of such models easier and more robust, but modeling still requires a fair amount of expertise and care. Despite the challenges, EXAFS has been proven to give reproducible and reliable measures of the local structure around selected atoms that cannot be obtained in any other way, and the number of scientists using EXAFS in both mature and new fields of science continues to grow.

REFERENCES

Als-Nielsen J, McMorrow D (2001) Elements of Modern X-ray Physics. John Wiley & Sons

Booth CH, Bridges F (2005) Improved self-absorption correction for fluorescence measurements of extended X-ray absorption fine-structure. Physica Scripta T115:202-204

Brown GE, Calas G, Waychunas GA, Petiau J (1998) X-ray absorption spectroscopy; applications in mineralogy and geochemistry. Rev Mineral Geochem 18:431-512

Bunker G (2010) Introduction to XAFS: A Practical Guide to X-ray Absorption Fine Structure Spectroscopy. Cambridge University Press

Calvin S (2013*)* XAFS for Everyone. CRC Press

Filipponi A, Di Cicco A, Natoli CR (1995) X-ray-absorption spectroscopy and n-body distribution functions in condensed matter. Phys Rev B 52:15122–15134

IXAS (2012) International X-ray Absorption Society. *http://www.ixasportal.net/*

Kelly SD, Hesterberg D, Ravel B (2008) Analysis of Soils and Minerals using X-ray Absorption Spectrocopy. *In:* Methods of Soil Analysis Part 5 - Mineralogical Methods. Ulery AL, Drees LR (eds), Soil Science Society of America, p 387-464

Koningsberger DC, Prins R (eds) (1998) X-ray Absorption: Principles, Applications, Techniques of EXAFS, SEXAFS, and XANES. John Wiley & Sons

Lytle FW, Sayers DE, Stern EA (1989) Report on the international workshop on standards and criteria in x-ray absorption spectroscopies. Physica B 158:701-722

Manceau A, Marcus MA, Tamura N (2002) Quantitative speciation of heavy metals in soils and sediments by synchrotron X-ray techniques. Rev Mineral Geochem 49:341-428

Newville M (2001a) IFEFFIT: interactive XAFS analysis and FEFF fitting. J Synchrotron Radiat 8:322-324

Newville M (2001b) EXAFS analysis using FEFF and FEFFIT. J Synchrotron Radiat 8:96-100

Newville M, Livins P, Yacoby Y, Rehr JJ, Stern EA (1993) Near-edge X-ray-absorption fine structure of Pb: A comparison of theory and experiment. Phys Rev B 47:14126-14131

Newville M, Boyanov B, Sayers DE (1999) Estimation of uncertainties in XAFS data. J Synchrotron Radiat 6:264-265

Pfalzer P, Urbach JP, Klemm M, Horn S, denBoer ML, Frenkel AI, Kirkland JP (1999) Elimination of self-absorption in fluorescence hard-x-ray absorption spectra. Phys Rev B 60:9335-9339

Ravel B, Newville M (2005) ATHENA, ARTEMIS, HEPHAESTUS: data analysis for X-ray absorption spectroscopy using IFEFFIT. J Synchrotron Radiat 12:537-541

Rehr JJ, Albers RC (2000) Theoretical approaches to x-ray absorption fine-structure. Rev Mod Phys 72(3):621-654

Rehr JJ, Mustre de Leon J, Zabinsky SI, Albers RC (1991) Theoretical X-ray absorption fine structure standards. J Am Chem Soc 113:5135-5140

Stern EA (1988) Principles of EXAFS. *In:* X-ray Absorption: Principles, Applications, Techniques of EXAFS, SEXAFS, and XANES. Koningsberger DC, Prins R (eds) John Wiley & Sons, Chapter 1

EBSCOhost - printed on 2/13/2023 5:26 AM via . All use subject to https://www.ebsco.com/terms-of-use

Stern EA (1993) Number of relevant independent points in x-ray-absorption fine-structure spectra. Phys Rev B 48:9825-9827

Stern EA, Heald SM (1983) Principles and Applications of EXAFS. *In:* Handbook of Synchrotron Radiation. Koch EE (ed) North-Holland, p 995-1014

Sutton SR, Bertsch PM, Newville M, Rivers M, Lanzirotti A, Eng P (2002) Microfluorescence and microtomography analyses of heterogeneous earth and environmental materials. Rev Mineral Geochem 49:429-483

Teo BK (1986) EXAFS: Basic Principles and Data Analysis. Springer-Verlag

XAFS.ORG (2003) *http://xafs.org* {Site as of 2013 will be: *http://www.ixasportal.net/wiki/doku.php*}

EBSCOhost - printed on 2/13/2023 5:26 AM via . All use subject to https://www.ebsco.com/terms-of-use

Reviews in Mineralogy & Geochemistry
Vol. 78 pp. 75-138, 2014
Copyright © Mineralogical Society of America

X-ray Absorption Near-Edge Structure (XANES) Spectroscopy

Grant S. Henderson[1], Frank M.F. de Groot[2], Benjamin J.A. Moulton[1]

[1]Department of Earth Sciences
University of Toronto
22 Russell St
Toronto, Ontario, M5S 3B1
Canada

henders@es.utoronto.ca

[2]Inorganic Chemistry and Catalysis Department of Chemistry
Utrecht University
Universiteitsweg 99, 3584 CG Utrecht, Netherlands

f.m.f.degroot@uu.nl

PREFACE

The previous *Reviews in Mineralogy* volume on spectroscopic methods (Vol. 18 *Spectroscopic Methods in Mineralogy and Geology*, Frank C. Hawthorne, ed. 1988), contained a single chapter on X-ray absorption spectroscopy which reviewed aspects of both EXAFS (Extended X-ray Absorption Fine Structure) and XANES (X-ray Absorption Near-Edge Structure) (Brown et al. 1988, Chapter 11) However, since publication of that review there have been considerable advances in our understanding of XANES theory and applications. Hence EXAFS and XANES have been separated into their own individual chapters in the current volume. In this chapter we endeavor to bring the reader up to date with regard to current XANES theories, as well as, introducing them to the common applications of the technique in mineralogy, geochemistry and materials science. There have been several reviews of XANES (cf., Brown et al. 1988, Brown and Parks 1989, Manceau et al. 2002, Brown and Sturchio 2002, Mottana 2004, Rehr and Ankudinov 2005, de Groot 2001, 2005, and papers therein). In this chapter on XANES it is not our intention to provide a comprehensive review of all the XANES studies since 1988 but to summarize what X-ray edges are commonly investigated and what one can expect to be able to extract from the data. The reader is also advised to read the chapters in this volume on analytical transmission electron microscopy by Brydson et al. (2014, this volume) where (core level) electron energy loss (EELS) spectroscopy is discussed, and by Lee et al. (2014, this volume) on X-ray Raman spectroscopy (XRS), as these techniques provide element specific information similar to XANES.

X-ray absorption near-edge structure (XANES) spectroscopy using synchrotron radiation is a well-established technique providing information on the electronic, structural and magnetic properties of matter. In XANES, a photon is absorbed and an electron is excited from a core state to an empty state. To excite an electron in a given core-level, the photon energy has to be equal or higher than the binding energy of this core-level. This gives rise to the opening of a new absorption channel when the photon energy is scanned. The energy of an absorption edge therefore corresponds to the core-level energy, which is characteristic for each element, making XANES an element-selective technique.

1529-6466/14/0078-0003$10.00 http://dx.doi.org/10.2138/rmg.2014.78.3

EBSCOhost - printed on 2/13/2023 5:26 AM via . All use subject to https://www.ebsco.com/terms-of-use

In addition to the XANES region, at higher energies the extended X-ray absorption fine structure (EXAFS) region is found. The spectral shape in the near-edge region is determined by electronic density of states effects and gives mainly information about the electronic properties and the local geometry of the absorbing atom. The EXAFS region is dominated by single scattering events of the outgoing electron on the neighboring atoms, providing mainly information about the local geometric structure around the absorbing site. In this chapter we will focus on XANES.

INTRODUCTION

XANES is an important tool for the characterization of bulk minerals as well as for studies of mineral surfaces and adsorbents on mineral surfaces. The particular assets of XANES spectroscopy are its element specificity and the possibility to obtain detailed information in the absence of long range order. Below, it will be shown that the X-ray absorption spectrum in many cases is closely related to the density of unoccupied electronic states of a system. As such XANES is able to provide a detailed picture of the local electronic structure of the element studied.

Interaction of X-rays with matter

In XANES, the changes in the absorption of X-rays due to the photoelectric effect is measured. The XANES spectrum is given by the absorption cross section μ. An X-ray photon acts on charged particles such as electrons. As X-ray passes an electron, its electric field pushes the electron first in one direction, then in the opposite direction, in other words the field oscillates in both direction and strength, allowing the electron to capture the energy. The Fermi Golden Rule states that the XANES intensity (I_{XANES}) for the transition from a system in its initial state Φ_i to a final state Φ_f is given by:

$$I_{XAXES} \propto \left|\left\langle \varepsilon \left| \hat{e}_q \cdot r \right| \nu \right\rangle\right|^2 \rho$$

where $\hat{e}_q \cdot r$ is the electric dipole operator. The quadrupole transition is more than 100 times smaller and often can be neglected. In the case of the pre-edge structures of the metal *K*-edges, the quadrupole transition is important because the 3*d* density of states is much larger than the 4*p* density of states and the quadrupole peaks appear in the pre-edge region where there is no 4*p* density of states.

Binding energy

If an assembly of atoms is exposed to X-rays it will absorb some of the incoming photons. At a certain energy a sharp rise in the absorption will be observed. This sharp rise in absorption is called the absorption edge. The energy of the absorption edge is determined by the binding energy of a core level. Exactly at the edge, the photon energy is equal to the binding energy, or more precisely the edge identifies transitions from the ground state to the lowest electron-hole excited state.

The core hole binding energy is formally defined in relation to the core electron ionization energy, as is measured in an X-ray photoemission experiment. The ionization energy is the amount of energy required to remove an electron from an atom, as one would do in an X-ray photoemission spectroscopy (XPS) experiment (cf., Nesbitt and Bancroft 2014, this volume). In case of a solid, the ionization energy is corrected by the work function, the energy difference between the lowest empty state and the vacuum level. The core hole binding energies of all metals are tabulated in the X-ray data booklet (Thompson and Vaughan 2011). The XANES edge energy is not necessarily exactly the same as the core hole binding energy. The two processes are respectively:

EBSCOhost - printed on 2/13/2023 5:26 AM via . All use subject to https://www.ebsco.com/terms-of-use

$$\text{XPS: } \Psi_0 > \Psi_0\underline{c} + \varepsilon$$

$$\text{XAS: } \Psi_0 > \Psi_0\underline{c}v$$

In XPS the ground state (Ψ_0) is excited to the ground state plus a core hole ($\underline{c}$), where the electron (ε) is excited to higher energy, while in XAS the ground state is excited with a core-to-valence excitation ($\underline{c}v$). The XPS binding (E_B) is defined as the photon energy (Ω) minus the measured kinetic energy of the electron (E_k) and corrected for the work function (ϕ):

$$E_B = \Omega - E_k - \phi$$

The work function is the minimal energy to emit an electron from the material. In metals the XAS edge energy can be assumed to be equal to the XPS binding energy, because exactly at the XPS binding energy a transition is possible to the lowest empty state. Experimentally the XAS edge energy can be slightly higher than the XPS binding energy, for example if the transition to the lowest empty state is forbidden by selection rules.

Single electron excitation approximation and selection rules

In first approximation XANES can be described as the excitation of a core electron to an empty state. In the Fermi golden rule, the initial state wave function is rewritten as a core wave function and the final state wave function (ε) as a valence electron wave function (v). This implicitly assumes that all other electrons do not participate in the X-ray induced transition. In this approximation, the Fermi golden rule can be written as:

$$I_{XAXES} \propto \left|\left\langle \varepsilon \left| \hat{e}_q \cdot r \right| v \right\rangle\right|^2 \rho$$

The X-ray absorption selection rules determine that the dipole matrix element is non-zero if the orbital quantum number of the final state differs by one from the initial state ($\Delta L = \pm 1$, i.e., $s \rightarrow p$, $p \rightarrow s$ or d, etc.) and the spin is conserved ($\Delta S = 0$). In the dipole approximation, the shape of the absorption spectrum should look like the partial density of the ($\Delta L = \pm 1$) empty states projected on the absorbing site, convoluted with a Lorentzian. This Lorentzian broadening is due to the finite lifetime of the core-hole, leading to an uncertainty in its energy according to Heisenberg's principle. The single electron approximation gives an adequate simulation of the XANES spectral shape if the interactions between the electrons in the final state are relatively weak. This is the case for all excitations from 1*s* core states (*K*-edges).

Calculations of XANES spectra

The dominant method to calculate the density of states is Density Functional Theory (DFT) where either band structure, multiple scattering or chemical DFT codes can be used (cf., Jahn and Kowalski 2014, this volume). Programs to calculate the X-ray absorption spectral shape include FEFF, Wien2k, QuantumEspresso, ADF and ORCA. Depending on the specific method used one has to use a number of "technical" parameters such as the number of states used, the specific exchange-correlation potential and semi-empirical parameters such as the Hubbard U (the two-electron repulsion energy). An overview of the various software packages can be presently found at *http://www.xafs.org* but will move to *http://www.ixasportal.net/wiki/doku.php* shortly.

Core hole effects and hole-electron excitations. Following the final state rule (von Barth and Grossmann 1982), one has to calculate the distribution of empty states in the final state of the absorption process. The final state includes a core hole on the absorbing site. The inclusion of the core hole introduces a significantly larger unit cell in case of reciprocal space calculations. In case of real-space calculations, the inclusion of a core hole is straightforward and only the potential of the central atom is modified. It has been shown for many examples that the inclusion of the core hole improves the agreement with experiment (Taillefumier et al. 2002). It is not well established if the inclusion of a fullcore hole gives the best description of

EBSCOhost - printed on 2/13/2023 5:26 AM via . All use subject to https://www.ebsco.com/terms-of-use

the XANES spectral shape. For example, one can use the exchange core hole (XCH) method, or methods that explicitly calculate the creation of hole-electron excitation such as Time-Dependent DFT (DeBeer-George et al. 2008).

Multiplet effects. The core hole that is part of the XANES final state does not only have an influence on the potential, but the core state also has a wave function. In case of a 1*s* core state, this wave function can be neglected. In case of 2*s* and 3*s* wave functions the overlap is larger but the only effect that plays a role is the spin-up or spin-down character of the core hole. The spin-moment of the core hole interacts with the valence electrons (or holes) giving rise to an exchange splitting in 2*s* and 3*s* XANES. The same exchange interaction plays a role in 2*s* and 3*s* XPS spectra, which are more often studied than their XANES counterparts (L_1 and M_1 edges, Okada et al. 1994). Things become dramatically more complex in those cases where a core hole carries an orbital momentum. The core hole spin-orbit coupling that separates the 2*p* XANES spectra into their $2p_{3/2}$ (L_3) and $2p_{1/2}$ (L_2) parts. In addition, the 2*p* wave function can have significant overlap with the valence electrons. In case of 3*d*-systems, the 2*p*3*d* electron-electron interactions are significant and significantly modify the spectral shape. The term "multiplet effect" is used to indicate this core-valence electron-electron interaction (de Groot 1994).

EXPERIMENTAL ASPECTS OF XANES

Doing a XANES experiment at a beamline

Prior to doing experiments one has to select an appropriate beamline at a suitable synchrotron radiation facility and it's a good idea to check on what costs will be involved should your experiments be allocated beamtime. Often facilities cover travel and living expenses for researchers, but not always. A proposal has to be written and submitted to the facility (online and by a set deadline) outlining the type of experiments that will be done, edges to be investigated, type of samples, energy resolution required and probable length of time to do the experiments (usually in terms of 8 hour shifts), as well as, any special requirements such as use of wet and dry labs, high pressure or temperature equipment, etc. These proposals are then peer reviewed and beamtime allocated based on competitive review of all the proposals requiring access to the experimental beamline and synchrotron radiation facility. If the experiments are approved it is allocated a set number of shifts for their experiment. Once at the beamline to run experiments, it is important to remember that they must be performed during the limited time allocated, so it is important to utilize all available time. This means that experiments will run 24 hours per day requiring more than a single person to be present (usually 2-3 people are required). Samples must be prioritized in case of problems with the X-ray beam since a variety of unexpected disruptions may occur, such as loss of the X-ray beam, computer glitches etc. that may reduce available experimental time. It is also advisable to have extra samples available to run in case the experiments go quicker and smoother than anticipated (not usually the case!).

For example, for Fe XANES with an edge energy of ~7110 eV, the beamline must be capable of collecting data over the appropriate energy range of interest (from ~20 eV before the edge to ~150 eV above the edge for a typical XANES experiment. The theoretical width of the peak responsible for the 1*s* state to higher energy states is ~1.5 eV (Krause and Oliver 1979) so that the beamline optics must ideally be sufficient to resolve features of this width, i.e., energy resolution should be at least 2 times better. In addition, the data need to be collected at a step size that will resolve subtle experimental features such as shoulders on the pre-edge peaks. Usually the step size in the pre-edge region is set at 0.1 or 0.2 eV and slightly larger step sizes (0.5 eV) across the edge itself with an even larger step size for the EXAFS region, 1.0 eV close to the edge and up to 5 eV at higher energies. The energy range must also be calibrated, for example using metallic reference foils. Furthermore, an internal standard should be used if experiments are going to be performed on the same samples and

EBSCOhost - printed on 2/13/2023 5:26 AM via . All use subject to https://www.ebsco.com/terms-of-use

edges at *different* beamlines as the energy position may change slightly from beamline to beamline due to different facility characteristics. In addition, for quantitative measurements of iron oxidation states a set of standards must be used with well-known oxidation states, preferably determined using another technique such as Mossbauer or wet chemical analysis, and the standards must have the Fe in somewhat similar matrices to those of the unknown samples. This means that for quantitative Fe redox measurements on glasses, glass standards should be used while for minerals mineral standards should be used (cf., e.g., Galoisy et al. 2001; Berry et al. 2003a; Wilke et al. 2005; Cottrell et al. 2009). Finally it is important that the experimental conditions from one experimental run to another be the same, which means that a quick energy calibration should be run periodically throughout experimental runs, as well as, immediately after restoration of the beam following any beam disruption such as a beam dump. Depending upon the resolution, signal-to-noise and time required to collect a spectrum, multiple spectra (usually 2 or 3) are collected on the same sample and averaged. It is also important to check that the sample is not being affected by the beam (beam damage) so some time should be allocated to collecting spectra with and without moving the position of the beam on the sample. This is particularly important for redox studies where the beam itself may change the redox state of the sample.

Data reduction

Once the data have been collected and individual spectra checked for "glitches," such as random spikes in the data which must be removed, the data need to be reduced to a suitable form for analysis and interpretation. XANES data reduction is relatively simple and may be done with a variety of available software. Data reduction steps include possible correction for self-absorption effects, removal of a pre-edge background (usually a linear fit or a Victoreen polynomial) and normalization of the edge jump to one.

In some publications the background continuum is removed from the XANES spectrum. Background continuum removal is important for EXAFS analysis, but for XANES analysis it is not obvious what advantage is gained from such continuum removal. In fact, theoretical XANES simulations based on DFT calculate the whole XANES spectral shape including the background continuum. The background continuum is removed using some sort of arctan or error function but correction that has been widely used since the late 80's is an arctan function (cf., Poe et al. 2004; Höche et al. 2011). An example of an arctan fit from Wilke et al. (2001) is shown in Figure 1. Outka and Stohr (1988) note that there are several different types of continuum steps that can be observed and it is important to account for the step if the spectra are going to be modeled using some sort of fitting of the peaks by Gaussian, Lorentzian or pseudo-Voigt peak profiles. Unfortunately, the placement and width of the background subtraction functions is not well defined. Outka and Stohr's (1988) prefer an error function because the width of the function is related to a known parameter; the instrumental resolution, while the width of the arctan is related to the life time of the excited state which may not be known. As to the position of the step, Outka and Stohr (1988) suggest it should be placed 1 to several eV below the core level ionization energy. Regardless of how the continuum step is modeled it is important that all the experimental data be treated in a consistent manner with background removal fully described and justified.

Prior to analysis and interpretation of the pre-edge features one further correction needs to be applied. The background of the edge under the pre-edge features needs to be removed and this is done by fitting a polynomial such as a spline function that smoothly reproduces the slope of the data prior to the pre-edge and immediately following the pre-edge peaks. For extracting the pre-edge the background may also be described by the tail of a Gaussian or Lorentzian function (cf., Farges et al. 2004). One example for background removal by a spline function is shown in the inset in Figure 1. The data are now ready to be analyzed and interpreted.

EBSCOhost - printed on 2/13/2023 5:26 AM via . All use subject to https://www.ebsco.com/terms-of-use

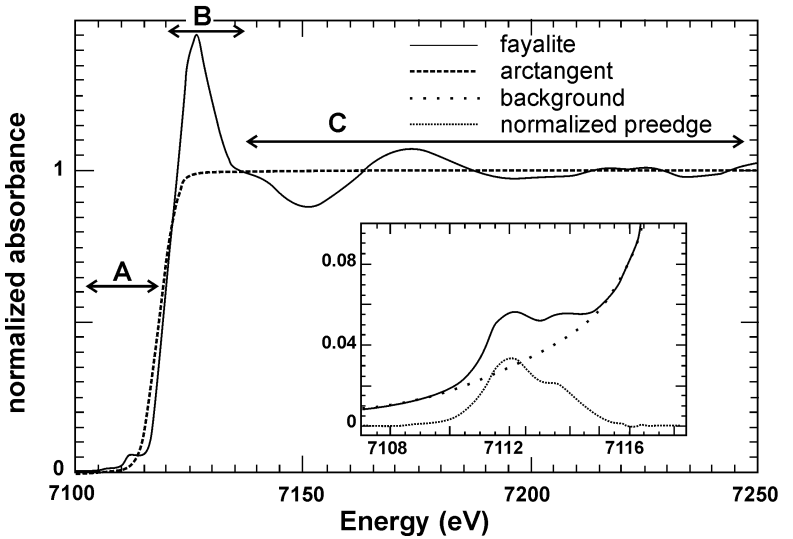


Figure 1. The arctan function and normalization of the pre-edge. The inset shows the background fit for the pre-edge region (after Wilke et al. 2001). The pre-edge (A), edge (B) and post-edge (C) regions are indicated. The inset shows the background removal under the pre-edge features.

XANES DETECTION MODES

Transmission detection of XANES

A XANES spectrum originates from the fact that the probability of an electron to be ejected from a core level is dependent on the energy of the incoming beam. For this reason the energy of the X-rays is scanned during an experiment. The X-ray interacts with the sample of interest and the intensity after the sample is measured. An important factor of transmission detection is the requirement for a homogeneous sample. Variations in the thickness or pinholes are reasons for the so-called thickness effect that can significantly affect the spectral shape by introducing a non-linear response (Schroeder et al. 1996). Transmission experiments are standard for hard X-rays, but due to the attenuation length of less than one micron, soft X-ray XANES is usually not measured in transmission mode, except in the case of Transmission X-ray Microscopy (TXM) beamlines (de Smit et al. 2008).

Electron yield detection of XANES

The decay of the core hole gives rise to an avalanche of electrons, photons and ions escaping from the surface of the substrate. By measuring any of these decay products, it is possible to measure samples of arbitrary thickness. An important prerequisite for the use of decay channels is that the channels that are measured are linearly proportional to the absorption cross section. With the total electron yield method, one detects all electrons that emerge from the sample surface, independent of their energy. One can detect the current that flows to the sample or detect the emitted electrons. The interaction of electrons with solids is much larger than the interaction of X-rays with solids. This implies that the electrons that escape from the sample must originate close to the surface. The probing depth of total electron yield (TEY) lies in the range between approximately 1 to 10 nm, depending on the edge strength and the material studied. A quantitative study on the oxygen *K*-edge determined an electron escape depth of 1.9 nm (Abbate et al. 1992).

EBSCOhost - printed on 2/13/2023 5:26 AM via . All use subject to https://www.ebsco.com/terms-of-use

Fluorescence yield detection of XANES

The fluorescence decay of the core hole can be used as the basis for the absorption measurement. The amount of fluorescent decay increases with energy and dominates over Auger decay for hard X-ray experiments. The photon created in the fluorescent decay has a mean free path of the same order of magnitude as the incoming X-ray, which implies that there will be saturation effects if the sample is not dilute. For materials dilute in the studied element the background absorption μ_B dominates the absorption at the specific edge and the measured fluorescence intensity (also known as fluorescence yield (FY)) is proportional to the absorption coefficient. For less dilute materials the spectral shape is modified and the highest peaks will appear compressed with respect to the lower peaks, an effect known as self-absorption or saturation. In case of the *L*-edges of transition metal compounds and the *M*-edges of rare earths the fluorescence decay is strongly energy dependent, which implies that for those systems FY detection is not directly proportional to the X-ray absorption spectral shape (de Groot 2012).

Partial Fluorescence Yield detection of XANES

Recently, a range of partial fluorescence yield methods have been developed. We briefly discuss two important approaches, respectively inverse partial fluorescence yield (IPFY) and high-energy fluorescence detection (HERFD). IPFY measured the integrated fluorescence of an element in the system other than the edge element that is measured. It can be shown that such an approach effectively yields a fluorescence yield spectrum that is effectively not sensitive to saturation effects (Achkar et al. 2011). HERFD uses a high-resolution fluorescence detector to scan through a XANES spectrum. HERFD-XANES measurements are often performed in connection to resonant inelastic X-ray scattering (RIXS) experiments and relate to a constant-emission-energy cross-section through the RIXS plane. Furthermore, by extracting the constant-incident cross-section at the position *K*-edge pre-edge *L*-edge or *M*-edge-like spectra may be recorded (Caliebe et al. 1998; Glatzel and Bergmann 2005). For systems where multiplet effects are important, the HERFD-XANES can be modified from the XANES spectral shape (Suljoti et al. 2009). Hämäläinen et al. (1991) showed that HERFD-XANES effectively removes the lifetime broadening. This largely enhances the accuracy in the determination of the pre-edge spectral shapes and their intensities. HERFD detection also allows the detection of XANES spectra that are selective to the valence, spin-state or site symmetry (de Groot 2001; Glatzel and Bergmann 2005). One can tune the energy of the fluorescence detector to the peak position of one valence and vary the energy of the incoming X-ray, thereby measuring the X-ray absorption spectrum of that particular valence.

Electron energy loss spectroscopy and X-ray Raman

It can be shown that electron energy loss spectroscopy (EELS) as detected in an electron microscope can measure exactly the same spectral shape as XANES. This is the case under the assumptions that the primary electron energy is higher than a few thousand eV and that the scattering angle is small. Details on EELS spectroscopy are discussed in the chapter by Brydson et al. (2014, this volume).

X-ray Raman spectroscopy is the X-ray analog of optical and UV Raman. A hard X-ray, typically with an energy of about 10.000 eV impinges on the sample and the scattered radiation is measured at an energy lower than 10.000 eV. Like normal Raman one can study vibrational excitations (meV range) and electronic excitations (eV range). In addition, one can study core electron excitations that relate to energy losses of several hundred eV. Note that such core level X-ray Raman could also be named X-ray energy loss spectroscopy (XELS) and as such is the direct X-ray analog of electron energy loss spectroscopy (EELS). As is the case for EELS, the core excitation spectra from X-ray Raman spectroscopy can be described in analogy with XANES under the assumption of small scattering moments. X-ray Raman has a great potential for *in situ* measurements and it presents a hard X-ray alternative to conventional XANES

EBSCOhost - printed on 2/13/2023 5:26 AM via . All use subject to https://www.ebsco.com/terms-of-use

experiments in the study of systems with light elements, including Li, B, C, N and O (Lee et al. 2014, this volume).

XANES microscopy

XANES experiments can be performed with X-ray microscopes. A number of transmission X-ray microscopes (TXM) or scanning transmission X-ray microscopes (STXM) exist for the soft X-ray range and the hard X-ray range. Typical resolutions that can be obtained are of the order of 20 nm. We refer to dedicated reviews for more details on the characteristics of the X-ray optics, etc. In the present review we assume that the TXM microscopes essentially allow doing XANES spectroscopy with 20 nm spatial resolution. If the sample is rotated in the beam the extension to XANES tomography is straightforward (Gonzalez-Jimenez et al. 2012).

XANES ANALYSIS OF METAL *K*-EDGES

An important set of environmental and mineralogical studies involve the 1*s* X-ray absorption spectra (*K*-edges) of the 3*d*-metals. We will discuss respectively the shape, the energy position and the white line intensity of the 1*s* XANES spectra. The 1*s* edges of the 3*d* transition metals have energies ranging from about 4 to 9 KeV. Cabaret and co-workers have carried out DFT calculations for TiO_2 (Cabaret et al. 1999). The complete spectral shape of TiO_2 is reproduced and it can be concluded that the 1*s* XANES of 3*d* transition metals does correspond to the metal *p*-projected density of state. In addition, the pre-edge region is found to be an addition of dipole and quadrupole transitions.

In many mineralogical applications, the systems studied are not exactly known. The metal 1*s* edges do show fine structure and edge shifts that can be used without the explicit calculation of the density of states. For example, the Fe^{3+} edges are shifted to higher energy with respect to the Fe^{2+} edges. The shift to higher energies with higher valence is a general phenomenon that can be used to determine the valence of 3*d* transition metals in unknown systems.

Special energy positions of X-ray absorption edges

We will define the following special energy positions in the XANES edge structure:

- The X-ray absorption edge (E_{edge})
- The pre-edge energy (E_{pre})
- The transition with the lowest excitation energy (E_B)
- The energy where the escaping electron would have exactly zero energy (E_0)

In case of the *K*-edges of transition metal systems, it is not a trivial task to determine the energy position of a XANES edge E_{edge}. There are, at least, three different methods to define the energy of the edge: (a) the inflection point, (b) the energy where the intensity is 50% of the edge maximum and (c) the average of the energies at 20% and 80% of the edge maximum. The inflection point can be accurately determined from the maximum of the first derivative. In case of a single, non-structured edge the methods (a) to (c) all find exactly the same energy. The situation becomes more complicated with a spectrum for which a clear shoulder is visible on the leading edge. For example, iron metal has an edge on which a clear shoulder is visible. The inflection point might lose its value in such a case and, in fact, there can be two inflection points. In our opinion there is no clear criterion to decide which procedure should be followed. Much depends on the spectral details of the observed spectra. The best procedure would perhaps be the use of two or three methods for the edge determination. In case of many 3*d*-transition metal systems, a clear pre-edge is visible due to transitions to 3*d*-states. The pre-edge energy (E_{pre}), defined as the first maximum of the pre-edge can also be used as an experimental indicator.

EBSCOhost - printed on 2/13/2023 5:26 AM via . All use subject to https://www.ebsco.com/terms-of-use

We define the transition with the lowest energy as the binding energy, noting that this energy is not necessarily the same as in XPS as discussed above. Within a ground state calculation, the lowest unoccupied state is determined by the Fermi level can be determined from the comparison with a simulation of the XANES spectral shape. However, if the final state rule is used, the extra core hole potential can shift the edge excitation energy to lower energy, losing its direct relation to the ground state Fermi level. In X-ray photoemission experiments, E_0 is defined as the vacuum level, i.e., the energy at which the electron would have zero kinetic energy. The energy difference between E_F and E_0 is the work function.

Despite the variety of special edge energies including several procedures to determine them, the use of consistent procedures to determine energy positions can lead to clear trends, for example a relation between edge energies and the formal valence of the system. An example is the determination of the pre-edge energies and the edge energies of a series of vanadium oxides by Wong et al. (1984). They find a linear relation between the edge position and the formal oxidation state. In addition, a linear relation was found between the pre-edge energy and the formal oxidation state. The slope of the pre-edge and edge energies is different, respectively about 2 eV/valence for the edge energy and 0.6 eV/valence for the pre-edge energy. This also implies that the energy difference between the pre-edge position and the edge position is linear with the formal oxidation state.

An interesting issue relates to the relative energy position of the edge and pre-edge peak position of octahedral and tetrahedral sites. In the case of iron coordination compounds, equivalent energy positions are found (Westre et al. 1997) whereas for example in the case titanium, copper and aluminum a systematic shift is observed with the tetrahedral peak shifted by approximately 1 eV in the case of copper (Yamamoto et al. 2002).

The pre-edge region

The pre-edge region is related to transitions from the 1*s* core state to the 3*d*-bands. Both direct 1*s*3*d*-quadrupole transitions and dipole transitions to 4*p*-character hybridized with the 3*d*-band are possible. For the quadrupole transitions the matrix elements are less than 1% of the dipole transition, but on the other hand the amount of 3*d*-character is by far larger than the *p*-character. This can make, depending on the particular system, the contributions of quadrupole and dipole transitions equivalent in intensity in the pre-edge region.

The pre-edge structures in systems with isolated metal ions. First we discuss the pre-edge spectra in systems with isolated metal ions in coordination compounds. The general model to interpret these pre-edges is to consider them as quadrupole transitions into empty 3*d*-states. Quadrupole transitions have intrinsic transition strengths of approximately 0.1% of the dipole transitions, but because of the high density of states for the 3*d*-band they are visible as small peaks with ~1 to 3% intensity in most, octahedral, transition metal systems. If inversion symmetry is broken, for example in tetrahedral complexes, the metal 3*d* and 4*p* states mix and there are direct dipole transitions into the 4*p*-character of the 3*d*-band.

The position and number of peaks are sensitive to the oxidation state and coordination of Fe. Their energy separation corresponds to the bound state spectroscopic levels of a Z+1 ion (cf., Westre et al. 1997). Because the 1*s* core hole has no effect on the relative energy positions, the $3d^5$ Fe^{3+} spectra can be modeled using the ground state orbital configuration of $3d^6$ (Schulman et al. 1976; Calas and Petiau 1983). This is because the core hole generated by the promotion of the excited electron to the 3*d* orbitals, is close enough to the nucleus (Z) that the outer orbitals see a configuration similar to the next highest atom on the periodic table (Z+1) (cf., Sutton et al. 2000). Consequently, the pre-edge features can thus be interpreted using ligand field theory or charge transfer multiplet theory (cf., de Groot 2005; de Groot and Kotani 2008). Octahedral complexes only have quadrupole transitions and these transitions can be simulated from $3d^N$ to $1s^1 3d^{N+1}$ multiplet calculations. This approach has been used by Westre et al. (1997) to explain the pre-edge structures in iron coordination compounds.

EBSCOhost - printed on 2/13/2023 5:26 AM via . All use subject to https://www.ebsco.com/terms-of-use

Tetrahedral transition metal complexes, or in general systems where inversion symmetry is broken, have dipole-quadrupole mixing (Westre et al. 1997; DeBeer-George et al. 2005). In the case of tetrahedral symmetry, the local dipole-quadrupole mixing *only* involves the t_2-states, not the *e*-states. Because inversion symmetry is broken, the metal 3*d* and metal 4*p* states mix with each other and form a set of combined 3*d*+4*p* symmetry states. As such, the dipole (D) and quadrupole (Q) transitions reach the same final states, and their peaks are visible at the same energy.

The pre-edge structures in systems with ligand-bridged metal ions. In case of oxides with oxygen-bridged metal ions the spectral situation is more complex. In addition to the local effects, there can be effects due to non-local transitions, as has been shown for the case of TiO_2 (Cabaret et al. 1999). The case of TiO_2 is described in detail in the next section. An example of non-local pre-edge structure can be found in the cobalt *K*-edge XANES of $LiCoO_2$. Figure 2 shows the normal *K*-edge XANES spectrum in comparison with the HERFD XANES. The peak at 7718 eV is related to the main edge, in other words to the dipole transitions to the 4*p* band. The 1*s* XANES spectrum of $LiCoO_2$ contains two clearly observable pre-edges A and B. $LiCoO_2$ is a non-magnetic (S = 0) low-spin oxide and its ground state has a filled t_{2g} band and an empty e_g band. This implies the presence of a single 1*s*3*d* quadrupole peak, which seems in contrast with the two peaks in experiment. Detailed angular dependent experiments showed that the first peak (A) at 7709 eV has quadrupole nature and the second peak (B) at 7711 eV has dipole character (Vankó et al. 2008). This second pre-edge peak of dipole character is absent in low-spin Co(III) complexes such as the $Co(acac)_3$ complex. Both systems are low-spin trivalent cobalt systems, where $Co^{III}(acac)_3$ has isolated Co ions, while in $LiCoO_2$ there are oxygen mediated Co-Co interactions. These observations confirm that the first peak is the local 1*s*3*d* quadrupole transition, while the second peak is a dipole 1*s*4*p* transition to the 4*p* character of the 3*d*-band. These non-local pre-edge transitions have been observed for the cobalt oxides (Vankó et al. 2008), TiO_2 (Cabaret et al. 1999; Shirley 2004; Uozumi et al. 1992), iron oxides (Caliebe et al. 1998; Glatzel et al. 2008) and MnO_2 (Farges 2005). Shukla et al. (2006) observed very small non-local transitions, alternatively called off-site transitions, in La_2CuO_4.

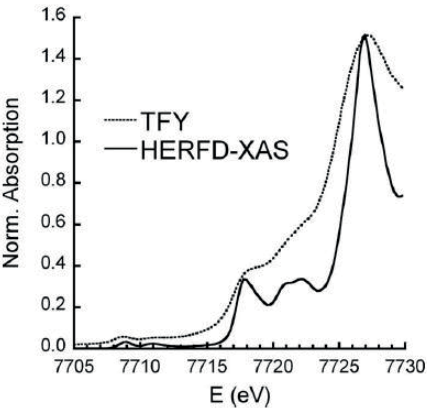


Figure 2. Comparison between XAS spectra recorded at the Co *K* edge using total fluorescence yield (dashed line) and using HERFD XANES (solid line).

The edge region and peaks at higher energies in the XANES region

In addition to the edge shift discussed above, the shape of the edge region can be interpreted in relation to reference compounds, for example the XANES edge structure of a metal in oxides. Some studies interpret spectral features at higher energies. A well-known example is the use of the $1/R^2$ rule, which relates the energy of a peak in the XANES with the distance *R* between the absorbing atom and its neighbors. This rule effectively uses electron scattering, similar as used in the EXAFS region of the spectrum. The scattering vector *k* is proportional to $\sqrt{E_k}$. In the chapter on EXAFS it is shown that within the single scattering approximation the distance *R* is inversely proportional to the scattering vector *k*, yielding as a result the $1/R^2$ rule. The $1/R^2$ rule has been applied successfully for the determination of bond lengths in (adsorbed) small molecules (Stohr 1992) and melts (Wilke et al. 2007).

EBSCOhost - printed on 2/13/2023 5:26 AM via . All use subject to https://www.ebsco.com/terms-of-use

XANES analysis of metal *L*-edges

The metal *L*-edges of the 3*d* transition metals are dominated by multiplet effects as described in the introduction. We will first briefly explain multiplet theory and multiplet analysis. For more details we refer to dedicated reviews on the calculations of *L*-edge spectra (de Groot 1994, 2001). In this review we focus on the consequences for practical *L*-edge analysis applied to minerals. The multiplet effects are too large to make any sensible connection to the empty density of states, as is possible for the *K*-edges. However the *L*-edges can be analyzed without theoretical simulations, focusing on respectively the spectral shifts, the integrated intensity, the branching ratio and XMCD experiments for improved site symmetry analysis.

Multiplet analysis of *L*-edges

L-edges to transition metal compounds with partly filled 3*d* states are dominated by transitions to the empty 3*d* states. In first approximation the transition to the 4*s* states and higher states are neglected. They can be subtracted from the experimental spectra by an edge jump subtraction procedure (Wasinger et al. 2003). We approximate the ground state as $3d^N$ and the final state as $2p^5 3d^{N+1}$. A description of the *L*-edge needs the following interactions for the ground state and the final state:

1. An adequate description of the chemical bonds for molecules and band structure for solids, which can be approximated with model Hamiltonians, for example crystal field theory or charge transfer theory.
2. The intra-atomic 3*d*3*d* multipole interactions described with the F^2 and F^4 Slater integrals that can be reformulated as the Racah B and C parameters.
3. The 3*d* spin-orbit coupling
4. The core hole spin-orbit coupling, yielding a distinction between the L_3 and L_2 edge.
5. The core hole potential.
6. The core-valence exchange interaction, the direct spin-spin coupling of the core spin and the valence spins, within the multiplet model described with the G1 Slater integral.
7. The higher order term of the core-valence exchange interaction described with the G3 Slater integral.
8. The core hole – valence hole multipole interactions. The 2*p* and 3*p* core holes have a dipole-dipole interaction with the 3*d* holes, described with the F^2 Slater integral.

The basis for the crystal-field multiplet and charge-transfer multiplet calculations is the observation that the *L*-edges of many transition metal systems yield quasi-atomic spectra that can be described well with the atomic $3d^N$ to $2p^5 3d^{N+1}$ transition, where all other effects are included into an effective electric field. This implies that the translation symmetry is neglected and the hybridization described with an effective field. The local electron-electron interactions and the 3*d* spin-orbit coupling are treated explicitly. All final state effects of the 2*p* core hole are treated explicitly, including the core hole spin-orbit coupling and the atomic multiplet interactions. They are calculated for an isolated atom or ion and transferred to a molecule or solid. The charge-transfer multiplet (CTM) model has been initially developed by Theo Thole, partly in collaboration with Kozo Okada, Hirohiko Ogasawara, Akio Kotani, Gerrit van der Laan and George Sawatzky (Thole et al. 1988). The program of Theo Thole, modified by Hirohiko Ogasawara, has been incorporated into a user friendly interface CTM4XAS that can calculate the XAS, XPS, XES and RIXS spectra of transition metal systems and rare earths (Stavitski and de Groot 2010).

EBSCOhost - printed on 2/13/2023 5:26 AM via . All use subject to https://www.ebsco.com/terms-of-use

QUALITATIVE SPECTRAL ANALYSIS OF THE *L*-EDGES

Energy shifts

It turns out that the *L*-edge also shifts in energy with valence (cf., Nesbitt and Bancroft 2014, this volume). The shift is approximately 1.5 eV per formal valence change, as determined empirically for a number of elements. Because the *L*-edge spectral shape is a multi-peaked complex structure, it is difficult to assign an energy to a particular peak position. Instead it is more customary to determine the center of gravity of the complete *L*-edge. A complicating issue is the edge jump due to continuum states that should be subtracted.

Intensities of the *L*-edges

According to the optical sum rule of a 2*p* to 3*d* transition, the integrated intensity of the *L*-edge yields the number of empty 3*d* states. To derive this value it is important to normalize the experimental spectrum to the edge jump and to subtract the edge jump from the experimental spectrum. Because *L*-edges are often measured with electron yield or fluorescence yield, without normalization to the edge jump, no significant number can be determined.

The branching ratio

An experimental parameter that has been often analyzed is the branching ratio, the intensity ratio between the L_3 and the L_2 edge. The advantage is that this number can be determined without normalization to the edge jump but in order to obtain a reliable number the edge jumps must be subtracted. The branching ratio is sensitive to the ground state symmetry, especially its spin state. This makes the branching ratio also sensitive to the valence (Thole and van der Laan 1988).

Polarization dependence and XMCD

Spectral analysis can be refined if polarization dependent spectra can be measured. Linear polarization needs an ordered system, for example a crystal with tetragonal symmetry. Systems that are ferro(i)magnetic or paramagnetic systems that can be magnetized can be measured with X-ray circular magnetic dichroism (XMCD). For example XMCD can be used to determine the relative site and valence occupations of mixed spinel systems, as is discussed below.

XANES ANALYSIS OF LIGAND *K*-EDGES

The *K*-edges of the ligands binding to the metal can be calculated with DFT calculations. In case of ligand *K*-edges the comparison with DFT calculations is often very good. The most important experimental parameter that can be determined without calculations is the edge-normalized intensity of the 3*d*-band. The integrated intensity of the peaks that overlap with 3*d* states yields the amount of ligand character in the 3*d*-band. In other words this yields the ligand-*p* – metal-*d* covalency (Hedman et al. 1990). Another parameter is the position of the first peak. While the metal edges shift to higher energy with the metal valence, the ligand edges shift to lower energy with increased metal valence, essentially because it costs less energy to extract a core electron from a more negatively charged ion.

APPLICATIONS OF XANES IN MINERALOGY AND GEOCHEMISTRY

Transition metals: *K*-edges

By far the most common application of XANES in Earth sciences has traditionally been in investigating the oxidation state and coordination environment of transition metals, particularly iron (Fe), in minerals and amorphous materials such as glasses and melts. Below we focus on the transition metals that have been most commonly studied in recent years. While

EBSCOhost - printed on 2/13/2023 5:26 AM via . All use subject to https://www.ebsco.com/terms-of-use

they by no means represent the full range of transition metals that have been investigated, many of the comments, pitfalls and experimental requirements outlined, are applicable to any transition metal *K*-edge XANES study. We use iron as the main example.

Iron – pre-edge and edge features. Iron is one of the most geologically important elements as it is the most abundant element found within the crust (Earth!) that exhibits different oxidation and coordination states in minerals and in magmas. Its coordination and redox state can strongly influence the physical and chemical behavior of magmas. An important method for accurately determining the reduced (Fe^{2+})-to-oxidized (Fe^{3+}) ratio or Fe^{3+}/Fe_{total} within minerals and solid materials is by Mössbauer spectroscopy. However, Mossbauer spectroscopy lacks the sensitivity required for samples with small amounts of iron (<1 wt%). The Fe *K*-edge, measured in fluorescence yield mode, is sensitive to small amounts of iron because hard X-rays measure a bulk signal. It is usually collected from ~7100 eV to ~7300 eV[1] but features beyond ~7150 eV are related to the EXAFS and are not considered here.

As discussed above, the *K*-edge XANES consists of a pre-edge region, a main peak characteristic of the edge jump and secondary features beyond the main edge peak. While the main peak and higher energy features may be of use in comparing unknown Fe *K*-edge XANES spectra with spectra from known mineral or glass standards; the so called "fingerprinting" technique, it is relatively unused for determining coordination and oxidation states of Fe in minerals and amorphous materials. As discussed above in "XANES analysis of metal *L*-edges," the main TM *K*-edge peaks shift to higher energy with increasing oxidation state (e.g., Schulman et al. 1976; Berry et al. 2003a), in the case of iron by ~5 eV but the principle features used for determining oxidation state and coordination are the pre-edge features.

As described above, the pre-edge peaks are due to $1s \rightarrow 3d$ transitions. In a non-centrosymmetric site (i.e., tetrahedral) the peak intensity is increased due to electric dipole contributions as a result of mixing of the $3d$ with $4p$ orbitals. Consequently, the intensity of the peaks increases with decreasing coordination due to the loss of inversion symmetry (Westre et al. 1997). Extracting quantitative numbers for oxidation state and coordination environment requires fitting of the peaks with either Gaussian or pseudo-Voigt peak profiles (Fig. 3) (Hawthorne and Waychunas 1988) give a discussion of peak fitting methods) and determination of the centroid of the fitted peaks. The centroid is the area weighted average of the position of the component used in the fit. The number of peaks fit, their positions and intensities varies depending upon whether there is Fe^{2+} and/or Fe^{3+} and whether *the different* Fe oxidation states are in 4-fold (tetrahedral, $^{[4]}$Fe), 6-fold (octahedral, $^{[6]}$Fe), 5-fold (square pyramid or trigonal bipyramid, $^{[5]}$Fe) or higher coordination.

In minerals with no mixing of Fe^{2+} and Fe^{3+}, Fe^{2+} in tetrahedral coordination exhibits 2 pre-edge features at ~7111 eV and ~7113 eV. However, four peaks are predicted by theory (Westre et al. 1997; Arrio et al. 2000). When in octahedral coordination, three features are observed in experimental spectra although site distortion may reduce the intensity of the third peak (Wilke et al. 2001) and three peaks are predicted by theoretical calculations (Westre et al. 1997; Arrio et al. 2000). When Fe^{2+} is in 5-fold coordination two peaks are observed in the experimental spectrum, similar to when in tetrahedral coordination and 3 peaks predicted by theory. Finally when in 8-fold coordination, two maxima are observed in the pre-edge region.

Tetrahedral Fe^{3+} has one pre-edge peak with a centroid at 7113.5 eV. There are two peaks predicted but the second peak intensity is too low to be resolved in the experimental data. Five coordinated Fe^{3+} also exhibits a single peak when in trigonal bipyramidal coordination

1 Note throughout the following sections the energy range shown is the region over which the spectra are normally collected. For the precise edge energy the reader should consult the X-ray data booklet compiled by Thompson and Vaughan (2011) which can be downloaded from http://xdb.lbl.gov.

EBSCOhost - printed on 2/13/2023 5:26 AM via . All use subject to https://www.ebsco.com/terms-of-use

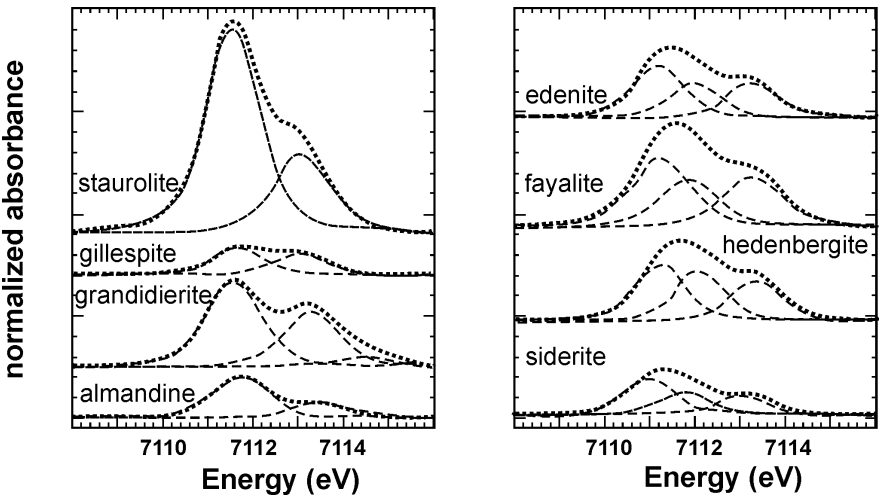


Figure 3. Examples of curve fits for mineral phases containing Fe^{2+} and Fe^{3+} (after Wilke et al. 2001).

and two peaks when in a square pyramid configuration (2 predicted). Farges (2001) has investigated a number of grandidierites where Fe^{2+} is located in a trigonal bipyramid site. The spectra exhibit two pre-edge peaks due to Fe^{2+} at ~7111.7 eV and minor Fe^{3+} at ~7113.3, respectively. The most intense pre-edge peak, due to Fe^{2+} in the trigonal bipyramid site, has a centroid at ~7112 ± 0.05 eV. $^{[6]}Fe^{3+}$ compounds have two components whose centroids are at 7112.8 eV and 7114.3 eV, in agreement with theoretical predictions (Westre et al. 1997; Arrio et al. 2000).

Iron – presence of both oxidation states. In mineral phases that contain both oxidation states, analysis and interpretation of the pre-edge becomes more problematic. One approach is to use a linear combination of different spectra (see below). In this approach one attempts to match the experimental spectrum by summing different percentages of standard spectra of phases containing only Fe^{2+} or Fe^{3+} (Fig. 4).

The centroid position is an excellent measure of oxidation state of Fe when a material is composed solely of either ferrous or ferric iron, an Fe^{2+} pre-edge can be observed at a centroid position of 7112 eV and for Fe^{3+} 1.5 eV higher in energy at 7113.5 eV (cf., Wilke et al. 2001, 2004, 2005, 2009). Note that the edge itself is shifted ~5 eV higher in energy for Fe^{3+} versus Fe^{2+}. For a given coordination state there is a linear response between centroid position and integrated pre-edge intensity. However, when there are mixtures of geometries, site distortion, and oxidation state, the response becomes non-linear (Wilke et al. 2001). Figure 5 plots the integrated pre-edge intensity versus centroid position for binary mixtures of Fe^{2+} and Fe^{3+} in different coordination states and clearly shows non-linear behavior between the two different oxidation states. Analysis of the pre-edge feature then requires some careful thought with regard to the intensity of the main peak, its shoulders, if any, as well as the relative intensities of the pre-edge features.

Titanium. Titanium *K*-edge XANES (~4900-5000 eV) has been primarily used to investigate the coordination state of Ti in glasses and melts (cf., Greegor et al. 1983; Yarker et al. 1986). However, regardless of the material being studied it is the pre-edge features, like that of Fe, that are used to determine the coordination environment of Ti. The pre-edge features are again due to quadrupole $1s \rightarrow 3d$ transitions similar to the Fe *K*-edge above (cf., Fig. 1) (Grunes 1983; Waychunas 1987; Uozumi et al. 1992). In the case of Ti, however, we do not

EBSCOhost - printed on 2/13/2023 5:26 AM via . All use subject to https://www.ebsco.com/terms-of-use

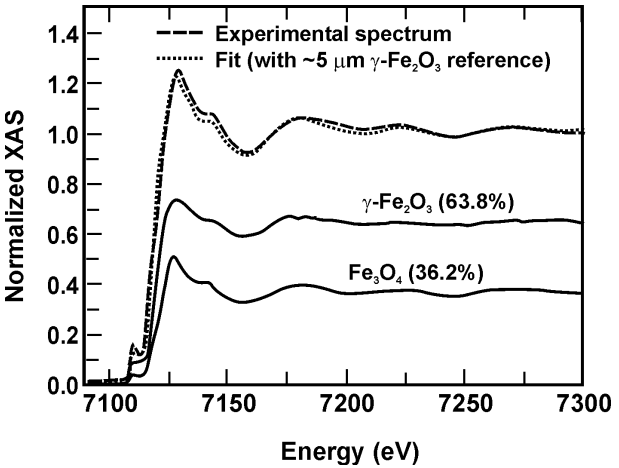


Figure 4. Fit of experimental spectrum of iron oxide nanoparticles by a linear combination of the spectra of maghemite (γ-Fe_2O_3) and magnetite (Fe_3O_4) (after Espinosa et al. 2012).

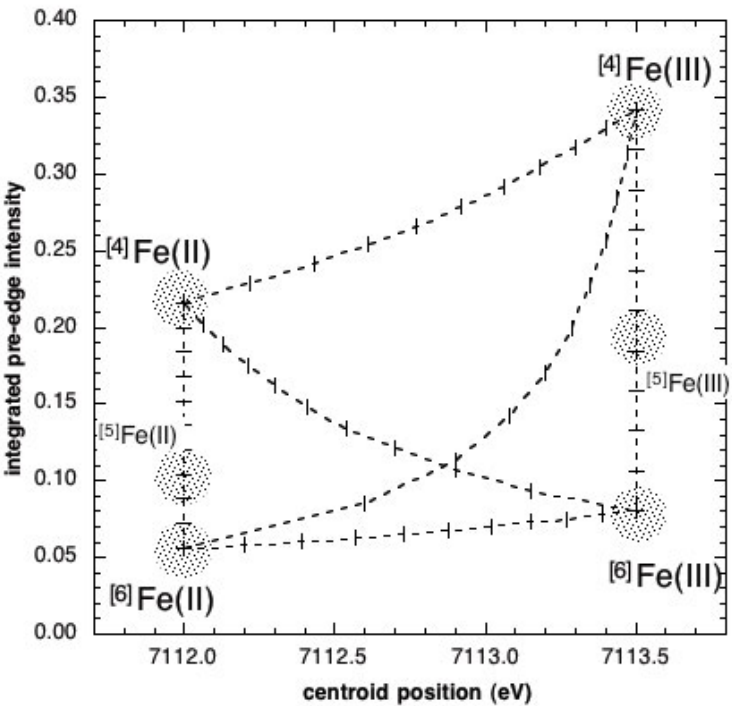


Figure 5. Relationship between centroid position of the pre-edge features, Fe coordination and oxidation state, (after Wilke et al. 2001, 2005; Petit et al. 2001) (provided courtesy of M Wilke).

normally have to worry about the presence of a second oxidation state like Ti^{3+}. At least under conditions relevant to most mineralogical and geochemical processes, because very strong reducing conditions must be present to produce Ti^{3+}.

EBSCOhost - printed on 2/13/2023 5:26 AM via . All use subject to https://www.ebsco.com/terms-of-use

Titanium *K*-edge spectra with Ti^{4+} in 6-fold coordination ($^{[6]}$Ti) exhibit from 1-3 weak intensity pre-edge peaks (Fig. 6). These peaks are conventionally labeled A_1, A_2, and A_3, (at ~4968, ~4971 and ~4974 eV) with a shoulder observed on the low energy side of the A_2 peak. However, observation of the shoulder depends on the spectral resolution of the data and may not always be observed. Cabaret et al. (1999, 2010) used a full-potential linearized augmented plane wave (LAPW) method of calculating the pre-edge dipolar and quadrupolar transitions. They showed that the A_1 peak is due to a quadrupolar, t_{2g}, transition (Ti 1*s* → Ti 3*d* (t_{2g})) while A_3 is entirely dipolar in nature (Ti 1*s* → Ti 4*p*). However, the A_2 peak has contributions from both dipolar (Ti 1*s* → Ti 4*p*) and quadrupolar transitions (Ti 1*s* → Ti 3*d* (e_g)). In addition they also concluded that the A_2 and A_3 contributions are related to medium range order as they are derived from the hybridizations of the central Ti-4*p* orbital with the second shell Ti-3*d* orbitals.

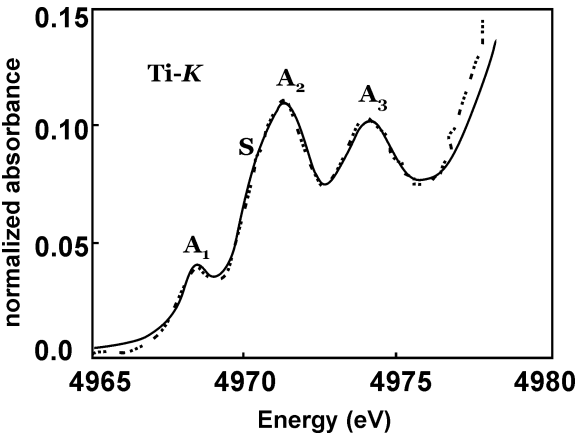


Figure 6. Pre-edge features observed in rutile (TiO_2) Ti *K*-edge XANES spectrum (after Uozumi et al. 1992).

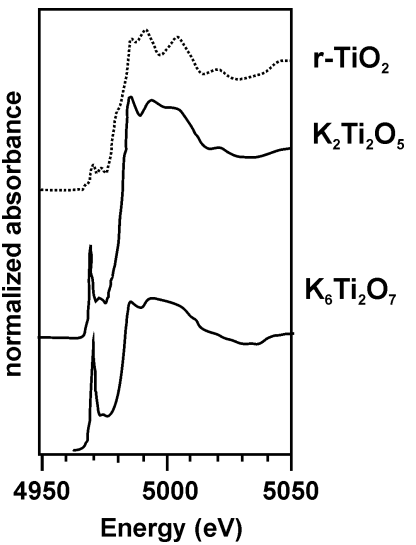


Figure 7. Ti *K*-edge spectra for selected crystalline phases containing $^{[4]}$Ti ($K_2Ti_2O_7$), $^{[5]}$Ti ($K_2Ti_2O_5$) and $^{[6]}$Ti (r-TiO_2) (after Farges et al.1996a, 1997).

When Ti is 4-fold ($^{[4]}$Ti) or 5-fold ($^{[5]}$Ti) coordinated there is an increase in intensity of the A_2 peak due to increased mixing of the 3*d* quadrupole and 4*p* dipole states as the polyhedra become less centrosymmetric (cf., Fig. 7) or the centrosymmetry is broken by atomic vibrations (Brouder et al. 2010). Farges et al. (1996a) have defined three regions characteristic of Ti in $^{[4]}$Ti, $^{[5]}$Ti, and $^{[6]}$Ti coordination (Fig. 8) based on both the intensity and position of the A_2 pre-edge peak as well as its intensity. The pre-edge intensity, determined by comparing the intensity of the pre-edge (4850-4950 eV) region and the average intensity of the XAFS region (5050-5200 eV) shows a general negative correlation with increasing Ti coordination. In addition, the position of the pre-edge peak is at lower energy for $^{[4]}$Ti relative to $^{[6]}$Ti by ~ 2 eV. The pre-edge peak characteristic of $^{[4]}$Ti is found at ~4969 eV with an intensity 80% or greater of the intensity of the main edge while the pre-edge feature of $^{[6]}$Ti is at ~4971 eV with a relative intensity of ~25% of the main edge. The five-fold ($^{[5]}$Ti) pre-edge peak occurs at energies intermediate between $^{[4]}$Ti and $^{[6]}$Ti values at~ 4970 eV with a relative intensity between 40-80% of the main edge. It is important to remember that it is *intensity* and *position* together that define the coordination. Using only one or the other is insufficient.

EBSCOhost - printed on 2/13/2023 5:26 AM via . All use subject to https://www.ebsco.com/terms-of-use

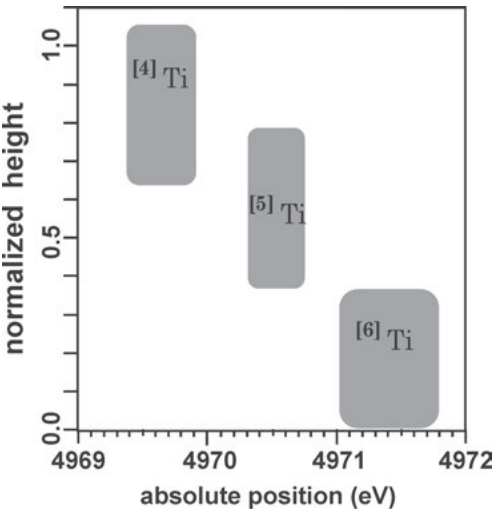


Figure 8. Plot of normalized pre-edge intensity versus energy position showing the three areas corresponding to $^{[4]}$Ti, $^{[5]}$Ti and $^{[6]}$Ti (after Farges et al. 1996a, 1997).

In addition to being useful for determining the Ti coordination, the pre-edge features can also be used to estimate particle size. The intensity ratio of A_2 to A_3 increases as particle size decreases (Luca et al. 1998). The Ti *K*-edge itself consists of three or more features in the region of ~4950-5050 eV. These features can be described by multiple scattering effects between the ejected X-ray photo electron and the surrounding atoms or to transitions involving Ti $1s \rightarrow$ Ti $4p$ orbitals possibly with core hole effects (Poumellec et al. 1991a,b). Spectral features can be reproduced quite well using one of the theoretical codes available: either one of the multiple scattering or *ab inito*/first principles band structure codes noted above. In particular, the partial (or projected) density of states (p-DOS) is most useful for interpreting XANES spectra in general as this provides information on which orbitals are involved in the electronic transitions. Unfortunately the p-DOS is often not provided in simulation publications although it is commonly calculated during the simulations and a quick E-mail to the principle author is often helpful for obtaining it. Furthermore, using a "fingerprint" approach of comparing standards containing Ti in different crystal chemical environments one can use the linear combination method to help identify unknown Ti phases and different phases in samples containing mixtures of Ti-containing minerals etc.

When Ti^{4+} is reduced to Ti^{3+} the XANES spectrum and pre-edge features may still be analyzed to determine the Ti coordination state in a similar manner to unreduced samples. However, both the pre-edge and edge features are shifted to lower energy relative to the energy positions of features in the unreduced samples containing only Ti^{4+} (Simon et al. 2007; Ollier et al. 2008). The magnitude of the energy shift depends upon how much Ti^{4+} has been reduced to Ti^{3+}.

Other transition metals. Essentially all of the first row transition metal *K*-edges have been investigated in minerals to some extent and a variety of examples are given below.

Titanium(Ti): Grunes 1983; Waychunas 1987; Uozumi et al. 1992; Paris et al. 1993; Dingwell et al. 1994; Farges et al. 1996a,b, 1997; Romano et al. 2000; Jiang et al. 2007; Cormier et al. 2011.

Vanadium (V): Nabavi et al. 1990; Abbate et al. 1993; Giuli et al. 2004; Sutton et al. 2005; Simon et al. 2007; Burke et al. 2012; Höche et al. 2013.

EBSCOhost - printed on 2/13/2023 5:26 AM via . All use subject to https://www.ebsco.com/terms-of-use

Chromium (Cr): Brigatti et al. 2000; Berry and O'Neil 2004; Berry et al. 2006;Villain et al. 2007; Gaudry et al. 2007; Odake et al. 2008; Juhin et al. 2008; Farges 2009; Fandeur et al. 2009; Frommer et al. 2009, 2010; Burke et al. 2012.

Manganese (Mn): Manceau et al. 1992; Farges 2005; Alvarez et al. 2007; Fandeur et al. 2009; Chalmin et al. 2009; Manceau et al. 2012.

Iron (Fe): Waychunas et al. 1983; Galoisy et al. 2001; Petit et al. 2001; Wilke et al. 2001; Farquhar et al. 2002; Berry et al. 2003a; Wilke et al. 2001, 2005, 2006; Magnien et al. 2008; Cottrell et al. 2009; Berry et al. 2010; Beck et al. 2012; Dyar et al. 2012; Rivard et al. 2013.

Cobalt (Co): Manceau et al. 1992; Choy et al. 2001.

Nickel (Ni): Manceau et al. 1992; Galoisy and Calas 1993; Farges et al. 1994; Giuli et al. 2000; Farges et al. 2001a,b; Fandeur et al. 2009; Curti et al. 2009; Essilfie-Dughan et al. 2012.

Copper (Cu): England et al. 1999; Alcacio et al. 2001; Mavrogenes et al. 2002; Berry et al. 2006; Cook et al. 2012.

Zinc (Zn): Pattrick et al. 1998; Waychunas et al. 2003.

In most cases, it is the pre-edge features that are used to determine oxidation state and coordination environment and, in particular, the position and intensity of the centroid of the pre-edge peaks rather than the position of the edge itself (cf., Cabaret et al. 2010). Reviews of TM *K*-edges have been given by de Groot (1993, 2008, 2009). Furthermore, the second and third row TMs are being increasingly studied as well with not only *K*-edges but also with *L*- *M*- and *N*-edges. Obtaining XANES spectra from these elements is a little more trying technically due to interference affects from the close proximity of other elemental edges.

Transition metals: *L*-edges

The 3*d* transition metal *L*-edges have been less studied, partly because of their large surface sensitivity. *L*-edges are also sensitive to changes in coordination and oxidation state, and because of their lower intrinsic broadening contain more information with regards to the electronic structure of the transition metal ions (Fister et al. 2007). The theory of XANES spectra of transition metal *L*-edge is described above. In case of Ti^{4+} oxides the peak splitting within each edge is primarily due to the t_{2g} e_g symmetry of the *d*-orbitals in a centrosymmetric environment (O_h symmetry for octahedral and 8-fold coordination) and is related (but not equal) to the crystal field splitting parameter 10D*q*. Further splitting of the higher energy peak within the L_3 edge has been attributed to distortion of the coordination environment (de Groot et al. 1992; Crocombette and Jollet 1994), possible second-neighbor interactions (Crocombette and Jollet 1994), coupling of electronic and vibrational states due to a dynamic Jahn-Teller effect (Brydson et al. 1989) or core hole effects (Crocombette and Jollet 1994). Without multiplet effects, the intensity ratio between the L_3 and L_2 edges is 2:1 and this ratio is observed for systems involving 4*d* electrons but not for 3*d* systems due to the large multiplet effects (de Groot et al. 1994).

L-edge spectra of 3*d* metals are collected in a similar manner to the *K*-edges above. However, experiments are carried out on what are commonly referred to as "soft X-ray" beamlines. These beamlines are usually limited in energy to <10 keV and in most cases require vacuum sample chambers. Spectra are collected over an energy range that covers both edges if possible with a step size equal to the lifetime broadening of about 0.1 to 0.2 eV. Data reduction is similar to that for *K*-edges with removal of the pre-edge background and fitting of an arctan or error function as above. However, with *L*-edges more than one such function usually must be fit to account for the L_3- and L_2-edge. The positions and heights of the functions are not well

EBSCOhost - printed on 2/13/2023 5:26 AM via . All use subject to https://www.ebsco.com/terms-of-use

known and consequently the fitting of such functions tends to be determined simply on what gives the "best fit" to the data.

In order to use the *L*-edges for determining coordination environments in minerals and glasses it is essential to carefully analyze the subtle changes in relative peak intensities and positions (cf., Henderson et al. 2003; Henderson and St-Amour 2004; Cormier et al. 2011). In addition, second nearest neighbors may also affect the spectra (Höche et al. 2013) and must be taken into account when selecting appropriate mineral standards for comparison or linear combination modeling (cf., Fig. 9).

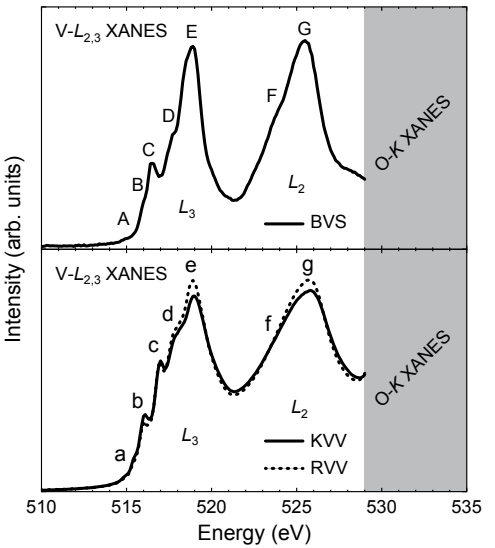


Figure 9. V $L_{2,3}$ spectra (~515-530 eV) for Ba ($Ba_2VSi_2O_8$) (top), potassium ($K_2VV_2O_8$) and rubidium ($Rb_2VV_2O_8$) vanadium fresnoites (bottom). Spectra in the bottom panel has V in two oxidation states and coordinations (V^{4+} (CN = 5) and V^{5+} (CN = 4) yet are quite similar to the top spectrum with V only in a single oxidation and coordination state (Used by permission of Mineralogical Society of America, from Höche et al. 2013, American Mineralogist, 98, Fig. 3, p 668).

Titanium L-edges. Some characteristic Ti *L*-edge spectra (~ 455-475 eV) are shown in Figure 10. The spectra are quite distinct for different Ti oxidation states (Ti^{3+}, Ti^{4+}) and for different coordination environments ($^{[4]}$Ti, $^{[5]}$Ti, $^{[6]}$Ti). As noted above the lower valence state spectrum (Ti^{3+}) is at slightly lower energy relative to the higher valence state (Ti^{4+}). Titanium in 4-fold coordination exhibits two peaks in the L_3-edge with the higher energy peak being somewhat asymmetric with no splitting. This contrasts with $^{[6]}$Ti where the second peak is split and where the relative intensities of the split peaks reverses for anatase versus rutile or brookite. Five-fold Ti exhibits a small t_{2g} peak and a sharp e_g peak and the splitting between the two peaks in the L_3-edge is reduced relative to $^{[4]}$Ti and $^{[6]}$Ti. At the L_2-edge the splitting and relative intensities of the t_{2g} and e_g peaks decreases from $^{[6]}\text{Ti} \rightarrow {}^{[4]}\text{Ti} \rightarrow {}^{[5]}$Ti. In addition, $^{[5]}$Ti has an additional small peak on the low energy side of the L_2-edge which may be due to differences between the t_{2g} orbitals. However, caution must be used when determining coordination state since numerous factors affect the peak intensities and positions (see above). This is particularly important when investigating mineral phases where Ti can occupy more than one site (cf., Henderson and Foland 1996) and consequently the *L*-edge spectra are an average of the multiple sites. In all cases it is advantageous to have some sort of theoretical calculations available to aid interpretation (see above plus Höche et al. 2013).

Iron L-edges. The Fe^{2+}/Fe^{3+} ratio is usually given as the fraction Fe^{3+}, $Fe^{3+}/\Sigma Fe$. Systematic studies of the Fe 2*p* EELS spectra of a series of minerals give a reliable method to determine this ratio, based on the determination of the ratio of the Fe^{3+} and Fe^{2+} peaks in the L_3-edge (van

EBSCOhost - printed on 2/13/2023 5:26 AM via . All use subject to https://www.ebsco.com/terms-of-use

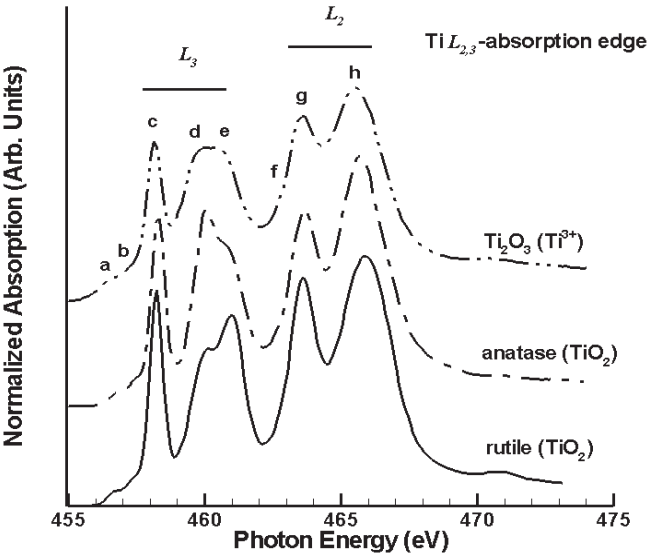


Figure 10. Representative spectra of the Ti *L*-edge. The L_3 and L_2 edges are indicated.

Aken and Liebscher 2002). An important application of the iron *L*-edges is the determination of the occupation of the tetrahedral and octahedral sites and the variation of divalent and trivalent ions for Fe in spinel ferrites, including $CoFe_2O_4$, $MnFe_2O_4$, $NiFe_2O_4$, $ZnFe_2O_4$ and $MgFe_2O_4$. The line shape of the Fe 2*p* XAS spectrum of $MnFe_2O_4$ is similar to those of both α-Fe_2O_3 and γ-Fe_2O_3 indicating that the valence states of Fe ions in $MnFe_2O_4$ are mainly trivalent. Pattrick et al. (2002) analyzed a series of mixed spinel ferrite systems with 2*p* XAS and XMCD. By comparison with multiplet spectra, the site occupancies of the cations have been determined. It turns out that the different mixed (Co, Ni, Zn, Mg) ferrite spinels show considerable variation in site occupancies. Incomplete site speciation is found and the preference of Co, Ni and Mg for the octahedral site and Zn for the tetrahedral site is confirmed. An overview of the 2*p* XAS and XMCD spectra of spinel ferrites have been given by Pearce et al. (2006). The Fe *L*-edge XANES has recently been reviewed by Miedema and de Groot (2013).

Other transition metal L-edges. Cressey et al. (1993) give a general introduction of the use of transition metal *L*-edges in mineralogy. Charnock et al. (1996) analyzed the *L*-edges of Fe, Co and Ni sulfides, selenides and tellurides. They also discuss the related iron and nickel spectra. A recent paper is the determination of the valence of cobalt in carrolite $CuCo_2S_4$ by Pattrick et al. (2008). Cobalt *L*-edges of oxides have been published by van Elp et al. (1991), de Groot et al. (1993), Mizokawa et al. (2005) and Coker et al. (2008).

Silicon and aluminum *K*- and *L*-edges

Silicon K-edge. The Si *K*-edge (~1830-1890 eV) is the lowest energy soft X-ray edge for which EXAFS data can be obtained. Edges occurring at lower energies are not able to provide a large enough energy range for EXAFS analysis due to interference from other elemental edges for most geochemically relevant materials. The edge itself has been extensively investigated both in minerals (cf., Li et al. 1993, 1994, 1995a; Gilbert et al. 2003) and glasses/melts (cf., Davoli et al. 1992; Henderson 1995; Henderson and Fleet 1997; Henderson and St-Amour 2004; de Wispelaere et al. 2004; de Ligny et al. 2009). Furthermore, a significant amount of work has been published on this edge using electron energy loss (EELS), parallel electron

EBSCOhost - printed on 2/13/2023 5:26 AM via . All use subject to https://www.ebsco.com/terms-of-use

energy loss (PEELS) or energy loss near edge spectroscopy (ELNES) and this literature can be very helpful for interpreting soft X-ray XANES spectra (cf., McComb et al. 1991; Garvie et al. 1994, 2000; Sharp et al. 1996; Poe et al. 1997; van Aken et al. 1998; Garvie and Buseck 1999).

The spectrum for α-quartz exhibits 5 main peaks labeled A-F in Figure 11a. While there have been a number of theoretical studies of the quartz and stishovite Si *K*-edge that reproduce the experimental spectra well (cf., Wu et al. 1998; Soldatov et al. 2000; Mo and Ching 2001; Taillefumier et al. 2002) they have not provided a detailed analysis of the p-DOS to enable explicit assignment of the peaks in the spectra. Li et al. (1994, 1995a) used previous molecular orbital studies and gas phase spectra of tetrahedral analogues to assign the peaks in quartz. They assigned the pre-edge peak (peak A) to a dipolar(?) $1s \rightarrow 3s$ transition. Peak B representing the main edge transition (also called white line or shape resonance in older literature) is due to a $1s \rightarrow 3p$ transition, peaks D and F to $1s \rightarrow 3d/p$ states and peaks C and E to multiple scattering from the structure beyond the first coordination sphere. Similar peaks and assignments can be made for stishovite (Fig. 11b) where Si is in 6-fold coordination ($^{[6]}$Si). However, the position of the edge is shifted to higher energy by ~2.2 eV consistent with other elemental edges when there is a change to higher coordination (see above and below).

The Si *K*-edge, compared to other soft X-ray edges, is relatively insensitive to structural changes, at least for silicate minerals (Fig. 11c). This is mostly a result of the nature of the SiO_4 tetrahedron, which is fairly well defined in most minerals and does not exhibit a large amount of distortion or variation in Si-O bond lengths relative to other polyhedra. Comparison of the SiO_2 polymorphs (Fig. 11b) shows that the pre-edge peak intensity tends to increase in the higher pressure phases, probably due to increased mixing of $3p$ states with the Si $3s$ (Li et al. 1994). Li et al. (1995a) also noted that there is a general shift in the position of the *K*-edge to higher energy with increasing polymerization (Fig. 11c), a weak correlation with Si-O bond length (shift to higher energy with shorter Si-O bond distance) and some dependence of the edge position on the nature of the next nearest neighbors (NNN) In addition, Bender et al. (2002) have shown that the position of the edge shifts to lower energy as the Q species (Q^n, where n is the number of bridging oxygens attached to the silicon) shifts from Q^4 to Q^0.

In SiO_2 glass (Fig. 11a) the *K*-edge spectrum is more diffuse with peaks C-F being suppressed in intensity relative to crystalline SiO_2. This is due to the inherent disordered nature of glasses, which have a broad range of Si-O-Si angles and Si-O, and Si-Si distances compared to crystalline materials. Only four main peaks are observed. The pre-edge peak A occurs as a weak broadening at the base of the main edge feature, the main transition (Peak B), a weak peak around 1852 eV (Peak C) and a higher energy peak F due to transition of $1s \rightarrow 3d/p$ states, and whose intensity is related to the Si-O-Si angle, becoming more intense as this angle decreases (Davoli et al. 1992). The weak feature labeled C may be due to either transitions from $1s \rightarrow 3d/p$ states or multiple scattering. Unfortunately as noted above, the Si *K*-edge of glasses and melts exhibits even less compositionally dependent variation in peak positions and intensities than crystalline phases and is very uniform. By and large, the only changes observed in glasses (other than a shift of the edge due to a coordination change of Si) are in the ~1848-1855 eV region, are very subtle, and are most probably related to changes in the medium-range structure. An exception to this is a shoulder to the high-energy side of the main peak (B) at ~1849 eV which occurs in some glasses (cf., Fleet et al. 1997; Cabaret et al. 2001; Henderson and St-Amour 2004). It has been assigned to $^{[6]}$Si in phosphate glasses (Fleet et al. 1997) and silica-modified titanias (Iwamoto et al. 2005), or to changes in medium-range structure in alkali and alkaline-earth containing silicate glasses (Henderson and St-Amour 2004) and borosilicate glasses (Cabaret et al. 2001), initiated by the presence of a network modifier (Cabaret et al. 2001; Levelut et al. 2001). Its apparent presence in the Si *K*-edge spectra of a wide range of glass and amorphous compositions is intriguing but has not been explored further.

EBSCOhost - printed on 2/13/2023 5:26 AM via . All use subject to https://www.ebsco.com/terms-of-use

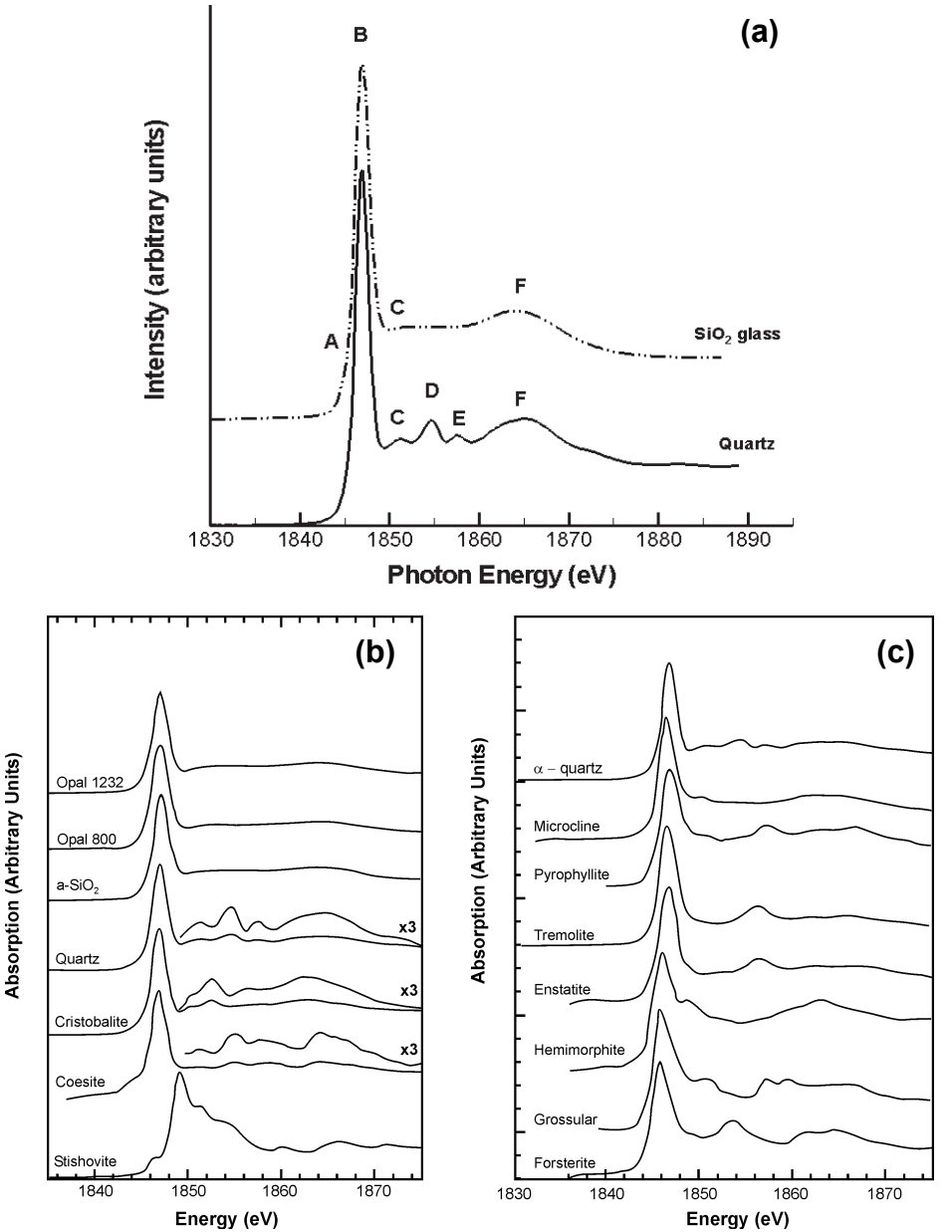


Figure 11. Si *K*-edge spectra, α-quartz and SiO_2 glass (a) opal, a-SiO_2 (glass) and SiO_2 polymorphs (after Li et al. 1994) (b) and minrals (c) (after Li et al. 1995b).

Silicon L-edge. Like the *K*-edge above, the Si *L*-edge (~100-140 eV) has also been reasonably well studied both by ELNES and XANES (McComb et al. 1991; Kasrai et al. 1993, 1996b; Li et al. 1993, 1994; Sharp et al. 1996; Poe et al. 1997; Garvie and Buseck 1999; Garvie et al. 2000; Gilbert et al. 2003). Peak assignments are similar to that of the Si *K*-edge

EBSCOhost - printed on 2/13/2023 5:26 AM via . All use subject to https://www.ebsco.com/terms-of-use

(see Fig. 12). However, no pre-edge feature is observed and peak A (Fig. 12) is split by spin-orbit (LS) coupling into two features ~1 eV apart due to the Si $2p_{3/2}$ (L_3) and $2p_{1/2}$ (L_2) states. This splitting may not be observed if the resolution of the monochromator is insufficient (older literature) or if there is broadening of the peaks due to instrumental affects or inherent broadening such as in amorphous materials. Li et al. (1993) suggest that the strongest feature (peak B) is shifted by ~2 eV to higher energy in stishovite with $^{[6]}$Si relative to α-quartz with $^{[4]}$Si, as observed for the *K*-edge. However, Sharp et al. (1996) using ELNES do not observe this. A large number of minerals have been investigated by Garvie and Buseck (1999) using PEELS. They observe a linear increase in energy of the edge onset with increasing polymerization and that the edge features are affected by the NNN and their bonding environments. Although it should be remembered that PEELs lacks the energy resolution of XANES and consequently some features, such as the LS doublet, are not clearly resolved.

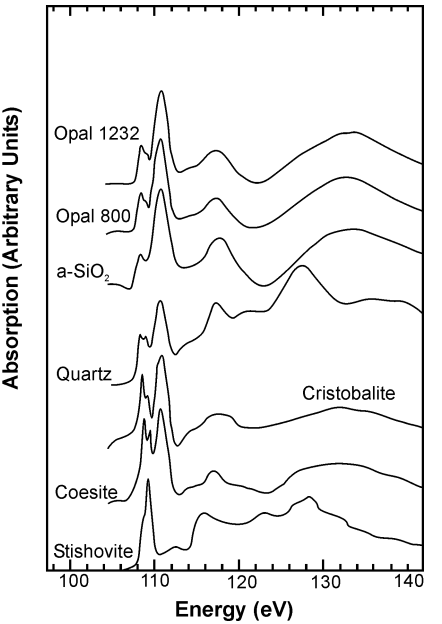


Figure 12. Si *L*-edge spectra of the SiO_2 polymorphs (after Li et al. 1994).

Aluminum K-edge. The aluminum *K*-edge (~1550-1650 eV) has been extensively utilized in mineralogical and geochemical studies (McKeown et al. 1985; McKeown 1989; Ildefonse et al. 1994, 1995, 1998; Li et al. 1995b; Fröba et al. 1995; Wu et al. 1997a; Giuli et al. 2000; Romano et al. 2000; Arai and Sparks 2002; van Bokhoven et al. 2003; Neuville et al. 2004a, 2010; de Wispelaere et al. 2004; Khare et al. 2005; Hu et al. 2008; Xu et al. 2010; Rivard et al. 2013). In general the Al *K*-edge for 4-fold coordinated Al ($^{[4]}$Al) occurs at ~1566 eV and usually exhibits a single edge maximum or peak. The Al *K*-edge of 6-fold coordinated Al ($^{[6]}$Al) is ~1.5-2.0 eV higher in energy relative to that of $^{[4]}$Al and usually exhibits a peak with a maximum at ~1568 eV and a secondary but relatively strong peak at ~1572 eV (see Fig. 13). The shift to higher energy for the higher coordination is simply because the core hole is more effectively screened in octahedral coordination (van Bokhoven et al. 2001).

Both edges have multiple peaks usually labeled A-E by various authors[2]. In Figure 13 the experimental spectrum for berlinite ($AlPO_4$), containing only $^{[4]}$Al, exhibits 5 main peaks. Peak A is the Al edge due to Al $1s \rightarrow 3p$ transitions and, as noted above, its intensity will depend on the screening of the core hole (Cabaret et al. 1996). In some spectra a pre-edge feature may also be observed (cf., Corundum in Fig. 13) and this is due to $1s \rightarrow 3s$ dipolar transitions that would normally be forbidden by quantum mechanical selection rules but become allowed due to effects from vibrations (Li et al. 1995b; Manuel et al. 2012). This pre-edge feature will increase in intensity with increasing temperature and shift to lower energy (Manuel et al. 2012). The other peaks have been variously assigned to multiple scattering (B and D), $1s \rightarrow 3d$ transitions (C and E), (Li et al. 1995b) or to multiple scattering from medium range environment (Cabaret et al. 1996). Their positions and intensity will depend upon Al site multiplicity, bond angles

2 Note it is important to be careful when comparing peak assignments from one author to the next as they do not necessarily label peaks the same or in a consistent manner

EBSCOhost - printed on 2/13/2023 5:26 AM via . All use subject to https://www.ebsco.com/terms-of-use

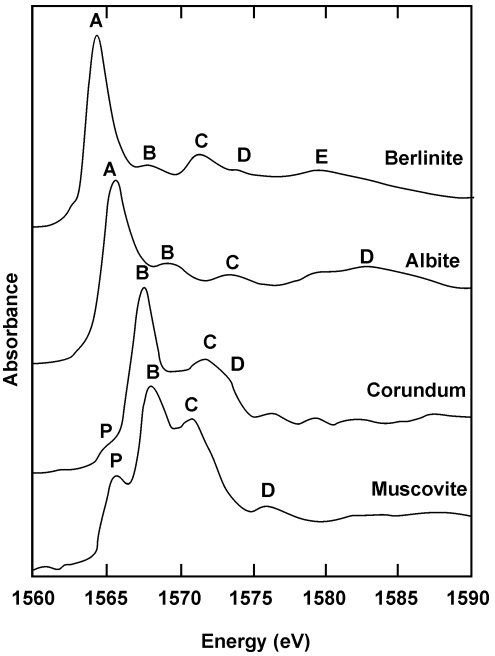


Figure 13. Al K-edge spectra of Berlinite ($AlPO_4$, [4]Al), Albite ($NaAlSi_3O_8$, [6]Al), corundum (Al_2O_3, [6]Al) and muscovite ($KAl_2(AlSi_3O_{10})(OH)_2$, [4]Al and [6]Al) after Ildefonse et al. 1994;Cabaret et al. 1996). Note that muscovite has both [4]Al and [6]Al and has XANES peaks characteristic of both coordinations.

and lengths, and NNN (Fröba et al. 1995; Li et al. 1995b; Wu et al. 1997a; Ildefonse et al. 1998). For example, the edge position of peak A in berlinite is at higher energy than for other [4]Al only compounds because the NNN to Al are phosphorous, which decrease the electronic density around the Al.

The spectrum for corundum (Al_2O_3) with only [6]Al exhibits a pre-edge peak (P) at 1565 eV, a sharp edge peak (A) at ~1568 eV due to Al $1s \rightarrow 3p$ transitions along with a secondary peak (B) at ~1572 eV due to $1s \rightarrow 3d$ transitions (Ildefonse et al. 1998). Peak C has been assigned to multiple scattering (Li et al. 1995b). However, the spectra for [6]Al minerals are more variable than those of [4]Al containing phases due to variations in site symmetry, site occupancy and Al-O bond lengths (Ildefonse et al. 1998).

Aluminum may also occur in 5-fold coordination ([5]Al), especially in calcium aluminosilicate glasses and melts (Neuville et al. 2004a). However, discriminating between [4]Al or [6]Al and [5]Al is difficult. Certainly in minerals such as the Al_2SiO_5 polymorphs (sillimanite, andalusite and kyanite) with [4]Al and [6]Al, [5]Al and [6]Al and all [6]Al, respectively, it is not possible to unambiguously determine features that are characteristic of [5]Al (Ildefonse et al. 1998). Li et al. (1995b) have interpreted a peak at ~1567.8 eV in their spectra as being due to [5]Al and lying between peaks at 1566.7 and 1568.7 eV characteristic of [4]Al and [6]Al, respectively although their peak assignments having been brought into question (Ildefonse et al. 1998). Nevertheless van Bokhoven et al. (1999), Chaplais et al. (2001), Hu et al. (2008), and Neuville et al. (2009) have all assigned a peak in their Al *K*-edge spectra to the presence of [5]Al based on its position mid-way between peaks characteristic [4]Al and [6]Al.

Aluminum L-edge. Relative to the Al *K*-edge there have been relatively few mineralogical studies (Bianconi 1979; Balzarotti et al. 1984; Chen et al. 1993a,b; van Bockhoven et al. 2001; Hu et al. 2008; Weigel et al. 2008; Shaw et al. 2009; Zhang et al. 2009; Neuville et al. 2010; Xu et al. 2010), involving the Al *L*-edge (~75-90 eV) despite the increased resolution of *L*- versus *K*-edges (see above). However, like the silicon above, there has been a significant amount of work published on this edge using EELS, PEELS and ELNES and this literature can be very helpful for interpreting the spectra.

Like other *L*-edges the main features of the spectra arise from excitation of an Al $2p$ electron to unoccupied *s* and *d*-like states but in this case are termed excitons since the excitation energy lies in the band gap (cf., Weigel et al. 2008 and references therein). The edge is split into two components the $2p_{3/2}$ (L_3) and $2p_{1/2}$ (L_2) due to LS coupling. Figure 14a shows a high-resolution spectrum for corundum (sapphire) as well as the transitions contributing to the spectrum. The split feature at ~79 eV (inset) is the $L_{2,3}$ edge. The edge is shifted to lower

EBSCOhost - printed on 2/13/2023 5:26 AM via . All use subject to https://www.ebsco.com/terms-of-use

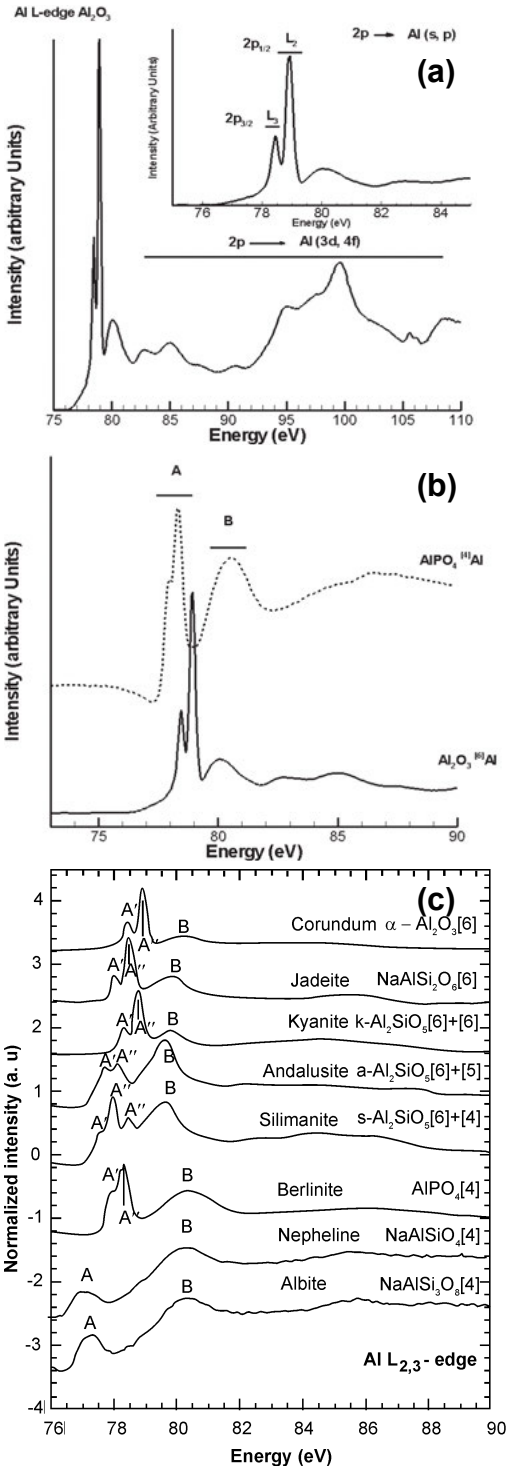


Figure 14. a) Al *L*-edge spectrum of corundum (variety sapphire) showing the transitions responsible for the spectral features. The inset show the $L_{2,3}$ peaks, b) High-resolution spectra (uncorrected) of berlinite (top, $^{[4]}$Al) and corundum (bottom, $^{[6]}$Al) along with peaks conventionally labeled A and B, c) XANES Al $L_{2,3}$-edge spectra of crystals and glasses (the numbers in brackets indicate the Al CN.) (after Weigel et al. 2008).

energy by ~1.5 eV for $^{[4]}$Al versus $^{[6]}$Al (Fig. 14b) similar to the Si $L_{2,3}$ edge (see above). This is because the core hole is more effectively screened in octahedral coordination (van Bokhaven et al. 2001). The position of the edge jump is also affected by a number of other factors. It is shifted to lower energy by increased bond covalency, the presence of Si as next nearest neighbors (NNN) and the presence of alkalis; the least polarizing NNN cations move the edge jump to lower energy. Weigel et al. (2008) investigated a number of mineralogical phases with varying Al coordination (Fig. 14c). The Al $L_{2,3}$ edges exhibit variations in position, intensities, and degree of splitting. There are two main spectral regions labeled A and B following the convention of Chen et al. (1993a). The A feature is the $L_{2,3}$ edge while the B feature, due predominantly to Al 2*p* transitions to unoccupied Al 3*s* states, is common to all spectra but varies in intensity relative to A due to site distortion and selection rules (in octahedral coordination) (Hansen et al. 1994) and increased *s-p* hybridization (for tetrahedral coordination). Furthermore it tends to be at higher energy relative to peak A in tetrahedral compared to octahedral environments.

The Al $L_{2,3}$ edge (A feature) exhibits more than two peaks in the phases with more than a single Al coordination environment. This is because the $L_{2,3}$ edges of the two sites are overlapping. For example, in the sillimanite spectrum the low energy A′

EBSCOhost - printed on 2/13/2023 5:26 AM via . All use subject to https://www.ebsco.com/terms-of-use

peak is the L_3 edge of $^{[4]}$Al, the high energy A‴ peak the L_2 edge of $^{[6]}$Al while the intermediate peak is a superposition of the L_2 edge of $^{[4]}$Al and the L_3 edge of $^{[6]}$Al (Weigel et al. 2008). The resolution of the A feature depends to some extent on the number of Al sites in the crystal structure, their site occupancies and NNN distribution, all of which tend to broaden the edge. Glass spectra are inherently broad due to their disordered nature, lack of symmetry and wide distribution of bond lengths and angles.

Weigel et al. (2008) also showed that there is a correlation between the position of the peak maximum of the Al L_3-edge and the Al-O bond length: the smaller the Al-O bond length the lower the energy of the edge. In addition, the relative intensities of the L_3- and L_2-edges can be used to calculate the exchange energy (see above and Eqn. 1 of Chen et al. 1993a and Weigel et al. 2008).

Alkalis (Li, Na, K, Rb, Cs)

Lithium K-edge. There are very few experimental XANES studies of the Li *K*-edge (~50-100 eV) because of the difficulty of making measurements at these very low energies as well as the overlap in energy with other elemental edges. The majority of studies have been related to the electrochemical and battery industries (cf., Tsuji et al. 2002; Kobayashi et al. 2007; Lu et al. 2011). The Li *K*-edge for some common compounds is shown in Figure 15.

Generally, the *K*-edge spectra exhibit a relatively intense peak at ~ 62 eV with secondary peaks between 62-65 eV and possibly a broad peak at ~70 eV. The intense sharp feature at 62 eV is a core exciton probably resulting from a 1*s* transition to unoccupied 2*p* states. In lithium halides, this core exciton peak exhibits a linear dependence on the electronegativity of the halide (Fig. 15a); the larger the electronegativity difference between Li and the halide the higher the peak energy (Handa et al. 2005). In some spectra the core exciton peak is relatively weak and appears as a low energy shoulder (Fig. 15b). Its position is also dependent on the

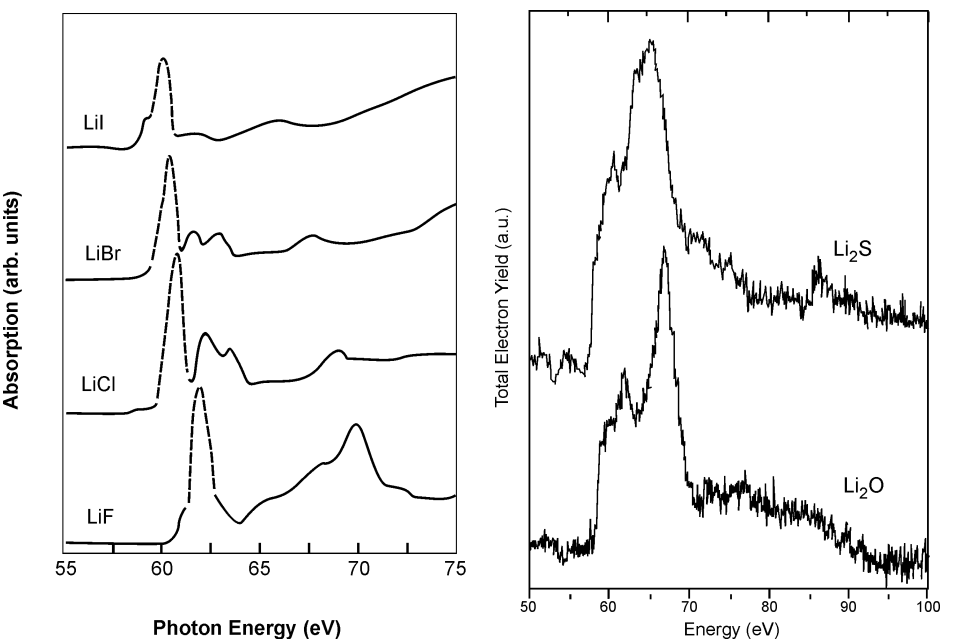


Figure 15. Li K-edge spectra of the Li halides (*left*) and a comparison of Li_2O and Li_2S (*right*), (after Handa et al. 2005 and Tsuji et al. 2002).

EBSCOhost - printed on 2/13/2023 5:26 AM via . All use subject to https://www.ebsco.com/terms-of-use

oxidation state of the anionic group attached to the Li. The peak shifts to higher energy with decreasing oxidation state (Tsuji et al. 2002). There have been some theoretical simulations (Jiang and Spence 2004; Mauchamp et al. 2006, 2008; Olovsson et al. 2009a,b) but they do not provide sufficient details on the p-DOS to aid interpretation of the experimental spectra. The low energy of the Li *K*-edge makes in-situ experiments difficult. Recently an XRS study of the Li *K*-edge was performed using hard X-rays (Miedema et al. 2012).

Sodium K-edge. The first comprehensive Na *K*-edge (~1065-1125 eV) study of minerals and glasses was that of McKeown et al. (1985) although the energy resolution was relatively poor. Since then there have been several studies of alkali halides (Murata et al. 1988; Fujikawa et al. 1989; Kasrai et al. 1991; Hudson et al. 1994) but few studies of other minerals and glasses. Mottana et al. (1997) looked at Ca-Na pyroxenes while Neuville et al. (2004b) have looked at a range of mineral phases and glasses. Glasses have also been investigated by Cormier and Neuville (2004) who looked at Ca-Na glasses and De Wispelaere et al. (2004) who investigated Na silicate and sodium-alumino-silicate glasses. Representative spectra are shown in Figure 16. The sodium *K*-edge of crystalline phases, other than the halides, consists of essentially two peaks at ~1078 eV and ~1082 eV (Cormier and Neuville 2004) with a pre-edge peak occurring at ~ 1174 eV. This pre-edge peak is not always present and arises from a dipolar $1s \rightarrow 3s$ transition (Murata et al. 1988; Teodorescu et al. 2000). The first main peak at ~1078 eV has been assigned to a Na $1s \rightarrow 3p$ transition while the origin of the second peak at ~ 1082 eV remains ambiguous but is usually assigned to multiple scattering beyond the immediate Na environment as are peaks above ~1090 eV (cf., Neuville et al. 2004b). A similar assignment can be made for the alkali halides (Teodorescu et al. 2000; Kikas et al. 2001; Prado and Flank 2005). Peaks are also reproduced quite well by multiple scattering theory (Hudson et al. 1994; Riedler et al. 2001a,b). There is a correlation between the higher energy peaks in the halides and the $1/R^2$ rule (see above).

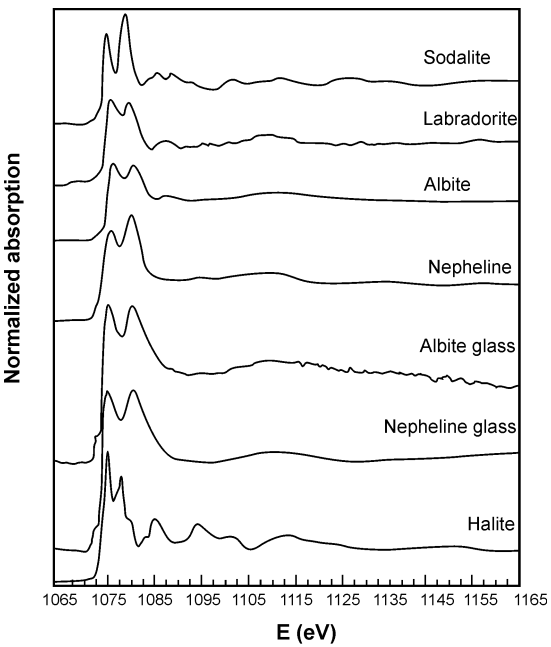


Figure 16. Na K-edge spectra of selected minerals and glasses (after Neuville et al. 2004b).

The two main peaks and their relative intensities appear to be a reasonable indicator of Na coordination environment when compared to model compounds (McKeown et al. 1985; Neuville et al. 2004b). The more ordered the Na environment the narrower the peaks. In addition, the intensity of the second peak tends to increase relative to the first peak as Na coordination increases (Cormier and Neuville 2004). There also appears to be an edge shift to lower energy with increasing Al/Na ratio, at least up to a ratio of 1.0 (McKeown et al. 1985), but the overall shape of the spectra are not affected significantly with Al substitution for Si (Cormier and Neuville 2004).

EBSCOhost - printed on 2/13/2023 5:26 AM via . All use subject to https://www.ebsco.com/terms-of-use

Potassium K-edge. The majority of K *K*-edge (Fig. 17) studies have been on micas (cf., Mottana 2004; Cibin et al. 2005, 2006, 2010; Marcelli et al. 2006; Brigatti et al. 2008) often using a polarized incident beam in order to look at the angular dependence of the *K*-edge with respect to the layered mica structure. The shape of the K *K*-edge (~3595-3680 eV) is similar to that of the Na *K*-edge with two main peaks being observed at ~3610 eV and ~3615 eV. The edge onset shifts to higher energy with increasing K coordination for minerals with similar K environments (Cibin et al. 2005; Marcelli et al. 2006).

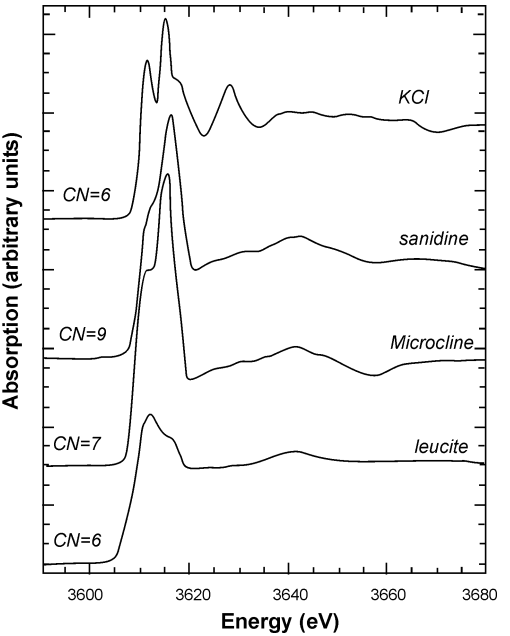


Figure 17. K *K*-edge spectra of some common minerals (after Cibin et al. 2005).

Additional peaks are observed at ~3625, ~3630 and ~3640 eV with the peak at ~3625 eV exhibiting a correlation in micas with the out of plane tetrahedral rotation of the tetrahedral sheet and the environment around the interlayer cation (Marcelli et al. 2006), while the peak at ~3630 eV appears to be related to the interplanar spacing between the interlayer and tetrahedral sheet (Brigatti et al. 2008). Brigatti et al. (2008) also suggest that the peak at ~3640 eV is related to the peak at ~3630 eV and has some link to the distance between the A and T sites in micas. Simulations, both multiple scattering and first principles DFT calculations, reproduce the experimental spectra quite well (Lavrentyev et al. 1999; Vinson et al. 2011; Xu et al. 2011). However, detailed p-DOS calculations and analysis of the individual peaks are not given.

Rubidium K-edge. The Rb *K*-edge (~15150-15260 eV) arises from Rb 1*s* transition to unoccupied p states but like the Cs edge below is broadened due to core-hole lifetime broadening (~3 eV)(cf., Soldatov et al. 1996 and references therein). In the case of RbBr there is some indication that the Rb *p* states are hybridized with the Br *p* states. In addition, the edge onset shifts with change in Rb oxidation state (Rb^+ to Rb^-) moving to lower energy with increasing electronegativity (Fussa-Rydel et al. 1988).

Some representative spectra are shown in Figure 18. While there is some variation in the edge features these subtle changes have not been investigated further and the behavior of the Rb *K*-edge remains relatively unexplored.

Cesium K-edge. The Cs *K*-edge is at very high energy (~35940-36040 eV) and almost featureless because of core-hole broadening (~14 eV). Consequently there are few studies of this edge (usually in the gas phase). The Cs L_3-edge (energy?) has less broadening and is at lower energy but it too has not been utilized to any large extent (cf., Rossetti et al. 2011).

Alkaline-Earths (Be, Ca, Mg, Sr, Ba)

Beryllium K-edge. As far as we are aware there are no published Be *K*-edge (~110-160 eV) XANES experimental data. However, there are Be *K*-edge spectra obtained by X-ray Raman (Soininen et al. 2001). The *K*-edge exhibits two relatively sharp peaks at ~119 eV and~124

EBSCOhost - printed on 2/13/2023 5:26 AM via . All use subject to https://www.ebsco.com/terms-of-use

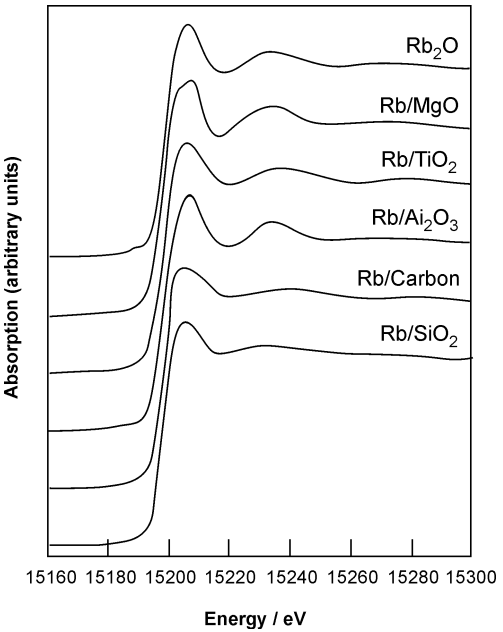


Figure 18. Rb *K*-edge on various support substrates at 77K (after Doskocil et al. 1997).

ordination numbers greater than 9. However, the post-edge shape of the XANES envelope is characteristic for higher coordinated (> 9) Ca (Sowery et al. 2004).

The XANES spectrum often exhibits one or more small pre-edge features at ~4040 eV, a shoulder on the low energy side of the edge at ~4045 eV, the main edge at ~4050 eV, with several higher energy peaks at ~4060 eV. The XANES has been modeled successfully using multiple scattering (Xu et al. 2013). However, Cabaret et al. (2013) have recently carried out first principle DFT calculations on the Ca *K*-edge in graphite intercalation compounds. They provide a detailed analysis of the interatomic interactions contributing to the edge features, which can be used to aid

eV. The latter peak is somewhat less intense. There is also a broad low intensity peak at ~139 eV. The first peak is due to a core exciton and the overall spectrum is reproduced quite well by theoretical calculations (Soininen et al. 2001; Gao 2010) but there has been no detailed analysis of the individual peaks.

Calcium K-edge. The Ca *K*-edge (~4020-4100 eV) has been used to determine Ca coordination in minerals (Paris et al. 1995; Quartieri et al. 1995) and glasses (Cormier and Neuville 2004; Neuville et al. 2004a) using the "fingerprinting" method of comparison with known mineral standards (Fig. 19). There appears to be a linear relationship between the energy of the edge and coordination (Sowrey et al. 2004), at least up to a Ca coordination of 9. The edge shifts to higher energy (~ 1 eV) as Ca coordination increases. The relationship does not hold for co-

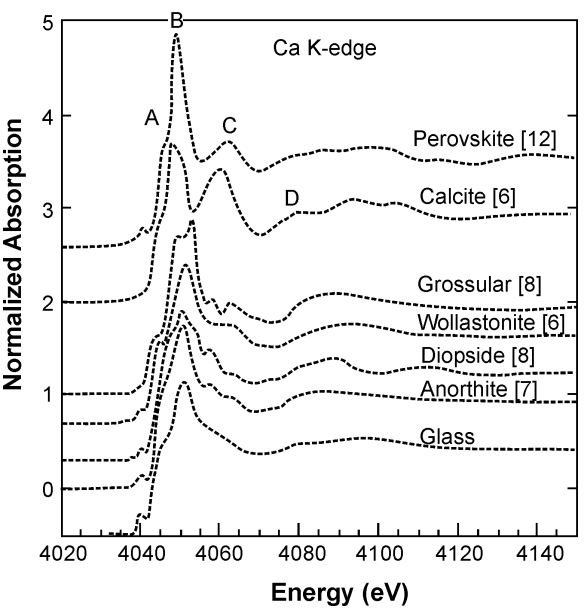


Figure 19. Ca K-edge spectra of anorthite glass and some common Ca containing minerals, (after Cormier and Neuville 2004).

EBSCOhost - printed on 2/13/2023 5:26 AM via . All use subject to https://www.ebsco.com/terms-of-use

the interpretation of Ca XANES features in other phases. Cabaret et al. (2013) assign the pre-edge feature to a quadrupolar $1s \rightarrow 3d$ transition that becomes dipole allowed due to mixing with Ca 4*p* states. It does not occur if the Ca is in a centrosymmetric site. Peak A is due to Ca $1s \rightarrow$ Ca 4*p* states mixed with 3*d* and 4*s* states of NNN Ca atoms. In the graphite intercalation compounds there is also a contribution from π* states (see C *K*-edge). Similar contributions may occur with other types of ligands. Peak B is due to Ca 4*p* interactions with NNN Ca 3*d* and 4*s* states and ligand π* states. The main peak C above is due to Ca 4*p* states mixed with NNN Ca 4*p* states and ligand σ* states (see C *K*-edge). The peak D is a result of in plane hybridization between Ca 4*p* states but is variable in intensity and position and not fully explained by DFT calculations.

Magnesium K-edge. Mg *K*-edge (~1300-1400 eV) XANES has been used to investigate the coordination of Mg in a variety of minerals such as calcite and aragonite (Finch and Alison 2007), pyroxenes (Mottana et al. 1999), perovskites (Andrault et al. 1998), garnet and spinel (Ildefonse et al. 1995; Quartieri et al. 2008; Neuville et al. 2009), silicates and phyllosilicates (Li et al. 1999; Miehé-Brendlé et al. 2010), and several other mineral phases (cf., Trcera et al. 2009 and references therein). It has also been used to study the Mg coordination in glasses (Li et al. 1999; Trcera et al. 2009) and melts (Neuville et al. 2009). The spectrum consists of around 5 or more peaks; three in the region of 1300-1320 eV (labeled A-C in Fig. 20) and two broader peaks at ~1323 and ~1331 eV (labeled D′ and D in Fig. 20). Additional shoulders and smaller peaks may also be observed depending upon the composition of the sample, as well as, a pre-edge feature at ~1305 eV. The pre-edge peak is due to a dipolar $1s \rightarrow p$ transition of the Mg atom possibly with contributions from the empty Mg 3*s* states (Trcera et. 2009).

The edge has been shown to move to higher energy (~2.5 eV) between $^{[4]}$Mg and $^{[8]}$Mg (Trcera et al. 2009) with increasing Mg coordination and this can be used to discriminate $^{[4]}$Mg/$^{[6]}$Mg, and

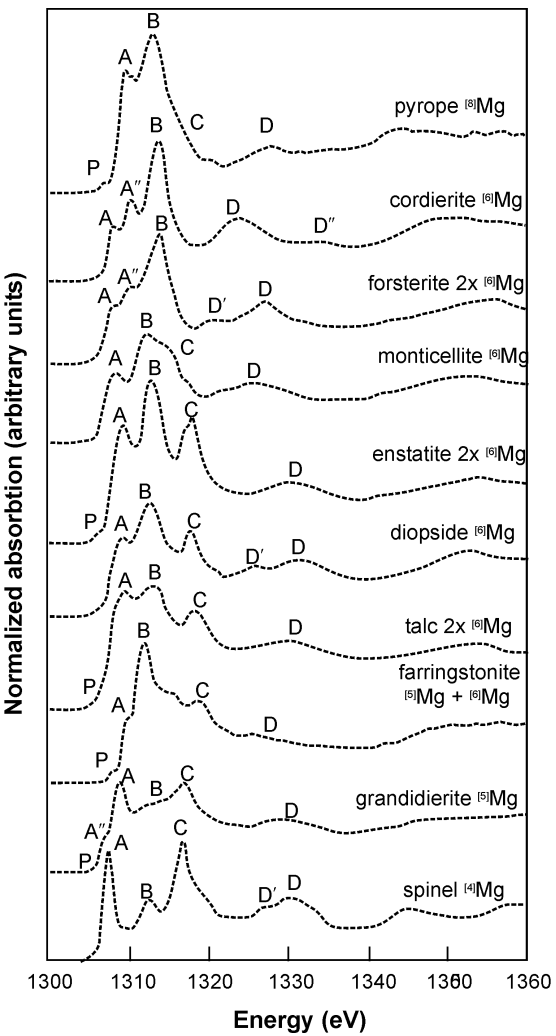


Figure 20. Mg *K*-edge spectra for a variety of minerals (after Trcera et al. 2009). The splitting of the A peak is due to different Mg site occupancies.

EBSCOhost - printed on 2/13/2023 5:26 AM via . All use subject to https://www.ebsco.com/terms-of-use

$^{[6]}$Mg/$^{[8]}$Mg sites (Ildefonse et al. 1995). However, it is not possible to resolve $^{[5]}$Mg. The shift is related to increasing Mg-O bond lengths as the coordination changes (Li et al. 1999). However, caution should be used in using the edge shift as it is also correlated with site distortion, shifting to lower energy with increasing site distortion of MgO_4 or MgO_6 polyhedra (Trcera et al. 2011).

Peaks A/D and B are due to Mg $1s \rightarrow 3p$ transitions of the absorber atom mixed with other Mg *s* (peaks A/D) and *p* states (peak B), respectively and can be correlated with Mg site occupancies in minerals. Peak D and higher energy peaks also involve contributions from the Mg *d* orbitals (Mizoguchi et al. 2006). The appearance of peak C seems to have some sort of relationship to the presence or absence of Fe in minerals (Trcera et al. 2009). Early multiple scattering studies (cf., Wu et al. 1996; Cabaret et al. 1998) indicated that the spectrum was sensitive to changes in short and medium range order. Recently, Trcera et al. (2009, 2011) have carried out first principle DFT calculations. Unlike the Ca *K*-edge, the Mg *K*-edge does not appear to be sensitive to the degree of polymerization in glasses. However, the energy positions and intensities of the main peaks do depend on the nature of the alkali cation present in the glass. Peak A shifts to lower energy as the atomic number of the alkali increases and peak C exhibits a correlation with the Mg-alkali distance. Peak B is not sensitive to the nature of the alkali present (Trcera et al. 2009).

Strontium K-edge. The Sr *K*-edge (~16080-16200 eV) has been used to investigate the Sr environment in carbonate phases and solutions (Kohn et al. 1990; Pingitore et al. 1992; Greegor et al. 1997; Parkman et al. 1998; Finch and Alison 2007; Borchert et al. 2013). The Sr *K*-edge (Fig. 21) is distinct when Sr is contained in calcite (Sr in 6-fold coordination) with a double peak feature at ~16115 and ~16130 eV, and a broader peak at ~16160 eV whereas in aragonite (Sr in 9-fold coordination) it has a single peak at ~16115 eV and a broad peak at ~16150 eV (Finch and Alison 2007).

Barium K-edge. As far as we are aware there are no Ba *K*-edge (~37435-37485 eV) studies of minerals or glasses. However, the Ba L_3-edge (~5200-5300 eV) has been used to identify various Ba-containing carbonate and biomineral phases (cf., Finch et al. 2010) and glasses (cf., Handa et al. 2006).

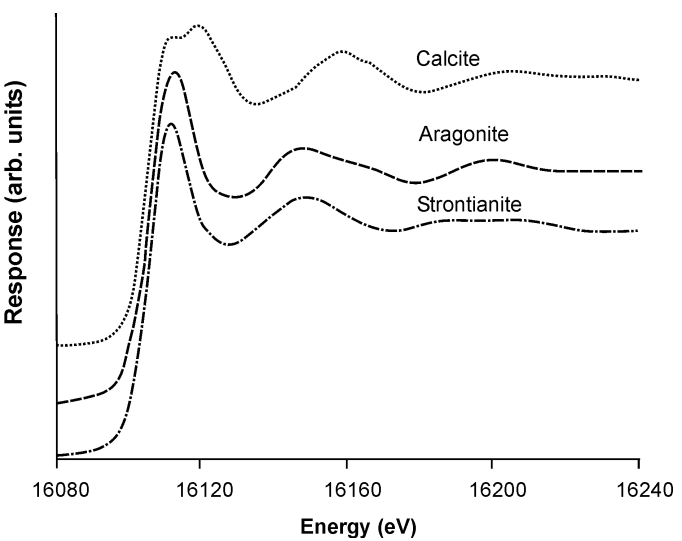


Figure 21. Strontium *K*-edge of three common Sr-containing minerals, (after Finch and Alison 2007).

EBSCOhost - printed on 2/13/2023 5:26 AM via . All use subject to https://www.ebsco.com/terms-of-use

Ligand edges (C, O, B, S, P)

Carbon K-edge. The carbon *K*-edge (~280-320 eV) of graphite (Mele and Ritsko 1979; Terminello et al. 1991) is shown in Figure 22, and is due to exciton transitions of the C 1*s* electron to unoccupied C 2*s* and 2*p* states. Furthermore it is divided into what are termed σ* (>290 eV) and π*states (<290 eV). The former involve the C 2*s*, $2p_x$ and $2p_y$ orbitals and the latter the C $2p_z$ orbital (Skytt et al. 1994). The σ* states lie in the plane of the C-C bond while the π* states are perpendicular to the C-C plane. As a consequence of this π* states are particularly sensitive to changes in incident beam orientation (Rosenberg et al. 1986; Brühwiler et al. 1995), as well as, the nature of the functional groups attached to the C (Boese et al. 1997). The σ* states are sensitive to the nature of the C-C and C=C bonds; C-C σ* states have peak energies lower than C=C σ* states (Hitchcock et al. 1986).

Diamond has also been studied (Morar et al. 1985; Ma et al. 1992, 1993) and exhibits a characteristic sharp σ* exciton peak at ~289 eV similar to that of graphite (~292 eV). Furthermore, the ratio of the π*/σ* states has been used to measure irradiation damage to the surface of the diamond (Reinke et al. 2000).

Currently, the C *K*-edge is widely utilized for discriminating the nature of carbon compounds in soils (Jokic et al. 2003; Solomon et al. 2005, 2012), amino acids (Kaznacheyev et al. 2002), and carbonyl compounds (Urquhart and Ade 2002). In recent years it is routinely employed in STXM experiments on organic materials (cf., Brandes et al. 2008; Lawrence et al. 2012).

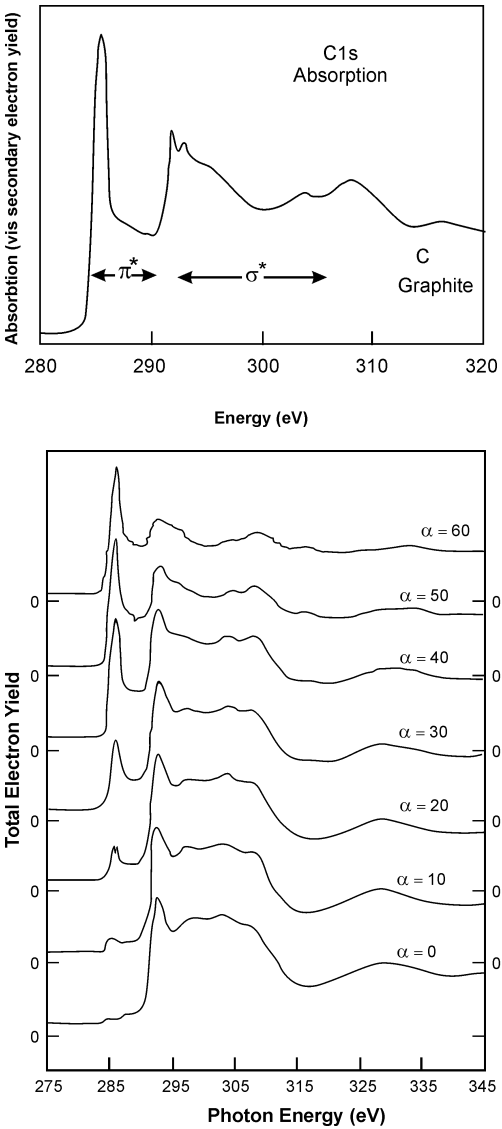


Figure 22. C *K*-edge of graphite showing σ* and π*states (*top*, after Terminello et al. 1991) and orientational effects of the incident beam on the sample surface, (*bottom*, after Rosenberg et al. 1986).

Oxygen K-edge. Oxygen *K*-edge XANES (~520-580 eV) generally results from an O 1*s* transition to O 2*p* anti-bonding states mixed with cation orbitals (cf., de Groot et al. 1989; Cabaret et al. 2007). Of particular interest is that the edge is sensitive to interactions with the cations bound to the oxygen (Fig. 23) and consequently contains information not just on the oxygens but also on the surrounding cations (cf., Wang and Henderson 2004; Henderson et al. 2007, 2009; Cabaret et al 2007; Zhang et al. 2010).

EBSCOhost - printed on 2/13/2023 5:26 AM via . All use subject to https://www.ebsco.com/terms-of-use

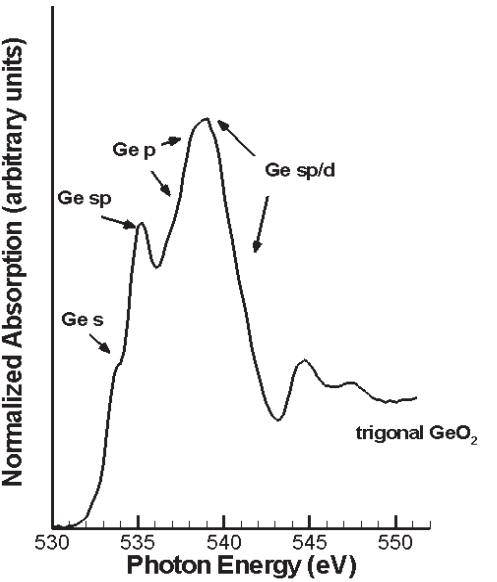


Figure 23. O *K*-edge spectrum of crystalline trigonal GeO_2 showing the peaks due to the O 1s → O 2*p* transition and the cation orbitals with which the O 2*p* state is hybridized/mixed (cf., Wang and Henderson 2004; Cabaret et al. 2007).

However, the spectra are complex and influenced by a number of factors other than the nature of the cation bonded to the oxygen. These include whether or not oxygen is bridging (BO) or non-bridging (NBO), the coordination geometry and nature of the cations to which the O is bonded, and the bond angles between the oxygen and surrounding cations. Consequently interpretation of O *K*-edge spectra is non-trivial and requires knowledge of the atomic structure of the sample, as well as, theoretical calculations. When O is bonded to only one other cation such as in simple oxides like SiO_2, GeO_2, or Al_2O_3 where the O atoms are all bridging and only attached to a single type of cation then the O *K*-edge spectra are relatively uncomplicated. However, the complexity is greatly increased when there are both NBOs and BOs, different Q^n species and oxygen is bonded to more than one type of cation. This is seen in Figure 24a where in corundum the oxygen is bridging and attached to a single type of 6-fold aluminum, in berlinite the oxygen is also bridging but now shared between tetrahedral Al and P, while in $CaAl_2O_4$ there are three types of Ca (one 9- and two 7-fold sites) and O is shared between these and six Al sites in 4-fold coordination (Neuville et al. 2010). In general, transitions due to NBOs occur at slightly lower energy than transitions involving BOs because NBO bonds are shorter than BO and have higher electron density (Jiang 2002). In addition, the simulations of $CaAl_2O_4$ O *K*-edge spectra by Jiang (2002) suggest that as the Ca coordination increases, the peak associated with oxygen, shifts to lower energy by ~0.5 eV. Whether or not this is general behavior for O *K*-edge peaks as cation coordination changes, remains unresolved.

Furthermore, for O *K*-edge spectra there is also the possibility of forming beam-induced O_2 "defects" on the surface of the sample, particularly for data collected in TEY mode. These "defects" occur as a relatively intense sharp pre-edge peak around 533 eV (peak a in Fig. 24b). It is due to an O 1*s* transition to π* states of O-O bonds in O_2 molecules that have diffused to the surface (Jiang 2006; Jiang and Spence 2006).

When oxygen is associated with a transition metal in an octahedral environment, the O *K*-edge spectrum is strongly influenced by the unoccupied *d* orbitals of the transition metal. Consequently, O *K*-edge spectra are very similar across the first row transition metals. Figure 24c shows O *K*-edge spectra for rutile (TiO_2), anatase (TiO_2) and Ti_2O_3. They are similar to other studies (Brydson et al. 1987, 1989; de Groot et al. 1989; Ruus et al. 1997; Wu et al. 1997b). The spectra exhibit two prominent peaks at ~531.0 and 533.7 eV). These peaks arise from the transition of an oxygen 1*s* electron to O 2*p* σ* states that are hybridized with empty transition metal 3*d* orbitals (de Groot et al. 1989). The splitting into two peaks (labeled a and b) is due to t_{2g}-e_g splitting of the 3*d* orbitals and the intensity is related to the degree of covalency between the oxygen atoms and the transition metal (de Groot et al. 1989). The second set of bands in the ~540-546 eV range are due to oxygen 1*s* transitions to O 2*p* states

EBSCOhost - printed on 2/13/2023 5:26 AM via . All use subject to https://www.ebsco.com/terms-of-use

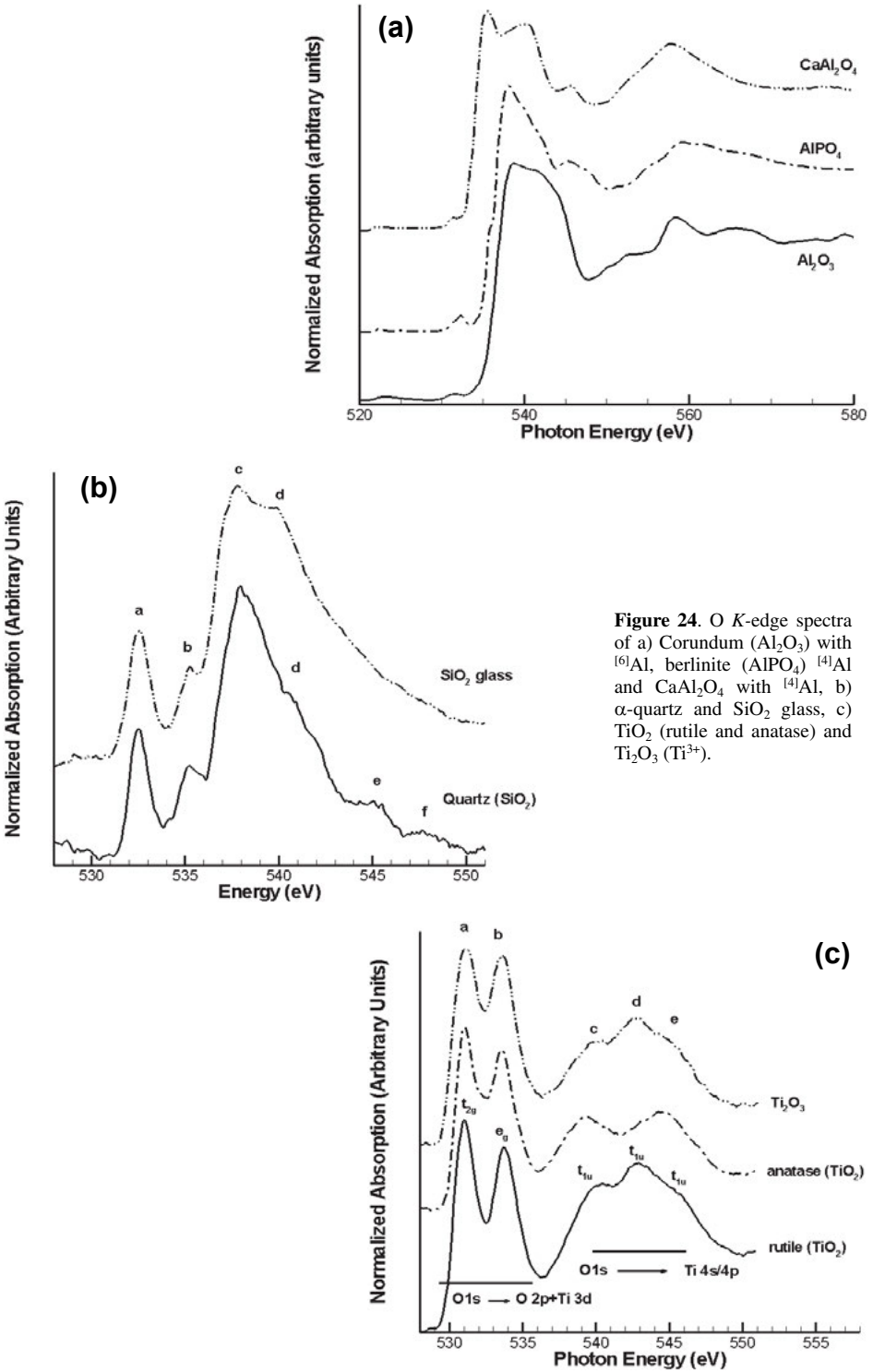


Figure 24. O *K*-edge spectra of a) Corundum (Al_2O_3) with $^{[6]}$Al, berlinite ($AlPO_4$) $^{[4]}$Al and $CaAl_2O_4$ with $^{[4]}$Al, b) α-quartz and SiO_2 glass, c) TiO_2 (rutile and anatase) and Ti_2O_3 (Ti^{3+}).

EBSCOhost - printed on 2/13/2023 5:26 AM via . All use subject to https://www.ebsco.com/terms-of-use

that are hybridized with transition metal 4*s* and 4*p* states (de Groot et al. 1989). Furthermore, the peaks in this region can be assigned to transitions to the lowest unoccupied t_{iu} states (peaks c and d) and to higher lying t_{iu} type orbitals (peak e) (Bydson et al. 1989). There is also a weak shift to higher energy of the O *K*-edge when the formal number of *d*-electrons increases on the Ti, i.e., when going from Ti^{4+} to Ti^{3+} (Yoshiya et al. 1999). When the transition metal is in 4- or 5-fold coordination similar mixing occurs but spectral interpretation is more complicated (Wu et al. 2002; Henderson et al. 2003) because of the t_{2g}-e_g inversion (4-fold) and the loss of degeneracy of the *d*-orbitals (5-fold).

Boron K-edge. Interest in this edge (~195-210 eV) stems mainly from the potential use of borosilicate glasses in the encapsulation of high-level nuclear waste and the need to determine the B coordination in these materials (cf., Peuget et al. 2006, 2007). There have been several B *K*-edge XANES studies of borate and borosilicate minerals (Hallmeier et al. 1981; Brydson et al. 1988; Sauer et al. 1993; Li et al. 1995c, 1996; Garvie et al. 1995; Kasrai et al. 1998; Fleet and Muthupari 1999, 2000; Fleet and Liu 2001). In general, the spectra of B_2O_3 ($^{[3]}$B), sassolite ($B(OH)_3$)($^{[3]}$B), BPO_4 ($^{[4]}$B) and danburite ($Ca[B_2Si_2O_8]$) ($^{[4]}$B) are often used as reference spectra for interpreting other B containing phases (Fig. 25).

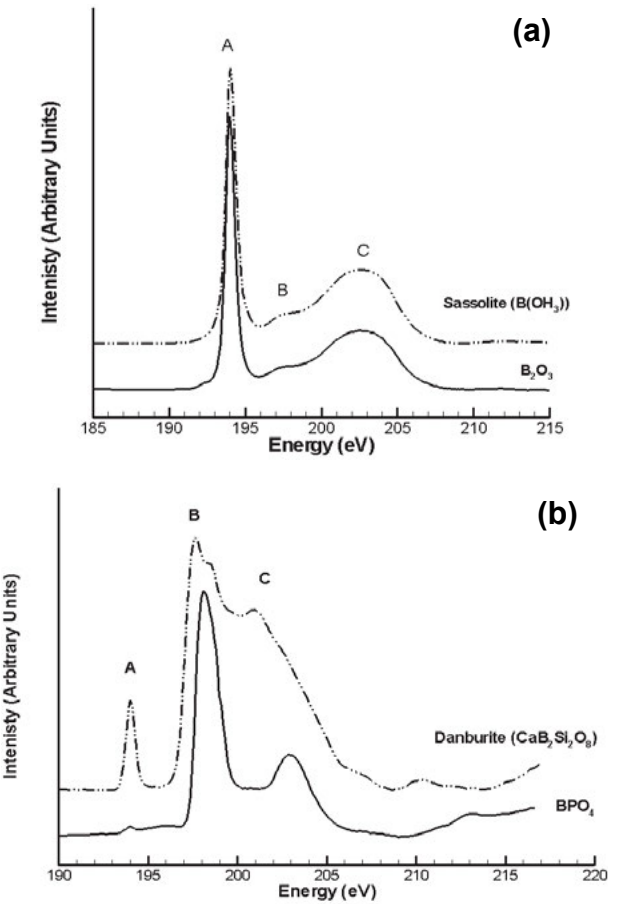


Figure 25. B *K*-edge XANES spectra of a) B_2O_3 and Sassolite ($B(OH)_3$) containing 100% $^{[3]}$B and b) BPO_4 and danburite ($Ca[B_2Si_2O_8]$) containing nominal 100% $^{[4]}$B.

EBSCOhost - printed on 2/13/2023 5:26 AM via . All use subject to https://www.ebsco.com/terms-of-use

In B_2O_3 (Fig. 25a) peak A is assigned to a [3]B transition from $1s \rightarrow 2p_z$ (π^*) states, which project normal to the plane of BO_3 groups (Schwarz et al. 1983). A weak peak, B (around 197.5 eV) arises from a dipole-forbidden transition from [3]B $1s \rightarrow a_1'$ (B $3s$ + O $2s$ + O $2p$) (σ^*) states (Ishiguro et al. 1982). BO_3 site distortion enhances this transition, due to the mixing of valence $2p$ π or σ^* antibonding and $2s$ states. The broad feature C around 198-205 eV consists of at least three distinct peaks at 200, 202 and 204 eV. They are assigned to transitions of B $1s$ electrons to unoccupied B-O sigma antibonding (σ^*) orbitals of e' (B $2p_x$ + B $2p_y$ + O $2s$ + O $2p$) symmetry, which are calculated to be ~10 eV above the B $2p_z$ orbital. Again Ishiguro et al. (1982) assign this peak to B $3p$ and $4p$ rather than $2p$ interactions.

For the BPO_4 and danburite spectra (Fig. 25b) in which only [4]B should be present, we can assign the peaks to transitions of B $1s$ electrons to unoccupied sigma antibonding ($^*\sigma$) states of t_2 (B $2p$ + O $2p$) symmetry (peaks around 198 eV) and a_1 (B $2s$ + O $2p$) symmetry (peak at 200 eV) while the broad feature (labeled C in Fig. 25) may be assigned to transitions of B $1s$ electrons to the unoccupied σ^* orbitals of a_1 and t_2 symmetry (Schwarz et al. 1983; Sauer et al. 1993; Garvie et al.1995). However, distortion of BO_4 tetrahedra may result in loss of degeneracy of the σ^* (t_2) orbital and peak broadening (Schwarz et al. 1983; Garvie et al. 1995; Fleet and Muthupari 1999, 2000) may occur which is observed as a shoulder at 199 eV on the high-energy side of the main peak.

Recent first principles calculations of the p-DOS have been carried out for crystalline B_2O_3, and BPO_4 (Ferlat et al. to be published). They show that some of the intensity of the main peak at 194 eV for B_2O_3 is also due to mixing with O $2p$ states while in the higher energy region (198-205 eV) the strongest contributor is a B $1s \rightarrow 2p$ transition at ~ 203-204 eV. At lower energy (198-200 eV) there are strong contributions from B $2s$ and B second neighbor $2p$ and $3p$ transitions while to the high energy side of the broad envelope second neighbor B $2s$ transition are the major contributors to the intensity. Simulations for BPO_4 show that the slight asymmetry of the peak at ~197 eV to the high energy side is due to a contribution from B $2s$ states and the high energy peak at ~202-205 eV results from contributions primarily from second neighbor P $3p$ interactions along with lesser contributions from B $2p$/$3p$ interactions.

Boron -- effects of sample preparation. Spectra for compounds with nominal 100% [4]B often exhibit a sharp peak at 194 eV characteristic of [3]B. Earlier studies attributed this to the conversion of [4]B to [3]B by the X-ray beam or to reaction of the sample with OH (Sauer et al. 1993; Garvie and Buseck 1996) during sample preparation. Certainly for ELNES studies possible beam induced conversion may be likely, given the highly focused nature of the beam. Kasrai et al. (1998) considered that the [4]B transformed to [3]B when samples were crushed and ground and that mechanical disruption was the major source of the conversion. This suggestion is supported by the results shown in Figure 26 in which the B *K*-edge spectrum of a danbu-

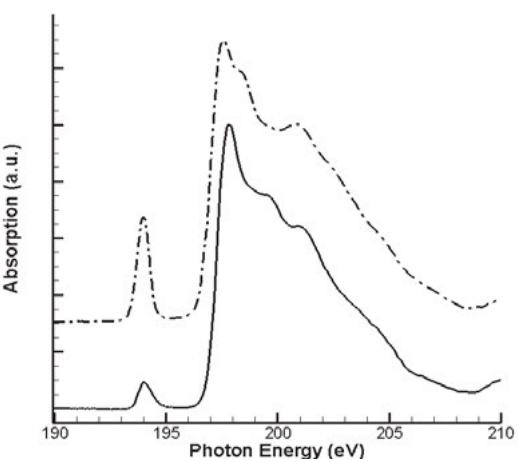


Figure 26. B *K*-edge XANES spectra of Danburite collected after different preparation conditions: crushed and under N_2 (*upper*); crushed fragments with a "fresh" surface exposed immediately prior to insertion in the sample chamber (*lower*).

EBSCOhost - printed on 2/13/2023 5:26 AM via . All use subject to https://www.ebsco.com/terms-of-use

rite sample has been collected under different experimental conditions. There is a significant difference between a sample crushed and ground in N_2 versus the same sample just crushed and not ground in N_2. The conversion is most likely a result of the increased surface area of the ground sample, with $^{[3]}$B forming at the expense of $^{[4]}$B simply because at the surface of the particles the planar BO_3 unit is likely to be geometrically preferred.

Representative spectra of minerals nominally containing only $^{[3]}$B, only $^{[4]}$B and mixed $^{[3/4]}$B are shown in Figure 27 and their compositions given in Table 1. In the nominal 100% $^{[4]}$B minerals a sharp feature characteristic of $^{[3]}$B (peak A) can be seen at ~194 eV because all of the samples were ground prior to data collection. This peak may exhibit subtle asymmetry in some $^{[3]}$B and mixed $^{[3/4]}$phases although it is more prevalent in the $^{[3]}$B only phases. Fleet and Muthupari (2000) attributed this to distortion of the BX_3 (where X = O, OH) group. However, Dong et al. (to be published) suggest it occurs due to separation of the B 2*p* and O 2*p* contributions to this peak. One should also note the high degree of variation in the intensity and positions of peaks B and C in all three groups of spectra. The overlap of peak B in the $^{[3]}$B spectra at ~198 eV with peak B in the $^{[4]}$B phases will lead to complications with extraction of quantitative B coordination numbers (see below). In addition, Fleet and Liu (2001) curve fit the spectral envelope in the 195-215 eV range in mixed $^{[4]}$B mineral phases and noted a correlation between splitting of the fitted B peak and divergence of tetrahedral B-O bond length. However, Dong et al. (to be published) do not observe this.

Table 1. Formulae of minerals shown in Figure 27.

Mineral	Formula
Minerals with only trigonal B	
Sassolite	$[B(OH)_3]$
Sussexite	$Mn_2(OH)[B_2O_4(OH)]$
Szaibelyite	$Mg_2(OH)[B_2O_4(OH)]$
Vonsenite	$Fe_2Fe^{3+}O_2(BO_3)$
Warwickite	$(Mg,Ti,Fe^{3+},Al)_2O(BO_3)$
Minerals with both trigonal and tetrahedral B	
Colemanite	$Ca[B_3O_4(OH)_3](H_2O)$
Hydroboracite	$CaMg[B_3O_4(OH)_3]_2(H_2O)_3$
Inyoite	$Ca[B_3O_3(OH)_5](H_2O)_4$
Inderite	$Mg[B_3O_3(OH)_5](H_2O)_5$
Kurnakovite	$Mg[B_3O_3(OH)_5](H_2O)_5$
Howlite	$Ca_2B_5SiO_9(OH)_5$
Boracite (low)	$Mg_3[B_3O_{10}]_2(BO_3)Cl$
Minerals with only tetrahedral B	
Datolite	$CaBSiO_4(OH)$
Pinnoite	$Mg[B_2O(OH)_6]$
Reedmergnerite	$Na[BSi_3O_8]$
Searlesit	$NaBSi_2O_5(OH)_2$
Serendibite	$Ca_2(Mg,Fe^{2+})_3(Al,Fe^{3+})_{4.5}B_{1.5}Si_3O_{23}$
Sinhalite	$AlMg(BO_4)$

Fleet and Muthupari (2000) also noted a correlation between the position of the $^{[3]}$B peak at ~194 eV and the B-O bond length. They observed that the peak shifted to lower energy as the B-O bond length increased. This correlation is observed for minerals containing only $^{[3]}$B (Fig. 28a, squares) but is less certain in minerals containing both coordination states (cf., Fig. 28a triangles). Dong et al. (to be published) speculate that it is related to more effective binding of the photoelectron to the nucleus due to the shorter B-O bond. In addition, there is a correlation between the position of the 194 eV peak and the increasing complexity of the B linkages (Fleet and Muthupari 2000; Dong et al. unpublished data) due to increasing positive charge on the B atom (Fleet and Muthupari 2000).

Determining the $^{[3]}$B/$^{[4]}$B ratio. Sauer et al. (1993) noted that the spectra of $^{[3]}$B is dominated by a sharp peak at ~194 eV and that of $^{[4]}$B by a relatively sharp peak at ~199 eV. They also suggested that spectra of mixed $^{[3]}$/$^{[4]}$B phases were essentially the sum of the

EBSCOhost - printed on 2/13/2023 5:26 AM via . All use subject to https://www.ebsco.com/terms-of-use

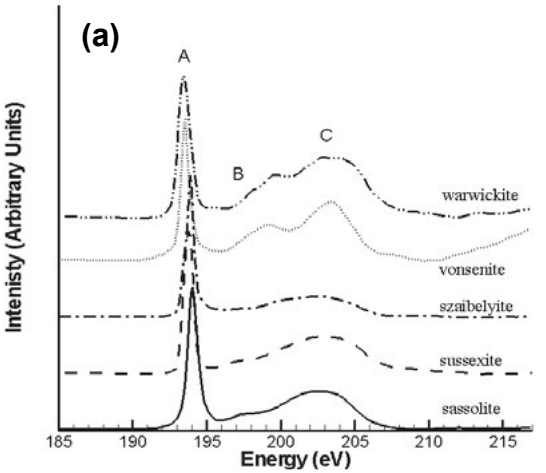
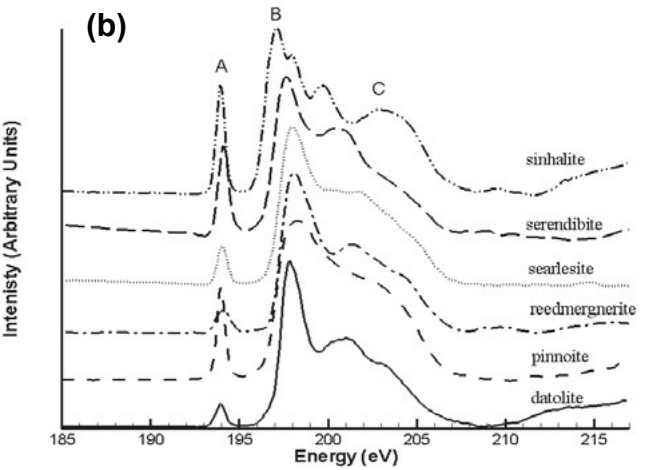
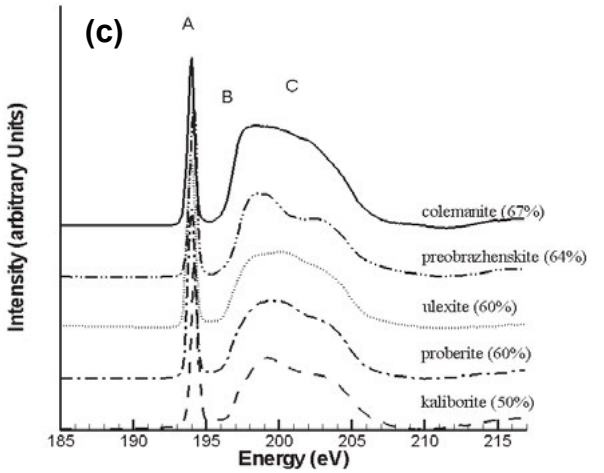


Figure 27. Representative spectra of minerals nominally containing a) 100% [3]B, b) 100% [4]B and c) mixed [3]B and [4]B (classified by nominal [4]B percentage).





EBSCOhost - printed on 2/13/2023 5:26 AM via . All use subject to https://www.ebsco.com/terms-of-use

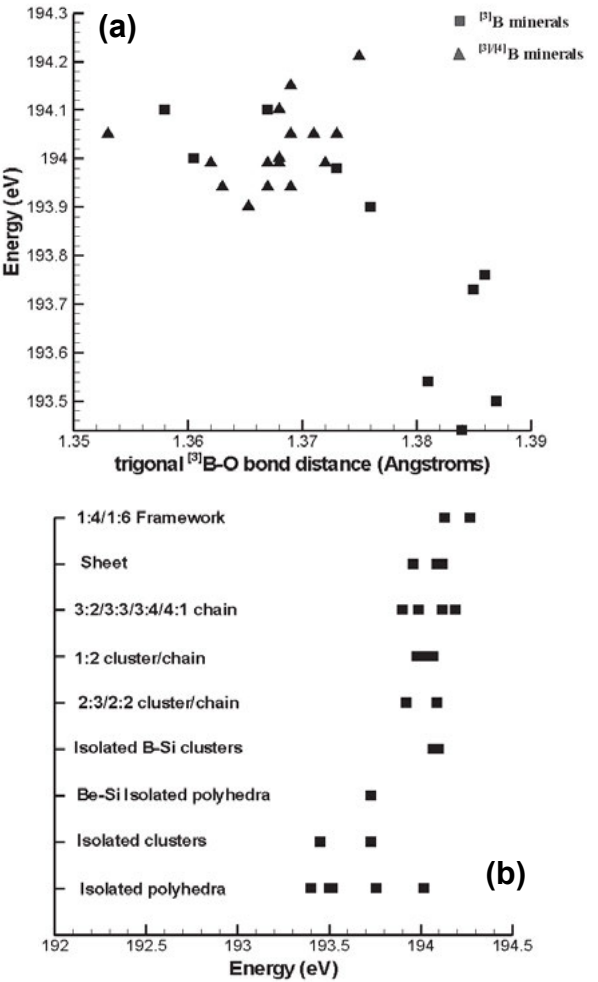


Figure 28. Correlation between position of the [3]B peak at ~194eV versus a) average B-O bond length and b) on the extended structure of the BX_3 (where X =O,OH) group in borate and borosilicate minerals containing only [3]B or [3]/[4]B.

individual [3]B and [4]B spectra and consequently quantitative [3]/[4]B ratios could be determined by a simple integration of the intensities of peaks characteristic of [3]B via the following equation;

$$f_{tri} = \frac{J(\pi^*) / (J(\Delta E))}{\left[J(\pi^*) / (J(\Delta E))\right]_{ref}} \quad (1)$$

Where f_{tri} is the fraction of [3]B in an unknown, $J(\pi^*)$ and $J(\pi^*)_{\text{ref}}$ are the intensities of the π^* peaks (~194 eV) of the unknown, and a reference material containing 100% [3]B, $J(\Delta E)$ and $J(\Delta E)_{ref}$ are the integrated intensities in the energy window ΔE (~18-20 eV) above the respective B *K*-edges. This method has also been used by Garvie et al. (1995) and Fleet and Muthupari (2000), with some slight modification of the energy windows. Fleet and Muthupari (2000) noted that the area and position of the peak due to [3]B at ~194 eV was sensitive to the [3]B

EBSCOhost - printed on 2/13/2023 5:26 AM via . All use subject to https://www.ebsco.com/terms-of-use

content and the B-O bond length. In addition, the area of the peak assigned to [4]B at ~ 198 eV was also sensitive to concentration of [4]B but quantification was difficult because of overlap with the broad feature at 203-204 eV due to both [3]B and [4]B. This latter overlap makes accurate determination of the relative coordination numbers somewhat problematic. Figure 29 shows a plot of calculated versus nominal [3]B concentration in mixed coordination phases. It is clear that this method underestimates the proportion of [3]B at high [3]B contents and overestimates it at low [3]B contents.

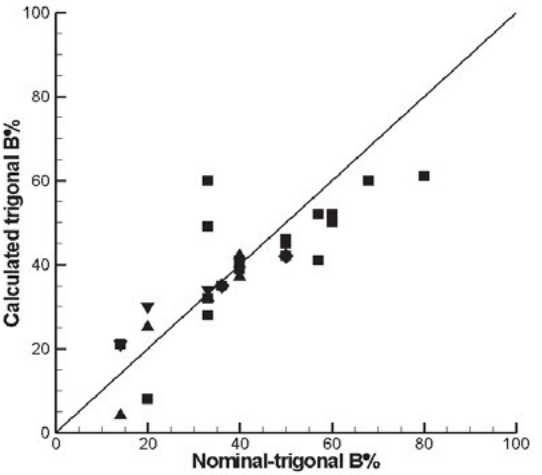


Figure 29. Proportion of [3]B calculated using the total area method: squares (Dong et al. unpublished data), triangles (Fleet and Muthupari 2000), gradient (Sauer et al. 1993), diamonds (Garvie et al. 1995).

Borate and borosilicate minerals may also form superstructural units (cf., Hawthorne et al. 1996). Sipr et al. (2007) have investigated theoretically, the influence of superstructural units on the XANES spectra of B-containing minerals. They note that spectra of minerals containing boroxyl rings, diborate and tridiborate units differ from a simple superposition of spectra containing isolated [3]B and [4]B units as opposed to spectra of structures containing pentaborate and triborate units. They find that boroxyl ring structures should be recognized by a small sub peak ~25 eV above the edge while diborate and ditriborate units will produce "fine structure" around the main XANES peak (cf., Sipr et al. 2007; Sipr and Rocca 2010).

Sulfur K-edge. Recent reviews of sulfur XANES have been given by Fleet (2005) and Wilke et al. (2011) and references therein. Sulfur is a ubiquitous volatile element in the Earth that occurs naturally in a wide variety of oxidation states from 2– to 6+ and consequently the sulfur *K*-edge (~2460-24520 eV) can vary by up to 12 eV in energy (Li et al. 1995d; Fleet 2005; Fleet et al. 2005; Almkvist et al. 2010). The two most common oxidation states for sulfur in solids of earth systems are oxidized S^{6+} (sulfate oxy-anion; SO_4^{2-}) and reduced S^{2-} (sulfide) (Fig. 30). The S *K*-edge of sulfur found as sulfate, such as in gypsum ($CaSO_4 \cdot 2H_2O$), displays a sharp feature at 2482 eV due to core level transitions of a 1*s* electron to the t_2 (3*p*-like) anti-bonding orbitals (Li et al. 1995d). This peak is found in other sulfates including $MgSO_4 \cdot 2H_2O$, K_2SO_4, Na_2SO_4, anhydrite, celestite, barite and hauyn (Li et al. 1995d; Wilke et al. 2008; Alonso Mori et al. 2009; Klimm et al. 2012). The peak is relatively sharp due to the narrow S-O bond distribution in the SO_4^{2+} groups. Higher energy peaks within sulfate spectra are attributed to multiple scattering by nearest- and NNN.

In contrast, monosulfide minerals (Fig. 31) show greater variation in edge position and intensity due to the meta-sulfide bond covalency (or ionicity), as well as, the degree of site distortion. Farrell et al. (2002) have studied monosulfide solid solutions in Fe-Mn-Mg sulfide system and CaS. A pre-edge feature (peak a) shifts to higher energy in the order FeS (2469.9 eV), MnS (2471.0 eV), CaS (2473.8 eV) while it is absent in the MgS spectra. The peak results from excitation of a 1*s* electron to unoccupied 3*d* antibonding states which is allowed due to hybridization of the metal 3*d* electrons with the S 3*p* σ* antibonding states (Tossell 1977). It is strongest in iron sulfides, due to the presence of unoccupied e_g orbitals (Farrell

EBSCOhost - printed on 2/13/2023 5:26 AM via . All use subject to https://www.ebsco.com/terms-of-use

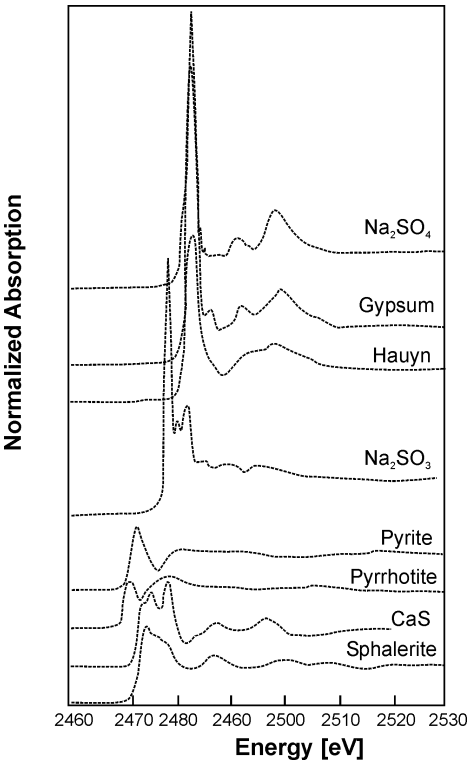


Figure 30. Compilation of S *K*-edge XANES of sulfur compounds with varying S oxidation state, (after Wilke et al. 2011).

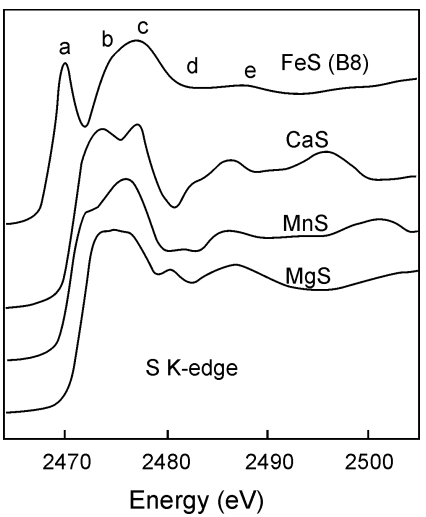


Figure 31. S K-edge spectra after Farrell et al. (2002) showing the effect of filling the 3*p* like anti-bonding states.

and Fleet 2001; Farrell et al. 2002), and weakest in CaS, due low-lying Ca 3*d* antibonding orbitals that reduce the band gap (Stepanyuk et al. 1989; Farrell et al. 2002). MgS has no low-lying metal 3*d* (e_g) orbitals available to hybridize with the S antibonding states and consequently exhibits no pre-edge feature. Farrell et al. (2002) attribute peaks b and c to 1*s* to 3*p* σ* antibonding states hybridized with Fe 4*s* and 4*p* σ* antibonding states in the conduction band. Furthermore they conclude that the relative intensity of peaks b and c are proportional to the available unoccupied t_{2g}-like and e_g-like antibonding orbitals, as well as, to the degree of hybridization between 3*p* σ* antibonding and 4*s* and 4*p* σ* antibonding states. Finally peaks at higher energies (approx. >2480 eV) have been assigned to multiple scattering.

The spectra of FeS, NiS and CoS have been simulated by Soldatov et al. (2004) using multiple-scattering codes. The simulations reproduce the experimental spectra reasonably well when a core hole bandwidth of 0.59 eV is taken into account and clusters of sufficient size are used. In both, experimental and calculated spectra all three peaks show a progressive shift to higher energies and higher intensity in the order FeS - NiS - CoS consistent with the $1/R^2$ rule (see above). The lattice parameters a and c decrease from FeS to CoS and consequently peaks b and c increase in energy in these spectra.

While in most mineral phases the sulfur is present as either S^{6+} or S^{2-} recent studies on silicate glasses from ocean island basalts (e.g., Loihi Seamount) and from synthesis at high pressure and temperature have shown evidence for the coexistence of both sulfide and sulfate species (Jugo et al. 2010). From these observations on mixed S-species in glasses the following relationship was derived to calculate the proportion of S^{6+} in the total sulfur content:

EBSCOhost - printed on 2/13/2023 5:26 AM via . All use subject to https://www.ebsco.com/terms-of-use

$$\frac{S^{6+}}{\sum S} = -C \ln\left\{\frac{\left[I(S^{6+})/\sum I - A\right]}{B}\right\}$$

where A, B and C are the coefficients 1.2427, −0.94911 and 0.81354, respectively and $\Sigma I = I(S^{6+}) + I(S^{2-})$ where $I(S^{2-})$ is the integrated intensity over the region 2475.7-2480 eV and $I(S^{6+})$ is the integrated intensity over the region 2481.5-2484 eV (Jugo et al. 2010). This relationship has been calibrated for a variety of synthetic glasses and fit parameters are dependent on the integrated area of the spectra and the regions defined as either sulfide or sulfate. This model works well for sulfur in silicate glasses as the edge position of sulfate is constant and the edge for sulfide does vary only in a limited range. Wilke et al. (2011) note that relationship varies depending on the composition of the glass, mostly due the variability of the spectra for the sulfide species. More discussion regarding the quantification of sulfur species can be found in Jugo et al. (2010), Wilke et al. (2011) and Klimm et al. (2012).

Finally, in early studies of S in silicate melts many authors report S^{4+}. However Wilke et al. (2008) have shown that this is an artifact of beam damage during XANES or electron microprobe analysis. Recently, Klimm et al. (2012) noted that beam damage is more important for iron-free melts than their iron-bearing counterparts. Although S^{4+} (as sulfite) is unlikely to be a common species in magmatic systems it may be important in other geochemical environments, particularly in vapor and fluids as SO_2. In solids, the sulfite oxy-anion, as found in Na_2SO_3, is in trigonal pyramidal geometry and the S *K*-edge is at 2478 eV (Alonso Mori et al. 2009; Almkvist et al. 2010).

Alonso Mori et al. (2009) have carried out a number of *ab initio* calculations of the S *K*-edge using multiple scattering, density functional theory and atomic multiplet theory. They compared their calculations with experimental data collected on sulfides (S^{2-}), sulfites (S^{4+}) and sulfates (S^{6+}). They found that the number, position and intensity of the experimental peaks depend primarily on the nature of the S first neighbors although next-nearest neighbors could also play a role. The main edge in sulfates and sulfites was due to a transition of the S 1*s* core electron to the 3*p*-like lowest unoccupied level that also has an O 2*p* component and some S 3*d* contribution. However, the main edge of sulfite occurs at lower energy than that of sulfates. For sulfides, the energy of the main edge shifts to lower energy from Zn to Cd and Hg. This is due to increased hybridization from the cation d orbitals. Overall there is ~12 eV energy shift in the edge on going from sulfides to sulfates and this edge shift is characteristic of the S oxidation state in oxycompounds but much less so for sulfides where the S atom is directly bound to the metal cations.

S $L_{2,3}$-edge. Sulfur $L_{2,3}$-edge (~160-200 eV) has been reviewed by Chen (1997) and Fleet (2005). The *L*-edge has not been as widely applied as the *K*-edge because the spectra are more complex than the S *K*-edge due to increased contributions from hybridized anti-bonding states (see below), they tend to have low signal to noise and are surface sensitive due to the low penetration depth of soft X-rays.

Sulfate *L*-edge spectra are simpler to interpret than sulfide spectra. Li et al. (1995d) obtained S $L_{2,3}$-edge spectra of typical sulfate minerals (Fig. 32). There is a distinct edge feature lying between 170.2-171.2 eV that exhibits splitting due to LS coupling resulting in the L_2 and L_3 doublet separated by ~1.2 eV (Fleet 2005). In gypsum, Li et al. (1995d) have assigned a S $2p_{3/2} \rightarrow a_1$ (3*s*-like) transition to the edge shoulder at 170.3 eV (peak A_1) and the S $2p_{1/2} \rightarrow a_1$ (3*s*-like) to the edge maximum at 171.3 eV (peak A_2). In addition to the edge doublet there is clearly a shoulder at higher energy, peak C, as well as an intense peak (E) centered at ~180 eV. Li et al. (1995d) have assigned peaks C and E to S 2*p* to t_2 and *e* transitions, respectively, though this interpretation has been questioned as it simplifies the hybridized nature of these higher energy contributions (Chen 1997; Farrell et al. 2002; Fleet 2005).

EBSCOhost - printed on 2/13/2023 5:26 AM via . All use subject to https://www.ebsco.com/terms-of-use

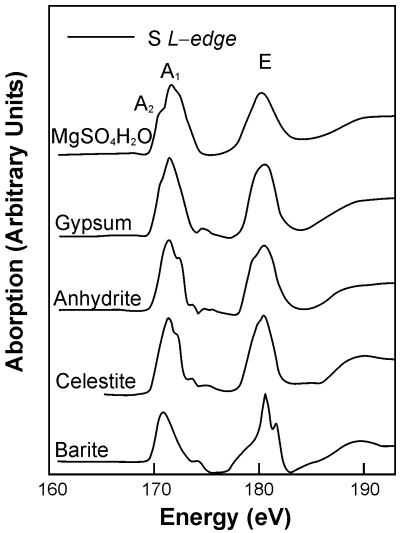


Figure 32. S *L*-edge spectra of simple sulfate minerals (after Li et al. 1995d).

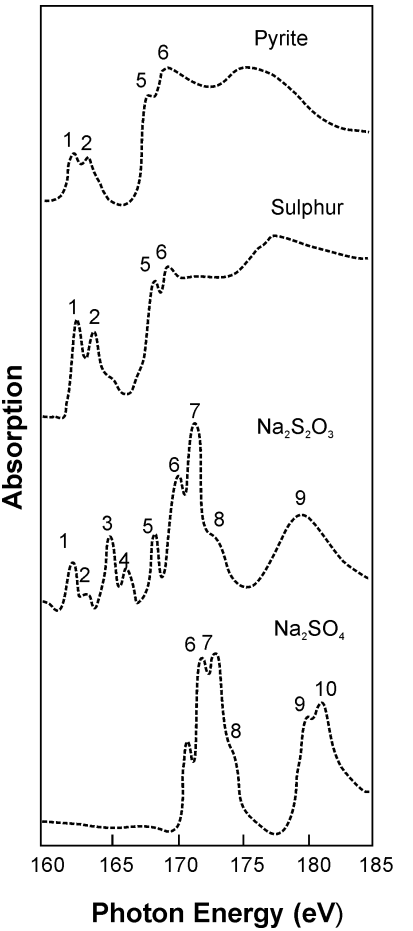


Figure 33. S L-edge spectra showing the strong LS doublet at ~162-163 eV (after Kasrai et al. 1996a).

The LS doublet is more distinct but lower in intensity than the post-edge features in sulfide minerals. For example, both native sulfur (S^0) and pyrite (S^{1-}) have a doublet at approximately the same position: 162.7 and 163.9 eV for sulfur versus 162.4 and 163.5 eV for pyrite (Fig. 33) (Kasrai et al. 1996a). For organic sulfur-bearing compounds (e.g., disulfides, alkyl sulfides, aryl sulfides and thiophenes) the S $L_{2,3}$-edge spectra of Sarret et al. (1999, 2002) exhibit at least three separate prominent peaks starting at ~163-164.5 eV separated by about 2 eV. These peaks strongly correlate with those found in thiophene have been used in characterizing unknown kerogens through linear combination fitting, however discrepancies still remain (Sarret et al. 2002).

A second doublet is also observed in the S $L_{2,3}$-edge in the spectra of pyrite and native sulfur (peaks 5 and 6 in Fig. 33) (Kasrai et al. 1996a). This doublet has also been recorded by Farrell et al. (2002) for CaS. The origin of this second doublet is currently attributed to an "echo" or shadow effect of the LS doublet due to multiple scattering or a transition to localized levels higher in the conduction band (Farrell et al. 2002). Earlier work by Kasrai et al. (1988) used peaks 10-45 eV above the edge to evaluate interatomic distances using the $1/R^2$ rule. They found a strong correlation for PbS, ZnS and MoS_2. Fleet (2005) further discussed the $1/R^2$ rule as applied to galena, PbS, correlating energy with interatomic distance for peaks down to 11 eV above the main edge feature.

Simulations of the S $L_{2,3}$-edge of FeS, NiS and CoS have been performed by Soldatov et al. (2004) using multiple-scattering theory. Their results reproduce the positions of the pre-edge, the edge and two higher energy peaks however, the pea*k*-to-background ratios are not in

EBSCOhost - printed on 2/13/2023 5:26 AM via . All use subject to https://www.ebsco.com/terms-of-use

agreement with experiment. Moreover, the pre-edge feature is much stronger in the calculated spectra than in the experimental data. Nevertheless the simulations do show the shift to higher energy, FeS → CoS in order of decreasing lattice spacing as observed experimentally. Soldatov et al. (2004) calculate the density of states of CoS and NiS and observe a "'normal" hybridization between Ni *d* and the S *p* unoccupied states, as well as, a second hybridization where the S *p* states are repulsed away from the Ni *d* states. Soldatov et al. (2004) note that this phenomenon has been previously reported for rare earth sulfides (Soldatov and Gusatinskii 1984), CeO_2 (Soldatov et al. 1994), orthoferrite (Povahzynaja et al. 1995), and stishovite (Soldatov et al. 2000). Finally, they use this energy separation as a measure of the covalency of the bonding in sulfide minerals concluding that NiS bonds are the most covalent in character and FeS are the least covalent (Soldatov et al. 2004).

Phosphorous. Phosphorous is an essential nutrient in the Earth's biosphere as well as an incompatible element in most magmatic and hydrological processes. It has a variety of oxidation states between P^0, in its elemental form, and P^{5+} as $(PO_4)^{3-}$. In nature, it is almost always found as the latter. Industrially, phosphate minerals are crucial components in fertilizers and phosphate minerals in rocks are often a major sink for rare-earth elements. P *K*-edge XANES has been applied to studies of phosphate minerals (Okude et al. 1999; Ingall et al. 2011), phosphate glasses (Yin et al. 1995; Nicholls et al. 2004); and soils (Beauchemin et al. 2003; Prietzel et al. 2010 and references therein; Kar et al. 2011; Xiong et al. 2012). On the other hand, a substantial amount of P *L*-edge data comes from the thin film and tribology literature where phosphorous and sulfur are key ingredients in lubricants (Kasrai et al. 2003; Nicholls et al. 2007 and references therein). Recently Kruse et al. (2009) have reviewed the phosphorous $L_{2,3}$-edge XANES of a number of commonly used crystalline and organic reference compounds.

Phosphorous K-edge. The position of the P K edge (~2140-2190 eV) can shift by ~ 8 eV (Prietzel et al. 2010) depending upon oxidation state (higher energy with increasing oxidation) and is affected by the nature of the ligand attached to the P. The edge shifts to higher energy with increasing ligand electronegativity (Yin et al. 1995). Thus ligand bonding has a strong effect on edge position similar to the cation effect in sulfide minerals (see above). Therefore, when using standards to determine oxidation state, it is important to use standards of the same ligand type (e.g., oxide-bearing or sulfur-bearing) not only similar oxidation state.

P *K*-edge spectra for several compounds are shown in Figure 34. Each spectrum has a sharp edge feature (peak 1) as well as two to three higher energy peaks The sharp edge in all spectra is attributed to a 1*s* core level to the t_2^* (*p*-like) anti-bonding orbitals (Yin et al. 1995). They attributed peaks 2-4 to shape resonances or multiple scattering. The main edge shifts to higher energies with the ligand: from C→S→O (Yin et al. 1995).

A range of phosphate minerals have been investigated by Ingall et al. (2011) at the P *K*-edge and are shown in Figure 35. The 12 apatite specimens all show similar spectral features despite varying carbon, hydroxyl and fluorine contents. A sharp edge peak is centered at 2155.6 eV with a high energy shoulder at (~2157 eV) that is approximately half to a third the intensity of the main edge, and two higher energy peaks centered at 2163.3 eV and 2170 eV. The edge is assigned to a transition of a 1*s* electron to the t_2^* (*p*-like) anti-bonding orbital. Non-apatite calcium-poor phosphate minerals (e.g., whiteite) display sharp edge features between 2153.0 and 2154.0 eV. The non-apatite calcium phosphates have lower intensity edge shoulders and a range of post-edge peaks. Aluminum-bearing phosphate minerals display no shoulder on the main edge and as a result have the narrowest edge (FWHM around 0.9 eV). Oxidized iron- and manganese-bearing phosphates display a unique pre-edge feature at 2150.1 eV associated with the presence of oxidized iron (Fe^{3+}). A single pre-edge feature is also observed in the spectra of chromium and cobalt phosphate minerals (Okude et al. 1999) and the copper-bearing phosphate, cornetite (Ingall et al. 2011). Xenotime has five sharp peaks that are attributed

EBSCOhost - printed on 2/13/2023 5:26 AM via . All use subject to https://www.ebsco.com/terms-of-use

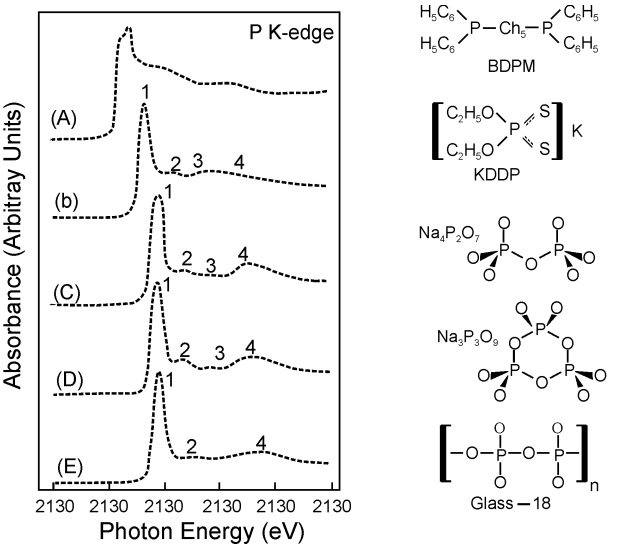


Figure 34. P *K*-edge XANES (*left*) of P bound to different ligands (*right*) (after Yin et al. 1995).

to interactions between phosphate and the outer orbitals of group 3 elements. Finally, Ingall et al. (2011) also note that pyromorphite and the uranium-bearing phosphates (e.g., coconinoite, meta-autunite) have a distinctive pre-edge doublet feature (~2151 and ~2152 eV). Thus the P *K*-edge of these general mineral groups may be used to constrain the contents of unknown mineral samples via "fingerprinting" and linear combination modeling.

Phosphorous L-edge. The $L_{2,3}$-edge (~130-155 eV) is comprised of the LS coupled doublet at ~134.5-137.5 and 136-141 eV (Fig. 36) corresponding respectively to the $2p_{1/2}$ and $2p_{3/2} \rightarrow a^*_1$ transitions (Yin et al. 1995). The $L_{2,3}$ edge is generally insensitive to the chemical environment. A broad peak at ~138-139 eV, about 2 eV above the edge, can be assigned to a $1s \rightarrow 3p$ anti-bonding state transition similar to that of the Si *L*-edge (Harp et al. 1990; Kruse et al. 2009). A further peak at ~147 eV due to $2p$ to $3d$ transitions is sensitive to the molecular symmetry and local environment.

The separation between the LS doublet varies for different phosphorous-bearing phases (Kasrai et al. 1999; Varlot et al. 2001). Na- and K-bearing phosphates have similar spectral features to Ca- and Mg-bearing phosphates. When Fe (or other TM) is bound to the phosphate quadrupolar transitions become allowed and a pre-edge peak is observed.

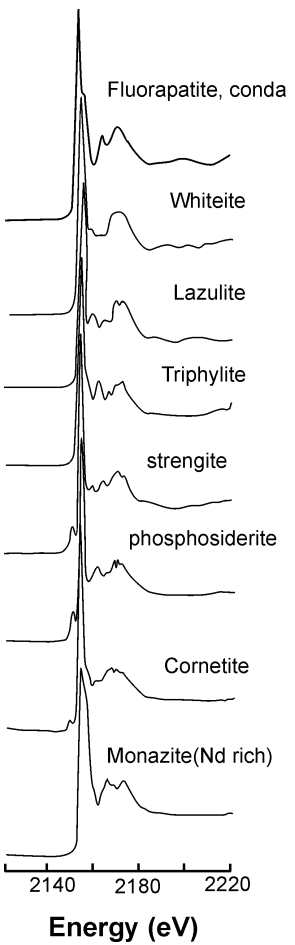
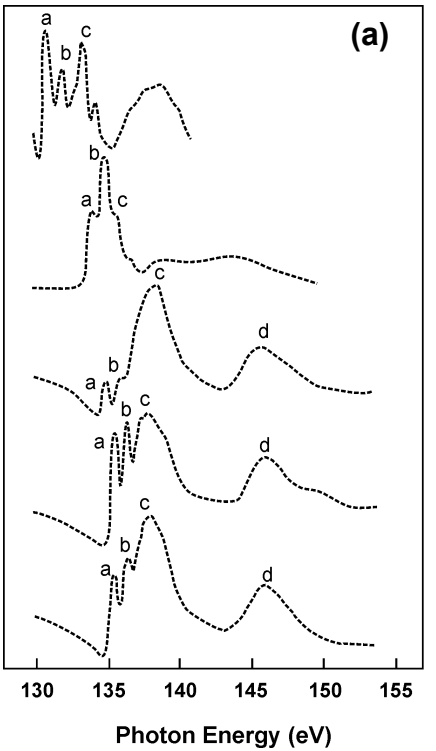
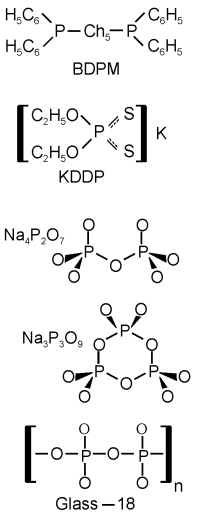


Figure 35. P *K*-edge spectra of selected phosphate minerals (after Ingall et al. 2011).

EBSCOhost - printed on 2/13/2023 5:26 AM via . All use subject to https://www.ebsco.com/terms-of-use





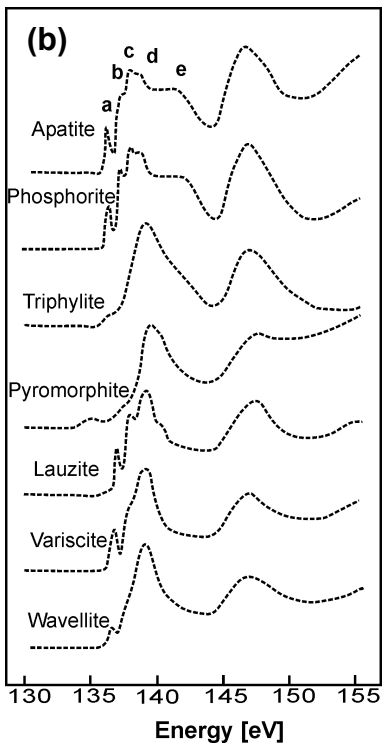


Figure 36. a) P $L_{2,3}$-edge of a phosphorous compounds with a variety of ligands (C, S and O), (After Yin et al. 1995). b) P *L*-edge XANES of a variety of mineral standards (after Kruse et al. 2009): Note the LS doublet (peaks a and b) is merged with antibonding orbital peaks C and D.

EBSCOhost - printed on 2/13/2023 5:26 AM via . All use subject to https://www.ebsco.com/terms-of-use

SOME EXAMPLES OF STUDIES UTILIZING XANES

In the following section we highlight the use of XANES in more detail by discussing some recent studies.

Assessing trace element substitution in minerals: Cerium speciation (Ce^{3+}/Ce^{4+}) in Ti-rich minerals

Titanite is a ubiquitous mineral that concentrates incompatible elements through incorporation of these elements into the large seven-fold site that holds Fe^{2+} and the rare earth elements. King et al. (2013) determined the oxidation state of cerium (Ce) within two titanites (one green and one brown) using Ce L_3-edge (5723 eV) XANES. King et al. (2013) combine the oxidation state information with known ionic radii to evaluate possible substitution mechanisms for Ce in titanites. Their model evaluates favorable from unfavorable trace substitutions in the context of the lattice strain model (Brice 1975; Blundy and Wood 1994) arguing that favorable substitutions minimize the overall changes in combined ionic radii and valence (King et al. 2013). King et al. (2013) used Ce^{3+} ($CePO_4$) and Ce^{4+} (CeO_2) standards and used linear combination fitting to determine the $Ce^{3+/4+}$ ratio needed to evaluate their substitution model. The green titanite was calculated to contain 71% of Ce in the 3+ oxidation state whereas the brown titanite contains 46% Ce^{3+} (Fig. 37).

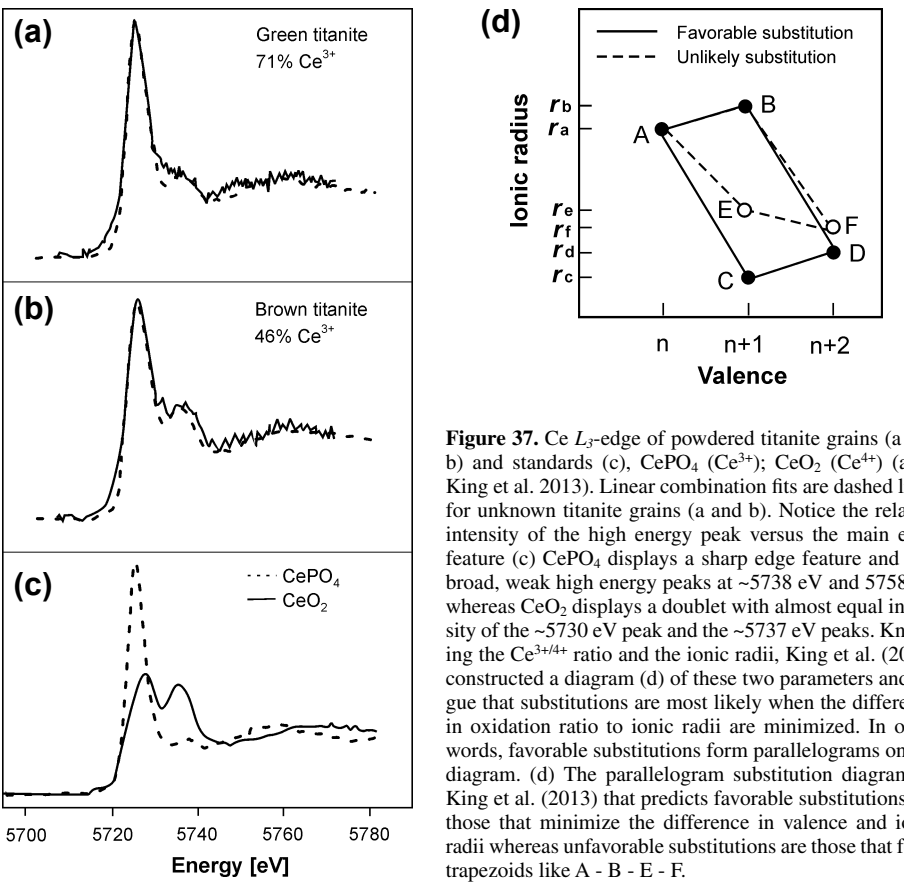


Figure 37. Ce L_3-edge of powdered titanite grains (a and b) and standards (c), $CePO_4$ (Ce^{3+}); CeO_2 (Ce^{4+}) (after King et al. 2013). Linear combination fits are dashed lines for unknown titanite grains (a and b). Notice the relative intensity of the high energy peak versus the main edge feature (c) $CePO_4$ displays a sharp edge feature and two broad, weak high energy peaks at ~5738 eV and 5758 eV whereas CeO_2 displays a doublet with almost equal intensity of the ~5730 eV peak and the ~5737 eV peaks. Knowing the $Ce^{3+/4+}$ ratio and the ionic radii, King et al. (2013) constructed a diagram (d) of these two parameters and argue that substitutions are most likely when the difference in oxidation ratio to ionic radii are minimized. In other words, favorable substitutions form parallelograms on the diagram. (d) The parallelogram substitution diagram of King et al. (2013) that predicts favorable substitutions are those that minimize the difference in valence and ionic radii whereas unfavorable substitutions are those that form trapezoids like A - B - E - F.

EBSCOhost - printed on 2/13/2023 5:26 AM via . All use subject to https://www.ebsco.com/terms-of-use

Assessing changes in oxidation state of Nb and Ta with varying f_{O_2} at 1.5 GPa as a possible explanation for the negative Nb/Ta anomaly or "arc signature" of melts

Burnham et al. (2012) tested the hypotheses that the Nb-Ta anomlies that define the "arc signature" are related to oxidation state of the Nb or Ta. Both Nb and Ta are high field strength elements that are typically found in octahedral coordination, have a 5+ oxidation state and nearly identical ionic radii (0.69 and 0.68 Å). In this coordination Nb-Ta anomalies in arc magmas have an unknown source. The relative depletion of Nb and Ta has been shown to vary implying that these elements are capable of geochemical fractionation despite having the same charge and radii. One obvious explanation would be that the oxidation state varies with f_{O_2}, melt composition and pressure. Burnham et al. (2012) collected Nb *K*-edge (Fig. 38) and the Ta L_3-edge (Fig. 39) to observe the expected edge shift if differing oxidation states were present. However, the Nb *K*-edge and Ta L_3-edge show no major changes. The Ta L_3-edge position is consistent with the Ta_2O_5 standard (Ta^{5+}; 9983.06 eV) though there is a subtle splitting of the edge. The Nb *K*-edge is consistent with Nb^{5+} standard edge position (18 991.0 eV) and only shows subtle changes in its pre-edge features. Clearly over a wide range of f_{O_2}'s at ambient and high pressures both Nb and Ta remain in the 5+ oxidation state and in the same structural environment. Ultimately, Burnham et al. (2012) conclude that the anomalous

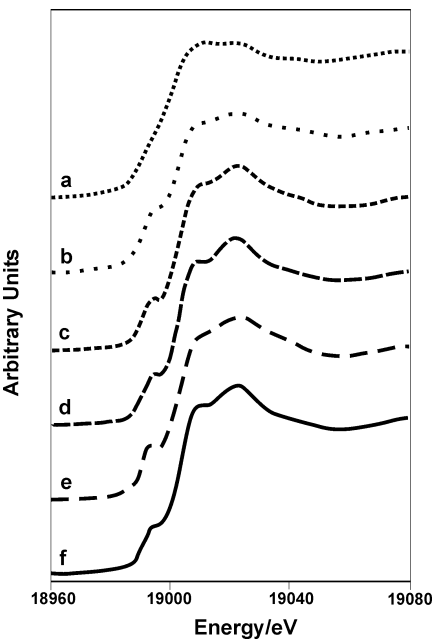


Figure 38. Nb *K*-edge spectra after Burnham et al. (2012). a) NbO_2 in BN. b-e) Overlain ambient pressure spectra of various compositions at end-member f_{O_2}'s; IW +6.7 and IW –4.3. f) Overlain 1.5 GPa spectra of compositions 1110 (IW-4.2) and 1111 (>>IW). See Burnham et al. (2012) for exact compositions. The identical edge positions across all f_{O_2}'s and across all compositions indicates constant oxidation state. Notice the subtle changes in pre-edge features.

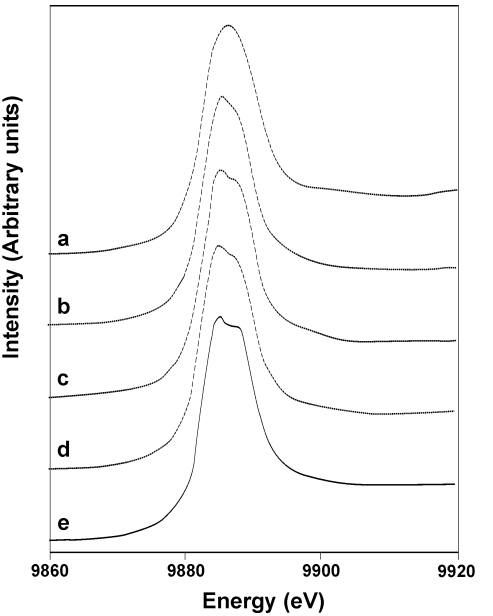


Figure 39. Ta L_3-edge spectra after Burnham et al. (2012). a) Ta_2O_5 in BN glass standard. b-d) Overlain ambient pressure spectra for various compositions at IW +6.7 and IW-3.3. e) Overlain 1.5 GPa pressure spectra for compositions 1110 (IW-4.2) and 1111 (>>IW). Notice the slight separation of the LS doublet with varying SiO_2 content and increasing pressure.

EBSCOhost - printed on 2/13/2023 5:26 AM via . All use subject to https://www.ebsco.com/terms-of-use

Ta-Nb "arc signature" is derived from partitioning due to small differences in ionic radii or polarizability.

In situ high-temperature determination of Cr oxidation state in basaltic melts: A novel XANES furnace design

Berry et al. (2003b) developed a furnace design for carrying out *in situ* high temperature XANES experiments on melts to resolve Cr speciation within iron-bearing basaltic melts under controlled oxygen fugacity (f_{O_2}). This is crucial as iron-bearing melts always display Cr^{3+} upon quenching samples because of the electron exchange reaction $Cr^{2+} + Fe^{3+} \rightarrow Fe^{2+} + Cr^{3+}$ during quenching. This quench effect in the presence of iron may be an important phenomenon for many other transition metals and redox sensitive elements. Moreover, models that involve the partitioning of redox sensitive elements between crystals and magmas are dependent upon the correct oxidation state assignment, which in turn is controlled by the f_{O_2}. Thus it is critical to constrain the oxidation state of elements under different f_{O_2} at melt conditions rather than in the quenched products.

Under typical terrestrial oxidation conditions Cr occurs in both the 3+ and 2+ oxidation states in iron-free glasses, whereas in iron-bearing glasses only Cr^{3+} has been observed. The controlled-atmosphere furnace uses a $Pt_{0.6}/Rh_{0.4}$ wire heater within an aluminum tube approximately 75 mm in diameter and 300 mm in length and which has two windows in a 90° configuration for the incident and fluorescent X-rays. A Pt/Re wire or strip is used to suspend the molten samples in the furnace, which are held to the strip by surface tension. The sample tube is kept slightly above atmospheric pressure. Cr *K*-edge spectra were collected using a focused beam of 2 mm × 1 mm on an alkali-free "model" mid-ocean ridge basalt which was pre-equilibrated at 1673 K and a log f_{O_2} of −8 before being used in the controlled f_{O_2} experiments under varying temperature conditions. The *in situ* spectra were compared with iron-free standards.

In iron-free glasses the Cr^{3+} pre-edge feature arises from $1s \rightarrow 3d$ quadrupolar transitions (see above). However, in Cr^{2+} a low-energy shoulder is observed on the edge which arises from $1s \rightarrow 4s$ dipolar transitions (Fig. 40). Across the −6 to −10 f_{O_2} range the Cr *K*-edge exhibits a pre-edge shoulder that decreases with increasing f_{O_2} and shifts to lower energy with increasing temperature indicating a change in Cr oxidation state. These results indicate that there is a clear need for *in situ* high temperature studies of redox sensitive elements.

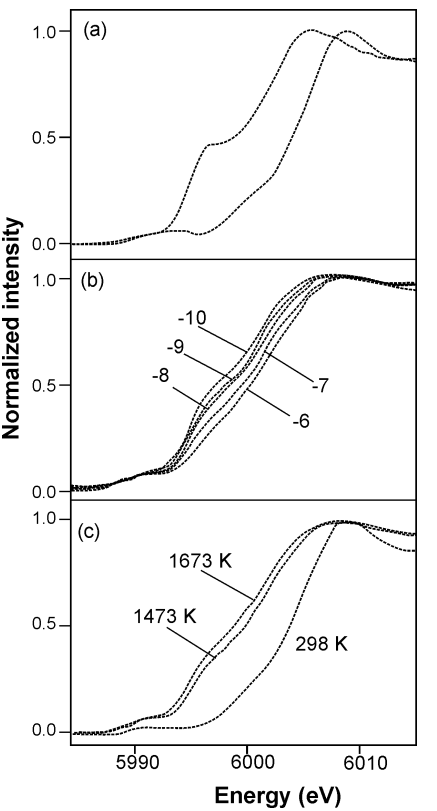


Figure 40. Cr *K*-edge measurements after Berry et al. (2003b). a) Iron-free diopside-anorthite glasses doped with Cr^{2+} and Cr^{3+}. Note the prominent low energy shoulder on the edge of the Cr^{2+} standard.

EBSCOhost - printed on 2/13/2023 5:26 AM via . All use subject to https://www.ebsco.com/terms-of-use

The behavior of Br in CO_2-bearing fluids in low-temperature geological settings: A Br K-edge study on synthetic fluid inclusions

Evans et al. (2007) investigated the behavior of RbBr (Fig. 41) salts in CO_2-bearing fluid inclusions trapped in synthetic quartz. RbBr was used as an analogue of NaCl as the absorption edge of Br (13474 eV) is a hard X-ray range and thus may penetrate the quartz crystal whereas the absorption edges of Cl lies <3000 eV and is attenuated by the quartz matrix.

The CO_2-free fluid inclusion shows a prominent edge maximum at 13482 eV and a broad high-energy peak 13499 eV. As X_{CO_2} increases the energy separation between the two peaks is reduced. This trend appears to be independent of temperature. In fluid inclusions with X_{CO_2} between 0.02 - 0.2 the Br *K*-edge displays a prominent pre-edge, at ~13476.5 eV. Furthermore, with increasing temperature the pre-edge peak decreases in intensity and ultimately disappears above 423 K. Burattini et al. (1991) have assigned the pre-edge peaks in Br *K*-edge spectra to transitions between the 1*s* core level electrons to an unfilled bound *p* states. Covalently bonded Br exhibits an intense pre-edge feature (e.g., Burattini et al. 1991; Feiters et al. 2005) while

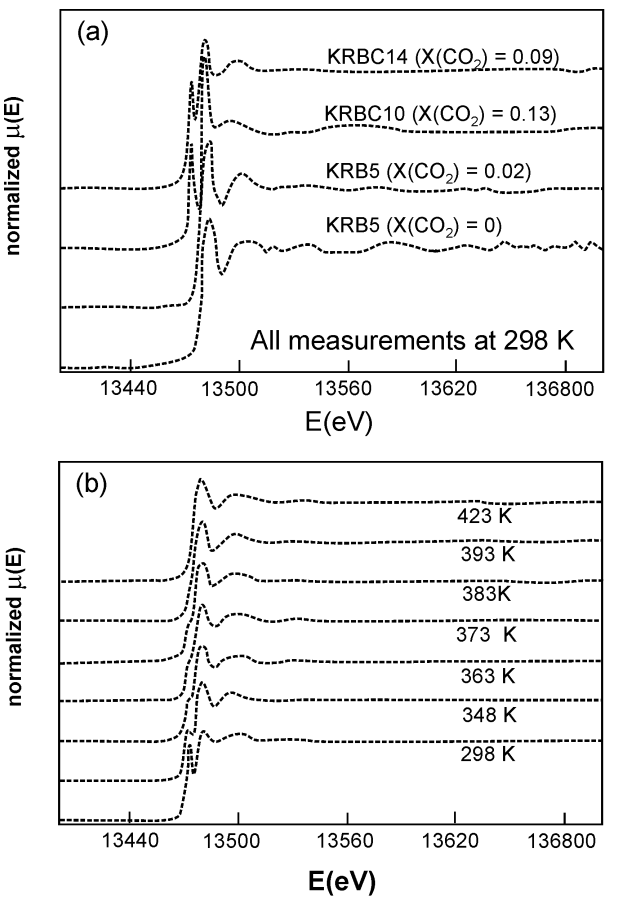


Figure 41. Br *K*-edge spectra of synthetic RbBr salt fluid inclusions in quartz crystals (after Evans et al. 2007). a) Br *K*-edge as a function of CO_2 content. Note the intense pre-edge peak at X_{CO2} = 0.09 and 0.13. b) Br *K*-edge as a function of temperature. Notice the decrease in pre-edge feature with increasing temperature. No pre-edge feature is seen at 423 K.

EBSCOhost - printed on 2/13/2023 5:26 AM via . All use subject to https://www.ebsco.com/terms-of-use

neither Br in electrolytic solution nor solid RbBr salt do. This implies that the Br in these fluid inclusions is covalently bonded. Burattini et al. (1991) also observe that the distance between the two main edge features decreases when the polarity of the solvent is low. In addition, Evans et al. (2007) have observed an increase in the intensity of the pre-edge peak with increasing CO_2 and its disappearance at high temperatures. These observations indicate that with increasing CO_2 content the RbBr-CO_2-H_2O solution reacts to form covalently bonded C- and Br-bearing compounds or that CO_2 produces strongly polar molecules to form within the hydrothermal solution. Ultimately, Evans et al. (2007) conclude that the chemical bonding of Br in the presence of CO_2 is unexplained by current solution chemistry models, which has important implications for the role of halogens in solution.

ACKNOWLEDGMENTS

For comments, collaborations and discussions, we would like to thank Pieter Glatzel, Bert Weckhuysen, David Prendergast, George Calas, Laurence Galoisy, Laurent Cormier, Delphine Cabaret, Gerald LeLong, Guillaume Ferlat, Daniel Neuville, Mike Bancroft and Masoud Kasrai. Thanks to Karyn Gorra for preparation of the figures. Mike Bancroft, Masoud Kasrai and Max Wilke are thanked for constructive reviews.

REFERENCES

Abbate M, Goedkoop JB, de Groot FMF, Grioni M, Fuggle JC, Hofmann S, Petersen H, Sacchi M (1992) Probing depth of soft X-ray absorption spectroscopy measured in total-electron-yield mode. Surf Interface Anal 18:65-69

Abbate M, Pen H, Czyzyk MT, Degroot FMF, Fuggle JC, Ma YJ, Chen CT, Sette F, Fujimori A, Ueda Y, Kosuge K (1993) Soft X-ray absorption-spectroscopy of vanadium-oxides. J Electron Spectrosc Relat Phenom 62:185-195

Achkar AJ, Regier TZ, Wadati H, Kim YJ, Zhang H, Hawthorn DG (2011) Bulk sensitive X-ray absorption spectroscopy free of self-absorption effects. Phys Rev B 83:081106

Alcacio TE, Hesterberg D, Chou JW, Martin JD, Beauchemin S, Sayers DE (2001) Molecular scale characteristics of Cu(II) bonding in goethite-humate complexes. Geochim Cosmochim Acta 65:1355-1366

Almkvist G, Boye K, Persson I (2010) *K*-edge XANES analysis of sulfur compounds:an investigation of the relative intensities using internal calibration. J Synchrotron Radiat 17:683-688

Alonso Mori R, Paris E, Giuli G, Eeckhout SG, Kavcic M, Zitnik M, Bucar K, Pettersson LGM, Glatzel P (2009) Electronic structure of sulfur studied by X-ray absorption and emission spectroscopy. Anal Chem 81:6516-6525

Alvarez M, Rueda EH, Sileo EE (2007) Simultaneous incorporation of Mn and Al in the goethite structure. Geochim Cosmochim Acta 71:1009-1020

Andrault D, Neuville DR, Flank AM, Wang Y (1998) Cation sites in Al-rich $MgSiO_3$ perovskites. Am Mineral 83:1045-1053

Arai Y, Sparks DL (2002) Residence time effects on arsenate surface speciation at the aluminum oxide-water interface. Soil Sci 167:303-314

Arrio MA, Rossano S, Brouder C, Galoisy L, Calas G (2000) Calculation of multipole transitions at the Fe *K*- pre-edge through p-d hybridization in the Ligand Field Multiplet model. Europhys Lett 51:454-460

Balzarotti AAF, Girlanda R, Martino G (1984) Electronic energy levels of α-Al_2O_3 from L_3 edge photoabsorption of aluminum and small cluster CNDO calculations. Phys Rev B 29:5903-5908

Beauchemin S, Hesterberg D, Chou J, Beauchemin M, Simard RR, Sayers DE (2003) Speciation of phosphorus in phosphorus-enriched agricultural soils using X-ray absorption near-edge structure spectroscopy and chemical fractionation. J Environ Qual 32:1809-1819

Beck P, De Andrade V, Orthous-Daunay FR, Veronesi G, Cotte M, Quirico E, Schmitt B (2012) The redox state of iron in the matrix of CI, CM and metamorphosed CM chondrites by XANES spectroscopy. Geochim Cosmochim Acta 99:305-316

Bender S, Franke R, Hartmann E, Lansmann V, Jansen M, Hormes J (2002) X-ray absorption and photoemission electron spectroscopic investigation of crystalline and amorphous barium silicates. J Non-Cryst Solids 298:99-108

EBSCOhost - printed on 2/13/2023 5:26 AM via . All use subject to https://www.ebsco.com/terms-of-use

Berry AJ, O''Neill HSC (2004) A XANES determination of the oxidation state of chromium in silicate glasses. Am Mineral 89:790-798

Berry AJ, O'Neill HS, Jayasuriya KD, Campbell SJ, Foran GJ (2003a) XANES calibrations for the oxidation state of iron in a silicate glass. Am Mineral 88:967-977

Berry AJ, Shelley JMG, Foran GJ, O'Neill HS, Scott DR (2003b) A furnace design for XANES spectroscopy of silicate melts under controlled oxygen fugacities and temperatures to 1773 K. J Synchrotron Radiat 10:332-336

Berry AJ, Hack AC, Mavrogenes JA, Newville M, Sutton SR (2006) A XANES study of Cu speciation in high-temperature brines using synthetic fluid inclusions. Am Mineral 91:1773-1782

Berry AJ, Yaxley GM, Woodland AB, Foran GJ (2010) A XANES calibration for determining the oxidation state of iron in mantle garnet. Chem Geol 278:31-37

Bianconi A (1979) Core excitons and inner well resonances in surface soft X-ray absorption (SSXA) spectra. Surf Sci 89:41-50

Blundy J, Wood B (1994) Prediction of crystal-melt partition-coefficients from elastic-moduli. Nature 372:452-454

Boese J, Osanna A, Jacobsen C, Kirz J (1997) Carbon edge XANES spectroscopy of amino acids and peptides. J Electron Spectrosc Relat Phenom 85:9-15

Borchert M, Wilke M, Schmidt C, Kvashnina K Jahn S (2013) Complexation of Sr in aqueous solutions equilibrated with silicate melts: implications for fluid-melt partitioning. Mineral Mag 77:739

Brandes JA, Cody GD, Rumble D, Haberstroh P, Wirick S, Gelinas Y (2008) Carbon *K*-edge XANES spectromicroscopy of natural graphite. Carbon 46:1424-1434

Brown GE Jr (1990) Spectroscopic studies of chemisorption reaction mechanisms at mineral/water interfaces. Rev in Mineral 23: 314-384

Brown GE Jr, Calas G, Waychunas GA, Petiau J (1988) X-ray absorption spectroscopy and its applications in mineralogy and geochemistry. Rev Mineral 18: 431-512

Brown GE Jr, Sturchio NC (2002) An overview of synchrotron radiation applications to low temperature geochemistry and environmental sciences. Rev in Mineral 49:1-115

Brown GE Jr, Parks GA (1989) Synchrotron-based X-ray absorption studies of cation environments in earth materials. Rev Geophys 27:519-533

Brice JC (1975) Some thermodynamic aspects of growth strained crystals. J Cryst Growth 28:249-253

Brigatti MF, Lugli C, Cibin G, Marcelli A, Giuli G, Paris E, Mottana A, Wu ZY (2000) Reduction and sorption of chromium by Fe(II)-bearing phyllosilicates: Chemical treatments and X-ray absorption spectroscopy (XAS) studies. Clay Clay Miner 48:272-281

Brigatti MF, Malferrari D, Poppi M, Mottana A, Cibin G, Marcelli A, Cinque G (2008) Interlayer potassium and its neighboring atoms in micas:Crystal-chemical modeling and XANES spectroscopy. Am Mineral 93:821-830

Brouder C, Cabaret D, Juhin A, Sainctavit P (2010) Effect of atomic vibrations on the X-ray absorption spectra at the K edge of Al in α-Al_2O_3 and of Ti in TiO_2 rutile. Phys Rev B 81:115125

Brühwiler P, Maxwell A, Puglia C, Nilsson A, Andersson S, Mårtensson N (1995) π^* and σ^* excitons in C 1s absorption of graphite. Phys Rev Lett 74:614-617

Brydson R, Williams BG, Engel W, Sauer H, Zeitler E, Thomas JM (1987) Electron-energy Loss spectroscopy (EELS) and the electronic-structure of titanium dioxide. Solid State Commun 64:609-612

Brydson R, Vvedensky DD, Engel W, Sauer H, Williams BG, Zeitler E, Thomas JM (1988) Chemical information from Electron-loss Near-edge Structure - Core hole effects in the beryllium and boron *K*-edges in rhodizite. J Phys Chem 92:962-966

Brydson R, Sauer H, Engel W, Thomas JM, Zeitler E, Kosugi N, Kuroda H (1989) Electron-energy loss and X-ray absorption-spectroscopy of rutile and anatase - A test of structural sensitivity. J Phys-Condens Mat 1:797-812

Brydson R, Brown A, Benni LG, Livi K (2014) Analytical transmission electron microscopy. Rev Mineral Geochem 78:219-269

Burattini E, Dangelo P, Giglio E, Pavel NV (1991) EXAFS study of probe molecules in micellar solutions. J Phys Chem 95:7880-7886

Burke IT, Mayes WM, Peacock CL, Brown AP, Jarvis AP, Gruiz K (2012) Speciation of Arsenic, Chromium, and Vanadium in Red Mud Samples from the Ajka Spill Site, Hungary. Environ Sci Technol 46:3085-3092

Burnham AD, Berry AJ, Wood BJ, Cibin G (2012) The oxidation states of niobium and tantalum in mantle melts. Chem Geol 330:228-232

Cabaret D, Sainctavit P, Ildefonse P, Flank AM (1996) Full mutiple-scattering calculations on silicates and oxides at the Al *K*-edge. J Phys-Condens Mat 8:3691-3704

Cabaret D, Sainctavit P, Ildefonse P, Flank AM (1998) Full multiple scattering calculations of the X-ray absorption near edge structure at the magnesium K-edge in pyroxene. Am Mineral 83:300-304

EBSCOhost - printed on 2/13/2023 5:26 AM via . All use subject to https://www.ebsco.com/terms-of-use

Cabaret D, Joly Y, Renevier H, Natoli CR (1999) Pre-edge structure analysis of Ti *K*-edge polarized X-ray absorption spectra in TiO_2 by full-potential XANES calculations. J Synchrotron Radiat 6:258-260

Cabaret D, Le Grand M, Ramos A, Flank AM, Rossano S, Galoisy L, Calas G, Ghaleb D (2001) Medium range structure of borosilicate glasses from Si *K*-edge XANES:a combined approach based on multiple scattering and molecular dynamics calculations. J Non-Cryst Solids 289:1-8

Cabaret D, Mauri F, Henderson GS (2007) Oxygen-edge XANES of germanates investigated using first-principles calculations. Phys Rev B 75:184205

Cabaret D, Bordage A, Juhin A, Arfaoui M, Gaudry E (2010) First-principles calculations of X-ray absorption spectra at the *K*-edge of 3*d* transition metals:an electronic structure analysis of the pre-edge. Phys Chem Chem Phys 12:5619-33

Cabaret D, Emery N, Bellin C, Hérold C, Lagrange P, Wilhelm F, Rogalev A, Loupias G (2013) Nature of empty states in superconducting CaC_6 and related Li-Ca ternary graphite intercalation compounds using polarized X-ray absorption near-edge structure at the Ca *K*- edge. Phys Rev B 87:075108

Calas G, Petiau J (1983) Coordination of iron in oxide glasses through high-resolution *K*-edge spectra – Information from the pre-edge. Solid State Commun 48:625-629

Caliebe WA, Kao CC, Hastings JB, Taguchi M, Kotani A, Uozumi T, de Groot FMF (1998) 1*s*2*p* resonant inelastic X-ray scattering in Fe_2O_3. Phys.Rev B 58:13452-13458

Chalmin E, Farges F, Brown GB Jr (2009) A pre-edge analysis of Mn *K*-edge XANES spectra to help determine the speciation of manganese in minerals and glasses. Contrib Mineral Petrol 157:111-126

Chaplais G, Prouzet E, Flank AM, Le Bideau J (2001) Al^{27} MAS NMR and XAS cross-study of the aluminophosphonate $Al(OH)(O_3PC_6H_5)$. New J Chem 25:1365-1367

Charnock J, Henderson CMB, Mosselmans J, Pattrick R (1996) 3*d* transition metal *L*-edge X-ray absorption studies of the dichalcogenides of Fe, Co and Ni. Phys Chem Minerals 23*:*403-408

Chen JG (1997) NEXAFS investigations of transition metal oxides, nitrides, carbides, sulfides and other interstitial compounds. Surf Sci Reports 30:1-152

Chen JM, Simonson JK, K.H. T, Rosenberg RA (1993a) Correlation between interatomic distances and teh X-ray absorption near-edge structure of singe-crystal sapphire. Phys Rev B 48:10047-10050

Chen JM, Rosenberg RA, Simons JK, Tan KH (1993b) X-ray absorption near-edge structure of single-crystal sapphire using synchrotron-radiation – The interatomic-distance correlation. Jpn J Appl Phys Part 1 32:788-790

Choy JH, Jung H, Yoon JB (2001) Co *K*-edge XAS study on a new cobalt-doped-SiO_2 pillared clay. J Synchrotron Radiat 8:599-601

Cibin G, Mottana A, Marcelli A, Brigatti MF (2005) Potassium coordination in trioctahedral micas investigated by *K*-edge XANES spectroscopy. Mineral Petrol 85:67-87

Cibin G, Mottana A, Marcelli A, Brigatti MF (2006) Angular dependence of potassium *K*-edge XANES spectra of trioctahedral micas: Significance for the determination of the local structure and electronic behavior of the interlayer site. Am Mineral 91:1150-1162

Cibin G, Mottana A, Marcelli A, Cinque G, Xu W, Wu Z, Brigatti MF (2010) The interlayer structure of trioctahedral lithian micas: An AXANES spectroscopy study at the potassium *K*-edge. Am Mineral 95:1084-1094

Coker VS, Pearce CI, Pattrick RAD, van der Laan G, Telling ND, Charnock JM, Arenholz E, Lloyd JR (2008) Probing the site occupancies of Co-, Ni-, and Mn-substituted biogenic magnetite using XAS and XMCD. Am Mineral 93:1119-1132

Cook NJ, Ciobanu CL, Brugger J, Etschmann B, Howard DL, de Jonge MD, Ryan C, and Paterson D (2012) Determination of the oxidation state of Cu in substituted Cu-In-Fe-bearing sphalerite via μXANES spectroscopy. Am Mineral 97:476-479

Cormier L, Neuville DR (2004) Ca and Na environments in Na_2O–CaO–Al_2O_3–SiO_2 glasses: influence of cation mixing and cation-network interactions. Chem Geol 213:103-113

Cormier L, Dargaud O, Menguy N, Henderson GS, Guignard M, Trcera N, Watts B (2011) Investigation of the Role of Nucleating Agents in MgO-SiO_2-Al_2O_3-SiO)-TiO_2 Glasses and Glass-Ceramics:A XANES Study at the Ti *K*- and $L_{2,3}$-Edges. Cryst Growth Des 11:311-319

Cottrell E, Kelley KA, Lanzirotti A, Fischer RA (2009) High-precision determination of iron oxidation state in silicate glasses using XANES. Chem Geol 268:167-179

Cressey G, Henderson C, van der Laan G (1993) Use of *L*-edge x-ray-absorption spectroscopy to characterize multiple valence states of 3*d* transition-metals - a new probe for mineralogical and geochemical research. Phys Chem Miner 20:111-119

Crocombette JP, Jollet F (1994) Ti 2*p* X-ray absorption in titanium dioxides. J Phys Condens Matter 6:10811-10821

Curti E, Dähn R, Farges F, Vespa M (2009) Na, Mg, Ni and Cs distribution and speciation after long-term alteration of a simulated nuclear waste glass: A micro-XAS/XRF/XRD and wet chemical study. Geochim Cosmochim Acta 73:2283-2298

EBSCOhost - printed on 2/13/2023 5:26 AM via . All use subject to https://www.ebsco.com/terms-of-use

Davoli I, Paris E, Stizza S, Benfatto M, Fanfoni M, Gargano A, Bianconi A, Seifert F (1992) Structure of densified vitreous silica – silicon and oxygen XANES spectra and multiple-scattering calculations. Phys Chem Miner 19:171-175

de Groot FMF (1993) X-ray-absorption of transition metal oxides – An overview of the theoretical approaches. J Electron Spectrosc Relat Phenom 62:111-130

de Groot FMF (1994) X-ray absorption and dichroism of transition metals their compounds. J Electron Spectrosc Relat Phenom 67:529-622

de Groot FMF (2001) High-resolution X-ray emission and X-ray absorption spectroscopy. Chem Rev 101:1779-1808

de Groot FMF (2005) Multiplet effects in X-ray spectroscopy. Coord Chem Rev 249:31-63

de Groot FMF (2008) Ligand and metal X-ray absorption in transition metal complexes. Inorg Chim Acta 361:850-856

de Groot FMF (2009) XANES spectra of transition metal compounds. *In*: 14th International Conference on X-Ray Absorption Fine Structure, 190. DiCicco A, Filipponi A (eds) Iop Publishing Ltd, Bristol, #012004

de Groot FMF (2012) Dips and peaks in fluorescence yield X-ray absorption are due to state-dependent decay. Nature Chem 4:766-767

de Groot FMF, Kotani A (2008) Core Level Spectroscopy of Solids. Taylor and Francis CRC press.

de Groot FMF, Grioni M, Fuggle JC, Ghijsen J, Sawatzky GA, Petersen H (1989) Oxygen 1*s* X-ray-absorption edges of transition metal oxides. Phys Rev B 40:5715-5723

de Groot FMF, Figueiredo MO, Basto MJ, Abbate M, Petersen H, Fuggle JC (1992) 2*p* X-ray absorption of titanium in minerals. Phys Chem Miner 19:140-147

de Groot FMF, Abbate M, Vanelp J, Sawatzky GA, Ma YJ, Chen CT, Sette F (1993) Oxygen-1*s* and cobalt-2*p* X-ray absorption of cobalt oxides. J Phys Cond Matt 5:2277-2288

de Groot FMF, Hu ZW, Lopez MF, Kaindl G, Guillot F, Tronc M (1994) Differences between L3 and L2 x-ray absorption spectra of transition metal compounds. J Chem Phys 101:6570-6576

de Ligny D, Neuville DR, Cormier L, Roux J, Henderson GS, Panczer G, Shoval S, Flank AM, Lagarde P (2009) Silica polymorphs, glass and melt: An *in situ* high temperature XAS study at the Si *K*-edge. J Non-Cryst Solids 355:1099-1102

de Smit E, Swart I, Creemer JF, Hoveling GH, Gilles MK, Tyliszczak T, Kooyman PJ, Zandbergen HW, Morin C, Weckhuysen BM, de Groot FMF (2008) Nanoscale chemical imaging of a working catalyst by scanning transmission X-ray microscopy. Nature 456:222-226

De Wispelaere S, Cabaret D, Levelut C, Rossano S, Flank AM, Parent P, Farges F (2004) Na-, Al- and Si *K*-edge XANES study of sodium silicate and sodium aluminosilicate glasses:influence of the glass surface. Chem Geol 213:63-70

DeBeer-George S, Brant P, Solomon EI (2005) Metal and ligand *K*-Edge XAS of organotitanium complexes: Metal 4*p* and 3*d* contributions to pre-edge intensity and their contributions to bonding. J Am Chem Soc 127:667-674

DeBeer-George S, Petrenko T, Neese F (2008) Prediction of iron *K*-edge absorption spectra using time-dependent density functional theory. J Phys Chem A 112:12936-12943

Dingwell DB, Paris E, Seifert F, Mottana A, Romano C (1994) X-ray-absorption study of Ti-bearing silicate-glasses. Phys Chem Miner 21:501-509

Doskocil EJ, Bordawekar SV, Davis RJ (1997) Alkali-support interactions on rubidium base catalysts determined by XANES, EXAFS, CO_2 adsorption, and IR spectroscopy. J Catal 169:327-337

Dyar MD, Breves EA, Emerson E, Bell SW, Nelms M, Ozanne MV, Peel SE, Carmosino ML, Tucker JM, Gunter ME, Delaney JS, Lanzirotti A, Woodland AB (2012) Accurate determination of ferric iron in garnets by bulk Mossbauer spectroscopy and synchrotron micro-XANES. Am Mineral 97:1726-1740

England KER, Charnock JM, Pattrick RAD, Vaughan DJ (1999) Surface oxidation studies of chalcopyrite and pyrite by glancing-angle X-ray absorption spectroscopy (REFLEXAFS). Mineral Mag 63:559-566

Espinosa A, Serrano A, Llavona A, Jimenez de la Morena J, Abuin M, Figuerola A, Pellegrino T, Fernández JF, Garcia-Hernandez M, Castro GR, Garcia MA (2012) On the discrimination between magnetite and maghemite by XANES measurements in fluorescence mode. Meas Sci Technol 23:015602

Essilfie-Dughan J, Hendry MJ, Warner J, Kotzer T (2012) Microscale mineralogical characterization of As, Fe, and Ni in uranium mine tailings. Geochim Cosmochim Acta 96:336-352

Evans KA, Mavrogenes J, Newville M (2007) The effect of CO_2 on the speciation of bromine in low-temperature geological solutions: an XANES study. J Synchrotron Radiat 14:219-26

Fandeur D, Juillot F, Morin G, Olivi L, Cognigni A, Webb SM, Ambrosi JP, Fritsch E, Guyot F, Brown Jr GE (2009) XANES evidence for oxidation of Cr(III)) to Cr(VI) by Mn-oxides in a lateritic regolith developed on serpentinized ultramafic rocks of New Caledonia. Environ Sci Technol 43:7384-7390

Farges F (2001) Crystal chemistry of iron in natural grandidierites: an X-ray absorption fine-structure spectroscopy study. Phys Chem Miner 28: 619-629

Farges F (2005) Ab initio and experimental pre-edge investigations of the Mn *K*-edge XANES in oxide-type materials. Phys Rev B 71:155109

EBSCOhost - printed on 2/13/2023 5:26 AM via . All use subject to https://www.ebsco.com/terms-of-use

Farges F (2009) Chromium speciation in oxide-type compounds: application to minerals, gems, aqueous solutions and silicate glasses. Phys Chem Miner 36:463-481
Farges F, Brown GE Jr, Calas G, Galoisy L, Waychunas GA (1994) Structral transformation in Ni-bearing $Na_2Si_2O_5$ glass and melt. Geophys Res Lett 21:1931-1934
Farges F, Brown GE Jr, Rehr JJ (1996a) Coordination chemistry of Ti (IV) in silicate glasses and melts: I. XAFS study of titanium coordination in oxide model compounds. Geochim Cosmochim Acta 60:3013-3038
Farges F, Brown GE Jr, Navrotsky A, Gan H, Rehr JJ (1996b) Coordination chemistry of Ti(IV) in silicate glasses and melts: II. Glasses at ambient temperature and pressure. Geochim Cosmochim Acta 60:3039-3053
Farges F, Brown GE Jr, Rehr JJ (1997) Ti *K*-edge XANES studies of Ti coordination and disorder in oxide compounds:Comparison between theory and experiment. Phys Rev B 56:1809-1819
Farges F, Brown GE Jr, Petit PE, Munoz M (2001a) Transition elements in water-bearing silicate glasses/melts. Part I. A high-resolution and anharmonic analysis of Ni coordination environments in crystals, glasses, and melts. Geochim Cosmochim Acta 65:1665-1678
Farges F, Munoz M, Siewert R, Malavergne V, Brown GE, Behrens H, Nowak M, Petit ME (2001b) Transition elements in water-bearing silicate glasses/melts. Part II. Ni in water-bearing glasses. Geochim Cosmochim Acta 65:1679-1693
Farges F, Lefrère Y, Rossano S, Berthereau A, Calas G, Brown GE Jr (2004) The effect of redox state on the local structural environment of iron in silicate glasses: a combined XAFS spectroscopy, molecular dynamics, and bond valence study. J. Non-Cryst Solids 344: 176-188
Farquhar ML, Charnock JM, Livens FR, Vaughan DJ (2002) Mechanisms of arsenic uptake from aqueous solution by interaction with goethite, lepidocrocite, mackinawite, and pyrite: An X-ray absorption spectroscopy study. Environ Sci Technol 36:1757-1762
Farrell SP, Fleet ME (2001) Sulfur *K*-edge XANES study of loal electronic structure in ternary monosulfide solid solution [$(Fe, Co, Ni)_{0.923}S$]. Phys Chem Miner 28:17-27
Farrell SP, Fleet ME, Stekhin I, Kravtsova AN, Soldatov AV, Liu X (2002) Evolution of local electronic structure in alabandite and niningerite solid solutions Am Mineral 87:1321-1332
Feiters MC, Kupper FC, Meyer-Klaucke W (2005) X-ray absorption spectroscopic studies on model compounds for biological iodine and bromine. J Synchrotron Radiat 12:85-93
Finch AA, Allison N (2007) Coordination of Sr and Mg in calcite and aragonite. Mineral Mag 71:539-552
Finch AA, Allison N, Steaggles H, Wood CV, Mosselmans JFW (2010) Ba XAFS in Ba-rich standard minerals and the potential for determining Ba structural state in calcium carbonate. Chem Geol 270:179-185
Fister TT, Seidler GT, Rehr JJ, Kas JJ, Elam WT, Cross JO, Nagle KP (2007) Deconvolving instrumental and intrinsic broadening in core-shell X-ray spectroscopies. Phy Rev B 75: 174106
Fleet ME (2005) XANES spectroscopy of sulfur in Earth materials. Can Mineral 43:1811-1838
Fleet ME, Liu X (2001) Boron *K*-edge XANES of boron oxides: Tetrahedral B-O distances and near-surface alteration. Phys Chem Miner 28:421-427
Fleet ME, Muthupari S (1999) Coordination of Boron in alkail borosilicate glasses using XANES. J Non-Cryst Solids 255:233-241
Fleet ME, Muthupari S (2000) Boron *K*-edge XANES of borate and borosilicate minerals. Am Mineral 85:1009-1021
Fleet ME, Muthupari S, Kasrai M, Prabakar S (1997) Sixfold coordinated Si in alkali and alkali-CaO silicophosphate glasses by Si *K*-edge XANES spectroscopy. J Non-Cryst Solids 220:85-92
Fleet ME, Liu X, Harmer SL, King PL (2005) Sulfur *K*-edge XANES spectroscopy: Chemical state and content of sulfur in silicate glasses. Can Mineral 43:1603-1618
Fröba M, Wong J, Behrens P, Sieger P, Rowen M, Tanaka T, Rek Z, Felsche J (1995) Correlation of multiple-scattering features in XANES spectra of Al and Si *K*-edges to the Al-O-Si bond-angle in aluminosilicate sodalites – An emperical-study. Physica B 208:65-67
Frommer J, Nachtegaal M, Czekaj I, Weng TC, Kretzschmar R (2009) X-ray absorption and emission spectroscopy of Cr-III hydroxides: analysis of the *K*-pre-edge region. J Phys Chem A 113:12171-12178
Frommer J, Nachtegaal M, Czekaj I, Kretzschmar R (2010) The Cr X-ray absorption *K*-edge structure of poorly crystalline Fe(III)-Cr(III)-oxyhydroxides. Am Mineral 95:1202-1213
Fujikawa T, Okazawa T, Yamasaki K, Tang JC, Murata T, Matsukawa T, Naoe SI (1989) Full multiple-scattering approach to Na *K*-edge XANES of NaCl-KCl mixed crystal. J Phys Soc Japan 58:2952-2961
Fussa-Rydel O, Dye JL, Teo BK (1988) Rubidium X-ray-absorption (EXAFS and XANES) studies of Rb- and complexed Rb^+ in alkalides and electrides. J Am Chem Soc 110:2445-2451
Galoisy L, Calas G (1993) Structural environment of nickel in silicate glass melts systems. 1. Sepctroscopic determination of coordination states. Geochim Cosmochim Acta 57:3613-3626
Galoisy L, Calas G, Arrio MA (2001) High-resolution XANES spectra of iron in minerals and glasses:Structural information from the pre-edge region. Chem Geol 174:307-319

EBSCOhost - printed on 2/13/2023 5:26 AM via . All use subject to https://www.ebsco.com/terms-of-use

Gao SP (2010) Ab initio calculation of ELNES/XANES of BeO polymorphs. Phys Status Solidi B 247:2190-2194
Garvie LAJ, Buseck PR (1996) Parallel electron energy-loss spectroscopy of boron in minerals. Rev Mineral 33:821-843
Garvie LAJ, Buseck PR (1999) Bonding in silicates: Investigations of the Si $L_{2,3}$ edge by parallel electron energy-loss spectroscopy. Am Mineral 84:946-964
Garvie LAJ, Craven AJ, Brydson R (1994) Use of electron-energy-loss near-edge fine-structure in the study of minerals. Am Mineral 79:411-425
Garvie LAJ, Craven AJ, Brydson R (1995) Parallel elecrton energy-loss spectroscopy (PEELS) study of B in minerals: The electron energy-loss near-edge structure (ELNES) of the B *K*-edge. Am Mineral 80:1132-1144
Garvie LAJ, Rez P, Alvarez JR, Buseck PR, Craven AJ, Brydson R (2000) Bonding in alpha-quartz (SiO_2): A view of the unoccupied states. Am Mineral 85:732-738
Gaudry E, Cabaret D, Brouder C, Letard I, Rogalev A, Wilhlem F, Jaouen N, Sainctavit P (2007) Relaxations around the substitutional chromium site in emerald: X-ray absorption experiments and density functional calculations. Phys Rev B 76:094110
Gilbert B, Frazer BH, Naab F, Fournelle J, Valley JW, De Stasio G (2003) X-ray absorption spectroscopy of silicates for in situ, sub-micrometer mineral identification. Am Mineral 88:763-769
Giuli G, Paris E, Wu ZY, Berrettoni M, Della Ventura G, Mottana A (2000) Nickel site distribution and clustering in synthetic double-chain silicates by experimental and theoretical XANES spectroscopy. Phys Rev B 62:5473-5477
Giuli G, Paris E, Mungall J, Romano C, Dingwell D (2004) V oxidation state and coordination number in silicate glasses by XAS. Am Mineral 89:1640-1646
Glatzel P, Bergmann U (2005) High resolution 1s core hole X-ray spectroscopy in 3*d* transition metal complexes. Coord Chem Rev 249:65-95
Glatzel P, Mirone A, Eeckhout SG, Sikora M, Giuli G (2008) Orbital hybridization and spin polarization in the resonant 1s photoexcitations of Fe_2O_3. Phys Rev B 77:115133
Gonzalez-Jimenez ID, Cats K, Davidian T, Ruitenbeek M, Meirer F, Liu Y, Nelson J, Andrews JC, Pianetta P, de Groot FMF, Weckhuysen BM (2012) Hard X-ray nanotomography of catalytic solids at work. Angew Chem 51:11986-11990
Greegor RB, Lytle FW, Sandstrom DR, Wong J, Schultz P (1983) Investigation of TiO_2-SiO_2 glasses by X-ray absorption-spectroscopy. J Non-Cryst Solids 55:27-43
Greegor RB, Pingitore NE, Lytle FW (1997) Strontianite in coral skeletal aragonite. Science 275:1452-1454
Grunes LA (1983) Study of the *K*-edges of 3*d* Transition-metals in pure and oxide form by X-ray-absorption spectroscopy. Phys Rev B 27:2111-2131
Hallmeier KH, Szargan R, Meisel A, Hartmann E, Gluskin ES (1981) Investigation of core-excited quantum yield spectra of highly symmetric boron compounds. Spectrochim Acta A 37:1049-1053
Hamalainen K, Siddons DP, Hastings JB, Berman LE (1991) Elimination of the inner-shell lifetime broadening in X-ray absorption spectroscopy. Phys Rev Lett 67:2850-2853
Handa K, Kojima K, Taniguchi K, Ozutsumi K, Ikeda S (2005) Studies on the Extremely Soft X-ray absorption spectrometry at BL2. Memoires of the SR Center Ritsumeikan University 7:3-6
Handa K, Ide J, Nishiyama Y, Ozutsumi K, Dalba G, Ohtori N, Umesaki N (2006) XAS study of barium borate glasses and crystals. Phys Chem Glasses-B 47:445-447
Hansen PL, Brydson R, McComb DW, Richardson I (1994) EELS fingerprint of Al-coordination in silicates. Microsc Microanal Microstruct 5:173-182
Harp GR, Han ZL, Tonner BP (1990) X-ray-absorption near-edge structures in intermediate oxidation-states of silicon in silicon-oxides during thermal-desorption. J Vac Sci Technol A 8:2566-2569
Hawthorne FC (ed) (1988) Spectroscopic Methods in Mineralogy and Geochemistry. Volume 18. Reviews in Mineralogy. Mineralogical Society of America, Washington
Hawthorne FC, Waychunas GA (1988) Spectrum fitting methods. Rev Mineral 18:63-98
Hawthorne FC, Burns PC, Grice JD (1996) The crystal chemistry of boron. Rev Mineral 33:41-115
Hedman B, Hodgson KO, Solomon EI (1990) X-ray absorption edge spectroscopy of ligands bound to open-shell metal ions. J Am Chem Soc 112:1643-1645
Henderson CMB, Foland KA (1996) Ba- and Ti-rich primary biotite from the Brome alkaline igneous complex, Monteregion Hills, Quebec: mechansims of substitution. Can Mineral 34: 1241-1252.
Henderson GS (1995) A Si *K*-edge EXAFS/XANES study of sodium-silicate glasses. J Non-Cryst Solids 183:43-50
Henderson GS (2007) The germanate anomaly:What do we know? J Non-Cryst Solids 353:1695-1704
Henderson GS, Fleet ME (1997) The structure of titanium silicate glasses investigated by Si *K*-edge X-ray absorption spectroscopy. J Non-Cryst Solids 211:214-221
Henderson GS, St-Amour JC (2004) A Si *K*-edge XANES study of Ti containing alkali/alkaline-earth silicate glasses. Chem Geol 213:31-40

EBSCOhost - printed on 2/13/2023 5:26 AM via . All use subject to https://www.ebsco.com/terms-of-use

Henderson GS, Liu X, Fleet ME (2003) Titanium coordination in silicate glasses investigated using O *K*-edge X-ray absorption spectroscopy. Mineral Mag 67:597-607

Henderson GS, Neuville DR, Cormier L (2007) An O K-edge study of calcium aluminates. Can J Chem 85:801-805

Henderson GS, Neuville DR, Cormier L (2009) An O *K*-edge XANES study of glasses and crystals in the CaO-Al_2O_3-SiO_2 (CAS) system. Chem Geol 259:54-62

Hitchcock AP, Newbury DC, Ishii I, Stohr J, Horsley JA, Redwing RD, Johnson AL, Sette F (1986) Carbon *K*-shell excitation of gaseous and condensed cyclic hydrocarbons - C_3H_6, C_4H_8, C_5H_8, C_5H_{10}, C_6H_10, C_6H_{12}, AND C_8H_8. J Chem Phys 85:4849-4862

Höche T, Mäder M, Bhattacharya S, Henderson GS, Gemming T, Wuth R, Rüssel C, Avramov I (2011) $ZrTiO_4$ crystallization in nanosized liquid-liquid phase-seperation droplets in glass-a quantitative XANES study. CrystEngComm 13:2550-2556.

Höche T, Ikeno H, Mäder M, Henderson GS, Blyth RIR, Sales BC, Tanaka I (2013) Vanadium $L_{2,3}$ XANES experiments and first-principles multielectron calculations: Impact of second-nearest neighboring cations on vanadium-bearing fresnoites. Am Mineral 98:663-670

Hu YF, Xu RK, Dynes JJ, Blyth RIR, Yu G, Kozak LM, Huang PM (2008) Coordination nature of aluminum (oxy)hydroxides formed under the influence of tannic acid studied by X-ray absorption spectroscopy. Geochim Cosmochim Acta 72:1959-1969

Hudson E, Moler E, Zheng Y, Kellar S, Heimann P, Hussain Z, Shirley D (1994) Near-edge sodium and fluorine *K*-shell photoabsorption of alkali halides. Phys Rev B 49:3701-3708

Ildefonse P, Kirkpatrick RJ, Montez B, Calas G, Flank AM, Lagarde P (1994) Al^{27} MAS NMR and aluminum X-ray-absorption near-edge structure study of imogolite and allophanes. Clay Clay Miner 42:276-287

Ildefonse P, Calas G, Flank AM, Lagarde P (1995) Low Z-elements (Mg, Al, and Si) *K*-edge X-ray-absorption spectroscopy in minerals and disordered-systems. Nucl Instrum Methods Physics B 97:172-175

Ildefonse P, Cabaret D, Sainctavit P, Calas G, Flank AM, Lagarde P (1998) Aluminium X-ray absorption near edge structure in model compounds and Earth's surface minerals. Phys Chem Miner 25:112-121

Ingall ED, Brandes JA, Diaz JM, de Jonge MD, Paterson D, McNulty I, Elliott WC, Northrup P (2011) Phosphorus *K*-edge XANES spectroscopy of mineral standards. J Synchrotron Radiat 18:189-197

Ishiguro E, Iwata S, Suzuki Y, Mikuni A, Sasaki T (1982) Boron *K* photoabsorption spectra of BF_3, BCl_3, and BBr_3. J Phys B 15:1841-1854

Iwamoto S, Iwamoto S, Inoue M, Yoshida H, Tanaka T, Kagawa K (2005) XANES and XPS study of silica-modified titanias prepared by the glycothermal method. Chem Mater 17:650-655

Jahn S, Kowalski PM (2014) Theoretical approaches to structure and spectroscopy of earth materials. Rev Mineral Geochem 78:691-743

Jiang N (2002) on detection of non-bridging oxygen in glasses by electron-energy-loss spectroscopy. Solid State Commun 122:7-10

Jiang N (2006) Structure and composition dependence of oxygen K edge in $CaAl_2O_4$. J Appl Phys 100:013703

Jiang N, Spence J (2004) Core-hole effects on electron energy-loss spectroscopy of Li_2O. Phys Rev B 69:115112

Jiang N, Spence JCH (2006) Interpretation of oxygen K pre-edge peak in complex oxides. Ultramicroscopy 106:215-219

Jiang N, Su D, Spence J (2007) Determination of Ti coordination from pre-edge peaks in Ti *K*-edge XANES. Phys Rev B 76:214117

Jokic A, Cutler JN, Ponomarenko E, van der Kamp G, Anderson DW (2003) Organic carbon and sulfur compounds in wetland soils:Insights on structure and transformation processes using *K*-edge XANES and NMR spectroscopy. Geochim Cosmochim Acta 67:2585-2597

Jugo PJ, Wilke M, Botcharnikov RE (2010) Sulfur *K*-edge XANES analysis of natural and synthetic basaltic glasses:Implications for S speciation and S content as function of oxygen fugacity. Geochim Cosmochim Acta 74:5926-5938

Juhin A, Calas G, Cabaret D, Galoisy L, Hazemann JL (2008) Structural relaxation around substitutional Cr^{3+} in pyrope garnet. Am Mineral 93:800-805

Kar G, Hundal LS, Schoenau JJ, Peak D (2011) Direct chemical speciation of P in sequential chemical extraction residues using P *K*-Edge X-Ray absorption near-edge structure spectroscopy. Soil Science 176:589-595

Kasrai M, Fleet ME, Sham TK, Bancroft GM, Tan KH, Brown JR (1988) A XANES study of the S *L*-edge in sulfide minerals:Application to interatomic distance determination. Solid State Commun 68:507-511

Kasrai M, Fleet M, Bancroft G, Tan K, Chen J (1991) X-ray-absorption near-edge structure of alkali halides:The interatomic-distance correlation. Phys Rev B 43:1763-1772

Kasrai M, Yin Z, Bancroft GM, Tan KH (1993) X-ray fluorescence measurements of X-ray absorption near edge structure at the Si, P, and S *L* edges. J Vac Sci Technol A 11:2694-2699

EBSCOhost - printed on 2/13/2023 5:26 AM via . All use subject to https://www.ebsco.com/terms-of-use

Kasrai M, Brown JR, Bancroft GM, Yin Z, Tan KH (1996a) Sulfur characterization in coal from X-ray absorption near edge spectroscopy. Int J Coal Geol 32:107-135

Kasrai M, Lennard WN, Brunner RW, Bancroft GM, Bardwell JA, Tan KH (1996b) Sampling depth of total electron and fluorescence measurments in Si *L*- and *K*-edge absorption spectroscopy. Appl Surf Sci 99:303-312

Kasrai, M, Fleet ME, Muthupari S, Li D, Bancroft GM (1998) Surface modification study of borate materials from B K-edge X-ray absorption spectroscopy. Phys Chem Miner 25:268-272

Kasrai M, Vasiga M, Fuller MS, Bancroft GM, Fyfe K (1999) Study of the effects of Ca sulfonate on antiwear film formation by X-ray absorption spectroscopy using synchrotron radiation. J Synchrotron Radiat 6:719-721

Kasrai M, Suominen Fuller M, Bancroft GM (2003) X-ray absorption study of the effect of calcium sulfonate on antiwear film formation generated from neutral and basic ZDDPS: Part 1-Phosphorous species. Tribology Trans 46:534-542

Kaznacheyev K, Osanna A, Jacobsen C, Plashkevych O, Vahtras O, Agren H, Carravetta V, Hitchcock AP (2002) Innershell absorption Spectroscopy of amino acids. J Phys Chem A 106:3153-3168

Khare N, Hesterberg D, Martin JD (2005) XANES investigation of phosphate sorption in single and binary systems of iron and aluminum oxide minerals. Environ Sci Technol 39:2152-2160

Kikas A, Nommiste E, Ruus R, Saar A, Martinson I (2001) Core excitons in Na *K* photoabsorption of NaF: Resonant Auger spectroscopy. Phys Rev B 64:235120

King PL, Sham TK, Gordon RA, Dyar MD (2013) Microbeam X-ray analysis of Ce^{3+}/Ce^{4+} in Ti-rich minerals: A case study with titanite (sphene) with implications for multivalent trace element substitution in minerals. Am Mineral 98:110-119

Klimm K, Kohn SC, O'Dell LA, Botcharnikov RE, Smith ME (2012) The dissolution mechanism of sulfur in hydrous silicate melts. I: Assessment of analytical techniques in determining the sulfur speciation in iron-free to iron-poor glasses. Chem Geol 322-323:237-249

Kobayashi H, Emura S, Arachi Y, Tatsumi K (2007) Investigation of inorganic compounds on the surface of cathode materials using Li and O *K*-edge XANES. J Power Sources 174:774-778

Kohn SC, Charnock JM, Henderson CMB, Greaves GN (1990) The structural environments of trace elements in dry and hydrous silicate glasses: a manganese and strontium K-edge X-ray absorption spectroscopy study. Contrib Mineral Petrol 105:359-368

Krause MO, Oliver JH (1979) Natural widths of atomic *K* and *L* levels, *K*-alpha X-ray lines and several KLL Auger lines. J Phys Chem Ref Data 8:329-338

Kruse J, Leinweber P, Eckhardt KU, Godlinski F, Hu Y, Zuin L (2009) Phosphorus $L_{2,3}$-edge XANES: Overview of reference compounds. J Synchrotron Radiat 16:247-259

Lavrentyev AA, Gabrelian BV, Nikiforov IY, Rehr JJ (1999) Ab initio XANES calculations for KCl and PbS. J Phys Chem Solids 60:787-790

Lawrence JR, Dynes JJ, Korber DR, Swerhone GDW, Leppard GG, Hitchcock AP (2012) Monitoring the fate of copper nanoparticles in river biofilms using scanning transmission X-ray microscopy (STXM). Chem Geol 329:18-25

Lee DK, Eng PJ, Mao H-K (2014) Probing of pressure-induced bonding transitions in crystalline and amorphous earth materials: insights from X-ray Raman scattering at high pressure. Rev Mineral Geochem 78:139-174

Levelut C, Cabaret D, Benoit M, Jund P, Flank AM (2001) Multiple scattering calculations of the XANES Si *K*-edge in amorphous silica. J Non-Cryst Solids 293:100-104

Li D, Bancroft GM, Kasrai M, Fleet ME, Feng XH, Tan KH, Yang BX (1993) High-resolution Si *K*-edge and $L_{2,3}$-edge XANES of alpha quartz and stishovite. Solid State Commun 87:613-617

Li D, Bancroft GM, Kasrai M, Fleet ME, Secco RA, Feng XH, Tan KH, Yang BX (1994) X-ray-absorption spectroscopy of silicon dioxide (SiO_2) polymorphs – The structural characterization of opal. Am Mineral 79:622-632

Li D, Bancroft GM, Fleet ME, Feng XH (1995a) Silicon *K*-edge XANES spectra of silicate minerals. Phys Chem Minerals 22:115-122

Li D, Secco RA, Bancroft GM, Fleet ME (1995b) Pressure-induced coordination change of Al in silicate melts from the Al *K*-edge XANES of high-pressure $NaAlSi_2O_6$, $NaAlSi_3O_8$ glasses. Geophys Res Lett 22:3111-3114

Li D, Bancroft GM, Fleet ME, Hess PC, Yin ZF (1995c) Coordination of B in K_2O-SiO_2-B_2O_3-P_2O_5 glasses using B *K*-edge XANES. Am Mineral 80:873-877

Li D, Bancroft GM, Kasrai M (1995d) S *K*- and *L*-edge X-ray absorption spectroscopy of sulfides and sulfates: Applications in mineralogy and geochemistry. Can Mineral 33:949-960

Li D, Bancroft GM, Fleet ME (1996) B *K*-edge XANES of crystalline and amorphous inorganic materials. J Electron Spectrosc Relat Phenom79:71-73

EBSCOhost - printed on 2/13/2023 5:26 AM via . All use subject to https://www.ebsco.com/terms-of-use

Li D, Peng MS, Murata T (1999) Coordination and local structure of magnesium in silicate minerals and glasses: Mg *K*-edge XANES study. Can Mineral 37:199-206

Lu Y-C, Kwabi DG, Yao KPC, Harding JR, Zhou J, Zuin L, Shao-Horn Y (2011) The discharge rate capability of rechargeable Li–O_2 batteries. Energy Environ Sci 4:2999-3007

Luca V, Djajanti S, Howe RF (1998) Structural and electronic properties of sol-gel titanium oxides studied by X-ray absorption spectroscopy. J Phys Chem B 102:10650-10657

Ma Y, Wassdahl N, Skytt P, Guo J, Nordgren J, Johnson P, Rubensson JE, Boske T, Eberhardt W, Kevan S (1992) Soft-X-ray resonant inelastic scattering at the C *K*-edge of diamond. Phys Rev Lett 69:2598-2601

Ma Y, Skytt P, Wassdahl N, Glans P, Guo J, Nordgren J (1993) Core excitons and vibronic coupling in diamond and graphite. Phys Rev Lett 71:3725-3728

Magnien V, Neuville DR, Cormier L, Roux J, Hazemann JL, de Ligny D, Pascarelli S, Vickridge I, Pinet O, Richet P (2008) Kinetics and mechanisms of iron redox reactions in silicate melts:The effects of temperature and alkali cations. Geochim Cosmochim Acta 72:2157-2168

Manceau A, Gorshkov AI, Drits VA (1992) Structural chemistry of Mn, Fe, Co and Ni in manganese hydrous oxides. 1. Information from XANES spectroscopy. Am Mineral 77:1133-1143

Manceau A, Marcu MA, Tamura N (2002) Qunatitative speciation of heavy metals in soils and sediments by synchrotron X-ray techniques. Rev Mineral Geochem 49: 341-428

Manceau A, Marcus MA, Grangeon S (2012) Determination of Mn valence states in mixed-valent manganates by XANES spectroscopy. Am Mineral 97:816-827

Manuel D, Cabaret D, Brouder C, Sainctavit P, Bordage A, Trcera N (2012) Experimental evidence of thermal fluctuations on the X-ray absorption near-edge structure at the aluminum K edge. Phys Rev B 85:224108

Marcelli A, Cibin G, Cinque G, Mottana A, Brigatti MF (2006) Polarized XANES spectroscopy:The *K* edge of layered K-rich silicates. Radiat Phys Chem 75:1596-1607

Mauchamp V, Boucher F, Ouvrard G, Moreau P (2006) Ab initio simulation of the electron energy-loss near-edge structures at the Li K edge in Li, Li_2O, and $LiMn_2O_4$. Phys Rev B 74:115106

Mauchamp V, Moreau P, Ouvrard G, Boucher F (2008) Local field effects at Li *K*-edges in electron energy-loss spectra of Li, Li_2O and LiF. Phys Rev B 77:045117

Mavrogenes JA, Berry AJ, Newville M, Sutton SR (2002) Copper speciation in vapor-phase fluid inclusions from the Mole Granite, Australia. Am Mineral 87:1360-1364

McComb DW, Hansen PL, Brydson R (1991) A study of silicon ELNES in nesosilicates. Microscopy Microanalysis Microstructures 2:561-568

McKeown DA (1989) Aluminum X-ray-absorption near-edge spectra of oxide minerals – Calculation versus experimental-data. Phys Chem Miner 16:678-683

McKeown DA, Waychunas GA, Brown GE Jr (1985) EXAFS and XANES study of the local coordination environment of sodium in a series of silica-rich glasses and selected minerals within the Na_2O-Al_2O_3-SiO_2 system. J Non-Cryst Solids 74:323-348

Mele EJ, Ritsko JJ (1979) Fermi-level lowering and the core exciton spectrum of intercalated graphite. Phys Rev Lett 43:68-71

Miedema PS, Ngene P, van der Eerden AMJ, Weng TC, Nordlund D, Sokaras D, Alonso-Mori R, Juhin A, de Jongh PE, de Groot FMF (2012) In situ X-ray Raman spectroscopy of $LiBH_4$. Phys Chem Chem Phys 14:5581-5587

Miedema PS, de Groot FMF (2013) The iron *L* edges: Fe 2*p* X-ray absorption and electron energy loss spectroscopy, J Electron Spectrosc Relat Phenom 187:32-48

Miehé-Brendlé J, Tuilier MH, Marichal C, Gallego JC, Reinholdt M (2010) Mg environments in the octahedral sheet of 2:1 talc-like hybrid phyllosilicates: A comparative XAFS study. Euro J Inorg Chem 35:5587-5591

Mizoguchi T, Tatsumi K, Tanaka I (2006) Peak assignments of ELNES and XANES using overlap population diagrams. Ultramicroscopy 106:1120-1128

Mizokawa T, Tjeng L, Lin H, Chen C, Kitawak, R, Terasaki I, Lambert S, Michel C (2005) X-ray absorption study of layered Co oxides with a Co-O triangular lattice. Phys Rev B 71:193107

Mo SD, Ching WY (2001) X-ray absorption near-edge structure in alpha-quartz and stishovite:Ab initio calculation with core-hole interaction. Appl Phys Lett 78:3809-3811

Morar JF, Himpsel FJ, Hollinger G, Hughes G, Jordan JL (1985) Observation of a C-1s core exciton in diamond. Phys Rev Lett 54:1960-1963

Mottana A (2004) X-ray absorption spectroscopy in mineralogy: Theory and experiment in the XANES region. EMU Notes Mineral 6:465-552

Mottana A, Murata T, Wu ZY, Marcelli A, Paris E (1997) The local structure of Ca-Na pyroxenes .1. XANES study at the Na *K*-edge. Phys Chem Miner 24:500-509

Mottana A, Murata T, Marcelli A, Wu ZY, Cibin G, Paris E, Giuli G (1999) The local structure of Ca-Na pyroxenes. II. XANES studies at the Mg and Al *K*-edges. Phys Chem Miner 27:20-33

EBSCOhost - printed on 2/13/2023 5:26 AM via . All use subject to https://www.ebsco.com/terms-of-use

Murata T, Matsukawa T, Naoe S (1988) XANES and EXAFS studies on *K*-shell absorption in $K_{1-x}Na_xCl$solid solutions. Solid State Commun 66:787-790

Nabavi M, Taulelle F, Sanchez C, Verdaguer M (1990) XANES V-51 NMR-study of vanadium oxygen compounds. J Phys Chem Solids 51:1375-1382

Nesbitt HW, Bancroft GM (2014) High resolution core- and valence-level XPS studies of the properties (structural, chemical and bonding) of silicate minerals and glasses. Rev Mineral Geochem 78:271-329

Neuville DR, Cormier L, Flank A-M, Briois V, Massiot D (2004a) Al speciation and Ca environment in calcium aluminosilicate glasses and crystals by Al and Ca *K*-edge X-ray absorption spectroscopy. Chem Geol 213:153-163

Neuville DR, Cormier L, Flank A-M, Prado RJ, Lagarde P (2004b) Na *K*-edge XANES spectra of minerals and glasses. Eur J Mineral 16:809-816

Neuville DR, de Ligny D, Cormier L, Henderson GS, Roux J, Flank A-M, Lagarde P (2009) The crystal and melt structure of spinel and alumina at high temperature: An in-situ XANES study at the Al and Mg *K*-edge. Geochim Cosmochim Acta 73:3410-3422

Neuville DR, Henderson GS, Cormier L, Massiot D (2010) The structure of crystals, glasses, and melts along the $CaO\text{-}Al_2O_3$ join: Results from Raman, Al *L*- and *K*-edge X-ray absorption, and ^{27}Al NMR spectroscopy. Am Mineral 95:1580-1589

Nicholls M, Najman MN, Zhang Z, Kasrai M, Norton PR, Gilbert P (2007) The contribution of XANES spectroscopy to tribology. Can J Chem 85:816-830

Nicholls MA, Norton PR, Bancroft GM, Kasrai M (2004) X-ray absorption spectroscopy of tribofilms produced from zinc dialkyl dithiophosphates on Al–Si alloys. Wear 257:311-328

Odake S, Fukura S, Arakawa M, Ohta A, Harte B, Kagi H (2008) Divalent chromium in ferropericlase inclusions in lower-mantle diamonds revealed by micro-XANES measurements. J Mineral Petrol Sci 103:350-353

Okada K, Uozumi T, Kotani A (1994) Split-off formation in the final state of photoemission of Ti compounds. J Phys Soc Japan 63:3176-3184

Okude N, Nagoshi M, Noro H, Baba Y, Yamamoto H, Sasaki TA (1999) P and S *K*-edge XANES of transition-metal phosphates and sulfates. J Electron Spectrosc Relat Phenom101:607-610

Ollier N, Lombard P, Farges F, Boizot B (2008) Titanium reduction processes in oxide glasses under electronic irradiation. J Non-Cryst Solids 354:480-485

Olovsson W, Tanaka I, Mizoguchi T, Puschnig P, Ambrosch-Draxl C (2009a) All-electron Bethe-Salpeter calculations for shallow-core X-ray absorption near-edge structures. Phys Rev B 79:041102(R)

Olovsson W, Tanaka I, Puschnig P, Ambrosch-Draxl C (2009b) Near-edge structures from first principles all-electron Bethe-Salpeter equation calculations. J Phys-Condens Mat 21:104205

Outka DA, Stöhr J (1988) Curve fitting analysis of near-edge core excitation spectra of free, adsorbed, and polymeric molecules. J Chem Phys 88:3539-3554

Paris E, Mottana A, Della Ventura G, Robert JL (1993) Titanium valence and coordination in synthetic richterite – Ti-richterite amphiboles – A synchrotron-radiation XAS study. Eur J Mineral 5:455-464

Paris E, Wu ZY, Mottana A, Marcelli A (1995) Calcium environment in omphacitic pyroxenes – XANES experimental-data versus one-electron multiple-scattering calculations. Eur J Mineral 7:1065-1070

Parkman RH, Charnock JM, Livens FR, Vaughan DJ (1998) A study of the interaction of strontium ions in aqueous solution with the surfaces of calcite and kaolinite. Geochim Cosmochim Acta 62:1481-1492

Pattrick RAD, Mosselmans JFW, Charnock JM (1998) An X-ray absorption study of doped sphalerites. Eur J Mineral 10:239-249

Pattrick RAD, van der Laan G, Henderson CMB (2002) Cation site occupancy in spinel ferrites studied by X-ray magnetic circular dichroism: developing a method for mineralogists. Eur J Miner 14:1095-1102

Pattrick RAD, Coker VS, Pearce CI, Telling ND, van der Laan G (2008) The oxidation state of copper and cobalt in carrolite, $CuCo_2S_4$. Can Mineral 46:1317-1322

Pearce CI, Henderson CMB, Pattrick RAD, van der Laan G, Vaughn DJ (2006) Direct determination of cation site occupancies in natural ferrite spinels by L_2, L_3 X-ray absorption spectroscopic and X-ray magnetic circular dichroism. Am Mineral 91:880-893.

Petit PE, Farges F, Wilke M, Sole VA (2001) Determination of the iron oxidation state in Earth materials using XANES pre-edge information. J Synchrotron Radiat 8:952-954

Peuget S, Broudic V, Jégou C, Frugier P, Roudil D, Deschanels X, Rabiller H, Noel PY (2007) Effect of alpha radiation on the leaching behaviour of nuclear glass. J Nucl Materials 362:474-479

Peuget S, Cachia JN, Jégou C, Deschanels X, Roudil D, Broudic V, Delaye JM, Bart JM (2006) Irradiation stability of R7T7-type borosilicate glass. J Nucl Materials 354:1-13

Pingitore NE, Lytle FW, Davies BM, Eastman MP, Eller PG, Larson EM (1992) Mode of incorporation of Sr^{2+} in calcite – Determination by X-ray-absorption-spectroscopy. Geochim Cosmochim Acta 56:1531-1538.

Poe B, Romano C, Henderson GS (2004) Raman and XANES spectroscopy of permanently densified vitreous silica. J Non-Cryst Solids 341: 162-169

EBSCOhost - printed on 2/13/2023 5:26 AM via . All use subject to https://www.ebsco.com/terms-of-use

Poe B, Seifert F, Sharp T, Wu Z (1997) ELNES spectroscopy of mixed Si coordination minerals. Phys Chem Miner 24:477-487

Poumellec B, Cortes R, Tourillon G, Berthon J (1991a) Angular-dependence of the Ti *K*-edge in rutile TiO_2. Phys Status Solidi B 164:319-326

Poumellec B, Durham PJ, Guo GY (1991b) Electronic-structure and X-ray-absorption-spectrum of rutile TiO_2. J Phys-Condens Mat 3:8195-8204

Povahzynaja NA, Shvejtzer IG, Soldatov AV (1995) Electronic structure of $SmFeO_3$ –X-ray absorption fine-structure analysis. J Phys-Condens Mat 7:4975-4981

Prado RJ, Flank AM (2005) Sodium K edge XANES calculation in 'NaCl' type structures. Phys Scripta T115:165-167

Prietzel J, Thieme J, Paterson D (2010) Phosphorus speciation of forest-soil organic surface layers using P *K*-edge XANES spectroscopy. J Plant Nutr Soil Sci 173:805-807

Quartieri S, Chaboy J, Merli M, Oberti R, Ungaretti L (1995) Local structural environment of calium in garnets – A combined structure-refinement and XANES investigation. Phys Chem Miner 22:159-169

Rehr JJ, Ankudinov A (2005) Progress in the theory and interpretation of XANES. Coord Chem Rev 249:131-140

Reinke P, Knop-Gericke A, Havecker M, Schedel-Niedrig T (2000) Interaction of diamond with water: An in situ XANES investigation. Surf Sci 447:229-236

Riedler M, de Castro ARB, Kolmakov A, Lofken JO, Nowak C, Soldatov AV, Wark A, Yalovega G, Moller T (2001a) Na 1s photoabsorption of free and deposited NaCl clusters: Development of bond length with cluster size. Phys Rev B 64:245419

Riedler M, de Castro ARB, Kolmakov A, Löfken JO, Nowak C, Soldatov AV, Wark A, Yalovega G, Möller T (2001b) Photoabsorption of NaCl clusters at the Na *K*-edge: Development of the bond length with the cluster size. J Chem Phys 115:1319-1323

Rivard C, Montarges-Pelletier E, Vantelon D, Pelletier M, Karunakaran C, Michot LJ, Villieras F, Michau N (2013) Combination of multi-scale and multi-edge X-ray spectroscopy for investigating the products obtained from the interaction between kaolinite and metallic iron in anoxic conditions at 90 °C. Phys Chem Miner 40:115-132

Romano C, Paris E, Poe BT, Giuli G, Dingwell DB, Mottana A (2000) Effect of aluminum on Ti-coordination in silicate glasses: A XANES study. Am Mineral 85:108-117

Rosenberg RA, Love PJ, Rehn V (1986) Polarization-dependent C(K) near-edge X-ray-absorption fine structure of graphite. Phys Rev B 33:4034-4037

Rossetti I, Sordelli L, Ghigna P, Pin S, Scavini M, Forni L (2011) EXAFS-XANES Evidence of in Situ Cesium Reduction in Cs-Ru/C Catalysts for Ammonia Synthesis. Inorg Chem 50:3757-3765

Ruus R, Kikas A, Saar A, Ausmees A, Nommiste E, Aarik J, Aidla A, Uustare T, Martinson I (1997) Ti 2*p* and O 1s X-ray absorption of TiO_2 polymorphs. Solid State Commun 104:199-203

Sarret G, Connan J, Kasrai M, Bancroft G, Charrie-Duhaut A, Lemoine S, Adam P, Albrecht P, Eybert-Berard L (1999) Chemical forms of sulfur in geological and archealogical asphaltenes from Middle East, France and Spain determined by sulfur *K* and *L*-edge X-ray absorption near-edge structure spectroscopy. Geochim Cosmochim Acta 63:3767-3779

Sarret G, Mongenot T, Connan J, Derenne S, Kasrai M, Bancroft GM, Largeau C (2002) Sulfur speciation in kerogens of the Orbagnoux deposit (Upper Kimmeridgian, Jura) by XANES spectroscopy and pyrolysis. Org Geochem 33:877-895

Sauer H, Brydson R, Rowley PN, Engel W, Thomas JM (1993) Determination of coordinations and coordination-specific site occupancies by electron energy-loss spectroscopy: An investigation of boron-oxygen compounds. Ultramicroscopy 49:198-209

Schroeder SLM, Moggridge GD, Chabala E, Ormerod RM, Rayment T, Lambert RM (1996) In situ studies of catalysts under reaction conditions by total electron-yield. Farad Disc 105:317-336

Schulman RG, Yafet Y, Eisenberger E, Blumberg WE (1976) Observation and interpretation of X-ray absorption edges in iron compounds and proteins. Proc Natl Acad Sci USA 73:1384-1388

Schwarz WHE, Mensching L, Hallmeier KH, Szargan R (1983) *K* shell excitations of BF_3, CF_4 and MBF_4. Chem Phys 82:57-65

Sharp T, Wu Z, Seifert F, Poe B, Doerr M, Paris E (1996) Distinction between six- and fourfold coordinated silicon in SiO_2 polymorphs via electron loss near edge structure (ELNES) spectroscopy. Phys Chem Miner 23:17-24

Shaw SA, Peak D, Hendry MJ (2009) Investigation of acidic dissolution of mixed clays between pH 1.0 and-3.0 using Si and Al X-ray absorption near edge structure. Geochim Cosmochim Acta 73:4151-4165

Shirley EL (2004) Ti ls pre-edge features in rutile: A Bethe-Salpeter calculation. J Electron Spectrosc Relat Phenom 136:77-83

Shukla A, Calandra M, Taguchi M, Kotani A, Vanko G, Cheong SW (2006) Polarized resonant inelastic X-ray scattering as an ultrafine probe of excited states of La_2CuO_4. Phys Rev Lett 96:0770006

EBSCOhost - printed on 2/13/2023 5:26 AM via . All use subject to https://www.ebsco.com/terms-of-use

Simon SB, Sutton SR, Grossman L (2007) Valence of titanium and vanadium in pyroxene in refractory inclusion interiors and rims. Geochim Cosmochim Acta 71:3098-3118

Sipr O, Rocca F (2010) Electronic structure effects on B *K*-edge XANES of minerals. J Synchrotron Radiat 17:367-373

Sipr O, Simunek A, Rocca F (2007) B *K*-edge XANES of superstructural units in borate glasses. AIP conference proceedings 882:446-448

Skytt P, Glans P, Mancini D, Guo JH, Wassdahl N, Nordgren J, Ma Y (1994) Angle-resolved soft-X-ray fluorescence and absorption study of graphite. Phys Rev B 50:10457-10461

Soininen JA, Hamalainen K, Caliebe WA, Kao CC, Shirley EL (2001) Core-hole-electron interaction in X-ray Raman scattering. J Phys-Condens Mat 13:8039-8047

Soldatov AV, Gusatinskii AN (1984) Energy delocalization of the rare-earth F-states in some compounds. Phys Status Solidi B 125:K129-K132

Soldatov AV, Ivanchenko TS, Dellalonga S, Kotani A, Iwamoto Y, Bianconi A (1994) Crystall-structure effects in the Ce L_3-edge X-ray-absorption spectrum of CeO_2 – Mutiple scattering resonances and many-body final-states. Phys Rev B 50:5074-5080

Soldatov AV, Stekhin IE, Ingalls R (1996) Electronic structure of RbBr during the phase transition: X-ray absorption near-edge structure analysis. J Phys-Condens Mat 8:7829-7835

Soldatov AV, Kasrai M, Bancroft GM (2000) unoccupied electronic states of stishovite: X-ray absorption fine structure theoretical analysis. Solid State Commun 115:687-692

Soldatov AV, Kravtsova AN, Fleet ME, Harmer SL (2004) Electronic structure of MeS (Me = Ni,Co,Fe):X-ray absorption analysis. J Phys-Condens Mat 16:7545-7556

Solomon D, Lehmann J, Harden J, Wang J, Kinyangi J, Heymann K, Karunakaran C, Lu Y, Wirick S, Jacobsen C (2012) Micro- and nano-environments of carbon sequestration:Multi-element STXM–NEXAFS spectromicroscopy assessment of microbial carbon and mineral associations. Chem Geol 329:53-73

Solomon D, Lehmann J, Kinyangi J, Liang BQ, Schafer T (2005) Carbon *K*-edge NEXAFS and FTIR-ATR spectroscopic investigation of organic carbon speciation in soils. Soil Sci Soc Am J 69:107-119

Sowrey FE, Skipper LJ, Pickup DM, Drake KO, Lin Z, Smith ME, Newport RJ (2004) Systematic empirical analysis of calcium-oxygen coordination environment by calcium *K*-edge XANES. Phys Chem Chem Phys 6:188

Stavitski E, de Groot FMF (2010) The CTM4XAS program for EELS and XAS spectral shape analysis of transition metal L edges. Micron 41:687-694

Stepanyuk VS, Szasz A, Farberovich OV, Grigorenko AA, Kozlov AV, Mikhailin VV (1989) An electronic band structure calculation and the optical properties of alkaline-earth sulphides. Phys Status Solidi B 155:215-220

Stöhr J (1992) NEXAFS Spectroscopy. Springer Verlag, Berlin

Suljoti E, de Groot FMF, Nagasono M, Glatzel P, Hennies F, Deppe M, Pietzsch A, Sonntag B, Föhlisch A, Wurth W (2009) Spin-orbit mediated interference in the radiative and nonradiative channels of the La 4d core resonances. Phys Rev Lett 103:137401

Sutton SR, Dyar MD, Delaney JS, Newville M, Rossman GR (2000) Interpretation of Fe *K* XANES Pre-edge spectra of hematite based on cobalt optical spectra. APS Activity report 2000

Sutton SR, Karner J, Papike J, Delaney JS, Shearer C, Newville M, Eng P, Rivers M, Dyar MD (2005) Vanadium *K* edge XANES of synthetic and natural basaltic glasses and application to microscale oxygen barometry. Geochim Cosmochim Acta 69:2333-2348

Taillefumier M, Cabaret D, Flank AM, Mauri F (2002) X-ray absorption near-edge structure calculations with the pseudopotentials: Application to the *K*-edge in diamond and alpha-quartz. Phys Rev B 66:195107

Teodorescu CM, Esteva JM, Womes M, El Afif A, Karnatak RC, Flank AM, Lagarde P (2000) Sodium 1s photoabsorption spectra of Na and NaF clusters deposited in rare gas matrices. J Electron Spectrosc Relat Phenom 106:233-245

Terminello LJ, Shuh DK, Himpsel FJ, Lapianosmith DA, Stohr J, Bethune DS, Meijer G (1991) Unfilled orbitals of C-60 and C-70 from carbon *K*-shell X-ray-absorption fine-structure. Chem Phys Lett 182:491-496

Thole BT, van der Laan G (1988) Branching ratio in X-ray absorption spectroscopy. Phys Rev B 38:3158-3171

Thole BT, van der Laan G, Butler PH (1988) Spin-mixed ground state of Fe Phthalocyanine and the temperature dependent branching ratio in X-ray absorption spectroscopy. Chem Phys Lett 149:295-299

Thompson AC, Vaughan D (2011) X-ray data booklet. Lawrence Berkeley National Laboratory, University of California, Berkeley, CA 94720

Tossell JA (1977) SCF–Xα scattered wave MO studies of the electronic structure of ferrous iron in octahedral coordination with sulfur. J Chem Phys 66:5712

Trcera N, Cabaret D, Rossano S, Farges F, Flank AM, Lagarde P (2009) Experimental and theoretical study of the structural environment of magnesium in minerals and silicate glasses using X-ray absorption near-edge structure. Phys Chem Miner 36:241-257

EBSCOhost - printed on 2/13/2023 5:26 AM via . All use subject to https://www.ebsco.com/terms-of-use

Trcera N, Rossano S, Madjer K, Cabaret D (2011) Contribution of molecular dynamics simulations and ab initio calculations to the interpretation of Mg *K*-edge experimental XANES in K_2O-MgO-3SiO_2 glass. J Phys-Condens Mat 23:255401

Tsuji J, Nakamatsu H, Mukoyama T, Kojima K, Ikeda S, Taniguchi K (2002) Lithium *K*-edge XANES spectra for lithium compounds. X-Ray Spectrom 31:319-326

Uozumi T, Okada K, Kotani A, Durmeyer O, Kappler JP, Beaurepaire E, Parlebas JC (1992) Experimental and theoretical investigation of the pre-peaks at the Ti *K*-edge absorption-spectra in TiO_2. Europhys Lett 18:85-90

Urquhart SG, Ade H (2002) Trends in the carbonyl core (C 1s, O 1s) → pi*c=o transition in the near-edge X-ray absorption fine structure spectra of organic molecules. J Phys Chem B 106:8531-8538

van Aken PA, Liebscher B (2002), Quantification of ferrous/ferric ratios in minerals. Phys Chem Miner 29:188-200

van Aken PA, Sharp TG, Seifert F (1998) Electron-beam induced amorphization of stishovite:Silicon-coordination change observed using Si *K*-edge extended electron energy-loss fine structure. Phys Chem Miner 25:83-93

van Bockhoven JA, Nabi T, Sambe, Remaker DE, Koningsberger DC (2001) Interpretation of the Al *K*- and $L_{II/III}$-edges of aluminum oxides:differences between tetrahedral and octahedral Al explained by different local symmetries. J Phys-Condens Mat 13:10247-10260

van Bokhoven JA, Sambe H, Ramaker DE, Koningsberger DC (1999) Al *K*-edge near-edge X-ray absorption fine structure (NEXAPS) study on the coordination structure of aluminum in minerals and Y zeolites. J Phys Chem B 103:7557-7564

van Bokhoven JA, van der Eerden AMJ, Koningsberger DC (2003) Three-coordinate aluminum in zeolites observed with in situ X-ray absorption near-edge spectroscopy at the Al *K*-edge: Flexibility of aluminum coordinations in zeolites. J Am Chem Soc 125:7435-7442

Van Elp J, Wieland J, Eskes H, Kuiper P, Sawatzky G, de Groot FMF, Turner T (1991) Electronic-Structure of CoO, Li-Doped CoO, and $LiCoO_2$. Phys Rev B 44:6090-6103

Vankó G, de Groot FMF, Huotari S, Cava RJ, Lorenz T, Reuther M (2008) Intersite 4*p*-3*d* hybridization in cobalt oxides: A resonant X-ray emission spectroscopy study. arXiv:0802.2744

Varlot K, Kasrai M, Bancroft GM, Yamaguchi ES, Ryason PR, Igarashi J (2001) X-ray absorption study of antiwear films generated from ZDDP and borate micelles. Wear 249:1029-1035

Villain O, Calas G, Galoisy L, Cormier L (2007) XANES determination of chromium oxidation states in glasses: Comparison with optical absorption spectroscopy. J Am Ceram Soc 90:3578-3581

Vinson J, Rehr JJ, Kas JJ, Shirley EL (2011) Bethe-Salpeter equation calculations of core excitation spectra. Phys Rev B 83:115106

von Barth U, Grossmann G (1982) Dynamical effects in X-ray spectra and the final-state rule. Phys Rev B 25:5150-5179

Wang HM, Henderson GS (2004) Investigation of coordination number in silicate and germanate glasses using O *K*-edge X-ray absorption spectroscopy. Chem Geol 213:17-30

Wasinger EC, de Groot FMF, Hedman B, Hodgson KO, Solomon EI (2003) *L*-edge X-ray absorption spectroscopy of non-heme iron sites. J Am Chem Soc 125:12894-12906

Waychunas GA (1987) Synchrotron Radiation XANES spectroscopy of Ti in minerals: Effects of Ti bonding distances, Ti valence, and site geometry on adsorption edge structure. Am Mineral 72:89-101

Waychunas GA, Apted MJ, Brown GE Jr (1983) X-ray *K*-edge absorption spectra of Fe minerals and model compounds: Near-edge structure. Phys Chem Miner 10:1-9

Waychunas GA, Fuller CC, Davis JA, Rehr JJ (2003) Surface complexation and precipitate geometry for aqueous Zn(II) sorption on ferrihydrite:II. XANES analysis and simulation. Geochim Cosmochim Acta 67:1031-1043

Weigel C, Calas G, Cormier L, Galoisy L, Henderson GS (2008) High-resolution Al $L_{2,3}$-edge X-ray absorption near edge structure spectra of Al-containing crystals and glasses: Coordination number and bonding information from edge components. J Phys-Condens Mat 20:135219

Westre TE, Kennepohl P, DeWitt JG, Hedman B, Hodgson KO, Solomon EI (1997) A multiplet analysis of Fe *K*-edge 1s → 3*d* pre-edge features of iron complexes. J Am Chem Soc 119:6297-6314

Wilke M, Farges F, Petit PE, Brown GE Jr, Martin F (2001) Oxidation state and coordination of Fe in minerals: An Fe *K*-XANES spectroscopic study. Am Mineral 86:714-730

Wilke M, Partzsch GM, Bernhardt R, Lattard D (2004) Determination of the iron oxidationstate in basaltic glasses using XANES at the K-edge. Chem Geol 213: 71-87

Wilke M, Partzsch GM, Bernhardt R, and Lattard D (2005) Determination of the iron oxidation state in basaltic glasses using XANES at the *K*-edge. Chem Geol 213:71-87

Wilke M, Schmidt C, Farges F, Malavergne V, Gautron L, Simionovici A, Hahn M, Petit P (2006) Structural environment of iron in hydrous aluminosilicate glass and melt-evidence from X-ray absorption spectroscopy. Chem Geol 229:144-161

EBSCOhost - printed on 2/13/2023 5:26 AM via . All use subject to https://www.ebsco.com/terms-of-use

Wilke M, Farges F, Partzsch GM, Schmidt C, Behrens H (2007) Speciation of Fe in silicate glasses and melts by in-situ XANES spectroscopy. Am Mineral 92:44-56

Wilke M, Jugo PJ, Klimm K, Susini J, Botcharnikov R, Kohn SC, Janousch M (2008) The origin of S^{4+} detected in silicate glasses by XANES. Am Mineral 93:235-240

Wilke M, Hahn O, Woodland AB, Rickers K (2009) The oxidation state of iron determined by Fe K-edge XANES-application to iron gall ink in historical manuscripts. J. Anal At Spectrom 24:1364-1372

Wilke M, Klimm K, Kohn SC (2011) Spectroscopic Studies on Sulfur Speciation in Synthetic and Natural Glasses. Rev Mineral Geochem 73:41-78

Wong J, Lytle FW, Messmer RP, Maylotte DH (1984) K-edge absorption spectra of selected vanadium compounds. Phys Rev B 30:5596-5610

Wu Z, Mottana A, Marcelli A, Natoli CR, Paris E (1996) Theoretical analysis of X-ray absorption near-edge structure in forsterite, Mg_2SiO_4-Pbnm, and fayalite, Fe_2SiO_4-Pbnm, at room temperature and extreme conditions. Phys Chem Mineral 23:193-204

Wu Z, Marcelli A, Mottana A, Giuli G, Paris E (1997a) Al coordination and local structure in minerals: XAFS determinations and multiple-scattering calculations for K-feldspars. Europhys Lett 38:465-470

Wu ZY, Ouvrard G, Gressier P, Natoli CR (1997b) Ti and O *K* edges for titanium oxides by multiple scattering calculations: Comparison to XAS and EELS spectra. Phys Rev B 55:10382-10391

Wu ZY, Jollet F, Seifert F (1998) Electronic structure analysis of α-SiO_2 via X-ray absorption near-edge structure at the Si *K*, $L_{2,3}$ and O *K*-edges. J Phys-Condens Mat 10:8083-8092

Wu Z, Paris E, Langenhorst F, Seifert F. (2002) Oxygen-metal bonding in Ti-bearing compounds from O 1s spectra and ab initio full mutiple scattering calculations. J Synchrotron Radiat 9:394-400

Xiong W, Peng J, Hu Y (2012) Use of X-ray absorption near edge structure (XANES) to identify physisorption and chemisorption of phosphate onto ferrihydrite-modified diatomite. J Colloid Interf Sci 368:528-32

Xu RK, Hu YF, Dynes JJ, Zhao AZ, Blyth RIR, Kozak LM, Huang PM (2010) Coordination nature of aluminum (oxy)hydroxides formed under the influence of low molecular weight organic acids and a soil humic acid studied by X-ray absorption spectroscopy. Geochim Cosmochim Acta 74:6422-6435

Xu W, Chen DL, Chu WS, Wu ZY, Marcelli A, Mottana A, Soldatov A, Brigatti MF (2011) Quantitative local structure determination in mica crystals: ab initio simulations of polarization XANES at the potassium *K*-edge. J Synchrotron Radiat 18:418-426

Xu W, Liu L, Cui M, Zheng L, Hu Y, Marcelli A, Wu Z (2013) Electronic structure and hybridization of CaS by means of X-ray absorption spectroscopy at Ca and S *K*-edges. J Synchrotron Radiat 20:110-115

Yamamoto T, Tanaka T, Suzuki S, Kuma R, Teramura K, Kou Y, Funabiki T, Yoshida S (2002) NO reduction with CO in the presence of O_2 over Cu/Al_2O_3. Top Catal 18:113-118

Yarker CA, Johnson PAV, Wright AC, Wong J, Greegor RB, Lytle FW, Sinclair RN (1986) Neurton-diffraction and EXAFS evidence for TiO_5 units in vitreous K_2O-TiO_2-$2SiO_2$. J Non-Cryst Solids 79:117-136

Yin ZF, Kasrai M, Bancroft GM, Tan KH, Feng XH (1995) X-ray-absorption spectroscopic studies of sodium polyphosphate glasses. Phys Rev B 51:742-750

Yoshiya M, Tanaka I, Kaneko K, Adachi H (1999) First principles calculations of chemical shifts in ELNES/NEXAFS of titanium oxides. J Phys-Condens Mat 11:3217-3228

Zhang GY, Hu YF, Xu RK, Dynes JJ, Blyth RIR, Kozak LM, Huang PM (2009) Carbonate induced structural perturbation of Al hydroxides. Clay Clay Miner 57:795-807

Zhang JY, Xiao ZR, Kuo JL (2010) Calculation of near *K*-edge X-ray absorption spectra and hydrogen bond network in ice XIII under compression. J Chem Phys 132:184506

EBSCOhost - printed on 2/13/2023 5:26 AM via . All use subject to https://www.ebsco.com/terms-of-use

Reviews in Mineralogy & Geochemistry
Vol. 78 pp. 139-174, 2014
Copyright © Mineralogical Society of America

Probing of Pressure-Induced Bonding Transitions in Crystalline and Amorphous Earth Materials: Insights from X-ray Raman Scattering at High Pressure

Sung Keun Lee

School of Earth and Environmental Sciences
Seoul National University, Seoul, 151-742 Korea

sungklee@snu.ac.kr

Peter J. Eng

Consortium for Advanced Radiation Sources
and
James Franck Institute
University of Chicago, Chicago, Illinois 60637, U.S.A.

Ho-kwang Mao

Geophysical Laboratory
Carnegie Institution of Washington, Washington D.C., 20015, U.S.A.

Center for High Pressure Science and Technology Advanced Research
1690 Cailun Rd., Pudong, Shanghai 201203, P.R. China

INTRODUCTION

Knowledge of the electronic structure of crystalline and non-crystalline earth materials at ambient and high pressure are essential in order to understand the atomic origins of electronic, thermodynamic, and mechanical properties of these materials in the Earth's crust as well as Earth and planetary interiors (Hemley 1998; Laudernet et al. 2004; Stixrude and Karki 2005; Mao and Mao 2007; Price 2007; Stixrude 2007). Pressure-induced changes in the electronic structure of crystalline and amorphous silicates and oxides (glasses and melts) with low-z elements (e.g., Si, O, B, Li, C, etc.) have implications for diverse geophysical and magmatic processes relevant to the evolution and differentiation of the earth (e.g., mantle convection and mantle melting) (Stebbins 1995; Wolf and McMillan 1995; Lee 2005, 2011; Mysen and Richet 2005; Murakami and Bass 2010). Despite this importance, the analysis of the effect of pressure on the electronic structure and the nature of bonding in the crystalline and, particularly, non-crystalline oxides has remained one of the challenging problems in mineral physics and geochemistry, as well as, condensed matter physics. This is mostly because of the lack of suitable experimental probes of electronic bonding around these light elements in the earth materials under pressure.

Advances in *in situ* high pressure technologies, together with progress in X-ray optics in synchrotron radiation and first principle calculations have revealed structural details of bonding transitions of crystalline earth materials at high pressure (Hemley 1998; Mao and Mao 2007; Price 2007; Stixrude 2007). The non-resonant synchrotron inelastic X-ray scattering (NRIXS, also known as X-ray Raman, XRS) is one of the relatively new synchrotron X-ray probes of local structures with element-specificity. It explores the electronic bonding transitions in soft X-ray absorption edges using hard X-rays (e.g., ~ 10 keV) by tuning the energy loss (energy

1529-6466/14/0078-0004$05.00 http://dx.doi.org/10.2138/rmg.2014.78.4

EBSCOhost - printed on 2/13/2023 5:26 AM via . All use subject to https://www.ebsco.com/terms-of-use

of incident X-rays – energy of scattered X-rays) to the binding energy of electrons in elements of interest (Mao et al. 2003, 2006, 2010; Schulke 2007; Lee et al. 2008b; Rueff and Shukla 2010). Progress in XRS has been combined with advances in *in situ* high pressure technology and consequently, in the last 6-7 years it has been possible to examine the detailed pressure-induced electronic bonding transitions in low-*z* oxide glasses, molecules, and crystals by tuning the *K*-edges of elements in the 2nd row of the periodic table and/or to the *L-M* edges of heavier elements both at ambient and at high pressure (e.g., Schulke 2007; Rueff and Shukla 2010). The observed XRS results for amorphous oxides under compression contribute to the understanding of the atomistic origins of anomalous changes in melt properties in the Earth's interiors.

While the following list is by no means complete, important classes of materials studied by XRS at ambient pressure include Li, LiC_6 LiF, Li_3N, Li-borate glass, phases used for Li-batteries, and Li-peroxide (with Li *K*-edge) (Schulke et al. 1991, 1986; Krisch et al. 1997; Nagasawa et al. 1997; Hamalainen et al. 2002; Fister et al. 2008a, 2011b; Chan et al. 2011; Karan et al. 2012), Be crystals and BeO (with Be *K*-edge) (Schulke et al. 1986; Nagasawa et al. 1989). The C *K*-edge was used to explore bonding details of graphite (Tohji and Udagawa 1987; Schulke et al. 1988; Nagasawa et al. 1989), carbon in diverse aromatic rings, C_{60} (Rueff et al. 2002; Gordon et al. 2003), and hydrocarbons (Feng et al. 2008; Fister et al. 2008b; Sakko et al. 2011). B *K*-edge XRS has provided structural details of BN (Watanabe et al. 1996), B_2O_3, Na-, and Li-borate glasses (Lee et al. 2005, 2007, 2008a). The utility of O-K edge XRS has been demonstrated in the study of H_2O and its polymorphs (Bowron et al. 2000; Bergmann et al. 2002b; Wernet et al. 2004, 2005; Cai et al. 2005; Tse et al. 2008; Fister et al. 2009). Oxygen environments of oxide glasses (SiO_2, B_2O_3, GeO_2, alkali borate glasses, and $MgSiO_3$) and silicate crystals (SiO_2, $MgSiO_3$) have also been investigated using XRS (Lin 2007; Lee et al. 2008a, 2005, 2007, 2008b; Fukui et al. 2009a; Lelong et al. 2012; Yi and Lee 2012). Recently, Na *K*-edge XRS provided the core-electron excitation spectra for NaF and NaCl (Nagle et al. 2009). Application of XRS has been extended to the characterization of oxide thin films (Fister et al. 2011a).

XRS can be particularly effective in studying the electronic structure at high pressure and has been used to yield the electronic structure of helium (He *K*-edge) (Mao et al. 2010), carbon polymorphs (graphite, diamond, amorphous carbon, C *K*-edge) (Mao et al. 2003; Lin et al. 2011), BN (with boron *K*-edge) (Meng et al. 2004), dense oxygens (Meng et al. 2008), H_2O polymorphs (O *K*-edge) (Cai et al. 2005; Tse et al. 2008), and oxide glasses under static compression (see the "*Pressure-Induced Structural Changes in Crystalline and Amorphous Earth Materials: Insights from X-ray Raman Scattering*" section below). Because the features in XRS spectra are sensitive to local "short-range" structure, the technique has been particularly useful in revealing structural changes in non-crystalline oxides at high pressure (Lee et al. 2005; Lin 2007; Fukui et al. 2009a; Lelong et al. 2012). For instance, B *K*-edge XRS studies of borate glasses at high pressure showed the first unambiguous experimental evidence for the formation of highly coordinated boron (i.e., $^{[4]}B$) at high pressure (Lee et al. 2005, 2007, 2008a). O *K*-edge XRS studies of diverse low-*z* oxide glasses suggested the pressure-induced increases in the fraction of triply coordinated oxygen associated with cation coordination changes (Lin 2007; Lee et al. 2008b, 2012; Lelong et al. 2012). Topological disorder also tends to increase with pressure as shown by the increase in the width of the O *K*-edge feature with pressure (Lee et al. 2008b). The O *K*-edge XRS of shock compressed multi-component quaternary oxide glasses showed evidence for the topologically driven densification in model basaltic glasses. This has strong geochemical implications for impact processes (Lee et al. 2012). Atomic configurations around network modifying cations in alkali silicate glasses were explored using Li *K*-edge XRS (Lee et al. 2007).

In addition to *K*-edges of low-*z* elements, XRS technique has also been useful to probe the edge features for loosely bound electrons in earth materials (e.g., *L*- and *M*- and higher

EBSCOhost - printed on 2/13/2023 5:26 AM via . All use subject to https://www.ebsco.com/terms-of-use

edges) (see the "*Remaining Challenges and Outlook: Applications of New K-, L-, M-edge XRS, XRS with Momentum Transfer, In Situ High Temperature and Pressure XRS Study for Multi-Components Glasses*" section for further details). These examples showed that XRS is beneficial for revealing the rich information of electron bonding transitions surrounding low-z elements in diverse crystalline and non-crystalline solids at 1 atm that are traditionally difficult to explore using other conventional techniques.

In this chapter, we provide an overview of the recent progress and insights provided by XRS on the electronic structure of key earth materials. Particular emphasis will be placed on the pressure-induced bonding transitions in dense molecules and non-crystalline oxides. We note that excellent accounts of earlier studies on fundamentals of XRS can be found in the previous review (Schulke 2007). The general application of IXS technique at high pressure (including that of XRS) can also be found in the previous reviews (Schulke 2007; Rueff and Shukla 2010). Short but helpful reviews of XRS techniques with experimental setups can also be found in (Bergmann et al. 2002a, 2004; Fister et al. 2006). There are also extensive reviews and discussion of O *K*-edge studies of H_2O polymorphs and thus these will not be discussed in detail here (e.g., Bowron et al. 2000; Bergmann et al. 2002b; Wernet et al. 2004; Cai et al. 2005; Tse et al. 2005, 2008; Fister et al. 2009). In the current chapter, we first outline the brief theoretical principles of X-ray Raman spectroscopy and experimental setups required for XRS measurement at high pressure. We then present the recent XRS results of the electronic bonding transitions in earth materials. A brief account of theoretical calculations of XRS spectra for mantle minerals is also presented. We also present several new XRS spectra for $CaSiO_3$ glass at ambient and high pressure in order to demonstrate the utility of XRS. Finally, we discuss the future challenges in exploring the structure of diverse earth materials at high pressure using XRS spectroscopy.

BRIEF REMARKS ON THEORETICAL BACKGROUNDS AND XRS EXPERIMENTS AT HIGH PRESSURE

Brief theoretical backgrounds

Recent advances in synchrotron X-ray optics, multi-element IXS analyzers specifically for XRS experiments, and improved diamond anvil cells (DACs) have revealed previously unknown details of the atomic configurations of crystalline materials at high pressure. Although detailed theoretical backgrounds and principles of inelastic X-ray scattering (IXS) can be found in recent reviews and textbooks (Schulke 2007; Rueff and Shukla 2010), brief theoretical background of non-resonant (NR) IXS is presented to provide the necessary information to understand the advantages (and disadvantages) of the method.

In the XRS process, the intensity of inelastically scattered photons is estimated with varying scattering angle (2θ) (and thus momentum transfer, $q = k_1 - k_2$) (Fig. 1). Energy loss (ΔE) in the process is achieved from the difference between energy of incident X-ray photon (E_{ins}) and scattered X-ray photon (E_{scat}). Spectra are collected by varying E_{ins} (with a monochrometer) at a fixed analyzer energy of E_{scat}. The experimental measurable in the above process is the non-resonant double differential scattering cross section (DDSCS) of X-ray and is defined as a change in number of scattered photons (σ) with respect to changes in solid angle (Ω_2) and frequency of scattered photon (ω_2) as shown below (Fourier transform of the DDSCS results in electron density as a function of time and spatial coordinates):

$$\frac{d^2\sigma}{d\Omega_2 d\omega_2} = r_0^2 \left(\frac{\omega_2}{\omega_1}\right) \left|\varepsilon_1 \cdot \varepsilon_2\right|^2 S\left(q,\omega\right) \tag{1}$$

where r_0 is classical electron radius (= e^2/mc^2) and $S(q, \omega)$ is dynamic structure factor, which

EBSCOhost - printed on 2/13/2023 5:26 AM via . All use subject to https://www.ebsco.com/terms-of-use

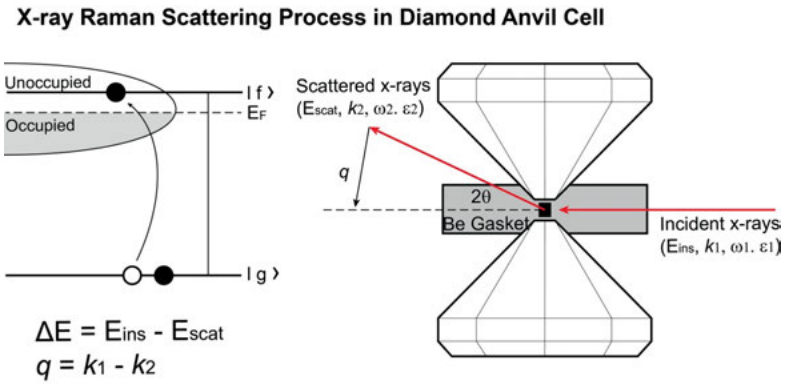


Figure 1. X-ray Raman scattering processes in a diamond anvil cell. E_{ins}, k_1, ω_1, and ε_1 are energy, wave vector, frequency, and polarization vector of the incident photon, respectively. E_{iscat}, k_2, ω_2, and ε_2 are those for the scattered photon. $|g\rangle$ and $\langle f|$ are the initial and final electronic states. E_F is the Fermi energy.

can be expressed as shown below:

$$S(q,\omega)=\sum_{g,f}\left|\langle f\,|\,e^{iq\cdot r}\,|\,g\rangle\right|^2\delta\left(E_g-E_f+\hbar\omega\right) \tag{2}$$

where g and f denote ground and final states and E_g and E_f are electronic energy levels of the ground and final states, respectively (Fig. 1) and thus $\langle f\,|\,e^{iq\cdot r}\,|\,g\rangle$ is the transition matrix that shows the correlation between the ground and excited states. The non-resonant scattering cross section is thus shown below:

$$\frac{d^2\Omega}{d\Omega_2 d\omega_2}=\left(\frac{d\sigma}{d\Omega_2}\right)_{Th}\sum_{g,f}\left|\langle f\,|\,e^{iq\cdot r}\,|\,g\rangle\right|^2\delta\left(E_g-E_f+\hbar\omega\right) \tag{3}$$

where Thomson scattering by a free electron is defined below:

$$\left(\frac{d\sigma}{d\Omega_2}\right)_{Th}=r_0^2\left(\frac{\omega_2}{\omega_1}\right)\left|\varepsilon_1\cdot\varepsilon_2\right|^2 \tag{4}$$

In the non-resonant IXS process relevant to X-ray Raman Scattering (XRS), the incident energy (~10 keV) is much larger than the binding energy (less than 1 keV for low-z elements) of core electrons. At small scattering angle, $q{\cdot}r$ is much smaller than 1 (<<1), and the transition matrix can thus be approximately described by:

$$\langle f\,|\,e^{iq\cdot r}\,|\,g\rangle\cong\langle f\,|\,g\rangle+i\left(f\,|\,q\cdot r\,|\,g\right)-1/2\langle f\,|\left(q\cdot r\right)^2|\,g\rangle+\ldots \tag{5}$$

Assuming orthogonality of initial and final state wave functions ($\langle f\,|\,g\rangle = 0$), the first order term is dominant and the resulting double differential scattering cross section can be described below:

$$\frac{d^2\Omega}{d\Omega_2 d\omega_2}=\left(\frac{d\sigma}{d\Omega_2}\right)_{Th}\sum_{g,f}\left|\langle f\,|\,r\,|\,g\rangle\right|^2\delta\left(E_g-E_f+\hbar\omega\right) \tag{6}$$

As shown in Equation (6) above, under the dipole transition selection rule, the transition matrix for the XRS cross section at low scattering vector (i.e., $\langle f\,|\,r\,|\,g\rangle$) is identical to that of XAS, thus providing identical spectra to X-ray absorption near-edge structure (XANES) spectra (see Schulke 2007; Rueff and Shukla 2010; Henderson et al. 2014, this volume for

EBSCOhost - printed on 2/13/2023 5:26 AM via . All use subject to https://www.ebsco.com/terms-of-use

a review). In addition, with increasing momentum transfer, q (and thus scattering angle), transitions from non-dipole contributions can also be observed. Higher order terms in Equation (6) (e.g., $\langle f | (q \cdot r)^2 | g \rangle$ can be prevalent and the bonding nature relevant to momentum transfer (q-dependence) during the IXS process can be examined (Mizuno and Ohmura 1967; Suzuki 1967; Tohji and Udagawa 1987, 1989; Bergmann et al. 2000) (see the section "*Comparison with other core-electron excitation spectroscopy and traditional experimental probes at high pressure"* below for brief remarks on previous studies of q-dependence in XRS spectrum). With high brilliance synchrotron hard X-rays (~10 keV), XRS allows us to probe the configurations around low-z element (typically from He to Na K-edges) of diverse materials (as well as high L and M edges of third and fourth elements) without using an ultrahigh vacuum environment, yielding bulk sensitivity with resolution of XAS.

Comparison with other core-electron excitation spectroscopy and traditional experimental probes at high pressure

Comparison with other core-electron excitation spectroscopy. Local electronic bonding structure with the transition matrix, $\langle f | r | g \rangle$ in Equation (6) can be obtained using several experimental techniques that probe the energy-loss near-edge structure (ELNES) of the elements of interest stemming from an excitation of core (or valence) electron to unbound states (Fig. 1). These techniques unveil element-specific electronic bonding environments (i.e., local atomic structures, bonding nature, coordination number, and chemical environments) around atoms of interest. One of the popular techniques is X-ray absorption spectroscopy [XAS, either X-ray absorption near-edge structure (XANES) and extended X-ray absorption fine structure (EXAFS)] (see Newville 2014, this volume; Henderson et al. 2014, this volume). Additionally, electron scattering techniques using transmission electron microscopy (TEM) offer electron energy loss spectroscopy (EELS), yielding spectral response function with identical transition matrix elements (e.g., see Brown et al. 1995; de Groot 2001; Wilke et al. 2001; Stohr 2003; Brydson et al. 2014, this volume and references therein). XRS compliments these established techniques involving excitation of core and/or valence electrons into unoccupied electronic states.

Whereas the local electronic bonding natures of low-z glasses and crystals at ambient pressures have been extensively studied using soft X-ray XANES spectroscopy (e.g., Seifert et al. 1996; Wu et al. 1996; Garvie et al. 2000; Henderson et al. 2009), application of XAS is often more suitable for high-z elements using hard X-ray because its application to soft X-ray region requires vacuum conditions (used to minimize the scattering from air molecules). Furthermore, conventional synchrotron XAS may not be suitable for probing low-z oxides at high pressures due to the inability of the soft X-rays to penetrate the sample environments to sustain its high pressure condition (e.g., Be gasket of a diamond anvil cell). Due to limited penetration depth of the soft X-ray photon for low-z element XAS, XAS of these elements is often more suitable for probing of surface structure. While the EELS technique can be potentially useful for studying quenched materials (compressed and decompressed within a DAC) and to probe electronic excitations of low-z elements, it suffers limitations in its *in situ* investigation of electronic bonding transitions in oxide materials at high pressure as *in situ* high pressure techniques cannot be combined with TEM. Furthermore, the electron beam during sample preparation and measurement may alter the sample. In summary, X-ray Raman scattering (XRS) is one of the non-resonant inelastic X-ray techniques and is obtained using hard X-rays. XRS is thus an element-specific (tuning with electron binding energy), *in situ* experimental probe of bulk oxides with low-z elements at extreme conditions (and at ambient pressure) using hard X-rays. It provides sensitivity similar to that of soft X-rays (similar transition matrix for scattering cross section); therefore, it allows us to probe the detailed local bonding nature of low-z elements in crystalline and amorphous oxides, molecular solids, and liquids *in situ* at high pressures (Bergmann et al. 2002a; Mao et al. 2003; Wernet et al. 2004; Cai et al. 2005; Lee et al. 2005b, 2007, 2008b, 2008b; Lin et al. 2007; Schulke 2007; Meng et al. 2008, 2004; Fukui et al. 2009; Rueff and Shukla 2010).

EBSCOhost - printed on 2/13/2023 5:26 AM via . All use subject to https://www.ebsco.com/terms-of-use

As an example of the utility and uniqueness of XRS at 1 atm, Figure 2 shows typical IXS spectra for $CaSiO_3$ glass at 1 atm. The elastic X-ray signal is dominant at an energy loss (i.e., energy difference between incident energy and elastic energy) of 0 eV. The broad feature at ~10-140 eV is due to the Compton scattering peak. The Compton scattering peak position moves to higher energy and the Compton peak width also gets broader with increasing scattering angle (2θ). The spectra also show the first experimental results for Ca *M*-edge features [Ca $M_{2\text{-}3}$ (from Ca 3*p* state to an unbound state) at energy loss of ~28 eV and Ca M_1 (Ca 3*s* state to an unbound state) edge at ~45 eV] of non-crystalline solids. The spectral features at an energy loss at ~100-120 eV are due to the Si *L*-edge (corresponding to electron excitation form Si 2*p* to unbound state) XRS spectra for the glass (background due to Compton scattering is not subtracted here) (Fig. 2B). Figure 2C shows O *K*-edge XRS spectrum for the $CaSiO_3$ glass where typical and broad O *K*-edge features for oxide glasses at 538-540 eV are presented: the O *K*-edge feature is due to an excitation of a core electron from the oxygen 1*s*-state into unoccupied oxygen 2*p*-states that are hybridized with the silicon 3*s*- and 3*p*-states of four-coordinated Si atoms in corner-sharing SiO_4 (see section "*Remaining Challenges and Outlook: Applications of New K-, L-, M-edge XRS, XRS with Momentum Transfer, In Situ High Temperature and Pressure XRS Study for Multi-Components Glasses*" for further details of O *K*-edge XRS spectra for oxide glasses). Note that these multi-element and multiple-edge XRS spectra were collected without need of a vacuum chamber that is necessary for soft-x ray XAS studies of low-*z* elements. As previously mentioned, while the transition matrix in the XRS scattering cross section (Eqn. 6) is identical to that of XAS, multipole transitions can be probed by exploring the momentum transfer (when $q \cdot r$ becomes larger). The q dependence on XRS spectra for diverse materials has been explored in order to study the nature of the bonding processes in such phenomena as the indirect band gap of dielectrics, the nature of excitons, and orbital symmetry (Caliebe et al. 2000; Hamalainen et al. 2002; Soininen et al. 2006) (see Schulke 2007 and references therein).

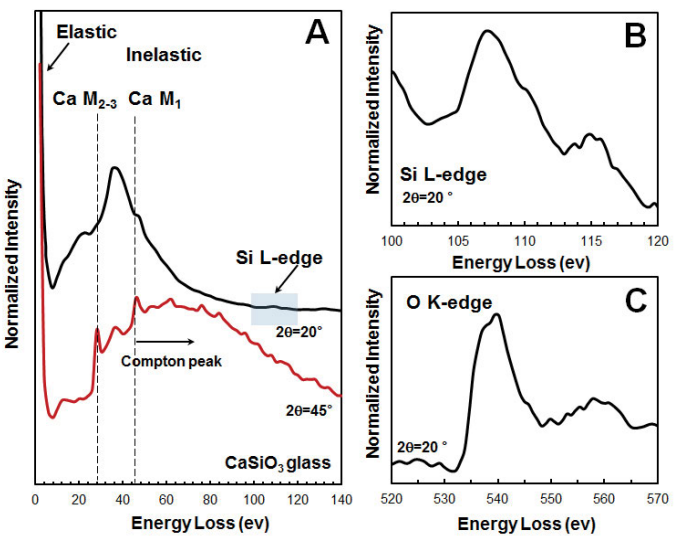


Figure 2. XRS spectra for $CaSiO_3$ glass with varying scattering angle (2θ) as labeled. The spectrum is plotted as normalized scattered intensity versus energy loss (incident energy – elastic energy). Elastic energy is 9.694 keV. (A) Ca $M_{2\text{-}3}$, Ca M_1 edges, Si *L*-edge X-ray Raman scattering (XRS) spectra and Compton scattering peak for $CaSiO_3$ glass. (B) Si *L*-edge XRS spectra for $CaSiO_3$ glass at scattering angle of 20°. (C) O *K*-edge XRS spectra for $CaSiO_3$ glass at scattering angle of 20°.

EBSCOhost - printed on 2/13/2023 5:26 AM via . All use subject to https://www.ebsco.com/terms-of-use

Comparison with other high pressure probes of structure of non-crystalline oxides. XRS compliments other established spectroscopic and scattering techniques that give unique data on the structure of materials under compression. As we provide extensive discussion on the application of XRS techniques to explore the structure and bonding nature of glasses or non-crystalline solids, here we briefly mention the advantages of XRS techniques over other high-pressure probes of glass structure.

Elastic X-ray scattering techniques provide essential information of the electron density of materials (and its structure factor) and average lattice structure, making it mostly suitable for studying crystalline materials under compression. Applications of synchrotron elastic X-ray scattering to low-z glass, including oxide glasses (silicates, borates) at high pressure has been limited due to the highly attenuating sample environment and small atomic scattering factors of low-z elements (e.g., oxygen, silicon, boron). While neutron scattering experiments for low-z glasses can overcome this problem and are potentially promising, they require relatively large sample volumes, which limits the current pressure range of study to below 10-20 GPa (e.g., Salmon et al. 2013). Additionally, with an increasing number of components, the overlap among structure factors or pair-correlation functions from both elastic X-ray and neutron scattering becomes problematic. The detailed pair correlation functions for cation-anion (or cation-cation, anion-anion) pairs are thus difficult to obtain as the number of components in oxide glasses increases.

Vibrational spectroscopy (such as Raman and IR) has been effective in providing vibrational density of states of materials (mostly for crystalline and molecules) at high pressure and can be performed *in situ*. The spectra for amorphous oxides are often quite broad even at 1 atm and due to an increase in topological disorder with pressure, the modes (or peaks) gets even further broadened, often yielding ambiguous results at high pressure.

This trend in an increase in overlap among modes or structure factors is inherent in any experimental measurement for amorphous materials under compression. This problem can be partly resolved using element-specific experimental probes, such as XRS and multi-nuclear solid-state nuclear magnetic resonance (NMR). Previous solid-state NMR studies of oxide glasses have provided improved resolution among the detailed atomic structures in the glasses and thus their pressure-induced structural changes (see Allwardt et al. 2005a,b; Kelsey et al. 2009a,b; Lee 2010, 2011). For example, it has been shown that the pressure-induced structural changes are characterized by the formation of bridging oxygen (BO) linking $^{[4]}$Si and highly coordinated Si and Al at the expense of nonbridging oxygen (NBO) at high pressure (Xue et al. 1994; Yarger et al. 1995; Lee 2010, 2011). However, solid-state NMR studies require 10-20 mg samples, limiting the maximum quench pressure for oxide glasses to 10-12 GPa (Xue et al. 1989; Yarger et al. 1995; Lee et al. 2003; Allwardt et al. 2004). Therefore the structure of glasses for the NMR experiments represents that of super-cooled liquids at the glass transition temperature, below which the melt structures are frozen at high pressure. *In situ* high-pressure NMR spectroscopy of solids is currently not possible. The inherent difficulties of the current technologies pose major challenges for probing structural changes of low-z glasses over a wide pressure ranges. The XRS technique can resolve most of the aforementioned problems of conventional experimental probes, as well as yield a new opportunity to study the bonding changes in low-z systems at high pressure.

Current limitations of XRS technique. We also note that there are several disadvantages of XRS spectroscopy. Because XRS utilizes inelastically scattered X-ray photons, the intensity of the X-ray Raman signal is several orders of magnitude smaller than that of an elastic X-ray signal. The XRS process is thus intrinsically inefficient, requiring relatively long collection times to provide statistically meaningful experimental results with sufficient signal/background ratios: as for the spectra presented in the current review, collection time varies from several hours to ~ a day depending on the atoms of interest, as well as, the type and dimension of the

EBSCOhost - printed on 2/13/2023 5:26 AM via . All use subject to https://www.ebsco.com/terms-of-use

sample (see below for further details). The stability (and drift) of the synchrotron X-ray beam should thus be regularly checked during collection of the XRS signal. Furthermore, XRS has only been applied to a limited number of elements from He up to Na *K*-edge. This is largely because the X-ray Raman signal intensity decreases with atomic number.

Practical glitches involving XRS experiments under static compression. XRS studies involving low-*z* elements enable us to unveil structural details of densification in oxide glasses at pressures up to ~ 50 GPa. Application of XRS to oxide glasses synthesized at higher pressure above 50-70 GPa remains to be explored. This has been limited due mostly to the following experimental technical difficulties. First, as the gap between diamond anvils decreases with increasing pressure, unless a beam size of a few μm with significantly improved photon flux could be used, it is difficult to get sufficient q-ranges for the IXS experiment with radial X-ray radiation through the Be gasket. Taking into consideration the ranges of pressure in the Earth's and planetary interiors (up to 360 GPa to the Earth's inner core) and variations in composition in the diverse earth and planetary materials, a considerable amounts of future studies spanning much higher pressure conditions are necessary. Additionally, as previously mentioned, X-ray attenuation depth of the many oxides (including iron oxides) is rather small (~ 10 μm for 10 keV X-rays). The limited sample volume due to small X-ray attenuation length makes it difficult to get sufficient signal from the sample at high pressure: sample volume of oxides interacting with incident X-rays can decrease significantly because of the small X-ray attenuation length of many transition metal bearing crystalline and amorphous oxides. The combination of sample dimension for high pressure research and X-ray attenuation lengths needs to be taken into consideration to optimize sample size for XRS with a DAC. Third, the pressure gradient in the DAC increases with increasing pressure. Depending on the size (FWHM) of the X-ray beam, the IXS signals from a sample with varying pressure range (instead of a single pressure condition) can be collected with a typical size of 60 μm (H) × 20 μm (V). It should also be mentioned that, with the possible exceptions of B and C *K*-edge XRS studies, currently it takes ~day(s) of beamtime to achieve a signal to noise (and/or background) ratio in the oxygen and other *K*- and *L*- edge XRS spectra under typical experimental conditions for the current XRS beam lines with ~ 1 eV resolution. This makes it difficult to check reproducibility of the experimental results. New cell design with enhanced X-ray flux and reduced beam size would thus be necessary. Better X-ray optics with focusing and enhancing signals from a few μm beam are being developed for XRS techniques and will be eventually overcome the aforementioned limitations.

XRS experiments

Hard X-rays at 3rd generation synchrotron radiation sources with flux densities of approximately 10^{13}-10^{14} photons/s/eV are used to collect XRS spectra. While most of the experimental XRS data shown here were obtained from sector 16 ID-D (HPCAT) and 13-IDC (GSECARS) at the Advanced Photon Source (APS), NRIXS spectra can be collected at other 3rd generational synchrotron radiation facilities including SPring-8 (BL12-XU), and the European Synchrotron Radiation Facility (ESRF) (e.g., Bergmann et al. 2002a; Fister et al. 2006, 2007; Lelong et al. 2012).

The experimental conditions for XRS studies at high pressure using a DAC have been reported previously (Mao et al. 2003; Schulke 2007; Rueff and Shukla 2010). The detailed information of instrumentation and X-ray optics can be found in recent manuscripts (Bergmann et al. 2002a; Fister et al. 2006, 2007). Current progress and review of DAC techniques can also be found elsewhere (Mao and Mao 2007; Shen and Wang 2014, this volume). In the typical XRS experiment, samples are loaded into the sample chamber of a gasket (typically made from Be or BN) in a DAC with a few ruby spheres as the pressure calibrant (Mao and Mao 2007). A pressure medium is not often used in the typical XRS study for materials at high pressure. This is in order to minimize scattering and/or absorption from the medium. The stress condition

EBSCOhost - printed on 2/13/2023 5:26 AM via . All use subject to https://www.ebsco.com/terms-of-use

in the DAC is therefore uniaxial without the pressure medium, although the orientation effect in glass is less important that in the crystals. Future experiments with hydrostatic conditions (with the pressure medium) are certainly necessary to explore the effect of stress conditions on the pressure-induced changes in electronic bonding environment. Diamonds with varying flat culets have been used for high-pressure X-ray Raman experiments up to 74 GPa (Fukui et al. 2008).

XRS spectra are collected by scanning the energy of the incident beam relative to the analyzer with a fixed elastic energy (E_0) that varies depending on analyzer setting (e.g., 9.886 keV at the BL12XU, 9.692 at the GSECARS, and 9.686 keV at the HPCAT). A linear array of multiple spherical Si(660) analyzers operating in a backscattering geometry were used for the study at the APS and an array of multiple Si(555) analyzers are used for experiments performed at BL12-XU (see Lee 2008 and references therein). The backscattered X-rays are focused into a single detector with the typical instrument energy resolution of 1.0 eV. While the resolution can be further enhanced (~ meV) for verification of detailed edge features (or probing of phonon dynamics of solids) (e.g., by implementing spectrometer optics utilizing the higher-order asymmetric Bragg back scattering optics; Shvyd'ko et al. 2006; Stetsko et al. 2011), the ~1 eV resolution is adequate for revealing many major *K*-edge features in the XRS spectra for crystalline and amorphous oxides and their shifts as a function of pressure and momentum transfer.

The X-ray Raman scattering signals are collected at varying scattering angles, but typically ~15-30° for high pressure experiments. The X-ray beam size (FWHM) varies but is typically ~60 μm (W) × 20 μm (H) at the GSECARS and HPCAT and 20 μm (W) × 20 μm (H) at the BL12-XU. Raw XRS spectra are background-subtracted, and most spectra are normalized to the continuum energy tail (see section "*Pressure-Induced Structural Changes in Crystalline and Amorphous Earth Materials: Insights from X-Ray Raman Scattering*" below). In addition, by comparing the spectra from different beam lines, the uncertainty in the edge energy of the spectra can be identified and is usually less than 0.4 eV: this aspect has been discussed in the recent manuscript (Lee et al. 2008b, supplementary information). The pressure uncertainties and the pressure gradient across the sample can be obtained from multiple measurements from the ruby spheres before and after the X-ray measurements.

PRESSURE-INDUCED STRUCTURAL CHANGES IN CRYSTALLINE AND AMORPHOUS EARTH MATERIALS: INSIGHTS FROM X-RAY RAMAN SCATTERING

Recent experimental results utilizing multi-edge, multi-element XRS spectroscopy are summarized in this section. We first present previous XRS studies involving the boron *K*-edge (~190 eV), carbon *K*-edge (~280 eV), and oxygen *K*-edge (~530 eV), which are often suitable for XRS measurements at high pressure (yielding moderate quality of signal/background ratios with ~100-300 μm X-ray attenuation length, depending on sample density). These prominent element edges are thus relatively well-understood. We then provide an overview of previous XRS studies involving other lesser known or/and poorly studied edges (and thus more difficult to probe), such as helium *K*-edge (~23 eV), lithium *K*-edge (~60 eV), and nitrogen *K*-edge (~410 eV). We also briefly mention the previous (and the new) XRS studies involving L and *M*-edges of Ca and Si in glasses. We have not attempted to provide an extensive review of all the experimental results using IXS as excellent accounts of these diverse IXS measurements of materials under compression can also be found in the reviews of Rueff and Shukla (2010) and Schulke (2007).

EBSCOhost - printed on 2/13/2023 5:26 AM via . All use subject to https://www.ebsco.com/terms-of-use

Application of *K*-edge XRS to materials under high pressure

Boron K-edge XRS study of earth materials under compression. Boron *K*-edge XRS (as well as XANES) has been one of the most effective probes for B coordination environments ($^{[3]}$B, and $^{[4]}$B) because these two distinct B coordination environments are relatively well-distinguished in the XRS spectrum: as for boron containing phases at 1 atm, previous XAS studies showed that these $^{[3]}$B (characterized with π* bonding at ~ 194 eV), and $^{[4]}$B (with features at ~ 197-200 eV) environments are well-resolved (see Fleet and Muthupari 1999, 2000 and references therein). XRS has been utilized to explore the structural details (direct and quantitative measurements of B coordination transition) of crystalline boron nitride and archetypal amorphous borates and alkali borate glasses with varying pressure up to ~ 30 GPa.

Pressure-induced bonding transitions in crystalline boron nitride (BN). BN was one of the first crystals explored using XRS at high pressure. Hexagonal boron nitride (*h*-BN) and hard cubic phase (*c*-BN) have diverse technological applications (Meng et al. 2004). Boron *K*-edge XRS spectroscopy revealed pressure-induced bonding transitions of boron and nitrogen in *h*-BN to a hexagonal close-packed wurtzite type structure (*w*-BN). The sp^2- and *p*-bonding in *h*-BN is transformed into sp^3-bonding stemming from the formation of a three-dimensional tetrahedron framework in *w*-BN (Meng et al. 2004). Figure 3 shows boron (B) *K*-edge XRS spectra for BN with varying pressure. The XRS spectra at 1 atm show the π and σ bonds characteristics of *h*-BN (as labeled). Pressure-induced changes in intensities of π* and σ* bonds (indicating the presence of π and σ bonds) were apparent. These changes show an orientation dependence, leading to the preferred orientation of *h*-BN where its *c* axis is parallel to the DAC axis. After further increase in pressure up to 14 GPa, the *w*-BN phase was formed as indicated

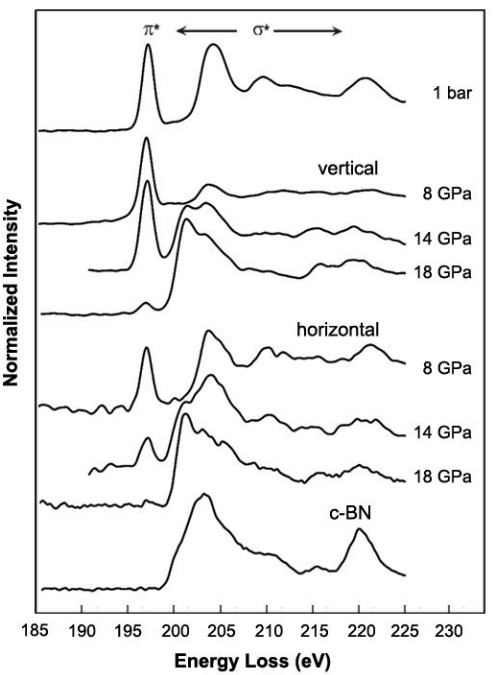


Figure 3. Boron *K*-edge XRS spectra of BN with varying pressure. The spectra are plotted as normalized scattered intensity versus energy loss (incident energy – elastic energy). The spectra were collected in both vertical and horizontal geometries to probe bonds in directions parallel and perpendicular to the *c* axis of BN (modified from Meng et al. 2004).

EBSCOhost - printed on 2/13/2023 5:26 AM via . All use subject to https://www.ebsco.com/terms-of-use

by the appearance of the new feature at ~ 196 eV in the B *K*-edge XRS spectrum. While the XRS features for *w*-BN and *c*-BN are rather similar, their relative intensities of XRS features (in the range from 194 to 200 eV and at 215 eV) are slightly distinct, indicating the difference in the distribution of electronic densities of state for each phase (Meng et al. 2004).

Pressure-induced changes in boron coordination environments in pure borate (B_2O_3) glasses at high pressure. While the structure of borate glasses at 1 atm is relatively well known mainly from ^{11}B NMR (see Eckert 1992 and the references therein), pressure-induced changes in coordination for low-*z* glasses, including borates, remain unsolved in modern physical chemistry, condensed matter physics, glass sciences, and earth science due to the lack of suitable experimental probes. Pure borate glasses have fundamental importance as prototypical glass formers (along with silica). Pressure-induced coordination transformation of the B cations can provide insights into structural evolution of multicomponent covalent oxide glasses with pressure (Wolf and McMillan 1995; Yarger et al. 1995; Poe et al. 1997).

Figure 4 (top) shows the boron *K*-edge XRS spectra for B_2O_3 and $Na_2B_4O_7$ glasses at 1 atm: Note that at 1 atm all boron atoms in the B_2O_3 glass are $^{[3]}$B and $Na_2B_4O_7$ glass consists of ~ 45% of $^{[4]}$B) and thus we show the XRS spectrum for $Na_2B_4O_7$ glass to show the spectral features for $^{[4]}$B. The feature at 194 eV corresponds to the transition of a core boron 1*s* election to an unoccupied boron antibonding $2p_z$ orbital (labeled π*) and is due to three-coordinated boron ($^{[3]}$B) in the glasses. The broader features centered at ~203 eV corresponds predominantly to a transition from a B 1*s* to unoccupied B-O σ* antibonding orbital (labeled σ*) and is also associated with $^{[3]}$B (Schwarz et al. 1983). The XRS spectrum for $Na_2B_4O_7$ glass (with ~ 45% of $^{[4]}$B) show another σ* feature around at 198-200 eV that corresponds to a 1s to 2*p*/2*s* σ* antibonding orbital transition in four-coordinated boron ($^{[4]}$B) (Fleet and Muthupari 1999, 2000). The decrease in π* intensity for $Na_2B_4O_7$ glass (compared with that of B_2O_3 glass) indicates an increase in

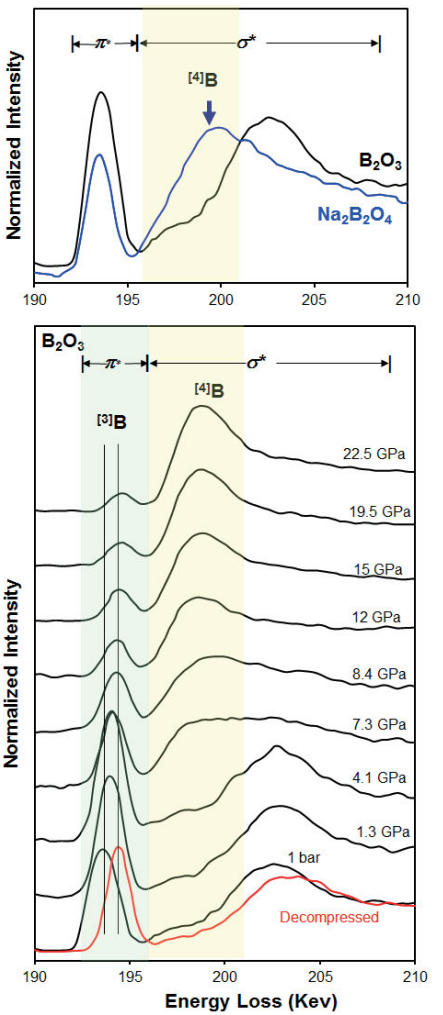


Figure 4. (*top*) Boron *K*-edge XRS spectra for B_2O_3 (black) and $Na_2B_4O_7$ (blue) glass at 1 atm [plotted as Normalized scattered intensity vs. Energy loss (incident energy – elastic energy of 9.692 keV)] (modified from Lee et al. 2005). (*bottom*) Boron *K*-edge XRS spectra for B_2O_3 glass at pressures ranging from 1 bar to 22.5 GPa. Some pressure uncertainty exists due to the slow equilibration of *v*-B_2O_3 after each pressure change. The experiment was repeated with different DACs and observed similar pressure response was observed, suggesting that this behavior is intrinsic to the sample, as reported previously (modified from Lee et al. 2005).

EBSCOhost - printed on 2/13/2023 5:26 AM via . All use subject to https://www.ebsco.com/terms-of-use

$^{[4]}$B bonds and is consistent with NMR measurements and XANES study of *v*-B_2O_3 (Fleet and Muthupari 1999, 2000).

Figure 4 (bottom) shows boron *K*-edge XRS spectra for B_2O_3 glass under varying pressures (Lee 2005). XRS spectra show negligible changes at pressures up to ~4.1 GPa. At 7.3 GPa, π* intensity (due to $^{[3]}$B) drops drastically and the σ* component due to $^{[4]}$B (~198-200 eV) increases. With a further increase in pressure up to 22.5 GPa, most of the $^{[3]}$B is transformed into the $^{[4]}$B. While the coordination transformation is reversible, the energy shift of the π* peak remains upon decompression, implying permanent densification associated with boron topology due to a decrease in boroxol ring fraction (tri-membered planar borate ring) (see Lee 2005, 2010 and references therein). The XRS results for B_2O_3 glass provided the first '*in situ*' and unambiguous experimental evidence of a reversible coordination transformation along with an irreversible topological densification in borate glasses.

Pressure-induced changes in boron coordination environments in alkali borate glasses at high pressure: implications for densification mechanisms of oxide glasses. The cation field strength (i.e., charge/ionic radii) of network-modifying cations (e.g., Li^+, Na^+) affects the thermodynamic properties and viscosity of silicates melts at both ambient and high pressure (e.g., Navrotsky 1995). The effect of cation field strength on the densification in oxide glasses has been recently explored using the XRS technique. The XRS results revealed the marked difference in densification behavior in borate glasses with varying cation field strength: B *K*-edge XRS spectra for borate and alkali borate glasses ($Li_2B_4O_7$ and $Na_2B_4O_7$) were probed at high pressure up to 30 GPa with an aim to provide pressure-induced coordination transformation from $^{[3]}$B to $^{[4]}$B (Lee et al. 2007, 2008a). Figure 5A presents the B *K*-edge XRS spectra for $Li_2B_4O_7$ glasses with varying pressures up to 30 GPa. With increasing pressure, the σ* ($^{[4]}$B) feature near 198-200 eV increases while π* intensity ($^{[3]}$B) gradually decreases. Figure 5B present the XRS spectra of $Na_2B_4O_7$ glasses with varying pressure. A π* feature at approximately 194 eV ($^{[3]}$B) decreases while the σ* feature associated with $^{[4]}$B increases, consistent with the trends reported for pure borate and Li-borate glasses (Lee et al. 2005, 2007).

Quantification of boron coordination environments. The quantitative fractions of boron coordination states provide information necessary to establish effect of pressure on the bonding transitions. As the quantification of the spectra can be of practical importance, the procedure of yielding quantitative $^{[3]}$B fraction is given below (Fig. 6): the raw XRS spectra were background-subtracted and then were normalized to the continuum energy tail above approximately 210 eV, leading to spectra with a plateau above approximately 205 eV (Fig. 6, blue spectrum). Then, linear backgrounds extending from a π* peak (around 193-194 eV) to 210 eV were subtracted as suggested by previous B *K*-edge XANES studies (e.g., Fleet and Muthupari 1999, 2000) to obtain quantitative fraction of boron coordination environments. Figure 6 presents the XRS spectra before and after linear background subtraction for the quantification of $X(^{[3]}B_{sample})$ in the borate glasses studied here. The total intensity of the spectra [*J*(total)] from 192 eV to 210 eV was subsequently obtained. Then, the spectral intensity for π* feature [*J*(π*)] was obtained by fitting it with a single Gaussian function. The ratio between [*J*(π*)] and [J(total)] was then calculated [i.e., *J*(π*)/*J*(total)]. The ratio was further normalized to the ratio of spectral intensity in the B *K*-edge of reference material with 100% $^{[3]}$B, i.e., pure B_2O_3 glass at 1 atm [$[J(\pi^*)/J(\text{total})]_{\text{pure } B_2O_3 \text{ glass}}$]. Its estimated value is 0.354, which is in excellent agreement with the average value predicted from the borate crystals with only $^{[3]}$B (0.354, Garvie et al. 1995). The mole fraction of $^{[3]}$B in sample borate glass [$X(^{[3]}B)$] is thus calculated from the following relation:

$$X\left(^{[3]}B_{sample}\right) = \frac{\left[J(\pi^*)/J(total)\right]_{sample}}{\left[J(\pi^*)/J(total)\right]_{pure\ B_2O_3\ glass}} \quad (7)$$

EBSCOhost - printed on 2/13/2023 5:26 AM via . All use subject to https://www.ebsco.com/terms-of-use

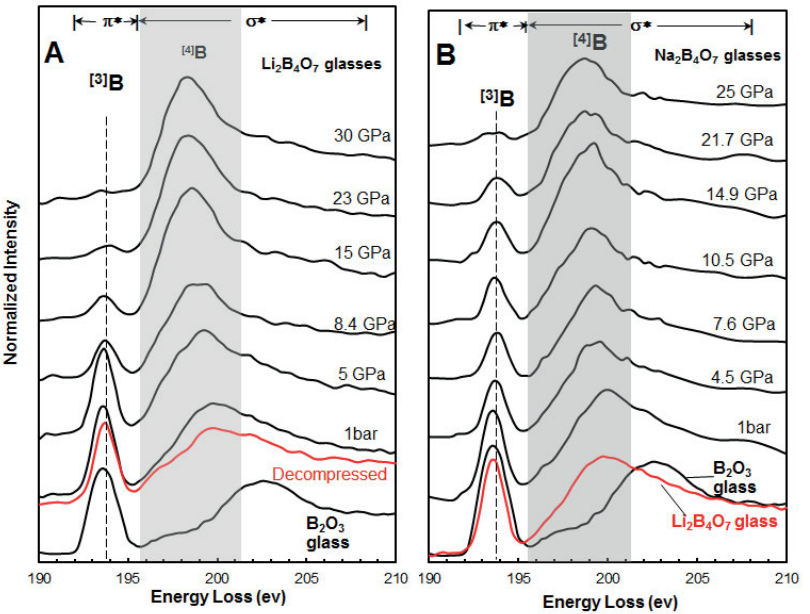


Figure 5. (A) Boron *K*-edge XRS spectra for $Li_2B_4O_7$ glass and B_2O_3 glass (*bottom*) at pressures ranging from 1 bar to 30 GPa as labeled. Thin line refers to XRS spectra for $Li_2B_4O_7$ glass decompressed to 1 atm from 30 GPa. The spectra are plotted as normalized scattered intensity vs. energy loss (incident energy – elastic energy (9.687 keV) (Modified from Lee et al. 2007). The inelastic X-rays were collected with a linear array of six spherical Si(660) analyzers operating in a backscattering geometry, and at an angle of 30° (for ambient condition) and 18° (for high-pressure experiment) off the incident beam direction. The monochromatic X-rays produced by a cryogenically cooled double crystal Si(111) monochromator were focused to 20 × 20 μm (H × V) with a large KB mirror pair. While previous studies of B_2O_3 glasses high pressure reported that pressure response of cold pressed glass appeared to be slow, necessitating the equilibration time of about several hours (Wright et al. 2000; Lee et al. 2005), this slow pressure equilibration was not observed for Li-borate glasses. (B) Boron *K*-edge X-ray Raman scattering spectra of Na-diborate ($Na_2B_4O_7$) glasses with varying pressure, as labeled. The spectra are plotted as the normalized scattered intensity vs. the energy loss (incident energy–elastic energy) (modified from Lee et al. 2008).

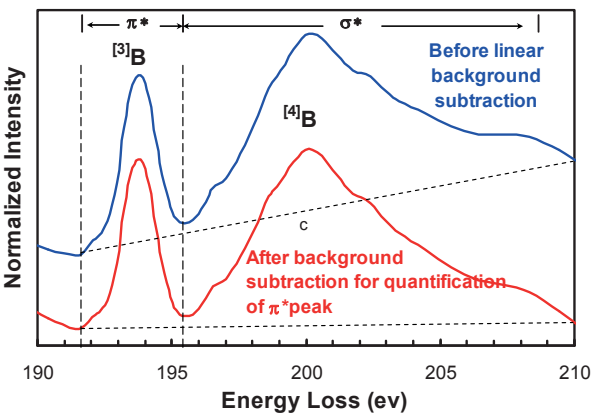


Figure 6. Quantification of boron *K*-edge XRS spectrum for Na-diborate ($Na_2B_4O_7$) glass at 1 atm (blue spectrum). Linear background subtracted spectrum for the Na-borate glasses for quantification of π* was also shown (red spectrum).

EBSCOhost - printed on 2/13/2023 5:26 AM via . All use subject to https://www.ebsco.com/terms-of-use

The robustness of the above method has been tested in previous studies (e.g., Garvie et al. 1993; Sauer et al. 1993), although it could somewhat overestimate $^{[3]}$B at low concentrations and may underestimate it at high concentrations. Furthermore, the $^{[3]}$B fractions in Na- and Li-diborate glasses at 1 atm (approximately 50%) are rather consistent with predicted fraction from B-11 NMR (about 55%). Whereas slightly better agreement (3-4 % deviation from NMR) can be reached by extending the spectral range above 210 eV as suggested by the earlier quantification of $^{[3]}$B fraction in borosilicate glasses for larger Na_2O/B_2O_3 ratio (> 1) (Fleet and Muthupari 1999), the $\left[J(\pi^*)/J(total)\right]_{pure\ B_2O_3\ glass}$ decreases with extension of spectral range and it further deviates from 0.354. This suggests that the spectral intensity up to 210 eV is reasonable approximation for the quantification of $^{[3]}$B fraction ($X^{[3]}B$). We note that upon calibration of $^{[3]}$B fraction based on the above procedure, $^{[4]}$B fraction ($X^{[4]}B$) is simultaneously calibrated as a function of concentration and pressure because of constraints in the mole fractions of these two species (i.e., $X^{[4]}B = 1 - X^{[3]}B$). Uncertainty in the current method may result from the absence of a high pressure borate standard with known $^{[3]}$B fraction.

Figure 7 shows the variation in the $^{[3]}$B fraction in alkali borate glasses with pressure (Lee et al. 2007, 2008a). The pressure-induced boron coordination transformation from $^{[3]}$B to $^{[4]}$B in Na-diborate glass (blue line) is *linear* with pressure: $^{[3]}$B proportion in Na-borate glasses (blue line) decreases with pressure from ~ 47 ± 4% (at 1 atm) to 16% ± 4% at 25 GPa. The results for Li-borate glasses (red line) show a *nonlinear* coordination transformation with *multiple* $(\partial^{[3]}B/\partial P)_T$. Pure borate and Li-borate glasses show three distinct regions of $(\partial^{[3]}B/\partial P)_T$ values: in low-pressure ranges (I) $(\partial^{[4]}B/\partial P)_T$ is the smallest. In the intermediate-pressure range (II) a dramatic coordination changes (and thus largest $(\partial^{[4]}B/\partial P)_T$) are observed. With further increases in pressure [range (III)], a considerably smaller $(\partial^{[4]}B/\partial P)_T$ were observed (Lee et al. 2007, 2008a). The observed trends demonstrate the effect of cation field strength (in particular, ionic radii) on the densification behavior of borates (Lee et al. 2008a). While the small ionic radii of Li^+ (0.76 Å) may not alter the densification mechanisms observed for pure borate glasses, the larger ionic radii of Na^+ (1.02 Å) in borates significantly affect the structural transition with pressure. $(\partial^{[4]}B/\partial P)_T$ may be regarded as the measure of an energy barrier for the boron coordination transformation. On the basis of this premise, pure and Li-borate glasses have at least three distinct energy barriers for coordination transformation and thus multiple densification mechanisms. For Na-borate glasses, the change is more gradual with a single transformation energy barrier for boron coordination transformation (Lee et al. 2008a).

A conceptual model was introduced to account for the observed trends, utilizing pressure flexibility (the resistance to structural changes with increased pressurization) defined by the variance of the ratio of energy difference between high and low pressure states to its pressure gradient (see Lee et al. 2008a and references therein). It should also

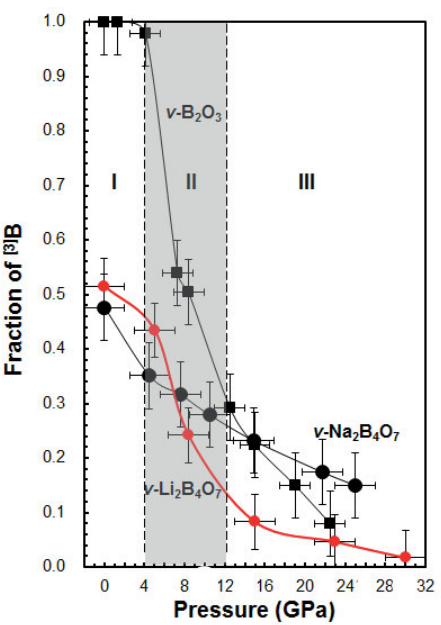


Figure 7. Pressure dependence of the $^{[3]}$B fraction for $Na_2B_4O_7$ glass and $Li_2B_4O_7$ glass. The black dashed lines for I, II, and III represent distinct pressure ranges with varying $(\partial^{[4]}B/\partial P)_T$ values (modified from Lee et al. 2008).

EBSCOhost - printed on 2/13/2023 5:26 AM via . All use subject to https://www.ebsco.com/terms-of-use

be mentioned that before the first application of X-ray Raman scattering technique, little was known about the structure of borate glasses at high pressure. However, the progress in these techniques make borate glasses one of only a few model oxide glasses in which detailed densification mechanisms have been established (Lee et al. 2008a). We believe that the aforementioned model can be applied to diverse glass forming liquids with varying degree of fragility.

Oxygen K-edge XRS studies of earth materials under pressure. The O *K*-edge XRS (and thus XAS) features of oxides provide the electronic structure around oxygen from the information of the unoccupied oxygen 2*p*-state, and thus detailed oxygen coordination environments (de Groot 2001). Previous O-K edge XANES studies have shown that the O *K*-edge features (~0.5-1 eV) depend on local structures and chemical compositions, and overall topology of cations around the oxygen (e.g., Si-O and O-O bond lengths, oxygen coordination environments, and Si-O-Si bond angles) (Ching and Rulis 2008 and references therein). The previous studies have also shown that the O *K*-edge is useful for probing the pressure-induced changes in local electronic structures in crystalline oxides at high pressure (Lee et al. 2008b). For example, oxygen *K*-edge X-ray Raman spectra for SiO_2 and $MgSiO_3$ polymorphs and amorphous phases show characteristic *K*-edge features stemming from their local atomic configurations (corner sharing, edge-sharing, and Si coordination number) and topology (bond angle and length) around oxygen (Lin 2007; Lee et al. 2008b; Fukui et al. 2009a; Yi and Lee 2012).

Oxygen *K*-edge XRS has also been applied to the study of fluids and non-crystalline materials, revealing the pressure-induced changes in the electron bonding transitions in glasses (SiO_2, B_2O_3, GeO_2, $MgSiO_3$), H_2O, and O_2 phases at high pressures (Wernet et al. 2004; Lee et al. 2008b; Meng et al. 2008; Fister et al. 2009). In particular, revealing the bonding nature of H_2O polymorphs with varying pressure and temperature conditions is essential to understand their characteristic properties. Earlier XRS studies of water and related phases with varying pressure, first unveiled the utility, as well as, the capability of the technique by probing the intermediate-range structure of liquid water (Wernet et al. 2004). Additionally, O *K*-edge XRS experiments for ice phases have revealed characteristic O *K*-edge features due to their distinctive local configurations (Bergmann et al. 2002a; Cai et al. 2005; Meng et al. 2008; Fister et al. 2009): the features are also dependent on the proton positions as well as oxygen topologies. As a review of previous O *K*-edge XRS study of H_2O polymorphs can be found elsewhere (e.g., Fister et al. 2009), these phases will not be discussed here. Other phases are discussed in the following section. Additionally, the X-ray induced dissociation of H_2O phase under pressure is briefly mentioned (Mao et al. 2006).

Pressure-induced electron bonding transitions in dense oxygen. O *K*-edge XRS studies of O_2 polymorphs at high pressure showed the pressure-induced bonding mechanisms in the dense fluid (i.e., intermolecular bonding) and molecular solids (i.e., intercluster bonding) (Meng et al. 2008). Figure 8 presents O *K*-edge XRS spectra for oxygen in dense fluid and solid β-, δ-, and ε-phases up to 38 GPa at room temperature. The peak position of gas-phase O_2 is schematically illustrated (a π* peak at 530.8 eV and two weak

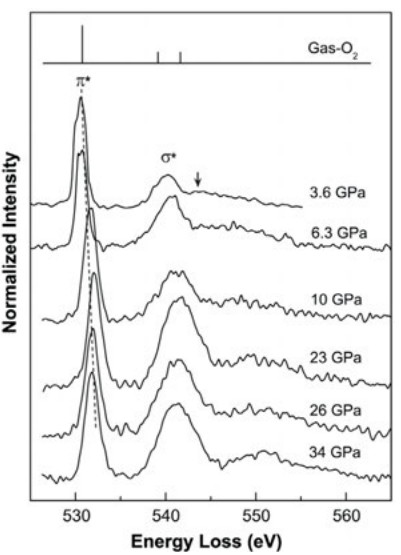


Figure 8. Oxygen *K*-edge XRS spectra for oxygen in dense fluid and solid β-, δ-, and ε-phases up to 38 GPa at room temperature (modified from Meng et al. 2009).

EBSCOhost - printed on 2/13/2023 5:26 AM via . All use subject to https://www.ebsco.com/terms-of-use

σ_u* peaks at 539.2 eV and 541.7 eV). Additionally, the intensity of the second σ* feature of fluid-O_2 at 3.6 GPa is smaller than those of the gas phase. The peak width of the second peak (arrow) is also broadened upon pressurization, indicating a broadening of the Rydberg states in the condensed fluid phase. The XRS spectra for high-pressure oxygen phases show similar spectral features (π* and σ*). Below 10 GPa, the σ* edge peak position of the dense fluid phase gradually moves to higher energy while the π* peak energy remains constant up to 10 GPa. Upon transition to the ε-phase at 10 GPa, a ~1 eV shift in the π* peak is observed. With further increase in pressure from 10 to 38 GPa, both π* and σ* transition energies show slight but gradual increases (and then decrease) with pressure. The relative intensity of the π* feature decreases with pressure for low pressure phases while it does not change much for the ε-phase (see Meng et al. 2008 for further discussion). At low pressure, below 10 GPa, the results indicate that densification of O_2 molecules enhances intermolecular interactions, leading to π orbital delocalization. The ε-phase consists of $(O_2)_4$ clusters and an increase in interactions between $(O_2)_4$ clusters in the ε-phase leads to stronger intercluster bonding with increasing pressure (Meng et al. 2008).

X-ray–induced dissociation of H_2O and formation of an O_2-H_2 alloy at high pressure. The XRS technique requires long exposure to moderately high energy (~10-keV) X-ray radiation (up to several days). X-ray radiation of a sample at high pressure, if the absorption conditions are met, can often induce the dissociation of molecules. Recent O *K*-edge XRS spectra of H_2O have revealed the X-ray radiation- and pressure-induced dissociation of H_2O polymorphs: ice VII was converted into a molecular alloy of O_2 and H_2 (Fig. 9) (Mao et al. 2006). The O *K*-edge XRS spectra for dense water below 0.9 GPa, ice VI between 1 and 2 GPa, and ice VII just above 2 GPa show characteristic peaks at ~ 540 eV. At higher pressures above 2.5 GPa, a sharp peak at 530 eV is observed. The peaks are due to O–O π∗ bonding in O_2 molecule, indicating X-ray-induced dissociation of H_2O molecules. The peak intensity grew with increasing time of exposure to the incident X-ray beam of ~10 keV and the change is apparently irreversible. The authors pointed out that the X-ray-induced dissociation in ice VII was most effective with X-ray

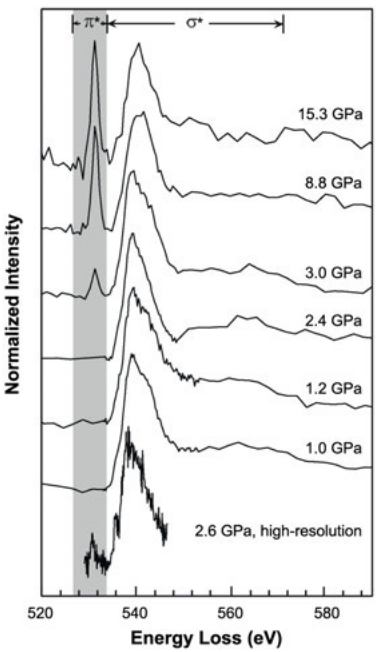


Figure 9. Oxygen *K*-edge XRS spectra of H_2O at high pressure after 12 hours of X-ray irradiation. The spectra are plotted as the normalized scattered intensity vs. the energy loss (incident energy–elastic energy). The bottom spectrum was collected at BL12XU, SPring-8 (9.886-keV X-ray radiation with high-energy resolution of 300 meV). The XRS spectra for H_2O collected at 1.0, 1.2, 2.4, 3.0, 8.8, and 15.3 GPa were collected with X-ray radiation elastic energy of 9.687 keV at beamline 13-IDC of the GSECARS, Advanced Photon Source with resolution of 1 eV (modified from Mao et al. 2006).

EBSCOhost - printed on 2/13/2023 5:26 AM via . All use subject to https://www.ebsco.com/terms-of-use

radiation energy of ~ 10 keV with a low absorbance Be gasket while at higher energy radiation (e.g., 30 keV) through the diamond anvil did not induce the dissociation (Mao et al. 2006).

Oxygen K-edge XRS study of archetypal oxide glasses (SiO_2, GeO_2, and B_2O_3) at high pressure. The oxygen configurations in amorphous oxides at high pressure can be directly probed using O *K*-edge XRS. The formation of highly coordinated framework cations (e.g., $^{[5,6]}$Si, $^{[5,6]}$Ge, $^{[4]}$B) in the fully polymerized prototypical single component oxide glasses such as SiO_2, GeO_2, and B_2O_3 glasses should be accompanied by the formation of the triply coordinated oxygen ($^{[3]}$O) (here we used the term "oxygen tricluster" for the triply coordinated oxygen as expected from the compositions, Lee et al. 2008b). Formation of oxygen triclusters has been suggested to be a dominant factor affecting the melt properties at ambient and high pressure (Angell et al. 1982; Diefenbacher et al. 1998; Stebbins and Xu 1997).

- **SiO_2.** O *K*-edge XRS feature at 543 eV for SiO_2 glass at 39 GPa has been interpreted as the formation of stishovite-like $^{[6]}$Si in SiO_2 glass at high pressures (Lin et al. 2007). The coordination transformation of Si in the fully polymerized SiO_2 glass is inevitably resulting in the formation of oxygen atoms that are triply coordinated by $^{[5,6]}$Si. The edge feature at 543 eV could thus result from the formation of the triply coordinated oxygen.

- **B_2O_3.** The change in pressure-induced boron coordination also leads to a variation of oxygen environments with pressure (Lee et al. 2005). Figure 10 shows the oxygen *K*-edge XRS spectra for *v*-B_2O_3 at 1 atm and 8.4 GPa where a decrease in sharp features at 536 eV and an increase in σ* (543 eV) with broadening of the feature were observed. This change is due to the fact that unpaired *p* orbitals in oxygen contribute to form $^{[4]}$B by forming a σ bond with p_z in the $^{[3]}$B with increasing pressure. Formation of $^{[4]}$B at high pressure leads to decrease in the fraction of boroxol rings content and it is likely due to be accompanied by the formation of peculiar oxygen environment, with oxygen triply coordinated by three $^{[4]}$B (Lee et al. 2005).

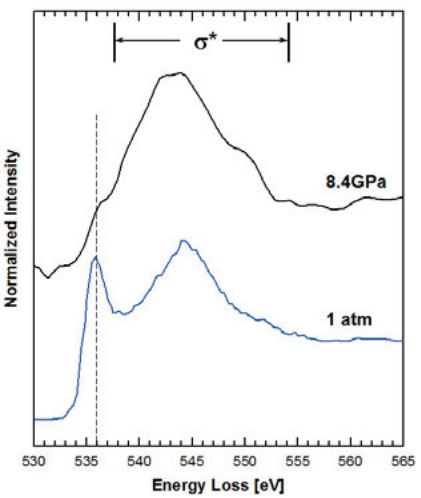


Figure 10. Oxygen *K*-edge XRS spectra for B_2O_3 glasses at 1 atm and 8.4 GPa. (Modified from Lee et al. 2004). The spectra are plotted as the normalized scattered intensity vs. the energy loss (incident energy–elastic energy).

- **GeO_2.** GeO_2 glass at high pressure has been recently studied with O *K*-edge XRS (current study and Lelong et al. 2012). While GeO_2 is isochemical to SiO_2 glass, the GeO_2 glass is more compressible (i.e., a larger compressibility) than SiO_2 glass and thus it show changes in short-range structure at much lower pressure ranges (see Micoulaut et al. 2006 and references therein). The previous XRS spectra exhibit characteristic pressure-induced changes in the O *K*-edge feature with double peaks (similar to that of rutile- type GeO_2 phase) (Lelong et al. 2012). On the basis of XRS studies of crystalline polymorphs with various Ge coordination states, the authors were able to obtain detailed Ge coordination environments ($^{[4.5.6]}$Ge) in GeO_2 glasses with pressure. Figure 11 shows the oxygen *K*-edge XRS spectra for GeO_2 glasses at 1 atm and 15 GPa An increase in the σ* region at ~544 eV is observed with pressure, consistent with those for SiO_2 glass under pressure at ~40 GPa. The fea-

EBSCOhost - printed on 2/13/2023 5:26 AM via . All use subject to https://www.ebsco.com/terms-of-use

ture could stem from the formation of highly coordinated Ge in the glasses and thus triply coordinated oxygen (which results from the formation of $^{[5.6]}$Ge).

Oxygen K-edge XRS study of crystalline $MgSiO_3$ polymorphs and $MgSiO_3$ glasses at high pressure. Crystalline and non-crystalline $MgSiO_3$ at high pressure have strong geophysical and geochemical implications for the mantle minerals and melts in earth and planetary interiors Knowledge of the electronic and atomic structure of amorphous and crystalline $MgSiO_3$ polymorphs is essential to understand their elasticity, thermodynamic and transport properties in the mantle (e.g., Hemley 1998; Price 2007 and references therein). The potential presence of silicate melts at the top of the transition zone and in the core-mantle boundary has been suggested and it could have significant influences on the dynamics and properties of Earth's interior (Revenaugh and Sipkin 1994; Song et al. 2004; Caracas and Cohen 2006; Sakamaki et al. 2006; Agee 2008). $MgSiO_3$-rich silicate melts were among the primary components of the early magma ocean. Despite essential roles of silicate melts in many geophysical and geochemical problems, little is known about the nature of bonding transitions in $MgSiO_3$ melts under the conditions of Earth's interior. O *K*-edge XRS studies of $MgSiO_3$ glass at high pressure up to 40 GPa suggested the formation of oxygen triclusters (oxygen coordinated with three Si frameworks; $^{[3]}$O) above 20 GPa in $MgSiO_3$ glass (Lee et al. 2008b).

Figure 12 shows the O *K*-edge spectra of $MgSiO_3$ glass with a dominant feature at 538-539 eV which show negligible changes in the pressure range between 1 atm and ~ 12 GPa (Lee et al. 2008b). Above 20 GPa, the spectra show a distinct feature at around 544-545 eV, wherein the spectral features gradually shift to higher energies with increasing pressure. The occurrence of the spectral feature near 545 eV at high pressures could arise from a variety of complex pressure-induced structural changes in the $MgSiO_3$ glass, such as the formation of the $^{[3]}$O triclusters, an increase (or decrease) in the Mg-O distance, reduction in non-bridging oxygens, and formation of oxygen linking

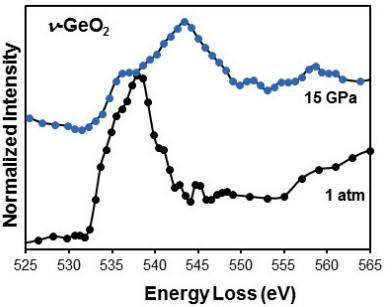


Figure 11. Oxygen *K*-edge XRS spectra for GeO_2 glasses at 1 atm and 15 GPa. The spectra are plotted as the normalized scattered intensity vs. the energy loss (incident energy–elastic energy).

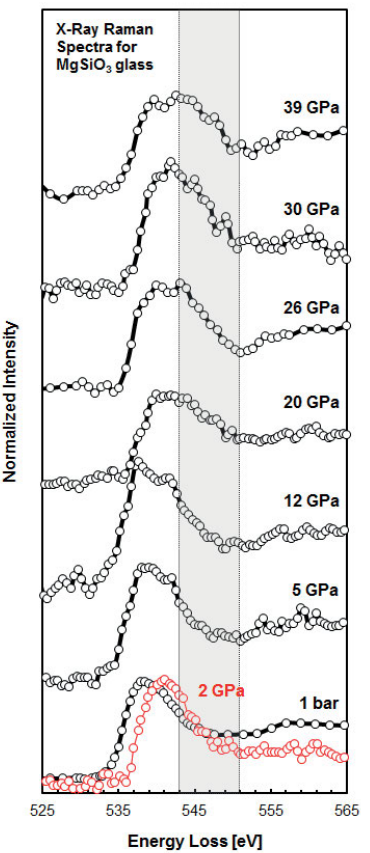


Figure 12. Oxygen *K*-edge XRS spectra for $MgSiO_3$ glasses at high pressures [plotted as normalized scattered intensity vs. energy loss (incident energy – elastic energy). Points refer to the step size of the energy scan of the experiments (modified from Lee et al. 2008).

EBSCOhost - printed on 2/13/2023 5:26 AM via . All use subject to https://www.ebsco.com/terms-of-use

$^{[4]}$Si and highly coordinated silicon such as $^{[4]}$Si-O-$^{[5,6]}$Si and $^{[6]}$Si-O-$^{[6]}$Si. However, the exact atomistic origin for the feature is not clear (see section "*Insights from quantum chemical calculations*" below). Therefore, the authors studied the oxygen *K*-edge XRS for model crystalline $MgSiO_3$ and SiO_2 phases with known short-range local structures (Fig. 13). Detailed comparison of the O *K*-edge features for amorphous SiO_2 glass at 1 atm and $MgSiO_3$ glass, as well as polymorphs at high pressure, indicate that both NBO (Mg-O-$^{[4]}$Si) and BO ($^{[4]}$Si-O-$^{[4]}$Si) have similar oxygen *K*-edge features (Lee et al. 2008b). Although recent *ab initio* calculations of O *K*-edge features of crystalline chain silicates reported that bridging oxygen (BO) and nonbridging oxygen (NBO) in crystalline chain silicates show distinct oxygen *K*-edge features (Yi and Lee 2012) and see section "*Insights from quantum chemical calculations*" below for detailed analysis of an XRS spectrum with first principle calculations and references therein), a similar distinction was not observed in the oxygen *K*-edge spectra for the silicate glasses due to their inherent topological disorder (Lin et al. 2007; Lee et al. 2008b). The spectrum for ilmenite-type $MgSiO_3$ shows distinctive features at 537 and 541 eV. This peculiar feature for the edge-sharing oxygen configuration is similar to that of stishovite (Lin et al. 2007), indicating close proximity of oxygen with its second nearest neighbors. The oxygen *K*-edge spectrum of perovskite with all corner-sharing $^{[6]}$Si-O-$^{[6]}$Si shows an increase in the intensity at approximately 543 eV, indicating pressure-induced Si coordination transformation. The feature in the quartz spectrum at around 546 eV apparently originates from its long-range periodicity (Davoli 1992).

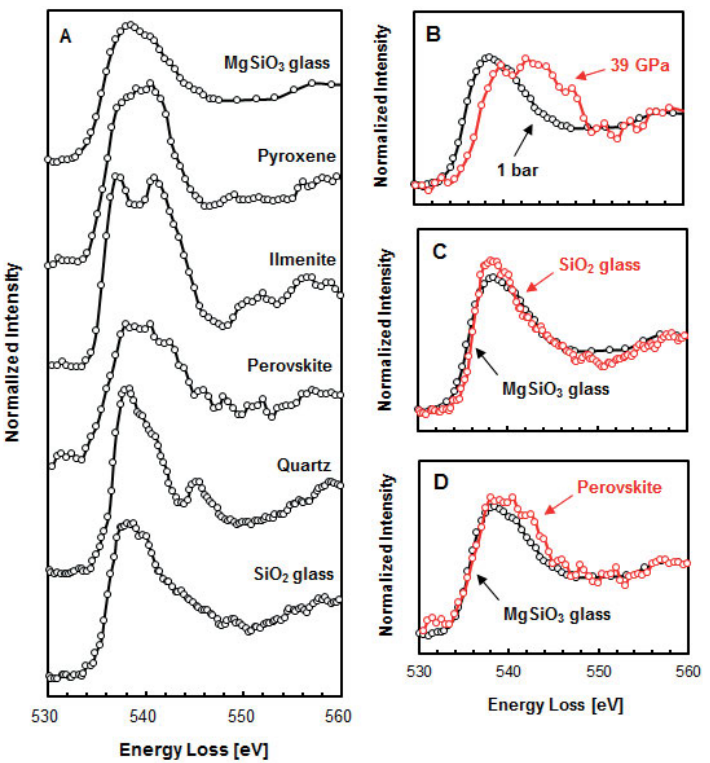


Figure 13. (A) Oxygen *K*-edge XRS spectra for crystalline and amorphous SiO_2 and $MgSiO_3$ at 1 atm and their high-pressure polymorphs. (B) Oxygen *K*-edge spectra for amorphous SiO_2 and $MgSiO_3$ at 1 atm. (C) Oxygen *K*-edge spectra for pyroxene (enstatite) and quartz. (D) Oxygen *K*-edge X-ray Raman scattering spectra for $MgSiO_3$ glass at 1 atm and perovskite (modified from Lee et al. 2008).

EBSCOhost - printed on 2/13/2023 5:26 AM via . All use subject to https://www.ebsco.com/terms-of-use

The significantly different oxygen coordination environments for perovskite and glass at 1 atm (i.e., $^{[6]}$Si-O-$^{[6]}$Si for perovskite *vs.* $^{[4]}$Si-O-$^{[4]}$Si and Mg-O-$^{[4]}$Si for $MgSiO_3$ glass at 1 atm) cannot explain the significant changes observed for the glasses at high pressures (Lee et al. 2008b). However, as similar *K*-edge features at ~ 544 eV in fully polymerized glasses have been observed and indicated that the features are due to the formation of oxygen tricluster associated with the formation of highly coordinated Si (see section "*XRS experiments*"), the oxygen *K*-edge feature at ~544 eV in the $MgSiO_3$ glass at pressures above 20 GPa may be attributed to the formation of the triply coordinated oxygen and changes in the short- to medium-range structures that are associated with the formation of the triclusters. The continuous increase in the fraction of the triclustered $MgSiO_3$ melt at high pressures and temperatures thus needs to be taken into account in future modeling of properties of mantle melts in order to improve our understanding of the microscopic origins of the anomalous pressure dependence of solubility of elements (noble gases and volatiles) into silicate melts with pressure relevant to the Earth's deep mantle and the geochemical and geophysical processes in the Earth's interior (Lee et al. 2008b). Note that there are number of other possibilities that lead to the formation of the peak at ~ 545 eV (Yi and Lee 2012): the theoretical confirmation of this proposal for the formation of oxygen tricluster in the glasses remains to be explored (see section "*Insights from quantum chemical calculations*" for further details).

Carbon K-edge XRS study

Bonding changes in compressed graphite. Carbon is one of the most important elements in the Earth system. The carbon atoms in crystalline diamond are characterized by sp^3-hybridized orbitals with all four valence electrons, forming $^{[4]}$C atoms. The carbon atoms in crystalline graphite are characterized by sp^2-hybridized orbitals forming $^{[4]}$C atoms. Amorphous carbon consists of 100% sp^2 bonding at 1 atm and shows high thermal stability and chemical durability. Carbon *K*-edge XRS has been used to explore the pressure-induced bonding transitions in graphite under compression (Mao et al. 2003). Figure 14 shows the C *K*-edge X-ray Raman scattering spectra for graphite in horizontal and vertical directions with varying pressure where detailed characterization of carbon in sp^2 and sp^3 bonding under compression are revealed. The peaks labeled π* and σ* correspond to the 1*s*-π_g* and 1*s*-σ_u* transitions, respectively. The C *K*-edge XRS spectrum for the *a*-plane showed only carbon atoms with σ-bonding regardless of pressures. The *c*-axis spectrum showed π-bonding but its intensity decreases ~50% at pressure above ~17 GPa. After the transition, the σ* bond intensity apparently increases at the expense of the π*. The results confirm that the π-bonds between graphite layers convert to σ-bonds with increasing pressure. Combined with XRD results, the results showed that at high pressure above 17 GPa, bridging carbon between graphite layers form σ-bonds, while the nonbridging

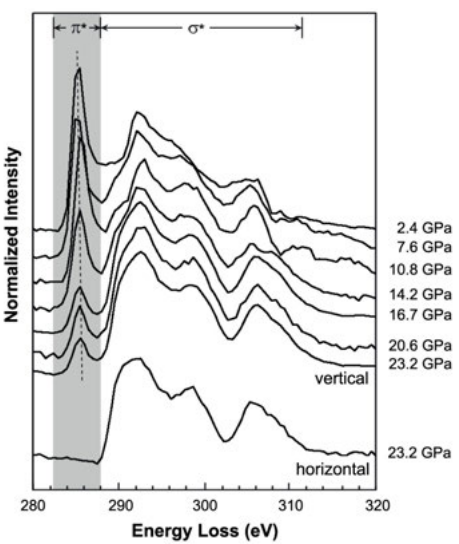


Figure 14. Carbon *K*-edge XRS spectra for graphite in horizontal and vertical directions with varying pressure. The spectrum is plotted as normalized scattered intensity vs. energy loss (incident energy – analyzer energy). The top seven spectra were collected by orienting the DAC to probe the bonds in the *c* plane (vertical direction, *c* axis parallel to the DAC axis) and the bottom spectra to probe bonds in the *a* plane (modified from Mao et al. 2003).

EBSCOhost - printed on 2/13/2023 5:26 AM via . All use subject to https://www.ebsco.com/terms-of-use

carbon remains unpaired. It was also reported that the high-pressure graphite phase is super hard, leading to a formation of indentations on the surface of diamond anvils (Mao et al. 2003).

Pressure-induced bonding changes in amorphous carbon allotrope. The pressure-induced bonding transitions in amorphous carbon forming diamond-like amorphous carbon were probed using XRS (Lin et al. 2011). Figure 15 shows C *K*-edge XRS spectra for amorphous carbon with varying pressure (compression and decompression as labeled). The peak at ~285 eV corresponds to the 1*s* to antibonding π* transition, and the broad band at higher energy features the σ* bonding (from 1*s* to σ*). Upon compression, the XRS spectra show a gradual decrease in the π* intensity and an increases in the σ* peak. The C *K*-edge XRS spectrum for the amorphous carbon at ~44 GPa shows complete σ* bonding, forming $^{[4]}$C (and thus formation of a 100% sp^3-bonded carbon). Upon decompression, the π* peak (sp^2 bonding) intensity gradually increases, indicating reversible sp^2-sp^3 bonding transitions (Lin et al. 2011).

Nitrogen K-edge XRS study. Nitrogen *K*-edge XRS has been utilized to probe pressure-induced bonding changes in BN polymorphs (Meng et al. 2004): please note that boron *K*-edge XRS study of the same materials has been discussed previously (see section "*Pressure-induced bonding transitions in crystalline boron nitride (BN)*"). Here, we discuss the pressure-induced structural transitions in the BN polymorphs using nitrogen *K*-edge. Figure 16 shows N *K*-edge XRS spectra for BN with varying pressure. The XRS spectrum at 1 atm shows the π and σ bonds, characteristic of *h*-BN. The π and σ bonds show pressure-induced changes in edge features and intensities. After further compression to 14 GPa, formation of the new features at approximately 410 eV is indicative of a phase transition to a hexagonal close-packed wurtzite structure

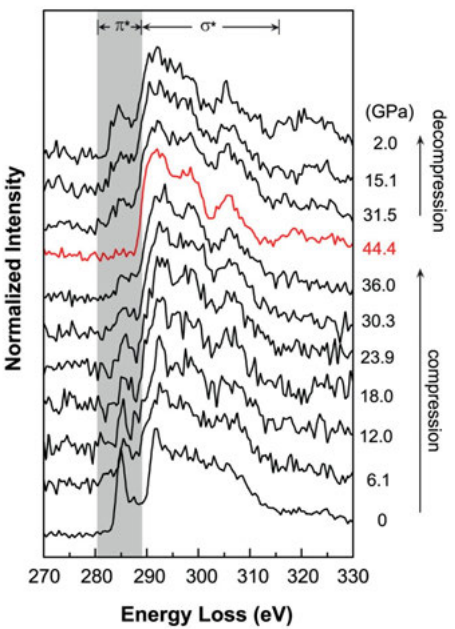


Figure 15. Carbon *K*-edge XRS spectra for amorphous carbon with varying pressure (as labeled compression and decompression). The spectra are plotted as normalized scattered intensity vs. energy loss (incident energy–analyzer elastic energy of 9.887 keV). Scattering angle of 30° was used (modified from Lin et al. 2011).

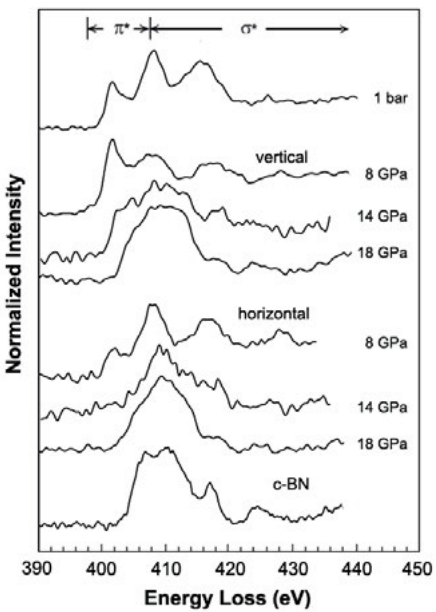


Figure 16. Nitrogen *K*-edge XRS spectra of BN with varying pressure. The spectra are plotted as normalized scattered intensity versus energy loss (incident energy – elastic energy) (modified from Meng et al. 2004).

EBSCOhost - printed on 2/13/2023 5:26 AM via . All use subject to https://www.ebsco.com/terms-of-use

(*w*-BN) (Meng et al. 2004). The overall similarity between the two electronic structures shown in the XRS spectra suggests that the bonding in *w*-BN is similar to that in *c*-BN: both *w*-BN and *c*-BN consist of sp^3 bonding between B and N. Whereas detailed interpretation of XRS features necessitates the first principle calculations of the BN polymorphs, slight difference in XRS features for *w*-BN and *c*-BN phases indicates differences in their electronic density of states: the *c*-axis bond of *w*-BN has a more ionic nature than other bonds, while all bonds in c-BN are identical (Meng et al. 2004).

Helium K-edge XRS study: electronic structure of crystalline ^{4}He at high pressures. It is challenging to obtain an XRS signal for He due to overlap with other excitations and the backgrounds in the XRS spectra. However, a recent He *K*-edge study revealed the pressure-induced bonding transition in He (Mao et al. 2010): background from Be gasket spectrum and diamond spectrum were subtracted to yield the spectra shown in the figure (Mao et al. 2010). Figure 17 shows the He *K*-edge XRS spectrum for ^{4}He with varying pressure. The edge features include an exciton peak at ~23-26 eV, a series of additional excitations and a continuum tail at 26 to 45 eV. At 11 GPa the He was compressed to form a hexagonal close-packed (hcp) He single crystal. The XRS spectrum of ^{4}He at 13.4 GPa reveals a steep edge at ~ 23.7 eV, a sharp exciton peak at ~24.4 eV, a broad series of unresolved peaks at ~27.5 eV, and a continuum at higher energy. The presence of the broad peaks at 26-45 eV suggests the existence of the Wannier exciton (weekly bound electron-hole pair), in addition to the presence of the Frenkel exciton (tightly bound electron-hole pair) (Marder 2000; Mao et al. 2010).

Lithium K-edge XRS study: Pressure-induced structural transitions in Li in silicate glasses. In addition to intrinsic disorder associated with the distribution of network formers

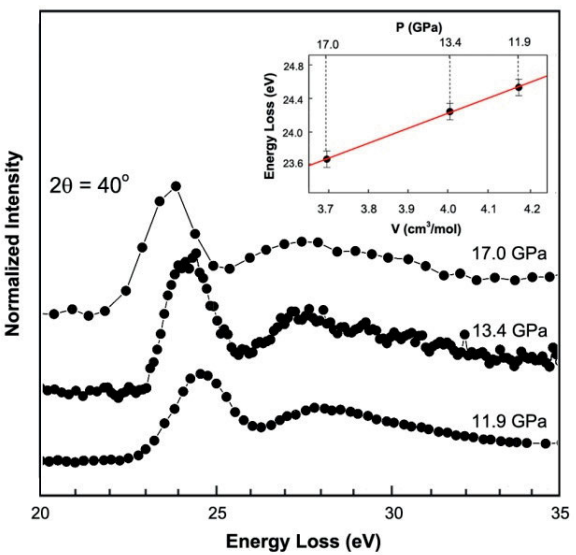


Figure 17. Helium *K*-edge XRS spectra for ^{4}He sample with varying pressure (as labeled). The spectra are plotted as normalized scattered intensity vs. energy loss (incident energy–analyzer elastic energy). To get sufficient counting statistics, the authors were able to accumulate the signal and background from ^{4}He for one month of beam time at 13ID-C of the GSECARS and 16ID-D [21] of the High Pressure Collaborative Access Team (HPCAT) at the Advanced Photon Source (APS), and the Taiwan Beamline BL12XU [20] at SPring-8, Japan. A scattering angle of 40° was used, which corresponds to momentum transfer $\boldsymbol{q}$ of 0.992, 0.998, and 0.972 for 11.9, 13.4, and 17, respectively. A panoramic DAC with large diamond anvils of 630 μm culet diameter was used. The exciton peak position with molar volume is also shown (inset) (modified from Mao et al. 2010).

EBSCOhost - printed on 2/13/2023 5:26 AM via . All use subject to https://www.ebsco.com/terms-of-use

(e.g., Si, Al, B, and Ti etc.), inherent structural disorder in the oxide glasses and melts includes topological disorder due to the distribution of cation-oxygen distance and bond angle variations involving network modifying cations (e.g., alkali and alkaline earth elements, such as Li, Na, Ca, Mg). The atomic environment of network modifying cations in oxide glasses is important for understanding transport properties including electric conductivity (Greaves and Ngai 1995; Jund et al. 2001; Lee and Stebbins 2003). Li *K*-edge studies have been utilized to probe electronic structures around Li in the crystalline oxides at 1 atm (Krisch et al. 1997; Sandi et al. 1998; Bergmann et al. 2002a; Tsuji et al. 2002). The coordination environment for Li in borate glasses has been recently studied using Li *K*-edge XRS up to 5 GPa (Lee et al. 2007).

Figure 18 presents Li *K*-edge XRS spectrum for Li-borate glasses at 5 GPa (Lee et al. 2007). The result shows XRS features similar to that at 1 atm. Note that the broad Be plasmon feature (inset), due to Be gasket used in the DAC, complicates Li *K*-edge spectrum. Nevertheless, the Be plasmon was effectively subtracted. Two weak features around 60 and 63 eV were observed. The features are similar to those reported for crystalline Li-halides and Li-silicates and are due to a transition from 1*s* core electrons to valence band free orbitals (Bergmann et al. 2002b; Tsuji et al. 2002). The Li *K*-edge XRS spectra at 1 atm and 5 GPa are rather similar as expected from the similarity in the B *K*-edge XRS spectra measured at similar pressure ranges (Lee et al. 2007).

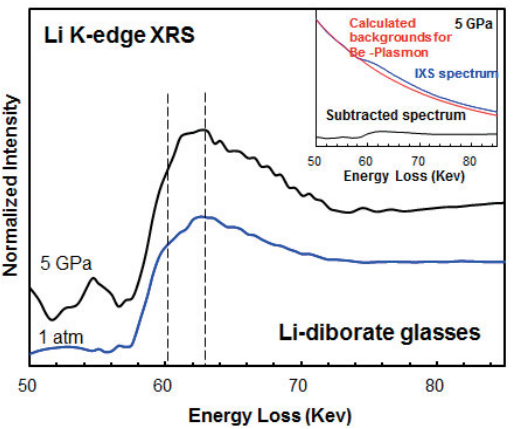


Figure 18. Lithium *K*-edge XRS spectra for Li-B_2O_3 glasses at 1 atm and 5 GPa. The inset shows the Be plasmon background subtraction methods for XRS spectra at 5 GPa: a contribution from the Be plasmon was fitted using a complex polynomial function and then subtracted from the spectrum (modified from Lee et al. 2007).

Insights from quantum chemical calculations

Experimental XRS studies have provided detailed information on pressure-induced bonding transitions in crystalline and amorphous earth materials at pressures up to ~70 GPa [e.g., 50 GPa for the O *K*-edge of SiO_2 glass (Lin et al. 2007), ~39 GPa for the O *K*-edge of $MgSiO_3$ glass (Lee et al. 2008b), ~74 GPa for the Si *L*-edge of SiO_2 glass (Fukui et al. 2008)]. The current pressure limit of ~40-70 GPa for XRS experiment (mostly limited by X-ray beam size and scattering geometry with the diamond anvil cell) poses a challenge to probing the detailed bonding environments in diverse silicate polymorphs stable above ~70 GPa. For example, because one of the important oxide phases in the Earth's mantle, $MgSiO_3$ post-perovskite (PPv) is stable near the core-mantle boundary at a pressure of ~120-135 GPa. The electronic bonding nature of the phase cannot be experimentally probed using current *in situ* high-pressure XRS experimental techniques.

For the analysis of XRS features, inputs from *ab initio* calculations (cf., Jahn and Kowalski 2014, this volume) are often necessary to establish the relationship between atomic configurations and edge features. Theoretical calculations (e.g., *ab initio* calculations) allow us to predict XRS spectra (or any core electron excitation spectroscopy, energy loss near edge spectroscopy) for crystalline oxides at high pressure, overcoming the current difficulties of *in situ* high-pressure experiments (Lin et al. 2007; Aryal et al. 2008; Meng et al. 2008; Fukui et al. 2009). Typical core electron excitation spectra (e.g., XAS, XRS, and EELS) for earth materials with low-*z* element have traditionally been calculated using multiple scattering theory. The method has been

EBSCOhost - printed on 2/13/2023 5:26 AM via . All use subject to https://www.ebsco.com/terms-of-use

useful for reproducing the core-electron excitation spectrum for high-z elements (Wu et al. 1997; Cabaret et al. 1998; Rehr and Albers 2000; Krayzman et al. 2006; Eustace et al. 2010; Jorissen and Rehr 2010; Rehr et al. 2010) but it has met with limited success for calculations of spectra involving low-z elements (e.g., see Rehr and Albers 2000, de Groot 2001 and references therein for detailed discussion as well as the previous theoretical efforts on oxides). *Ab initio DFT* theory has been effective in calculation of core-electron excitation spectrum for low-z elements such as silicate oxides (Rez et al. 1999; Mizoguchi et al. 2000; Mo and Ching 2000; Schwarz et al. 2002; Tanaka et al. 2002; Ikeno et al. 2004; Kim et al. 2005; Cabaret et al. 2007; Sakko et al. 2007, 2010; Fukui et al. 2009; McLeod et al. 2010). The core-hole effect from the 1s-orbital of oxygen needs to be taken into consideration for the calculations of XRS spectra involving low-z elements (Tamura et al. 1995; Prewitt and Downs 1998; Mizoguchi et al. 2000; Luitz et al. 2001; Hebert et al. 2003; Hebert 2007). For example, O K-edge XRS experiments for SiO_2 polymorphs were well-reproduced by the oxygen 2p-projected electronic PDOS (e.g., Fukui et al. 2009 and references therein). The theoretical implementation of full-potential linearized augmented plane wave (FP-LAPW) methods have been effective in reproducing experimental XAS (and thus XRS) spectra for metal and simple phases (Blaha 2001; Hebert et al. 2003; Hebert 2007; Jorissen 2007; Fukui et al. 2009): Note again that XAS and XRS provide similar spectra under the dipole approximation (see "*Comparison with other core-electron excitation spectroscopy and traditional experimental probes at high pressure*" section above). The O K-edge XAS spectra of crystalline GeO_2 was successfully reproduced by the calculated theoretical spectra (Cabaret et al. 2007). Recent theoretical calculations of the O K-edge XRS features of SiO_2 glass at high pressure give insights into its densification mechanisms (Wu et al. 2012). These advances have recently been applied to calculate O K-edge XRS spectra for $MgSiO_3$ perovskite and post-perovskite) and those for dense oxygen crystals. The relevant results are briefly summarized below.

The electronic origins of XRS features in the ε-phase of oxygen with pressure were explored using *ab initio* calculations (Meng et al. 2008). Figure 19 shows the calculated O K-edge XRS spectra with increasing pressures from 10 to 47 GPa (Meng et al. 2008). With increasing pressure, both π* and σ* peaks moves to higher energy, consistent with the XRS experiments (Meng et al. 2008). A continuous decrease in π* intensity in the ε-phase with

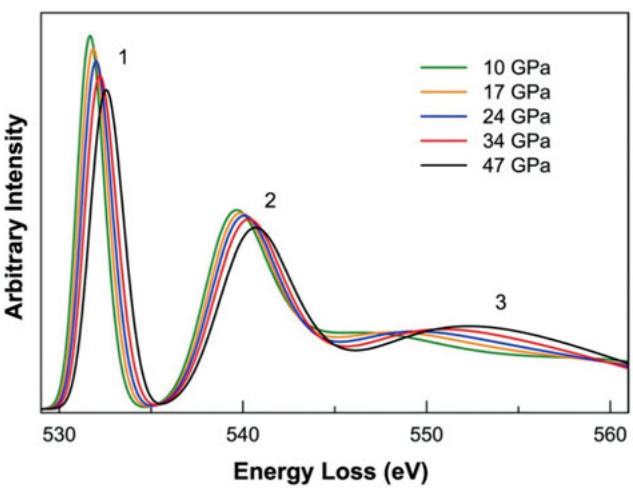


Figure 19. Calculated oxygen K-edge XRS spectra of the ε-phase with varying pressure as labeled. Peaks labeled as '1', '2', and '3' correspond to contribution from electronic transitions of 1s electron to π*, σ*, and the continuum states, respectively (modified from Meng et al. 2009).

EBSCOhost - printed on 2/13/2023 5:26 AM via . All use subject to https://www.ebsco.com/terms-of-use

pressure indicates an increase in the π orbital delocalization. The results suggest an increase in the intercluster interaction with pressure in the ε-phase. With further increase in pressure the broad feature at ~550 eV stemming from the σ*-like continuum state increases, suggesting prevalence of intercluster interaction in the ε-phase. We also note that similar *ab initio* methods have been applied to reproduce oxygen *K*-edge XRS spectra for SiO_2 glass with varying pressure. The results revealed that the pressure-induced structural transitions in Si coordination number can also affect the energy shift in the O *K*-edge XRS features (Wu et al. 2012).

Direct probing of the local electronic structure of mantle minerals, such as $MgSiO_3$ perovskite and post-perovskite, is challenging. The O *K*-edge XRS spectra for SiO_2 and $MgSiO_3$ polymorphs (i.e., α-quartz, stishovite, ortho-enstatite, ilmenite-type $MgSiO_3$, $MgSiO_3$ perovskite, and post-perovskite) were calculated based on the FP-LAPW method to achieve improved insight into the origins of distinctive O *K*-edge features for $MgSiO_3$ polymorphs from their short-range structures and topology using the Wien2k code (Blaha 2001) (see Yi and Lee 2012 for computational details). Figure 20A shows the calculated O *K*-edge XRS spectrum for $MgSiO_3$ PPv. Two crystallographically distinct oxygen sites of $MgSiO_3$ PPv are a corner-sharing oxygen atom, $^{[6]}$Si-O1-$^{[6]}$Si [O1 site], and an edge-sharing oxygen atom, $^{[6]}$Si-O2-$^{[6]}$Si [O2 site], as shown in Figure 20B. The full spectrum was calculated by combining the results from these two sites. Both the O1 and O2 sites of $MgSiO_3$ PPv yield characteristic O *K*-edge features as shown in Figure 20C. Figure 20D shows the calculated PDOS for oxygen, confirming that the oxygen 2*p*-state component contributes to the overall shape of the total O *K*-edge XRS spectrum (Yi and Lee 2012).

Figure 21 shows the calculated O *K*-edge XRS spectra for SiO_2 and $MgSiO_3$ polymorphs (Yi and Lee 2012). The calculated spectra are consistent with the experimental O *K*-edge XRS (red) spectra (Lin et al. 2007; Lee et al. 2008b) (see section "*X-ray–induced dissociation of H_2O and formation of an O_2-H_2 alloy at high pressure*" above). While future XRS experimental confirmation for $MgSiO_3$ PPv with improved X-ray optics and photon flux remains to be explored, the spectrum is expected to be similar to the calculated O *K*-edge XRS spectrum for $MgSiO_3$ PPv shown here.

The *ab initio* calculations provide crystallographic site-specific analysis of O *K*-edge features (Yi and Lee 2012). Figure 22 presents the calculated O *K*-edge XRS spectra for $MgSiO_3$ polymorphs (Yi and Lee 2012). It is clear that the O *K*-edge spectrum shift to higher energy (~ 3-4 eV) with increasing degree of densification in atomic arrangement in $MgSiO_3$ polymorphs (from enstatite to PPv) (Fig. 22A). O *K*-edge features for the corner-sharing oxygen moves to higher energy from enstatite to PPv (121 GPa) (Fig. 22B). The features are mainly affected by the silicon coordination environment, O-O proximity, and Si-O bond lengths. A peak shift for edge-sharing oxygens in ilmenite-$MgSiO_3$ and PPv is also observed (Fig. 22C). A similar trend in pressure-induced edge energy shift has been reported for simple elements (e.g., O, Ne, and Cl), solid oxygen, as well as archetypal single component oxide glasses (see section "*Oxygen K-edge XRS study of archetypal oxide glasses (SiO_2, GeO_2, and B_2O_3) at high pressure*" above) (Cruz et al. 2005; Lin 2007).

Figure 23 shows the O *K*-edge XRS spectra for $MgSiO_3$ glass at 1 atm and 39 GPa compared with the calculated O *K*-edge features for $MgSiO_3$ Pv and PPv. The O *K*-edge feature for $MgSiO_3$ glass at ~39 GPa is comparable to the changes in the O *K*-edge features of $MgSiO_3$ Pv and PPv. The spectral differences between the local oxygen configurations of $MgSiO_3$ Pv and PPv and the changes in the O *K*-edge features imply that a densification of crystalline silicates (via formation of highly coordinated Si and enhanced proximity between oxygen atoms) leads to a shift of edge features into higher energy region.

EBSCOhost - printed on 2/13/2023 5:26 AM via . All use subject to https://www.ebsco.com/terms-of-use

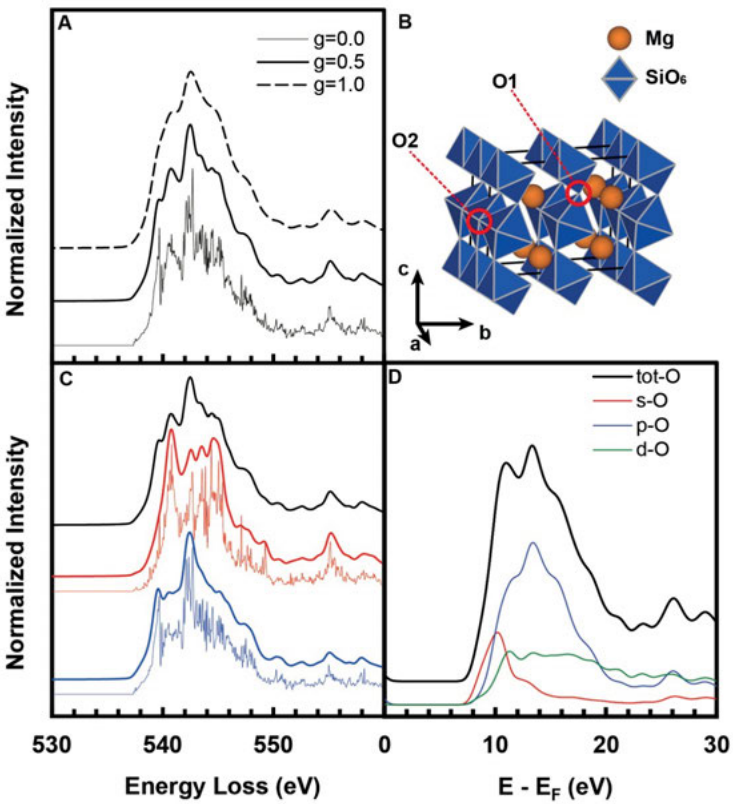


Figure 20. (A) Calculated oxygen *K*-edge XRS spectra for $MgSiO_3$ Post-Perovskite (PPv); the spectrometer broadening parameters (g) for Gaussian broadening FWHM are 0.0 eV (thin black solid), 0.5 eV (black solid), and 1.0 eV (black dashed). (B) The crystal structure of $MgSiO_3$ PPv and the crystallographically distinct oxygen sites (O1, corner-sharing oxygen; O2, edge-sharing oxygen). (C) O *K*-edge XRS spectra for $MgSiO_3$ PPv for each oxygen site and total O *K*-edge XRS spectrum (black solid), corner-sharing oxygen (O1, red solid), and edge-sharing oxygen (O2, blue solid). The Gaussian broadening (g) FWHM of 0.5 eV is used. (D) PDOS for each orbital of $MgSiO_3$ PPv. The Gaussian broadening FWHM for PDOS is 0.04 Ry (red solid, oxygen *s*-state; blue solid, oxygen *p*-state; green solid, oxygen *d*-state; black solid, total DOS of oxygen); the crystal structure of $MgSiO_3$ PPv is shown in the inset (Modified from Yi and Lee 2012). Quantum chemical calculations were performed using the Wien2k code, which utilizes a full-potential linear augmented plane wave plus local orbital methods (FP-LAPW+lo) (Blaha 2001). For computational details see Yi and Lee (2012).

REMAINING CHALLENGES AND OUTLOOK: APPLICATIONS OF NEW *K*-, *L*-, *M*-EDGE XRS, XRS WITH MOMENTUM TRANSFER, *IN SITU* HIGH-TEMPERATURE AND HIGH-PRESSURE XRS STUDY FOR MULTI-COMPONENTS GLASSES

In the previous sections, we have provided a summary of previous XRS studies on several popular *K*-edges (e.g., carbon, nitrogen, boron, oxygen) as well as less utilized *K*-edges (e.g., helium and lithium). Here, we briefly discuss additional XRS studies utilizing *L*- and *M*-edges for loosely bound electrons, XRS studies with momentum transfer, and XRS experiment involving multi-component oxide glasses. We then discuss other current and challenges and future studies.

EBSCOhost - printed on 2/13/2023 5:26 AM via . All use subject to https://www.ebsco.com/terms-of-use

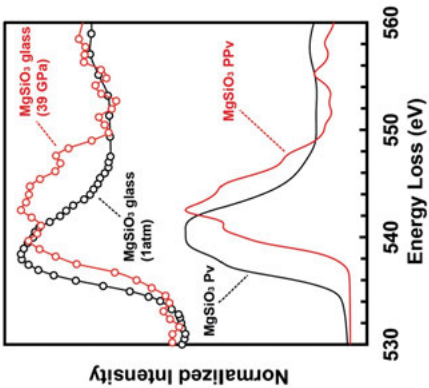


Figure 23 (***above***). Oxygen *K*-edge XRS spectra for $MgSiO_3$ glass at 1 atm and 39 GPa, and for $MgSiO_3$ perovskite and post-perovskite as labeled. The Gaussian broadening FWHM for the calculated O *K*-edge ELNES spectra is 1.0 eV (modified from Yi and Lee 2012).

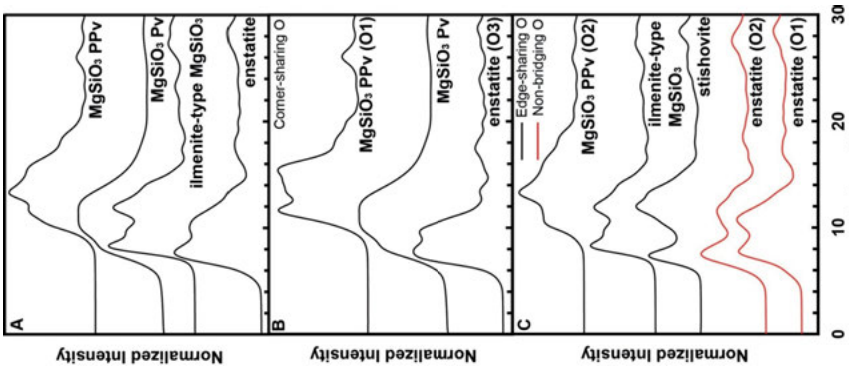
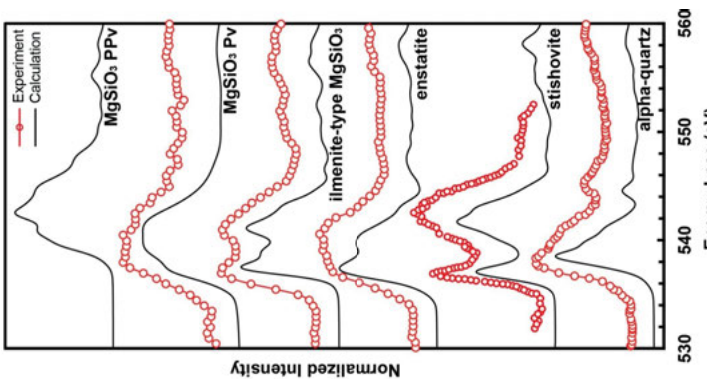


Figure 21 (***on left***). Calculated O *K*-edge XRS spectra (black solid line) for SiO_2 (α-quartz, stishovite) and $MgSiO_3$ (ortho-enstatite, ilmenite, perovskite, and post-perovskite) polymorphs with the corresponding X-ray Raman scattering experimental results (open circles with solid line) from previous works (Lee et al. 2008b; Lin et al. 2007) (modified from Yi and Lee 2012).

Figure 22 (***on right***). (A) Calculated O *K*-edge XRS spectra for $MgSiO_3$ high pressure polymorphs as labeled. (B) Calculated O *K*-edge XRS spectra for corner-sharing oxygen sites in $MgSiO_3$ high pressure polymorphs. (C) Calculated O *K*-edge XRS spectra for edge-sharing oxygen site in SiO_2 and $MgSiO_3$ polymorphs as labeled. The spectrometer broadening parameter (g) of Gaussian broadening FWHM of 1.0 eV was used (modified from Yi and Lee 2012).



EBSCOhost - printed on 2/13/2023 5:26 AM via . All use subject to https://www.ebsco.com/terms-of-use

Application of *L*- and *M*-edge XRS techniques to oxides and silicates under pressure

While the application of XRS can be effective for providing *element specific* information on atomic configurations, its application has focused on the low-z elements in the 2nd row of periodic table. Furthermore, the XRS features in the 10-100 eV region can be complicated by diverse sources of background signals (e.g., Compton scattering peak, Be plasmon) that overlap with the IXS features in these region. Be plasmon due to Be gasket can be effectively removed as shown in the previous Li *K*-edge study (Lee et al. 2007). As the Compton peak position moves to higher energy and its peak width gets broader with increasing scattering angle (2θ), the inelastic X-ray scattering spectrum within 10-100 eV region can be probed by carefully adjusting scattering angle and geometry (Lee et al. unpubl data). In Figure 2, we also showed Ca *M*-edges (20-40 eV) for Ca-silicate glasses. Similar approaches can be applied to diverse Ca-bearing silicates and oxide under extreme pressure. However, *L*-, *M*-, and *N*-edge XRS spectra for high-z elements have also provided useful information on electronic structures by probing excitations of electron from *p* and *d* orbitals to unbound states. The edges studied using XRS at 1 atm are the *L*-edges (from 2*p* to virtual states) of Na, Si, and Ba, *M*-edges (from 3*p* to virtual states) of 3*d* metals, *N*-edges (from 4*d* to unbound states) features of barium, lanthanum and cerium materials, and *O*-edges (from 5*d* to unbound states) features from compounds consisting of actinides (see Sternemann et al. 2007a,b and Gordon et al. 2011 and references therein). The application of theses edges focused on the structure of simple systems at 1 atm. With a possible exception of a recent Si *L*-edge (~120 eV) study of SiO_2 glasses under pressure above 70 GPa (Fukui et al. 2008), these edges have not been explored for the silicates and oxides at high pressure.

In order to explore the pressure-induced changes in the structure of network modifying cations in silicate glasses at high pressure, Ca *L*-edge XRS spectrum for $CaSiO_3$ glass at 1 atm and 21 GPa are presented (Fig. 24). The two features at ~349 and 353 eV are due to an excitation of an electron from the Ca 2*p*-state with total angular momentum of 3/2 and 1/2 into unoccupied states (labeled as, L_3, L_2 transitions), respectively (cf., Henderson et al. 2013). The L_3/L_2 ratio at high pressure is somewhat smaller than that at 1 atm: because the signal to background (S/B) ratio is low for the spectrum at high pressure, the change in L_3/L_2 ratio may result from spectral uncertainty. However, the change could also imply structural changes (e.g., average coordination number) around Ca in the glasses at high pressure. Furthermore, it may suggest the presence of a potential spin transition (from high spin (L_3) to low spin (L_2)) at pressure. Further experimental and theoretical efforts are necessary to provide atomistic origins of the change.

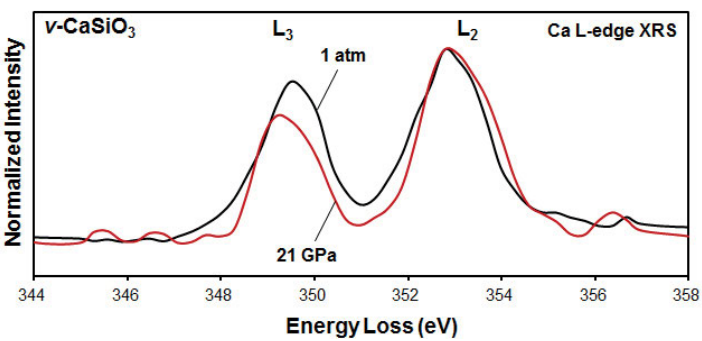


Figure 24. Calcium *L*-edge XRS spectrum for $CaSiO_3$ glass with varying pressure. The features at ~349 and 353 eV are due to an excitation of a core electron from the Ca 2*p*-state with total angular momentum of 3/2 and 1/2 into unoccupied states (labeled as., L_3, L_2 transitions), respectively.

EBSCOhost - printed on 2/13/2023 5:26 AM via . All use subject to https://www.ebsco.com/terms-of-use

Application of XRS technique to multi-component oxide glasses under pressure

While materials with relatively simple compositions (pure elements, single component and binary earth materials) have been thus far studied, further efforts to reveal the structures of multi-component earth materials are necessary to account for the variations in the properties of natural earth materials. Intrinsic disorder inherent in multicomponent (i.e., beyond quaternary) oxide glasses, however, makes it difficult to resolve their atomic structures at both ambient and elevated pressure conditions as peak overlap (or double differential scattering cross section) increases with increasing numbers of components. While this aspect could also pose a serious problem for any spectroscopic and scattering technique, an element specific like XRS could be potentially useful in revealing the densification mechanisms of these multi-component oxide glasses.

Indeed, XRS has been applied to probe local atomic configuration around oxygen in multi-component model basaltic glasses (Ca-Mg aluminosilicate melt of diopside-anorthite eutectic composition, $Di_{64}An_{36}$) at 1 atm and the glass under shock compression (Lee et al. 2012). The structures of shock compressed glasses are essential to understand the changes in the corresponding melt properties under dynamic compression and magmatic processes in the Earth's interior (Ahrens 1996; Okuno et al. 1999; Reynard et al. 1999; Akins et al. 2004; Shimoda et al. 2004; Tschauner et al. 2009). O *K*-edge XRS provides an opportunity to reveal the shock-induced transitions in atomic environments around oxygen in unshocked and shocked model basaltic glasses (Lee et al. 2012). Figure 25 shows the O *K*-edge X-ray Raman spectra for unshocked (black) and shocked $Di_{64}An_{36}$ glass (red spectrum) (Lee et al. 2012). A dominant peak at 538-540 eV is prevalent for both unshocked and shocked glass and is due to an excitation of a core electron from the oxygen 1*s*-state into unoccupied oxygen 2*p*-states stemming from four-coordinated Si atoms, similar to features in other silicate glasses at 1 atm (Lin et al. 2007; Lee et al. 2008b). Shock compression apparently leads to a slight edge energy shift (~1 eV). O *K*-edge features move to higher energy with an increasing degree of densification in Mg-silicate polymorphs due to an increase in the energy of unoccupied oxygen 2*p*-states (Yi and Lee 2012).

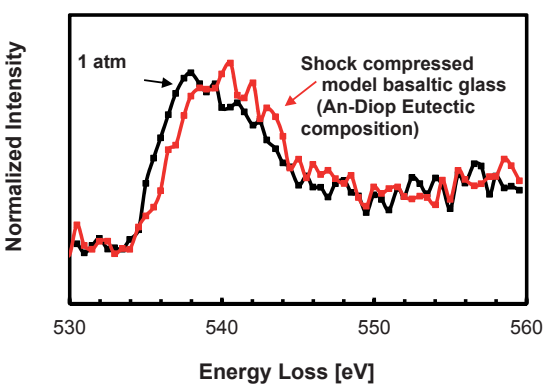


Figure 25. Oxygen *K*-edge XRS spectra for glass with a diopside–anorthite eutectic composition ($Di_{64}An_{36}$) quenched from melts at 1 atm and recovered after shock compression. The spectra were plotted as normalized scattered intensity vs. energy loss (incident energy – elastic energy). The X-ray Raman scattering spectra for the unshocked and shocked $Di_{64}An_{36}$ glass were collected at HPCAT sector 16ID-D of the APS. X-ray Raman spectra were collected for the samples (~200 μm) attached to 100-μm glass fibers mounted directly on the goniometer. The spectra were collected by scanning the energy of the incident beam relative to the analyzer with a fixed elastic energy (E_0) of ~9.886 keV at a scattering angle of 20°. A linear array of 17 spherical Si(555) analyzers operating in a backscattering geometry was used. The X-ray beam size was approximately 50 μm(H) × 30 μm(V) (modified from Lee et al. 2012).

EBSCOhost - printed on 2/13/2023 5:26 AM via . All use subject to https://www.ebsco.com/terms-of-use

The current result thus suggests a densification of the $Di_{64}An_{36}$ glass upon shock compression. We note that due to the pronounced uncertainty in spectral features (stemming from low signal/background ratio of the spectrum and insufficient signal averaging), the observed shift should not be regarded as strong evidence for noticeable structural transitions (e.g., coordination number of Si) after shock-compression but may result from mostly topological changes (bond angle and lengths and medium-range structure) (Lee et al. 2012).

Application of new *K*-edges (elements in the 3rd row of the periodic table) and momentum transfer XRS to crystals under pressure

The XRS signal intensity tends to decrease with increasing atomic number of elements (e.g., Na, Mg) and thus it is still a challenge to collect sufficiently high quality XRS spectra for Na and Mg in silicates and oxides. Note that Na *K*-edge XRS has probed the electronic structures of NaCl and NaF (Nagle et al. 2009). These edges have not been utilized for oxides and silicates at 1 atm so far but the edge features will be potentially useful to probe the local structure of other Na compounds as well as Na-bearing silicate glasses and minerals. Its application to diverse glasses and crystals at high pressure also remains to be explored. Additionally, revealing the momentum-transfer dependent edge feature can provide studies of non-dipole transitions in materials (Caliebe et al. 2000; Hamalainen et al. 2002; Soininen et al. 2006; Gordon et al. 2011). This aspect has not been fully utilized for the study of earth materials under pressure but is potentially useful in resolving the detailed nature of bonding in iron bearing oxide glasses and/or transition metal sites in the earth materials.

***In situ* high-temperature and high-pressure XRS studies**

Further study of effect of high temperature is another target of future research. Current experiments are mostly for room temperature applications. The future development of measurement techniques (involving laser heating) operating at higher temperature ranges seems necessary to explore the effect of temperature on electronic bonding transitions in oxides under pressure. Conventional external heating and/or laser heating technique can be implemented with DAC, allowing us explore the effect of both temperature and pressure on electronic bonding simultaneously (Mao and Mao 2007)

Outlook and prospects

As XRS beamlines have been experiencing major experimental improvements and upgrades during the last couple of years in several synchrotron radiation sources, and technical advances with X-ray optics and DAC cell design are likely to be continued, development of efficient XRS protocols with improved DAC cell design and X-ray optics with better photon flux is certainly expected. These notable advances may also hold some promise for studying the structure of diverse earth materials under pressure. Additionally, because the application of XRS to earth materials at high pressure is relatively new and has only been applied to a limited number of earth materials, current XRS methods with ~ 1 eV resolution and with fluxes of ~10^{13} photons/s/eV can still be extremely useful to probe structural transitions in oxide glasses and crystals under compression. While many challenges remain, the XRS technique is a promising tool for probing pressure-induced changes in detailed atomic structures at elevated pressures.

ACKNOWLEDGMENTS

This research was supported by National Research Foundation, Korea (2012-026-411) and partly supported by the Korea Meteorological Administration Research and Development Program under Grant CATER 2012-8030 to S.K. Lee. We are grateful for careful and constructive suggestions by Grant Henderson and two anonymous reviewers. We sincerely thank colleagues and collaborators, Jinfu Shu, Jung-Fu Lin, Yue Meng, Matt Newville, Wendy Mao, Paul Chow, Sun Young Park, Hyo-Im Kim, Oliver Tschauner, Paul Asimow, Ligang Bai, Yuming Xiao,

EBSCOhost - printed on 2/13/2023 5:26 AM via . All use subject to https://www.ebsco.com/terms-of-use

Hyunna Kim, Bum Han Lee, Yoosoo Yi, Yong Q. Cai, Nozomu Hiraoka, Takuo Okuchi, Michael Y. Hu, Paul Chow, Baosheng Li, Hiroshi Fukui, Yang Ding, Chicang Kao, John Tse, Yu Lin, and Choong-Shik Yoo for the invaluable contributions to the results presented here. GSECARS was supported by DOE-BES-Geosciences, NSF-Earth Sciences and the State of Illinois. HPCAT operations are supported by DOE-NNSA under Award No. DE-NA0001974 and DOE-BES under Award No. DE-FG02-99ER45775, with partial instrumentation funding by NSF. APS is supported by DOE-BES, under Contract No. DE-AC02-06CH11357. Lee SK thanks travel supports from LG fellowship.

REFERENCES

Agee CB (2008) Static compression of hydrous silicate melt and the effect of water on planetary differentiation. Earth Planet Sci Lett 265:641-654

Ahrens TJ (1996) Application of shock compression science to Earth and planetary physics. *In*: Shock Compression of Condensed Matter. Schmidt SCTWC (*Ed*) p 3-8

Akins JA, Luo SN, Asimow PD, Ahrens TJ (2004) Shock-induced melting of $MgSiO_3$ perovskite and implications for melts in Earth's lowermost mantle. Geophys Res Lett 31:L14612

Allwardt JR, Schmidt BC, Stebbins JF (2004) Structural mechanisms of compression and decompression in high pressure $K_2Si_4O_9$ glasses: An investigation utilizing Raman and NMR spectroscopy of high-pressure glasses and crystals. Chem Geol 213:137-151

Allwardt JR, Poe BT, Stebbins JF (2005a) The effect of fictive temperature on Al coordination in high-pressure (10 GPa) sodium aluminosilicate glasses. Am Mineral 90:1453-1457

Allwardt JR, Stebbins JF, Schmidt BC, Frost DJ, Withers AC, Hirschmann MM (2005b) Aluminum coordination and the densification of high-pressure aluminosilicate glasses Am Mineral 90:1218-1222

Angell CA, Cheeseman PA, Tamaddon S (1982) Pressure enhancement of ion mobilities in liquid silicates from computer simulations studies to 800 kbar. Science 218:885-887

Aryal S, Rulis P, Ching WY (2008) Density functional calculations of the electronic structure and optical properties of aluminosilicate polymorphs (Al_2SiO_5). Am Mineral 93:114-123

Bergmann U, Mullins OC, Cramer SP (2000) X-ray Raman spectroscopy of carbon in asphaltene: Light element characterization with bulk sensitivity. Anal Chem 72:2609-2612

Bergmann U, Glatzel P, Cramer SP (2002a) Bulk-sensitive XAS characterization of light elements: from X-ray Raman scattering to X-ray Raman spectroscopy. Microchem J 71:221-230

Bergmann U, Wernet P, Glatzel P, Cavalleri M, Pettersson LGM, Nilsson A, Cramer SP (2002b) X-ray Raman spectroscopy at the oxygen K edge of water and ice: Implications on local structure models. Phys Rev B 66:092107

Bergmann U, Groenzin H, Mullins OC, Glatzel P, Fetzer J, Cramer SP (2003) Carbon K-edge X-ray Raman spectroscopy supports simple, yet powerful description of aromatic hydrocarbons and asphaltenes. Chem Phys Lett 369:184-191

Bergmann U, Groenzin H, Mullins OC, Glatzel P, Fetzer J, Cramer SP (2004) X-ray Raman spectroscopy - A new tool to study local structure of aromatic hydrocarbons and asphaltenes. Pet Sci Technol 22:863-875

Blaha P, Schwarz K, Madsen G, Kvasnicka D, Luitz J (2001) WIEN2k. Techn. Univ. Wien, Austria, Wien.

Bowron DT, Krisch MH, Barnes AC, Finney JL, Kaprolat A, Lorenzen M (2000) X-ray-Raman scattering from the oxygen K edge in liquid and solid H_2O. Phys Rev B 62:R9223-R9227

Brown GE Jr, Farges F, Calas G (1995) X-ray scattering and X-ray spectroscopy studies of silicate melts. Rev Mineral Geochem 32:317-410

Brydson R, Brown A, Benni LG, Livi K (2014) Analytical transmission electron microscopy. Rev Mineral Geochem 78:219-269

Cabaret D, Sainctavit P, Ildefonse P, Flank AM (1998) Full multiple scattering calculations of the X-ray absorption near edge structure at the magnesium K-edge in pyroxene. Am Mineral 83:300-304

Cabaret D, Mauri F, Henderson GS (2007) Oxygen K-edge XANES of germanates investigated using first-principles calculations. Phys Rev B 75:184205

Cai YQ, Mao HK, Chow PC, Tse JS, Ma Y, Patchkovskii S, Shu JF, Struzhkin V, Hemley RJ, Ishii H, Chen CC, Jarrige I, Chen CT, Shieh SR, Huang EP, Kao CC (2005) Ordering of hydrogen bonds in high-pressure low-temperature H_2O. Phys Rev Lett 94:025502

Caliebe WA, Soininen JA, Shirley EL, Kao CC, Hamalainen K (2000) Dynamic structure factor of diamond and LiF measured using inelastic X-ray scattering. Phys Rev Lett 84:3907-3910

Caracas R, Cohen RE (2006) Theoretical determination of the Raman spectra of $MgSiO_3$ perovskite and post-perovskite at high pressure. Geophys Res Lett 33:L12S05

EBSCOhost - printed on 2/13/2023 5:26 AM via . All use subject to https://www.ebsco.com/terms-of-use

Chan MKY, Shirley EL, Karan NK, Balasubramanian M, Ren Y, Greeley JP, Fister TT (2011) Structure of Lithium Peroxide. J Phys Chem Lett 2:2483-2486

Cruz SA, Díaz-García C, Pathak AP, Soullard J (2005) Pressure dependence of the mean excitation energy of atomic systems. Nucl Instrum Methods B 230:46-52

Davoli I, Paris E, Stizza S, Benfatto M, Fanfoni M, Gargano A, Bianconi A, Seifert F (1992) Structure of densified vitreous silica - silicon and oxygen Xanes spectra and multiple-scattering calculations. Phys Chem Miner 19:171-175

de Groot F (2001) High resolution X-ray emission and X-ray absorption spectroscopy. Chem Rev 101:1779-1808

Diefenbacher J, McMillan PF, Wolf GH (1998) Molecular dynamics simulations of $Na_2Si_4O_9$ liquid at high pressure. J Phys Chem B 102:3003-3008

Eckert H (1992) Structural characterization of noncrystalline solids and glasses using solid state NMR. Prog Nucl Mag Reson 24:159-293

Eustace DA, McComb DW, Craven AJ (2010) Probing magnetic order in EELS of chromite spinels using both multiple scattering (FEFF8.2) and DFT (WIEN2k). Micron 41:547-553.

Feng YJ, Soininen JA, Ankudinov AL, Cross JO, Seidler GT, Macrander AT, Rehr JJ, Shirley EL (2008) Exciton spectroscopy of hexagonal boron nitride using nonresonant X-ray Raman scattering. Phys Rev B 77:165202

Fister TT, Seidler GT, Wharton L, Battle AR, Ellis TB, Cross JO, Macrander AT, Elam WT, Tyson TA, Qian Q (2006) Multielement spectrometer for efficient measurement of the momentum transfer dependence of inelastic X-ray scattering. Rev Sci Instrum 77:063901

Fister TT, Seidler GT, Rehr JJ, Kas JJ, Elam WT, Cross JO, Nagle KP (2007) Deconvolving instrumental and intrinsic broadening in core-shell X-ray spectroscopies. Phys Rev B 75:174106

Fister TT, Seidler GT, Shirley EL, Vila FD, Rehr JJ, Nagle KP, Linehan JC, Cross JO (2008a) The local electronic structure of alpha-Li_3N. J Phys Chem 129:044702

Fister TT, Vila FD, Seidler GT, Svec L, Linehan JC, Cross JO (2008b) Local electronic structure of dicarba-closo-dodecarboranes $C_2B_{10}H_{12}$. J Am Chem Soc 130:925-932

Fister TT, Nagle KP, Vila FD, Seidler GT, Hamner C, Cross JO, Rehr JJ (2009a) Intermediate-range order in water ices: Nonresonant inelastic X-ray scattering measurements and real-space full multiple scattering calculations. Phys Rev B 79:174117

Fister TT, Fong DD, Eastman JA, Iddir H, Zapol P, Fuoss PH, Balasubramanian M, Gordon RA, Balasubramaniam KR, Salvador PA (2011a) Total-reflection inelastic X-Ray scattering from a 10-nm thick $La_{0.6}Sr_{0.4}CoO_3$ thin film. Phys Rev Lett 106:037401

Fister TT, Schmidt M, Fenter P, Johnson CS, Slater MD, Chan MKY, Shirley EL (2011b) Electronic structure of lithium battery interphase compounds: comparison between inelastic X-ray scattering measurements and theory. J Phys Chem 135:224513-224513

Fleet ME, Muthupari S (1999) Cordination of boron in alkali borosilicate glasses using XANES. J Non-Cryst Solids 255:233-241

Fleet ME, Muthupari S (2000) Boron K-edge XANES of borate and borosilicate minerals. Am Mineral 85:1009-1021

Fukui H, Kanzaki M, Hiraoka N, Cai YQ (2008) Coordination environment of silicon in silica glass up to 74 GPa: An X-ray Raman scattering study at the silicon L-edge. Phys Rev B 78:012203

Fukui H, Kanzaki M, Hiraoka N, Cai YQ (2009) X-ray Raman scattering for structural investigation of silica/silicate minerals. Phys Chem Miner 36:171-181

Garvie LAJ, Rez P, Alvarez JR, Buseck PR, Craven AJ, Brydson R (2000) Bonding in alpha-quartz (SiO_2): A view of the unoccupied states. Am Mineral 85:732-738

Garvie LAJ, Craven AJ (1995) Parallel electron energy-loss spectroscopy (PEELS) study of B in minerals: The electron energy-loss near edge structure (ELNES) of the B K-edge. Am Mineral 80:1132-1144

Gordon ML, Tulumello D, Cooper G, Hitchcock AP, Glatzel P, Mullins OC, Cramer SP, Bergmann U (2003) Inner-shell excitation spectroscopy of fused-ring aromatic molecules by electron energy loss and X-ray Raman techniques. J Phys Chem A 107:8512-8520

Gordon RA, Seidler GT, Fister TT, Nagle KP (2011) Studying low-energy core-valence transitions with bulk sensitivity using q-dependent NIXS. J Electron Spectrosc 184:220-223

Greaves GL, Ngai KL (1995) Reconciling ionic-transport properties with atomic-structure in oxide glasses. Phys Rev B 52:6358-6380

Hamalainen K, Galambosi S, Soininen JA, Shirley EL, Rueff JP, Shukla A (2002) Momentum dependence of fluorine *K*-edge core exciton in LiF. Phys Rev B 65:155111

Hebert C (2007) Practical aspects of running the WIEN2k code for electron spectroscopy. Micron 38:12-28

Hebert C, Luitz J, Schattschneider P (2003) Improvement of energy loss near edge structure calculation using Wien2k. Micron 34:219-225

Hemley RJ (ed) (1998) Ultrahigh-Pressure Mineralogy: Physics and Chemistry of the Earth's Deep Interior. Reviews in Mineralogy 37. Mineralogical society of America, Washington, DC

EBSCOhost - printed on 2/13/2023 5:26 AM via . All use subject to https://www.ebsco.com/terms-of-use

Henderson GS, Neuville DR, Cormier L (2009) An O K-edge XANES study of glasses and crystals in the CaO-Al_2O_3-SiO_2 (CAS) system. Chem Geol 259:54-62
Henderson GS, de Groot FMF, Moulton BJA (2014) X-ray absorption near-edge structure (XANES) spectroscopy. Rev Mineral Geochem 78:75-138
Ikeno H, Tanaka I, Miyamae L, Mishima T, Adachi H, Ogasawara K (2004) First principles calculation of Fe $L_{2,3}$-edge X-ray absorption near edge structures of iron oxides. Mater Trans 45:1414-1418
Jahn S, Kowalski PM (2014) Theoretical approaches to structure and spectroscopy of earth materials. Rev Mineral Geochem 78:691-743
Jorissen K (2007) The ab initio Calculation of Relativistic Electron Energy Loss Spectra. Department of Physics, Doctor of Philosophy. University of Antwerp.
Jorissen K, Rehr JJ (2010) Calculations of electron energy loss and X-ray absorption spectra in periodic systems without a supercell. Phys Rev B 81:245124
Jund P, Kob W, Jullien R (2001) Channel diffusion of sodium in a silicate glass. Phys Rev B 64:4303-4308.
Karan NK, Balasubramanian M, Fister TT, Burrell AK, Du P (2012) Bulk-sensitive characterization of the discharged products in Li-O-2 batteries by nonresonant inelastic X-ray scattering. J Phys Chem C 116:18132-18138
Kelsey KE, Stebbins JF, Mosenfelder JL, Asimow PD (2009a) Simultaneous aluminum, silicon, and sodium coordination changes in 6 GPa sodium aluminosilicate glasses. Am Mineral 94:1205-1215
Kelsey KE, Stebbins JF, Singer DM, Brown GE Jr, Mosenfelder JL, Asimow PD (2009b) Cation field strength effects on high pressure aluminosilicate glass structure: Multinuclear NMR and La XAFS results. Geochim Cosmochim Acta 73:3914-3933
Kim S, Kim Y, Hong J, Tanaka I, No K (2005) Electronic structure and X-ray-absorption near-edge structure of amorphous Zr-oxide and Hf-oxide thin films: A first-principles study. J Appl Phys 97:073519
Krayzman V, Levin I, Woicik JC, Yoder D, Fischer DA (2006) Effects of local atomic order on the pre-edge structure in the Ti K X-ray absorption spectra of perovskite $CaTi_{1-x}Zr_xO_3$. Phys Rev B 74:224104
Krisch MH, Sette F, Masciovecchio C, Verbeni R (1997) Momentum transfer dependence of inelastic X-ray scattering from the Li *K*-edge. Phys Rev Lett 78:2843-2846
Laudernet Y, Clerouin J, Mazevet S (2004) Ab initio simulations of the electrical and optical properties of shock-compressed SiO_2. Phys Rev B 70:165108
Lee SK (2005) Microscopic origins of macroscopic properties of silicate melts: implications for melt generation and dynamics. Geochim Cosmochim Acta 69:3695-3710
Lee SK (2010) Effect of pressure on structure of oxide glasses at high pressure: Insights from solid-state NMR of quadrupolar nuclides. Solid State Nucl Magn Reson 38:45-57
Lee SK (2011) Simplicity in melt densification in multi-component magmatic reservoirs in Earth's interior revealed by multi-nuclear magnetic resonance. Proc Natl Acad Sci USA 108:6847-6852
Lee SK, Stebbins JF (2003) The distribution of sodium ions in aluminosilicate glasses: A high field Na-23 MAS and 3QMAS NMR study. Geochim Cosmochim Acta 67:1699-1709
Lee SK, Fei Y, Cody GD, Mysen BO (2003) Order and disorder of sodium silicate glasses and melts at 10 GPa. Geophys Res Lett 30:1845
Lee SK, Eng PJ, Mao HK, Meng Y, Newville M, Hu MY, Shu JF (2005) Probing of bonding changes in B_2O_3 glasses at high pressure with inelastic X-ray scattering. Nat Mater 4:851-854
Lee SK, Eng PJ, Mao HK, Meng Y, Shu J (2007) Structure of alkali borate glasses at high pressure: B and Li K-edge inelastic X-ray scattering study. Phys Rev Lett 98:105502
Lee SK, Eng P, Mao HK, Shu JF (2008a) Probing and modeling of pressure-induced coordination transformation in borate glasses: Inelastic X-ray scattering study at high pressure. Phys Rev B 78:214203
Lee SK, Lin JF, Cai YQ, Hiraoka N, Eng PJ, Okuchi T, Mao HK, Meng Y, Hu MY, Chow P, Shu JF, Li BS, Fukui H, Lee BH, Kim HN, Yoo CS (2008b) X-ray Raman scattering study of $MgSiO_3$ glass at high pressure: Implication for triclustered $MgSiO_3$ melt in Earth's mantle. Proc Natl Acad Sci USA 105:7925-7929
Lee SK, Park SY, Kim H-I, Tschauner O, Asimow P, Bai LG, Xiao YM, Chow P (2012) Structure of shock compressed model basaltic glass: Insights from O K-edge X-ray Raman scattering and high-resolution Al-27 NMR spectroscopy. Geophys Res Lett 39:L05306
Lelong G, Cormier L, Ferlat G, Giordano V, Henderson GS, Shukla A, Calas G (2012) Evidence of fivefold-coordinated Ge atoms in amorphous GeO_2 under pressure using inelastic X-ray scattering. Phys Rev B 85:134202
Lin JF, Fukui H, Prendergast D, Okuchi T, Cai YQ, Hiraoka N, Yoo CS, Trave A, Eng P, Hu MY, Chow P (2007) Electronic bonding transition in compressed SiO_2 glass. Phys Rev B 75:012201
Lin Y, Zhang L, Mao HK, Chow P, Xiao YM, Baldini M, Shu JF, Mao WL (2011) Amorphous Diamond: A High-Pressure Superhard Carbon Allotrope. Phys Rev Lett 107:175504
Luitz J, Maier M, Hebert C, Schattschneider P, Blaha P, Schwarz K, Jouffrey B (2001) Partial core hole screening in the Cu L_3-edge. Eur Phys J B 21:363-367
Mao HK, Mao WL (2007) Theory and practice - diamond-anvil cells and probes for high P-T mineral physics studies. *In:* Treatise on Geophysics. Gerald S (Ed) Elsevier, Amsterdam. p 231-267

EBSCOhost - printed on 2/13/2023 5:26 AM via . All use subject to https://www.ebsco.com/terms-of-use

Mao WL, Mao HK, Eng PJ, Trainor TP, Newville M, Kao CC, Heinz DL, Shu JF, Meng Y, Hemley RJ (2003) Bonding changes in compressed superhard graphite. Science 302: 425-427
Mao WL, Mao HK, Meng Y, Eng PJ, Hu MY, Chow P, Cai YQ, Shu JF, Hemley RJ (2006) X-ray-induced dissociation of H_2O and formation of an O_2-H_2 alloy at high pressure. Science 314:636-638
Mao HK, Shirley EL, Ding Y, Eng P, Cai YQ, Chow P, Xiao YM, Shu JF, Hemley RJ, Kao CC, Mao WL (2010) Electronic structure of crystalline He-4 at high pressures. Phys Rev Lett 105:186404
Marder (2000) Condensed Matter Physics. John Wiley
McLeod JA, Wilks RG, Skorikov NA, Finkelstein LD, Abu-Samak M, Kurmaev EZ, Moewes A (2010) Band gaps and electronic structure of alkaline-earth and post-transition-metal oxides. Phys Rev B 81:245123
Meng Y, Mao HK, Eng PJ, Trainor TP, Newville M, Hu MY, Kao CC, Shu JF, Hausermann D, Hemley RJ (2004) The formation of sp(3) bonding in compressed BN. Nat Mater 3:111-114
Meng Y, Eng PJ, Tse JS, Shaw DM, Hu MY, Shu JF, Gramsch SA, Kao C, Hemley RJ, Mao HK (2008) Inelastic X-ray scattering of dense solid oxygen: Evidence for intermolecular bonding. Proc Natl Acad Sci USA 105:11640-11644
Micoulaut M, Cormier L, Henderson GS (2006) The structure of amorphous, crystalline and liquid GeO_2. J Phys-Condens Mat 18:R753-R784
Mizoguchi T, Tanaka I, Yoshiya M, Oba F, Ogasawara K, Adachi H (2000) Core-hole effects on theoretical electron-energy-loss near-edge structure and near-edge X-ray absorption fine structure of MgO. Phys Rev B 61:2180
Mizuno Y, Ohmura Y (1967) Theory of X-ray Raman scattering. J Phys Soc Japan 22:445-&
Mo SD, Ching WY (2000) Ab initio calculation of the core-hole effect in the electron energy-loss near-edge structure. Phys Rev B 62:7901-7907
Murakami M, Bass JD (2010) Spectroscopic evidence for ultrahigh-pressure polymorphism in SiO_2 glass. Phys Rev Lett 104:025504
Mysen BO, Richet P (2005) Silicate Glasses and Melts: Properties and Structure. Elsevier, Amsterdam.
Nagasawa H, Mourikis S, Schulke W (1989) X-ray Raman spectrum of Li, Be, and graphite in a high-resolution inelastic synchrotron X-ray scattering experiment. J Phys Soc Japan 58:710-717
Nagasawa H, Mourikis S, Schulke W (1997) Momentum-transfer dependence of the near edge structure of Li. J Phys Soc Japan 66:3139-3146
Nagle KP, Seidler GT, Shirley EL, Fister TT, Bradley JA, Brown FC (2009) Final-state symmetry of Na 1s core-shell excitons in NaCl and NaF. Phys Rev B 80:045105
Navrotsky A (1995) Energetics of silicate melts. *In*: Structure, Dynamics, and Properties of Silicate Melts. Stebbins JF, McMillan PF, Dingwell DB (Eds.) Mineralogical Society of America, Washington, D.C. p 121-143
Newville M (2014) Fundamentals of XAFS. Rev Mineral Geochem 78:33-74
Okuno M, Reynard B, Shimada Y, Syono Y, Willaime C (1999) A Raman spectroscopic study of shock-wave densification of vitreous silica. Phys Chem Miner 26:304-311
Poe BT, McMillan PF, Rubie DC, Chakraborty S, Yarger JL, Diefenbacher J (1997) Silicon and oxygen self-diffusivities in silicate liquids measured to 15 Gigapascals and 2800 Kelvin. Science 276:1245-1248
Prewitt CT, Downs RT (1998) High-pressure crystal chemistry. Rev Mineral Geochem 37:283-317
Price GD (2007) Mineral physics: past, present, and future. *In*: Treatise on Geophysics. Vol 2. Gerald S (Ed) 2. Elsevier, Amsterdam, p 1-6
Rehr JJ, Albers RC (2000) Theoretical approaches to X-ray absorption fine structure. Rev Mod Phys 72:621-654
Rehr JJ, Kas JJ, Vila FD, Prange MP, Jorissen K (2010) Parameter-free calculations of X-ray spectra with FEFF9. Phys Chem Chem Phys 12:5503-5513
Revenaugh J, Sipkin SA (1994) Seismic evidence for silicate melt atop the 410 km mantle discontinuity. Nature 369:474-476
Reynard B, Okuno M, Shimada Y, Syono Y, Willaime C (1999) A Raman spectroscopic study of shock-wave densification of anorthite ($CaAl_2Si_2O_8$) glass. Phys Chem Miner 26:432-436
Rez P, Alvarez JR, Pickard C (1999) Calculation of near edge structure. Ultramicroscopy 78:175-183
Rueff J-P, Shukla A (2010) Inelastic X-ray scattering by electronic excitations under high pressure. Rev Mod Phys 82:847-896
Rueff JP, Joly Y, Bartolome F, Krisch M, Hodeau JL, Marques L, Mezouar M, Kaprolat A, Lorenzen M, Sette F (2002) X-ray Raman scattering from the carbon *K*-edge in polymerized C_{60}: experiment and theory. J Phys-Condens Mat 14:11635-11641
Sakamaki T, Suzuki A, Ohtani E (2006) Stability of hydrous melt at the base of the Earth's upper mantle. Nature 439:192-194
Sakko A, Hakala M, Soininen JA, Hamalainen K (2007) Density functional study of X-ray Raman scattering from aromatic hydrocarbons and polyfluorene. Phys Rev B 76:205115
Sakko A, Rubio A, Hakala M, Hamalainen K (2010) Time-dependent density functional approach for the calculation of inelastic X-ray scattering spectra of molecules. J Phys Chem 133:174111

EBSCOhost - printed on 2/13/2023 5:26 AM via . All use subject to https://www.ebsco.com/terms-of-use

Sakko A, Galambosi S, Inkinen J, Pylkkanen T, Hakala M, Huotari S, Hamalainen K (2011) Inelastic X-ray scattering and vibrational effects at the K-edges of gaseous N_2, N_2O, and CO_2. Phys Chem Chem Phys 13:11678-11685

Sauer H, Brydson R, Rowley PN, Engel W, Thomas JM (1993) Determination of coordination and coordination specific site occupancy by electron-energy loss spectroscopy: An investigation of boron-oxygen compounds. Ultramicroscopy 49:198-209

Sandi G, Song K, Carrado KA, Winans RE (1998) A NEXAFS determination of the electronic structure of carbons for lithium-ion cells. Carbon 36:1755-1758

Schulke W (2007) Electron Dynamics by Inelastic X-ray Scattering. Oxford University Press

Schulke W, Bonse U, Nagasawa H, Kaprolat A, Berthold A (1988) Interband-transitions and core excitations in highly oriented pyrolytic-graphite studied by inelastic synchrotron X-ray scattering: Band structure information. Phys Rev B 38:2112-2123

Schulke W, Gabriel KJ, Berthold A, Schulteschrepping H (1991) Interlayer states of LiC_6 investigated by inelastic X-ray scattering spectroscopy (IXSS) using Li core excitation. Solid State Commun 79:657-660

Schulke W, Nagasawa H, Mourikis S, Lanzki P (1986) Dynamic structure of electrons in Li metal: Inelastic synchrotron X-ray scattering results and interpretation beyond the random-phase approximation. Phys Rev B 33:6744-6757

Schwarz K, Blaha P, Madsen GKH (2002) Electronic structure calculations of solids using the WIEN2k package for material sciences. Comput Phys Commun 147:71-76

Schwarz WHE, Mensching L, Hallmeier KH, Szargan R (1983) K-shell excitation of BF_3, CF_4 and MBF_4 compounds. Chem Phys 82:57-65

Seifert F, Sharp T, Poe B, Wu Z (1996) ELNES Si L-, K-edge and O K-edge spectroscopy as a tool for distinction of four- vs six-coordinated silicon in high-pressure phases. Phys Chem Miner 23:227-227

Shen G, Wang Y (2014) High-pressure apparatus integrated with synchrotron radiation. Rev Mineral Geochem 78:745-777

Shvyd'ko Y V, Lerche M, Kuetgens U, Ruter HD, Alatas A and Zhao J (2006) X-ray Bragg diffraction in asymmetric backscattering geometry. Phys Rev Lett 97:235502

Shimoda K, Okuno M, Syono Y, Kikuchi M, Fukuoka K, Koyano M, Katayama S (2004) Structural evolutions of an obsidian and its fused glass by shock-wave compression. Phys Chem Miner 31:532-542

Soininen JA, Mattila A, Rehr JJ, Galambosi S, Hamalainen K (2006) Experimental determination of the core-excited electron density of states. J Phys-Condens Matter 18:7327-7336

Song TRA, Helmberger DV, Grand SP (2004) Low-velocity zone atop the 410-km seismic discontinuity in the northwestern United States. Nature 427:530-533

Stebbins JF (1995) Dynamics and structure of silicate and oxide melts: nuclear magnetic resonance studies. Rev Mineral 32:191-246

Stebbins JF, Xu Z (1997) NMR evidence for excess non-bridging oxygen in aluminosilicate glass. Nature 390, 60-62

Stetsko YP, Keister JW, Coburn DS, Kodituwakku CN, Consolo A, Cai YQ (2011). Multiple-wave diffraction in high energy resolution back-reflecting x-ray optics. Phys Rev Lett 107:155503

Sternemann H, Soininen JA, Sternemann C, Hamalainen K, Tolan M (2007a) Near-edge structure of nonresonant inelastic X-ray scattering from L-shell core levels studied by a real-space multiple-scattering approach. Phys Rev B 75:075118

Sternemann H, Sternemann C, Tse JS, Desgreniers S, Cai YQ, Vanko G, Hiraoka N, Schacht A, Soininen JA, Tolan M (2007b) Giant dipole resonance of Ba in Ba_8Si_{46}: An approach for studying high-pressure induced phase transitions of nanostructured materials. Phys Rev B 75:245102

Stixrude L (2007) Properties of rocks and minerals - seismic properties of rocks and minerals, and structure of the Earth. *In*: Treatise on Geophysics. Gerald S (ed) Elsevier, Amsterdam p 7-32.

Stixrude L, Karki B (2005) Structure and freezing of $MgSiO_3$ liquid in Earth's lower mantle. Science 310:297-299

Stohr J (2003) NEXAFS Spectroscopy. Springer, New York

Suzuki T (1967) X-ray Raman scattering experiment. I. J Phys Soc Japan 22:1139

Tamura E, van Ek J, Fröba M, Wong J (1995) X-Ray absorption near edge structure in metals: relativistic effects and core-hole screening. Phys Rev Lett 74:4899

Tanaka I, Mizoguchi T, Yoshiya M, Ogasawara K, Adachi H, Mo SD, Ching WY (2002) First principles calculation of ELNES by LCAO methods. J Electron Microsc 51:S107-S112

Tohji K, Udagawa Y (1987) Novel-approach for structure-analysis by X-ray Raman-scattering. Phys Rev B 36:9410-9412

Tohji K, Udagawa Y (1989) X-ray Raman scattering as a substitute for soft X-ray extended X-ray absorption fine-structure. Phys Rev B 39:7590-7594

EBSCOhost - printed on 2/13/2023 5:26 AM via . All use subject to https://www.ebsco.com/terms-of-use

Tschauner O, Asimow PD, Kostandova N, Ahrens TJ, Ma C, Sinogeikin S, Liu Z, Fakra S, Tamura N (2009) Ultrafast growth of wadsleyite in shock-produced melts and its implications for early solar system impact processes. Proc Natl Acad Sci USA 106:13691-13695

Tse JS, Shaw DM, Klug DD, Patchkovskii S, Vanko G, Monaco G, Krisch M (2008) X-ray Raman spectroscopic study of water in the condensed phases. Phys Rev Lett 100:095502

Tsuji J, Nakamatsu H, Mukoyama T, Kojima K, Ikeda S, Taniguchi K (2002) Lithium K-edge XANES spectra for lithium compounds. X-Ray Spectrom 31:319-326

Watanabe N, Hayashi H, Udagawa Y, Takeshita K, Kawata H (1996) Anisotropy of hexagonal boron nitride core absorption spectra by X-ray Raman spectroscopy. Appl Phys Lett 69:1370-1372

Wernet P, Nordlund D, Bergmann U, Cavalleri M, Odelius M, Ogasawara H, Naslund LA, Hirsch TK, Ojamae L, Glatzel P, Pettersson LGM, Nilsson A (2004) The structure of the first coordination shell in liquid water. Science 304:995-999

Wernet P, Testemale D, Hazemann JL, Argoud R, Glatzel P, Pettersson LGM, Nilsson A, Bergmann U (2005) Spectroscopic characterization of microscopic hydrogen-bonding disparities in supercritical water. J Phys Chem 123:154503

Wilke M, Farges F, Petit PE, Brown GE Jr, Martin F (2001) Oxidation state and coordination of Fe in minerals: An FeK-XANES spectroscopic study. Am Mineral 86:714-730

Wolf GH, McMillan PF (1995) Pressure effects on silicate melt structure and properties. Rev Mineral 32:505-562

Wright AC, Stone CE, Sinclair RN, Umesaki N, Kitamura N, Ura K, Ohtori N, Hannon AC (2000) Structure of pressure compacted vitreous boron oxide. Phys Chem Glass 41:296-299

Wu M, Liang Y, Jiang J-Z, Tse JS (2012) Structure and properties of dense silica glass. Scientific Reports 2:398

Wu ZY, Ouvrard G, Gressier P, Natoli CR (1997) Ti and O K-edges for titanium oxides by multiple scattering calculations: Comparison to XAS and EELS spectra. Phys Rev B 55:10382-10391

Wu ZY, Seifert F, Poe B, Sharp T (1996) Multiple-scattering calculations for SiO_2 polymorphs: A comparison to ELNES and XANES spectra. J Phys-Condens Mat 8:3323-3336

Xue X, Stebbins JF, Kanzaki M, Tronnes RG (1989) Silicon coordination and speciation changes in a silicate liquid at high pressures. Science 245:962-964

Xue X, Stebbins JF, Kanzaki M (1994) Correlations between O^{17} NMR parameters and local structure around oxygen in high-pressure silicates and the structure of silicate melts at high pressure. Am Mineral 79:31-42

Yarger JL, Smith KH, Nieman RA, Diefenbacher J, Wolf GH, Poe, BT, McMillan, PF (1995) Al coordination changes in high-pressure aluminosilicate liquids. Science 270:1964-1967

Yi YS, Lee SK (2012) Pressure-induced changes in local electronic structure of SiO_2 and $MgSiO_3$ polymorphs: Insights from ab initio calculations of O K-edge energy-loss near-edge structure spectroscopy. Am Mineral 97:897-909

EBSCOhost - printed on 2/13/2023 5:26 AM via . All use subject to https://www.ebsco.com/terms-of-use

Reviews in Mineralogy & Geochemistry
Vol. 78 pp. 175-217, 2014
Copyright © Mineralogical Society of America

Luminescence Spectroscopy

Glenn A. Waychunas

Geochemistry Department, Earth Sciences Division
E. O. Lawrence Berkeley National Laboratory
One Cyclotron Road, MS 74-316C
Berkeley, California 94720, U.S.A.

gawaychunas@lbl.gov

INTRODUCTION

One of the most astonishing properties of minerals is luminescence, usually observed under ultraviolet light excitation in the laboratory or field as a bit of a curiosity, but increasingly a subject of detailed study utilizing electron beam and laser instrumentation that reveals highly specific electronic structure information and mineral histories.

Volume 18, Chapter 14 of *Reviews in Mineralogy & Geochemistry* (RiMG) presented an overview of mineral luminescence, including an introduction to some of the relevant processes and mechanisms, and a brief catalog of observations for some commonly luminescent minerals (Waychunas 1988). Later, Volume 48 Chapter 19 of RiMG contained a thorough survey of luminescence in apatite minerals (Waychunas 2002) and since then, the *EMU Notes in Mineralogy Series* Volume 6, Chapter 2 reviewed luminescence techniques with classic examples (Nasdala et al. 2004). In the present chapter the emphasis is on methodology and application with luminescent studies undertaken in the last two decades. During this time three types of investigations have seen more prominence: 1) mineralogical studies using gated laser-excitation to reveal luminescent mechanisms, electronic structure and specific activators; 2) use of cathodoluminescence in petrology to give information on provenance and thermal/radiation history, and to aid in phase and trace impurity identification; and 3) thermoluminescence measurements to yield thermal history and age information. These three types of investigations and typical results constitute the main body of this chapter, once the general aspects of luminescence phenomena have been introduced.

Luminescence spectroscopy has traditionally been done with instrumentation common to optical (UV-vis-IR) analysis, but this has evolved with the advent of sophisticated and flexible laser excitation systems, and efficient cathodoluminescence apparatus for electron microprobe and SEM installations, both of which have greatly extended both the specific information content and sensitivity of analysis. Accordingly more space is spent on these newer approaches in this chapter, though a discussion of terminology, basic mechanisms and processes, and luminescent centers is introduced using classical methodology to make it compatible with the optical spectroscopy chapter in this and past volumes.

THE TYPES AND PHYSICAL PROCESSES OF LUMINESCENCE

Luminescence

Luminescence is the emission of light from a substance separate from black body (thermal emission), and incorporates excitations produced by higher energy photons (UV, X-ray, gamma ray), by chemical agents such as free radicals or energetic ions (chemiluminescence

1529-6466/14/0078-0005$05.00 http://dx.doi.org/10.2138/rmg.2014.78.5

EBSCOhost - printed on 2/13/2023 5:26 AM via . All use subject to https://www.ebsco.com/terms-of-use

and candoluminescence), by particle radiation (e.g., alpha particles), by electrons (cathodoluminescence, beta-excited luminescence), by ions (ionoluminescence), sound (sonoluminescence), and by mechanical action (triboluminescence). The excitation energy usually needs to be greater than the energy of the emitted photons, but it is possible to have luminescence due to the sum of two electronic absorptions (two photon transitions) or thermal plus electronic photon absorptions where the emitted photon energies are larger than the single highest energy excitation photon (anti-Stokes luminescence). Another pathway is the use of a low energy photon (thermal or electronic) to trigger decay of a previously excited state that did not result in luminescence (thermoluminescence, optical-stimulated luminescence or OSL).

Fluorescence

Fluorescence (or Photoluminescence – PL) is the emission of a visible photon (generally, though sometimes this term is used for IR or UV emission) after absorption of a photon with higher energy, the difference being called the Stokes shift (Fig. 1). Under ideal circumstances it is possible to observe resonant emission, i.e. at the same energy as the excitation, corresponding to no loss of thermal energy in the absorber prior to emission. Depending on the electronic transitions connected with absorption and emission, fluorescence can have a broad range of lifetimes. Fluorescence is commonly studied with UV excitation, and mineral luminescence is frequently discussed with respect to the common UV bands UVA, UVB and UVC, and the readily available UV sources, excited Hg vapor 366 nm UVA emission, UVC-excited UVB phosphors ranging from ca. 300-325 nm, and excited Hg vapor 254 nm UVC emission, respectively. However for complete analysis the entire excitation spectrum of mineral fluorescence is required for all strong emission bands.

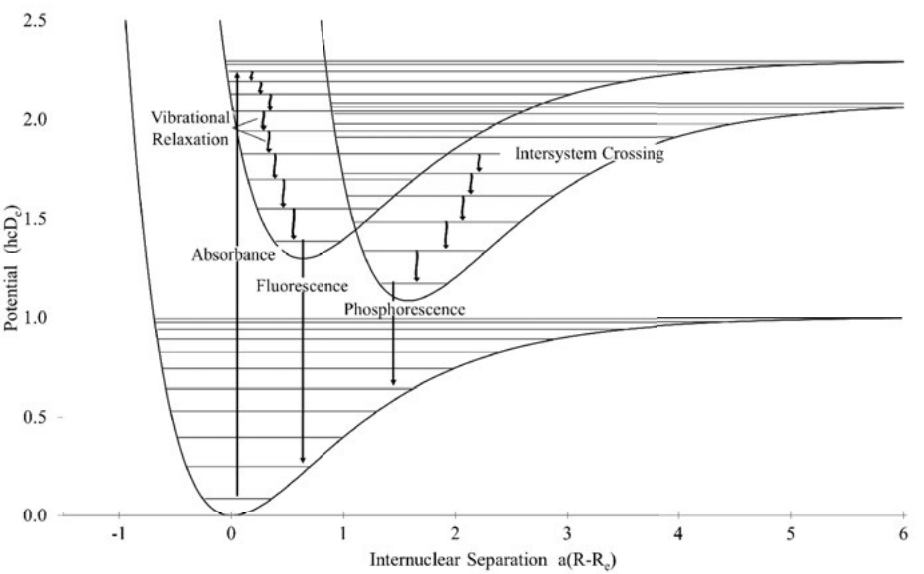


Figure 1. Fluorescence and phosphorescence processes in a configurational coordinate diagram. The internuclear separation change upon excitation (e.g., metal-oxygen bond) is scaled in the figure but typically may be on the order of 5-10% in inorganic systems. Fluorescence is shifted in energy from the absorption due to one or more vibrational excitations. Phosphorescence is a separate emission transition from a triplet spin state (in organic molecules) to a ground singlet state, or generally a spin-forbidden transition. Each potential energy curve defines an electronic state of an activator system. (modified image from Wikimedia commons).

EBSCOhost - printed on 2/13/2023 5:26 AM via . All use subject to https://www.ebsco.com/terms-of-use

Phosphorescence

Phosphorescence and Afterglow are terms referring to luminescence emission once the excitation source is extinguished, but the usage of "phosphorescence" in the literature is inconsistent. Phosphorescence was originally used to describe the long fluorescence lifetimes associated with singlet-triplet (spin-forbidden) electronic transitions in organic solids (Fig. 1). In many such cases the lifetimes of excited states can approach seconds, and hence a long-lived emission post excitation is readily visible to the eye. This term has come to be used for all emission that is "slow" by eye, though spin-forbidden emission in transition metal oxides and silicates with lifetimes of milliseconds is usually considered fluorescence. Also Thermoluminescence is often what is seen when a source is turned off, representing the slow emission of shallow depth trapped electrons from ambient temperature. The term Afterglow avoids all the confusion, and is simply defined as whatever is observed once excitation is stopped.

Thermoluminescence

Thermoluminescence (TL) is thermally activated fluorescence, with the trigger being stimulation of electrons that have entered trapping states during excitation (Fig. 2). In the energy band model electron trapping states are present below the conduction band and above the Fermi energy (mean level of highest energy filled electronic states). The thermal trigger is thus the energy difference between trapping level and the bottom of the conduction band. The energy difference is called the trap "depth" and is expressed in energy units or as equivalent temperature (k*T*). Once electrons are freed from traps they enter the conduction band where they can move through the structure until interacting with a luminescence center where they can recombine to produce an excited state that subsequently can decay to the ground state and emit light. Alternatively, trapping states can be on structural positions close enough to activator centers so that there can be direct energy transfer without involving the conduction band. This happens in minerals with high concentration of trapping states, and produces different TL decay

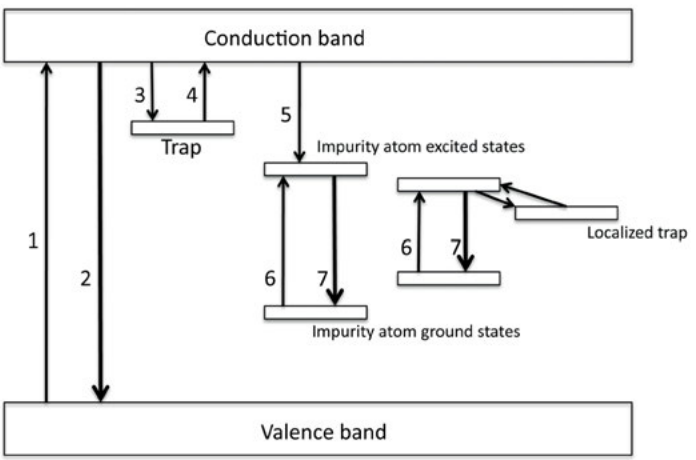


Figure 2. Thermoluminescence process in a simple band model. Excitation at the band gap energy (1) can lead to band gap emission (2) or to electron trapping (3). Thermal energy or photon excitation can lead to emptying of the trap (4) returning the electron to the conduction band and possible reemission (2). Impurity atoms having ground and excited states in the band gap can also be excited from the conduction band or from released trapped electrons (5). The atoms can also be excited directly (6) without involving the conduction band, leading to localized emission (7). Defects physically near an impurity atom can also function as traps for an impurity atom.

EBSCOhost - printed on 2/13/2023 5:26 AM via . All use subject to https://www.ebsco.com/terms-of-use

profiles. Typical TL trapping centers may be damaged sites produced by radioactivity (e.g., ion vacancies or interstitials), stacking faults, or other structural defects. Ion substitutions in a structure that are positively charged and thus can bond an excited electron generated locally, e.g., As^{5+} substituting for Si^{4+} in Mn^{2+} activated willemite (Zn_2SiO_4) are another type of trap. TL also can be excited by photons as optically stimulated luminescence (OSL) (or IRSL in the case of infrared photons), and this is particularly effective using powerful diode lasers. OSL is notably used in radiation dosimetry technology but has a significant geological application in dating sediments up to several tens of thousands of years old. Bos (2007) described the theory behind the basic TL process for a system with one trapping center and one recombination center, which affords a good introduction to the process. A more detailed theoretical treatment including the full complexity of the phenomenon and including simulation calculations is available (Chen and Pagonis 2011).

Cathodoluminescence

Cathodoluminescence (CL) can be observed in any electron-beam device and is now popularly measured quantitatively in SEM and electron probe microanalyzer (EPMA) instruments, as well as bench-top optical microscope based systems. As electrons in a beam device have energies far in advance of UV photons (usually thousands of eV compared to 3-10 eV or so) besides direct excitation, a cascade of processes (Fig. 3) ensue in a solid that all affect excitation of luminescence (Garlick 1962; Götze and Kempe 2009). Besides this, the energy density for electron beam excitation far exceeds what is available except with high power focused lasers, so that even very weak excitation processes may be activated and contribute to emission. Activation is to a depth on the order of microns in general, but any high energy X-ray and UV photons produced in the cascade may excite luminescence over a larger volume. This type of excitation has many advantages over classical spectroscopy, but there are also accompanying limitations. It can be an excellent phase identification tool, able to map small phases that might be hard to distinguish by regular optical means, or even by EPMA. It also can reveal very small amounts of activators, e.g., trivalent rare earths, Mn^{2+}, as well as structural defects that may trap electrons by creating localized states (Götze and Kempe 2009). As structural defects are related to the temperature of formation, and other physical processes that the sample may

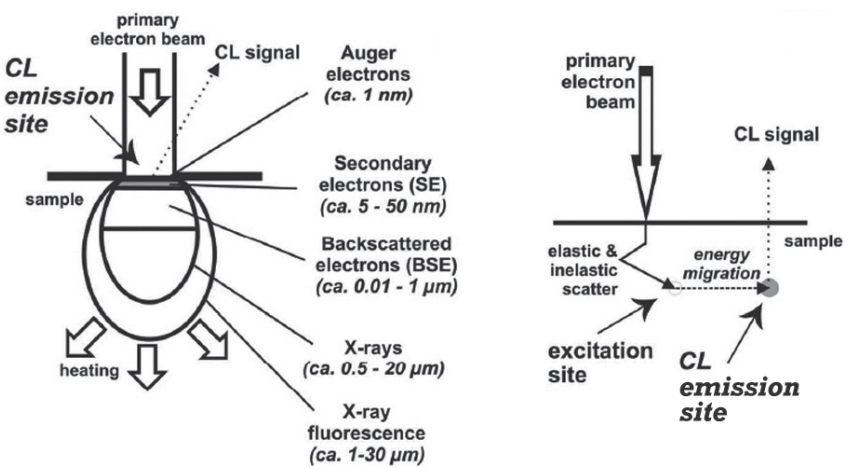


Figure 3. Interactions of an electron beam with a solid surface showing the affected volume of a sample and types of emitted radiation (*left*), and indirect process of exciting cathodoluminescence (*right*). X-ray emission includes both characteristic and continuum varieties. [Used with permission of Springer-Verlag from Götze and Kemp (2009), Fig. 1.2.]

EBSCOhost - printed on 2/13/2023 5:26 AM via . All use subject to https://www.ebsco.com/terms-of-use

have undergone, CL can be a powerful tool in evaluating formation or alteration history. All of this can be done on a micron or smaller scale, enabling imaging of impurities, crystal defects, growth patterns and other formation or alteration features (Yacobi and Holt 1990). Limitations include inability to measure excitation spectra, so all analysis is done via emission spectra, and restrictions on time-resolution methodology. Hence CL is not always a strong technique for identification of activators except possibly by comparison with spectra from synthetic well-characterized materials, and with use of other types of complementary spectroscopy. This works particularly well with rare earth activators that have sharp *f*-*f* transitions whose energy is generally independent of site in the host material. Defects that give rise to CL are often more complicated to identify, although a significant effort has been devoted to silica defect characterization. CL emission spectra are likely to deviate markedly from fluorescence spectra created with UV light, as the threshold for exciting luminescence centers is far smaller with CL.

X-ray excited optical luminescence

X-ray excited optical luminescence (XEOL) is a relatively new technique that takes advantage of the characteristic energies of elemental X-ray absorption. In this method specific luminescent centers or activators (see below) can be preferentially probed as causes of emission, hence directly identifying the responsible impurity. XEOL can be used with XAS spectroscopy to recover the X-ray absorption spectrum (EXAFS or XANES) of the emission center, hence potentially revealing if it is a substituent, defect site or minor phase inclusion, and the local molecular structure in its vicinity (Taylor et al. 2013). Time-resolved studies into the picosecond regime are also possible taking advantage of synchrotron bunch timing structures (Ko et al. 2006; Mosselmans et al. 2012).

Activators, sensitizers, and quenchers

Activators. Activators are substituents in a mineral that confer luminescent activity. Usually they have electronic structure with absorption transitions in the UV, and emission transitions in the visible. A simple example is Cr^{3+} with transitions in the UV, blue, and red, all exciting fluorescence in the red. The Cr^{3+} transitions are associated with 3*d* electronic states, and are said to be metal ion states. Other activators have energy states with a large ligand contribution, and the states are more properly described by molecular orbitals (MOs) of mixed character. An example is MoO_4^{2-}, molybdate, where the main luminescent transition is a charge-transfer band, i.e., a transition from a mainly metal MO to an excited state that is mainly ligand type. In such a case the activator is the entire molybdate cluster. In insulating minerals, the electronic states of the activator are usually located in the band gap energy range and hence excitation can be localized to the activator if it is photon-excited, e.g., with a fluorescence spectrometer or with UV radiation. Band gap excitation would dominate in the case of cathodoluminescence (Fig. 2 arrow 5).

Sensitizers. These combine with activators to foster luminescence, and operate in several ways. If the potential activator has only forbidden (weak) excitation transitions, then instead of being activated directly, say by UV, it can instead receive the excitation energy from the sensitizer. The classic case is Mn^{2+} luminescence in calcite. Mn^{2+} has 3*d* transitions that are spin forbidden and thus very weak, so Mn^{2+}-activated luminescence excited by UV is extremely weak without a sensitizer. (However it is observable with the intense energy density possible with CL or laser excitation.) If the sensitizer is Pb^{2+}, there is strong absorption in UVC due to Pb^{2+} charge-transfer excitation. The excitation energy is directly transferred to a nearby Mn^{2+}, assuming proximity due to sufficient concentration, which will then emit in the orange-red. The forbidden emission transition has a lifetime of many milliseconds, giving rise to afterglow regardless of the absence of trapping levels. Similarly, rare earth impurities can absorb UVA and UVB energy and sensitize Mn^{2+} emission. Sensitizers may include an entire structural unit of a mineral, such as a silicate network, that absorbs UV preferentially.

EBSCOhost - printed on 2/13/2023 5:26 AM via . All use subject to https://www.ebsco.com/terms-of-use

Quenchers. These are ions whose electronic states can efficiently accept excitation energy by a variety of processes and convert it entirely into thermal energy. Hence they remove excitation energy from other excited activators and provide an alternative "nonradiative" pathway to return to the ground state. Important examples are ions with strong charge-transfer absorption bands. Quenching can also occur from self-absorption effects at high activator concentrations, from defects in a structure that provide pathways for nonradiative energy transfer, and by increased temperature. Temperature-quenching affects luminescence by making it more likely for the excited state of an activator or luminescent center to intersect the ion's own ground state, or that of another activator or defect, and thus bleed off all excitation energy into thermal vibrations. Some concepts for activators, sensitizers and quenching are shown in Figure 4.

Activators, sensitizers, and quenchers may be substitutional impurities in a structure, such as Mn^{2+} Fe^{2+}, and Pb^{2+} in calcite, or they may be intrinsic constituents, such as molybdate or tungstate in powellite and scheelite, respectively. Or, they may be defect states such as vacancies with strongly trapped electrons or charge-compensating ions. Radiation damage often can create defect states that can act as luminescent centers. In some cases the defects include multiple substitutions and clusters with various charge states. This is the situation with nitrogen defects in diamond, the luminescence of which have been thoroughly studied (e.g., Gaft et al. 2005).

Defect states are important electron traps and we customarily distinguish defects that can bind electrons that can readily be removed by thermal (or optical) excitation creating TL and OSL, from more tightly bound electronic states that are stable to higher temperatures. However defect states can exist over a wide range of energies. CL in quartz is due to a large number of possible defect states created by lattice vacancies, dangling bonds, and charge states produced by heterovalent cation substitutions (e.g., Al for Si) among other possibilities (Götze et al. 2001, 2005). Quartz has been extensively studied, but it is likely that related defect states exist in many silicates and the topic has been incompletely explored.

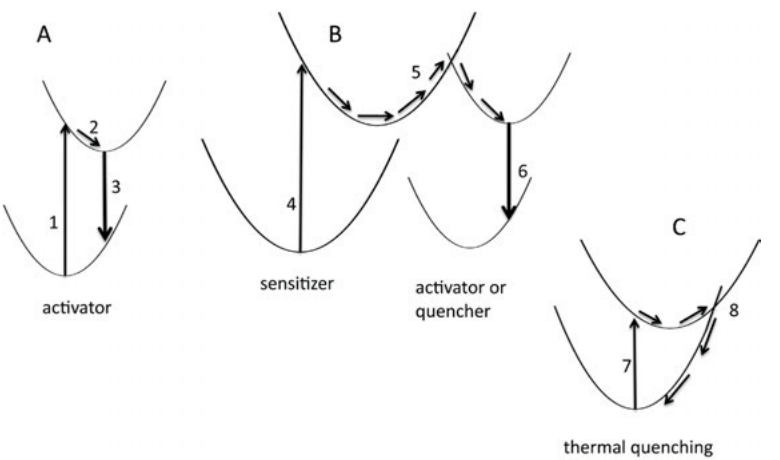


Figure 4. Activators, sensitizers and quenching impurities. Configurational coordinate diagrams showing approximate topologies. (A) Activator excitation (1), vibrational relaxation (2), emission (3). (B) Sensitizer excitation (4), intersystem crossing to excited state of activator (5), emission from activator (6). Note that the activator is essentially quenching possible emission from the sensitizer. (C) temperature quenching of activator. At sufficiently high temperature the ground and excited state can intersect allowing energy to bleed off as vibrational relaxation (radiationless transition).

EBSCOhost - printed on 2/13/2023 5:26 AM via . All use subject to https://www.ebsco.com/terms-of-use

Emission and excitation spectra

Absorption spectra record the energies of electronic transitions from ground to various excited states of an activator or luminescence center, while emission spectra record only the transition from the particular excited state that produces emission. In rare cases two excited states of the same activator may both produce emission from a single type of excitation, if they are near in energy, or can transfer energy between one another. Excitation spectra record the electronic transitions that give rise to a given emission, and hence they show all electronic transitions to higher energies that can transfer energy to the excited state and produce emission. This means that comparison of the excitation spectrum of an unknown activator with characteristic absorption spectra of the same ion or center can identify that ion as the activator, as they must have the same energy levels and energy level spacings. This is shown for a simple case in Figure 5 where the electronic states of Cr^{3+} in octahedral coordination by oxygen (the case for ruby) are shown. One can see the absorption and excitation spectra are equivalent, while only the ground state ^2E is seen in the emission spectrum. Another example of excitation/absorption spectrum comparison is Fe^{3+} in tetrahedral coordination in feldspar, as is shown in Figure 15 of Waychunas (1988). Collection and analysis of spectral data is analogous to optical absorption spectroscopy (see Rossman 2014, this volume), inasmuch as selection rules and electronic states are identified in the same manner. Excellent summaries are available that discuss general aspects of luminescence spectroscopy (e.g., Blasse and Grabmaier 1994; Henderson and Imbusch 2006), while mineralogical luminescence spectroscopy has been presented mainly as catalogs of spectra with chemical and structural interpretations (Gorobets and Rogojine 2002; Gaft et al. 2005), besides the review chapters noted earlier.

An important difference between luminescence and optical absorption spectra is the fact that all luminescence spectra depend on two transitions, an absorption and emission process. In the case of sensitized luminescence there is an additional energy transfer between centers. Essentially all luminescence processes also involve the generation of vibrations that depend on local structure. Whereas calculation of optical spectra absorption transition probabilities is possible, excited state calculations necessary to simulate the emission transition as well as all energy transfer processes are relatively more difficult. Hence there is direct modeling

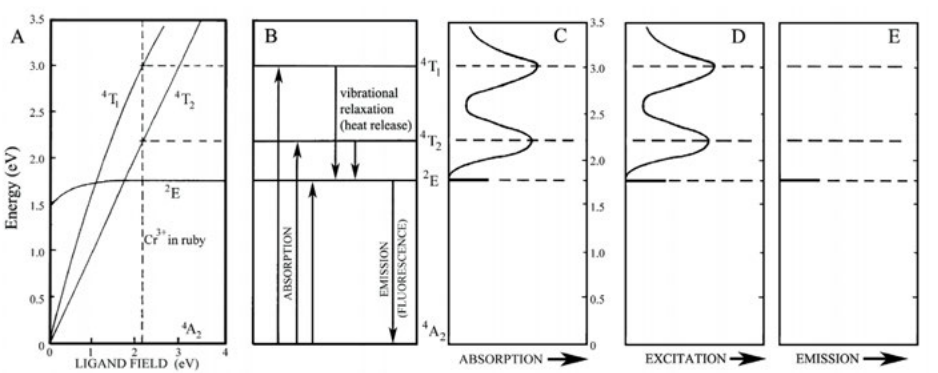


Figure 5. Relationship of excitation, emission and absorption spectra. (A) Section of Tanabe-Sugano diagram for $3d^3$ ion (Cr^{3+}) in an octahedral crystal field in ruby showing electronic states involved in luminescence. Ligand field in ruby is indicated by dashed vertical line and horizontal dashed lines indicate energies for the transitions. Note that the state field dependencies (slopes of the curves) correlate to band width. (B) Transitions for absorption in ruby ($^4A_2 \rightarrow {}^4T_1, {}^4T_2$), vibrational relaxations (see Fig. 1), and fluorescence emission transition. (C) Absorption spectrum consistent with B. (D) Excitation spectrum showing absorption bands leading to fluorescence emission. (E) Emission spectrum (single narrow band).

EBSCOhost - printed on 2/13/2023 5:26 AM via . All use subject to https://www.ebsco.com/terms-of-use

of luminescence spectra only for certain materials applications, notably laser crystals, and the results are generally semi-quantitative. More precise calculations are possible for organic molecules in solvents.

Semiconductor vs. insulator models

Luminescence processes differ between insulating (large band gap) and semiconducting (narrow band gap) minerals. In insulators the electronic states responsible for photoluminescence are usually within the band gap, and hence most excitations are localized. With semiconducting materials the transitions include the conduction band, and are thus delocalized. Such transitions produce photoconductivity, as electrons are added to the conduction band via excitation. Luminescence in photoconductive minerals is relatively less important in mineralogy, as most rock-forming minerals that frequently show luminescence are large band gap insulators (feldspars, quartz, amphiboles, pyroxenes, carbonates, halides, phosphates). Exceptions are ZnS, and a few rare sulfides and halides, and these can show very interesting luminescent properties. For example, impurities in ZnS can produce practically any emission color. Band properties are also important in thermoluminescent systems where trapped electrons are assumed freed into the conduction band even in large band gap minerals. The high excitation energy of cathodoluminescence can also involve the band gap in creating electron-hole pairs and a cascade of luminescent processes.

Luminescence in organic molecules and structures

Most of this chapter deals with inorganic systems, but just as mineralogy-geochemistry has evolved during the past few decades to embrace systematic and pervasive interactions with organic reactions and biogeochemical processes, the importance of luminescence studies of organic environmental materials is likely to increase dramatically. The overall description of luminescent processes above is applicable to organic molecules and condensates with some differences. Electronic transitions in organic molecular structures that give rise to luminescence usually involve π-bonding molecular orbitals and hence are generally associated with aromatic structures and molecules with multiple C=C double bonds. These systems are well described using configurational coordinate diagrams, and historically a vast amount of literature has been written on luminescence in organic systems exploring the associations of molecule structure with electronic structure, and thus the changes in fluorescence and the efficiency of fluorescence with variations in ring structure, side organic chains, types of functional groups and many other chemical aspects (Valeur 2001).

Some general trends in molecular structure include: 1) shift in the energy of the lowest excited state as aromatic systems are extended. Hence larger π-bonded systems have absorption bands that shift to lower energies, and often have lower energy emission bands; 2) shifts in excited state energies associated with electron-withdrawing substituents such as F^-, Cl^- and Br-; and 3) significant changes in efficiency with configurational changes, and with the nature of solvating species, e.g., water versus less polarized molecular media.

Luminescence spectroscopy with organic materials are commonly done using statistical and "fingerprint" approaches as the materials are usually comprised of a large number of species, and analysis of spectra as if only a few species are present is not effective. Hence approaches such as total luminescence spectra analysis (see next section) are commonly utilized, and analysis often involves correlation of features or bands with standards. It is expected that this area will advance to more detailed molecular specificity as selective excitation and time-resolved measurements are more commonplace.

Total Luminescence Spectra

A relatively new way to present and use luminescence spectra is by plotting measured luminescence intensity vs. emission and excitation wavelengths in a 2D or 3D plot (Fig. 6),

EBSCOhost - printed on 2/13/2023 5:26 AM via . All use subject to https://www.ebsco.com/terms-of-use

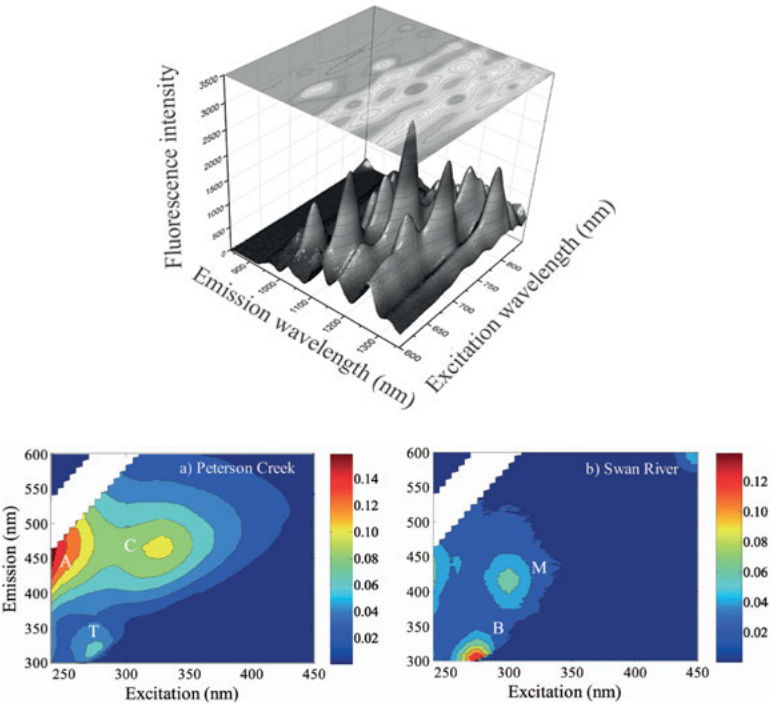


Figure 6. TLS plots. *Top*: three dimensional representations showing the derivation of the 2D emission-excitation matrix (EEM) plot. Modified from OriginLab webpage. *Bottom*: Examples of EEMs modified from Fellman et al. (2010) for DOM in natural waters.

called a total luminescence spectrum (TLS) or an excitation-emission matrix spectrum (EEM). Instead of analyzing particular spectral features and electronic structure, the 2D maps can function as fingerprints of a given luminescence system, which is useful when all samples have complex mixtures of fluorescent agents, e.g., organic contaminants. An example of this is found in evaluating cell culture components (Li et al. 2011), and for dissolved (DOM) and solid organic matter (NOM) that show characteristic changes in organic species (Alberts and Takacs 2004; Baker et al. 2008; Fellman et al. 2010) between size fractions and localities. The advantage of the approach is that statistical and chemometric analysis can be used to determine trends in speciation without detailed processing of very many individual spectra and model spectra. This is extremely advantageous for dynamic evaluation of ecosystems and water quality. Alternatively, the TLS plot can be interrogated (i.e., sliced) to provide excitation or emission spectra at particular emission or excitation wavelengths, respectively. Hence the TLS provides a very complete image of the luminescent electronic system of the sample.

SPECIFIC LUMINESCENCE METHODOLOGY AND APPLICATIONS

Time-gated laser excitation and emission techniques

Time-gated laser methods take advantage of the fact that electronic transitions in minerals have much different lifetimes depending on the nature of the transition (electric dipole, magnetic dipole, charge transfer, etc.), and the symmetry of the electronic states involved. Hence it is possible to select one type of transition to study even in an impure material that

EBSCOhost - printed on 2/13/2023 5:26 AM via . All use subject to https://www.ebsco.com/terms-of-use

may have many kinds of activators. Laser excitation also has high energy density, and hence can excite luminescence even at low activation levels. In execution both the laser excitation and detector must be gated (i.e., with both a time-delay and window duration) in order to separate out clean spectra (Fig. 7). These characteristics have been exploited by a number of researchers, notably Gaft and colleagues (Gaft et al. 2005), to explore mineral luminescence activation. This work has been extremely successful, such that most types of impurity activation can be effectively studied in this way, though complementary chemical analysis at the parts per billion (or better) level is usually required to narrow the chemical possibilities during interpretation. Luminescence created by radiation-induced defects can also be examined with this technology, but in such cases complementary analysis of the defect centers is crucial to making unambiguous interpretations. Such difficulty with respect to identifying defect activation in unusual (so-called "Terlingua Type") calcite luminescence (Gaft et al. 2008) suggested that ESR or perhaps optically-excited EXAFS studies (XEOL) would be needed to ultimately connect the states observed with definite impurities. Another version of laser-excited luminescence spectroscopy is termed time-resolved laser fluorescence spectroscopy (TRLFS), and is usually focused only on lifetime analysis. It has become popular for measurement of fluorescence lifetimes in solutions, at interfaces and in particles.

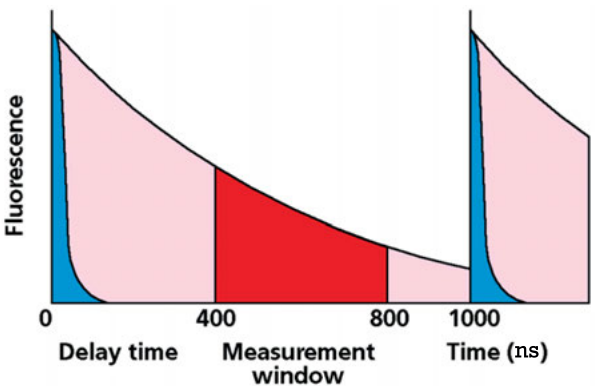


Figure 7. Basic concept for time-resolved laser-excited fluorescence analysis. Laser pulse width is considered to be very short (e.g., 1 picosecond), and the interval between pulses here is 1000 ns = 1 microsecond. After a delay of 400 ns the spectrometer is gated on and spectra collected. This window is kept open for 400 ns. The process is repeated for each laser excitation pulse. In this case only the long lifetime fluorescence will contribute to the emission spectrum. To collect the short lifetime fluorescence spectrum no delay and a very brief gated window would be used. By using several gates and delays the different spectral contributions can be separated. Additional ways to separate spectral contributions, e.g., using different excitation energies, different temperatures and polarization, can be used in combination with time-resolution (modified image from Wikimedia commons).

EXAMPLES OF APPLICATIONS

Activator determination

Pb^{2+}. Divalent lead functions as both an activator and a sensitizer in calcite, but is probably an important activator in many more species than have been examined to date. Unfortunately, without use of laser excitation and time-resolved luminescence spectroscopy, it is difficult to unravel Pb^{2+} luminescent activity from that due to Ce^{3+} and Eu^{2+}, and perhaps other possible activators. This has been shown very clearly by work of Gaft et al. (2002) in exploring the luminescence of hardystonite, hydrozincite and calcite. Figure 8 shows

EBSCOhost - printed on 2/13/2023 5:26 AM via . All use subject to https://www.ebsco.com/terms-of-use

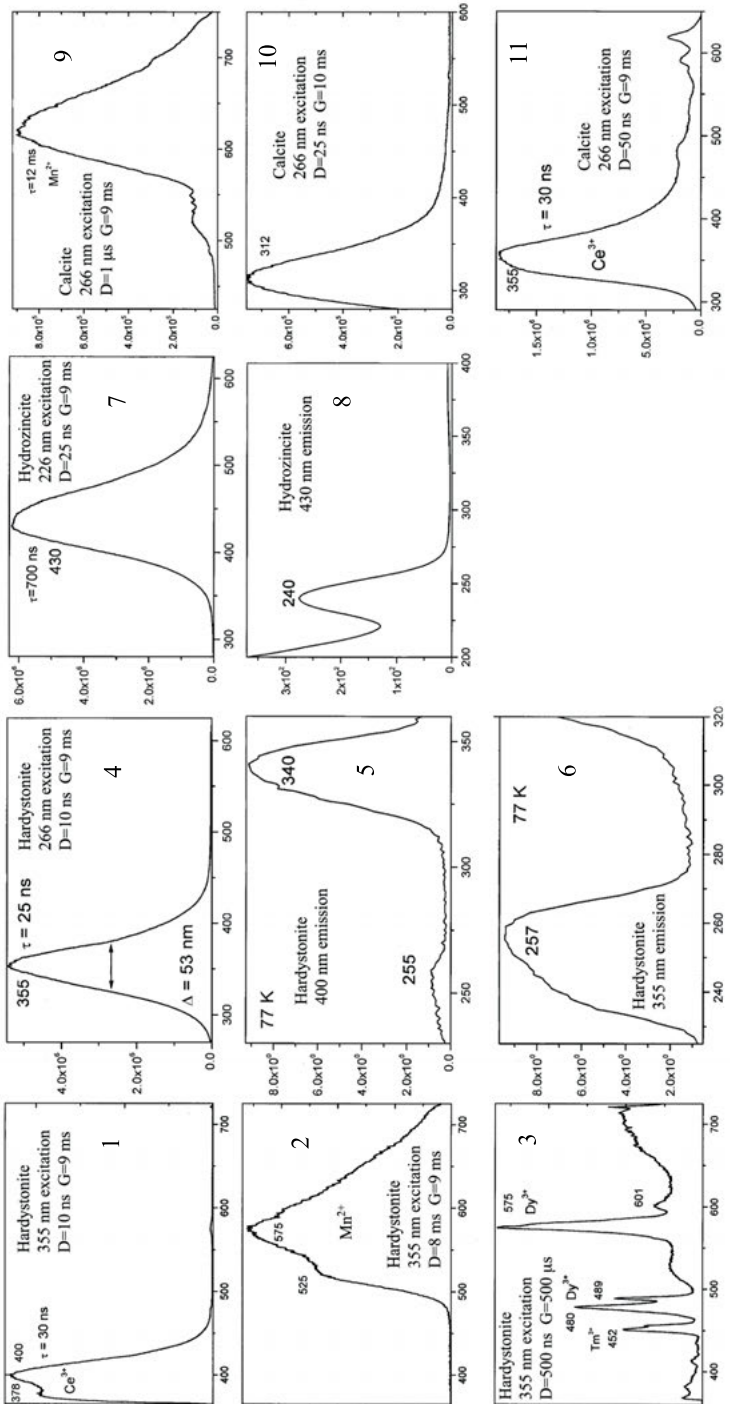


Figure 8. Time gated luminescence of Pb^{2+} in minerals. (1-3) luminescence emission spectra laser excited at 355 nm from hardystonite (Franklin, New Jersey) recorded at different delay and gate timing, separates different activator contributions. (4) Emission excited at 266 nm gives rise to a different energy and shape band, not consistent with Ce^{3+}, and lifetime and excitation spectra (5-6) indicate Pb^{2+}. (5) Excitation spectrum for 400 nm cerium emission band. (6) Excitation spectrum for 355 nm emission band. (7) emission spectrum for hydrozincite excited at 226 nm. (8) Excitation spectrum corresponding to the emission band in (7). Note similarities with Pb^{2+} bands in hardystonite. (9-10) emission from calcite (Franklin, NJ) with different time resolution, corresponding to Mn^{2+} and Pb^{2+} activators. (11) Emission from calcite (Stepnyak, Kazakhstan) showing mainly Ce^{3+} activation. Modified from Gaft et al. (2005).

EBSCOhost - printed on 2/13/2023 5:26 AM via . All use subject to https://www.ebsco.com/terms-of-use

time-resolved luminescence spectra for all three minerals. In hardystonite, a rare mineral from Franklin, NJ, emission can occur from Pb^{2+}, Ce^{3+}, Mn^{2+}, and several rare earths. After laser pulse excitation at 355 nm the emission due to Ce^{3+}, with bands at 378 and 400 nm, is observed alone using a delay of 10 ns and a long gate period. However with the same excitation wavelength if the luminescence is observed after a delay of 8 ms, the short lifetime Ce^{3+} emission is no longer present, and now only long lifetime (spin-forbidden) Mn^{2+} emission is observed. At intermediate delays and varying gate periods, emission from rare earths can be detected and partially separated. In contrast, the luminescence emission from Pb^{2+} at 355 nm is strongly excited by 266 nm excitation, and cleanly observed with a delay of 10 ns. Collection of excitation spectra at the emission wavelengths with similar time-resolution and gating shows distinct excited states for the Pb and Ce activators, which could not be resolved using steady-state conventional approaches. In the case of hydrozincite, a common result of weathering of Pb-Zn ore, strong luminescence is generally observed in natural samples using UVC ultraviolet lamps, but not observed in pure synthetic hydrozincite. Figure 8 shows the emission with excitation at 226 nm, a delay of 25 ns and a long gate period. The emission is a single band at 430 nm and the excitation spectrum indicates a large Stokes shift. These luminescence characteristics are consistent with Pb^{2+} in an octahedral Zn site in hydrozincite. For natural calcite, Ce^{3+}, Pb^{2+} and Mn^{2+} emission can be separated using different delays and gate periods. Mn^{2+} emission at 630 nm dominates for longer delays and very long gate periods, but shorted delays and brief gate periods reveal the Pb^{2+} emission at 312 nm and the Ce^{3+} emission at 355 nm.

The lifetimes of the excited state of these ions in these species, all presumed to be in octahedral oxygen coordination, are also characteristic. Ce^{3+}, like many trivalent lanthanides *f-f* transitions are typically in the tens of nanoseconds, while the charge-transfer state for Pb^{2+} is in the hundreds of nanoseconds, and the spin-forbidden Mn^{2+} in the several to tens of milliseconds. Hence both electronic structure as evidenced by emission and excitation band positions and spacings, and excited state lifetimes, serve to distinguish these activators.

S_2^- and O_2^- ions. Charged disulfide and dioxide (superoxide) radicals are unstable in solutions but can be found as stabilized species in minerals, with both potentially acting as luminescence centers (Taraschan 1978). Until recently, luminescence associated with S_2^- was not reproducibly characterized, with varying reported band positions, but this has been partially explained with the use of time-resolved spectroscopy (Gaft et al. 2009). The disulfide radical is found in feldspathoid minerals and presents dramatic and unique luminescent emission in tugtupite (red color), sodalite (orange color) and scapolite (yellow color). Some species, notably hackmanite, exhibit tenebresence (or photochromatic behavior), where strong physical coloration is created by exposure to UV, then bleached away with exposure to daylight. The transient color presumably is due to excitation of an electron from the S_2^- or S_2 disulfide molecule anion into a local trap, which creates a light absorption center similar to an F center. The trapped electrons can be freed by suitable excitation, analogous to thermoluminescence, but here changing coloration without light emission. Luminescence is due to excitation of the S_2^- radical. At room temperature with 355 nm excitation, the S_2^- emission is a broad band at about 605 nm in sodalite, and some vibronic structure is evident at 77K due to the vibrations of the S-S molecule. At 77 K with an 80 ns delay and 1 ms gate very strong vibronic structure is seen (Fig. 9). Differing reports of the band positions appears to be related to the existence of several types of disulfide centers, likely related to variations in local chemistry (e.g., Al, Si ratio, charge-compensating ions). Time-resolved experiments also allow other luminescent centers to be identified in sodalites, including Fe^{3+} in tetrahedral coordination (red-orange emission), and Mn^{2+} (green emission), Eu^{2+} (violet emission), Pb^{2+} (UV emission) all probably substituting for Na. Related to S_2^- is the isoelectronic superoxide radical O_2^- which has been identified in zeolites, anhydrite and fluorite minerals (Taraschan 1978), and which creates a blue or blue-green emission. This is an important radical in organic and bioorganic chemistry, and probably is a more

EBSCOhost - printed on 2/13/2023 5:26 AM via . All use subject to https://www.ebsco.com/terms-of-use

prevalent activator of luminescence than has been realized. Still another "dimer" center analog is the Se_2^- radical, which is responsible for the strong coloration seen in red ultramarines (Schlaich et al. 2000).

Zircon luminescence. Although luminescence in zircon is a useful tool for identifying zonation and alteration or growth history using CL, the activation processes for luminescence in natural zircon have been incompletely characterized, thus reducing potential geochemical information from spectral analysis of the emission. Zircon typically contains trivalent REE substituting into the Zr site, but can also incorporate transition metals into both the Zr octahedral site and the Si tetrahedral site, and additional species into radiation-produced defect, and interstitial sites. In particular, the characteristic broad band yellow emission at about 575 nm in most natural zircon crystals could not be assigned to specific activators by using conventional luminescence spectroscopy. However Gaft et al. (2002) showed by using time-resolved methods that this band was related to damage produced by neutron or alpha irradiation. They doped a synthetic zircon with Eu, leading to Eu^{3+} emission centers (Fig. 10a) that produced sharp emission bands yielding a net orange luminescence. Subsequent irradiation with neutrons generated a much stronger yellow emission band that overwhelmed the Eu^{3+} activation (Fig. 10b). A separate undoped synthetic zircon sample also showed the same broad yellow emission after alpha irradiation (Fig. 10c). The strength of this yellow band was found to increase with radiation dose, and in all cases had spectral characteristics very close to that seen in most natural zircon crystals, e.g., peak width, asymmetry and lifetime (Fig. 10d). A variety of delay times and gate periods indicated only one type of emission center, although the width would seem to suggest a range of local variations at this site. EPR evidence suggested that this band is associated with silicate defects, but a precise assignment could not be made. In both naturals and synthetics the broad emission is removed by annealing at 900 °C or above, and reinstated by alpha or neutron radiation, but not caused by X-ray, beta, or gamma irradiation. These findings indicate that natural uranium, thorium or other radioactive impurity in zircon probably gives rise to the luminescence indirectly through defect generation.

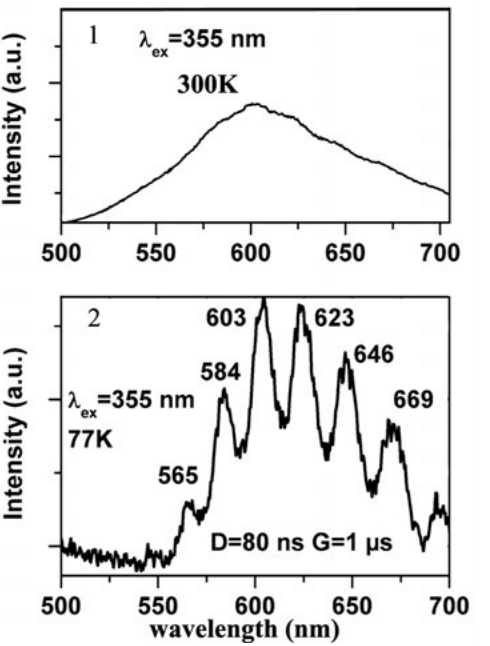


Figure 9. S_2^- in sodalite luminescence spectra. (1) Room temperature emission with 355 nm laser excitation. Vibronic bands are weakly visible. (2) time-gated emission spectrum at 77 K, also 355 nm excitation. Vibronic bands dominate the spectrum. Modified from Gaft et al. (2009).

Other emission bands were also examined by Gaft et al. (2002) including synthetic zircons doped with Mn^{2+}, Fe^{3+}, the uranyl ion, Pb^{2+}, and other elements. Mn^{2+} has a similar radius to Zr^{4+}, but likely is not stable in the zircon structure, instead substituting as Mn^{4+}. Both types of Mn give rise to characteristic emission bands, which are also affected by the presence of co-activators. However time resolved spectroscopy has not revealed either of these substitutions explicitly in natural zircon crystals. In contrast, Fe^{3+} doping was shown to correlate with a broad emission band often observed in natural zircons, and probably due to Fe^{3+} in the tetra-

EBSCOhost - printed on 2/13/2023 5:26 AM via . All use subject to https://www.ebsco.com/terms-of-use

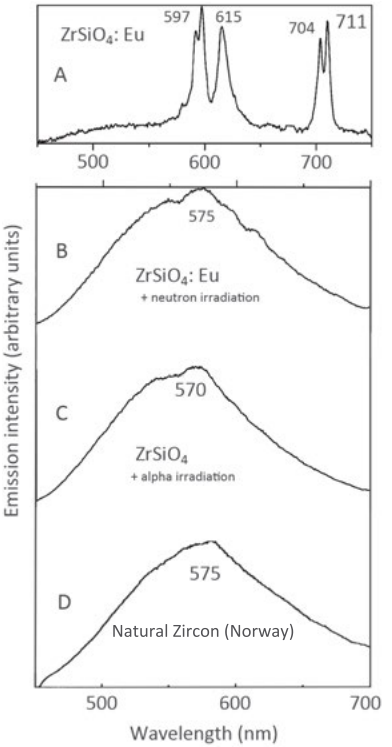


Figure 10. Time-gated luminescence in zircon. (A) Synthetic zircon doped with Eu^{3+}. (B) sample from (A) after neutron irradiation. Broad band emission centered about 575 nm dominates spectrum. (C) Synthetic zircon after alpha irradiation. (D) Luminescence spectrum of a natural zircon from Norway showing very similar broad band emission. Delay is 10 ns, gate width is 9 ms. Excitation at 337 nm. Modified from Gaft et al. (2000, 2002).

hedral site (Fig. 11A). Ti^{3+} and Cr^{3+} emission was ruled out as causes of this broad band, long lifetime emission. Uranyl and P^{5+} doping generated uranyl emission similar to that observed in natural zircon, with a characteristic vibronic structure and the emission peaking around 510 nm (Fig. 11B). However doping without P^{5+} produced no emission. This suggests a charge-coupled substitution involving P^{5+} substituting for Si^{4+} may be required to stabilize uranyl in the structure. Pb-doped synthetic zircons produce a broad-band emission at 515 nm, but this band is not seen in natural zircon crystals.

These various studies thus suggest that the yellow emission of zircon is radiation dose dependent and closely connected to U or other alpha-emitter concentration, but zircon may also have emission due to a red band from Fe^{3+} activation, and from direct uranyl activation. REE also produce emission centers, most notably trivalent Dy^{3+}, and to a lesser extent Tb^{3+} but these have not been thoroughly evaluated using time-resolved methods. Observations on synthetic zircons with various REE doping have been done using CL excitation (Hanchar et al. 2001).

Site occupancy and partitioning

If the optical absorption spectrum for a given valence state of a substitutional impurity differs significantly between mineral structural sites that compete for its occupation, it may be possible to determine site occupation and partitioning by either optical or luminescence spectroscopy. For the optical case, if the electronic structure of the impurity is different in each site there would be shifts

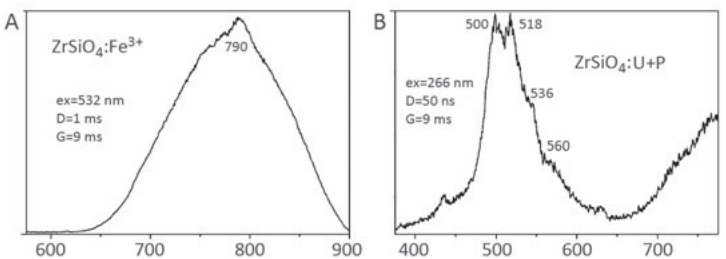


Figure 11. Iron and uranyl in zircon. (A) Fe^{3+} believed to be substituting in the tetrahedral silicon site. (B) Uranyl showing vibronic structure due to axial oxygens in a synthetic zircon with co-substituent P. It is believed that there is a charge-coupled substitution, such as $2\ P^{5+} + UO_2^{2+} = Zr^{4+} + 2\ Si^{4+}$, but this has not yet been verified. Zircon doped only with uranyl shows no emission, possibly due to reduction of the uranyl and substitution of U^{4+} for Zr^{4+}. Modified from Gaft et al. (2002).

EBSCOhost - printed on 2/13/2023 5:26 AM via . All use subject to https://www.ebsco.com/terms-of-use

or other changes in absorption features, differences in relative absorption strength, and changes in directional absorption, such as pleochroism. Success for use as a site partitioning measurement depends on interferences from other substitutional ions, and availability of suitable reference samples for optical analysis. In the luminescence case most of the information comes from a single emission transition that can be sensitive to crystal field splitting (e.g., with transition metals in minerals with large band gaps). However, more information potentially comes from time-resolved measurements as luminescence lifetimes can differ for the same ion in slightly different sites, and selective manipulation of excitation energy and timing can separate out potential interferences. This has been seen best with site occupation and partitioning determined for substituents in Ca sites, especially Mn^{2+}, but also REE.

Mn^{2+} in carbonates, silicates and apatite. Mn^{2+} in octahedral coordination by oxygen has electronic states with crystal field dependence shown in Figure 12. The Tanabe-Sugano $3d^5$ diagram for lower strength crystal fields (appropriate for oxygen, water and hydroxide ligands) has the ground state $^6A_{1g}$ and transitions to the various crystal field excited states, all with net spin 4, are spin-forbidden. Transitions can occur from different vibrational levels of the ground state. Most probable are transitions from near the bottom at lower temperature. All transitions to states above ^4G (T_1) cross this level and hence can decay by loss of vibrational energy into this state. Luminescence occurs from near the lowest vibrational state of ^4G (T_1) to the ground state, which subsequently relaxes further to its own lower vibrational levels. The separation of the lowest excited and ground state thus determine the energy of the luminescent transition, and this in turn depends on the crystal field. A stronger crystal field increases splitting among the ^4G states and lowers the energy of the excited state, while the reverse occurs in a weaker crystal field. For a given coordination, shorter metal-oxygen distances produce a larger crystal field, while for a given metal-oxygen distance, reduced coordination produces a smaller field. In the case of Mn^{2+}, a $3d^5$ ion with all $3d$ orbitals filled with one electron each, the crystal field splitting of states is identical whether octahedral or tetrahedral coordination obtains (although state names are changed reflecting the differences in local symmetry). Hence, we expect if the

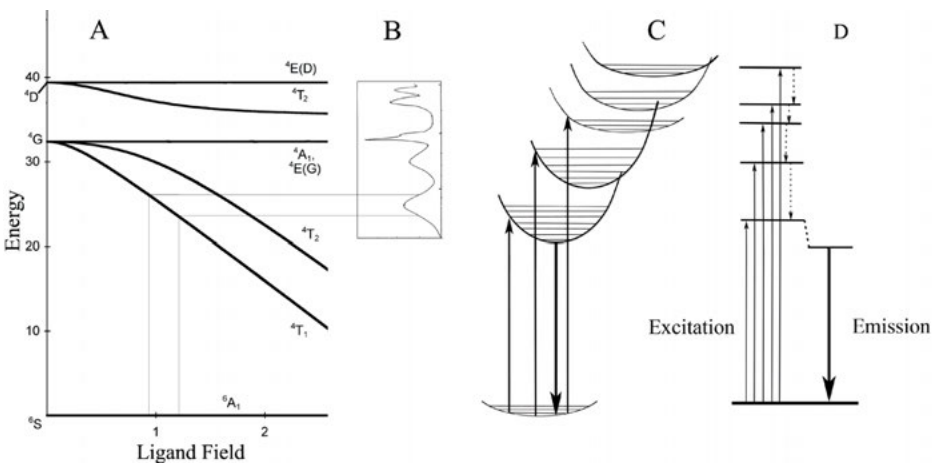


Figure 12. Mn^{2+} octahedral electronic structure. (A) Tanabe-Sugano diagram for $3d^5$ electronic states in an octahedral crystal field. Additional lines indicate how absorption spectrum (B) peak widths depend on variations in crystal field and slope of the state energy/field dependence. (C) Corresponding configurational coordinate diagram showing state vibrational sub levels and approximate energy relationships. Note state crossings on right side indicating the energetic vibrational relaxation of the system without emission. (D) Corresponding simple energy level diagram for the system showing excitation transitions and emission transition.

EBSCOhost - printed on 2/13/2023 5:26 AM via . All use subject to https://www.ebsco.com/terms-of-use

octahedral luminescence is near 630 nm, then the tetrahedral Mn^{2+} luminescence is at shorter wavelengths, which is observed (e.g., Mn^{2+} replacing Zn in willemite, emission at 525 nm). For more subtle changes among octahedral sites the energy change is smaller, but definite. For example in dolomite Mn^{2+} has emission of 655 nm in the smaller Mg site, and 578 nm in the larger Ca site, magnesite has Mn^{2+} emission at 654 nm, and calcite has Mn^{2+} emission at 615 nm (Ali et al. 1993).

In apatite Mn^{2+} can occupy either of the Ca sites, M1 and M2, but is favored in M1 (Hughes et al. 2004). Mn^{2+} in M1 tends to have a broad emission band in the orange-yellow near 587 nm, while Mn^{2+} in M2 has a yellow narrow emission band near 567 nm (Gaft et al. 1997). This is for a typical fluorapatite, but apatite structures may contain considerable arsenate and in some cases Si (britholite substitution – $REE^{3+}+Si^{4+} \leftrightarrow Ca^{2+}+P^{5+}$) replacing phosphate, or divalent lead, strontium, or REE replacing Ca, and these substitutions change the unit cell size, increase the mean Mn^{2+}-O distances, and thus shift the emission spectra of Mn^{2+}. The expanded cell due to Pb^{2+} and Sr^{2+} reduces the crystal field splitting and hence shifts the M1 emission wavelength to shorter wavelengths, e.g., from orange into yellow. Significant large ion substitutions also change the site occupation, forcing more Mn^{2+} into M1. Other possible substitutions include Cl^- or OH^- for F^- which expands the unit cell and would be expected to create a shift to shorter wavelengths and more yellow emission.

REE elements. REE have incompletely filled 4*f* shells that are shielded by the outermost $5s^2$ and $5p^6$ shells. Hence transitions between 4*f* electronic states are largely insensitive to crystal fields and mineral structure, and absorption and emission bands tend to be at the same energies in most phases. This also means that distinguishing between site occupation, e.g., in apatite, is not easily done via electronic spectroscopy. In addition there is only a small variation between configurational coordinate (molecular spacing or bond length) between ground and excited states, and so the emission lines are very sharp. 4*f* to 4*f* transitions are parity forbidden, which does make their intensity (probability) sensitive to local symmetry. Greater transition probability is seen in mixed state transitions, e.g., 4*f* to 5*d*, or charge-transfer transitions. The former are strongest in divalent rare earths such as Eu^{2+} and Sm^{2+}, while the latter are strongest in highly oxidized REE (Ce^{4+}, Tb^{4+}). Figure 13 shows a simple model for why Eu^{2+} emission bands vary markedly in width, depending on how the crystal field determines the excited state from which emission occurs. For small crystal fields the emission is in the ultraviolet from a $4f^7$ to $4f^7$ transition, and is a sharp band. If the emission is from the $4f^65d$ to $4f^7$ transition then the crystal field dependence of the $4f^65d$ state smears out the emission band (see Fig. 12). The color of emission is also highly sensitive to the crystal field of the host mineral.

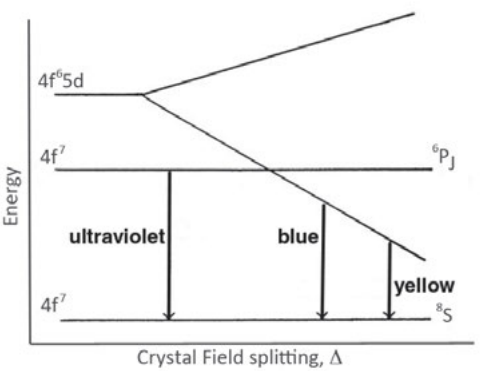


Figure 13. Eu^{2+} electronic energy levels and transition energies as a function of crystal field.

Sorting out which REE have luminescent activity in a mineral, and identifying them from other activators is extremely difficult if not impossible using steady state luminescence spectroscopy as the primary tool for investigation. However, time-resolved spectroscopy can effectively separate the characteristics of most centers affording an unprecedented description of the luminescence. In the case of apatite, the REE can substitute onto the two Ca sites, in

EBSCOhost - printed on 2/13/2023 5:26 AM via . All use subject to https://www.ebsco.com/terms-of-use

combination with transition metal activators. Transition metals can also occupy the tetrahedral sites, and both REE and transition metals can occupy defect sites. Defect sites might be vacancies created by substitution of highly charged REE into the Ca sites, necessitating a Ca vacancy (Chen et al. 2002). Such a vacancy could be a hole trap creating thermoluminescent behavior. Other defects may be created by substitution of a large molecular unit, such as uranyl, for some combination of structural species. Figure 14 shows the time-resolved emission spectra from a green fluorapatite from Norway (Gaft et al. 2001) and how changes in the delay and gate timing influences the appearance of the specific REE in the emission spectra. Ce^{3+} in the two Ca sites has different excited state lifetimes due to changes in the site symmetry and this allows delays that reveal both site contributions (Figs. 14A and 14B). For a much longer delay Ce^{3+} is not seen, and the Dy^{3+} and Eu^{3+} emission appears (Fig. 14D). For a much shorter delay (and very short gate) the Eu^{2+} emission can be resolved (Fig. 14C).

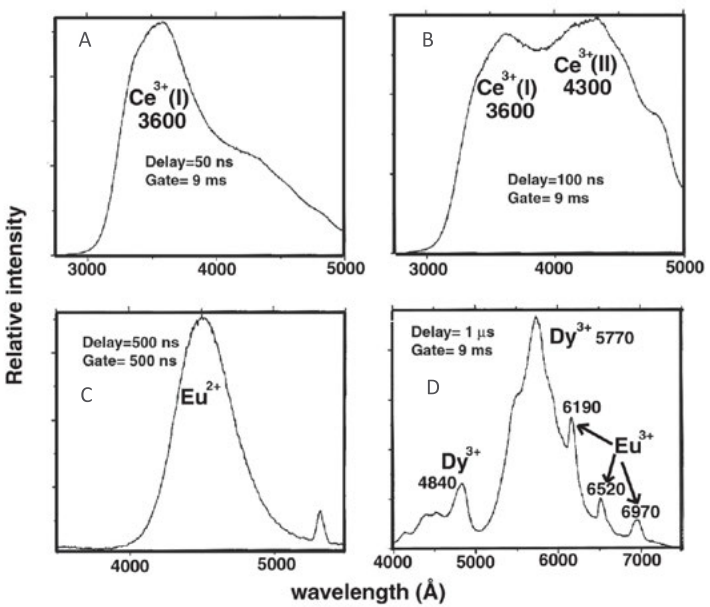


Figure 14. Green fluorapatite TR REE spectra showing large differences due to excited state lifetimes. (A) Ce^{3+} in M1 visible with short delay. (B) Ce^{3+} in M2 becomes visible with slightly longer delay. (C) 500 ns delay shows only long lifetime Eu^{2+} emission. (D) Much longer delay allows Dy^{3+} and Eu^{3+} bands to be separated. Modified from Gaft et al. (2001).

Figure 15 shows use of excitation wavelength and temperature to sort out REE emission in a red apatite specimen from Norway (Gaft et al. 2001). For UVC excitation (Fig. 15A) Tb^{3+} bands are strongly excited, as well as Eu^{3+} in the M1 site. At excitation in the UVA range (Fig. 15B) the Eu^{3+} in the M2 site is more evident and the Tb^{3+} weakened. At an intermediate wavelength of 337 nm Figures 15C and 15D show the effects of temperature, with sharpening of the Eu^{3+} bands. These examples show the power of time-resolved laser excitation analysis in combination with temperature control.

Organic-derived luminescence

NOM and DOM. Natural organic matter (NOM) and dissolved organic matter (DOM) have luminescent activity that can potentially be used to characterize the types of organics

EBSCOhost - printed on 2/13/2023 5:26 AM via . All use subject to https://www.ebsco.com/terms-of-use

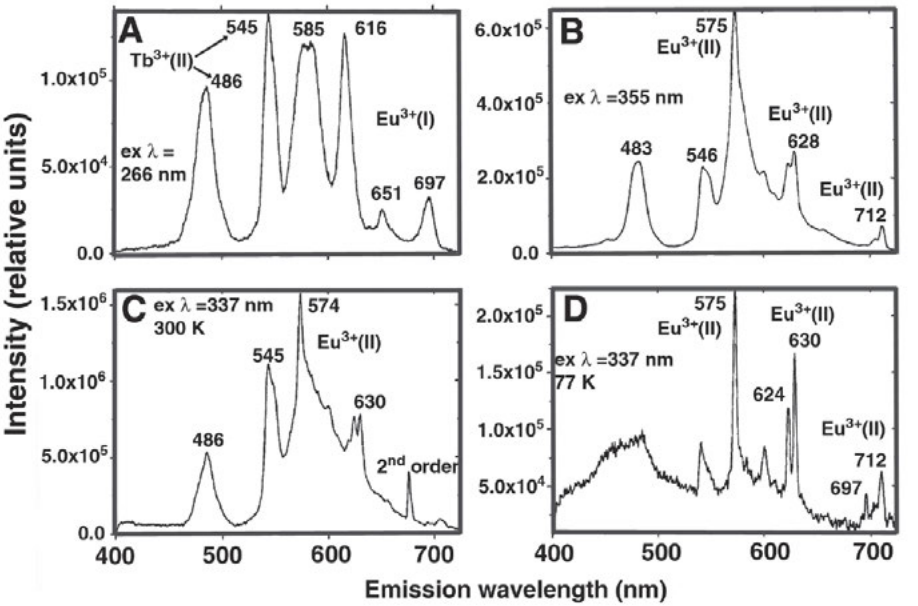


Figure 15. Red fluorapatite REE spectra. Effect of excitation wavelength and temperature. (A) Steady state UVC excitation at 266 nm shows bands from Tb^{3+} in M2 and Eu^{3+} in M1. (B) Steady state UVA excitation at 355 nm preferentially excites Eu^{3+} in M2. (C) and (D): comparison of emission spectra with 337 nm excitation at two temperatures. Eu^{3+} bands are sharpened at lower temperatures. All spectra collected with 10 ms delay and 500 ms gate Modified after Gaft et al. (2001).

present and reveal reactivity, provenance and historical information, providing an important addition to classical analysis techniques (Chen et al. 2003; Zsolnay 2003; Hudson et al. 2007; Baker et al. 2008; Mladenov et al. 2008, 2010; Miller et al. 2009). This is especially important in diagnosing water quality (Bridgeman et al. 2011), but can also be used to judge the effect of land use on DOM character and recycling, the extent of DOM lability, biological activity and biogeochemical transformations, and the effects of photochemical processes (Fellman et al. (2010). Not all compounds within NOM and DOM are efficiently luminescent, but there are enough so that characterization of the overall distribution of chemical types and functional group entities can be determined, thus allowing an improved chemical assessment. Luminescence analysis now also allows rapid analysis with high precision, and is relatively inexpensive.

There are essentially two types of luminescent natural organic matter described for natural water systems, one that is derived principally from terrestrial plants and contains high concentrations of humic and fulvic acids and related compounds (including lignin, tannins, polyphenols and melanins), and another that is derived largely from biota, algae and other larger organisms and has compounds that are high in proteins or related organic molecules. Tyrosine-like and tryptophan-like protein-derived molecules give rise to bands at 304-320 nm and 330-368 nm, respectively, from excitation via UVC. Humic-like molecules produce emission bands at 420-460 nm with UVA and UVB excitation, at 448-480 nm with UVC excitation, and at 370-430 nm for UVB excitation, these being attributed to high molecular weight humics, high molecular weight aromatic humics, and low molecular weight humics, respectively. Marine humics tend to fall in the low molecular weight category.

EBSCOhost - printed on 2/13/2023 5:26 AM via . All use subject to https://www.ebsco.com/terms-of-use

Analysis has been done with a number of strategies, and indices have been developed to define the chemical state of DOM. For example, the fluorescent index (FI) utilizes the ratio of emission strength at two wavelengths to judge the proportion of aromatic versus nonaromatic functional groups. The increased presence of aromatic emission indicates a larger biotic source. Other indices utilize analysis by examination of the TLS (EEM), which provides much more information than use of only emission spectra (Coble 1996). For example, Baghoth et al. (2011) were able to define seven chemical components in spectra of water in a water treatment plant (Fig. 16 and Table 1). Each component is associated with a unique aspect of the EEM, and could not be separated from emission spectra alone. Indices derived from analysis of this type include the humification index, which extracts information about the source, degree of humification, and relative contributions of particular types of molecules. A powerful tool for analysis of EEMs is the PARAFAC technique, which uses multivariate modeling combined with parallel factor analysis (Cory and McKnight 2005; Fellman et al. 2010; Baghoth et al. 2011). An interesting use of this methodology is to deduce the redox state of the organic matter from the luminescence activity (Macalady and Walton-Day 2009).

Interactions between dissolved organic matter and metals. The interaction of humic and fulvic acids with ionic species in solution is an extremely important application in environmental chemistry, although the complexity of the molecules and number of functional

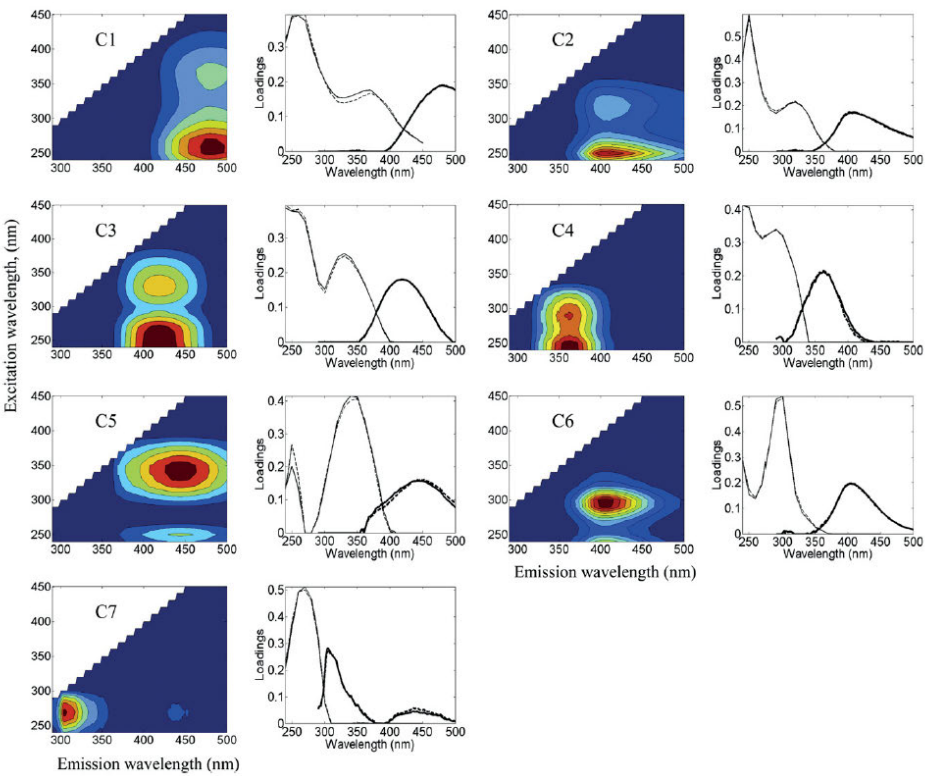


Figure 16. Fluorescent components in dissolved organic matter (DOM). Excitation vs. emission spectra plots (EEM). See Table 1 for identification. Plots beside each EEM show approximate spectra derived from the EEM datasets. Thinner lines on the left side are excitation, thicker lines on the right are emission. [Used with permission of Elsevier from Baghoth et al. (2011), Fig. 2.]

EBSCOhost - printed on 2/13/2023 5:26 AM via . All use subject to https://www.ebsco.com/terms-of-use

Table 1. NOM luminescence components separated by excitation-emission matrices.

Component	Excitation nm	Emission nm	Description
C1	260, 360	480	terrestrial humics
C2	250, 320	410	terrestrial/anthropogenic humics
C3	<250, 330	420	marine and terrestrial humics
C4	<250, 290	360	amino acids
C5	250, 340	440	terrestrial humics
C6	<250, 300	406	marine and terrestrial humics
C7	270	306	amino acids

groups makes interpretation of interactions with metals and anions challenging. However luminescent studies can provide some insights that complement other spectroscopic analyses. For example, the luminescence emission of the humic bands in the 420-480 nm region can be affected by formation of humic-metal organometallic complexes. The luminescence can be reduced or even quenched (Esteves da Silva et al. 1998) by Cu^{2+} and other species, or it can be modified or intensified (Sharpless and McGown 1999) by complexation with Al^{3+}, which may change the shape of the humic acid molecule (Elkins and Nelson 2001). Even if the effect of the complexing species is only to quench luminescence, information on complexation kinetics, stability and binding site can be addressed, such as for Hg^{2+} interacting with DOM (Lu and Jaffe 2001).

There is a major effort in nanomaterials and other kinds of cutting-edge electronic materials to utilize energy transfer processes between metal ion centers and substrates or other centers using organic ligands. For example new types or organic phosphors are being developed using organic molecule absorbers that transfer energy with high efficiency to a chelated REE or transition metal ion. Such materials studies may allow enhanced understanding of luminescence from trace metals bound in natural organic matter.

Cathodoluminescence techniques

Cathodoluminescence combines high excitation density and thus sensitivity, with high spatial resolution if using an SEM, EPMA, or similar electron-beam instrument. This means that high resolution maps of hyperspectral emission spectra can be acquired, which may be linked to petrological changes in the samples, such as growth and sectoral zoning, impurity uptake, changes in precipitating solution temperature, and other factors. This type of methodology is one of the most used in mineralogical and petrological luminescence analysis, and is increasing in application in part due to the availability of excellent software for collection and image analysis.

The main issue in quantitative analysis is standardization, and the nonlinearity of the concentration of the impurity concentration and the luminescence intensity, which can be a difficult problem when comparing disparate types of samples. Identification of impurities or the source of the emission is complicated by the fact that all luminescent centers may be activated by the intense beam. Hence many mineralogical studies work with samples where only one or a few types of emission dominate. Alternatively, the methodology is popular as it is cost-effective to add a detector system to an SEM or EPMA and achieve high-resolution optical fluorescence mapping in synchrony with standard back-scattered electron imaging and/or X-ray mapping.

Effective cathodoluminescence imaging and spectroscopy can also be studied without an SEM or EPMA, by use of a device originally devised to do cathodoluminescence with a standard petrographic microscope for the examination of thin sections. This is the Luminoscope

EBSCOhost - printed on 2/13/2023 5:26 AM via . All use subject to https://www.ebsco.com/terms-of-use

(another instrument is the Technosyn) which uses a cold cathode electron gun and relatively low vacuum (10-50 mTorr) in the sample chamber. The lower vacuum allows ionization in the stage to bleed off sample surface charge, and thus no conductive sample coating is needed for analysis. Such instruments allow the true cathodoluminescence colors to be seen by the eye, but generally have much lower sensitivity, and considerably lower spatial resolution as the electron beam focus (e.g., ~1 mm) is larger than in a modern SEM (1's to 10's of microns), and magnification is dramatically reduced due to hardware limitations inherent to that kind of system (e.g., ultra long working distance objectives).

Scanning cathodoluminescence microscopy

As stated by Goldstein et al. (2003), a typical modern SEM or EPMA focus of 1 μm allows for spatial resolution of 10-50 Å. However emission is usually measured as a grayscale unless the electron beam instrument has an optical spectrometer or spectrograph (e.g., Gatan/ChromaCL2, JEOL/xCLent) that can differentiate emission energies. SEMs may be equipped with primary color filters that will produce three filtered grayscale images that can be combined into a false color image. This technique apparently yields fairly accurate cathodoluminescence colors (Boggs et al. 2002), though high-resolution color spectra that may be analyzed in detail are obviously preferable. Scanning cathodoluminescence microscopy is limited if the sample has strong long-lived phosphorescence or afterglow. This is a problem in calcite, dolomite, and fluorite samples. If one only wishes to measure relative cathodoluminescent activity, the red-orange emission from the carbonate samples can be blocked with an optical filter, and the blue emission, which does not show much afterglow, can be detected preferentially.

Other issues with samples include beam-damage quenching of the luminescence, and the need to carbon-coat nonconductive samples. A recent advance for CL imaging is the use of hyperspectral approaches (Edwards et al. 2007; Bruckbauer et al. 2011) which collect complete spectra from every sampled spot on a surface, allowing detailed comparisons from area to area at different wavelengths which in turn may reveal differences in the CL activators in different regions of the sample.

Quantitativeness. Overall quantitativeness is an issue with CL spectral analysis, as the emission intensity of a given band is not a simple function of a single impurity or defect concentration. Hence studies of spectra to yield impurity concentrations, although using sophisticated peak fitting, tend to be semiquantitative at best. The CL spectra cannot be calculated from first principles to reproduce what is observed using natural or synthetic-doped materials. The situation appears most ideal for low concentrations of REE (below 500 ppm) as shown by Habermann (2002) in synthetic calcite samples, where effects of interacting activators and sensitizers are less important. Mn^{2+} in carbonates and feldspars also appeared to give CL intensity proportional to concentration at Mn concentration below 1000 ppm and Fe^{2+} (quencher) below 3000 ppm. Habermann (2002) has an excellent discussion of self-quenching and other effects that affect quantitativeness of luminescent emission. Perhaps a more crucial general issue are differences in the wavelength resolution, and quantum efficiency (i.e., spectral response) over the wavelength range of interest, of the spectrometer, spectrograph, or detector used. If these are not appropriately calibrated or standardized, spectra from the same mineral may be quantitatively different (Barbarand and Pagel 2001). These authors also show how much a CL signal may decrease under constant electron beam bombardment and that this decrease is a function of the specific activator. Degradation of CL may be due to the formation of a "dead zone" due to electron-activated chemistry at the mineral surface (Swart et al. 2007). All these considerations suggest that quantitative analysis must be approached with caution and characterization by several spectroscopic methods is warranted.

EBSCOhost - printed on 2/13/2023 5:26 AM via . All use subject to https://www.ebsco.com/terms-of-use

APPLICATIONS

Quartz

Early work by Zinkernagel (1978) showed that quartz from different petrological environments had different CL emission colors. More recent work has verified the original findings (e.g., Götze et al. 2001; Richter et al. 2003). Quartz in plutonic rocks, as phenocrysts in volcanic rocks, and in high-grade metamorphic rocks has dominantly a blue-violet emission; matrix quartz grains in volcanic rocks has red CL; pegmatitic quartz has green or blue CL that is transient and is reduced in the electron beam; moderate metamorphosed rocks have quartz with brownish CL; and authigenic quartz has very weak or no CL emission. This visual analysis suffers from standardization, and the issues mentioned in the preceding paragraph, and the most quantitative work now utilizes collection of full optical emission spectra, allowing differentiation of more variations in the quartz emission bands and hence provenance types. Earlier spectral analysis suggested that quartz had two CL emission bands, in the red and blue, and that the variation between these bands yielded the visual colors. However more recent analysis shows the presence of many more bands, some of which have been identified by characterization with other spectroscopic techniques, notably electron spin resonance (ESR) to detect paramagnetic impurities and defect sites, complementary UV-excited fluorescence, and thermoluminescence (Götze et al. 2001; Götze and Kempe 2009). Many of the emission bands are believed associated with a specific impurity-coupled defect, or with vacant oxygen or silicon sites (Weil 1984, 1993). Table 2 (data from Stevens-Kalceff et al. 2000 and Götze et al. 2001) lists the fluorescent, CL, and X-ray induced emission bands for SiO_2 polymorphs and amorphous forms identified up to 2000. Figure 17 shows representative quartz grain CL spectra for various polymorphs of quartz and geological conditions. Figure 18 shows spectra from quartz grains having different provenance or zonation.

CL imaging of quartz grains can be used to analyze chemical, defect or mechanical zonation in volcanic, plutonic and metamorphic rocks, the presence of healed fractures, deformation structures in tectonically deformed rocks, and shock structures in quartz affected by meteorite impacts. In sedimentary rocks CL can be used to aid provenance determination (Boggs and Krinsley 2006). Zoning in quartz in plutonic rock grains is due to changes in impurity and/or defect content and is affected by temperature, pressure, magma composition and, in the case of fine oscillatory or sectoral zoning, diffusional variations during near-equilibrium growth (D'Lemos et al. 1997; Müller 2000). The brighter emission in the fine oscillatory bands is thought to be due to regions where Al^{3+} and Ti^{4+} substitute for Si^{4+}. The presence of Al^{3+} requires a charge compensating interstitial alkali ions but Ti^{4+} does not, although it will produce local lattice distortion. Zonation structure in some cases may allow inference of changes in the magma chamber and hence details of the history of the geological province (Müller et al. 2010; Agangi et al. 2011). Fractures in quartz grains within plutonic rocks that are filled with later silica give weak red CL emission that is consistent with relatively low temperatures in the formation solution. The original fracturing could be caused by a beta to alpha quartz transition during cooling of the primary grains. In contrast, sealed fractures in quartz grains in volcanic rocks are apparently rather rare, and have not been well characterized. Deformation structures in metamorphic quartz create many types of CL patterns which are the subject of much discussion, but the CL spectrum itself does not seem to be informative beyond a rough measurement of resetting temperature. Pegmatitic quartz shows bluish green very uniform CL that is sensitive to electron bombardment and is removed after 60-100 s of exposure (Götze et al. 2005). The emission is from two bands at 505 and 390 nm that may be related to trace element impurities linked with charge-compensating alkalis. The 390 nm emission is also found in hydrothermally-grown synthetic quartz (Götze et al. 2001). Interestingly, the emission bands common to other higher temperature quartz near 450, 580 and 650 nm, and believed due to silicon and oxygen vacancy-related luminescence centers, are

EBSCOhost - printed on 2/13/2023 5:26 AM via . All use subject to https://www.ebsco.com/terms-of-use

Table 2. Characteristic quartz luminescence emission bands (data from Götze et al. (2001).

Emission nm	Proposed Origin	Method
175	Intrinsic (pure SiO_2)	CL[1]
290	Oxygen deficient center	PL[2], CL[2], CL[3]
340	Oxygen vacancy	TL[4]
	$[AlO_4/Li^+]$ center	CL[5]
	$[TiO_4/Li^+]$ center	TL[6]
380-390	$[AlO_4/M^+]$ center ($M^+ = Li^+, Na^+, H^+$)	RL[7], CL[8]
	$[H_3O_4]^0$ hole center	TL[9]
420	Intrinsic defect	CL[10], CL[11]
450	Intrinsic defect	CL[12], RL[12]
	Self-trapped exciton	CL[13], CL[14], CL[10], CL[11]
500	$[AlO_4]^0$ center	CL[15]
	extrinsic emission	RL[14]
	$[AlO_4]^0$, $[GeO_4/M^+]^0$ center	TL[4]
	$[AlO_4/M^+]$ center ($M^+ = Li^+, Na^+, H^+$)	TL[16], CL[17], CL[18]
580	Oxygen vacancy	TL[4]
	Self-trapped exciton	CL[10]
	E' center	CL[19]
620-650	Nonbridging oxygen hole center	PL[20]
	Oxygen vacancy	CL[8]
	Nonbridging oxygen hole center with precursors (hydroxyl, peroxy)	CL[21], CL[10]
705	Substitutional Fe^{3+}	CL[22], CL[23]

CL=cathodoluminescence, TL=thermoluminescence, PL=photoluminescence, RL=radioluminescence

1 Entzian and Ahlgrimm (1983)
2 Jones and Embre (1976)
3 Skuja and Entzian (1986)
4 Rink et al. (1993)
5 Demars et al. (1996)
6 Plötze and Wolf (1996)
7 Alonso et al. (1983)
8 Luff and Townsend (1990)
9 Yang and McKeever (1990)
10 Stevens Kalceff and Phillips (1995)
11 Gorton et al. (1997)
12 Trukhin and Plaudis (1979)
13 Walker (1985)
14 Itoh et al. (1988)
15 Nassau and Prescott (1975)
16 Katz and Halperin (1988)
17 Ramseyer and Mullis (1990)
18 Perny et al. (1992)
19 Götze et al. (1999)
20 Siegel and Marrone (1981)
21 Remond et al. (1992)
22 Pott and McNicol (1971)
23 Kempe et al. (1999)

generally missing from pegmatitic quartz suggesting uniform lower temperature conditions during growth.

Ti dissolved in quartz has been shown to be a versatile geothermometer (Wark and Watson 2006) due to quartz stability over a wide range of geological *P* and *T* conditions. CL imaging can indicate a domain or zonation structure due to Ti, which can then be quantitatively measured (e.g., by EPMA) to apply the thermometry (Spear and Wark 2009). In principle this approach may allow detailed temperature and recrystallization information to be extracted from rock textures and grain Ti profiles, perhaps leading to a better understanding of the processes for redistribution of silica during metamorphic reactions.

Feldspars

Feldspar CL has been studied in detail and has rich spectral information, usually associated with specific impurities, as well as complex image features both of which can

EBSCOhost - printed on 2/13/2023 5:26 AM via . All use subject to https://www.ebsco.com/terms-of-use

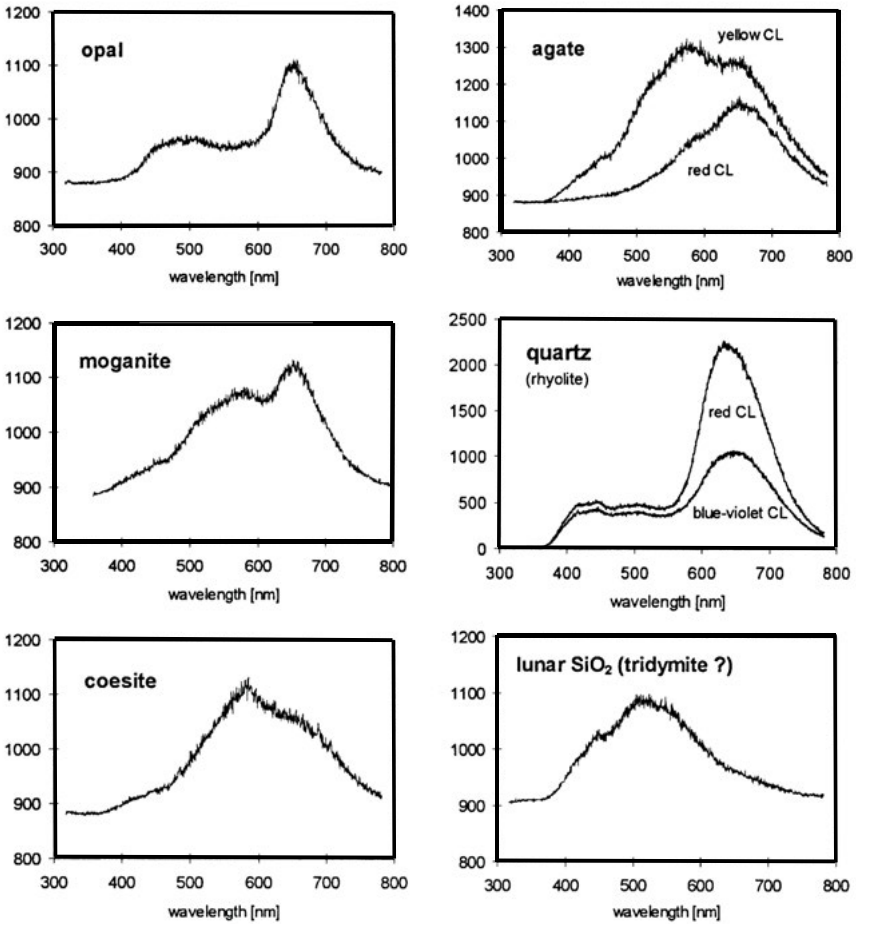


Figure 17. Quartz polymorph CL spectra. The ordinate axis is intensity in measured detector counts. Modified from Götze et al. (2001).

be related to growth or alteration history (e.g., Gonzalez-Acebron et al. 2012). Because the feldspar structure allows substitution of large metal ions and alkalis, as well as replacements for tetrahedral silicon, a host of activators can be accommodated. First observations are due to Smith and Stenstrom (1965) who identified blue and red CL from alkali feldspars. Later work showed high sensitivity to formation conditions and alteration (Marshall 1988), the lack of CL in authigenic feldspar, and detected an increasing number of possible activators and luminescent centers. In general, feldspars from plutonic and metamorphic rocks often show bright CL emission of blue, greenish-yellow, violet and red due to varying amplitude of three emission bands around 420-500 nm, 540-570 nm and 690-760 nm (Götze et al. 2000). Alkali feldspars usually show only blue or red CL, but plagioclase feldspars show a wide range of coloration ostensibly due to greater possibilities for di- and trivalent substitutions and structural changes in the structure from albite to anorthite. As temperature, pressure, and redox conditions in the growth environment affect activator substitution, it is possible to make inferences about formation conditions from detailed analysis of the CL spectra (Rokatschuk et al. 1989).

EBSCOhost - printed on 2/13/2023 5:26 AM via . All use subject to https://www.ebsco.com/terms-of-use

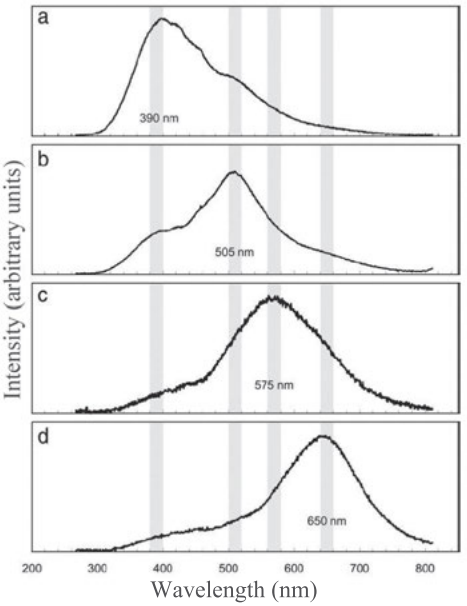


Figure 18. Quartz CL spectra showing effects of provenance. (A) Al-rich zone in hydrothermal quartz form Swiss Alps. (B) High grade metamorphic quartz from New Zealand. (C) Hydrothermal quartz from West Germany with a green-emitting growth zone. (D) Different growth zone in same crystal as (C) but showing brown emission after 200 s of irradiation. Vertical lines show correlation of major emission bands. Modified from Preusser et al. (2009).

Reviews (e.g., Götze et al. 2000) have summarized specific impurities linked with spectral features, as well as types of patterns in CL imaging. However the identity of the major activator contributors to feldspar CL have been disputed because, as shown in Table 3 (adapted from Götze et al. 2000), there are multiple possible activators for each color or band location. An example is work on albite from the A-type Georgeville granite in Nova Scotia (Dalby et al. 2010). This albite has uniform physical texture and gives bright CL which is either blue or red, showing interesting internal growth zoning. The emission spectrum consists of several bands, but a band near 720 nm is more prominent in the red CL areas, while a band peaking in the UV at about 280 nm is prominent only in the blue-emitting CL areas. The red band has been attributed to Fe^{3+} replacing Al^{3+} in a tetrahedral site (e.g., White et al. 1986) and X-ray microprobe and synchrotron X-ray fluorescence analysis demonstrated that this red band was correlated with total Fe content. However XAS experiments indicated that Fe^{3+} was located in both the blue and red emitting areas, so that the differences in emission might be more related to local Si-Al order as well as a Fe preference for tetrahedral occupation. The blue emission was correlated with higher concentrations of Ca, Ti, Pb and REE, but there seemed to be only small changes in the spectrum over the 350-500 nm range between the red and blue emitting areas where the expected main blue-emission bands occur. Hence, clear association of the blue emission and its cause could not be made. However alkali feldspar CL analyzed in detail by Finch and Klein (1999) in samples from South Greenland, gave more definite results. They separated blue and red CL sections of feldspar grains for further spectral study using EPR and SIMS. The blue emission correlated with Al substitution for Si (the Al-O^- Al center) and no other reasonable source of blue emission (Eu^{2+}, Ti^{4+} Parsons et al. 2008, Ti^{3+}, Ga^{3+}). The visible red emission correlated with Fe^{3+} only on the T1 site, while the peak shifted into the IR in disordered feldspars. The difference between these Fe^{3+} features was thus attributed to Fe^{3+} ordering, and changes in formation or alteration conditions. Analysis of the Fe^{3+} CL emission over a wide range of feldspar compositions gave similar results (Krbetschek et al. 2002).

The position of the Fe^{3+} peak was found to be systematically related to composition with low An plagioclases having the band peaking in the IR at about 740 nm, but shifting into the red as far as 680 nm in pure anorthite. In alkali feldspars a similar trend is seen, with the shift from 730 nm to about 700 nm occurring as orthoclase content increases (Götze et al. 2000). Both trends are consistent with decreased crystal field at the tetrahedral site with higher An and Or content, respectively, in analogy to Mn^{2+} peak shifts in carbonates.

EBSCOhost - printed on 2/13/2023 5:26 AM via . All use subject to https://www.ebsco.com/terms-of-use

Table 3. Characteristic luminescence features and activators observed in feldspars.

Activator	Emission Color	Position (nm)	Technique	Reference
Tl^{+}	UV	280	PL	Gorobets et al. (1989)
Pb^{2+}	UV	280	RL	Taraschan et al. (1973)
Ce^{3+}	UV	324-335	PL	Gaft et al. (2005)
	blue-green	490	CL	Laud et al. (1971)
Eu^{2+}	blue	420	CL	Mariano and Ring (1975)
			TL, RL	Jaek et al. (1996)
		402-410	PL	Gaft et al. (2005)
Cu^{2+}	blue	420	CL	Mariano et al. (1973)
			TL, RL	Jaek et al. (1996)
Al-O^{-}-Al	blue	450-480	TL, RL	Marfunin (1979)
			CL	Walker (1985)
			CL	Slaby et al. (2008)
		440	CL	Kayama et al. (2010)
Ti^{4+}, Al-O-Ti	blue	460	CL	Parsons et al. (2008)
			CL	Lee et al. (2007)
Ti^{4+}		436	CL	Kayama et al. (2010)
		408	CL	Kayama et al. (2010)
Ti^{3+}	blue	460	CL	Mariano et al. .(1973)
			CL	Geake et al. (1973)
Ga^{3+}	bluish-green	500	CL	De St. Torre and Smith (1988)
O—Si…M^{+}	bluish green	500-510	TL, RL	Marfunin and Bershov (1970)
Mn^{2+}	greenish-yellow	559	CL	Sippel and Spencer (1970)
		570	CL	Mariano et al. (1973)
		540	CL	Mora and Ramseyer (1992)
		550-565	CL, TL	Götze et al. (1996)
Dy^{3+}	yellow-orange	487, 546, 576	PL	Gaft et al. (2005)
Sm^{3+}	red		CL	Mariano et al. (1973)
	blue-IR		CL	Götze et al. (1996)
	red	603, 645	PL	Gaft et al. (2005)
Eu^{3+}	red	614, 624	PL	Gaft et al. (2005)
Fe^{3+}	red/IR	700	CL	Mariano et al. (1973)
		705-730	CL	Sippel and Spencer (1970)
		700-780	CL	Geake et al. (1973)
		690-760	RL	Boroznovskaya et al. (1982)
		680-745	CL	Mora and Ramseyer (1992)
		688-740	CL, TL	Götze et al. (1996)
T2 site Ab-rich		796	CL	Kayama et al. (2010)
Ti site Ab-rich		754	CL	Kayama et al. (2010)
T2 site Or-rich		739	CL	Kayama et al. (2010)
T1 site Or-rich		717	CL	Kayama et al. (2010)
Tb^{3+}, Nd^{3+}	blue-IR		CL	Götze et al. (1996, 1999)
Cr^{3+}	IR	880	RL	Boroznovskaya et al. (1996)

REE are common activators of CL in feldspars, especially from Eu^{2+}, which substitutes for $Ca^{2+}$and produces an emission band at 420 nm and is seen in hydrothermal and regionally metamorphosed feldspars, but much less commonly in granitoids and pegmatites (Gorobets et al. 1989). Ce^{3+} activation has been found in regionally metamorphosed plagioclases, and shows variations according to the conditions of formation (Kusnetsov and Kramarenko 1995).

EBSCOhost - printed on 2/13/2023 5:26 AM via . All use subject to https://www.ebsco.com/terms-of-use

It is noteworthy that lunar feldspars have emission bands similar to those found in terrestrial feldspars, although alkali feldspars are rare in returned lunar material. However alkali feldspars show strong blue CL, attributed to Al substitution for Si, and plagioclase shows a range of CL colors due to the presence of the tetrahedral Fe^{3+} band at about 700 nm, a Mn^{2+} band at 570 nm, and a blue band at 410-450 nm, possibly due to several activators or defect centers (Götze 2009). Figure 19 shows some representative spectra for plagioclase having different activators including REE.

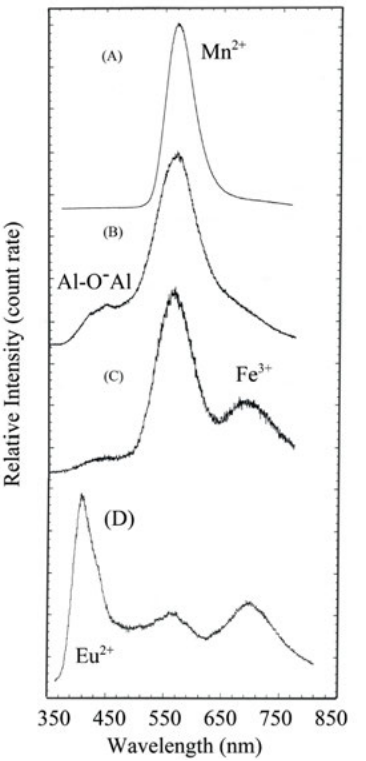


Figure 19. Plagioclase CL spectra showing common activated luminescence emission. (A) Mn^{2+} in the large cation site has emission around 550-560 nm. (B) Mn^{2+} combined with Al-O- Al defect centers. (C) Mn^{2+} and Fe^{3+} (tetrahedral site) produce a net red-orange emission depending on Fe content. (D) Blue CL from Eu^{2+} activation in the large cation site. Mn^{2+} and Fe^{3+} are also commonly present. Modified from Götze et al. (1998, 2000).

Zircon

Zircon shows very characteristic CL concentric growth zoning attributed to variation in the U and Y (Rubatto and Gebauer 2000), or to Dy^{3+} (Hanchar et al. 2001 and John Hanchar, personal communication) content, during crystallization. Changes in the zonation lead to inferences about separate geological events which can be analyzed further via secondary ion mass spectrometry (SIMS) or laser ablation indictively coupled mass spectrometry (LA-ICPMS) technology to extract U-Pb age information (e.g., Hanchar and Miller 1993; Hanchar and Rudnick 1995; Kempe et al. 2000; Grant et al. 2009). The activators for UV-excited luminescence and CL of zircon have been incompletely characterized. REE are found in all natural zircon crystals with the heavy REE (HREE) in higher concentrations, as well as a UO_2^{2+} signature, but the dominating broad band yellow emission seen in CL and under UV remains mysterious, as does a blue emission possibly associated with silicate. Gaft et al. (2005) noted that the yellow broad band emission is structureless down to a temperature of 4.6 K, making it difficult to develop conclusions about the electronic structure. Likely the band is a result of the superposition of many emission states related to impurity or intrinsic defect ordering (Kempe et al. 2000). Despite this limitation CL imaging is extremely useful in detecting growth or alteration history, and thus providing targets for different types of in-situ analyses for U-Pb, O, trace elements, and tracer isotopes (e.g., Lu-Hf) although differentiating original growth from later modifications must be done cautiously (Kempe et al. 2000).

Carbonates

Dolomites and other carbonate rocks usually show strong CL, as long as the concentration of quenching impurities is not too high or there is not too much Fe^{2+} present in the sample. The main activator is Mn^{2+}, though REE can also be important activators (Habermann et al. 1996; Machel 2000; Habermann 2002) and organic impurities may also create CL emission. In unusual cases radiation damage centers likely paired with REE impurities (Gaft et al. 2008) may be important activators producing striking luminescence. Mn^{2+} has spin forbidden transitions, and hence is a weak UV-excited luminescent center without sensitizers (generally

EBSCOhost - printed on 2/13/2023 5:26 AM via . All use subject to https://www.ebsco.com/terms-of-use

Pb^{2+} or Ce^{3+}), but this is much less important with the energy density available with SEM-based CL instruments.

The Mn^{2+} electronic structure in an octahedral site in carbonates has been well studied, and spectral changes with site occupation in dolomites, and due to compositional (hence lattice parameter) variations have been documented (Walker et al. 1989; Ali et al. 1993). In particular dolomite CL shows two bands (Fig. 20) that result from occupation by Mn^{2+} in the Ca sites (more yellow CL) and Mn^{2+} in the Mg sites (red CL). From the electronic structure (Fig. 12) one can see that transitions to the ground state depend on the crystal field splitting, so that smaller octahedral sites have more splitting resulting in a lower energy luminescent transition. This effect is also seen in Mg^{2+} containing calcite where the solid solution reduces the mean site size, increasing the splitting and shifting the emission toward the red. As physical conditions can affect Mn^{2+} site partitioning, these spectral shifts can be used in principle to discern formation and alteration temperatures or events. Variations in redox conditions, e.g., as a function of burial, will affect the uptake and availability of divalent manganese, as well as quencher divalent iron. REE in calcite and dolomite generally give rise to sharp bands characteristic of trivalent lanthanides (Fig. 20), but have limited use as petrogenetic indicators. There is a rich literature of CL imaging in carbonates related to petrological conditions and diagenesis, some of it summarized in Boggs and Krinsley (2006).

In aragonite, the Mn^{2+} emission is shifted to higher energy producing a yellow-green to green CL coloration that is clearly different from calcite (Richter et al. 2003). The green emission results from a larger Ca site with lower crystal field splitting. Similarly, the small Mg site in magnesite gives rise to a red CL emission at an energy close to the Mg site in dolomite.

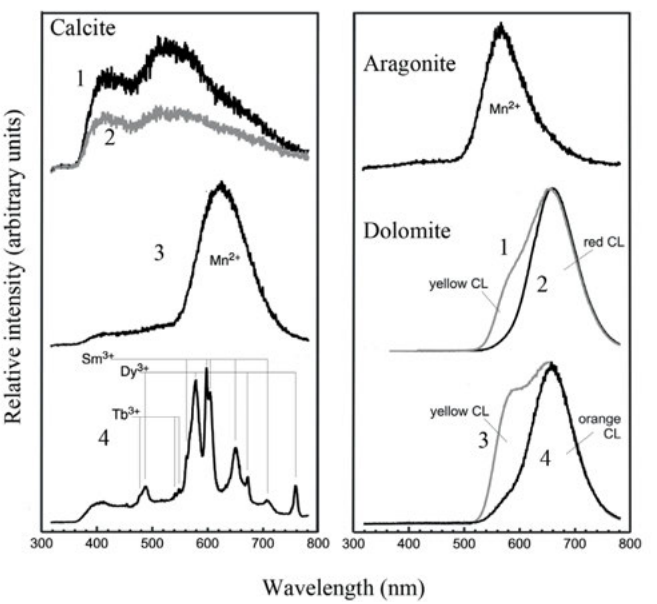


Figure 20. Natural carbonate CL. *Left*: (1) stalagmite clear zone, (2) same stalagmite colored zone. Emission may be due to organic impurities both in the structure and between grains. (3) Mn^{2+} activated calcite. (4) REE activated carbonate in stalagmite. *Right*: (top) Aragonitic bivalve with Mn^{2+} activation. (1-4) dolomite Mn^{2+} emission: (1,2) dolomite from Permian evaporite deposit. (3,4) dolomite from hydrothermal deposit. The colors of the CL emission are shown, but the spectra show well the changing two-component emission structure attributable to the two kinds of cation sites. Modified from Richter et al. (2003).

EBSCOhost - printed on 2/13/2023 5:26 AM via . All use subject to https://www.ebsco.com/terms-of-use

Apatite

CL in apatite follows what has been observed for UV-excited luminescence, with a wide range of possible colors, and can be quite spectacular (Waychunas 2002). The literature is fairly extensive, but the study by Barbarand and Pagel (2001) is representative of some of the critical issues when attempting quantitative analysis, including detector sensitivity (Fig. 21), and beam damage. Many apatites seem to have strong emission largely from Ce^{3+} and Mn^{2+} activation, producing strong blue and yellow-orange bands near 360-420 nm and 570-580 nm, respectively. But additional REE emission including Sm^{3+}, Dy^{3+}, Tb^{3+}, Eu^{2+}, Eu^{3+} is also very commonly observed (Roeder et al. 1987). REE zonation is common in apatites and CL can yield information on growth and dissolution and even permeability and porosity (Dempster et al. 2003). The two most commonly observed types of zoning in fluorescence under ultraviolet light are concentric zoning and sectoral zoning (Rakovan and Waychunas 1993, 2013; Rakovan 2009). In cathodoluminescence, excited by electrons rather than ultraviolet light, a third and often striking type of zoning can be observed, intrasectoral zoning (Rakovan and Reeder 1994). Luminescence and color variations, ultimately related to concentric zoning but appearing similar to sectoral zoning, can occur when the last stages of crystal growth take place preferentially on certain faces and not equally on all crystal faces.

Redox conditions of growth solutions may also be preserved in the CL emission, e.g., through changes in Mn^{2+} emission, Eu^{2+} versus Eu^{3+}, or levels of Ce^{3+}. The site partitioning of the trivalent REE and Mn^{2+} between the M1 and M2 sites can potentially be determined using CL, but this is more quantitatively approached with time-resolved laser excitation. Apatite that occurs as part of organism skeletons (francolite) has not been studied in detail with CL, but may offer information on life conditions of the organism and its environment.

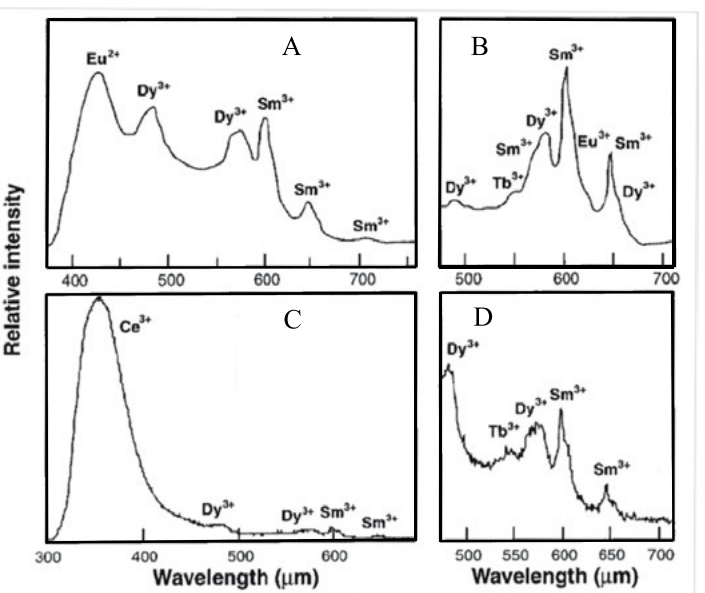


Figure 21. Durango apatite CL collected with different apparatus. (A) Nuclide Luminoscope with photomultiplier detector. (B) Patco Luminoscope with Princeton Instruments CCD camera and Acton Research spectrometer. (C,D) Oxford Instrument MonoCL with a Philips XL30 SEM. Major differences are in part due to lack of UV sensitivity in (A) and (B), and Ce^{3+} is improperly assigned to Eu^{2+} emission. Modified from Barbarand and Pagel (2001).

EBSCOhost - printed on 2/13/2023 5:26 AM via . All use subject to https://www.ebsco.com/terms-of-use

Thermoluminescence techniques

Classical approaches. TL can be divided into two separate types of studies: 1) detailed spectroscopic analysis to identify spectral features which potentially can be assigned to specific defects in natural minerals. This information can provide a better understanding of the electronic and optical properties, and it can assist activator-sensitizer identification, site symmetry determination, or determination of luminescence mechanism; or 2) as a technique to measure defect production from integrated radiation damage, and hence for dosimetry, or conversely with known dose rates to establish an exposure age. Of these two areas, dosimetry seems to be an increasing part of the literature.

The first type of study is frequently combined with time-resolved laser excitation analysis (Gaft et al. 2005) and CL for mineralogical characterization, and this connection was considered in an earlier section. Two types of information can be obtained: 1) the trapping levels or temperatures for which TL is stimulated; 2) and the TL emission spectra at each temperature, representing the recombination or luminescent centers. In the case of dosimetry, TL is a well-established method for obtaining information on radiation exposure, being developed just after WWII, and first applied to archaeological dating in the 1960's (Aitken et al. 1964) and then later to geological samples (Wintle and Huntley 1980).

Thermoluminescence investigations often start with collection of luminescence in a sample as a function of temperature, using a constant temperature ramp up. The resulting function is called a Glow Curve and often shows well-defined peaks at particular temperatures (Fig. 22). Each peak is due to the emptying of a trapped electron from a trap depth (energy below the conduction band) defined by the temperature, and hence can be considered as a kind of excitation spectrum. As emission spectra can be collected at each temperature defined by a glow curve peak, it is possible in ideal situations to associate particular activators or defect centers with each peak and thus trapping energy. However as many centers can contribute to a single glow curve peak, and also because emission spectra may change during a TL temperature scan, it is usually important to collect multiple emission spectra during the full temperature scan. These are assembled into a 3D glow curve that can be analyzed for both trap energy distribution, and the nature of recombination centers. Shallow traps (corresponding to temperatures below 200 °C) are not useful for dating methods as they are slowly emptied just by long exposures at ambient conditions. Glow curve peaks at 300 °C or more are used for geological dating, though even deep traps can sometimes empty by means of various recombination processes. The TL stability in K feldspars, studied by Strickertsson (1985), is such that only glow curve peaks at 299, 384 and 470 °C were stable and useful for dating or dosimetry. At high temperatures quenching can occur. In this case an excited state may interact with other electronic states creating a nonradiative path to the ground state (see Figs. 4 and 12).

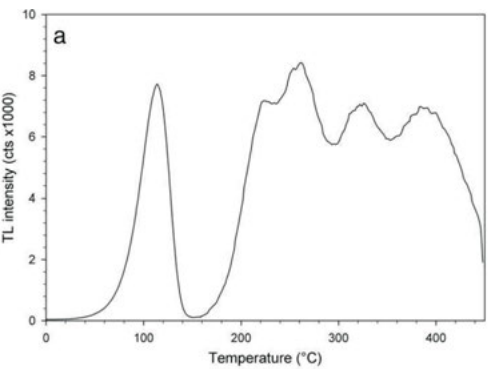


Figure 22. Example of Glow Curve from Nigerian quartz. At least five distinct bands are visible, corresponding to 5 different electron trapping levels. [Used with permission of Elsevier from Preusser et al. (2009), Fig. 1a.]

Optical stimulation approaches. Optically stimulated luminescence (OSL) does not require temperature scanning, and has the additional advantage of being insensitive to latent

EBSCOhost - printed on 2/13/2023 5:26 AM via . All use subject to https://www.ebsco.com/terms-of-use

TL contained in the mineral at the time of sediment deposition that can affect traditional TL measurements. Hence for dating purposes OSL can be more accurate, especially for sediments deposited in water (Aitken 1994). However the spectra differ from that of TL in form and mode of collection. Early measurements of OSL used a 514 nm (green) argon laser operated in continuous mode (Huntley et al. 1985) with quartz. Subsequently it was shown that longer wavelengths also generated OSL but were progressively inefficient. The green light simulation approach was found to work with feldspar, but in contrast to quartz it was found that infrared light could be used to excite luminescence efficiently (Hütt et al. 1988; Botter-Jensen et al. 1994). This paradoxical observation appears to be due to two-photon transitions, effectively producing stimulation as if from green light. The infrared and green light techniques are sometimes referred to as IRSL and GLSL, respectively. Use of green light or other visible light restricts the optical emission spectroscopy that can be done with OSL, and hence mainly UV emission is studied in detail. Use of IR stimulation allows more detailed emission spectroscopy, as well as excitation spectroscopy (called stimulation spectroscopy in this case) Godfrey-Smith and Cada (1996).

The mode of data collection in OSL varies, but for continuous mode the OSL signal is a decaying one that has a fast component followed by slower and slower decay rates (Fig. 23). Another popular mode of data collection is the linearly modulated (LM-OSL) mode wherein the power of the stimulation source is increased with time. For the same sample as in Figure 23, the LM-OSL curve looks quite different (Fig. 24) revealing three distinct slow components.

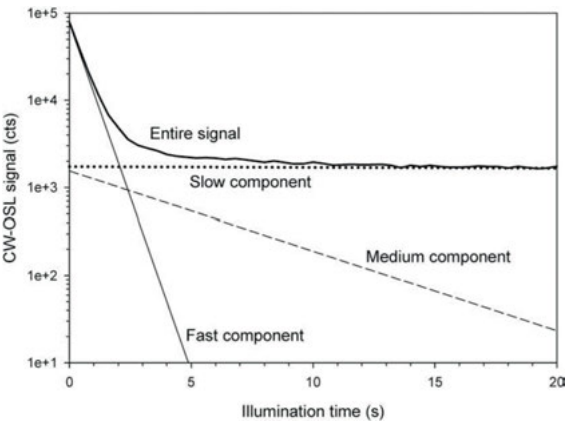


Figure 23. CW-OSL (continuous wave optically simulated luminescence) decay curve from quartz grains in a lacustrine deposit from New South Wales, Australia showing components having dramatically different decay rates. [Used with permission of Elsevier from Preusser et al. (2009), Fig. 11.]

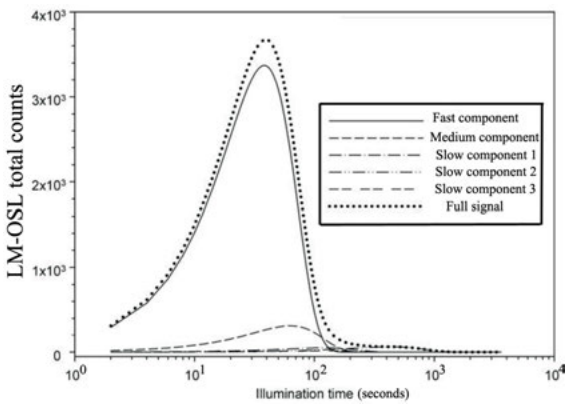


Figure 24. LM-OSL (linearly modulated optically stimulated luminescence) curve for same sample as in Figure 23. This type of plot reveals three slow components, and hence there are five identifiable components resolved using the two approaches. Modified from Preusser et al. (2009).

EBSCOhost - printed on 2/13/2023 5:26 AM via . All use subject to https://www.ebsco.com/terms-of-use

The ratios of these components predict success in dating measurements, with dominance of the faster component being preferred (Steffen et al. 2009).

OSL stimulation spectroscopy does not have the resolution to reveal detailed electronic structure as with fluorescence excitation spectroscopy. However differences between samples of quartz and feldspar from different localities have been observed (Godfrey-Smith and Cada 1996) though it remains to be shown if such observations are useful to dosimetry applications, or geological applications. Emission spectra have been collected with continuously improving instrumentation which now include Fourier transform spectroscopy (Huntley et al. 1988; Rieser et al. 1994; Martini et al. 1996) enabling TL/OSL spectra to be collected simultaneously at all wavelengths as a function of stimulation time.

Applications

Glow curve peaks, emission spectra and defects in quartz. There is considerable similarity between the emission spectra obtained from CL and TL/OSL despite the much different excitation and energy conversion processes (Krbetschek et al. 1997). Quartz CL emission spectra generally show broad emission bands centered at 390, 505, 575 and 650 nm (Preusser et al. 2009) with the blue 390 and red 650 bands dominating. Broad bands centered in the ranges 360-440, 460-500 and 600-650 nm are seen in TL/OSL emission spectra. These bands can be discussed with respect to their association with TL glow curve peaks (Fig. 22). For example, the 110 °C peak coincides with strong emission near 380 nm which has been attributed to a recombination process at $[AlO_4]^0$ (Al^{3+} substitution for Si^{4+} with an additional trapped hole) centers in synthetic quartz crystals (Martini et al. 1995; Vartanian et al. 2000). The 325 C peak is associated with emission near 420 nm and thought to be due to recombination at an $[AlO_4]^-$ center (Itoh et al. 2002). The 375 °C peak is also used as the main dosimetric peak as it has the best stability over long periods, and is connected with emission in both the blue and red bands. These are very sensitive to the geological conditions of formation and alteration as are the analogous bands observed with CL studies. The red band has been attributed to defects involving Al substitution with nearby H^+, but the precise details of this center have not been confirmed (Hashimoto et al. 1994; Stokes and Fattahi 2003; Westaway and Prescott 2012). The blue emission has been associated with $[AlO_4]^0$ centers, with Ti centers, and possibly with Ge centers. Some of the molecular geometries of these and other defects are shown in Figure 25. Clearly, even though it should be possible to associate certain defect populations with TL trapping levels and emission spectra, there remains much ambiguity. Study of the TL emission and excitation spectrum has shown that there are characteristic reproducible differences for quartz samples having different provenance (see e.g., Kuhn et al. 2000; Fig. 26). However it does not appear that this sensitivity has been as thoroughly investigated as it has been for CL spectral analysis, but it potentially allows defect and impurity density to be measured perhaps by combining both methods, and without the need for UHV electron beam instruments like the SEM or electron microprobe. A single temperature "slice" from the matrix spectra of Figure 26 is shown in Figure 27.

Age dating. The basic premise behind TL/OSL dating is that quartz or feldspar grains have had all of their potential trapping states emptied by prolonged exposure to natural light, and that after eventual burial away from light penetration the traps are filled only by local radiation sources. Hence TL would be proportional to the radiation dose after burial, and if the dose rate were known, the duration of burial could be estimated. However it is very difficult to measure the total amount of trapped electrons in a mineral grain accurately, as one would need to sample all light energies emitted with appropriate normalization values for detector efficiency among other complexities. In practice then a single band, usually in the UV for quartz, and in the violet for feldspar is measured using a single aliquot regenerative-dose (SAR) protocol. In this method a sample is first stimulated to release all of its naturally trapped electrons creating TL, which is measured. It is then reradiated with a known dose of radiation and restimulated so that the amount of TL for a specific dose can be determined, and thus with multiple such doses a dose-

EBSCOhost - printed on 2/13/2023 5:26 AM via . All use subject to https://www.ebsco.com/terms-of-use

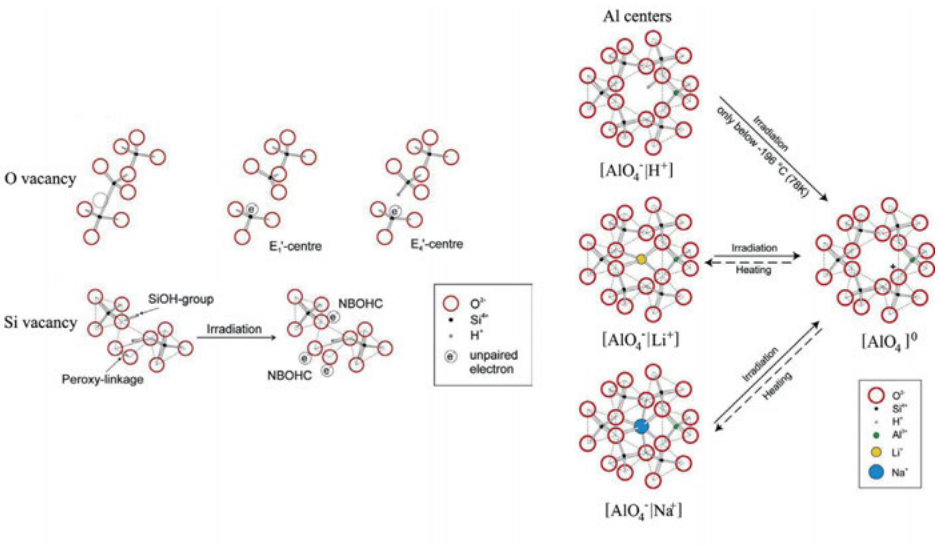


Figure 25. Defects in quartz associated with luminescent activity. Left: intrinsic vacancy and electron trapping centers. Right: proton and alkali impurity defects. Modified from Preusser et al. (2009).

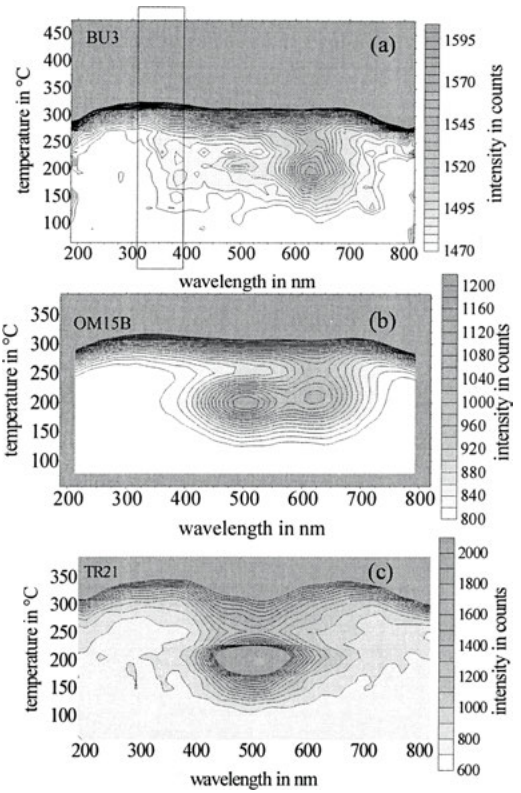


Figure 26. Representative TL matrix spectra showing differences due to provenance. (a) Aeolian sediment, Germany giving an orange-red emission. (b) Aeolian sediment, Oman giving two bands—one blue-green and the other orange-red. (c) Aeolian sediment, India showing only a blue-green emission band. [Used with permission of Elsevier from Kuhn et al. (2000), Fig. 2.]

EBSCOhost - printed on 2/13/2023 5:26 AM via . All use subject to https://www.ebsco.com/terms-of-use

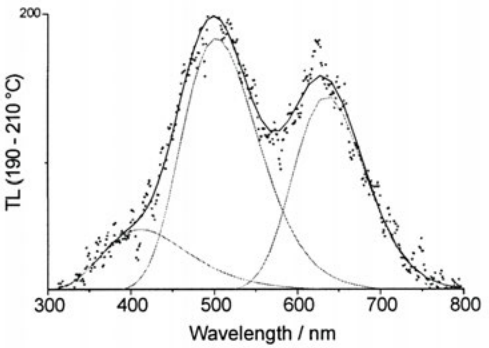


Figure 27. 190-210 °C temperature slice across a matrix such as depicted in Figure 26 showing three resolvable emission bands. The sample is aeolian sand from India, though a different locality from that shown in Figure 26 (c). [Used with permission of Elsevier from Kuhn et al. (2000), Fig. 3.]

response curve (Wintle and Murray 2006) can be generated. The curve then allows the original measured dose to be evaluated. An obvious difficulty of this technique is that it assumes dosing with one type of source, e.g., gamma ray, is equivalent to the natural exposure which comes from gamma rays of various energies, cosmic rays, and other sources. Nevertheless strategies have emerged to yield accurate results when compared with other dating methods. TL/OSL can be used for ages of a few hundred up to about 100,000 years, so it is directly comparable to ^{14}C dating, but in principle can be more generally applied. Studies comparing TL/OSL dating with other procedures show general good agreement, to within approximately 5% relative. Both sediments and volcanic rocks can be studied using this method.

Carbonate TL. Analysis of calcite and rhombohedral carbonates (Calderon et al. 1996) and aragonite (Coy-Yll et al. 1988) TL emission spectra generally agree with CL and fluorescence spectra, with gross spectral parameters consistent with Mn^{2+} as the main activator and following trends well-known from those other types of studies. For example, in rhombohedral carbonates, the main emission due to the $^4T_{1g} \rightarrow {}^6A_{1g}$ transition, decreases in energy as the lattice parameters and the mean M-O distance increase. For dolomite, at low Mn^{2+} concentrations, the difference in the emission from Mn^{2+} in the larger A and smaller B sites can be resolved. However TL emission spectra seem to be more sensitive to impurity concentration than other spectra (Calderon et al. 1996) as concentration quenching appears at 600 ppm Mn. Similarly, in the glow curves, at low Mn concentrations fine stimulation structure is revealed, but this is washed out at high concentrations. Other bands assumed not due to Mn^{2+} have been less explored, but in dolomite the blue emission band can be strong in natural samples, and is markedly enhanced by X-ray irradiation (Soliman et al. 2004). This emission corresponds to a glow curve peak at 240-270 °C and is assumed to be due to lattice defects.

However, the main debate in the literature is in the nature of trapping centers in carbonates, and the precise mechanisms for activation of the luminescence. The consensus, first suggested by Calderon et al. (1983, 1984) for calcite is that electron trapping is dominated by carbonate groups, creating a localized CO_3^{-3} center. Variations in this center may have to do with structural imperfections, dislocations etc., and give rise to glow curve peaks at 260-280 °C and 320-350 °C. Irradiation of natural samples enhances these glow curve peaks, and adds another at lower temperature. Such samples also have enhanced defect-related UV emission in addition to the Mn (yellow-orange-red) emission. When the trapped electrons are freed they ultimately combine with trapped holes at impurity centers, which for Mn^{2+} creates an excited state that (after some nonradiative decay to lower energy excited states) leads to emission. As with other materials studied with TL there are luminescence mechanisms proposed that utilize these centers both with and without interaction with energy bands. In aragonite and the orthorhombic carbonates there is a difference in the interpretation of TL Mn^{2+} emission spectra compared to

EBSCOhost - printed on 2/13/2023 5:26 AM via . All use subject to https://www.ebsco.com/terms-of-use

that in CL spectra. The large average M-O distances in orthorhombic carbonates are consistent with a smaller crystal field splitting than for the rhombohedral carbonates, and hence emission ought to occur at shorter wavelengths as seen in CL (Richter et al. 2003). However the main emission in the TL is observed between 630 and 650 nm, overlapping the longer wavelength range for rhombohedral carbonates. As the Mn^{2+} site in aragonite has lower than octahedral symmetry, the electronic transitions may differ due to removal of degeneracies and subsequent splitting of excited states. However this alone does not explain the differences between CL and TL emission.

Carbonates have been investigated for TL and OSL dating, particularly with cave speleothems. However other methods appear to be more accurate (Vaks et al. 2007; Wintle 2008). A single-aliquot protocol for TL dating using biogenic carbonates has been advanced (Stirling et al. 2012) that may allow dating to over 3 million years.

Fluorite TL. Fluorite has long been known to display strong thermoluminescence in response to fairly gentle heating, even from the heat of a hand. The variety that shows such strong TL is known as chlorophane and the luminescence is generally a blue-green color. A specimen from Franklin, New Jersey was studied long ago by Ginther and Kirk (1957) who found glow curve peaks at 60, 150 and 240 °C. In synthetic fluorite, only the 240 °C peak was seen at higher Mn^{2+} concentrations, with the lower temperature peaks seen only at Mn^{2+} concentrations of fractions of a percent. Interestingly, a small additional amount of Y^{3+} or Ce^{3+} led to strengthening of the lower temperature glow curve peaks at higher Mn^{2+} content, and in the case of Y^{3+} shifted it down to 50 °C. Hence Mn^{2+}, Y^{3+} activated fluorite is a candidate for describing chlorophane behavior.

Fluorite is used commercially as a radiation dosimeter. In this case mainly REE are used as activators, and lower temperature TL is undesirable as it allows trapped electron states to be emptied under dosimeter storage or during radiation collection. Alternatively, fluorite is a sensitive dosimeter that collects a high density of trapped electrons at relatively low radiation levels. For most natural fluorites the REE also are the most important activators and recombination centers. Typical glow curves show peaks at 120, 200 and 265-300 °C and corresponding emission spectra with many trivalent REE peaks (Calderon et al. 1992; Balogun et al. 1999). However Dy^{3+}, Ce^{3+} and Sm^{3+} appear to be the most significant trapping and recombination centers. Natural fluorite can be optically simulated using a blue LED source and it has been proposed as a replacement for synthetic fluorite dosimeters (Polymeris et al. 2006; Yegingil et al. 2012) with a least dose measuring capacity of 10^{-6} Gy. Figure 28 shows a glow curve for a gamma-ray irradiated natural fluorite from Nigeria and the corresponding dose-response curves (Balogun et al. 1999).

Developing areas for luminescence applications

Surface and interface characterization using TRLFS and other luminescence methods. It has long been known that molecules with luminescent properties may have substantial changes in luminescent intensity, spectral features or excited-state lifetimes when sorbed at the mineral-water interface. Sorption may reduce fluorescence lifetimes by creating new pathways for energy dissipation at the interface. Sorption to a magnetic surface is especially sensitive, affording other energy transfer pathways, and the luminescence may be very short or even not observed. Changes in water or other ligand field around a solvated ion also can affect fluorescence lifetimes, usually increasing the lifetime as the number of waters decreases (Tan et al. 2010). Both these effects are incompletely understood, but allow for high potential sensitivity to sorption topology. Besides lifetimes, the fluorescence emission spectrum may also be altered, e.g., by changes in transition probability or by small shifts in band positions. As high power laser excitation can produce statistically useful emission spectra at very low concentrations, this methodology can in principle be used to investigate the geometry of sorption at trace levels where EXAFS or NMR cannot be profitably applied.

EBSCOhost - printed on 2/13/2023 5:26 AM via . All use subject to https://www.ebsco.com/terms-of-use

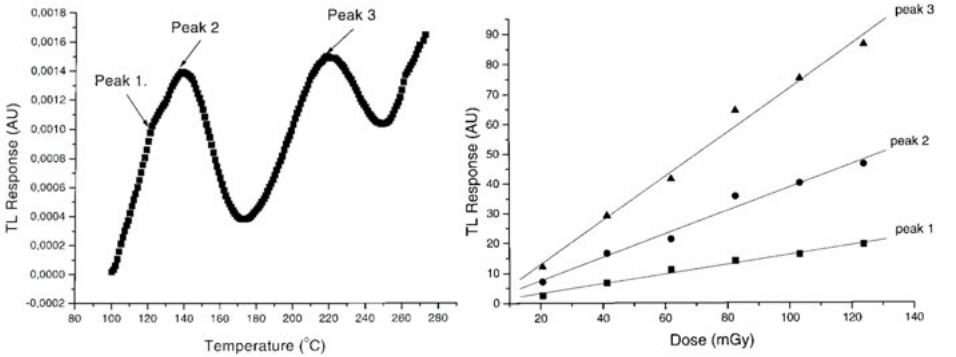


Figure 28. *Left*: Glow curve for gamma-irradiated natural fluorite from Nigeria, showing three peaks or features. *Right*: Dose-response curves for the glow peaks indicated. [Used with permission of Elsevier from Balogun et al. (1999), Figs. 1 and 2.]

One highly luminescent species studied with this in mind is uranyl (UO_2^{2+}), which has been examined at many mineral-water interfaces, in solution, and as a variety of solvated multinuclear complexes. An example of such interface work is that of Baumann et al. (2005) on gibbsite surfaces using time-resolved laser fluorescence spectroscopy (TRLFS). They found two types of sorption topology, an inner sphere complex with a lifetime of 330 ns which was attributed to bidentate attachment to two reactive OH^- groups attached to a single Al at the gibbsite platelet edge, and another species with much longer lifetime of 5.6 μs, attributed to a cluster of sorbed polynuclear uranyl. With increased pH the lifetime of the polynuclear species increased, suggesting that it was growing in size. Another uranyl study on a clay mineral surface included the effect of humic materials. Krepelova et al. (2007) found two sorbed species with different fluorescent lifetimes on kaolinite surfaces both with and without the presence of humic acid (HA). In the former case, both species appear to be bidentate mononuclear complexes, but with different degrees of water coordination. In the latter case with humic acid, the uranyl was identified as having some water coordination displaced by binding to the HA. The spectral emission bands were considerably shifted from dilute uranyl in perchlorate solution, as expected by the hydration change. However the lifetimes were considerably longer (4-40 μs) than those in the gibbsite study for nominally similar surface complexes.

A combined EXAFS and TRLFS study was done by Walter et al. (2005) on pristine and leached albite surfaces, the latter representing degrees of weathering. In this case the EXAFS analysis could in principle be used to link the fluorescence parameters to discrete complexation topology. On the pristine surface one well defined species was deduced from EXAFS, a bidentate mononuclear complex effectively sharing an edge of a silicate tetrahedron on the albite surface, and having a U-Si distance of 3.09 Å. TRLFS detected this complex as having a lifetime of 11 μs, but also indicated the presence of other surface complexes at higher uranyl concentrations not discernable in the EXAFS data, and having shorter lifetimes. The shorter lifetimes suggest another type of inner sphere complex, possibly a type of hydroxylated uranyl complex. On the leached surfaces the EXAFS could not be quantitatively analyzed, but it was suggested that monodentate-mononuclear complexes dominated. The fluorescence lifetimes were around 20 μs, also indicating a different surface complex, or at least a complex with different water coordination.

REE. Other actinides and rare earths are also good subjects for luminescence studies at surfaces, including Cm, Gd, Eu, Sm, Np, and Am (Tan et al. 2010). Cm^{3+} sorbed on clays has been studied by Huittinen et al. (2010) and by Rabung et al. (2005), and Eu^{3+} on kaolinite and

EBSCOhost - printed on 2/13/2023 5:26 AM via . All use subject to https://www.ebsco.com/terms-of-use

smectite by Stumpf et al. (2002). Cm^{3+} sorbs as several types of inner sphere complexes on the studied clay mineral surfaces, with surface precipitation also being observed. Fluorescent lifetimes much different from aqueous species indicated that no outer sphere complexation occurred, and it was concluded that the same type of surface hydroxyl was involved in binding in all cases, namely the $\equiv$Al-O-Cm^{3+} type. In contrast, changes in the emission spectra of Eu^{3+} suggest a coordination change with increasing pH. This is supported by lifetime measurements which showed a lifetime of 110 μs at pH less than 4, and one of 330 μs at pH greater than 7. These changes are consistent with water ligand coordination reduction with change from outer sphere to inner sphere complexation. With added carbonate a ternary complex was suggested (clay surface-Eu^{3+}-CO_3) based on lifetime changes that indicated a loss of 2-3 water ligands. Eu^{3+} has also been studied sorbed on calcite surfaces (Piriou et al. 1997) showing both inner sphere and Ca replacement based on lifetime analysis. Competitive sorption on sedimentary humic acids among Eu^{3+}, Ca^{2+} and Cu^{2+} has also been probed (Marang et al. 2009) showing that Cu replaces Eu^{3+} on several sorption sites, while Ca acts more to modify the humic acid itself, enhancing the luminescence of the bound europium. Analogous studies are possible for organic sorption on mineral surfaces, and these could potentially allow study of competitive sorption among different organic structures for particular types of mineral surface sites. Such studies would be highly complementary to vibrational spectroscopy now possible using ATR-FTIR and other methods, but with potentially much higher sensitivity.

ACKNOWLEDGMENTS

GW wishes to acknowledge support from the Department of Energy, DOE-BES under contract number DE-AC02-05CH11231, and also support while a visitor at The University of New South Wales, Australia by the School of Civil and Environmental Engineering and Deputy Dean David Waite. The manuscript benefited from comments and corrections suggested by John Hanchar, Grant Henderson and an anonymous referee.

REFERENCES

Agangi A, McPhie J, Kamenets VS (2011) Magma chamber dynamics in a silicic LIP revealed by quartz: The Mesoproterozoic Gawler Range Volcanics. Lithos 126:68-83

Aitken MJ (1994) Optical dating: a non-specialist review. Quart Sci Rev 13:503-508

Aitken MJ, Tite MS, Reid J (1964) Thermoluminescent dating of ancient ceramics. Nature 202:1032-1133

Alberts JJ, Takacs M (2004) Total luminescent spectra of IHSS standard and reference fulvic acids, humic acids and natural organic matter: comparison of aquatic and terrestrial source terms. Org Geochem 35:243-256

Ali AE, Barbin V, Calas G, Cervelle B, Ramseyer K, Bouroulec J (1993) Mn^{2+}-activated luminescence in dolomite, calcite and magnesite: quantitative determination of manganese and site distribution by EPR and CL spectroscopy. Chem Geol 104:189-202

Alonso PJ, Halliburton LE, Kohnke EE, Bossoli RB (1983) X-ray induced luminescence in crystalline SiO_2. J Appl Phys 54:5369-5373

Baghoth SA, Sharma SK, Amy GL (2011) Tracking natural organic matter (NOM) in a drinking water treatment plant using fluorescence excitation-mission matrices and PARAFAC. Water Res 45:797-809

Baker A, Tipping E, Thacker SA, Gondar D (2008) Relating dissolved organic matter fluorescence and functional properties. Chemosphere 73:1765-1772

Balogun FA, Ojo JO, Ogundare FO, Fasasi MK, Hussein LA (1999) TL response of a natural fluorite. Radiat Meas 30:759-763

Barbarand J, Pagel M (2001) Cathodoluminescence of apatite crystals. Am Mineral 86:473-484

Baumann N, Brendler V, Arnold T, Geipel G, Bernhard G (2005) Uranyl sorption onto gibbsite studied by time-resolved laser-induced fluorescence spectroscopy (TRLFS). J Coll Interface Sci 290:318-324

Blasse G, Grabmaier BC (1994) Luminescent Materials. Springer Berlin

Boggs S, Krinsley D (2006) Applications of CL Imaging to the Study of Sedimentary Rocks. Cambridge Univ Press

Boggs S, Kwon Y-I, Goles GG, Seyedolali A, Dypvik H (2002) Is quartz CL color a reliable provenance tool? A quantitative examination. J Sediment Res 72:408-415

EBSCOhost - printed on 2/13/2023 5:26 AM via . All use subject to https://www.ebsco.com/terms-of-use

Borosnovskaya NN, Lesnov FP, Scherbakova MYa (1982) On the X-ray luminescence of Fe^{3+} in calcic plagioclase (in Russian). Geokhimiya 9:129-131

Borosnovskaya NN, Makagon VM, Zhukova AI (1996) Luminogen generation in rare-earth pegmatite K-feldspar as affected by geochemical and crystal-chemical factors (in Russian). Geokhimiya 12:1202-1209

Bos AJJ (2007) Theory of thermoluminescence. Radiat Meas 41:S45-S56

Botter-Jensen L, Duller GAT, Poolton NRJ (1994) Excitation and emission spectrometry of stimulated luminescence from quartz and feldspars. Radiat Meas 23:613-616

Bridgeman J, Bieroza M, Baker A (2011) The application of fluorescence spectroscopy to organic matter characterization in drinking water treatment. Rev Environ Sci Biotechnol 10:277-290

Bruckbauer J, Edwards PR, Wang T, Martin RW (2011) High resolution cathodoluminescence hyperspectral imaging of surface features in INGaN/GaN multiple quantum well structures. Appl Phys Lett 98:141908-141908-3

Calderon T, Aguilar M, Coy-Yll R (1983) Relationship between blue color and radiation damage in calcite. Radiat Effects 76:187-191

Calderon T, Aguilar M, Jaque F, Coy-Yll R (1984) Thermoluminescence from natural calcites. J Phys C 17:2027-2038

Calderon T, Aguilar M, Coy-Yll R (1988) A new model of TL in carbonates. Thermochim Acta 133:213-218

Calderon T, Khanlary MR, Rendell HM, Townsend PD (1992) Luminescence from natural fluorite crystals. Nucl Tracks Radiat Meas 20:475-485

Calderon T, Townsend PD, Beneitez P, Garcia-Guinea J, Millan A, Rendell HM, Tookey A, Urbina M, Wood RA (1996) Crystal field effects on the thermoluminescence of manganese in carbonate lattices. Radiat Meas 26:719-731

Chen J, LeBoeuf EJ, Dai S, Gu B (2003) Fluorescence spectroscopic studies of natural organic matter fractions. Chemosphere 50:639-647

Chen N, Pan Y, Weil JA, Nilges MJ (2002) Electron paramagnetic resonance study of synthetic fluorapatite: Part 2. Gd^{3+} at the Ca1 site, with a neighboring Ca1 vacancy. Am Mineral 87:47-55

Chen R, Pagonis V (2011) Thermally and Optically Stimulated Luminescence. Wiley Chichester, West Sussex, UK

Coble PG (1996) Characterization of marine and terrestrial DOM in seawater using excitation-emission matrix spectroscopy. Marine Chem 51:325-346

Cory RM, McKnight DM (2005) Fluorescence spectroscopy reveals ubiquitous presence of oxidized and reduced quinones in DOM. Environ Sci Technol 39:8142-8149

Coy-Yll R, Calderon T, Aguilar M (1988) Thermoluminescence and radioluminescence in aragonite. Mineral Petrol 39:39-53

D'Lemos RS, Kearsley AT, Pembroke JW, Watt GR, Wright P (1997) Complex quartz growth histories in granite revealed by scanning cathodoluminescence techniques. Geol Mag 134: 549-552

Dalby KN, Anderson AJ, Mariano AN, Gordon RA, Mayanovic RA, Wirth R (2010) An investigation of cathodoluminescence in albite from the A-type Georgeville granite, Nova Scotia. Lithos 114:86-94

De St. Torre L, Smith DGW (1988) Cathodoluminescent gallium-enriched feldspars from the Thor Lake rare-metal deposits, Northwest Territories. Can Mineral 26:301-308

Demars C, Pagel M, Deloule E, Blanc P (1996) Cathodoluminescence of quartz from sandstones: interpretation of the UV range by determination of trace element distributions and fluid inclusion P-T-X properties in authigenic quartz. Am Mineral 81:891-901

Dempster TJ, Joliver M, Tubrett MN, Braithwaite CJR (2003) Magmatic zoning in apatite: a monitor of porosity and permeability in granites Contrib Mineral Petrol 145:568-577

Edwards PR, Martin RW, Lee MR (2007) Combined cathodoluminescence hyperspectral imaging and wavelength dispersive X-ray analysis of minerals. Am Mineral 92:235-242

Elkins KM, Nelson DJ (2001) Fluorescence and FTIR spectroscopic studies of Suwanee river fulvic acid complexation with aluminum, terbium and calcium. J Inorg Biochem 87:81-96

Entzian W, Ahlgrimm C (1983) Vergleiche Untersuchungen zur Kathodolumineszenz von SiO_2. Wiss Z W-Pieck-Univ Rostock, Naturweiss Reihe 32:27-29

Esteves da Silva JC, Machado AS, Oliveira CJ, Pinto MS (1998) Fluorescence quenching of anthropogenic fulvic acids by Cu(II), Fe(III) and UO_2^{2+}. Talanta 45:1155-1165

Fellman JB, Hood E, Spencer RGM (2010) Fluorescence spectroscopy opens new windows into dissolved organic matter dynamics in freshwater ecosystems: A Review. Limnol Oceanogr 55:2452-2462

Finch AA, Klein J (1999) The causes and petrological significance of cathodoluminescence emissions from alkali feldspars. Contrib Mineral Petrol 135:234-243.

Gaft M, Nagli L, Panczer G, Waychunas G, Porat N (2008) The nature of unusual luminescence in natural calcite $CaCO_3$. Am Mineral 93:158-167

Gaft M, Panczer G, Nagli L, Yeates H (2009) Laser-induced time-rresolved luminescence of tugtupite, sodalite and hackmanite. Phys Chem Miner 36:127-141

EBSCOhost - printed on 2/13/2023 5:26 AM via . All use subject to https://www.ebsco.com/terms-of-use

Gaft M, Panczer G, Reisfeld R, Uspensky E (2001) Laser-induced time-resolved luminescence as a tool for rare-earth element identification in minerals. Phys Chem Miner 28:347-363
Gaft M, Reisfeld R, Panczer G (2005) Luminescence Spectroscopy of Minerals and Materials. Springer Berlin
Gaft M, Reisfeld R, Panczer G, Boulon G, Shoval S, Champagnon B (1997) Accommodation of rare earths and manganese by apatite. Opt Mater 8:149-156
Gaft M, Seigel H, Panczer G, Reisfeld R (2002) Laser-induced time-resolved luminescence spectroscopy of Pb^{2+} in minerals. Eur J Mineral 14:1041-1048
Garlick GFJ (1962) The kinetics and efficiency of cathodoluminescence. Brit J Appl Phys 13:541-547
Geake JE, Walker G, Telfer DY, Mills AA, Garlick GFJ (1973) Luminescence of lunar, terrestrial, and synthetic plagioclase, caused by Mn^{2+} and Fe^{3+}. *In:* Proceedings 4th Lunar Science Conference 3:3181-3189
Ginther RJ, Kirk RD (1957) The thermoluminscence of CaF_2:Mn. J Electrochem Soc 104:365-369
Godfrey-Smith DI, Cada M (1996) IR stimulation spectroscopy of plagioclase and potassium feldspars, and quartz. Rad Protect Dos 66:379-38
Goldstein J, Newbury DE, Joy DC, Lyman CE, Echlin P, Lifshin E, Sawyer L, Michael JR (2003) Scanning Electron Microscopy and X-ray Microanalysis. Springer Berlin
González-Acebrón L, Götze J, Barca D, Arribas J, Mas R, Pérez-Garrido C (2012) Diagenetic albitization in the Tera Group, Cameros Basin (NE Spain) recorded by trace elements and spectral cathodoluminescence. Chem Geol 313:148-162
Gorobets BS, Gaft ML, Podolskiy AM (1989) Luminescence of Minerals and Ores (in Russian). Ministry of Geology USSR, Moscow
Gorobets BS, Rogojine AA (2002) Luminescent Spectra of Minerals (English version). RPC VIMS Moscow
Gorton NT, Walker G, Burley SD (1997) Experimental analysis of the composite blue CL emission in quartz. J Lumin 72-74:669-671
Götze J (2009) Cathodoluminescence microscopy and spectroscopy of lunar rocks and minerals. *In:* Cathodoluminescence and its application in the Planetary Sciences. Gucsik A (ed) Springer Berlin, p. 87-110
Götze J, Kempe U (2009) Physical principles of cathodoluminescence (CL) and its applications in the geosciences. *In:* Cathodoluminescence and its application in the Planetary Sciences. Gucsik A (ed) Springer Berlin, p. 1-22
Götze J, Krbetschek M R, Habermann D, Wolf D (2000) High resolution cathodoluminescence studies of feldspar minerals. *In:* Cathodoluminescence in Geosciences. Pagel M, Barbin V, Blanc P, Ohnenstetter (eds.) Springer Berlin, p 245-270
Götze J, Krbetschek MR, Habermann D, Rieser U, Wolf D (1996) Investigation of feldspars by spectral TL, CL and IROSL. *In:* Third European Meeting Spectroscopic Methods in Mineralogy, Kiev, Programme and Abstracts. p 215
Götze J, Plötze M, Fuchs H, Habermann D (1999) Defect structure and luminescence behavior of agate-results of electron paramagnetic resonance (EPR) and cathodoluminescence (CL) studies. Mineral Mag 63:149-163
Götze J, Plötze M, Habermann (2001) Origin, spectral characteristics and practical applications of the cathodoluminescence (CL) of quartz: a review. Mineral Petrol 71:225-250
Götze J, Plotze M, Trautmann T (2005) Structure and luminescence characteristics of quartz from pegmatites. Am Mineral 90:13-21
Grant ML, Wilde SA, Wu F, Yang J (2009) The application of zircon cathodoluminescence imaging, Th–U–Pb chemistry and U–Pb ages in interpreting discrete magmatic and high-grade metamorphic events in the North China Craton at the Archean/Proterozoic boundary. Chem Geol 261:155-171
Habermann D (2002) Quantitative cathodoluminescence (CL) spectroscopy of minerals: possibilities and limitations. Mineral Petrol 76: 247-259.
Habermann D, Neuser RD, Richter DK (1996) REE-activated cathodoluminescence of calcite and dolomite: high-resolution spectrometric analysis of CL emission (HRS-CL). Sediment Geol 101:1-7
Hanchar JM, Finch RJ, Hoskin PWO, Watson EB, Cherniak DJ, Mariano AN (2001) Rare earth elements in synthetic zircon: Part 1. Synthesis, and rare earth element and phosphorus doping. Am Mineral 86:667-680
Hanchar JM, Miller CF (1993) Zircon zonation patterns as revealed by cathodoluminescence and backscattered electron images: implications for interpretation of complex crustal histories. Chem Geol 110:1-13
Hanchar JM, Rudnick RL (1995) Revealing hidden structures: The application of cathodoluminescence and back-scattered electron imaging to dating zircons from lower crustal xenoliths. Lithos 36:289-303
Hashimoto T, Sakaue S, Aoki H, Ichino M (1994) Dependence of TL-property changes of natural quartzes on aluminium contents accompanied by thermal annealing treatment. Radiat Meas 23:293-299
Henderson B, Imbusch GF (2006) Optical Spectroscopy of Inorganic Solids. Oxford
Hudson N, Baker A, Reynolds D (2007) Fluorescence analysis of dissolved organic matter in natural, waste and polluted waters-a review. River Res Appl 23:631-649

EBSCOhost - printed on 2/13/2023 5:26 AM via . All use subject to https://www.ebsco.com/terms-of-use

Hughes J M, Ertl A, Bernhardt H-J, Rossman G R, Rakovan J (2004) Mn-rich fluorapatite from Austria: Crystal structure, chemical analysis, and spectroscopic investigations. Am Mineral 89:629-632

Huittinen N, Rabung T, Andrieux P, Lehto J, Geckeis H (2010) A comparative batch sorption and time-resolved laser fluorescence spectroscopy study on the sorption of Eu(III) and Cm(III) on synthetic and natural kaolinite. Radiochim Acta 98:613-620

Huntley DJ, Godfrey-Smith DI, Thewalt ML (1985) Optical dating of sediments. Nature 313:105-107

Huntley DJ, Godfrey-Smith DI, Thewalt ML, Berger GW (1988) Thermoluminescence spectra of some mineral samples relevant to thermoluminescent dating. J Lumin 39:123-136

Hütt G, Jack I, Tchonka J (1988) Optical dating: K-feldspars optical response simulation spectra. Quat Sci Rev 7:381-386

Itoh C, Tanimura K, Itoh N (1988) Optical studies of self-trapped excitons in SiO_2. J Phys C, Solid State Phys 21:4693-4702

Itoh N, Stoneham D, Stoneham AM (2002) Ionic and electronic processes in quartz: mechanisms of thermoluminescence and optically stimulated luminescence. J Appl. Phys 92:5036-5044

Jaek I, Hütt G, Vasiltchenko E (1996) Luminescence of the natural alkali feldspars artificially doped by Eu- and Cu- ions. *In:* Third European Meeting Spectroscopic Methods in Mineralogy, Kiev, Programme and Abstracts. p 23

Jones CE, Embree D (1976) Correlations of the 4.77-4.28 eV luminescence band in silicon dioxide with oxygen vacancy. J Appl Phys 47:5365-5371

Katz S, Halperin A (1988) The low temperature phosphorescence and thermoluminescence of quartz crystals. J Lumin 39:137-143

Kayama M, Nakano S, Nishido H (2010) Characteristic of emission centers in alkali feldspar: A new approach by using cathodoluminescence spectral deconvolution. Am Mineral 95:1783-1795

Kempe U, Götze J, Dandar S, Habermann D (1999) Magmatic and metasomatic processes during formation of the Nb-Zr-REE deposits from Khaldzan Buregte (Mongolian Altai): indications from a combined CL-SEM study. Mineral Mag 63:165-167

Kempe U, Gruner T, Nasdala L, Wolf D (2000) Relevance of cathodoluminescence for the interpretation of U-Pb Zircon ages, with an example of an application to a study of zircons from the Saxonian granulite complex, Germany. *In:* Cathodoluminescence in Geosciences. Pagel M, Barbin V, Blanc P, Ohnenstetter D (eds) Springer Berlin, p 415-455

Ko JYP, Zhou X-T, Heigl F, Regier T, Blyth R, Sham T-K (2006) X-ray absorption Near-edge structure (XANES) of calcium L3,2 edges of various calcium compounds and X-ray excited optical luminescence (XEOL) studies of luminescent calcium compounds. AIP Conf Proc 882:538-540

Krbetschek MR, Götze J, Dietrich A, Trautmann T (1997) Spectral information from minerals relevant for luminescence dating. Radiat Meas 27:695-748

Krepelova A, Brendler V, Sachs S, Baumann N, Bernhard G (2007) U(VI)-Kaolinite surface complexation in absence and presence of humic acid studied by TRLFS. Environ Sci Tech 41:6142-6147

Kuhn R, Trautmann T, Singhvi AK, Krbetschek MR, Wagner GA, Stolz W (2000) A study of thermoluminescence emission spectra and optical stimulation spectra of quartz from different provenances. Radiat Meas 32:653-657

Kusnetsov GV, Kramarenko NK (1995) Kinetic luminescence characteristics of Ce^{3+} in plagioclases as a guide for facial classification of granitoids (in Russian). Miner Zhurn 17:86-90

Laud KR, Gibbons EF, Tien TY, Stadler HL (1971) Cathodoluminescence of Ce^{3+} and Eu^{2+}-activated alkaline earth feldspars. J Electrochem Soc 118:918-923

Lee MR, Parsons I, Edwards PR, Martin RW (2007) Identification of cathodoluminescence activators in zoned alkali feldspars by hyperspectral imaging and electron probe microanalysis. Am Mineral 92:243-253

Li B, Ryan PW, Shanahan M, Leister KJ, Ryder AG (2011) Fluorescence excitation-emission matrix (EEM) spectroscopy for rapid identification and quality evaluation of cell culture media components. Appl Spectrosc 65:1240-1249

Lu X, Jaffe R (2001) Interaction between Hg(II) and natural dissolved organic matter: A fluorescence spectroscopy based study. Water Res 35:1793-1803

Luff BJ, Townsend PD (1990) Cathodoluminescence of synthetic quartz. J Phys Condens Matter 2:8089-8097

Macalady DL, Walton-Day K (2009) New light on a dark subject: On the use of fluorescence data to deduce redox states of natural organic matter (NOM). Aquat Sci 71:135-143

Machel HG (2000) Application of cathodoluminescence to carbonate diagenesis. *In:* Cathodoluminescence in Geosciences, Pagel M, Barbin V, Blanc P, Ohnenstetter D (eds) Springer, Berlin/Heidelberg, p 271-301

Marang L, Eidner S, Kumke M, Benedetti MF, Reiller PE (2009) Spectroscopic characterization of the competitive binding of Eu(III), Ca(II), and Cu(II) to a sedimentary originated humic acid. Chem Geol 264:154-161

Marfunin AN, Bershov LV (1970) Electron-hole centers in feldspars and their possible crystalchemical and petrological significance (in Russian). Dokl Akad Nauk 193:412-414

EBSCOhost - printed on 2/13/2023 5:26 AM via . All use subject to https://www.ebsco.com/terms-of-use

Marfunin AS (1979) Spectroscopy, Luminescence and Radiation Centers in Minerals. Springer-Verlag, Berlin
Mariano AN, Ito J, Ring PJ (1973) Cathodoluminescence of plagioclase feldspars. Geol Soc Am, Abstracts and Program 5:726
Mariano AN, Ring PJ (1975) Europium-activated cathodoluminescence in minerals. Geochim Cosmochim Acta 39:649-660
Marshall DJ (1988) Cathodoluminescence of Geological material. Allen and Unwin, London.
Martini M, Paravisi S, Liguori C (1996) A new high sensitive spectrometer for 3-D thermoluminescence analysis. Radiat Prot Dosim 66:447-450
Martini M, Paravisi S, Spinolo G, Vedda A (1995) Role of $[AlO_4]^0$ centers in the 380 nm thermoluminescence of quartz. Phys Rev B 52:138-142
Miller MP, Chapra SC, Williams MW (2009) A model of degradation and production of three pools of DOM in an alpine lake. Limnol Oceanogr 54:2213-2227
Mladenov N, Zheng Y, Miller MP, Nemergut DR, Legg T, Simone B, Hageman C, Rahman MM, Ahmed KM, McKnight DM (2010) Dissolved organic matter sources and consequences for iron and arsenic mobilization in Bangladesh aquifers. Environ Sci Technol 44:123-128
Mladenov NP, Huntsman-Mapila P, Wolski P, Wellington R, Masamba L, McKnight DM (2008) Dissolved organic matter accumulation, reactivity, and redox state in ground water of a recharge wetland. Wetlands 28:747-759
Mora CI, Ramseyer K (1992) Cathodoluminescence of coexisting plagioclases, Boehls Butte anorthosite: CL activators and fluid flow paths. Am Mineral 77:1258-1265
Mosselmans JFW, Taylor RP, Quinn PD, Finch AA, Cibin G, Gianolio D, Sapelkin AV (2012) A time resolved microfocus facility at the Diamond Light Source. J Phys: Conf Ser 425:1-4
Müller A (2000) CL and characterization of defect structures in quartz with applications to the study of granitic rocks. Doctoral dissertation, Georg-August-Universität zu Gottingen.
Müller A, van den Kerkhof, AM, Behr H-J, Kronz A, Koch-Muller M (2010) The evolution of late-Hercynian granites and rhyolites documented by quartz—a review (for 2009). Earth Environ Sci Trans 100:185-204
Nasdala L, Götze J, Hanchar J M, Gaft M, Krbetschek M R (2004) Luminescence techniques in Earth Sciences. *In:* Spectroscopic Methods in Mineralogy. Beran A, Libowitzky E (eds) EMU Notes in Mineralogy, p 43-92
Nassau K, Prescott BE (1975) A reinterpretation of smoky quartz. Phys Stat Sol 29:659-663
Parsons I, Steele DA, Lee MR, Magee CW (2008) Titanium as a cathodoluminescence activator in alkali feldspar. Am Mineral 93:875-879.
Perny B, Eberhardt P, Ramseyer K, Mullis J, Pankrath R (1992) Microdistribution of Al, Li and Na in α-quartz: possible causes and correlation with short-lived cathodoluminescence. Am Mineral 77:534-544
Piriou B, Fedoroff M, Jeanjean J, Bercis L (1997) Characterization of the sorption of Europium (III) on calcite by site-selective and time-resolved luminescence spectroscopy. J Colloid Interface Sci 194:440-447
Plötze M, Wolf D (1996) EPR- und TL-Spektren von Quartz: Bestrahlungsabhängigkeit der $[TiO_4^-/Li^+]^0$-Zentrum. Ber Deutsch Mineral Gesellsch 8:217 {Abstract}
Polymeris GS, Kitis G, Tsirliganis NC (2006) Correlation between TL and OSL properties of CaF_2:N. Nucl Inst Meth Physics Res B251:133-142
Pott GT, McNicol BD (1971) Spectroscopic study of the coordination and valence of Fe and Mn ions in and on the surface of aluminas and silicas. Disc Faraday Soc 52:121-131
Preusser F, Chithambo ML, Götte T, Martini M, Ramsayer K, Sendezera EJ, Susino GJ, Wintle AG (2009) Quartz as a natural luminescent dosimeter. Earth Sci Rev 9:184-214
Rabung T, Pierret MC, Bauer A, Geckeis H, Bradbury MH, Baeyens B (2005) Sorption of Eu(III)/Cm(III) on a Ca-montmorillonite and Na-illite, Part 1. Batch sorption and time-resolved laser fluorescence spectroscopy experiments. Geochim Cosmochim Acta 69:5393-5402
Rakovan J (2009) Word to the wise-Sectoral Zoning. Rocks & Minerals 84:171-176
Rakovan J, Reeder RJ (1994) Differential incorporation of trace elements and dissymmetrization in apatite: The role of surface structure during growth. Am Mineral 79:892-903
Rakovan J, Waychunas GA (1996) Luminescence in minerals. Min Record 27: 7-19
Rakovan J, Waychunas GA (2013) Color and luminescence in apatite, $Ca_5(PO_4)_3(F,Cl,OH)$. *In:* Lithographie Monograph 17: Apatite the Great Pretender. Rakovan J, Staebler GA, Dallaire DA, Bunk DW (eds) Lithographie LLC, p 11-17
Ramseyer K, Mullis O (1990) Factors influencing short-lived blue cathodoluminescence of alpha-quartz. Am Mineral 75:791-800
Remond G, Cesbron F, Chapoulie R, Ohnenstetter D, Roques-Carmes C, Schvoerer M (1992) Cathodoluminscence applied to the microcharacterization of mineral materials: A present status in experimentation and interpretation. Scanning Microscopy 6:23-68
Richter DK, Götte Th, Götze J, Neuser RD (2003) Progress in application of cathodoluminescence (CL) in sedimentary petrology. Mineral Petrol 79:127-166

EBSCOhost - printed on 2/13/2023 5:26 AM via . All use subject to https://www.ebsco.com/terms-of-use

Rieser U, Krebetcheck MR, Stolz W (1994) CCD-camera based high sensitivity TL/OSL-spectrometer. Radiat Meas 23:523-528
Rink WJ, Rendell H, Marseglia EA, Luff BJ, Townsend PD (1993) Thermoluminescence spectra of igneous quartz and hydrothermal vein quartz. Phys Chem Minerals 20:353-361
Roeder PL, MacArther D, Ma X-P, Palmer GR, Mariano AN (1987) Cathodoluminescence and microprobe study of rare-earth elements in apatite. Am Mineral 72:801-811
Rokatschuk TA, Tscherbakov IB, Steschin VA (1989) Genetic interpretation of the distribution of centres in plagioclases. Miner Zhurn 11:60-67
Rossman GR (2104) Optical spectroscopy. Rev Mineral Geochem 78:371-398
Rubbato D, Gebauer D (2000) Use of cathodoluminescence for U-Pb zircon dating by ion microprobe: some examples from the western Alps. *In:* Cathodoluminescence in Geosciences. Pagel M, Barbin V, Blanc P, Ohnenstetter D (eds) Springer Berlin, p 373-400
Schlaich H, Lindner G G, Feldmann J, Göbel E O, Reinen D (2000) Optical properties of Se_2^- and Se_2 color centers in the red selenium ultramarine with the sodalite structure. Inorg Chem 39:2740-2746
Sharpless CM, McGown LB (1999) Effects of aluminum-induced aggregation on the fluorescence of humic substances. Environ Sci Technol 33:3264-3270
Siegel GH, Marrone MJ (1981) Photoluminescence in as-drawn and irradiated silica optical fibers: an assessment of the role of nonbridging oxygen defect centers. J Non-Cryst Solids 45:235-247
Sippel RF, Spencer AB (1970) Cathodoluminescence properties of lunar rocks. Science 167:677-679
Skuja LN, Entzian W (1986) Cathodoluminescence of intrinsic defects in glassy SiO_2, thermal SiO_2 films, and a-quartz. Phys Status Solidi A 96:191-198
Slaby E, Götze J, Simon K, Wörner G (2008) K-feldspar phenocrysts in microgranular magmatic enclaves: Cathodoluminescence and geochemical studies on crystal growth as a marker of magma mingling dynamics. Lithos 105:85-97
Smith JV, Stenstrom RC (1965) Electron-excited luminescence as a petrologic tool. J Geol 73:627-635
Soliman C, Massoud AM, Hussein MA (2004) Thermoluminescence of the blue emission band of dolomite. Nucl Instrum Methods Modern Phys Res B 222:163-168
Spear FS, Wark DA (2009) Cathodoluminescence imaging and titanium thermometry in metamorphic quartz. J Metamorphic Geol 27:187-205
Steffen D, Preusser F, Schlunegger F (2009) OSL quartz age underestimation due to unstable signal components. Quat Geochronol 4:353-362
Stevens-Kalceff MA, Phillips MR (1995) Cathodoluminescence microcharacterization of the defect structure of quartz. Phys Rev B 52:3122-3134
Stevens-Kalceff MA, Phillips MR, Moon AR, Kalceff W (2000) Cathodoluminescence microcharacterization of silicon dioxide polymorths. *In:* Cathodoluminescence in Geosciences. Pagel M, Barbin V, Blanc P, Ohnenstetter D (eds) Springer Berlin, p 193-224
Stirling RJ, Duller GAT, Roberts HM (2012) Development of a single-aliquot protocol for measuring equivalent dose in biogenic carbonates Radiat Meas 47:725-731
Stokes S, Fattahi M (2003) Red emission luminescence from quartz and feldspar for dating applications: an overview. Radiat Meas 37:383-395
Strickertsson K (1985) the thermoluminescence of potassium feldspars-glow curve chracteristics and initial rise measurements. Nucl Tracks Radiat Meas 10:613-617
Stumpf T, Bauer A, Coppin F, Fanghänel T, Kim JI (2002) Inner-sphere, outer-sphere and ternary surface complexes: a TRLFS study of the sorption process of Eu(III) onto smectite and kaolinite. Radiochim Acta 90:345-349
Swart HC, Terblans JJ, Coetsee E, Ntwaeaborwa OM, Dhlamini MS, Nieuwoudt S, Holloway PH (2007) Review on electron stimulated surface chemical reaction mechanism for phosphor degradation. J Vac Sci Technol A 25:917-921
Tan X, Fang M, Wang X (2010) Sorption speciation of lanthanides/actinides on minerals by TRLFS, EXAFS and DFT studies: A review. Molecules 15:8431-8468
Taraschan AN (1978) Luminescence of Minerals. Naukova Dumka, Kiev (in Russian).
Taraschan AN, Serebrennikov AI, Platonov AN (1973) Features of lead ions luminescence in amazonite (in Russian). *In:* Constitution and Properties of Minerals 7:106-111
Taylor RP, Finch AA, Mosselmans JFW, Quinn PD (2013) The development of a XEOL and TR XEOL detection system for the I18 microfocus beamline Diamond light source. J Lumin 134:49-58
Trukhin AN, Plaudis AE (1979) Investigation of intrinsic luminescence of SiO_2. Sov Phys Sol State 21:644-646
Vaks A, Bar-Matthews M, Ayalon A, Matthews A, Halicz L, Frumkin A (2007) Desert speleothems reveal climatic window for African exodus of early modern humans. Geology 35:831-834
Valeur B (2001) Molecular Fluorescence: Principles and Applications. Wiley-VCH Verlag GmbH Weinheim 387pp
Vartanian E, Guibert P, Roque C, Bechtel F, Schvorer M (2000) Changes in OSL properties of quartz by preheating: an interpretation. Radiat Meas 32:647-652

EBSCOhost - printed on 2/13/2023 5:26 AM via . All use subject to https://www.ebsco.com/terms-of-use

Walker G (1985) Mineralogical applications of luminescence techniques. *In:* Chemical Bonding and Spectroscopy in Mineral Chemistry. Berry FJ, Vaughan DJ (eds) Chapman and Hall, London, p 103-140
Walker G, Abumere OE, Kamaluddin B (1989) Luminescence spectroscopy of Mn^{2+} centres in rock-forming carbonates. Mineral Mag 53:201-211
Walter M, Arnold T, Geipel G, Scheinost A, Bernhard G (2005) An EXAFS and TRLFS investigation on uranium (VI) sorption to pristine and leached albite surfaces. J Coll Interface Sci 282:293-305
Wark DA, Watson EB (2006) TitaniQ: a titanium-in-quartz geothermometer. Contrib Mineral Petrol 152:743-754
Waychunas GA (1988) Luminescence, X-ray emission and new spectroscopies. Rev Mineral Geochem 18:638-698
Waychunas GA (2002) Apatite luminescence. Rev Mineral Geochem 48:701-742
Weil JA (1984) A review of electron spin spectroscopy and its application to the study of paramagnetic defects in crystalline quartz. Phys Chem Minerals 10:149±165
Weil JA (1993) A review of the EPR spectroscopy of the point defects in α-quartz: the decade 1982-1992. *In:* Physics and Chemistry of SiO_2 and the Si–SiO_2 interface 2. Helms CR, Deal BE (eds) Plenum Press, New York, p 131-144
Westaway K, Prescott J (2012) Investigating signal evolution: A comparison of red and UV/blue TL, and UV OSL emissions from the same quartz sample. Radiat Meas 47:909-915
White WB, Matsumura M, Linnehan DG, Furukawa T, Chandrasekhar BK (1986) Absorption and luminescence of Fe^{3+} in single-crystal orthoclase. Am Mineral 71:1415-1419
Wintle AG (2008) Fifty years of luminescence dating. Archaeometry 50:276-312
Wintle AG, Huntley DJ (1980) Thermoluminescence dating of ocean sediments. Can J Earth Sci 17:348-360
Wintle AG, Murray AS (2006) A review of quartz optically simulated luminescence characteristics and their relevance in single-aliquot regeneration dating protocols. Radiat Meas 41:369-391
Yacobi BG and Holt DB (1990) Cathodoluminescence Microscopy of Inorganic Solids. Plenum Press, New York
Yang XH, McKeever SWS (1990) Point defects and the pre-dose effect in quartz. Radiat Prot Dosim 33:27-30
Yegingil Z, Nur N, Dogan T, Yazici N, Topaksu M (2012) Effects of annealing and high radiation dose on the thermoluminescence characteristics of natural fluorite. Radiat Meas 47:981-987
Zinkernagel U (1978) Cathodoluminescence of quartz and its application to sandstone petrology. Contrib Sedimentol 8:1-69
Zsolnay A (2003) Dissolved organic matter: artefacts, definitions, and functions. Geoderma 113:187-209

EBSCOhost - printed on 2/13/2023 5:26 AM via . All use subject to https://www.ebsco.com/terms-of-use

EBSCOhost - printed on 2/13/2023 5:26 AM via . All use subject to https://www.ebsco.com/terms-of-use

Reviews in Mineralogy & Geochemistry
Vol. 78 pp. 219-269, 2014
Copyright © Mineralogical Society of America

Analytical Transmission Electron Microscopy

Rik Brydson[1], Andy Brown[1], Liane G. Benning[2]
[1]Institute for Materials Research
[2]School of Earth and Environment
University of Leeds
Leeds, LS2 9JT, United Kingdom
R.M.Drummond-Brydson@leeds.ac.uk

Ken Livi
High-Resolution Analytical Electron Microbeam Facility
Integrated Imaging Center
Department of Earth and Planetary Sciences
Johns Hopkins University
Baltimore, Maryland 21218, U.S.A.

INTRODUCTION

Analytical transmission electron microscopy (TEM) is used to reveal sub-micrometer, internal fine structure (the *microstructure* or *ultrastructure*) and chemistry in minerals. The amount and scale of the information which can be extracted by TEM depends critically on four parameters; the resolving power of the microscope (usually smaller than 0.3 nm); the energy spread of the electron beam (of the order of an electron volt, eV); the thickness of the specimen (almost always significantly less than 1 μm), and the composition and stability of the specimen. An introductory text on all types of electron microscopy is provided by Goodhew et al. (2001), while more detailed information on transmission electron microscopy may be found in the comprehensive text of Williams and Carter (2009).

INTRODUCTION TO ANALYTICAL TRANSMISSION ELECTRON MICROSCOPY (TEM)

Basic design of transmission electron microscopes (TEM)

The two available modes of TEM—CTEM and STEM—differ principally in the way they address the specimen. Conventional TEM (CTEM) is a wide-beam technique, in which a close-to-parallel electron beam floods the whole area of interest and the image (or diffraction pattern), formed by an imaging (objective) lens after the thin specimen from perhaps 10^6-10^7 pixels on a digital camera, is collected in *parallel*. Scanning TEM (STEM) deploys a fine focused beam, formed by a probe-forming lens before the thin specimen, to address each pixel (here, a dwell point) in *series* and form a sequential image as the probe is scanned across the specimen. Figures 1 and 2 summarize these different instrument designs; here it should be noted that many modern TEM instruments are capable of operating in both modes, rather than being instruments dedicated to one mode of operation.

In both types of instrument analytical information from a small region is usually collected using a focused beam. The smallest region from which an analysis can be collected is defined by the diameter of this beam and hence the corresponding through-thickness volume in the

1529-6466/14/0078-0006$10.00 http://dx.doi.org/10.2138/rmg.2014.78.6

EBSCOhost - printed on 2/13/2023 5:26 AM via . All use subject to https://www.ebsco.com/terms-of-use

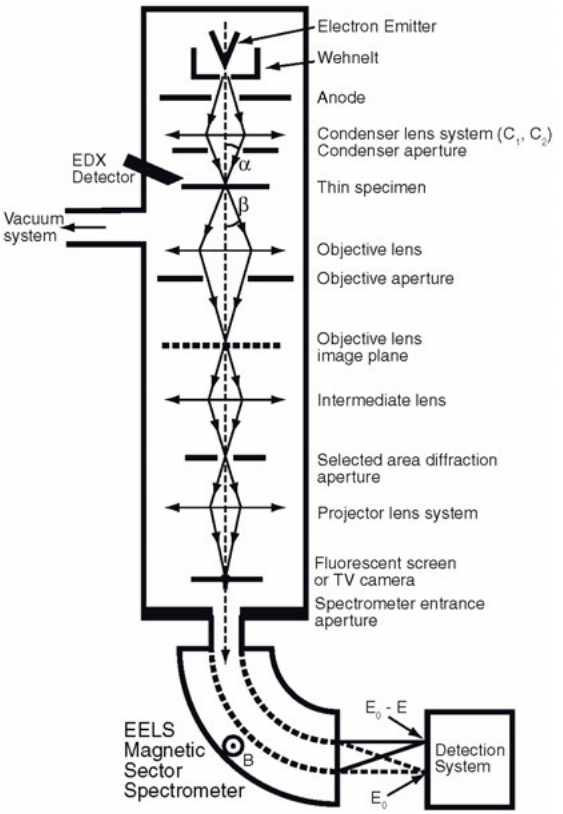


Figure 1. Schematic diagram of the layout of an analytical conventional transmission electron microscope (CTEM) fitted with an energy dispersive X-ray (EDX) detector and an electron energy loss (EEL) spectrometer (after Brydson 2001, 2011). α and β denote the convergence and collection angles. E_o is incident beam energy, E is the energy loss of the fast electron and B is the magnetic field in the spectrometer.

specimen within which various elastic and inelastic scattering (energy-loss) processes take place.

In both CTEM and STEM, electrons are produced from an electron emitter, focused and collimated into a beam and finally accelerated to a given beam energy. Key instrumental components, which affect the microscope resolution and analytical performance, are:

- the electron emitter which can operate via either a thermionic or field emission mechanism or a combination of the two; field emission provides the brightest, most monochromatic and coherent source of electrons.
- the accelerating voltage (E_o, typically in the range 60-300 kV) and hence incident electron energy; the higher the accelerating voltage the higher the resolution and the larger the sample penetration (although, in certain cases depending on the elements present and their chemical bonding, sample damage via sputtering may be an issue above a certain threshold energy).

In the CTEM (Fig. 1), two or more electromagnetic condenser lenses demagnify the probe to a size typically between a few micrometers and a few nanometers—the excitation of these lenses controls both the beam diameter and the beam divergence/convergence angle. For these

EBSCOhost - printed on 2/13/2023 5:26 AM via . All use subject to https://www.ebsco.com/terms-of-use

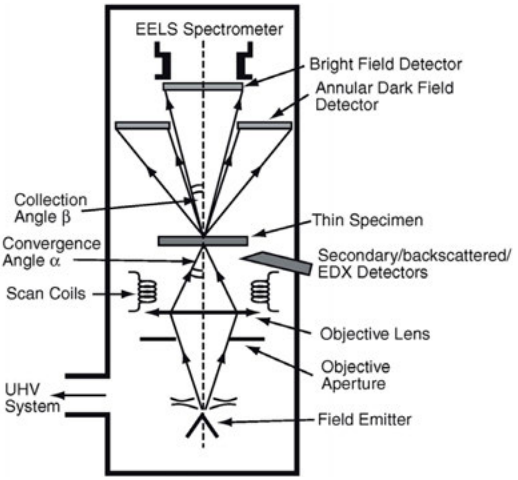


Figure 2. Schematic diagram of the layout of a dedicated analytical scanning transmission electron microscope (STEM) fitted with an energy dispersive X-ray (EDX) detector and an electron energy-loss (EEL) spectrometer (after Brydson 2001, 2011). α and β denote the convergence and collection angles, respectively. Note this is a dedicated UHV STEM configuration with the electron emitter at the base of the microscope for reasons of stability; in the more usual hybrid CTEM/STEM instruments, STEM mode is achieved using the TEM condenser lens system (Fig. 1) which is prior to the specimen and is used to converge a probe which is then scanned across the specimen.

condenser-lens systems the first condenser (C1 or spot size) controls the demagnification of the source, while the second (C2 or intensity) controls the size of the spot at the specimen and hence the beam divergence/convergence.

The specimen is in the form of a thin (< 100 nm) 3 mm diameter disc of either the material itself or the material supported on an electron transparent film. The specimen is usually inserted into the vacuum of the TEM via an airlock and fixed into a side-entry specimen rod that can be translated or tilted (about one or two axes).

In the CTEM (see Fig. 1), the main electromagnetic objective lens forms the first intermediate, real space, projection image of the illuminated specimen area (in the image plane of the lens) as well as the corresponding reciprocal space diffraction pattern (in the back focal plane of the lens). Here the image magnification relative to the specimen is typically 50-100 times. For a given electron emitter and accelerating voltage, the image resolution in CTEM is principally determined by imperfections or aberrations in this objective lens. An objective aperture can be inserted in the back focal plane of the objective lens to limit beam divergence in reciprocal space of the transmitted electrons contributing to the magnified image. Typically there are a number of circular objective apertures ranging from 10 to 100 μm in diameter. The projector lens system consists of a first projector or intermediate lens that focuses on either the objective lens image plane (microscope operating in imaging mode) or the back focal plane (microscope in diffraction mode). The first projector lens is followed by a series of three or four further projector lenses—each of which magnify the image or diffraction pattern by typically up to 20 times. The Selected Area Electron Diffraction (SAED) aperture usually lies in the image plane of one of the projector lenses (due to space considerations) and if projected back to the first intermediate image and hence the specimen effectively allows the selection of a much smaller area (typically ranging from a few tenths of a micron to a few microns) on the specimen for the purposes of forming a diffraction pattern. The overall microscope system can provide a total magnification of up to a few million times on the electron fluorescent microscope

EBSCOhost - printed on 2/13/2023 5:26 AM via . All use subject to https://www.ebsco.com/terms-of-use

viewing screen or, below this, the camera (either a photographic plate or a phosphor coupled to a two dimensional charge coupled diode (CCD) array).

In the STEM (see Fig. 2), as opposed to CTEM, there is usually only a condenser lens system, which is better called a probe-forming lens; confusingly in a STEM this is often referred to as an objective lens—however, the important distinction from the case of CTEM is that this objective lens lies before the specimen. This lens system is used to form a small diameter (typically a nanometer or less) probe that is serially scanned in a two-dimensional raster across the specimen. At each point the transmitted beam intensity is measured—thus building up a serial image of the specimen. Two intensities are usually recorded: that falling on an on-axis bright field (BF) detector that collects electrons that have undergone relatively small angles of scattering (principally undiffracted, Bragg diffracted and inelastically scattered electrons which gives images equivalent to CTEM BF images), as well as that incident on a high-angle annular dark-field (HAADF) detector that principally collects higher-angle (beyond the diffracted spots) incoherently elastically scattered electrons (so called *Z*-contrast images). In a STEM instrument, the resolution of the scanned image (as well as the analytical resolution described above) is determined largely by the beam diameter generated by the probe-forming lens and this is also limited by lens aberrations. As discussed in the introduction, there are now many hybrid CTEM/STEM instruments, which can operate in both modes.

Interactions between the electron beam and the specimen

The high-energy incident electron beam of the TEM interacts with the sample in a number of ways. Low-angle, coherent elastic scattering (diffraction) of electrons (through 1°-10°) occurs via the interaction of the incident electrons with the electron cloud associated with atoms in a solid—this is used for CTEM and STEM bright field imaging. High-angle, incoherent elastic (back)scattering (through 10-180°) occurs via interaction of the negatively charged electrons with the nuclei of atoms—this is used for STEM dark field imaging. The cross section or probability for elastic scattering varies roughly as the square of the mean atomic number of the sample, whereas inelastic scattering, which provides the analytical signal, generally involves much smaller scattering angles than is the case for elastic scattering; the cross section of inelastic scattering varies linearly with atomic number.

Inelastic scattering of electrons by solids predominantly occurs via four major mechanisms:

1. *Phonon scattering*, where the incident electrons excite phonons (atomic vibrations) in the material. Typically the energy loss is < 1 eV, the scattering angle is quite large (~10°) and for carbon, the average distance between such scattering events—the mean free path, Λ—is ~1 μm. This is the basis for heating of the specimen by an electron beam.

2. *Plasmon scattering*, where the incident electrons excite collective, ''resonant'' oscillations (plasmons) of the valence (bonding) electrons associated with a solid. Here, the energy loss from the incident beam is between 5-30 eV and Λ is ~100 nm, causing this to be the dominant scattering process in electron-solid interactions.

3. *Single-electron excitation*, where the incident electron transfers energy to single atomic electrons resulting in the ionization of atoms. The mean free path for this event is of the order of μm. Lightly bound valence electrons may be ejected from atoms and, if they escape from the specimen surface, may be used to form secondary electron images in scanning electron microscopy (SEM). Energy losses for such excitations typically range up to 50 eV. If inner-shell electrons are removed, the energy loss can be up to keV. For example, the energy loss required to ionize carbon 1*s* (i.e., *K* shell) electrons is 284 eV. The energy loss of the incident beam can be used in electron energy-loss spectroscopy (EELS) analysis and the secondary emissions (e.g., X-ray or Auger electron production; see Fig. 3) produced when the ionized atom relaxes can

EBSCOhost - printed on 2/13/2023 5:26 AM via . All use subject to https://www.ebsco.com/terms-of-use

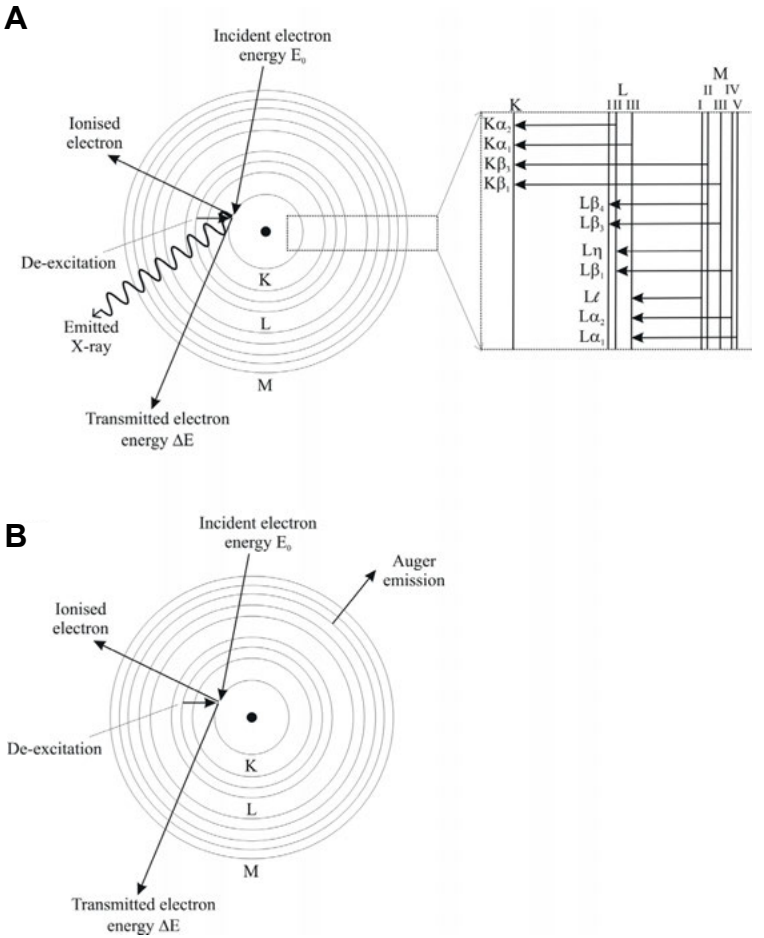


Figure 3. Energy dispersive X-ray analysis in the TEM (after Brydson 2011). De-excitation mechanisms for an atom which has undergone *K*-shell ionization by primary electrons: (A) emission of a characteristic K_α X-ray (the inset details possible ionization processes and emission of X-rays) and (B) emission of a KLM Auger electron.

also be used for analytical purposes in the techniques of either energy dispersive or wavelength dispersive X-ray (EDX/WDX) spectroscopy.

4. *Direct radiation losses*, the principal of which is Bremsstrahlung X-ray emission caused by the deceleration of electrons by the solid; this forms the background in the X-ray emission spectrum upon which are superimposed characteristic X-ray peaks produced by single-electron excitation and subsequent relaxation. The Bremsstrahlung energy losses can take any value and can approach the total incident beam energy in the limit of full deceleration.

Brief review of imaging mechanisms in CTEM and STEM. All TEM images are two dimensional projections of the internal structure of a thin specimen region. In recent years, however, there has been considerable interest in reconstructing the three dimensional nature of the specimen using tomographic techniques (see Weyland and Midgley (2007) in Hutchison

EBSCOhost - printed on 2/13/2023 5:26 AM via . All use subject to https://www.ebsco.com/terms-of-use

and Kirkland (2007)). Notwithstanding, unless they are STEM EDX or EEL spectrum images or energy filtered CTEM images (see "*EDX and EELS Imaging*" section below), all TEM images are based principally on the elastically scattered components of the incident electron beam although the images may contain some underlying inelastically scattered contribution (Williams and Carter 2009).

There are three basic contrast mechanisms which contribute to all CTEM images:

1. *Mass-thickness contrast*: sample regions (whether amorphous or crystalline) that are thicker or of higher density will scatter the electrons more strongly and hence more electrons will be scattered through high angles and be lost in their passage down the narrow bore of the microscope column so making these areas appear darker in the image.
2. *Diffraction contrast*: crystalline regions of the sample oriented at the Bragg angle for diffraction will excite diffracted beams, which correspondingly reduce the amplitude of the unscattered beam. Insertion of an objective aperture in the back focal plane can accentuate this effect via formation of bright field (BF) images (the unscattered beam selected with diffracting regions appearing dark) or dark field (DF) images (a diffracted beam selected, with diffracting regions appearing bright). Any microstructural feature which changes the corresponding diffraction condition (such as a grain boundary, stacking fault, strain field or a line defect etc.) will, in principle, show up in diffraction contrast.
3. *Phase contrast*: this relies on the interference between the unscattered beam and different diffracted beams to produce an interference pattern (visible at high magnification) which reflects the lattice periodicity; effectively lattice planes and hence atomic positions are imaged but may appear light or dark depending on the microscope conditions (objective lens defocus, beam energy, etc.) and the sample thickness.

Some examples of these three CTEM contrast mechanisms are given in Figure 4A as well as in many subsequent figures in the chapter. In addition to imaging, as discussed in the Introduction, the diffraction pattern in the back focal plane may be viewed. The area of the specimen from which the diffraction pattern originates can be defined using the SAED aperture (using effectively parallel illumination) or the probe can be converged to a small area on the specimen so as to form diffraction discs (whose radius depends on the convergence angle) rather than spots. The diffraction pattern allows the degree of crystallinity as well as the exact crystallographic phase of the material to be determined as well as the incident beam direction through the crystal. See Figure 4B for a schematic diagram and also Figures 16 and 19 for an example diffraction patterns.

STEM bright field images contain all the same contrast mechanisms as CTEM bright field images, whereas STEM dark field images (particularly HAADF which relies on Rutherford scattering from the nuclei) images are relatively insensitive to structure and orientation but strongly dependent on atomic number (Z contrast), with the intensity varying as Z^{ζ} where ζ lies between 1.5 and 2. If the specimen is uniformly thick in the area of interest the HAADF intensity can be directly related to the average atomic number in the column at each pixel. Figure 4C shows an example BF and DF STEM image. If the beam is less than one atom dimension in diameter, for instance in an aberration-corrected STEM (see later), then atom column compositional resolution is therefore possible (strictly, only if we have strong channeling of the probe down the atomic columns which occurs when the sample is oriented along a low Miller index zone axis).

Analytical signals. Based on the description in the section "*Interactions between the electron beam and the specimen*", the two major techniques for chemical nanoanalysis in the

EBSCOhost - printed on 2/13/2023 5:26 AM via . All use subject to https://www.ebsco.com/terms-of-use

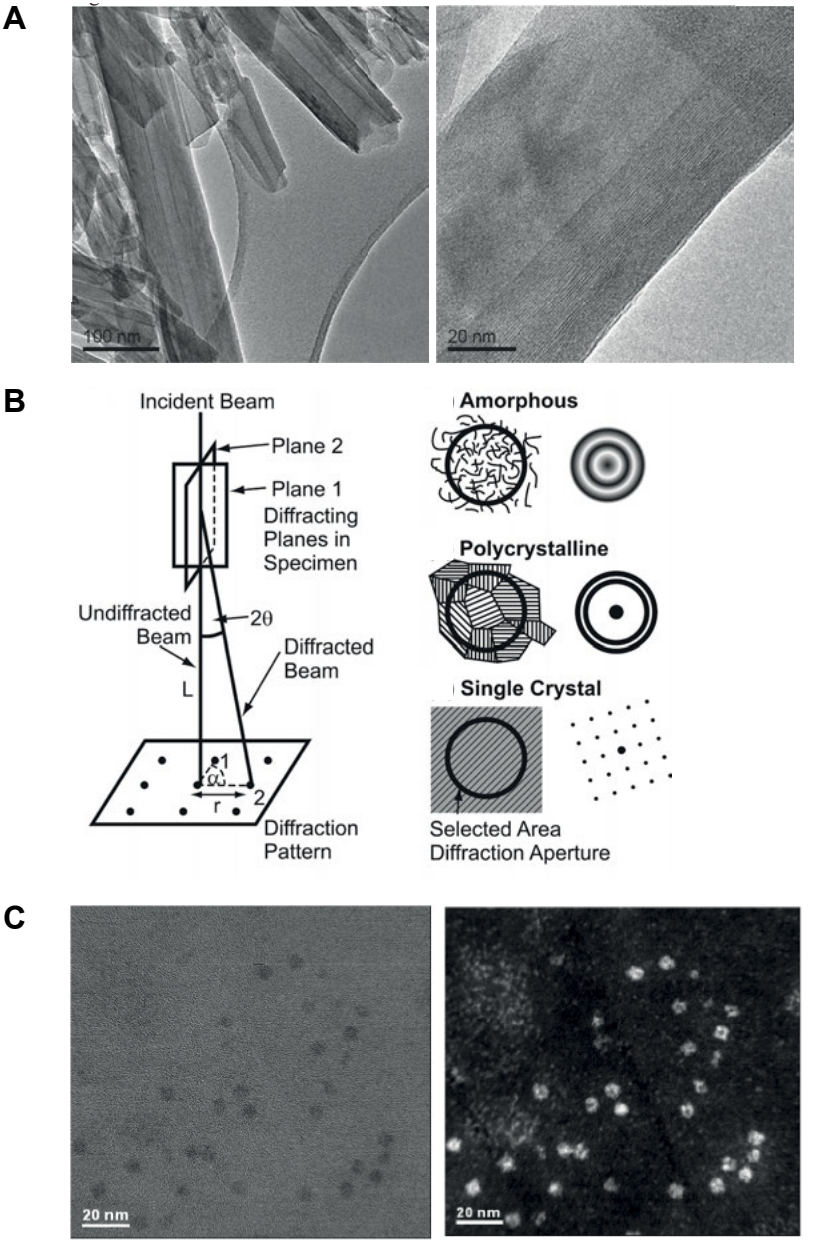


Figure 4. (A) TEM bright field image of a tubular halloysite clay mineral showing both CTEM mass thickness contrast (from the amorphous carbon support film and the halloysite tubes) and CTEM diffraction contrast from some of the halloysite tubes oriented at the Bragg angle for diffraction. At higher magnification CTEM phase contrast is evident in the (002) basal plane lattice fringes of tube walls (Brydson and Hillier, unpublished). (B) Schematic diagram of the geometry of electron diffraction in the CTEM and the form of the selected area diffraction pattern for amorphous, polycrystalline and single crystal sample regions. Examples of real diffraction patterns are shown in Figure 16 and subsequent figures. (C) Example of (*left*) a STEM BF image and (*right*) a STEM high angle annular dark field image from a cluster of iron storage proteins, ferritin molecule mineral-cores (doped ferrihydrite) cores within a tissue section (see Pan et al. 2009).

EBSCOhost - printed on 2/13/2023 5:26 AM via . All use subject to https://www.ebsco.com/terms-of-use

transmission electron microscope are both concerned with inelastic interactions and are based on the analysis of either the energy or wavelength of the emitted X-rays (EDX or WDX), or the direct energy losses of the incident electrons (EELS).

As shown in Figure 5, X-rays produced when the electron probe interacts with the specimen are most commonly detected from the incident surface using a low take-off angle Energy Dispersive X-ray (EDX) detector (i.e., the detector is approximately in the same plane as the sample, some 20° to the horizontal), so as to allow the detector to be brought close to the sample and also to minimize the predominantly forward-peaked Bremsstrahlung background contribution to the X-ray emission spectrum. Even though the detector is inserted to within a few mm of the sample surface, it collects only a small proportion (usually only a few percent) of the isotropically emitted X-ray signal owing to the limited solid collection angle of the detector (typically significantly less than 1 Steradian, from a total possible solid angle of 4π Steradians). Generally, the specimen is tilted towards the detector (typically through ca. 15°) so as to provide a clear X-ray trajectory between the irradiated area and the detector. The volume of the specimen that produces X-rays is controlled by the electron probe size (and hence condenser-lens currents) as well as beam broadening within the specimen that increases with (among other things) thickness and average atomic number and decreases with

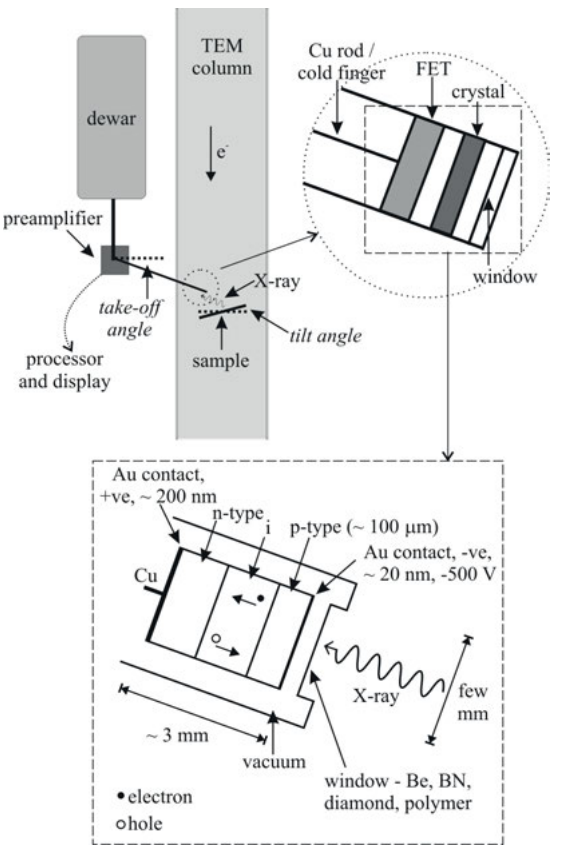


Figure 5. Energy dispersive X-ray analysis in the TEM (after Brydson 2011). Schematic diagram showing the components and location of an EDX detector in a TEM.

EBSCOhost - printed on 2/13/2023 5:26 AM via . All use subject to https://www.ebsco.com/terms-of-use

microscope accelerating voltage. High take-off angle X-ray detectors also exist and these do not require the specimen to be tilted towards the detector.

Below the microscope viewing screen, the self-contained EELS spectrometer (which almost always possesses a variable entrance aperture itself) and detection system collects the transmitted electron signal that is composed of both elastically and inelastically scattered electrons. In both Figures 1 and 2, α and β are known as the convergence and collection semi-angles, respectively. Note certain commercial EELS systems (particularly those initially developed for the purposes of energy-filtered imaging) employ an in-column design with the EEL spectrometer placed between the objective and projector lenses. Further details are given in the "*EDX and EELS Imaging*" section below.

As discussed in the introduction, apart from the case of energy filtered CTEM (see "*EDX and EELS Imaging*" section below), analytical information is most usually collected using a focused probe. In this respect STEMs are ideal analytical machines since they easily allow the simultaneous recording of images and X-ray emission spectra, furthermore retraction of the bright-field detector allows electrons to enter an EEL spectrometer while still simultaneously recording the HAADF image. Generally, STEMs can collect analytical EDX and EELS data in one of two ways: firstly, by scanning the beam over an area and collecting the signal from the whole scanned area and, secondly, by scanning the beam slowly and recording the analytical signal serially at each point (known as spectrum imaging). Dedicated STEMs employ extremely small probe sizes produced by cold field-emission electron sources that can provide extremely high energy resolution (EELS) and high spatial resolution (EELS and EDX) measurements.

The specimen

A specimen suitable for study by analytical TEM should be thin enough for electron transmission without significant spreading of the electron beam, yet be representative of the material about which we wish to draw conclusions. These simple requirements imply that in most cases we must prepare a thin specimen (typically less than 50 nm for high resolution studies) from a larger sample, and in all cases we must assure ourselves that the processes of preparation, mounting and examination do not change, in any uncontrolled way, the important features of the specimen. Specimen preparation is therefore an absolutely crucial aspect of analytical TEM. This is discussed in the "*Example of the practical application of EDX: clay minerals – Sample preparation*" and "*Developments in TEM specimen preparation*" sections below. However, for the vast majority of mineralogical and geological samples this usually involves cleaving or crushing a sample in an agate mortar and pestle, dispersing in a suitable inert liquid and drop-casting onto a TEM grid with a thin, usually amorphous and often holey support film. An alternative procedure, which retains the microstructural relationships in the overall specimen, involves the thinning and polishing of a bulk 3 mm disc of material cut using a drill or ultrasonic disc cutter. Course-scale thinning of the disc is usually performed mechanically using standard polishing procedures employing silicon carbide, diamond and alumina or silica abrasives of progressively decreasing roughness. Final thinning to electron transparency (ca. 100 nm) can be achieved via either: accurate and controlled mechanical polishing (tripod polishing); chemical polishing using jets of acids or alkalis or, very commonly, ion milling using a broad low energy argon ion beam. More recently the use of focused ion beam (FIB) specimen preparation techniques, although not without their specific problems associated with sample damage, has radically altered the preparation of thin TEM specimens from site-specific areas within larger samples, in particular cross sections of interfaces and surfaces (see Fig. 20 and also Giannuzzi 2004).

When analyzing the sample, the specimen should resist both contamination and damage induced by the primary electron beam. For a given incident beam energy, beam damage of the specimen is generally a function of the energy deposited within the specimen volume (known

EBSCOhost - printed on 2/13/2023 5:26 AM via . All use subject to https://www.ebsco.com/terms-of-use

as dose) which is dependent on the incident energy of the electron beam, the interaction cross section for the specimen, the electron fluence (i.e., the total number of electrons incident per unit area of specimen) and, in some cases, the fluence rate (usually quoted in current per unit area) can be important. In many cases, for a given set of microscope conditions, there is a "safe" fluence or fluence rate below which damage is negligible.

Beam damage of the specimen can occur by two dominant mechanisms: knock-on damage in which an atom or ion is displaced from its normal site, and ionization damage (in some contexts called radiolysis) in which electrons are perturbed leading to chemical and then possibly structural changes (Egerton et al. 2004; Williams and Carter 2009). The latter can also eventually result in specimen heating. Both types of damage are very difficult to predict or quantify with accuracy, because they depend on the bonding environment of the atoms in the specimen. In most circumstances, however, the knock-on cross section increases with primary beam energy, while the ionization cross section decreases. Thus there is a compromise to be struck for each specimen to find a beam energy that is low enough not to cause significant atomic displacement but is high enough to suppress radiolysis.

Recent developments in analytical TEM

As mentioned previously, the image resolution in CTEM is primarily determined by the imperfections or aberrations in the objective lens, while in a STEM instrument the resolution of the scanned image (as well as the analytical resolution for EDX and EELS) is determined largely by the beam diameter generated by the probe-forming lens which is also limited by aberrations. In both cases the most serious lens aberration is spherical aberration, whereby electrons travelling at differing distances from the central optic axis of the lens are focused to different positions. In recent years, technical difficulties have been overcome (principally due to increases in computing power) which has allowed both the diagnosis and correction of an increasing number (and type) of these lens aberrations (Hawkes 2008). Aberration correction could in principle be applied to any magnetic lens in any microscope. In practice there are two key areas where it is employed (in some cases in tandem) to correct spherical aberration: (i) in the condenser/illumination or probe-forming system (STEM) and (ii) in the objective or imaging lens (CTEM). With the correction of spherical aberration, the next resolution-limiting lens aberration, particularly at low accelerating voltages, is chromatic aberration whereby electrons of differing energies are focused to different positions. At the time of writing there are a number of schemes being developed and implemented for chromatic aberration correction (Leary and Brydson 2011). One of the main benefits of the correction of aberrations in STEM is in the reduction of the "beam tails" so that a fine beam positioned on a specified column of atoms does not "spill" significant electron intensity into neighboring columns. This has big implications for the STEM-based techniques of HAADF or "*Z* contrast" imaging, EELS and EDX analysis and even tomography (Brydson 2011).

Particularly with the advent of micro-electromechanical systems (MEMS) technology, it is now becoming increasingly possible to control many environmental parameters associated with the specimen while in many cases simultaneously imaging or spectroscopically analyzing a region of interest. Possible *in situ* experiments that have been demonstrated include: specimen heating or cooling, specimen straining or compression, the control of local electric or magnetic fields, measurement of local specimen conductivity, illumination of the specimen with photons, even imaging the specimen under the presence of environmental atmospheres of gas or even (flowing) liquids (see chapter by Gai (2007) in Hutchison and Kirkland (2007)).

Finally, as mentioned at the beginning of subsection "*Brief review of imaging mechanisms in CTEM and STEM,*" methodologies for three dimensional TEM image reconstructions using either tilt series tomography (see chapter by Weyland and Midgley (2007) in Hutchison and Kirkland (2007)) or single particle analysis (Pan et al. 2009) have been applied in areas

EBSCOhost - printed on 2/13/2023 5:26 AM via . All use subject to https://www.ebsco.com/terms-of-use

potentially akin to geology and mineralogy. In terms of analytical TEM, the basic possibilities are any signal, which monotonically increases with increasing thickness such as HAADF images and potentially EDX and EEL spectrum images or energy filtered TEM images (EFTEM) (see section below on "*EDX and EELS imaging*").

ELEMENTAL QUANTIFICATION – EDX AND EELS

EDX

As discussed previously (section "*Interactions between the electron beam and the specimen*"), following ionization of atoms in a sample by an electron beam, one possible de-excitation process is X-ray emission. The energy of the X-ray photon emitted when a single outer electron drops into the inner shell hole is given by the difference between the energies of the two excited states involved. A set of dipole selection rules determines which transitions are observed and these are labeled due to a standard notation: e.g., *K* excitation for ionization of 1*s* electrons, *L* for 2*s* (L_1) and 2*p* (actually spin orbit split into L_2 for $2p_{1/2}$, L_3 for $2p_{3/2}$) electrons etc. with corresponding subscripts (α, β, etc.) denoting the electron from the upper energy level which fills the ionized hole. Due to the well-defined nature of the various atomic energy levels, it is clear that the energies of the set of emitted X-rays will have characteristic values for each of the atomic species present in the specimen and by measuring these energies of the X-rays emitted from the sample, it is possible to determine which elements are present at the particular position of the electron probe. Figure 6 shows a typical electron-generated X-ray emission spectrum from Molybdenum oxide. The Mo K_α, K_β and L_α X-ray lines as well as the O K_α line are superimposed upon the Bremsstrahlung background. The latter X-rays are not characteristic of any particular atom but depend principally on specimen thickness. To a first approximation, peak intensities are roughly proportional to the atomic concentration of the element and, through careful measurements and comparison to elemental/mineralogical standards, EDX can detect levels of elements down to 0.1 at%. Many further example EDX spectra are given in subsequent figures.

EDX detectors collect X-rays in a near-parallel fashion and rely on the creation of electron-hole pairs in a biased doped silicon crystal (see Fig. 5); the number of electron-hole pairs and hence current is directly proportional to the energy of the incident X-ray. Fast electronics allow

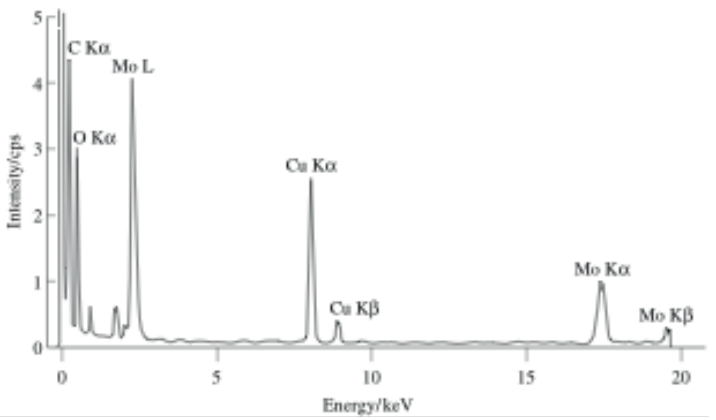


Figure 6. Schematic energy dispersive X-ray (EDX) emission spectrum from a sample of molybdenum oxide on a carbon support film. The copper K_α and K_β X-ray peaks are due to the TEM specimen holder and support grid.

EBSCOhost - printed on 2/13/2023 5:26 AM via . All use subject to https://www.ebsco.com/terms-of-use

separate pulses of X-rays to be discriminated and measured. EDX detectors often have some form of window (either beryllium or, for a thinner more sensitive window, a polymer) which, depending on the material and thickness, may reduce sensitivity to light elements ($Z < 11$).

New developments in EDX detectors employ silicon-drift detector (SDD) technology that have several advantages: 1) SD detectors can be designed to fit closer to the sample and subtend a greater solid collection angle so collecting more X-rays per unit time; 2) several SDD's can be linked in parallel to cover a solid collection angle approaching 1 Steradian. This requires a high level of integration of the detectors into the microscope optical design, and thus, is only available from the microscope manufacturer at the time of the publication of this chapter; 3) SDD technology can handle large amounts of incident X-rays ($10^{5\text{-}6}$ counts/s), levels that would normally saturate the conventional Si(Li) detectors ($10^{3\text{-}4}$ counts/s); 4) liquid nitrogen cooling is not necessary for SDD, which are Peltier cooled. This technology is still in the early stages of implementation on the TEM and promises to improve significantly elemental detection limits and also X-ray mapping capabilities.

Compared to the alternative method of detection via X-ray wavelength (Wavelength Dispersive X-ray Spectroscopy, WDX) rather than energy EDX, EDX is cheaper to implement and very fast in terms of acquisition, but it has a much poorer resolution and hence sensitivity to all elements, particularly light elements. WDX is generally confined to dedicated analytical Scanning Electron Microscopes (SEMs) known as Electron Probe Microanalyzers (EPMA), while EDX detectors may be fitted as an add-on attachment to most SEMs and TEMs.

Practical EDX acquisition and quantification. Identifying which elements are present in significant amounts from an EDX spectrum such as that shown in Figure 6 or Figure 7, is relatively routine. The positions and relative heights of the various X-ray peaks are either tabulated in references or, more commonly, are stored in a database associated with the

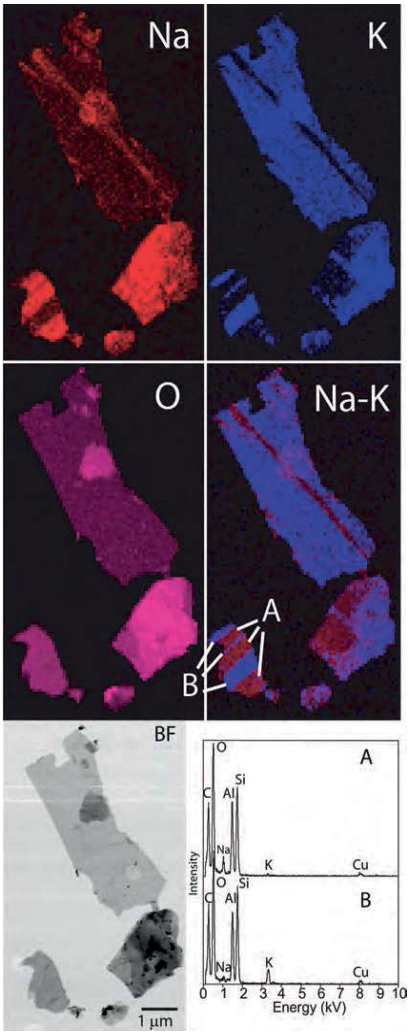


Figure 7. STEM/EDX spectrum image of mixed Na-K white micas (down c*) (from Livi et al. 2008). The Na-K X-ray image is generated by: 1) normalizing the Na and K by the O image that stands in as a proxy for thickness variations, and then 2) generating a false color (RB) image from the combined normalized maps (in electronic version Na is red and K is blue, while in print version of Na-K image Na is darker grey and K is lighter grey). The thickness variation is then effectively removed. EDX spectra integrated from areas A and B are given in the lower right. The carbon peak comes from the carbon support film and Cu is from the Cu mesh support grid.

EBSCOhost - printed on 2/13/2023 5:26 AM via . All use subject to https://www.ebsco.com/terms-of-use

software package of the EDX system. Working from the high-energy end of the spectrum, for internal consistency, it is necessary to confirm manually that if the *K* lines for a particular element are present, then the corresponding *L* (and possibly *M* lines) is also evident. Pre-processing of the spectrum prior to quantification involves both background subtraction and correction for escape peaks due to X-ray absorption in the surface of the detector and sum peaks due to the near simultaneous arrival (and hence detection) of two X-rays at high count rates. This may be performed using deconvolution techniques involving Fourier transformation and filtering, or alternatively both the background and escape and sum fractions may be modeled mathematically. Such facilities are an integral part of many currently available EDX software packages.

After the spectrum has been processed, the characteristic X-ray peaks are matched, using least squares methods, either to stored spectra or to computed profiles. Such a procedure can also deal with the problem of overlapping peaks. Alternatively, simple integration of areas under the peaks may be performed. Once the characteristic line intensities have been extracted the next step is to turn these into a chemical composition present in the irradiated sample volume. For quantification it is necessary to know the relevant cross sections for X-ray excitation by the accelerated electrons as well as the absorption characteristics of the window, electrode and dead layer of the X-ray detector, so as to correct the measured X-ray intensities. The most usual approach to tackling this problem is to use a proportionality factor known as a *k*-factor; this may be calculated from first principles or, more usually, it is measured experimentally. The latter approach employs a standard compound of known composition that contains the elements of interest. The basic equation for the analysis of inorganic materials is:

$$\frac{C_A}{C_B} = k_{AB}\frac{I_A}{I_B}$$

where C denotes the concentration in wt% and I denotes the characteristic X-ray peak intensity above the background, for both elements A and B. k_{AB} is the appropriate proportionality or *k*-factor, also known as a Cliff-Lorimer factor, which is independent of specimen composition and thickness but varies with accelerating voltage. Frequently, *k*-factors are measured for several element pairs that have a common element such as Si; k_{AB} is then simply given by $k_{AB} = k_{ASi}/k_{BSi}$. EDX software packages often provide a set of *k*-factors, obtained for a particular detector system at a given electron beam accelerating voltage, known as a virtual standards pack. If the specimen is very thin (a few tens of nanometers), it is possible to neglect the following phenomena: (i) the differing absorption, within the material itself, of the various characteristic X-rays generated in the specimen as they travel to the specimen exit surface en route to the detector, and (ii) fluorescence of one characteristic X-ray by another higher-energy characteristic X-ray. If however, the specimen is thicker, or for quantification of the concentration of a light element present in a heavy element matrix then, for accuracy, we have to correct for these effects, in particular absorption. The absorption correction employs an iterative procedure that initially assumes a starting composition for the specimen based on the uncorrected X-ray intensities. The absorption of different energy X-rays in this specimen en route to the detector is then accounted for using a Beer-Lambert-type expression to give a new composition that is subsequently used as input to a further absorption correction. This procedure is repeated until the change in composition falls below some preset level of required accuracy. Fluorescence by characteristic X-rays is only really significant when there are two elements of interest with similar X-ray energies and the energy of one X-ray is just above the absorption edge of another X-ray (e.g., elements close to each other in the periodic table). Fluorescence is made considerably worse by the presence of a large concentration of the fluorescing element combined with a small concentration of the fluoresced species.

With careful measurement and analysis, EDX can detect levels of elements down to 0.1 at% with an accuracy of roughly 5%. However, the absorption of low-energy X-rays becomes

EBSCOhost - printed on 2/13/2023 5:26 AM via . All use subject to https://www.ebsco.com/terms-of-use

a severe problem for elements of $Z < 11$ and this can make light-element quantification extremely unreliable without the use of very carefully and individually determined *k*-factors.

In terms of element detectability using analytical TEM, two important quantities are firstly, the *minimum mass fraction* (MMF), which is the smallest composition (expressed in either wt% or at%) detectable; secondly, the *minimum detectable mass* (MDM) is the minimum number of atoms detectable in the analytical volume probed. Generally for analytical transmission electron microscopy, the MMF is rather poor compared to many other analytical techniques principally due to either the low total signal detected (EDX) or the large background contribution (EELS). The ability to form small, intense electron probes means that it is possible to analyze very small total sample masses and, for a given detectable MMF, this results in a low MDM, which is one of the major benefits of analytical transmission electron microscopy; aberration correction can significantly improve this capability (see section on "*Recent developments in analytical TEM*" and Brydson 2011).

When EDX is used in the TEM, the thin nature of the TEM sample (as opposed to a bulk SEM sample) leads to much reduced broadening of the electron beam during its passage through the specimen (the so-called interaction volume) and, since EDX analysis will collect all X-rays produced isotropically within the beam-broadened volume within the specimen, the elemental analysis will possess a high spatial resolution. In practice at 100 keV, a 100 nm thick sample typically gives a beam broadening of the order of a few nanometers and by generating a small focused STEM probe, EDX spectrum imaging maps can now routinely demonstrate resolutions of 5-10 nm in thin sample areas (see Fig. 7 and also Fig. 18). However, it is important to realize that the smaller you make the probe, the more you reduce the current within the probe as electrons are "lost" in the (sometimes fixed) apertures in the column; this then means that fewer X-rays are generated lowering the spectrum signal to noise ratio (SNR). Aberration corrected STEMs, can achieve ultrafine electron probes with more current and very high (even atomic column) resolution EDX maps have been demonstrated, most probably at the risk of increased beam damage and hydrocarbon contamination (Brydson 2011). However, such high spatial resolution mapping requires the use of high solid angle, high throughput EDX SDDs which can significantly increase count rates both collected and processed by the detector. This has significantly enhanced EDX spectrum imaging capabilities both in terms of acquisition times and spatial resolution.

Below we outline the major issues associated with the practical application of TEM/EDX in mineralogical research.

Example of the practical application of EDX: clay minerals

The development of TEM techniques has been very beneficial to the study of clay minerals owing to their grain size (<1 μm) being generally below the resolution of electron microprobe (EPMA) techniques. Analytical TEM using light element detectors has become a standard tool for "nanopetrologists" interested in the compositions of individual crystals of clay minerals (see Merriman and Peacor 1999 for description of EDX applications to low-grade metamorphism). The purpose of this section is not to summarize the extensive work of analytical TEM applications to clay minerals, but to outline some protocols that should be adhered to when attempting to obtain quantitative data on nanoparticles. Potential pitfalls become apparent when the analytical volumes decrease in our attempts to obtain greater resolution and detail of intergrowths and mineral boundaries—especially in beam sensitive minerals.

Sample preparation. Several factors can influence elemental analysis during sample preparation. These include elements introduced during the preparation or alteration of sample composition during the process of thinning the sample.

EBSCOhost - printed on 2/13/2023 5:26 AM via . All use subject to https://www.ebsco.com/terms-of-use

- *Choice of TEM support grid metal.* Copper, which is a common choice for the grid metal, has an L_α X-ray line that interferes with the analysis of sodium. The tantalum and tungsten *M* lines overlap with silicon and may complicate background subtraction in that keV range. Molybdenum will overlap with sulfur, and steel will complicate analysis of iron, nickel and chromium. It is important to understand how your support grid metal will influence your analysis. Choose a metal to meet your analytical needs. If need be, manufacture your own using hole punches and drills.
- *Ar ion milling.* Argon ion milling can cause smearing of elements across mineral interfaces (Schmidt et al. 1999). Ion milling can also cause loss of volatile elements through heating of the specimen during milling. To minimize these effects, liquid nitrogen cooled milling is recommended. However, make sure the sample is not the coldest component in the mill or else contaminants will condense on the sample. Oxidation or reduction can take place in the vacuum of the ion mill. An example of this is the reduction of pyrite to nanocrystalline pyrrhotite (unpublished data).

  Ion milling creates an amorphous layer on the top and bottom of mineral samples. The proportion of amorphous material in analytical volumes will increase as the thickness of the foil decreases. Low-energy polishing may remove much of the amorphous layers and this is facilitated by new ion mills with ion guns capable of operating at very low energies.
- *Focused Ion Beam (FIB) cross sectioning.* During the production of FIB sections, implantation of gallium will occur. The Ga L_α interferes with Na K_α analysis, so a good final polish at low keV and low beam current is necessary to remove the implanted gallium and amorphous material that may have been added during foil preparation. Good preparation of FIB sections will produce uniformly thin foils. It is then necessary to determine if the foil thickness will satisfy the Cliff-Lorimer thin-film criteria.
- *Crushed grain mounts on TEM support films.* These mounts are extremely useful in cases where spatial relationships between grains are not needed. Sample preparation times are short (5 min) and there is little chance of sample contamination if care is taken. A few issues are important to pay attention to though. Use clean thin holey- or lacey-carbon support films and deionized-distilled water (or freshly-opened 200 proof alcohol) as the suspension fluid. Silicon, sulfur, sodium, chlorine and calcium can be found as contaminants introduced during the manufacturing process or from suspension solution. Check the presence of these elements by analyzing areas of the support film close to the grain of interest. The use of deionized-distilled water can sometimes leach sodium and potassium from minerals such as albite and especially Na-rich sheet silicates. With these minerals, use tap water as the suspension fluid and check for sodium, chlorine, and calcium contamination on the support film.
- *Tripod polishing.* Tripod polishing is good for large mineral grains and their interfaces, but not fine-grained or loosely aggregated particles. Crystal bond adhesive is typically used to fix samples to the pedestal and this adhesive makes it difficult to thin small particles without loosening them.

Calibration of EDX detector. Although instrument manufacturers sell detectors with estimated efficiency parameters, it is highly recommended that empirical *k*-factors be determined for each detector. It is best to determine these *k*-factors for specific conditions (i.e., incident keV, pulse processing rate, peak integration width) using known mineral standards.

Sample geometry. Make sure the sample is tilted towards the detector during analysis, but not too high a tilt since this will increase the fluorescence of the support grid metal (e.g.,

EBSCOhost - printed on 2/13/2023 5:26 AM via . All use subject to https://www.ebsco.com/terms-of-use

Cu) by bremsstrahlung radiation. Make sure there is a clear path for X-rays to enter the EDX collimator. If not, this can cause subtle absorption of light relative to heavy X-rays. It is important to know, for a given image magnification, the direction in which the EDX detector lies. This can be accomplished by partially retracting the sample holder carefully and determining the tilt axis and tip direction of the holder. This should be determined for all magnifications since the image rotation often changes with magnification. When analyzing grain mounts, large particles and even support grid bars can occlude X-ray detection, therefore, take care to determine if you are on the detector side of the particle or grid for unobstructed X-ray collection.

Sample thickness. Quantitative AEM analyses require that the Cliff-Lorimer thin-film criteria (C-LTFC) be satisfied for all elements analyzed. This criterion has been stated as the thickness of the foil where absorption of any element is less than 3% (Williams and Carter 2009). A more practical criterion would be the thickness that the ratio of any two elements changes by less than 3%. This can be calculated or determined empirically through analyses along the foil wedge. Be aware that the thinnest C-LTFC will be for samples containing both light and heavy X-rays (e.g., sodium and iron). One tip to determine if there is absorption of low-energy X-rays, is to observe the slope of the background below 1 kV. This should continue to rise up to the cutoff of the lower-level discriminator setting value, or in some systems, the zero-strobe peak. Absorption corrections can be made in most commercial software packages if the thickness is known, although this is not trivial to measure.

An alternative method for correcting for samples thicker than the C-LTFC was proposed by van Cappellen and Doukhan (1994). This method uses the calculated cation to oxygen ratio to determine if electroneutrality is satisfied (i.e., if proper oxygen stoichiometry is met). An absorption correction is applied to balance cation and oxygen atom proportions. This method is not applicable if the valences of elements such as iron and manganese are not known.

The generation of STEM/EDX images present an interesting problem that the variation of sample thickness influences the intensity of an X-ray signal independently of compositional variation. This can lead to false conclusions of concentration variance where there is none or hide variations that exist. Figure 7 presents a case where the relative compositional constancy of an element (in this case oxygen) can be used to ratio with other elements and generate first order thickness-normalized images. Livi et al. (2008) investigated the occurrence of K- and Na-rich intergrowths in very low-grade prograde metamorphic white micas. They obtained low-dose STEM/EDX images of white mica flakes with the basal normal parallel to the electron beam. Although the flakes were relatively flat, some thickness variation existed which degraded the image quality and increased the difficulty of interpretation of intensity variations. They took advantage of the fact that O content was nearly identical in both the paragonite (Na) and muscovite (K) rich regions and normalized the Na and K X-ray intensity maps to the O map, in proxy for thickness. The O map clearly indicates where thickness changes are, and the improvement in image quality can been seen in the combined red (Na) and blue (K) image. By this processing, the unusual boundaries of the Na-K intergrowths in the lower right crystal can be discerned.

This type of "quick" thickness correction will break down when the thickness variation of the sample is more extreme. The best solution for thickness variation is to perform a full quantitative reduction of each spectrum at every pixel. This, first of all, is best done when the data is collected as a "spectrum" image that stores a full spectrum at every pixel. Then there has to be an estimate of the thickness at every pixel. For minerals with known stoichiometry, the method of van Cappellen and Doukhan (1994) could be used and the resultant image is a fully quantitative map. In some cases, the continuum background may be used as a reference image if sufficient counts are generated. Alternatively, the simultaneous EELS acquisition of the zero-loss and plasmon peaks could be used to estimate the thickness (Egerton 2011). In this method,

EBSCOhost - printed on 2/13/2023 5:26 AM via . All use subject to https://www.ebsco.com/terms-of-use

there has to be a balance between the need for high beam fluxes for good EDX statistics and low fluxes to ensure that the EELS detector is not damaged or saturated. In all of these methods, there is an increase in the variation of the element intensity due to the summation of errors in each map. As in any analytical method, it is a good idea to perform an error analysis to determine the initial count rate needed to distinguish the desired compositional contrast.

Besides the Cliff-Lorimer method, recently a new EDX quantitative method called the ζ (zeta)-factor approach has been developed which incorporates both the absorption correction and also the fluorescence correction (Williams and Carter 2009) and, in addition to estimating composition, provides a simultaneous determination of the specimen thickness. ζ-factors can be recorded from pure element standard thin films provided the beam current and hence the electron fluence during EDX acquisition is known.

Microscope operating conditions. The microscope conditions focus on establishing an electron fluence (electrons/nm^2) during which there is statistically no loss of elements due to volatilization or diffusion. It does not matter if the structure becomes altered or amorphous, as long as the chemical composition remains constant. However, structural alteration is often accompanied by compositional changes—especially when considering oxidation changes of transition elements (Livi et al. 2012). Fluence is a function of four parameters: 1) Beam current—which is set by the first condenser lens and the emission current (gun bias) in a conventional source TEM, and additionally by the gun lens setting and extraction voltage in a FEG; 2) Beam diameter—which is set by the second condenser lens or the particular lens settings for a scanning beam (microprobe or nanoprobe modes); 3) Analysis time—which should include the time to set up the acquisition (beam placement and computer setup and the scan rate during STEM analysis; 4) Microscope accelerating voltage (strictly this affects dose).

Time-series analyses should be used to determine the highest fluence possible to maximize precision and spatial resolution before loss of any element occurs. Fluence in the STEM is often varied by the scan rate of the beam. However, areas scans in STEM are often achieved by not only scanning quickly over the area displayed on the computer or CRT, but also include two dwell positions outside the view area. In order to reduce distortions in scanned images, two reference positions are established: one just outside the initial corner of the image and one at the starting point of each scanned line. X-rays generated from these reference points are included in the acquired spectrum and are disproportionally counted. Since they are analyzed at greater fluences than the viewed area, they may experience greater beam damage and bias the integrated area analysis.

Fluence in conventional TEM mode is varied by beam diameter and shape. In cases where analyses of linear features are required (a thin edge, elongated precipitate, or an interface), the condenser lens stigmation can be set to elongate the beam parallel to that feature. This lowers the fluence and maintains spatial resolution in one direction without loss of X-ray production. An alternative could be to move the beam along a feature of interest during X-ray collection.

A special case for clay minerals occurs due to their thin sheet morphology in grain mounts. This produces thin areas for analysis, but elements like sodium and potassium can diffuse during condensed beam analysis. To mitigate this, it is recommended to spread the beam (in CTEM mode) such that it extends to just larger than the sheet. Sodium and potassium will diffuse within the grain, but there will be less volatilization.

Adhering to these protocols will help ensure the acquisition of high-quality EDX analyses. The evaluation of the accuracy of analyses may sometimes be achieved through calculation of mineral formulae and determination if site occupancies are reasonable. However, the possibility of mixed valence elements, vacancies, missing species from the analyses (e.g., H_2O, CO_2, lithium, beryllium and boron) and non-stoichiometry render mineral formulae inaccurate.

EBSCOhost - printed on 2/13/2023 5:26 AM via . All use subject to https://www.ebsco.com/terms-of-use

EELS

As discussed previously, Electron Energy-Loss Spectroscopy (EELS) in a S/TEM involves analysis of the inelastic scattering suffered by the transmitted electron beam (Brydson 2001; Egerton 2011). Measurement of the transmitted electron-energy distribution is achieved by dispersing the electrons according to their kinetic energy (and hence energy loss during passage through the sample) using an electron spectrometer most usually based on a magnetic field normal to the electron beam, as shown in Figure 1. The electron energy loss spectrum is almost exclusively recorded in parallel using a scintillator optically coupled to either a one- or two-dimensional photodiode array detection system. This produces a spectrum consisting of typically 1000 channels or pixels. The dispersion of the spectrometer may be varied so that different spectral energy ranges can be made incident on the detector, typically varying from about 100 eV to up to 2000 eV wide. In practice owing to the large dynamic range in the EEL spectrum (up to 10^8), a whole EEL spectrum is nearly always recorded in separate energy portions by applying an offset voltage to a drift tube through which the electrons travel during their passage through the dispersing magnetic field. This shifts the spectrum across the detector and each individual spectral section needs to be energy calibrated using either an accurate drift tube voltage applied to shift a known feature such as the intense zero loss peak, or the known energy of a reference feature within a particular spectral region (such as the carbon K-edge onset).

The various inelastic scattering processes outlined above each provides valuable information on the sample area that is irradiated by the electron probe. The technique can provide high-resolution elemental analysis and mapping as well as a means of determining the local electronic structure, in crude terms the local chemical bonding. These are discussed in more detail in subsequent sections.

Practical EELS acquisition and general features in the EEL spectrum. Practically, there are two main ways to operate the microscope when recording EEL spectra:

1. Operate in STEM mode with the electron probe focused onto the specimen with a semi-angle of convergence (α) typically in the range 2-15 mrad (see Fig. 2). The area irradiated by the probe effectively determines the spatial resolution for analysis. The highly forward peaked EELS signal is collected over a semi-angle (β) defined by the spectrometer entrance aperture (SEA) and the camera length (effectively the magnification of the diffraction pattern) or alternatively, in a dedicated STEM, a post-specimen collector aperture may be employed to define β. In general, for efficient signal collection, the collection semi-angle should be chosen so as to be significantly larger than the convergence semi-angle.
2. Operate in TEM diffraction mode with a near parallel beam and the selected area diffraction (SAED) aperture effectively defining the area of analysis (typically ranging from 150 nm to a few microns in diameter); in this mode, both the camera length of the diffraction pattern and the SEA define the collection semi-angle (β). Here the collection semi-angle should be chosen so as to efficiently collect as many inelastically scattered electrons as possible so as to give a good signal to noise ratio while not inducing a large background contribution to the spectrum; typically this would be a value in the range 5-15 mrad at 200 keV incident beam energy.

Additionally please note that in energy filtered TEM (see later) the microscope is operated in TEM image mode.

As mentioned above, spectra are most often recorded using a scintillator and a two-dimensional array of a CCD, identical to that used for the digital recording of TEM images. These systems rely on the measurable discharge (over a certain integration time) of a large array

EBSCOhost - printed on 2/13/2023 5:26 AM via . All use subject to https://www.ebsco.com/terms-of-use

of self-scanning, cooled silicon diodes by photons created by the direct electron irradiation of a suitable scintillator. This spectral signal is superimposed on that due to thermal leakage currents as well as inherent electronic noise from each individual diode and together these are known as dark current that can be subtracted from the measured spectrum; gain variations and cross-talk between individual diode elements can also be measured and corrected for following spectrum acquisition.

Once recorded and pre-processed, the various energy losses observed in a typical EEL spectrum are shown schematically in Figure 8A, which displays the scattered electron intensity as a function of the decrease in kinetic energy (the energy loss, E) of the transmitted fast electrons. This represents the response of the electrons in the solid to the electromagnetic disturbance introduced by the incident electrons. As noted previously, the intensity at 2000 eV energy loss is typically eight orders of magnitude less than that at the zero-loss peak and therefore, for clarity, in Figure 8A a gain change has been inserted in the linear intensity scale at 150 eV. In a specimen of thickness less than the mean free path for inelastic scattering (roughly 100 nm at 100 keV), by far the most intense feature in the spectrum is the zero-loss

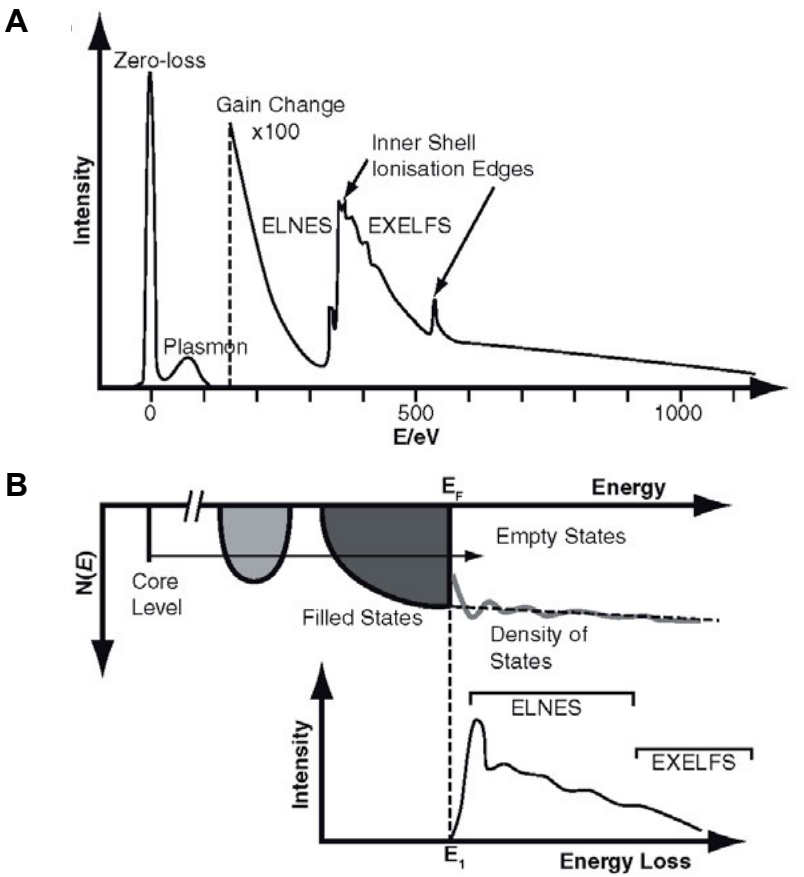


Figure 8. Schematic diagram of (A) a general EEL spectrum (with a linear intensity scale and a gain change at ca. 150 eV) showing all of the observable features and (B) an enlarged version the (background-subtracted) ELNES intensity indicating how it reflects transitions from atomic core levels to the unoccupied DOS above the Fermi level (after Brydson 2001, 2011).

EBSCOhost - printed on 2/13/2023 5:26 AM via . All use subject to https://www.ebsco.com/terms-of-use

peak at 0 eV energy loss that contains all the elastically and quasi-elastically (i.e., vibrational- or phonon-) scattered electron components. Neglecting the effect of the spectrometer and detection system, the Full Width Half-Maximum (FHWM) of the zero-loss peak is usually limited by the energy spread inherent in the electron source. In a TEM, the energy spread will generally lie between 0.3-3 eV, depending on the type of emitter (cold field emission < Schottky < LaB_6 thermionic < tungsten thermionic emitter), and this parameter often determines the overall spectral energy resolution. In recent years, the use of electron monochromators has improved achievable spectral energy resolutions to 0.1 eV or less, generally at the expense of probe current.

The low-loss region of the EEL spectrum, extending from 0 to about 50 eV, corresponds to the excitation of electrons in the outermost atomic orbitals that are delocalized in a solid due to interatomic bonding and may extend over several atomic sites. This region therefore reflects the solid-state character of the sample. The smallest energy losses (10-100 meV) arise from phonon excitation, but these are usually subsumed in the zero-loss peak. The dominant feature in the low-loss spectrum arises from collective, resonant plasmon oscillations of the valence electrons. The energy of the plasmon peak is governed by the density of the valence electrons, and its width by the rate of decay of this resonant mode. In a thicker specimen (> 100 nm) there are additional (harmonic) peaks at multiples of the plasmon energy, corresponding to the excitation of more than one plasmon; the intensities of these multiple Plasmon peaks follow a Poisson statistical distribution. A further feature in the low-loss spectra of insulators are peaks, known as interband transitions, which correspond to the excitation of single valence electrons to low-energy unoccupied electronic states above the Fermi level. Besides more detailed analysis, the low-loss region can be used to determine the relative (or absolute) specimen thickness and to correct for the effects of plural inelastic scattering when performing quantitative microanalysis on thicker specimens (see ahead).

Correspondingly, the high-loss region of the EEL spectrum extends from about 50 eV to several thousand electron volts and corresponds to the excitation of electrons from localized orbitals on a single atomic site to extended, unoccupied electron energy levels just above the Fermi level of the material (Fig. 8B). This region therefore more reflects the atomic character of the specimen. As the energy loss progressively increases, this region exhibits steps or edges superimposed on the monotonically decreasing background intensity that usually follows an inverse power law, $I = AE^{-r}$. These edges correspond to excitation of inner-shell electrons and are therefore known as ionization edges. The various EELS ionization edges are classified using the standard spectroscopic notation similar to that employed for labeling X-ray emission peaks; e.g., K excitation for ionization of 1s electrons, L_1 for 2s, L_2 for $2p_{1/2}$, L_3 for $2p_{3/2}$ and M_1 for 3s, etc. The subscript, in for example $2p_{1/2}$, refers to the total angular momentum quantum number, j, of the electron that is equal to the orbital angular momentum, l, plus the spin quantum number, s, which can couple either positively or negatively.

Practical EELS quantification. Since the energy of the ionization edge threshold is determined by the binding energy of the particular electron subshell within an atom—a characteristic value, the atomic type may be easily identified with reference to a tabulated database. The signal under the ionization edge extends beyond the threshold, since the amount of kinetic energy given to the excited electron is not fixed. The intensity or area under the edge is proportional to the number of atoms present, scaled by the cross section for the particular ionization process, and hence this allows the technique to be used for *quantitative analysis*. EELS is particularly sensitive to the detection and quantification of light elements ($Z < 11$) as well as transition metals and rare earths.

Problems can arise if the sample thickness is greater than the mean free path for inelastic scattering, in this case plural inelastic scattering (i.e., a few such inelastic scattering events) will occur. This will significantly increase the low loss Plasmon intensities, leading to an increase in

EBSCOhost - printed on 2/13/2023 5:26 AM via . All use subject to https://www.ebsco.com/terms-of-use

the background contribution making it difficult to identify the presence of edges in a spectrum. A further effect of plural inelastic scattering is the transfer of intensity away from the edge threshold towards higher energy losses due to the increase of double scattering events involving a plasmon excitation followed by an ionization event or vice versa. It is possible to remove this plural inelastic scattering contribution (at the expense of some added noise) from either the whole EEL spectrum or a particular spectral region by Fourier transform deconvolution techniques. Two techniques are routinely employed, one, known as the Fourier-log method, requires the whole spectrum over the whole dynamic range as input data. This large signal dynamic range can be a problem with data recorded in parallel. The second, known as the Fourier-ratio method, requires a spectrum containing the feature of interest (i.e., an ionization edge) that has had the preceding spectral background removed. A second spectrum containing the low-loss region from the same specimen area is then used to deconvolute the ionization edge spectrum.

After some initial data processing, such as dark-current subtraction, gain correction (which are both a function of the response of the detection system outlined previously) and also possibly deconvolution to remove the effects of multiple inelastic scattering in thicker specimen regions, in order to quantify the elemental analysis it is necessary to measure the intensities under the various edges. This is achieved by fitting a background (in many cases a power law, $I = AE^{-r}$, where A is a constant, r the inverse power law exponent and E the energy loss) to the spectrum immediately before the edge. This is then subtracted (Fig. 9A) and the intensity is measured in an energy window, Δ, which begins at the edge threshold and usually extends some 50 to 100 eV above the edge. The next step is to compute the inelastic partial cross section, σ, for the particular inner-shell scattering event under the appropriate experimental conditions, i.e., $\sigma(\alpha, \beta, \Delta, E_o)$, where the bracketed terms simply represent the variables on which the partial cross section depends. This partial cross section is calculated for the case of a free atom using simple hydrogenic or Hartree–Fock–Slater wavefunctions and is generally an integral part of the analysis software package. The measured edge intensity is normalized (i.e., divided) by the partial cross section so that either different edge intensities can be compared (Fig. 9B,C), or the intensity can be directly interpreted in terms of an atomic concentration within the specimen volume irradiated by the electron probe. For the latter case, the measured edge intensity is divided by both the partial cross section and the combined zero loss and low loss intensity measured over the same energy window, Δ; the result is usually expressed in terms of an areal density in atoms/nm^2 multiplied by the specimen thickness (Pan et al. 2008, 2009).

An example of relative EELS elemental quantification on minerals is provided in Figure 18 and also Engel et al. (1988). Apart from the case of light elements as well as many of the transition metal and rare earth elements, detection limits for EELS are generally worse than those for EDX and typically lie between 0.1 and 1 at%. This is principally due to the limited spectral range of the technique relative to EDX as well as the steep and intense background signal upon which the ionization signal lies. Meanwhile, analytical accuracies in elemental quantification usually lie in the range 5-10%.

EEL SPECTROMETRY

EEL low-loss spectroscopy

The low-loss region of the EEL spectrum provides a high signal intensity, which is often recorded as one spectral region containing the zero loss peak, or, alternatively, the zero loss is displaced off the detector to increase the SNR. The low loss is dominated by the bulk plasmon excitation, which may be thought of as a resonant collective oscillation of the valence electron gas of the solid (as pictured in the Drude-Lorentz model for metals) stimulated by the fast incident electron. Employing the free-electron model of solids, which works surprisingly well for a range of elements and compounds including minerals, the bulk plasmon energy, E_p, is

EBSCOhost - printed on 2/13/2023 5:26 AM via . All use subject to https://www.ebsco.com/terms-of-use

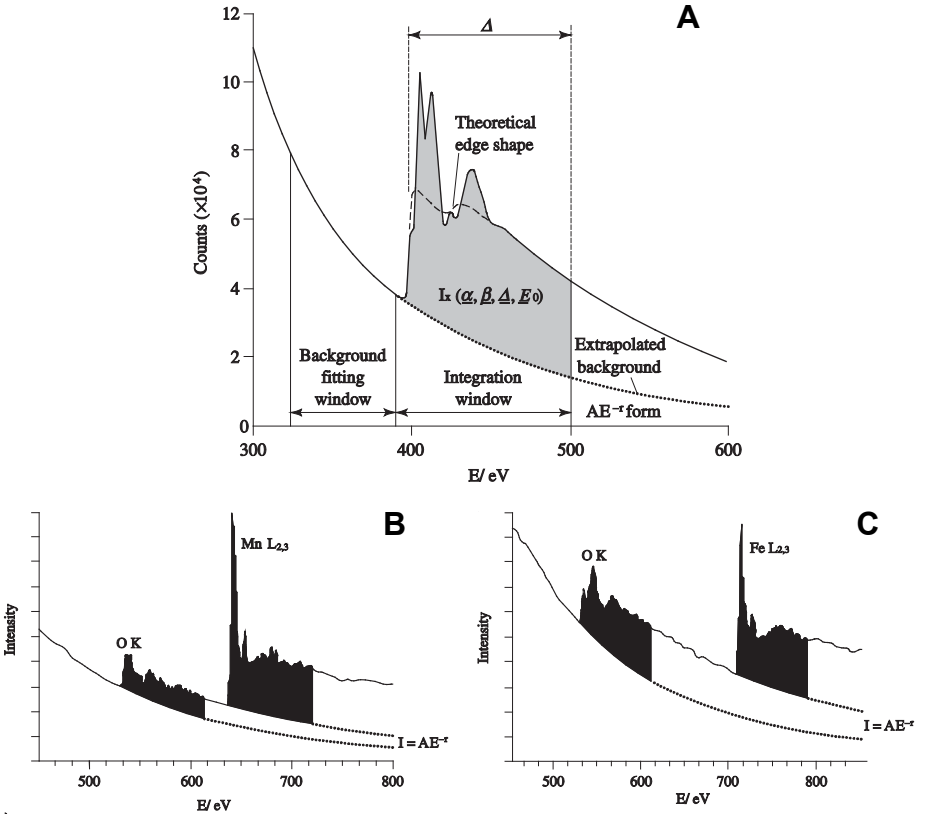


Figure 9. Diagram showing the details of EELS quantification procedures (after Brydson 2001). (A) The nitrogen *K*-edge from thin sample of boron nitride with a power law background fitted in a window prior to the edge and extrapolated over a window of width, Δ, under the edge. Also shown is a theoretical N *K*-edge cross-section calculated using the Hydrogenic model after convolution with the low loss region of the spectrum to simulate the effects of multiple inelastic scattering. EEL spectra of (B) MnO and (C) α-Fe_2O_3. In both cases fitted power law ($I = AE^{-r}$) backgrounds are indicated by dotted lines. The shaded areas extend for an energy window, Δ = 80 eV, above each edge threshold and are used to quantify the elemental analysis as described in the text.

predicted to be proportional to the square root of the valence electron density. Free-electron metals, such as aluminum, show very sharp plasmons, while in minerals, which are generally insulators and semiconductors, the plasmon peak is considerably broader since the valence electrons are damped by scattering with the ion-core lattice. The sensitivity of the plasmon peak position to changes in valence-electron density, potentially allows any chemical or structural rearrangements in, for example, different microstructural phases or changes in the degree of ordering to be detected as shifts in this plasmon energy. For example, the plasmon energy of graphitizing carbons (see Fig. 10A) correlates well to the long-range structural order (graphitic character and sp^2 carbon content) and density of the specimens, which in turn is a function of their thermal history (Daniels et al. 2007). See Figure 13 for a selection of low loss spectra.

In addition to plasmon oscillations, the low-loss region may also exhibit interband transitions, i.e., single electron transitions from the valence band to unoccupied states in the conduction band, which appear as peaks superimposed on the main plasmon peak (see Fig. 10A). If a mineral is an insulator and possesses a bandgap there should be no interband

EBSCOhost - printed on 2/13/2023 5:26 AM via . All use subject to https://www.ebsco.com/terms-of-use

transitions below the bandgap energy and thus, once the zero loss peak has been modeled, extrapolated and removed from the rest of the spectrum, it is possible to extract the bandgap associated with an initial rise in intensity in the low-loss region, as seen in Figure 10B-D for the case of diamond.

A full analysis of the low-loss region is based upon the extraction of the dielectric function, ε, of the material. This is a complex quantity, which represents the response of the entire solid to the disturbance created by the incident electron. The same response function describes the interaction of photons with a solid and this means that energy-loss data may be correlated with the results of optical measurements in the visible and UV regions of the electromagnetic spectrum, including quantities such as refractive index, absorption and reflection coefficients.

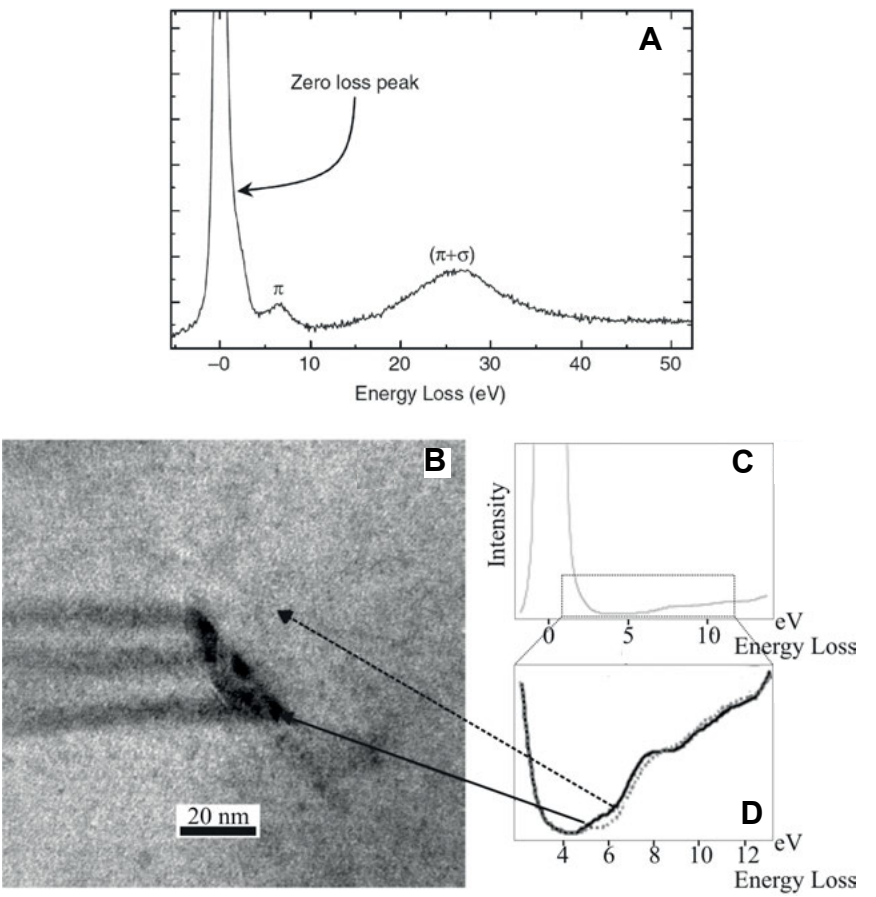


Figure 10. (A) The EELS low loss region of a partially graphitic carbon. The feature at 6.5 eV arises from an interband transition between the π bonding and π* antibonding orbitals. The bulk valence plasmon (at ca. 26 eV) arises from a collective oscillation of the valence electrons. (B) STEM BF image of a stacking fault arrangement in CVD single crystalline diamond comprising of primary and secondary faults. (C) EEL spectra taken at locations of the arrows, i.e., in the perfect crystal (grey) and near the stacking fault (black). The difference can be seen more clearly in the expanded view in (D) where enhancement in the joint density of states in the vicinity of the partial dislocations bounding the stacking fault occurs due to energy states below the conduction band edge (~5.5 eV) and due to contribution of sp^2 bonding (~7 eV). See Bangert et al. (2005) for further details.

EBSCOhost - printed on 2/13/2023 5:26 AM via . All use subject to https://www.ebsco.com/terms-of-use

EELS core-loss fine structure

For solids, the change in the cross section for inner-shell ionization as a function of energy loss (known as the energy differential cross section) and therefore the detailed shape of the ionization edge is not in fact solely that due to an isolated atom (as is assumed in the basic EELS quantification process). In reality it is proportional to a site- and symmetry-projection of the unoccupied density of electron energy states (DOS). Since the exact form of both the occupied and unoccupied DOS will be appreciably modified by the presence of bonding between atoms in the solid, this will therefore be reflected in the detailed ionization edge fine structure known as electron loss near-edge structure (ELNES) (Ahn 2004).

In many cases it is found that, for a particular elemental ionization edge, the observed ELNES exhibits a structure that, principally, is specific to the arrangement, i.e., the number of atoms and their geometry, as well as the type of atoms solely within the first coordination shell (Brydson et al. 1988, 1989). This occurs whenever the local DOS of the solid is dominated by atomic interactions within a molecular unit and is particularly true in many non-metallic systems such as semiconducting or insulating minerals where we can often envisage the energy band structure as arising from the broadened molecular orbital levels of a giant molecule. If this is the case, we then have a means of qualitatively determining nearest-neighbor coordinations using characteristic ELNES shapes known as coordination fingerprints. This is similar to the use of near-edge structure (XANES or NEXAFS) in the analogous (though less spatially resolved) technique of X-ray absorption spectroscopy (XAS) (de Groot and Kotani 2008, see also Fig. 16). A wide range of cations (e.g., aluminum, silicon, magnesium, various transition metals, etc.) in different coordinations and anion units (e.g., borate, boride, carbonate, carbide, sulfate, sulfide, nitrate, nitride, etc.) in inorganic solids show this behavior that can be of great use in phase identification and local structure determination (see Fig. 11A; and also see review by Drummond-Brydson et al. (2004) in Ahn (2004)).

For certain edges, as well as for certain compounds, the concept of a local coordination fingerprint breaks down. In these cases, the unoccupied DOS cannot be simply described on such a local level and ELNES features are found to depend critically on the arrangement of the atoms in outer-lying coordination shells allowing medium-range structure determination. This opens up possibilities for the differentiation between different structural polymorphs, the characterization of the structure of localized defects, intergrowths or interfaces as well as the accurate determination of lattice parameters, vacancy concentrations and substitutional site occupancies in complex structures (Scott et al. 2001).

Using density functional band structure calculations (or their equivalents) it is possible to model the unoccupied DOS and compare this directly with measured ELNES (see Fig. 11). The calculated electron energy bands need to be integrated into a density of electronic states which need to be resolved into a site projection in the unit cell for the atom undergoing ionization and also an angular momentum symmetry projection for the exact final states which are accessed by the excited electron under the dipole selection rule (which states that the change in orbital angular momentum, Δl, between the initial and final states of the transition is ± 1). Currently a number of different approaches are commonly used, among which are: WIEN2K (*http://www.wien2k.at*; Schwarz et al. 2002); CaSTEP (*http://www.castep.org/*; Clark et al. 2005); FEFF (*http://leonardo.phys.washington.edu/feff/*; Ankudinov et al. 1998), all of which now have specific modules to enable output of EELS spectra. Wien2k is what is known as an all electron code and expands the electron wavefunctions as plane waves, whereas CaSTEP is a pseudopotential code, approximating tightly bound inner core levels as part of the potential term so allowing more complex systems to be handled. Both codes perform calculations in reciprocal space and thus require a periodic system (i.e., a unit cell). Meanwhile FEFF calculates electronic states by considering multiple (elastic) scattering (MS)

EBSCOhost - printed on 2/13/2023 5:26 AM via . All use subject to https://www.ebsco.com/terms-of-use

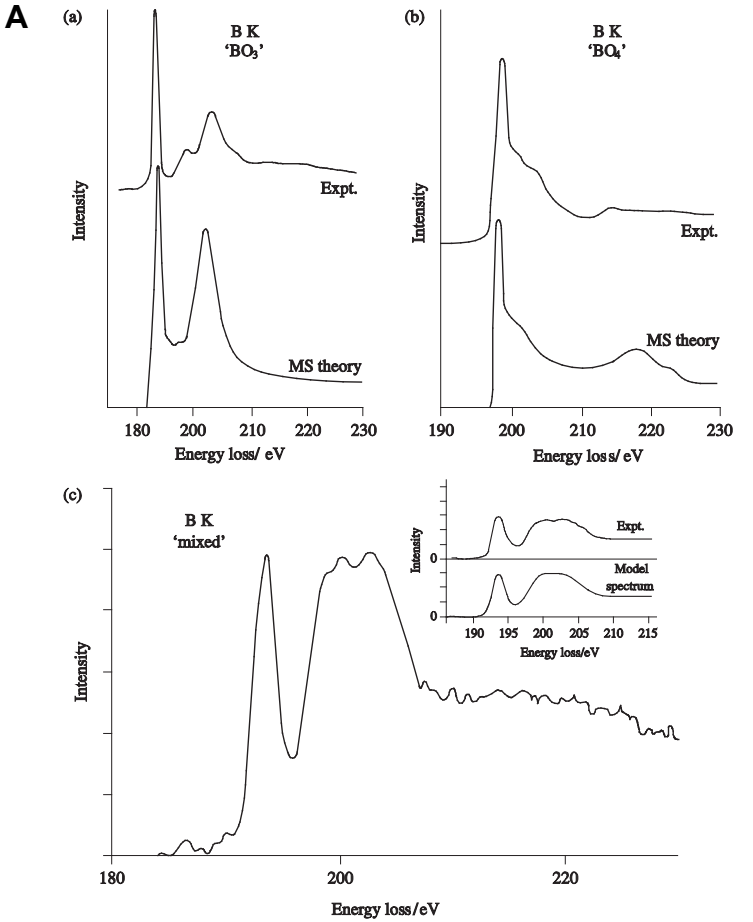


Figure 11. (A) An example of ELNES coordination fingerprinting after Sauer et al. (1993). A comparison of the B K-ELNES from: (a) the mineral vonsenite containing trigonal planar BO_3 groups; (b) the mineral rhodizite containing tetrahedral BO_4 groups and (c) a mixed coordination boron-doped Fe,Cr oxide. In (a) and (b) the experiment (*Expt.*) is compared to the results of single shell MS calculations (*MS Theory*) indicating the existence of trigonal and tetrahedral B K-ELNES coordination fingerprints. Inset in (c), the experimental data has been modeled using a linear combination the B K-coordination fingerprints in the ratio 3:1 (trigonal: tetrahedral).
figure continued on next page

of the excited electron with a real space cluster, which more easily allows the study of non-periodic structures.

As well as determining coordinations, ELNES can be used for the spatially resolved determination of the formal valency or oxidation state of elements in minerals (see Fig. 11B). The valence state of the atom undergoing excitation influences the ELNES in two distinct ways. Firstly, changes in the effective charge on an atom lead to shifts in the binding energies of the various electronic energy levels (both the initial core level and the final state) that often manifest as an overall chemical shift of the edge onset. Secondly, the valence of the excited atom can affect the intensity distribution in the ELNES. This predominantly occurs in edges that exhibit considerable overlap between the initial and final states and hence a strong interaction between the core hole and the excited electron leading to the presence of

EBSCOhost - printed on 2/13/2023 5:26 AM via . All use subject to https://www.ebsco.com/terms-of-use

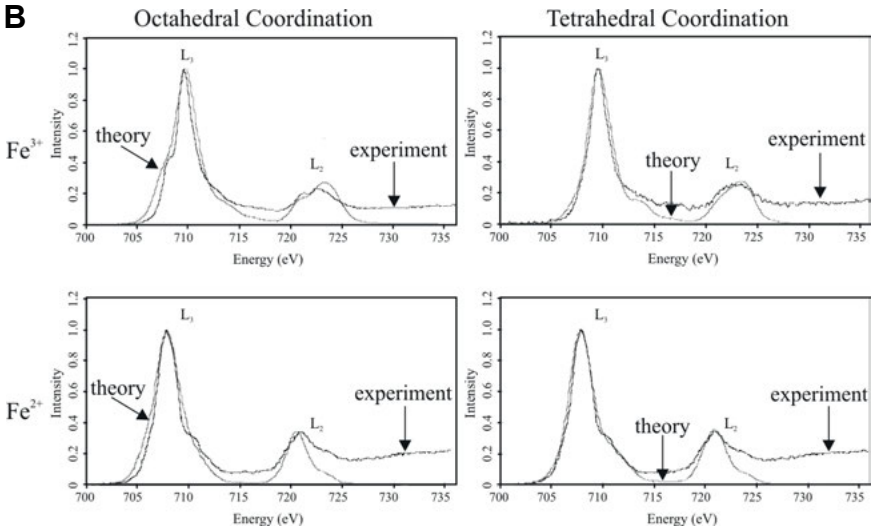


Figure 11. ***continued from previous page.*** (B) An example of ELNES valence state fingerprinting (see Calvert et al. 2005). Fe $L_{2,3}$-edges from the minerals hematite and orthoclase (containing Fe^{3+} in octahedral and tetrahedral coordination respectively), and hedenbergite and hercyanite (both containing Fe^{2+} in octahedral and tetrahedral coordination respectively); the blue curves are the experimental EELS results while the green curves are the results of theoretical modeling using atomic multiplet theory (Brydson 2001; Ahn 2004). Note the shift to higher energy (from 707.5 eV to 709.5 eV) with increasing oxidation state of Fe. Theoretical data calculated by Derek Revill and Andrew Scott, University of Leeds.

quasiatomic transitions (so called since the observed ELNES is essentially atomic in nature and only partially modified by the crystal field due to the nearest-neighbor atoms). Examples of such spectra are provided by the $L_{2,3}$-edges of the 3*d* and 4*d* transition metals and their compounds and the $M_{4,5}$- edges of the rare-earth elements. These spectra exhibit very strong, sharp features known as white lines, which result from transitions to energetically narrow d or f bands. This makes detection and quantification of these elements extremely easy. Rather than using band structure calculations, such spectra are more appropriately modeled using atomic multiplet theory, in the presence of a crystal field of a particular ligand field symmetry. As an example, Figure 14 shows the $L_{2,3}$-edges from a number of manganese minerals, containing manganese in either the +IV, +III or +II oxidation state. Transitions from the Mn 2*p* shell are actually split into two components separated by the spin orbit splitting of the ionized 2*p* core level: an L_3-edge followed at higher energy loss by a broader L_2-edge. It is clear that both the L_3- and L_2-edges exhibit a chemical shift to higher energy loss with increasing manganese valence (this remains true when elemental manganese is also considered). Additionally, the relative intensities in the two separate white line components also clearly depend on the valence of the excited atom thus leading to the possibility of oxidation-state identification in an unknown sample. A mineralogical example of this type of analysis is provided by the study of chromium valence in hydrogarnets (Hiller et al. 2007).

Finally, EELS may be used to extract local structural information such as the length of chemical bonds. There are two approaches to bond-length determination: the first is to analyze the weak oscillations occurring ~40-50 eV above the edge onset known as extended energy loss fine structure (EXELFS—the electron equivalent of EXAFS in XAS). Since these oscillations are weak, high statistical accuracy (i.e., high count rates and long acquisition times) is required if useful information is to be extracted. The second procedure employs the energy position of

EBSCOhost - printed on 2/13/2023 5:26 AM via . All use subject to https://www.ebsco.com/terms-of-use

the broad ELNES peaks some 20-30 eV above the edge onset, known as multiple scattering resonances (MSR). As their name suggests, these features arise from a resonant scattering event involving the excited electron and a particular shell of atoms. The energies of these features above the edge onset have been shown to be proportional to $1/R^2$, where R is the bond length from the ionized atom. Identification of such MSR permits a semi-quantitative determination of nearest neighbor, and in some cases second nearest neighbor bond lengths (Kurata et al. 1993; see also Daniels et al. 2007).

EDX AND EELS IMAGING

As mentioned at the beginning of this chapter, besides simple analysis using a focused probe in say CTEM, using STEM it is possible to raster the electron probe across the specimen and record an EDX or EEL spectrum at every specimen pixel (x,y)—this technique being generally termed "Spectrum Imaging." The complete dataset may then be processed (either off- or increasingly on-line) to form a quantitative one dimensional line scan or two dimensional map of the sample using either standard elemental quantification procedures for elemental composition using either EDX (see for example Figs. 7 and 20) or EELS outlined previously. Alternatively the position and/or intensity of characteristic low loss or ELNES features may be used so as to obtain line scans or maps related to variations in chemical bonding (Egerton 2011).

Processing of any series of EDX or EELS line scans or maps may be done using a number of techniques including the construction of simple scatter plots and identification of data clusters or employing more detailed multivariate statistical analysis (MSA) methods to determine the significant principal components. Such methods can be used to highlight distinct chemical phases within a sample region either in terms of elemental concentrations (EDX or EELS), or even local coordinations or valence states of particular elements (EELS). MSA can also be used to identify the principal components identified as noise which can then be removed so as to regenerate a noise-reduced dataset (Egerton 2011). This processed dataset can improve element detectability and quantification as well as identification of changes in ELNES as a function of spatial coordinate. More recent developments in STEM spectrum imaging involve fully computerized beam control and beam blanking which allows complex, discontinuous areas in a microstructure to be scanned during the acquisition of a spectrum image (Sader et al. 2010).

Subject to the constraints of radiation damage, the inherent high spatial resolution of the EEL spectrum imaging technique has allowed maps of elemental distributions to be formed at sub-nanometer and even atomic resolution (Bosman et al. 2007). This is because EELS employs an aperture before the spectrometer and detector, which defines the collection angle (β) and can therefore be used to limit the region of the beam-broadened volume contributing to the recorded spectrum. Future developments will include the more routine production of atomic resolution chemical maps using variations in ELNES. Recently the possibility of near atomic resolution EDX maps has also been demonstrated (Watanabe 2009), despite the inherent problems of probe broadening in the specimen.

Finally, STEM/EELS spectrum imaging is directly comparable to direct energy filtered imaging in the CTEM (EFTEM). EFTEM involves the selection of specific energy loss electrons, or narrow range of energy losses (''an energy window''—typically between a few eV and a few tens of eV) from the transmitted electron beam via the insertion of an energy selecting slit after the EEL spectrometer (see Fig. 12 and see also Ahn 2004). This energy filter is then combined with subsequent image-forming optics. The spectrometer and post-spectrometer image-forming system may form part of a post column imaging filter or the microscope system may employ an in-column design with the EEL spectrometer and slit placed between the objective and projector lenses. Generally, EFTEM is better suited to mapping from larger fields of view with relatively short acquisition times than STEM/EEL spectrum imaging. The spatial resolution of EFTEM

EBSCOhost - printed on 2/13/2023 5:26 AM via . All use subject to https://www.ebsco.com/terms-of-use

is limited to about 1 nm or so which is poorer than that of EEL spectrum imaging, particularly since the development of aberration corrected probes.

Using only zero loss (elastically) scattered electrons to form EFTEM images and diffraction patterns increases contrast and resolution, allowing easier interpretation than with unfiltered data (see Fig. 12). Chemical mapping may be achieved by acquiring and processing images formed by electrons that have undergone either a specific low energy loss event (such as an interband transition or a plasmon event) or an inner-shell ionization event, using either the whole ionization edge or a specific ELNES feature indicative of a certain bonding characteristic. For the mapping of elemental distributions using EFTEM, two approaches are commonly employed:

1. jump-ratio mapping employs two energy windows and hence energy-filtered images, one positioned just before the ionization edge and one positioned just after the edge; the post-edge image is divided by a pre-edge image to produce a semi-quantitative map of the elemental distribution that is sensitive to small concentrations and is relatively free of noise and also diffraction contrast present in crystalline materials.

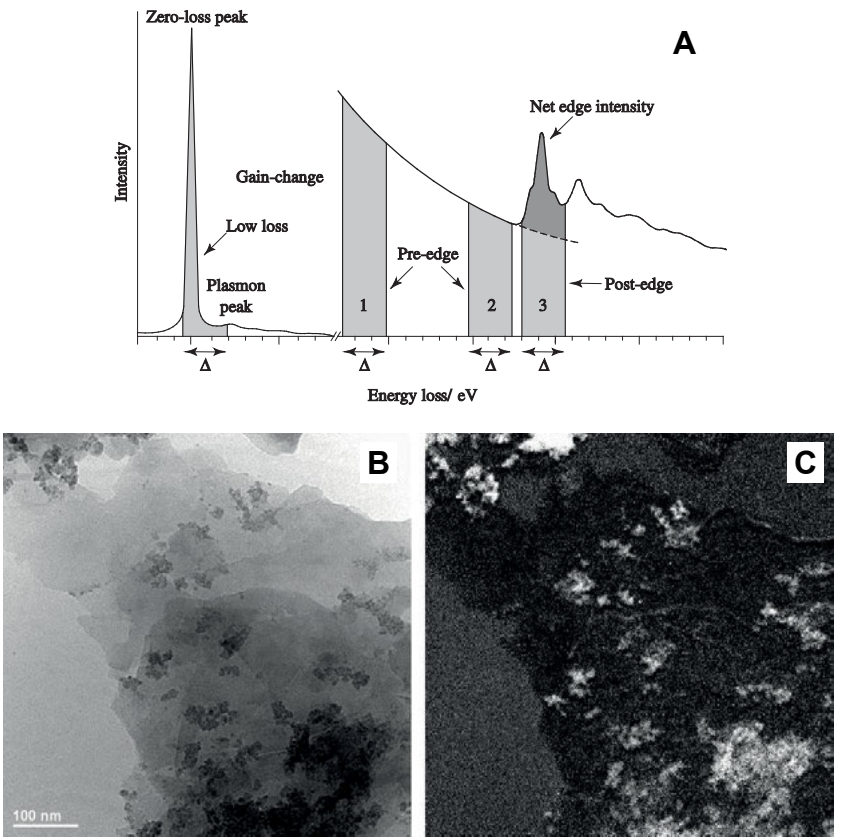


Figure 12. (A) Schematic diagram of EEL spectrum showing possible energy windows, of width Δ, used for energy filtered TEM imaging and mapping, (B) TEM bright field image and (C) corresponding Fe $L_{2,3}$-edge energy filtered EELS elemental (three window) map of a glacial sediment showing iron-rich nanoparticles (iron oxyhydroxides) on larger clay particles (from Raiswell et al. 2006).

EBSCOhost - printed on 2/13/2023 5:26 AM via . All use subject to https://www.ebsco.com/terms-of-use

2. true, quantitative elemental mapping (see Fig. 12C; Raiswell et al. 2006), where image intensity is proportional to concentration) usually employs three energy windows, two pre-edge windows and a post edge window; the two pre-edge images are used to extrapolate the background contribution to the post-edge image and this extrapolated background image is then subtracted from the post-edge image to produce a quantitative elemental map where image intensity is directly related to areal density.

Below we outline a practical application of TEM/EELS in mineralogical research.

EXAMPLE OF THE PRACTICAL APPLICATION OF EELS: EELS OF MANGANESE IN MINERALS AND ENVIRONMENTAL HEALTH

Introduction

Manganese is a 3*d* transition metal (TM) with the electron configuration [Ar]$4s^2 3d^5$. The partially-filled *d*-shells control the oxidation state of manganese which can exist in the formal oxidation states between 0 and +VII. In natural systems, manganese exists in the +II, +III and +IV valence states, often in multivalent minerals. In reduced igneous and metamorphic environments, manganese is most commonly +II and +III in solid solution with other transition elements in oxides, silicates and carbonates. Reviews of manganese occurrences in economically important deposits can be found in Huebner (1976), Roy (1968) and Hewett and Fleischer (1960). In more surficial environments, manganese is dominated by +III and +IV bearing oxides, but still may contain +II impurities. Manganese-oxides are found in mixtures of nanosized phases in various degrees of crystalline perfection in a wide variety of oceanic and terrestrial environments, such as soils, ocean floors, fresh-water sediments, and deserts. An important fraction of Manganese-oxides under oxic conditions may have formed from oxidation of Mn(II) by O_2 via microbially-mediated processes.

Although manganese-oxide minerals in the environment are generally far less abundant than other minerals, such as iron-oxides, the importance of manganese-oxides in controlling environmental chemical processes is not in accordance with their abundance (Post 1999). An important aspect of manganese-oxides is their capability to oxidize a wide variety of redox-active chemical species including many inorganic or organic contaminants in the environment, such as pharmaceuticals, metals and metalloids (Murray and Dillard 1979; Oscarson et al. 1981; Manceau et al. 1997; Fredrickson et al. 2002). The oxidation reactions can significantly impact the toxicity, bioavailability and mobility of the contaminants. Augmenting the high redox potential and extraordinary sorption properties is the high surface area of manganese oxides with nanoparticulate size. These characteristics make manganese-oxides one of the most important components of the aquatic and terrestrial ecosystems. An excellent review of the types and structures of manganese oxides in deposits and the environment can be found in Post (1999).

Analytical considerations for EELS determination of manganese valence

Manganese presents analytical considerations similar to its periodic table neighbors. Like other TM elements, manganese transitions accessible to EELS analysis include the *L* and *M* ionization edges. As with all the TM elements, the L_3/L_2 white-line transition ratio of Mn deviates from the expected value of 2 (Leapman and Grunes 1980). These deviations may be used to determine information about the coordination number and formal valence state. Unlike iron, which has only two valence states, manganese has the three common states listed above. However, the simultaneous coexistence of all three states has yet to be quantitatively addressed through EELS and current studies have only dealt with Mn(II)/Mn(III) and Mn(III)/Mn(IV) combinations.

EBSCOhost - printed on 2/13/2023 5:26 AM via . All use subject to https://www.ebsco.com/terms-of-use

Near edge structure of Mn $M_{2,3}$-edge

Little quantitative work has been done on the $M_{2,3}$ transitions of manganese. Early work was initiated by Rask et al. (1987) and Hofer and Wilhem (1993). Figure 13 illustrates the changes in the near-edge structure of the $M_{2,3}$ edge at about 50 eV for different valence states. They follow similar trends of iron (van Aken et al. 1999) in that the pre-peak intensity, position and ratio with the main peak is a function of oxidation state. Mansot et al. (1994) correlated the energy of both the maxima and the inflection point of the $M_{2,3}$ edge pre-peak. They were able to reproduce the mean valence value of manganese oxybromides within 4% relative error using these features.

The advantage of using the M edge relative to the Mn $L_{2,3}$ edge is that the M edge is more intense and the nearby zero-loss peak acts as a precise internal energy calibration. The disadvantage of the M edge is its proximity to the plasmon peak complicating background subtraction and it is highly affected by sample thickness. Another disadvantage of the M edge is the overlap of other TM elements commonly associated with manganese such as Mg L and Fe M (that are often in higher concentration than manganese). This limits the use of the M edge for quantification to simple, nearly pure, manganese minerals often only found in synthetic samples. Because of this, later methods for manganese valence determinations focused on the $L_{2,3}$ edge.

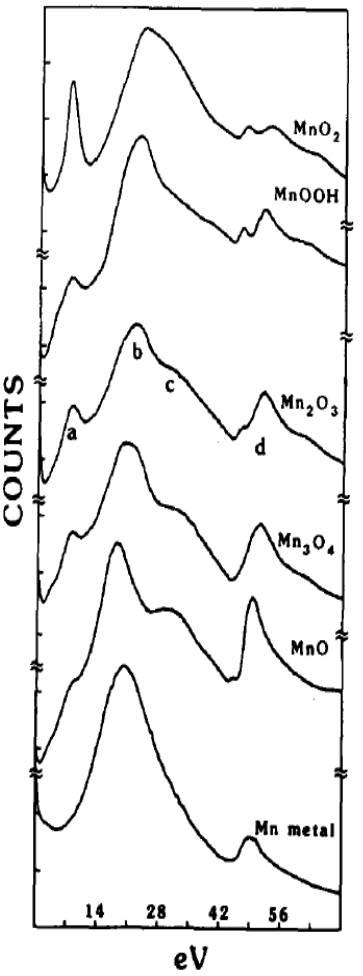


Figure 13. Low loss spectra of five manganese oxides and manganese metal. Included in this region are the plasmon peak (b) and the manganese $M_{2,3}$-peak (d) and interband transitions (a) and (c) all of which change with manganese oxidation state (from Rask et al. 1987).

Near edge structure of Mn $L_{2,3}$-edge

Early studies of the Mn L edge ELNES were done by Sparrow et al. (1984), Otten et al. (1985) and Rask et al. (1987) using a serial EEL spectrometer with a nominal resolution of ≥2 eV. Otten et al. (1985) and Rask et al. (1987) identified a chemical shift of $L_{2,3}$ edge with oxidation state to span approximately 4 eV between Mn(II) and Mn(IV). Subsequent reported absolute values of the L_3 edge for the three most common oxidation states for manganese vary considerably (Table 1). All three also reported a change in the L_3/L_2 ratio that decreased with increasing oxidation state in simple manganese oxides. From these initial studies, the usefulness of EELS for the determination of mean valence in minerals with mixed valence states was predicted.

Later, Garvie and Craven (1994a) and Garvie et al. (1994) used a parallel EEL spectrometer with a resolution of 0.3 eV that gave greater detail of NES. Twenty-five manganese-containing materials were studied covering oxidation states 0, +II, +III, +IV and +VII with different numbers of coordinating oxygen anions (Fig. 14). With respect to Mn(II), differences in the sharpness of the a and c peaks of L_3 edge for various Mn(II) minerals were apparent. Peak a

EBSCOhost - printed on 2/13/2023 5:26 AM via . All use subject to https://www.ebsco.com/terms-of-use

Table 1. Review of reported absolute energy loss values of the L_3 edge peak maxima for the three most common oxidation states for manganese (modified from Schmidt and Mader 2006)

Reference	Mn-L_3 energy-loss (eV)			
	Mn(II)	Mn(III)	Mn(IV)	Δ(Mn(II)-Mn(IV))
Mansot et al. (1994)	637.8	639.3	640.7	2.9
Paterson and Krivanek (1990)	639.0	639.6	642.1	3.1
Kurata and Colliex (1993)	639.5	642.0	643.0	3.5
Garvie and Craven (1993)	640	642	644	4
Loomer et al. (2007)	640.2	642	643.5	3.3
Schmidt and Mader (2006)	640.8	643.0	643.8	3
Laffont and Gibot (2010)	641.2	642.8	644.0	2.8
Rask et al. (1987)	642.4	643.8	646.4	4
Pecher et al. (2003)	639.7	641.35	643.05	3.35
Glatzel et al. (2004)	640.2	643.0	644.4	4.2
Average	640.1	641.9	643.5	3.4

is present in manganosite and rhodochrosite, but suppressed in MnF_2 and rhodonite or absent in lithiophilite, spessartine and jacobsite. It is apparent that the spectra are fingerprints for individual structures, but quantitative systematics for the bonding environment are lacking.

In the Mn(III) bearing minerals manganite, norrishite, gaudefroyite and bixbyite, Garvie and Craven (1994a) found that there were few differences between L_3 edges–even at high energy resolution. However, in Mn(IV) minerals, the L_3 edge contains 2 main peaks (a,b) and minerals studied are all similar in shape except for the sharpness of peak a. This distinction is reduced by spectrometers with lower resolution (e.g., 0.8 eV – Livi et al. 2012; 1.0 eV – Zhang et al. 2010; 1.6 eV – Loomer et al. 2007).

Mn(VII) in potassium permanganate has empty d-orbitals and is tetrahedrally coordinated. The spectrum obtained by Garvie and Craven (1994a) was sharp, but relatively featureless. Potassium permanganate proved to be extremely beam sensitive.

Quantification of valence by $L_{2,3}$-ELNES

Comparisons of four different methods for the extraction of the mean manganese valence from the $L_{2,3}$ white line intensities were made by Reidl et al. (2006). These methods—Pearson step function (Pearson et al. 1993), curve fitting, Walsh-Dray (Stolojan et al. 1999) and no subtraction—all differed in their handling of the subtraction of the continuum background and the integration of the white-line peaks. Reidl et al. (2006) found the Walsh-Dray method to be most precise in estimating the continuum background when analyzing $Mn(III)_2O_3$, $Mn(IV)O_2$ and $BaMn(VI)O_4$. Schmidt and Mader (2006) compared the relative precision of the white-line intensity ratio method as compared to the changes in the absolute energy positions of the peaks ($\Delta E(L_2\text{-}L_3)$). They concluded that although $\Delta E(L_2\text{-}L_3)$ changes systematically with mean valence, it has a greater error.

Loomer et al. (2007) studied the L_3/L_2 white line intensity ratio with the addition of internal energy calibration supplied by the Ti L_2 edge from added TiO_2 anatase nanocrystals. Although their resolution was relatively poor (1.6 eV resolution), they were successful at reproducing manganese valence within 3% error. Two aspects of this study are important: 1)

EBSCOhost - printed on 2/13/2023 5:26 AM via . All use subject to https://www.ebsco.com/terms-of-use

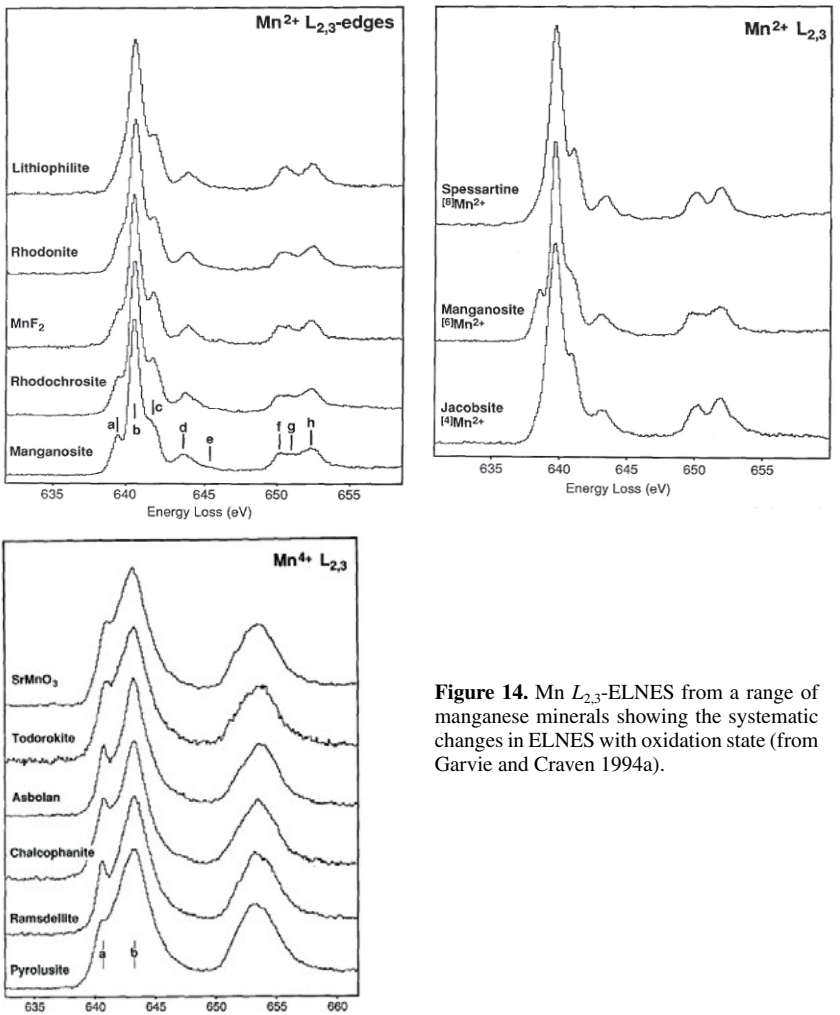


Figure 14. Mn $L_{2,3}$-ELNES from a range of manganese minerals showing the systematic changes in ELNES with oxidation state (from Garvie and Craven 1994a).

high-resolution EELS is not a requirement for successful EELS analysis of manganese valence if an internal energy standard is employed, 2) the L_3/L_2 white line intensity ratio flattens near the Mn(IV)-rich part of the calibration curve increasing the uncertainty in estimates dominated by Mn(IV) (Fig. 15) This is unfortunate since many environmentally important phases are rich in Mn(IV).

Zhang et al. (2010) assessed methods for determination of Mn(III)-Mn(IV) mixtures, and like Loomer et al. (2007), used an internal standard but in the form of Ti metal. This allowed for the examination of the O *K* edge without contamination of O from TiO_2. They compared $\Delta E(L_2\text{-}L_3)$, ΔE(Mn L_3-O *K*), the L_3/L_2 white line intensity ratio, Gaussian peak decomposition and multiple linear least-squares (MLLS) fitting of reference spectra methods. They concluded that of the calibration curve methods (first three methods), ΔE(Mn L_3-O *K*) was most precise (± 0.02 valence units). The failure of this method occurs when Mn is mixed with other oxide components and the position of the O *K* peak cannot be predicted. MLLS fitting results were subject to the selection of an appropriate standard, but yielded uncertainties (±0.03) that were

EBSCOhost - printed on 2/13/2023 5:26 AM via . All use subject to https://www.ebsco.com/terms-of-use

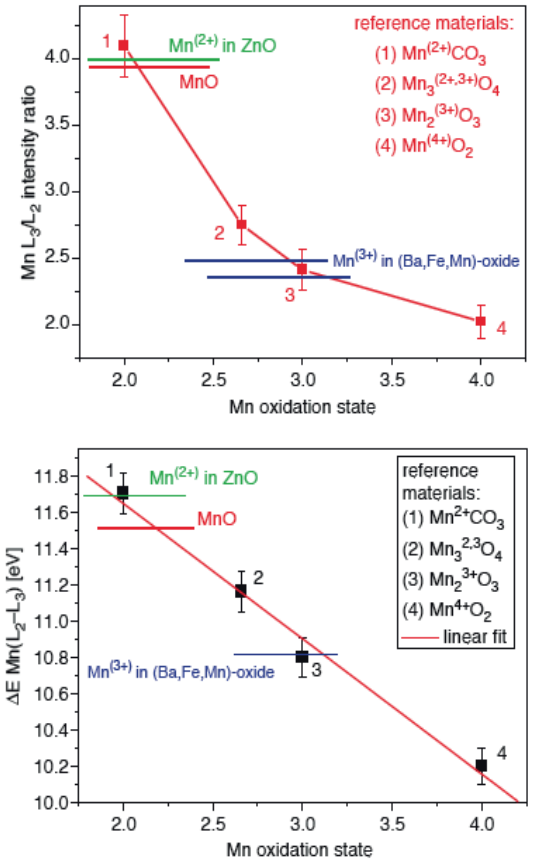


Figure 15. Calibration curves showing (*top*) Mn(L_3/L_2) white-line intensity ratio, and (*bottom*) Mn white line energy-difference ΔE Mn (L_2-L_3) versus Mn oxidation state in $MnCO_3$, Mn_3O_4, Mn_2O_3 and MnO_2 reference materials. The Mn(L_3/L_2) intensity ratios and energy-difference ΔE Mn (L_2-L_3) as measured in Mn-doped ZnO and (Ba,Fe,Mn) oxide are indicated by horizontal lines (from Schmidt and Mader 2006).

comparable to the ΔE(Mn L_3-O K) method without having to be pure manganese oxides. The Gaussian peak fit method was unsuccessful at modeling Mn(III)-Mn(IV) mixtures due to the similarity of shape and small separation of the Mn(III) and Mn(IV) L_3 peaks. Livi et al. (2012) followed Zhang et al. (2010) and used MLLS fitting methods to obtain average errors of ±0.05 (2σ).

Beam damage

Otten et al. (1985) was the first study to identify beam damage in manganese oxides during EELS analysis. This was corroborated and expanded upon by Garvie and Craven (1994c) for the phyllomanganate mineral asbolan. They conclude that damage of asbolan begins as a loss of oxygen on the surface of crystals and proceeds inward–progressively reducing the mean valence state. Evidence of loss of hydrogen from hydroxide minerals comes from an initial oxidation of manganese in $MnBO_2$ from Mn(II) to Mn(III) which was followed by a reduction back to Mn(II) as oxygen was subsequently lost (Garvie et al. 1994). Livi et al. (2012) determined the electron "safe dose" for beam sensitive todorokite and birnessite minerals. Accurate estimates of the mean valence values were possible for all varieties of birnessite minerals except for the

EBSCOhost - printed on 2/13/2023 5:26 AM via . All use subject to https://www.ebsco.com/terms-of-use

very poorly crystalline or amorphous δ-MnO_2. They point out that each variety of environmental mineral displayed a different damage profile, and every new study will require time-series analysis to determine the effects of beam damage. Future analysis of environmental minerals would benefit from advancements in low-dose imaging methods such as increased sensitivity of CCD cameras.

Applications

Varella et al. (2009) investigated the manganite (perovskite) $La_xCa_{1-x}MnO_3$ system with 2D atomic resolution. Although this is an engineered material, the study successfully demonstrated that the manganese mean valence could be measured on an atomic scale as La:Ca varied, and in some cases, could detect differences between non-equivalent O sites. The most precise estimate of manganese valence took advantage of systematic variations in the O K-ELNES main peak to pre-peak separation ($\Delta E\ K_M$-K_P). Luo et al. (2009) provided a theoretical basis for the correlation of $\Delta E\ K_M$-K_P with manganese oxidation state–although they conclude that $\Delta E\ K_M$-K_P is due to changes in the Ca:La proportion. Further empirical evidence that $\Delta E\ K_M$-K_P systematics may hold for simple manganese oxides may be found in Rask et al. (1987), Kurata and Colliex (1993) and Zhang et al. (2010). This has not been thoroughly studied and may not prove viable when other elements (such as Fe) are present.

Manganese nodules found at hydrothermal vents present a rich area for the application of EELS valence determination (see Hayes et al. 1985 for a description of the variety of manganese minerals found in Pacific nodules). However, this field has not been exploited as of yet. In one study, Buatier et al. (2004) performed an initial investigation of manganese valence in manganese crusts in active hydrothermal deposits on the flanks of the Juan de Fuca Ridge. Buatier et al. (2004) identified todorokite, birnessite and veil-like amorphous phases. EELS analysis showed the first two phases to have a mean valence of 3.7, while the amorphous material gave valences close to +II. Unfortunately, no time-series data were presented, so the validity of the low valence of the amorphous material is in question due to the likelihood of severe beam damage. The study does illustrate the value of combined X-ray diffraction, scanning electron microscopy, analytical TEM and EELS methods to identify all constituents of these complex mixtures, including amorphous material.

A preliminary report on EELS characterization of manganese minerals from the N'chwaning II mine in the Kalahari Manganese Field by Calvert et al. (2008) indicated that supposedly single valence mineral species were in fact of mixed valence.

The recent attention to the toxicity of manganese inhalation has led to some investigation of both the sources of manganese (e.g., welding fume) and its translocation to the central nervous system and other organs. Most analytical TEM studies of manganese in tissue employ the location of manganese through EDX analysis. However, there are two notable studies that use EELS. Richman et al. (2011) used STEM/EDX/EELS to characterize both the size and composition of manganese-weld fume. They demonstrated the usefulness of combining annular dark-field imaging to determine weld particle size/shape with EELS of oxygen, manganese and iron (major fume elements) and EDX of silicon and other minor elements (not readily accessible by EELS with 0.3 eV dispersion). The maps generated by EELS were far superior to those by EDX due to greater counting statistics. In addition, the O K-ELNES can also be used to deduce differences in crystal structure (rock salt vs. spinel). Richman et al. (2011) demonstrated that, in half the samples studied, there was a positive correlation of manganese content of breath exhale condensate with particle size in welders of the study group. The physicochemical properties of nanoparticles were important in understanding the amount of manganese delivered to the lungs, the depth to which nanoparticles will penetrate in the lungs, their residence time, and their surface area and reactivity. In this study, the statistically valid conclusion was drawn that smaller particles had longer residence time in the lung, while larger particles were exhaled more quickly.

EBSCOhost - printed on 2/13/2023 5:26 AM via . All use subject to https://www.ebsco.com/terms-of-use

Although manganese is found in all parts of the body, it is inhomogeneously distributed. Morello et al. (2008) investigated those areas in rats that have higher contents on the assumption that hyperaccumulation would occur during elevated manganese exposure. They used electron spectroscopy imaging in an in-column energy-filtering TEM to image high concentrations of manganese in mitochondria of astrocytes (glial nerve cells) and neurons, and to a lesser extent, in nuclei of astrocytes and neurons. This contrasted with biochemical assay results that suggested accumulation in nuclei. Morello et al. (2008) explain this discrepancy as a difference in spatial resolution between the two techniques. This application illustrates how EELS in the TEM can more accurately locate manganese accumulations in sub-cellular organelles than traditional biochemical assays. Developments in sample preparation methods (to minimize soluble manganese loss during fixing), cryo-analytical TEM preparation, and increased sensitivity of detectors will undoubtedly improve the quality of EELS applications to biological sciences in the future.

GENERAL APPLICATION OF EELS, SAED AND EDX

Finally we present an overview of the integrated use of the various imaging and spectroscopic techniques available in a modern analytical TEM to general mineralogical research.

The use of TEM for detailed mineral characterization accelerated rapidly in the 1970's with the development of ion beam milling for the preparation of electron transparent thin sections of rocks and minerals (see for example the review by Champness 1977). Since then, applications of TEM in the geosciences have kept abreast of the many developments in instrumentation, specimen preparation and analytical techniques (see for example, Lee 2010). It is now possible to image and chemically map a specimen atom column by atom column using spherical aberration corrected STEM combined with energy dispersive X-ray spectroscopy (EDX) (D'Alfonso et al. 2010) and/or electron energy loss spectroscopy (EELS) (Bosman et al. 2007). In order to achieve this resolution, one must prepare a suitably thin, representative specimen and control the applied electron dose in order to limit any irradiation induced artifacts (Egerton and Malac 2004; Egerton et al. 2010).

Most modern TEMs can readily provide atomic lattice imaging and, when equipped with the appropriate spectrometers, chemical information at the nanoscale if not the atomic. Identification of nanoscale segregation of elements within earth and planetary materials can bring new insight into the dynamic processes these materials undergo. Here we highlight recent examples of the characterization of environmentally important nanoparticle systems while highlighting a consistent theme of representative specimen preparation and analysis.

Use of (S)TEM to assess transport and retardation mechanisms of trace metal contaminants

Nanoparticles and colloids are a consistent feature of low temperature surface waters and ground waters. They remain suspended and are transported in moving groundwater and have a high surface area such that a relatively insoluble metal can be readily adsorbed onto the NP/colloid surface. Thus nanoparticles play a critical role in the transport of trace metal contaminants and it is therefore key to understand the binding sites of these colloids in order to further understand trace metal transport and retardation. Over the years there have been relatively detailed analyses of nanoparticle characteristics, with analytical STEM and CTEM emerging as powerful tools for the identification and characterization of trace metal contaminants on and within nanoparticulate phases. CTEM alone has been used to identify particles bearing toxic elements (Hochella et al. 1999; Suzuki et al. 2002) while analytical STEM combined with CTEM have been used to identify and characterize nanoparticulate

EBSCOhost - printed on 2/13/2023 5:26 AM via . All use subject to https://www.ebsco.com/terms-of-use

metal contaminants in a range of environmental, colloidal matrices (Utsunomiya and Ewing 2003; Utsunomiya et al. 2009). Using CTEM to identify contaminants in low concentration and localized to a nanoparticulate phase is limited because the image contrast alone will not identify the contaminant. The full analytical capability of the STEM however is very useful since the strong electron scattering of the contaminant metal can be used to identify (by HAADF-STEM) and map (by STEM-EDX or by CTEM-EFTEM) the metal contaminants in or on host particles. Subsequent CTEM (lattice imaging, electron diffraction and EELS) can be used to identify the speciation and crystal phase of the two.

In general, analytical S/TEM analysis is not used as a standalone characterization technique but more often it can provide nanoscale information to support bulk analytical data. For example (see Fig. 16), the identification of Cr(III) substitution in hematite within samples from the Ajka red mud spill site, Hungary relied on a combination of CTEM-selected

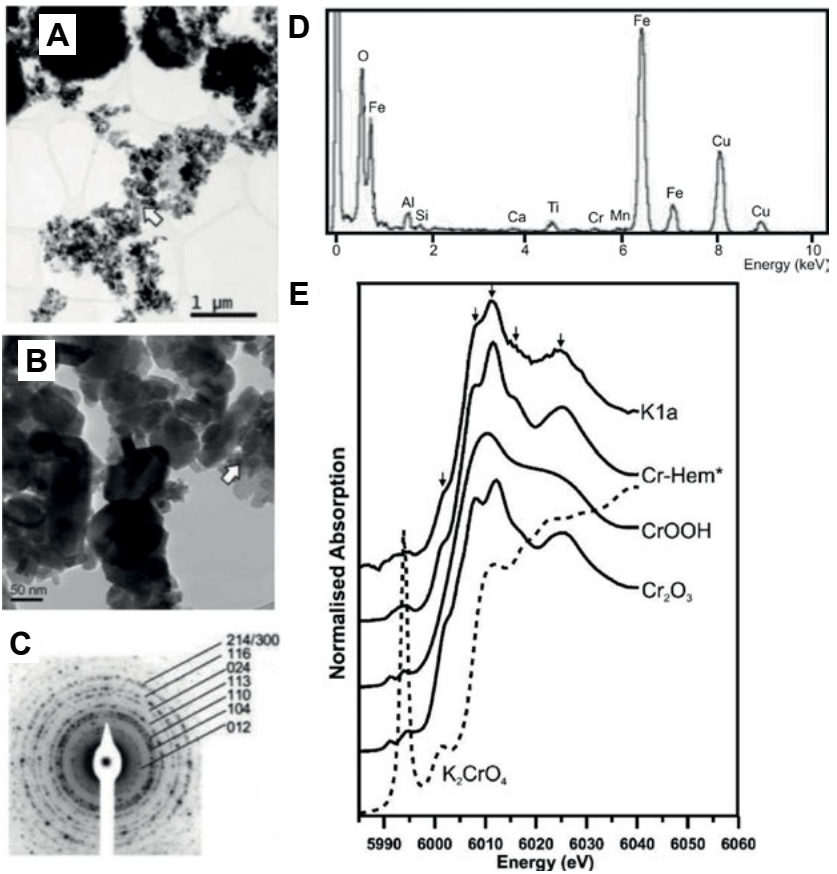


Figure 16. Identification of Cr(III) substitution in hematite within samples from the Ajka red mud spill site, Hungary (after Burke et al. (2012). (A) Low-resolution bright field TEM image of the red mud particles from the spill site. (B) Higher magnification image of area highlighted by white arrow in A. (C) Polycrystalline selected area electron diffraction pattern indexed to hematite. (D) EDX spectrum collected from the point shown with a white arrow in B, confirming the additional presence of Ti and Cr in the hematite phase. (E) Normalized Cr *K*-edge XANES spectra collected from the red mud sample (K1a) and three Cr(III) and one Cr(VI) containing standards. The spectrum from the red mud is consistent with the spectra collected from the Cr(III)-substituted hematite and Cr_2O_3 standards.

EBSCOhost - printed on 2/13/2023 5:26 AM via . All use subject to https://www.ebsco.com/terms-of-use

area electron diffraction and spot EDX analysis to identify Cr within a fine-grained hematite structure and X-ray absorption spectroscopy to identify the valence state of the Cr (Burke et al. 2012).

Similarly X-ray Absorption Spectroscopic (XAS) analysis of soils from a chromite ore processing residue disposal site indicated Cr is present as a mixed Cr(III)-Fe(III) oxyhydroxide phase and this was confirmed by STEM-EDX and BF-TEM imaging (Whittleston et al. 2011). The retention of Cr(III) within the soil was shown to be due to reductive precipitation of Cr(VI) by Fe(II).

Indeed, multiple approaches are essential to understanding metal speciation in complex heterogeneous sediments given the wide concentration range relevant to contaminated natural and engineered environments. For example (see Fig. 17 the association and speciation of the fission product, technetium-99, found in radioactive wastes, was examined under reducing conditions over a range of concentrations in estuarine sediments (Burke et al. 2010; Lear et al. 2010). Anoxic incubation experiments were conducted with direct (transmission electron microscopy and gamma camera imaging) and indirect (incubation experiments and chemical extractions) experimental techniques employed. The combination of low and high concentration measurements supported the hypothesis that removal of Tc from solution may be controlled by reduction of Tc(VII) to Tc(IV) by biogenic Fe(II) in sediments. STEM-EDX and TEM-EELS were employed specifically to show that the Tc was localized and co-associated with nanometer size Fe(II)-rich particles in the relatively high concentration sediments.

The multiple approaches are equally applicable to a biological setting. For example (see Fig. 18), evidence for a Si-specific intracellular mechanism for Al detoxification in aquatic snails, involving regulation of orthosilicic acid [$Si(OH)_4$] was supported by intracellular identification of hydroxyaluminosilicates (HAS) in exposed snails by analytical STEM (White et al. 2008). In snails preloaded with $Si(OH)_4$, behavioral toxicity in response to subsequent exposure to Al was abolished. Similarly, recovery from Al-induced toxicity was faster when $Si(OH)_4$ was provided, together with rapid loss of Al from the major detoxificatory organ (digestive gland). Temporal separation of Al and Si exposure excluded the possibility of their interaction ex vivo. Elemental mapping using analytical STEM and CTEM revealed nanometer-scale co localization of Si and Al within excretory granules in the digestive gland, consistent with recruitment of $Si(OH)_4$, followed by high-affinity Al binding to form particles similar to allophane, an amorphous HAS.

This work highlights the value of analytical STEM to the emerging field of nanoparticle toxicology where one of the goals is to assess the impact of engineered nanoparticles on the environment. For example, Ag nanoparticles are now extensively produced and used in consumer products and sulfidation is thought to be the dominant degradation product as they are released into the environment (Levard et al. 2011). Silver sulfide (α-Ag_2S) nanoparticles have been identified in the final stage sewage sludge materials of a full-scale municipal wastewater treatment plant using analytical STEM (Kim et al. 2010).

Developments in TEM specimen preparation

The crossover of geological and biological specimens also requires consideration of the recent developments in specimen preparation for TEM. Most nanoparticle work relies on drop-casting particles or particle suspensions directly onto amorphous carbon (or sometimes silicon or silicon nitride) support films for TEM. For valuable or potentially toxic particulates one can also use resin impregnation of a suspension and then after hardening, thin sections can be cut for TEM by an ultramicrotome (for example Burke et al. 2010). The drop-casting method is simple and can be used following the completion of solution based reactions to chart the progress of a reaction (for example, Penn and Banfield 1998). More recent developments are taken from biological specimen preparation where thin layers of particle suspensions are rapidly frozen

EBSCOhost - printed on 2/13/2023 5:26 AM via . All use subject to https://www.ebsco.com/terms-of-use

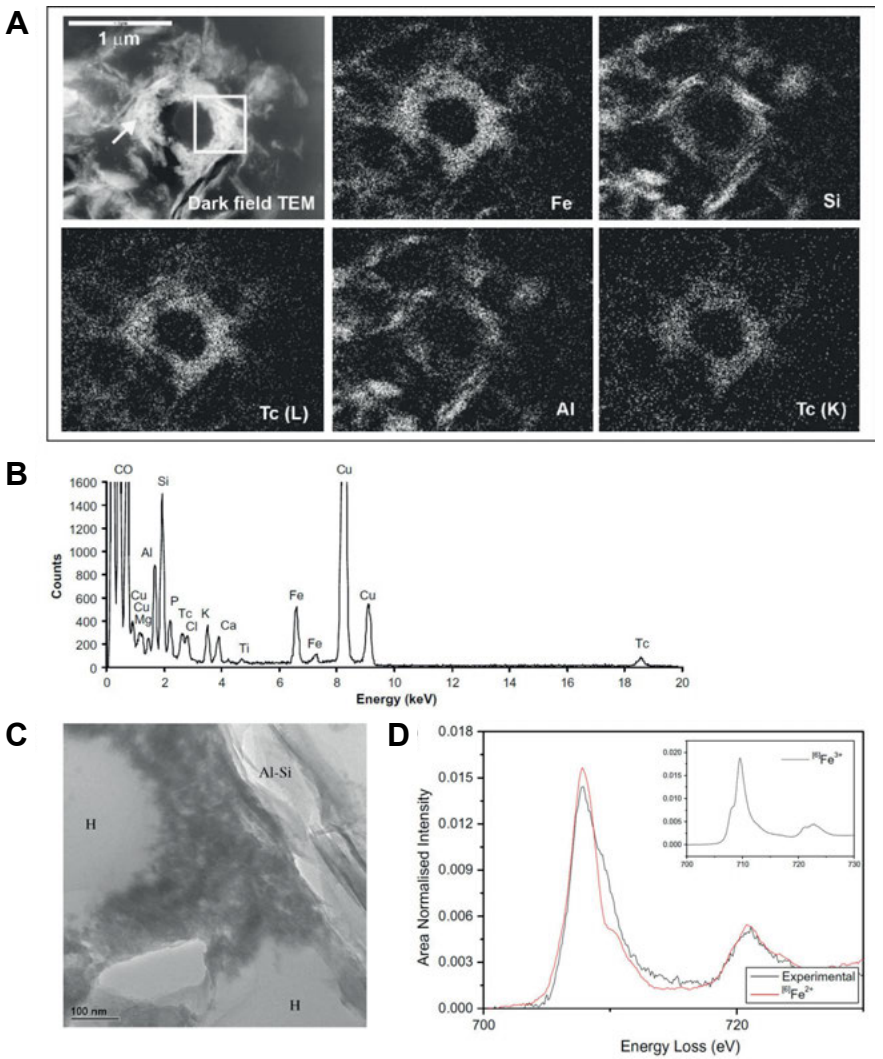


Figure 17. Identification of the association of the fission product, technetium-99, in estuarine sediments examined under reducing conditions (after Burke et al. 2010). (A) Annular dark field STEM image and elemental X-ray maps showing the distribution of Fe, Si, Al and Tc (L_α and K_α X-rays) in sediments incubated with 0.5% (w/w) Tc. Clearly, Tc is co-localized with Fe, and Si is co-localized with Al. (B) EDX spectrum of the whole region shown in A. Cu and C peaks are present due to stray X-rays emitted by the TEM grid and films, respectively. Tc L_α X-rays at 2.42 keV are indistinguishable from S K_α X-rays at 2.31 keV, but Tc K_α X-rays at 18.38 keV do not overlap in energy with any other elemental X-rays measured here, confirming the presence of Tc. (C) Bright field TEM image of the sediment shown to be Fe- and Tc-rich (inside white box in A showing a network of fine particles that are amorphous (by electron diffraction) next to larger Al and Si-rich crystals. (D) Background stripped Fe $L_{2,3}$-edge electron energy loss spectrum (black line) acquired from the Tc-rich region. The general shape of the edge and the position of the L_3 peak maxima (at 707 eV energy loss) is consistent with a spectrum from an Fe(II) rich region. For reference a spectrum from a well characterized Fe(II) bearing mineral (hedenbergite; $CaFe\text{-}Si_2O_6$, where the Fe is octahedrally coordinated to O) is shown in red and inset is a reference spectrum from a well characterized Fe(III) bearing mineral (hematite; $\alpha\text{-}Fe_2O_3$).

EBSCOhost - printed on 2/13/2023 5:26 AM via . All use subject to https://www.ebsco.com/terms-of-use

in solution allowing the hydrodynamic state of the particles and agglomerates to be observed (Hondow et al. 2012). These cryo-quenching approaches and subsequent TEM imaging and analyses recently helped quantify in a time resolved manner the kinetics and mechanisms of several geological relevant reactions (e.g., Tobler et al. 2009; Van Driessche et al. 2012). In the geosciences, recent developments include the use of TEM imaging to track and quantify the kinetics of nanoparticle formation and transformation. For example, conventional and cryo-TEM imaging helped quantify the nucleation and growth of amorphous silica (Tobler et al. 2009). Similarly, using TEM imaging, SAED and associated pair distribution quantifications, the formation and aging of nanocrystalline iron sulfide phases (amorphous FeS, machinawite, greigite and pyrite; Csákberényi-Malasics et al. 2012), which control the biogeochemical cycling of iron and sulfur in anoxic and suboxic marine sediments has been quantified. Finally, only by using novel fast-quenching techniques combined with high-resolution TEM imaging combined with EDX and SAED could the processes that control the nucleation, growth and transformation of calcium sulfate phases from aqueous solution be evaluated (see Fig. 19; Van Driessche et al. 2012). These studies showed that not only important geological processes but also crucial industrial applications can be accurately studied using the novel imaging, sample preparation and analytical approaches developed in the last few years.

Liquid cell imaging within the TEM is also progressing rapidly however the attainable spatial resolution still remains significantly less good than that available by CTEM (Klien et al. 2011). Finally, FIB sectioning of TEM specimens has been used to successfully examine mineral weathering products (Lee et al. 2007) and the interface between microbes and minerals (Obst et al. 2005; Bonneville et al. 2009). Avoiding preparation artifacts such as over-thinning with the ion beam and bending of the samples is a major issue with these types of samples. As section depth increases, it becomes more difficult to keep the sides flat, and over-thinning of certain areas can occur because the profile of the ion beam itself is not parallel and this has to be accommodated by tilting the face of the section to be milled a few degrees off axis from the incident ion beam (Ishitani et al. 1994). Deep sections also have less support, and non-rigid materials such as the cellular components of the above samples can bend. Once this occurs protruding "bulges" will be milled away more quickly than the rest of the section, potentially leaving holes (Ward et al. 2013). This can be avoided by leaving relatively thick sections (say 100-150 nm) however this should be balanced against the required spatial resolution of the (S)TEM analysis (for example, the spatial resolution obtainable by EDX decreases with increasing specimen thickness because of the increased interaction volume that generates X-rays from the incident beam in the thicker sections; Williams and Carter 1996).

FIB-preparation of very thin sections suitable for atomic resolution HAADF-STEM, with parallel sides and a sample depth of 2 to 3 μm have been successfully achieved (Bals 2007; Schaffer 2012). Recently, analytical TEM of FIB prepared mineral-fungi sections has been used to demonstrate weathering of natural minerals (biotite) by fungal hypha, with the conclusion that this proceeds by a combination of biomechanical forcing and chemical dissolution (Bonneville et al. 2009). For the case of Bonneville et al. (2009), careful FIB preparation followed by analytical TEM has demonstrated that weathering of biotite by fungal hypha proceeds by a combination of biomechanical forcing and chemical dissolution. Here (see Fig. 20), CTEM and SAED analysis of the fungus-biotite interfaces revealed intimate fungal mineral attachment, biomechanical forcing, and altered interlayer spacings while STEM-EDX identified substantial depletion of potassium (~50 nm depth) with STXM analysis of the same sections showing oxidation of the biotite Fe(II) and finally CTEM once again showing the formation of vermiculite and clusters of Fe(III) oxides. Modeling of the nanometer-scale elemental fluxes obtained at the hypha-mineral interface by STEM-EDX demonstrates how the weathering of rocks may be accelerated to release nutrients to plants (Bonneville et al. 2011).

EBSCOhost - printed on 2/13/2023 5:26 AM via . All use subject to https://www.ebsco.com/terms-of-use

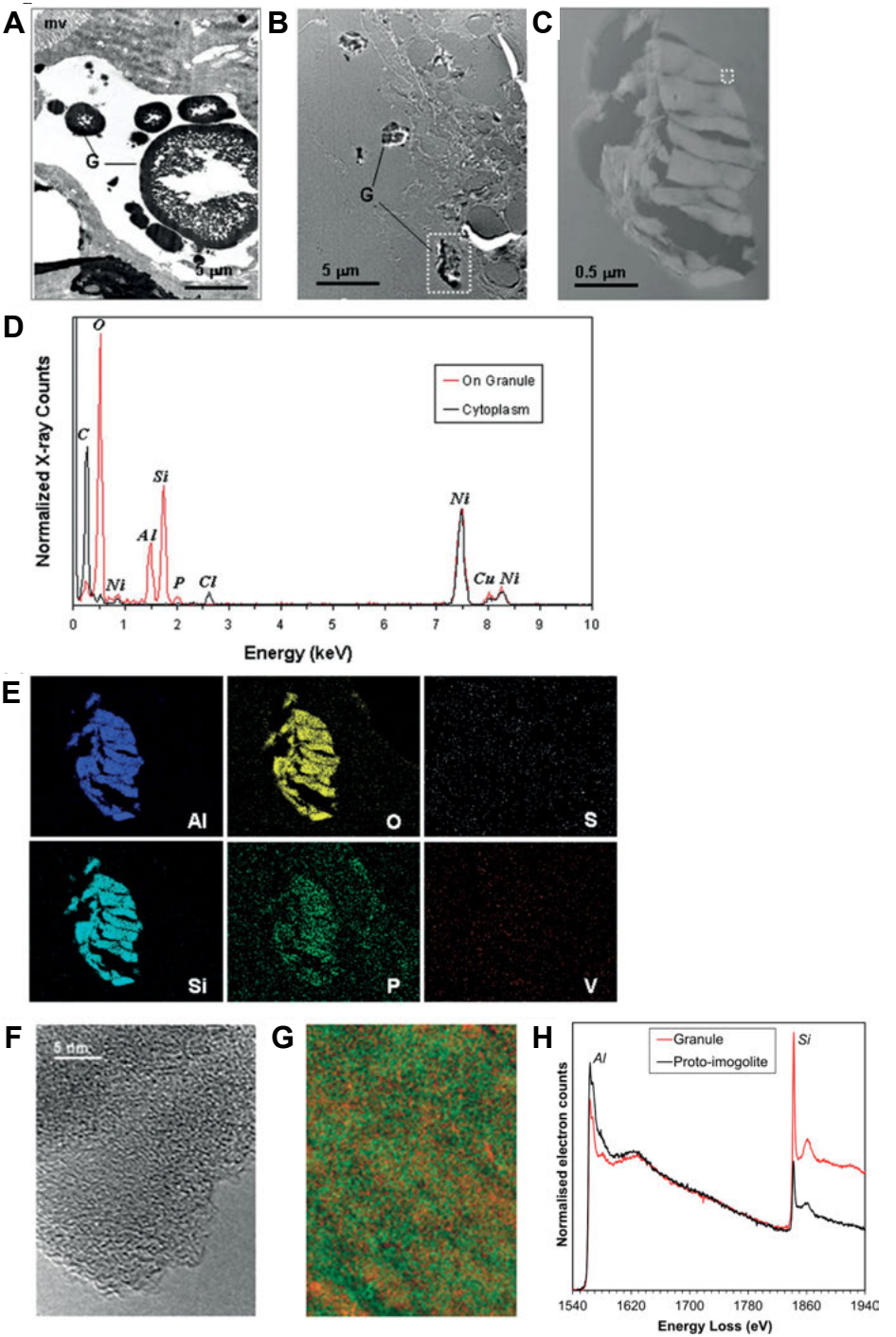


Figure 18. *caption on next page*

EBSCOhost - printed on 2/13/2023 5:26 AM via . All use subject to https://www.ebsco.com/terms-of-use

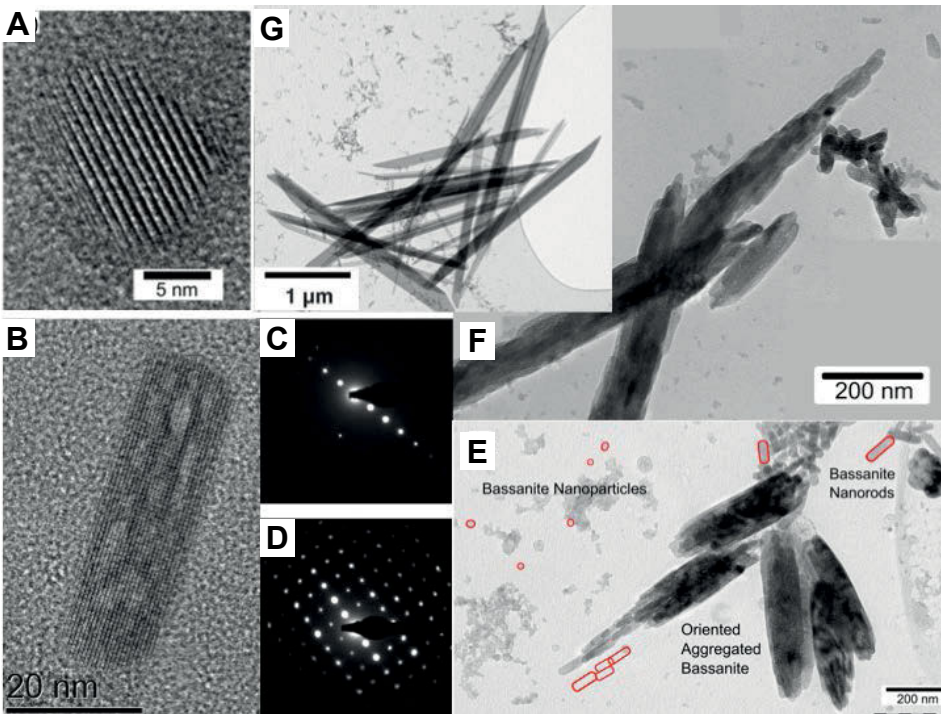


Figure 19. Using fast and time-resolved sample quenching and associated TEM imaging and analyses Van Driesche et al. (2012) have documented how a geologically important mineral phase, gypsum, forms from aqueous solutions via a multi-stage reaction chain. In a first step the homogeneous precipitation of nanocrystalline (A) calcium sulfate hemihydrate, bassanite ($CaSO_4 \cdot 0.5H_2O$) occurs; interestingly at this nanoscale this happens below its predicted solubility. The so formed rounded nanocrystals transform to bassanite nanorods (B) with corresponding SAED pattern in (C). These nanorods later self-assemble into aggregates that are co-oriented along their *c*-axis (E) and corresponding SAED pattern in (D). These oriented aggregates develop into overall morphologies reminiscent of the dihydrate gypsum ($CaSO_4 \cdot 2H_2O$), yet crystallographically they are still just self-assembled oriented bassanite nanorods (F). Only in a final stage, do these bassanite aggregates hydrate to transform to gypsum crystals (G).

Figure 18 (*on facing page*). Evidence for a Si-specific intracellular mechanism for Al detoxification in aquatic snails, *Lymnaea stagnalis* (after White et al. 2008). (A) Digestive gland thin sections were taken from snails exposed to Al (500 µg L^{-1}) for 15 days and stained with heavy metals to show membrane-bound granules (G) in an excretory cell, bordered by microvilli (mv). (B) Unstained section (for elemental analysis) with granules still evident. (C) Bright-field STEM image of granule outlined in B. (Some diamond knife damage during sectioning is evident). (D) Spot EDX spectra from the granule and the surrounding cytoplasm showing the granule composition to be consistent with an aluminosilicate phase containing some phosphorus. The counts are normalized to the background signal from the Ni support grid. (E) STEM-EDX maps of the granule shown in C, demonstrating the co-localization of Al, Si, O, and minor amounts of P. S and V (negative control) were not detected. (F) TEM image of the area outlined in C, indicating that the granule is non-crystalline. (G) EF-TEM false colour elemental map shows nanoscale co-localization of Al (red in electronic version) and Si (green in electronic version) [both Al and Si are light grey in print version]. (H). Al *K*- and Si *K*-edge electron energy loss spectra from a digestive gland granule (red in electronic version and grey in print version) and from synthetic proto-imogolite (black in both electronic and print versions): gift from Dr. D. Lumsdon, The Macaulay Institute, Aberdeen). Similarity in shape of the Al *K*-edges suggests that the allophane phase of the granule is similar in structure to proto-imogolite.

EBSCOhost - printed on 2/13/2023 5:26 AM via . All use subject to https://www.ebsco.com/terms-of-use

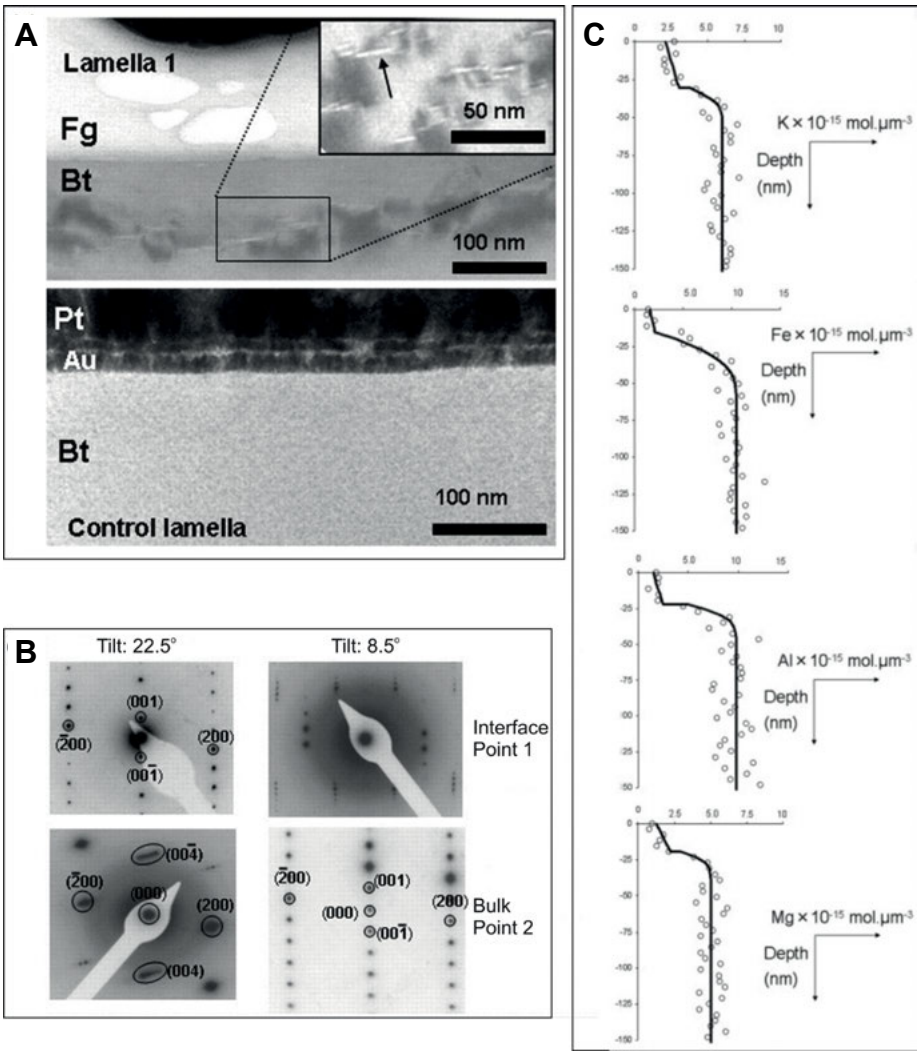


Figure 20. Evidence for biomechanical forcing and chemical dissolution, weathering of biotite by fungal hypha (after Bonneville et al. 2009). (A) BF-TEM image of the cross-section of a hypha (Fg)-biotite (Bt) interface, labeled lamella 1 and compared to a cross section of pristine biotite, labeled control lamella. Both cross-sections were prepared by focused ion beam milling. Strong diffraction contrast and micro-cavities (image inset) are visible in the biotite incubated with the fungal hypha and indicate physical alteration of the mineral. (B) Selected area electron diffraction patterns of the interfacial versus bulk biotite in lamella 1 indicate a misorientation of the biotite at the interface compared to that in the bulk (indexed to biotite monoclinic structure; JCPDS reference 01-074-2578). The biotite crystal structure was tilted from a relative angle of 8.5° in the bulk (point 2) to an angle of 22.5° at the interface with the hypha tip (point 1) to obtain the same $[0\,\bar{1}0]$ zone axis diffraction patterns. (C) STEM-EDX derived elemental (symbols) and modeled (lines) concentration depth-profiles over the 150 nm below the hypha-biotite interface for K, Al, Fe and Mg in a FIB section exposed to a fungal hypha for ~ 70 days, demonstrating clear chemical alteration of the biotite (Bonneville et al. 2011).

EBSCOhost - printed on 2/13/2023 5:26 AM via . All use subject to https://www.ebsco.com/terms-of-use

Developments in analyzing poorly crystalline, beam sensitive materials

It is well known that the electron beam in a TEM/STEM may cause some form of specimen alteration during examination and may affect the integrity of the information sought from the specimen (Hobbs 1987; Egerton and Malac 2004; Reimer and Kohl 2008). For example, in the last section we discussed the FIB preparation and analysis of biotite, which is sensitive to damage by the high energy electron beam of the TEM (Bell and Wilson 1981). At 300 keV, mass loss occurs as a function of accumulated electron fluence (Ma et al. 1998) and this is therefore a major concern when using the focused probe of a STEM (operating at 197 keV in the case of Bonneville et al. 2009). There are reports of a threshold dose for electron beam induced damage of minerals such as vermiculite (Baumeister and Hahn 1976) and a threshold fluence for a biotite has also recently been identified (Ward et al. 2013). This has been obtained following a cumulative electron fluence protocol developed for the TEM-EELS analysis of ferritin and ferrihydrite (Pan et al. 2006, 2010) and for the STEM-EDX analysis of hydroxyapatite nanoparticles (Eddisford et al. 2007). Furthermore, similar time dependent exposure of amorphous calcium carbonate (ACC) nanoparticles to a high voltage electron beam (200 keV) immediately induced the formation of 2-5 nm ordered subdomains, which grew and transformed into larger (5-20 nm) crystalline domains (Fig. 21; Rodriguez-Blanco et al. 2008). This process occurred within the confinement of the large spherical ACC nanoparticles and this crystallization is likely the results of dehydration of the initially highly hydrated ACC. However, the nature of the resulting crystalline domains (i.e., whether they correspond to 'proto-vaterite' or proto-calcite' is unclear as the mechanisms of this beam-induced crystallization may differ from that occurring in aqueous solution (Rodriguez-Blanco et al. 2011). A quantitative understanding of the stability and transformation mechanisms of ACC into geologically stable calcium carbonate polymorphs has major implications for biomineral formation, which themselves often form from an initial hydrated ACC. For example, the formation of coccoliths and foraminifera, the dominant calcium carbonate biominerals in our world's oceans, controls the global carbon cycle. Using novel imaging and analytical techniques as described above can help us better understand how the formation of such biominerals may be affected by for example changes in climate (i.e., increase in atmospheric pCO_2 and associated ocean acidification).

As indicated above, near-edge core-excitation spectroscopy, such as energy loss near-edge structure (ELNES) analysis, has been demonstrated as a useful tool for studying mineral oxidation states and coordination environments (Garvie et al. 1994, 2004; Garvie and Craven 1994b). Fe $L_{2,3}$-ELNES specifically has been used to investigate the effects of electron dose (via control of electron fluence) in hydrated iron phosphate, ferrihydrite and ferritin/haemosiderin cores in an iron- overloaded human liver biopsy (see Fig. 22) and the results demonstrate the reduction of iron and its transformation from octahedral to tetrahedral co-ordination under progressively increasing electron dose, consistent with the preferential loss of iron coordinating ligands (O, OH and H_2O) (Pan et al. 2010).

By considering the cumulative effect of electron fluence on a mineral, one can extrapolate back to the pristine structure or chemical state and, for the case of ferrihydrite (Fh), this characterization is very topical because of the potential presence of 'coordination under saturated' tetrahedral ferric iron sites. First described in 1967, there is still some controversy over the precise atomic structure of Fh because its size and defective nature make a definitive characterization challenging. One structural model, proposed in 1993 and based on powder XRD analysis, describes Fh as three intermixed phases where iron occupies octahedral interstices only (Drits et al. 1993). Recently (2007-2010), a new model challenging the standard view has been proposed, based predominantly on structural refinement of atomic pair-distribution functions (PDF) measured in the synchrotron using total X-ray scattering (Michel et al. 2007, 2010). Fh is described in this model as a single phase in which iron

EBSCOhost - printed on 2/13/2023 5:26 AM via . All use subject to https://www.ebsco.com/terms-of-use

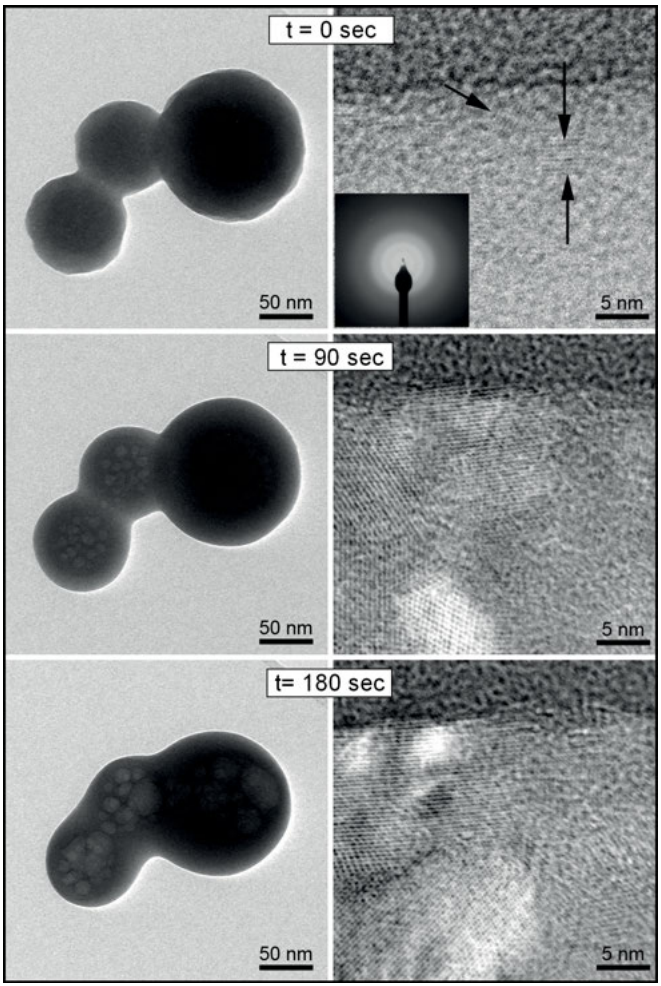


Figure 21. Bright field TEM image time series of the crystallization of amorphous calcium carbonate (ACC) upon exposure to the electron beam. From top to bottom, changes in ACC morphology (*left*) and internal structure and ordering (*right*) as a function of time. The insert in the upper right image shows a SAED pattern of ACC revealing only diffuse rings related to poorly ordered materials (from Rodriguez-Blanco et al. 2008).

occupies both tetrahedral (≤ 10-20%) and octahedral interstices. This new model has received some criticism (Rancourt and Muenier 2008; Manceau 2009, 2010, 2011, 2012; Barron et al. 2012) and additional support (Maillot et al. 2011; Xu et al. 2011; Harrington et al. 2011; Peak and Regier 2012; Guyodo et al. 2012). The TEM measurement of Fe $L_{2,3}$-ELNES from 6-line Fh has contributed to this debate however it has not provided a definitive measure of the tetrahedral iron content because of the uncertainty in the extrapolation back to very low electron fluence (Pan et al. 2010).

More recently, Vaughan et al. (2012) have shown X-ray scattering profiles of synthetic 2-line ferrihydrite that are consistent with other reports for ferrihydrite. The measurement of ~93% octahedrally coordinated ferric iron by extrapolation of the Fe $L_{2,3}$-ELNES to very

EBSCOhost - printed on 2/13/2023 5:26 AM via . All use subject to https://www.ebsco.com/terms-of-use

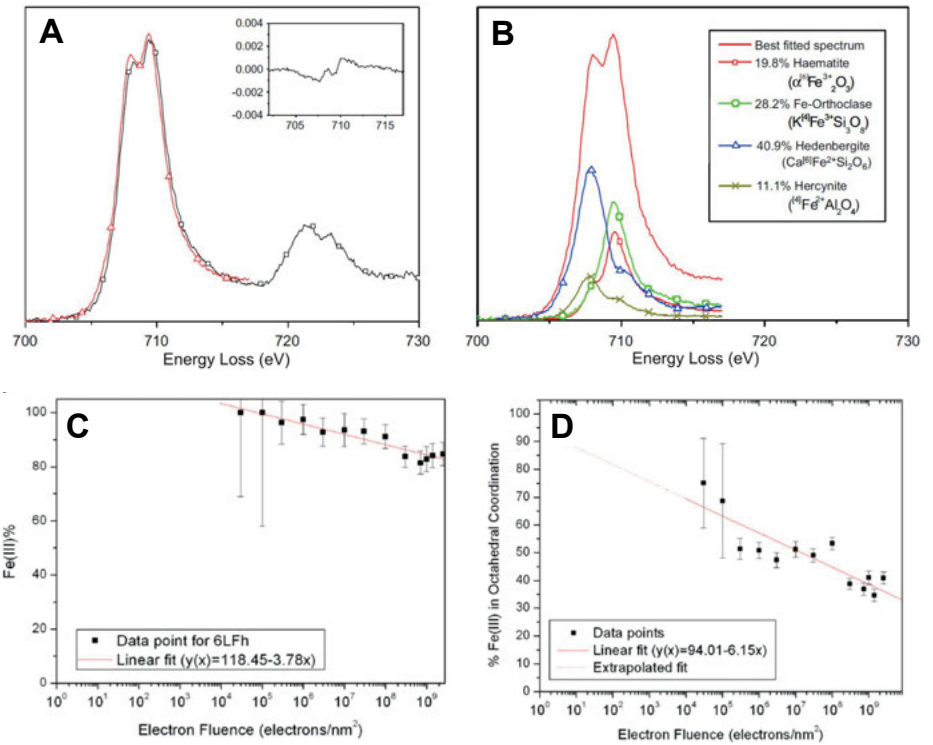


Figure 22. Fitting Fe $L_{2,3}$-edge TEM EEL spectra to estimate the octahedral ferric Fe content of ferrihydrite (after Pan et al. 2010). (A) An example of the result of a non-linear least squares (NLLS) fitting to a Fe L_3-energy loss edge (i.e., 702-717 eV energy loss) of iron phosphate dihydrate. The experimental spectrum is black and the best fit spectrum is red. The inset shows the residual intensity following subtraction of the best fit curve. (B) The relative proportions of the four reference spectra that, when combined, produce the best fit to the experimental spectrum. (C) The NLLS fitting coefficient estimate of the percentage content of total ferric iron (octahedral + tetrahedral coordination) in 6-line ferrihydrite (6LFh) at each accumulated electron fluence. (D) The estimated percentage of octahedrally coordinated ferric iron in 6-line ferrihydrite at each accumulated electron fluence. The extrapolated ferric and octahedral content at very low fluence are 100% and 95% respectively.

low electron fluence is not, however, in complete agreement with the most recently proposed structural model described above (see Fig. 23). Nitrate has also been detected and inferred to be a surface contaminant, because its presence does not apparently affect the bulk structure. It may be that the incorporation of nitrate affects the surface co-ordination states of the iron and so the measurement of tetrahedral iron. This highlights the need for careful and consistent synthesis and characterization of ferrihydrites before comparison with structural models is made.

CONCLUSIONS

This review of the chemical analysis of mineralogical micro- and nano-structures *in situ* within the transmission electron microscope has highlighted the two major techniques of energy dispersive X-ray analysis and electron energy-loss spectroscopy.

This article has summarized the basic aspects of the excitation mechanisms, the interpretation, the acquisition and processing of both EDX and EELS spectra. Details of instrumenta-

EBSCOhost - printed on 2/13/2023 5:26 AM via . All use subject to https://www.ebsco.com/terms-of-use

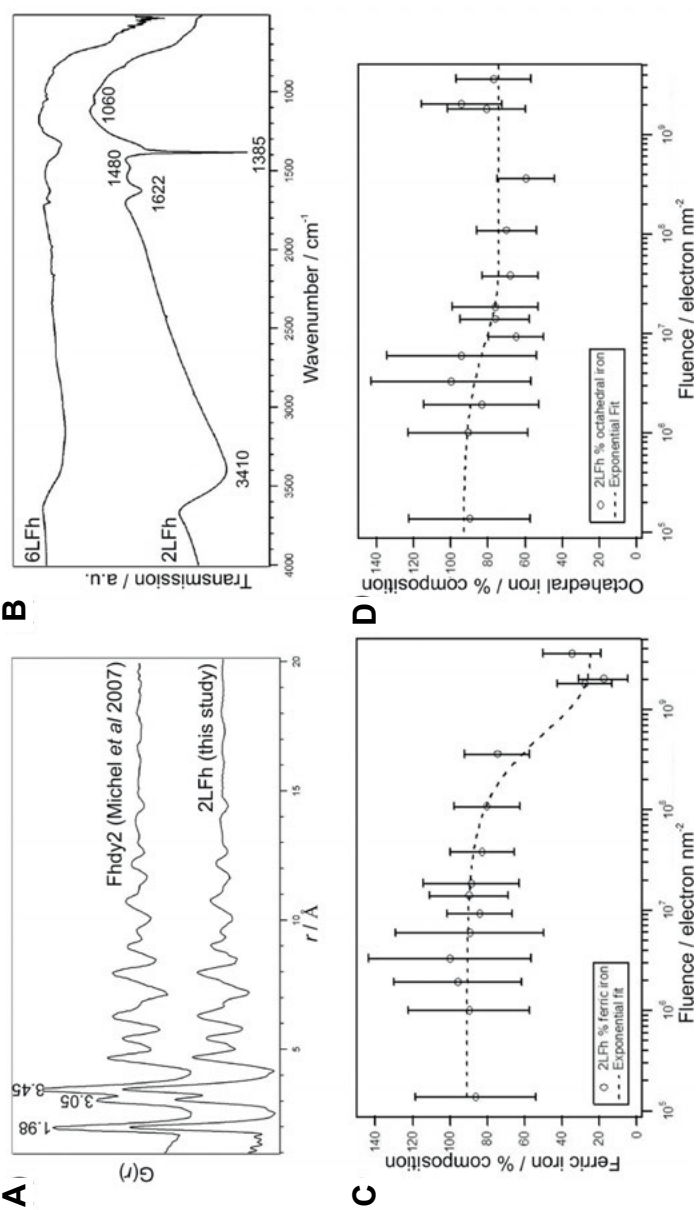


Figure 23. Characterization of 2-line ferrihydrite (after Vaughan et al. 2012). (A) Comparison of the total X-ray scattering pair distribution function data for 2-line ferrihydrite produced by Vaughan et al. (2012) to that produced by Michel et al. (2007). The atom-atom separations of the first three correlations, are labeled in units of Å. The profiles of the two samples are very similar. (B) Fourier transform infrared spectra obtained from 2 and 6-line ferrihydrite produced by Vaughan et al. (2012). The 2-line ferrihydrite has a steeper background and a sharp peak at 1385 cm^{-1} that can be attributed to nitrate. Fe-L_3 ELNES analysis of the ferric (C) and octahedral (D) iron content of 2-line ferrihydrite as a function of cumulative electron fluence, following the procedure of Pan et al. (2010). The extrapolated ferric and octahedral content at very low fluence are 91% and 93% respectively.

EBSCOhost - printed on 2/13/2023 5:26 AM via . All use subject to https://www.ebsco.com/terms-of-use

tion have been discussed including the practical usage of the techniques as applied to minerals together with the types of chemical information that can be extracted. This has been facilitated by the provision of a limited set of examples, although it should be stressed that the interested reader should consult the references within this review and further reading material for a much more complete list of potential applications. In addition, we have attempted to highlight the benefits (and in some cases complications) introduced by the use of small, highly converged, aberration corrected probes.

REFERENCES

Ahn CC (ed) (2004) Transmission EELS in Materials Science, 2nd Edition. Wiley, Weinheim

Ankudinov AL, Ravel B, Rehr JJ, Conradson SD (1998) Real space multiple scattering calculation of XANES. Phys Rev B 58:7565-7576. See also *http://leonardo.phys.washington.edu/feff/*

Bals S, Tirry W, Geurts R, Yang Z, Schryvers D (2007) High-quality sample preparation by low kV FIB thinning for analytical TEM measurements. Microsc Microanal 13:80-86

Bangert U, Harvey AJ, Schreck M, Hörmann F (2005) Extended defect related energy loss in CVD diamond revealed by spectrum imaging in a dedicated STEM. Ultramicroscopy 104:46-56

Barron V, Torrent J, Michel FM (2012) Critical evaluation of the revised akdalaite model for ferrihydrite — Discussion. Am Mineral 97:253-254

Baumeister W, Hahn M (1976) An improved method for preparing single crystal specimen supports: H_2O_2 exfoliation of vermiculite. Micron (1969) 7:247-251

Bell LA, Wilson CJL (1981) Deformation of biotite and muscovite: TEM microstructure and deformation model. Tectonophysics 78:201-228

Bonneville S, Smits MM, Brown A, Harrington J, Leake JR, Brydson R, Benning LG (2009) Plant-driven fungal weathering: Early stages of mineral alteration at the nanometer scale. Geology 37:615-618

Bonneville S, Morgan DJ, Schmalenberger A, Bray A, Brown A, Banwart SA, Benning LG (2011) Tree-mycorrhiza symbiosis accelerate mineral weathering: Evidences from nanometer-scale elemental fluxes at the hypha-mineral interface. Geochim Cosmochim Acta 75:6988-7005

Bosman M, Keast VJ, García-Muñoz JL, D'Alfonso AJ, Findlay SD, Allen LJ (2007) Two-dimensional mapping of chemical information at atomic resolution. Phys Rev Lett 99:086102

Brydson R (2001) Electron Energy-loss Spectroscopy. BIOS (now Taylor Francis), Oxford.

Brydson R (ed) (2011) Aberration-Corrected Analytical Transmission Electron Microscopy. Wiley, West Sussex

Brydson R, Sauer H, Engel W, Thomas JM, Zeitler E (1989) Coordination fingerprints in electron loss near-edge structures - determination of the local site symmetry of aluminum and beryllium in ultrafine minerals. J Chem Soc Chem Comm 1989:1010-1012, doi: 10.1039/C39890001010

Brydson R, Williams BG, Engel W, Lindner T, Muhler M, Schlogl R, Zeitler E, Thomas JM (1988) Electron energy-loss spectroscopy and the crystal-chemistry of rhodizite: near-edge structure. J Chem Soc Farad Trans 1 84:631-646

Buatier MD, Guillaume D, Wheat CG, Hervé L, Adatte T (2004) Mineralogical characterization and genesis of hydrothermal Mn oxides from the flank of the Juan the Fuca Ridge. Am Mineral 89:1807-1815.

Burke IT, Livens FR, Lloyd JR, Brown A, Law GTW, McBeth JM, Ellis B, Lawson RS, Morris K (2010) Fate of technetium in reduced sediments: comparison of direct and indirect analysis. Appl Geochem 25(2):233-241

Burke IT, Mayes WM, Peacock CL, Brown AP, Jarvis AP, Gruiz K (2012) Speciation of arsenic, chromium and vanadium in red mud samples from the Ajka spill site, Hungary. Environ Sci Technol 46:3085-3092

Calvert CC, Brown A, Brydson R (2005) Determination of the local chemistry of iron in inorganic and organic materials. J Electron Spectrosc Relat Phenom 143:173

Calvert CC, Gutzmer J, Banks DA and Rainforth WM (2008) EELS characterisation and valence determination of Mn minerals from the Kalahari Manganese Field in South Africa. J Phys Conf Ser 126:012045

Champness PE (1977) Transmission electron microscopy in earth science. Ann Rev Earth Planet Sci 5:203-226

Clark SJ, Segall MD, Pickard CJ, Hasnip PJ, Probert MJ, Refson K, Payne MC (2005) First principles methods using CASTEP. Z Kristallogr 220:567-570. See also http://www.castep.org/

Csákberényi-Malasics D, Rodriguez-Blanco JD, Rečnik A, Benning LG, Pósfai M (2012) Structural properties and transformations of precipitated FeS. Chem Geol 294-295:249-258

D'Alfonso AJ, Freitag B, Klenov D, Allen LJ (2010) Atomic-resolution chemical mapping using energy-dispersive X-ray spectroscopy. Phys Rev B 81:100101

EBSCOhost - printed on 2/13/2023 5:26 AM via . All use subject to https://www.ebsco.com/terms-of-use

Daniels H, Brydson R, Rand B, Brown A (2007) Investigating carbonization and graphitization using electron energy loss spectroscopy (EELS) in the transmission electron microscope (TEM). Philos Mag 87:4073-4092

de Groot F, Kotani A (2008) Core Level Spectroscopy of Solids. Taylor & Francis CRC press.

Drits VA, Sakharov BA, Salyn AL, Manceau A (1993) Structural model for ferrihydrite. Clay Miner 28:185-207

Drummond-Brydson RM, Sauer H, Engle W (2004) Probing Materials Chemistry Using ELNES. In: Transmission Electron Energy Loss Spectrometry in Materials Science and The EELS Atlas, 2nd Edition. Ahn CC (ed) Wiley-VCH Verlag GmbH & Co., p 223-270

Eddisford P, Brown A, Brydson R (2007) Identifying and quantifying the mechanism of electron beam induced damage and recovery in hydroxyapatite. J Phys Conf Ser 126:12008

Egerton RF (2011) Electron Energy-loss spectroscopy in the Electron Microscope (3rd Edition). Springer, New York.

Egerton RF, Li P, Malac M (2004) Radiation damage in the TEM and SEM. Micron 35:399-409

Egerton RF, McLeod R, Wang F, Malac M (2010) Basic questions related to electron-induced sputtering in the TEM. Ultramicroscopy 110:991-997

Engel W, Sauer H, Zeitler E, Brydson R, Williams BG, Thomas JM (1988) Electron energy-loss spectroscopy and the crystal-chemistry of rhodizite. 1. Instrumentation and chemical-analysis. J Chem Soc Farad Trans 1 84:617-629

Fredrickson JK, Zachara JM, Kennedy DW, Liu C, Duff MC, Hunter DB, Dohnalkova A (2002) Influence of Mn oxides on the reduction of uranium(VI) by the metal-reducing bacterium *Shewanella putrefaciens*. Geochim Cosmochim Acta 66:3247-3262

Gai PL (2007) *In situ* environmental transmission electron microscopy. *In:* Nanocharacterisation. Hutchison AI, Kirkland JL (eds) RCS Publishing, p 268-290

Garvie LAJ, Craven AJ (1994a) High-resolution parallel electron energy-loss spectroscopy of Mn $L_{2,3}$-edges in inorganic manganese compounds. Phys Chem Miner 21:191-206

Garvie LAJ, Craven AJ (1994b) Electron-beam-induced reduction of Mn4+ in manganese oxides as revealed by parallel EELS. Ultramicroscopy 54:83-92

Garvie LAJ, Craven AJ, Brydson R (1994) Use of electron energy-loss near-edge fine structure in the study of minerals. Am Mineral 79:411-425

Garvie LAJ, Zega TJ, Rez P, Buseck PR (2004) Nanometer-scale measurements of $Fe^{3+}/\Sigma Fe$ by electron energy-loss spectroscopy; a cautionary note. Am Mineral 89:1610-1616

Giannuzzi LA (ed) (2004) Introduction to Focused Ion Beams: Instrumentation, Theory, Techniques and Practice. Springer

Glatzel P, Bergmann U, Yano J, Visser H, Roblee JH, Gu W, de Groot FMF, Christou G, Pecoraro VL, Cramer SP, Yachandra VK (2004) The electronic structure of Mn in oxides, coordination complexes, and the oxygen-evolving complex of photosystem II studied by resonant inelastic X-ray scattering. J Am Chem Soc 126: 9946-9959

Goodhew PJ, Humphreys FJ, Beanland R (2001) Electron Microscopy and Analysis. Taylor and Francis

Guyodo Y, Sainctavit P, Arrio MA, Carvallo C, Penn RL, Erbs JJ, Forsberg BS, Morin G, Maillot F, Lagroix F, Bonville P, Wilhelm F, Rogalev A (2012) X-ray magnetic circular dichroism provides strong evidence for tetrahedral iron in ferrihydrite. Geochem Geophys Geosyss 13:1525-2027

Harrington R, Hausner DB, Xu W, Bhandari N, Michel FM, Brown Jr GE, Strongin DR, Parise JB (2011) Neutron pair distribution function study of two-line ferrihydrite. Environ Sci Technol 45:9883-9890

Hawkes PW (ed) (2008) Advances in Imaging and Electron Physics, Volume 153. Elsevier

Haynes BW, Law SL, Barron DC, Kramer GW, Maeda R, Magyar MJ (1985) Pacific manganese nodules: Characterization and processing. Bulletin of the Department of the Interior, Bureau if Mines 679:43

Hewett DF, Fleischer M (1960) Deposits of manganese oxides. Econ Geol 55:1-55

Hillier S, Lumsdon DG, Paterson E, Brydson R (2007) Hydrogarnet: A host phase for Cr(VI) in chromite ore processing residue (COPR) and other high pH wastes. Environ Sci Technol 41:1921-1927

Hobbs LW (1987) Radiation effects in analysis by TEM. *In*: Introduction to Analytical Electron Microscopy. Hren JJ, Goldstein JI, Joy DC (eds) Plenum Press, New York, p 399-445

Hochella MF Jr, Moore JN, Golla U, Putnis A (1999) A TEM study of samples from acid mine drainage systems: Metal-mineral association with implications for transport. Geochim Cosmochim Acta 63:3395-3406

Hofer F, Wilhem P (1993) EELS microanalysis of the elements Ca to Cu using $M_{2,3}$ edges. Ultramicroscopy 49:189-197

Hondow N, Brydson R, Brown A, Wang P, Holton MD, Brown MR, Rees P, Summers HD (2012) Quantitative characterization of nanoparticle agglomeration within biological media. J Nanopart Res 14:977-991

Huebner JS (1976) The manganese oxides – a bibliographic commentary. Rev Mineral 3:SH-1–SH-17

Hutchison JL, Kirkland AI (2007) Nanocharacterisation. Royal Society of Chemistry, London.

EBSCOhost - printed on 2/13/2023 5:26 AM via . All use subject to https://www.ebsco.com/terms-of-use

Ishitani T, Tsuboi H, Yaguchi T, Koike H (1994) Transmission electron microscope sample preparation using focused ion beam. J Electron Microsc 43:322-326

Kim B, Park C-S, Murayama M, Hochella MF Jr (2010) Discovery and characterization of silver sulfide nanoparticles in final sewage sludge products. Environ Sci Technol 44:7509-7514

Klein KL, Anderson IM, De Jonge N (2011) Transmission electron microscopy with a liquid flow cell. J Microscopy 242:117-123

Kurata H, Colliex C (1993) Electron-energy-loss core-edge structures in manganese oxides. Phys Rev B 48:2102-2108

Kurata H, Lefevre E, Colliex C, Brydson R (1993) Electron-energy-loss near-edge structures in the oxygen k-edge spectra of transition-metal oxides. Phys Rev B 47:13763-13768

Laffont L, Gibot P (2010) High resolution electron energy loss spectroscopy of manganese oxides: Application to Mn_3O_4 nano particles. Mater Charact 61:1268-1273

Leapman RD, Grunes LA (1980) White-line ratios in the 3d transition metals. Phys Rev Lett 45:397-401.

Lear G, McBeth JM, Boothman C, Gunning DJ, Ellis B, Lawson R, Morris K, Burke, IT, Bryan N, Livens FR, Lloyd JR (2010) Probing the biogeochemical behavior of technetium using a novel nuclear imaging approach. Environ Sci Technol 44:156-162

Leary R, Brydson R (2011) Chromatic aberration correction: the next step in electron microscopy. Adv Imag Elect Phys 165:73-130

Lee M (2010) Transmission electron microscopy (TEM) of earth and planetary materials: a review. Mineral Mag 74(1):1-27

Lee MR, Brown DJ, Smith CL, Hodson ME, MacKenzie M, Hellmann R (2007) Characterization of mineral surfaces using FIB and TEM: A case study of naturally weathered alkali feldspars. Am Mineral 92:1383-1394

Levard C, Reinsch BC, Michel FM, Oumahi C, Lowry GV, Brown GE Jr (2011) Sulfidation processes of PVP-coated silver nanoparticles in aqueous solution: impact on dissolution rate. Environ Sci Technol 45:5260-5266

Livi KJT, Christidis G, Árkai P, Veblen DR (2008) White mica domain formation: A model for paragonite, margarite, and muscovite formation during prograde metamorphism. Am Mineral 92:1288-1302

Livi KJT, Lafferty B, Zhu M, Zhang S, Gaillot A-C, Sparks DL (2012) Electron energy-loss safe-dose limits for manganese valence measurements in environmentally relevant manganese oxides. Environ Sci Technol 46:970-976

Loomer DB, Al TA, Weaver L, Cogswell S (2007) Manganese valence imaging in Mn minerals at the nanoscale using STEM-EELS. Am Mineral 92:72-79

Luo W, Varela M, Tao J, Pennycook SJ, Pantelides ST (2009) Electronic and crystal-field effects in the fine structure of electron energy-loss spectra of manganites. Phys Rev B 79:052405

Ma C, Fitzgerald JD, Eggleton RA, Llewellyn DJ (1998) Analytical electron microscopy in clays and other phyllosilicates: Loss of elements from a 90-nm stationary beam of 300-keV electrons. Clays Clay Miner 46:301-316

Maillot F, Morin G, Wang Y, Bonnin D, Ildefonse P, Chaneac C, Calas G (2011) New insight into the structure of nanocrystalline ferrihydrite: EXAFS evidence for tetrahedrally coordinated iron(III). Geochim Cosmochim Acta 75:2708-2720

Manceau A (2009) Evaluation of the structural model for ferrihydrite derived from real space modeling of high energy X-ray diffraction data. Clay Miner 44:19-34

Manceau A (2010) PDF analysis of ferrihydrite and the violation of Pauling's Principia. Clay Miner 45:225-228

Manceau A (2011) Critical evaluation of the revised akdalaite model for ferrihydrite. Am Mineral 96:521-533

Manceau A (2012) Critical evaluation of the revised akdalaite model for ferrihydrite—Reply. Am Mineral 97:255-256

Manceau A, Drits VA, Silvester E, Bartoli C, Lanson B (1997) Structural mechanism of Co^{2+} oxidation by the phyllomanganate buserite. Am Mineral 82:1150-1175

Mansot JL, Leone P, Euzen P, Palvadeau P (1994) Valence of manganese, in a new oxybromide compound, determined by means of electron energy loss spectroscopy. Microsc Microanal Microstruct 5:79-90

Merriman RJ, Peacor DR (1999) Very low-grade metapelites: mineralogy, microfabrics and measuring reaction progress. *In:* Low-Grade Metamorphism. Frey M, Robinson D (eds) Blackwell Science Ltd, Oxford, p 10-60

Michel FM, Ehm L, Antao SM, Lee PL, Chupas PJ, Liu G, Strongin DR, Schoonen MAA, Phillips BL, Parise JB (2007) The structure of ferrihydrite, a nanocrystalline material. Science 316:1726-1729

Michel FM, Barron V, Torrent J, Morales MP, Serna CJ, Boily J-F, Liu Q, Ambrosini A, Cismasu AC, Brown GE (2010) Ordered ferrimagnetic form of ferrihydrite reveals links among structure, composition, and magnetism. Proc Nat Acad Sci 107:2787-2792

EBSCOhost - printed on 2/13/2023 5:26 AM via . All use subject to https://www.ebsco.com/terms-of-use

Morello M, Canini A, Mattioli P, Sorge RP, Alimonti A, Bocca B, Forte G, Martorana, A, Bernardi G, Sancesario G (2008) Sub-cellular localization of manganese in the basal ganglia of normal and manganese-treated rats: An electron spectroscopy imaging and electron energy-loss spectroscopy study. NeuroToxicol 29:60-72

Murray JW, Dillard JG (1979) Oxidation of cobalt (II) adsorbed on manganese-dioxide. Geochim Cosmochim Acta 43:781-787

Obst M, Gasser P, Mavrocordatos D, Dittrich M (2005) TEM-specimen preparation of cell/mineral interfaces by focused ion beam milling. Am Mineral 90:1270-1277

Oscarson DW, Huang PM, Defosse C, Herbillon A (1981) Oxidative power of Mn(IV) and Fe(III) oxides with respect to As(III) in terrestrial and aquatic environments. Nature 291:50-51

Otten MT, Miner B, Rask JH, Buseck PR (1985) The determination of Ti, Mn and Fe oxidation states in minerals by electron energy-loss spectroscopy. Ultramicroscopy 18:285-290

Pan Y, Brown A, Brydson R, Warley A, Li A, Powell J (2006) Electron beam damage studies of synthetic 6-line ferrihydrite and ferritin molecule cores within a human liver biopsy. Micron 37:403-411

Pan YH, Brown A, Sader K, Brydson R, Gass M, Bleloch A (2008) Quantification of absolute iron content in mineral cores of cytosolic ferritin molecules in human liver. Mater Sci Technol Lond 24(6):689-694

Pan YH, Sader K, Powell J, Bleloch A, Gass M, Trinick J, Warley A, Li A, Brydson R, Brown A (2009) Atomically resolved in situ quantitative analytical electron microscopy of human hepatic ferritin mineral**.** J. Struct Biol 166(1):22-31

Pan YH, Vaughan G, Brydson R, Bleloch A, Gass M, Sader K, Brown A (2010) Electron-beam-induced reduction of Fe^{3+} in iron phosphate dihydrate, ferrihydrite, haemosiderin and ferritin as revealed by electron energy-loss spectroscopy. Ultramicroscopy 110:1020-1032

Patterson JH, Krivanek OL (1990) ELNES of 3*d* transition-metal oxides II: Variations with oxidation state and crystal structure. Ultramicroscopy 32:319-325

Peak D, Regier T (2012) Direct observation of tetrahedrally coordinated Fe(III) in ferrihydrite. Environ Sci Technol 46:3163-3168

Pearson DH, Ahn CC, Fultz B (1993) White lines and d-electron occupancies for the 3d and 4d transition metals. Phys Rev B 47:8471

Pecher K, McCubbery D, Kneedler E, Rothe J, Bargar J, Meigs G, Cox L, Nealson K, Toner B (2003) Quantitative charge state analysis of manganese biominerals in aqueous suspension using Scanning Transmission X-ray Microscopy (STXM). Geochim Cosmochim Acta 67:1089-1098

Penn RF, Banfield JF (1998) Imperfect oriented attachment: Dislocation generation in defect-free nanocrystals. Science 281:969

Post JE (1999) Manganese oxide minerals: Crystal structures and economic and environmental significance. Proc Natl Acad Sci USA 96:3447-3454

Raiswell R, Tranter M, Benning LG, Siegert M, De'ath R, Huybrechts P, Payne T (2006) Contributions from glacially derived sediment to the global iron (oxyhydr)oxide cycle: Implications for iron delivery to the oceans. Geochim Cosmochim Acta 70:2765-2780

Rancourt DG, Meunier J-F (2008) Constraints on structural models of ferrihydrite as a nanocrystalline material. Amer Mineral 93:1412-1417

Rask JH, Miner BA, Buseck PR (1987) Determination of manganese oxidation states in solids by electron energy-loss spectroscopy. Ultramicroscopy 21:321-326

Reidl T, Gemming T, Wetzig K (2006) Extraction of EELS white-line intensities of manganese compounds: Methods, accuracy, and valence sensitivity. Ultramicroscopy 106:284-291

Reimer L, Kohl H (2008) Transmission Electron Microscopy. Springer -Verlag, Berlin.

Richman JD, Livi KJT, Geyh AS (2011) A scanning transmission electron microscopy method for determining manganese composition in welding fume as a function of primary particle size. J Aerosol Sci 42:408-418

Rodriguez-Blanco JD, Shaw S, Benning LG (2008) How to make 'stable' ACC: protocol and structural characterization. Mineral Mag 72(1):283-286

Rodríguez-Blanco JD, Shaw S, Benning LG (2011) The kinetics and mechanisms of amorphous calcium carbonate (ACC) crystallization to calcite, via vaterite. Nanoscale 3:265-271

Roy S (1968) Mineralogy of different genetic types of manganese deposits. Econ Geol 63:760-786

Sader K**,** Schaffer B, Vaughan G, Brydson R, Brown A, Bleloch A (2010) Smart acquisition EELS. Ultramicroscopy 110:998-1003

Sauer H, Brydson R, Rowley PN, Engel W, Thomas JM (1993) Determination of coordinations and coordination-specific site occupancies by electron energy-loss spectroscopy - an investigation of boron oxygen compounds. Ultramicroscopy 49:198-209

Schaffer M, Schaffer B, Ramasse Q (2012) Sample preparation for atomic-resolution STEM at low voltages by FIB. Ultramicroscopy 114:62-71

Schmidt D, Livi KJT, Frey M (1999) Reaction progress in chloritic material: an electron microbeam study of the Taveyanne greywacke, Switzerland. J Metamorph Geol 17:229-241

EBSCOhost - printed on 2/13/2023 5:26 AM via . All use subject to https://www.ebsco.com/terms-of-use

Schmidt HK, Mader W (2006) Oxidation states of Mn and Fe in various compound oxide systems. Micron 37:426-432

Schwarz K, Blaha P, Madsen GKH (2002) Electronic structure calculations of solids using the WIEN2k package for material sciences. Comput Phys Commun 147:71-76. See also *http://www.wien2k.at/*

Scott AJ, Brydson R, MacKenzie M, Craven AJ (2001) A theoretical investigation of the ELNES of transition metal carbides and nitrides for the extraction of structural and bonding information. Phys Rev B 63:245105

Sparrow TG, Williams BG, Rao CNR, Thomas JM (1984) L_3/L_2 whiteline intensity ratios in the electron energy-loss spectra of 3d transition-metal oxides. Chem Phys Lett 108:547-550

Stolojan V, Walsh C, Yuan J, Brown L (1999) Calibration of the relationship between white-line intensity and valence states for the first transition series. In: Electron Microscopy and Analysis 1999: Proceedings of the Institute of Physics Electron Microscopy and Analysis Group Conference, University of Sheffield, 24-27 August 1999. Kiely CJ (ed) CRC Press. Inst Phys Conf Ser 161:235-237

Suzuki Y, Kelly SD, Kemner KM, Banfield JF (2002) Radionuclide contamination - Nanometre-size products of uranium bioreduction. Nature 419:134-134

Tobler DJ, Shaw S, Benning LG (2009) Quantification of initial steps of nucleation and growth of silica nanoparticles: an *in situ* SAXS and DLS study. Geochim Cosmochim Acta 73(18)5377-5393

Utsunomiya S, Ewing RC (2003) Application of high-angle annular dark field scanning transmission electron microscopy (HAADF-STEM), STEM-energy dispersive X-ray spectrometry (EDX), and energy-filtered (EF)-TEM to the characterization of nanoparticles in the environment. Environ Sci Technol 37:786-791

Utsunomiya S, Kersting AB, Ewing RC (2009) Groundwater nanoparticles in the far-field at the Nevada Test Site: mechanism for radionuclide transport. Environ Sci Technol 43:1293-1298

van Aken PA, Styrsa VJ, Liebscher B, Woodland AB, Redhammer GJ (1999) Microanalysis of $Fe^{3+}/\Sigma Fe$ in oxide nad silicate minerals by investigation of electron energy-loss near-edge structures (ELNES) at the Fe $M_{2,3}$ edge. Phys Chem Miner 26:584-590

van Cappellen EV, Doukhan J-C (1994) Quantitative transmission X-ray micro-analysis of ionic compounds. Ultramicroscopy 53:343-349

Van Driessche AES, Benning LG, Rodriguez-Blanco JD, Ossorio M, Bots P, García-Ruiz JM (2012) The role and implications of bassanite as a stable precursor phase to gypsum precipitation. Science 336:69-72

Varella M, Oxley MP, Luo W, Tao J, Watanabe M, Lupini AR, Pantelides ST, Pennycook SJ (2009) Atomic-resolution imaging of oxidation states in manganites. Phys Rev B 79:085117

Vaughan G, Brydson R, Brown A (2012) Characterisation of synthetic two-line ferrihydrite by electron energy loss spectroscopy. J Phys Conf Ser 371:12079

Ward MB, Kapitulčinová D, Brown AP, Heard PJ, Cherns D, Cockell CS, Hallam KR, Ragnarsdóttir KV (2013) Investigating the role of microbes in mineral weathering: Nanometer-scale characterisation of the cell-mineral interface using FIB and TEM. Micron 47:10-17; doi: *http://dx.doi.org/10.1016/j.micron.2012.12.006*

Watanabe M (2009) Atomic-resolution chemical analysis by electron energy-loss spectrometry and X-ray energy dispersive spectrometry in aberration-corrected electron microscopy. *In:* Proceedings of the 7th International Symposium on Atomic Level Characterizations for New Materials and Devices '09 (ALC'09). The 141st Committee on Microbeam Analysis of Japan Society for the Promotion of Science, p 400-405

Weyland M, Midgley PA (2007) Electron tomography. *In:* Nanocharacterisation. Hutchison AI, Kirkland JL (eds) RCS Publishing, p 184-267

White KN, Ejim AI, Walton RC, Brown AP, Jugdaohsingh R, Powell JJ, McCrohan CR (2008) Avoidance of aluminum toxicity in freshwater snails involves intracellular silicon-aluminum bio-interaction. Environ Sci Technol 42(6): 2189-2194

Whittleston RA, Stewart DI, Mortimer RJG, Tilt ZC, Brown AP, Geraki K, Burke IT (2011) Chromate reduction in Fe(II)-containing soil affected by hyperalkaline leachate from chromite ore processing residue. J Hazard Mater 194:15-23

Williams DB, Carter CB (2009) Transmission Electron Microscopy. Plenum Press, New York

Xu W, Hausner DB, Harrington R, Lee PL, Strongin DR, Parise JB (2011) Structural water in ferrihydrite and constraints this provides on possible structure models. Amer Mineral 96:513-520

Zhang S, Livi KJT, Gaillot A-C, Stone AT, Veblen DR (2010) Determination of manganese valence states in (Mn^{3+}, Mn^{4+}) minerals by electron energy-loss spectroscopy. Am Mineral 95:1741-1746

EBSCOhost - printed on 2/13/2023 5:26 AM via . All use subject to https://www.ebsco.com/terms-of-use

EBSCOhost - printed on 2/13/2023 5:26 AM via . All use subject to https://www.ebsco.com/terms-of-use

Reviews in Mineralogy & Geochemistry
Vol. 78 pp. 271-329, 2014
Copyright © Mineralogical Society of America

High Resolution Core- and Valence-Level XPS Studies of the Properties (Structural, Chemical and Bonding) of Silicate Minerals and Glasses

H.W. Nesbitt

Department of Earth Sciences
University of Western Ontario
London, Ontario N6A5B7, Canada

hwn@uwo.ca

G.M. Bancroft

Department of Chemistry
University of Western Ontario
London, Ontario N6A5B7, Canada

INTRODUCTION

Core-level and valence-level X-ray Photoelectron Spectroscopy (XPS), developed in the late 1950's and 1960's by Siegbahn and coworkers (Siegbahn et al. 1969; Carlson 1975; Barr 1993; Fadley 2010) has become an invaluable tool over the last 40 years for studying mainly the surface properties and reactivity of a wide range of minerals, predominantly oxides (for reviews, see: Heinrich and Cox 1994; Chambers 2000; Salmeron and Schlogl 2008, and references in Bancroft et al. 2009; Newburg et al. 2011), sulfides (for reviews, see Hochella 1988; Bancroft and Hyland 1990; Nesbitt 2002; Murphy and Strongin 2009) and silicates (for a review see Hochella 1988; references in Biino and Groning 1998; Oelkers 2001; Zakaznova-Herzog et al. 2008). The large majority of these studies have focused on the first few surface monolayers of the minerals because of the surface sensitivity of the technique (~2-20 monolayers for photon energies of ≤ 1486 eV (Hochella 1988; Nesbitt 2002), and in many such cases, XPS has become the technique of choice for surface studies. Silicate XPS studies generally have focused on three surface applications outlined by Hochella (1988): (1) studies of the oxidation state of near surface atoms (e.g., Fe); (2) studies of sorption reactions on mineral surfaces; and (3) studies of the alteration and weathering of mineral surfaces. Fewer reports have focused on the fourth application of Hochella (1988), the study of the bulk atomic structure and chemical state properties of minerals and glasses. This is surprising perhaps, because the large majority (usually >90 %) of XPS line intensities comes from the bulk mineral in XPS studies using the typical laboratory Al K_α X-ray sources (1486.6 eV). To emphasize this point, the surface S 2*p* peaks from the first S monolayer on a sulfide such as pyrite are barely visible in a 1486 eV Al K_α spectrum (Schaufuss et al. 1998), and one needs to employ photon energies about 50 to 100 eV greater than the binding energy of the photopeak being studied (i.e., 210 eV for the S 2*p* line at ~160 eV) to obtain maximum surface sensitivity (Nesbitt et al. 2000).

XPS studies of silicates

Considering the plethora of silicate minerals (Deer et al. 2004), there are surprisingly few XPS studies of their bulk properties, and this is more striking if compared with the number of oxide and sulfide studies. Yin et al. (1971) published the O 1*s* spectrum of an orthopyroxene;

1529-6466/14/0078-0007$10.00 http://dx.doi.org/10.2138/rmg.2014.78.7

EBSCOhost - printed on 2/13/2023 5:26 AM via . All use subject to https://www.ebsco.com/terms-of-use

but the bridging oxygen (designated BO with an O bonded to two Si atoms, Si-O-Si) and non-bridging oxygen (designated NBO with O bonded to one Si and one cation, Si-O-M, where M = Na, K, Ca etc.) signals were not resolved, and were incorrectly assigned primarily because the spectra were too broad (≥2 eV) to be interpreted properly. Although others collected additional spectra of silicate minerals at similar resolution (e.g., Hochella 1988; Hochella and Brown 1988), there appeared to be relatively little chemical or structural bulk information that could be obtained on crystalline silicates. There were reported, however, some very early conventional XPS (Mg or Al K_α sources) *valence level* spectra of amorphous thin films of SiO_2 (DiStefano and Eastman 1971a,b; Fischer et al. 1977) and these have reasonable resolution. The importance of this oxide to the electronics industry explains the emphasis (Himpsel et al. 1988). The bulk properties of some silicate glasses have been probed successfully by XPS (e.g., Bruckner et al. 1978, 1980; Veal et al. 1982; Jen and Kalinowski 1989; Matsumoto et al. 1998). They used O 1*s* core level spectra to determine ratios of bridging to non-bridging oxygen (and other properties) in primarily Na-silicate glasses. The spectra, however, were still broad (although Matsumoto's spectra had narrower peaks); and possible beam damage, which modifies the O 1*s* spectra (Sharma et al. 2001; Nesbitt et al. 2011) was apparently not recognized. Until the last few years, there had been no concerted, systematic effort to conduct XPS core level studies of the bulk chemical properties of either silicate minerals or glasses.

The disparity between the number of papers for silicates and sulfides/oxides is still greater with respect to high resolution synchrotron-based XPS studies, which today provide the best spectral resolution with either high surface sensitivity (Schaufuss et al. 1998; Mattila et al. 2004) or high bulk sensitivity (Fadley 2010), depending on the source energy used. There are now a large number of such oxide and sulfide synchrotron XPS studies (see Murphy and Strongin 2009; Newburg et al. 2011); but the **only** silicate studied with *synchrotron-based* XPS is, to our knowledge, that of thin, amorphous films of SiO_2 (Himpsel et al. 1988).

There is likewise a paucity of silicate valence band XPS studies of crystalline silicate minerals. A valence band spectrum of olivine reported in the 1980's (Al-Kadier et al. 1984) was broad, noisy and mostly featureless. Ching et al. (1983, 1985) reported XPS valence band studies of crystalline Na and Li silicate compounds and Di Pomponio et al. (1995) published valence bands of crystalline SiO_2 phases. Core level spectra are not reported by these studies. There are but a few published valence band XPS studies of Li, Na and Ca silicate glasses (e.g., Ching et al. 1983, 1985; Jiang et al. 2003). It appears that XPS studies of silicates are probably two decades behind the oxide and sulfide XPS studies.

Technical advances

Why is there a dearth of XPS studies of the bulk properties of silicate minerals? The answer likely lies with the difficulty of analyses using conventional XPS instruments. Unlike sulfides, which are mostly semiconductors, the vast majority of silicates (and oxides) are non-conductors, leading to charging and differential charging problems. These are mostly responsible for the large Si 2*p* and O 1*s* linewidths and poor line shapes for the silicates compared to XPS studies of semiconductor sulfides. Second, well characterized thin films or "perfect" cleavage surfaces, often used for non-conductor oxide studies (e.g., Chambers 2000), are usually not available for silicates. As a result, reported linewidths for silicate minerals up until 2004 have usually been ≥ 2eV (e.g., Hochella 1988; Hochella and Brown 1988; Biino and Groning 1998; Seyama et al. 1996, 2004) whereas much narrower linewidths are obtained for sulfides (less than 1 eV with laboratory sources and ~ 0.5 eV with synchrotron sources, Schaufuss et al. 1998; Nesbitt et al. 2000; Mattila et al. 2004; Murphy and Strongin 2009). Linewidths for silicate glass surfaces (usually fractured) have been somewhat better (~ 1.8 eV linewidths for O 1*s*, and as low as ~1.5 eV in Matsumoto et al. 1998) using both non-monochromatic Mg K_α and Al K_α sources (e.g., Bruckner et al. 1978, 1980; Mekki and Salim 1999) and monochromatized Al K_α based instruments (Veal et al. 1982; Sharma et al.

EBSCOhost - printed on 2/13/2023 5:26 AM via . All use subject to https://www.ebsco.com/terms-of-use

2001; Matsumoto et al. 1998). The BO and NBO O 1*s* peaks, however, remained rather poorly resolved except for the O 1*s* spectra in Matsumoto et al. (1998).

XPS has been very useful for Hochella's three surface applications noted above. But these studies used XPS "survey scans" to obtain near-surface compositions and generally did not show "narrow scan" XPS spectra from which chemical state information (e.g., oxidation states, bonding partners) is obtained. Indeed, in an early attempt to extract chemical bulk information from XPS spectra of common silicates, Adams et al. (1972) suggested that there was little chemical information available from the very broad lines. Progress in XPS resolution of non-conductor silicate minerals did not improve appreciably between 1971 and about 2000. As mentioned above, the broad O 1*s* spectrum of pyroxene obtained by Yin et al. (1971) did not resolve the bridging (BO) and non-bridging (NBO) oxygen signals and the two O signals remained unresolved in 1988 (Hochella and Brown 1988). The two signals remained only partially resolved in silicate glasses until the study of Matsumoto et al. (1998), followed by our studies (see references in Dalby et al. 2007; Nesbitt et al. 2011; Sawyer et al. 2012). In spite of the poor resolution, there were nevertheless many studies which demonstrated the potential of conventional XPS to identify changes in bonding and structure through binding energy shifts, and these shifts have been useful in distinguishing different coordination environments in silicates and aluminosilicates (e.g., Hochella 1988; Biino and Groning 1998).

Focus of the review

In this review, we focus on recent studies (since 2003) using a modern Kratos Axis Ultra XPS instrument which has minimized or eliminated differential charging of nonconductors, thereby decreasing dramatically spectral linewidths. This instrument employs a magnetic confinement system that traps a "sea" of low energy non-directional electrons above the sample, ready to neutralize positive charging on all parts of imperfect surfaces caused by electron emission after X-rays strike the sample surface. With this technical advance, it is possible to obtain much more chemical information on bulk (and surface) properties of silicate minerals and glasses derived from both core-level and valence-level spectra. Other modern XPS instruments (for example, the VG Scientific ESCALAB 250Xi) have charge compensation systems that can yield linewidths on non-conductors similar to the Kratos Axis Ultra instrument. For example, Unveren et al. (2004), showed equivalent Cr 2*p* linewidths on Cr_2O_3 powders from the two instruments. However, to our knowledge, there are **no** published reports of any high resolution spectra of **silicates** with other XPS instruments, although Alan Buckley recently demonstrated to us that the ESCALAB instrument gave the same Si 2*p* linewidths to our linewidths on a quartz sample. As a result, in this article we focus on XPS results from the Kratos instrument; and hopefully, studies using other XPS instruments will generate equivalent published results. The mineralogy and geochemistry communities have not yet been fully involved in such silicate studies, and most of the examples of silicate spectra will be from our laboratory. We trust the potential of the technique is made obvious with this review. Before focusing on recent results, some background into XPS theory and practice are summarized, with particular emphasis on optimum resolution obtainable for silicate minerals and glasses.

FUNDAMENTAL PRINCIPLES OF XPS

Photoionization and analysis depths

Fundamental principles have been well reviewed in the previous volume in this series (Hochella 1988) and in other reviews (e.g., Bancroft and Hyland 1990; Nesbitt 2002). A summary of these principles begins with a "broadscan" XPS spectrum of a bronzite orthopyroxene $[(Mg_{0.8}Fe_{0.2})_2Si_2O_6]$, which extends over a broad range of binding energies (Fig. 1). The spectrum was taken with Al K_α radiation (1486.6 eV) at the UWO Surface Science Western

EBSCOhost - printed on 2/13/2023 5:26 AM via . All use subject to https://www.ebsco.com/terms-of-use

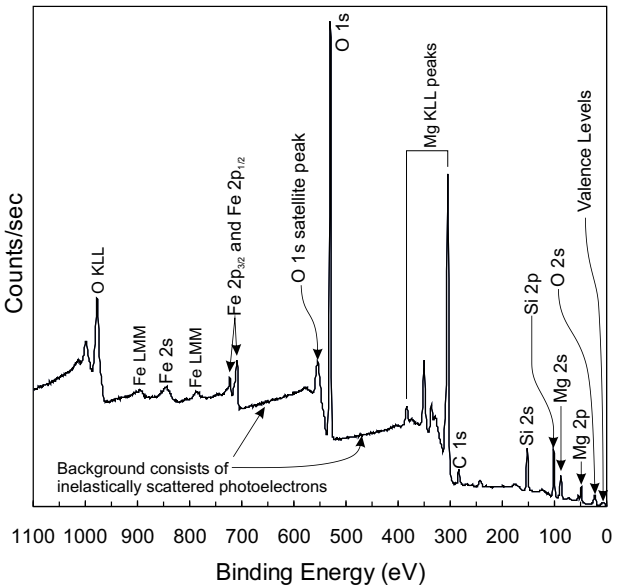


Figure 1. XPS broadscan spectrum of vacuum-fractured orthopyroxene (bronzite) with pertinent photopeaks and Auger lines labeled (original diagram with XPS data from Zakaznova-Herzog et al. 2006).

laboratory with the Kratos Axis Ultra XPS instrument. Monochromatized Al K_α radiation is directed at the sample, and the X-rays ionize the atoms from the surface to 1000's of Å depth in solid phases (Henke et al. 1993)

$$A + h\nu \rightarrow A^+ + e^- \quad (1)$$

where A is an atom in the solid which absorbs an X-ray of energy hν, A^+ is the photo-ionized product and e^- is the photoelectron produced whose kinetic energy is measured by an analyzer. With the intensity of common X-ray sources, multiply charged atoms are not formed because A^+ relaxes to A very rapidly, and before the atom is again excited by a photon. Auger electrons and X-ray photons are emitted in the relaxation process (Hochella 1988). Although the X-rays penetrate 1000's of Å into the mineral, the photoelectrons produced are strongly attenuated in the solid so that effectively all electrons collected by the analyzer are derived from about 20 to 30 monolayers (~50 Å) depth (discussed subsequently). The photoelectrons which undergo no interaction with the solid (referred to as elastically scattered electrons) have a common energy characteristic of the orbital from which they are derived, thus they produce a narrow peak in the broadscan. Those electrons which interact with the solid (mostly from deeper in the sample) lose kinetic energy, and are referred to as inelastically scattered electrons. These contribute to the background rather than to the peaks (see Fig. 1). The kinetic energy (KE) of the photoelectron of Equation (1) is given approximately by the Einstein photoelectric equation (neglecting small work function terms and charging of the sample):

$$BE = h\nu - KE \quad (2)$$

where BE is the binding energy of the electron to the nucleus, hν is the incident photon energy, and KE is the kinetic energy of the ejected photoelectron measured by a magnetic or electrostatic analyzer (see Carlson 1975; Hochella 1988; Nesbitt 2002). In practice, the KE of the photoelectrons is scanned, for example, by varying voltages on a lens or hemispherical analyzer (Hochella 1988), and the plot shown in Figure 1 is obtained by recording the number

EBSCOhost - printed on 2/13/2023 5:26 AM via . All use subject to https://www.ebsco.com/terms-of-use

of photoelectrons per unit of time as a function of KE (or BE using Eqn. 2 to convert KE to BE). Inelastically scattered electrons lose kinetic energy by interactions with the solid; thus their BE is calculated by Equation (2) to be located at a higher BE than the elastically scattered photoelectrons derived from the same orbital: hence the stronger background on the high BE side of every peak in Figure 1. High vacuum conditions are required to minimize surface contamination, and to minimize the collisions of photoelectrons with gas molecules which decrease the signal intensity (and increase the background). In principle, one can evaluate the BEs for all electrons in all elements, except H, if photons of sufficient energy can be generated.

Non-conductors and sample charging

All analyzed samples lose electrons (via photoionization and release of Auger and secondary electrons), but these are immediately replaced in conductors and semiconductors by having the sample grounded to the instrument. Grounding cannot neutralize bulk non-conductors. If not neutralized, the positive charge on the sample decreases the KE of the ejected electron and increases the BE of the photoelectron calculated from Equation (2). For imperfect surfaces, different parts of the sample may charge to different extents, leading to photoelectrons with variable KE, and to broad, often asymmetric, peaks. With the early non-monochromatized Mg K_α and Al K_α sources, the positive charge on non-conductors is partially effectively neutralized by electrons from the nearby X-ray source. Since the introduction of monochromatized sources (see Siegbahn 1971) in the 1970's (where the X-ray source is far from the sample), this positive charge build-up could not be neutralized by electrons from the X-ray source, and electron "flood" guns were introduced which directionally flood the sample with low energy electrons. This has decreased the differential charging and decreased linewidths greatly on "near-perfect" surfaces (e.g., cleavage surfaces and some polymer surfaces) because the linewidth of the monochromatized sources are ≤0.4 eV compared to 0.8 eV and 1.0 eV, respectively, for non-monochromatized Mg K_α and Al K_α sources. The linewidths of spectra collected from material with irregular surfaces (e.g., fracture surfaces and powdered samples) were not usually decreased (with a notable exception from the results of Matsumoto et al. 1998), primarily because "shadowed" parts of the surface were not neutralized by the directional electrons of the flood gun. Peaks consequently remained above 2 eV in most mineral studies (e.g., the O 1*s* spectra of silicates taken on a state-of-the-art commercial instrument; Hochella and Brown 1988; Seyama et al. 1996, 2004; Pokrovsky and Schott 2000a,b). For fractured glass samples as noted above, the O 1*s* linewidths using both types of sources still approach 2 eV (Bruckner et al. 1978, 1980; Sharma et al. 2001), with the exception of the results of Matsumoto et al. (1998) who obtained linewidths close to 1.5 eV. It is interesting to note that Stipp and Hochella (1991) deliberately used a non-monochromatic source to obtain good spectra of cleaved $CaCO_3$ because the "monochromatic source caused unstable sample charging resulting in peak broadening." The problem of differential charge neutralization on non-conductors was largely overcome by introduction of a unique charge compensation system, as evident from the study of Nesbitt et al. (2004), who showed that S 2*p* spectra of the non-conductor As_2S_3 were the same as that collected from semi-conductor sulfides. Linewidths were narrowest using the charge compensation system but the non-monochromated Mg K_α S 2*p* spectrum was much better than the spectrum collected with the monochromated Al K_α source using a conventional flood gun, thus corroborating the observation of Stipp and Hochella (1991).

The Kratos instrument employs a magnetic confinement system, where a "sea" of low energy electrons floats above the entire sample, and available to neutralize any positive charge on all parts of the sample, regardless of surface morphology (i.e., surface "highs," "lows" or "slopes"). This system has decreased differential charging greatly, leading to much narrower linewidths, and to collection of a much greater amount of chemical state information. Samples still charge in this instrument (but uniformly), and it is still critical to use a standard to calibrate BE of all spectral peaks (Hochella 1988). Furthermore, the standard must be internal to the

EBSCOhost - printed on 2/13/2023 5:26 AM via . All use subject to https://www.ebsco.com/terms-of-use

spectrum. The C 1*s* peak at 284.8 or 285.0 eV represents adventitious carbon which is universally present, and is the most common internal standard (e.g., the small C 1*s* peak of Fig. 1).

It is also important here to emphasize that the X-rays and electrons impinging on the sample can damage the sample and change relative intensities (Sharma et al. 2001; Dalby et al. 2007; Nesbitt et al. 2011). To circumvent this damage, it is necessary to take many spectra over time to monitor such changes and then extrapolate the intensities back to zero time. Multiple spectra are also important to obtain the best linewidths on non-conductors because the charge compensation may change slightly over time, resulting in peak broadening even with modern neutralization systems.

Photopeak assignments and intensities

The BEs for all orbital energy levels of all elements have been well characterized to within a few eV (Siegbahn 1969; Carlson 1975), and it is now routine to assign the peaks in spectra (e.g., Fig. 1) to atomic orbitals from which the photoelectrons originate. Each element generally produces numerous peaks. For oxygen, the O KLL Auger peak is near 1000 eV (Al K_α source), the O 1*s* peak is at ~530 eV and the O 2*s* peak is at ~ 25 eV; whereas Fe gives rise to the Fe 2*p* peaks at ~705eV and the Fe 3*p* peak at ~50 eV as well as numerous Auger peaks (Fig. 1, Fe LMM peaks). Identification of the numerous peaks produced by each element is used to confirm the element's presence. Those emitted from the Fe 2*p*, Fe 2*s*, Mg 2*s*, Mg 2*p*, Si 2*s*, Si 2*p* and C 1*s* orbitals are noted in Figure 1, along with the Fe LMM, Mg KLL and O KLL Auger peaks. A small amount of adventitious carbon is present as indicated by the C1*s* photopeak at ~285 eV and valence band photoelectrons (mostly O 2*p*) have a BE of ~ 3-10 eV.

Although these BEs of core level orbitals are characteristic of the element, they may vary somewhat (up to 10 eV) due to the nature of the bonding and the valence of the element. This shift is referred to as a "chemical shift" (Carlson 1975; Bancroft and Hu 1999). Other complications may arise. Energy levels from two elements may overlap. Weak to strong, broad Auger peaks may be observed; and their "BEs" are dependent on, and shift with, the energy of the source (Hochella 1988). Energy loss features (e.g., satellite peaks) are associated with photopeaks, but are located at somewhat higher BE than the associated photopeak and generally are much broader than the photopeak; the peak at ~550 eV is one such feature (Fig. 1) and is associated with the O 1*s* photopeak (Hochella 1988). These "peaks" accompany all photoelectron peaks in this spectrum, but may not be detectable where the photopeak is of low intensity.

Photoelectrons derived from all p, d and f orbitals nearly always give rise to spin-orbit doublets. These are due to the coupling of the orbital angular momentum (1 for a p electron) and spin angular momentum (± ½) giving a so-called $2p_{3/2}$ and $2p_{1/2}$ doublet with relative intensities given by 2:1, the multiplicity ratio (Hochella 1988; Bancroft and Hyland 1990). These two peaks are apparent in Figure 1 for the Fe 2*p* orbital at ~ 705 eV and 720 eV. The Si 2*p* and Mg 2*p* energy splittings are too small to be seen in Figure1 but will be addressed subsequently.

The peak intensities vary enormously from the very strong O 1*s* peak to the extremely weak valence band spectrum (mostly O 2*p* character). This is primarily due to different photo-ionization cross sections for the different orbitals (Fig. 2, Yeh and Lindau 1985; Bancroft and Hyland 1990). The strongest peak for a given element is normally used for surface analysis. The 1*s* level is employed for the light elements (Li, Be, B, C, N, O, F, Ne, and Na), the 2*p* electrons for Mg, Al, Si, P, S, Cl, Ar, and the first row transition elements and the 3*d* and 4*f* levels for heavy element analysis. The 1*s*, 2*p*, 3*d* and 4*f* levels usually have the highest ionization cross sections using Al K_α radiation (Fig. 2) and have the narrowest linewidths (discussed subsequently). In Figure 1, the Si 2*s* and Si 2*p* levels have similar peak heights but the Si 2*p* level has a narrower linewidth and this line usually is used to extract chemical state information for Si in silicates. The broad Auger peaks (the O KLL peak) generally are not used to extract chemical state information.

EBSCOhost - printed on 2/13/2023 5:26 AM via . All use subject to https://www.ebsco.com/terms-of-use

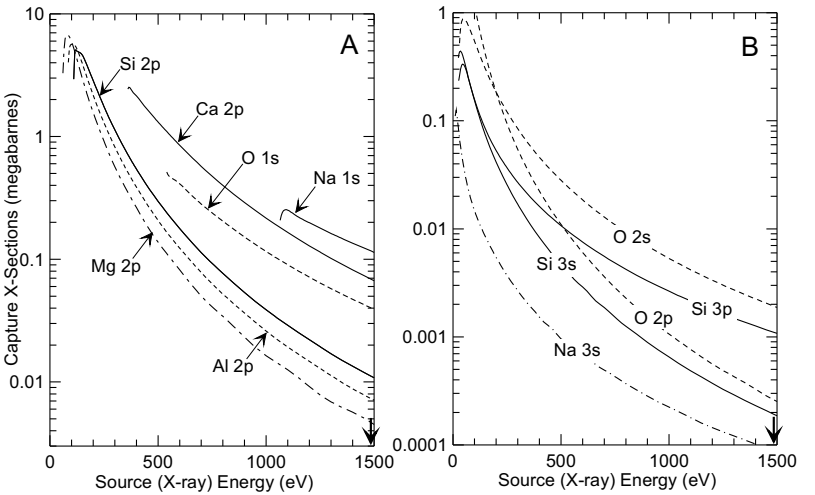


Figure 2. Photoionization cross sections as a function of photon (X-ray) source energy. A) O 1*s*, Si 2*p*, Ca 2*p*, Fe 2*p* and Mg 2*p* core level orbital: B) O 2*s*, Si 3*s*, Si 3*p*, O 2*p*, Na 3*s* valence levels (original diagram with cross-sections from Yeh and Lindau 1985).

Depth of analysis

The analysis depth varies largely with both the photon energy and the angle of take-off (Fig. 3; Tanuma et al. 1991). Photoelectrons with 1400 eV KE have an escape depth or attenuation length of around 8-10 monolayers (~20 Å), (attenuation length corresponds to 63% of the total possible intensity, I_0; Hochella 1988). Photoelectrons with just 50 eV KE, however, have an escape depth of about two monolayers (~5Å) (Fig. 3A). The so-called analysis depth, sampling depth, or information depth (corresponding to 95% of the possible intensity I_0) is three times the above depths (Tanuma et al. 1991). The angle of take-off is 90° for our spectrometer, which minimizes surface sensitivity and maximizes bulk sensitivity (Fig. 3B). An example of the huge difference in analysis depth is shown in Figure 4 for pyrite (Schaufuss et al. 1998; Nesbitt et al. 2000). A unit cell with the 011 face emphasized is shown in Figure 4A. Using a 1487 eV photon source, where the KE of S 2*p* photoelectrons is ~1320 eV, the surface contribution is represented by a very small shoulder on the low BE side of the main peak (Fig. 4B). A 260 eV photon source (~100 eV KE of S 2*p* photoelectrons), reveals two distinct surface contributions. The sum of the intensities of the surface peaks "a" and "b" is comparable to the intensity of the bulk peak "c" (Fig. 4C). Note the spin orbit doublets in these spectra have an intensity ratio of very close to 2:1.

Linewidths

The observed overall linewidth Γ_{TOT} (normally designated FWHM, the full width at half maximum) can be written to a first approximation:

$$\Gamma_{TOT}^{\ 2} = \Gamma_{instrumental}^{\ 2} + \Gamma_{solid}^{\ 2} \quad (3)$$

where:

$$\Gamma_{instrumental}^{\ 2} = \Gamma_{source}^{\ 2} + \Gamma_{electron\ analyzer}^{\ 2} \quad (4)$$

and:

$$\Gamma_{solid}^{\ 2} = \Gamma_{H}^{\ 2} + \Gamma_{extra}^{\ 2} \quad (5)$$

EBSCOhost - printed on 2/13/2023 5:26 AM via . All use subject to https://www.ebsco.com/terms-of-use

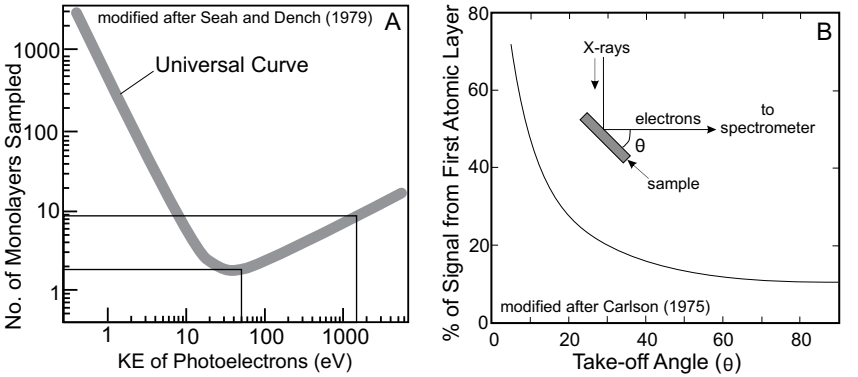


Figure 3. A) Monolayers of sample from which photoelectrons are derived (escape depth) as a function of the kinetic energy of the photoelectron emitted. The escape depth, when multiplied by 3, yields the depth from which 95% of the photoelectrons are derived in a solid (the analysis or information depth). B) the percentage of the total signal derived from the first atomic layer of Al metal, as a function of the take-off angle (Γ), which is 90° for our Kratos spectrometer.

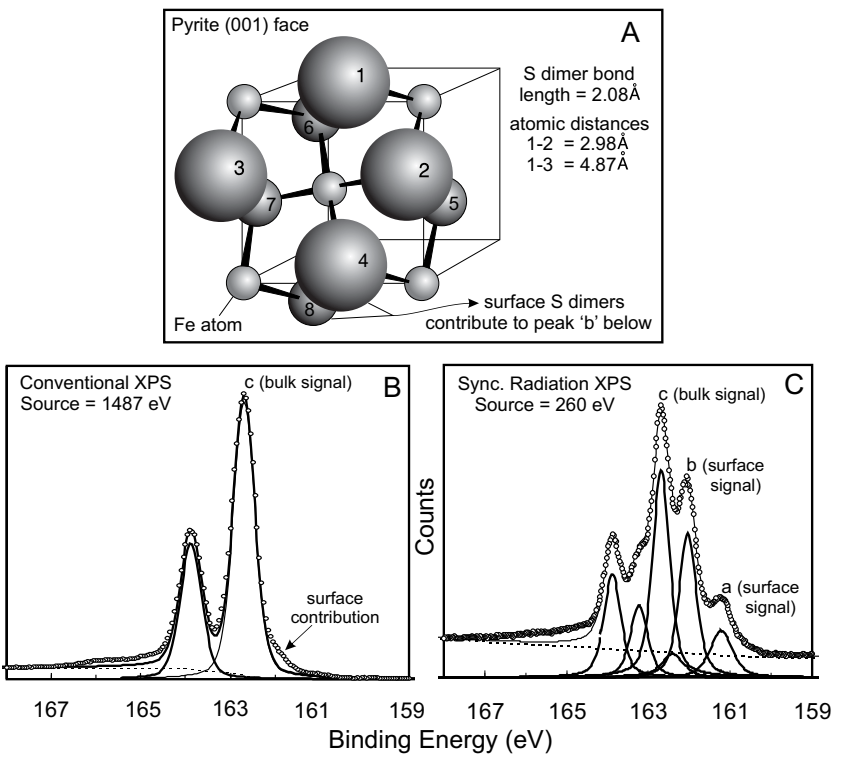


Figure 4. A) Pyrite unit cell showing arrangement of atoms associated with the 001 surface. The small spheres represent Fe atoms and they are located at the corners and centers of faces. The large (1-4) and intermediate-sized spheres (5-8) represent S atoms of dimers (3 and 7 is a dimer). Large spheres are above the 001 and the intermediate-sized spheres are below it. B) S 2*p* XPS spectrum of pyrite taken with a conventional instrument with an Al K_α source. C) S 2*p* XPS spectrum of pyrite collected using a synchrotron source tuned to maximize the surface contributions (modified after Nesbitt et al. 1998, 2000).

EBSCOhost - printed on 2/13/2023 5:26 AM via . All use subject to https://www.ebsco.com/terms-of-use

As shown by Equation (4), the two contributions to the instrumental width $\Gamma_{instrumental}$ come from the source linewidth Γ_{source} and the width from the electron analyzer $\Gamma_{electron\ analyzer}$. In early XPS studies, non-monochromatized Mg K_α and Al K_α radiation were used, with linewidths Γ_{source} of 0.8 and 1.0 eV respectively. Since the late 1970's, most instruments have employed monochromatized Al K_α radiation, with Γ_{source} of ≤0.4 eV. However, monochromatized SR can yield Γ_{source} of less than 0.1 eV. The electron linewidths, $\Gamma_{electron\ analyzer}$, on modern instruments can be as low as 0.1 eV. Thus, from Equation (4), the $\Gamma_{instrumental}$ for a laboratory monochromatized Al K_α source can be as low as ~0.3-0.4 eV, whereas $\Gamma_{instrumental}$ for a SR source can be less than 0.1 eV.

The Heisenberg lifetime (or natural lifetime) width Γ_H (Eqn. 5) is given by the Heisenberg uncertainty principle, which in units of eV becomes:

$$\Gamma_H = \frac{4.56 \times 10^{-16}}{t_{1/2}} \tag{6}$$

where $t_{1/2}$ is the half-life of the hole state (the core-ionized atom). These lifetimes are controlled by the fluorescence and Auger rates which determine how quickly electrons fill the hole created by photoionization (Carlson 1975; Bancroft and Hyland 1990; Krause and Oliver 1979; McGuire 1971). From both theoretical calculations and experiment, these natural linewidths are close to 0.1 eV for the light elements (Table 1).Two points are worth noting. First, Γ_H generally increases across a row in the periodic table (e.g., from C 1*s* to O 1*s*, or Si 2*p* to S 2*p*). Second, these widths can vary from compound to compound for a given energy level (e.g., 38 meV for SiH_4 and 79 meV for SiF_4). However, it is immediately apparent from the above discussion that $\Gamma_{instumental}$ and Γ_H are not significant contributors to the very large silicate total linewidths mentioned above (i.e., ~2 eV for non-conducting, bulk silicate solids), and Γ_{extra} must be the dominant contribution to Γ_{TOT}.

Table 1. Natural lifetime linewidths (Γ_H) in meV.

Line	Experimental Width	Theoretical Width
C 1*s*	95 (CH_4) [1], 99 (CO_2) [2], 77 (CF_4) [3]	96 [4]
O 1*s*	160 (H_2O) [5]	150 (H_2O) [6]
Si 2$p_{3/2}$	38 (SiH_4), 79 (SiF_4) [7]	32 (SiH_4), 14 (SiF_4) [7,8]
S 2$p_{3/2}$	70 (H_2S) [9]	54 (S) [10]
Ti 2$p_{3/2}$	100 [11] (Ti)	220 [10], 100 [11,12] (Ti)

References:

1) Carroll et al. (1999)
2) Carroll et al. (2000)
3) Carroll et al. (2002)
4) Coville and Thomas (1991)
5) Sankari et al. (2003)
6) Carravetta and Agren (1987)
7) Thomas et al. (2002)
8) Larkins (1994)
9) Svensson et al. (1994)
10) Krause and Oliver (1979)
11) Nyholm et al. (1981)
12) McGuire (1971)

A few spectra illustrate the above points. The very high resolution spectra of gas phase SiF_4 and $SiCl_4$ shown in Figures 5A and 5B (Thomas et al. 2002) have exceedingly narrow peaks (<0.1 eV width) for both the Si 2$p_{3/2}$ and Si 2$p_{1/2}$ levels. Nine peaks are resolved for both the 2$p_{3/2}$ and 2$p_{1/2}$ levels. These are due to so-called "final state vibrational splitting" (FSVS) the origins of which are illustrated in Figure 5C. The vibrational peaks arise when the Si-X (X=H, O, F, Cl) bond length of the final (ion or excited) state is substantially **different** from that in the corresponding ground state (Carlson 1975; Bozek et al. 1991; Bancroft and Hu 1999). The

EBSCOhost - printed on 2/13/2023 5:26 AM via . All use subject to https://www.ebsco.com/terms-of-use

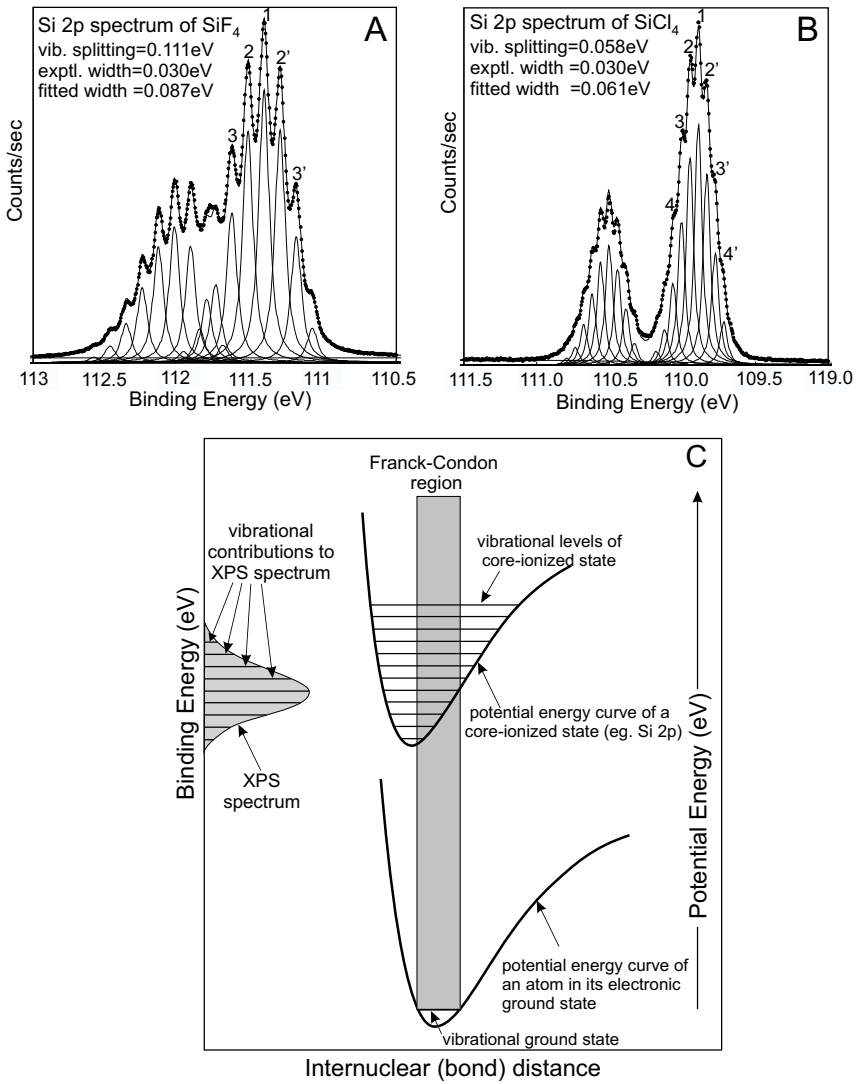


Figure 5. The experimental high resolution Si 2*p* spectra (instrumental resolution of 30 meV) of A) SiF_4 (modified after Thomas et al. 2002 and Bancroft et al. 2009) and B) $SiCl_4$ (after Thomas et al. 2002 and Bancroft et al. 2009) fit to nine vibrational peaks for both the Si 2*p* spin orbit components. C) Morse potentials for the ground state (lower curve) and the core-ionized (also final or ion) state. Horizontal lines of the ion state represent vibrational levels. Upon excitation, an electron initially in its electronic and vibrational ground state may access numerous vibrational states of the ion state giving rise to numerous vibrational peaks in an XPS spectrum.

Si atom in the lowest vibrational state ν_0 of the ground state is excited by a photoelectron to produce an excited "core-ionized state" which contains a series of vibrational states ν_1, $\nu_{2,}$..... ν_9. If the bond length in the core-ionized state (or ion state) is the same as the ground state, only one narrow peak corresponding to the transition ν_0 (ground state) $\rightarrow$ ν_0 (ion state) will be observed. However, for Si in the above molecules, the ion state Si-X bond length is ~0.04 Å smaller than the ground state Si-X bond length, a large number of ion state vibrational levels

EBSCOhost - printed on 2/13/2023 5:26 AM via . All use subject to https://www.ebsco.com/terms-of-use

will be accessed—with intensities governed by Frank-Condon factors (Carlson 1975; Bancroft and Hu 1999, their Fig. 8)—and yield a large vibrational envelope and a broad peak in the XPS spectrum. Note from the left hand side of Figure 5C that the ν_0 (ground state) $\rightarrow$ ν_0 (ion state) transition (formally the Si 2*p* BE) yields a very weak peak in the spectrum.

In the gas phase, there are only two significant contributions to the Si 2*p* individual linewidths for these tetrahedral gas phase molecules: the instrumental linewidth ($\Gamma_{instrumental}$), and the inherent Heisenberg lifetime linewidth (Γ_H). The total observed linewidth (Γ_{TOT}) is approximated well by:

$$\Gamma_{TOT}^2 = \Gamma_{instrumental}^2 + \Gamma_H^2 \quad (7)$$

For the SiF_4 spectrum (Fig. 5A), Γ_{TOT} = 87 meV and $\Gamma_{instrumental}$ = 30 meV (both observed), yielding Γ_H = 82 meV for each of the vibrational peaks, which agrees well with the experimentally derived value of 79 meV obtained by Thomas et al. (2002) through deconvolution of the SiF_4 spectrum (Fig. 5A). Thomas et al. (2002) also demonstrated that the individual vibrational peaks are Lorentzian in shape as expected when Γ_H dominates the linewidth. Taken as a group, however, the overall envelope evolves toward a Gaussian line shape as the number of vibrational contributions to the envelope increases. The XPS spectrum collected with a conventional source width of >0.3 eV cannot resolve the individual vibrational contributions, but yields instead a broad XPS spectrum (Fig. 5C, left) with the line shape having a significant Gaussian contribution. This example also illustrates that $\Gamma_{instrumental}$ = 30 meV (instrumental or experimental linewidth) adds less than 10 meV to the total linewidth above the Heisenberg linewidth Γ_H.

Solid state spectra have shown broader (usually much broader) linewidths than observed for gases. An early illustration of minimum silicate linewidths is given in the Himpsel et al. (1988) study of very thin films of SiO_2 on semiconducting Si (Fig. 6) taken with Synchrotron Radiation (SR). No charging or differential charging is expected for this Si wafer, and none has occurred, as evident from the Si $2p_{3/2}$ linewidth (FWHM) of Si metal which is close to 0.5 eV. The Si $2p_{3/2}$ linewidth from SiO_2 is, by contrast, 1.24 eV. Although broader than the Si 2*p* linewidth for Si metal, it is much narrower than the ~2 eV Si 2*p* linewidths of silicates reported in the literature (see above). More recent SRXPS studies of Si metal observed very narrow Si $2p_{3/2}$ linewidths of about 0.25 eV (Karlsson et al. 1994).

All literature up to 2004 reported Si 2*p* and O 1*s* linewidths (FWHM) for silicate minerals and glasses to be much broader than the 1.24 eV linewidth reported by Himpsel et al. (1988). As an example, Figure 7 shows the O 1*s* spectrum of a vacuum- fractured pyroxene (jadeite) with linewidths of 1.7 eV and 1.9 eV for the bridging and non-bridging peaks, respectively

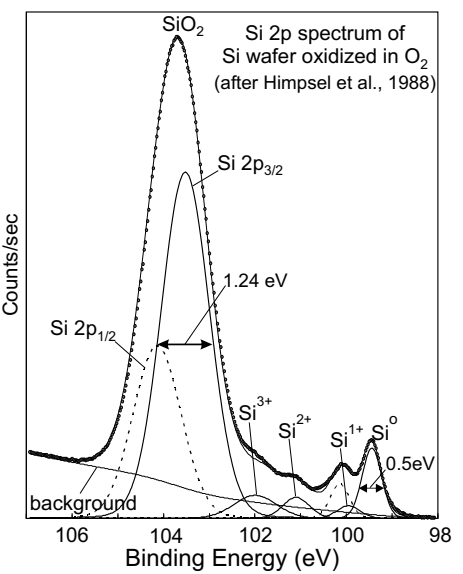


Figure 6. Si $2p_{3/2}$ core level XPS spectra of SiO_2 grown on the Si(111) face through exposure to O_2 gas. Dots represent the data of Himpsel et al. (1988). Peaks drawn with solid lines represent the Si $2p_{3/2}$ contributions and dotted lines represent the Si $2p_{1/2}$ contributions. The solid line through the data points is the fit. The Si $2p_{3/2}$ linewidth of elemental Si is about 0.5 eV and the Si $2p_{3/2}$ linewidth of SiO_2 is much broader (~1.24 eV) as a result of vibrational contributions (modified after Bancroft et al. 2009).

EBSCOhost - printed on 2/13/2023 5:26 AM via . All use subject to https://www.ebsco.com/terms-of-use

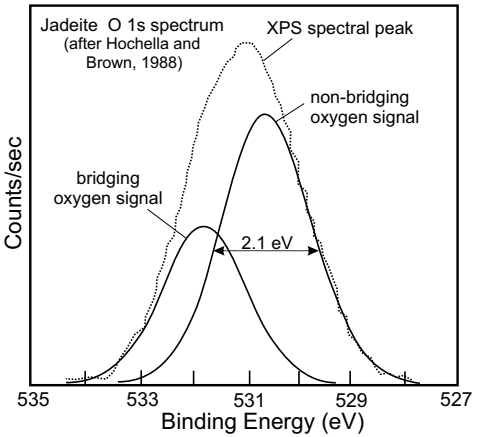


Figure 7. Observed O 1*s* spectrum of jadeite (a pyroxene of approximate composition $NaAlSi_2O_6$). Two peaks have been fitted, a bridging oxygen and non-bridging oxygen peak (modified from Hochella and Brown 1988). The peaks are very broad.

(Hochella and Brown 1988). From these spectra it is immediately apparent that $\Gamma_{instrumental}$ and Γ_H are not significant contributors to Γ_{TOT} in the pyroxene spectrum, and the Γ_{extra} term must dominate the silicate linewidths (Eqns. 3, 4, 5). To emphasize this point, note that the S 2*p* linewidths in Figure 4 are also much narrower than the silicate widths. Typically, linewidths for sulfides are < 0.5 eV when taken with a $\Gamma_{instrumental}$ of ~0.1 eV. The silicate linewidths are dominated by a contribution not common to the sulfides; and the controlling factor on the silicate linewidths must be assigned to Γ_{extra}.

What is the controlling factor for these large silicate linewidths? The major contributors are: differential charging, phonon broadening (common to all solids), and "final state" vibrational splitting/broadening (FSVB) noted for the Si gas phase molecules (Bancroft et al. 2009). Other effects such as ligand field splitting may be important in non-cubic compounds on the Si $2p_{3/2}$ level (Svensson et al. 1994; Bancroft et al. 2009), but not on the Si $2p_{1/2}$ or O 1*s* levels. To determine the factors controlling linewidths, one must first address charge broadening to obtain minimum linewidths for non-conductor silicates.

Si 2*p* AND O 1*s* LINEWIDTHS: EXPERIMENT AND THEORY

Evidence for minimum linewidths for silicates

The Kratos charge compensation system eliminates differential broadening for most insulators, as demonstrated by Nesbitt et al. (2004). They focused on the question: does one obtain the *same* linewidth on a non-conductor as on an analogous semiconductor? Previous high resolution studies on Si, Ge, Sn, P, and As gas phase molecules revealed: first, that the As 3*d* line had a rather narrow inherent lifetime linewidth (≤ 0.2 eV) with little or no vibrational broadening in the ion state (Liu et al. 1992); and second, that the total As 3*d* linewidths for the semiconductor FeAsS was < 0.4 eV using high resolution synchrotron radiation (Schaufuss et al. 2000). The As 3*d* level of two analogous minerals, the non-conductor orpiment (As_2S_3) and the semiconductor arsenopyrite (FeAsS) were studied. The charge compensation system is required only for the non-conductor; and this mineral gave a severe test of the charge compensation system because fracturing yielded a surface with an irregular fibrous texture. The resulting room temperature As 3*d* spectra for the two minerals are illustrated in Figures 8A and 8B. The As 3*d* linewidths for both minerals are identical at 0.52 eV, and the line shapes are the same. In an independent study of the As 3*d* line in As metal on the same instrument (Mark Biesinger at SSW, personal communication) also obtained an As 3*d* linewidth of 0.51 eV. These

EBSCOhost - printed on 2/13/2023 5:26 AM via . All use subject to https://www.ebsco.com/terms-of-use

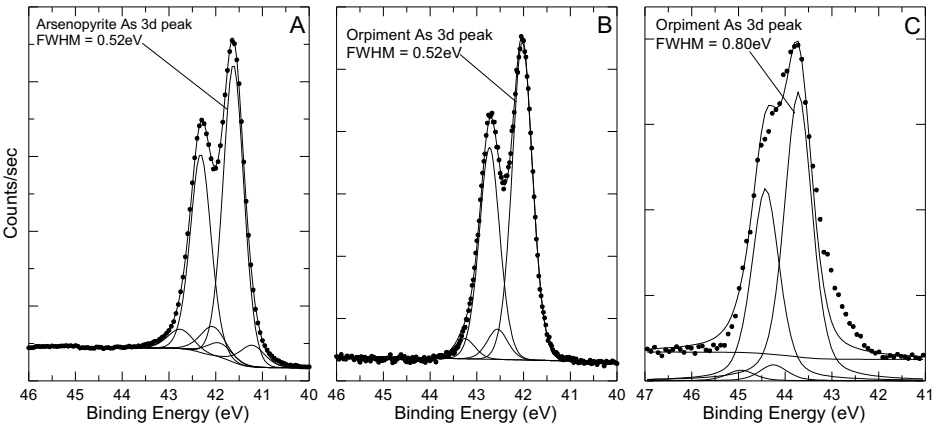


Figure 8. As 3*d* XPS spectra of A) FeAsS, and B) As_2S_3 where both spectra were taken with the Kratos XPS instrument. C) the As 3*d* spectrum taken with a SSX 100 XPS. The linewidth for the semiconductor (FeAsS) and the non-conductor (As_2S_3) are the same (modified from Nesbitt et al. 2004).

results demonstrate that the charge compensation system works extremely well, and gives no observable differential charge broadening. The effects of differential broadening are, however, apparent in Figure 8C, which shows an As 3*d* spectrum of the non-conductor (orpiment) collected with a modern SSX-100 XPS instrument using a monochromatic Al K_α source and a traditional directional flood gun. This spectrum is broader and gives unexplainable broadening in the peak tails, all a result of surface charging. The small peaks in Figures 8A and 8B are due to surface species (Schaufuss et al. 2000).

The 0.52 eV linewidths obtained for the As 3*d* spectra of orpiment and arsenopyrite are readily explained. They result primarily from the instrumental width of 0.35 eV (X-ray source contribution primarily), from ground state phonon broadening of ~0.1 eV (Leiro et al. 1998), and from the As 3*d* inherent width of ≤ 0.2 eV (Liu et al. 1992). With the As 3*d* linewidth explained, differential charging clearly has not contributed to the spectrum, and with this knowledge the silicates were addressed.

Consistent Si 2*p* and O 1*s* linewidths and line shapes have been obtained for many different silicates (Nesbitt et al. 2004; Zakaznova-Herzog et al. 2005, 2006). Their widths are about 1.0 to 1.1 eV (Si $2p_{3/2}$) and 1.2 to 1.3 (O 1*s*) eV, regardless of the type of silicate, and regardless of the orientation or nature of the surface analyzed (e.g., rough fracture surfaces or smooth cleavage surfaces), thus suggesting that charge broadening does not contribute to linewidths of these silicates. Additional evidence in now summarized.

Figures 9 and 10 show the optimized Si 2*p* and O 1*s* spectra for fractured quartz and olivine, respectively (Zakaznova-Herzog et al. 2005), along with the Mg 2*p* spectrum for olivine. As noted by Zakaznova-Herzog et al. (2005), these spectra show well-behaved peak shapes and much narrower linewidths than collected previously. In Figures 9A,B, the fit to the low binding energy part of the peak is optimized, and these two fits indicate that these peaks are slightly asymmetric as predicted by the asymmetric vibrational envelopes in Figure 5 (see also the next sections on Si 2*p* and O 1*s* vibrational contributions). If the overall fits are least-squares optimized as in Figures 9C,D and Figures 10A,B,C the fits to the Si $2p_{3/2}$ and Mg $2p_{3/2}$ peaks are very good, but the O 1*s* peaks show some small misfit in the tails at both high and low BE (Figs. 9D and 10B). For the olivine O 1*s* spectrum (Fig. 10B), the tail at high BE is especially noticeable, and this will be discussed in the ensuing section "*Silicate glasses: uncertainties in BO% from O 1s spectra*." The total, Si $2p_{3/2}$, O 1*s* and Mg $2p_{3/2}$ linewidths (Fig. 10A,B,C) are,

EBSCOhost - printed on 2/13/2023 5:26 AM via . All use subject to https://www.ebsco.com/terms-of-use

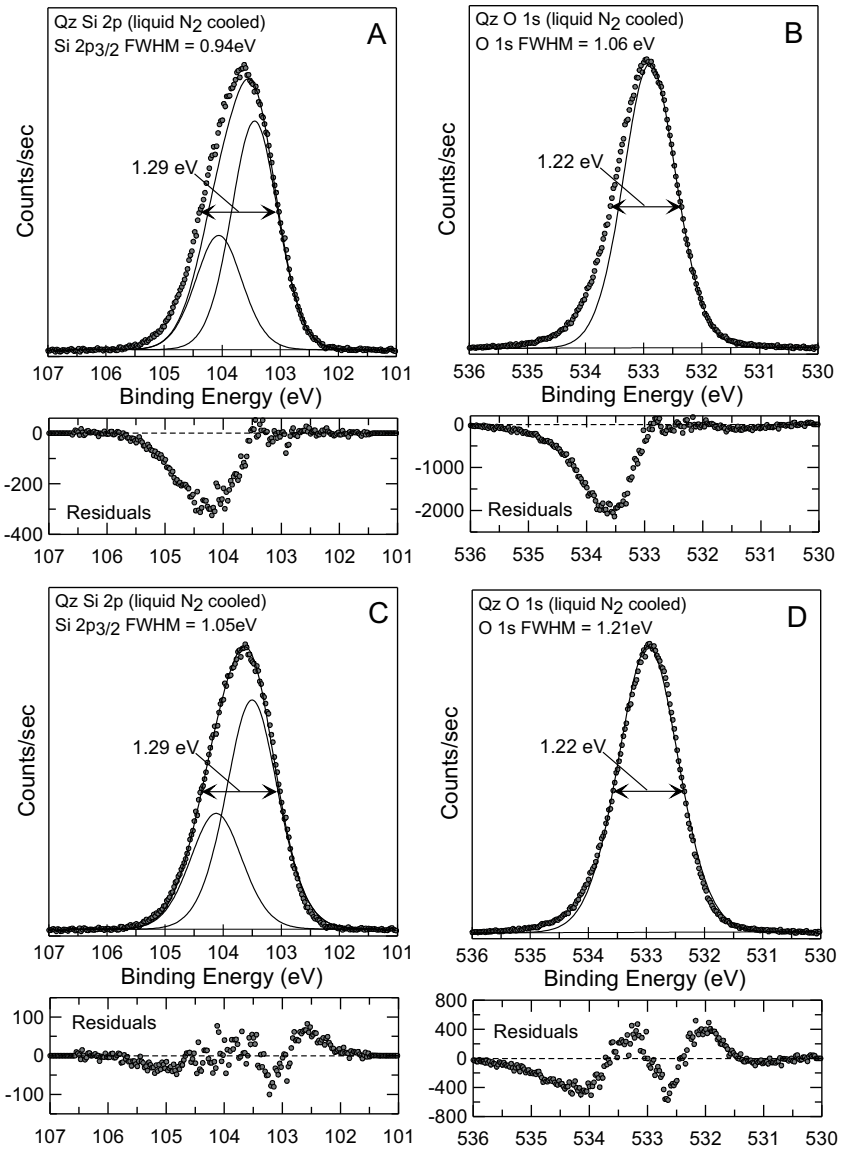


Figure 9. Core level spectra of α-quartz (modified from Zakaznova-Herzog et al. 2005). A) Si 2*p* spectrum of quartz where the Si 2*p* spin-orbit doublet is fitted to give the best fit to the low BE side of the peak. This provides the best indication of peak symmetry and is most apparent in the residuals plot below the spectrum. B) O 1*s* spectrum of quartz where the fitted peak is constrained to fit best the low binding energy side of the peak to emphasize the asymmetry of the spectrum. C) A root-mean-square best fit to the Si 2*p* spectrum of quartz. D) A root-mean-square best fit to the O 1*s* spectrum of quartz (an original Figure with data for Figs. 9A and 9B from Zakaznova-Herzog et al. 2005).

EBSCOhost - printed on 2/13/2023 5:26 AM via . All use subject to https://www.ebsco.com/terms-of-use

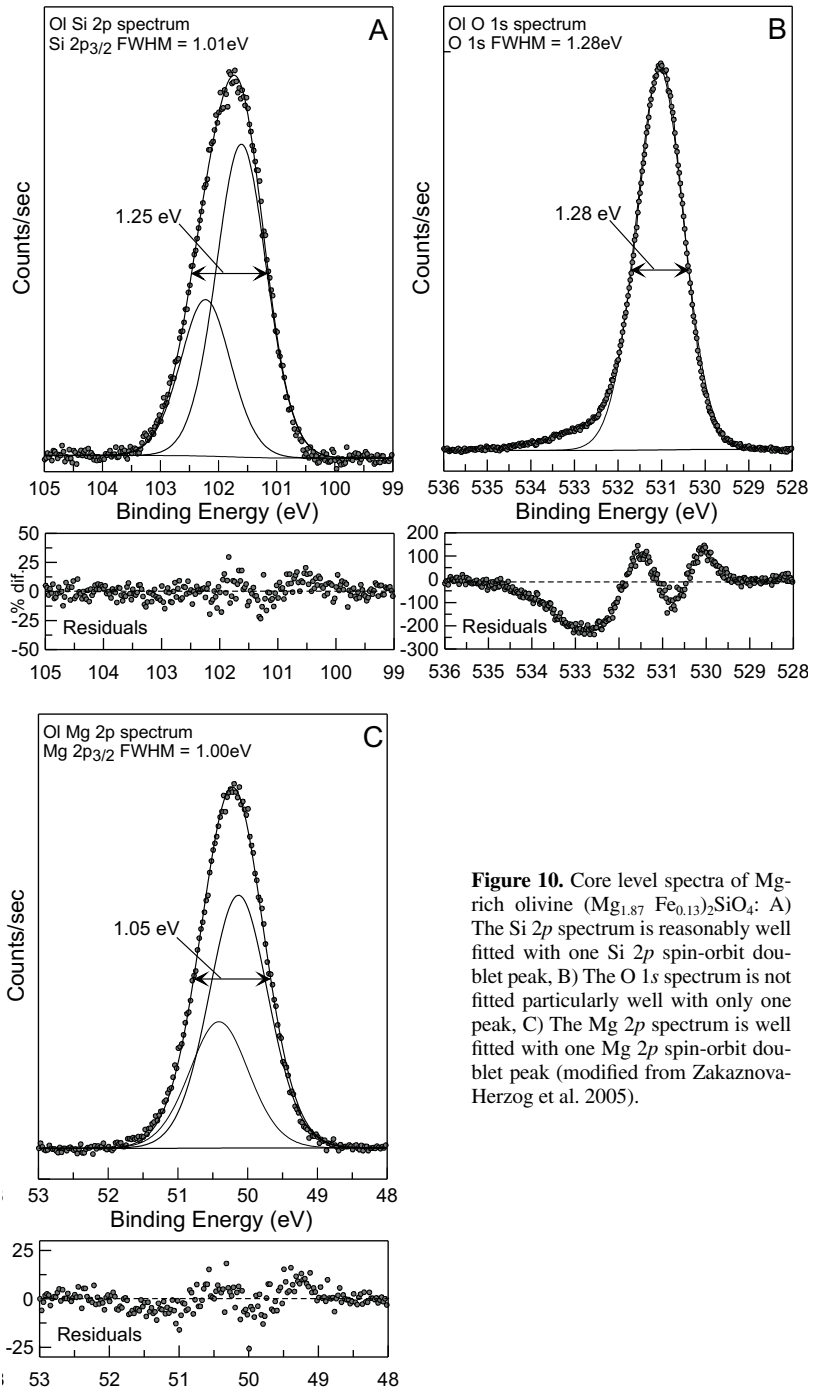


Figure 10. Core level spectra of Mg-rich olivine ($Mg_{1.87}$ $Fe_{0.13})_2SiO_4$: A) The Si 2*p* spectrum is reasonably well fitted with one Si 2*p* spin-orbit doublet peak, B) The O 1*s* spectrum is not fitted particularly well with only one peak, C) The Mg 2*p* spectrum is well fitted with one Mg 2*p* spin-orbit doublet peak (modified from Zakaznova-Herzog et al. 2005).

EBSCOhost - printed on 2/13/2023 5:26 AM via . All use subject to https://www.ebsco.com/terms-of-use

respectively, 1.01 eV, 1.00 eV and 1.28 eV. Although narrower than obtained for other XPS studies, they are nevertheless much broader than the As 3*d* widths shown in Figures 8A and 8B. As well, the O 1*s* and Si $2p_{3/2}$ silicate linewidths collected are similar, as apparent from the data of Table 2. Some of these data were obtained from our laboratory, and some are from other laboratories with the same Kratos instrument (Schindler et al. 2009a,b). As previously mentioned earlier in the "*Focus of the review*" section, an ESCALAB 250 spectrometer also obtained a similar Si 2*p* linewidth on quartz, showing that other charge compensation systems will yield equivalent results (Unveren et al. 2004). The O 1*s* linewidths for the silicates listed in Table 2 are between 1.2 and 1.3 eV, whereas the Si $2p_{3/2}$ linewidths are 0.1-0.2 eV narrower than the O 1*s* linewidths for the same silicate. Note that these are average values from several spectra, and the linewidths in Figures 9 and 10 for individual spectra can be slightly different (<0.04 eV) from the widths in Table 2. Even SiO_2 pastes and powders give similar linewidths (Shchukarev et al. 2004), although the narrowest lines generally are obtained from clean fracture surfaces of minerals. In addition, the Si $2p_{3/2}$ and O 1*s* linewidths of quartz decrease very little on going from 300 K to 120 K. Also included in Table 2 are the linewidths from three oxide phases: TiO_2, $CaCO_3$ and Cu_2O. The Ti $2p_{3/2}$ and O 1*s* linewidths for fractured TiO_2 (Nesbitt et al. unpublished) are similar to those obtained on thin, non-charging films of TiO_2 (Cheung et al. 2007), providing additional evidence that differential charge broadening has been eliminated for fractured nonconductor surfaces. The linewidths for $CaCO_3$ (Nesbitt et. al.

Table 2. O 1*s* and M 2*p* XPS linewidths (FWHM, averaged from several spectra), M-O symmetric stretching frequencies, and Debye temperatures or solid silicates and oxides.

Compound	*T* (K)	ΔE[a] (eV)	M $2p_{3/2}$[b] FWHM (eV)	O 1*s* FWHM (eV)	M-O Stretch (cm^{-1})	Θ_D (K)
α-SiO_2 (1)	120	0.4	1.09 (0.01)	1.23 (0.01)	1081	528,562
	300	0.4	1.13 (0.01)	1.23 (0.01)		
SiO_2 glass (1)	300	0.4	1.16	1.27	1095	~645
SiO_2 paste (2)	300	0.4		~1.3		
Mg_2SiO_4 (1) (3)	300	0.4	0.99 (0.03)	1.24 (0.03) 1.2 (3)	830	763,647
Uranophane(3)	300	0.4		1.1		
$CaCO_3$ (4)	300	0.4	1.03(0.03)	1.32 (0.03)	1082 (7,8)	469 (9)
TiO_2 (4)	300	0.4	0.97 (0.02)	1.10 (0.01)	628 (7,8)	775(9)
(5)	300	~0.4	0.9	1.0		
Cu_2O (6)	300	0.18	1.0	0.66	553 (7,8)	181-184 (10)

Notes & References:

a) Total Instrumental resolution (photon plus electron) in eV.

b) Errors from our work are in parentheses

1) Bancroft et al. (2009), and references for the M-O stretch and Θ_D

2) Shchukarev et al. (2004)

3) Uranophane is: $Ca(H_2O)_5[(UO_2)(SiO_3(OH)_2]$ Schindler et al. (2009a,b)

4) Nesbitt et al. unpublished results

5) Cheung et al. (2007)

6) Harmer et al. (2009). The O 1*s* spectrum was taken with an instrumental resolution of 0.18 eV at 610 eV, but the Cu 2*p* spectrum was taken at 1500 eV with an instrumental resolution of 0.35 eV

7) Gadsen (1975)

8) Farmer (1974)

9) Robie and Edwards (1966)

10) Lippman and Schneider (2000); White (1978)

EBSCOhost - printed on 2/13/2023 5:26 AM via . All use subject to https://www.ebsco.com/terms-of-use

unpublished) are much narrower than the linewidths (O 1*s* 1.8-2.0 eV; C 1*s* ~1.6 eV) obtained previously by Stipp and Hochella (1991) using a non-monochromatic Mg K_α source. Of all the samples we have run, calcite has been the most challenging to obtain minimum linewidths, and explains why Stipp and Hochella (1991) used a non-monochromatic source rather than the higher resolution monochromatic source. Much narrower O 1*s* linewidths (<0.7 eV) have been observed for heavy metal oxides such as Cu_2O (Harmer et al. 2009), and they resolved a surface chemical shift similar to those seen for the sulfides and arsenosulfides. The M-O symmetric vibrational frequencies are given in Table 2 along with Debye temperatures which are important in determining broadening from FSVB and phonon broadening (Citrin et al. 1974; Leiro et al. 1998; Bancroft et al. 2009). With these observations, we conclude that aspects other than charge broadening control the Mg 2*p*, Si $2p_{3/2}$ and O 1*s* linewidths in silicates and we now examine FSVB and phonon broadening as the important linewidth contributors.

Si 2*p* vibrational contributions

There is a contribution from phonon broadening such as characterized by Citrin et al. (1974) and Leiro et al. (1998), but Bancroft et al. (2009) have shown that it alone cannot account for the widths observed. The high resolution gas phase Si 2*p* spectrum of SiF_4 (Bozek et al. 1991; Thomas et al. 2002) and the close gas phase analogue to silicates, $Si(OCH_3)_4$, (Sutherland et al. 1992) strongly point to unresolved ion state vibrational splitting (FSVB) as the major cause of the broadening in the Si 2*p* spectrum of silicates. After consideration of all possible contributions, Bancroft et al. (2009) concluded that the major contribution is from final state vibrational splitting as seen on the gas phase Si spectra (Fig. 5). They also concluded that vibrational broadening is the major control on O 1*s* spectra of silicates and its causes and effects are now addressed.

With ejection of a core electron during photoionization, there is a change in the Si-O bond length in going from the ground state to the excited (or ion) state (see previous section on "*Linewidths*"), the changed bond length (Δr) allows access to numerous vibrational levels of the ion state (Fig. 5C). The most likely transition from a ground state to an ion state vibrational level (ground or excited) is within the Franck Condon region (Fig. 5C), which is the region close to the intersection of the ion state potential energy curve with the vibrational levels. The most probable transition yields the most intense vibrational line in an XPS spectrum (Fig. 5C). The Si-O bond length in solid SiO_2 and the gas phase analogue $Si(OCH_3)_4$ were calculated using Car-Parrinello molecular dynamics (CPMD) within the density functional theory formalism (Bancroft et al. 2009) to determine the influence of 3 dimensional network bonding in solid SiO_2 relative to gas phase analogue $Si(OCH_3)_4$. The calculated ground state Si-O bond lengths were within 0.015 Å of the experimental values for both SiO_2 and $Si(OCH_3)_4$ (Bancroft et al. 2009), and these bond lengths are virtually identical at 80 K and 300 K (within 0.003 Å). The change in Si-O bond lengths, Δr, after Si 2*p* ionization are similar for both solid state SiO_2 and molecular $Si(OCH_3)_4$, and the Si-O bond lengths decrease by 0.04 Å in *both* compounds. The Si 2*p* vibrational envelope (and overall broadening) in both gas phase and solid state compounds are consequently expected to be similar, although the Si-O symmetric stretching frequency in SiO_2 (1081 cm^{-1}) is significantly larger than for $Si(OCH_3)_4$ (842 cm^{-1}) or olivine (830 cm^{-1}). Our calculations yield Δr values similar to values obtained previously using other theoretical methods on Si gas phase molecules (Thomas et al. 2002); the calculations consequently provide reasonable results compared to other theoretical calculations on gas phase molecules. Other bond lengths in the ion state increase to compensate for the decrease in Si-O bond length.

The calculations indicate that the vibrational profile in the solid state Si 2*p* spectra should be similar to that for gaseous $Si(OCH_3)_4$. The prediction has been tested by taking the vibrational contributions to the SiF_4 and $Si(OCH_3)_4$ and assigning them our instrumental resolution of 0.4 eV rather than the 0.1 eV for the gas phase spectra in Figure 5. In addition, the original BE separations (splitting) between each vibrational peak were retained. The simulated Si 2*p* spec-

EBSCOhost - printed on 2/13/2023 5:26 AM via . All use subject to https://www.ebsco.com/terms-of-use

tra are shown in Figures 11A and B respectively for vibrational splitting of 895 cm^{-1} (0.111 eV) (Fig. 11A) and 992 cm^{-1} (0.123 eV) (Fig. 11B). As expected, the vibrational splittings are no longer resolved in the simulations, and even the spin orbit splitting is indistinct. The $Si(OCH_3)_4$ spectrum, which should be a reasonable analogue for quartz and olivine Si 2*p* spectra, is indeed qualitatively similar to the Si 2*p* spectra of these solids (Figs. 9A, 10A). Specifically, the overall peak shape is asymmetric but the Si $2p_{1/2}$ contribution is not resolved due to the breadth of the vibrational peaks. The total linewidth of the simulated spectrum for $Si(OCH_3)_4$ is 0.80 eV (Fig. 11B), which approaches the Si $2p_{3/2}$ total linewidths observed for quartz and olivine (1.1 eV, Table 2).

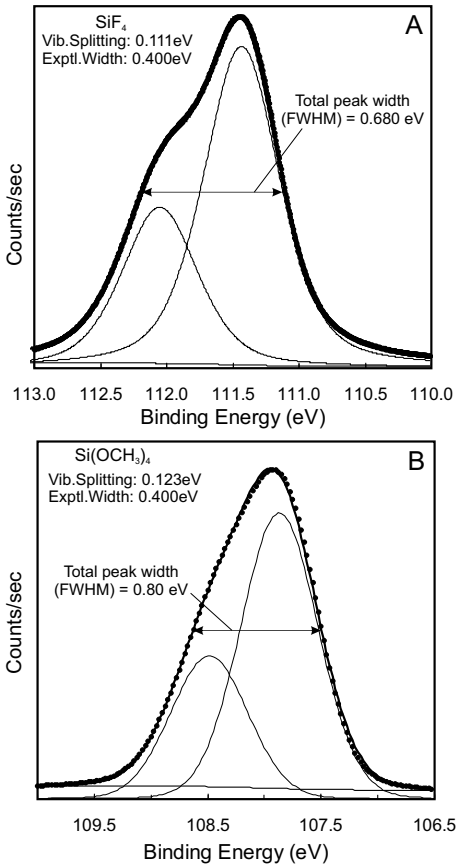


Figure 11. Simulated spectra of A) SiF_4 and B) $Si(OCH_3)_4$ using the Kratos Ultra Axis instrumental (or experimental) resolution of 0.4 eV. Each *vibrational* peak of SiF_4 and $Si(OCH_3)_4$ shown in Figure 5 was assigned a linewidth of 0.4 eV (the instrumental linewidth). The individual peaks then were summed to obtain the simulated Si 2*p* spectra of SiF_4 and $Si(OCH_3)_4$. The vibrational splitting is the energy separating each vibrational peak. The vibrational contributions to Si $2p_{1/2}$ signal are half the intensity of the associated vibrational contribution of the Si $2p_{3/2}$ peak, have the same FWHM and are located at 0.617 eV greater binding energy (Sutherland et al. 1992) than the associated vibrational peak in the Si $2p_{3/2}$ peak (modified from Bancroft et al. 2009).

"Broadened" Si 2*p* spectra were again simulated for the three gas phase species, SiF_4, $SiCl_4$ and $Si(OCH_3)_4$ by varying the vibrational peak widths from 0.15 eV (e.g., a synchrotron source width) to 0.8 eV (Mg K_α source width), and then measuring the overall peak width of the Si $2p_{3/2}$ signal. The variation in Si $2p_{3/2}$ linewidths for the different vibrational peak widths is provided in Figure 12, along with a linear best fit. The effect of line shape was investigated by varying the vibrational peak shape from 85% Lorentzian (in the original spectrum) to 50% Lorentzian (because of the large expected Gaussian component from the 0.4 eV electron/photon contributions). The changes had little effect on the total Si $2p_{3/2}$ linewidths; the linewidths in Figure 11, for example, decreased by less than 0.02 eV from 85% to 50% Lorentzian peak shape.

Four observations are apparent from Figure 12. First, the overall linewidths vary linearly with the individual peak width (instrumental, phonon, etc., see below) of each vibrational peak. Second, the Si $2p_{3/2}$ width increases markedly with the vibrational frequency for similar vibrational envelopes. Thus the linewidths at an individual peak width with an instrumental resolution of 0.4 eV (vertical dashed line) are: 0.50 eV, 0.68 eV and 0.80 eV for $SiCl_4$, SiF_4, and $Si(OCH_3)_4$, respectively. Third, the slopes of these lines (see equations in Fig.12) decrease from 0.82 eV for $SiCl_4$ to 0.74 eV for SiF_4, to 0.62 eV for $Si(OCH_3)_4$, as the vibrational splitting in these molecules increases. Fourth, the Si $2p_{3/2}$ width approaches the single vibrational peak width at large values for a (single) vibrational peak width. At a (single) vibrational peak width of 0.8 eV, for example, the

EBSCOhost - printed on 2/13/2023 5:26 AM via . All use subject to https://www.ebsco.com/terms-of-use

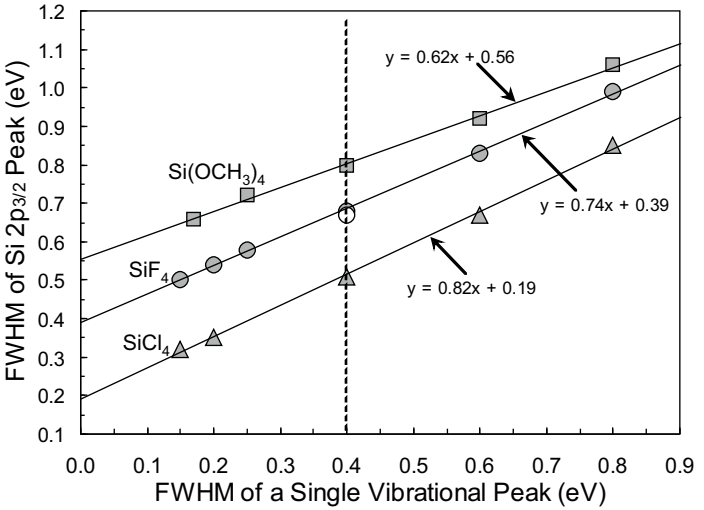


Figure 12. The full width at half maximum (FWHM) of the Si $2p_{3/2}$ peak obtained by our spectral simulations are shown for the three gas phase Si 2*p* spectra. An instrumental linewidth of 0.4 eV (the Kratos instrumental linewidth) was used for all simulations. From top to bottom, the simulations are for $Si(OCH_3)_4$, SiF_4 and $SiCl_4$. The linear relationship is indicated by the least squares fits for all three molecules. The vertical dashed line gives the expected total width of the Si $2p_{3/2}$ peak for the three different molecules (modified from Bancroft et al. 2009).

Si $2p_{3/2}$ linewidth is 0.83 eV for $SiCl_4$. From the relations shown in Figure 12, one would expect progressively narrower linewidths for TiO_2 and Cu_2O because the M-O stretching frequencies are substantially smaller than for the silicates and carbonate (Table 2).

O 1*s* vibrational contributions

The O 1*s* linewidth is similarly controlled by vibrational contributions. The changes in O-Si bond length (Δr) after O 1*s* ionization for both quartz and $Si(OCH_3)_4$ are similar, with the O-Si bond length *increasing* by 0.05-0.06 Å in *both* compounds (Bancroft et al. 2009). As for Si 2*p* vibrational envelopes, O 1*s* vibrational envelopes for the two compounds should be similar. Furthermore, a larger vibrational envelope and broader overall linewidth is expected for O 1*s* spectra compared to Si 2*p* spectra because of the larger Δr on O 1*s* ionization (Fig. 5C). The O 1*s* linewidths (e.g., 1.22 eV in Fig. 9D, 1.23 eV in Table 2) are always slightly broader than the component Si $2p_{3/2}$ line (e.g., 1.05 eV in Fig. 9C, 1.09 eV in Table 2), indicating that the number of component vibrational peaks is probably larger for O 1*s* than for the Si 2*p* spectra. Similar $|\Delta r|$ values for both the gas phase and solid state compounds implies that relaxation upon ionization is similar in both states of matter; and the Si 2*p* vibrational broadening effects observed in $Si(OCH_3)_4$ gas should also be observed in solid silicates. Also, the O 1*s* peak is expected to be slightly asymmetric as seen in the Si 2*p* gas phase spectra (Fig. 5), and as discussed above for Figures 9B,D and 10B. Indeed, Shchukarev et al. (2004) show a two peak fit to their O 1*s* spectra of SiO_2 pastes because of this asymmetry (Bancroft et al. 2009).

Effects of phonon broadening

The simulated Si $2p_{3/2}$ linewidth of 0.8 eV is narrower than the observed linewidth of 1.1 eV for quartz (Fig. 9A) or 1.0 eV for olivine (Fig. 10A) and as discussed in Bancroft et al. (2009), phonon broadening largely accounts for this difference. Phonon broadening also is responsible for the decrease in the Si $2p_{3/2}$ linewidth (1.13 eV to 1.09 eV in Table 2) as the temperature decreases from 300 K (T_1) to 120 K (T_2) respectively.

EBSCOhost - printed on 2/13/2023 5:26 AM via . All use subject to https://www.ebsco.com/terms-of-use

The phonon linewidth Γ_{PB} (0) (T = 0 K) can be estimated using the approximate formula (Leiro et al. 1998):

$$\Gamma_{PB}{}^2(T_1) - \Gamma_{PB}{}^2(T_2) = \frac{8}{3}\Gamma_{PB}{}^2(0)\frac{(T_1 - T_2)}{\Theta_D} \quad (8)$$

Taking the Θ_D = 528 K (Table 1) for α-quartz, and substituting the above values into Equation (8) yields a $\Gamma_{PB}(0)$ value of 0.39 eV (Bancroft et al. 2009) which probably is an upper limit. Thus the vibrational and phonon broadening are the major contributors to the silicate linewidths. Also, the low Θ_D value for Cu_2O (Table 2) is probably the major factor in the small O 1*s* linewidth for this compound.

To conclude, ***all*** silicate XPS spectra are expected (predicted) to give similar linewidths, with Si $2p_{3/2}$ and O 1*s* spectra having linewidths of ~1.05 eV and ~1.25 eV respectively, which are confirmed subsequently. In addition, a weak asymmetry (Fig. 9A,B) is often apparent in these spectra. Other lines (e.g., Mg 2*p*, Ca 2*p*) in silicates are usually of width similar to the O 1*s* linewidth, although Na 1*s* lines tend to be somewhat broader, as expected by the core equivalent model (Zakaznova-Herzog et al. 2006).

Experimental and fitting considerations

Minimum linewidths can be readily obtained only on fractured or cleaved surfaces, with a relatively clean, high vacuum system. High quality Si 2*p* and O 1*s* individual spectra with high resolution (total instrumental resolution of 0.35 eV), small spot size (300 μm), excellent statistics, and a large number of points (step sizes of 25-50 meV, dwell time per point of 100 msec) can be acquired in a few minutes with the Kratos instrument. Deposition of adventitious C on the sample can broaden the peaks significantly; but our spectra usually show a very small C1*s* peak (Fig. 1). As mentioned previously, Shchukarev et al. (2004) obtained minimum linewidths on SiO_2 slurries; but our limited experience with fine powders indicates that minimum linewidths are more difficult to obtain with powders than from samples fractured or cleaved in the vacuum of the introduction chamber. Also, spectra should be collected as quickly as practicable, and collection of narrow scans in cycles is required to document changes to spectra over time. In this regard, and although *differential* charging appears to be eliminated in our spectra, very small changes in overall sample charging still occurs in the Kratos instrument, and spectra collected over long periods will usually be slightly broader than those collected over short periods. By collecting spectra in 3 to 5 cycles, changes to the peak shape and BE can be monitored. If counting statistics are a concern the cycles can be added, ensuring that there is compensation of shifts in BE of the peak. For glasses, the ensuing section shows that beam damage is also important, and this cycling is critical to get accurate BO:NBO values.

Spectral fitting also needs discussion. Symmetric composite Lorentzian/Gaussian functions using a Shirley background (Shirley 1972) to all core level spectra of silicates and sulfides has been used in this laboratory (CasaXPS software, available from http//www.casaxps.com). The background is usually slightly higher at low BE than at high BE (see Fig. 1), and normally has a very small effect (<1%) on the calculated peak areas. There are a few situations (not found in our studies of silicates) where the background is higher at low BE; but, in any case, it is critical to use a consistent method for fitting the background for a given set of spectra. The peak function normally used is 30% Lorentzian/70% Gaussian (Nesbitt et al. 2004; Zakaznova-Herzog et al. 2005, 2006, 2008; Schindler et al. 2009b) which gives a good fit to sulfide and silicate spectra. What is the best function to fit these spectra, and is it important for area measurements? Fits to the olivine and quartz spectra in Figures 9 and 10 are nearly as good with 50% Lorentzian character. Generally, increased Lorentzian character yields slightly decreased linewidths. For example, if 50% Lorentzian is used in the quartz spectrum in Figure 9, the O 1*s* linewidths decrease to 1.22 eV from 1.25 eV, with the area of the peak increasing by 1%. The RMS residuals are identical for the 30% and 50% fits; the best statistical fit may not be apparent. The

EBSCOhost - printed on 2/13/2023 5:26 AM via . All use subject to https://www.ebsco.com/terms-of-use

small asymmetries seen on the O 1*s* peaks in quartz (Fig. 9B,D) do not affect the overall O 1*s* area appreciably. As shown in Figure 9D, the positive and negative residuals cancel each other out in the area determination- as they should for a least squares fit. The effect of peak shape and asymmetry on the determination of BO% in glasses will be discussed further in the section "*Silicate glasses: uncertainties in BO% from O 1s spectra*."

Chemical shifts in silicates

The Si 2*p* and O 1*s* BEs vary considerably depending on the chemical environment of Si or O, as shown in Figures 5, 6 and 7. For example, in Figure 5, the Si 2*p* BE in SiF_4 is about 1.5 eV larger than in $SiCl_4$; and in Figure 6, the Si 2*p* BE increases by about 4 eV from Si to SiO_2, with the intermediate Si-O species giving Si 2*p* BE between Si and SiO_2. The O 1*s* BE is also sensitive to the neighboring atoms around the O as shown in Figure 7. The bridging O (Si-O-Si) has a higher BE than the non-bridging O (Si-O-Na). These shifts in BE are referred to as chemical shifts, and were recognized and rationalized in the initial XPS studies of Siegbahn et al. (1969).

How do these shifts arise? Qualitatively, the Si 2*p* BE increases from $SiCl_4$ to SiF_4 or from Si to SiO_2 because the electronegative F or O withdraws more Si 3*p* (and Si 3*s*) valence electrons than Cl or Si respectively. These Si 3*p* valence electrons shield (to a very small amount) the core Si 2*p* electrons. Thus, a greater removal of Si 3*p* electron density (in SiF_4 or SiO_2) results in less shielding of the Si 2*p* electrons than in $SiCl_4$ or Si respectively, the Si 2*p* electrons are drawn closer to the Si nucleus, and the Si 2*p* BE increases from $SiCl_4$ to SiF_4 or Si to SiO_2. Considering the difference (close to 2 eV) in O 1*s* BE between the BO and NBO oxygen atoms (Fig. 7), the replacement of Si in BO with the electropositive Na in NBO leads to a more negative O in NBO and a smaller O 1*s* BE for NBO. Similarly, the Si 2*p* BE also becomes smaller (also by close to 2 eV) when the electropositive Mg in olivine replaces Si in quartz (Figs. 9C and 10A). Some of the electrons from the Na or Mg reside both on the O and the Si via the covalent Si-O bond.

Siegbahn et al. (1969) formulated a simple electrostatic model to explain chemical shifts (Bancroft and Hu 1999). Considering that the core electron density lies near the center of an electrostatic sphere having a radius given by the mean radius $\langle r_v \rangle$ of a valence electron charge q_v, then the potential felt by the core electrons (V_i) inside this sphere is given by $q_v e^2/r_v$. The chemical shift from an atom to a compound, or one compound to another is then given by:

$$\Delta V_i = \frac{\Delta q_v e^2}{r_v} \tag{9}$$

assuming that $\langle 1/r_v \rangle$ is a constant for a given element. Carlson and coworkers (see Carlson 1975, Table 5.7) tabulated $\langle 1/r_v \rangle$, and $\langle e^2/r_v \rangle$ in eV for a change in electron charge (Δq_v) of 1. For example, the ΔV_i values (for $\Delta q_v = 1$) for the valence orbitals of interest to us are: O 2*p* (31.6 eV), Na 3*s* (8.8 eV), Si 3*p* (13.8 eV), K 4*s* (7.0 eV). Thus, complete removal of one 3*s* electron on going from a Na atom to a Na^+ ion should give a chemical shift of 8.8 eV. We might expect the O 1*s* chemical shifts to be large because of the large ΔV_i value above. However, one electron from Na is donated to the 6 coordinating O atoms which will decrease greatly the expected O 1*s* chemical shift.

However, there are two other significant contributions to the chemical shift, both of which decrease the above expected values by about 50%. These are: first, a point charge term from the ionic charges surrounding the atom of interest (e.g., the Na+ surrounding the O in the NBO linkage which causes an *increase* in BE which counteracts the decrease in BE from the addition of 2*p* electrons considered above); and second, a relaxation energy shift ΔR due to differences in relaxation of the Si 2*p*, Na 1*s* or O 1*s* electrons after photoionization. This ΔR can be determined by obtaining experimentally the shifts in Auger lines together with the BE shifts (Aksela et al. 1985), and is much smaller than the electrostatic terms. However, the point charge

EBSCOhost - printed on 2/13/2023 5:26 AM via . All use subject to https://www.ebsco.com/terms-of-use

term can be 50% of the Equation (9) term (Bancroft and Hu 1999), but the trend is *always* determined by Equation (9) (i.e., lower electron density on an atom results in a larger BE). Because it is not simple to calculate accurate charges on all atoms in silicates, we use Equation (9) to discuss qualitatively the trends in electron density on the Si and O atoms for the O 1*s* and Si 2*p* BE differences above (~2 eV) for BO (Si-O-Si) in SiO_2, and a NBO (Si-O-M) (M = Mg in olivine or Na, K in silicate glasses).

The large $<1/r_v>$ value for the O 2*p* valence electrons (31.6 eV) versus the Si 3*p* valence electrons (13.8 eV) would initially lead us to predict that the O 1*s* chemical shift should be much larger than the Si 2*p* chemical shift. There are two effects that alter this first impression greatly. First, going from BO to NBO, four O atoms will donate the extra electron density from the M atom to the covalently bound Si (all silicates have the SiO_4 moiety), and so the Si 2*p* shift would be 4 times the O 1*s* shift atom *if* the Si and O share the electron density from M equally. With the above $<1/r_v>$ values for Si 3*p* and O 2*p*, the Si 2*p* shift would then be larger than the O 1*s* shift [(4×13.8)/31.6 = 1.75)]. The second effect—the more electronegative O will retain much more electron density from M than the Si—will decrease this ratio considerably to closer to 1.

Surface core-level shifts in silicates

Discussion of the O 1*s* spectra in Figures 9, 10 and 11, did not include consideration of contributions from surface core-level shifts in silicates (e.g., as seen in Fig. 4C for the S 2*p* spectrum of FeS_2) and comment is warranted. Effects of surface chemical shifts on determination of BO% in glasses are considered in the later section on "*Silicate glasses: uncertainties in BO% from O 1s spectra*." Surface core level shifts are best observed using low photoelectron KE (usually about 50 eV for maximum surface sensitivity) with synchrotron radiation on faces of metals (Hufner 1996), and semiconductors. Eastman (1980) first observed core level shifts using a high resolution synchrotron source. He observed surface peaks in GaAs and GaSb spectra located at about 0.3 eV *lower* binding energy on the As 3*d* and Sb 4*d* signals, and at about 0.3 eV *higher* BE on the Ga signal. As explanation of the surface peaks, when the Ga-As or Ga-Sb bond is broken at the surface, the bonding electrons migrate to the more electronegative As or Sb, making them more negative than the fully coordinated bulk atoms, thus resulting in a surface peak located at lower BE than the bulk As 3*d* or Sb 4*d* peak. For Ga, the converse is true, yielding a positive BE shift for the surface peak compared with the bulk Ga peak. Only one surface peak is seen in all metals and binary semiconductors. For FeS_2 (Nesbitt et al. 1998; Schaufuss et al. 1998) the S 2*p* spectrum shows two surface species (with a possible third as seen by Mattila et al. 2004), a surface Fe S-S (shifted 0.65 eV from the bulk peak); and a broader surface $Fe^{3+}S$ (shifted 1.4 eV from the bulk peak), where the S-S bond has been broken, and the Fe^{2+} is oxidized to Fe^{3+} when the S-S is reduced to S. As noted earlier in the "*Depth of analysis*" section, at 1486.6 eV photon energies surface peaks become very weak (Fig. 4B, surface contribution ≤ 8% of the bulk peak) whereas these surface peaks approach 50% of the bulk peak intensity at ~260 eV (Fig. 4C, about 100 eV above the spectral line energy). As for GaAs and GaSb, Harmer and Nesbitt (2004) have shown that the surface chemical shift on the cation Fe in both FeS_2 and $FeAs_2$ analogues is positive and comparable in magnitude to the S 2*p* shifts.

There have been no surface chemical shifts observed for silicates. The analysis depth for SiO_2, was measured at 29 Å (Lu et al. 1995). This is slightly greater than those for sulfides (e.g., FeS at 22 Å, Mycroft et al. 1995) so that surface core level peaks should be somewhat weaker in silicates than sulfides (<8% of the bulk peak). Harmer et al. (2009) recently observed a surface chemical shift (a large value of 0.95 eV) on the O 1*s* level in Cu_2O. Somewhat surprisingly, the surface peak had a much lower intensity than expected. The surface contribution was 9% of the bulk peak at 610 eV photon energy (where O 1*s* photoelectrons carry ~70 eV KE) and this decreased to 6% at 800 eV photon energy (O 1*s* electron carry ~270 eV KE), indicating a decrease of ~ 1.5% per 100 eV KE increase. At 1486 eV photon energy the KE of the

EBSCOhost - printed on 2/13/2023 5:26 AM via . All use subject to https://www.ebsco.com/terms-of-use

photoelectrons is ~ 950 eV so that and the intensity of the surface peaks should be very small, and we estimate the surface peak should be 2% (or less) of the bulk peak (Fig. 3A, Nesbitt et al. 2011). There is also a possible surface related peak at high BE on the O 1*s* spectrum of comparable intensity at 800 eV photon energy to the above low BE peak, so that the total surface contribution of the surface O 1*s* peaks on Cu_2O at 1486 eV is expected to be less than 4% of the bulk peak. On ionic solids such as KCl, the surface peak on the Cl 2*p* spectrum is at a 0.4eV BE lower than the bulk peak (Patenen et al. 2012). Thus, it is highly probable that the surface chemical shifts in silicates will be < 0.6 eV at lower BE than the main line, and <4% of the intensity of the bulk peak, using 1486 eV photons.

The much broader lines observed for silicates compared with FeS_2, GaAs or Cu_2O, suggest that surface chemical shifts on Si 2*p* or O 1*s* peaks may never be observed on silicates; instead the area of the surface peak is **included** in the area of the one peak that is normally fit. To illustrate this point, the O 1*s* spectrum of quartz is employed (Fig. 13). A one peak fit with the normal 30% Lorentzian, 70% Gaussian is shown in Figure 13A. The fit is good, with a slight asymmetry on the high BE side due probably to the expected vibrational asymmetry mentioned previously. The peak shape and slight asymmetry do not affect the overall area of the peak as shown above. Figure 13B includes a surface peak whose intensity is ~ 10% the bulk peak, with a –0.5 eV surface chemical shift. As just emphasized, the 10% intensity is an overestimate. The overall fit is no better than for the single peak fit, and the area of the two peaks in Figure 13B is within 0.05% of the one peak fit in Figure13A! The area of a surface contribution with the above-noted characteristics is included in a one peak fit; ergo, surface peaks do not affect ap-

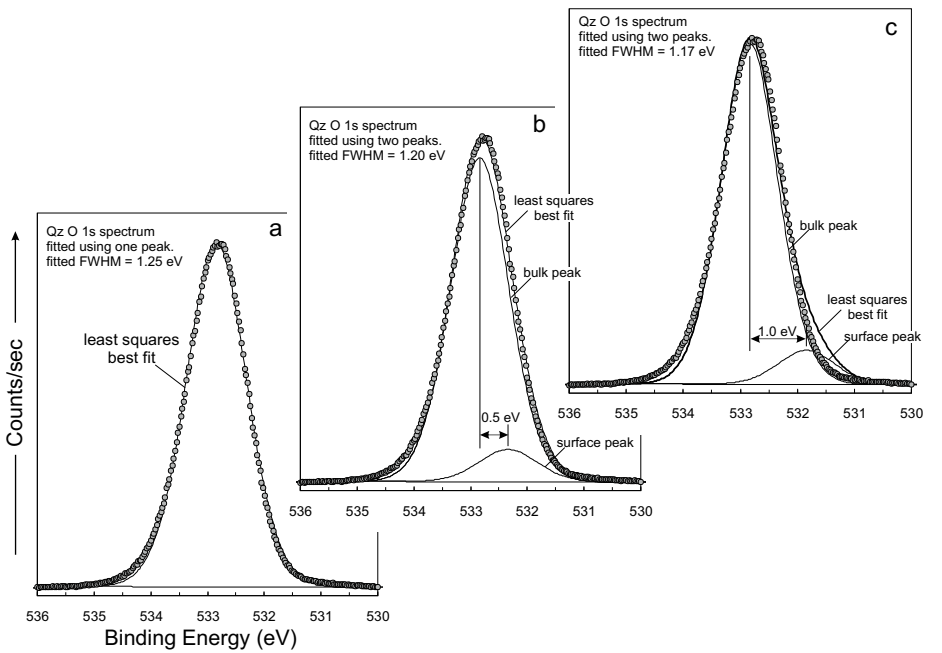


Figure 13. The effect of a possible surface core-level shift on the quartz O 1*s* peak shape and area. A) one major peak with no surface contribution yields a reasonable fit to the data; B) one major peak with an additional surface peak (which is 10% the intensity (area) of the major peak and is shifted 0.5 eV to lower binding energy) yields a fit as statistically good as the one peak fit; C) one major peak and an additional surface peak (which is 10% the intensity of the major peak and is shifted 1.0 eV) gives a decidedly poor fit to the spectral data.

EBSCOhost - printed on 2/13/2023 5:26 AM via . All use subject to https://www.ebsco.com/terms-of-use

preciably O 1*s* peak areas of silicates. If the surface chemical shift were greater, say 1.0 eV (Fig. 13C), an asymmetry on the low BE tail becomes apparent and would be noticed on inspection of the spectrum.

In summary, surface chemical shifts in silicates are probably ~ 0.5 eV or less, and experience to date indicates that a one peak gives an excellent estimate for the **overall** area of O 1*s* and Si 2*p* peaks even if there are small surface core level shifts. The one peak O 1*s* fits thus give the total intensity of **both** bulk and surface species. Surface chemical shifts will also have a very small effect on the determination of BO% for silicate glasses as discussed later in the section "*Silicate glasses: uncertainties in BO% from O 1s spectra*."

CORE LEVEL BULK APPLICATIONS

Crystalline silicates

Pyroxenes. High resolution is critical to resolve and characterize the O 1*s* spectra of silicates which include both structural BO and NBO (e.g., pyroxenes, Deer et al. 2004). With the higher resolution, the O 1*s* spectrum of diopside [$Ca(Mg_{0.8}Fe_{0.2})Si_2O_6$], for example, reveals two *resolved* peaks as observed in Figure 14A (compare with Fig. 7). The two contributions can be immediately assigned based on previous results, the high energy peak to the O atoms in the bridging Si-O moiety (Si-O-Si) (BO), and the low energy peak to the O atoms in the M-O-Si moiety (M= Mg, Ca, Fe) (NBO). The BEs for these two peaks are similar respectively to the BO in quartz, and the NBO in olivine. The ratio of areas of the two peaks NBO:BO

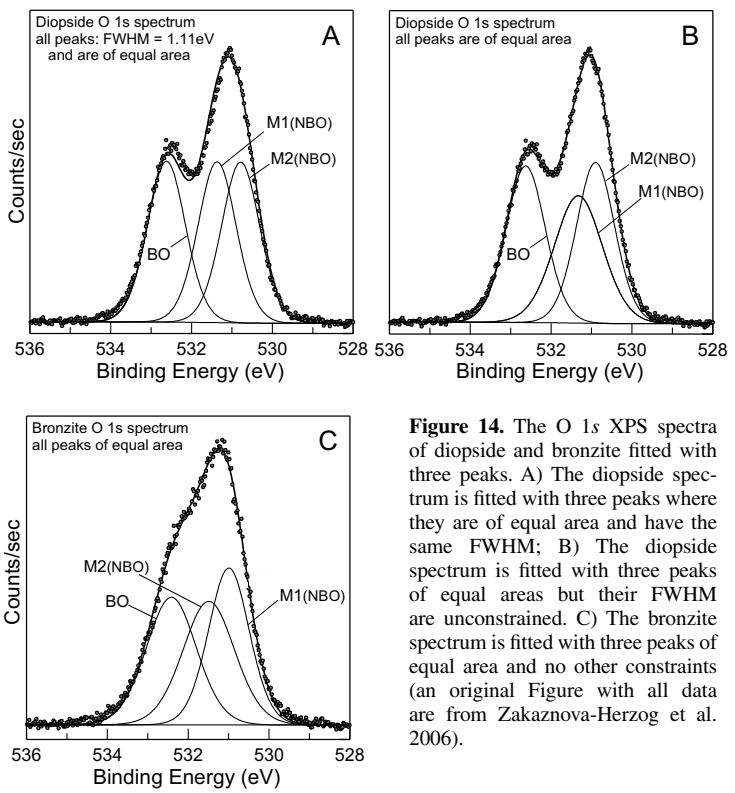


Figure 14. The O 1*s* XPS spectra of diopside and bronzite fitted with three peaks. A) The diopside spectrum is fitted with three peaks where they are of equal area and have the same FWHM; B) The diopside spectrum is fitted with three peaks of equal areas but their FWHM are unconstrained. C) The bronzite spectrum is fitted with three peaks of equal area and no other constraints (an original Figure with all data are from Zakaznova-Herzog et al. 2006).

EBSCOhost - printed on 2/13/2023 5:26 AM via . All use subject to https://www.ebsco.com/terms-of-use

should be 2:1 for diopside (there are four NBO and 2 BO in the Si_2O_6 moiety), but a two peak fit with identical linewidths (Zakaznova-Herzog et al. 2006) gives a ratio of 1.6:1. Examination of the diopside crystal structure (Clark et al. 1968) indicates three crystallographically distinct O atoms in the Si_2O_6 unit with proportions of 2:2:2, the moieties being Si-O-Si, (Mg,Fe)-O-Si, and Ca-O-Si. Three peak fits are shown in Figure 14A and 14B. In Figure 14A, the linewidths for all peaks were constrained to be equal, and the areas and peak positions were allowed to vary. Each peak in the fit to Figure 14A can be assigned based on the order of electronegativities Si>>Mg>Ca: the high BE peak at > 532 eV to the O in the Si-O-Si moiety, the middle peak to (Mg, Fe)-O-Si and the low BE peak at ~530.5 eV to Ca-O-Si. Nevertheless, the overall fit to the spectrum is unsatisfactory in the region between about 531 eV and 533 eV binding energy. A better fit (Fig. 14B) is obtained where the areas of the three peaks are constrained to be equal and the linewidths are allowed to vary. The major difference in this second fit is the breadth of the middle peak which is represents the (Mg, Fe)-O-Si moiety as previously noted. The broader width of the middle peak is expected because the Fe resides with the Mg in the so-called M1 site, and the Fe-O-Si moiety would give a larger O 1*s* BE than Mg-O-Si because the electronegativity of Fe^{2+} is greater than that of Mg^{2+}; in effect the middle peak is a composite peak with an Mg-O-Si and a Fe-O-Si contribution at slightly different energies.

A similar three peak fit is given for the O 1*s* spectrum of a bronzite [$(Fe_{0.2}Mg_{0.8})_2Si_2O_6$] in Figure 14C.The separation between the middle and low energy peaks is only 0.9 eV whereas the energy splitting between these peaks in diopside is 1.2 eV. The effect is that the high energy BO peak of bronzite is not resolved, and instead produces a shoulder on the two low energy NBO peaks. The Fe^{2+} and Mg^{2+} are known to order on the M2 and M1 sites respectively (Bancroft et al. 1967; Clark et al. 1968), and we can readily assign the middle and low energy peaks to (Mg,Fe)-O-Si (Mg,Fe are in M2) and Mg-O-Si (Mg is in M1) respectively as shown in Figure 14C.

Uranyl silicates. Schindler et al. (2009a,b) collected the XPS spectra of many uranyl minerals using single crystals and the Kratos instrument, obtaining the same resolution as we obtained for silicate spectral studies. Their O 1*s* spectrum of Mg-rich olivine, for example, yielded an O 1*s* BE and linewidth of 531.2 eV and 1.2 eV respectively in excellent agreement with our results of 531.0 eV and 1.23 eV (Fig. 5, Table 2). Different instrumental settings were used for the two different spectra of uranophane and siddyite, to test reproducibility of the spectra. The spectrum of an "isolated" SiO_4 unit (e.g., olivine) was useful in fitting the complicated O 1*s* spectra of the three uranyl silicates which contain isolated $SiO_{3\phi}$ (ϕ = O, OH) units: uranophane and uranophane-β of composition $Ca(H_2O)_5[(UO_2)(SiO_3(OH)]_2$, and soddyite of composition $[(UO_2)_2(SiO_4)(H_2O)_2]$. The O 1*s* spectra of the three minerals (Fig. 15) yield a maximum just below 531.0 eV, a prominent shoulder at ~532 eV and a small shoulder at 533.3 eV. Using the SiO_4 peak position and width for the isolated SiO_4 unit previously noted, a reasonable four peak fit to all spectra was obtained using similar BEs and linewidths: 530.6-530.9 eV to the uranyl O=U=O unit, 531.2-531.5 eV to the SiO_4 unit, 532.2-532.5 eV to the OH, and 533.1-533.6 eV to the structural interstitial H_2O. The BE for O=U=O, OH and H_2O are also in good agreement with those in the literature (Zakaznova-Herzog et al. 2008; Schindler et al. 2009b). The OH and H_2O peaks are broader than the low BE peaks, probably because of larger expected vibrational splitting for these species. Some spectra show a very small peak at ~530 eV which is assigned to a U-O-U unit. This species does not occur in the bulk structure of these minerals but it may be a surface contribution situated along edges of basal surfaces of these minerals.

The relative intensities of the peaks in Figure 15 do not agree quantitatively with the expected structural values, but small changes to widths and positions of these peaks can alter the ratios significantly. For example, the closely equal intensities for the O=U=O and SiO_4 peaks in the uranophanes is not expected from the structural 2:3 ratio for these species (Notice that in Fig. 15D, the ratio is closer to 3:2). The much lower intensity for the SiO_4 peak, relative to the O=U=O peak in soddyite is expected from the structural 1:4 ratio, but again the fitted ratio is

EBSCOhost - printed on 2/13/2023 5:26 AM via . All use subject to https://www.ebsco.com/terms-of-use

about 1:2. In addition, the relative intensities of the OH and H_2O peaks do not agree well with the expected intensities. Some of the discrepancy may be explained by loss of these species in the vacuum and the X-ray beam (Ilton et al. 2007).

The U $4f_{7/2}$ spectra of five U-bearing minerals are shown in Figure 16 (Schindler et al. 2009a). Note that the U $4f$ spin orbit splitting is large (~11 eV), so that the $4f_{5/2}$ line is not vis-

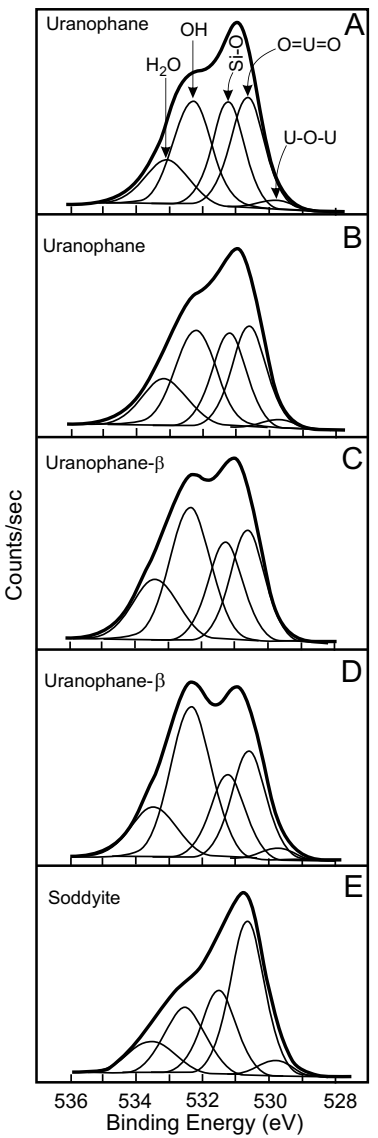


Figure 15. The O 1*s* spectra of uranophane, uranophane-β and soddyite. The assignment of peaks is given at the top of the Figure. The Figure is modified after Schindler et al. (2009b).

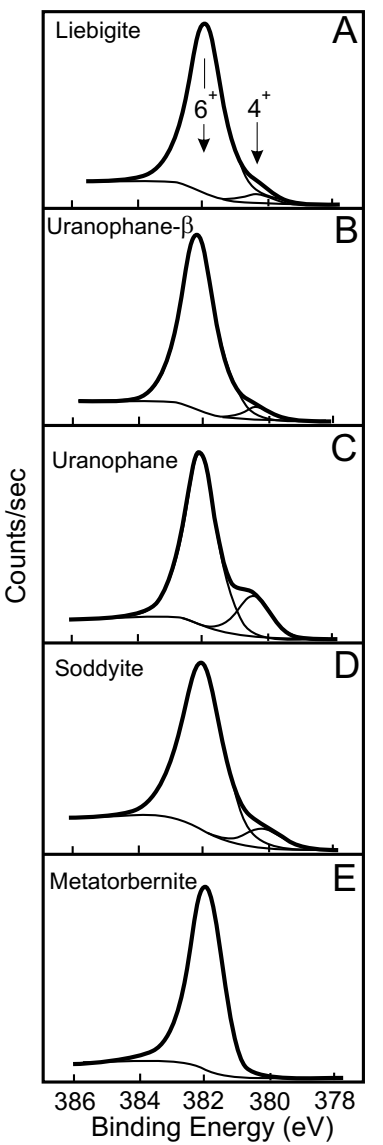


Figure 16. The U $4f_{7/2}$ spectra of liebigite, uranophane, uranophane-β, soddyite and metatorbernite. The peak assignments are provided in Figure 16A. The Figure is modified after Schindler et al. (2009a).

EBSCOhost - printed on 2/13/2023 5:26 AM via . All use subject to https://www.ebsco.com/terms-of-use

ible in these spectra. The major peak at ~382 eV (again, of width ~1.2 eV) can be immediately assigned to the U^{6+} in these minerals. The BEs of the U 4*f* line are sensitive to the change in U-O bonding properties for a large number of different types of uranyl minerals. The U 4*f* peak migrates to higher BE with a decrease in Lewis basicity of the anion group, shifting from 381.3 eV for O/OH groups, to 381.6 eV for O/ (MO_n) (M = Si, P, C, S), to 382.0 eV for (MO_n) groups such as the SiO_4 minerals shown here. This general trend results from the increase of covalency of the U-O bond with increasing Lewis basicity of the anion group (Schindler et al. 2009a). The observation of small peaks at lower BE which are assigned to U^{4+} is unexpected. Is it possible, as discussed by Schindler et al. that U^{4+} was incorporated onto a structural site on formation or was incorporated in the interstitial structure. The authors did not rule out radiation reduction of the U^{6+}, as observed by Ilton et al. (2007). Such reduction is common in the silicate glasses as discussed subsequently.

Novel uranium silicates containing U oxidation states of 4+, 5+ and 6+, several researchers (e.g., Lee et al. 2009, Liu and Lii 2011) have used XPS to characterize the oxidation state of the U. This knowledge is important for chemical and structural characterization of complex novel U silicates such as $Cs_2USi_6O_{15}$ and $Cs_2K(UO)_2Si_4O_{12}$. For example, the U $4f_{7/2}$ BE of 379.7 eV for $Cs_2USi_6O_{15}$ is characteristic of U^{4+} (Liu and Lii 2011); and the U $4f_{7/2}$ spectrum for $Cs_2K(UO)_2Si_4O_{12}$ confirms the presence of both U^{4+} and U^{5+} (Lee et al. 2009).

Silicate glasses: general aspects

Introduction. Silicate glasses have been used in a wide range of areas for hundreds of years (Lewis 1989; Varshneya 1994), and Henderson 2005 has recently published an authoritative review on silicate glass structure. A large number of XPS studies have been performed over the last 40 years (many in the last few years) predominantly to characterize the glass composition and to obtain structural information via BO:NBO values from O 1*s* spectra. There have been, however, other applications. For example, transition metals are used to color glasses, and to tailor electrical and magnetic properties (Mekki and Salim 1999; Duan et al. 2011 and references), including optical lasing, magnetic, and fluorescent applications (Mekki 2005; Tian et al. 2011 and references). Modified silicate glasses and glass ceramics are widely used for medical applications, and again XPS is a primary tool to characterize these glasses (Wren et al. 2011; Li and Kim 2011 and references).

Until the last six years, there has been limited use of XPS techniques to study glass structure of silicates, with the work of Bruckner et al. (1980), Veal et al. (1982) and Matsumoto (1998) being exceptions. NMR and Raman spectra by contrast have been much more widely used (Stebbins 1987; Zhang et al. 1997; Herzog and Zakaznova-Herzog 2011; Maekawa et al. 1991; Malfait et al. 2007 and references). There are three reasons why XPS has not been used to the extent that NMR has been. First, XPS is generally considered to be, and used mostly as, a surface technique rather than as a technique to obtain bulk structural properties. We have shown above that for Al K_α radiation, the addition of a small surface peak makes no difference to the overall area under the peak (Fig. 13). Quantitative XPS *bulk* measurements are thus feasible. Second, until 1998 (Matsumoto et al. 1998), the resolution of the BO and NBO peaks in glasses were rather poor (and variable) making it difficult to accurately quantify BO:NBO and BO% or X_{BO} values. The recent advancements in charge neutralization previously discussed makes the quantification of the NBO:BO ratio and X_{BO} much more simple and accurate. Dalby et al. (2007) presented well resolved spectra with consistent linewidths and line shapes for Pb-silicate glasses; as did Nesbitt et al. (2011) (Fig. 17) and Sawyer et al. (2012) for Na and K silicate glasses. The O 1*s* spectra of Na-silicate glasses include three distinct peaks, a Na KLL Auger peak and the O 1*s* BO and NBO peaks (Fig. 17). The broad, highest BE peak is a Na KLL Auger line but it is not related to the O 1*s* signals. There are other NaKLL Auger lines at lower KE (Nesbitt et al. 2011; Fig. 1). The Auger peak should be fitted so that its contribution to the highest BE portion of the O 1*s* peak is taken into account when determining areas under

EBSCOhost - printed on 2/13/2023 5:26 AM via . All use subject to https://www.ebsco.com/terms-of-use

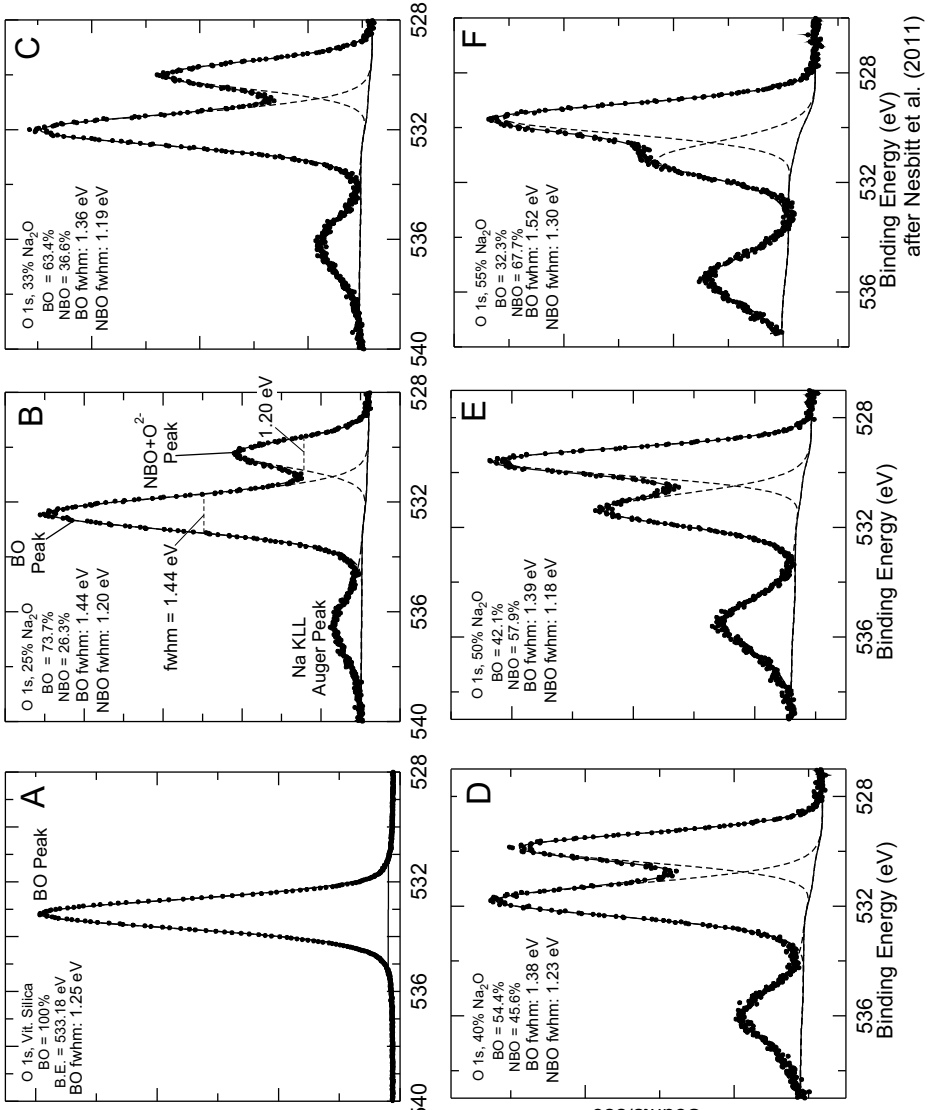


Figure 17. O 1*s* spectra of: A) vitreous silica; B to F) Na-silicate glasses containing respectively, 25%, 33%, 40%, 50% and 55% Na_2O. Each spectrum consists of three contributions, the Na KLL Auger peak (highest BE), the Bridging Oxygen (BO) peak and the Non-Bridging Oxygen (NBO) peak at lowest binding energy. Each of the three peaks was fitted with a separate peak (dashed curves). The intensity of the Na KLL Auger peak increases systematically with Na_2O content. The BO peak decreases and the NBO peak increases systematically with Na_2O content. The full width at half maximum and the percentages of BO and NBO are listed in the upper left corner (an original Figure with all data from Nesbitt et al. 2011).

EBSCOhost - printed on 2/13/2023 5:26 AM via . All use subject to https://www.ebsco.com/terms-of-use

the other peaks. The other peaks represent BO and NBO, the latter being located at the lower binding energy (Bruckner et al. 1978; Dalby et al. 2007; Nesbitt et al. 2011; Sawyer et al. 2012). The electron density argument outlined in the "*Chemical shifts*" in silicates section explains qualitatively their relative binding energies as shown in the next section. The O 1*s* spectra of Pb and K silicates (Dalby et al. 2007: Sawyer et al. 2012) consist of only the two resolved BO and NBO peaks (for example, Fig. 18A, B for two Pb silicate glasses, adapted from Dalby et al. (2007) and Nesbitt et al. (2014a)). The two peak O 1*s* fits shown in Figure 17 are excellent, with virtually every data point on the fitted line. Also, there is no hint of asymmetry in these spectra. The earlier O 1*s* spectra of Pb silicates do not have quite as good statistics and are not as well resolved, but the fits are still good. In contrast to the O 1*s* spectra, the Si 2*p* spectra of the Na silicates (Fig. 19) consist of only one doublet of varying linewidth, and the fits are not quite as good as the O 1*s* fits. These spectra (and others) will be discussed in detail in the following sections of this review, with a strong focus of using the O 1*s* spectra to determine BO%, NBO%, and free O^{2-}% in silicate glasses.

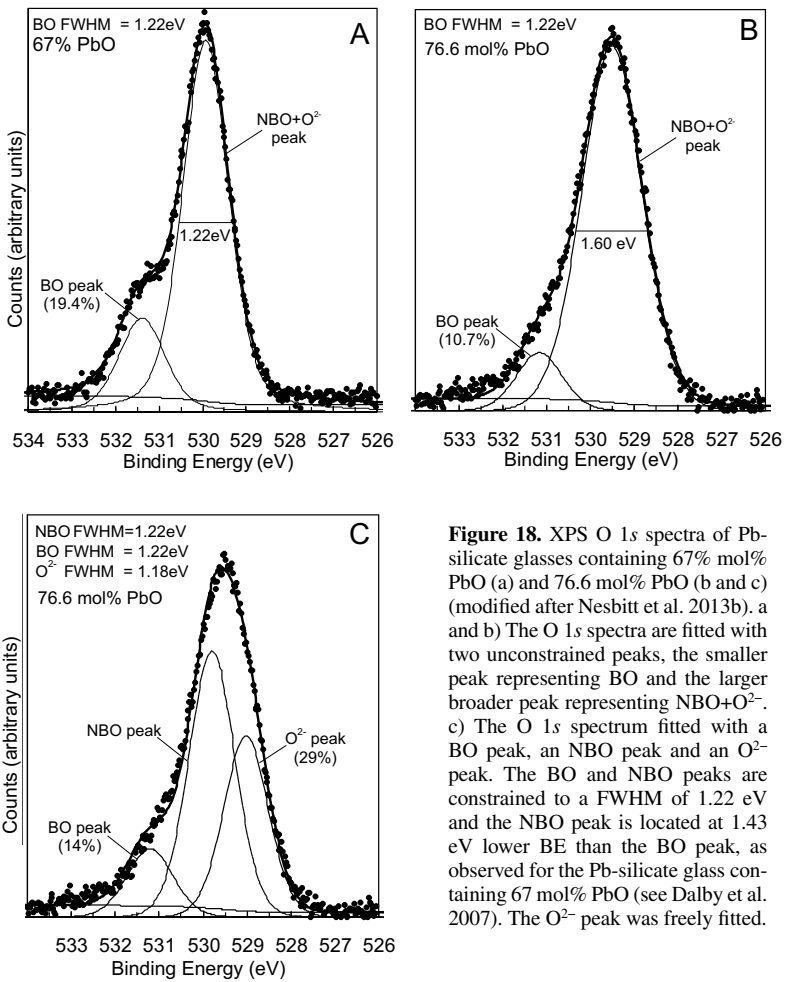


Figure 18. XPS O 1*s* spectra of Pb-silicate glasses containing 67% mol% PbO (a) and 76.6 mol% PbO (b and c) (modified after Nesbitt et al. 2013b). a and b) The O 1*s* spectra are fitted with two unconstrained peaks, the smaller peak representing BO and the larger broader peak representing NBO+O^{2-}. c) The O 1*s* spectrum fitted with a BO peak, an NBO peak and an O^{2-} peak. The BO and NBO peaks are constrained to a FWHM of 1.22 eV and the NBO peak is located at 1.43 eV lower BE than the BO peak, as observed for the Pb-silicate glass containing 67 mol% PbO (see Dalby et al. 2007). The O^{2-} peak was freely fitted.

EBSCOhost - printed on 2/13/2023 5:26 AM via . All use subject to https://www.ebsco.com/terms-of-use

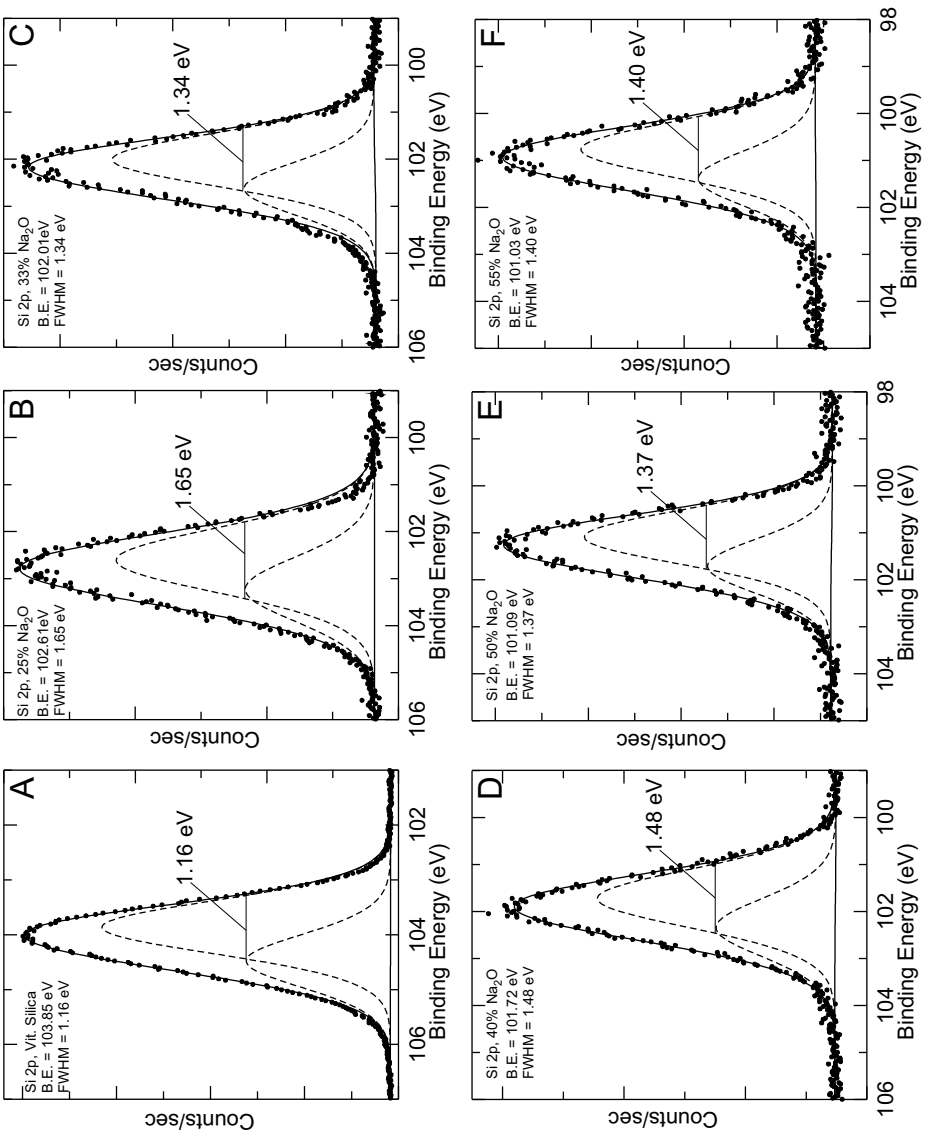


Figure 19. Si 2*p* spectra of: A) vitreous silica; B to F) Na-silicate glasses containing respectively, 25%, 33%, 40%, 50% and 55% Na_2O. Each spectrum has been fitted with an Si 2*p* spin-orbit doublet peak where the Si $2p_{3/2}$ Binding Energies and FWHM are given in the top left corner of each diagram. The FWHM of the Si $2p_{3/2}$ is also shown on each diagram (lines with double arrowheads). The FWHM of the fitted peaks do *not* vary systematically with Na_2O content (an original Figure with all data from Nesbitt et al. 2011). Note: the vitreous silica spectrum is shown here but the spectrum for 25% Na_2O was inadvertently shown in the original paper; Nesbitt et al. (2011).

EBSCOhost - printed on 2/13/2023 5:26 AM via . All use subject to https://www.ebsco.com/terms-of-use

Binding energies in Na silicate glasses. The addition of alkalis to silicate glasses affects the binding energies of all photopeaks (Matsumoto et al. 1998), and the relationship of the Na 1*s*, Si 2*p*, O 1*s* (BO) and O 1*s* (NBO) BEs to the Na_2O content of Na-silicate glasses is illustrated in Figure 20 (Nesbitt et al. 2014b). These plots agree well with those of Matsumoto et al. (1998) after considering that their C 1*s* standard is at 284.6 eV rather than our 285.0 eV. For example, our slope for the O 1*s* BO peak (Fig. 20C) of −0.037 eV/mol compares well with the Matsumoto et al. (1998) slope of −0.04 eV/mol; and our intercept of 533.2 eV is in good agreement with the Matsumoto et al. (1998) value of 533.1 eV after adding 0.4 eV for the different C 1*s* standard BE given above. Increased Na_2O concentrations clearly cause the BE of each photopeak to shift to lower BE values. As discussed in the "*Chemical shifts in silicates*" section, the 3*s* valence electrons of Na are shared by (or effectively transferred to) the more electronegative atoms (i.e., O and Si) of the glass thus increasing the electron density over O atoms within their coordination sphere (i.e., NBO *and* BO atoms). Because molecular orbitals of the glass extend over Si centers, the electron density over all atoms of the glass increases, thus decreasing the BE for all Si and O atoms. Qualitatively, the rather similar slopes for the Si 2*p* and O 1*s* lines can be rationalized using the discussion in the "*Chemical shifts in silicates*" section. Thus, the three major contributing factors are: the differences in the $<1/r_v>$ values for the Si 3*p* and O 2*p* valence electrons, the stoichiometry of the silicate glass (four O atoms donate electrons to the Si in the SiO_4 moiety), and the large electronegativity of O compared to Si. The comparison of O 1*s* and Si 2*p* slopes is complicated by the fact that the Si 2*p* spectra contain a distribution of BE from the different Q species distribution in each glass having a range of BE of probably close to 1 eV. Also, it is probably unexpected at first glance that the BO slope (Fig. 20C) is larger than the NBO slope (Fig. 20D).

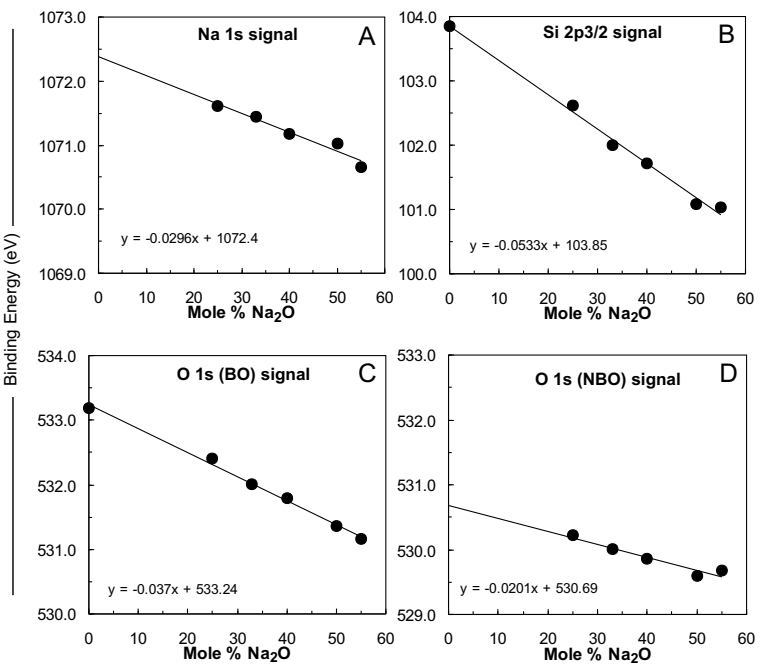


Figure 20. Binding Energies of the Na 1*s*, Si 2*p*, O 1*s* (BO) and O 1*s* (NBO) core level signals as a function of the mol % of Na_2O in vitreous silica and Na-silicate glasses. A linear least squares fit was performed on the data of each diagram and the results of the fit are included (an original Figure with all data from Nesbitt et al. 2011).

EBSCOhost - printed on 2/13/2023 5:26 AM via . All use subject to https://www.ebsco.com/terms-of-use

It is also interesting to note that the Na 1*s* slope is also negative (Fig. 20A). Increased Na_2O content causes the electron density over all Na atoms to increase (decreasing the Na 1*s* BE). For each incremental increase in Na_2O, a progressively smaller portion of the Na 3*s* electronic charge is transferred to the O and Si resulting in an increase in Na 3*s* electron density with increasing Na content. Thus, the Na-O bond becomes more covalent with increasing Na content. Detailed calculations should provide a more quantitative evaluation and better understanding of these trends.

Bulk chemical analysis by XPS. Although XPS is usually considered to be a surface analytical technique (see "*Depth of analysis*" section above), bulk chemical analyses are readily obtained, as previously discussed in Hochella (1988) and Bancroft and Hyland (1990) (see also "*Surface core-level shift in silicates*" section, Figure 13 and related discussion). There are, however, some important considerations when selecting peaks to be used for bulk chemical analysis. Kinetic energies of photoelectrons should be similar to ensure that the depth of analysis is the same for all elements (Fig. 3A). This condition, unfortunately, cannot be met using conventional instrumentation because photopeaks differ greatly in BE, and conventional XPS instruments with fixed source energies do not allow selection of the source energy (i.e., rearranging Eqn. 2 yields KE = hν – BE). Fortunately most elements produce a number of photopeaks or Auger peaks, and any line may be used to obtain bulk compositions. The Si 2*p* and Al 2*p* lines have binding energies near 100 and 75 eV respectively so that photoelectrons from these orbitals have the similar KEs (~1400 eV) and hence are derived from approximately the same depth interval. The O 1*s* peak, by contrast, is at about 530 eV (KE of ~950 eV), and reference to Figure 3A demonstrates that O 1*s* photoelectrons are derived from a shallower depth than those from the Si 2*p* or Al 2*p* lines. Si atoms are therefore "over-sampled" with respect to O, and the resulting analysis will over estimate the amount of Si in the sample. This difference is corrected for (with difficulty because escape depths vary from one compound to another) in some XPS spectrometer software in their "sensitivity factors" (dominated by differences in cross sections, Bancroft and Hyland 1990) but other software packages do not make the correction. Use of appropriate standards overcomes this problem, and bulk chemical analysis of glasses with errors of about 2% (absolute difference) can be obtained. In the absence of standards, and with judicious choice of photopeaks, semi-quantitative bulk chemical analyses of glasses can be obtained, but errors are substantial (5% to 10% absolute; e.g., Nesbitt et al. 2011; Sawyer et al. 2012; Sharma et al. 2001).

Beam damage also affects analytical results (Sharma et al. 2001), as discussed subsequently for the O 1*s* spectra. The effect can be circumvented by an appropriate sampling strategy. The first spectrum collected should be a broadscan (from which compositions are derived) which generally takes 3 to 5 minutes, thus minimizing the effects of beam damage. A broadscan should be collected at the end of the analytical session to determine the extent of damage (with respect to composition). Narrow scans should be collected in cycles where each narrow scan is collected a number of times so that changes in spectra over time are documented. If, for example, 5 cycles were collected with each cycle including the Na 1*s*, O 1*s* Si 2*p* narrow scans, changes in the three spectra can be monitored (e.g., Nesbitt et al. 2011; Sawyer et al. 2012).

Si 2p linewidths. Bancroft et al. (2009) argue that the Si 2*p* and O 1*s* linewidths of quartz and olivine are determined by two major contributions, vibrational broadening (FSVB) and phonon broadening. There are, however, additional factors contributing to small increases in Si 2*p* linewidths of silicate glasses. As example, the narrowest, root-mean-square (RMS) fit to the one quartz Si 2*p* spectrum yields a Si $2p_{3/2}$ linewidth of 1.05 eV (Fig. 9C; Zakaznova-Herzog et al. 2005) whereas the RMS fit to vitreous silica gives a broader Si $2p_{3/2}$ linewidth of 1.16 eV (Fig. 19A). The absence of long range order apparently results in slightly broader peaks, perhaps because there are more energetically distinct Si sites in silicate glasses.

EBSCOhost - printed on 2/13/2023 5:26 AM via . All use subject to https://www.ebsco.com/terms-of-use

A more important contributor to linewidth is the number of unique Si moieties (Q-species) in a silicate glass. Whereas the number of Q-species observed in most crystalline silicates is limited, five Q-species may coexist in silicate glasses (e.g., Stebbins 1987); and each Q-species will give rise to a separate, energetically distinct, Si 2*p* signal. If the energy separating each signal is small, a separate signal for each will not be observed. Instead, one broad Si 2*p* peak will result (Sprenger et al. 1993). From a thermodynamic perspective, all five species are present in an equilibrated melt, although some may be below detectability (Stebbins 1987). Based on electronegativity arguments, the Si 2*p* peak for the Q^4 species should be located at the highest binding energy and that of the Q^0 species should be located at the lowest binding energy, with the Q^3, Q^2 and Q^1 species located sequentially, between the two extremes, as deduced by Sprenger et al. (1993) using other criteria.

Vitreous silica contains only Q^4-species and its Si $2p_{3/2}$ linewidth is 1.16 eV (Fig. 19A) and about 10% greater than that of quartz (1.05 eV, Fig. 9C). Olivine contains only Q^0-species and its Si $2p_{3/2}$ linewidth is 1.01 eV (Fig. 10A) and its linewidth is therefore expected to be about 10% greater value in a glass or 1.1 eV. Because similar vibrational broadening contributes to all Q-species in XPS spectra, all Q-species should have linewidths of about 1.1 eV.

It is now possible to discuss the trends in Si 2*p* linewidths in Figure 19. Where one Q-species of a glass is greatly dominant, the Si 2*p* peaks should be narrow (e.g., vitreous silica, Fig. 19A) and in a glass where two species are equally abundant, a much broader Si 2*p* peak should result (e.g., Fig. 19B). Whether one species or two species dominates in a Na-silicate glass depends on the Na_2O content of the glass (Stebbins 1987; Maekawa et al. 1991). These considerations suggest that Si 2*p* spectral widths should vary with Na_2O content of glasses but not in a systematic manner: the Si 2*p* linewidth will not increase or decrease monotonically with respect to Na_2O content. Instead it will increase or decrease as Q-species proportions change (Fig. 19A to F), and fits using one doublet may not be satisfactory (note the fit to the wings of Figs. 19B,C). As for mineral spectra, Si 2*p* spectra of glass are reproducible for a given composition (linewidths within 0.02 eV).

The effect of changed Q-species abundance is more apparent in K-silicate glasses. A series of K-silicate glasses collected by Sawyer et al. (2012) displayed unusual Si 2*p* peak shapes, some showing distinct shoulders and others displaying distinct asymmetry (Fig. 21). These are the first XPS data to indicate the presence of Q-species and their effects on the Si 2*p* spectra. Furthermore, the Q-species distributions derived from the XPS spectra are broadly consistent with abundances obtained from NMR studies (Maekawa et al. 1991; Malfait et al. 2007), as emphasized by Sawyer et al. (2012). There is consequently good evidence that Q-species abundances affect the shape and breadth of Si 2*p* XPS spectra of silicate glasses. Unfortunately the resolution is not sufficient to reliably quantify Q-species abundances.

Silicate glasses: O 1*s* spectra, and NBO and BO linewidths

The O 1*s* NBO and BO linewidths for the silicate glasses (Figs. 17 and 18) are similar to linewidths of crystalline silicate minerals as explained by Bancroft et al. (2009). NBO linewidths of Na-silicate glasses (Fig. 17, lowest BE peak in each spectrum) range from 1.18 to 1.30 eV and average 1.22 eV, a value similar to the NBO linewidth for olivine which contains only SiO_4^{4-} tetrahedra (Fig. 10). The FWHM of the BO signal of vitreous silica (1.25 eV, Fig. 17A), is similar to that of quartz (1.23 eV, Table 2) and to the above NBO linewidths. The FWHM of *all* oxygen signals (NBO or BO) to the O 1*s* spectrum of silicate minerals or glasses should be 1.2 eV to 1.3 eV (Bancroft et al. 2009), and should be determined primarily by final-state vibrational and phonon broadening; each O 1*s* signal is expected to have about the same linewidth.

In contrast to the above conclusion, the linewidths of the BO signals for Na-silicate glasses (Figs. 17B to F, and Nesbitt et al. 2011) range from 1.36 eV to 1.52 eV and all are broader

EBSCOhost - printed on 2/13/2023 5:26 AM via . All use subject to https://www.ebsco.com/terms-of-use

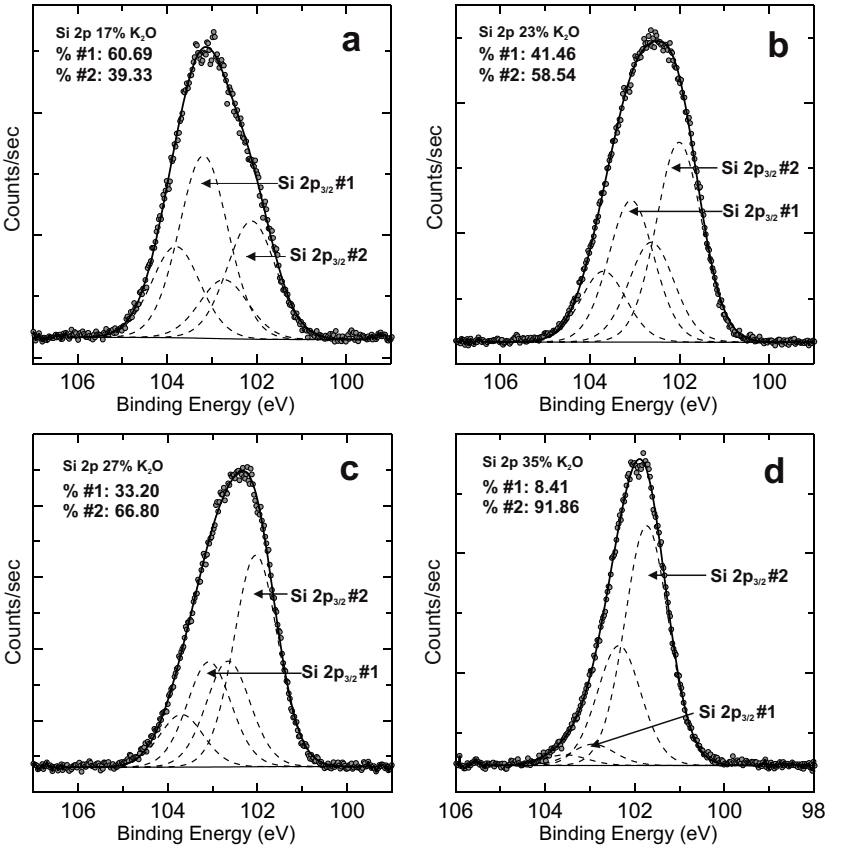


Figure 21. Si 2*p* spectra of K-silicate glasses. A to D) K-silicate glasses containing respectively 17%, 23%, 27% and 35% K_2O. The peak shapes vary dramatically and non-systematically with K_2O content of the glasses. Sawyer et al. (2012) fitted two Si 2*p* spin-orbit split doublet peaks to each spectrum (dashed peaks) and observed that their relative intensities were similar to those observed for the dominant Q-species in these glasses. The area for each doublet is provided in the upper left corner of each diagram (modified from Sawyer et al. 2012).

than the vitreous silica linewidth (Fig. 17A). Structural properties of crystalline Na-disilicate ($Na_2Si_2O_5$) and metasilicate (Na_2SiO_3) provide an explanation. McDonald and Cruickshank (1967) and Ching et al. (1983) note that Na is bonded to some BO atoms (referred to as the BO-Na moiety) but not to others (referred to as the BO moiety) in these crystals. The BO-Na bond length is 2.40 Å and is similar to NBO-Na bond lengths which range between 2.28 Å and 2.54 Å. The two BO moieties likely exist in Na-silicate glasses and the Car-Parrinello Molecular Dynamics calculations of Tilocca and de Leeuw (2006) indicate that Na atoms are enclosed in a coordination shell of 5-6 oxygen atoms, of which 60% are NBOs and 40% BO atoms. Nesbitt et al. (2011) and Sawyer et al. (2012) argued that each type of BO moiety (i.e., BO-Na and BO moieties) should give rise to a separate BO peak (each of 1.2 to 1.3 eV in FWHM) due to electron density differences over the O atom of each moiety. The BO-Na moiety should be located at slightly lower BE than the BO moiety, thus providing an explanation for the broadened BO peak in Na-silicate glasses (Figs. 17B to F) over that of vitreous SiO_2 (Fig. 17A).

EBSCOhost - printed on 2/13/2023 5:26 AM via . All use subject to https://www.ebsco.com/terms-of-use

Silicate glasses: uncertainties in BO% from O 1*s* spectra

The next few sections of this review consider the uncertainties associated with BO% derived from glass O 1*s* XPS spectra. The discussion is relevant because oxygen speciation in glasses is controversial, mainly because the abundance of free O^{2-} derived from XPS measurements is greater than previously considered. These aspects were addressed in three publications (Dalby et al. 2007; Nesbitt et al. 2011; and Sawyer et al. 2012) but they are worth revisiting to emphasize the nature and magnitude of uncertainties related to O 1*s* XPS analyses. In this regard, the uncertainties associated with BO% for Na and K silicate glasses are ±2%, and ±3% for the Pb silicate glasses.

X-ray beam damage effects on BO%. Aside from the complications of glass synthesis (homogeneity) and exposure of clean fracture surfaces for analysis, collection of high quality core level spectra of silicate glasses can be complicated by exposure to the X-ray beam. Sharma et al. (2001) demonstrated that the X-ray beam affected Na-Ca-silicate glass (the Na and Ca migrate to the surface) and X-ray beam damage (and/or damage from secondary electrons associated with photoemission) was observed in the three binary glass systems studied in this laboratory, the Pb-silicate, Na-silicate and K-silicate glasses (Dalby et al. 2007; Nesbitt et al. 2011; Sawyer et al. 2012). The phenomenon was not apparent during analysis of crystalline silicates such as olivines and pyroxenes; but it seems that glasses containing alkalis, alkaline earths and other divalent ions migrate in response to the X-ray beam. Of particular importance, and probably as a result of migration of network modifiers such as Na and K, the O 1*s* BO signal commonly is enhanced relative to the NBO signal with increased time of exposure (Dalby et al. 2007; Nesbitt et al. 2011; Sawyer et al. 2012). The problem can be circumvented by plotting BO mol% against exposure time and extrapolating to zero exposure time (Fig. 22). The first spectrum taken has a BO% close to the extrapolated value (within 1%) and the second spectrum is within 2% of the extrapolated value. Similar plots for the Pb and K silicate glasses (Dalby et al. 2007; Sawyer et al. 2012) also demonstrate that the first O 1*s* spectrum collected gives BO% typically within 1% of the extrapolated value. Because the spectra were collected in cycles from O 1*s* to Si 2*p* to Na 1*s*, it would be possible to limit the beam damage if just a few O 1*s* spectra were obtained without taking the other core level spectra. Alternatively, low source intensities would limit beam damage but would also diminish count rates. Regardless of the technique used to minimize beam

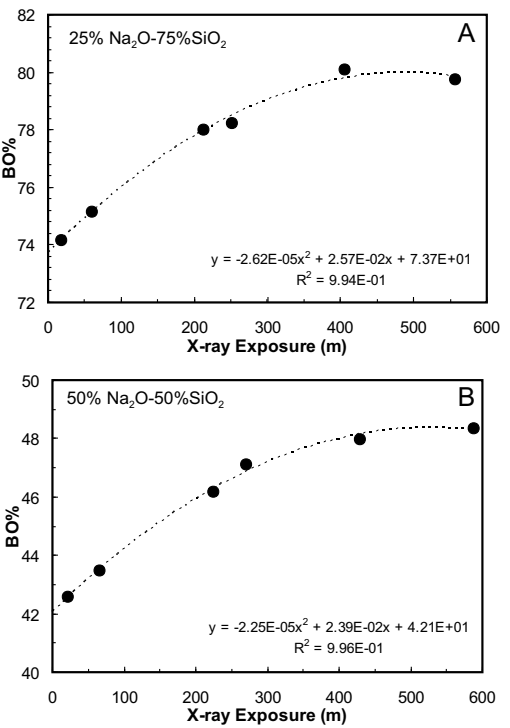


Figure 22. The change to the Bridging Oxygen (BO) peak as a function of exposure to the X-ray beam. A quadratic least-squares fit to the data was performed to obtain the intercept at zero exposure time for A) Na-silicate glass containing 25% Na_2O and; B) Na-silicate glass containing 50% Na_2O. The data are from Nesbitt et al. (2011).

EBSCOhost - printed on 2/13/2023 5:26 AM via . All use subject to https://www.ebsco.com/terms-of-use

damage, O 1*s* and other spectra should be collected in cycles so that changes in the spectra can be monitored.

Bruckner et al. (1978, 1980), Veal et al. (1982), Jen and Kalinowski (1989), Sprenger et al. (1993), Matsumoto et al. (1998) and others conducted XPS studies on Na-silicate and Na-Al-silicate glasses but none addressed the effects of X-ray beam damage. Some of these data consequently are suspect (Nesbitt et al. 2011). Bruckner et al. (1978) and Jen and Kalinowski (1989) used an achromatic Mg K_α source to collect O 1*s* spectra of Na-silicate glasses and obtained spectra of reasonable resolution but beam damage may still arise using a Mg K_α source, and the extent of beam damage incurred by use of this source remains to be investigated.

Fitting and reproducibility. It is worth considering the effect of different fitting procedures on the calculated BO%. BO:NBO ratios derived from fitting O 1*s* spectra are insensitive to the % Lorentzian used (Table 3, for the 40% Na_2O glass – see Fig. 17D, Nesbitt et al. 2011) because the peak areas of *both* peaks change proportionately with different peak shapes. Thus, Table 3 shows that the RMS value for the 30% Lorentzian fit is lowest, but the BO % changes from 54.2% to 54.5% (less than 0.6% change) on going from a 20% to 80% Lorentzian fit. The linewidths for each peak decrease substantially (by 0.08 eV or 7%) using 20% to 80% Lorentzian fits but there is almost no change in the calculated BO% (Table 3). Similarly, a small asymmetry on both O 1*s* peaks (not noticeable for the spectrum in Figure 17D but seen in Figures 9B,D and 10B) will not affect the BO% significantly. First, the residual plot in Figure 9D shows that the positive and negative residuals come close to cancelling each other (as they should for a "best" fit), so that the total fitted area of this peak is not sensitive to the asymmetry. More importantly, both BO and NBO areas will be equally affected by any small asymmetry (as for the above fits to different % Lorentzian shapes), so that the BO% is largely insensitive to this asymmetry. The effect of background correction was explored in another fit on this same glass. A completely independent fit for the 40% Na_2O glass using 30% Lorentzian peak gave 54.2% compared to 54.4% listed in the original publication, the difference resulting from a slightly different background correction. Thus, the *fitting* errors on the BO % calculated from the well resolved O 1*s* spectra of silicate glasses are typically less than 1%.

The plots in Figure 22 for Na glasses show BO% for multiple analyses (of the same sample) over time of X-ray exposure. For both glasses, the first spectrum yielded BO% within 1% of the extrapolated value. Similar effects were seen for the Pb and K glasses (Fig. A2C, AD, Dalby et al. 2007; Fig. 7, Sawyer et al. 2012). Separate spectra on two different fractured samples of the 15% K_2O glass yielded 84.0% and 85.6% BO (Sawyer et al. 2012). Similarly, two different

Table 3. A comparison of fits with different Gaussian/Lorentzian % to the O 1*s* spectra of the 40% Na_2O glass (Fig. 17D, Nesbitt et al. 2011).

% Lorentzian	Relative RMS	BO FWHM	NBO FWHM	BO%	NBO%
20	1.02	1.39	1.24	54.2	45.8
30	**1.00**[1]	1.38	1.23	54.2[2]	45.8
40	1.04	1.35	1.20	54.3	45.7
60	1.13	1.33	1.18	54.4	45.6
80	1.31	1.30	1.16	54.5	45.5

Notes:
1) These root mean square residuals are normalized to the value for the 30% fit.
2) This spectrum was independently refit for this review, and the %BO for the 30% fit is slightly different than the 54.4% tabulated in Table 3 of Nesbitt et al. (2011).

EBSCOhost - printed on 2/13/2023 5:26 AM via . All use subject to https://www.ebsco.com/terms-of-use

fractured samples of two Pb silicate glasses (50% PbO and 67% PbO) yielded BO% within 0.3% and 1.2%, respectively. Fitting contributes about 1% error to BO%.

Values for the several Na and K glasses are in reasonable agreement with those determined on fractured samples by Matsumoto et al. (1998) analyzed alkali silicate glasses using a different XPS instrument and somewhat poorer resolution. For Na glasses, their BO% results (compared to ours in brackets) for glasses containing 25% Na_2O, 33% Na_2O, and 40% Na_2O glasses are: 72.6% (73.7%), 61.9% (63.4%), and 52.3% (54.4%), respectively. Their results are consistently lower than ours but they did not show their fits, and their unreported peak widths are > 1.5 eV, so we consider that our results are more precise and probably more accurate. However, the agreement is within the 2% errors which is the uncertainty that both papers assign to these values.

Surface chemical shifts. There is generally good agreement between X_{BO} values derived from O 1*s* XPS spectra and derived from ^{29}Si NMR results for Pb, Na and siliceous (K_2O%<0.2) K silicate glasses (Maekawa et al. 1991; Fayon et al. 1998; Dalby et al. 2007; Nesbitt et al. 2011; Sawyer et al. 2012). The agreement demonstrates that no systematic differences exist between the two techniques; ergo, surface peaks have introduced no bias to X_{BO} values derived from O 1*s* XPS spectra. This is expected for at least two reasons. First, as discussed in a previous section, the intensity of surface peaks for oxides should be < 5% of the total O 1*s* XPS signal (Harmer et al. 2009) using conventional X-ray sources. As shown in the next paragraph, this level of surface contribution cannot change the X_{BO} values by more than the 0.02 errors assigned. Second, the M-O (M = Na, K, Ca, Mg) bond dissociation energies (Speight 2005) are much smaller than the Si-O bond dissociation energy, strongly indicating that there would be more M-O bonds ruptured at the surface than Si-O bonds. This would, of course, yield more surface Si-O_{NBO} than surface Si-O_{BO} contributions; and as shown below, this would lead to an *enhancement* of the bulk X_{BO}.

Two extreme cases are now presented to illustrate that surface contributions cannot affect BO% outside the experimental uncertainties (±2 mol%). The scenarios draw from Figure 13 and the BO and NBO+O^{2-} peaks of the 35 mol% K-silicate glass of Sawyer et al. (2012). The O 1*s* XPS spectrum of this glass indicates 65.7 mol% (X_{BO} = 0.657) BO, with the remainder (34.3%) being NBO+O^{2-} (Sawyer et al. 2012, their Fig. 6i). Consider the first case where: (a) there is a surface peak included in the fitted BO peak; (b) the surface peak represents 5% of the total O 1*s* signal; and (c) the NBO+O^{2-} peak has *no* surface peak. The true BO_{bulk} signal is obtained by removing the surface signal, and BO_{bulk} = (65.7-5.0) = 60.7%. The NBO+O^{2-} contribution remains at 34.3%. Normalization to 100% then yields the true BO_{bulk} percentage = 63.9.0% (i.e., 100*60.7/95) which is within the quoted experimental uncertainty for the K silicate glasses (±2 mol%; Sawyer et al. 2012). The second extreme case is the reverse situation, with the BO peak having *no* surface peak, and the NBO peak includes a 5% surface peak. For this situation, the area of the BO_{bulk} is unaffected by the surface contribution, and it represents 65.7 mol% of the total O 1*s* signal, with the NBO_{bulk} decreasing by 5% to 32.6 mol%. This then yields a true BO_{bulk} percentage of 66.8%. As noted above, this *increase* in the BO% is more likely, but is well within the quoted errors of 2 mol%. The other fitting errors (from peak shapes, background corrections and small O 1*s* asymmetry) (see "*Experimental and fitting considerations*" section) are less than 1% of the BO% (or X_{BO}). In summary, measured X_{BO} values cannot be different from true bulk values by more than ±0.02 (or ±2 mol%).

Surface H_2O and OH. Although the O 1*s* spectra are taken within minutes after fracturing the glass in high vacuum, small amounts of impurities can be observed in the spectra. Very small amounts of carbon (usually < 5% of the intensity of the O 1*s* peak, Fig. 1) are deposited on the surface of nearly all mineral and glass samples as evident by development of a C 1*s* XPS peak at approximately 285 eV binding energy. This peak does not affect the analysis of O 1*s* peaks, and it is valuable for calibrating binding energies as indicated previously. The

EBSCOhost - printed on 2/13/2023 5:26 AM via . All use subject to https://www.ebsco.com/terms-of-use

effects of adsorption of H_2O, however, may affect O 1*s* signals. Adsorption of H_2O onto a fresh fracture surface of glasses or minerals may cause the molecule to dissociate, with H^+ bonding to dangling NBO and OH^- bonding to an unsatisfied Si dangling bond (where a BO-Si bond was ruptured on fracture). The first monolayer likely would be OH, which will represent about 5 mol% of the total O 1*s* signal. Additional H_2O likely would be adsorbed in molecular form because the molecule does not dissociate when adsorbed onto a hydroxylated surface (Knipe et al. 1995). Chemisorbed and physisorbed H_2O is located at > 533 eV binding energy (Knipe et al. 1995) and its presence will be obvious in O 1*s* XPS spectra of glasses. No such contribution has been observed for silicate glasses studied in this laboratory, indicating that, if present at all, there is no more than a monolayer of OH^- on the glass surfaces (i.e., a max. ~ 5 mol% O contribution to the O 1*s* spectrum).

Detection of hydroxide is difficult for glasses. As example, a small shoulder on the high BE side of the olivine O 1*s* spectrum (Fig. 10B, with ~ 5% of the total O 1*s* intensity) may indicate the presence of surface OH (Zakaznova-Herzog et al. 2005), although its origin remains uncertain. The OH peak (BE of 532.5 eV) overlaps the BO peak of vitreous silica (at 533.2 eV) and is likely to overlap BO signals of most glasses. It may be identified, however, by line broadening of the BO peak. Many studies have shown that these O 1*s* peaks from surface OH and H_2O have linewidths of > 1.5 eV due to large vibrational broadening (e.g., Biesinger et al. 2004, 2009; Knipe et al. 1995), which is appreciably broader than the 1.2 eV linewidths of the NBO and BO peaks. The BO peak should consequently broaden with accumulation of surface OH. The presence of OH will affect BO% and it is worth looking at two numerical examples to appreciate the extent of this effect. OH does not appreciably affect BO% for glasses with less than 40% Na_2O, K_2O or PbO, but could be quantitatively significant for glasses containing more than 50 mol% modifier oxide.

We consider two cases where the OH peak is 5% (representing a monolayer) of the total O intensity (NBO plus BO peaks). Considering the 35 mol% K_2O glass considered above with BO= 65.7% and NBO= 34.3% (Sawyer et al. 2012) and assuming the area of the BO peak includes a 5% OH peak, the "true" BO% would be 63.9% [100×60.7/(60.7+34.3)] which is within experimental uncertainty (±2 mol%, Sawyer et al. 2012). The 50 mol% Pb silicate glass has 56.4 mol% NBO+O^{2-} and 42.6 mol% BO (Dalby et al. 2007). A 5% OH peak under the BO peak leads to a "corrected" BO of 39.6 mol% [100×37.6/(37.6+56.4)] representing a 3 mol% error in the BO mol%, the error quoted for Pb-silicate glasses (Dalby et al. 2007). Pb-glasses containing more than 50 mol% PbO would fall outside the quoted uncertainty. There cannot be, however, much OH in the O 1*s* spectra of the Pb-silicate glasses. Considering the glass containing 67 mol% PbO (Fig. 18B), the fitted BO linewidth is very narrow at 1.22 eV. An OH peak which is ~25% of the total BO intensity (5% OH, 14.4% BO, Fig. 18A) and which has a width of ~ 1.5 eV would lead to a broadening of at ~ 0.1 eV, which is not observed. The fit in Figure 18B is excellent—the high energy wing, where the broadening from OH would be obvious, is not evident. Finally, the O 1*s* photopeak is slightly but inherently asymmetric to its high binding energy side (Bancroft et al. 2009), and the asymmetry may be mistaken for OH^- or H_2O signals.

Na glasses become more hygroscopic with increasing Na content, and a substantial increase in OH contribution to the BO peak from 20% Na_2O to 55% Na_2O should increase the BO% linewidth across this series. However, the O 1*s* linewidth does not increase regularly across this series of glasses (Fig. 17). Indeed the linewidths for the 50% Na_2O glass (1.39 eV) are narrower than for the 25% Na_2O glass (1.44 eV) showing that OH is not the cause of the linewidth changes in the Na glasses. Rather, there is more than one BO species as discussed in a previous section.

Our XPS values for most of the Pb, Na, and K samples agree with ^{29}Si MAS NMR results and this agreement is perhaps the most convincing evidence that there are no systematic errors

EBSCOhost - printed on 2/13/2023 5:26 AM via . All use subject to https://www.ebsco.com/terms-of-use

in our BO% (or X_{BO} values). The agreement is remarkable considering the very different techniques and measurements. In summary, all of the above evidence indicates that there are no systematic errors in the O 1*s* XPS BO% values. Only, an OH peak can have significant systematic effect on our values; and even in this case there are very few of our glasses where the quoted BO% could be outside the quoted uncertainties (±2% for the Na and K glasses, and ±3% for the Pb glasses).

Determination of free oxide O^{2-} and its importance

Toop and Samis (1962) proposed the presence of the three O species (BO, NBO and free O^{2-}) in silicate melts, and calculated activity and other thermodynamic relationships based on the model of Fraser (1977). The actual abundance of O^{2-} in melts, however, has been largely ignored during the last 30 years and remains contentious (Nesbitt et al. 2014b) in spite of its likely importance in affecting reactivity of melts and their physical properties such as diffusion and viscosity as has been emphasized (Stolper 1982). The results described below illustrate the role of O 1*s* XPS studies in assessment of oxygen speciation in glasses.

O^{2-} in Na silicate glasses. The O 1*s* peaks for Na, K and Pb silicate glasses are well resolved, and accurate measurements of the area under the two O 1*s* peaks can be made (e.g., Figure 17; Matsumoto et al. 1998; Dalby et al. 2007; Sawyer et al. 2012). All fits were performed with *no* constraints other than adopting a 30% Lorentzian, 70% Gaussian lineshape function. To quantify the fraction of BO, areas under the BO and NBO+O^{2-} peaks are summed and the mol fraction of BO (X_{BO}) is determined according to:

$$X_{BO} = \frac{\left[\text{Area of BO Peak}\right]}{\left[\text{Area of BO Peak} + \text{Area of NBO} + O^{2-}\text{Peak}\right]} \tag{10}$$

The resulting X_{BO} values for Na-silicate glasses are plotted Figure 23A (black squares). The size of the square represents approximately the uncertainties in both dimensions (experimental uncertainty is ±0.02 in mol fraction or ±2 in mol%, Nesbitt et al. 2011). The results agree with the previous XPS results of Matsumoto (1998) (black circles) and with X_{BO} values obtained from the ^{29}Si NMR spectra (shaded squares) of Nesbitt et al. (2011), and Stebbins (1987) (shaded circles). The calculation of X_{BO} from Q-species abundances is simple, and is provided elsewhere (Nesbitt et al. 2011, 2014a). The earlier X_{BO} values calculated from the XPS data of Veal et al. (1982) (Fig. 23A, open diamonds) were derived from poorly resolved O 1*s* XPS peaks. More importantly, Veal et al. (1982) did not correct for beam damage, and their anomalously large X_{BO} values probably result from exposure to the X-ray source (see Nesbitt et al. 2011). The remarkable agreement of the XPS and NMR results up to $X_{Na_2O} = 0.40$ for Na-silicate glasses demonstrates that there are no significant systematic errors in X_{BO} or quoted chemical composition obtained by the two totally independent, disparate, measurements, thus dispelling concerns that surface chemical shifts or surface contamination affect the XPS results.

Two curves labeled K = infinity and K = 14 are shown on Figure 23A where *K* is the equilibrium constant *K* for the reaction:

$$BO + O^{2-} \rightarrow 2NBO \tag{11}$$

The associated mass-action equation is:

$$K = \frac{(NBO)^2}{\left[(BO)(O^{2-})\right]} \tag{12}$$

Where Reaction (11) goes to *completion*, every mole of Na_2O reacts with a BO to form two moles of NBO. For this condition, *K* = infinity and there can be no free oxide present for melt or glass compositions where $X_{Na_2O} < 0.67$ (the orthosilicate composition) and NBO =Na (molar basis). For *K* = 14, Reaction (11) does not go to completion, and some Na_2O remains

EBSCOhost - printed on 2/13/2023 5:26 AM via . All use subject to https://www.ebsco.com/terms-of-use

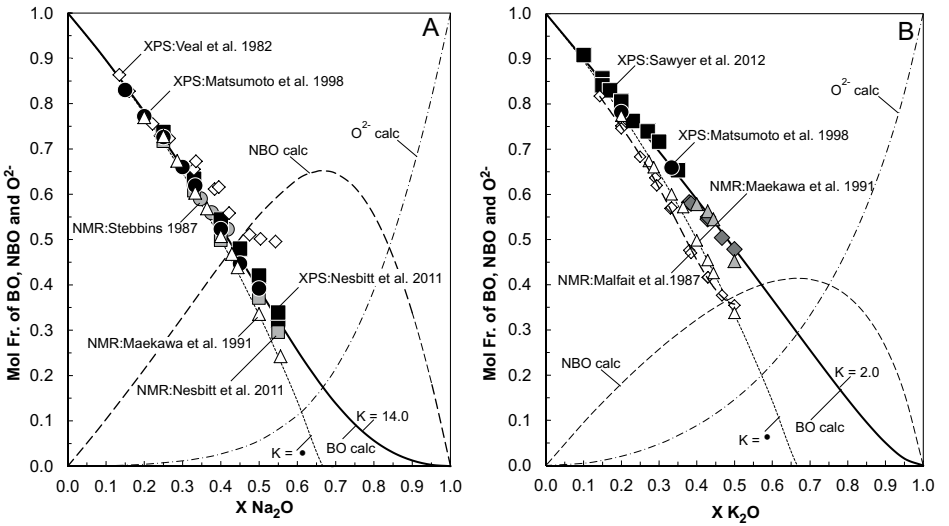


Figure 23. Mol fraction of oxygen species derived from experimental results and calculation are plotted as a function of glass composition. A) Numerous XPS and ^{29}Si MAS NMR experimental results are plotted for Na-silicate glasses. B) Numerous XPS and ^{29}Si MAS NMR experimental results are plotted for K-silicate glasses. On both diagrams BO values derived from experimental results are plotted as symbols. The solid, short dashed, dash-dot curves are calculated BO, NBO, O^{2-} values obtained with K = 14 (Na-silicate glasses) and K = 2.0 (K-silicate glasses) for the mass action equation $K = (X_{NBO})^2/\{(X_{BO})(X_{O^{2-}})\}$, which relates to the reaction $1BO + 1O^{2-} \rightarrow 2NBO$. The dotted curve is calculated from the above mass action equation assuming that K is infinite (K = ∞), which implies that the above reaction goes to completion in both Na- and K-silicate glasses. If the assumption were true, important corollaries are that O^{2-} cannot coexist with BO and that only one species, NBO, exists at the orthosilicate composition (X_{Na_2O} and X_{K_2O} = 0.666). Most of the data from Nesbitt et al. (2011).

unreacted with BO. For this condition, some free O^{2-} (O bonded only to Na) is present in the glass and NBO<Na (molar basis) for compositions less than X_{Na_2O} = 0.67. Furthermore, the amount of O^{2-} increases with increasing Na content. Above X_{Na_2O} =0.40, the original NMR results (Maekawa et al. 1991) lie on the dotted line (labeled *K* = infinity); in contrast, the NMR and XPS results of Nesbitt et al. (2011) lie on the solid line (within experimental uncertainty), indicating appreciable free oxide in these glasses (Fig. 23A, dot-dash curve). The amounts are quantified in a recent publication (Nesbitt et al. 2014b). Evidence for free oxide is experimentally detectable by XPS in glasses where $X_{Na_2O} > 0.35$ and it increases markedly to >15 mol% at the orthosilicate composition (i.e., 67 mol% Na_2O). The errors in these values are again ±2%. All results of Maekawa et al. (1991) lie on the dotted line (K = infinity), and they may have assumed that Reaction (11) goes to completion (i.e., NBO=Na on a molar basis), thereby assuming that O^{2-} was absent from the Na-silicate glasses studied. Note that the discrepancy between the X_{BO} values from of Nesbitt et al. (2011) ($X_{O^{2-}} \sim 0.32$) and the Maekawa et al. (1991) NMR results ($X_{O^{2-}} \sim 0.23$) for the 55% Na_2O sample is about 30%! It is also possible that the glasses used by Maekawa et al. (1991) had different thermal histories than those used by Nesbitt et al. (2011).

The conditional equilibrium constant (K) is sensitive to the amount of O^{2-} present. As example, the NMR and XPS results for the 50% Na_2O glass of Nesbitt et al. (2011) yield respectively about 3 and 6 mol% BO (Nesbitt et al. 2014b). The K values derived from the NMR and XPS results are about 20 and 14 respectively. Although the NMR and XPS results are within experimental uncertainty, the corresponding uncertainty in K values is nevertheless large.

EBSCOhost - printed on 2/13/2023 5:26 AM via . All use subject to https://www.ebsco.com/terms-of-use

O^{2-} in Pb silicate glasses. O 1*s* XPS results for Pb silicate glasses (Dalby et al. 2007) and X_{BO} values obtained from ^{29}Si NMR (Fayon et al. 1998) agree over the entire composition range up to $X_{PbO} = 0.7$. Both techniques give X_{BO} values consistent with K = 14 for Reaction (11), indicating that the reaction does not go to completion in Pb-silicate glasses. Fayon et al. (1998) did not use the constraint that PbO = 2NBO (i.e., K = infinity), hence did not assume that O^{2-} was absent. These Pb silicate XPS and NMR results provide strong confirmation that the XPS results are accurate within experimental uncertainty, and also that NMR results are consistent with XPS results where unsubstantiated constraints are not applied to evaluate Q-species abundances. These XPS and NMR results show conclusively that there is at least 15% free O^{2-} at 67% PbO, and significant amounts of free O^{2-} at lower Pb contents.

The most direct evidence for free O^{2-} in silicate glasses is provided by the O 1*s* XPS spectrum of a Pb-silicate glass containing 76.6% PbO (Fig. 18B,C, Nesbitt et al. 2014b). A two peak fit (Fig. 18B) shows the normal BO and NBO peaks. At this composition there should be no BO signal if K = infinity; the BO peak shows that K cannot be infinite. The NBO+O^{2-} peak is strikingly broader (1.6 eV) than for the 67 mol% glass (Fig. 18A) indicating that a second, strong peak contributes to the 76 mol% glass (Fig. 18B) which was weak or absent from the 67 mol% glass (Fig. 18A). A three peak fit, constraining the linewidths and the NBO position from the earlier O 1*s* NBO positions, yields Figure 18C. The low BE peak at 529.0 eV is due to free O^{2-}, with its BE agreeing with the O 1*s* BE for PbO (Nesbitt et al. 2014b) as expected. The large amount of free O^{2-} (29%) agrees with that expected from the K = 14 curve.

O^{2-} in K silicate glasses. There is agreement between XPS and ^{29}Si MAS NMR results for all the Pb-silicate glasses (Dalby et al. 2007) and for most Na silicate glasses (Fig. 23A). With respect to K silicate glasses, however, disagreement between the XPS and ^{29}Si NMR results becomes noticeable where $X_{K2O} > 0.2$. The X_{BO} values derived from XPS (Matsumoto et al. 1998; Sawyer et al. 2012) are plotted on Figure 23B as solid squares and dots respectively, whereas the NMR data plot on the curve labeled K = infinity (Maekawa et al. 1991) or below this curve (Malfait et al. 2007). The X_{BO} values derived from the NMR data of Maekawa et al. (1991) all plot on the curve labeled K = infinity (Fig. 23B, open triangles) and this suggests that they used the relationship NBO = K to constrain the areas in their Q-species assignments. Malfait et al. (2007) fitted freely their ^{29}Si MAS NMR spectra, and their data plot *below* the curve labeled K = infinity (Fig. 23B, open diamonds fitted with dashed curve). It is physically impossible to access the region below the curve labeled K = infinity if the samples are pure. Hence the Q-species distributions derived from the free fits are inaccurate, and are the result of spectra too poorly resolved to extract accurate Q-species abundances. Malfait et al. (2007) recognized the problem and recalculated their Q-species abundances using two constraints which effectively constrained X_{BO} values to fall on the curve K = infinity where NBO = K (Fig. 23B). There is no evidence for the assumptions made (e.g., NBO/Si = 2.0 or that NBO=K), and their assignments are consequently suspect.

In an attempt to resolve the above discrepancy between XPS and NMR results, we first considered (Nesbitt et al. 2014b) the ^{29}Si NMR spectrum of the K-metasilicate (K_2SiO_3) glass which has four relatively well resolved peaks. Maekawa et al. (1991) was uncertain about Q-species assignments to the K-metasilicate glass. They assigned Q^0, Q^1, Q^2 and Q^3 species to the four peaks and obtained an NBO/Si value of 2.44. Next they assigned Q^1, Q^2, Q^3 and Q^4 species to the four peaks and obtained an NBO/Si value of 1.44. In their words, "the values of 2.44 or 1.44 for NBO/Si are derived, respectively, instead of the stoichiometric value (2.00)." They consequently adopted a third assignment consisting of a Q^1, *two* Q^2 and a Q^3 species which yielded NBO/2.0 = 2.0 for the metasilicate glass. The condition that NBO/Si = 2.0, holds for pyroxenes and wollastonite (i.e., crystalline metasilicates), but glasses have no long range order and there is no reason why NBO/Si should necessarily equal 2.0 for the K_2SiO_3. As conclusive evidence, the ratio is not realized in the Pb- Na- or Mg-metasilicate glasses

EBSCOhost - printed on 2/13/2023 5:26 AM via . All use subject to https://www.ebsco.com/terms-of-use

(discussed above). In addition, in his review, Henderson (2005) emphasizes that there is no independent experimental evidence for two Q^2 species in alkali silicate glasses.

Consistent with the Pb and Na glass XPS results, Nesbitt et al. (2014b) discarded the assumptions of Maekawa et al. (1991) and assumed instead that the four peaks in the K-metasilicate glass spectrum could be assigned initially to Q^1, Q^2, Q^3 and Q^4 as initially considered (but rejected) by Maekawa et al. (1991). With this reassignment, the X_{BO} values for both sets of NMR data (shaded diamond and triangle) lie on or very close to the K = 2 line defined by our XPS data. There is equally good agreement for the K-metasilicate and all the other glasses with the K = 2 line if the four peaks are assigned instead to Q^1, Q^2, and *two* Q^3 species. All the X_{BO} values plot well above the K = infinity curve indicating appreciable O^{2-} is present.

The assignment of two Q^3 species rather than two Q^2 species is given additional credence from Raman and NMR results. McMillan et al. (1995) and Matson et al. (1983) both conclude that there are two Q^3-species in siliceous K-silicate glasses and Duer et al. (1995) observed two Q^3-species in Na-disilicate glasses (33.3 mol% K_2O) and emphasized that these could not have been observed in ^{29}Si MAS NMR spectra. In addition, early studies by Zhang et al. (1997), Shaller et al. (1999), and Umesaki et al. (1988) proposed the presence of a few percent O^{2-} in Ca-silicate, La-doped Na-silicate and Li silicate glasses respectively to explain their NMR and Raman spectra. Nasikas et al. (2012) conducted an NMR study of Ca-Mg silicate glasses containing between 67 and 72 mol% CaO+ MgO and identified ~ 10% O^{2-} using ^{29}Si MAS NMR and ^{17}O MAS NMR spectra. Numerous molecular dynamics (MD) calculations indicate the presence of O^{2-} in Na, Ca, Mg and Pb-silicate glasses (Du and Cormack 2004; Sen and Tangeman 2008; de Koker et al. 2009; Martin et al. 2009; Karki 2010; Davis et al. 2011; Nasikas et al. 2012; Nesbitt et al. 2014b). Additional experimental and theoretical studies of the K-silicate glasses (for example, NMR and XPS studies on the same glasses) is obviously now required to understand fully the the oxygen and Q-species distributions in K-silicate glasses.

CORE LEVEL SURFACE STUDIES OF SILICATES

Adsorption on silicate and oxide surfaces

The focus of this review has been on bulk XPS studies of silicates; but as indicated in the introduction, the majority of XPS studies has been focused on the first three surface applications outlined by Hochella (1988): 1) the oxidation state of near surface atoms; 2) adsorption studies on mineral surfaces; 3) studies of the alteration and weathering of mineral surfaces. The following section emphasizes some recent surface applications, and illustrates how the new, higher resolution will affect future surface studies. The combination of effective charge compensation with the extreme surface sensitivity obtainable with synchrotron sources (via sources tuned to appropriate energies) harkens to tremendous opportunities in the near-future to study silicate insulator surfaces and their reactivity at a level previously unattained.

Ilton et al. (2000, 2004) studied the adsorption/reduction of transition metals (e.g., Cr and U) on micas (biotites) of general formula $K(Fe,Mg)_3(Al,Si)_3O_{10}(OH)_2$ and showed that transition metals and actinides are readily adsorbed on micaceous surfaces, and can be reduced by the Fe^{2+} in the micas. Their spectra were taken with a state-of-the-art, high intensity, high resolution Scienta instrument; but the charge compensation system was inferior to that of the Kratos, and peak broadening occurred. The primary goal of the U study was to determine whether soluble U^{6+} can be reduced to the less soluble U^{4+} at micaceous surfaces thus limiting its mobility in the environment. Low concentrations of U^{6+} (e.g., 5 μM) were reacted with cut mica faces for 1-20 hours. Their U 4*f* XPS spectra were shown for solutions without NaCl and with 25 mM NaCl added to the solution. Only U^{6+} was observed in the experiment where the solution contained no NaCl. Although there was some asymmetry on the U^{6+} peak, there was no obvious change in the spectra with reaction time in solution. With NaCl added, the peak

EBSCOhost - printed on 2/13/2023 5:26 AM via . All use subject to https://www.ebsco.com/terms-of-use

shifted to lower binding energies characteristic of U^{4+}. Ilton et al. (2004) found that the amount of adsorption, and the amount of reduction, increased with the Fe content in the three micas studied. The amount of Na^+ and K^+ in solution also influenced the amount of U^{6+} adsorbed; and the amount of U^{4+} produced was dependent on the nature of the surface, with U^{4+} detected only on edges and rough basal surfaces of the micas. A mechanism involving oxidation of the Fe^{2+} in the micas was proposed, with the U^{6+} being reduced to U^{4+} by two Fe^{2+} which are oxidized to Fe^{3+}. The U $4f_{7/2}$ linewidths (~2eV) collected by Ilton et al. (2004) were substantially broader than those reported by Schindler et al. (2009a,b) using the Kratos instrument. Comparison of the spectra collected with the two instruments demonstrates the great advantage of using good charge compensation systems for surface studies of insulators.

Ilton et al. (2000, 2004) did not report the Fe 2*p* spectra from the micas which would have provided additional evidence that Fe^{2+} was the oxidant. Fe 2*p* spectra are complicated, and even with good charge compensation the spectra are difficult to interpret. Nevertheless, and as noted by Hochella (1988), it is possible to distinguish the two Fe oxidation states by the Fe $2p_{3/2}$ chemical shift, where the ferric iron is located at higher BE than ferrous iron. XPS studies of the Fe $2p_{3/2}$ lines on Fe compounds using the Kratos higher resolution (Grosvenor et al. 2004) clearly differentiate between the Fe^{2+} and Fe^{3+} spectra. In a similar type of study, Chakraborty et al. (2011) used XPS and XANES (X-ray Absorption Near Edge Structure) spectroscopy to monitor the adsorption of aqueous As on biotite surfaces. The high resolution As 3*d* XPS spectra showed that As $^{5+}$ was not reduced on the biotite after 30 days, confirming their XANES and thermodynamic results.

Many experimental and theoretical studies (Gupta and Sen 1974, 1975; Carlson 1975; Biesinger et al. 2004; Grosvenor et al. 2004) have shown that the 2*p* spectra of transition metals such as Cr^{3+}, Mn^{4+} ($3d^3$ configurations), and Fe^{3+} ($3d^5$ configuration), are split into a number of lines due to the electrostatic interaction of the $2p^5$ hole state with the $3d^3$ or $3d^5$ valence states. This "multiplet splitting" is normally not resolved (e.g., the Cr study by Ilton et al. 2000). With the higher resolution obtained with the Kratos instrument, some of the four major multiplet peaks in the Cr $2p_{3/2}$ spectrum of pure solid $CrCl_3$ have been resolved with individual linewidths of less than 1 eV, although the overall Cr $2p_{3/2}$ linewidth is still greater than 2 eV (Biesinger et al. 2004).

To our knowledge there are no studies of silicates where both oxidant and reductant have been monitored at silicate surfaces. This section consequently finishes with an example where the oxidation states of both the reductant and oxidant, and intermediate reaction products, were identified on an oxide mineral surface. Nesbitt et al. (1998b) conducted a study where adsorption and oxidation of H_3AsO_3 onto birnessite (MnO_2) surfaces were documented. The net reaction is:

$$MnO_2 + H_3AsO_3 + 2H^+ = Mn^{2+} + H_3AsO_4 + H_2O \quad (13)$$

The initial, unreacted MnO_2 spectrum indicated about 70% Mn(IV), about 25% Mn(III) and about 5% Mn(II). After 90 minutes reaction time, Mn(IV) had decreased to 30%, Mn(III) was 67% and Mn(II) was about 3%, indicating that Mn(IV) had been reduced to Mn(III). Some AsO_3^{3-}(surf) had been oxidized to AsO_4^{3-}(surf), and both were observed on the surface at near-equal amounts; the oxidant (Mn^{4+}) and reductant (AsO_3^{3-}) were observed on the same surface, as were their reaction products.

The large amount of Mn(III) can only be derived from Mn(IV) as shown in the reaction:

$$2MnO_2 + H_3AsO_3 + H_2O = 2MnOOH + H_3AsO_4 \quad (14)$$

Mn(III) production requires only one electron to be transferred to the Mn^{4+} in MnO_2, even though two electrons must be extracted from As^{3+} to produce As^{5+}. Monitoring the Mn 2*p* XPS spectrum it was observed that Mn(III) accumulated in the near-surface of birnessite with

EBSCOhost - printed on 2/13/2023 5:26 AM via . All use subject to https://www.ebsco.com/terms-of-use

its largest amount being observed at 90 minutes reaction time. Along with accumulation of Mn(III), OH^- accumulated at the surface (as apparent in the O 1*s* spectrum), suggesting that an intermediate reaction product was MnOOH. After 90 minutes, Mn(III) decreased in abundance (Nesbitt et al. 1998b), suggesting that the surface Mn^{3+} of MnOOH undergoes reductive dissolution in the following reaction:

$$2MnOOH + H_3AsO_3 + 4H^+ = 2Mn^{2+} + H_3AsO_4 + 3H_2O \quad (15)$$

The sum of Reactions (14) and (15) divided by 2 yields Reaction (13).

These types of study could be conducted at much greater surface sensitivity if the Kratos charge compensation system were incorporated into the end station of a synchrotron beam line where photon energies could be optimized for maximum surface sensitivity. With selection of appropriate photon energies, exceptional surface sensitivity can be obtained (Nesbitt et al. 2000), and with an appropriate charge compensation system, the surface and bulk peaks would be the narrowest possible. This is particularly important for studies of 3*d* metals with complex metal 2*p* spectra.

Leaching of silicates

There are a large number of XPS studies of leaching of silicates (for reviews, see Hochella 1988; Oelkers 2001; Zakaznova-Herzog et al. 2008) where changes to core level XPS intensities are monitored to document the change in elemental compositions at the leached surface of the solid. The older instrumentation used in most of these studies did not allow collection of high resolution narrow scans of leached silicate surfaces; but recent advances in XPS technology, particularly with respect to charge compensation, allow detailed chemical state information to be collected for the leached layer from both O 1*s* and valence band spectra (e.g., Zakaznova-Herzog et al. 2008).

There is agreement among most XPS studies that cations such as Mg^{2+} and Ca^{2+} of leached olivines and pyroxenes are depleted in the surface layer. The general consensus is that the exchange of Mg^{2+} (and Ca^{2+}) for $2H^+$ is the initial leaching step and that exchange extends to a depth of about 20Γ (e.g., Rosso and Rimstidt 2000; Schott et al. 1981; Schott and Berner 1985; Oelkers and Schott 2001; Zakaznova-Herzog et al. 2008). Few studies, however, have presented high resolution, narrow scans of O 1*s*, Si 2*p* or other photolines.

The study of Zakaznova-Herzog et al. (2008) is an exception, and this study illustrates the importance of the high resolution achievable with the Kratos instrument. They collected XPS spectra of olivine and pyroxenes for pristine surfaces (Figs. 9, 10, 13) and for surfaces leached in pH 2 solutions (e.g., Fig. 24) and the following discussion emphasizes the level of detail that now can be obtained for pristine and leached silicates. The initial reaction is exchange of Mg^{2+} for $2H^+$ at the olivine surface:

$$2H^+_{(aq)} + Mg_2SiO_4 \rightarrow Mg^{2+}_{(aq)} + H_2Mg(M1)SiO_{4(surf)} \quad (16)$$

where the Mg^{2+} of the M2 site is exchanged with the $2H^+$ which is bonded to oxygen to produce two OH groups bonded to Si; that is an Si-NBO moiety → Si-OH moiety and the surface complex is denoted as $H_2Mg(M1)SiO_{4(surf)}$.

Evidence for the surface complex, $H_2Mg(M1)SiO_{4(surf)}$, is obtained from both the O 1*s* core level and the valence level XPS spectra of olivine. We present the valence band (VB) spectra first because it provides unique information. The details of the valence band interpretations are given in the next section of this review. The VB band spectra for pristine and leached olivine are similar (Fig. 24) with the exception of a weak signal at about 13.5 eV BE in the VB spectra of leached olivine. Collection of many spectra at different leach times has verified the presence of this 13.5 eV peak (Zakaznova-Herzog 2008, their Fig. 9). Density functional calculations were performed to simulate the spectrum for the $H_2Mg(M1)SiO_4$ surface complex, and the

EBSCOhost - printed on 2/13/2023 5:26 AM via . All use subject to https://www.ebsco.com/terms-of-use

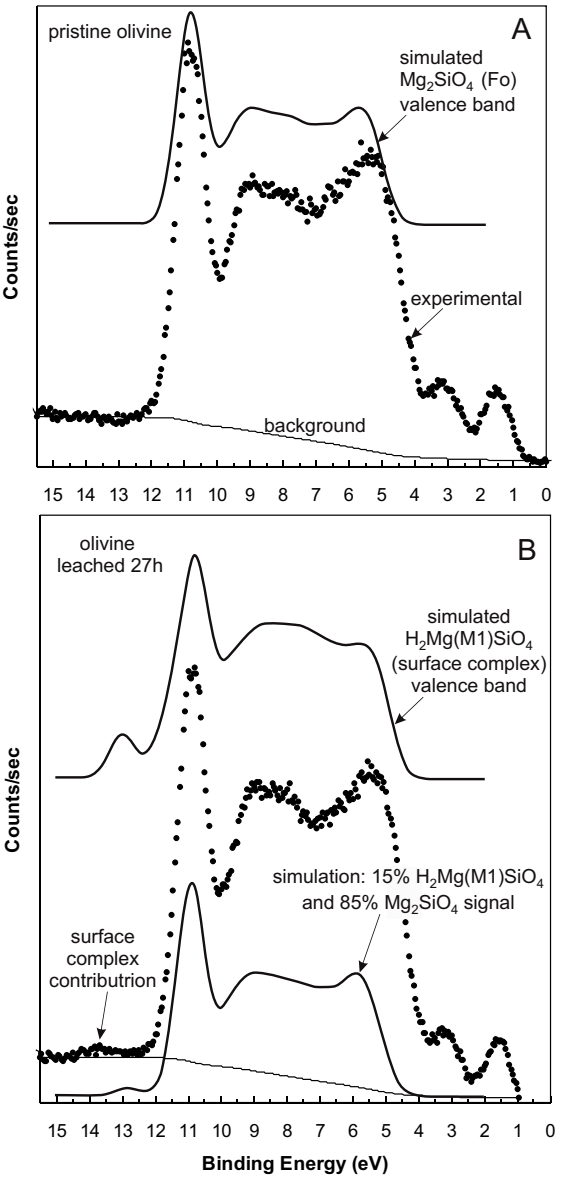


Figure 24. XPS valence band spectra of pristine and leached olivine (dots), and valence bands calculated using density functional theory (DFT). A) XPS valence band spectrum of pristine olivine (dots), and a Shirley background for the data. The solid curve is the forsterite (Mg_2SiO_4) valence band calculated using DFT. The experimental data displays two peaks at about 1.5 and 3.0 eV. These are the Fe 3*d* e_g and t_{2g} contributions. These Fe orbitals are not included in the DFT calculation (Nesbitt et al. 2011). B) XPS valence band of olivine leached in pH = 2 solution for 27 hours (dots). Top curve is the calculated valence band for the species $H_2Mg[M1]SiO_4$ and the bottom curve is the simulated valence band of forsterite where 15% of the signal is that of the surface complex (i.e., top curve of Fig. 23B) and 85% is that of pristine forsterite (i.e., solid curve of Fig. 23A). An original diagram with all data, the conditions for the experiments and details of the DFT calculations are from Zakaznova-Herzog et al. (2008).

EBSCOhost - printed on 2/13/2023 5:26 AM via . All use subject to https://www.ebsco.com/terms-of-use

calculations verify the existence of a peak at ~ 13 eV BE (Zakaznova-Herzog 2008, their Figs. 11A and B). The simulated spectra are obtained by convoluting the calculated Density of States (DOS) with the theoretical XPS cross sections as discussed in the next section. The calculations reveal an intense, narrow peak of Si 3*s* character DOS at 12.9 eV for the $H_2Mg(M1)SiO_4$ surface complex. The predicted 12.9 eV peak is in reasonable agreement with the observed 13.5 eV. The result provides reasonable evidence for the presence of the surface complex, hence for initial exchange of $2H^+$ with Mg^{2+} in the M2 site of olivine.

The intensity of the surface complex peak at 13.5 eV is very weak and an explanation is warranted. If the simulated VB spectrum for $H_2Mg(M1)SiO_{4(surf)}$ is considered to be one monolayer thick, it should contribute about 15% of the intensity of the overall spectrum, with 85% coming from unaltered (pristine) underlayers of olivine. The resulting simulation has a peak at ~13 eV with similar intensity to the 13.5 eV peak in experimental spectrum (Zakaznova-Herzog et al. 2008, their Figs. 11A and B, Fig. 24B,bottom). The experimental data and calculations are in close agreement, thus providing confidence that the $H_2Mg(M1)SiO_{4(surf)}$ surface complex is developed on olivine leached surfaces, and strongly supports the conclusions of previous studies that H-Mg exchange takes place in the near surface region of olivine and pyroxenes.

There are also changes in core level photopeaks associated with leaching. The O 1*s* spectrum of leached olivine (Zakaznova-Herzog et al. 2008) shows an increase in intensity of the 532 eV BE peak shown in Figure 10B, due to OH in Equation (13). The pristine diopside O 1*s* spectrum displays a strong spectral minimum at about 531.9 eV (Fig. 25A). The same diopside leached for 3 days (Fig. 25B) shows no such minimum, and the XPS signal has gained appreciable intensity in the region of 532 eV. The intensity is due to OH^- accumulation in the near-surface (solid peak in Fig. 25B) according the following reaction scheme (Zakaznova-Herzog et al. 2008). Diopside leaching begins at the mineral solution interface with exchange of $2H^+$ for Ca^{2+} of the M2 site:

$$CaMgSi_2O_6 + 2H^+ \rightarrow Ca^{2+} + H_2Mg(M1)Si_2O_{6(surf)} \quad (17)$$

where the two H atoms of $H_2Mg(M1)Si_2O_{6(surf)}$ are attached to O atoms to produce OH^- groups, This electrophilic exchange reaction is followed by a second, slower electrophilic reaction, where the $H_2Mg(M1)SiO_{4(surf)}$ is attacked by two additional H^+:

$$H_2Mg(M1)SiO_{4(surf)} + 2H^+ \rightarrow Mg^{2+} + H_4SiO_{4(surf)} \quad (18)$$

After this reaction, all Mg-O-Si bonds at the surface have been ruptured and Mg^{2+} has been released to solution. The two electrophilic reactions are followed by a nucleophilic attack of H_2O (or H_3O^+) on bridging oxygen atoms (Si-O-Si moiety in the near-surface) resulting ultimately in the release of $H_4SiO_{4(aq)}$ to solution. Once steady state is achieved (all reactions proceed at the same rate), congruent dissolution then ensues as is seen in most leaching studies (e.g., Pokrovsky and Schott 2000a,b).

The leached diopside spectrum in Figure 25B shows a substantial gain in intensity at about 532 eV (due to OH^-) which "fills in" the valley in the pristine spectrum (Fig. 24A). The best fit to the pristine diopside O 1*s* spectrum (Fig. 25A) is superimposed on that of the leached spectrum (dotted lines, Fig. 25B), thus emphasizing the gain in intensity due to the OH^- signal (in bold, Fig. 25B). Also apparent is a slight broadening of linewidths for the leached sample. Whereas the three peaks fitted to the pristine signal (Fig. 25A) have a FWHM up to 1.4 eV, a FWHM value of 1.5 to 1.6 eV is required to fit properly the leading and trailing edges of the leached sample. Nevertheless, the O 1*s* linewidths are remarkably similar for both pristine and leached samples. The intensity of the OH^- peak in diopside (~ 14%) is about double that from olivine (Zakaznova-Herzog et al. 2008) as expected from Equations (13) for olivine and (14) and (15) for diopside.

EBSCOhost - printed on 2/13/2023 5:26 AM via . All use subject to https://www.ebsco.com/terms-of-use

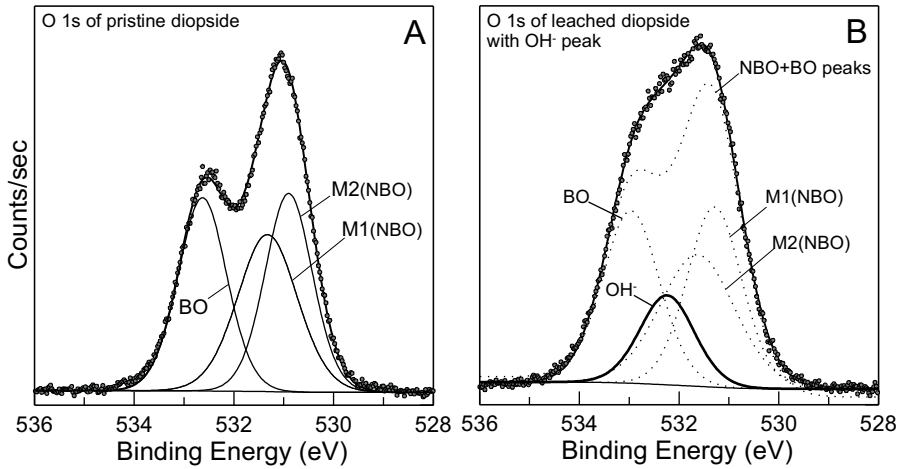


Figure 25. XPS O 1*s* spectra of pristine diopside and diopside leached for 3 days in pH 2 solution. A) The O 1*s* spectrum of pristine diopside is fitted with three peaks of equal area (solid curves). B) The dots are the O 1*s* spectrum of leached diopside and the dotted curves represent the three-peak fit to the prisitine diopside (of Fig. 24A). The solid curve represents the O 1*s* contribution of OH^- and constitutes 15% of the total O 1*s* signal. It accounts for the difference between the pristine and leached spectra of diopside. An original diagram with all data are taken from files used by Zakaznova-Herzog et al. (2008). Our fits to the two spectra are shown and are slightly broader than those of Zakaznova-Herzog et al. (2008).

VALENCE LEVEL BULK APPLICATIONS

Nature of the contributions to the valence band

***Crystalline minerals*.** As shown in Figure 1, the orbital contributions to the VB (e.g., O 2*s*, Si 3*p*, O 2*p*, Si 3*p* orbitals) are weak compared with the O 1*s*, Si 2*s*, Si 2*p* core level contributions. The large intensity differences are due to the large cross sections of the core level orbitals (Fig. 2A, O 1*s*, Si 2*s*, Si 2*p*) compared with the much smaller cross sections for the valence level orbitals (Fig. 2B, O 2*s*, Si 3*p*, O 2*p*, Si 3*p* orbitals). For example, the O 2*p* cross section at 1486 eV excitation energy is 200 times less than the O 1*s* cross section [2×10^{-4} Megabarns (MB) compared to the 4×10^{-2} MB (Yeh and Lindau 1985)]. Because of the low intensities, long counting times (hours) are required to obtain good valence spectra, and any charging or surface decomposition can severely degrade the quality of the spectra. As noted earlier, the only good, high resolution, valence spectra of a crystalline natural silicate mineral that had been recorded with X-rays are the spectra of crystalline and amorphous SiO_2 (Fischer et al. 1977; Di Pomponio et al. 1995).

The small photon cross sections of the valence orbitals make it difficult to collect good quality VB spectra for non-conductor silicates. Of greatest concern is surface charging and charge shifting of peaks during collection of the spectra. These spectra can be, however, collected using the Kratos Ultra Axis instrument; and VB spectra have been collected with this instrument for quartz, olivines and pyroxenes (Zakaznova et al. 2005, 2006). The second goal was to determine the sensitivity of these spectra to different tetrahedral linkages in silicates (e.g., SiO_4^{4-} units in olivines, $Si_2O_6^{4-}$ units in pyroxenes, and polymeric $(SiO_2)_n$ in quartz). With collection of high resolution VB spectra, the third objective was to test the quality of theoretical calculations by comparing the calculated spectra to the experimental high resolution spectra. Until about 2005, such calculations had been reported for VB partial density of states (PDS) for only crystalline SiO_2 (e.g., Laughlin et al. 1979; Li and Ching 1985; Di Pomponio et al. 1995), and a few synthetic Na and Li silicate structures (Ching et al. 1983, 1985).

EBSCOhost - printed on 2/13/2023 5:26 AM via . All use subject to https://www.ebsco.com/terms-of-use

The VB spectra of quartz (SiO_2), olivine $[Mg_{0.87}Fe_{0.17}]_2SiO_4$, diopsidic clinopyroxene $[Ca(Mg_{0.8}Fe_{0.2})Si_2O_6]$, and bronzite $[Mg_{0.8},Fe_{0.2}]_2Si_2O_6]$ are shown in Figure 26 (Zakaznova-Herzog et al. 2005, 2006). The binding energy of the VB of each mineral is located between ~15 eV to ~1eV. The O 2*s* peaks are not shown but are located between 20 eV and 25 eV BE. The resolution and counting statistics are sufficiently good to reveal narrow peaks (e.g., peak 5 in the olivine spectrum). Indeed, peak 5 in the olivine spectrum has a width of about 1.2 eV which is comparable to the Si 2*p* and O 1*s* linewidths of olivine, indicating that there has been little or no differential charging or charge shifting during the several hours of VB spectral accumulation. The highest energy contribution to the olivine valence band is at about 11 eV BE (Fig. 26, peak 5), and it shifts systematically to higher BE from olivine to the pyroxenes and to quartz, which reflects SiO_2 connectivity from separate tetrahedra (olivine) to chains of tetrahedra (pyroxenes) and to the 3D network of quartz. The Fe 3*d* band, and particularly the Fe 3*d* t_{2g} orbitals, populate the top of the olivine and pyroxene valence bands (peaks 1 and 2) and are the highest occupied molecular orbital. As such, this band is the most energetic and most susceptible to reaction with reagents, whether oxidant or acid. Also, Mg-end members of olivine (forsterite), orthopyroxene (enstatite) and clinopyroxene (diopside) contain no Fe; hence the Fe 3*d* peaks

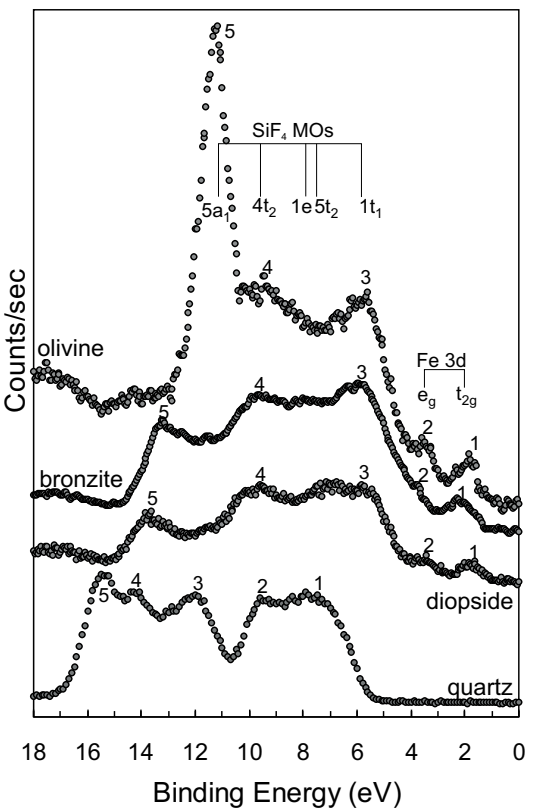


Figure 26. Valence band spectra of olivine, bronzite (orthoproxene), diopside (clinopyroxene) and quartz. The peaks of the four minerals are numbered 1 to 5 and correspond to the five peaks of Zakaznova-Herzog et al. (2005). The Molecular Orbitals (MOs) of SiF_4 are shown and as noted by Zakaznova-Herzog et al. (2005) are similar to the olivine peaks in the valence band if the Fe 3*d* peaks are ignored. The valence band structures of SiF_4 gas and of the SiO_4 units of olivine are similar. An original diagram with data taken from Zakaznova-Herzog et al. (2005, 2006, 2008), with modifications.

EBSCOhost - printed on 2/13/2023 5:26 AM via . All use subject to https://www.ebsco.com/terms-of-use

of Figure 26 (olivine, peaks 1, 2) would be absent. The top of their valence bands therefore will be determined by peak 3, which are predominantly O 2*p* non-bonding orbital contributions (Zakaznova-Herzog et al. 2005, 2006). The entire VB band spectrum of forsterite consequently spans less than 6 eV, whereas the quartz spectrum (peaks 1 to 5) spans more than 8 eV.

Peaks 1-5 in quartz and 3-5 in olivine can be broadly understood as due to molecular orbitals for a tetrahedral SiO_4 unit; and these peaks are qualitatively similar to the spectra for analogous tetrahedral $Si(OCH_3)_4$ and SiF_4 gas phase molecules (Yates et al. 1985; Sutherland et al. 1993). Thus, the shifted SiF_4 gas phase molecular orbital energies from the VB spectrum in Figure 26 shows the same relative energies and range of energies as the olivine spectrum. The low BE peaks in both spectra can be associated with the non-bonding O 2*p* $1e$, $5t_2$, and $1t_1$ orbitals. The higher energy peaks (3, 4 in quartz, and 4, 5 in olivine) can be associated with the $5a_1$ and $4t_2$ bonding orbitals resulting from O 2*p*-Si 3*p* mixing. Fischer et al. (1977) and Di Pomponio et al. (1995) assigned peak 5 of quartz as a K 3*p* line from a K impurity, but the assignment cannot be correct because our sample contains no detectable K; consequently, the simple MO treatment cannot account for peak 5 in the quartz spectrum. The two weak, low energy lines in the olivine spectrum are due to the crystal field split Fe 3*d* orbitals- the e_g and t_{2g} levels (Zakaznova-Herzog et al. 2005).

Theoretical calculations have reproduced qualitatively the VB band spectra of crystalline SiO_2, and several Li, Na silicates (Ching et al. 1983, 1985; Di Pomponio et al. 1995). No detailed comparison, however, of theory and experiment was made for two major reasons: first, the density of states were not converted to photoemission intensities (see below); and second, the spectral quality was not as good with the older XPS instruments and charge neutralization systems. The theoretical and experimental valence band spectra for olivine are given in Figure 24A. The partial density of states (PDS) were calculated using the known crystal structures (Deer et al. 2004) within the pseudopotential density functional theory (DFT) using the program SIESTA (Zakaznova-Herzog et al. 2005). As Zakaznova-Herzog et al. (2005) demonstrate, the majority of the PDS in the outer valence region arises from the O 2*p* electrons, with very substantial contributions from the Si 3*p* electrons and smaller contribution from Si 3*s*. The Mg 3*s* and 3*p* valence electrons have cross sections that are *much* smaller than either the O or Si valence electrons (Zakaznova-Herzog et al. 2005), and make *no* significant contribution to the VB spectra of olivines or any other silicate. This is also true of all alkali or alkaline earth elements in silicates. To convert these PDSs to a photoelectron spectrum, the Gelius model (Gelius 1974) is employed, which has been used very successfully for gas phase molecules (Bancroft and Hu 1999). The photoionization cross section for a MO is determined by the atomic orbital components of that MO multiplied by the appropriate atomic cross sections. Mathematically, the intensity of the j^{th} MO (I_j^{MO}) is proportional to:

$$I_j^{MO} \propto \sum P_{A\lambda} \sigma_{A\lambda}{}^{AO} \tag{19}$$

where $P_A\Gamma$ is the probability of finding an electron in the j^{th} MO belonging to the atomic AΓ orbital and $\sigma_A\Gamma^{AO}$ are the atomic cross sections for all orbitals Γ of atoms A in an MO (Fig. 2). These probabilities are given from the population analysis from an MO calculation. For these solids, the PSD values have been used instead of the $P_A\Gamma$ for molecules. Thus, each PSD is multiplied by the atomic cross sections, and summed at a given energy.

The comparison of experimental valence band spectra with calculation has been made by Zakaznova-Herzog et al. (2005, 2006), and after aligning peak 5 in the experimental and calculated spectrum, there is generally good agreement—thus the Gelius treatment works very well for solids as well as molecules. As an example of the agreement, the experimental valence spectrum for Mg-rich olivine and the calculated valence spectrum for forsterite (Mg_2SiO_4) are illustrated in Figure 24A. If the Fe 3*d* peaks are ignored there is excellent agreement with experiment. DFT calculations were also performed on an olivine containing Fe, and although

EBSCOhost - printed on 2/13/2023 5:26 AM via . All use subject to https://www.ebsco.com/terms-of-use

all the relative intensities are in good agreement, the Fe 3*d* peaks 1 and 2 are situated at greater binding energy relative to peaks 3-5 than observed experimentally.

The same type of DFT calculations were performed for idealized diopside and bronzite of compositions $CaMgSi_2O_6$ and $Mg_2Si_2O_6$, respectively and comparison with experimental results are reasonable (Zakaznova-Herzog et al. 2006). The calculations reproduce all the major features including the relative energies and intensities, the implication being that the different cations and small structural differences make relatively little difference to these spectra. Because Ca and Mg orbital contributions are minimal in the pyroxenes, and major contributions to their valences bands are dominantly O 2*p* with smaller contributions of Si 3*p* character, the $Si_2O_6^{4-}$ unit determines in large part the pyroxene spectral properties. Nevertheless, subtle differences between the spectra are reproduced by the calculations. For example, peaks 3 and 4 are shifted to slightly higher energy in bronzite than in diopside (Fig. 26); and there is a larger splitting between peaks 3 and 4 in bronzite than in diopside. Many more such valence band spectra of silicates need to be obtained and calculated; and as discussed in the last section of this review, these spectra can be important aids in determining structural changes in silicates and modified silicate surfaces.

Vitreous silica and alkali-silicate glasses. The VB spectra of vitreous SiO_2 has been documented by many and some very early work provided spectra with good resolution (e.g., Stephenson and Binkowski 1976; Laughlin et al. 1979). They are as good as any published during the following 30 years. The VB spectrum illustrated in Figure 27 is, however, of greater resolution (collected in our laboratory, Nesbitt et al. 2014b). Figure 27A includes the entire valence band and the O 2*s* level, (spectrum standardized to the C 1*s* line at 285.0 eV). The high resolution results from two technical advances; the development of good charge compensation systems, and the development of more efficient analyzers. The first compensates for surface charging and the latter increases count rates dramatically. The latter advance is as important as the former advance because the photon cross sections of the orbitals contributing to valence bands generally are very small at 1487 eV photon energy (Fig. 2). The efficient analyzers consequently allow collection of high resolution VB spectra in a reasonable time and with good counting statistics.

The O 2*s* state, centered at about 25.5 eV (Fig. 27B), is strongly asymmetric and in this respect much different from the O 1*s* core-level spectrum (Fig. 19A). Theoretical studies provide the explanation for the strong asymmetry in that they indicate numerous orbital contributions to the peak. MO calculations of Uchino et al. (1991) and de Jong and Brown (1980) indicate that the O 2*s* band consists mostly of non-bonding O 2*s* character which is nearly localized on the O atom but some Si 3*s*, Si 3*p* character is present. de Jong and Brown (1980) calculate 5 separate contributions to the O 2*s* band spanning a BE range of almost 4 eV, which is about the FWHM of the collected spectrum. Their calculations indicate that σ, π and non-bonding orbitals of mostly O 2*p* character contribute to and broaden the O 2*s* band. In addition, asymmetry on the O 2*s* peak may result from the breakdown of the one-electron approximation in Equation (1) (Langhoff et al. 1981), giving a number of overlapping peaks from states that are admixtures of single-hole and multi-hole states. The O 2*s* line cannot be considered a core-level line, yet the band is mostly localized. One peak fitted to conform to the leading edge of the O 2*s* band yields a FWHM of 2.26 eV, which is much broader than the O 1*s* core level peak of vitreous silica (Fig. 19A), indicating that the O 2*s* spectrum is more complex than the truly core-level O 1*s* line. Furthermore, and although the fitted peak is already broad, it an entirely inadequate fit to the entire O 2*s* band. At least one additional peak is needed to obtain a reasonable fit. Additional theoretical approaches are required to explain its asymmetry and breadth.

The valence band of vitreous silica extends from about 17 eV to 4 eV binding energy. The measured VB-Conduction Band (CB) energy gap is about 9 eV (DiStefano and Eastman 1971), and at least 4 eV of this gap is shown in Figure 27C. The bottom of the CB consequently is

EBSCOhost - printed on 2/13/2023 5:26 AM via . All use subject to https://www.ebsco.com/terms-of-use

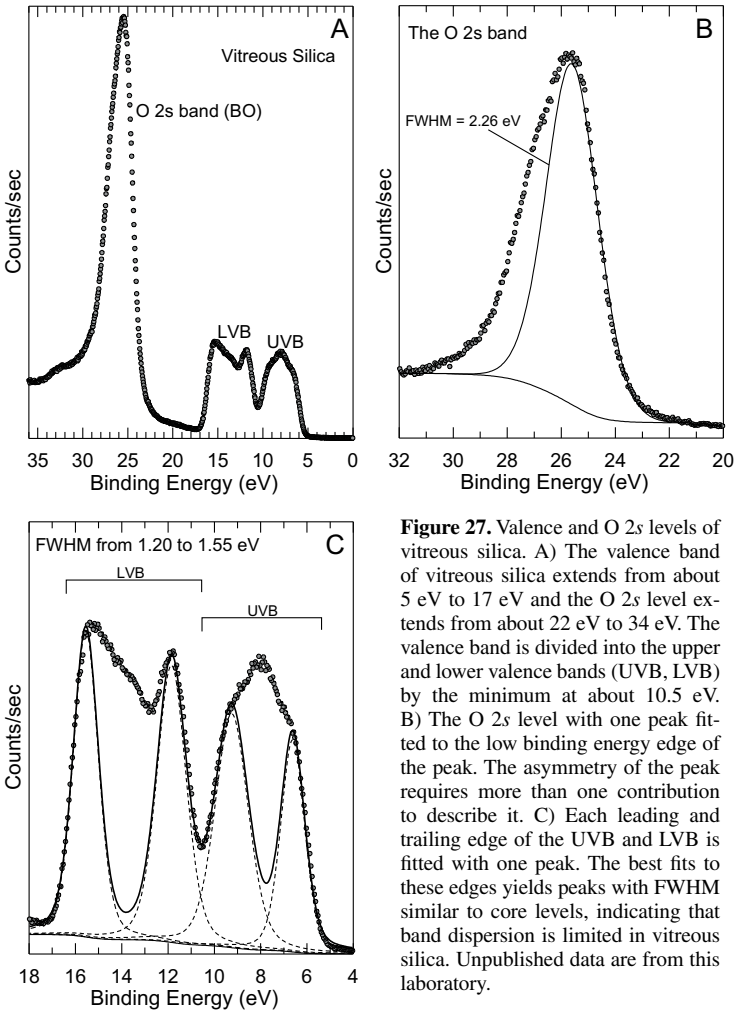


Figure 27. Valence and O 2*s* levels of vitreous silica. A) The valence band of vitreous silica extends from about 5 eV to 17 eV and the O 2*s* level extends from about 22 eV to 34 eV. The valence band is divided into the upper and lower valence bands (UVB, LVB) by the minimum at about 10.5 eV. B) The O 2*s* level with one peak fitted to the low binding energy edge of the peak. The asymmetry of the peak requires more than one contribution to describe it. C) Each leading and trailing edge of the UVB and LVB is fitted with one peak. The best fits to these edges yields peaks with FWHM similar to core levels, indicating that band dispersion is limited in vitreous silica. Unpublished data are from this laboratory.

at about +5 eV BE, assuming that the BE scale is accurately standardized. The valence band of vitreous silica is conveniently divided into the upper and lower valence band (Fig. 27C, UVB and LVB respectively) by a minimum located at about 10.5 eV. Numerous theoretical approaches, most of which are in agreement, interpret the UVB (5 to 10.5 eV) to represent mostly O 2*p* non-bonding orbital contributions; whereas the LVB is considered to be composed mostly O 2*p* (with hybridized Si sp^3 states) bonding orbital contributions (Sarnthein et al. 1995; Tilocca and de Leeuw 2006).

The leading and trailing edges of both the UVB and the LVB have been fitted with a 70% Gaussian- 30% Lorentzian peak shape, and the linewidths range between 1.20 and 1.55 eV. The peak widths are as narrow as the vitreous silica Si 2*p* and O 1*s* core level line widths (Figs. 18A and 20A). The linewidths demonstrate that the upper and lower valence bands do not vary (or wander) appreciably in energy within the first Brillouin zone. These band widths may be controlled as much by final state vibrational and phonon broadening (as for the Si 2*p* and O 1*s* linewidths) as by band energy wandering within the Brillouin zone. The conclusion

EBSCOhost - printed on 2/13/2023 5:26 AM via . All use subject to https://www.ebsco.com/terms-of-use

is consistent with the theoretical treatment of the band structure for α-quartz (Laughlin et al. 1979). They calculated the band energies for quartz and the bands in the UVB varied by less than 2 eV across the first Brillouin zone. The quartz valence band is strikingly similar to the VB of vitreous silica in all respects (Stephenson and Binbkowski 1976) as apparent by comparing the VB of α-quartz in Figure 26 with that of vitreous silica (Fig. 27A). Band dispersion within the UVB of both phases likely is similar and apparently less than 2 eV, implying that individual bands of the UVB are almost as narrow as core levels. The narrow valence band contributions open the possibility of using VB XPS spectra to determine which orbitals are quenched and which are formed when SiO_2 polymorphs and vitreous silica are engaged in reactions with other substances provided high resolution XPS spectra are collected.

The valence band spectra for three Na-silicate glasses spanning the compositional range 20% Na_2O to 55% Na_2O are illustrated in Figure 28 (Nesbitt et al. 2014b). The highest binding energy line is the Na 2*s* core level signal. It is present in the three spectra shown but is not considered part of the VB. The peak labeled the O 2*s* band is composite and consists of a BO peak and an NBO peak with the latter located at somewhat lower BE than the BO peak. The relative intensities of the BO and NBO component change systematically with Na_2O content. A fit to the O 2*s* band of the 20% Na_2O glass is shown (Fig. 28A). The high BE fitted peak (i.e., the BO peak) has a FWHM of 3.04 eV and the lower BE fitted peak (NBO peak) has a linewidth of 1.67 eV. Both are much broader than observed for the O 1*s* spectrum (e.g., Fig. 20). As for vitreous silica, there are

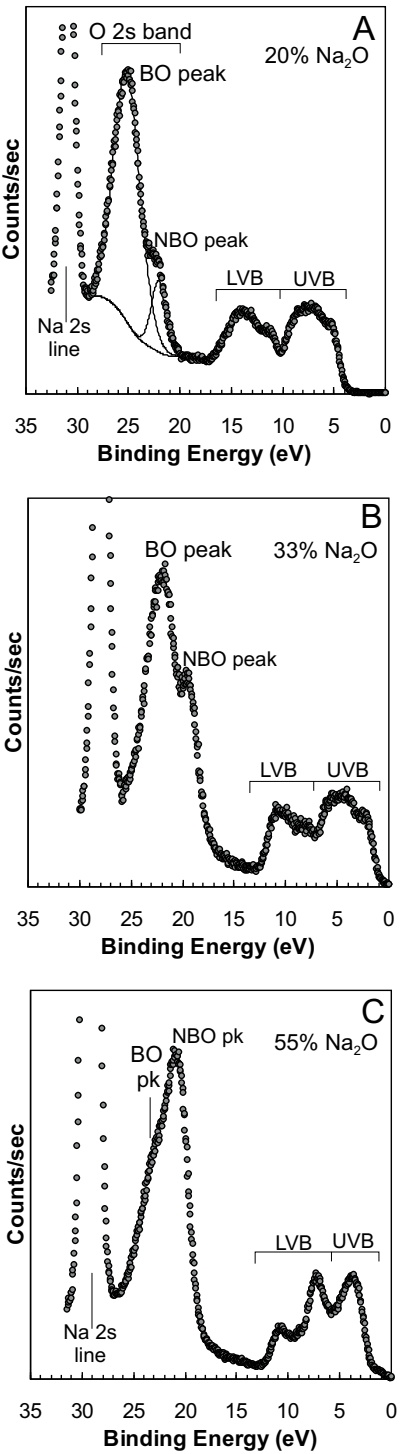


Figure 28. Valence band, O 2*s* and Na 2*s* levels of Na-silicate glasses illustrating the change in the BO:NBO with glass composition. A) The valence band of Na-silicate glass containing 20% Na_2O. The O 2*s* level has been fitted with two peaks (see text for comment). B) The valence, O 2*s* and Na 2*s* levels of Na-silicate glass containing 33% Na_2O. C) The valence, O 2*s* and Na 2*s* levels of Na-silicate glass containing 55% Na_2O. All data are from this laboratory (Nesbitt et al. 2014b). These spectra will be accurately calibrated in the forthcoming publication.

EBSCOhost - printed on 2/13/2023 5:26 AM via . All use subject to https://www.ebsco.com/terms-of-use

apparently numerous MO contributions to the O 2*s* band of the Na-silicates, and these cannot be used to evaluate the proportions of BO and NBO in the glass without much more study.

The valence band of the Na-silicates can be divided into upper and lower valence band, and are labeled UVB and LVB (respectively) in Figure 28. The valence band, O 2*s* and Na 2*s* bands shift systematically to lower BE with increased Na_2O content, as for the core level lines in Figure 20. In addition, measurements of the areas of the UVB and LVB indicate that there is a progressive shift in peak intensity, from the UVB to the LVB with increased Na_2O content. The details of these findings will be reported elsewhere (Nesbitt et al. 2014a). The shift in VB intensity is consistent with the recent Car-Parrinello molecular dynamics calculations of Na-silicate glass containing 30% Na_2O (Tilocca and de Leeuw 2006). They observed that the UVB is composed primarily of O 2*p* non-bonding contributions whereas the LVB consists primarily of orbitals of O 2*p* BO character (with some Si 3*p* character). The shift in intensity from LVB to UVB consequently is expected with increased Na_2O content because a greater proportion of NBO atoms are expected.

The VB structure of the glass containing 55% Na_2O (Fig. 28C) is different from the glasses containing 20% and 33% Na_2O. Three distinct peaks are developed but the nature of the contributions to these peaks is unknown. To our knowledge there are no DFT or molecular dynamics of sodic glasses containing very high Na_2O contents. This may be a fruitful area of research, both from theoretical and experimental perspectives. At some composition, the Na-silicate glass must change character from a silicate-based framework to an oxide (O^{2-}) based framework. The 55% Na_2O glass may represent the initiation of the transition.

ACKNOWLEDGEMENTS

We are very pleased to acknowledge our dedicated colleagues doing silicate XPS research in the last eight years: our experimental colleagues M.C. Biesinger, K.N. Dalby, R. Davidson, G.S. Henderson, R.Ho, Y. Huang, P.A. King, N.S. McIntyre, A.R. Pratt, R.A. Secco, W. Skinner, Z.Yan, and V.P Zakaznova-Herzog; and our theoretical colleagues X. Gao, D.M. Shaw, and J.S. Tse.

We are very grateful to M.C. Biesinger and the Surface Science Western (SSW) staff for all their technical and experimental assistance. We also thank the Canadian Foundation for Innovation and NSERC (Canada) for funding the XPS spectrometer and many salary and operating expenses.

We are very grateful to one of the referees, Alan Buckley, for a very comprehensive review of our manuscript, and especially for running the XPS spectra of quartz on his ESCALAB 250Xi instrument. The manuscript has been greatly improved as a result of his generous contributions.

REFERENCES

Adams I, Thomas JM, Bancroft GM (1972) An ESCA study of silicate minerals. Earth Planet Sci Lett 16:429-432

Aksela S, Bancroft GM, Bristow DJ, Aksela H, Schrobilgen GJ (1985) Auger energy shifts and core level relaxation energies in XeF_2, XeF_4, and XeF_6. J Chem Phys 82:4809-4812

Al-Kadier M, Tolon C, Urch DH (1984) Photoelectron and X-ray spectroscopy of minerals. J Chem Soc Faraday Trans 2:669-679

Bancroft GM, Hu Y (1999) Photoelectron spectra of inorganic molecules in the gas phase using synchrotron radiation. *In*: Inorganic Electronic Structure and Spectroscopy. Solomon EI, Lever ABP (eds), John Wiley and Sons, New York 1:443-512

Bancroft GM, Hyland MM (1990) Spectroscopic Studies of adsorption/reduction reactions of aqueous metal complexes on sulfide surfaces. Rev Mineral 23:511-558

EBSCOhost - printed on 2/13/2023 5:26 AM via . All use subject to https://www.ebsco.com/terms-of-use

Bancroft GM, Burns RG, Howie RA (1967) Determination of the cation distribution in the orthopyroxene series by the Mossbauer effect. Nature 213:1221-1223

Bancroft GM, Nesbitt HW, Ho R, Shaw DM, Tse JS, Biesinger MC (2009) Toward a comprehensive understanding of solid state core-level XPS linewidths: experimental and theoretical studies on the Si 2p and O 1s linewidths in silicates. Phys Rev B 80:075405

Barr TL (1993) Modern ESCA, The Principles and Practice of X-Ray Photoelectron Spectroscopy. CRC Press, Boca Raton, Florida

Biesinger MC, Brown C, Mycroft JR, Davidson RD, McIntyre NS (2004) X-ray photoelectron spectroscopy studies of chromium compounds. Surf Interface Anal 36:1550-1563

Biesinger MC, Payne BP, Lau LWM, Gerson AR, Smart RStC (2009) X-ray photoelectron spectroscopic chemical state quatification of mixed nickel metal, oxide and hydroxide systems. Surf Interface Anal 41: 324-332

Biino G, Groning P (1998) X-ray photoelectron spectroscopy (XPS) used as a structural and chemical surface probe on aluminosilicate minerals. Eur J Mineral 10:423-427

Bozek JD, Bancroft GM Cutler JN, Tan KH (1991) Vibrationally resolved core-level photoelectron spectroscopy: Si 2p levels of SiH_4 and SiF_4 molecules. Phys Rev Lett 65:2757-2761

Bruckner R, Chun H-U, Gorretzki H (1978) Photoelectron spectroscopy (ESCA) on alkali silicate- and soda aluminosilicate glasses. Glasstechn Ber - Glass Sci Technol 1:1-7

Bruckner R, Chun H-U, Gorretzki H, Sammet M (1980) XPS measurements and structural aspects of silicate and phosphate glasses. J Non-Cryst Solids 42:49-60

Carlson TA (1975) Photoelectron and Auger Spectroscopy. Plenum Press, New York

Carravetta V, Agren H (1987) Stieltjes imaging method for molecular Auger transition rates: application to the Auger spectrum of water. Phys Rev A 35:1022-1032

Carroll TX, Berrah N, Bozek JD, Hahne J, Kukk E, Saethre LJ, and Thomas TD (1999) Carbon 1s photoelectron spectrum of methane: vibrational excitation and core-hole lifetime. Phys Rev A 59:3386-3393

Carroll TX, Hahne J, Thomas TD, Saethre LJ, Berrah N, Bozek JD, Kukk E (2000) Carbon 1s core-hole lifetime in CO_2. Phys Rev A 61:042503 (1-7)

Carroll TX, Borve KN, Saethre LJ, Bozek JD, Kukk E, Hahne J, Thomas TD (2002) Carbon 1s photoelectron spectroscopy of CF_4 and CO: Search for chemical effects on the carbon 1s hole-state lifetime. J Chem Phys 116:10221-10228

Chakraborty S, Bardelli F, Mullet M, Greneche JM, Varma S, Ehrhardt JJ, Banerjee D, Charlet L (2011) Spectroscopic studies of arsenic retention onto biotite. Chem Geol 281:83-92

Chambers SA (2000) Epitaxial growth and properties of thin film oxides. Surf Sci Reports 39:105-180

Cheung SH, Nachimuthu P, Joly AG, Engelhard MH, Bowman MK, Chambers SA (2007) N incorporation and electronic structure in N-doped TiO_2 (110) rutile. Surf Sci 601:1754-1762

Ching WY, Murray RA, Lam DJ, Veal BW (1983) Comparative Studies of electronic structures of sodium metasilicate and α amd β phases of sodium disilicate. Phys Rev B 28:4724-4735

Ching WY, Li YP, Veal BW, Lam DJ (1985) Electronic structures of lithium metasilicate and lithium disilicate. Phys Rev B 32:1203-1207

Citrin PH, Eisenberger P, Hamann DR (1974) Phonon broadening of X-ray photoemission linewidths. Phys Rev Lett 33:965-969

Clark JR, Appleman DE, Papike JJ (1968) Bonding in eight ordered clinopyroxenes isostructural with diopside. Contrib Mineral Petrol 20:81-85

Coville M, Thomas TD (1991) Molecular effects on inner-shell lifetimes: possible test of the one-center model of Auger decay. Phys Rev A 43:6053-6056

Dalby KN, Nesbitt HW, Zakaznova-Herzog VP, King PA (2007) Resolution of Bridging oxygen signals from O 1s spectra of silicate glasses using XPS: Implications for O and Si speciation. Geochim Cosmochim Acta 71:4297-4313

Davis MC, Sanders KJ, Grandinetti PJ, Gaudio SJ, Sabyasachi S (2011) Structural investigations of magnesium silicate glasses by ^{29}Si 2D magic-angle flipping NMR. J Non-Cryst Solids 357:2787-2795

de Jong BHWS, Brown GE (1980) Polymerization of silicate and aluminate tetrahedra in glasses, melts, and aqueous solutions – I. Electronic structure of $H_6Si_2O_7$, $H_6AlSiO_7^{1-}$, and $H_6Al_2O_7^{2-}$. Geochim Cosmochim Acta 44:491-511

de Koker NP, Stixrude L, Karki BB (2009) Thermodynamics, structure, dynamics, and freezing of Mg_2SiO_4 liquid at high pressure. Geochim Cosmochim Acta 72: 1427-1441.

Deer WA, Howie RA, Zussman J (2004) An Introduction to Rock-Forming Minerals. Longmans, London, John Wiley, New York, Geological Society, London Vols.1A, 1B, 2A, 2B, 3A, 4B

Di Pomponio A, Continenza A, Lozzi L, Passacantando M, Santucci S, Picozzi P (1995) Electronic properties of crystalline and amorphous SiO_2 investigated via all-electron calculations and photoemission spectroscopy Solid State Commun 95: 313-317

DiStefano TH, Eastman DE (1971a) Photoemission Measurements of the Valence Levels of Amorphous SiO_2. Phys Rev Lett 27:1560-1562

EBSCOhost - printed on 2/13/2023 5:26 AM via . All use subject to https://www.ebsco.com/terms-of-use

DiStefano TH, Eastman DE (1971b) The band edge of amorphous SiO_2 by photoinjection and photoconductivity measurements. Solid State Commun 9:2259-2261
Du J, Cormack AN (2004) The medium range structure of sodium silicate glasses: a molecular dynamics simulation. J Non-Cryst Solids 349:66-79
Duan X, Song C, Yu F, Yuan D, Li X (2011) X-ray photoelectron spectroscopy studies of Co-doped ZnO-Ga_2O_3-SiO_2 nano-glass-ceramic composites. Appl Surf Sci 257:4291-4295
Duer MJ, Elliot SR, Gladden LF (1995) An investigation of the structural units of sodium disilicate glass: a 2-D ^{29}Si NMR Study. J Non-Cryst Solids 189:107-117
Eastman DE, Chiang TC, Heimann P, Himpsel FJ (1980) Surface core-level binding-energy shifts for GaAs(110) and GaSb(110). Phys Rev Lett 45:656-659
Fadley CS (2010) X-ray photoelectron spectroscopy: progress and perspectives. J Electron Spectros Relat Phenom 178-179:2-32
Farmer VC (1974) The Infrared Spectra of Minerals. Mineralogical Society, London, England
Fayon F, Bessada C, Massiot D, Farnam I, Coutres JP (1998) ^{29}Si and ^{207}Pb NMR study of local order in lead silicate glasses. J. Non-Cryst Solids 232-234:403-408
Fischer B, Pollak RA, DiStefano TH, Grobman WD (1977) Electronic structure of SiO_2, $Si_xGe_{1-x}O_2$, and GeO_2 from photoemission spectroscopy. Phys Rev B 15:3193-3199
Fraser DG (1977) Thermodynamic properties in silicate melts. *In:* Thermodynamics in Geology. Fraser DG (ed) D. Reidel Dordrecht, p 301-326
Gadsen JA (1975) Infrared Spectra of Minerals and Related Inorganic Compounds. Butterworths, London, England (1975)
Gelius U (1974) Recent progress in ESCA studies of gases. J Electron Spectrosc Relat Phenom 5:985-1057
Grosvenor AP, Kobe BA, Biesinger MC, McIntyre NS (2004) Investigation of mutiplet splitting of Fe 2p XPS spectra and bonding in iron compounds. Surf Interface Anal 36:1550-1563
Gupta RP, Sen SK (1974) Calculations of multiplet structure of core p-vacancy levels. Phys Rev B 10:71-79
Gupta RP, Sen SK (1975) Calculations of multiplet structure of core p-vacancy levels II. Phys Rev B 12:15-19
Harmer SL, Nesbitt HW (2004) Stabilization of pyrite (FeS_2), marcasite (FeS_2), arsenopyrite (FeAsS) and lollingite ($FeAs_2$) surfaces by polymerization and auto-redox reactions. Surf Sci 564:38-52
Harmer SL, Skinner WM, Buckley AN, Fan L-J (2009) Species formed at cuprite fracture surfaces; observation of O 1s core level shift. Surf Sci 603:537-545
Heinrich VE, Cox PA (1994) The Surface Science of Metal Oxides. Cambridge University Press, Cambridge, U.K.
Henderson GS (2005) The structure of silicate melts: a glass perspective. Can Mineral 43:1921-1925
Henke BL, Gullikson EM, Davis JC (1993) X-ray interactions:photoabsorption, scattering, transmission and reflection at e = 50-30000 eV, Z = 1-92. At Data Nucl Data Tables 54 (#2):181-342
Herzog F, Zakaznova-Herzog VP (2011) Quantitative Raman spectroscopy: challenges, shortfalls, and solutions-application to calcium silicate glasses. Am Mineral 96:914-927 and references
Himpsel FJ, McFeely FR, Taleb-Ibrahimi A, Yarmoff J, Hollinger G (1988) Microscopic structure of the SiO_2/Si Interface. Phys Rev B 38:6084-6096
Hochella MF Jr, Brown GE (1988) Aspects of silicate and bulk structure analysis using X-ray photoelectron spectroscopy (XPS). Geochim Cosmochim Acta 52:1641-1648
Hochella MF Jr (1988) Auger electron and X-ray photolectron spectroscopies. Reviews in Mineral 18:573-637
Hufner S (1996) Photoelectron Spectroscopy: Principles and Applications. Springer-Verlag, Berlin
Ilton ES, Moses CO, Veblen D (2000) Using X-ray photoelectron spectroscopy to discriminate among different sorption sites of Micas: with implications for heterogeneous reduction of chromate at the mica-water interface. Geochim Cosmochim Acta 64:1437-1450
Ilton ES, Haiduc A, Moses CO, Heald SM, Elbert DC, Veblen DR (2004) Heterogeneous reduction of uranyl by micas: crystal chemical and solution controls. Geochim Cosmochim Acta 68:2417-2435
Ilton ES, Boily JF, Bagus PS (2007) Beam induced reduction of U(VI) during photoelectron spectroscopy: The utility of the U4f satellite structure for identifying uranium oxidation states in mixed valence uranium oxides. Surface Science 601:908-916
Jen JS, Kalinowski MR (1989) An ESCA study of the bridging to non-bridging oxygen ratio in sodium silicate glass and the correlations to glass density and refractive index. J Non-Cryst Solids 38-39:21-26
Jiang N, Denlinger JD, Spence JCH (2003) Electronic structure and oxygen bonding in $CaSiO_3$ silicate. J Phys Condens Matter 15:5523-5534
Karki BB (2010) First-principles molecular dynamics simulations of silicate melts: structural and dynamical properties. Rev Mineral Geochem 71:355-389
Karki BB, Bhattarai D, Mookherjee M, Stixrude L (2010) Visualization-based analysis of structural and dynamical properties of simulated hydrous silicate melt. Phys Chem Miner 37:103-117
Karlsson CJ, Owman F, Landmark E, Chao Y-C, Martensson P, Uhrberg, RI (1994) Si 2p core-level spectroscopy of the Si(111)-1x1):H and Si(111)-1x1):D surfaces: vibrational effects and phonon broadening. Phys Rev Lett 72**:**4145

EBSCOhost - printed on 2/13/2023 5:26 AM via . All use subject to https://www.ebsco.com/terms-of-use

Knipe SW, Mycroft JR, Pratt AR, Nesbitt HW, Bancroft GM (1995) X-ray photoelectron spectroscopic study of water adsorption on iron sulphide minerals. Geochim Cosmochim Acta 59:1079-1090

Krause MO, Oliver JH (1979) Natural widths of atomic K and L levels, K_α X-ray lines and several KLL Auger lines. J Phys Chem Ref Data 8:329-340

Langhoff PW, Langhoff SR, Rescigno TV, Schirmer J, Cederbaum LS, Domke W, Von Niessen W (1981) Theoretical studies of inner-valence-shell photoionization cross sections in N_2 and CO. Chem Phys 58:71-91

Larkins FP (1994) Influence of core hole screening on molecular Auger rates and inner shell lifetimes. J Electron Spectrosc Relat Phenom 67:159-162

Laughlin RB, Joannopoulos JD, Chadi DJ (1979) Bulk electronic structure of SiO_2. Phys Rev B 20:5228-5237

Lee CS, Wong SL, Lii KH (2009) $Cs_2K(UO)_2Si_4O_{12}$: A mixed valence uranium (IV,V) silicate. J Am Chem Soc 131:15116-15117

Leiro JA, Laajalehto K, Kartio I, Heimonen M (1998) Surface core-level shift and phonon broadening in PbS(100). Surf Sci 412/413:L918-L923

Lewis MH (1989) Glasses and Glass Ceramics. Chapman and Hall, London, New York

Li M, Kim DP (2011) Silicate glass coated microchannels through a phase conversion process for glass-like electrokinetic performance. Lab Chip 11:1126-1131

Li YP, Ching WY (1985) Band structures of all polycrystalline forms of silicon dioxide. Phys Rev B 31:2172-2179

Lippman T, Schneider JR (2000) Topological analyses of cuprite, Cu_2O, using high-energy synchrotron data. Acta Crystallogr A 56:575-584

Liu HK, Lii KH (2011) $Cs_2USi_6O_{15}$: A tetravalent uranium silicate. Inorg Chem 50:5870-5872

Liu ZF, Bancroft GM, Cutler JN, Sutherland DG, Tan KH (1992) Vibrational structure in core-level photoelectron spectra: periodic trends. Phys RevA 46:1688-1691

Lu ZH, McCaffrey JP, Brar B, Wilk GD, Wallace RM, Feldman LC, Tay SP (1995) SiO_2 film thickness metrology by X-ray photoelectron spectroscopy. Appl Phys Lett 71:2764-2766

Maekawa H, Maekawa T, Kawamura K, Yokokawa T (1991) The structural groups of alkali silicate glasses determined by ^{29}Si MAS-NMR. J Non-Cryst Solids 127:52-64

Malfait WJ, Halter WE, Morizet Y, Meier BH, Verel R (2007) Structural control on bulk melt properties: Single and double quantum ^{29}Si NMR spectroscopy on alkali-silicate glasses. Geochim Cosmochim Acta 71:6002-6018

Martin GB, Spera FJ, Ghiorso MS, Nevins D (2009) Structure, thermodynamic, and transport properties of molten Mg_2SiO_4: Molecular dynamics simulations and model EOS. Am Mineralo 94:693-703

Matson DW, Sharma SK, Philpotts JA (1983) The structure of high-silica alkali-silicate glasses: A Raman spectroscopic investigation. J Non-Cryst Solids 58:323-352

Matsumoto S, Nanba T, Miura Y (1998) X-ray photoelectron spectroscopy of alkali silicate glasses. J Ceram Soc Japan 106:415-421

Mattila S, Leiro JA, Heinonen M (2004) XPS study of the oxidized pyrite surface. Surf Sci 566-568:1097-1101

McDonald WS, Cruickshank DWJ (1967) A reinvestigation of the structure of sodium metasilicate Na_2SiO_3. Acta Crystallogr 22:37-43

McGuire EJ (1971) L-shell Auger and Coster-Kronig electron spectra. Phys Rev A 3:1801-1810

McMillan PF, Wolfe GH (1995) Vibrational spectroscopy of silicate liquids. Rev Mineral 32:247-315

Mekki A (2005) X-ray photoelectron spectroscopy of CeO_2-Na_2O-SiO_2 glasses. J Electron Spectrosc Relat Phenom 142:75-81

Mekki A, Salim M (1999) XPS study of transition metal doped silicate glasses. J Electron Spectrosc Relat Phenom 101-103:227-232

Murphy R, Strongin DR (2009) Surface reactivity of pyrite and related sulfides. Surf Sci Reports 64:1-45

Mycroft JR, Nesbitt HW, Pratt AR (1995) X-ray photoelectron and Auger electron spectroscopy of air-oxidized pyrrhotite: Distribution of oxidized species with depth. Geochim Cosmochim Acta 59:721-733

Nasikas NK, Edwards TG, Sen S, Papatheodorou GN (2012) Structural characteristics of novel Ca-Mg orthosilicate and suborthosilicate glasses: results from ^{29}Si and ^{17}O NMR spectroscopy. J Phys Chem B 116:2696-2702

Nesbitt HW (2002*)* Interpretation of X-ray Photoelectron Spectra with applications to mineralogy and geochemistry, *In*: Synchrotron Radiation, Earth, Environmental and Materials Sciences Applications. Henderson GS, Baker DS (ed) Mineralogical Association of Canada Short Course 30:131-158

Nesbitt HW, Bancroft GM, Pratt AR, Scaini MJ (1998a) Sulfur and iron surface states on fractured pyrite surfaces. Am Mineral 83:1067-1076

Nesbitt HW, Canning GW, Bancroft GM (1998b) XPS study of reductive dissolution of 7Å birnessite by H_3AsO_3, with constraints on reaction mechanism. Geochim Cosmochim Acta 62:2097-2110

EBSCOhost - printed on 2/13/2023 5:26 AM via . All use subject to https://www.ebsco.com/terms-of-use

Nesbitt HW, Scaini M, Hochst H, Bancroft GM, Schaufuss AG, Szargan R (2000) Synchrotron XPS evidence for Fe^{2+}-S and Fe^{3+}S surface species on pyrite fracture-surfaces, and their 3D electronic states. Am Mineral 85:850-857

Nesbitt HW, Bancroft GM, Davidson R, McIntyre NS, Pratt AR (2004) Minimum XPS core-level line widths of insulators, including silicate minerals. Am Mineral 89:878- 882

Nesbitt HW, Bancroft GM, Henderson GS, Ho R, Dalby KN, Huang Y, Yan Z (2011) Bridging, non-bridging and free (O^{2-}) oxygen in Na_2O-SiO_2 glasses: An X-ray photoelectron spectroscopic (XPS) and nuclear magnetic resonance (NMR) study. J Non-Cryst Solids 357:170-180

Nesbitt HW, Bancroft GM, Sawyer R, Tse J, Secco RA, Henderson GS (2014a) Oxygen speciation in anhydrous and hydrous silicate glasses and melts: evidence from molecular dynamics simulations and XPS experiments. Chem Geol, in review

Nesbitt HW, Bancroft GM, Ho R (2014b) XPS Valence Level study of vitreous silica and Na_2O-SiO_2 glasses: Identification of molecular orbitals and reactivity of silicate glasses. Am Mineral, in prep

Newburg JT, Starr DE, Yamamoto S, Kaya S, Kendelewicz T, Mysak ER, Porsgaard S, Salmeron MB, Brown GE, Nillson A, Blum H (2011) Formation of hydroxyl and water layers on MgO films studied with ambient pressure XPS. Surf Sci 605:89-94

Nyholm R, Martensson N, Lebugle A, Axelman U (1981)Auger and Coster- Kronig broadening effects in the 2p and 3p photoelectron spectra from the metals Ti-Zn. J Phys F 11:L727-L1733

Oelkers EH (2001) General description of multi-oxide silicate mineral and glass dissolution. Geochim Cosmochim Acta 65:3703-3719

Oelkers EH, Schott J (2001) An experimental study of enstatite dissolution rates as a function of pH, temperature, and aqueous Mg and Si concentration, and the mechanism of pyroxene/pyroxenoid dissolution. Geochim Cosmochim Acta 65:1219-1231

Patenen M, Bancroft GM, Aksela S, Aksela H (2012) Direct Experimental determination of the K 2p and Cl 2p core-level binding energy shifts between molecular and solid KCl: linebroadening effects. Phys Rev B 85:125419 (1-7)

Pokrovsky OS, Schott J (2000) Forsterite surface composition in aqueous solutions: A combined potentiometric, electrokinetic and spectroscopic approach. Geochim Cosmochim Acta 64:3299-3312

Pokrovsky OS, Schott J (2000b) Kinetics and mechanism of forsterite dissolution at 25 °C and pH from 1 to 12. Geochim Cosmochim Acta 64:3313-3325

Robie RA, Edwards JL (1966) Some Debye temperatures from single-crystal elastic constant data. J Appl Phys 37:2659-2663

Rosso JJ, Rimstidt JD (2000) A high resolution study of forsterite dissolution rates. Geochim Cosmochim Acta 64:97-811

Salmeron M, Schlogl R (2008) Ambient pressure photoelectron spectroscopy: a new tool for surface science and nanotechnology. Surf Sci Reports 63:169-199

Sankari R, Ehra M, Natatsuji H, Senba Y, Hosokawa K, Yoshida H, De Fanis A, Tamenori Y, Aksela S, Ueda K (2003) Vibrationally resolved O 1s photoelectron spectrum of water. Chem Phys Lett 380:647-653

Sarnthein J, Car R, Pasquarello A (1995) Model of vitreous SiO_2 generated by an *ab initio* molecular-dynamics quench from the melt. Phys Rev B 52:12690-12695

Sawyer R, Nesbitt HW, Secco RA (2012) Three types of oxygen in K_2O- SiO_2 glasses: an X-ray photoelectron spectroscopy (XPS) study. J Non-Cryst Solids 358:290-302

Schaufuss AG, Nesbitt HW, Kartio I, Laajalehto K, Bancroft GM, Szargan R (1998) Reactivity of surface chemical states on fractured pyrite. Surface Science 411:321-328

Schaufuss AG, Nesbitt HW, Kartio I, Laajalehto K, Bancroft GM, Szargan R (2000) Reactivity of surface sites on fractured arsenopyrite (FeAsS) toward oxygen. Am Mineral 85:1754-1766

Schindler M, Hawthorne FC, Freund MS, Burns PC (2009a) XPS spectra of uranyl minerals and synthetic uranyl compounds. I: the U 4f spectrum. Geochim Cosmochim Acta 73:2471-2487

Schindler M, Hawthorne FC, Freund MS, Burns PC (2009b) XPS spectra of uranyl minerals and synthetic uranyl compounds. II: the O 1s spectrum. Geochim Cosmochim Acta 73:2488-2509

Schott J, Berner RA (1985) Dissolution Mechanisms of pyroxene and olivines during weathering. *In:* The Chemistry of Weathering, J.I. Drever (ed) D. Reidel Publishing Co., p 35-53

Schott J, Berner RA, Sjoberg EL (1981) Mechanism of pyroxene and amphibole weathering-I. Experimental studies of iron-free minerals. Geochim Cosmochim Acta 45:2123-2135

Seah MP, Dench WA (1979) Quantitative electron spectroscopy of surfaces: a standard database for electron inelastic mean free paths in solids. Surf Interface Anal 1:2-11

Sen S, Tangeman J (2008) Evidence for anomalously large degree of polymerization in Mg_2SiO_4 glass and melt. Am Mineral 93:946-949

Seyama H, Soma M, Tanaka A (1996) Surface characterization of acid-leached olivines by X-ray photoelectron spectroscopy. Chem Geol 129:209-216

EBSCOhost - printed on 2/13/2023 5:26 AM via . All use subject to https://www.ebsco.com/terms-of-use

Seyama H, Wang,D, Soma M (2004) X-ray photoelectron microscopic imaging of the chemical bonding state of Si in a rock sample. Surf Interface Anal 36:609-612

Shaller T, Stebbins JF, Wilding MC (1999) Cation clustering and formation of free oxide ions in sodium amd potassium lanthanum silicate glasses: nuclear magnetic resonance and Raman spectroscopic findings. J Non-Cryst Solids 243:146-157

Sharma A, Jain H, Miller AC (2001) Surface modification of a silicate glass during XPS experiments. Surf Interface Anal 31:369-374

Shchukarev A, Rosenqvist J, Sjoberg S (2004) XPS study of the silica- water interface. J Electron Spectroscopy 137-140:171-176

Shirley DA (1972) High resolution X-ray photoemission spectrum of the valence bands of Au. Phys Rev B 5:4709- 4714

Siegbahn K, Nordling C, Johansson G, Hedman J, Heden PF, Hamrin K, Gelius U, Bergmark T, Werme LO, Manne R, Baer Y (1969) ESCA Applied to Free Molecules. North Holland, Amsterdam, London

Speight JG (2005) Lange's Handbook of Chemistry (70th Anniversary Edition). McGraw Hill Standard Handbook, New York Table 4.11, p. 4.41-4.51

Sprenger D, Bach H, Meisel W, Gutlich P (1993) Discrete bond model (DBM) of sodium silicate glasses derived from XPS, Raman and NMR measurements. J Non-Crystal Solids 159:187-203

Stebbins JF (1987) Identification of multiple structural species in silicate glasses by ^{29}Si NMR. Nature 330:465-467

Stephenson DA, Binkowski N.J. (1976) X-Ray Photoelectron Spectroscopy of Silica in Theory and Experiment. J Non-Crystal Solids 22:399-421

Stipp SL, Hochella MF (1991) Structure and bonding environments at the calcite surface as observed with X-ray photoelectron spectroscopy (XPS) and low energy electron diffraction (LEED). Geochim Cosmochim Acta 55:1723-1736

Stolper E (1982) Water in silicate glasses: an infrared spectroscopic study. Contrib Mineral Petrol 81: 1-17

Sutherland DGJ, Bancroft GM, Tan KH (1992) Vibrational splitting in Si 2p core-level photoelectron spectra of Si molecules J Chem Phys 97:7918-7931

Sutherland DGJ, Kasrai M, Bancroft GM, Liu ZF, Tan KH (1993) Si L- and K-edge X-ray absorption near-edge spectroscopy of gas phase $Si(CH_3)_x(OCH_3)_{4-x}$: models for solid state analogues Phys Rev B 48: 14989-15001

Svensson S, Ausmees A, Osborne SJ, Bray G, Gel'mukhanov F, Agren H, Nives de Brito A, Sairenen O-P, Kivimaki A, Nommiste E, Aksela H, Aksela S (1994) Observation of an anomalous decay ratio between the molecular field split levels in the S 2p core photoelectron and LVV Auger spectrum of H_2S. Phys Rev Lett 72:3021-3024

Tanuma S, Powell CJ, Penn DR (1991) Calculations of electron inelastic mean free paths III. Surf Interface Anal 17:927-939

Thomas TD, Miron C, Weisener P, Morin P, Carroll TX, Saethre LJ (2002) Anomalous natural linewidth in the 2p photoelectron spectrum of SiF_4. Phys Rev Lett 89**:**223001 (1-4)

Tian P, Cheng J, Zhang G (2011) X-ray photoelectron spectroscopy of Sm^{3+}-doped CaO-MgO-Al_2O_3-SiO_2 glasses and glass ceramics. Appl Surf Sci 257:4896-4900

Tilocca A, de Leeuw NH (2006) Structural and electronic properties of modified sodium and soda-lime silicate glasses by Car-Parrinello molecular dynamics. J Mater Chem 16:1950-1995

Toop GW, Samis CS (1962) Activities of ions in silicate melts. Trans Metal Soc Am 224:878-887

Uchino T, Iwasaki M, Sakka T, Ogata Y(1991) Ab initio molecular orbital calculations on the electronic structure of sodium silicate glasses. J Phys Chem 95:5455-5462

Umeski N, Iwamoto N, Tatsumisago M, Minami T (1988) A structural study of rapidly quenched glasses in the system Li_2O-SiO_2. J Non-Crystal Solids 106:77-80

Unveren E, Kemnitz E, Hutton S, Lippitz A, Unger WES (2004) Analysis of highly resolved X-ray photoelectron Cr 2p spectra obtained with a Cr_2O_3 powder sample prepared with adhesive tape. Surf Interface Anal 36:92-95

Varshneya AK (1994) Fundamentals of Inorganic Glasses. Academic Press, London

Veal BW, Lam DJ, Paulikas AP (1982) XPS study of CaO in sodium silicate glass. J Non-Cryst Solids 49:309-320

White GK (1978) Thermal expansion of cuprous oxide at low temperatures. J Phys C 11:2171-2174

Wren AW, Laffir FR, Kidari A, Towler MR (2011) The structural role of titanium in Ca-Sr-Zn-Si/Ti glasses for medical applications. J Non-Cryst Solids 357:1021-1026

Yates BW, Tan KH, Bancroft GM, Coatsworth LL, Tse JS (1985) Photoelectron study of the valence levels of CF_4 and SiF_4 from 20 to 100 eV. J Chem Phys 83:4906-4916

Yeh JJ, Lindau I (1985) Atomic subshell photoionization cross sections and asymmetry parameters: $1 \leq Z \leq 103$. At Data Nucl Data Tables 32:1-155

Yin LI, Ghose S, Adler I (1971) Core binding energy difference between bridging and non-bridging oxygen atoms in a silicate chain. Science 173:633-635

EBSCOhost - printed on 2/13/2023 5:26 AM via . All use subject to https://www.ebsco.com/terms-of-use

Zakaznova-Herzog VP, Nesbitt HW, Bancroft GM, Tse JS, Gao X, Skinner W (2005) High-resolution valence band XPS spectra of the nonconductors quartz and olivine. Phys Rev B 72:205113 (1-13)

Zakaznova-Herzog VP, Nesbitt HW, Bancroft GM, Tse JS (2006) High resolution core and valence band XPX spectra of non-conductor pyroxenes. Surf Sci 600:3175-3186

Zakaznova-Herzog VP, Nesbitt HW, Bancroft GM, Tse JS (2008) Characterization of leached layers on olivine and pyroxenes using high resolutiuon XPS and density functional theory. Geochim Cosmochim Acta 72:69-86

Zhang P, Gandinetti PJ, Stebbins JF (1997) Anionic species determination in $CaSiO_3$ glass using two-dimensional ^{29}Si NMR. J Phys Chem 101:4004-4008

EBSCOhost - printed on 2/13/2023 5:26 AM via . All use subject to https://www.ebsco.com/terms-of-use

EBSCOhost - printed on 2/13/2023 5:26 AM via . All use subject to https://www.ebsco.com/terms-of-use

Reviews in Mineralogy & Geochemistry
Vol. 78 pp. 331-369, 2014
Copyright © Mineralogical Society of America

Analysis of Mineral Surfaces by Atomic Force Microscopy

Jacques Jupille

Institut des Nanosciences de Paris CNRS and UPMC
4, place Jussieu
75005 Paris, France

Jacques.Jupille@insp.jussieu.fr

INTRODUCTION

Chemistry and physics of mineral surfaces and interfaces are pivotal in understanding the many processes occurring in the extremely diverse domains in which mineral matter is encountered, such as geochemistry of soils and aquifers (Morse and Arvidson 2002), interaction with microbial organisms (Brown et al. 1999), catalysis (Corma 1995) and nanotechnology (Fu and Wagner 2007). The study of mineral surfaces as archetypes of surfaces of insulators mostly started twenty years ago, which is rather recent with respect to the general evolution of surface science. The likely origin of such delay, surprising given the ubiquity of mineral matter, was the difficulty in operating methods dominated by electron probes to deal with insulating substrates and to the deterrent effect of the complex chemical composition of the encountered compounds. In the burgeoning development of the analysis of mineral surfaces, techniques of investigation which belong to the well-stocked toolkit available to surface science currently involve both versatile enough traditional methods and emerging techniques that have proved relevant. Photoelectron spectroscopy, synchrotron-based diffraction and absorption are cornerstones techniques for the analysis of all surfaces, including those of mineral compounds, as well as pure photon probes which are not affected by the insulating nature of substrates, such as infrared spectroscopy, Raman spectroscopy and X-ray diffraction.

In the 1990's, a strong incentive for the development of analysis of mineral surfaces came from the emergence of atomic force microscopy (AFM) which had the potential ability to probe surfaces of insulators and which is a powerful tool for the study of surface topography and structure at sub-nanometer-scale resolution (Binnig et al. 1986). Extremely flexible, the technique can be used in any condition, either vacuum or gas or liquid phases, and on any substrate. The instrument itself is of small size, commercially available, friendly to use and can be operated at a very high scientific level at a reasonable cost. AFM is the appropriate near field microscopy for the study of surfaces of minerals since, while being mostly insulators, mineral substrates are currently found in wet environments and in contact with organic compounds or biologic matter.

AFM has become central in a number of issues regarding mineral matter: dissolution, precipitation and growth examined on surfaces of both single crystals and particles; hydration, acid- base behavior, electrostatic charging for surfaces in moisture or in aqueous solution; atomically resolved exploration of surface structures. After a general presentation of the experimental AFM methods, the objective of the present Chapter is to review the specific approaches that are used in each of these domains on the basis of examples.

1529-6466/14/0078-0008$05.00 http://dx.doi.org/10.2138/rmg.2014.78.8

EBSCOhost - printed on 2/13/2023 5:26 AM via . All use subject to https://www.ebsco.com/terms-of-use

EXPERIMENTAL METHODS

Near-field microscopies were invented in the 1980s. The scanning tunneling microscopy (STM) is based on the current that tunnels from a conducting tip to a substrate (Binnig et al. 1982, 1983). It can only be operated on conducting and semiconducting substrates. The atomic force microscopy (AFM), that was implemented a few years later (Binnig et al. 1986), allows measurements on any substrate, either conducting or insulating. AFM is performed by means of a tip mounted at the end of a small cantilever beam. Upon placing the tip in contact with or at the vicinity of the surface of a sample, the forces acting between tip and sample cause a deflection of the cantilever, detection of which gives rise to the imaging process.

In STM, the imaging signal is the tunneling current which takes place between the tip and surface. The tunneling current decreases exponentially with the tip-surface distance z (Hofer et al. 2003):

$$I(z) \propto k\sqrt{2\varphi z} \tag{1}$$

Here k is a constant and φ is the work function of the two surfaces. The optimal separation between tip and sample is commonly a fraction of interatomic distance. The current is extremely sensitive to the tip-surface distance so that it mostly relies on the atoms of the tip apex that are closest to the surface. The rest of the tip has little influence on the tunneling current. The relative simplicity of the active part of the tip-sample system and the easy detection of the typical tunneling currents (of the order of magnitude of 10^{-9} A) makes atomically resolved imaging rather common. The defined physical process involved in STM imaging (Tersoff and Hamann 1985) explains the agreement found between observation and simulation (Hofer et al. 2003).

In contrast, in atomic force microscopy, the control parameter is the deflection of the lever which results from the complex set of forces exerted between tip and sample that involve the long-range attractive van der Waals forces and the short-range repulsive Pauli forces. Due to electromagnetic field fluctuations, van der Waals forces are universal. If the tip apex is represented by a sphere of radius R and the surface by a plane, the van der Waals force is given by:

$$F_{vdW}(z) = \frac{AR}{6z^2} \tag{2}$$

as a function of the tip-surface distance z (A is the Hamaker constant). In AFM, van der Waals forces arise from macroscopic parts of the tip-substrate ensemble. They are of the order of 10^{-9} N which is more difficult to detect than typical STM tunneling current. This makes the imaging process more uneasy than in STM (Giessibl 1994; Shluger et al. 1999; Hofer et al. 2003).

Other macroscopic forces are encountered in specific systems. Not found in general theories, they are rather simulated in dedicated models. They comprise image and electrostatic forces, magnetic forces (Garcia and Perez 2002; Hofer et al. 2003) and capillary forces (Weisenhorn et al. 1989; Garcia and Perez 2002). Image forces are typically observed when an ionic compound is facing an electrically conductive medium. Electrostatic forces arise from contact potential differences and charges accumulated in tip and substrate. Charges may result from crystal cleavage, tip-sample contact upon scanning, interface with a solution and, if in vacuum, ion bombardment during sample and tip preparation. The attractive capillary forces are an important issue for studies in the ambient conditions. When surface and tip are hydrophilic, a meniscus is formed when the tip approaches the substrate in moisture. Capillary forces can profoundly affect measurements (Garcia and Perez 2002; Butt et al. 2005). Similar effects occur when tip and surface are covered with pollutants (Weisenhorn et al. 1989; Giessibl and Binnig 1992).

At the surface of ionic solids, the main contrast between anionic sites and cationic sites arises from the interaction of the tip with the alternating electrostatic potential and with the

EBSCOhost - printed on 2/13/2023 5:26 AM via . All use subject to https://www.ebsco.com/terms-of-use

surface polarization induced by the electric field of the tip (Livshits et al. 1999). By exploring contrast imaging for an MgO tip model over NaCl, LiF and MgO surfaces, it has been predicted that the best contrast that can be achieved in noncontact AFM stems from chemical forces at tip-surface distances of 0.4-0.6 nm which are similar to optimum distances in STM (Livshits et al. 1999). Small with respect to the above macroscopic forces, chemical forces can distinguish atomic identities and can lead to chemical contrast in images (Shluger et al. 1999; Garcia and Perez 2002; Giesssibl 2003; Hofer et al. 2003; Barth et al. 2011). Fingerprints of the surface chemical contrast being short- range forces, force gradients appear to be better probes of surface structures than forces, which have prompted the use of noncontact AFM to study surface structure at atomic level (Giessibl 1994, 1995).

AFM set-ups

In AFM, the imaging process is based on the detection of the parameters characterizing the deflection of the cantilever that occurs when the tip is approaching the sample. A schematic representation of AFM is given in Figure 1. The sample is mounted on a piezoelectric tube that allows displacements (i) in the z direction to control the tip-sample distance interaction and (ii) in the x and y in-plane directions for imaging. The feedback loop that drives the relative vertical position of the tip with respect to the surface (z direction) is found in all AFM modes. The control of phase and amplitude of the vibrating tip is needed to operate AFM in tapping mode and noncontact mode (see below). Tips are commonly made of silicon or silicon nitride. The radius of the tip apex is typically a few tens of nanometers. Different techniques have been used to detect the deflection of the lever, including scanning tunneling microscopy and capacitive measurements. Popular methods are to date optical beam detection which is based on the reflection of a laser beam on the lever (Meyer and Amer 1988, 1990) and self-sensing piezoresistive or piezoelectric levers (Giessibl et al. 2011). Atomic force microscopy is an extremely flexible method. By means of specific set-ups, it can be used in air, water and ultra-high vacuum (UHV). First operated in the so-called contact mode as the tip is bought into intimate contact with the surface, AFM was soon after its invention run in dynamic modes (Martin et al. 1987; Albrecht et al. 1991) in which surfaces are probed by vibrating tips, either in intermittent contact with the substrate or in noncontact mode.

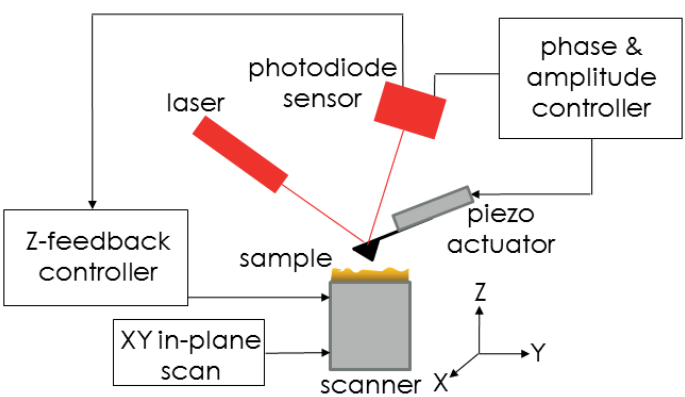


Figure 1. Schematic representation of an AFM device. The sample is mounted on a piezoelectric tube that allows displacements (i) in the z direction to control the tip-sample distance interaction and (ii) in the x and y in-plane directions for imaging. The deflection of the cantilever is detected by the optical beam deflection method (Meyer and Amer 1988, 1990). The relative vertical position of the tip is controlled by a z-feedback loop. The control of phase and amplitude of the oscillating cantilever is needed to operate AFM in tapping mode and noncontact mode.

EBSCOhost - printed on 2/13/2023 5:26 AM via . All use subject to https://www.ebsco.com/terms-of-use

Contact mode. In the so-called contact mode, the tip is in hard contact with the surface. The instrument can be operated in two ways (Maurice 1996). In constant force mode, the deflection of the lever is kept constant during sample rastering by adjusting the height of the sample via the *z*-feedback circuit. Tip-surface interactions can be dominated either by attractive van der Waals forces or by repulsive forces. Alternatively, in constant height mode, the tip is brought into contact with the surface and the deflection of the lever upon scanning reflects the short-range repulsive forces acting on the tip. The *z*-piezo is used to keep the tip and surface in contact. This mode allows fast scans. It is best adapted to rather flat surfaces of hard substrates in the absence of capillary forces. Indeed, soft substrates are susceptible to tip-induced scratch and both tip and surface may be damaged under scanning high relief if the *z*-piezo fails to compensate for changes in height. In contact mode, dimensional measurements are perturbed by various tip–sample interactions whose effects can be minimized by appropriate choices of tip and cantilever (Yacoot and Koenders 2008).

Scanning macroscopic crystals (Giessibl and Binnig 1992; Maurice 1996; Pachon-Rodriguez et al. 2011) or nanoparticles (Bickmore et al. 2001; Kuwahara 2006) by a tip in contact mode may damage surfaces. AFM in contact mode is mostly operated in the repulsive regime where repulsive short-range forces balance the van der Waals attraction. The force exerted by the tip on the substrate involves a contribution parallel to the surface which corresponds to frictional forces. Together with adhesive forces they may erode the surface parallel to the scan direction (Maurice 1996) and strongly modify dissolution rates (Kuwahara 2006) and step velocity (Pachon-Rodriguez et al. 2011). In microtopography studies, interaction forces can be minimized (Dove and Platt 1996) by an appropriate implementation of the microscope (Dove and Platt 1996; Maurice 1996) and, more specifically, by adjusting the set-point to minimize the force applied to the substrate (Shiraki et al. 2000; Larsen et al. 2010). For dissolution and growth experiments, tips are commonly operated with forces ~ 10 nN (Hillner et al. 1992a; Xu et al. 2010).

It has been predicted that a monoatomic tip penetrates into a graphite substrate when the force exerted exceeds ~ 10 nN and breaks atomic bonds beyond 50 nN (Abraham and Batra 1989). Nevertheless, any limit may be questioned. Tip-induced erosion has been observed when scanning with tip loads < 10 nN (Nakahara et al. 1995; Pachon-Rodriguez et al. 2011) and even in attractive mode (Nakahara et al. 1995). KBr(100) surfaces were imaged with atomic resolution in the attractive regime with a loading force of ~ 1 nN whereas higher values were shown to lead to surface damage and contamination of the cantilever with sample material (Giessibl and Binnig 1992). The higher limit of the loading force was even estimated to less than 10^{-10} N (Ohnesorge and Binnig 1993) from experimental observations of calcite surfaces in water. These values are to be compared to the limit of 10^{-9} N predicted for a tip apex made of a unique atom (Abraham et al. 1988) and can be inferred by dividing the binding energy per bond by the bonding length (Giessibl 1994). A way to control that the contact of the tip does not affect the morphology of the sample surface in given conditions, is to check whether the observed phenomenon is robust with respect to tests that involve operation of the tip at a higher frequency or a higher load than those currently used, scans in different directions, analysis of unfiltered images, change of tips and substrates (Maurice 1996; Shiraki et al. 2000).

AM-AFM and FM-AFM. In the dynamic operation mode of AFM, or noncontact AFM, the cantilever is oscillated at or near its resonance frequency to map the force gradient between the tip and surface when scanning over the surface. The occurrence of force gradients result in changes in phase and amplitude of the lever oscillations which are controlled by mounting the lever on an actuator (Fig. 1). Detection is based on either the Amplitude Modulation (AM) technique (Martin et al. 1987), or the Frequency Modulation (FM) technique (Albrecht et al. 1991) or phase variation (Loppacher et al. 1999). Amplitude, frequency and phase can be alternatively used as feedback parameters to map out the scanned surface. Force gradient

EBSCOhost - printed on 2/13/2023 5:26 AM via . All use subject to https://www.ebsco.com/terms-of-use

measurements are much more sensitive to change in tip-surface interaction than direct forces measurements. In particular, noncontact AFM can achieve atomic resolution via the detection of the chemical forces in vacuum (Giessibl 1995; Reichling and Barth 1999; Garcia and Perez 2002; Hofer et al. 2003; Lauritsen and Reichling 2010; Barth et al. 2011) and in gas or liquids (Fukuma et al. 2005a,b,c; Rode et al. 2009).

AM-AFM and FM-AFM can be compared on the basis of their response to a change in the tip- sample interaction (Albrecht et al. 1991). In AM-AFM mode, the cantilever is operated at a constant frequency near resonance and the feedback parameter is the oscillation amplitude. The occurrence of a force gradient between the tip and sample modifies the compliance of the lever which gives rise to a shift in the amplitude of the lever vibration. A change in amplitude results in a new steady-state and two transient components, a transient decay and a beat term, which involve time constants ~Q/ω_0 indicative of the time needed by the lever to reach its new stationary amplitude. The tip is oscillated with small amplitude of ~1 nm and the cantilever stiffness is decreased to improve the sensitivity (Martin et al. 1987). In AM-AFM, high (low) Q values lead to slow (fast) responses, which makes the technique suitable for analysis in air and in liquids but prevents its use in vacuum conditions in which Q values are quite high (Albrecht et al. 1991).

The frequency modulation AFM (FM-AFM) will be labeled herein noncontact AFM (nc-AFM) since it is often referred to in this way (Hofer et al. 2003; Lauritsen and Reichling 2010; Barth et al. 2011). Change in the force gradient changes the oscillator frequency that is detected within a single oscillation cycle on a time scale of $\tau_{FM} \approx 1/\omega_0$. Therefore, the method allows improvement of the sensitivity through increased Q values (Albrecht et al. 1991). In nc-AFM mode, the cantilever is excited at its resonance frequency (~ 50-300 kHz) at a constant oscillation amplitude of ~10-40 nm in vacuum and less than 1 nm in water (Fukuma et al. 2005a,b,c; Rode et al. 2009). In the vicinity of the surface, the force gradient causes a shift Δf—detuning—in the cantilever resonance frequency f. When scanning the surface in the so-called constant detuning mode, variations in detuning Δf due to change in force gradient are used to generate a feedback signal that keeps the detuning constant, which results in a topographic image of the surface (Reichling and Barth 1999; Enevoldsen et al. 2008; Ostendorf et al. 2008). Alternatively, changes in detuning Δf can be directly recorded while compensating for variations in tip-surface distance (Barth et al. 2001; Foster et al. 2001; Rode et al. 2009; Schütte et al. 2010), which may be viewed as an approximation to the constant height mode (Barth et al. 2001). The z regulation can even be switched off (Rahe et al. 2008). A detailed diagram of the nc-AFM set-up and detailed explanation on the amplitude and phase controllers can be found in Couturier et al. (2005).

The parameters which characterize nc-AFM devices are commonly determined by trial and error on the basis of commercially available products. Attempts to optimize those parameters suggest that, although existing systems are correctly operated, stiffer cantilevers would allow (i) a strong reduction of the oscillation amplitude and, in turn, an increased sensitivity to the surface potentials responsible for chemical contrast and (ii) a decrease in thermal noise and detector noise that are both inversely proportional to the oscillation amplitude (Giessibl 1997; Giessibl et al. 2000; Garcia and Perez 2002). Suggested sensors are tuning forks (Giessibl et al. 2004, 2011). Other current challenging issues are the achievement of high-effective Q-factors (Lübbe et al. 2010) and the improvement of the signal to noise ratio. In this respect, it has been proposed to mount a laser diode outside the vacuum chamber and to connect it to the AFM set-up by an optical fiber (Torbrügge et al. 2008).

Tapping Mode AFM (TM-AFM). AM-AFM and FM-AFM were initially both operated without contact with the substrate. The successful development of an AM mode in which the tip probes the surface in the repulsive regime at the lower turning point of each periodic excursion led to the so-called "tapping-mode" (TM-AFM) (Zhong et al. 1993) also referred

EBSCOhost - printed on 2/13/2023 5:26 AM via . All use subject to https://www.ebsco.com/terms-of-use

to as "intermittent contact AFM". In contrast with AM-AFM which was operated with small oscillation amplitude of the lever (Martin et al. 1987), tapping mode is run by oscillating the tip with oscillation amplitudes that are typically from 20 to 100 nm to eliminate capture by the surface fluid layer. Stiff cantilevers with spring constants of 20 to 50 nN and high Q factors up to ~ 1000 are used to overcome the tip-surface sticking (Zhong et al. 1993). Moreover, although contrast formation is due to repulsive forces, the operation mode minimizes the tip and sample degradation by reducing the contact and lateral forces and by shortening the time during which the tip is in contact with the sample. In Figure 2, AFM images recorded in contact mode of a silica surface covered with residual polymer coating are compared to TM-AFM images of the same surface. Images recorded in tapping mode appear not only better resolved than contact mode images, but also more reliable (Zhong et al. 1993). The technique, which is intermediate between contact mode and noncontact mode, is easier to operate than noncontact mode. Imaging is based on the detection by the feedback system of the changes in oscillation amplitude caused by the intermittent contact of the tip with the sample surface. Used in air and in liquid, the tapping mode is often preferred to contact mode to avoid tip/sample degradation (Zhong et al. 1993). The method is particularly relevant to clay mineral surface studies (Bickmore et al. 1999; Bosbach et al. 2000; Kuwahara 2006; Can et al. 2010).

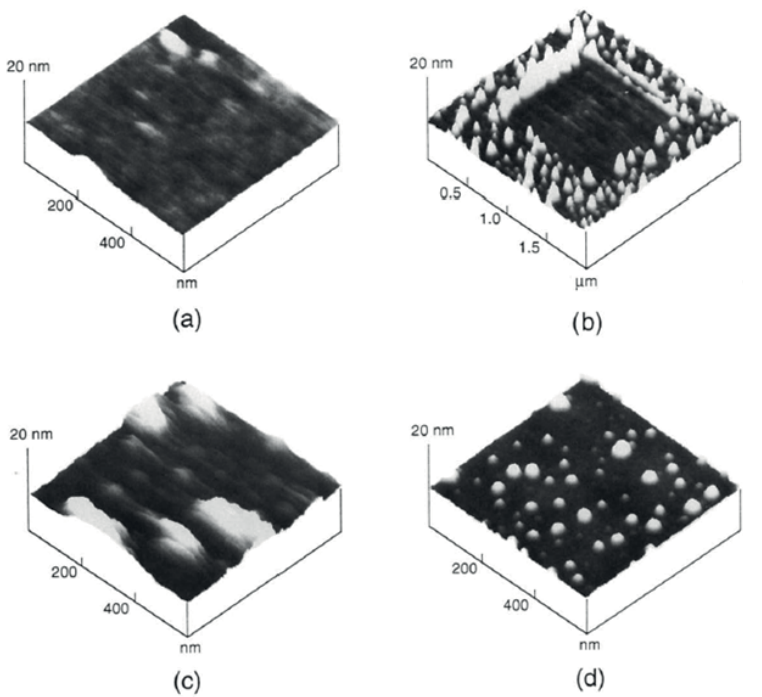


Figure 2. AFM images of a silica optical fiber surface containing residual polymer coating, recorded in constant force mode and in tapping mode (Zhong et al. 1993). All images are presented as acquired, except for a global plane subtraction: (a) AFM image in constant force mode using a pyramidal Si_3N_4 tip: smeared out surface features are partly assigned to tip deterioration; (b) The enlarged scan area of (a) acquired immediately after enlargement shows the "scan mark" corresponding the area scanned in (a); (c) AFM image in contact mode using an etched silicon tip: the resolution is improved but smearing features are still visible along the scan direction; (d) Topographic image of the same sample surface recorded using the tapping mode AFM: the image was reproducible and did not degrade after several scans. [Used by permission of Elsevier, from Zhong et al. (1993), *Surf. Sci. Lett.* 290, Fig. 1, p. L691.]

EBSCOhost - printed on 2/13/2023 5:26 AM via . All use subject to https://www.ebsco.com/terms-of-use

Experimental conditions

As commonly observed in surface studies, the properties of mineral substrates depend on their history. Therefore, the preparation of well-defined surfaces is a prerequisite condition for a reliable analysis. Special attention is also paid to liquid cells since these are needed for the achievement of experimental conditions representative of realistic environments.

Surface preparation. Surface analysis requires a strict control of contamination of the substrate under examination. For example, it has been noticed that water perfectly wets freshly cleaved calcite but forms droplets on this substrate after exposure during a few hours to the surrounding atmosphere, which indicates that the surface becomes hydrophobic; in the same series of experiments, it was also observed that a calcite crystal cleaved in vacuum without baking shows some surface contamination immediately following fracture (Stipp and Hochella 1991). For vacuum studies, the adventitious carbon which comes from the conditions of preparation of the sample modifies the reactivity of the surface (Stipp and Hochella 1991) and significantly changes the surface potential (Toikka and Hayes 1997). Samples manipulated in ambient conditions are exposed to water vapor and CO_2 from the surrounding atmosphere prior to being analyzed. On calcite (Stipp et al. 1996) and barite (Bokern et al. 2002), amorphous films that extended over nanometers while escaping visual inspection and light microscope examination were observed by AFM (Fig. 3). To record reliable data, one must use freshly cleaved surfaces (Stipp and Hochella 1991; Reichling and Barth 1999; Larsen et al. 2010), or samples kept in controlled conditions, and check the cleanliness of the substrate under study by the techniques available in the experimental set-up in which experiments are performed.

Surfaces can be cleaved either in vacuum or in dry conditions to avoid contamination. However, they often exhibit charges that prevent AFM analysis. Electrical neutrality can be achieved by either annealing in vacuum (Barth and Henry 2007), or exposure to a high enough relative humidity (Xu et al. 1998), or by setting up a bias voltage (Foster et al. 2001).

Liquid cells. Dedicated liquid cells have been implemented to allow variable temperature and pressure within the cell during the analysis of minerals at the contact of solutions (Jordan and

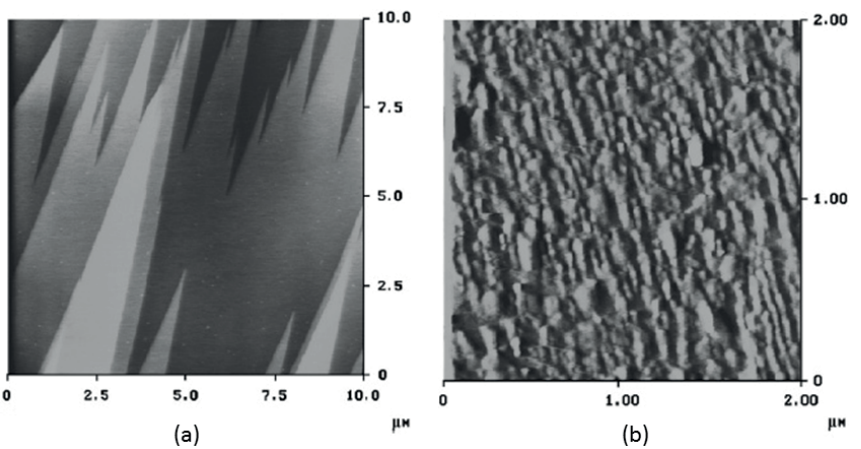


Figure 3. AFM height images of cleaved barite (001) surfaces (Bokern et al. 2002): (a) In air just after cleavage with steps due to direction of cleavage; (b) After exposure for two days to ambient conditions. The barite surface is coated with a 4-8 nm thick film which is soft enough to be displaced by the scanning tip. The rough film was attributed to dissolution and precipitation of species formed in the hydration layer that covers the barite surface in moist air. [Used by permission of Elsevier, from Bokern et al. (2002), *J. Cryst. Growth* 246, Figs. 1 and 2, p. 142.]

EBSCOhost - printed on 2/13/2023 5:26 AM via . All use subject to https://www.ebsco.com/terms-of-use

Rammensee 1996; Higgins et al. 1998). The objective was in particular the study of kinetics of dissolution that are too slow to be observed by AFM in normal conditions. Thermal equilibrium can be reached by circulating a hot solution which is neutral with respect to the dissolution process prior to undertaking experiments. Specific designs involving a pressurization of the cell are needed for operation at a temperature higher than the ambient boiling point of the solution. A hydrothermal cell has been designed by Higgins et al. to perform *in situ* AFM analysis in aqueous solution up to 423 K under a pressure of 6×10^5 Pa (Higgins et al. 1998). Temperature, pressure and flow rate are controlled, although pressure and flow rate are not independent.

Flow rates may influence data (Hillner et al. 1992a,b; Dove and Platt 1996). Fluxes too high cause distortions of the cantilever and drifts in images. Fluxes too low fail to feed the surface with fresh solution and create an apparent diffusion-limited regime. An indication of the relevance of the flow rates chosen to run an experiment is the independence of the step velocities on those rates (Xu et al. 2010). Great care must be taken about the preparation of solutions. Solutions can be bubbled by argon to remove CO_2 traces when appropriate (Shiraki et al. 2000). When performing measurements from the solution in parallel to the microscopic analysis by AFM, the surface exposed to the solution must be controlled and its area has to be carefully determined (Shiraki et al. 2000). Coating the sides of the crystal restricts dissolution to the crystalline face under study (Shiraki et al. 2000). Solutions are currently not recirculated (Hillner et al. 1992a).

Dissolution and growth take place at the extreme surface of materials, although they are analyzed in conditions in which it is not easy to control that the substrate under study is in a suitable shape. The elimination of carbon contamination requires specific pre-treatments (Franks and Meagher 2003). Impurities also come from the solutions used in the experiments. Stipp and Hochella (1991) prepared and stored solutions in all-glass systems, with careful cleaning by nitric acid, milliQ and distilled MilliQ water. To avoid unwanted dissolution of silica from glass containers, Larsen et al. (2010) preferred to use Teflon jars and polypropylene bottles filled with MilliQ water prior to being annealed, rinsed and dried.

DISSOLUTION, PRECIPITATION AND GROWTH

The dissolution of minerals is central to Earth crust history, geochemical cycles and human activities. Many efforts have been devoted over decades to the determination of reaction rates of the mineral matter via the study of powders in aqueous solution. Nevertheless, macroscopic approaches hardly lead to a description of the specific sites of the surface of the material which control reaction rates. Indeed, the knowledge of the effects of crystallographic orientations and surface defects on dissolution, growth and adsorption rates is a prerequisite to go beyond kinetics and understand mechanisms (Gratz et al. 1990; Dove and Rimstidt 1994). Made of dissimilar ions, mineral compounds often show anisotropic behaviors in aqueous solutions. In the early 1990s, the capacity of the emergent AFM technique to explore *in situ* the microtopography of surface samples with lateral and vertical resolution in the nanoscale range allowed a number of specific observations regarding the behavior of mineral substrates in solution.

Studies have mainly focused on carbonates (Morse and Arvidson 2002; Duckworth and Martin 2004; Morse et al. 2007)—particularly calcite (Hillner et al. 1992a,b, 1993; Gratz et al. 1993; Dove and Hochella 1993; de Leeuw et al. 1999; Shiraki et al. 2000; Teng et al. 2000; Arvidson et al. 2003, 2006; Kristensen et al. 2004; Lüttge and Conrad 2004; McEvoy et al. 2006; De Yoreo et al. 2009; Larsen et al. 2010; Ruiz-Agado et al. 2010; Xu et al. 2010) and sulfates (Bosbach and Rammensee 1994; Bosbach and Hochella 1996; Bosbach et al. 1998; Risthaus et al. 2001; Bockern et al. 2002; Fan and Teng 2007; Bose et al. 2008; Pachon-Rodriguez et al. 2011; Kuwahara 2011). On clay mineral particles, edge surfaces and steps are known to be more prone to exchange with the surrounding solution than basal planes. These

EBSCOhost - printed on 2/13/2023 5:26 AM via . All use subject to https://www.ebsco.com/terms-of-use

active sites which represent a minor percentage of the total area can be characterized by *ex situ* (Brady et al. 1996; Zbik and Smart 1998) and *in situ* (Bickmore et al. 1999) AFM studies.

However, the AFM analysis encounters kinetic limits regarding the analysis of moving steps and edges. Moreover, discrepancies appear between microscopic and macroscopic data (Arvidson et al. 2003; Metz et al. 2005). Therefore, the determination of dissolution and growth rates by AFM techniques questions the comparison between data recorded in different conditions.

Determination of reaction rates at crystal surfaces from step velocities

Anisotropic dissolution. An archetype of anisotropic behaviors of crystallographically oriented surfaces is the $(10\bar{1}4)$ plane of calcite (Fig. 4) in which both calcium and carbonate ions form rectangular sublattices. This plane is easily obtained by cleavage of the rhombohedral lattice of calcite. In both dissolution (Hillner et al. 1992a,b; de Leeuw et al. 1999; Shiraki et al. 2000; Arvidson et al. 2003; Xu et al. 2010; Ruiz-Agado et al. 2010) and growth processes (Hillner et al. 1992a,b, 1993; Gratz et al. 1993; Teng et al. 2000; Kristensen et al. 2004; McEvoy et al. 2006; De Yoreo et al. 2009; Larsen et al. 2010) moving steps are characterized by AFM, using the methods of Land et al. (1997) (Fig. 5) and Teng et al. 2000) (Fig. 6). Inhibition of dissolution (Dove and Hochella 1993; Lüttge and Conrad 2004; Arvidson et al. 2006) and effects of the solution composition (Ruiz-Agado 2010, 2012) have also been examined. Structurally non-equivalent obtuse $[\bar{4}41]^+$ and $[4\bar{8}1]^+$ and acute $[\bar{4}41]^-$ and $[4\bar{8}1]^-$ steps are evidenced on the $(10\bar{1}4)$ plane of calcite (Figs. 6 and 7). Moving steps are observed by AFM. Inhibition of dissolution has also been examined (Dove and Hochella 1993; Lüttge and Conrad 2004; Arvidson et al. 2006). Reactions rates are determined via the measurement by AFM of step velocities. The volume V of calcite dissolved per unit area and unit of time is defined by (Shiraki et al. 2000)

$$V = v_{step} n h_{step} \tag{3}$$

where v_{step} and h_{step} are the step velocity and height, respectively, and n is the number of steps per unit area. The step velocity v_{step} is an average between velocities of obtuse and acute steps

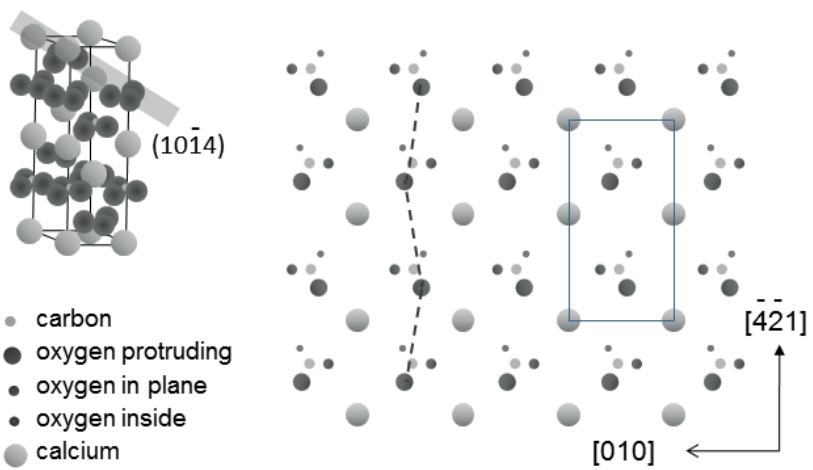


Figure 4. Calcite $(10\bar{1}4)$ cleavage plane. The surface unit cell is shown. The position of the carbonates with respect to the surface is indicated via the position of the oxygen atoms. A zig-zag chain found by protruding oxygen atoms is featured by a dotted line. A schematic of the hexagonal unit cell is on the left. The shaded zone indicates the cleavage direction.

EBSCOhost - printed on 2/13/2023 5:26 AM via . All use subject to https://www.ebsco.com/terms-of-use

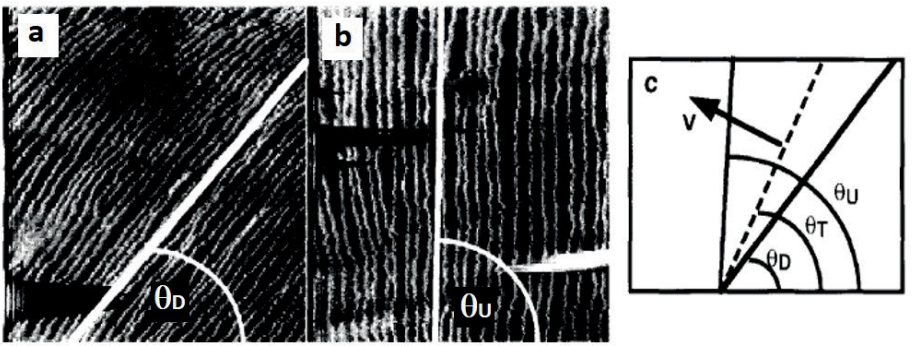


Figure 5. Method for determining step velocity using AFM (a) down scan and (b) up scan imaging; (c) schematic representation of step speed (Eqn. 5) and step direction (Eqn. 6) as determined from measurements. Experiments were performed on carnavalin. [Used by permission of Elsevier, from Land et al. (1997), *Surf. Sci.* 384, Fig. 3, p. 141.]

which differ most of the time. The rate of dissolution per unit area is

$$R_{topography} = \frac{v_{step}}{V_m}\Delta h = \frac{v_{step}}{V_m}\tan\theta \tag{4}$$

where V_m is the molar volume and Δh (Fig. 5b) is the slope of the calcite surface (height over a unit length) which is equivalent to tanθ. The apparent slopes that result from the step motion upon scanning (Figs. 5c,d) was accounted for by the method of Land et al. (1997) which gives the step velocity as a function of the angles θ_U and θ_D of the steps with respect to the scanning direction for scan up and scan down, respectively (Figs. 5a-c):

$$v_{step} = \frac{RS}{2N}\left(\cot\theta_D - \cot\theta_U\right)\sin\theta_T \tag{5}$$

$$\theta_T = \cot^{-1}\left(\frac{\cot\theta_U + \cot\theta_D}{2}\right) \tag{6}$$

where R is the scan rate per time unit, S is the scan size, N is the number of lines in the image and θ_T is the angle between the horizontal and the true orientation of the step motion (Land et al. 1997). An alternative method to determine the step speed is to scan the surface with the slow scan axis disabled as illustrated in Figure 6 in the case of the growth of calcite (Teng et al. 2000).

Changes in anisotropy of step velocities. Changes in step velocity were used to determine velocity ratios during calcite dissolution (Larsen et al. 2010). At constant pH (fixed at 8.5 using KOH) and ionic strength (set at 0.1 M with KCl), the (Ca^{2+}) to (CO_3^{2-}) activity ratio, ξ, was varied from 0.1 to 100 to observe the spiral growth of calcite. The saturation index, which is defined as:

$$SI = \log\left(\frac{a_{Ca^{2+}} \cdot a_{CO_3^{2-}}}{K}\right) \tag{7}$$

where K is the equilibrium constant of dissolution of calcite, was fixed to 0.6. The geometry of the spiral growth pyramids observed by AFM (Fig. 7a) was characterized by differential interference contrast (DIC) microscopy to determine the absolute growth velocities of obtuse and acute steps. The initial growth solution, with ξ = 1, produced pyramids with spreading

EBSCOhost - printed on 2/13/2023 5:26 AM via . All use subject to https://www.ebsco.com/terms-of-use

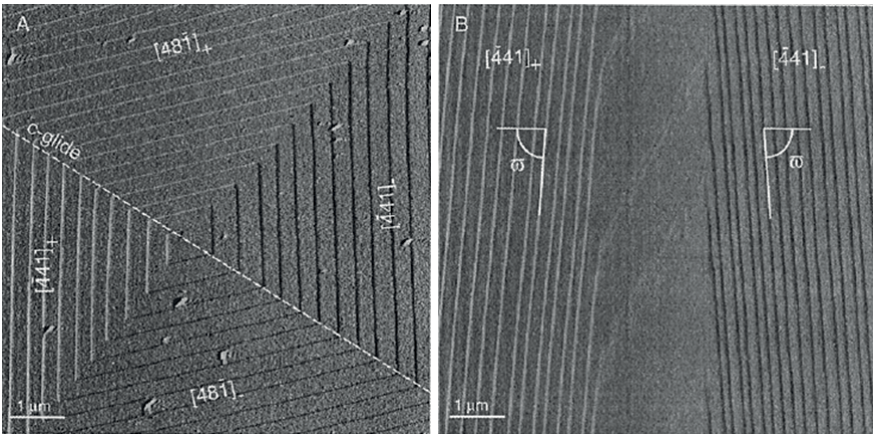


Figure 6. AFM imaging of a spiral hillock formed during the growth of the (10$\bar{1}$4) surface of calcite in supersaturated $CaCO_3$ solution (Teng et al. 2000). On the left image, the slow scanning direction was enabled whereas it was disabled on the right image. Steps are mono-molecular with a height of 0.3 nm. The angle $\bar{\omega}$ which allows to determine the step velocity has been measured on the two sides (right) of the glide line (left) to determine the velocity of both acute and obtuse steps. [Used by permission of Elsevier, from Teng et al. (2000), *Geochim Cosmochim Acta* 64, Figs. 1, p. 2258.]

velocities that were almost identical on the acute and obtuse sides and, thus, the angle θ (as defined in Fig. 7b) was essentially 180°. Within the experimental solutions ($\xi \neq 1$), the change in the relative velocities of acute and obtuse steps results in change in θ. Neglecting the shift of the apex of the pyramid because of the very small aspect ratio (height/diameter ~ 10^{-3}) of the hillock, the following relationship is derived from Figure 7b:

$$\frac{o}{x}\sin\left(\frac{\theta+\gamma}{2}\right) \quad \text{and} \quad \frac{a}{x}=\sin\left(\frac{\theta-\gamma}{2}\right) \tag{8}$$

where x is the distance from the apex of the pyramid to the obtuse/acute corners of the pyramid, a and o are distances from the apex to the acute and obtuse steps, respectively. The angles θ and ϕ are defined in Figure 7b. Increase in lengths o and a results from step motions, so that

$$\frac{o}{a}=\frac{v_o}{v_a}=\frac{\sin\left[\dfrac{\theta+\gamma}{2}\right]}{\sin\left[\dfrac{\theta-\gamma}{2}\right]} \tag{9}$$

Larsen et al. (2010) have used the analytical model of Zhang and Nancollas (1998) known as 'kinetic ionic ratio' which accounts for the interaction of dissimilar ions with kink sites on the basis of the Kossel model (Kossel 1927). The step velocity is expressed as a function of the product $r = (k_A/k_B)(a_A/a_B)$ of the ratios of the activities a_A and a_B of the A and B ions and of the rate constants k_A and k_B for their incorporation at step sites. Quite successful to represent the velocity of obtuse steps, the model failed to account for acute steps since dissimilar crystallographic directions cannot be described on the basis of the sodium chloride lattice. Therefore, the acute step velocity was represented empirically. For both obtuse and acute steps, velocity decreases with increasing relative Ca^{2+} activity, consistent with the results from batch experiments, where bulk growth rate is strongly influenced by changes in the Ca^{2+}:CO_3^{2-} activity ratio. A reversal in the relative obtuse and acute step velocities was observed at log ξ = 0.1 indicating that, because a high CO_3^{2-} activity is required to accelerate the growth of acute

EBSCOhost - printed on 2/13/2023 5:26 AM via . All use subject to https://www.ebsco.com/terms-of-use

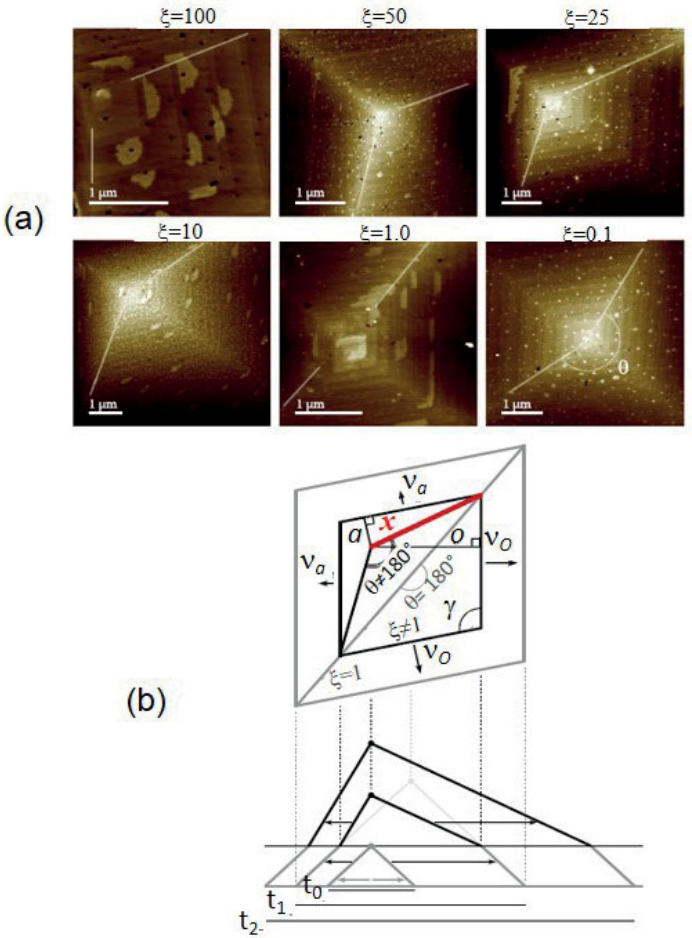


Figure 7. Geometry of a spiral pyramid of growing calcite upon change in growth conditions (Larsen et al. 2010): (a) AFM images of growing pyramids recorded in air, after removal from the solution, for different values of the activity ratio ζ (given in Figure). Obtuse steps are oriented toward the south and east; (b) schematic representation. For an activity ratio ζ = 1 (see text), the angle between the acute and obtuse "side" is 180° (light grey color). Change in the activity ratio (ζ ≠ 1) results in difference in velocity for acute and obtuse steps. The apex of the pyramid shifts towards the slower steps and the above angle diverges from 180°. Starting from a change in ζ at a time t_0, changes in shape are shown at different time t_1 and t_2. The distance x between the apex and the corner of the pyramid was then used to determine relative step velocities via Equations (8) and (9). A velocity reversal was inferred for ζ ≈ 0.1, the velocity of the obtuse steps becoming faster below that value. Texts and symbols are rewritten for clarity. [Used by permission of Elsevier, from Larsen et al. (2010), *Geochim Cosmochim Acta* 74, Figs. 4 and 5, pp. 2104-2105.]

steps, Ca^{2+} is attached at higher rate than CO_3^{2-}. The authors suggested that the velocity reversal depends on both the activity product (constant in their experiments) and the activity ratio and that the incorporation of ions is controlled by dehydration of ions and geometry of step sites. Therefore, the high Ca^{2+}:CO_3^{2-} concentration ratio observed in natural waters is a significant parameter that must be considered in models describing calcite growth kinetics (Larsen et al. 2010). More generally, impurity molecules or background electrolytes can strongly affect dissolution and growth, as in the specific case of calcite (Ruiz-Agado 2010, 2012).

EBSCOhost - printed on 2/13/2023 5:26 AM via . All use subject to https://www.ebsco.com/terms-of-use

Size and shape of clay minerals

In a way comparable to surface of bulk crystals, clay minerals particles show very anisotropic surfaces on which edge surface areas, steps and basal planes play quite different roles regarding the chemical activity and surface charging (Wieland and Stumm 1992; Zhou and Gunter 1992). Observations of the microtopography of kaolinite nanoparticles by *ex situ* AFM have proven that the contribution of edge surface areas and basal surface steps to the total surface charge has often been underestimated (Brady et al. 1996; Zbik and Smart 1998) and that the ionization of edge sites dominates; it has even been shown that ionization of the basal planes of kaolinite particles is not needed to account for the observed proton adsorption (Brady et al. 1996). On the basis of AFM observations that the talc basal planes carry a permanent negative charge, while the charge on edge surfaces is highly pH-dependent, the DLVO (after Derjaguin, Landau, Verwey and Overbeek) theory could be applied to those anisotropically-charged particles to demonstrate that the attractive interaction between talc basal planes and edge surfaces dominates the rheological behavior of talc particle suspensions (Yan et al. 2013).

The direct observation of nanoparticles in solution faces several difficulties. Particles must be fixed on a substrate that sticks particles but not the tip and which is smooth enough to allow the unambiguous observation of the supported powder. Three experimental methods for preparing supported clay particles for AFM analysis in aqueous solutions were proposed (Bickmore et al. 1999). Two techniques rely on the surface charge of phyllosilicates which combines a dominant structural negative charge delocalized on basal planes and a pH variable charge with a point of zero net proton charge (PZNPC) between 2-6. A first suggestion is to fix particles at the surface of a polished sapphire crystal where point of zero charge is between 8-9. It was observed that phlogopite particles were stabilized sufficiently for TM-AFM analysis for pH values below the point of zero charge (PZC) of sapphire (positively charged substrate) and above the PZNPC of the clay particles (negatively charged particles) (Fig. 8a). The very flat surface allows the analysis of particles of any size and shape. However, the technique is best suited for particles with strong permanent surface charge. A second method consists in using a polyethyleneimine(PEI)-coated mica surface which has an isoelectric point (IEP) of about 10 and shows a large positive charge for pH values lower than its IEP (Fig. 8b). The adhesion of particles on the PEI-coated mica is stronger than on alumina so that contact mode AFM can be used to image particles. The pH values at which particles stick on the substrate are mostly accounted for by the expected surface charges although, in some cases, surface roughness and hydrogen bonds are stressed to play a role. A third way to prepare clay minerals for *in situ* analysis in aqueous solution was to deposit particles on a thermoplastic adhesive film spread over a steel plate. The method is suitable for any kind of particles, regardless of the surface charge, provided they are of well-defined shape and of rather large size. *In situ* study by AFM of dissolution profiles (Fig. 8c) and measurements of change in particle dimensions using computerized analysis have allowed the determination of reaction rates normalized to the edge surface area (ESA), the comparison to rates normalized to the total surface area (TSA) (Bosbach et al. 2000; Bickmore et al. 2001, 2002; Tournassat et al. 2003; Brandt et al. 2003; Köhler et al. 2005; Kuwahara 2006, 2008; Can et al. 2010) and the measurement of friction coefficients (Kosoglu et al. 2010).

Limits of the AFM observation

AFM analysis of step velocity. The direct determination of reaction rates through measurements of step velocities suffers from several limits. The accurate determination of the number of steps per unit area requires the choice of a wide enough scanfield (Jordan and Rammensee 1996) and measurements of step velocities by the methods described above (Land et al. 1997; Larsen et al. 2010) need appropriate scan speeds. Step velocities that are either too slow or too fast cannot be accurately determined. Step motion must be stationary, and steps must be long enough to lead to reliable values of step velocity (Higgins and Hu 2006). Steps must move by ~10 times the lateral resolution per image (Higgins and Hu 2006). Conversely,

EBSCOhost - printed on 2/13/2023 5:26 AM via . All use subject to https://www.ebsco.com/terms-of-use

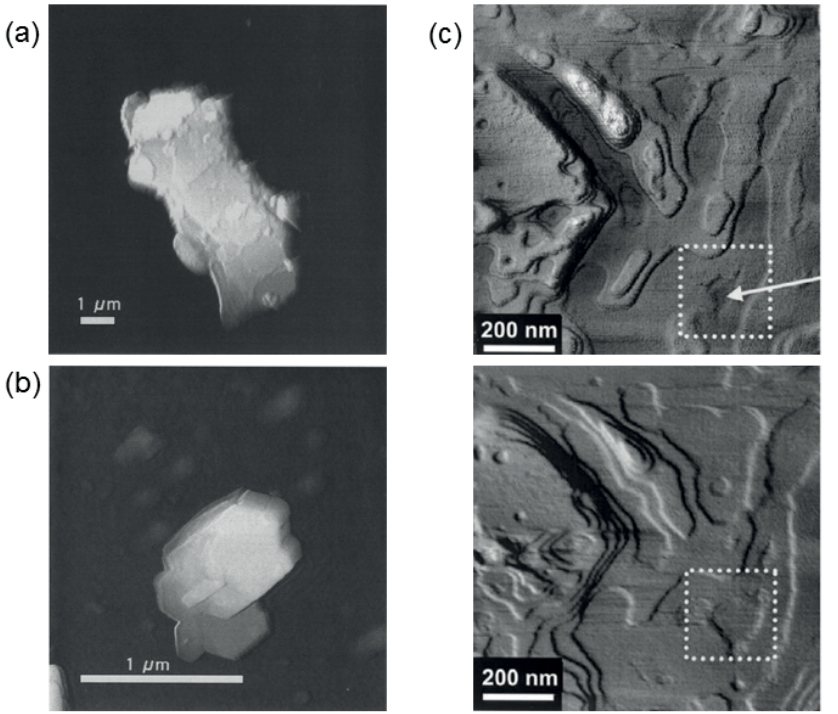


Figure 8. Tapping mode AFM height images of clay mineral particles: (a) Ground phlogopite particle electrostatically fixed to a polished sapphire substrate under deionized water. Maximum particle height = 789 nm (Bickmore et al. 1999); (b) Kaolinite particle fixed to a PEI-coated mica substrate under deionized water. Maximum particle height = 201 nm (Bickmore et al. 1999); (c) *In situ* dissolution sequence at pH 2 and 29±1° of a (001) surface of a chlorite particle mounted onto a sample holder which was coated by a thin layer of thermoplastic adhesive. Top: opening of an etch pit within a TOT layer. Bottom: the same surface captured 1200s after top figure; the etch pit marked by the square is now 1 nm in depth, corresponding to one TOT sheet (Brandt et al. 2003). [Used by permission of The Clay Mineral Society publisher of *Clays and Clay Minerals*, from Bickmore et al. (1999), *Clay Clay Miner* 47, Figs. 1 and 4, pp. 576-577 and of Elsevier from Brandt et al. (2003), *Geochim Cosmochim Acta* 67, Fig. 5, p. 1459.]

steps with velocities that strongly overcome the scan speed are hardly observed (Lasaga and Lüttge 2001). Moreover, an increased scan velocity may cause scan- induced erosion of the surface (Maurice 1996). Finally, the instrument bandwidth limits the measurable step velocity (Higgins and Hu 2006).

It is generally estimated that AFM can be used to observe dissolution or growth processes occurring at rates in the range of 10^{-10}-10^{-5} mole m^2 s^{-1} (Dove and Platt 1996; Jordan and Rammensee 1996) on the basis of step velocity ranging between 10^{-4} to 10 nm s^{-1}. Dissolution rates of celestite and barite are easily measured (Dove and Platt 1996). Those of calcite (Dove and Platt 1996), dolomite (Lasaga and Lüttge 2001), brucite (Jordan and Rammensee 1996) and gypsum (Bosbach and Hochella 1996) lie in the upper limit of the observable range. For the many mineral surfaces that show much lower rates of dissolution than those, dissolution can be monitored by an appropriate choice of circulating solutions (Bosbach and Rammensee 1994) as well as by an increase in temperature (Higgins et al. 1998).

Effect of tip pressure on the apparent step speed. The tip-induced erosion of surfaces is an important issue for AFM analysis of reaction rates at mineral surfaces (Dove and Platt 1996;

EBSCOhost - printed on 2/13/2023 5:26 AM via . All use subject to https://www.ebsco.com/terms-of-use

Maurice 1996; Shiraki et al. 2000; Butt et al. 2005; Larsen et al. 2010). Contact mode scanning was often shown to result in an enhanced wear of substrates, in particular in the presence of water. For example, the local dissolution rate of calcite was seen to be increased by over an order of magnitude for normal forces of 270 nN in aqueous solution whereas no wear features could be observed in dry conditions (Park et al. 1996). Using mica and silicon tips, it has been demonstrated that defects produced by the rupture of Si–O bonds at the surface, which are not visible in contact mode AFM images, have a noticeable contribution to friction (Kopta and Salmeron 2000). For forces that depend on the hardness and solubility of the substrate, the most common observation is an erosion of atomic steps which results in an increase in step velocity upon dissolution (Park et al. 1996; Nakahara et al. 1995). Frictional forces are higher when the tip moves up a step than when it moves down (Nakahara et al. 1995). Tapping mode AFM is frequently used to reduce tip-sample interaction (Zhong et al. 1993; Hansma et al. 1994), in particular to study the microtopography of nanoparticles in solution (Bickmore et al. 1999, 2001, 2002; Brandt et al. 2003; Tournassat et al. 2003; Metz et al. 2005; Kuwahara 2006; Can et al. 2010).

However, surfaces may be modified by scanning with weak or even negative loads (Nakahara et al. 1995). In the case of $NaNO_3$ surfaces exposed to moist air, it was observed (i) that the growth rate of tip-induced ridges does not depend linearly on the applied force and (ii) that ridges appear at a relative humidity of 35-40% but not above 50%, as if the stress was mediated by the water film via either a dielectric shielding mechanism or an increase in pressure beneath the tip (Nakahara et al. 1995). During the dissolution of a cleaved gypsum crystal, two dissolution regimes were observed as a function of the tip pressure (Pachon-Rodriguez et al. 2011) (Fig. 9a). Forces higher than 10 nN resulted in a jump in step velocity with respect to step speed observed below that value (Fig. 9b). The high force behavior was explained by a wear mechanism (Park et al. 1996) whereas the rate enhancement at forces < 10 nN was suggested to arise from a contribution of the elastic strain to the chemical potential, as a consequence of the tip-induced increase in the pressure solution (Pachon- Rodriguez et al. 2011).

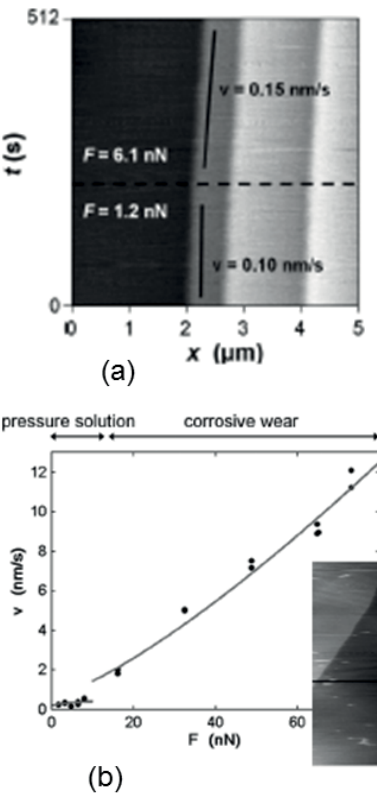


Figure 9. AFM imaging in contact mode of the dissolution of gypsum (Pachon-Rodriguez et al. 2011). Step velocity was determined by the method of Teng et al. (2000): (a) At a constant saturation index (Eqn. 7), an increase in load (indicated in the figure) was seen to increase the step speed; (b) Two dissolution regimes were identified as a function of the load. Below 10 nN, the rate of dissolution increases as a function of the strain exerted on the lattice. Above that value, the tip was suggested to erode the substrate. [Reprinted Figs. 1 and 4 from Pachon-Rodriguez et al., *Phys. Rev. Lett.* 107, 146102 (2011). Copyright (2011) by the American Physical Society.]

EBSCOhost - printed on 2/13/2023 5:26 AM via . All use subject to https://www.ebsco.com/terms-of-use

AFM rates versus bulk rates

For a given system, values of dissolution and growth rates determined by different groups on the basis of the measurement of step velocities on crystal surfaces are often in good agreement, which means that data are reproducible (Shiraki et al. 2000). However, those rates are systematically lower than rates derived from the analysis of powders in solutions, with discrepancies that are often of one or two orders of magnitude (Jordan and Rammensee 1996; Morse and Arvidson 2002; Arvidson et al. 2003; Lüttge et al. 2003; Morse et al. 2007) as illustrated in Figure 10 (Morse and Arvidson 2002). Reasons invoked are the CO_2 pressure, grain size, crystallographic orientations (step density that must be higher on powders than on crystal surfaces), contaminants which are more efficient on extended surfaces than on powders (Arvidson et al. 2003) and the suspicion of incongruent dissolution behavior (Lüttge et al. 2003). Authors also point to the difficulty of definition of the reactive area in the sense that some extremely reactive sites, such as outcrops of dislocation or micro-damaged areas, might not be correctly sampled by microscopic analyses (Shiraki et al. 2000; Lüttge et al. 2003; Morse et al. 2007). Finally, diffusion of products away from the surface has to be properly accounted for; indeed, measurement of the surface reaction rate constant for gypsum in water using holographic interferometry, free from the influence of mass transport, gives clues to explain the inconsistency between published dissolution rates of calcite and aragonite (Colombani 2008).

Regarding clay minerals, the comparison between data is an important issue to achieve unified descriptions of nanoparticles in solution. Specific surface areas of clay nanoparticles are commonly determined by the Brunauer-Emmett-Teller (BET) method. However, the reliability of the BET method for the calculation of reactive surface area is questioned since, for a given clay mineral, depending on the history, exfoliation and porosity can increase the BET surface area while the edge surface area remains constant (Metz et al. 2005).

The above discrepancies also raise questions about mechanisms, in particular regarding the link between dissolution mechanisms and concentrations of dissolved components:

- On the basis of the observation of steps moving away from etch pits into the surface, the stepwave model (Lasaga and Lüttge 2001; Arvidson et al. 2003; Kurganskaya et al. 2012) (Fig. 11) suggests (i) that the mechanism of dissolution (etch pits opening up or not) depends on undersaturation and (ii) that the main role of etch pits is to serve as sources of train of steps (Lasaga and Lüttge 2001; Arvidson et al. 2003, Kurganskaya et al. 2012). In the same spirit, the use of the basal/edge surface ratios for characterizing dissolution rates was questioned on the basis of the observation of strong variations of those ratios during the course of dissolution of mica (Kurganskaya et al. 2012). Arvidson et al. have noticed about the debates on microscopic and macroscopic measurements that the issue is not to determine the "best number" (Arvidson et al. 2003) but to build up models that combine mechanistic information from AFM to kinetic data from bulk solutions (Arvidson et al. 2003; Morse et al. 2007).
- Although the BCF (Burton, Cabrera and Franck 1951) model has been demonstrated to apply to the dissolution of quartz (Gratz et al. 1991), its application to the case of calcite is unclear. Using high- resolution *in situ* atomic force microscopy (AFM) and kinetic Monte Carlo simulations of step-edge structure, steps were shown to exhibit low kink density and weak step edge fluctuations. A mechanism determined by the kinetics of attachment and detachment was suggested (De Yoreo et al. 2009).
- Sorption may strongly perturb dissolution and growth. Using frictional force microscopy for imaging *in situ* a calcite substrate immersed in aqueous solutions, ions such as Cd^{2+}, Sr^{2+}, and La^{3+} were seen to either initiate or passivate surface growth; the monomolecular surface played a central role, serving as both dissolution sites for the substrate and nucleation sites for the overgrowth (Hay et al. 2003).

EBSCOhost - printed on 2/13/2023 5:26 AM via . All use subject to https://www.ebsco.com/terms-of-use

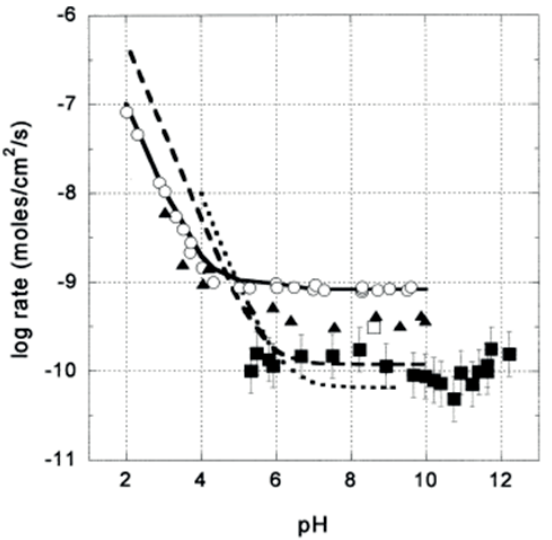


Figure 10. Comparison of values of the dissolution rate of calcite that were derived from AFM data with those determined in solution (Morse and Arvidson 2002): closed squares are AFM rates and closed triangles are bulk rates (both from Shiraki et al. 2000). Although AFM-derived values are smaller than the average, they are within the range of the bulk values determined under similar conditions (Shiraki et al. 2000). Other data which show higher dissolution rates are from measurements in solution (see Morse and Arvidson for references). [Used by permission of Elsevier, from Morse and Arvidson (2002), Earth-Sci. Rev. 58, Fig. 10, p. 67.]

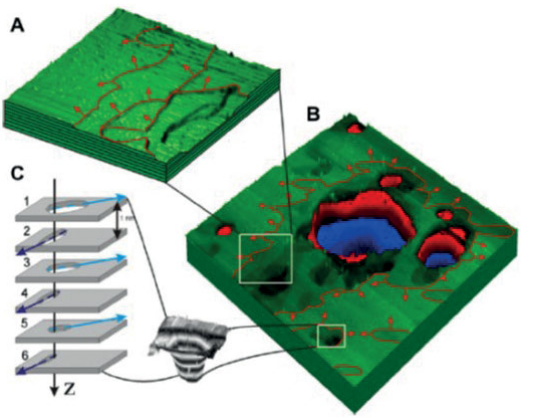


Figure 11. Schematic illustration of stepwave formation on muscovite (001) surface (Kurganskaya et al. 2012): (a) consecutive steps moving from a dislocation center; (b) steps generated around etch pits and point defects form a unique stepwave; (c) TOT layers shown as parallel plates. [Used by permission of Elsevier, from Kurganskaya et al. (2012), G*eochim Cosmochim Acta* 97, Fig. 6, p. 127.]

Another concern is the change in surface orientation in the course of a reaction, in line with the more general suggestion that the reactive area should have both a geometric and an energetic definition (Lüttge 2005, 2006). For example, the formation of (111) facets during the dissolution of the periclase (001) surface (Jordan et al. 1999) is consistent with the observation (Hacquart and Jupille 2007, 2009) supported by numerical simulation (Geysermans et al. 2009) that MgO(111) is the stable hydroxylated orientation of MgO.

FORCE MEASUREMENTS

In contact with aqueous solutions, surfaces become charged. Surfaces charges are involved in the DLVO theory which combines long range dispersion forces and double layer interaction. In aqueous solution, the surface hydroxyl groups react with proton and hydroxyl

EBSCOhost - printed on 2/13/2023 5:26 AM via . All use subject to https://www.ebsco.com/terms-of-use

groups of the solution to create either a positively or negatively charged surface. The surface charge is positive (negative) for pH lower (higher) than that of the isoelectric point (IEP) of the surface at which the zeta potential of the surface is zero (Parks 1965). The surface charge may also be anisotropic or may appear at specific sites corresponding to lower coordination numbers, vacancies, impurities or adsorbates. Another major phenomenon occurs at the vicinity of a surface in water. Over distances of a few nanometers from a surface in water solution, the water density profile and interaction forces oscillate with a periodicity close to molecular diameter. The interactions giving rise to the layered structure of the water are called hydration forces (Israelachvili and Pashley 1983; Israelachvili 1991). Water structuration and charges control the particles growth (Jolivet 2000), the stability of colloids (Israelachvili 1991) and the adhesion processes (Fowkes 1990). These phenomena are of crucial importance for mineral surfaces that are prone to hydration and charging. This has given rise to many specific developments (or adaptation) of experimental AFM approaches.

Hydration forces

The DLVO theory fails to account for the interfacial phenomena that involve objects that approach at distances less than a few nanometers. In aqueous solutions, the formation of structured water layers at interfaces is the main cause of the non-DLVO behavior (Israelachvili 1991). The phenomenon has little effect on the force measurements aimed at probing surface charges since the DLVO approach applies for tip-substrate distances used in these measurements (Lin et al. 1993; Franks and Meagher 2003). Conversely, structured water layers may have important consequences at distances shorter than a few nanometers and, more specifically, for AFM analysis of surfaces at sub- nanometer distances.

Structured water layers. A direct confirmation of the importance of hydration on mineral surfaces comes from force-distance measurements between silica microspheres and muscovite mica surfaces (Acuna and Toledo 2011). The surface roughness of both microspheres and substrates was estimated to be in sub-nanometer range. The excess repulsive force determined by subtracting the DLVO theory from the experimental data (Fig. 12a) was fitted by an empirical double exponential law, which is close to that found for the glass-silica interaction,

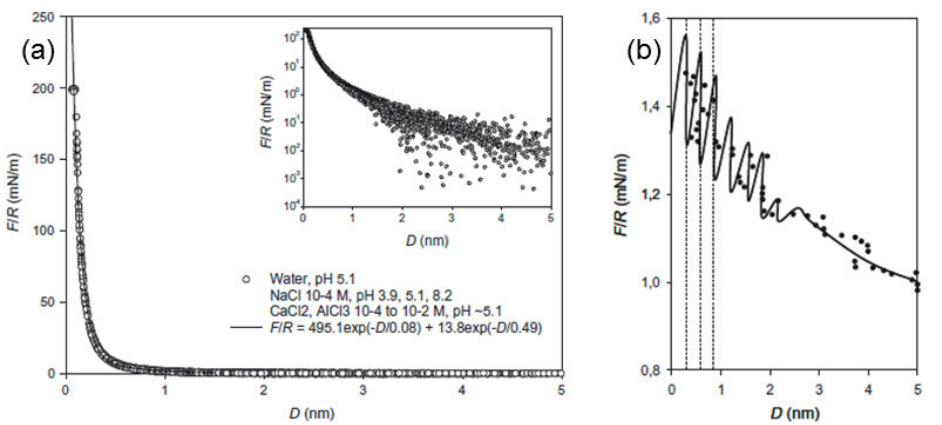


Figure 12. Repulsive forces between glass microspheres of 20 mm in size and a muscovite mica surface. Experiments were performed in various solutions at pH ~ 5.1 (Acuna and Toledo 2011): (a) Excessive repulsive force obtained by subtracting values derived from DLVO theory from the sum of a series of AFM measurements; (b) AFM measurement performed in a $10^{-4}M$ aqueous NaCl solution at pH ~5.1. The line is to guide the eyes. The period of 0.25 nm of the oscillations is assigned to successive water layers (see also Fig. 18). [Used by permission of Elsevier, from Acuna and Toledo (2011), *J. Colloid Interf. Sci*. 361, Figs 1 and 2, p. 399.]

EBSCOhost - printed on 2/13/2023 5:26 AM via . All use subject to https://www.ebsco.com/terms-of-use

and is poorly sensitive to the nature and concentration of the electrolyte, and to the pH of the solution. The examination of a single force curve revealed oscillations with a period of about 0.25 nm (Fig. 12b) that were attributed to water layers in the same way as those that were observed between two mica surfaces (Israelachvili and Pashley 1983).

Hydrophilic and hydrophobic attraction. Structured water layers are also involved in apparently macroscopic phenomena. An example is given by the flotation of fluorite and calcite. Fluorite has a much better flotation response than calcite, which indicates that adsorption of surfactants is easier on fluorite than on calcite. Force measurements between calcium dioleate spheres and cleaved fluorite and calcite surfaces were compared to the DLVO theory derived from the calculation of the van der Waals contribution and of the electrical double-layer contribution (Fa et al. 2005). Since calcium dioleate and calcite are negatively charged at pH 8.1 at which the experiments were performed, the observed repulsion between the two surfaces was assigned to electrostatic interactions. However, the sizeable attraction which is observed in experiments for small sphere-surface distances escapes the DLVO theory. Molecular dynamic simulation was undertaken to determine the water structure at the hydrophilic surfaces of fluorite and calcite. On fluorite, the layered structure involves three layers with a separation of 0.26 nm that is larger than a water molecule. On calcite five or six water layers are formed which are denser than in the case of fluorite. Therefore, the structure of the water layer plays a central role in the attraction/repulsion of hydrophobic dioleate spheres at hydrophilic surfaces.

Determination of the point of zero charge (PZC)

Acid-base interactions. Acid-base interactions play a pivotal role in dissolution, precipitation, agglomeration, transport of matter in aqueous solutions and adhesion (Fowkes 1990) between dissimilar media. Surface charges that develop as a function of concentration and pH in aqueous solution are a driving force for the partition of the ionic species between solutions and surfaces and for the behavior of suspensions of colloidal particles (Israelachvili 1991). Under the assumption that H^+ and OH^- are potential determining ions for oxides in aqueous solutions, the nature of the surface charges that appear on surfaces as a result of the dissociation of water molecule is expressed as a function of pH (Parks et al. 1965). The point of zero net proton charge (PZNPC) is defined as the pH at which proton uptake is balanced by proton removal. It characterizes the Brönsted acidity or basicity of a substrate. More generally, the point of zero charge (PZC) is defined as the pH at which positive and negative charges arising from adsorption of H^+, OH^- and other ions are in equal numbers (Sposito 1998). A closely related parameter is the ζ potential which is the potential at the plane of shear between the surface with adlayers adsorbed from the solution and the bulk of the solution. The pH at which the ζ potential is zero is called isoelectric point (IEP) (Parks 1965). In the absence of ions specifically adsorbed from the solution, the PZC and IEP are similar and the two terms are alternatively used by authors. The pH values corresponding to PZC and IEP are commonly derived from titrations performed on powder suspensions.

The drawback of the determination of the donor-acceptor character of surfaces by analyzing powders is the absence of information on crystallographic orientations. Indeed, acid-base properties are expected to depend on the structure of surfaces since the ability of the surface sites to capture protons relies on coordination numbers (Goniakowski and Noguera 1995). Measurements on defined orientations are prerequisites to obtain reference data by combining experimental and theoretical approaches. In this context, the examination of the PZC of α-Al_2O_3(0001) by AFM is by far the most common study. The frequent comparison of AFM data with measurements made on powders (Franks and Meagher 2003) or by other approaches such as Second Harmonic Generation (SHG) (Stack et al. 2001; Fitts et al. 2005), Sum-Frequency Generation (SFG) (Stack et al. 2001), Sum-Frequency Vibrational Spectroscopy (SFVS) (Sung et al. 2011), streaming potential (Franks and Meagher 2003), offers an opportunity to evaluate the reliability of AFM in characterizing acid-base properties of surfaces.

EBSCOhost - printed on 2/13/2023 5:26 AM via . All use subject to https://www.ebsco.com/terms-of-use

Point of zero charge of alumina surfaces. From the DLVO behavior, it is expected that the double layer forces measured between tip and surface are proportional to surface potentials. Consequently, in the region in which electrostatic forces dominate van der Waals forces, the tip-surface interaction is repulsive when surface and tip bear charges of similar sign, attractive when charges are of opposite sign (Lin et al. 1993). Therefore, when pH is varied, a switch in the attractive/repulsive regime occurs at the PZC of the substrate. AFM measurements dedicated to the study of PZC are performed by approaching the surface with either a conventional AFM silicon nitride tip (Lin et al. 1993; Stack et al. 2001) or a silica microsphere (made hydrophilic) glued on a cantilever (Veeramasuneni et al. 1996; Meagher et al. 2002; Franks and Meagher 2003; Tulpar et al. 2005) (Fig. 13a). Set-ups are similar to those used to probe double layer forces (Ducker et al. 1991; Acuna and Toledo 2011).

Alumina surfaces are prepared in very similar manner by the various groups. Polished alumina crystals are cleaned by nitric acid etch and rinses in purified or deionized water, and/or in ethanol, acetone, surfactant solutions, with differences that appear marginal (Stack et al. 2001; Meagher et al. 2002; Franks and Meagher 2003; Fitts et al. 2005; Sung et al. 2011). When it has been analyzed, the level of the residual contamination by carbon was judged acceptable (Franks and Meagher 2003). As determined by AFM, the pH at which PZC was observed ranges from 4 to 6 (Larson et al. 1997; Stack et al. 2001; Meagher et al. 2002; Franks and Meagher 2003; Tulpar et al. 2005). AFM data were confirmed by measurements performed in parallel on the same surfaces by different techniques, as for example SFG (Stack et al. 2001) and streaming potential (Franks and Meagher 2003). Separate measurements by SHG (Fitts et al. 2005) and SFVS (Sung et al. 2011) on similar crystal surfaces were also compared to AFM data. The overall consistency of the data demonstrates the reliability of measurements. Nevertheless, values of pH at which PZC of flat surfaces is observed are significantly lower than those observed on powders (Franks and Gan 2007; Franks and Meagher 2003). A puzzling point is that the PZC of plasma-etched alumina crystal surfaces is found at pH similar

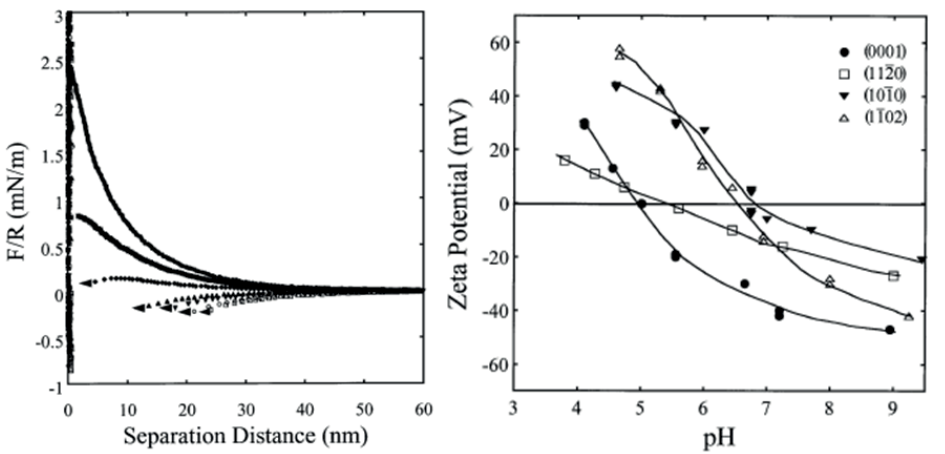


Figure 13. Interaction forces in an electrolyte between a silica microsphere glued at the end of a cantilever and an alumina surface (Franks and Meagher 2003): (a) (1 $\bar{1}$02) face of an α-alumina crystal in 0.001 M KBr solutions with, from top to bottom curves, pH values of 9.25, 8.0, 6.95, 6.45, 6.0, 5.3 and 4.65. As pH decreases, forces switch from repulsive (positive forces) to attractive. Arrows indicate jump-to-contact; (b) Zeta potential for various crystal orientations that were derived from forces measurements similar to those shown on the left figure. Intersects with the zero line give the values of pH corresponding to PZCs. [Used by permission of Elsevier, from Franks and Meagher (2003), *Colloid Surface A* 214, Figs 3 and 6, pp. 106 and 107.]

EBSCOhost - printed on 2/13/2023 5:26 AM via . All use subject to https://www.ebsco.com/terms-of-use

(9.3) to those of alumina powders. It was observed at pH = 9.3, in excellent agreement with electrokinetic measurements recorded in parallel (pH = 9.1) (Veeramasuneni et al. 1996), and at pH = 8.5 (Tulpar et al. 2005).

Therefore, differences in PZC between flat surfaces on the one hand and powders and plasma-etched surfaces on the other hand, are reproducibly observed, independently on the technique which is used. Indeed, the pH values corresponding to PZC depends on the surface orientation, as observed for (001) and (101) faces of goethite (Gaboriaud and Ehrhardt 2003), and there exists a tendency for high index crystal surfaces to exhibit PZC at higher pH (Franks and Meagher 2003; Fitts et al. 2005) which can be understood on the basis of the expected properties of low-coordinated surface atoms (Goniakowski and Noguera 1995). For α-alumina surfaces of various orientations, the PZC is found at pH ranging between 5 and ~ 7 by AFM, with α-Al_2O_3 faces in the order (0001) ≈ $(11\bar{2}0)$ < $(1\bar{1}02)$ ≈ $(10\bar{1}0)$ (Frank and Meagher 2003; Fitts et al. 2005; Sung et al. 2011) (Fig. 13b). Although the PZCs of more open crystal orientations are found at higher pH values (~ 7) than the basal α-Al_2O_3(0001) orientation, the difference does not fill the gap between flat surfaces and powders whose PZCs are observed in the pH range 8 to 9.4. The reason commonly invoked to explain the discrepancies is that the low-coordinated sites of the external surface of powder particles may not be correctly reproduced by single crystal surfaces since the charging behavior of surface hydroxyls depends upon the number of aluminum atoms to which the hydroxyl is bound as well as the coordination of the aluminum ion (octahedral or tetrahedral) (Franks and Gan 2007).

Kelvin Force Probe Microscopy (KPFM)

Principle of the method. The detection of local changes in surface potential using AFM in noncontact mode was first developed to detect charges (Weaver and Abraham 1991) and probe difference in work function (Nonnenmacher et al. 1991) at metallic and semiconduconductor surfaces with lateral sub-micrometric resolution. Implemented on AFM set-ups, the so-called Kelvin Probe Force Microscopy (KPFM) technique (Nonnenmacher et al. 1991) was based on the same principle as the Kelvin method which consists in measuring the current $i(t)$ through a plate capacitor vibrating at a frequency ω that is approached in close proximity to a surface:

$$i(t) = V_{CPD}\Delta C\omega\cos(\omega t) \tag{10}$$

where VCPD is the contact potential difference (CPD) and ΔC the change in capacitance (Nonnenmacher et al. 1991). An additional voltage applied to the plate until the current vanishes gives the measure of the VCPD. The KPFM machine was aimed at achieving high lateral resolution (Nonnenmacher et al. 1991; Weaver and Abraham 1991). The method was first operated in ambient conditions, in AM-AFM mode in which the amplitude of the cantilever oscillation induced by the electrostatic force is measured directly (Kikukawa et al. 1995). It was then run in nc-AFM mode in ultra-high vacuum to achieve contact potential and topographic analysis (Kitamura and Iwatsuki 1998). The force gradient is detected by applying between tip and sample a voltage $V = [V_{dc} + V_{ac}\sin(\omega t)]$ that combines dc and ac voltages. If z is the tip-sample distance, the resulting electrostatic force F_{el} given by

$$F_{el} = -\frac{1}{2}V^2\frac{\partial C}{\partial z} \tag{11}$$

involves a dc component and two ac components oscillating at ω and 2ω, respectively (Hudlet et al. 1995). The amplitude of the ω contribution is minimized when the tip-sample dc voltage V_{dc} component is equal to VCPD (Glatzel et al. 2003). In addition, the amplitude V_{ac} of the ac component contributes quadratically to the topographic image that can therefore be recorded at the same time as the KPFM image, provided amplitude, phase shift and Kelvin-probe feedback are controlled (Loppacher et al. 2004).

EBSCOhost - printed on 2/13/2023 5:26 AM via . All use subject to https://www.ebsco.com/terms-of-use

An alternative use of nc-AFM to probe contact potential was developed by applying a dc bias on electrically conducting tips (Sturm et al. 2005). On alumina films, the bias dependence of the response of the charges was quantitatively explained (Sturm et al. 2005) by a model involving the electric force gradient between the fixed charge and its image in the tip and by accounting for the image of the tip in the sample (Terris et al. 1989; Hudlet et al. 1995). The sign and the distribution of the charges over the sample depth were sketched and correlations between height profiles and charge suggested a relationship between surface charge and microstructure (Sturm et al. 2005).

A shortcoming of the KPFM analysis based on the locking detection of the force gradient is the lack of quantitative meaning of the measurements. Glatzel et al. have measured the work function difference between gold islands and highly oriented pyrolytic graphite (HOPG) substrates on which they were deposited (Glatzel et al. 2003). The expected value of ≈ 400 mV was neither found in AM- mode nor in FM-mode, although the analyzed gold islands (50-100 nm) were significantly larger than the tip radii (10 nm). Indeed, the measurements were strongly dependent on the tip shape. Long tips were seen to be more appropriate for KPFM measurements (Glatzel et al. 2003), in agreement with a model which predicts that good resolution in potential maps is obtained by long tips on cantilevers of minimal width and surface area (Jacobs et al. 1998).

Surface charges on insulating materials. The surface double layer arising at the surface of ionic materials containing cationic impurities (extrinsic case) has been studied on alkali halide surfaces that possess a net negative charge originating from negative cation vacancies (Barth and Henry 2007). The space charge region arising at the surface in the presence of cation impurities requires negative cation vacancies to preserve charge neutrality. Kelvin probe force microscopy (KPFM) images recorded on cleaved KCl(100) crystals annealed at 420-470 K to reach an equilibrium charge state are shown in Figure 14 (Barth and Henry 2007). A bias voltage involving dc and ac components was applied at the rear side of the sample and the tip was grounded. The contact potential was mapped out by minimizing the electrostatic tip-surface interaction. At the corners of crossing steps or along steps of higher indices otherwise evidenced by the topographic analysis (Fig. 14a), KPFM images revealed bright spots (Fig. 14b) that were assigned to negative surface charges, as indicated by the more positive CPD voltage needed to compensate electrostatic forces on those spots. Indeed, in the representation of the interaction of the tip with a point charge (Terris et al. 1989), the negative charge created by the positive bias compensates for the positive image charge arising from a negative surface charge that is in turn balanced by a positive charge at the back of the crystal (Barth and Henry 2007). The size of the bright spots (≈ 20 nm) was comparable to the tip radius (Fig. 14b).

Surfaces of doped ionic compounds were also studied. The surface double layer observed at the surface of NaCl(100):Mg^{2+} (NaCl crystals doped by Mg^{2+} impurities) was suggested to explain the progressive discharge of the charging observed just after cleavage of ionic crystals (Barth and Henry 2007). Then, the structures of Susuki precipitates at the surfaces of NaCl(100):Mg^{2+} and NaCl(100):Cd^{2+} were imaged at atomic resolution by nc-AFM (Barth and Henry 2008). The positions of the Na^{+}, Cl^{-}, Mg^{2+} and Cd^{2+} ions in the cubic structure of the precipitates were identified by the combination of numerical simulations and nc-AFM atomically resolved images of the surface (Foster et al. 2009). The technique provides a general tool for characterizing ionic surfaces at atomic scale.

Work function vs. topography of thin films. Thin films can be probed by STM, as well as work function change. However, atomic force microscopy is the only technique that can analyze simultaneously the topography and the work function change, as in the AM-AFM ultra-high vacuum study of KBr and NaCl thin films deposited on a Cu(111) crystal (Glatzel et al. 2009). The topographic image, its schematic representation and the corresponding KPFM image are presented in Figures 15a, 15b and 15c, respectively (Glatzel et al. 2009). The active

EBSCOhost - printed on 2/13/2023 5:26 AM via . All use subject to https://www.ebsco.com/terms-of-use

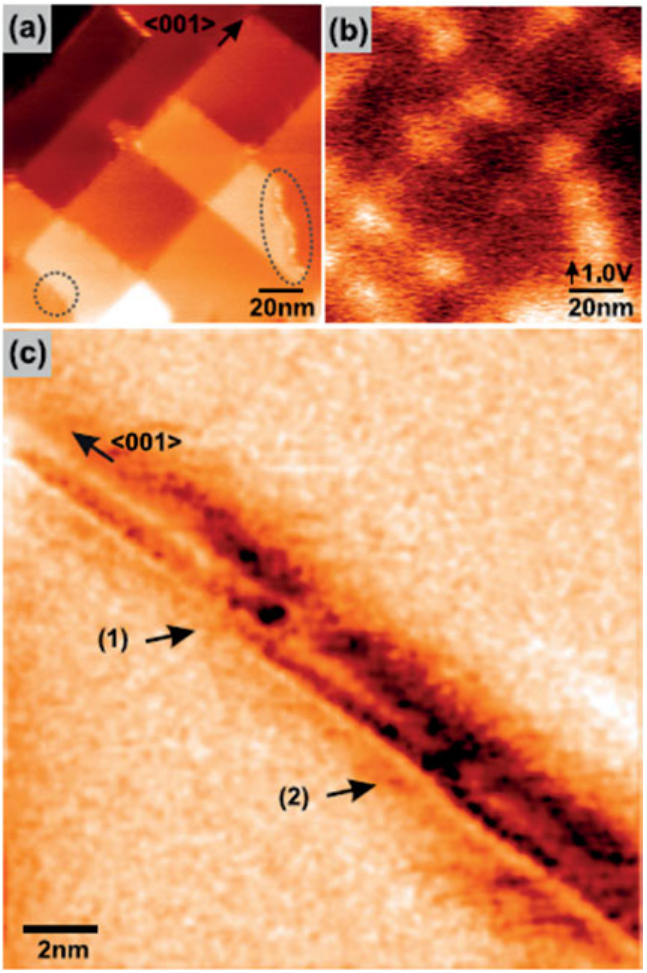


Figure 14. Kelvin probe force microscopy (KPFM) measurements on the KCl(100) surface (Barth and Henry 2007): (a) surface topography (150×150 nm^2)—with atomically flat terraces separated by monoatomic high steps—analyzed simultaneously with (b) potential image during KPFM measurements on a (001) surface of a pure KCl crystal; voltage differences which show charges at crossing points between steps and on steps with higher indices; (c) constant height zooming (18×18 nm^2) of the area shown in an ellipse in (a) without the KPFM modulation. Kinks on the <100> steps are marked by arrows. Black holes suggest stronger tip-substrate interaction (stronger detuning) in the vicinity of kinks. [Reprinted Fig. 1 from Barth and Henry, *Phys. Rev. Lett.* 98, 136804 (2007). Copyright (2007) by the American Physical Society.]

adjustment of the dc component of the voltage to determine the contact potential difference variation tends to continuously eliminate electrostatic forces between tip and substrate, which allows a determination of heights in good conditions (Sadewasser and Lux-Steiner 2003). Based on a method proposed by Sadewasser and Lux-Steiner (2003), Glatzel et al. (2009) simulated the tip-sample interaction. The tip was described with a staircase profile to represent a series of parallel plate capacitors. Theoretical heights compared within 10 to 20% to measurements (Glatzel et al. 2009).

EBSCOhost - printed on 2/13/2023 5:26 AM via . All use subject to https://www.ebsco.com/terms-of-use

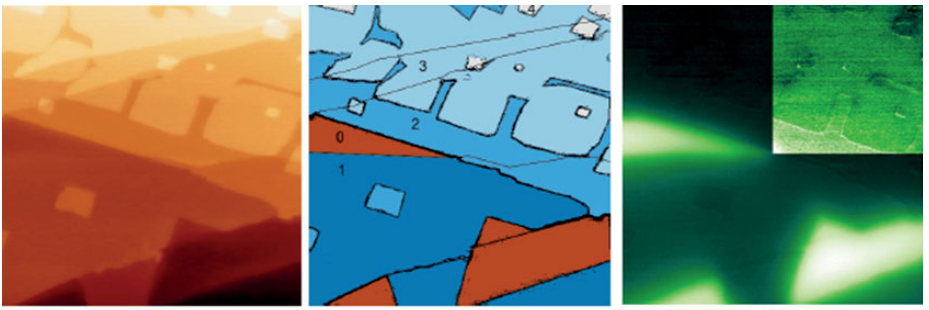


Figure 15. Simultaneous imaging of the topography and contact difference potential for NaCl(100) films supported on Cu(111) (Glatzel et al. 2009): (a) Topography of a 300×300 nm^2 area shown schematically in (b) to highlight the different layer heights (numbered from 0 (bare copper surface) to 3); (c) Contact potential image (VCPD = 600 mV) which presents a clear contrast between the bare copper surface and covered areas as well as between different layer heights. The zone shown with a better contrast in the inset corresponds to the middle right of the image (a), which gives an estimate of the resolution that is achieved by the method. [Used by permission of IOP Publishing Ltd, from Glatzel et al. (2009), *Nanotechnology* 20, Fig 1, p. 264016-3.]

ATOMICALLY RESOLVED SURFACE STRUCTURES

The complexity of the control parameters of AFM with respect to STM makes the achievement of images at atomic resolution in force microscopy more difficult than in tunneling microscopy (Giessibl 1994). Nevertheless, atomic resolution was achieved soon after the invention of STM on many surfaces and in particular on mineral surfaces using AFM in contact mode and then in noncontact mode.

Structures in contact mode

Atomically resolved AFM in contact mode. Atomically resolved AFM images were recorded on many surfaces of mineral crystals. The surface structure of illite/smectite nanoparticles supported on freshly cleaved HOPG was evidenced by AFM in contact mode and, in the case of very thin clay particles, compared with STM analysis (Lindgreen et al. 1991). The cleaved barite (001) surface analyzed by AFM in variable deflection mode in saturated $BaSO_4$ solution was suggested to be bulk-terminated (Bosbach et al. 1998). AFM analysis of NaCl(001) (Meyer and Amer 1990), LiF(001) (Meyer et al. 1991), KBr(001) (Giessibl and Binnig 1992) were performed in contact mode. Atomic scale dislocation defects were observed on the (001) surface of mineral anhydrite analyzed in contact mode (Sokolov et al. 1999). Atomically resolved images of clinochlore, muscovite (Sokolov et al. 1997) and mineral astrophyllite (Sokolov and Henderson 2000) were obtained in the presence on electric double layers to decrease the tip load by compensating for the long-range attractive force.

The $(10\bar{1}4)$ cleavage plane of calcite (Fig. 4) has been over years a test bed for structural analysis by AFM. AFM measurements in contact mode were operated either in air (Stipp et al. 1994) or in liquid phase (Hillner et al. 1992a,b; Rachlin et al. 1992; Ohnesorge and Binnig 1993; Stipp et al. 1994; Liang et al. 1996). Most atomically resolved AFM images have revealed the zigzag rows attributed to the protruding oxygen atoms (Fig. 4)—although the lateral amplitude of the zigzag chain was seen to vary from 0.07 nm to 0.21 nm (Liang et al. 1996)—and have identified the rectangular surface unit cell (Rachlin et al. 1992; Ohnesorge and Binnig 1993; Stipp et al. 1994; Liang et al. 1996). A contrast in intensity between oxygen rows such that every second carbon row appears brighter was described as "paired rows" (Stipp et al. 1994). A modulation along the [010] direction results in a (2×1) structure (Stipp et

EBSCOhost - printed on 2/13/2023 5:26 AM via . All use subject to https://www.ebsco.com/terms-of-use

al. 1994) first seen by LEED (Stipp and Hochella 1991). It was suggested to be due to twisting of some surface carbonate groups after cleavage (Stipp et al. 1994).

Atomic resolution in attractive regime. When approaching a surface, the tip jumps toward the surface when the force gradient of the interaction potential between tip and substrate V_{ts} exceeds that of the spring, which corresponds to the fulfillment of the following condition between the second derivatives of the potential energies (Burnham and Colton 1989; Giessibl 1997; Garcia and Perez 2002):

$$\max\left|\frac{d^2V_{ts}}{dz^2}\right| > k \tag{12}$$

where V_{ts} is the tip-sample attractive force interaction potential and k is the cantilever stiffness. The jump-to-contact corresponds to a switch between attractive and repulsive regime. Attempts were made to reduce the load in the repulsive regime (Sokolov et al. 1997, 1999; Sokolov and Henderson 2000, 2002). Atomic resolution could also be achieved by compensating for long-range attractive forces by long-range forces due to an electrical double layer (Sokolov et al. 1997; Sokolov and Henderson 2000). The tip was even operated in attractive regime (Giessibl and Binnig 1992). Indeed, atomically resolved images of KBr (001) surfaces were recorded without damaging the surface using AFM operated in attractive regime with tip-substrate forces of ≈−1 nN , and differences in contrast (Fig. 16) were assigned to the two kinds of ions (Giessibl and Binnig 1992).

The limit of the tip-surface interaction in contact mode has been explored by Ohnesorge and Binnig (1993). They analyzed the cleaved surface $(10\bar{1}4)$ of calcite by AFM in water to avoid the occurrence of capillary forces (Drake et al. 1989) and to screen the van der Waals forces. The AFM was operated in the so-called variable-deflection mode in which the deflection is directly recorded as the signal data since no feedback is applied. The elimination of the jump-to-contact (Weisenhorn et al. 1989) evidenced by the absence of hysteresis in the approach and retract curves allowed the collection of images at any tip height. Since the maximum attractive force (4.5×10^{-11} N) was of the order of magnitude of the van der Waals attraction between two single atoms at equilibrium distance, the AFM image was suggested to correspond to individual surface atoms probed by single tip atoms. Reproducible zigzag arrays were assigned to the protruding surface oxygen atoms and surface calcium ions were identified. Upon further approach of the surface, the tip front atom entered the repulsive regime while secondary microtips imaged the surface in a similar way as the primary tip at the onset of the tip approach. At the end of the tip approach, in the repulsive regime, distorted structures were attributed to elastic deformations (Ohnesorge and Binning 1993).

Surface structures analyzed by AFM in dynamic mode

Structural analysis in nc-AFM mode has developed because the atom-site dependent contribution to the AFM signal is enhanced by measuring the gradient of the interaction force instead of the force itself (Giessibl 1994, 1995). Moreover, noncontact AFM is nondestructive since the tip-substrate interaction is restricted to attractive forces. Since the mid 1990's, nc-AFM has become pivotal for structural study of insulator surfaces in the laboratory (Giessibl 1994, 1995; Barth and Reichling 1999).

Atomic resolution by nc-AFM in vacuum. Atomically resolved images were collected in vacuum by nc-AFM on many mineral surfaces, including rutile (Fukui et al. 1997a,b; Rahe et al. 2008), fluorite (Reichling and Barth 1999), reconstructed α-$Al_2O_3(0001)$ (Barth and Reichling 2001), magnesium oxide (Barth and Henry 2003), cerium oxide (Namai et al. 2003), Mica (Rahe et al. 2008), calcite (Schütte et al. 2010), and antigorite (Palacios-Lidon et al. 2010). Strong progress has been made in theoretical modeling. The combination of numerical simulations with experiments provides information on the tip-surface system and allows study

EBSCOhost - printed on 2/13/2023 5:26 AM via . All use subject to https://www.ebsco.com/terms-of-use

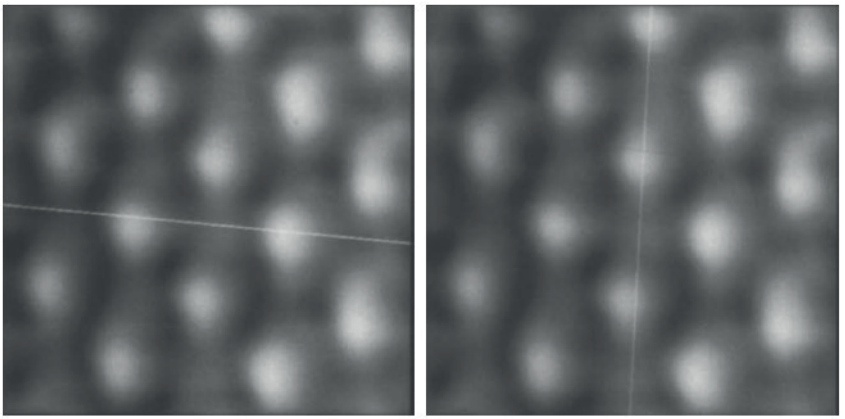


Figure 16. Analysis in attractive regime of the KBr(001) surface using AFM operated in static mode (Giessibl and Binnig 1992). 1.3×1.3 nm^2 AFM images. Differences in contrast along both [100] and [010] cuts were assigned to the two kinds of ions. [Used by permission of Elsevier, from Giessibl and Binnig (1992), *Ultramicroscopy* 42-44, Fig. 5, p. 286.]

of surface structure and properties with atomic resolution (Shluger et al. 1999; Garcia and Perez 2002; Hofer et al. 2003; Barth et al. 2011).

The structure of the $(10\bar{1}4)$ cleavage plane of calcite (Fig. 4) has been studied using nc-AFM in vacuum (Schütte et al. 2010) and in water (Rode et al. 2009). Analyses performed in water are discussed in the next paragraph. AFM in ultra-high vacuum was operated in almost constant height mode in which contrast arises from frequency shift. Cleaved crystals were annealed to 480 K for 1 h to remove surface charges. The n-doped silicon cantilevers were sputtered by argon ions at 2 keV for 5 min to remove contaminants. Atomic-scale defects on AFM images demonstrated the atomic imaging of the $(10\bar{1}4)$ calcite surface (Fig. 17). The deviation of the zigzag chain along the $[\bar{4}21]$ direction (Rachlin et al. 1992; Ohnesorge and Binnig 1993; Stipp et al. 1994; Liang et al. 1996) and the row pairing (Stipp et al. 1994) were observed (Fig. 17a). The formation of the (2×1) structure (Stipp et al. 1994) was confirmed (Fig. 17b,c). The observation performed in vacuum discards any foreign adsorbate as being at the origin of the structure, which appears instead as a true reconstruction of the calcite surface, in agreement with lattice energy minimization (Kristensen et al. 2004). However, the occurrence of the (2×1) reconstruction depends in a reproducible manner on the tip-sample distance. It is visible at large and small tip distance as a contrast modulation of the dark lines, but not observed at intermediate separations. This phenomenon and the dramatic changes in deviation of the zigzag chain and changes in contrast of the (2×1) reconstruction which accompany changes in tip apex (Fig. 17a,b) are suggested to explain the running controversies about the structure of the $(10\bar{1}4)$ cleavage plane of calcite.

Noncontact AFM in aqueous solution. In liquids, the very low quality factor of cantilever has long prevented the use of nc-AFM for atomically resolved analysis of surfaces. A few years ago, on the basis of detailed analyses of AFM noise (Fukuma et al. 2005a) and set-up (Fukuma et al. 2005b,c), nc-AFM could be operated in liquid to image surfaces at atomic resolution. The frequency noise in liquid is much larger than in vacuum due to the low Q factor of the cantilever resonance which results in a low force sensitivity and a low spatial resolution in nc-AFM. The optimal signal-to-noise ratio was achieved by using oscillation amplitudes of the order of atomic distances which, in addition, enhance the sensitivity to short-range forces. In vacuum environments, small-amplitude operation requires tips stiff enough to avoid tip

EBSCOhost - printed on 2/13/2023 5:26 AM via . All use subject to https://www.ebsco.com/terms-of-use

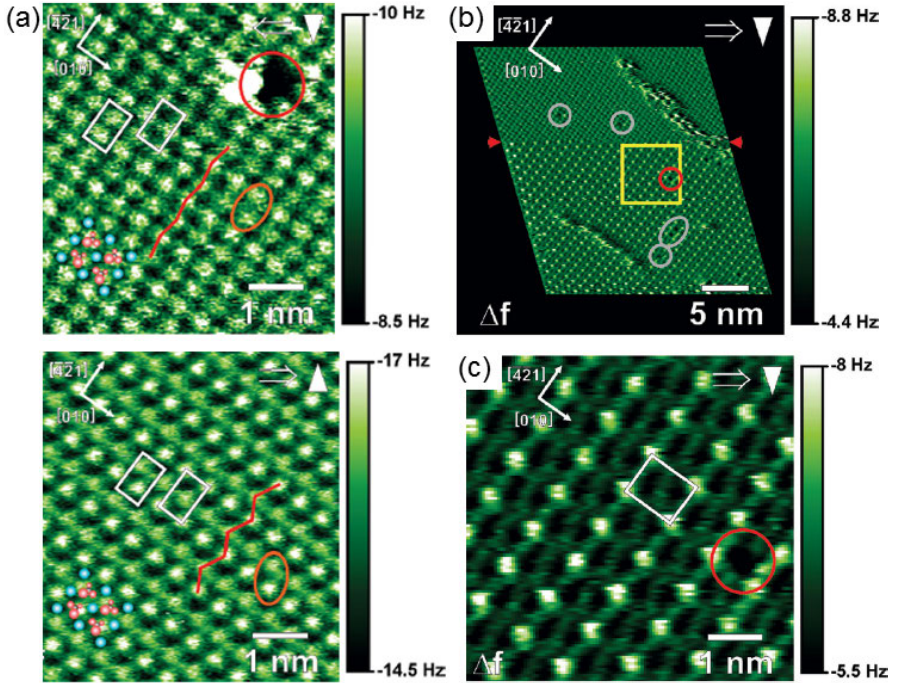


Figure 17. FM-AFM analysis of the $(10\bar{1}4)$ surface of calcite in vacuum at quasi-constant height (Schütte et al. 2010). Scanning directions are indicated on images by arrows in the upper right: (a) imaging at room temperature: differences in contrast in the zigzag chains observed along the $[\bar{4}21]$ direction were assigned to the so-called row-pairing (sites surrounded by ellipses). Rectangles correspond to unit cells. The change in deviation of the zigzag chain from top (0.1 nm) to bottom (0.2 nm) follows a change in tip since the two images have been collected on different days with different tip apex. On top right, an atomic-size defect demonstrates true atomic resolution imaging; (b) imaging at 110 K (downward image) the (2×1) reconstruction. A sudden change in contrast (shown by arrows) observed during the scan is assigned to a sudden change in tip apex; (c) zoom on the bottom of (b). [Used by permission of American Chemical Society, from Schütte et al. (2010), *Langmuir* 26, Figs. 2 and 4, pp. 8297 and 8299.]

adhesion, which partially reduces the benefit of sensitivity enhancement. In contrast, due to the reduced long range attractive interaction forces in liquid, small oscillation amplitudes do not lead to tip adhesion (Fukuma et al. 2005b,c). Moreover, great care was taken about the laser detection. The laser power was kept at a level such that the noise performance of the sensor was essentially limited to the photodiode shot noise to avoid unwanted contributions. The "optical interference noise" due to laser scattering, which is of particular importance in liquid cells, was reduced. The laser beam was collimated and focused to achieve a laser spot size close to the size of the cantilever. The reflectivity of the backside of the lever was improved with a metal coating. The noise performance was tested both in air (Fukuma et al. 2005a) and in liquid environments (Fukuma et al. 2005a,b). During the analysis of the cleaved muscovite mica in water by nc-AFM, it has been observed that, when images were recorded with atomic resolution, the tip- substrate distance was shorter than the distance between the surface and the first structured layer. This means that atomic resolution can only be achieved if the tip penetrates continuously the structured water layer (Fukuma et al. 2005a,b).

The perturbation of the analysis of the surface by both water-induced forces and structuring of the water layer was evidenced by a study of a mica surface in solution (Kimura et al. 2010).

EBSCOhost - printed on 2/13/2023 5:26 AM via . All use subject to https://www.ebsco.com/terms-of-use

Forces were mapped (Fig. 18a) by means of a nc-AFM set-up in a plane perpendicular to a cleaved muscovite mica surface in 1M KCl aqueous solution. Forces $F(z)$ were probed in the direction normal to the surface (z) in successive in-plane (x) positions so as to draw a two dimensional picture. The AFM was operated with low-noise deflection sensor and vibration amplitudes of 0.2 nm peak to peak. The hysteresis of the $F(z)$ curves allowed to check that the scanning velocity was low with respect to the relaxation time of water molecules. The water layers in the vicinity of the mica surface show a faint structure which reflects the periodicity of the hexagonal structure of the substrate (Fig. 18b). Different tip-substrate interactions have been observed at centers and borders of the hexagons of the surface lattice (Figs. 18c,d). Specific contrasts observed on some sites were attributed to solvated potassium ions (Figs. 18e,f). The exploration in three dimensions of the vicinity of the muscovite mica surface in water shows (i) the occurrence of structured water layers and (ii) the perturbation of the analysis of the solid surface by those structured layers.

The $(10\bar{1}4)$ cleavage plane of calcite was analyzed in Milli-Q water using a similar nc-AFM set-up (Rode et al. 2009). Gold-coated p-doped silicon tips were used. The cantilever oscillation amplitude was kept constant at a level of 0.2-2.0 nm. Images were obtained in constant height mode, with contrast arising from frequency shift. The observation of monoatomic surface defects and of steps was taken as an evidence for the achievement of atomic resolution. Images patterns with zigzag rows were assigned to the protruding oxygen atoms of the carbonate surface groups that defined unit cell dimensions of 0.5 nm in the [010] direction and 0.8 nm in the $[\bar{4}21]$ direction. In addition, pairs of two dots were attributed to the so-called row

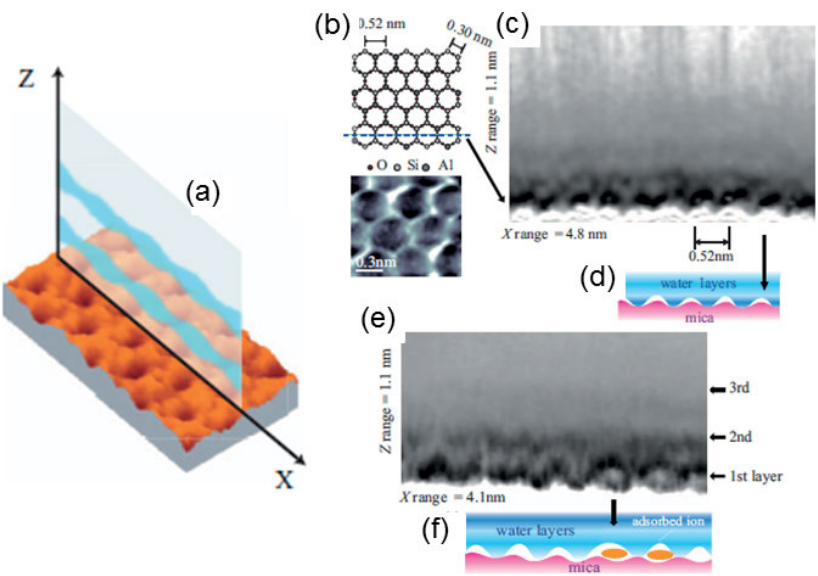


Figure 18. Two-dimensional force mapping by FM-AFM at the vicinity of a cleaved muscovite mica surface in water (Kimura et al. 2010): (a) schematic representation of the experiment. A two- dimensional (2D) mapping of the shift in frequency Δf was performed by measuring Δf along the vertical direction (z) at successive in-plane positions (x); (b) schematic representation and AFM image of the surface structure; (c) 2D mapping shows the layered structure of water at the vicinity of the surface as well as the in-plane structure which fits the periodicity of the substrate; (d) representation of (c); (e) other 2D mapping which shows, on some sites, repulsive forces that are attributed to solvated potassium ions; (f) schematic representation of (e). [Used by permission of American Institute of Physics, from Kimura et al. (2010), *J. Chem. Phys.* 132, Figs 1 and 2, p. 194705- 2 and 3.]

EBSCOhost - printed on 2/13/2023 5:26 AM via . All use subject to https://www.ebsco.com/terms-of-use

pairing. Rows of bright dots separated by more discrete rows were observed. The identification of calcium atoms (Rachlin et al. 1992) was confirmed. However, the (2×1) structure (Stipp et al. 1994; Schütte et al. 2010) was not clearly observed.

Chemical identity of surface atoms. The capability of nc-AFM to determine the chemical identity of the surface atoms was demonstrated in a series of publications on cleaved CaF_2(111) surfaces (Reichling and Barth 1999; Foster et al. 2001, 2002; Barth et al. 2001) (Fig. 19a). The distance control loop was operated at a small gain to achieve an effective constant height mode and to use the frequency detuning to reflect the tip-surface interaction. Tips were bought in contact with the calcium fluoride surface prior to imaging, likely to collect a small part of the sample to give the tip apex a defined ionic termination. This is quite a common method in nc-AFM (Hofer et al. 2003). A bias was applied to the tip to reduce the effect of residual charging due to cleavage. Reproducible experimental images with triangular features having their apex along <211> surface directions were obtained by scanning the CaF_2(111) surface (Fig. 19b) (Foster et al. 2001). A statistical examination of intensity profiles reveals a secondary peak the intensity of which is about half that of the main peak and located at a distance of 0.25 ± 0.05 nm (Fig. 19b).

Since the apex of the tip may generate a positive or negative electrostatic potential, theoretical simulations were performed by terminating the tip with a nanocube of MgO whith terminal ion of either Mg^{2+} or O^{2-} to produce either a positive or negative potential (Foster et al. 2001). The theoretical image obtained with a magnesium-terminated tip (Fig. 19c) nicely agrees with the experimental pattern (Fig. 19b). In simulation, maximum detuning corresponds to the most protruding F^- ions (labeled (2) in Fig. 19c) with an enhancement of the contrast due to a local outward displacement of these ions when the tip passes over the surface. The second F^- layer (labeled (3)) is also felt by the tip. In the intensity profile, it gives rise to a secondary maximum located at 0.22 nm from the main feature. The simulation shows that the Ca^{2+} ion corresponds to a dip in detuning (labeled (1)).The simulation predicts that the use of a tip terminated by an

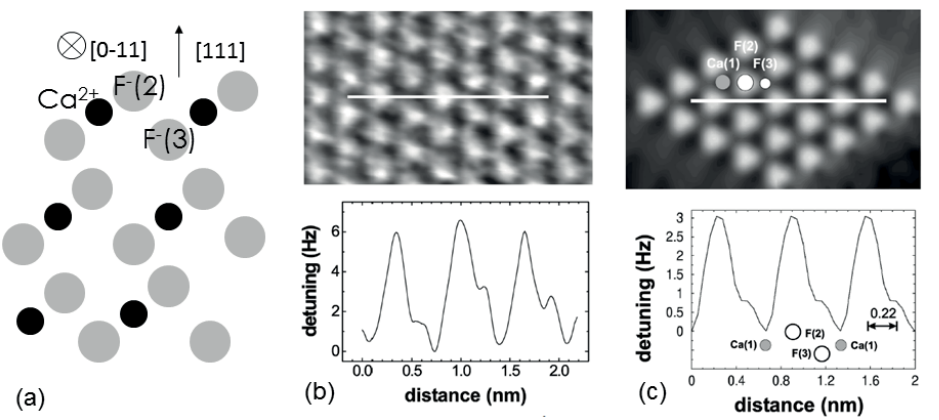


Figure 19. Chemical identity of the surface atoms of CaF_2(111) by FM-AFM (Foster et al. 2001): (a) schematic representation of the lattice of fluorite with (111) surface orientation (side view); (b) experimental image recorded at constant height. The intensity profile is given along the [121] direction indicated by the white line; (c) the numerical simulation with a tip apex terminated by Mg^{2+} gives rise to a positive potential (see text), in agreement with experimental findings of (b). A combination of protruding F^- (2) ions and F^- (3) ions from the second layer (see (a)) gives rise to bright triangles. The repulsive forces between Ca^{2+} and Mg^{2+} lead to dark patches. This means that the tip, which was prepared by contact with the fluorite surface was likely terminated by a calcium ion. [Reprinted Figs. 2 and 3 from Foster et al. (2001). Copyright (2001) by the American Physical Society.]

EBSCOhost - printed on 2/13/2023 5:26 AM via . All use subject to https://www.ebsco.com/terms-of-use

oxygen ion produces an image made of spots in the form of disks. Maximum detuning corresponds to the passage at the top of Ca^{2+} ions and a secondary maximum is expected between the two F^- ions. Such an image was actually recorded experimentally (Foster et al. 2002). The alternative occurrence of negative and positive potential at the tip apex likely depends on the contact on the fluorite surface.

Combined STM and AFM approaches. Insulating oxides have been much studied in the form of metal-supported films involving a few atomic layers to avoid charging and to benefit from the flexibility of scanning tunneling microscopy (STM) and spectroscopy (STS). Other incentives to develop thin films were (i) the control of surface defects and stoichiometry and (ii) the synthesis of new structures that do not exist in bulk materials (Nilius 2009).

However, nc-AFM and STM studies of bulk crystals can be combined in the case of some oxides, such as zinc oxide (Dulub et al. 2003), rutile (Onishi and Iwasawa 1994), hematite (Becker et al. 1996), and galena (Becker and Hochella 1996), that are conductive enough to allow STM analysis. Iwasawa and coworkers were first to stress the benefit that could be drawn from the combination of the essentially different STM (Onishi and Iwasawa 1994) and AFM (Fukui et al. 1997a) probes in a series of experiments on the TiO_2(110) rutile surface. The (110) face of the tetragonal D^{14}_{4h}-$P4_2/mnm$ rutile TiO_2 has a rectangular unit cell. The surface exhibits parallel rows of alternating five- and six-coordinated titanium atoms in the [001] direction. On the six-fold coordinated titanium, there are rows of bridging oxygen atoms that are protruding above the surface. The STM imaging at positive sample bias to probe unoccupied states exhibits alternating bright and dark rows running in the [001] direction. First-principle calculations demonstrated that bright rows corresponded to the five-fold coordinated surface Ti atoms, in agreement with the expectation that the tunneling current probes electronic states rather than surface geometry (Diebold et al. 1996). Titania surfaces are easily reduced via the creation of oxygen vacancies in the bridging oxygen row. On STM images, these appear as faint spots on the dark rows. Isolated hydroxyl groups that result from the dissociation of water molecules on oxygen vacancies give rise to brighter spots and double hydroxyl groups lead to even brighter features. By nc-AFM imaging of the TiO_2(110) surface, rows formally similar to those seen in STM are seen (Fukui et al. 1997a). However, it was shown that the contrast in nc-AFM was due to the sign of the charge on the tip apex (Lauritsen et al. 2006). By gentle contacts of the AFM tip on the TiO_2(110) surface, the image contrast could be reversed and switched from bright spots between bright rows to dark spots on bright rows (Fig. 20a,b). Increasing contrasts were observed for oxygen vacancies, single hydroxyl groups and double hydroxyl groups in this order (Fig. 20a,b). Numerical simulations of the tip-sample ensemble with a tip terminated by a MgO nanocube with either Mg^{2+} or O^{2-} termination, could mimic the experimental change in contrast (Fig. 20a,b) in a way comparable to the above described analysis of the alkali halide surface atoms.

Numerical simulation of nc-AFM images commonly use model of tips. Conversely, a quite elegant experiment has modeled tips by combining experiments and calculations. From an interplay between nc-AFM and STM data simultaneously recorded on TiO_2(110), and atomistic STM simulations based on multiple scattering theory, the state of the scanning tip was determined. The analysis of the AFM contrast reduced the number of tips to be considered in a full simulation and tips could be modeled. The technique may facilitate precise modeling and chemical identification of surface species (Enevoldsen et al. 2008).

CONCLUSIONS

Atomic force microscopy (AFM) is a very powerful technique for imaging mineral surfaces at sub-nanometer-scale resolution, regardless of the insulating character of the substrates, in any environment, vacuum, air and liquids. In AFM, the control parameter is the deflection

EBSCOhost - printed on 2/13/2023 5:26 AM via . All use subject to https://www.ebsco.com/terms-of-use

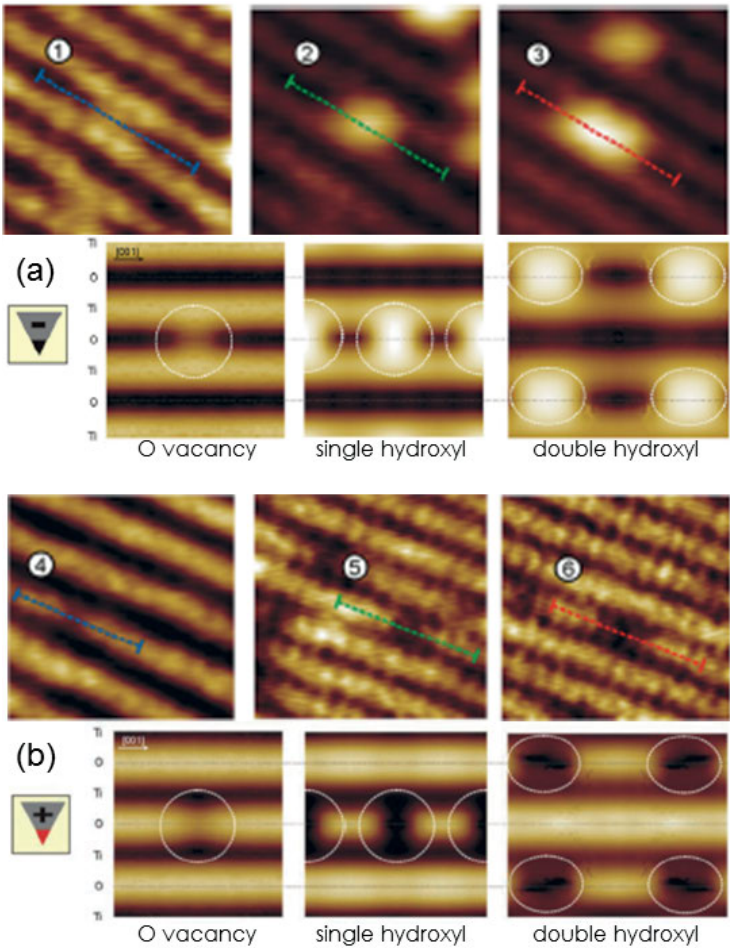


Figure 20. Noncontact AFM imaging and simulations of the rutile TiO_2(110) (Lauritsen et al. 2006). The tip was made positive or negative by contact with the substrate prior to sampling the structure (3×3 nm^2 images): (a) experiment and simulation with a negative tip apex. The images are formally similar to STM images. The five-coordinated Ti are seen as bright rows and vacancies (1), single (2) and double OH (3) give rise to bright spots of increasing brightness (brightness means attractive tip- surface forces). Simulated images are shown below the experimental images; (b) Conversely, the protruding oxygen rows appear bright when probed by the positive apex. Vacancies (4), single OH (5), double OH (6) correspond to dark spots. Therefore, in this case, the contrast in nc-AFM is dominated by electrostatic forces instead of dispersion and short-range repulsive forces. Simulated images are below the experimental data. [Used by permission of IOP Publishing Ltd, from Lauritsen et al. (2006), *Nanotechnology* 17, Figs. 3 and 5, pp. 3439 and 3440.]

of the lever which results from the complex set of long-range and short-range forces exerted between tip and sample. Because macroscopic parts of the tip-surface ensemble are involved in long-range interactions, high-resolution AFM images are more difficult to record than STM (scanning tunneling microscopy) images.

Firstly operated in the so-called contact mode, including constant height mode and constant force mode, AFM was soon after its invention run in dynamic modes in which surfaces are probed by vibrating tips. Detection is based on either the Amplitude Modulation

EBSCOhost - printed on 2/13/2023 5:26 AM via . All use subject to https://www.ebsco.com/terms-of-use

(AM) technique or Frequency Modulation (FM) technique. In AM-AFM, low Q values lead to fast responses, which make the technique suitable for analysis in air and in liquid. The successful development of an AM mode in which the tip probes the surface in the repulsive regime at the lower turning point of each periodic excursion led to the "tapping-mode" (TM-AFM) which is often preferred to contact mode to avoid tip/sample degradation.

Scanning surfaces by a tip in contact mode may damage surfaces, modify dissolution rates and step velocities. For dissolution and growth, tips are commonly operated with forces ~ 10 nN. Nevertheless, any limit may be questioned. Tip-induced erosion has been observed below that limit and even in attractive mode. During AFM studies, it is suggested to check whether the observed phenomena are robust with respect to tests in more stringent conditions.

In the early 1990's, the flexibility of the AFM technique enabled a breakthrough with regard to the dissolution and growth of mineral surfaces in solution. Indeed, macroscopic approaches relying on the analysis of powders in solution hardly lead to a description of the specific sites of the surface which control reaction rates. *In situ* AFM study of surfaces allowed a completely new mechanistic approach to the processes occurring at the mineral-solution interface. Models could be based on the analysis of individual crystallographic orientations, advancing and receding steps, moving edges, and formation of etch pits. However, rates calculated from AFM observation of moving steps are systematically lower than those determined by conventional powder methods. Discrepancies partly rely on the actual definition of reactive areas and on transport in solution. They also question the existing models, in particular regarding the link between dissolution mechanisms and concentrations of dissolved components.

Acid-base interactions play a pivotal role in dissolution, growth, agglomeration, transport of matter in aqueous solutions and adhesion. Acid-base properties are expected to depend on the structure of surfaces since the ability of the surface sites to capture protons relies on coordination numbers. A test case is the determination of the PZC of alumina surfaces. Reproducible experiments show that PZC for α-alumina crystal surfaces are found at much lower pH values (~ 5-7) than alumina powders (~ 9). The observation does not depend on the technique that is used since values derived from optical methods agree with those determined by near field microscopy. Although care must be taken about a possible contamination of flat surfaces in ambient conditions, the most likely reason for this behavior is that the powder surface exhibits a higher proportion of low-coordinated sites than crystal surfaces.

Atomic force microscopy was used soon after its invention to analyze the structure of mineral surfaces with atomic resolution. More recently, imaging of structure, chemical contrast and charges has been performed in AM-AFM, often called noncontact (nc) AFM. First developed in vacuum, the technique is now operated in gas and liquids by decreasing the oscillation amplitude of the cantilever. A major strength of nc-AFM is its ability to distinguish the chemical specificity of surface atoms. This leads not only to the analysis of the chemical contrast by controlling the charge of the tip termination, but also, in combination with numerical simulations, to defined tip-surface ensembles. Surface charges can be analyzed by Kelvin probe force microscopy (KPFM) at nanometer-scale resolution. Combinations of topographic analysis with tunneling microscopy or Kelvin probe microscopy and numerical simulations also open up great prospects.

ACKNOWLEDGMENTS

I am grateful for helpful comments and suggestions on the manuscript by a referee and Grant Henderson.

EBSCOhost - printed on 2/13/2023 5:26 AM via . All use subject to https://www.ebsco.com/terms-of-use

REFERENCES

Abraham FF, Batra IP (1989) Theoretical interpretation of atomic-force-microscope images of graphite. Surf Sci 209:L125-L132

Abraham FF, Batra IP, Ciraci S (1988) Effect of tip profile on atomic-force microscope images: A model study. Phys Rev Lett 60:1314-1317

Acuna SM, Toledo PG (2011) Nanoscale repulsive forces between mica and silica surfaces in aqueous solutions. J Colloid Interface Sci 361:397-399

Albrecht TR, Grütter P, Horne D, Rugar D (1991) Frequency modulation detection using high-Q cantilevers for enhanced force microscope sensitivity. J Appl Phys 69:668-673

Arvidson RS, Ertan IE, Amonette JE, Lüttge A (2003) Variation in calcite dissolution rates: A fundamental problem? Geochim Cosmochim Acta 67:1623-1634

Arvidson RS, Collier M, Davis KJ, Vinson MD, Amonette JE, Lüttge A (2006) Magnesium inhibition of calcite dissolution kinetics. Geochim Cosmochim Acta 70:583-594

Barth C, Henry CR (2003) Atomic resolution imaging of the (001) surface of UHV cleaved MgO by dynamic scanning force microscopy. Phys Rev Lett 91:196102

Barth C, Henry CR (2007) Surface double layer on (001) surfaces of alkali halide crystals: a scanning force microscopy study. Phys Rev Lett 98:136804

Barth C, Henry CR (2008) Imaging Suzuki precipitates on NaCl:Mg^{2+}(001) by scanning force microscopy. Phys Rev Lett 100:096101

Barth C, Reichling M (2001) Imaging the atomic arrangements on the high-temperature reconstructed α-Al_2O_3(0001) surface. Nature 414:54-57

Barth C, Foster AL, Reichling M, Shluger AL (2001) Contrast formation in atomic resolution scanning force microscopy on CaF_2(111): experiment and theory. J Phys Condens Matter 13:2061-2079

Barth C, Foster AS, Henry CR Shluger AL (2011) Recent trends in surface characterization and chemistry with high-resolution scanning force methods. Adv Mater 2011:477-501

Becker U, Hochella MF Jr (1996) The calculation of STM images, STS spectra, and XPS peak shifts for galena: New tools for understanding mineral surface chemistry. Geochim Cosmochim Acta 60:2413-2426

Becker U, Hochella MF Jr, Apra E (1996) The electronic structure of hematite {00l} surfaces: Applications to the interpretation of STM images and heterogeneous surface reactions. Am Mineral 81:1301-1314

Bickmore BR, Hochella MF Jr, Bosbach D, Charlet L (1999) Methods for performing atomic force microscopy imaging of clay minerals in aqueous solutions. Clay Clay Miner 47:573-581

Bickmore BR, Bosbach D, Hochella MF Jr, Charlet L, Rufe E (2001) *In situ* atomic force microscopy study of hectorite and nontronite dissolution: Implications for phyllosilicate edge surface structure and dissolution mechanisms. Am Mineral 86:411-423

Bickmore BR, Nagy KL, Sandlin PE, Crater TS (2002) Quantifying surface areas of clays by atomic force microscopy. Am Mineral 87:780-783

Binnig G, Quate CF, Gerber C (1986) Atomic Force Microscope. Phys Rev Lett 56:930-933

Binnig G, Rohrer H, Gerber C, Weibel E (1982) Surface studies by scanning tunneling microscopy. Phys Rev Lett 49:57-61

Binnig G, Rohrer H, Gerber C, Weibel E (1983) 7 × 7 Reconstruction on Si(111) resolved in real space. Phys Rev Lett 50:120-123

Bokern DG, Ducker WAC, Hunter KA, McGrath KM (2002) Surface imaging of a natural mineral surface using scanning-probe microscopy. J Cryst Growth 246:139-149

Bosbach D, Charlet L, Bickmore B, Hochella MF Jr (2000) The dissolution of hectorite: *in situ*, real time observations using atomic force microscopy. Am Mineral 85:1209-1216

Bosbach D, Hall C, Putnis A (1998) Mineral precipitation and dissolution in aqueous solution:*in situ* microscopic observations on barite (001) with atomic force microscopy. Chem Geol 151:143-160

Bosbach D, Hochella MF Jr (1996) Gypsum growth in the presence of growth inhibitors: a scanning force microscopy study. Chem Geol 132:227-236

Bosbach D, Rammensee W (1994) *In situ* investigation of growth and dissolution on the (010) surface of gypsum by scanning force microscopy. Geochim Cosmochim Acta 58:843-849

Bose S, Hu X, Higgins SR (2008) Dissolution kinetics and topographic relaxation on celestite (001) surfaces: The effect of solution saturation state studied using atomic force microscopy. Geochim Cosmochim Acta 72:759-770

Brady PV, Cygan RT, Nagy KL (1996) Molecular controls on kaolinite surface charge. J Colloid Interface Sci 183:356-364

Brandt F, Bosbach D, Krawczyk-Bärsch E, Arnold T, Bernhard G (2003) Chlorite dissolution in the acid pH-range:A combined microscopic and macroscopic approach. Geochim Cosmochim Acta 67:1451-1461

Brown GE, Henrich VE, Casey WH, Clark DL, Eggleston C, Felmy A, Goodman DW, Gratzel M, Maciel G, McCarthy MI, Nealson KH, Sverjensky DA, Toney MF, Zachara JM (1999) Metal oxide surfaces and their interactions with aqueous solutions and microbial organisms. Chem Rev 99:77-174

EBSCOhost - printed on 2/13/2023 5:26 AM via . All use subject to https://www.ebsco.com/terms-of-use

Burnham NA, Colton RJ (1989) Measuring the nanomechanical properties and surface forces of materials using an atomic force microscope. J Vac Sci Technol A 7:2906-2913
Burton WK, Cabrera N, Frank FC (1951) The growth of crystals and the equilibrium structure of their surfaces. Philos T Roy Soc A 243:299-358
Butt HJ, Cappella B, Kappl M (2005) Force measurements with the atomic force microscope: Technique, interpretation and applications. Surf Sci Rep 59:1-152
Can MF, Çinar M, Benli B, Özdemir O, Çelik MS (2010) Determining the fiber size of nano structured sepiolite using atomic force microscopy (AFM). Appl Clay Sci 47:217-222
Colombani J (2008) Measurement of the pure dissolution rate constant of a mineral in water. Geochim Cosmochim Acta 72:5634-5640
Corma A (1995) Inorganic solid acids and their use in acid-catalyzed hydrocarbon reactions. Chem Rev 95:559-614
Couturier G, Boisgard R, Dietzel D, Aimé JP (2005) Damping and instability in noncontact atomic force microscopy:the contribution of the instrument. Nanotechnology 16:1346-1353
de Leeuw NH, Parker SC, Harding JH (1999) Molecular dynamics simulation of crystal dissolution from calcite steps. Phys Rev B 60:13792-13799
De Yoreo JJ, Zepeda-Ruiz LA, Friddle RW, Qiu SR, Wasylenki LE, Chernov AA, Gilmer GH, Dove PM (2009) Rethinking classical crystal growth models through molecular scale insights: consequences of kink-limited kinetics. Cryst Growth Design 9:5135-5144
Diebold U, Anderson JF, Ng K-O, Vanderbilt D (1996) Evidence for the tunneling site on transition-metal oxides: TiO_2(110). Phys Rev Lett 77:1322-1325
Dove PM, Hochella MF Jr (1993) Calcite precipitation mechanisms and inhibition by orthophosphate: *in situ* observations by scanning force microscopy. Geochim Cosmochim Acta 57:705-714
Dove PM, Platt FM (1996) Compatible real-time rates of mineral dissolution by atomic force microscopy (AFM). Chem Geol 127:331-338
Dove PM, Rimstidt DJ (1994) Silica–water interactions. Rev Mineral 29:259-308
Drake B, Prater CB, Weisenhorn AL, Gould SAC, Albrecht TR, Quate CF, Cannell DS, Hansma HG, Hansma PK (1989) Imaging crystals, polymers, and processes in water with the atomic force microscope. Science 243:1586-1589
Ducker WA, Senden TJ, Pashley RM (1991) Direct measurement of colloidal forces using an atomic force microscope. Nature 353:239-241
Duckworth OW, Martin ST (2004) Dissolution rates and pit morphologies of rhombohedral carbonate minerals. Am Mineral 89:554-563
Dulub O, Diebold U, Kresse G (2003) Novel stabilization mechanism on polar surfaces: ZnO(0001)-Zn. Phys Rev Lett 90:016102
Enevoldsen GH, Pinto HP, Foster AS, Jensen MCR, Kühnle A, Reichling M, Hofer WA, Lauritsen JV, Besenbacher F (2008) Detailed scanning probe microscopy tip models determined from simultaneous atom-resolved AFM and STM studies of the TiO_2(110) surface. Phys Rev B 78:045416
Fa KQ, Nguyen AV, Miller JD (2005) Hydrophobic attraction as revealed by AFM force measurements and molecular dynamics simulation. J Phys Chem B 109:13112-13118
Fan C, Teng HH (2007) Surface behavior of gypsum during dissolution. Chem Geol 245:242-253
Fitts JP, Shang XM, Flynn GW, Heinz TF, Eisenthal KB (2005) Electrostatic surface charge at aqueous/α-Al_2O_3 single-crystal interfaces as probed by optical second-harmonic generation. J Phys Chem B 109:7981-7986
Foster AS, Barth C, Shluger AL, Reichling M (2001) Unambiguous interpretation of atomically resolved force microscopy images of an insulator. Phys Rev Lett 86:2373-2376
Foster AS, Barth C, Shluger AL, Nieminen RM, Reichling M (2002) Role of tip structure and surface relaxation in atomic resolution dynamic force microscopy:CaF_2(111) as a reference surface. Phys Rev B 66:235417
Foster AS, Barth C, Henry CR (2009) Chemical identification of ions in doped NaCl by scanning force microscopy. Phys Rev Lett 102:256103
Fowkes FM (1990) Quantitative characterization of the acid-base properties of solvents, polymers, and inorganic surfaces. J Adhes Sci Technol 4:669-691
Franks GV, Gan Y (2007) Charging behavior at the alumina-water interface and implications for ceramic processing. J Am Ceram Soc 90:3373-3388
Franks GV, Meagher L (2003) The isoelectric points of sapphire crystals and alpha-alumina powder. Colloid Surf A 214:99-110
Fu Q, Wagner T (2007) Interaction of nanostructured metal overlayers with oxide surfaces. Surf Sci Rep 62:431-498
Fukui K, Onishi H, Iwasawa Y (1997a) Atom-resolved image of the TiO_2(110) surface by noncontact atomic force microscopy. Phys Rev Lett 79:4202-4205

EBSCOhost - printed on 2/13/2023 5:26 AM via . All use subject to https://www.ebsco.com/terms-of-use

Fukui K, Onishi H, Iwasawa Y (1997b) Imaging of individual formate ions adsorbed on TiO_2(110) surface by noncontact atomic force microscopy. Chem Phys Lett 280:296-301
Fukuma T, Kimura M, Kobayashi K, Matsushige K, Yamada H (2005a) Development of low noise cantilever deflection sensor for multienvironment frequency-modulation atomic force microscopy. Rev Sci Instrum 76:053704
Fukuma T, Kobayashi K, Matsushige K, Yamada H (2005b) True atomic resolution in liquid by frequency-modulation atomic force microscopy. Appl Phys Lett 87:34101
Fukuma T, Kobayashi K, Matsushige K, Yamada H (2005c) True molecular resolution in liquid by frequency-modulation atomic force microscopy. Appl Phys Lett 86:193108
Gaboriaud F, Ehrhardt J (2003) Effects of different crystal faces on the surface charge of colloidal goethite (α-FeOOH) particles: An experimental and modeling study. Geochim Cosmochim Acta 67:967–983
Garcia R, Perez R (2002) Dynamic atomic force microscopy methods. Surf Sci Rep 47:197-301
Geysermans P, Finocchi F, Goniakowski J, Hacquart R, Jupille J (2009) Combination of (100), (110) and (111) facets in MgO crystals shapes from dry to wet environment. Phys Chem Chem Phys 11:2228-2233
Giessibl FJ (1994) Atomic force microscopy in ultrahigh vacuum. Jpn J Appl Phys 33:3726-3734
Giessibl FJ (1995) Atomic resolution of the silicon (111)-(7x7) surface by atomic force microscopy. Science 267:68-71
Giessibl FJ (1997) Forces and frequency shifts in atomic-resolution dynamic-force microscopy. Phys Rev B 56:16010-16015
Giessibl FJ (2003) Advances in atomic force microscopy. Rev Mod Phys 75:949-983
Giessibl FJ, Binnig G (1992) Investigation of the (001) cleavage plane of potassium bromide with an atomic force microscope at 4.2 K in ultra-high vacuum. Ultramicroscopy 42-44:281-289
Giessibl FJ, Hembacher S, Bielefeldt H, Mannhart J (2000) Subatomic features on the silicon (111)-(7 x 7) surface observed by atomic force microscopy. Science 289:422-425
Giessibl FJ, Hembacher, Herz M, Schiller Ch, J Mannhart J (2004) Stability considerations and implementation of cantilevers allowing dynamic force microscopy with optimal resolution:the qPlus sensor C. Nanotechnology 15:S79-S86
Giessibl FJ, Pielmeier F, Eguchi T, An T, Hasegawa Y (2011) Comparison of force sensors for atomic force microscopy based on quartz tuning forks and length-extensional resonators. Phys Rev B 84:125409
Glatzel T, Sadewasser S, Lux-Steiner MC (2003) Amplitude or frequency modulation-detection in Kelvin probe force microscopy. Appl Surf Sci 210:84-89
Glatzel T, Zimmerli L, Koch S, Such B, Kawai S, Meyer E (2009) Determination of effective tip geometries in Kelvin probe force microscopy on thin insulating films on metals. Nanotechnology 20:264016
Goniakowski J, Noguera C (1995) Theoretical investigation of hydroxylated oxide surfaces. Surf Sci 330:337-349
Gratz AJ, Bird P, Quiro GB (1990) Dissolution of quartz in aqueous basic solution, 106-236°C: surface kinetics of "perfect" crystallographic faces. Geochim Cosmochim Acta 54:2911-2922
Gratz AJ, Manne S, Hansma PK (1991) Atomic force microscopy of atomic-scale ledges and etch pits formed during dissolution of quartz. Science 251:1343-1346
Gratz AJ, Hillner PL, Hansma PK (1993) Step dynamics and spiral growth on calcite. Geochim Cosmochim Acta 57:491-495
Hacquart R, Jupille J (2007) Hydrated MgO smoke crystals from cubes to octahedra. Chem Phys Lett 439:91-94
Hacquart R, Jupille J (2009) Morphology of MgO smoke crystallites upon etching in wet environment. J Cryst Growth 311:4598–4604
Hansma PK, Cleveland JP, Radmacher M, Walters DA, Hillner PE, Benzanilla M, Fritz M, Vie D, Hansma HG, Prater CB, Massie J, Fukunaga L, Gurley J, Elings V (1994) Tapping mode atomic force microscopy in liquids. Appl Phys Lett 64:1738-1740
Hay MB, Workman RK, Manne S (2003) Mechanisms of metal ion sorption on calcite: composition mapping by lateral force microscopy. Langmuir 19:3727-3740
Higgins SR, Eggleston CM, Knauss KG, Boro CO (1998) A hydrothermal atomic force microscope for imaging in aqueous solution up to 150 °C. Rev Sci Instrum 69:2994-2998
Higgins SR, Hu X (2006) Near molecular-scale growth of natural minerals: Experimental methods and errors in length-dependent step speeds with scanning probe microscopy. J Electron Spectrosc 150:235-247
Hillner PE, Gratz AJ, Manne S, Hansma PK (1992a) Atomic-scale imaging of calcite growth and dissolution in real-time. Geology 20:359-362
Hillner PE, Manne S, Gratz AJ, Hansma PK (1992b) AFM images of dissolution and growth on a calcite crystal. Ultramicroscopy 42-44:1387-1393
Hillner PE, Manne S, Hansma PK, Gratz AJ (1993) Atomic force microscope: a new tool for imaging crystal growth processes. Faraday Discuss 95:191-197
Hofer WA, Foster AS, Shluger AL (2003) Theories of scanning probe microscopes at the atomic scale. Rev Mod Phys 75:1287-1331

EBSCOhost - printed on 2/13/2023 5:26 AM via . All use subject to https://www.ebsco.com/terms-of-use

Hudlet S, Saint Jean M, Roulet B, Berger J, Guthmann C (1995) Electrostatic forces between metallic tip and semiconductor surfaces. J Appl Phys 77:3308-3314
Israelachvili JN (1991) Intermolecular and Surface Forces. 2nd edition. Academic Press, London
Israelachvili JN, Pashley RM (1983) Molecular layering of water at surfaces and origin of repulsive hydration forces. Nature 306:249-250
Jacobs HO, Leuchtmann P, Homan OJ, Stemmer A (1998) Resolution and contrast in Kelvin probe force microscopy. J Appl Phys 84:1168-1173
Jolivet JP (2000) Metal Oxide Chemistry and Synthesis. John Wiley & Sons, New York.
Jordan G, Higgins SR, Eggleston CM (1999) Dissolution of the periclase (001) surface: A scanning force microscope study. Am Mineral 84:144-151
Jordan G, Rammensee W (1996) Dissolution rates and activation energy for dissolution of brucite (001): A new method based on the microtopography of crystal surfaces. Geochim Cosmochim Acta 60:5055-5062
Kikukawa A, Hosaka S, Imura R (1995) Silicon pn junction imaging and characterizations using sensitivity enhanced Kelvin probe force microscopy. Appl Phys Lett 66:3510-3512
Kimura K, Ido S, Oyabu N, Kobayashi K, Hirata Y, Imai T, Yamada H (2010) Visualizing water molecule distribution by atomic force microscopy. J Chem Phys 132:194705
Kitamura S, Iwatsuki M (1998) High-resolution imaging of contact potential difference with ultrahigh vacuum noncontact atomic force microscope. Appl Phys Lett 72:3154-3156
Köhler SJ, Bosbach D, Oelker EH (2005) Do clay mineral dissolution rates reach steady state? Geochim Cosmochim Acta 69:1997–2006
Kopta S, Salmeron M (2000) The atomic scale origin of wear on mica and its contribution to friction. J Chem Phys 113:8249-8251
Kosoglu LM, Bickmore BR, Filz GM, Madden AS (2010) Atomic force microscopy method for measuring smectite coefficients of friction. Clay Clay Miner 58:813-820
Kossel W (1927) Extending the law of Bravais. Nachr Ges Wiss Göttingen 135-143
Kristensen R, Stipp SLS, Refson K (2004) Modeling steps and kinks on the surface of calcite. J Chem Phys 121:8511-8523
Kurganskaya I, Arvidson RS, Fischer C, Lüttge A (2012) Does the stepwave model predict mica dissolution kinetics? Geochim Cosmochim Acta 97:120-130
Kuwahara Y (2006) *In situ* AFM study of smectite dissolution under alkaline conditions at room temperature. Am Mineral 91:1142-1149
Kuwahara Y (2008) *In situ* observations of muscovite dissolution under alkaline conditions at 25-50 degrees C by AFM with an air/fluid heater system. Am Mineral 93:1028-1033
Kuwahara Y (2011) *In situ* atomic force microscopy study of dissolution of the barite (001) surface in water at 30 degrees C. Geochim Cosmochim Acta 75:41-51
Land TA, DeYoreo JJ, Lee JD (1997) An *in situ* AFM investigation of canavalin crystallization kinetics. Surf Sci 384:136-155
Larsen K, Bechgaard K, Stipp SLS (2010) The effect of the Ca^{2+} to CO_3^{2-} activity ratio on spiral growth at the calcite $\{10\bar{1}4\}$ surface. Geochim Cosmochim Acta 74:2099-2109
Larson I, Drummond CJ, Chan DCY, Grieser F (1997) Direct force measurements between silica and alumina. Langmuir 13:2109-2112
Lasaga AC, Lüttge A (2001) Variation of crystal dissolution rate based on a dissolution stepwave model. Science 291:2400-2404
Lauritsen JV, Foster AS, Olesen GH, Christensen MC, Kühnle A, Helveg S, Rostrup-Nielsen JR, Clausen BS, Reichling M, Besenbacher F (2006) Chemical identification of point defects and adsorbates on a metal oxide surface by atomic force microscopy. Nanotechnology 17:3436-3441
Lauritsen JV, Reichling M (2010) Atomic resolution noncontact atomic force microscopy of clean metal oxide surfaces. J Phys Condens Matter 22:263001
Liang Y, Lea AS, Baer DR, Engelhard MH (1996) Structure of the cleaved $CaCO_3$ $(10\bar{1}4)$ surface in an aqueous environment. Surf Sci 351:172-182
Lin XY, Creuzet F, Arribart H (1993) Atomic-force microscopy for local characterization of surface acid-base properties. J Phys Chem 97:7272-7276
Lindgreen H, Garnæs J, Hansen PL, Besenbacher F, Lægsgaard E, Stensgaard I, Gould SAC, Hansma PK (1991) Ultrafine particles of North Sea illite/smectite clay minerals investigated by STM and AFM. Am Mineral 76:1218-1222
Livshits AI, Shluger AL, Rohl AL, Foster AS (1999) Model of noncontact scanning force microscopy on ionic surfaces. Phys Rev B 59:2436-2448
Loppacher C, Bammerlin M, Guggisberg M, Battiston F, Bennewitz R, Rast S, Baratoff A, Meyer E, Güntherodt HJ (1999) Phase variation experiments in noncontact dynamic force microscopy using phase locked loop techniques. Appl Surf Sci 140:287–292
Loppacher C, Zerweck U, Eng LM (2004) Kelvin probe force microscopy of alkali chloride thin films on Au(111). Nanotechnology 15:S9–S13

EBSCOhost - printed on 2/13/2023 5:26 AM via . All use subject to https://www.ebsco.com/terms-of-use

Lübbe J, Tröger L, Torbrügge S, Bechstein R, Richter C, Kühnle A, Reichling M (2010) Achieving high effective Q-factors in ultra-high vacuum dynamic force microscopy. Meas Sci Technol 21:125501
Lüttge A (2005) Etch pit coalescence, surface area, and overall mineral dissolution rates. Am Mineral 90:1776-1783
Lüttge A (2006) Crystal dissolution kinetics and Gibbs free energy. J Electron Spectrosc 150:248-259
Lüttge A, Conrad PG (2004) Direct observation of microbial inhibition of calcite dissolution. Appl Environ Microb 70:1627–1632
Lüttge A, Winkler U, Lasaga AC (2003) Interferometric study of the dolomite dissolution: A new conceptual model for mineral dissolution. Geochim Cosmochim Acta 67:1099-1116
Martin Y, Williams CC, Wickramasinghe HK (1987) Atomic force microscope–force mapping and profiling on a sub 100Å scale. J Appl Phys 61:4723-4729
Maurice PA (1996) Applications of atomic-force microscopy in environmental colloid and surface chemistry. Colloid Surface A 107:57-75
McEvoy AL, Stevens F, Langford SC, Dickinson JT (2006) Scanning-induced growth on single crystal calcite with an atomic force microscope. Langmuir 22:6931-6938
Meagher L, Maurdev G, Gee ML (2002) Interaction forces between a bare silica surface and an α- alumina surface bearing adsorbed polyelectrolyte and surfactant. Langmuir 18:2649-2657
Metz V, Raanan H, Pieper H, Bosbach D, Ganor J (2005) Towards the establishment of a reliable proxy for the reactive surface area of smectite. Geochim Cosmochim Acta 69:2581–2591
Meyer E, Heinzelmann H, Brodbeck D, Overney G, Overney R, Howald L, Hug H, Jung T, Hidber HA, Guntherodt HJ (1991) Atomic resolution on the surface of LiF(100) by atomic force microscopy. J Vac Sci Technol B 9:1329-1332
Meyer G, Amer NM (1988) Novel optical approach to atomic force microscopy. Appl Phys Lett 53:1045-1047
Meyer G, Amer NM (1990) Optical-beam-deflection atomic force microscopy: The NaCl(001) surface. Appl Phys Lett 56:2100-2101
Morse JW, Arvidson RS (2002) The dissolution kinetics of major sedimentary carbonate minerals. Earth-Sci Rev 58:51-84
Morse JW, Arvidson RS, Lüttge A (2007) Calcium carbonate formation and dissolution. Chem Rev 107:342-341
Nakahara S, Langford SC, Dickinson JT (1995) Surface force microscope observations of corrosive tribological wear on single crystal $NaNO_3$ exposed to moist air. Tribol Lett 1:277-300
Namai Y, Fukui KI, Iwasawa Y (2003) Atom-resolved noncontact atomic force microscopic and scanning tunneling microscopic observations of the structure and dynamic behavior of CeO_2(111) surfaces. Catal Today 85:79–91
Nilius N (2009) Properties of oxide thin films and their adsorption behavior studied by scanning tunneling microscopy and conductance spectroscopy. Surf Sci Rep 64:595-659
Nonnenmacher M, O'Boyle MP, Wickramasinghe HK (1991) Kelvin probe force microscopy. Appl Phys Lett 58:2921-2923
Ohnesorge F, Binnig G (1993) True atomic resolution by atomic force microscopy through repulsive and attractive forces. Science 260:1451-1456
Onishi H, Iwasawa Y (1994) STM-imaging of formate intermediates adsorbed on a TiO_2(110) surface. Chem Phys Lett 226:111-114
Ostendorf F, Torbrügge S, Reichling M (2008) Atomic scale evidence for faceting stabilization of a polar oxide surface. Phys Rev B 77:041405
Pachon-Rodriguez EA, Piednoir A, Colombani J (2011) Pressure solution at the molecular scale. Phys Rev Lett 107:146102
Palacios-Lidon E, Grauby O, Henry C, Astier JP, Barth C, Baronnet A (2010) TEM-assisted dynamic scanning force microscope imaging of (001) antigorite: Surfaces and steps on a modulated silicate. Am Mineral 95:673-685
Park NS, Kim MW, Langford SC, Dickinson JT (1996) Tribological enhancement of $CaCO_3$ dissolution during scanning force microscopy. Langmuir 12:4599-4604
Parks GA (1965) The isoelectric points of solid oxides, solid hydroxides, and aqueous complex systems. Chem Rev 65:177-198
Rachlin AL, Henderson GS, Goh MC (1992) An atomic force microscope (AFM) study of the calcite cleavage plane: Image averaging in Fourier space. Am Mineral 77:904-910
Rahe P, Bechstein R, Schütte J, Ostendorf F, Kühnle A (2008) Repulsive interaction and contrast inversion in noncontact atomic force microscopy imaging of adsorbates. Phys Rev B 77:195410
Reichling M, Barth C (1999) Scanning force imaging of atomic size defects on the CaF_2(111) Surface. Phys Rev Lett 83:768-771
Risthaus P, Bosbach D, Becker U, Putnis A (2001) Barite scale formation and dissolution at high ionic strength studied with atomic force microscopy. Colloid Surface A 191:201–214

EBSCOhost - printed on 2/13/2023 5:26 AM via . All use subject to https://www.ebsco.com/terms-of-use

Rode S, Oyabu N, Kobayashi K, Yamada H, Kühnle A (2009) True atomic-resolution imaging of $(10\bar{1}4)$ calcite in aqueous solution by frequency modulation atomic force microscopy. Langmuir 25:2850-2853
Ruiz-Agudo E, Kowacz M, Putnis CV, Putnis A (2010) The role of background electrolytes on the kinetics and mechanism of calcite dissolution. Geochim Cosmochim Acta 74:1256-1267
Ruiz-Agudo E, Putnis CV (2012) Direct observations of mineral-fluid reactions using atomic force microscopy:the specific example of calcite. Mineral Mag 76:227-253
Sadewasser S, Lux-Steiner MC (2003) Correct height measurement in noncontact atomic force microscopy. Phys Rev Lett 91:266101
Schütte J, Rahe P, Tröger L, Rode S, Bechstein R, Reichling M, Kühnle A (2010) Clear signature of the (2×1) reconstruction of calcite $(10\bar{1}4)$. Langmuir 26:8295-8300
Shiraki R, Rock PA, Casey WH (2000) Dissolution kinetics of calcite in 0.1 m NaCl solution at room temperature:An atomic force microscopic (AFM) study. Aquat Geochem 6:87-108
Shluger AL, Livshits AI, Foster AS, Catlow CRA (1999) Models of image contrast in scanning force microscopy on insulators. J Phys Condens Matter 11:R295–R322
Sokolov IY, Henderson GS (2000) Atomic resolution imaging using the electric double layer technique: friction vs. height contrast mechanisms. Appl Surf Sci 157:302–307
Sokolov IY, Henderson GS (2002) Simulation of the observability of atomic defects by atomic force microscopy in contact and noncontact modes. Surf Sci 499:135–140
Sokolov IY, Henderson GS, Wicks FJ (1999) Theoretical and experimental evidence for ''true'' atomic resolution under non-vacuum conditions. J Appl Phys 86:5537-5540
Sokolov IY, Henderson GS, Wicks FJ, Ozin GA (1997) Improved atomic force microscopy resolution using an electric double layer. Appl Phys Lett 70:844-846
Sposito G (1998) On points of zero charge. Environ Sci Technol 32:2815-2819
Stack AG, Higgins SR, Eggleston CM (2001) Point of zero charge of a corundum-water interface probed with optical Second Harmonic Generation (SHG) and Atomic Force Microscopy (AFM): New approaches to oxide surface charge. Geochim Cosmochim Acta 65:3055-3063
Stipp SL, Hochella MF Jr (1991) Structure and bonding environments at the calcite surface as observed with X-ray photoelectron spectroscopy (XPS) and low energy electron diffraction (LEED). Geochim Cosmochim Acta 55:1723-1736
Stipp SLS, Eggleston CM, Nielsen BS (1994) Calcite surface structure observed at microtopographic and molecular scales with atomic force microscopy (AFM). Geochim Cosmochim Acta 58:3023-3033
Stipp SLS, Gutmannsbauer W, Lehmann T (1996) The dynamic nature of calcite surfaces in air. Am Mineral 81:1-8
Sturm JM, Zinine AI, Wormeester H, Poelsema B, Bankras RG, Holleman J, Schmitz J (2005) Imaging of oxide charges and contact potential difference fluctuations in atomic layer deposited Al_2O_3 on Si. J Appl Phys 97:063709
Sung J, Zhang L, Tian C, Shen YR, Waychunas GA (2011) Effect of pH on the water/α-Al_2O_3(1102) interface structure studied by sum-frequency vibrational spectroscopy. J Phys Chem C 115:13887-13893
Teng HH, Dove PM, De Yoreo JJ (2000) Kinetics of calcite growth: surface processes and relationships to macroscopic rate laws. Geochim Cosmochim Acta 64:2255-2266
Terris BD, Stern JE, Rugar D, Mamin HJ (1989) Contact electrification using force microscopy. Phys Rev Lett 63:2669-2672
Tersoff J, Hamann DR (1985) Theory of the scanning tunneling microscope. Phys Rev B 31:805-813
Toikka G, Hayes RA (1997) Direct measurement of colloidal forces between mica and silica in aqueous electrolyte. J Colloid Interf Sci 191:102-109
Torbrügge S, Luebbe J, Troeger L, Cranney M, Eguchi T, Hasegawa Y, Reichling M (2008) Improvement of a dynamic scanning force microscope for highest resolution imaging in ultrahigh vacuum. Rev Sci Instrum 79:083701
Tournassat C, Neaman A, Villiéras F, Bosbach D, Charlet L (2003) Nanomorphology of montmorillonite particles:Estimation of the clay edge sorption site density by low pressure gas adsorption and AFM observation. Am Mineral 88:1989-1995
Tulpar A, Henderson DB, Mao M, Caba B, Davis RM, Van Cott KE, Ducker WA (2005) Unnatural proteins for the control of surface forces. Langmuir 21:1497-1506
Veeramasuneni S, Yalamanchili MR, Miller JD (1996) Measurement of interaction forces between silica and α-alumina by atomic force microscopy. J Colloid Interf Sci 184:594-600
Weaver JMR, Abraham DW (1991) High resolution atomic force microscopy potentiometry. J Vac Sci Technol B 9:1559-1561
Weisenhorn AL, Hansma PK, Albrecht T, Quate CF (1989) Forces in atomic force microscopy in air and water. Appl Phys Lett 54:2651-2653
Wieland E, Stumm W (1992) Dissolution kinetics of kaolinite in acidic aqueous solutions at 25 °C Geochim Cosmochim Acta 56:3339-3355

EBSCOhost - printed on 2/13/2023 5:26 AM via . All use subject to https://www.ebsco.com/terms-of-use

Xu L, Lio A, Hu J, Ogletree DF, Salmeron M (1998) Wetting and Capillary Phenomena of Water on Mica. J Phys Chem B 102:540-548

Xu M, Hu X, Knauss KG, Higgins SR (2010) Dissolution kinetics of calcite at 50-70° C: An atomic force microscopic study under near-equilibrium conditions. Geochim Cosmochim Acta 74:4285-4297

Yacoot A, Koenders L (2008) Aspects of scanning force microscope probes and their effects on dimensional measurement. J Phys D Appl Phys 41:103001

Yan L, Masliyah JH, Xu Z (2013) Understanding suspension rheology of anisotropically-charged platy minerals from direct interaction force measurement using AFM. Curr Opin Colloid Interface Sci 18:149-156

Zbik M, Smart R (1998) Nanomorphology of kaolinites: comparative SEM and AFM studies. Clay Clay Miner 46:153-160

Zhang JW, Nancollas GH (1998) Kink density and rate of step movement during growth and dissolution of an AB crystal in a nonstoichiometric solution. J Colloid Interf Sci 200:131-145

Zhong Q, Innis D, Kjoller K, Elings VB (1993) Fractured polymer silica fiber surface studied by tapping mode atomic-force microscopy. Surf Sci 290:L688-L692

Zhou Z, Gunter W (1992) The nature of the surface charge of kaolinite. Clay Clay Miner 40:365-368

EBSCOhost - printed on 2/13/2023 5:26 AM via . All use subject to https://www.ebsco.com/terms-of-use

EBSCOhost - printed on 2/13/2023 5:26 AM via . All use subject to https://www.ebsco.com/terms-of-use

Reviews in Mineralogy & Geochemistry
Vol. 78 pp. 371-398, 2014
Copyright © Mineralogical Society of America

Optical Spectroscopy

George R. Rossman

Division of Geological and Planetary Sciences
California Institute of Technology
Pasadena, California 91125-2500, U.S.A.

grr@gps.caltech.edu

INTRODUCTION

Optical spectroscopy is concerned with the measurement of the absorption, reflection and emission of light in the near-ultraviolet (~250 nm) through the mid-infrared (~3000 nm) portions of the spectrum. The human interface to the geological and mineralogical world is primarily visual. Optical spectroscopy is, in particular, well suited to investigating the origin of color in minerals. The reflection spectroscopy of minerals has been motivated to a large extent by interest in remote sensing. Emission spectra are usually studied in reference to luminescence phenomena. Studies of mineral color, metal ion site occupancy, oxidation states and concentrations have generally been done with absorption spectroscopy. This chapter concentrates on single crystal absorption spectroscopy.

Absorption of light by crystals can occur for a number of reasons. For many minerals, the presence of ions of transition elements (e.g., Ti, V, Cr, Mn, Fe, Co, Ni, Cu) in their various oxidation states is the cause of light absorption. In some minerals, the individual ions cause the light absorption while in others it is the interaction between ions such as between Fe^{2+} and Fe^{3+} that causes color. In some minerals, rare-earth elements are an important source of color. Some minerals are colored by small molecular units involving metal ions (UO_2^{2+}, CrO_4^{2-}) or anions (S_3^- in sodalites). Many sulfide minerals such as cinnabar (HgS) and realgar (As_4S_4) owe their color to band gaps in the semiconducting sulfides. Other important sources of color in minerals are the products of radiation damage which can be metal ions that have changed oxidation states, electron vacancies (called “hole” centers), or unpaired electrons located on crystal defects or on ions that are not normally associated with unpaired electrons. All of these are commonly studied, in part, with optical spectroscopy.

Historically, the study of the spectroscopy of minerals began in the attempt to understand the origin of color in minerals. The color and beauty of minerals and gems has, for thousands of years, attracted people to the materials of the geologic world. Serious study of mineral spectra together with interpretation of those spectra began in the mid 1900’s through the efforts of scientists such as Sof’ya Grum-Grzhimailo (Institute of Crystallography, Russia, who published from 1936 to 1972), Alexiei Platonov (National Academy of Sciences of Ukraine, who has published from 1964); and Roger Burns (MIT, who published from 1964 to 1995).

In principle, optical spectra can provide quantitative information about the concentration of common metal ions that are the chromophores (source of color) in crystals. In practice, improvements in methods for determining X-ray site occupancies, Mössbauer spectra, and other methods have generally surpassed optical spectroscopic methods for site occupancy determinations. Likewise, improved analytical methods such as LA-ICP-MS and improved electron microprobe analyses have proven easier to calibrate than optical spectroscopic methods. The primary advantage of the optical methods comes from the fact that the spectra

1529-6466/14/0078-0009$05.00 http://dx.doi.org/10.2138/rmg.2014.78.9

EBSCOhost - printed on 2/13/2023 5:26 AM via . All use subject to https://www.ebsco.com/terms-of-use

integrate the concentration of the metal ions from the entire volume of the crystal compared to what are generally near-surface analyses by most of the other quantitative methods. Nothing has surpassed optical spectra as a means of studying the origin of color in gems and minerals. Such studies are usually conducted together with quantitative analyses of the crystal.

GENERAL CONCEPTS

Numerous textbooks present discussions of the theories which govern electronic transitions. Ligand field theory and molecular orbital theory are commonly used to provide a theoretical underpinning to the light absorption of transition metal ions. Burns (1970) and Marfunin (1979), in particular, develop the theory with many mineralogical examples. Wildner et al. (2004) also present an extensive discussion of the theoretical underpinnings. A number of the important concepts were considered in the first edition of this volume (Rossman 1988) and are briefly outlined below.

Six types of processes generally contribute to the optical absorption spectra of minerals:

1) Electronic transitions involving electrons in the *d*-orbitals of ions of the first row transition elements such as Cr^{3+}, Mn^{3+}, Fe^{2+} and Fe^{3+}. These transitions involve rearrangement of the valence electrons, and give rise to absorption in the visible and near-infrared region. The spectra they produce are often called either crystal-field spectra or ligand-field spectra after the theories used to describe them. They are a major cause of color in many minerals and are, by far, the most studied.

2) Electronic transitions which involve displacement of charge density from one ion to another. These charge transfer processes are of two general types.

   The first typically involves charge transfer between an anion and a cation. The one most commonly encountered in mineral spectroscopy is the transfer of electron density from a filled oxygen orbital to a partially occupied Fe^{3+} orbital. These transitions usually require higher energies than crystal field transitions and produce absorption bands which are centered in the ultraviolet region. In the case of ions in higher oxidation states such as Fe^{3+} and Cr^{6+}, the wing of the absorption band will extend into the visible part of the spectrum, causing absorption which is strongest in the violet and extends towards the red. The yellow-brown color of some Fe^{3+} minerals is a result of this wing of absorption. There has been very little experimental work on this type of charge transfer in minerals due to the difficulty of preparing samples thin enough to keep these high intensity absorptions "on scale".

   The second type of charge transfer transition is intervalence charge transfer (IVCT), also called metal-metal charge transfer. It involves movement of electron density between metal ions in different oxidation states. The pairs or clusters of cations typically share edges or faces of coordination polyhedra. Relatively low concentrations of these pairs can produce appreciable absorption. The deep blue of sapphire is a familiar example of color caused by this type of transition. The Fe^{2+}-Fe^{3+} and Fe^{2+}-Ti^{4+} intervalence interactions are common. In some meteoritic minerals, the Ti^{3+}-Ti^{4+} interaction is also prominent.

3) Absorption edges result from electronic transitions between the top of a valence band and the bottom of the conduction band. Any photon with energy greater than this band gap will be absorbed. These types of absorption bands are usually encountered in sulfides. The red color of cinnabar is the result of a band gap which allows light with wavelength longer than 600 nm to pass while absorbing shorter wavelengths. The band-gap of most silicate minerals typically is located far into the ultraviolet region and, thus, generally does not contribute to the color of silicate minerals.

EBSCOhost - printed on 2/13/2023 5:26 AM via . All use subject to https://www.ebsco.com/terms-of-use

4) Overtones of vibrational transitions. The most commonly encountered bands in the near-infrared are the overtones of OH and H_2O groups. The spectrum of beryl contains both absorption from Fe^{2+} and from the vibrational modes of H_2O molecules. Vibrational overtones are readily recognized because they have much smaller widths than electronic transitions which can occur in the same spectral region. These transitions are both narrow and relatively low intensity, often located in the near-infrared portion of the spectrum. As such, they normally have little influence on the color of minerals. The blue color of thick layers of glacial ice is the result of absorption of light by these transitions.

5) Electronic transitions involving *f*-orbitals of uranium and the rare earth elements. These electronic transitions involve electrons in inner orbitals that are shielded from the coordination sphere of the central metal ion. Thus, absorption bands from the trivalent rare-earths tend to be much sharper than most of the bands from the third-row transition metals and tend to have only small shifts in wavelength with changes in the coordination number and geometry of the cation.

6) In many minerals, absorption of light is associated with electron-hole centers and molecular ions produced by ionizing radiation. The spectra of these centers can often be quite difficult to interpret. Smoky quartz, blue feldspar, green diamonds and blue calcite are examples of this process. Often, color in minerals arises from the combined action of *d*-orbital transitions from metal ions together with color centers from natural irradiation.

To better understand the first process involving electrons in the *d*-orbitals, we need to understand how the *d-d* transitions occur. We can first consider a transition metal ion floating freely in space with no other atoms nearby. In this case all five *d*-orbitals will have the same energy (Fig. 1a). If a conductive sphere of charge if brought around the metal ion, the orbitals will rise in energy because electrons in these orbitals experience more electrostatic repulsion (Fig. 1b). If the charge on the sphere is now separated into six discrete lumps of charge centered on the vertices of an octahedron, we have a situation resembling a metal ion in octahedral coordination. In this case, three of the orbitals "sneak" between the charge centers (the d_{xy}, d_{xz}, and d_{yz} orbitals) which effectively lowers their energy compared to the two orbitals which collide with the charge centers and experience greater repulsion (the $d_{x^2-y^2}$ and d_{z^2} orbitals). The energy separation between the lower three and upper two orbitals is commonly referred to by both the capital Greek letter "Δ", and the symbol "10dq".

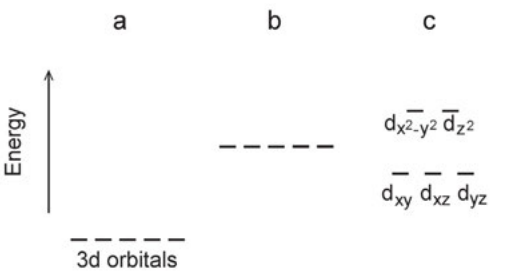


Figure 1. Diagrams illustrating the concept of orbitals splitting into groups of different energies when points of charge are located at the vertices of an octahedron.

When an electron that is located in a lower orbital encounters a photon of the appropriate energy, it can be promoted to a higher energy, empty orbital. When this occurs, light is absorbed, a *d-d* transition occurs, and, if the absorption process involves photons in the range of visible light, the mineral will have color. The absorbed energy is usually converted into heat and the crystal will become warmer by a tiny amount. Sometimes, much of the absorbed energy is dissipated through fluorescence.

Diagrams, known as Tanabe-Sugano diagrams, named after scientists who produced the first diagrams of their type (Tanabe and Sugano 1954a,b), help us to understand the origin of

EBSCOhost - printed on 2/13/2023 5:26 AM via . All use subject to https://www.ebsco.com/terms-of-use

the absorption bands in mineral systems that owe their color to the common metals of the third row transition elements (Ti, V, Cr, Mn, Fe, Co, Ni and Cu). Many books and web pages that deal with transition metal chemistry, coordination complexes and ligand field theory explain these diagrams and the theory behind them in greater detail.

The diagram in Figure 2 illustrates the energy states of Fe^{3+} in a situation where the ions (commonly oxide ions in minerals) bonded to the iron are arranged in perfect octahedral symmetry. The horizontal axis is related to the separation between the t_{2g} and the e_g orbitals normalized by a parameter "B", one of the Racah parameters, that is effectively related to the covalency of the bonding. The vertical axis is the energy of the various states of the system (in units of thousands of wavenumbers), again normalized by the parameter "B".

The lowest energy configuration of electrons in the orbitals is called the ground state. Each configuration is given a symbol that reflects the symmetry of the wave functions used to mathematically describe the system. The superscript prefix represents the number of unpaired electrons according to the formula $2s + 1$ where each unpaired electron has a spin number, s, of ½. For Fe^{3+} the ground state symbol is $^6A_{1g}$. It is the horizontal line located at zero energy. A typical value for Δ/B is illustrated by the intersection of the vertical dashed line in Figure 2 with the horizontal axis. Light of the appropriate energy will promote an electron and raise the system to the first excited state, labeled $^4T_{1g}$, indicated by the sloping black line at the energy where the dash line intersects the $^4T_{1g}$ line. The spin number changes from 5 unpaired electrons in the ground state to only 3 unpaired electrons in the first excited state because any promotion of an electron from the t_{2g} requires that two electron be paired.

The downward slope of the $^4T_{1g}$ line with increasing Δ/B is worth noting. As thermal energy causes the metal-oxygen bonds to vibrate, the value of Δ will change. Depending on when a photon interacts with a cation, the instantaneous Δ value will vary over a small range. Because of the slope of the $^4T_{1g}$ line, the value of E will also change. The result is that this optical absorption band will have considerable width. The same is true when the excitation take the ion to the $^4T_{2g}$ state. The next transition to a state with 3 unpaired electrons is actually a pair of states that just happen to fall at nearly the exact same energy, namely the $^4A_{1g}$ and ^4E_g states. The slope for these states is very shallow. As a result, when the metal-oxygen bonds change length during vibrations, there will be significantly less variation in the E/B value. The result is a narrow absorption band.

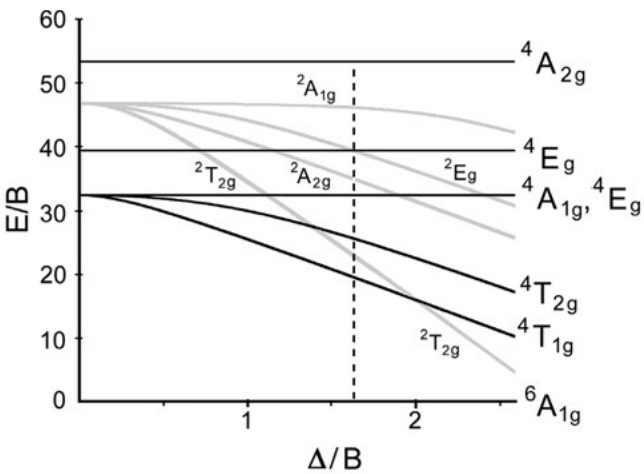


Figure 2. A portion of the Tanabe-Sugano diagram for Fe^{3+} in an octahedral environment.

EBSCOhost - printed on 2/13/2023 5:26 AM via . All use subject to https://www.ebsco.com/terms-of-use

An absorption band representing a transition to the next state, also with ^4E_g symmetry, is also narrow. This band is often not observed because it buried under other absorptions. Absorption bands at even higher energies are almost never observed in minerals. Additional states with the superscript 2 appear as grey lines on the diagram above. These are states of the system in which two electrons are both promoted to higher energy and paired. This type of transition is of very low probability and, if seen at all in a spectrum, will produce a band of very low intensity.

UNITS

Wavelength and energy

Wavelengths are usually presented in units of nanometers and energies are commonly presented in units of wavenumbers. Older literature presents wavelengths in Ångstroms (10 Å = 1 nm). In the physics-focused literature, energy may be expressed in electron volts (eV). Interconversions among the units commonly used for mineral spectra are:

Wavelength		Wavenumber		Energy	Color
333 nm	=	30,000 cm^{-1}	=	3.72 eV	ultraviolet
400 nm	=	25,000 cm^{-1}	=	3.10 eV	violet
500 nm	=	20,000 cm^{-1}	=	2.48 eV	green
750 nm	=	13,333 cm^{-1}	=	1.65 eV	red
1000 nm	=	10,000 cm^{-1}	=	1.24 eV	near infrared
2000 nm	=	5,000 cm^{-1}	=	0.62 eV	near infrared

Intensities

The intensity of an absorption band is related to the concentration of the absorbing ion in the crystal. Thus, optical spectra can be used for quantitative determinations of the amount of particular ions in crystals. There is a long history in the chemical sciences of using optical spectra for quantitative analyses. In mineralogy, there has been significantly less use of spectra for this purpose, in part because of the need to generate calibration standards, and in large part because of the added complexities associated with anisotropic crystals.

The intensity of light passing through a crystal at a given wavelength can be measured in units of percent transmission,

$$\%T = 100 \times I/I_0 \tag{1}$$

where I_0 is the intensity of light incident upon the crystal, and I is the intensity passing through the crystal. Most instruments present the intensity in absorbance units:

$$\text{Absorbance } (A) = -\log_{10}(I/I_0) \tag{2}$$

This unit is useful because, according to the Beer-Lambert law of solution colorimetry, the absorbance is linearly related to the concentration of the absorbing species and to the thickness of the sample:

$$\text{Absorbance} = \varepsilon \times \text{path} \times \text{concentration} \tag{3}$$

where path is in cm and concentration is in moles per liter. The molar absorptivity, also referred to as the extinction coefficient, ε, is a constant for each system of interest. The concentration in a "liter" of crystal can also be calculated as the following example demonstrates:

EBSCOhost - printed on 2/13/2023 5:26 AM via . All use subject to https://www.ebsco.com/terms-of-use

Consider the concentration of Fe^{2+} in a grossular garnet of density 3.61 and with 1.10 wt% FeO. One liter of the crystal (1000 cm^3) weighs 3610 grams, of which 1.1% or 39.71 g is FeO. The formula weight of FeO is 71.85, so the number of moles of FeO in one liter of crystal is 39.71/71.85 = 0.553 moles. There is one mole of Fe in FeO, so the concentration of Fe^{2+} is also 0.553 moles per liter.

THE EXPERIMENT – SAMPLE AND EQUIPMENT CONSIDERATIONS

Qualitative spectra, which tell where the absorption bands are, can be obtained by measuring the transmission of light through the sample without regard to sample preparation, as long as the sample is not too thick to allow adequate transmission for the instrument to measure. However, the samples are usually oriented (by morphology, optics or X-rays) so that light propagates along a crystal axis or an axis of the optical indicatrix. Windows are polished on the two sides of the sample to improve the transmission quality and to exactly define the sample thickness. For optimum results, the thickness of the sample should be adjusted (often by trial and error) so that the absorption bands are "on scale." Ideally, absorbances will not exceed 2 for the most accurate data on many spectrometers. For a darkly colored mineral such as augite, the optimal thickness may be a few tens of micrometers, whereas a pale blue beryl (aquamarine) may optimally be a centimeter thick.

Types of spectrometers

A variety of instrument types are now in use for measuring the optical spectrum of a mineral. Instruments that use diffraction gratings to disperse light use a tungsten-halogen bulb for visible and near-infrared wavelengths, and either a deuterium lamp or a xenon arc lamp for the ultraviolet region. The detection systems can include photomultiplier tubes, PbS detectors, diode-arrays, or CCD detectors. The diode-array systems use silicon diodes for the visible and UV regions, and InGaAs arrays for the near-infrared. They, and the CCD detectors, offer the advantage of simultaneous detection of many wavelengths at once (up to several hundred nanometers, depending on the spectroscopic resolution of the instrument). These spectrometers can work with samples on the order of 100 μm in diameter in the visible spectral region, but usually require larger diameters in the near-infrared because of the lower sensitivity of the detectors used in this energy region. In general, larger sample diameters give better quality data.

Commercial microscope spectrometers are available from a few vendors, although, some labs have constructed their own microscope systems from components. Microscope spectrophotometers can work with samples from a few micrometers to a few tens of micrometers in diameter although necessarily compromising the orientational purity of the incident light because the microscope optics converge the light on the sample and, as a result, do not maintain the *E*-vector perfectly parallel to the plane of the sample (Goldman and Rossman 1978).

Fourier Transform spectrophotometers are also used, with or without microscopes, particularly in the near-infrared region. Those with InGaAs detectors can work in the near-infrared region with samples a few tens of μm in diameter.

For minerals of symmetry lower than cubic, it is necessary to obtain separate spectra with linearly polarized light vibrating along each axis of the optical indicatrix. To obtain polarized light, either crystal polarizers or sheet polarizers are commonly used. Crystal polarizers, such as calcite polarizers of the Glan Taylor or Glan Thompson design provide excellent polarization ratios that are significantly higher than those that can be obtained from various types of film polarizers. An additional advantage of the calcite polarizers is the broad wavelength range over which they polarize light with high efficiency. Film polarizers commonly require separate polarizers for the UV, visible, and near-IR regions.

EBSCOhost - printed on 2/13/2023 5:26 AM via . All use subject to https://www.ebsco.com/terms-of-use

NOMENCLATURE OF THE DIFFERENT SPECTRA

While useful information can be obtained about the identity and oxidation state of ions in crystals from unoriented crystals that are studied in unpolarized light, a more quantitative and more fundamental understanding of the origin of color can usually only be obtained with orientated crystals studied with linearly polarized light. The number of spectra required to describe the spectrum of a mineral depends on the crystal system of the mineral.

Cubic crystals such as garnets require just one spectrum. Polarized light is not required and the sample can be oriented in any direction. Such crystals usually present minimal difficulties for orientation if zonation within the crystal is not an issue.

For uniaxial crystals (tetragonal and hexagonal crystals), two spectra are required. One is taken with polarized light vibrating parallel to the *c*-axis and other with light vibrating perpendicular to the *c*-axis. The spectra are usually called the $E\|c$ and $E\perp c$ spectra or the ε and ω spectra where ε corresponds to the ε index of refraction obtained with light polarized parallel to *c* ($E\|c$), and ω corresponds to the ω index of refraction obtained with light polarized perpendicular to the *c*-axis ($E\perp c$). In some of the literature, the $E\|c$ spectrum is called the π-spectrum and the $E\perp c$ spectrum, the σ-spectrum. With uniaxial crystals, any direction perpendicular to the *c*-axis will provide the $E\perp c$ spectrum.

In the case of optically biaxial crystals, three spectra are required. The three spectra needed to completely describe an orthorhombic crystal can be named, *a*, *b*, and *c* spectra (after the crystal axes to which the light is polarized), the α, β, and γ spectra (after the refractive indices that would be measured with light polarized in the respective directions), or the X, Y, and Z spectra (after the axes of the indicatrix in which the α, β, and γ refractive indices that would be measured. It is important to note that the order of the α, β, and γ refractive indices does not necessarily correspond to the a, *b*, and *c* axes. Unfortunately, particular care must be used in correlating the morphological directions of an orthorhombic crystal with the optical directions because different authors have used different conventions for naming both the morphologic and crystallographic axes.

For biaxial monoclinic crystals the spectra are usually called the α, β and γ spectra or sometimes the X, Y and Z spectra, where the α spectrum is obtained in the X vibration direction in which the α refractive index would be measured, Y = β and Z = γ. At a minimum, those three spectra are required to describe a monoclinic crystal. Dowty (1978) has discussed some of the special requirements for a full optical description of monoclinic minerals discussed further in the "*Intervalence Charge Transfer in Low Symmetry Crystals*" section later in this chapter.

INTENSITIES AND SELECTION RULES

Absorption bands can vary greatly in their intensity. Ruby with 0.1 % Cr^{3+} is deep red when 1 mm thick, whereas orthoclase with 0.1% Fe^{3+} is essentially colorless at the same thickness. A variety of selection rules derived from quantum mechanics governs the intensity of the various types of absorption phenomena. These rules are extensively discussed in books devoted to the chemical physics of optical spectroscopy such as Harris and Bertolucci (1978), the various editions of Cotton (1971), and the classic book by Wilson et al. (1955).

The Laporte selection rule

Transitions between two *d*-orbitals or two *p*-orbitals are forbidden, but transitions between *s*-and *p*-orbitals or between *p*-and *d*-orbitals are allowed (Laporte Selection Rule; Laporte and Meggers 1925).

This means that oxygen-to-metal charge-transfer transitions (from an oxygen *p*-orbital to a metal *d*-orbital) will occur with high probability. Photons of the appropriate energy will

EBSCOhost - printed on 2/13/2023 5:26 AM via . All use subject to https://www.ebsco.com/terms-of-use

stand a high probability of being absorbed, and the resulting absorption band will be intense. Ideally, transitions within the *d*-orbitals would be forbidden, but, in fact, will occur with low probability and will produce correspondingly low intensity absorptions. All of the examples of single metal ion spectra that follow are examples of transitions within the *d*-orbitals.

In practice, these "rules" do not rigidly control the intensity of spectra because there are various ways to weaken them. A common factor is mixing of *d*-and *p*-orbitals to produce a hybrid state which has character intermediate between the two extremes. Also, geometric distortions of otherwise fully symmetric coordination environments will relax the Laporte rule. Distortions from full symmetry can occur because of the local structure of the phase, or even during the vibrations of the metal-oxygen bonds. An example is provided by the mineral gillespite where the *d-d* transitions are Laporte-forbidden, but where coupling with vibronic motion of the Fe-O bonds makes the absorption of visible light possible (Burns et al. 1966). Nevertheless, the intensity of crystal-field absorption bands from ions of the common transition metals will be about a factor of 1000 times less than the oxygen-to-metal charge-transfer bands.

Spin-forbidden transitions

An additional selection rule is the *spin-multiplicity selection rule*. It states that the total number of unpaired electrons on an atom must remain the same before and after an electronic transition occurs. Because all orbitals in Mn^{2+} and Fe^{3+} are half-filled, the only possible electronic transitions involve pairing electrons in an orbital with the necessity of changing the spin of one of the electrons. Consequently, the Mn^{2+} and Fe^{3+} transitions are spin-forbidden. In fact, they can occur, but with very low probability. Spin-forbidden bands can occur in the spectrum of any ion with two or more valence electrons. An example appears in the spectra of Cr^{3+} in kyanite discussed in a following section.

QUANTITATIVE CONCENTRATIONS FROM OPTICAL SPECTRA

Optical spectra are widely used for quantitative analysis in solution chemistry. In principle, quantitative metal ion concentrations and even site occupancies could be obtained from the optical spectra of minerals. To determine quantitative site-occupancies or total cation content, the ε value from the Beer-Lambert law (commonly known as Beer's Law) must be known for the system of interest, and it must be reasonably constant in a solid solution series. These plots require an independent determination of the ion's concentration in a number of crystals (e.g., by electron microprobe analysis). In practice, very few mineral systems have been examined in enough detail to establish Beer's law plots. When such information is available, quantitative site occupancy data can be obtained. Those which have a nearly linear correlation between absorbance and concentration are Fe^{2+} in garnets (White and Moore 1972), olivines (Hazen et al. 1977), orthopyroxenes (Goldman and Rossman 1978) and feldspars (Mao and Bell 1973; Hofmeister and Rossman 1984).

The ε values for a number of other ions in minerals are available, but they represent a single measurement and do not explore the variation of ε with composition along a solid solution series or with concentration of the absorbing ion. In practice, optical spectra generally have not competed favorably with other analytical methods such as LA-ICP-MS or electron microprobe analysis for determining concentrations of cations, but, in some cases, optical methods have particular advantages such as integrating through the entire volume of a sample, and providing information about concentrations of cations in a particular crystal site. In principle, optical methods can also have the advantage of quantitatively working with a single oxidation state of a cation in a crystal if calibration standards are available.

EBSCOhost - printed on 2/13/2023 5:26 AM via . All use subject to https://www.ebsco.com/terms-of-use

IDENTIFICATION OF THE OXIDATION STATES OF CATIONS

One of the most useful aspects of optical spectra is its ability to identify the oxidation state of many common cations. This is based, in part, on the fact that different cations have different numbers of electrons involved in electronic transitions, and on the fact that different cations have different sizes and geometries that influence the electrostatic repulsion that their electrons feel from the neighboring ions when their valence electrons undergo electronic transitions.

The spectra of many cations are sufficiently distinctive to allow identification of their oxidation states (e.g. Fe^{2+} vs. Fe^{3+}; Mn^{2+} vs. Mn^{3+}; Cr^{3+} vs. Cr^{6+}). When a metal ion is present in two oxidation states, it is difficult to determine the quantitative ratio because of the general lack of adequate calibration standards that are available for the optical data. An example of how such calibrations can be done is the determination of Fe^{2+} and Fein feldspars (Hofmeister and Rossman 1984). Total iron is first determined by X-ray fluorescence and/or electron microprobe analysis and Fe^{3+} is determined by electron paramagnetic resonance (EPR) spectroscopy (Pan and Nilges 2014, this volume). Fe^{2+} is then determined by difference. These determinations are then used to calibrate the optical spectrum. Several examples of the spectra of cations in different oxidation states are presented in the following sections.

A GALLERY OF SPECTRA OF METAL IONS COMMONLY RESPONSIBLE FOR THE OPTICAL SPECTRA OF MINERALS.

Titanium

Ti^{4+} has no valence *d*-electrons and as such does not have absorption in the visible region by itself. Ti^{3+} has one valence electron which can be excited to a higher energy by visible light. Consequently, Ti^{3+} minerals will have absorption in the optical region. This oxidation state is formed only under conditions more reducing than those found in the terrestrial environment; Ti^{3+} is found primarily in meteorites, lunar samples and synthetic phases. Ti^{3+} in octahedral coordination is a comparatively weak absorber and is easily overpowered by other cations which might be present. Two complicating factors must be considered: Ti^{4+} can enter into intervalence charge transfer (IVCT) with Fe^{2+} to produce strong absorption (Manning 1977; Burns 1981). This process has been implicated in the color of a variety of minerals such as blue sapphire and orange-brown micas. Many early reports of Ti^{3+} in the spectra of terrestrial minerals are probably due to the Fe^{2+}-Ti^{4+} interaction. Ti^{4+} can also enter into interva1ence charge transfer with Ti^{3+} producing intense absorption in the red to near-infrared. The blue meteoritic hibonite (Fig. 3) is the result of this IVCT interaction.

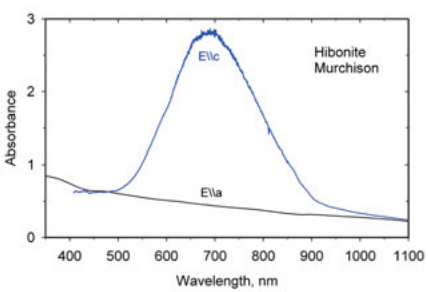


Figure 3. Spectrum of Ti^{3+}-Ti^{4+} IVCT in blue hibonite from the Murchison meteorite plotted for 1 mm thickness.

Vanadium

Trivalent vanadium is the cause of vivid colors in a number of minerals and gemstones. It produces a diversity of colors because the locations of its absorption bands are sensitive to the details of the size and symmetry of the vanadium site. The spectrum of vanadian tourmaline (Fig. 4) and grossular (Fig. 5) are representative. The spectroscopy of vanadium in minerals has been reviewed by Schmetzer (1982). The positions of the V^{3+} absorption bands are close to those of Cr^{3+} in the same site. Consequently, the color of a particular mineral is frequently

EBSCOhost - printed on 2/13/2023 5:26 AM via . All use subject to https://www.ebsco.com/terms-of-use

similar regardless of whether the chromophore is Cr^{3+} or V^{3+} (e.g., both green grossular and green beryl can be colored by either Cr or V).

Tetravalent vanadium is infrequently encountered but when present in minerals is normally in the form of the vanadyl ion (VO^{2+}) that is characterized by a spectrum that is centered in the red. Comparatively few mineralogical examples of this have been published. Canvaniste, $CaVOSi_4O_{10}{\cdot}4H_2O$, (Fig. 6) and apophyllite that contains a few thousand ppm of the vanadyl ion (Fig. 7) are two of the more common examples of this ion. Vanadate fluxes are sometimes used in mineral synthesis. The blue color of some of pyroxenes synthesized with these fluxes comes from ~0.1% substitutional vanadium in the form of the vanadyl ion in the large cation site.

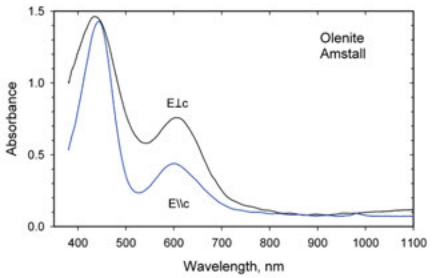


Figure 4. The spectrum of V^{3+} in the yellow-green tourmaline, olenite, from Amstahl, Austria, plotted as 1 mm thick. After Ertl et al. (2008).

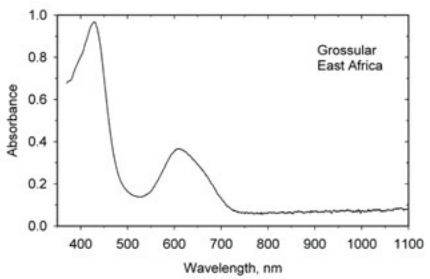


Figure 5. The spectrum of V^{3+}-containing grossular garnet (tsavorite variety) from East Africa, plotted as 1 mm thick.

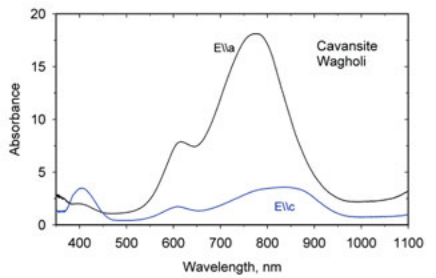


Figure 6. The spectrum of the VO^{2+} ion in blue cavansite from near Wagholi, Pune District, Maharashtra, India plotted as 1.0 mm thick.

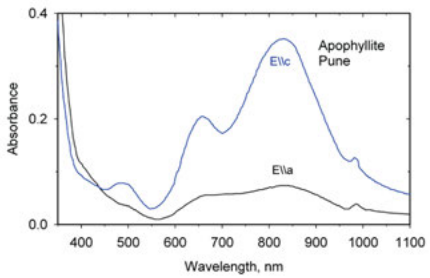


Figure 7. The spectrum of the VO^{2+} ion in green apophyllite from Pune, India, plotted as 1.0 mm thick. After Rossman (1974).

Chromium

Chromium is a moderately common minor component of many common minerals that contributes to the spectra of minerals in the trivalent state. The familiar red color of rubies and green color of emeralds are both due to Cr^{3+} in an aluminum site. Like vanadium, the exact position of the Cr^{3+} absorption bands will depend upon the particulars of the Cr site, including metal-oxygen distances, site distortion and degree of covalency. Because the molar absorptivity (ε value) of Cr^{3+} is high (typically 40-60) compared to Fe^{2+} (typically 3-6), a minor amount of Cr^{3+} (0.X%) can dominate the spectrum of many common ferro-magnesian silicates. The colors of green micas, pyroxenes, and amphiboles often result from traces of Cr^{3+} as much as from the primary iron component.

EBSCOhost - printed on 2/13/2023 5:26 AM via . All use subject to https://www.ebsco.com/terms-of-use

In the spectrum of many Cr^{3+} minerals, sharp, weak bands near 700 nm appear in the spectrum. These are spin-forbidden bands that result from a change in the number of unpaired electrons during the electronic transition. These bands are weak in the spinel spectrum (Fig. 8) but easily observed in the kyanite spectrum near 700 nm (Fig. 9).

Chromate, CrO_4^{2-}, produces intense colors due to its oxygen to Cr^{6+} charge-transfer band that is centered in the ultraviolet. The brilliant orange and yellow colors of crocoite ($PbCrO_4$) and vanadinite ($Pb_5(VO_4)_3Cl$) are from the chromate ion. In the case of vanadinite, a small amount of CrO_4^{2-} is involved in a solid solution with VO_4^{3-}. Because of the experimental difficulty of obtaining on-scale spectra of the intensely absorbing chromate bands, few single-crystal spectra of chromate in minerals are available.

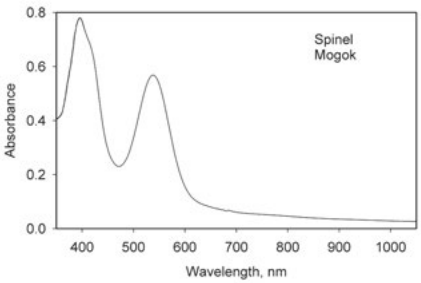


Figure 8. The spectrum of Cr^{3+} in red spinel, from Mogok, Myanmar, plotted as 1.0 mm thick.

Manganese

While small amounts of Mn^{2+} are found in many minerals, it is seldom a significant contributor to the spectrum of the phase. That is because all electronic transitions of Mn^{2+} are spin-forbidden. Therefore, the absorption by small amounts of Mn^{2+} in minerals is very weak and usually overpowered by the spectra of many other cations that may be present. The spectrum of Mn^{2+} in octahedral coordination consists of two weak bands at longer wavelength and a sharp band near 412 nm (Fig. 10). Only the sharp 412 nm band is seen in the spectrum of many minerals when minor amounts of Mn^{2+} occur in the presence of greater quantities of Fe^{2+}.

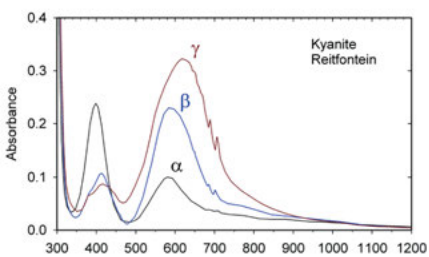


Figure 9. The spectrum of the Cr^{3+} in blue kyanite from a kyanite eclogite from the Reitfontein kimberlite, South Africa, plotted as 1 mm.

In contrast to Mn^{2+}, Mn^{3+} is an intense absorber which usually produces red through lavender colors. Common examples include piemontite, red tourmaline and pink micas. Mn^{3+} can also produce a green color such as found in the viridine variety of andalusite. Mn^{3+} spectra can vary from a dominant single band with shoulders in the case of sites of fairly regular symmetry as seen in the pink, Mn^{3+}-containing diaspore (AlO(OH)) spectrum (Fig. 11) to the well-separated pairs of bands that occur in the spectrum of green andalusite (Fig. 12) and orange kyanite (Fig. 13). In rare instances, Mn^{2+} enters tetrahedral sites such as found in the spectacularly fluorescent zinc silicate, willemite. Its spectrum is shown in Figure 14.

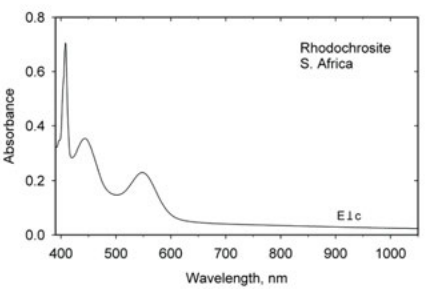


Figure 10. Spectrum of red rhodochrosite from the N'Chwaning Mines, Kuruman, South Africa, that shows the typical broad, broad, sharp band set going towards shorter wavelength.

EBSCOhost - printed on 2/13/2023 5:26 AM via . All use subject to https://www.ebsco.com/terms-of-use

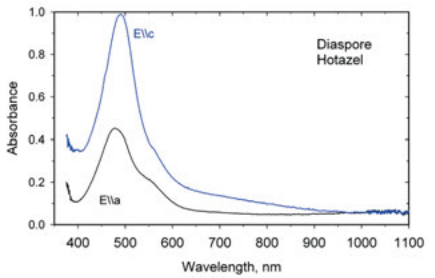


Figure 11. Spectrum of pink diaspore, AlO(OH), from Hotazel, S.W. Africa plotted as 1.0 mm thick. Its pink color of diaspore is due to Mn^{3+} substituting for Al.

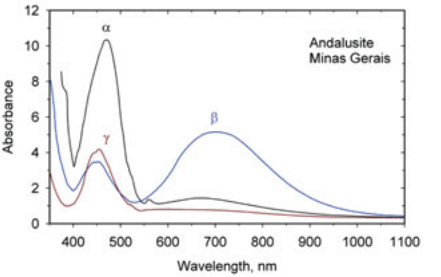


Figure 12. Spectrum of green andalusite from Minas Gerais, Brazil, plotted as 1.0 mm thick. Its green color arises from its content of ~1.08 wt% Mn.

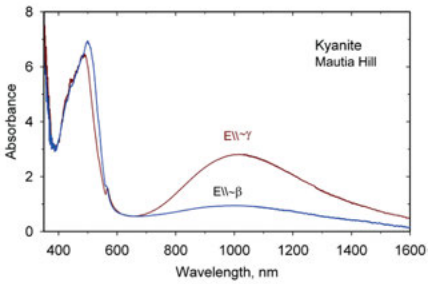


Figure 13. Spectrum of orange kyanite from Mautia Hill, Tanzania, that contains Mn^{3+} in aluminum sites plotted as 1.0 mm thick. After Chadwick and Rossman (2009).

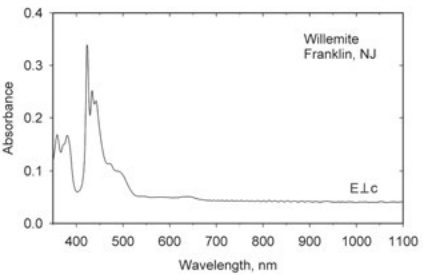


Figure 14. The spectrum of willemite, Zn_2SiO_4, from Franklin, New Jersey, containing Mn^{2+} in a tetrahedral site, plotted as 1.0 mm thick.

Iron

Iron is the most commonly encountered transition element in minerals and is responsible for the color of most rock-forming minerals. Fe^{2+} is usually found is sites that are somewhat distorted from an ideal octahedron. Its spectrum consists of a pair of bands centered near 1000 nm. The spectrum of siderite (Fig. 15) is representative of phases that contain Fe^{2+} sites that are not highly distorted from octahedral symmetry. The two components of the Fe^{2+} bands become more separated as the site becomes more distorted from octahedral geometry. In the case of the amphibole M(4) site and the pyroxene M(2) site, the two components can be separated by about 1000 nm (Fig. 16).

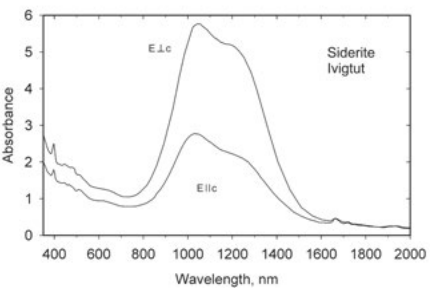


Figure 15. The spectrum of Fe^{2+} in siderite from Ivigtut, Greenland, that shows two overlapping bands in the 1000-1300 nm region from Fe^{2+} an octahedral site of only minor distortion. Plotted for 1.0 mm thickness.

Faye (1972) and Goldman and Rossman (1977) have discussed the relationship between the magnitude of the splitting and the nature of the Fe^{2+} site. The detailed analysis of an optical

EBSCOhost - printed on 2/13/2023 5:26 AM via . All use subject to https://www.ebsco.com/terms-of-use

absorption spectrum first requires knowledge of the symmetry of the cation site. Selection rules which establish the polarization of the various bands are then determined from group theory. An example of such an analysis for Fe^{2+} at the M2 site of orthopyroxene appeared in Appendix A of the first edition of this chapter (Rossman 1988).

For many common minerals, the spectrum is further complicated because of contributions from iron in multiple distinct sites. The spectrum of forsterite is a case in point (Fig. 17) where four distinct absorption bands occur in the 700-1600 nm region that represent two contributions each from both the M1 and M2 sites. Although the intensity of the M2 band in the γ-polarization is several times more intense then the M1 bands near 850 nm in the α- and β-polarizations, the concentration of Fe in the M2 site is not necessarily greater than the concentration in the M1 site. This is because the ε values (molar absorptivity) for the two sites are not equal. Iron in more-distorted sites tends to have a significantly higher probability for absorbing light than iron in a more regular site.

The electronic transitions of Fe^{3+}, like those of Mn^{2+}, are spin forbidden due to their d^5 electronic configuration. Any electronic transition demands that the ion goes from a configuration of five unpaired electrons to one with 3 unpaired electrons and 1 pair. Such transitions have low probability of happening. Consequently, minerals with dilute Fe^{3+} are pale colored due to weak absorption. They generally show a characteristic pattern of two broad, low-energy absorptions, labeled T_{1g} and T_{2g}, and a sharp band near 440 nm (Fig. 18). Because the wavelengths of the two broad bands are sensitive to the exact structural details of the Fe^{3+} site, they are of use in remote sensing to identify iron oxides and polymorphs of FeO(OH). Often, because of overlapping contributions from other ions, only the band at 440 nm is visible. Occasionally it is possible to observe additional Fe^{3+} bands near 376 nm as are seen in Figure 18.

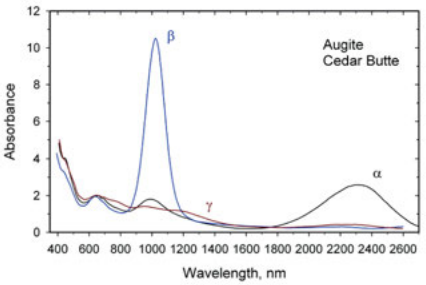


Figure 16. The spectrum of the clinopyroxene, augite, from Cedar Butte, Oregon. The spectrum is dominated by Fe^{2+} absorption near 1010 and 2300 nm from Fe^{2+} in the highly distorted M2 site. Weaker absorption from Cr^{3+} occurs near 650 and 400 nm.

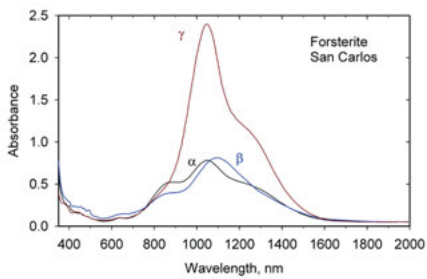


Figure 17. The spectrum of forsterite from San Carlos, Arizona, showing four bands in the 700-1500 nm region where two bands came from each of the M1 and M2 sites.

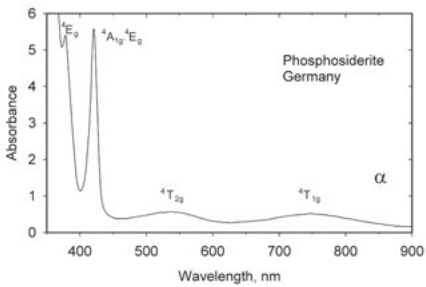


Figure 18. Spectrum of phosphosiderite, $FePO_4 \cdot H_2O$, from Kreuzberg, Germany, plotted as 1.0 mm thick that shows the typical pattern of two broad bands at lower energy followed by a sharper band near 440 nm.

The spectrum in Figure 18 presents an excellent opportunity to demonstrate the use of a Tanabe-Sugano diagram discussed in Figure 2 earlier in this chapter. Moving from low energy (right side) to high energy (left side) the

EBSCOhost - printed on 2/13/2023 5:26 AM via . All use subject to https://www.ebsco.com/terms-of-use

breadth of the first two bands (the $^6A_{1g} \rightarrow {}^4T_{1g}$ and $^6A_{1g} \rightarrow {}^4T_{2g}$ transitions) compared to the sharpness of the next two bands (the $^6A_{1g} \rightarrow {}^4A_{1g}, {}^4E_g$ and $^6A_{1g} \rightarrow {}^4E_g$ transitions) is obvious.

Sites of different coordination number present different Fe^{2+} spectra. The most extensively studied has been the spectrum of Fe^{2+} in the garnet 8-coordinated site. It consists of three bands in the near-infrared region plus spin-forbidden bands in the visible region (Fig. 19). Tetrahedral Fe^{2+} transitions occur at lower energies, usually consisting of a pair of bands centered in the 1800 to 2000 nm range (Fig. 20). If the Fe-O bond lengths were the same, the average energy of the tetrahedral absorptions would be 4/9 the average energy of the octahedral absorptions. The absorption intensity of tetrahedral Fe^{2+} is greater than octahedral Fe^{2+}. In general, a metal ion at a site which lacks a center of symmetry (non-centrosymmetric site) will have a greater probability of absorbing light then one at a centrosymmetric site. A very different pattern for four-coordinated iron is provided by Fe^{2+} in a square-planar site such as those of gillespite (Fig. 21) and eudialyte. Another example (Fig. 22) of Fe^{2+} in a non-octahedral site is provided by Fe^{2+} in the irregular geometry of the Ca-site in plagioclase feldspar.

Tetrahedral Fe^{3+} is encountered in a number of minerals including micas and pyroxenes and certain framework silicates such as feldspars (Fig. 23). Its absorption intensity is several times greater than that of Fe^{3+} in an octahedral site because of the non-centrosymmetric site.

An additional factor that strongly influences the colors of iron-containing minerals arises from a combination of absorption by the individual ions, Fe^{2+} and Fe^{3+}, and from intervalence charge transfer between Fe^{2+} and Fe^{3+} or between Fe^{2+} and Ti^{4+} , as well as from oxygen-to-Fe^{3+} charge transfer. The combination of these multiple causes of absorption contributes the dark color of many common iron-containing silicate minerals such as pyroxenes (Fig. 24), amphiboles and micas.

Cobalt

Cobalt is seldom encountered in minerals at concentrations high enough to impact the optical spectrum. When it does, it typically occurs in octahedral coordination as Co^{2+} and causes a pink color such as that in cobaltian-calcite (Fig. 25). When Co^{2+} is situated in a tetrahedral site, it is a strong absorber producing a blue color in synthetic spinels and contributes to the deep blue color of some rare, natural spinel crystals (Fig. 26).

Nickel

Nickel is an infrequent contributor to the spectra of minerals. It is usually present as Ni^{2+} at an octahedral site and gives rise to a green color in phases such as the chrysoprase, a variety of chalcedony that contains minute grains of nickel-containing layer silicates (Fig. 27). In addition to the Ni^{2+} features near 650, 730 and 1100 nm, the spectrum shows increasing absorption that rises towards short wavelengths. The rise results from wavelength-dependent scattering of light from the fine nickel silicate particles within the quartz host. A narrow water overtone feature is also present near 1400 nm. The annabergite spectrum (Fig. 28) shows the three major regions of absorption that arise from Ni^{2+} in an octahedral site.

Copper

Cu^{2+} is an intense absorber that produces the familiar green and blue colors of the numerous copper minerals such as azurite and malachite. Although there are many Cu^{2+} minerals, there has been very little work on their single crystal spectroscopy due to the difficulty of preparing the minerals thin enough for on-scale spectroscopy when the copper concentration is comparatively high. Elbaite tourmaline produces an especially beautiful blue color that results from the incorporation of Cu^{2+} in the Y-site (Fig. 29).

The Cu^{+} ion by itself does not contribute to the optical absorption spectrum of minerals. The color of Cu(I) oxides is due to band gap absorptions which are discussed in a following

EBSCOhost - printed on 2/13/2023 5:26 AM via . All use subject to https://www.ebsco.com/terms-of-use

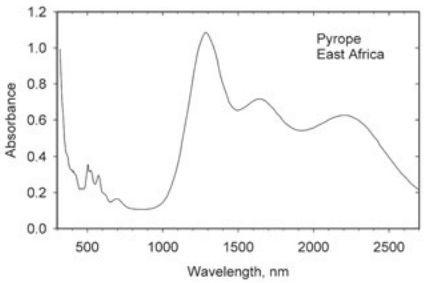


Figure 19. The spectrum a pyrope-almandine garnet with three components in the near-infrared at about 1250, 1600 and 2200 nm due to Fe^{2+} in the distorted eight-coordinated cubic site. Weaker, sharper features between 350 and 800 nm are spin-forbidden bands. Plotted as 1.0 mm thick.

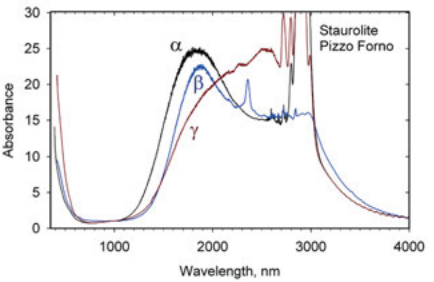


Figure 20. The spectrum of staurolite from Pizzo Forno, Switzerland, plotted as 1.0 mm thick that shows broad absorption bands from Fe^{2+} in a tetrahedral site with accompanying sharper bands from OH groups.

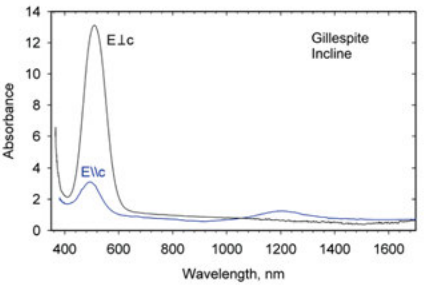


Figure 21. The spectrum of Fe^{2+} in the square-planar, four-coordinated site of gillespite, $BaFe^{2+}Si_4O_{10}$, from Incline, California, plotted as 1.0 mm thick.

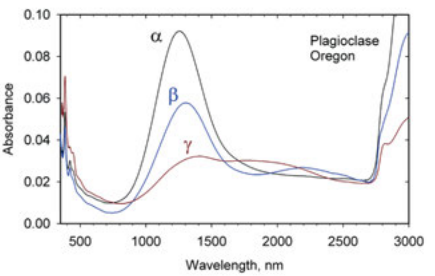


Figure 22. Spectrum of plagioclase feldspar (~An70) from Lake County, Oregon, plotted as 1.0 mm thick, showing the bands in the 1250 - 2300 nm region from about 0.3 wt% Fe^{2+} in the large, distorted Ca sites. Absorption from OH is in the 2800-3000 nm region. After Hofmeister and Rossman (1983).

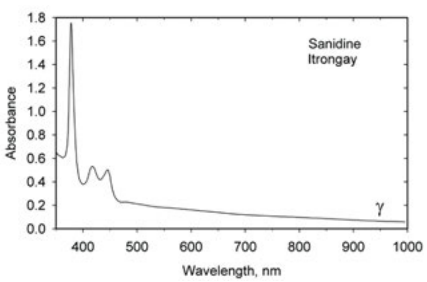


Figure 23. Spectrum in the gamma orientation of tetrahedral Fe^{3+} in sanidine with 0.42% Fe_2O_3 from Itrongay, Madagascar, plotted for 1.0 mm thickness.

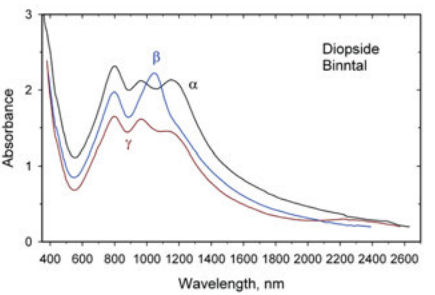


Figure 24. The spectrum of the clinopyroxene, diopside, from Binntal, Wallis, Switzerland, that shows strong absorption near 950 and 1050 nm from Fe^{2+} in the M1 site and a comparatively weak absorption near 1050 nm from Fe^{2+} in the M2 site. The band near 780 nm arises from Fe^{2+}- Fe^{3+} IVCT.

EBSCOhost - printed on 2/13/2023 5:26 AM via . All use subject to https://www.ebsco.com/terms-of-use

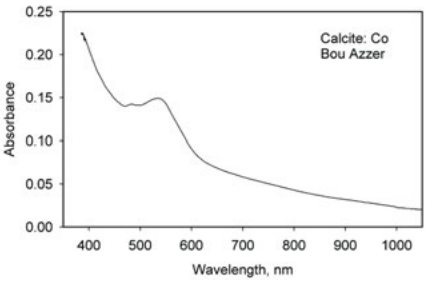


Figure 25. Pink cobaltian calcite that contains six-coordinated Co^{2+} from the Arhbar Mine, Bou Azzer, Morocco, plotted as 1.0 mm thick.

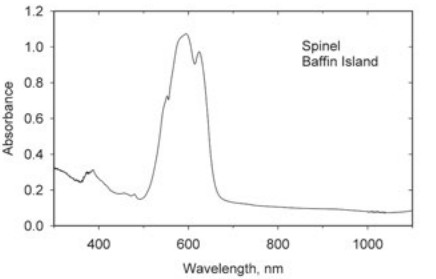


Figure 26. Spectrum of 1 mm thick blue spinel from Baffin Island, Canada, that contains tetrahedrally-coordinated Co^{2+}.

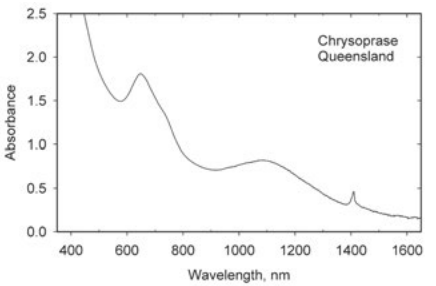


Figure 27. The unpolarized spectrum of Ni^{2+} in chrysoprase from Marlborough, Queensland, Australia, plotted for 1.0 mm.

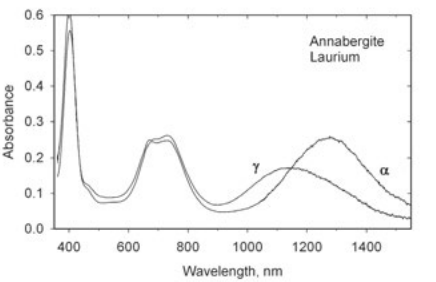


Figure 28. Absorption spectrum of Ni^{2+} in a (010) cleavage slab of annabergite, $Ni_3(AsO_4)_2{\cdot}8H_2O$, from Laurium, Greece, plotted for 0.10 mm thickness.

section. Cu(0) was implicated in the color of some unusual green and red plagioclase feldspars from basalt flows; absorption was attributed to small clusters of copper atoms (Hofmeister and Rossman 1985).

Rare Earth Elements and Uranium

The spectra of the rare earth elements in their normal 3+ oxidation state come from electronic transitions involving the *f*-orbitals that are comparatively shielded from the environment of the neighboring atoms. Because the *f*-orbitals are not involved with bonding, they are only weakly perturbed by the vibrations of the neighboring atoms and, as a result, their absorption bands are much narrower than those that involve *d*-orbitals. They show up as groups of sharp bands in the absorption spectra. Typically, these spectra are dominated by absorption features from Nd^{3+} and Pr^{3+}. The Nd^{3+} spectrum is most commonly encountered in minerals such as monazite (Fig. 30) and apatite (Fig. 31). In the apatite spectrum there is also a broader, underlying

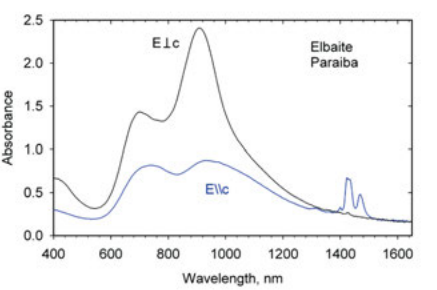


Figure 29. The spectrum of blue elbaite tourmaline from Paraiba, Brazil, showing strong absorption bands in the 700 to 1000 nm region from Cu^{2+} in the Y-site of the mineral. Also present are the first overtones of the O-H vibrations occur 1450 nm. Plotted for 1.0 mm thickness. After Rossman et al. (1991).

EBSCOhost - printed on 2/13/2023 5:26 AM via . All use subject to https://www.ebsco.com/terms-of-use

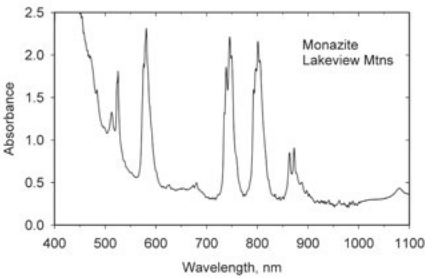


Figure 30. The unpolarized spectrum of monazite, $CePO_4$, from the Southern Pacific Silica Quarry, Lakeview Mountains, California, plotted as 1.0 mm thick from a (100) slab. The spectrum is dominated by narrow Nd^{3+} absorptions.

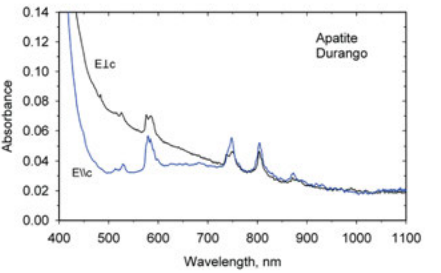


Figure 31. Spectrum of apatite from Durango, Mexico, showing sharper bands from Nd^{3+}. Plotted as 1.0 mm thick.

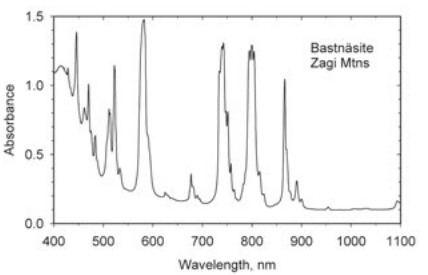


Figure 32. The spectrum of bastnäsite, $CeCO_3F$, from the Zagi Mountains, Pakistan, plotted as 1.0 mm thick in an unspecified orientation. In addition to Nd^{3+} features throughout the spectrum, Pr^{3+} bands in the 420 to 500 nm region are present.

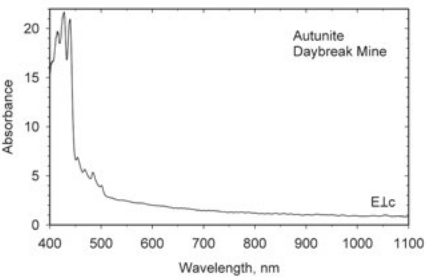


Figure 33. Spectrum of a (001) cleavage of autunite, $Ca(UO_2)_2(PO_4)_2{\cdot}10\text{-}12H_2O$, from the Daybreak Mine, Washington, shows vibronic structure of the UO_2^{2+} ion with several narrow features in the 400 to 500 nm region. Plotted as 1.0 mm thick.

absorption from radiation damage possibly related to the SO_3^- ion (Gilinskaya and Mashkovtsev 1995). Occasionally, features from Pr^{3+} are encountered in the 400-500 nm region such as occur in the spectrum of bastnäsite (Fig. 32).

Uranium is normally important in the spectrum of minerals that have the UO_2^{2+} ion in their structures. Typically this will cause a bright yellow color due to strong absorption in the 400 to 500 nm region of the spectrum such as is seen in the autunite spectrum (Fig. 33). The spectrum of uranium in a lower oxidation state is not commonly encountered except in the case of metamict zircons (Fig. 34).

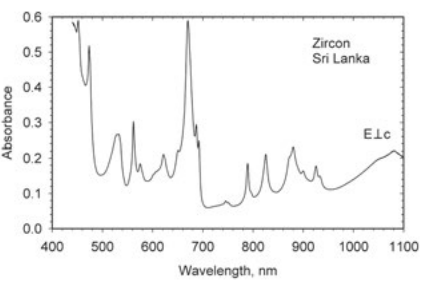


Figure 34. Spectrum of a partially metamict, yellow-green zircon from Sri Lanka plotted as 1.0 mm thick. Narrow bands, mostly from U^{4+}, dominate the spectrum.

EBSCOhost - printed on 2/13/2023 5:26 AM via . All use subject to https://www.ebsco.com/terms-of-use

INTERVALENCE CHARGE TRANSFER

Intervalence charge transfer (IVCT) is the dominant cause of color of many common rock-forming minerals such as amphiboles, pyroxenes, micas, tourmalines and aluminosilicates. In most minerals, the charge transfer is either between Fe^{2+} and Fe^{3+} or between Fe^{2+} and Ti^{4+}. One of the structurally least complicated examples is vivianite, $Fe^{2+}_3(PO_4)_2{\cdot}8H_2O$. Vivianite's structure contains simple pairs of Fe^{2+} in edge-shared octahedral isolated from other iron atoms by intervening phosphate ions and water molecules. When one of the Fe ions in the pair oxidizes to Fe^{3+}, an intervalence interaction between the two Fe ions occurs and a strong IVCT absorption develops in the spectrum (Fig. 35). Because all the Fe-Fe vectors are aligned in the same direction (along the *b*-axis), the absorption occurs in the *E**b* direction.

In systems that have more than two ions connected to each other, the IVCT interaction occurs, but the band center will appear at longer wavelengths (lower energies) than at which it is found in simpler systems such as vivianite. The spectrum (Fig. 36) of ilvaite is an excellent example. Ilvite, $CaFe^{2+}_2Fe^{3+}OSi_2O_7(OH)$, contains double chains of octahedra occupied by both Fe^{2+} and Fe^{3+}. Whereas the IVCT band in vivianite peaks near 680 nm, the IVCT band in ilvaite peaks near 1090 nm. A study of the role of iron-site polymerization on the IVCT spectrum was presented by Amthauer and Rossman (1984).

Intervalence charge transfer between two ions of different elements is well-known in the case of Fe^{2+}-Ti^{4+} interactions. Numerous examples exist (Mattson and Rossman 1988) including micas and tourmalines (Fig. 37). Because more energy is required to move an electron from Fe^{2+} to an ion of a different element, Fe^{2+}-Ti^{4+} IVCT occurs at higher energy (lower wavelength) than IVCT from Fe^{2+}-Fe^{3+}. The Fe^{2+}-Ti^{4+} IVCT usually occurs in the 400 to 500 nm region if the octahedral sites share a common edge. In other systems with more complicated structures containing both iron and titanium such as kyanite (Fig, 38) multiple IVCT bands occur in the spectrum that are commonly assumed to arise from Fe^{2+}-Ti^{4+} IVCT at higher energies and from Fe^{2+}-Fe^{3+} IVCT at lower energies.

Intervalence charge transfer in low-symmetry crystals

Low-symmetry crystals in the monoclinic and triclinic systems present additional complexities, particular when intervalence charge transfer occurs. The complexities arise from the fact that the metal-metal orientation may not coincide with a principal axis of the optical indicatrix. Thus, the "full" extent of absorption from the intervalence interaction will not occur in a principal optical direction.

Clinopyroxenes are monoclinic. The optical spectra of the clinopyroxene from the Angra Dos Reis meteorite (Fig. 39, top) show the profound difference in light absorption when light is linearly polarized to vibrate along the principle axes of the indicatrix. Under these conditions, the α, β and γ spectra are obtained for light vibrating along the X, Y, and Z axes of the indicatrix. One of these directions is confined to be parallel to the *b*-axis of the crystal, but the other two will occur in the (010) plane and will not align with either the *a*- or *c*-axis. In contrast to these directions, the spectra taken with extinction parallel to the *c*-axis shows higher intensity of the 490 nm Fe^{2+}-Ti^{4+} IVCT band than is seen when polarized along any of the principal axes of the indicatrix. That is because the *E*-vector is optimally aligned to cause electrons to exchange between the two ions in the chain of M1 sites that is aligned along the *c*-axis. Likewise, when the *E*-vector is aligned perpendicular to *c*, the IVCT interaction is not activated and essentially no indication of the 490 nm band is seen. While this has been recognized for several decades, very few monoclinic crystals have been studied in all five orientations.

The complete characterization of a triclinic crystal is even more complicated. The three principal spectra, α, β, and γ, taken along the axes of the indicatrix are commonly obtained.

EBSCOhost - printed on 2/13/2023 5:26 AM via . All use subject to https://www.ebsco.com/terms-of-use

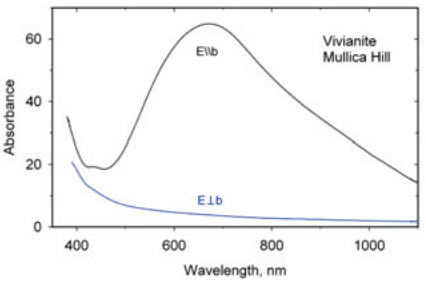


Figure 35. Spectrum of vivianite, $Fe^{2+}{}_3(PO_4)_2{\cdot}8H_2O$, from Mullica Hill, NJ, showing the intense absorption in the *E**b* direction arising from the interaction of Fe^{3+} with Fe^{2+}. After Amthauer and Rossman (1984).

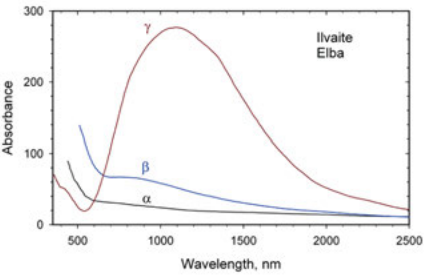


Figure 36. Spectrum of ilvaite, $CaFe^{2+}{}_2Fe^{3+}OSi_2O_7(OH)$, from Elba, Italy, plotted for 1.0 mm thickness. The spectrum is dominated by the IVCT from Fe^{2+}-Fe^{3+} interaction. After Amthauer and Rossman (1984).

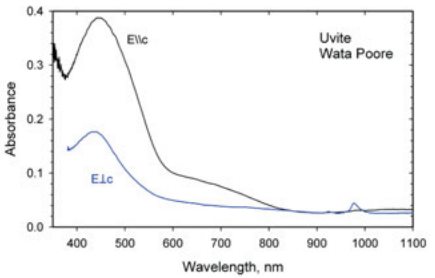


Figure 37. Spectrum of uvite tourmaline from the Wata Poore area, Kundar Province, Afghanistan, that is dominated by the broad Fe^{2+}-Ti^{4+} IVCT absorption near 450 nm.

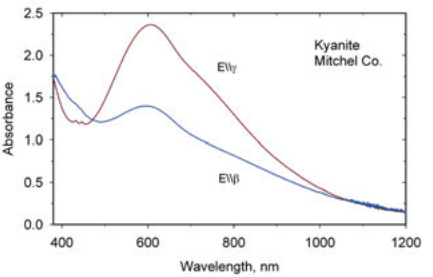


Figure 38. Spectrum of kyanite from Mitchel Co., North Carolina, showing two intervalence charge transfer bands that are assumed to arise between Fe^{2+} and Fe^{3+} (centered near 800 nm) and Fe^{2+} and Ti^{4+} (centered near 600 nm). Very weak Fe^{3+} features occur near 450 nm.

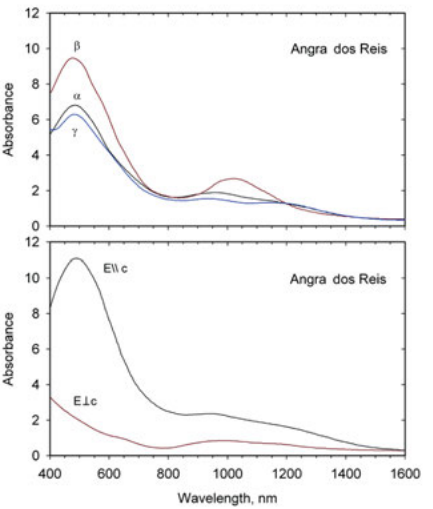


Figure 39. Spectra of the clinopyroxene in the Angra dos Reis meteorite taken (top) in the principal directions of the optical indicatrix (α, β and γ) compared to spectra taken (bottom) with the crystal oriented such that there are extinction directions parallel and perpendicular to the *c*-axis. From Mao et al. (1977) and plotted for 1 mm thickness.

EBSCOhost - printed on 2/13/2023 5:26 AM via . All use subject to https://www.ebsco.com/terms-of-use

Yet, other spectra parallel and appropriately perpendicular to the three crystal axes would also be obtained in a complete characterization. Such a complete characterization of a triclinic crystal has, most likely, never been done.

BAND GAPS

In semiconducting minerals, optical absorption occurs when electrons are promoted from the valance band to the conduction band. In contrast to absorptions from the common metal ions, these transitions rise rapidly once the photon energy exceeds the band gap. They also cause intense absorption. Minor components in the host phase may have energy levels between these bands and can cause additional absorption. Such absorption spectra of only a few minerals have been examined, in contrast to the much greater number of minerals in which metal ions cause ligand-field optical transitions. One important reason for this is that it is very difficult to prepare samples thin enough for such measurements. Normally studies of band gaps in oxides and sulfides are conducted on synthetic products made by evaporation techniques with samples only a few micrometers thick.

While it is difficult to obtain spectra of minerals that show the peak of the band gap absorptions, it is much easier to obtain spectra that show the onset of the band gap absorption. Figure 40 shows the onset of the band gap absorption in pyrite at about 1600 nm. Even though pyrite is opaque in the visible spectrum, if it is devoid of other impurities, it can become highly transparent in the near infrared. Other minor components, such as cobalt, can cause additional absorption as seen in Figure 40. Other highly colored minerals can have the onset of band gap absorption in the visible part of the spectrum. Figure 41 shows that in the case of cinnabar, transmission only occurs in the red portion of the spectrum (above 610 nm) which accounts for the red color of this mineral.

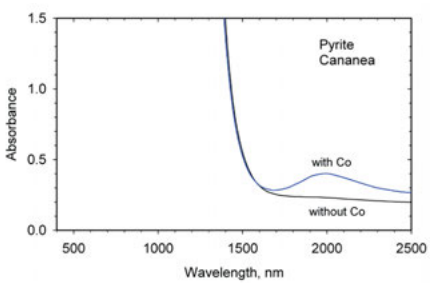


Figure 40. Absorption spectra of 0.2 mm thick slabs of Cananea, Mexico, pyrite showing the onset of the band gap absorption at about 1500 nm, and the effect of cobalt substitution in the pyrite on the near-infrared transmission. Data obtained from Kulis (1999).

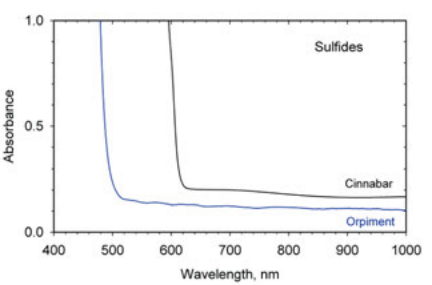


Figure 41. Onset of band gap absorption in 0.2 mm thick cleavage slabs of cinnabar from the Almadén Mine, Spain, and orpiment from the Getchell Mine, Nevada.

RADIATION-INDUCED COLOR CENTERS

Many minerals owe their color to the effects of natural irradiation through the decay of ^{40}K or the uranium series. ^{40}K is a naturally-occurring radioactive isotope with a half-life of 1.2×10^9 years. In one of its decay modes, it emits a gamma ray with an energy of 1.46 million electron volts that can penetrate tens of centimeters through typical silicate rock. The gamma ray energy is extremely large compared to the binding energy of a valence electron in metal

EBSCOhost - printed on 2/13/2023 5:26 AM via . All use subject to https://www.ebsco.com/terms-of-use

ions or oxide ions. Consequently, the gamma rays can strip electrons from the constituents of a crystal and change the oxidation state of both cations and anions. Furthermore, the ejected electron can travel through the crystal until it becomes trapped by various mechanisms such as by reducing an ion or by occupying an anion vacancy in the crystal. The various ions and trapped electrons can have their own electronic states and cause color. They are commonly referred to as color centers and display characteristic spectra that can be difficult to interpret at an atomic level. A few examples follow.

A mineral commonly colored by radiation-induced color centers is quartz in the form of dark-brown to black smoky quartz (Fig. 42). Although the absorption diminishes towards the near-infrared region, the amount of absorption in the visible region is enough to absorb most of the visible light resulting in a color close to black. If the amount of radiation damage is small, or if the crystal is thin, then some red and orange wavelengths will come through resulting in a brown color. The absorption is associated with the Al-content of the crystal and involves O^- (oxygen single minus ion). The atomistic interpretation of this spectrum remains incompletely understood (Weil 1984).

Colored diamonds owe their color to both minor components such as boron and nitrogen and to a variety of color centers. One of the color centers that arises from irradiation is the GR1 (general radiation 1) center shown in Figure 43. The spectrum is believed to arise from a carbon vacancy in the diamond induced by the irradiation. In addition to the broad absorption band, fine structure features in the spectrum corresponding to hindered rotational motion in the defect. Gemological laboratories that examine diamonds routinely obtain such spectra at LN_2 temperature which causes the fine structure to sharpen.

Topaz is commonly commercially irradiated to turn it blue for use as a gemstone. It also occurs in nature with a blue color. The absorption spectrum (Fig. 44) has not been related to any trace metal ion component, but is a direct product of the irradiation. The Al-O^--Al center involving the oxygen single minus ion is thought to be associated with the color, but the detailed cause of the absorption bands remains a matter of discussion (Rossman 2011).

Elbaite tourmaline is another mineral that commonly shows the effects of natural irradiation and which is irradiated in the commercial market for gemstones (Fig. 45). In this mineral, naturally occurring Mn^{2+}, when irradiated, is converted to Mn^{3+} by the natural flux of gamma rays (Reinitz and Rossman 1988). This process occurs in pegmatites which are rich in feldspar that contains weakly radioactive ^{40}K. Tens of millions of years of natural irradiation are required to bring about an intense color change. Other pegmatite minerals such

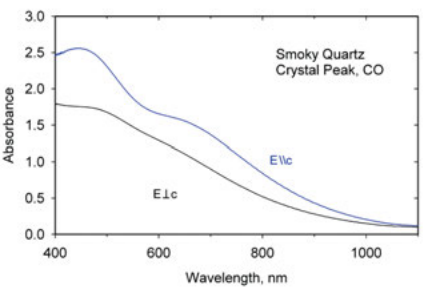


Figure 42. Smoky quartz associated with amazonite feldspar at Crystal Peak, Colorado, that shows multiple broad absorption features that are the result of natural irradiation. Plotted for 10 mm thickness.

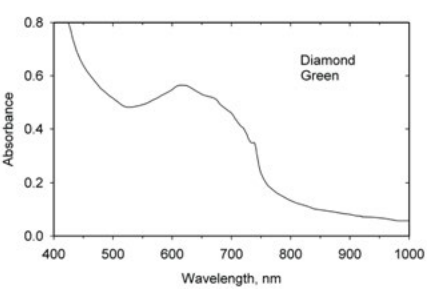


Figure 43. The room-temperature spectrum of a 3.0 mm thick green diamond showing a broad irradiation-induced absorption band centered about 650 nm.

EBSCOhost - printed on 2/13/2023 5:26 AM via . All use subject to https://www.ebsco.com/terms-of-use

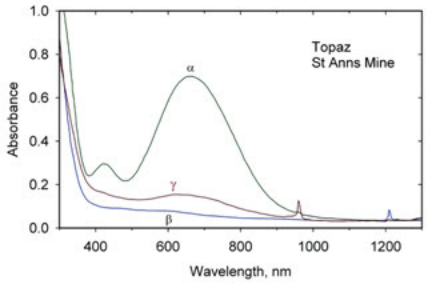


Figure 44. Spectrum of naturally irradiated blue topaz from the St Anns Mine, Zimbabwe, plotted as 10 mm thick. The narrow features are absorption from the OH in the crystal.

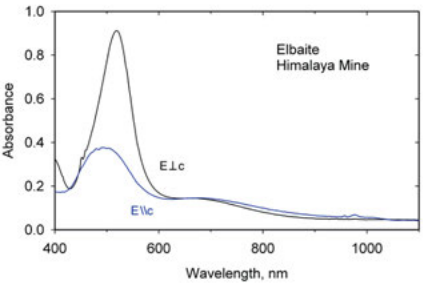


Figure 45. Spectrum of elbaite from the Himalaya Mine, Southern California, that has been artificially irradiated with gamma rays to increase the intensity of its color. Except for the absolute intensity of the features, the spectrum is identical to the spectrum of the naturally irradiated material. Prominent features are associated with the formation of Mn^{3+} from the irradiation of Mn^{2+} that naturally occurs in the crystal. Weak OH overtones occur near 980 nm. Plotted for 1.40 mm thickness.

as lead-containing potassium feldspar (amazonite variety), apatite, beryl (morganite variety) and spodumene (kunzite variety) are also commonly colored by natural ^{40}K irradiation.

VIBRATIONAL OVERTONES AND COMBINATIONS

Vibrational absorption is usually considerably narrower than the absorption from electronic transitions. Overtones of these motions and combinations of modes often show up in the spectra of minerals that contain water molecules or OH groups. Both water molecules and OH groups typically absorb in the 3500 cm^{-1} region. Their first overtone will be at about 7000 cm^{-1} which corresponds to about 1400 nm and the second overtone occurs at around 950 nm. Water bending occurs near 1600 cm^{-1}. The combination of water bending with a water stretching motion occurs around 5100 cm^{-1} (1600 + 3500 cm^{-1}) or 1950 nm. The exact wavelength of these features will vary with the hydrogen bonding state of the hydrous component.

These features are easily seen in the spectrum of beryl (Fig. 46) from Vldar Ukinsky, Ukraine. This particular sample has been heat-treated to make the blue aquamarine variety by removing the golden color component of the naturally-occurring crystals.

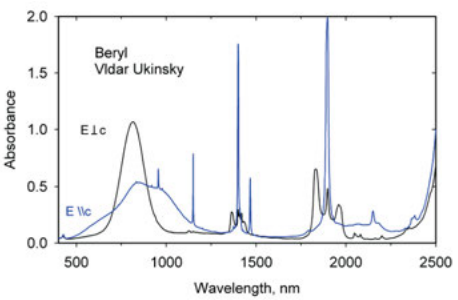


Figure 46. Beryl from Vldar Ukinsky, Ukraine, that displays numerous, sharp vibrational overtones and combination modes from water molecules. Iron absorption occurs in the 500-1200 region. 7.63 mm thick.

ARTIFACTS

Interference fringes

A problem that is often encountered while obtaining spectra is the presence of interference fringes which show up as regular variations in the intensity

EBSCOhost - printed on 2/13/2023 5:26 AM via . All use subject to https://www.ebsco.com/terms-of-use

of the spectrum that resemble sine waves (Fig. 38). They may arise from light that reflects from the back face of the crystal to the front face which, in turn, is reflected back in the direction in which light is propagating through the crystal. They may also arise from cracks or cleavages within the crystal, or even from the air gap between the crystal and the crystal holder. Their presence is dictated by the physics of optics, but there are strategies that can be used to minimize their presence. Anything that destroys the flatness of the crystal surface, or the index of refraction difference between the crystal and its surrounding medium (air or a glass slide, etc.) will minimize interference fringes. One surface of the crystal can be intentionally rounded to destroy its flatness. This works especially well for thicker crystals where the non-uniformity of the thickness does not introduce a significant error in quantitative intensity determinations. Alternatively, a surface can be lightly abraded to destroy the uniformity of the surface. Transparent, high-index liquids can be added to the surface of the crystal to destroy the index contrast. For crystals held on a supporting glass slide in microscope spectrometers, addition of a small amount of liquid such as water or glycerine between the crystal and the glass can prove helpful. The difficulty of the artifact is amplified when grating changes occur during scans over a wide wavelength range. The sudden discontinuity of the pattern at 600 nm in Figure 47 is the result of such a range change.

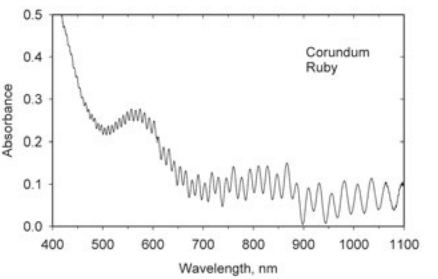


Figure 47. Interference fringes in the spectrum of the ruby variety of corundum produce periodic oscillations in the data.

Wood's grating anomaly

At certain wavelengths, sudden changes in the intensity of light diffracted by a grating can occur (Wood 1902). The magnitude of the change depends on the polarization of the light incident on the grating (Stewart and Gallaway 1962). If the orientation of the extinction direction of the crystal being studied is not aligned exactly with the polarizer, the resultant elliptically polarized light can produce artifacts in the spectrum that resemble narrow, weak absorption bands or sudden shifts in the baseline. If the spectroscopist is familiar with their instrument, such artifacts will be edited out of the final data. Occasionally, spectra with these artifacts have appeared in the literature.

TEMPERATURE AND PRESSURE DEPENDENCE

When crystals change temperature, the coefficient of thermal expansion demands that the length of metal-oxygen bonds will change, and perhaps, bond angles will change as well. These changes will influence the ligand fields surrounding metal ions and will result in changes in the wavelengths and bandwidths of spectra (Fig. 48). Such changes may occur anisotropically.

Likewise, when the external pressure is greatly increased, the metal-oxygen bonds and bond angles will change even if no phase change occurs. This, too, will result in a change in the ligand fields surrounding metal ions and will result in changes in the spectrum (Fig. 49). A similar change can occur in the luminescence spectrum of a phase when pressure is applied. The ruby pressure standard used in diamond cells (Silvera et al. 2007) is a direct application of this effect.

To illustrate the sensitivity of the optical absorption band position to changes in the metal-oxygen distance in a crystal, consider the case of Ti^{3+} dissolved in water in octahedral coordi-

EBSCOhost - printed on 2/13/2023 5:26 AM via . All use subject to https://www.ebsco.com/terms-of-use

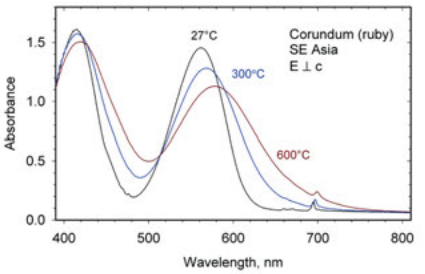


Figure 48. Temperature dependence of the $E \perp c$ orientation of Cr^{3+} in corundum (ruby variety).

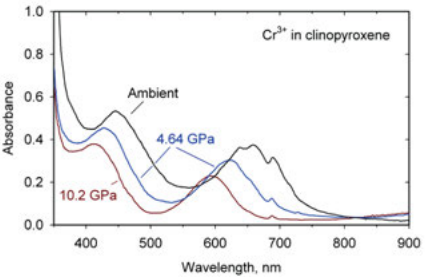


Figure 49. Pressure dependence of the unpolarized spectrum of Cr^{3+} in a 0.05 mm thick (010) slab of clinopyroxene from the Mir kimberlite pipe, Yakutia, Russia. From Taran et al. 2011.

nation with oxide ions as the species $Ti^{3+}(H_2O)_6$. This system has only one *d* electron in one of the t_{2g} orbitals. The electronic transition puts the electron in one of the higher-energy e_g orbitals where the energy separation between the t_{2g} and e_g orbitals is Δ. Crystal field theory tells us that the magnitude of Δ is proportional to $1/r^5$ where *r* is the metal-oxygen distance. The Ti-O distance is ideally 2.02 Å and the absorption band of Ti^{3+} dissolved in water is at about 20,300 cm^{-1} (493 nm). If we could compress the Ti-O bond by 1%, the absorption band would shift to 469 nm, and if we could compress the Ti-O band by 10%, the band would shift to 292 nm.

ABSORPTION BAND INTENSIFICATION

The intensities of certain metal ion absorption bands do not always scale with the concentration of the metal ion. Important example involves systems in which the concentration of Fe^{3+} is high or in which the Fe^{3+} ions are structurally paired. In these systems, antiferromagnetic interactions between Fe^{3+} ions provide a mechanism by which the intensity of absorption can increase dramatically. Such intensification has been observed by a number of authors (Krebs and Maisch 1971; Rossman 1975, 1976a,b; Bakhtin and Vinokurov 1978). This effect is related to the strength of the magnetic coupling between the pair of cations. Generally, shared O^{2-} ions lead to stronger magnetic coupling than shared OH^- ions. In favorable cases, the amount of absorption intensity enhancement can be more than an order of magnitude. The dark orange to red colors of many ferric iron minerals such as hematite (Rossman 1996) are caused by such interactions (Fig. 50). Iron in other oxides such as spinels is also subject to intensification (Andreozzi et al. 2001). Similar enhancement occurs in the d^5 Mn^{2+} system. Examples presented include galaxite, $MnAl_2O_4$ (Hålenius et al. 2007) and the helvite-genthelvite system, $(Mn,Zn)_4(Be_3Si_3O_{12})S$ (Hålenius 2011).

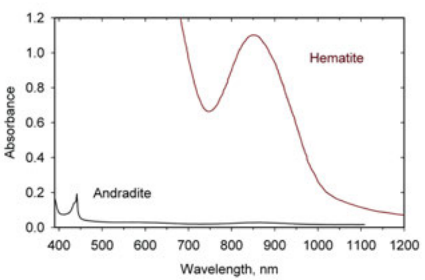


Figure 50. A spectrum that compares the intensity of the first Fe^{3+} absorption band near 860 nm in andradite garnet ($Ca_3Fe_2Si_3O_{12}$) and hematite (Fe_2O_3). In andradite, the Fe^{3+} ions are isolated from each other by intervening Ca and Si. In hematite, the Fe^{3+} ions are situated adjacent to each other where they experience magnetic interactions and intensification of the optical absorption bands. Spectra are presented such that both phases present an equal number of Fe^{3+} ions in the optical path.

EBSCOhost - printed on 2/13/2023 5:26 AM via . All use subject to https://www.ebsco.com/terms-of-use

The intensity of Fe^{2+} absorption bands (*d-d* transitions) can also be greatly enhanced by interactions with neighboring Fe^{3+} ions (Smith 1978; Amthauer and Rossman 1984; Mattson and Rossman 1987). This effect is in addition to the intervalence charge-transfer absorption which generates a new absorption feature. A detailed theoretical explanation of such enhancements has yet to appear.

Figure 51 shows three tourmalines that range from a blue elbaite with only Fe^{2+} through green elbaite with Fe^{2+} and a little Fe^{3+} to black dravite with significant amounts of both Fe^{2+} and Fe^{3+}. The noteworthy property is the comparative increase in the intensity of the $E \perp c$ spectrum compared to the $E \parallel c$ spectrum. In the lower spectrum of an elbaite with no Fe^{3+} the intensities of the Fe^{2+} bands in the 700 and 1200 nm regions are about the same in both polarizations. In the upper spectrum of a dravite with both Fe^{2+} and Fe^{3+}, there has been a remarkable increase in the intensity of the Fe^{2+} bands in the $E \perp c$ spectrum. In addition to the Fe^{2+} absorptions, the center spectrum shows an absorption band from Fe^{2+}-Ti^{4+} intervalence charge transfer at about 420 nm, and all spectra show OH overtones near 1400 nm.

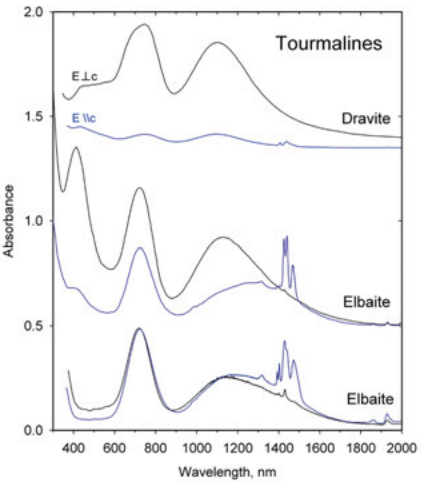


Figure 51. Tourmalines from bottom to top: blue elbaite from, Usakos, Namibia, plotted as 1.0 mm thick; center: dark green elbaite from northeastern Afghanistan plotted as 0.50 mm thick; top: black dravite from Sweeney Canyon, California, plotted as 0.02 mm thick.

COMPILATIONS OF MINERAL OPTICAL SPECTRAL DATA

The first edition of this chapter (Rossman 1988) presented an extensive list of references to published spectra of dominantly single-crystal mineral optical spectra emphasizing papers published after 1965 that deal with natural minerals. A greatly expanded and up-to-date, revised version of the original list with over 700 references is available at:

http://minerals.gps.caltech.edu/REFS/Index.html

Most of these references are now reasonably easy to find with on-line search programs such as SciFinder Scholar, Google Scholar, GeoRef, and Web of Science. The main exceptions are the references in the gemological literature that are not well-covered in the on-line search programs. Many spectra of the gem minerals have been presented in the literature from a variety of gemological organizations. Some of the literature can be accessed on the website of the Gemological Institute of America under the Article Topic –Color search.

http://www.gia.edu/gia-news-research

An online source of many gem spectra (but not always with oriented samples) is the Gemological Institute of America's gem project:

http://www.gia.edu/gia-gem-database

The extensive Russian language literature on mineral spectroscopy is under-represented in these lists, although the book by Platonov (1976) provides an entry into the extensive pre-1976 Russian literature primarily from the author's works and other Russian language papers. In addition, numerous mineral spectra and raw data, including data files for most of the spectra

EBSCOhost - printed on 2/13/2023 5:26 AM via . All use subject to https://www.ebsco.com/terms-of-use

in this chapter, are available at:

http://minerals.gps.caltech.edu/FILES/Visible/Index.html

The book by Burns (1970) remains the most comprehensive general introduction to the field of optical spectroscopy of minerals, with many examples of mineral spectra. The chapter by Burns (1985) serves as useful abbreviated introduction to the field. The book by Marfunin (1979) is a wide ranging introduction which goes more deeply into the theoretical aspects of mineral spectroscopy but which does not have many examples of actual data. Both Burns (1970) and Marfunin (1979) provide extensive lists of references to mineral spectra. Chapters in Strens (1976) are on optical spectra of minerals as are chapters in Berry and Vaughan (1985). Libraries of mineral spectra are available for the remote sensing community but do not include single crystal data.

The language of spectroscopy makes use of the terminology of group theory to describe individual orbitals, symmetry properties of molecular units, and individual electronic transitions. A variety of books from the chemical sciences discuss this nomenclature and the theory behind it, although none of these books is directed at mineralogical applications. Cotton (1971) is one of the most useful introductions to group theory from an inorganic perspective. The chapters by Wildner et al. (2004) in the European Mineralogical Union's *Spectroscopic Methods in Mineralogy* contain a detailed review of the theoretical concepts of crystal field theory which is used to understand the interaction of a metal ion's valence electrons with the atoms (ligands) that surround it.

An overview of color in minerals is presented by Nassau (1978). Nassau (2001) is a wide ranging introduction to color in solids including many examples of color and spectroscopy in minerals and gemstones. Several volumes of the *Reviews of Mineralogy and Geochemistry* series contain chapters devoted to the spectroscopy of specific mineral groups [volumes 2 (*Feldspars*, 2nd edition 1983), 7 (*Pyroxenes* 1980), 9a (*Amphiboles* 1981), 13 (*Micas* 1984), and 14 (*Microscopic to Macroscopic* 1985)].

CONCLUDING THOUGHTS

Originally, much of the interest in mineral spectroscopy was motivated by the desire to understand the origin of the color and beauty of minerals. It was further amplified by the desire to understand the sometimes spectacular changes seen in the color of minerals when observed in thin section with polarized light. Optical spectroscopy remains the indispensible tool for the study of color in minerals and continues to find wide application particularly in the study of the gem minerals.

Historically, there was also interest in determining the ratio of oxidation states of elements such as iron and manganese in minerals which furthered the desire to understand the quantitative aspects of mineral spectroscopy. It is certainly possible to derive quantitative information on the oxidation states of cations in crystals, but significant difficulties are associated with proper calibration of the methods. Today, the quantitative analysis aspects of site-specific analysis through optical spectroscopy have largely being replaced by other analytical methods, particularly by improved X-ray structural determinations. Improved analytical methods such as LA-ICP-MS can now more easily obtain elemental concentrations at low levels than can be obtained from optical spectroscopy with the attendant calibration and orientation issues. Nevertheless, optical spectroscopy does remains important in niche applications where the need to analyze the whole volume of a crystal exists, or where suitable oxidation state-specific alternative methods may not exist.

At this time, the single-crystal optical absorption spectra of a little over 100 mineral groups representing about 250 mineral species are available in print or online. They represent

EBSCOhost - printed on 2/13/2023 5:26 AM via . All use subject to https://www.ebsco.com/terms-of-use

the common rock-forming mineral groups and gemstones. This leaves on the order of 1000 colored, transparent minerals that have yet to be studied. A comparatively small number of these have been studied as powdered samples, but not as single crystals. Many of these unstudied phases are uncommon weathering products available only as tiny crystals. Many of these phases represent structures unknown in the widely practiced spectroscopy of metal ions and their coordination complexes in solutions. Their spectra may hold information important for the production of new pigments, for new electro-optic devices, or for new photocatalysts or for other unforeseen applications. Unless they are studied, we will never have this information. Clearly, much work remains to be done.

REFERENCES

Amthauer G, Rossman GR (1984) Mixed valence of iron in minerals with cation clusters. Phys Chem Miner 11:37-51

Andreozzi GB, Hålenius U, Skogby H (2001) Spectroscopic active $^{IV}Fe^{3+}$-$^{VI}Fe^{3+}$ clusters in spinel-magnesioferrite solid solution crystals: a potential monitor for ordering in oxide spinels. Phys Chem Miner 28:435-444

Bakhtin AI, Vinokurov (1978) Exchange-coupled pairs of transition metal ions and their effect on the optical absorption spectra of rock-forming silicates. Geokhimiya 1:87-95 (in Russian). Translation: Geochem Int 1079:53-60

Berry FJ, Vaughan DJ (1985) Chemical Bonding and Spectroscopy in Mineral Chemistry. Chapman and Hall, London

Burns RG (1970) Mineralogical Applications of Crystal Field Theory. Cambridge University Press, Cambridge.

Burns RG (1981) Intervalence transitions in mixed-valence minerals of iron and titanium. Ann Rev Earth Planet Sci 9:345-383

Burns RG (1985) Thermodynamic data from crystal field spectra. Rev Mineral 14:277-316

Burns RG, Clark MG, Stone AJ (1966) Vibronic polarization in the electronic spectra of gillespite, a mineral containing iron(II) in square-planar coordination. Inorg Chem 5:1268-1272

Chadwick KM, Rossman GR (2009) Orange kyanite from Tanzania. Gems Gemology 45:144-147

Cotton FA (1971) Chemical Applications of Group Theory. 2nd edition, J. Wiley, New York.

Dowty E (1978) Absorption optics of low-symmetry crystals - application to titanian clinopyroxene spectra. Phys Chem Miner 3:1773-181

Ertl A, Rossman GR, Hughes JM, Brandstätter F (2008) V^{3+}-bearing, Mg-rich strongly disordered olenite from a graphite deposit near Amstall, Lower Austria: A structural, chemical and spectroscopic investigation. Neues Jb Mineral 184:243-253

Faye GH (1972) Relationship between crystal-field splitting parameter, "Δ_{VI}", and M_{host}-O bond distance as an aid in the interpretation of absorption spectra of Fe^{2+}-bearing materials. Can Mineral 11:473-487

Gilinskaya LG, Mashkovtsev KI (1995) Centers of blue and green color in natural apatites according to EPR and optical-spectroscopy data. Zh Strukt Khim 36:89-101 (in Russian). Translation: J Struct Chem 36:76-86

Goldman DS, Rossman GR (1977) The identification of Fe^{2+} in the M(4) site of calcic amphiboles. Am Mineral 62:205-216

Goldman DS, Rossman GR (1978) Determination of quantitative cation distribution in orthopyroxenes from electronic absorption spectra. Phys Chem Miner 4:43-55

Hålenus U (2011) Absorption of light by exchange coupled pairs of tetrahedrally coordinated divalent manganese in the helvite-genthelvite solid solution. Periodico Mineral 80:105-111.

Hålenus U, Bosi F, Skogby H (2007) Galaxite, $MnAl_2O_4$, a spectroscopic standard for tetrahedrally coordinated Mn^{2+} in oxygen-based mineral structures. Am Mineral 92:1225-1231

Harris DC, Bertolucci MD (1978) Symmetry and Spectroscopy. Oxford University Press, New York

Hazen RM, Bell PM, Mao HK (1977) Comparison of absorption spectra of lunar and terrestrial olivines. Carnegie Inst Wash Yearbook 76:508-512

Hofmeister AM, Rossman GR (1983) Color in feldspars. Rev Mineral 2:271-280, 2nd edition

Hofmeister AM, Rossman GR (1984) Hofmeister AM, Rossman GR (1984) Determination of Fe^{3+} and Fe^{2+} concentrations in feldspar by optical and EPR spectroscopy. Phys Chem Mineral 11:213-224

Hofmeister AM, Rossman GR (1985) Exsolution of metallic copper from Lake County labradorite. Geol 13:644-647

Krebs JJ, Maisch WG (1971) Exchange effects in the optical-absorption spectrum of Fe^{3+} in Al_2O_3. Phys Rev B 4:757-769

Kulis J (1999) Trace Element Control on Near-Infrared Transparency of Pyrite. Master of Science Dissertation, New Mexico Institute of Mining and Technology, Socorro, New Mexico

Laporte O, Meggers WF (1925) Some rules of spectral structure. J Optic Soc Am Rev Sci Instrum 11:450-463

EBSCOhost - printed on 2/13/2023 5:26 AM via . All use subject to https://www.ebsco.com/terms-of-use

Manning PG (1977) Charge-transfer interactions and the origin of color in brown vesuvianite. Can Mineral 15:508-511
Mao HK, Bell PM (1973) Polarized crystal-field spectra of microparticles of the Moon. *In:* Analytical Methods Developed for Application to Lunar Sample Analyses. Am Soc Testing Materials STP 539:100-119
Mao HK, Bell PM, Virgo D (1977) Crystal-field spectra of fassaite from the Andra Dos Reis meteorite. Earth Planet Sci Lett 35:352-356
Marfunin AS (1979) Spectroscopy, Luminescence and Radiation Centers in Minerals. Springer Verlag, New York
Mattson SM, Rossman GR (1987) Fe^{2+}-Fe^{3+} interactions in tourmaline. Phys Chem Miner 14:163-171
Mattson SM, Rossman GR (1988) Fe^{2+}-Ti^{4+} charge transfer absorption in stoichiometric Fe,Ti minerals. Phys Chem Miner 16:78-82
Nassau K (1978) The origins of color in minerals. Am Mineral 63:219-229
Nassau K (2001) The Physics and Chemistry of Color: the Fifteen Causes of Color. 2nd edition. John Wiley and Sons, New York
Pan Y, Nilges MJ (2014) Electron paramagnetic resonance spectroscopy: basic principles, experimental techniques and applications to earth and planetary sciences. Rev Mineral Geochem 78:655-690
Platonov AN (1976) The Nature of the Color of Minerals. Scientific Publishers, Kiev (in Russian)
Reinitz IM, Rossman GR (1988) Role of natural radiation in tourmaline coloration. Am Mineral 73:822-825
Rossman GR (1974) Optical spectroscopy of green vanadium apophyllite from Poona, India. Am Mineral 59:621-622
Rossman GR (1975) Spectroscopic and magnetic studies of ferric iron hydroxy sulfates: Intensification of color in ferric iron clusters bridged by a single hydroxide ion. Am Mineral 60:698-704
Rossman GR (1976a) Spectroscopic and magnetic studies of ferric iron hydroxy sulfates: The series Fe(OH) $SO_4 \cdot nH_2O$ and jarosite. Am Mineral 61:398-404
Rossman GR (1976b) The optical spectroscopic comparison of the ferric iron tetrameric clusters in amarantite and leucophosphite. Am Mineral 61:933-938
Rossman GR (1988) Optical spectroscopy. Rev Mineral 18:207-254
Rossman GR (1996) Why hematite is red: Correlation of optical absorption intensities and magnetic moments of Fe^{3+} minerals. *In*: Mineral Spectroscopy: A tribute to Roger G. Burns. Dyar MD, McCammon *C*, Schaefer MW (eds) The Geochemical Society, Special Pub 5, p. 23-27
Rossman GR (2011) The color of topaz. Topaz, perfect cleavage. ExtraLapis 14:79-85
Rossman GR, Fritsch E, Shigley JE (1991) Origin of color in cuprian-elbaite tourmalines from Sao Jose de Batalha, Paraiba, Brazil. Am Mineral 76:1479-1484
Schmetzer K (1982) Absorption spectroscopy and color of vanadium(3+)-bearing natural oxides and silicates - a contribution to the crystal chemistry of vanadium. N Jb Mineral Abh 144:73-106
Silvera IF, Chijioke AD, Nellis WJ, Soldatov A, Tempere J (2007) Calibration of the ruby pressure scale to 150 GPa. Phys Stat Solidi B 244:460-467
Smith G (1978) Evidence for absorption by exchange-coupled Fe^{2+}–Fe^{3+} pairs in the near infra-red spectra of minerals. Phys Chem Miner 3:375-383
Stewart JE, Gallaway WS (1962) Diffraction anomalies in grating spectrophotometers. App Optics 1:421-429
Strens RJG (ed) (1976) The Physics and Chemistry of Minerals and Rocks. J. Wiley and Sons, New York
Tanabe Y, Sugano S (1954a) On the absorption spectra of complex ions I. J Phys Soc Japan 9:763-766
Tanabe Y, Sugano S (1954b) On the absorption spectra of complex ions II. J Phys Soc Japan 9:767-779
Taran MN, Ohashi H, Langer K. Vishnevskyy AA (2011) High-pressure electronic absorption spectroscopy of natural and synthetic Cr^{3+}-bearing clinopyroxenes. Phys Chem Mineral 38:345-356
Weil JA (1984) A review of electron spin spectroscopy and its application to the study of paramagnetic defects in crystalline quartz. Phys Chem Mineral 10:149-165
White WB, Moore RK (1972) Interpretation of the spin-allowed bands of Fe^{2+} in silicate garnets. Am Mineral 57:1692-1710
Wildner M, Andrut M, Rudowicz CZ (2004) Optical absorption spectroscopy in geosciences. Part I: Basic concepts of crystal field theory; Part 2: Quantitative aspects of crystal fields. In Beran A and Libowitzky E (eds) Spectroscopic Methods in Mineralogy, EMU Notes in Mineralogy 6, Budapest, Eötvös University Press, p 93-188
Wilson EB, Decius JC, Cross PC (1955) Molecular Vibrations. McGraw-Hill Book Company, Inc.
Wood RW (1902) XLII. On a remarkable case of uneven distribution of light in a diffraction grating system. Philos Mag Series 6, 4:396-402

EBSCOhost - printed on 2/13/2023 5:26 AM via . All use subject to https://www.ebsco.com/terms-of-use

Reviews in Mineralogy & Geochemistry
Vol. 78 pp. 399-446, 2014
Copyright © Mineralogical Society of America

Spectroscopy from Space

Roger N. Clark, Gregg A Swayze

U. S. Geological Survey
MS964, Box 25046 Federal Center
Denver, Colorado 80225, U.S.A.

rclark@usgs.gov
gswayze@usgs.gov

Robert Carlson

Jet Propulsion Laboratory, 183-601
California Institute of Technology
Pasadena, California 91109, U.S.A.

Robert.W.Carlson@jpl.nasa.gov

Will Grundy

Lowell Observatory
1400 West Mars Hill Road
Flagstaff, Arizona 86001, U.S.A.

W.Grundy@lowell.edu

Keith Noll

NASA/GSFC
MS 693
Greenbelt, Maryland 20771, U.S.A.

keith.s.noll@nasa.gov

ABSTRACT

This chapter reviews detection of materials on solid and liquid (lakes and ocean) surfaces in the solar system using ultraviolet to infrared spectroscopy from space, or near space (high altitude aircraft on the Earth), or in the case of remote objects, earth-based and earth-orbiting telescopes. Point spectrometers and imaging spectrometers have been probing the surfaces of our solar system for decades. Spacecraft carrying imaging spectrometers are currently in orbit around Mercury, Venus, Earth, Mars, and Saturn, and systems have recently visited Jupiter, comets, asteroids, and one spectrometer-carrying spacecraft is on its way to Pluto. Together these systems are providing a wealth of data that will enable a better understanding of the composition of condensed matter bodies in the solar system.

Minerals, ices, liquids, and other materials have been detected and mapped on the Earth and all planets and/or their satellites where the surface can be observed from space, with the exception of Venus whose thick atmosphere limits surface observation. Basaltic minerals (e.g., pyroxene and olivine) have been detected with spectroscopy on the Earth, Moon, Mars and some asteroids. The greatest mineralogic diversity seen from space is observed on the Earth and Mars. The Earth, with oceans, active tectonic and hydrologic cycles, and biological processes, displays the greatest material diversity including the detection of amorphous and crystalline inorganic materials, organic compounds, water and water ice.

1529-6466/14/0078-0010$05.00 http://dx.doi.org/10.2138/rmg.2014.78.10

EBSCOhost - printed on 2/13/2023 5:26 AM via . All use subject to https://www.ebsco.com/terms-of-use

Water ice is a very common mineral throughout the Solar System and has been unambiguously detected or inferred in every planet and/or their moon(s) where good spectroscopic data has been obtained.

In addition to water ice, other molecular solids have been observed in the solar system using spectroscopic methods. Solid carbon dioxide is found on all systems beyond the Earth except Pluto, although CO_2 sometimes appears to be trapped in other solids rather than as an ice on some objects. The largest deposits of carbon dioxide ice are found on Mars. Sulfur dioxide ice is found in the Jupiter system. Nitrogen and methane ices are common beyond the Uranian system.

Saturn's moon Titan probably has the most complex active extra-terrestrial surface chemistry involving organic compounds. Some of the observed or inferred compounds include ices of benzene (C_6H_6), cyanoacetylene (HC_3N), toluene (C_7H_8), cyanogen (C_2N_2), acetonitrile (CH_3CN), water (H_2O), carbon dioxide (CO_2), and ammonia (NH_3). Confirming compounds on Titan is hampered by its thick smoggy atmosphere, where in relative terms the atmospheric interferences that hamper surface characterization lie between that of Venus and Earth.

In this chapter we exclude discussion of the planets Jupiter, Saturn, Uranus, and Neptune because their thick atmospheres preclude observing the surface, even if surfaces exist. However, we do discuss spectroscopic observations on a number of the extra-terrestrial satellite bodies. Ammonia was predicted on many icy moons but is notably absent among the definitively detected ices with possible exceptions on Charon and possible trace amounts on some of the Saturnian satellites. Comets, storehouses of many compounds that could exist as ices in their nuclei, have only had small amounts of water ice definitively detected on their surfaces from spectroscopy. Only two asteroids have had a direct detection of surface water ice, although its presence can be inferred in others.

INTRODUCTION

The remote detection, identification, and mapping of materials using spectroscopy and imaging spectroscopy has been a rapidly advancing and maturing science over the last two decades, and promises significant advances into the future. Spectrometers and imaging spectrometers are now flying on many spacecraft throughout the Solar System, providing a wealth of new data that has led to many new discoveries. As of this writing, spectrometers and imaging spectrometers are in orbit or have recently flown past Mercury, Venus, Earth, Earth's Moon, Mars, several asteroids, Jupiter, Saturn, and on the way to Pluto. Aircraft-based sensors also play a key role in terrestrial imaging spectroscopy. This chapter will give a few examples of this very large and diverse field. The information is so vast, that the analogy for this chapter will be like taking a drink from Niagra Falls, thus we can cover only a small portion of the field. In order to limit the scope of this chapter, we limit discussions to spectroscopy of reflected solar radiation and thermally emitted light, and mostly exclude gamma-ray or radio wavelength spectroscopy. We only discuss remote detections across space (fly-by or orbiting spacecraft or in the case of the Earth, high altitude aircraft, above about 15 km). We exclude surface landers on other moons and planets.

Spectroscopy is a tool that has been used for decades to identify, understand, and quantify solid, liquid and gaseous materials, especially in the laboratory. In disciplines ranging from astronomy to chemistry, spectroscopic measurements are used to detect absorption features due to specific chemical bonds or electronic transitions, with detailed analyses used to determine the abundance and physical state of the detected absorbing species. Spectroscopic measurements have a long history in the study of the Earth and planets (e.g., Hunt 1977; Goetz et al. 1985; Pieters and Englert 1993; Clark 1999, Clark et al. 2003, 2007).

EBSCOhost - printed on 2/13/2023 5:26 AM via . All use subject to https://www.ebsco.com/terms-of-use

Reflectance and emittance spectroscopy of natural surfaces are sensitive to specific chemical bonds and transitions in materials, whether solid, liquid or gas. Spectroscopy has the advantage of being sensitive to both crystalline and amorphous materials, unlike some diagnostic methods, like X-ray diffraction. Spectroscopy's other main advantage is that it can be used up close (e.g., in the laboratory) to far away (e.g., to look down on the Earth, or up at other planets). Spectroscopy's historical disadvantage for materials identification is that it is sometimes too sensitive to small changes in the chemistry and/or structure of a material. The variations in material composition often cause shifts in the position and shape of absorption bands in the spectrum. Thus, with the vast variety of chemistry typically encountered in the real world, spectral signatures can be quite complex and sometimes unintelligible. However, that is now changing with increased knowledge of the natural variation in spectral features and the causes of the shifts. As a result, the previous disadvantage is turning into a huge advantage, allowing us to probe ever more detail about the chemistry of our natural environment (Pieters and Englert 1993; Clark 1999, Clark et al. 2003, 2007, 2013 and references therein).

Spectroscopic remote sensing from space, or high altitude aircraft requires the detection of reflected solar radiation at shorter wavelengths or thermally emitted light at longer wavelengths. The transition of predominantly reflected solar to predominantly emitted thermal radiation varies as a function of distance from the sun, and the object's albedo. The transition from reflected solar to emitted thermal emission occurs at approximately 1.5 μm at Mercury, 2.5 μm for our Moon, 3 μm for the Earth, 3.5 μm for Mars, ~6 μm for Jupiter's satellites, ~7 μm for Saturn's satellites, and beyond about 10 μm for the Neptune system (e.g., see Clark 1979).

Ice is probably the most abundance single mineral found in the Solar System. Ice technically refers to the mineral ice, solid H_2O, that is found naturally on the Earth. In the planetary sciences "ice" has become known as any volatile material that is frozen. Thus, in the planetary literature we discuss water ice, CO_2 ice, SO_2 ice, benzene ice, methane ice, etc. This chapter will also review such ices found on the surfaces of planets, their satellites, and small bodies in the Solar System.

The major elements that formed the solar system were hydrogen, carbon, nitrogen, and oxygen, often referred to as CHON material. When chemically combined, these elements produce molecules with low condensation temperatures—volatiles—with H_2O being the most refractory of these. Sulfur can also contribute to the volatile inventory, and the abundances of CHON + S material can be appreciable. The inferred molar elemental abundances present in the protoplanetary nebula, relative to hydrogen, of O, C, N, and S are 0.085, 0.036, 0.011, and 0.002, respectively (Anders and Grevesse 1989).

Under the reducing conditions produced by the presence of H_2, the expected closed-shell molecules are H_2O, CH_4, NH_3, and H_2S and these are observed as volatile gases or condensates in the atmospheres of the giant planets. Depending on thermal and chemical conditions in protoplanetary and protosolar nebulae, some or all of the above molecules, as well as those formed in more oxidizing conditions, will be incorporated in the forming satellites, comet nuclei, and dwarf planets. Examples of some stable volatiles formed under oxidizing conditions are CO, CO_2, N_2, and SO_2. Minor species may include CH_3OH, HCN, HCNO, etc. These volatiles condense in varying proportions at rates that are highly dependent on temperature and molecular interaction energies, ultimately forming the diverse ices that are found on outer solar system bodies.

In their pure states, molecules can condense in crystalline or amorphous forms, with crystalline compounds exhibiting a variety of polymorphs. The occurrence of a particular phase depends on the formation conditions, particularly the temperature and starting state (gaseous or liquid), and the subsequent thermal and irradiation history. For example, the freezing of liquid water produces hexagonal ice whereas amorphous, cubic, or hexagonal ice can be produced by condensation of the vapor at different temperatures.

EBSCOhost - printed on 2/13/2023 5:26 AM via . All use subject to https://www.ebsco.com/terms-of-use

Most minerals on and within solar system bodies are not pure, but contain other minerals or impurities. These mixed minerals can exist in many forms. The minor constituent can be randomly dispersed as isolated molecules within the crystalline or amorphous matrix (a solid solution). These molecules can be substitutional or interstitial, or trapped within defects or closed channels, sometimes existing as micro-atmospheres in voids (e.g., spectroscopically interacting O_2 molecules in H_2O ice, (Johnson and Jesser 1997; Loeffler et al. 2006) or CO_2 gaseous inclusions in minerals.

Closer to the sun, where temperatures in the solar nebula were hotter, rock forming minerals condensed in greater abundances. The solid surfaces of the terrestrial planets, Mercury, Venus, Earth and Mars are dominated by silicate and basaltic mineralogies and their weathering products.

DETECTION OF MINERALS AND THEIR SPECTRAL PROPERTIES

The main method for remotely detecting minerals and compounds is by studying sunlight reflected from the surface under study (reflectance spectroscopy), and/or the heat emitted in the thermal infrared (thermal emission spectroscopy). Materials absorb light at specific characteristic wavelengths, thus spectroscopy can be used to directly and unambiguously detect a compound (given sufficient spectral range, resolution and signal-to-noise ratio). Other methods of remote sensing, such as neutron absorption only sense the presence of atoms, so do not directly detect a specific chemical compound, and require instrumentation in close proximity to the surface (e.g., low orbit). Reflectance and emittance spectroscopy, however, can be used to probe surfaces both near and to the outer reaches of the Solar System from the Earth's surface as well as from spacecraft. See Clark (1999) for a review of the different types of transitions and vibrations that lead to absorption features in spectra.

While absorption features are diagnostic of material identities, it is the scattering processes that control the light returned from a surface to a detector. Scattering occurs from mineral-vacuum (or gas) interfaces, grain boundaries or crystal imperfections, or from discrete impurities mixed in the surface of a material such as a particulate coating. In order to make an unambiguous detection of a particular material there must be a high enough intensity signal returned to the detector over a sufficient spectral range and with sufficient resolution to resolve diagnostic spectral features. Figure 1 illustrates the issue of sufficient spectral resolution for three operational terrestrial sensors compared to a laboratory spectrum.

A significant problem in detecting materials from space using reflected sunlight is correction of remotely sensed data for effects of the solar spectrum, and absorption and scattering from any atmosphere between the surface and spectrometer. Figure 2 gives an example. Remotely sensing surface composition through such an atmosphere poses challenges. The atmospheric transmission and scattering effects must be accurately corrected, however the atmospheric models are still evolving and correction methods are complex. Clark et al. (2002, 2003) discusses various methods for correcting terrestrial imaging spectroscopy data. Transmission and aerosol scattering is a significant problem on only 4 bodies in the Solar System where we can observe the surface: Venus, Earth, Mars, and Titan, Venus being the most difficult. Model transmissions for the Earth, Mars and Titan are shown in Figure 3. The mid-infrared transmittance of the Earth's atmosphere is shown in Figure 4, which shows even less transmission, mostly due to absorption by water.

Another problem in remotely sensing compounds is that the apparent strength of spectral features changes with grain size of the material. Not only do the absorption features change shape, the overall shape of the spectrum can also change. This is illustrated in Figure 5 with Ice.

EBSCOhost - printed on 2/13/2023 5:26 AM via . All use subject to https://www.ebsco.com/terms-of-use

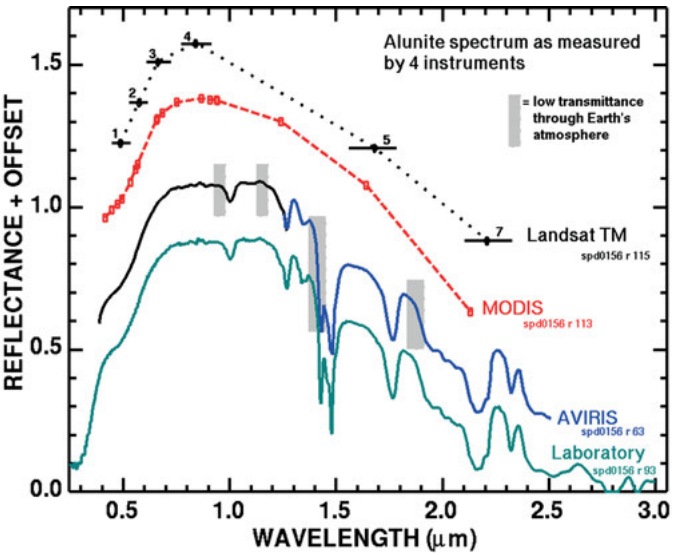


Figure 1. Comparison of sensors with different spectral resolutions. Landsat TM with 6 bands in the visible to near-infrared spectrum cannot resolve any absorptions typical in minerals. The MODerate resolution Imaging Spectrometer (MODIS) has enough spectral channels to barely resolve some spectral features in the visible portion of the spectrum, but not in the important near-infrared. The Airborne Visible and Infra-Red Imaging Spectrometer (AVIRIS), however, has sufficient spectral range and resolution to resolve many common absorption bands found in a wide variety of minerals and other compounds. The gray bands on the AVIRIS spectrum represent regions of the terrestrial atmosphere with strong absorptions. The spxnnnn entries are U.S. Geological Survey spectral IDs. Adapted from data in Clark (1999) and Clark et al. (2007).

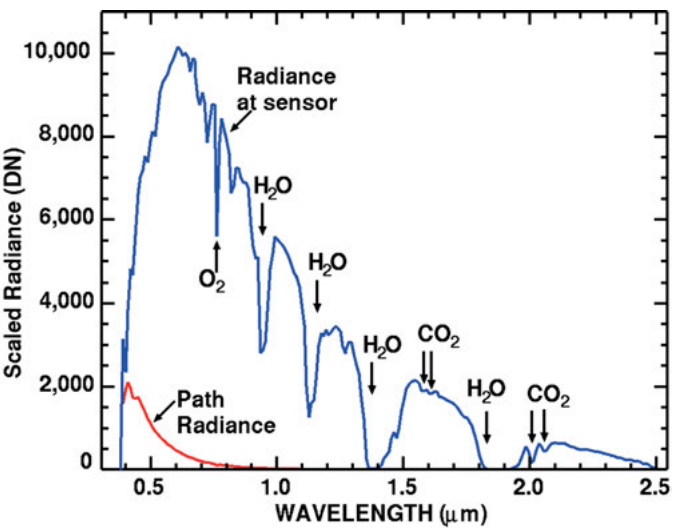


Figure 2. Observed signal of sunlight reflected from the Earth's surface measured at a height of 20 km by AVIRIS. The red line is the derived path radiance from the signal, light scattered by the atmosphere in the direction of the detector. To derive a surface reflectance spectrum, the solar spectrum, path radiance, and atmospheric absorption needs to be removed. DN stands for "Data Number" and is a relative scale. From Clark et al. (2002).

EBSCOhost - printed on 2/13/2023 5:26 AM via . All use subject to https://www.ebsco.com/terms-of-use

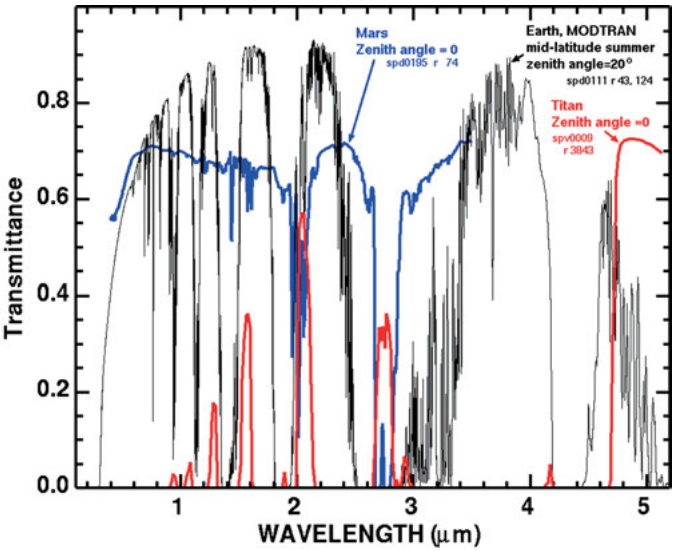


Figure 3. Model 1-way atmospheric transmission spectra for the Earth, Mars, and Titan. The dominant absorption in the Earth's atmospheric transmission is water vapor, with ozone providing the UV drop. The dominant absorption in Mars' atmospheric transmission is carbon dioxide and dust aerosol absorption plus scattering. The dominant absorption in Titan's atmospheric transmission is methane and hydrocarbon aerosol absorption plus scattering. Earth spectrum from Clark (1999), Mars from P. Irwin (personal communication, 1997), and Titan from Clark et al. (2010a). The transmission of Venus' atmosphere would be too low to register on this plot; transmission at 1 μm is <~ 0.00002 (Baines et al. 2000).

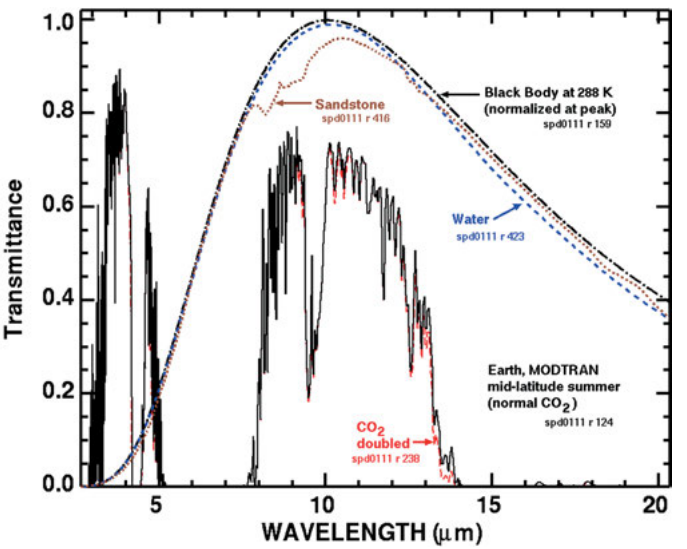


Figure 4. Atmospheric transmittance in the mid-infrared is compared to scaled grey-body spectra. Most of the absorption is due to water. Carbon dioxide has a strong 15-μm band, and the dotted red line shows the increased absorption due to doubling CO_2. Also shown is the black-body emission at 288 K and the grey-body emission from water and a sandstone scaled to fit on this transmittance scale. The water and sandstone curves were computed from reflectance data using: 1 - reflectance times a black-body at 288 Kelvin. Adapted from Clark (1999).

EBSCOhost - printed on 2/13/2023 5:26 AM via . All use subject to https://www.ebsco.com/terms-of-use

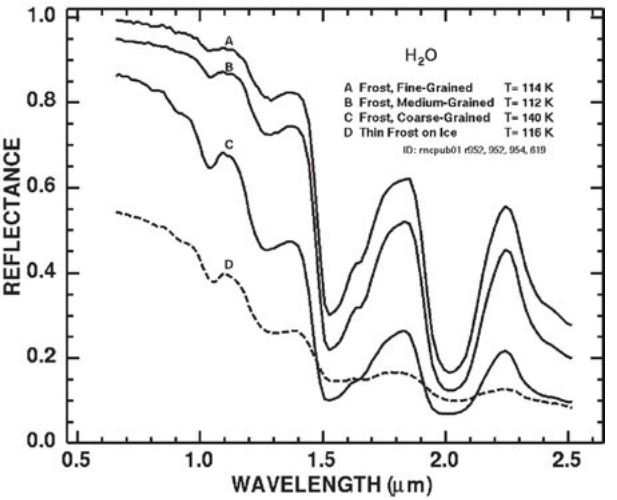


Figure 5. Illustration of changing ice absorption band shapes and strengths with grain size. The near-infrared spectral reflectance of A) a fine grained (~200 μm diameter) water frost, B) medium grained (~300 μm) frost, C) coarse grained (400-2000 μm) frost and D) an ice block containing bubbles and frost on the surface. The larger the effective grain size, the greater the mean photon path that photons travel in the ice, and the deeper the absorptions become. Curve D is very low in reflectance because of the large path length in ice but scattering from fine frost at the surface raises the reflectance. Adapted from data in Clark (1981), and Clark and Lucey (1984) with level corrections from the reflectance standard.

Spectroscopic characterization of minerals is well-covered in Pieters and Englert (1993), Clark (1999), and Clark et al. (2007), and references therein. Detection strategies are discussed in Clark et al. (2003) and references therein. Spectroscopy of ices are reviewed in Clark et al. (2013) and more briefly below.

Detection of a particular mineral on a planetary surface is only one aspect of understanding the geology and chemistry of the surface. Mapping the locations and geologic context greatly enhances our understanding of planetary surfaces, including their origin. Mapping solid and liquid compounds on a planetary surface is accomplished with imaging spectrometers. There are several types of imaging spectrometers. Two widely used diffraction grating types include whiskbroom scanners which collect spectra in a cross-track manner by using an oscillating mirror to sequentially reflect light from each spatial location in a scene to a spectrometer one pixel at a time, and pushbroom scanners which measure the spectra of all the pixels across an image simultaneously using an area array detector and the forward motion of the spacecraft. Whiskbroom scanner data are more easily calibrated because the same detector array measures the spectrum of every pixel in the scene, but dwell time on a given pixel is relatively short so images can be noisy. Pushbroom scanners have longer dwell times on each pixel so provide a less noisy image, but images are commonly plagued by along-track image artifacts caused by miscalibration of adjacent pixel array elements. See Goetz et al. (1985) and Clark et al. (2003) for more details. Whiskbroom systems include the NASA JPL classic Airborne Visible/Infrared Imaging Spectrometer (AVIRIS), flown on high altitude aircraft above the Earth (Green et al. 1990) and the NASA Visual and Infrared Mapping Spectrometer (VIMS) currently orbiting Saturn (Brown et al. 2005a). Pushbroom imaging spectrometers include the Compact Reconnaissance Imaging Spectrometer for Mars (CRISM) (Murchie et al. 2007) which is currently orbiting Mars on the Mars Reconnaissance Orbiter (MRO). Broadband imaging systems like the Mars Themis (Christensen et al. 2004) and HiRISE (McEwen et al. 2007) are not discussed because they are not spectrometers, nor imaging spectrometers.

EBSCOhost - printed on 2/13/2023 5:26 AM via . All use subject to https://www.ebsco.com/terms-of-use

MINERAL AND FROZEN VOLATILES SPECTRAL SIGNATURES

H_2O (ice)

Water ice phases and spectral features as a function of temperature are discussed in detail by Mastrapa et al. (2013). Ice forms multiple crystal structures, including cubic (Ic), hexagonal (Ih), and amorphous solids (Hobbs 1975 and references therein) which might be encountered on planetary surfaces in the solar system. The spectra of crystalline water ice (Fig. 5, and see Grundy and Schmitt 1998) display particularly broad absorptions because the water molecules are orientationally disordered. In hexagonal or cubic ice, the oxygen atoms are in a well-defined crystal structure, but the hydrogen bonds point randomly toward neighboring oxygen atoms.

Mastrapa et al. (2008) measured the optical constants of crystalline and amorphous ice from 20 to 120 K and reviewed formation conditions for amorphous versus crystalline water ice. Below about 135 K, amorphous ice is expected to condense from the vapor phase if the rate of growth is slow. Thus, we might expect amorphous ice to be present in the Jupiter system and beyond. However, as we will see, with the probable exception of the Jupiter system, where surfaces are being irradiated by particles caught in Jupiter's magnetic field, outer solar system surfaces are dominated by crystalline H_2O.

In amorphous ice, the absorptions shift to shorter wavelengths. The Fresnel peak near 3.1 μm also shifts to shorter wavelengths, and the temperature sensitive 1.65-μm absorption becomes very weak. See Clark et al. (2013).

SO_2 ice

SO_2, a colorless gas at room temperature, is a common terrestrial volcanic (and industrial) effluent and also present in Venus's atmosphere, possibly from recent volcanic activity. It is the major component emitted from Jupiter's volcanically active moon Io. SO_2 is a bent molecule of the form O-S-O and is a stable sulfoxide, with SO and S_2O being much less stable. Oxidation of SO_2 in the presence of H_2O produces sulfuric acid, evident in the Earth's atmosphere as acid rain and in Venus's atmosphere as the ubiquitous sulfuric acid clouds and haze.

SO_2 is more refractory than NH_3, it liquefies at ~263 K and freezes at ~200 K. Within the temperature range of 90 K to 120 K, appropriate for Jovian satellites, the SO_2 vapor pressure varies by five orders, from about 10^{-4} nbar to 10 nbar. SO_2 is amorphous when condensed at temperatures < 70 K, but crystallizes at temperatures > 70 K (Schmitt et al. 1994). Condensed SO_2 forms many different textures (Nash and Betts 1998). The condensation, evaporation, and metamorphism of pure SO_2 and mixed ices have been discussed by Sanford and Allamandola (1993).

Useful reviews of SO_2 properties by Schmitt et al. (1998b) and Nash and Betts (1998) are found in the Solar System Ices book (Schmitt et al. 1998a). Infrared and ultraviolet spectroscopy of SO_2 is summarized in Carlson et al. (2007).

Nitrogen ice (N_2)

Although nitrogen is cosmochemically abundant, the high volatility of N_2 ice makes it unstable except at extremely low temperatures characteristic of the outer edge of the Solar System. There are two low-pressure phases of N_2 ice. Above 35.61 K, the stable form is beta N_2 ice, an orientationally-disordered hexagonal close packing solid (Scott 1976). It is difficult to detect spectroscopically, because N_2 is a non-polar molecule in which vibrational absorptions are not easily excited. Only when an N_2 molecule collides with another molecule is a dipole moment temporarily induced, enabling a photon around 4.25 μm to excite its 1-0 fundamental vibrational mode (e.g., Shapiro and Gush 1966; Sheng and Ewing 1971). This collision-induced absorption is relatively broad (~100 cm^{-1} in wavenumber units), compared with gas-phase absorptions due to fixed dipole moments, owing to the modulation of the vibrational transition by the translational motion of the colliding pair. See Clark et al. (2013) for further review and references.

EBSCOhost - printed on 2/13/2023 5:26 AM via . All use subject to https://www.ebsco.com/terms-of-use

Hydrocarbons and other ices

Hydrocarbons are a diverse category of organic compounds, comprising numerous families without heteroatoms and with functional groups of solely hydrogen and carbon atoms. The simplest hydrocarbons are the alkanes – singly bonded molecules with no reactive functional groups. Hence, they tend to combust at relatively high temperatures, even though they are composed entirely of low atomic weight atoms, and have a generic chemical formula of C_nH_{2n+2}. If the carbon backbone contains a C-C double bond, the hydrocarbon is termed an alkene, and it has a formula of C_nH_{2n} (e.g., propene, C_3H_6); with a C-C triple bond, it is called an alkyne whose formula is C_nH_{2n-2} (e.g., propyne, C_3H_4). In the singly bonded alkanes, hydrogen atoms will bond to all the remaining positions on the carbon atom, and they are known as saturated hydrocarbons. Unsaturated hydrocarbons then, are those with doubly or triply bonded carbon atoms, and they will have less than their 'full' complement of hydrogen atoms. Together, these straight (or branched) chain hydrocarbons are known as 'aliphatic' compounds, and also include such derivatives as fatty acids (Wade 2005).

In general, spectra of different families share different spectral characteristics while spectral properties are similar within a family (also called group or series). For example, Figure 6 shows spectral differences among ices in the alkane, alkene, and alkyne groups from Clark et al. (2009). In alkanes, the C-H stretch fundamental occurs near 3.4 μm, whereas in the C-C double bonded alkenes, the C-H stretch shifts closer to 3.2 μm, and in the C-C triply bonded alkynes, the C-H stretch shifts to nearly 3.0 μm (Fig. 6).

The carbon skeleton can close in on itself in two ways: by creating a ring of singly-bonded carbon atoms of any length equal to or greater than three (cycloalkanes, known as alicyclic hydrocarbons), *or* by the overlapping of p orbitals from adjacent carbon atoms into pi (π) bonds to create a benzene ring (C_6H_6). The benzene ring with overlapping *p* orbitals is particularly stable, and forms the basis of the aromatic hydrocarbon family.

Most organic molecules are infrared active, displaying absorption features associated with stretching and bending vibrations. For example, the C-H stretch fundamental of aromatic

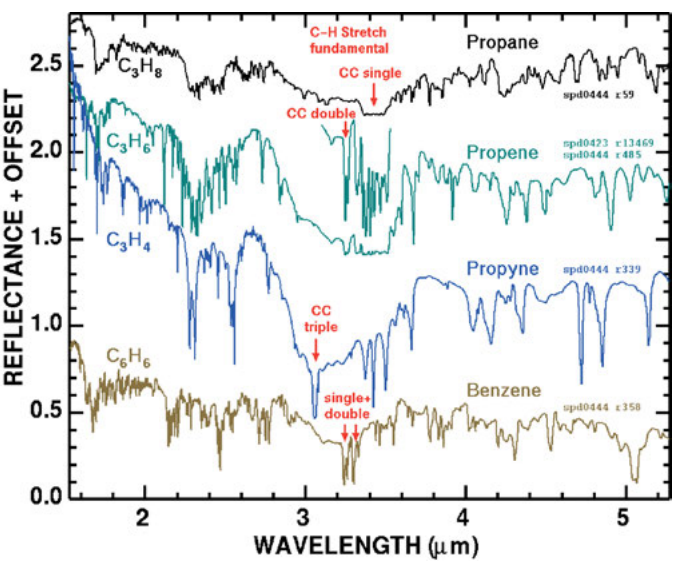


Figure 6. Reflectance spectra of propane, propene, propyne and benzene ices. From Clark et al. (2009).

EBSCOhost - printed on 2/13/2023 5:26 AM via . All use subject to https://www.ebsco.com/terms-of-use

hydrocarbons occurs near 3.3 μm (Fig. 6) and a bending mode absorption has been used to detect benzene ice on Saturn's moon Titan. Because these transitions are specific to the atoms and their chemical bonds, and are similar regardless of the type of larger molecule within which they are contained, an examination of the IR spectrum will reveal an enormous amount of information about an unknown compound (e.g., as seen in Fig. 6). Clark et al. (2009) observed that the spectral complexity of organic ices first increases as molecular weight increases, then decreases at higher molecular weights. The loss of spectral structure at high molecular weights is probably due to many overlapping absorptions averaging out small details.

Methane ice (CH_4)

Methane deserves special attention as the smallest and simplest alkane, as well as being the hydrocarbon most widely observed as an ice on solar system bodies. It is readily detected spectroscopically by means of numerous overtones and combinations of four fundamental vibrational transitions. These are a symmetric mode $\nu_1(A_1)$ at 2914 cm^{-1} (3.43 μm), a doubly degenerate $\nu_2(E)$ bending mode at 1526 cm^{-1} (6.55 μm), and triply degenerate stretching $\nu_3(F_2)$ and bending $\nu_4(F_2)$ modes at 3020 and 1306 cm^{-1} (3.31 and 7.66 μm), respectively (Grundy et al. 2002). Two different condensed phases occur at zero pressure. At temperatures below 20.4 K, CH_4 exists as a cubic crystal, whereas above that temperature, it loses its orientational order and long-range coordination, resulting in broadened bands similar to (but not identical to) those of liquid methane (e.g., Ramaprasad et al. 1978; Martonchik and Orton 1994). Temperature-dependent spectra have been measured for methane ice between 0.7 and 5 μm, revealing subtle changes with temperature that offer an as-yet unexploited potential for remote sensing of CH_4 ice temperatures (Grundy et al. 2002). Methane molecules dispersed in nitrogen ice exhibit slightly different spectral behavior, characterized by subtle wavelength shifts toward blue wavelengths as well as the loss of a weak transition at 1.69 μm (Quirico et al. 1997b). This property provides a way to remotely distinguish diluted from pure CH_4, as well as the potential to detect smaller quantities of nitrogen ice than can be readily detected through observation of the much weaker N_2 ice absorptions, with specific applications discussed later in this chapter.

MINERALS AND COMPOUNDS IN THE SOLAR SYSTEM DETECTED WITH SPECTROSCOPY

We will now discuss the detections of minerals and other compounds on planets and their satellites in our Solar System.

Terrestrial planets

Mercury. Vilas et al. (2012), Izenberg et al. (2012), and Riner and Lucey (2012) have searched for spectral features in the MErcury Surface, Space Environment, GEochemistry, and Ranging (MESSENGER) spacecraft data of the planet Mercury. To date, no plausible spectral features for identifying mineralogy, for example, pyroxene absorptions like those seen on the Moon have been found. It appears that the surface of Mercury is intensely space-weathered, where the surface minerals are partially destroyed, leaving rinds enriched in nano-phase metallic iron. See Hapke (2001) and Chapman (2004) for more on terrestrial space weathering, and Clark et al. (2012) for space weathering effects in the outer solar system.

Venus. Venus has a thick highly scattering atmosphere, making it the most difficult surface to be detected from space (excluding Jupiter, Saturn, Uranus, and Neptune whose surfaces, if they exist are impossible to see with UV to far infrared light). Three spacecraft have detected thermal emission from the surface using near-infrared wavelengths: Galileo NIMS (Carlson et al. 1991), Cassini VIMS (Baines et al. 2000), and Venus Express VIRTIS (Müller et al. 2008, Titov et al. 2009 and references therein). Baines et al. (2000) showed that it could be possible to use a few windows in the Venetian spectrum to detect broad electronic absorptions due to iron

EBSCOhost - printed on 2/13/2023 5:26 AM via . All use subject to https://www.ebsco.com/terms-of-use

in surface minerals and Hashimoto et al. (2008) have used these windows and suggested felsic materials in Venus's highlands.

Earth. The Earth is the only planet whose temperature is near the melting point of water where both liquid and solid water exists on the surface. This condition enables a complex hydrologic cycle of both solid and liquid water eroding, reshaping and weathering the surface. Active plate tectonics recycles crustal minerals, and creates active volcanism which leads to a variety of important mineral-forming conditions. Over three thousand minerals have been found naturally occurring on the Earth (e.g., Fleischer and Mandarino 1995). Dozens of minerals have been detected at the Earth's surface using spectroscopy from high-altitude aircraft (e.g., the NASA JPL Airborne Visible/Infrared Imaging Spectrometer, AVIRIS), commercial aircraft spectrometers, and spacecraft. The Earth's high carbon and nitrogen environment, energy sources, and hydrologic cycle provide a unique surface composition with abundant water, organic compounds, and life. The Earth's surface is dominated by liquid water, solid water, vegetation, and, in some locations, minerals in exposed rocks and soils.

While there are many imaging spectrometers on the way to, or have recently flown by or orbited, or are currently orbiting planets and satellites throughout the Solar System, very oddly there is only one (non-military) true imaging spectrometer in orbit around the Earth, the aging EO-1 Hyperion system (e.g., Barry et al. 2001). Because the Hyperion instrument is relatively old and its near-infrared performance is significantly lower than that of aircraft systems, many studies rely on systems like the NASA JPL Airborne Visible/Infrared Imaging Spectrometer (AVIRIS) system (Green et al. 1990) and other commercial systems which fly at lower altitudes.

The number of terrestrial applications of spectroscopy from space or aircraft is stunning, ranging from mineral mapping (e.g., Clark et al. 2003 and references therein) as shown in Figures 7a and 7b, acidic mine drainage and mineralization impact (e.g., Swayze et al. 2000), ecosystems mapping, vegetation species and chemistry (e.g., Kokaly et al. 2003; Clark et al. 2003; Ustin et al. 2009 and references therein), ice and snow mapping, including snow grain size and snow-water-vegetation mixtures (e.g., Clark et al. 2003; Painter et al. 2003 and references therein), mapping chlorophyll in water (Clark et al. 2003; Clark and Wise 2011), assessments of environmental disasters (the World Trade Center Disaster: Clark et al. 2001, 2006; the 2010 Gulf of Mexico Deepwater Horizon oil spill: Clark et al. 2010b), and detection of fires/thermal hot spots through thick smoke, determining temperature and sub-pixel areal extent (Clark et al. 2003, 2006). Remote sensing had been tried for decades to derive a method to determine the amount of oil on the ocean's surface without much success. But in the most recent disaster, the Gulf of Mexico 2010 oil spill, by using absorption features in oil and the spectral resolution of AVIRIS, Clark et al. (2010b) simultaneously solved for the oil:water ratio of intimate mixtures (e.g., water-in-oil emulsions), thickness of the mixture and their sub-pixel areal fraction to derive oil volume per pixel. Such unmixing is only possible using the many wavelengths provided by a visible to near-infrared imaging spectrometer.

The Earth's Moon. Water ice is thought to exist in the permanently shadowed craters on the moon and neutron spectrometer data from Lunar Prospector (Feldman et al. 1998, 2000, 2001) showed that hydrogen is present in the lunar polar regions. More recently Clark (2009), Pieters et al. (2009), and Sunshine et al. (2009) reported that adsorbed water is extensive in the lunar surface raising the likelihood that some of it has migrated and is trapped in the polar regions. Coleprete et al. (2010) reported detection of water vapor and water ice in the ejecta from the NASA LCROSS impact into South Pole crater Cabeus A. They also claim detection of other volatile compounds. Paige et al. (2010) reported temperatures as low as 38 K in Cabeus A, where many volatile compounds might exist as ices.

The Chandrayaan-1 spacecraft with the Moon Mineralogy Mapper (M^3) is the only imaging spectrometer to orbit the Moon covering the reflected solar spectral range. The M^3 instrument

EBSCOhost - printed on 2/13/2023 5:26 AM via . All use subject to https://www.ebsco.com/terms-of-use

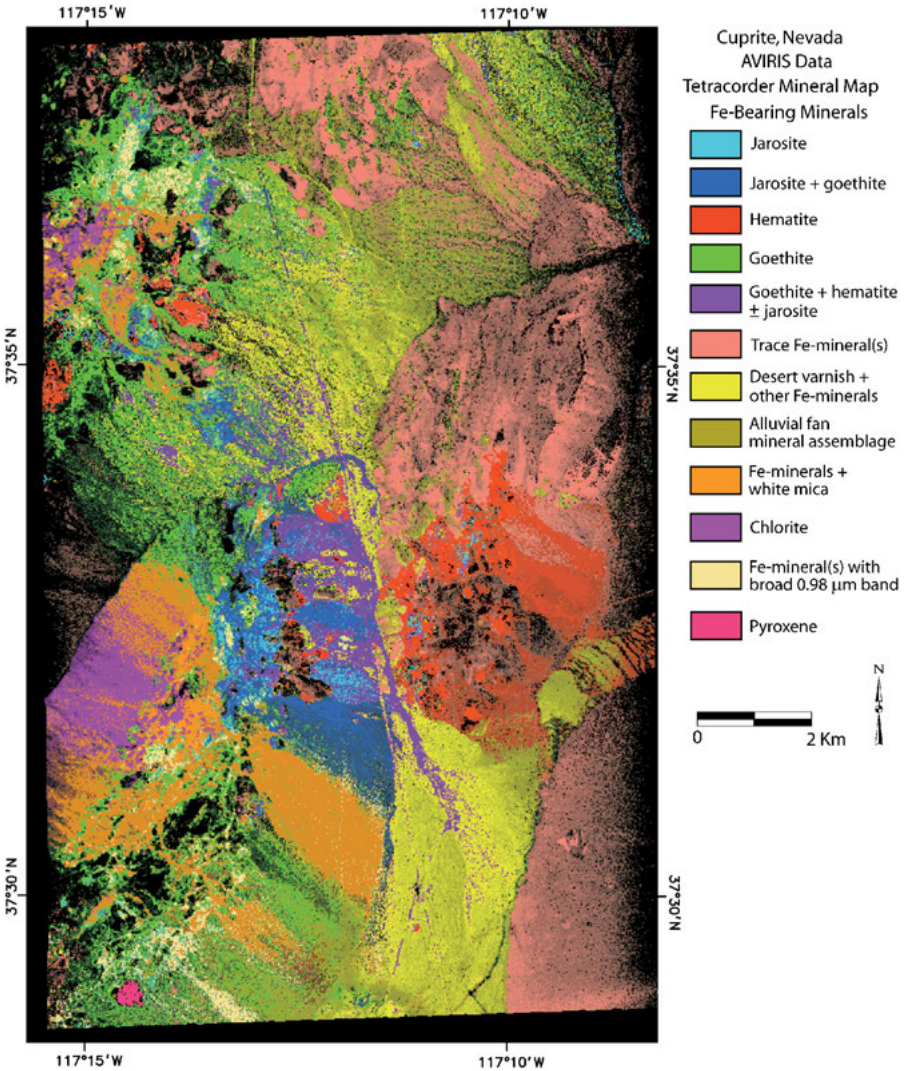


Figure 7. (a) Imaging spectroscopy mapping results from AVIRIS imaging spectrometer data over Cuprite, Nevada for absorptions in the 1-µm spectral region due to Fe^{2+} or Fe^{3+}. All the Fe^{2+} - Fe^{3+} absorptions overlap making separation difficult. Yet through spectroscopic analysis, not only can the minerals be distinguished, but mixtures could be distinguished based on the shape of the overlapping absorption features. From Swayze et al. (2003) with modifications.

has been used to detect and map a variety of minerals on the Moon, including the pyroxene solid solution series, olivines, feldspars and spinels (e.g., Pieters et al. 2011 and references therein). Kramer et al. (2011) showed an interesting link between the enigmatic lunar swirls which seem to lack hydroxyl that occurs in the surrounding rocks and soils.

Mars. Orbital high spectral resolution mapping of Mars over the last two decades with the Thermal Emission Spectrometer (TES) on Mars Global Surveyor (Christiansen et al. 1992), Observatoire pour la Minéralogie, L'Eau, les Glaces et l'Activitié (OMEGA) on Mars Express

EBSCOhost - printed on 2/13/2023 5:26 AM via . All use subject to https://www.ebsco.com/terms-of-use

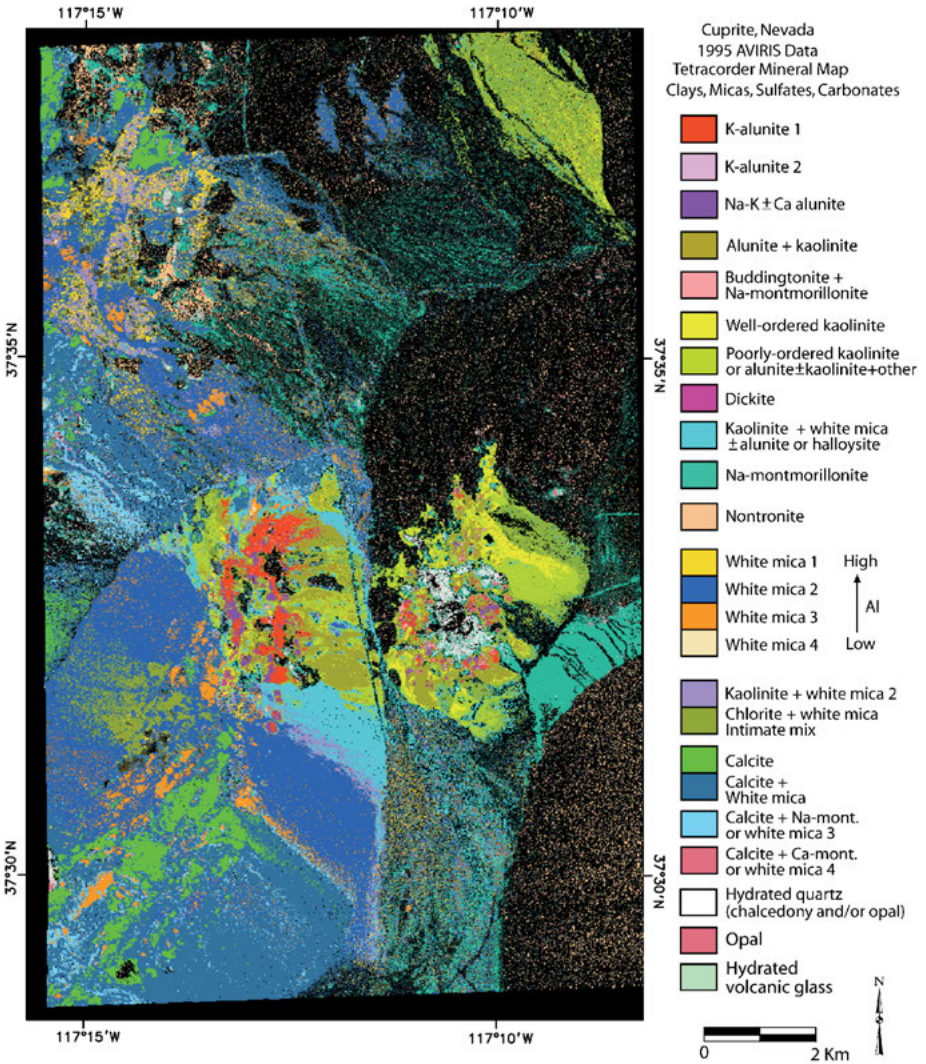


Figure 7. (b) Imaging spectroscopy mapping results from AVIRIS imaging spectrometer data over Cuprite, Nevada. The results distinguish kaolinite, alunite, carbonate, mica and other minerals, separate kaolinite from alunite-dominated areas, and also indicate where both occur as mixtures. From Swayze et al. (2003) with modifications.

(Bibring et al. 2004a), and the Compact Reconnaissance Imaging spectrometer for Mars (CRISM) on the Mars Reconnaissance Orbiter (Murchie et al. 2007) has led to numerous discoveries of mineral phases on the surface. One of the main goals that these imaging spectrometer share is the search for minerals formed during the early part of Martian history when water existed temporarily at the surface and for longer periods at depth. The spectral signatures of minerals frequently provide information about their environment of formation. Some minerals hint at metamorphic processes caused by elevated temperature and pressure caused by impacts. Clays and evaporites require water to form and are sensitive to formative pH conditions that can influence the preservation of fossils. Kaolin group minerals and the sulfate mineral alunite

EBSCOhost - printed on 2/13/2023 5:26 AM via . All use subject to https://www.ebsco.com/terms-of-use

may indicate the past presence of hydrothermal activity around hot spring deposits or acidic paleolakes. In this way, spectroscopists can use orbitally detected minerals as proxies to focus rover missions on the most promising sites in the search for evidence of past life.

During its operation from 1996 to 2006 the TES interferometer, which measured mid-infrared wavelengths for 3 km pixels on the surface, was used to discover concentrations of hematite in Meridiani Planum (Christensen et al. 2000), leading to its selection as a landing site for the Mars Exploration Rover Opportunity. Other mineralogic discoveries include olivine in Nili Fossi (Hoefen et al. 2003), globally distributed pyroxene (Christensen et al. 2001), and possibly carbonate (Bandfield et al. 2003) and zeolite minerals (Ruff 2004) distributed globally in the Martian dust. Originally, Christensen et al. (2001) thought TES data indicated the presence of basalt in the southern highlands and more silica-rich andesite in the northern plains. Wyatt and McSween (2002) argued that these more silica-rich spectral detections are actually weathered basalts with thin coatings of silica glass. Nevertheless, TES may have revealed the presence of rare exposures of granitoid rocks in the central uplifts of two adjacent craters (Bandfield et al. 2004) suggesting the presence of mechanisms that can produce highly differentiated magmas.

OMEGA led the way in orbital visible – near infrared spectroscopic mineral discoveries on Mars with its typical 1-2 km pixel resolution. Detailed variations in Fe-pyroxene distribution were documented by Mustard et al. (2005). Gendrin et al. (2005) identified the monohydrated Mg-sulfate kieserite in layered deposits on the surface while gypsum-rich sand dunes were identified by Langevin et al. (2005) at circumpolar latitudes. Poulet et al. (2005) observed sparsely distributed phyllosilicates such as montmorillonite, Fe/Mg smectite, and nontronite consistent with an early stage of neutral to alkaline Martian hydrologic activity. Based on these and other mineral discoveries, Bibring et al. (2006) recognized several eras of mineralogic evolution on Mars: the "phyllocian" (~4.5 to 3.8 billion years ago) where aqueous alteration at more neutral pH formed phyllosilicates in the oldest terrain, the "theiikian" (~3.8 to 3.3 billion years ago) where sulfates were formed in a more acidic environment, and the "siderikian" (~3.3 billion years ago to the present) where anhydrous ferric oxides formed from slow weathering primarily in the absence of liquid water.

CRISM, the latest orbital visible-near infrared spectrometer to orbit Mars, is a pushbroom imaging spectrometer that has two data collection modes: a targeted hyperspectral mode that measures light from 0.36 to 3.92 μm over 544 spectral channels at a spatial resolution up to 18 m per pixel, and a multispectral imaging mode that collects subsets (e.g., 72, 94, or 262) of its 544 channels at a spatial resolution of 100 to 200 m per pixel (Murchie et al. 2007). The hyperspectral mode produces full spatial resolution 10 × 10 km hourglass-shaped images with 18 m pixels or half spatial resolution 10 x 20 km images with 36 m pixels. In targeted mode, CRISM spectral sampling is approximately 6.5 nm. CRISM is gimbaled so it can swivel to perform continuous spectral measurements on a target while the spacecraft flies over the location. This allows higher spatial and spectral resolution measurements to be obtained with better signal-to-noise ratios. Gimbaling also allows acquisition of up to 11 images of the same target at varying emission angles during an overpass to facilitate separating surface absorptions from atmospheric ones. Recently, CRISM began acquiring targeted hyperspectral images with along-track overlap to produce images with 3-12 m pixel resolution over the most interesting areas (e.g., rover sites).

CRISM data can be calibrated to apparent reflectance by first converting the data from instrument units to I/F (the ratio of the reflected intensity to the incident intensity of sunlight), next photometrically correcting it, then assuming Lambertian scattering applies, dividing it by the cosine of the incidence angle, and lastly correcting it for atmospheric gas absorptions by dividing by a scaled atmospheric transmission spectrum of Olympus Mons as explained in Mustard et al. (2008). Image noise can then be reduced using a filtering algorithm that

EBSCOhost - printed on 2/13/2023 5:26 AM via . All use subject to https://www.ebsco.com/terms-of-use

replaces outlier pixels in the spectral and spatial dimensions of the image cube (Parente 2008). Remaining noise is further reduced in each column by dividing individual pixel spectra by a spectral average calculated from pixels lacking narrow vibrational absorptions from that column. Alternatively, a DISORT-based radiative transfer model can be used to convert I/F data to surface Lambert albedo resulting in spectra nearly free of atmospheric gas artifacts (McGuire et al. 2008). This last method is compute intensive so has been applied to only a select group of CRISM scenes.

CRISM has allowed planetary scientists to leverage its fine pixel resolution to identify, in unprecedented detail, an even broader array of carbonates, phyllosilicates, opaline silica, sulfates, and zeolites on the Martian surface. Ehlmann et al. (2008) identified Mg-carbonate in the Nili Fossae region formed by alteration of olivine by hydrothermal fluids or near-surface water that were not destroyed by more acidic conditions later in Martian history. A number of researchers (Murchie et al. 2009; Mustard et al. 2008; Bishop et al. 2008; Noe Dobrea et al. 2010) have noted that extensive phyllosilicate-rich layers, in some cases hundreds of meters thick, blanket old eroded highland areas. At the highest spatial resolution, these layers resolve in places into a lowermost Fe/Mg-smectite unit, a middle montmorillonite unit, and an upper kaolinite-rich unit suggestive of a weathering profile as conditions became more acidic with time. Curiosity, the Science Laboratory rover, successfully landed in and has begun exploring Gale Crater where CRISM has identified diverse phyllosilicate and sulfate mineralogy in a 5 km high pile of layered rocks believed to have recorded climatic conditions during the first billion years of Martian history (Milliken et al. 2010). Gale crater is 152 km in diameter and is just 5º south of the equator. Stratigraphic exposure in the central mound is more than twice that of the Earth's Grand Canyon (Thomson et al. 2011). The rover will traverse the central mound examining the lowermost section and then upper portion to determine if these sediments record the progressive "drying out" of Mars.

Ehlmann et al. (2009) summarizes spectral evidence for nontronite, Mg-rich smectite, chlorite, prehnite, serpentine, kaolinite, K-mica, opaline silica, Mg-carbonate, and the Na-zeolite analcime in and around the Nili Fossae region. They suggest these minerals may indicate that low-grade metamorphism or hydrothermal aqueous alteration has occurred in this region in the past. Milliken et al. (2008) identified opaline silica on Mars based on CRISM spectra that were initially confused with the Al-rich smectite montmorillonite. Under terrestrial conditions opal has a broader 2.2-μm absorption compared to that of montmorillonite (Fig. 8). But under simulated Martian conditions weakly hydrogen bonded water normally present under relatively humid terrestrial conditions is lost causing the 2.2-μm absorption to narrow so it forms a better spectral match to CRISM spectra of widespread Martian surface rocks. Ehlmann et al. (2011) argue that spectroscopic evidence of minerals from assemblages formed under anoxic high temperature conditions, a high ratio of primary to secondary minerals, and observed stratigraphic relations indicate substantial amounts of clay formed by hydrothermal groundwater circulation and that cold, arid conditions with only transient surface water existed at the surface since the early Noachian period nearly 4 billion years ago. This explanation diminishes the need for an atmosphere thick enough to support persistent liquid water and clay formation by near-surface weathering (Bibring et al. 2006; Ehlmann et al. 2011).

Sulfate deposits on Mars are similarly detectable. Bishop et al. (2009) identified szomolnokite, a monohydrated Fe-sulfate in light-toned mounds within Valles Marineris and hydrated silica with hydroxylated ferric sulfate on the surround plateau. Lichtenberg et al. (2010) noted that a wide expanse of hydroxylated ferric sulfate underlies what is probably a layer of szomolnokite deposited as part of an evaporitic sequence in Arma Chaos. Several workers (Farrand et al. 2009, Milliken et al. 2008) have identified the yellow Fe-sulfate hydroxide jarosite in areas where water may have been present. Wray et al. (2011) used CRISM to map the distribution of a bathtub-ring of sulfates (i.e., gypsum, poly- and mono-hydrated

EBSCOhost - printed on 2/13/2023 5:26 AM via . All use subject to https://www.ebsco.com/terms-of-use

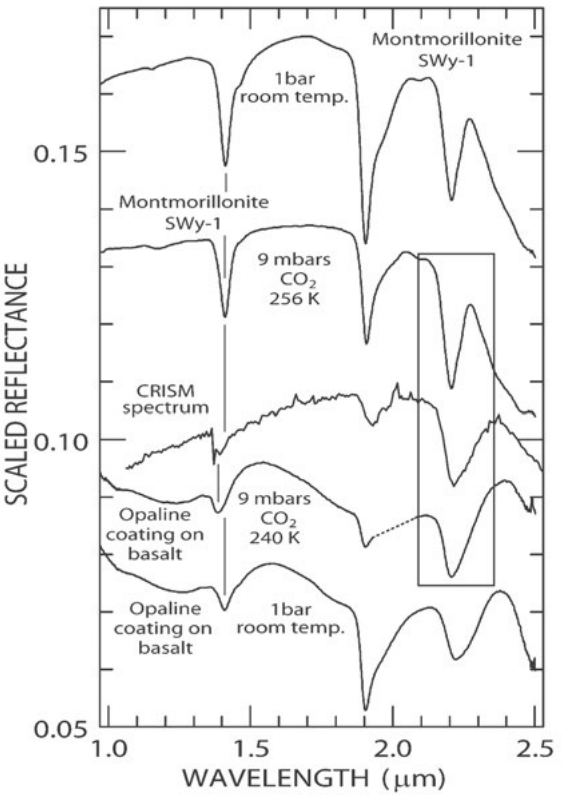


Figure 8. Laboratory spectra of montmorillonite and an opaline coating on a 3,000-5,000 year old basalt from Mauna Loa, Hawaii, at terrestrial conditions and simulated Martian surface conditions compared with an average of 120 spectra from MRO CRISM scene HRL000044AC collected over the plains around Valles Marineris south of Melas Chasma. Artifacts due to CO_2 have been replaced by the dashed line to facilitate spectral comparison. Box encloses CRISM spectrum and lab mineral spectra measured at simulated Martian conditions. Figure modified from Swayze et al. (2007).

Mg/Fe sulfates, and jarosite) and phyllosilicates (i.e., kaolinite, montmorillonite, and Fe/Mg-smectites) deposited as an evaporative scum by the receding waters of 900-meter deep paleolake that once partially filled Columbus Crater. Swayze et al. (2008) identified K-alunite in light toned layers on the floor of Cross Crater in the southern highlands in association with kaolinite, montmorillonite, and opal (Fig. 9). These minerals form partially concentric zones with alunite at the core suggestive of terrestrial relict acid-sulfate hydrothermal deposits. The relatively low-temperature (<100 °C) spectral signature of the alunite and its presence at the foot of the crater wall suggest it may have formed by precipitation in hydrothermal springs where acidic-water discharged into a lake that filled the crater to several hundred meters depth. Deposits in this crater and those in Columbus Crater would be excellent sites for future rover missions looking for evidence of past life.

As a general rule, the relative timing of phyllosilicate and sulfate deposition on Mars appears to be controlled by a progressively drying climate. Thollot et al. (2012) have found an exception, where a closed depression in the Noctis Labyrinthus region of Mars holds several hundred meters of stratified material enriched in phyllosilicates and sulfates, and both formed in situ during the Late-Hesperian epoch (3.4 to 3.0 billion years ago) after the Noachian period

EBSCOhost - printed on 2/13/2023 5:26 AM via . All use subject to https://www.ebsco.com/terms-of-use

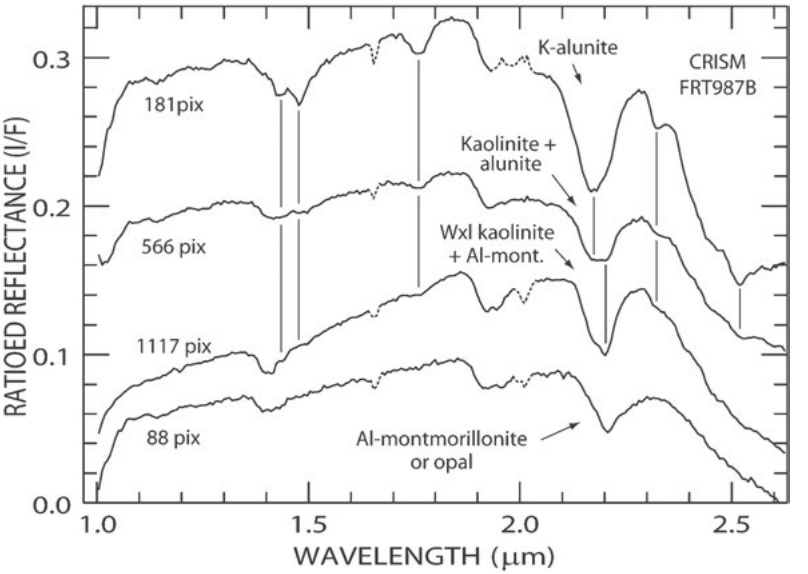


Figure 9. CRISM spectra of light-toned layered units on the floor of the 65 km diameter late Noachian Cross Crater in the southern highlands of Mars. Spectra were extracted from CRISM scene FRT0000987B; number of pixel spectra averaged listed at left end of each spectrum. Vertical lines mark position of diagnostic absorptions used to identify mineral phases and their mixtures. Wxl = well crystalline; Al-mont. = Al-montmorillonite. Figure modified from Swayze et al. (2008).

(4.1 to 3.8 billion years ago) when most phyllosilicates are thought to have formed. Their evidence suggests that the broadly diverse mineral assemblages formed from local volcanic activity and related hydrothermal alteration, and that geological setting may be just as important as geological timing when trying to understand orbitally detected mineral deposits.

Mars has seasonal and remnant polar caps of H_2O and CO_2 ices, as well as permafrost and geologic features indicative of glacial flow and sublimation of water ice from below the surface. Mars' seasonal polar caps extend down to about 50° latitude (e.g., James et al. 1993 and references therein). Due to present day obliquity, the southern hemisphere is drier than the northern hemisphere. The southern residual cap is dominated by CO_2 ice while the northern residual cap is dominated by H_2O ice (Farmer et al. 1976; Kieffer et al. 1976). However, it has recently been confirmed that an H_2O cap underlies the southern CO_2 remnant cap (Byrne and Ingersoll 2003; Bibring et al. 2004b).

More than 25% of the atmospheric CO_2 condenses each year to form the seasonal caps (Forget et al. 1995*;* Kieffer and Titus 2001). The NASA Phoenix lander and Mars Reconnaissance Orbiter, Compact Reconnaissance Imaging Spectrometer for Mars (CRISM), and the High-Resolution Imaging Science Experiment (HIRIS) instruments have quantified growth of the northern seasonal polar cap of H_2O and CO_2 at 68° N latitude (e.g., Cull et al. 2010; Fig. 10). During winter, the CO_2 ice grows to a depth of about 0.35 m with a thin layer of H_2O ice on the surface.

Asteroids and comets

Although asteroids generally show only silicate minerals on their surfaces, ice has been reported in two asteroids, 24 Themis (Rivkin and Emery 2008; Campins et al. 2009) and (65) Cybele (Licandro et al. 2011). Both objects have a weak absorption at 3-μm best described

EBSCOhost - printed on 2/13/2023 5:26 AM via . All use subject to https://www.ebsco.com/terms-of-use

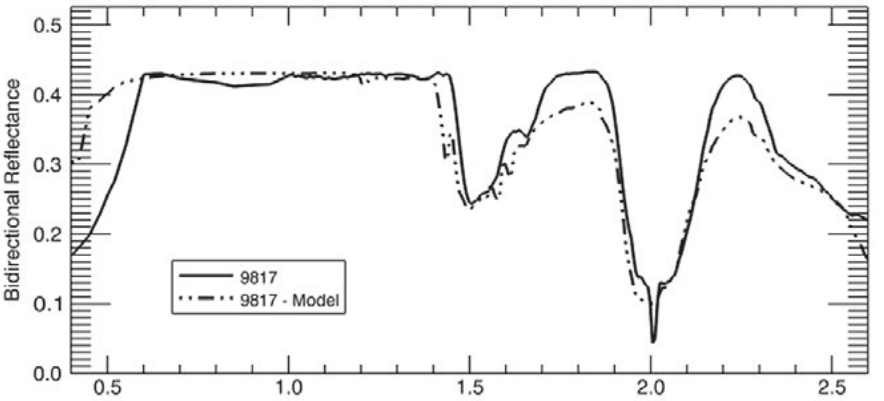


Figure 10. CRISM spectrum of the Mars Phoenix landing site (solid line) from orbit and model results (dotted lines) obtained at Ls~19.3°. Water ice dominates the spectrum with smaller amounts of CO_2 ice. The horizontal axis is the wavelength in microns. From Cull et al. (2010).

by water ice. However, strongly hydrogen bonded water can also display absorptions at the wavelengths where ice absorbs and higher signal-to-noise ratio spectra are needed to confirm this weak absorption. In addition, Themis has been reported to contain organic material (Campins et al. 2010; Rivkin and Emery 2010).

Comets are dark, with reflectances of only a few percent, and their surfaces are commonly thought of as carbonaceous lag deposits, the refractory remains left behind by the sublimation of dirty ice. While water is the major volatile species on comets, detection of water on the surface has been elusive. Davies et al. (1997) detected weak absorptions attributed to water ice in comet Hale-Bopp but the spectra included the coma. They also showed possible evidence for the ice being amorphous, but the low signal-to-noise ratio and weak absorption strength precludes a definitive detection when considering the far infrared spectrum of amorphous versus crystalline ice. Lellouch et al. (1998) also reported detection of ice in the coma of Comet Hale-Bopp. The temperatures they derived, 170 K, for their observations are too high for amorphous ice. A detection of ice on a comet nucleus without interference from the coma, comet Tempel 1, was reported by Sunshine et al. (2006) using the Deep Impact spacecraft where small exposures of ice were seen by the imaging spectrometer. The Deep Impact extended mission shows isolated patches of water ice on Comet Hartley 2 (Sunshine et al. 2012). While water ice has been detected on comets, to date, no other ices have been definitively detected via spectroscopy.

Jupiter system

Jupiter has four large moons, discovered 400 years ago by Galileo, and three of these (Europa, Ganymede, and Callisto) were found to have water ice surfaces (Kuiper 1957; Moroz 1965; Johnson and McCord 1971; Pilcher et al. 1972; Fink et al. 1973). Over the years these bodies have been studied using airborne (telescopes on terrestrial aircraft looking up) and ground-based spectroscopy using telescopes (Pollack et al. 1978; Clark 1980; Clark and McCord 1980), by infrared spectroscopy from the *Galileo* spacecraft in orbit around Jupiter (Fig. 11), and from the New Horizons flyby of the Jovian system (Grundy et al. 2007). While no water ice was found on the innermost of the Galilean satellites – Io –sulfur dioxide ice was identified by (Fanale et al. 1979; Hapke 1979; Smythe et al. 1979) on the surface of this moon, the most volcanically active object in the solar system. The vigorous heating that powers Io's volcanoes is the periodic solid-body tidal flexing arising from this moon's orbital eccentricity. An important aspect of Jupiter's satellites is the energetic radiation environment they suffer, far

EBSCOhost - printed on 2/13/2023 5:26 AM via . All use subject to https://www.ebsco.com/terms-of-use

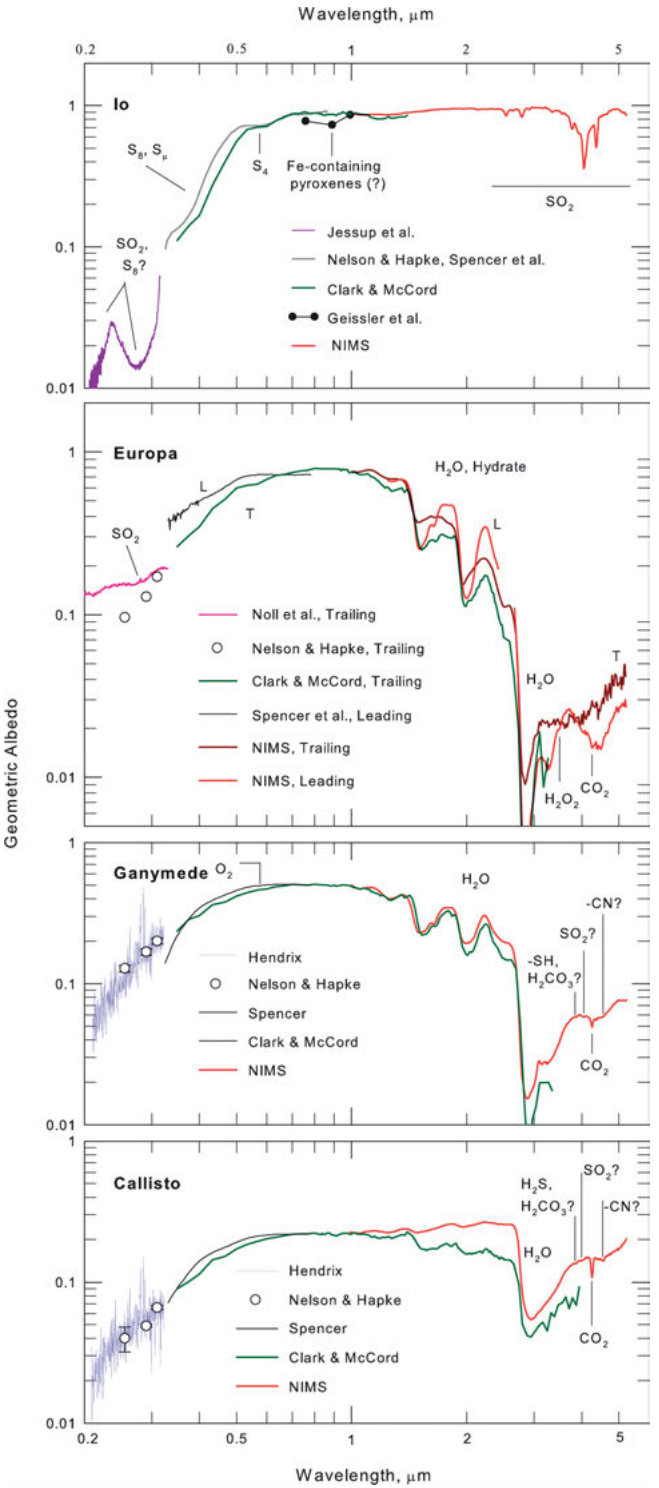


Figure 11. Reflectance spectra of the Galilean Satellites. Geometric albedo spectra derived from ground-based and spaceborne instruments are shown top to bottom as a function of distance from Jupiter. Volcanic Io exhibits a rich infrared spectrum of SO_2 with possible but unidentified polysulfur oxide (PSO) absorption present. The blue edge of sulfur is evident along with a feature at 5 μm due to the S_4 molecule. SO_2 and possibly S_8 absorptions are found in the ultraviolet region. Europa has a leading (L)-trailing (T) side dichotomy so we distinguish these cases. SO_2, polymeric sulfur, and likely S4 are present on the trailing hemisphere along with a hydrate shown at infrared wavelengths by distorted water bands. Nearly pure H_2O is present on Europa's leading side and there is less blue and ultraviolet absorption on that face compared to the sulfurous trailing side. Hydrogen peroxide and carbon dioxide are also apparent in Europa's infrared spectrum. Ganymede has less exposed ice and the geometric albedo is lower due to broad non-ice absorption. Callisto is almost completely covered with dark non-ice compounds and both Callisto and Ganymede show spectral features possibly due to a hydrosulfide or carbonic acid, possibly SO_2, and potentially a CN compound. Trapped O_2 is present on all three of the icy satellites. The Galileo ultraviolet spectrometer data shown for Callisto and Ganymede were kindly provided by A. Hendrix and here normalized to the geometric albedos derived by Nelson and Hapke. Data from Clark and McCord (1980), Nelson et al. (1987), Noll et al. (1995), Spencer et al. (1995), Hendrix et al. (1999), Jessup et al. (2002), Geissler et al. (2004), and Hendrix and Johnson (2008).

EBSCOhost - printed on 2/13/2023 5:26 AM via . All use subject to https://www.ebsco.com/terms-of-use

more powerful than elsewhere in the solar system. Consequently, the surfaces of these bodies, and particularly that of Io and Europa, will experience modification by radiation chemistry (see review by Johnson et al. 2004).

Gravity data show that Io is a differentiated silicate body with an Fe or Fe + FeS core, whereas the outer three Galilean moons contain significant water ice, with increasing H_2O content as one moves outward from Jupiter. Europa is differentiated and may have an internal structure similar to Io's but with an overlying 100-200 km H_2O mantle that comprises 10% of the satellite's mass. This H_2O cover is thought to consist of a 2-20 km icy crust covering an ocean of up to 100 km thickness. As in the case of Io, tidal flexing provides the heat to sustain a liquid ocean which is likely in contact with the rocky mantle. Ganymede, the largest satellite in the solar system and larger than Mercury, has more water than Europa, contributing to approximately half of the satellite's mass. An outer icy crust and mantle, about 200 km thick, is thought to cover an ocean that is sandwiched between layers of high-pressure ice in different phases. Beneath the H_2O mantle is a differentiated rocky body with a Fe-containing liquid core acting as a magnetic dynamo. Callisto is less differentiated than its sibling satellites, but has about the same relative water content and likely an ocean also, based on Galileo magnetic field data. However, due to their distance from Jupiter, tidal heating is much less efficient for these outer two satellites compared to Io and Europa.

In the following paragraphs we discuss the ice (SO_2 and H_2O) and non-ice surface compositions of Jupiter's Galilean satellites. General reviews can be found in recent publications (Bagenal et al. 2004; Lopes and Spencer 2007; Pappalardo et al. 2009; Dalton et al. 2010; Clark et al. 2013). Io and Europa's surface compositions are reviewed in Carlson et al. *(*2007) and Carlson et al. *(*2009), respectively.

Io. Io is the innermost of the four Galilean satellites and exhibits a young, volcanically active surface that is rapidly resurfaced at an average rate of about one cm per year. The surface is nearly completely covered by sulfur dioxide ice and elemental sulfur, the exceptions being in the hot volcanic areas and fresh lava flows where silicates may be exposed. Gaseous SO_2 is a volcanic effluent, derived from the degassing of hot magma, and is the dominant volcanic gas component, accompanied by minor amounts of SO and S_2 (Zolotov and Fegley 1998, 1999, 2000; Spencer et al. 2000) and other species such as NaCl (Lellouch et al. 2003), identified and mapped through ground-based microwave spectroscopy. SO_2 contributes nearly all of the absorption features in Io's spectra (Fanale et al. 1979; Hapke 1979; Smythe et al. 1979; Schmitt et al. 1994; Nash and Betts 1995; Carlson et al. 1997). The global abundance and grain sizes of the SO_2 particles indicate that optically thick SO_2 deposits of mm-size grains are concentrated in Io's equatorial regions (Carlson et al. 1997; Laver and de Pater 2008; 2009) and confirm earlier measurements of (McEwen 1988), who studied Io's surface using ultraviolet and visible Voyager images. These equatorial deposits are strongly associated with active volcanoes and arise from volcanic venting of gaseous SO_2 into the plumes and atmosphere with subsequent deposition onto colder surfaces as frost. The relatively large grain sizes indicate sublimation and condensation metamorphism for these deposits.

In contrast, fine grained SO_2 frost was found at mid-and high-latitudes (Carlson et al. 1997; Doute et al. 2001; Laver and de Pater 2008, 2009). SO_2 frost sublimates during the day due to relatively high surface temperatures. Although most of it re-condenses locally during the nighttime, SO_2 molecules slowly migrate toward higher latitudes and colder regions (Matson and Nash 1983). The high-latitude SO_2 deposits appear transparent under normal-incidence illumination and therefore are thought to be optically thin (Geissler et al. 2001). They tend to remain as small grains as originally condensed because of the colder environment and rapid radiolytic destruction of the SO_2 grains at higher latitudes (Wong and Johnson 1996). The poles of Io appear red due to the radiolytic destruction of SO_2 and the production of elemental sulfur. The possible condensation of SO_2 during the ~2.5 hour eclipses of Io by Jupiter during each

EBSCOhost - printed on 2/13/2023 5:26 AM via . All use subject to https://www.ebsco.com/terms-of-use

orbit has long been a subject of interest; see the recent review and time-resolved infrared spectra of Io at eclipse reappearance (Cruikshank et al. 2010a).

Sulfur dioxide is a thermochemical product of hot magmas and its presence is indicative of volcanic conditions. The ratios of SO and S_2 to SO_2 in the volcanic plumes are consistent with high-temperature volcanism in a silicate mantle that is deficient in Fe-metal (Zolotov and Fegley 2000). Being a high-temperature chemical product, SO_2 probably represents a very minor contribution to the satellites total mass. However, since it is a very volatile, it is likely that most of Io's SO_2 is at or near the surface. The solid and gaseous forms of SO_2 are evident in the surficial ices and the overlying sublimational and plume-derived atmosphere, but there is evidence that liquid SO_2 forms a near-surface "aquifer." Scarps and sapping channels provide one line of evidence (McCauley et al. 1979; McEwen et al. 2000; Moore et al. 2001) and uniform topographic infilling of a crater by SO_2 (Lopes et al. 2001) provides further evidence for SO_2 "ground water" (Fig. 12). It has been estimated that the upper 1 km of Io is rich in the volatiles SO_2 and sulfur (McEwen et al. 2000).

Io is intensely irradiated by Jupiter's magnetosphere, forming sulfur trioxide. The signature of SO_3, as well as S_8 and SO_2, may be present in thermal emission spectra of Io (Khanna et al. 1995; Hanel et al. 2003). A related species, disulfur monoxide (S_2O), was investigated by (Baklouti et al. 2008) but interference by strong SO_2 bands precluded its observation. Polysulfur oxides (PSO) may be present on Io and produce a broad absorption in the 4.5-μm region (Baklouti et al. 2008). Ion irradiation can also sputter surface atoms and molecules into an atmosphere around Io and into escape orbits. Neutral and ionized toroidal clouds are formed around Jupiter and provide a source of sulfur, oxygen, sodium, potassium, chlorine, and other possible species to other satellites. This is particularly important for Europa, where the tori strike the trailing hemisphere and provide a source of sulfur and other elements.

Sulfur on Io is emplaced on the surface by volcanic plumes, primarily as S_2, while sulfur volcanism may occur on Io and produce sulfur lava flows. Elemental sulfur can exist in a variety of forms (linear chains, cyclic) and with innumerable lengths. The most stable form is cyclo-octal and some of Io's sulfur is likely in this form, the remaining being polymeric with some tetrasulfur S_4 (Fig. 11, top panel).

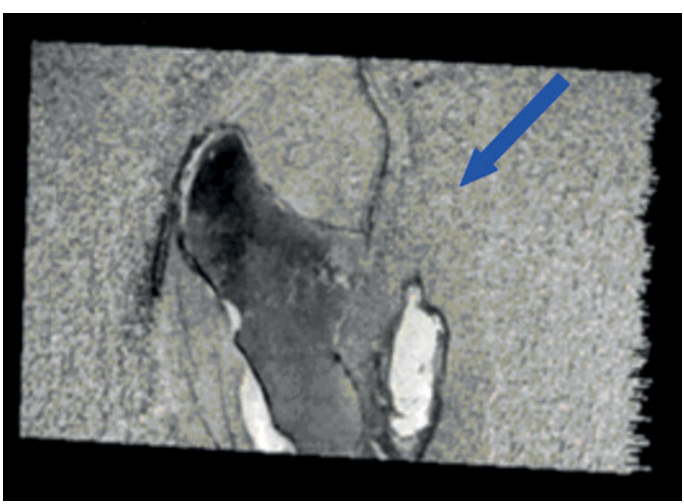


Figure 12. The interior of a volcanic caldera near Chaac (indicated by arrow) on the Galilean moon Io is filled with spectroscopically identified very pure SO_2 that appears white and to be topographically controlled inflows of liquid SO_2.

EBSCOhost - printed on 2/13/2023 5:26 AM via . All use subject to https://www.ebsco.com/terms-of-use

The high temperatures of Io's volcanoes, up to 1700 K, indicate silicate volcanism but the rapid resurfacing by plume and sublimated SO_2 has precluded definitive identifications of silicates on the surface. Geissler et al. (1999) found a region on Io with an absorption at 0.9 μm and suggested that it was caused by a ferrous iron feature present in Fe-containing magnesian orthopyroxenes. This is a plausible suggestion as such minerals are associated with the most primitive terrestrial rocks and possess a high melting temperature.

Europa. Europa orbits Jupiter at about 1.6 times the distance from Jupiter as Io and is the innermost of the water-ice-containing Galilean satellites. Although it contains less bulk H_2O than Ganymede or Callisto, the surface exhibits much more exposed water ice and hydrate than the other H_2O-icy Galileans due to its greater surface activity, a consequence of tidal heating (the crater age is a mere 50 My as reported by Zahnle et al. 2003). The leading hemisphere of Europa, in the sense of orbital motion, presents the purest ice as determined by infrared spectroscopy which probes the upper sub-millimeter depths of the surficial materials. Both amorphous and crystalline ice are present, with a greater proportion being the amorphous form (Hansen and McCord 2004). The presence of amorphous and crystalline phases are the result of two competing processes—the increase in disorder and amorphization of ice crystals by energetic particle bombardment, and thermally-induced phase transformation of amorphous ice to the lower energy cubic ice form or the even lower energy hexagonal ice phase.

The second major constituent on Europa is a hydrated species, predominant on the trailing side and associated with the dark material that produces Europa's hemispherical color dichotomy—the red, trailing hemisphere and the whiter, leading hemisphere. This icy hydrate is a complex of some molecule X (or groups of molecules) surrounded by hydration shells of water, often in stoichiometric proportions, as $X_n{\cdot}mH_2O$. One suggested source of this hydrate is a salty subsurface ocean, the X being a salt such as $MgSO_4$, forming hydrates such as epsomite $MgSO_4{\cdot}7H_2O$ and others (McCord et al. 1998b, 1999). A second hypothesis is that radiolysis of exogenic (Iogenic) sulfur implanted on Europa's trailing hemisphere produces hydrated sulfuric acid (Carlson et al. 1999b, 2002, 2005). The associated dark material is thought to be polymeric sulfur (Carlson et al. 1999b) since most salts and acids are colorless in the visible spectral region. The association of hydrate and dark material with geological features on the trailing side implies an endogenic process, either emplacement of material from the subsurface ocean or thermal modification of exogenically-derived material, forming lag deposits. Many hydrated salts exhibit spectral features in the infrared (Dalton et al. 2005; Clark et al. 2007). A linear (areal) mixing model has recently been applied and used to infer composition and variations across Europa's surface (Shirley et al. 2010; Dalton et al. 2012, 2013; Cassidy et al. 2013). The model used many hydrated materials in the fitting, each with a constant grain size, and with areal rather than intimate mixing. Since spectral characteristics are strongly grain-size dependent, the uniqueness of the solutions and identifications must be viewed with caution. Suggestive evidence for the presence of epsomite ($MgSO_4{\cdot}7H_2O$), based on a characteristic 2.07-μm feature, has been found recently by (Brown and Hand 2013). They suggest emplacement of Mg^{2+} and other cations from Europa's ocean as chlorides and subsequent radiolysis (see below) with H_2O ice and exogenic sulfur to produce sulfate salts. However, models with significant salt, like those proposed above, are incompatible with Europa's 3-μm to 5-μm spectrum, which is very dark compared to salts (e.g., see salt spectra in Clark et al. 2007). Future models and interpretations need to include intimate mixtures and the full spectral range of data available for Europa.

The magnetospheric environment at the orbit of Europa is almost as damaging as at Io, and several radiolytic species are observed. As mentioned above, native sulfur exists on the surface and is radiolyzed to the polymeric form and as the red chromophore tetrasulfur (Carlson et al 2009; Hand and Brown 2013). Molecular oxygen is found on Europa (Spencer and Calvin 2002), and is radiolytically formed and trapped in H_2O ice, as is hydrogen peroxide H_2O_2

EBSCOhost - printed on 2/13/2023 5:26 AM via . All use subject to https://www.ebsco.com/terms-of-use

(Carlson et al. 1999a). SO_2 is observed and is a radiolytic product of sulfate decomposition (Johnson et al. 2004; Carlson et al. 2009; Hendrix et al. 2011). CO_2 is also found (Smythe et al. 1998; Hand et al. 2007; Hansen and McCord 2008) and this ubiquitous molecule could be from endogenic or exogenic sources (see discussions below). These minor species may exist in Europa's near surface as mixed clathrate hydrates (Hand et al. 2006).

Ganymede. Ganymede is also a differentiated body, but is unique because it has an intrinsic magnetic field arising from dynamo motions within a molten iron core. Ganymede and Callisto contain more ice than Europa, but both exhibit darker, less icy surfaces than does Europa. The major source of this dark material is probably the direct infall of meteoritic material and from impact debris ejected from Jupiter's more plentiful but smaller outer satellites. This process should also occur on Europa, but Europa's vigorous current or recent surface activity has diluted and buried the meteoritic material within the ice shell.

Ganymede's surface has roughly equal proportions of amorphous and crystalline ice (Hansen and McCord 2004); the small proportion of amorphous ice compared to Europa is presumably due to the lower incident flux of high-energy magnetospheric radiation and shielding by Ganymede's magnetic field. Bright, icy polar caps are observed on this satellite and the boundary between the icy polar regions and the less icy lower latitudes closely coincides with the transition from open to closed magnetic field lines. This suggests surface brightening by energetic magnetospheric particles streaming in on open field lines and striking Ganymede's polar surfaces. This brightening may be produced by ice grain disruption (Johnson 1997), creating smaller grains and more scattering sites, which decreases the absorption and increases the albedo, or by sputtering and thermal segregation (Khurana et al. 2007).

A hydrate, possibly similar to Europa's, has been identified on Ganymede and suggested to have been formed from $MgSO_4$-rich brine emplaced from the ocean below (McCord et al. 2001). Ganymede once had an active surface but any such emplacement must have occurred in the distant past since the surface age is ~ 2Gy (Zahnle et al. 2003). With subsequent meteoritic infall and gardening, it is unclear how these salt minerals could be present in the high concentrations that were observed. The geological process that erupts material from a 200-km deep ocean is also unclear. A second class of hydrate, associated with dark crater rays, has been identified by Hibbits and Hansen (2007) and found to be similar to C-type asteroid or Callisto non-ice materials. This hydrate may be material from, or modified by, the impactor.

Three water-related radiolytic species are found on Ganymede: molecular oxygen (Spencer et al. 1995; Calvin et al. 1996), ozone (Noll et al. 1996; Hendrix et al. 1999a), and possibly hydrogen peroxide (Hendrix et al. 1999b). Transient, localized SO_2 concentrations have been suggested (Domingue et al. 1998) and spectral information indicates the presence of other species. Since these features are similar to those found in spectra of Callisto, they are described in the following section.

Callisto. Callisto, the outermost icy Galilean satellite, has a bulk composition that is about half H_2O and half rocky silicates. In contrast to the inner three Galilean satellites, Callisto is only partly differentiated, with denser rocky components that slowly settled, or are currently settling, to the center (Schubert et al. 2004). The lack of tidal heating and the low rate of gravitational settling may not provide sufficient energy to cause geological activity on the surface. Callisto has a very old surface, mostly covered with a layer of dark material, presumably from meteoritic infall and outer satellite-derived ejecta material. Both impact cratering and mass wasting have exposed the icy "bedrock" over approximately 10% of this ancient surface, showing the presence of water ice that is predominantly crystalline with grain sizes (diameters) of ~ 200-400 μm (Hansen and McCord 2004). Water molecules tend to segregate by sublimation and condensation on cold, bright ice surfaces, but the dark material also has an H_2O component, probably including adsorbed H_2O. Because the temperatures attained by the dark material are

EBSCOhost - printed on 2/13/2023 5:26 AM via . All use subject to https://www.ebsco.com/terms-of-use

high (~ 150-160 K), some of these water molecules sublimate during the day and re-condense at night, so thermal segregation is not complete. The radiolysis product O_2 has been observed on Callisto (Spencer and Calvin 2002) and H_2O_2 has been suggested (Hendrix et al. 1999b).

NH_3 has not been observed on the surface, but CO_2 is found on the surfaces of Callisto and Ganymede (Carlson et al. 1996; McCord et al. 1997; McCord et al. 1998a; Hibbitts et al. 2000, 2002, 2003) as well as on Europa as noted above. A tenuous CO_2 atmosphere has also been found on Callisto, indicating loss from the surface. The surficial CO_2 is not an ice, based on the spectral position of the absorption feature, and CO_2 ice is too volatile to be stable at Galilean satellite temperatures; instead the molecules appear to be trapped in the dark material. The source of CO_2 could be degassing from the interior (Moore et al. 1999) or an exogenic source or production mechanism. SO_2 has been suggested as a surface component based on ultraviolet (Lane and Domingue 1997; Noll et al. 1997) and infrared spectra (McCord et al. 1997, 1998a; Hibbitts et al. 2000). SO_2 is also quite volatile, and cannot exist as a direct condensate but could be trapped similar to CO_2. Hendrix and Johnson (2008) have questioned the ultraviolet SO_2 identification and interpreted Galileo ultraviolet spectra as absorption by carbonized organics. The radiolysis of organics in ice by energetic electrons as would occur in the Jovian magnetosphere does produce trapped CO_2 (Hand and Carlson 2012). Infrared evidence for the presence of aliphatic hydrocarbons has been suggested by (McCord et al. 1997, 1998a). Two other spectral features have been identified on both Callisto and Ganymede, one at 3.88 μm and thought to be due to a hydrosulfide compound (-SH) (McCord et al. 1997, 1998a) or the CO_2-related compound, carbonic acid (H_2CO_3) (Hage et al. 1998). Another common feature for these two satellites occurs at 4.57 μm and is possibly due to a –CN-containing tholin (McCord et al. 1997, 1998a).

Saturn system

It has long been known that the surfaces of Saturn's rings and major satellites, Mimas, Enceladus, Tethys, Dione, Rhea, Hyperion, Iapetus, and Phoebe are predominantly icy objects (e.g., Fink et al. 1975; Clark et al. 1984, 1986, 2005, 2008a; Roush et al. 1995; Cruikshank et al. 1998a, 2005; Grundy et al. 1999; Owen et al. 2001; Filacchione et al. 2007, 2008; Cuzzi et al. 2009). Whereas the reflectance spectra of these objects (Figs. 13-16) in the visible range indicate that a coloring agent is present on all surfaces, only Phoebe and the dark hemisphere of Iapetus display spectra markedly different from very pure water ice (e.g., Cruikshank et al. 2005; Clark et al. 2005, 2012; Jaumann et al. 2009 and references therein). The relative purity of the ice in Saturn's satellites and rings may be the result of a singular catastrophic event (e.g., Canup 2010; Asphaug and Reufer 2013).

Dark material was first inferred in the Saturn system by J. D. Cassini (1672), and verified by Murphy et al. (1972) and Zellner (1972). The nature of the dark material has been studied by numerous authors, sometimes with conflicting conclusions, including Cruikshank et al. (1983), Vilas et al. (1996), Jarvis et al. (2000), Owen et al. (2001), Buratti et al. (2002), and Villas et al. (2004). The new Cassini VIMS data provide a greater spectral range (0.35 to 5.1 μm in 352 wavelength channels) in reflected solar radiation, with higher precision, and show new absorption features not previously seen in these bodies (e.g., Buratti et al. 2005; Clark et al. 2005, 2008a, 2012; Cruikshank et al. 2007, 2008). These new VIMS observations also spatially resolve the satellite surfaces enabling maps of compounds to be made, leading to additional insights into the nature of the icy satellite surfaces. The spatial resolution of derived maps of materials from VIMS data is variable depending on fly-by distances, and ranges from tens of kilometers per pixel to sub kilometers per pixel.

The Cassini spacecraft entered the Saturn system in 2004, and the Visual and Infrared Mapping Spectrometer (VIMS) began obtaining spatially resolved spectra of Saturn's satellites and rings (Brown et al. 2005a; Figs. 13-16). The VIMS has provided a wealth of spatially

EBSCOhost - printed on 2/13/2023 5:26 AM via . All use subject to https://www.ebsco.com/terms-of-use

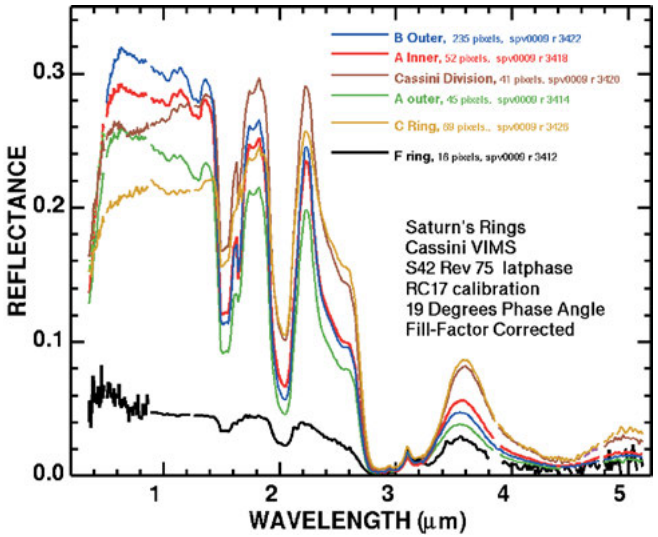


Figure 13. Cassini VIMS reflectance spectra of Saturn's rings corrected for fill factor. The spectra are dominated by absorptions from water ice and an UV absorber. Adapted from data in Cuzzi et al. (2009).

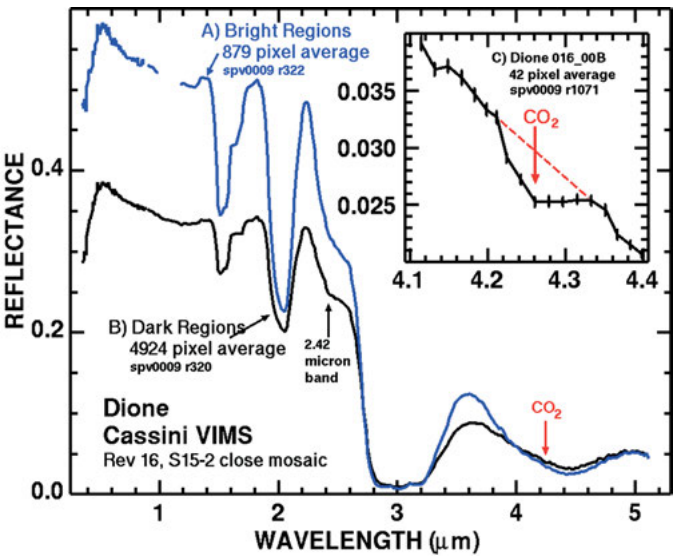


Figure 14. Spectra of bright and dark regions on Saturn's satellite Dione. Inset shows weak CO_2 observed in areas with dark material. From Clark et al. (2008a).

resolved compositional data on the satellites (e.g., Phoebe: Clark et al. 2005; Iapetus: Buratti et al. 2005, Cruikshank et al. 2007, 2008; Enceladus: Brown et al. 2006; Jaumann et al. 2006; Dione: Clark et al. 2008a; Jaumann et al. 2009; Clark et al. 2012) and rings (e.g., Nicholson et al. 2008; Cuzzi et al. 2009). The satellites and rings are dominated by crystalline H_2O ice with trace amounts of CO_2 (Fig. 15) and dark material (e.g., Fig. 14 and Fig. 16 spectra B and C) although it is not clear if the CO_2 is an ice, trapped, or both (Cruikshank et al. 2010b). Trace

EBSCOhost - printed on 2/13/2023 5:26 AM via . All use subject to https://www.ebsco.com/terms-of-use

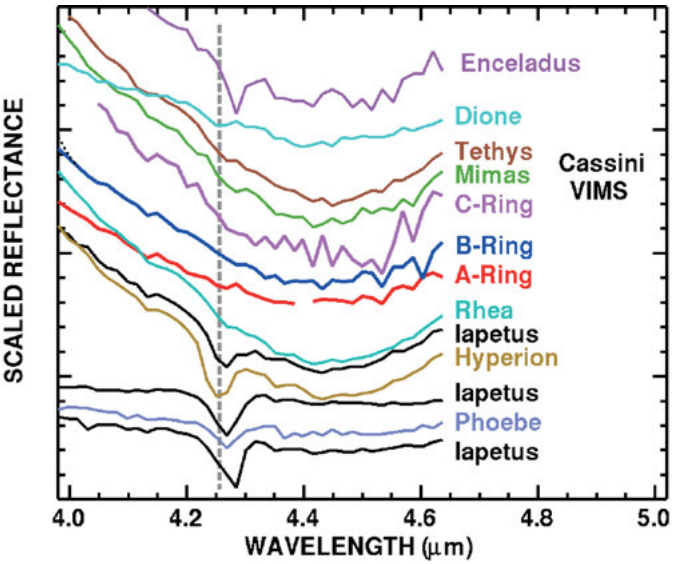


Figure 15. CO_2 on icy objects in the Saturn system detected by the absorption near 4.25 μm. No CO_2 has been detected in spectra of the rings. CO_2 absorption appears strongest on satellites with dark material. From Clark et al. (2008a).

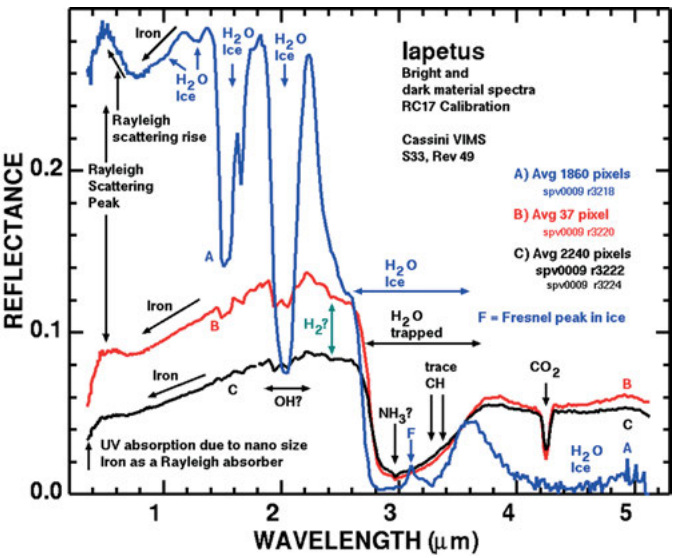


Figure 16. Spectra of Iapetus, showing a sequence from regions of dark material (black spectrum) to higher concentrations of water ice (blue). From Clark et al. (2012).

organics and ammonia absorptions are seen in some satellites but again, it is not clear if the absorptions are due to ices or trapped molecules. Unusual colors and spectral shapes of the satellites and rings in the UV to visible are currently explained by a combination of Rayleigh scattering by small particles (ice grains as well as contaminants) and an UV absorber by one of

EBSCOhost - printed on 2/13/2023 5:26 AM via . All use subject to https://www.ebsco.com/terms-of-use

the contaminants (Clark et al. 2008a,b, 2012; see reviews by Jaumann et al. 2009; Cuzzi et al. 2009; Hendrix et al. 2012).

The surface composition of Titan is still enshrouded in a cloud of mystery despite the initial flood of data from the Cassini spacecraft and the Huygens probe. Although the composition of Titan's atmosphere is known (Coustenis et al. 1999, 2003, 2005, 2006a,b, 2007; Flasar et al. 2005; Teanby et al. 2009 and references therein), with most of the observed gases having been predicted using models of UV photolysis and reactions of atmospheric methane and nitrogen (Yung and DeMore 1999; Vuitton et al. 2008 and references therein), the many less volatile molecules that coat and/or make up the solid surface have yet to be identified. Tholins are the solid end products of photolysis and electron discharge experiments done in terrestrial laboratories with gases common in Titan's atmosphere and are one type of mixture of compounds theorized to exist on Titan (e.g., Sagan et al. 1992; Imanaka et al. 2004; Quirico et al. 2008). Table 1b in Clark et al. (2010a) lists known solid compounds on Titan through 2009, and include benzene (firm), with many tentative or inferred compounds including ices of cyanoacetylene (HC_3N), toluene (C_7H_8), cyanogen (C_2N_2), acetonitrile (CH_3CN), H_2O, CO_2, and NH_3.

The Cassini RADAR has provided the highest spatial resolution images of Titan's surface from Saturn orbit but is a mono-frequency system that provides compositional information only through the dielectric constant of the surface at its operating wavelength of 2.16 cm (Elachi et al. 2005). Only the Descent Imager-Spectral Radiometer, DISR, on the Huygens probe and VIMS from the Cassini Saturn orbiter have the capability to provide combined spectral plus spatial information about the surface (Tomasko et al. 2005; Schroeder and Keller 2008; Sotin et al. 2005; Barnes et al. 2005, 2007, 2008; McCord et al. 2006, 2008; Rodriguez et al. 2006; Brown et al. 2008; Nelson et al. 2009; Soderblom et al. 2009; Clark et al. 2010a). The DISR was limited in wavelength range out to 1.7 μm but obtained very high spatial resolution over a limited area during the descent of the Huygens probe; VIMS measures wavelengths out to 5.1 μm (Fig. 17) and can cover large parts of the surface of Titan, but at much more limited spatial resolution (a few km /pixel are common and a few small areas have been spectrally imaged

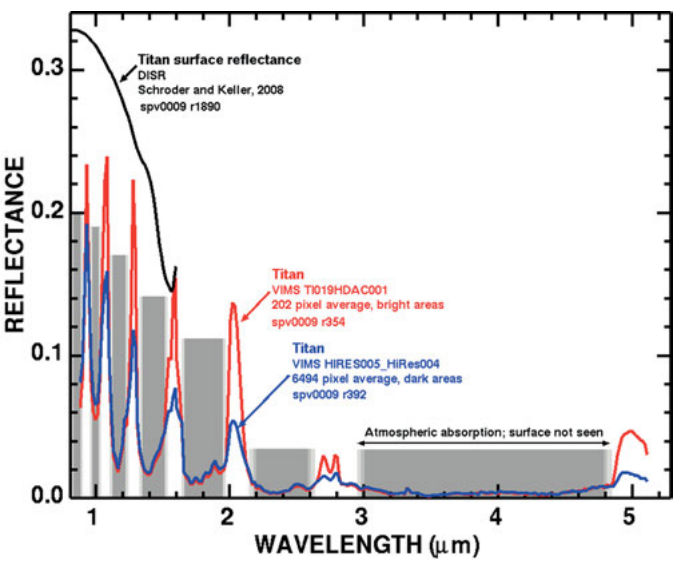


Figure 17. Reflectance spectra of Titan's bright (red line) and dark (blue line) regions. The gray areas in the plot are regions of strong absorption from atmospheric methane through which the surface is not detected. From Clark et al. (2010a).

EBSCOhost - printed on 2/13/2023 5:26 AM via . All use subject to https://www.ebsco.com/terms-of-use

at sub 300 meters). Terrestrially synthesized tholins do not match the spectral slope in data from the Huygens DISR (Tomasko et al. 2005; Schroeder and Keller 2008) or Cassini VIMS (McCord et al. 2006). The DISR spectra of Titan's surface show a blue spectral slope from 1 to 1.6 μm that is distinctly "un-tholin" like and show what qualitatively appears to be a water-ice absorption, but the complete H_2O feature was not covered by the spectrometer (Tomasko et al. 2005; Schroeder and Keller 2008). Schroeder and Keller concluded the absorption did not match water ice. Also, the 1.25-μm H_2O absorption was not observed even though expected in the models presented by Tomasko et al. (2005) and Schroeder and Keller (2008). *In situ* analyses have detected methane, ethane, and tentatively identified cyanogen, benzene, and carbon dioxide on the surface from the Huygens GCMS (Niemann et al. 2005). Ammonia and hydrogen cyanide were the main pyrolysis products of the aerosols measured by the Huygens *in situ* pyrolysis experiment during its descent (Israel et al. 2005) and those aerosols could rain down to the surface, but pyrolysis products are not necessarily compounds in the aerosols. Higher in Titan's thermosphere, benzene was first detected in the stratosphere by ISO and CIRS (Coustenis et al. 2003, 2007), and the Cassini Ion and Neutral Mass Spectrometer (INMS) instrument has detected high abundances of benzene along with toluene above 900 km (Waite et al. 2007). Toluene is an interesting molecule after benzene because toluene consists of a benzene ring with a methyl functional group, $-CH_3$, replacing one of the hydrogen atoms attached to the benzene ring. Toluene is a possible larger organic molecule that may be compatible with VIMS surface spectra of Titan.

Clark et al. (2010a) presented evidence for surface deposits of solid benzene, (C_6H_6) (Fig. 18), solid and/or liquid ethane, (C_2H_6), or methane (CH_4), and clouds of hydrogen cyanide (HCN) aerosols using diagnostic spectral features in data from the Cassini VIMS. Cyanoacetylene (2-propynenitrile, HC_3N) is indicated in spectra of some bright regions, but the spectral resolution of VIMS is insufficient to make a unique identification although it is a closer match to the feature previously attributed to CO_2. Acetylene (C_2H_2), expected to be more abundant than benzene on Titan according to some models, was not detected. Water ice, if present, must be covered with organic compounds to the depth probed by 1-μm to 5-μm wavelength photons: a few millimeters to centimeters. While many organic compounds have now been detected in the atmosphere and on Titan's surface, we still have only a small spectral database of solid organic compounds measured at Titan temperatures (about 92 K) to compare with spectra of Titan. Spectra of additional compounds are needed, along with higher spatial and

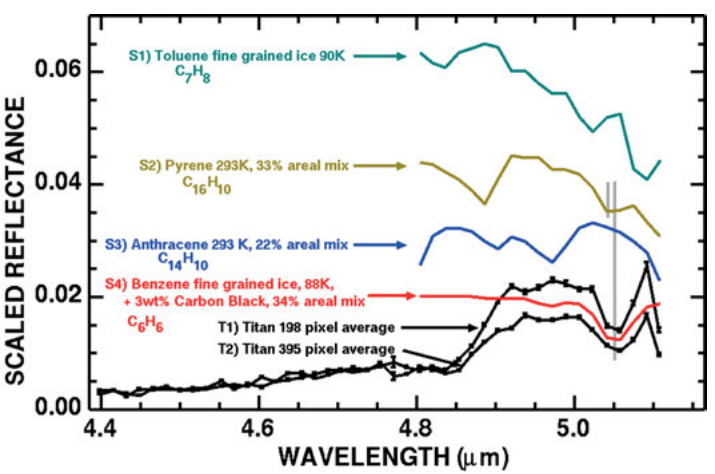


Figure 18. Spectra of Titan showing an absorption attributed to benzene ice. From Clark et al. (2010a).

EBSCOhost - printed on 2/13/2023 5:26 AM via . All use subject to https://www.ebsco.com/terms-of-use

spectral resolution data of Titan's surface in order to better understand the full compositional range of compounds there.

Saturn's moon Titan has a close analogy to Earth's hydrologic cycle where instead of liquid water, methane and ethane exist as liquids at the surface. Similar to liquid water lakes and rivers on the Earth, Titan has liquid methane and ethane lakes and rivers in a currently active methanologic cycle. These two bodies are unique in the Solar System in that regard.

Uranus system

The Uranus system was investigated by the Voyager II spacecraft in 1986, but that probe had no near-infrared spectral-imaging capability. Accordingly, compositional studies of the Uranian satellites and rings have relied on ground-based telescopic observations, progressing in parallel with advances in infrared instrumentation technology. Prior to the Voyager encounter, low spectral resolution (bandwidths ~2% of the wavelength) circular-variable filter (CVF) spectrophotometry led to detection of broad water ice absorptions at 1.5 and 2 μm on the five major satellites of Uranus: Miranda, Ariel, Umbriel, Titania, and Oberon (Cruikshank 1980; Cruikshank and Brown 1981; Soifer et al. 1981; Brown 1983; Brown and Clark 1984; Brown et al. 1991). Spectrometers based on infrared detector arrays enabled higher quality near-infrared spectra to be obtained (Fig. 19), with spectral bandwidths of around 0.1%, revealing the 1.65-μm water ice band on all five satellites, indicative of cold crystalline H_2O ice (Grundy et al. 1999; Bauer et al. 2002). An apparent dip in Miranda's spectrum near 2.2 μm has been tentatively attributed to ammonia ice (Bauer et al. 2002) but this identification has not yet been confirmed. Repeated observations of the other four satellites have shown no comparable 2.2-μm features, but did reveal the presence of a narrow triplet of CO_2 ice absorptions near 2 μm on Ariel, Umbriel, and Titania, but not Oberon (Grundy et al. 2003, 2006). Interestingly, the strengths of these CO_2 ice absorptions were found to be spatially variable, being strongest on the trailing hemispheres of the satellites, and also on the satellites closer to Uranus (whether or not Miranda fits this pattern remains to be tested). This spatial pattern is consistent with *in situ* production

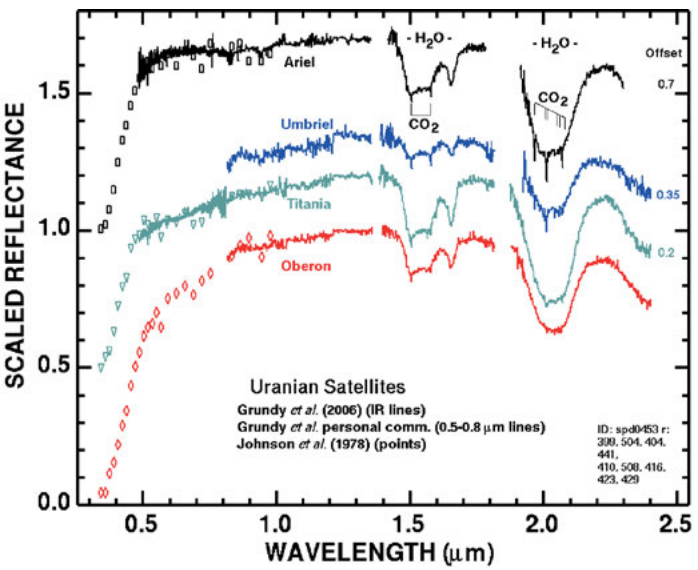


Figure 19. Reflectance spectra of the Uranian satellites showing strong water absorptions and narrow CO_2 absorptions. Note the asymmetric (toward longer wavelengths) 2-μm ice absorption of Oberon indicating the presence of sub-micron ice grains.

EBSCOhost - printed on 2/13/2023 5:26 AM via . All use subject to https://www.ebsco.com/terms-of-use

of CO_2 from local H_2O plus carbonaceous materials driven by Uranian magnetosphere charged particle radiolysis, balanced by relatively rapid sublimation loss (Grundy et al. 2006). Water ice absorptions were seen to exhibit the opposite pattern, being deepest on the leading hemispheres of Ariel, Umbriel, and Titania (although perhaps not Oberon; Grundy et al. 2006). This pattern of deeper water ice absorptions on leading hemispheres is also seen in the Jovian and Saturnian satellite systems, but the cause remains uncertain. Possibilities include preferential gardening of icy regoliths by impactors impinging on leading hemispheres (Zahnle et al. 2003), and preferential sputtering removal of H_2O ice via magnetospheric charged particle bombardment on trailing hemispheres (e.g., Cheng et al. 1986; Eviatar and Richardson 1986; Pospieszalska and Johnson 1989; Johnson 1990). No ices have been identified to date in spectra of the Uranian rings (e.g., Soifer et al. 1981; Pang and Nicholson 1984; Baines et al. 1998). The low albedos of Uranian satellites and ring particles implies the presence of a darkening agent, which has long been presumed to be carbonaceous in nature, although its precise composition remains unknown.

The Neptune system and beyond

The Neptune system was explored by Voyager 2 in 1989, providing a wealth of physical details. But, as with the Uranus system, almost all compositional information about ices in the Neptune system came from Earth-based observations. Neptune's largest satellite, Triton, provides particularly interesting and complex examples of outer solar system ice geology. Early Triton results came from a series of near-infrared CVF spectrometer observations (~2% spectral resolution) during the 1970s and 1980s, leading to the discovery of methane, nitrogen, and water ice absorptions (Cruikshank and Silvaggio 1979; Apt et al. 1983; Cruikshank and Apt 1984; Cruikshank et al. 1984, 1988, 1989; Rieke et al. 1985).

The advent of array spectrometers with cryogenic optics resulted in much higher quality spectra (Fig. 20), leading to the discovery of CO, CO_2, and C_2H_6 ices (Cruikshank et al. 1993; Bohn et al. 1994; DeMeo et al. 2010). The higher spectral resolution and signal precision enabled by these instruments revealed subtle wavelength shifts in the methane bands consistent

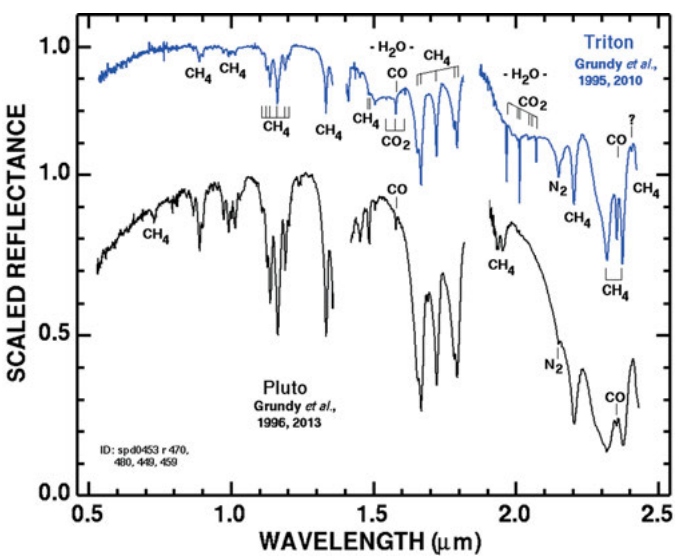


Figure 20. Near infrared spectra of Triton and Pluto are compared in this figure. Features arising from CH_4, CO, CO_2, H_2O, and N_2 are identified.

EBSCOhost - printed on 2/13/2023 5:26 AM via . All use subject to https://www.ebsco.com/terms-of-use

with the CH_4 molecules being dispersed in nitrogen ice (Cruikshank et al. 1993; Quirico et al. 1999), a situation anticipated from thermodynamic arguments (Lunine and Stephenson 1985). They also revealed the phase of Triton's water ice to be predominantly crystalline (Cruikshank et al. 2000; Grundy and Young 2004).

A picture of Triton emerged of a solar-powered, active world in which volatile N_2, CO, and CH_4 ices sublimate and condense in response to seasonal insolation on a substrate of H_2O and CO_2 ices (which are non-volatile at Triton surface temperatures), leading to an array of bizarre landforms and even jetting of sublimated nitrogen gas out of fissures, with possible aeolian transport of non-volatile H_2O and CO_2 ice dust (e.g., Brown et al. 1990; Hansen and Paige 1992; Stansberry et al. 1996; Grundy et al. 2002). Evidence for short-term changes in the visible wavelength parts of Triton's spectrum reinforced the perception of an active Triton (Hicks and Buratti 2004), as did the paucity of impact craters in Voyager images (Schenk and Zahnle 2007). To explain the large optical path-lengths required by the observed 2.15-μm N_2 absorption band, Triton's N_2 ice could have an unusually compacted texture, perhaps more like a sintered slab than the usual particulate soils encountered on planetary surfaces (e.g., Eluszkiewicz 1991; Grundy and Stansberry 2000). Based on seasonal models, latitudinal heterogeneity in the spatial distribution of Triton's ices is expected, but time-resolved spectroscopy reveals a longitudinal heterogeneity as well (Grundy et al. 2010). The N_2 and CO ices seem to co-occur, and to be much more abundant on Triton's Neptune-facing hemisphere. Despite being mostly dissolved in N_2 ice, Triton's CH_4 shows a very different longitudinal pattern, with its strongest absorption seen on Triton's trailing hemisphere. The H_2O and CO_2 ice absorptions show little or no longitudinal variation, as if they are globally distributed, perhaps as wind-blown dust.

To date, H_2O ice has only been detected on one other body in the Neptune system, the satellite Nereid (Brown et al. 1998, 1999). Little is known beyond photometric colors regarding compositions of Neptune's other satellites and rings (e.g., Dumas et al. 2002).

Objects at Neptune's heliocentric distance and beyond (the transneptunian region, also known as the Kuiper belt) have surface temperatures sufficiently low (<~50 K) for multiple ices to condense on their surfaces. The equilibrium temperature, T_{eq}, of a solid body is a function of both the heliocentric distance (a) of the objects and their albedos, (q), following the relation $T_{eq} = 280\ \mathrm{K}\ ((1-q)/a^2)^{1/4}$. For an object at 30 Astronomical Unitts (AU) with an albedo of 0.04 this gives T_{eq} =50.6 K. Larger heliocentric distances, a, and/or higher geometric albedos, q, lead to even lower temperatures. For objects near condensation thresholds, there is a positive feedback favoring the stability of icy surfaces once the threshold for formation is met. The stability of ices is also a function of surface gravity and the ability of a body to limit atmospheric escape. Schaller and Brown (2007) have calculated the expected stability for CH_4, N_2 and CO ices in outer solar system bodies and find that objects with diameters below 1000-1500 km are not expected to have retained significant amounts of these ices on their surfaces. The handful of larger objects in the Kuiper Belt can retain these materials, and apparently have.

Methane ice was first detected as a solid in the solar system in an infrared spectrum of Pluto (Cruikshank et al. 1976). More recently, solid CH_4 has been identified in the large Kuiper Belt Objects (KBO) Eris (Brown et al. 2005b), Sedna (Barucci et al. 2005), and Makemake (Licandro et al. 2006), as reviewed by de Bergh et al. (2013). The signal-to-noise ratio and wavelength coverage of spectra of small outer solar system objects have steadily improved.

For Pluto in particular, high signal-to-noise ratio spectra show that it shares many spectral features with Triton (Fig. 20) including multiple discrete features of CH_4, although the two clusters of features due to CO_2 ice in Triton's spectrum are absent from Pluto's spectrum. The quality and detail of the spectra allow for detailed analyses comparing band strengths and positions to constrain the detailed physical state of the ices on the surface. As with Triton, the beta N_2 2-0 absorption is interpreted as arising from optical path lengths in beta N_2 ice of the order

EBSCOhost - printed on 2/13/2023 5:26 AM via . All use subject to https://www.ebsco.com/terms-of-use

of many centimeters, implying unusually coarse particle sizes or perhaps a sintered glaze of N_2 ice, as noted above (e.g., Eluszkiewicz 1991; Grundy and Stansberry 2000). The existence of the ~2.16-μm side band in spectra of both Pluto and Triton has been used to place upper limits on the temperature of N_2 ice on those bodies (Grundy et al. 1993; Tryka et al. 1993, 1994).

Even without directly detecting its absorption bands, it may be possible to infer the presence of N_2 ice from its effect on absorptions from other species. For instance, when CH_4 is dispersed in N_2 ice, the much stronger CH_4 bands are shifted to slightly shorter wavelengths (Quirico and Schmitt 1997a), an effect which has been reported in spectra of Eris and Makemake, in addition to Pluto and Triton. Unfortunately, details of how the distinct CH_4 bands shift depend on the relative concentrations of N_2 and CH_4 are not yet fully understood (e.g., Brunetto et al. 2008; Cornelison et al. 2008), and the uniqueness of N_2 in its ability to shift CH_4 absorption bands has yet to be established. For instance, Tegler et al. (2010) report that dilution of CH_4 in argon ice produces similar shifts.

Pluto shows evidence for time-varying albedo features on its surface (Buie et al. 2010). Seasonal effects are expected to result in redistribution of surface ices over time. Grundy et al. (2013) have recently shown what appears to be seasonal evolution of features on Pluto over a decade of observation. Differing longitudinal variations of CH_4 and N_2 ices suggest that these two ices may be physically segregated on the surface. In contrast, CO and N_2 vary together with longitude, implying they are intimately mixed. Ethane ice has also been reported in spectra of Pluto, notably using bands at 2.27, 2.405, 2.457, and 2.461 μm (DeMeo et al. 2010), where it presumably forms through radiolysis and or photolysis of CH_4 (Moore and Hudson 2003).

Water ice has been detected on numerous Kuiper belt objects and Centaurs, both small and large (e.g., Dotto et al. 2003; Barkume et al. 2008; Guilbert et al. 2009). However, it seems to be absent from some of them. For most of the smaller objects, the bands are fairly shallow, consistent with their low albedos. Systematic changes in albedo and color from the Kuiper belt through the inner solar system could be linked to the sublimation loss of H_2O ice (Grundy 2009; Lamy and Toth 2009). Reports of weak absorptions at 2.2 μm in spectra of Kuiper belt objects have been tentatively attributed to ammonia or ammoniated species (e.g., Delsanti et al. 2010) and an absorption at 2.27 μm in spectra of several objects has been interpreted as resulting from methanol ice (Cruikshank et al. 1998b; Merlin et al. 2012).

The dwarf planet Haumea along with its largest satellite Hi'iaka are noteworthy for their particularly deep water ice bands (e.g., Barkume et al. 2006; Trujillo et al. 2007; Pinilla-Alonso et al. 2009). Several members of the Haumea collisional family also have similar water-rich spectral characteristics, suggesting they could be fragments of the icy mantle of a differentiated target body (Brown et al. 2007; Leinhardt et al. 2010).

A similar catastrophic impact scenario may apply in the Pluto system (Canup 2005, 2011). Unlike Pluto, the largest satellite Charon has a water ice dominated surface (Buie et al. 1987). Additionally, Charon's spectrum shows strong evidence for NH_3 ice (Cook et al. 2007). Charon may represent a sample of Pluto's mantle material which was too small to retain the more volatile CH_4, N_2, and CO ices which mask Pluto's own mantle from view. The compositions of Pluto's small satellites remain unknown.

SUMMARY

Minerals and ices are ubiquitous in the solar system. From the Earth and farther from the Sun, water ice and other more volatile ices are common. As our observational technology has improved, we have found more minerals and other solid compounds in more locations. If water ice in the poles of Mercury can be confirmed, water ice would be found throughout the solar system on every planet and/or their moons with the exception of Venus.

EBSCOhost - printed on 2/13/2023 5:26 AM via . All use subject to https://www.ebsco.com/terms-of-use

The Earth displays the greatest mineralogic diversity in the Solar System, due to two primary factors. First and foremost, the active volcanism, plate tectonics, and weather in a relatively warm environment provide the conditions for many chemical processes, leading to diverse compositions. Second, because we live on the Earth, we can study it in far greater detail than any other moon or planet.

But as we explore other worlds, we are finding they too have diverse mineralogy. On Mars, for example, it was difficult to prove a case for any clay minerals on the surface as recently as a decade or so ago. But now with orbiting imaging spectrometers with spatial resolutions as low as about 20 m, smaller outcrops are being found to contain diverse mineralogy indicative of a more complex geologic history.

There are outstanding issues. Some small absorptions seen in spectra of outer solar system objects have yet to be identified. For example, possible SO_2 absorptions on the outer three icy Galilean satellites need confirmation. A 2.42-μm absorption seen in spectra of Saturn's satellites, identified as trapped H_2, needs confirmation, and a 5.01-μm absorption seen in spectra of Titan remains unidentified. Some absorptions seen in CRISM spectra of Mars are also still unidentified or poorly understood. This implies a continuing need for improving spectral libraries of reference compounds.

Water ice dominates most icy objects in the outer solar system. But why is the ice so pure in Saturn's rings and most satellites, yet Titan is covered in organics? Similarly, Pluto is covered in organics yet its moon Charon displays a relatively pure water ice surface. What drives most surfaces to show such pure water surfaces with few other ices is unknown. Where are the expected signatures of ammonia or ammonia-water mixtures? If methane is so abundant on Pluto, Triton, Eris, Makemake, and Titan, why is it not abundant on other objects?

Why are some objects very high in albedo with relatively pure ice surfaces while others are very dark (e.g., Phoebe, the two faces of Iapetus, brighter Hyperion, dark Callisto versus brighter Ganymede and Europa)? Some of the answers certainly relate to resurfacing (e.g., Europa and Enceladus), whereas others display ancient heavily cratered surfaces that are still bright (e.g., Rhea) and still other ancient surfaces are dark (e.g., Phoebe). The mechanisms leading to these diverse surface compositions are not completely understood, although there is a trend in the Jupiter and Saturn systems for increasing darkening on moons farther from the planet, implying that dark dust preferentially coats the outer moons, probably from sources external to the system.

How are molecules complexed with one another, as in the case of CO_2 and CH_4 enclathrated in H_2O, and what are the spectroscopic and physical-chemical implications of the processes that lead to complexing?

If water condenses below 135 K, it is expected to be amorphous. Yet the spectra of water ice throughout the solar system is dominated by crystalline ice (where our spectra are of sufficient quality to distinguish between amorphous versus crystalline water ice), with the exception of icy satellites orbiting within Jupiter's inner magnetosphere where intense radiation can destroy the ice crystal structure**.** Even in the outer solar system beyond Saturn, where temperatures are well below 90 K, observed water ices are at least partially crystalline. Why we do not observe more amorphous ice is a mystery.

Spectroscopy and imaging spectroscopy have played major roles in exploring the solar system, and will continue to do so into the future.

ACKNOWLEDGMENTS

Portions of this work were funded by NASA Cassini VIMS (R. Clark, Team Member), NASA MRO CRISM team (R. Clark, co-I, with G. Swayze) and the Cassini Data Analysis

EBSCOhost - printed on 2/13/2023 5:26 AM via . All use subject to https://www.ebsco.com/terms-of-use

Program (R. Clark, PI). Portions were also funded by the U.S. Geological Survey Minerals Program (R. Clark and G. Swayze). Portions of this work were performed at the Jet Propulsion Laboratory, California Institute of Technology, under contract with NASA. (R. Carlson). W. Grundy gratefully acknowledges support from NASA grant NNX11AM53G to Lowell Observatory.

REFERENCES

Anders E, Grevesse N (1989) Abundances of the elements: Meteoritic and solar. Geochim Cosmochim Acta 53:197-214

Apt J, Carleton NP, Mackay CD (1983) Methane on Triton and Pluto: New CCD Spectra. Astrophys J 270:342-350

Asphaug E, Reufer A (2013) Late origin of the Saturn system. Icarus 223:544-565

Bagenal F, Dowling TE, McKinnon WB (eds) (2004) Jupiter. Cambridge University Press, Cambridge

Baines KH, Bellucci G, Bebring JP, Brown RH, Bussoletti E, Capaccioni F, Cerroni R, Clark RN, Coradini A, Cruikshank DP, Drossart P, Formisano V, Jauman R, Langevin Y, Matson DL, McCord TB, Mennella V, Nelson RM, Nicholson PD, Sicardy B, Sotin C, Hansen GB, Aiello JJ, Amici S, the Cassini VIMS team (2000) Detection of sub-micron radiation from the surface of Venus by the Cassini/VIMS. Icarus 148:307-311

Baines KH, Yanamandra-Fisher PA, Lebofsky LA, Momary TW, Golisch W, Kaminski C, Wild WJ (1998) Near-infrared absolute photometric imaging of the Uranian system. Icarus 132:266-284

Baklouti D, Schmitt B, Brissaud O (2008) S_2O, polysulfur oxide and sulfur polymer on Io‘s surface? Icarus 194:647-659

Bandfield JL, Glotch TD, Christensen PR (2003) Spectroscopic identification of carbonates in the Martian dust. Science 301:1084:1987

Bandfield JL, Hamilton VE, Christensen PR, McSween HY Jr (2004) Identification of quartzofeldspathic materials on Mars. J Geophys Res109:E10009, doi: 10.1029/2004JE002290

Barkume K.M, Brown ME, Schaller EL (2006) Water ice on the satellite of Kuiper belt object 2003 EL61. Astrophys J 640:L87-L89

Barkume KM, Brown ME, Schaller EL (2008) Near-infrared spectra of Centaurs and Kuiper belt objects. Astron J 135:55-67

Barnes JW, Brown RH, Soderblom L, Sotin C, Le Mouélic S, Rodriguez S, Jaumann R, Beyer RA, Buratti BJ, Pitman K, Baines KH, Clark R, Nicholson P (2008) Spectroscopy, Morphometry, and Photoclinometry of Titans Dunefields from Cassini/VIMS. Icarus 195:400-414, doi: 10.1016/j.icarus.2007.12.006

Barnes JW, Brown RH, Turtle EP, McEwen AS, Lorenz RD, Janssen M, Schaller EL, Brown ME, Buratti BJ, Sotin C, Griffith C, Clark R, Perry J, Fussner S, Barbara J, West R, Elachi C, Bouchez AH, Roe HG, Baines KH, Bellucci G, Bibring JP, Capaccioni F, Cerroni P, Combes M, Coradini A, Cruikshank DP, Drossart P, Formisano V, Jaumann R, Langevin Y, Matson DL, McCord TB, Nicholson PD, Sicardy B (2005) A 5-μm bright spot on Titan: Evidence for surface diversity: Science 310:92-94, http://www.sciencemag.org/cgi/content/full/310/5745/92

Barnes JW, Radebaugh J, Brown RH, Wall S, Soderblom L, Lunine J, Burr D, Sotin C, Le Mouélic S, Rodriguez S, Buratti BJ, Clark RN, Baines RN, Jaumann R, Nicholson PD, Kirk RL, Lopes R, Lorenz RD, Mitchell K, Wood CA (2007) Near-infrared spectral mapping of Titan’s mountains and channels. J Geophys Res 112:E11006, doi: 10.1029/2007JE002932

Barry P, Shepanski J, Segal C (2001) On-orbit spectral calibration verification of the Hyperion instrument, IGARSS presentation. http://eo1.gsfc.nasa.gov/new/validationReport/Technology/TRW_EO1%20Papers_Presentations/21.pdf

Barucci MA, Cruikshank DP, Dotto E, Merlin F, Poulet F, Dalle Ore C, Fornasier S, de Bergh C (2005) Is Sedna another Triton? Astron Astrophys 439:L1-L4

Bauer JM, Roush TL, Geballe TR, Meech KJ, Owen TC, Vacca WD, Rayner JT, Jim KTC (2002) The near infrared spectrum of Miranda: Evidence of crystalline water ice. Icarus 158:178-190

Bibring JP, Langevin Y, Mustard JF, Poulet F, Arvidson R, Grendrin A, Gondet B, Mangold N, Pinet P, Forget F, Berthe M, Bibring J-P, Gomez C, Jouglet D, Soufflot A, Vincendon M, Combes M, Drossart P, Encrenaz T, Fouchet T, Merchiorri R, Belluci G-C, Altieri F, Formisano V, Capaccioni F, Cerroni P, Coradini A, Fonti S, Korablev O, Kottsov V, Ignatiev N, Moroz V, Titov D, Zasova L, Loiseau D, Doute S, Schmitt B, Sotin C, Hauber E, Hoffmann H, Jaumann R, Keller U, Duxbury T, Neukum G (2006) Global mineralogical and aqueous mars history derived from OMEGA/Mars Express data. Science 312(5772):400-404, doi: 10.1126/science.1122659

EBSCOhost - printed on 2/13/2023 5:26 AM via . All use subject to https://www.ebsco.com/terms-of-use

Bibring J-P, Langevin Y, Poulet F, Gendrin A, Gondet B, Berthé M, Soufflot A, Drossart P, Combes M, Bellucci G, Moroz V, Mangold N, Schmitt B and the OMEGA team (2004b) Perennial water ice identified in the south polar cap of Mars. Nature 428:627-630

Bibring J-P, Soufflot A, Berthé M, Langevin Y, Gondet B, Drossart P, Bouyé M, Combes M, Puget P, Semery A, Bellucci G, Formisano V, Moroz V, Kottsov V, Bonello G, Erard S, Forni O, Gendrin A, Manaud N, Poulet F, Poulleau G, Encrenaz T, Fouchet T, Melchiori R, Altieri F, Ignatiev N, Titov D, Zasova L, Coradini A, Capacionni F, Cerroni P, Fonti S, Mangold N, Pinet P, Schmitt B, Sotin C, Hauber E, Hoffmann H, Jaumann R, Keller U, Arvidson R, Mustard J, Forget F (2004a) OMEGA: Observatoire pour le Minéralogie, l'Eau, les Glaces et l'Activité´. European Space Agency Special Publication 1240:37-49

Bishop JL, Noe Dobrea EZ, McKeown NK, Parente M, Ehlmann BL, Michalski JR, Milliken RE, Poulet F, Swayze GA, Mustard JF, Murchie SL, Bibring J-P (2008) Phyllosilicate diversity and past aqueous activity revealed at Mawrth Vallis, Mars. Science 321(5890):830-833, doi: 10.1126/science.1159699

Bishop JL, Parente M, Weitz CM, Noe Dobrea EZ, Roach LH, Murchie SL, McGuire PC, McKeown NK, Rossi CM, Brown AJ, Calvin WM, Milliken R, Mustard JF (2009) Mineralogy of Juventae Chasma: Sulfates in light-toned mounds, mafic minerals in the bedrock, and hydrated silica and hydroxylated ferric sulfate on the plateaus. J Geophys Res 114:E00D09, doi: 10.1029/2009JE003352

Bohn RB, Sandford SA, Allamandola LJ, Cruikshank DP (1994) Infrared spectroscopy of Triton and Pluto ice analogs: The case for saturated hydrocarbons. Icarus 111:151-173

Brown ME, Barkume KM, Blake GA, Schaller EL, Rabinowitz DL, Roe HG, Trujillo CA (2007) Methane and ethane on the bright Kuiper belt object 2005 FY9. Astron J 133:284-289

Brown ME, Hand KP (2013) Salts and radiation products on the surface of Europa. Astron J 145:110

Brown ME, Koresko CD, Blake GA (1998) Detection of water ice on Nereid. Astrophys J 508:L175-L176

Brown ME, Trujillo CA, Rabinowitz DL (2005b) Discovery of a planetary-sized object in the scattered Kuiper Belt. Astryphys J 635:L97-L100

Brown RH (1983) The uranian satellites and Hyperion: New spectrophotometry and compositional implications. Icarus 56:414-425

Brown RH, Baines KH, Bellucci G, Bibring JP, Buratti BJ, Bussoletti E, Capaccioni F, Cerroni P, Clark RN, Coradini A, Cruikshank DP, Drossart P, Formisano V, Jaumann R, Langevin Y, Matson DL (2005a) The Cassini visual and infrared mapping spectrometer investigation. Space Sci Rev 115(1-4):111-168

Brown RH, Clark RN (1984) Surface of Miranda: Identification of water ice. Icarus 58:288-292

Brown RH, Clark RN, Buratti BJ, Cruikshank DP, Barnes JW, Mastrapa RME, Bauer J, Newman S, Momary T, Baines KH, Bellucci G, Capaccioni F, Cerroni P, Combes M, Coradini A, Drossart P, Formisano V, Jaumann R, Langevin Y, Matson DL, McCord TB, Nelson RM, Nicholson PD, Sicardy B, Sotin C (2006) Composition and Physical Properties of Enceladus Surface. Science 311:1425-1428

Brown RH, Cruikshank DP, Pendleton Y, Veeder GJ (1999) Water ice on Nereid. Icarus 139:374-378

Brown RH, Johnson TV, Synnott S, Anderson JD, Jacobson RA, Dermott SF, Thomas PC (1991) Physical properties of the Uranian satellites. *In:* Uranus. Bergstralh JT, Miner ED, Matthews MS (eds) University of Arizona Press, Tucson, p 513-527

Brown RH, Kirk RL, Johnson TV, Soderblom LA (1990) Energy sources for Triton's geyser-like plumes. Science 250:431-435

Brown RH, Soderblom LA, Soderblom JM, Clark RN, Jaumann R, Barnes JW, Sotin C, Buratti B, Baines KH, Nicholson PD (2008) The identification of liquid ethane in Titan's Ontario Lacus. Nature 454:607-610

Brunetto R, Caniglia G, Baratta GA, Palumbo ME (2008) Integrated near-infrared band strengths of solid CH4 and its mixtures with N2. Astrophys J 686:1480-1485

Buie MW, Cruikshank DP, Lebofsky LA, Tedesco EF (1987) Water frost on Charon. Nature 329:522-523

Buie MW, Grundy WM, Young EF, Young LA, Stern SA (2010) Pluto and Charon with the Hubble Space Telescope. II. Resolving changes on Pluto's surface and a map for Charon. Astron J 139:1128-1143

Buratti BJ, Cruikshank DP, Brown RH, Clark RN, Bauer JM, Jaumann R, McCord TB, Simonelli DP, Hibbitts CA, Hansen GA, Owen TC, Baines KH, Bellucci G, Bibring JP, Capaccioni F, Cerroni P, Coradini A, Drossart P, Formisano V, Langevin Y, Matson DL, Mennella V, Nelson RM, Nicholson PD, Sicardy B, Sotin C, Roush TL, Soderlund K, Muradyan A (2005) Cassini visual and infrared mapping spectrometer observations of Iapetus: Detection of CO_2. Astrophys J 622:L149-L152

Byrne S, Ingersoll AP (2003) A sublimation model for Martian south polar ice features. Science 299:1051-1053

Calvin WM, Johnson RE, Spencer JR (1996) O_2 on Ganymede: Spectral characteristics and plasma formation mechanisms. Geophys Res Lett 23:673-676

Campins H, Hargrove K, Howell ES, Kelley MS, Licandro J, Mothi-Diniz T, Ziffer J, Fernandez Y, Pinilla-Alonso N (2009) Confirming water ice on the surface of Asteroid 24 Themis. American Astronomical Society, DPS meeting #41, #32.05 *http://adsabs.harvard.edu/abs/2009DPS....41.3205C*

Campins H, Hargrove K, Pillina-Alonso N, Howell ES, Kelley MS, Licandro J, Mothe-Dinez T, Fernandez Y, Ziffer J (2010) Water ice and organics on the surface of the Asteroid 24 Themis. Nature 464:1320-1321

Canup RM (2005) A giant impact origin of Pluto-Charon. Science 307:546-550

EBSCOhost - printed on 2/13/2023 5:26 AM via . All use subject to https://www.ebsco.com/terms-of-use

Canup RM (2010) Origin of Saturn's rings and inner moons by mass removal from a lost Titan-sized satellite. Nature 468:943-946

Canup RM (2011) On a giant impact origin of Charon, Nix, and Hydra. Astron J 141:35.1-9

Carlson RW, Anderson MS, Johnson RE, Schulman MB, Yavrouian AH (2002) Sulfuric acid production on Europa: The radiolysis of sulfur in water ice. Icarus 157:456-463

Carlson RW, Anderson MS, Johnson RE, Smythe WD, Hendrix AR, Barth CA, Soderblom LA, Hansen GB, McCord TB, Dalton JB, Clark RN, Shirley JH, Ocampo AC, Matson DL (1999a) Hydrogen peroxide on the surface of Europa. Science 283:2062-2064

Carlson RW, Anderson MS, Mehlman R, Johnson RE (2005) Distribution of hydrate on Europa: Further evidence for sulfuric acid hydrate. Icarus 177:461-471

Carlson RW, Baines KH, Encrenaz Th, Taylor FW, D Prossart, LW Kamp, Pollack JB, Lellouch E, Collard AD, Calcutt SB, Grinspoon DH, Weissman PR, Smythe WD, Ocampo AC, Danielson GE, Fanale FP, Johnson TV, Kieffer HH, Matson DL, McCord TB, Soderblom L (1991) Galileo infrared imaging spectroscopy measurements at Venus. Science 253:1541-1548

Carlson RW, Calvin WM, Dalton JB, Hansen GB, Hudson RL, Johnson RE, McCord TB, Moore MH (2009) Europa's Surface Composition. *In:* Europa. Pappalardo RT, McKinnon WB, Khurana KK (eds) Univ. Ariz. Press, Tucson, p 283-327

Carlson RW, Johnson RE, Anderson MS (1999b) Sulfuric acid on Europa and the radiolytic sulfur cycle. Science 286:97-99

Carlson RW, Kargel JS, Doute S, Soderblom LA, Dalton B (2007) Io's surface composition. *In:* Io after Galileo. Lopes RMC, Spencer JR (eds) Springer - Praxis, Chichester, p 193-229

Carlson RW, Smythe W, Baines K, Barbinis E, Becker K, Burns R, Calcutt S, Calvin W, Clark R, Danielson G, Davies A, Drossart P, Encrenaz T, Fanale F, Granahan J, Hansen G, Herrera P, Hibbitts C, Hui J, Irwin P, Johnson T, Kamp L, Kieffer H, Leader F, Lellouch E, LopesGautier R, Matson D, McCord T, Mehlman R, Ocampo A, Orton G, RoosSerote M, Segura M, Shirley J, Soderblom L, Stevenson A, Taylor F, Torson J, Weir A, Weissman P (1996) Near-infrared spectroscopy and spectral mapping of Jupiter and the Galilean satellites: Results from Galileo's initial orbit. Science 274:385-388

Carlson RW, Smythe WD, Lopes Gautier RMC, Davies AG, Kamp LW, Mosher JA, Soderblom LA, Leader FE, Mehlman R, Clark RN, Fanale FP (1997) The distribution of sulfur dioxide and other infrared absorbers on the surface of Io. Geophys Res Lett 24:2479-2482

Cassidy TA, Paranicas CP, Shirley JH, Dalton JB, Teolis BD, Johnson RE, Kamp L, Hendrix AR (2013) Magnetospheric ion sputtering and water ice grain size at Europa. Planet. Space Sci 77:64-73

Cassini GD (1672) Phil. Trans. 12:831. Quoted in Alexander, AFO'D, 1962, *The Planet Saturn*, McMillan, New York, 474

Chapman CR (2004) Space weathering of asteroid surfaces. Annu Rev Earth Planet Sci 32:539-567

Cheng AF, Haff PK, Johnson RE, Lanzerotti LJ (1986) Interactions of magnetospheres with icy satellite surfaces. *In*: Satellites. Burns JA, Matthews MS (eds) Univ. Arizona Press, Tucson, p 403-436

Christensen PR, Anderson DL, Stillman CC, Clark RN, Kieffer HH, Malin MC, Pearl JC, Carpenter JC, Bandera NB, Brown FG, Silverman S (1992) Thermal emission spectrometer experiment: Mars Observer Mission. J Geophys Res 97:7719-7734

Christensen PR, Bandfield JL, Clark RN, Edget KS, Hamilton VE, Hoefen T, Kieffer HH, Kuzmin RO, Lane MD, Malin MC, Morris RV, Pearl JC, Pearson R, Roush TL, Ruff SW, Smith MD (2000) Detection of crystalline hematite mineralization on Mars by the Thermal Emission Spectrometer: Evidence for near-surface water. J Geophys Res 105(E4):9623-9644, doi: 10.1029/1999JE001093

Christensen PR, Bandfield JL, Hamilton VE, Ruff SW, Kieffer HH, Titus TN, Malin MC, Morris RV, Lane MD, Clark RN, Jakosky BM, Mellon MT, Pearl JC, Conrath BJ, Smith MD, Clancy RT, Kuzmin RO, Roush T, Mehall GL, Gorelick N, Bender K, Murray K, Dason S, Greene E, Silverman S, Greenfield M (2001) Mars Global Surveyor Thermal Emission Spectrometer experiment: Investigation description and surface science results. J Geophys Res 106(E10):23823-23871, doi: 10.1029/2000JE001370

Christensen PR, Jakosky BM, Kieffer HH, Malin MC, McSween HY, Nealson K, Mehall GL, Silverman SH, Ferry S, Caplinger M, Ravine M (2004) The Thermal Emission Imaging System (THEMIS) for the Mars 2001 Odyssey mission. Space Sci Rev 110:85-130

Clark RN (1979) Planetary reflectance measurements in the region of planetary thermal emission. Icarus 40:94-103

Clark RN (1980) Ganymede, Europa, Callisto, and Saturn's Rings: Compositional analysis from reflectance spectroscopy. Icarus 44:388-409

Clark RN (1981) Water frost and ice: The near-infrared spectral reflectance 0.65-2.5 μm. J Geophys Res 86: 3087-3096

Clark RN (1999) Spectroscopy of rocks and minerals and principles of spectroscopy. *In:* Manual of Remote Sensing. Volume 3. Rencz AN (ed) John Wiley and Sons, New York, p 3-58

EBSCOhost - printed on 2/13/2023 5:26 AM via . All use subject to https://www.ebsco.com/terms-of-use

Clark RN (2009) Detection of adsorbed water and hydroxyl on the Moon. Science 326:562-564, doi: 10.1126/science.1178105

Clark RN, Lucey PG (1984) Spectral properties of ice-particulate mixtures and implications for remote sensing I: Intimate mixtures. J Geophys Res 89:6341-6348

Clark RN, McCord TB (1980) The Galilean satellites: new near-infrared spectral reflectance measurements (0.65-2.5 μm) and a 0.325-5 μm summary. Icarus 41:323-329

Clark RN, Brown RH, Owensby PD, Steele A (1984) Saturn's satellites: near-infrared spectrophotometry (0.65-2.5 μm) of the leading and trailing sides and compositional implications. Icarus 58:265-281

Clark RN, Fanale FP, Gaffey MJ (1986) Surface composition of natural satellites. *In:* Satellites. Burns JA, Matthews MS (eds) Univ. of Arizona Press, Tucson, p 437-491

Clark RN, Green RO, Swayze GA, Meeker G, Sutley S, Hoefen TM, Livo KE, Plumlee G, Pavri B, Sarture C, Wilson S, Hageman P, Lamothe P, Vance JS, Boardman J, Brownfield I, Gent C, Morath LC, Taggart J, Theodorakos PM, Adams M (2001) Environmental studies of the World Trade Center area after the September 11, 2001 attack. US Geological Survey Open File Report OFR-01-0429, http://pubs.usgs.gov/of/2001/ofr-01-0429/

Clark RN, Swayze GA, Livo KE, Kokaly RF, King TVV, Dalton JB, Vance JS, Rockwell BW, Hoefen T, McDougal RR (2002) Surface reflectance calibration of terrestrial imaging spectroscopy data: a tutorial using AVIRIS. *In:* Proceedings of the 10th Airborne Earth Science Workshop, JPL Publication 02-1, http://speclab.cr.usgs.gov/PAPERS.calibration.tutorial/

Clark RN, Swayze GA, Livo KE, Kokaly RF, Sutley SJ, Dalton JB, McDougal RR, Gent CA (2003) Imaging spectroscopy: Earth and planetary remote sensing with the USGS Tetracorder and expert systems. J Geophys Res 108(E12):5131, doi: 10.1029/2002JE001847

Clark RN, Brown RH, Jaumann R, Cruikshank DP, Nelson RM, Buratti BJ, McCord TB, Lunine J, Baines KH, Bellucci G, Bibring JP, Capaccioni F, Cerroni P, Coradini A, Formisano F, Langevin Y, Matson DL, Mennella V, Nicholson PD, Sicardy B, Sotin C, Hoefen TM, Curchin JM, Hansen G, Hibbits K, Matz KD (2005) Compositional maps of Saturn's moon Phoebe from imaging spectroscopy. Nature 435(7038):66-69, doi: 10.1038/nature03558

Clark RN, Swayze GA, Hoefen TM, Green RO, Livo KE, Meeker G, Sutley S, Plumlee G, Pavri B, Sarture C, Boardman J, Brownfield I, Morath LC (2006) Environmental mapping of the World Trade Center area with imaging spectroscopy after the September 11, 2001 attack. *In*: Urban Aerosols and Their Impacts: Lessons Learned from the World Trade Center Tragedy. ACS Symposium Series 919. Gaffney J, Marley NA (eds) Oxford University Press, p 66-83, plates 4.1-4.6

Clark RN, Swayze GA, Wise R, Livo E, Hoefen T, Kokaly R, Sutley SJ (2007) USGS digital spectral library splib06a. U.S. Geological Survey, Digital Data Series 231. *http://speclab.cr.usgs.gov/spectral.lib06/*

Clark RN, Curchin JM, Jaumann R, Cruikshank DP, Brown RH, Hoefen TM, Stephan K, Moore JM, Buratti BJ, Baines KH, Nicholson PD, Nelson RM (2008a) Compositional mapping of Saturn's satellite Dione with Cassini VIMS and implications of dark material in the Saturn System. Icarus 193:372-386

Clark RN, Cruikshank DP, Jaumann R, Filacchione G, Nicholson PD, Brown RH, Stephan K, Hedman M, Buratti BJ, Curchin JM, Hoefen TM, Baines KH, Nelson R (2008b) Compositional mapping of Saturn's rings and icy satellites with Cassini VIMS. *In*: Saturn After Cassini-Huygens., London, July, 2008 {abstract}

Clark RN, Curchin JM, Hoefen TM, Swayze GA (2009) Reflectance spectroscopy of organic compounds I: Alkanes. J Geophys Res 114:E03001, doi: 10.1029/2008JE003150

Clark RN, Curchin JM, Barnes JW, Jaumann R, Soderblom L, Cruikshank DP, Lunine J, Stephan K, Hoefen TM, Le Mouelic S, Sotin C, Baines KH, Buratti B, Nicholson P (2010a) Detection and mapping of hydrocarbon deposits on Titan. J Geophys Res 115:E10005, doi: 10.1029/2009JE003369

Clark RN, Swayze GA, Leifer I, Livo KE, Kokaly R, Hoefen T, Lundeen S, Eastwood M, Green RO, Pearson N, Sarture C, McCubbin I, Roberts D, Bradley E, Steele D, Ryan T, Dominguez R, and the Airborne Visible/Infrared Imaging Spectrometer (AVIRIS) Team (2010b) A method for quantitative mapping of thick oil spills using imaging spectroscopy. U.S. Geological Survey Open-File Report 20101167, 51, http://pubs.usgs.gov/of/2010/1167/

Clark RN, Wise RA (2011) Mapping with imaging spectroscopy, Fort Cobb Reservoir watershed, southwestern Oklahoma. *In:* Assessment of conservation practices in the Fort Cobb Reservoir watershed, southwestern Oklahoma. Becker CJ (ed) U.S. Geological Survey Scientific Investigations Report 2010–5257, 23

Clark RN, Cruikshank DP, Jaumann R, Brown RH, Curchin JM, Hoefen TM, Stephan K, Dalle Ore CM, Buratti BJ, Filacchione G, Baines KH, Nicholson PD (2012) The Composition of Iapetus: Mapping Results from Cassini VIMS. Icarus 218:831-860

Clark RN, Carlson R, Grundy W, Noll K (2013) Observed ices in the Solar System. *In*: The Science of Solar System Ices. Astrophysics and Space Science Library Series, Vol. 356. Gudipati MS, Castillo-Rogez J (eds) Springer, p 3-46, doi: 10.1007/978-1-4614-3076-6_1

EBSCOhost - printed on 2/13/2023 5:26 AM via . All use subject to https://www.ebsco.com/terms-of-use

Colaprete A, Schultz P, Heldmann J, Wooden D, Shirley M, Ennico K, Hermalyn B, Marshall W, Ricco A, Elphic RC, Goldstein D, Summy D, Bart GD, Asphaug E, Korycansky D, Landis D Sollitt L (2010) Detection of Water in the LCROSS Ejecta Plume. Science 330:463-468, doi: 10.1126/science.1186986

Cook JC, Desch SJ, Roush TL, Trujillo CA, Geballe TR (2007) Near-infrared spectroscopy of Charon: Possible evidence for cryovolcanism on Kuiper belt objects. Astrophys J 663:1406-1419

Cornelison DM, Tegler SC, Grundy W, Abernathy M (2008) Near-infrared laboratory spectroscopy of CH_4/N_2 ice mixtures: Implications for icy dwarf planets. Paper presented at The Science of Solar System Ices (ScSSI): A cross-disciplinary workshop, Oxnard CA, 2008 May 5-8

Coustenis A (2005) Formation and evolution of Titan's atmosphere. Space Sci Rev 116:171-184

Coustenis A, Achterberg R, Conrath B, Jennings D, Marten A, Gautier D, Nixon C, Flasar M, Teanby N, Bezard B, Samuelson RE, Carlson R, Lellouch E, Bjoraker G, Romani P, Taylor FW, Irwin P, Fouchet Th, Hubert A, Orton G, Kunde V, Vinatier S, Mondellini J, Abbas M, Courtin R (2006a) The composition of Titan's stratosphere from Cassini/CIRS mid-infrared spectra. Icarus 189:35-62

Coustenis A, Achterberg R, Conrath B, Jennings D, Marten A, Gautier D, Nixon C, Flasar F, Teanby N, Bezard B, Samuelson R, Carlson R, Lellouch E, Bjoraker G, Romani P, Taylor F, Irwin P, Fouchet T, Hubert A, Orton G, Kunde V, Vinatier S, Mondellini J, Abbas M, Courtin R (2007) The composition of Titan's stratosphere from Cassini/CIRS mid-infrared spectra. Icarus 189:35-62

Coustenis A, Bezard B, Gautier D (1989) Titan's atmosphere from Voyager integrated observations – II. The CH_3D abundance and D/H ration from the 900-1200 cm^{-1} spectral region. Icarus 82:67-80 {NOT USED?}

Coustenis A, Negrão A, Salama A, Schulz B, Lellouch E, Rannou P, Drossart P, Encrenaz T, Schmitt B, Boudon V, Nikitin A (2006b) Titan's 3-μm spectral region from ISO high-resolution spectroscopy. Icarus 180:176-185, doi:10.1016/j.icarus.2005.08.007

Coustenis A, Salama A, Schultz B, Ott S, Lellouch E, Encrenaz T, Gautier D, Feuchtgruber H (2003) Titan's atmosphere from ISO mid-infrared spectroscopy. Icarus 161:383-403

Coustenis A, Schmitt B, Khanna R, Trotta F (1999) Plausible condensates in Titan's stratosphere from Voyager infrared spectra. Planet Space Sci 47:1305-1329

Cruikshank DP (1980) Near infrared studies of the satellites of Saturn and Uranus. Icarus 41:246-258

Cruikshank DP, Apt J (1984) Methane on Triton: Physical state and distribution. Icarus 58:306-311

Cruikshank DP, Bell JF, Gaffey MJ, Brown RH, Howell R, Beerman C, Rognstad M (1983) The Dark Side of Iapetus. Icarus 53:90-104

Cruikshank DP, Brown RH (1981) The Uranian satellites: Water ice on Ariel and Umbriel. Icarus 45:607-611

Cruikshank DP, Brown RH, Calvin W, Roush TL, Bartholomew MJ, (1998a) Ices on the satellites of Jupiter, Saturn, and Uranus. *In*: Solar System Ices. Schmitt B, de Bergh C, Festou M (eds) Kluwer Academic, Dordrecht, p 579-606

Cruikshank DP, Brown RH, Clark RN (1984) Nitrogen on Triton. Icarus 58:293-305

Cruikshank DP, Brown RH, Giver LP, Tokunaga AT (1989) Triton: Do we see the surface? Science 245:283-286

Cruikshank DP, Brown RH, Tokunaga AT, Smith RG, Piscitelli JR (1988) Volatiles on Triton: The infrared spectral evidence, 2.0-2.5 microns. Icarus 74:413-423

Cruikshank DP, Dalton JB, Dalle Ore CM, Bauer J, Stephan K, Filacchione G, Hendrix CJ, Hansen CJ, Coradini A, Cerroni P, Tosi F, Capaccioni F, Jaumann R, Buratti BJ, Clark RN, Brown RH, Nelson RM, McCord TB, Baines KH, Nicholson PD, Sotin C, Meyer AW, Bellucci G, Combes M, Bibring JP, Langevin Y, Sicardy B, Matson DL, Formisano V, Drossart P, Mennella V (2007) Surface composition of Hyperion. Nature 448:54-57, doi: 101038/nature05948

Cruikshank DP, Emery JP, Kornei KA, Bellucci G, d'Aversa E (2010a) Eclipse reappearances of Io: Time-resolved spectroscopy (1.9-4.2 μm). Icarus 205:516-527, doi: 10.1016;j.icarus.2009.05.035

Cruikshank DP, Meyer AW, Brown RH, Clark RN, Jaumann R, Stephan K, Hibbitts CA, Sandford SA, Mastrapa RME, Filacchione G, Dalle Ore CM, Nicholson PD, Buratti BJ, McCord TB, Nelson RM, Dalton JB, Baines KH, Matson DL (2010b) Carbon dioxide on the satellites of Saturn: Results from the Cassini VIMS investigation and revision to the VIMS wavelength scale. Icarus 206:561-572, doi: 10.1016/j.icarus.2009.07.012

Cruikshank DP, Owen TC, Ore CD, Geballe TR, Roush TL, de Bergh C, Sandford SA, Poulet F, Benedix GK, Emery JP (2005) A spectroscopic study of the surfaces of Saturn's large satellites: H_2O ice, tholins, and minor constituents. Icarus 175:268-283

Cruikshank DP, Pilcher CB, Morrison D (1976) Pluto - Evidence for methane frost. Science 194:835-837

Cruikshank DP, Roush TL, Bartholomew MJ, Geballe TR, Pendleton YJ, White SM, Bell III JF, Davies JK, Owen TC, de Bergh C, Tholen DJ, Bernstein MP, Brown RH, Tryka KA, Dalle Ore CM (1998b) The composition of Centaur 5145 Pholus. Icarus 135:389-407

Cruikshank DP, Roush TL, Owen TC, Geballe TR, de Bergh C, Schmitt B, Brown RH, Bartholomew MJ (1993) Ices on the surface of Triton. Science 261:742-745

Cruikshank DP, Schmitt B, Roush TL, Owen TC, Quirico E, Geballe TR, de Bergh C, Bartholomew MJ, Dalle Ore CM, Doute S, Meier R (2000) Water ice on Triton. Icarus 147:309-316

EBSCOhost - printed on 2/13/2023 5:26 AM via . All use subject to https://www.ebsco.com/terms-of-use

Cruikshank DP, Silvaggio PM (1979) Triton: A satellite with an atmosphere. Astrophys J 233:1016-1020
Cruikshank DP, Wegryn E, Dalle Ore CM, Brown RH, Baines KH, Bibring JP, Buratti BJ, Clark RN, McCord TB, Nicholson PD, Pendleton YJ, Owen TC, Filacchione G, and the VIMS Team (2008) Hydrocarbons on Saturn's Satellites Iapetus and Phoebe. Icarus 193:334-343, doi: 10.1016/j.icarus.2007.04.036
Cull S, Arvidson RE, Mellon MT, Wiseman SJ, Clark RN, Titus TN, Morris RV, McGuire P (2010) Seasonal H_2O and CO_2 ice cycles at the Mars Phoenix landing site: 1. Prelanding CRISM and HiRISE observations. J Geophys Res 115:E00D16, doi: 10.1029/2009JE003340
Cuzzi J, Clark R, Filacchione G, French R, Johnson R, Marouf E, Spilker L (2009) Ring particle composition and size distribution. *In*: Saturn from Cassini/Huygens. Dougherty M, Esposito L, Krimigis S (eds) Springer, p 459-509, doi: 10.1007/978-1-4020-9215-2
Dalton JB, Cassidy T, Paranicas C, Shirley JH, Prockter LM, Kamp LW (2013) Exogenic controls on sulfuric acid hydrate production at the surface. Planet Space Sci 77:45-63
Dalton JB, Cruikshank DP, Stephan K, McCord TB, Coustenis A, Carlson RW, Coradini A (2010) Chemical Composition of Icy Satellite Surfaces. Space Science Review Series 153. Springer
Dalton JB, Prieto-Ballesteros O, Kargel JS, Jamieson CS, Jolivet J, Quinn RC (2005) Spectral comparison of heavily hydrated salts with disrupted terrains on Europa. Icarus 177:472-490
Dalton JB, Shirley JH, Kamp LW (2012) Europa's icy bright plains and dark linea: Exogenic and endogenic contributions to composition and surface properties. J Geophys Res Planets 117:E03003, doi: 10.1029/2011JE0033909
Davies JK, Geballe TR, Hanner MS, Weaver HA, Crovisier J, Bockelée-Morvan D (1997) Thermal infrared spectra of comet Hale-Bopp at heliocentric distances of 4 and 2.9 AU, Earth Moon Planets 78:293-298
de Bergh C, Schaller EL, Brown ME, Brunetto R, Cruikshank DP, Schmitt B (2013) The ices on transneptunian objects and Centaurs. *In:* The Science of Solar System Ices. Astrophysics and Space Science Library Series, Volume 356. Gudipati MS, Castillo-Rogez J (eds) Springer, p. 107-146, doi: 10.1007/978-1-4614-3076-6_1
Delsanti A, Merlin F, Guilbert-Lepoutre A, Bauer J, Yang B, Meech KJ (2010) Methane, ammonia, and their irradiation products at the surface of an intermediate-size KBO? A portrait of Plutino (90482) Orcus. Astron Astrophys 520:A40.1-15
DeMeo FE, Dumas C, de Bergh C, Protopapa S, Cruikshank DP, Geballe TR, Alvarez-Candal A, Merlin F, Barucci MA (2010) A search for ethane on Pluto and Triton. Icarus 208:412-424
Domingue DL, Lane AL, Beyer RA (1998) IUE's detection of tenuous SO2 frost on Ganymede and its rapid time variability. Geophys Res Lett 25:3117-3120
Dotto E, Barucci MA, Boehnhardt H, Romon J, Doressoundiram A, Peixinho N, de Bergh C, Lazzarin M (2003) Searching for water ice on 47171 1999 TC36, 1998 SG35, and 2000 QC243: ESO large program on TNOs and Centaurs. Icarus 162:408-414
Doute S, Schmitt B, Lopes-Gautier R, Carlson R, Soderblom L, Shirley J (2001) Mapping SO_2 frost on Io by the modeling of NIMS hyperspectral images. Icarus 149:107-132
Dumas C, Terrile RJ, Smith BA, Schneider G (2002) Astrometry and near-infrared photometry of Neptune's inner satellites and ring arcs. Astron J 123:1776-1783
Ehlmann BL, Mustard JF, Murchie SL, Bibring JP, Meunier A, Fraeman AA, Langevin Y (2011) Subsurface water and clay mineral formation during the early history of Mars. Nature 479(7371):53-60
Ehlmann BL, Mustard JF, Murchie SL, Poulet F, Bishop JL, Brown AJ, Calvin WM, Clark RN, Des Marais DJ, Milliken RE, Roach LH, Roush TL, Swayze GA, Wray JJ (2008) Orbital identification of carbonate-bearing rocks on Mars. Science 322(5909):1828-1832, doi: 10.1126/science.1164759
Ehlmann BL, Mustard JF, Swayze GA, Clark RN, Bishop JL, Poulet F, Des Marais DJ, Roach LH, Milliken RE, Wray JJ, Barnouin-Jha O, Murchie SL (2009) Identification of hydrated silicate minerals on Mars using MRO-CRISM: Geologic context near Nili Fossae and implications for aqueous alteration. J Geophys Res 114:E00D08, doi: 10.1029/2009JE003339
Elachi C, Wall S, Allison M, Anderson Y, Boehmer R, Callahan P, Encrenaz P, Flamini E, Franceschetti G, Gim Y, Hamilton G, Hensley S, Janssen M, Johnson W, Kelleher K, Kirk R, Lopes R, Lorenz R, Lunine J, Muhleman D, Ostro S, Paganelli F, Picardi G, Posa F, Roth L, Seu R, Shaffer S, Soderblom L, Stiles B, Stofan E, Vetrella S, West R, Wood C, Wye L, Zebker H (2005) Cassini Radar Views the Surface of Titan. Science 308:970-974
Eluszkiewicz J (1991) On the microphysical state of the surface of Triton. J Geophys Res 96:19217-19229
Eviatar A, Richardson JD (1986) Predicted satellite plasma tori in the magnetosphere of Uranus. Astrophys J 300:L99-L102
Fanale FP, Brown RH, Cruikshank DP, Clark RN (1979) Significance of absorption features in Io's IR absorption spectrum. Nature 280:761-763
Farmer CB, Davies DW, Laporte DD (1976) Mars: northern summer ice cap—water vapor observations from Viking 2. Science 194:1339-1341, doi: 10.1126/science.194.4271.1339

EBSCOhost - printed on 2/13/2023 5:26 AM via . All use subject to https://www.ebsco.com/terms-of-use

Farrand WH, Glotch TD, Rice JW, Hurowitz JA, Swayze GA (2009) Discovery of jarosite within the Mawrth Vallis region of Mars: Implications for the geologic history of the region. Icarus 204(2):478-488

Feldman WC, Lawrence DJ, Elphic RC, Barraclough BL, Maurice S, Genetay I, Binder AB (2000) Polar hydrogen deposits on the Moon. J Geophys Res 105:4175-4195

Feldman WC, Maurice S, Binder AB, Barraclough BL, Elphic RC, Lawrence DL (1998) Fluxes of fast and epithermal neutrons from Lunar Prospector: Evidence for water ice at the lunar poles. Science 281:1496-1500

Feldman WC, Maurice S, Lawrence DJ, Little RC, Lawson SL, Gasnault O, Wiens RC, Barraclough BL, Elphic RC, Prettyman TH, Steinberg JT, Binder AB (2001) Evidence for water ice near the Lunar Poles, J Geophys Res 106:23231-23252

Filacchione G, Capaccioni F, McCord TB, Coradini A, Cerroni P, Bellucci G, Tosi F, D'Aversa E, Formisano V, Brown RH, Baines KH, Bibring JP, Buratti BJ, Clark RN, Combes M, Cruikshank DP, Drossart P, Jaumann R, Langevin Y, Matson DL, Mennella V, Nelson RM, Nicholson PD, Sicardy B, Sotin C, Hansen G, Hibbitts K, Showalter M, Newmann S (2007) Saturn's icy satellites investigated by Cassini VIMS. I. Full-disk properties: 350-5100 nm reflectance spectra and phase curves. Icarus 186:259-290

Filacchione G, Capaccioni F, Tosi F, Cerroni P, McCord TB, Baines KH, Bellucci G, Brown RH, Buratti BJ, Clark RN, Cruikshank DP, Cuzzi JN, Jaumann R, Stephan K, Matson DL, Nelson RM, Nicholson PD (2008) Analysis of the Saturnian icy satellites full-disk spectra by Cassini-VIMS. Saturn After Cassini-Huygens, London, July, 2008 (abstract)

Fink U, Dekkers NH, Larson HP (1973) Infrared spectra of the Galilean satellites of Jupiter. Astrophys J 179:L155-L159

Fink U, Larson HP (1975) Temperature dependence of the water-ice spectrum between 1 and 4 microns: application to Europa, Ganymede, and Saturn's rings. Icarus 24:411-420

Flasar FM, Achterberg RK, Conrath BJ, Gierasch PJ, Kunde VG, Nixon CA, Bjoraker GL, Jennings DE, Romani PN, Simon-Miller AA, Bézard B, Coustenis A, Irwin PGJ, Teanby NA, Brasunas J Pearl JC, Segura ME, Carlson RC, Mamoutkine A, Schinder PJ, Barucci A, Courtin R, Fouchet T, Gautier D, Lellouch E, Marten A, Prangé R, Vinatier S, Strobel DF, Calcutt SB, Read PL, Taylor FW, Bowles N, Samuelson RE, Orton GS, Spilker LJ, Owen TC, Spencer JR, Showalter MR, Ferrari C, Abbas MM, Rauli nF, Edgington S, Ade P, Wishnow EH (2005) Titan's Atmospheric Temperatures, Winds, and Composition. Science 308:975-978

Fleischer M, Mandarino JA (1995) Glossary of Mineral Species 1995. The Mineralogical Record Inc., Tucson

Forget F, Hansen GB, Pollack JB (1995) Low brightness temperatures of Martian polar caps: CO_2 clouds or low surface emissivity? J Geophys Res 100(E10):21219-21234

Geissler P, McEwen A, Phillips C, Keszthelyi L, Spencer J (2004) Surface changes on Io during the Galileo mission. Icarus 169:29-64

Geissler P, McEwen AS, Keszthelyi L, Lopes-Gautier RMC, Granahan J, Simonelli DP (2001) Galileo imaging of SO_2 frosts on Io. J Geophys Res 106:33253-33266

Geissler PE, McEwen AS, Keszthelyi L, Lopes-Gautier R, Granahan J, Simonelli DP (1999) Global color variations on Io. Icarus 140:265-282

Gendrin A, Mangold N, Bibring JP, Langevin Y, Gondet B, Poulet F, Bonello G, Quantin C, Mustard J, Arvidson R, LeMouelic S (2005) Sulfates in Martian Layered Terrains: The OMEGA/Mars Express View. Science 307(5715):1587-1591, doi: 10.1126/science.1109087

Goetz AF, Vane G, Soloman JE, Rock BN (1985) Imaging spectrometry for Earth remote sensing. Science 228:1147-1153

Green RO, Conel JE, Carrere V, Bruegge CJ, Margolis JS, Rast M, Hoover G (1990) Determination of the In-Flight Spectral and Radiometric Characteristics of the Airborne Visible/Infrared Imaging Spectrometer (AVIRIS). *In:* Proceedings of the Second Airborne Visible/Infrared Imaging Spectrometer (AVIRIS) Workshop. JPL Publication 90-54, 15-22

Grundy WM (2009) Is the missing ultra-red material colorless ice? Icarus 199:560-563

Grundy WM, Buie MW, Spencer JR (2002) Spectroscopy of Pluto and Triton at 3-4 microns: Possible evidence for wide distribution of nonvolatile solids. Astron J 124:2273-2278

Grundy WM, Buie MW, Stansberry JA, Spencer JR, Schmitt B (1999) Near-infrared spectra of icy outer solar system surfaces: Remote determination of H_2O ice temperatures. Icarus 142:536-549

Grundy WM, Buratti BJ, Cheng AF, Emery JP, Lunsford A, McKinnon WB, Moore JM, Newman SF, Olkin CB, Reuter DC, Schenk PM, Spencer JR, Stern SA, Throop HB, Weaver HA, the New Horizons team (2007) New Horizons mapping of Europa and Ganymede. Science 318:234-237

Grundy WM, Olkin CB, Young LA, Buie MW, Young EF (2013) Near-infrared spectral monitoring of Pluto's ices: Spatial distribution and secular evolution. Icarus 223:710-721

Grundy WM, Schmitt B (1998) The temperature-dependent near-infrared absorption spectrum of hexagonal H_2O ice. J Geophys Res 103:25809-25822

Grundy WM, Schmitt B, Quirico E (1993) The temperature dependent spectra of alpha and beta nitrogen ice with application to Triton. Icarus 105:254-258

EBSCOhost - printed on 2/13/2023 5:26 AM via . All use subject to https://www.ebsco.com/terms-of-use

Grundy WM, Stansberry JA (2000) Solar gardening and the seasonal evolution of nitrogen ice on Triton and Pluto. Icarus 148:340-346
Grundy WM, Young LA (2004) Near infrared spectral monitoring of Triton with IRTF/SpeX I: Establishing a baseline. Icarus 172:455-465
Grundy WM, Young LA, Spencer JR, Johnson RE, Young EF, Buie MW (2006) Distributions of H_2O and CO_2 ices on Ariel, Umbriel, Titania, and Oberon from IRTF/SpeX observations. Icarus 184:543-555
Grundy WM, Young LA, Stansberry JA, Buie MW, Olkin CB, Young EF (2010) Near-infrared spectral monitoring of Triton with IRTF/SpeX II: Spatial distribution and evolution of ices. Icarus 205:594-604
Grundy WM, Young LA, Young EF (2003) Discovery of CO_2 ice and leading-trailing spectral asymmetry on the Uranian satellite Ariel. Icarus 162:222-229
Guilbert A, Alvarez-Candal A, Merlin F, Barucci MA, Dumas C, de Bergh C, Delsanti A (2009) ESO-Large Program on TNOs: Near-infrared spectroscopy with SINFONI. Icarus 201:272-283
Hage W, Liedl KR, Hallbrucker A, Mayer E (1998) Carbonic acid in the gas phase and its astrophysical relevance. Science 279:1332-1335
Hand KP, Brown ME (2013) Keck II Observations of hemispherical differences in H_{2O2} on Europa. Astrophys J Lett 766: I.21 (4pp)
Hand KP, Carlson RW (2012) Laboratory spectroscopic analyses of electron irradiated alkanes and alkenes in solar system ices. J Geophys Res 117:E03008
Hand KP, Carlson RW, Chyba CF (2007) Energy, chemical disequilibrium, and geological constraints on Europa. Astrobiology 7:1006-1022
Hand KP, Carlson RW, Cooper JF, Chyba CF (2006) Clathrate hydrates of oxidants in the Europan ice shell. Astrobiology 6:463-482
Hanel RA, Conrath BJ, Jennings DE, Samuelson RE (2003) Exploration of the Solar System by Infrared Remote Sensing. Cambridge Univ. Press, Cambridge
Hansen CJ, Paige DA (1992) A thermal model for the seasonal nitrogen cycle on Triton. Icarus 99:273-288
Hansen GB, McCord TB (2004) Amorphous and crystalline ice on the Galilean satellites: A balance between thermal and radiolytic processes. J Geophys Res 109:E01012, 1-19. doi: 10.1029/2003JE002149
Hansen GB, McCord TB (2008) Widespread CO_2 and other non-ice compounds on the anti-Jovian and trailing sides of Europa from Galileo/NIMS observations. Geophys Res Lett 35:L01202
Hapke B (1979) Io's surface and environs: A magmatic-volatile model. Geophys Res Lett 6:799-802
Hapke B (2001) Space weathering from Mercury to the asteroid belt. J Geophys Res 106:10,039-10,073
Hashimoto GL, Roos-Serote M, Sugita S, Gilmore MS, Kamp LW, Carlson RW, Baines KH (2008) Felsic highland crust on Venus suggested by Galileo Near-Infrared Mapping Spectrometer data. J Geophys Res 113:E00B24, doi: 10.1029/2008JE003134
Hendrix AR, Barth CA, Hord CW (1999a) Ganymede's ozone-like absorber: Observations by the Galileo ultraviolet spectrometer. J Geophys Res 104:14169-14178
Hendrix AR, Barth CA, Stewart AIF, Hord CW, Lane AL (1999b) Hydrogen peroxide on the icy Galilean satellites. Lunar and Planetary Science XXX, Vol. LPI Contribution 964. Lunar and Planetary Institute, Houston (CD-ROM). Abstract # 2043
Hendrix AR, Cassidy TA, Johnson RE, Paranicas C, Carlson RW (2011) Europa's disk-resolved ultraviolet spectra: Relationships with plasma flux and surface terrains. Icarus 212:736-743
Hendrix AR, Domingue D, Noll KS (2012) Ultraviolet properties of planetary ices. *In:* Solar System Ices. Astrophysics and Space Library, Volume 356. Murthy G (ed) Springer, p 73-105
Hendrix AR, Johnson RE (2008) Callisto: New insights from Galileo disk-rsolved UV measurements. Astrophys J 687:706-713
Hibbits CA, Hansen GB (2007) The other non-ice material on Ganymede: Dark ray ejecta (abstract). Bull Am Astron Soc 39:428
Hibbits CA, Pappalardo RT, Hansen GB, MCCord TB (2003) Carbon dioxide on Ganymede. J Geophys Res 108:2-1–2-21, doi: 10:1029/2002JE001956
Hibbitts CA, Klemaszewski JE, McCord TB, Hansen GB, Greeley R (2002) CO_2-rich impact craters on Callisto. J Geophys Res 107:14-1–14-12, 5084. 10.1029/2000JE001412
Hibbitts CA, McCord TB, Hansen GB (2000) The distributions of CO_2 and SO_2 on the surface of Callisto. J Geophys Res 105:22541-22557
Hicks MD, Buratti BJ (2004) The spectral variability of Triton from 1997-2000. Icarus 171:210-218
Hobbs (1975) Ice Physics. Oxford University Press, 856 pages
Hoefen TM, Clark RN, Bandfield JL, Smith MD, Pearl JC, Christensen PR (2003) Discovery of olivine in the Nili Fossae Region of Mars. Science 302(5645):627-630
Hunt GR (1977) Spectral signatures of particulate minerals, in the visible and near-infrared. Geophysics 42:501-513

EBSCOhost - printed on 2/13/2023 5:26 AM via . All use subject to https://www.ebsco.com/terms-of-use

Imanaka H, Khare BN, Elsila JE, Bakes ELO, McKay CP, Cruikshank DP, Sugita S, Matsui T, Zare RN (2004) Laboratory experiments of Titan tholin formed in cold plasma at various pressures: implications for nitrogen-containing polycyclic aromatic compounds in Titan haze. Icarus 168:344-366

Israel G, Szopa C, Raulin F, Cabane M, Niemann H, Atreya S, Bauer S, Brun JF, Chassefiere E, Coll P, Conde E, Coscia D, Hauchecorne A, Millian P, Nguyen MJ, Owen T, Riedler W, Samuelson R, Siguier JM, Steller M, Sternberg R, Vidal-Madjar C, (2005) Complex organic matter in Titan's atmospheric aerosols from in situ pyrolysis and analysis. Nature 438:796-798

Izenberg NRG, Holsclaw M, Domingue DL, McClintock WE, Klima RL, Blewett DT, Kochte MC, Helbert J, D'Amore M, Sprague AL, Vilas F, Solomon SC (2012) Ultraviolet through near-infrared reflectance variation on Mercury and the search for mineralogical telltales. 43rd Lunar and Planetary Science Conference, 2365, *http://www.lpi.usra.edu/meetings/lpsc2012/pdf/2365.pdf*

James PB, Kieffer HH, Paige DA (1993) The seasonal cycle of carbon dioxide on Mars. *In:* MARS (A93-27852 09-91), University of Arizona Press, p. 934-968

Jarvis KS, Vilas F, Larson SM, Gaffey MJ (2000) Are Hyperion and -Phoebe nlinked to Iapetus? Icarus 146: 125-132

Jaumann R, Clark RN, Nimmo F, Hendrix AR, Buratti BJ, Denk T, Moore JM, Schenk PM, Ostro SJ, Srama R (2009) Icy satellites: geological evolution and surface processes. *In*: Saturn after Cassini/Huygens. Dougherty MK, Esposito LW, Krimigis SM (eds) Springer, p 637-681, doi: 10.1007/978-1-4020-9215-2

Jaumann R, Stephan K, Buratti BJ, Hansen GB, Clark RN, Brown RH, Baines KH, Bellucci G, Coradini A, Cruikshank DP, Griffith CA, Hibbitts CA, McCord TB, Nelson RM, Nicholson PD, Sotin C, Wagner R (2006) Distribution of icy particles across Enceladus' surface as derived from Cassini VIMS measurements. Icarus 193(2008):407419, doi: 10.1016/j.icarus.2007.09.013

Jessup KL, Spencer J, Ballester GE, Yelle R, Roessler F, Howell RR (2002) Spatially resolved UV spectra of Io's Prometheus plume and anti-Jovian hemisphere. Bull Am Astron Soc 34:40.02

Johnson RE (1990) Energetic Charged-Particle Interactions with Atmospheres and Surfaces. Springer-Verlag, New York

Johnson RE (1997) Polar ''caps'' on Ganymede and Io revisited. Icarus 128:469-471

Johnson RE, Carlson RW, Cooper JF, Paranicas C, Moore MH, Wong M (2004) Radiation effects on the surfaces of the Galilean satellites. *In:* Jupiter. Bagenal F, McKinnon W (eds) Cambridge University Press, Cambridge, p 485-512

Johnson RE, Jesser WA (1997) O_2/O_3 microatmospheres in the surface of Ganymede. Astrophys J 480:L79-L82

Johnson TV, McCord TB (1971) Spectral geometric albedo of the Galilean satellites 0.3-2.5 microns. Astrophys J 169:589-593

Khanna RK, Pearl JC, Dahmani R (1995) Infrared-spectra and structure of solid-phases of sulfur- trioxide - Possible identification of solid SO_3 on Io surface. Icarus 15:250-257

Khurana KK, Pappalardo RT, Murphy N, Denk T (2007) The origin of Ganymede's polar caps. Icarus 191:193-202

Kieffer HH, Titus TN (2001) TES mapping of Mars' northern seasonal cap. Icarus 154:162-180

Kieffer S, Chase C Jr., Martin TZ, Miner ED, Palluconi FD (1976) Martian North Pole summer temperatures: dirty water ice. Science 194:1341-1344, doi: 10.1126/science.194.4271.1341

Kokaly RF, Despain DG, Clark RN, Livo KE (2003) Mapping the biology of Yellowstone National Park using imaging spectroscopy. Remote Sens Environ 84:437-456

Kramer GY, Besse S, Dhingra D, Nettles J, Klima R, Garrick-Bethell I, Clark RN, Combe JP, Head III JW, Taylor LA, Pieters CM, Boardman J, McCord TB (2011) The spectral peculiarities of Lunar swirls as seen by the Moon mineralogy mapper. J Geophys Res 116:E00G18, doi: 10.1029/2010JE003729

Kuiper GP (1957) Infrared observations of planets and satellites (abstract). Astron J 62:245

Lamy P, Toth I (2009) The colors of cometary nuclei: Comparison with other primitive bodies of the Solar System and implications for their origin. Icarus 201:674-713

Lane AL, Domingue DL (1997) IUE's view of Callisto: Detection of an SO_2 absorption correlated to possible torus neutral wind alterations. Geophys Res Lett 24:1143-1146

Langevin Y, Poulet F, Bibring JP, Gondet B (2005) Sulfates in the North Polar Region of Mars detected by OMEGA/Mars Express. Science 307:1584-1586

Laver C, de Pater I (2008) Spatially resolved SO2 ice on Io, observed in the near IR. Icarus 195:752-757, doi: 10.1016/j.icarus.2007.12.023

Laver C, de Pater I (2009) The global distribution of sulfur dioxide ice on Io, observed with OSIRIS on the WM Keck telescope. Icarus 201:172-181, doi: 10.1016/j.icarus.2008.12.037

Leinhardt ZM, Marcus RA, Stewart ST (2010) The formation of the collisional family around the dwarf planet Haumea. Astrophys J 714:1789-1799

Lellouch E, Crovisier J, Lim T, Bockelee-Morvan D, Leech K,Hanner MS, Altieri B, Schmitt B, Trotta F, Keller HU (1998) Evidence for water ice and estimate of dust production rate in comet Hale-Bopp at 2.9 AU from the Sun. Astron Astrophys 339:L9-L12

EBSCOhost - printed on 2/13/2023 5:26 AM via . All use subject to https://www.ebsco.com/terms-of-use

Lellouch E, Paubert G, Moses JI, Schneider NM, Strobel DF (2003) Volcanically emitted sodium chloride as a source for Io's neutral clouds and plasma torus. Nature 421:45-47

Licandro J, Pinilla-Alonso N, Pedani M, Oliva E, Tozzi GP, Grundy WM (2006) The methane ice rich surface of large TNO 2005 FY9: A Pluto-twin in the trans-neptunian belt? Astron Astrophys 445:L35-L38

Lichtenberg KA, Arvidson RE, Morris RV, Murchie SL, Bishop JL, Fernandez Remolar D, Glotch TD, Noe Dobrea E, Mustard JF, Andrews-Hanna J, Roach LH (2010) Stratigraphy of hydrated sulfates in the sedimentary deposits of Aram Chaos, Mars. J Geophys Res 115:E00D17, doi: 10.1029/2009JE003353

Loeffler MJ, Teolis BD, Baragiola RA, (2006) A model study of the thermal evolution of astrophysical ices. Astrophys J 639:L103-L106

Lopes RMC, Kamp LW, Doute S, Smythe WD, Carlson RW, McEwen AS, Geissler PE, Kieffer SW, Leader FE, Davies AG, Barbinis E, Mehlman R, Segura M, Shirley J, Soderblom LA (2001) Io in the near infrared: Near-Infrared Mapping Spectrometer (NIMS) results from the Galileo flybys in 1999 and 2000. J Geophys Res 106:33053-33078

Lopes RMC, Spencer JR (eds) (2007) Io after Galileo. Springer-Praxis, Chichester

Lunine JI, Stevenson DJ (1985) Physical state of volatiles on the surface of Triton. Nature 317:238-240

Martonchik JV, Orton GS (1994) Optical constants of solid and liquid methane. Appl Opt 33:8306-8317

Mastrapa RM, Bernstein MP, Sandford SA, Roush TL, Cruikshank DP, Dalle Ore CM (2008) Optical constants of amorphous and crystalline H_2O-ice in the near infrared from 1.1 to 2.6 μm. Icarus 197:307-320

Mastrapa RM, Grundy WM, Gudipati MS (2013) Observed ices in the Solar System. *In:* The Science of Solar System Ices. Astrophysics and Space Science Library, Volume 356. Gudipati MS Castillo-Rogez J (eds) Springer Science+Business Media, p 371-408, doi: 10.1007/978-1-4614-3076-6_1

Matson DL, Nash DB (1983) Ios atmosphere - Pressure control by regolith cold trapping and surface venting. J Geophys Res 88:4771-4783

McCauley JF, Smith BA, Soderblom LA, (1979) Erosional scarps on Io. Nature 280:736-738

McCord TB, Hansen GB , MatsonDL, Johnson TV, Crowley JK, Fanale FP, Carlson RW, Smythe WD, Martin PD, Hibbitts CA, Granahan JC, Ocampo A (1999) Hydrated salt minerals on Europa's surface from the Galileo near-infrared mapping spectrometer (NIMS) investigation. J Geophys Res 104:11827-11851

McCord TB, Hansen GB, Hibbitts CA (2001) Hydrated salt minerals on Ganymede's surface: Evidence of an ocean below. Science 292:1523-1525

McCord TB, Carlson RW, Smythe WD, Hansen GB, Clark RN, Hibbitts CA, Fanale FP, Granahan JC, Segura M, Matson DL, Johnson TV, Martin PD (1997) Organics and other molecules in the surfaces of Callisto and Ganymede. Science 278:271-275

McCord TB, Hansen GB, Buratti BJ, Clark RN, Cruikshank DP, D'Aversa E, Griffith CA, Baines KH, Brown RH, Dalle Ore CM, Filacchione G, Formisano V, Hibbitts CA, Jaumann R, Lunine JI, Nelson RM, Sotin C, and the Cassini VIMS Team (2006) Composition of Titan's surface from Cassini VIMS. Planet Space Sci 54:1524-1539

McCord TB, Hansen GB, Clark RN, Martin PD, Hibbits CA, Fanale FP, Granahan JC, Segura M, Matson DL, Johnson TV, Carlson RW, Smythe WD, Danielson GE, Team TN (1998a) Non-water-ice constituents in the surface material of the icy Galilean satellites from the Galileo near infrared mapping spectrometer investigation. J Geophys Res 103:8603-8626

McCord TB, Hansen GB, Fanale FP, Carlson RW, Matson DL, Johnson TV, Smythe WD, Crowley JK, Martin PD, Ocampo A, Hibbitts CA, Granahan JC (1998b) Salts on Europa's surface detected by Galileo's Near Infrared Mapping Spectrometer. Science 280:1242-1245

McCord TB, Hayne P, Combe JP, Hansen G, Barnes J, Rodriguez S, Le Mouelic S, Baines K, Buratti B, Sotin C, Nicholson P, Jaumann R, Nelson R, and the Cassini VIMS Team (2008) Titan's surface: Search for spectral diversity and composition using the Cassini VIMS investigation. Icarus 194:212-242

McEwen AS (1988) Global color and albedo variations on Io. Icarus 73:385-426

McEwen AS, Belton MJS, Breneman HH, Fagents SA, Geissler P, Greeley R, Head JW, Hoppa G, Jaeger WL, Johnson TV, Keszthelyi L, Klaasen KP, Lopes-Gautier R, Magee KP, Milazzo MP, Moore JM, Pappalardo RT, Phillips CB, Radebaugh J, Schubert G, Schuster P, Simonelli DP, Sullivan R, Thomas PC, Turtle EP, Williams DA (2000) Galileo at Io: Results from high-resolution imaging. Science 288:1193-1198, doi: 10.1126/science.288.5469.1193

McEwen AS, Eliason EM, Bergstrom JW, Bridges NT, Hansen CJ, Delamere WA, Grant JA, Gulick VC, Herkenhoff KE, Kreszthelyi L, Kirk RL, Mellon MT, Squyres SW, Thomas N, Weitz CM (2007) Mars Reconnaissance Orbiter's High 41934 Resolution Imaging Science Experiment (HiRISE). J Geophys Res 935:E05S02, doi: 10.1029/2005JE002605

McGuire PC, Wolff MJ, Smith MD, Arvidson RE, Murchie SL, Clancy RT, Roush TL, Cull SC, Lichtenberg KA, Wiseman SM, Green RO, Martin TZ, Milliken RE, Cavender PJ, Humm DC, Seelos FP, Seelos KD, Taylor HW, Ehlmann BL, Mustard JF, Pelkey SM, Titus TN, Hash CD, Malaret ER, (2008) MRO/CRISM retrieval of surface lambert albedos for multispectral mapping of Mars with DISORT-based radiative transfer modeling: Phase 1 – Using Historical Climatology for temperatures, aerosol optical depths, and atmospheric pressure. IEEE Trans Geosci Remote Sens 46(12):4020-4040

EBSCOhost - printed on 2/13/2023 5:26 AM via . All use subject to https://www.ebsco.com/terms-of-use

Merlin F, Quirico E, Barucci MA, de Bergh C (2012) Methanol ice on the surface of minor bodies in the solar system. Astron Astrophys 544:A20, doi: 10.1051/0004-6361/201219181

Milliken RE, Grotzinger JP, Thomson BJ (2010) Paleoclimate of Mars as captured by the stratigraphic record in Gale Crater. Geophys Res Lett 37:L04201, doi: 1029/2009GL041870

Milliken RE, Swayze GA, Arvidson RE, Bishop JL, Clark RN, Ehlmann BL, Green RO, Grotzinger JP, Morris RV, Murchie SL, Mustard JF, Weitz C (2008) Opaline silica in young deposits on Mars. Geology 36(11):847-850

Moore JM, Asphaug E, Morrison D, Spencer JR, Chapman CR, Bierhaus B, Sullivan RJ, Chuang FC, Klemaszewski JE, Greeley R, Bender KC, Geissler PE, Helfenstein P, Pilcher CB (1999) Mass movement and landform degradation on the icy Galilean satellites: Results of the Galileo nominal mission. Icarus 140:294-312

Moore JM, Sullivan RJ, Chuang FC, Head JW, III, McEwen AS, Milazzo MP, Nixon B E, Pappalardo RT, Schenk PM, Turtle EP (2001) Landform degradation and slope processes on Io: The Galileo view. J Geophys Res 106:33223-33240, doi: 10.1029/2000je001375

Moore MH, Hudson RL (2003) Infrared study of ion-irradiated N_2-dominated ices relevant to Triton and Pluto: Formation of HCN and HNC. Icarus 161:486-500

Moroz VI (1965) Infrared spectrophotometry of the Moon and the Galilean satellites of Jupiter. Sov Astron 9:999-1006

Müller N, Helbert J, Hashimoto G, Tsang CCC, Piccioni G, Drossart P and Venus Express/VIRTIS Team (2008) Venus surface thermal emission at one micrometer in VIRTIS imaging observations - evidence for variation of crust and mantle differentiation conditions. J Geophys Res 113:E00B17, doi: 10.1029/2008JE003118

Murchie S, Arvidson R, Bedini P, Beisser K, Bibring JP, Bishop J, Boldt J, Cavender P, Choo T, Clancy RT, Darlington EH, Des Marais D, Espiritu R, Fort D, Green R, Guinness E, Hayes J, Hash C, Heffernan K, Hemmler J, Heyler G, Humm D, Hutcheson J, Izenberg N, Lee R, Lees J, Lohr D, Malaret E, Martin T, McGovern JA, McGuire P, Morris R, Mustard J, Pelkey S, Rhodes E, Robinson, M, Roush T, Schaefer E, Seagrave G, Seelos F, Silverglate P, Slavney S, Smith M, Shyong W-J, Strohbehn K, Taylor H, Thompson P, Tossman B, Wirzburger M, Wolff M (2007) Compact Reconnaissance Imaging Spectrometer for Mars (CRISM) on Mars Reconnaissance Orbiter (MRO). J Geophys Res 112:EO5S03, doi: 10.1029/2006JE002682

Murchie SL, Mustard JF, Ehlmann BL, Milliken RE, Bishop JL, McKeown NK, Noe Dobrea EZ, Seelos FP, Buczkowski DL, Wiseman SM, Arvidson RE, Wray JJ, Swayze G, Clark RN, Des Marais DJ, McEwen AS, Bibring J-P (2009) A synthesis of Martian aqueous mineralogy after 1 Mars year of observations from the Mars Reconnaissance Orbiter. J Geophys Res 114:E00D06, doi: 10.1029/2009JE003342

Murphy RE, Cruikshank DP, Morrison D (1972) Radii, albedos, and 20-micron brightness temperatures of Iapetus and Rhea. Astrophys J Lett 177:L93-L96

Mustard JF, Murchie SL, Pelkey SM, Ehlmann BL, Milliken RE, Grant JA, Bibring J-P, Poulet F, Bishop J, Noe Dobrea E, Roach L, Seelos F, Arvidson RE, Wiseman S, Green R, Hash C, Humm D, Malaret E, McGovern JA, Seelos K, Clancy T, Clark R, Des Marais D, Izenberg N, Knudson A, Langevin Y, Martin T, McGuire P, Morris R, Robinson M, Roush T, Smith M, Swayze G, Taylor H, Titus T, and Wolff M (2008) Hydrated silicate minerals on Mars observed by the Mars Reconnaissance Orbiter CRISM instrument. Nature 454:305-309. doi: 10.1038/nature07097

Mustard JF, Poulet F, Gendrin A, Bibring J-P, Langevin Y, Gondet B, Mangold N, Bellucci G, Altieri F (2005) Olivine and pyroxene diversity in the crust of Mars. Science 307(5715):1594-1597, doi: 10.1126/science.1109098

Nash DB, Betts BH (1998) Ices on Io - composition and texture. *In:* Solar System Ices. Schmitt B, de Bergh C, Festou M (eds) Kluwer, Dordrecht, p 607-638

Nelson RM, Kamp LW, Matson DL, Irwin PGJ, Baines KH, Boryta MD, Leader FE, Jaumann R, Smythe WD, Sotin C, Clark RN, Cruikshank DP, Drossart P, Pearl JC, Hapke BW, Lunine J, Combes M, Bellucci G, Bibring JP, Capaccioni F, Cerroni P, Coradini A, Formisano V, Filacchione G, Langevin RY, McCord TB, Mennella V, Nicholson PD, Sicardy B (2009) Saturn's Titan: Surface change, ammonia, and implications for atmospheric and tectonic activity. Icarus 199:429-441

Nelson RM, Lane AL, Matson DL, Veeder GJ, Buratti BJ, Tedesco EF (1987) Spectral geometric albedos of the Galilean satellites from 0.24 to 0.34 micrometers: Observations with the International Ultraviolet Explorer. Icarus. 72:358-380

Nicholson PD, Hedman MM, Clark RN, Showalter MR, Cruikshank DP, Cuzzi JN, Filacchione G, Capaccioni F, Cerroni P, Hansen GB, Sicardy B, Drossart P, Brown RH, Buratti BJ, Baines KH Coradini A (2008) A close look at Saturn's rings with Cassini VIMS. Icarus 193:182-212, doi: 10.1016/j.icarus.2007.08.036

Niemann HB, Atreya S, Bauer S, Carignan G, Demick J, Frost R, Gautier D, Haberman J, Harpold D, Hunten D, Israel G, Lunine J, Kasprzak W, Owen T, Paulkovich M, Raulin F, Raaen E, Way S (2005) The abundance of constituents of Titan's atmosphere from the GCMS instrument on the Huygens probe. Nature 438:779-784

EBSCOhost - printed on 2/13/2023 5:26 AM via . All use subject to https://www.ebsco.com/terms-of-use

Noe Dobrea EZ, Bishop JL, McKeown NK, Fu R, Rossi CM, Michalski JR, Heinlein C, Hanus V, Poulet F, Mustard JF, Murchie S, McEwen S, Swayze G, Bibring J-P, Malaret E, Hash C (2010) Mineralogy and stratigraphy of phyllosilicate-bearing and dark mantling units in the greater Mawrth Vallis/west Arabia Terra area: Constraints on geological origin. J Geophys Res 115:E00D19, doi: 10.1029/2009JE003351

Noll KS, Johnson RE, Lane AL, Domingue DL, Weaver HA (1996) Detection of ozone on Ganymede. Science 273:341-343

Noll KS, Johnson RE, McGrath MA, Caldwell JJ (1997) Detection of SO_2 on Callisto with the Hubble Space Telescope. Geophys Res Lett 24:1139-1142

Noll KS, Weaver HA, Gonnella AM, (1995) The albedo spectrum of Europa from 2200 angstrom to 3300 angstrom. J Geophys Res Planets 100:19057-19059

Owen TC, Cruikshank DP, Dalle Ore CM, Geballe TR, Roush TL, de Bergh C, Pendleton YJ, Khare BN (2001) Decoding the domino: The dark side of Iapetus. Icarus 149:160-172

Paige DA, Siegler MA, Zhang JA, Hayne PO, Foote EJ, Bennett KA, Vasavada AR, Greenhagen BT, Schofield JT, McCleese DJ, Foote MC, DeJong E, Bills BG, Hartford W, Murray BC, Allen CC, Snook K, Soderblom LA, Calcutt S, Taylor FW, Bowles NE, Bandfield JL, Elphic R, Ghent R, Glotch TD, Wyatt MB, Lucey PG (2010) Diviner Lunar Radiometer Observations of Cold Traps in the Moons South Polar Region. Science 330:479-482, doi: 10.1126/science.1187726

Painter TH, Dozier J, Roberts DA, Davis RE, Green RO (2003) Retrieval of subpixel snow-covered area and grain size from imaging spectrometer data. Remote Sens Environ 85:64-77, doi: 10.1016/S0034-4257(02)00187-6

Pang KD, Nicholson PD (1984) Composition and size of Uranian ring particles. Lunar Planetary Science Conference XV, 627-628 (abstract)

Pappalardo RT, McKinnon WB, Khurana K (eds) (2009) EUROPA. Univ. of Ariz. Press, Tucson

Parente M (2008) A new approach to denoising CRISM images. Lunar Planetary Science Conference XXXIX, 2528.pdf (abstract)

Pieters CM, Besse S, Boardman J, Buratti B, Cheek L, Clark RN, Combe JP, Dhingra D, Goswami JN, Green R, Head JW, Isaacson P, Klima R, Kramer G, Lundeen S, Malaret E, McCord T, Mustard J, Nettles J, Petro N, Runyon C, Staid M, Sunshine J. Taylor LA, Thaisen K, Tompkins S, Whitten J (2011) Mg-Spinel Lithology: A New Rock-type on the Lunar Farside. J Geophys Res 116:E00G08, doi: 10.1029/2010JE003727

Pieters CM, Englert PA (1993) Remote geochemical Analysis: Elemental and Mineralogical Composition, Cambridge Univ. Press, New York

Pieters CM, Goswami JN, Clark RN, Annadurai M, Boardman J, Buratti B, Combe JP, Dyar MD, Green R, Head JW, Hibbitts C, Hicks M, Isaacson P, Klima R, Kramer G, Kumar S, Livo E, Lundeen S, Malaret E, McCord T, Mustard J, Nettles J, Petro N, Runyon C, Staid M, Sunshine J, Taylor LA, Tompkins S, Varanasi P (2009) Character and Spatial Distribution of OH/H_2O on the Surface of the Moon seen by M3 on Chandrayaan-1. Science 326:568-572, doi: 10.1126/science.1178658

Pilcher CB, Ridgeway ST, McCord TB (1972) Galilean satellites: Identification of water frost. Science 178:1087-1089

Pinilla-Alonso N, Brunetto R, Licandro J, Gil-Hutton R, Roush TL, Strazzulla G (2009) The surface of (136108) Haumea (2003 EL61), the largest carbon-depleted object in the trans-Neptunian belt. Astron Astrophys 496:547-556

Pollack JB, Witteborn FC, Erickson EF, Strecker DW, Baldwin BJ, Bunch TE, (1978) Near-infrared spectra of the Galilean satellites: Observations and compositional implications. Icarus 36:271-303

Pospieszalska MK, Johnson RE (1989) Magnetospheric ion bombardment profiles of satellites: Europa and Dione. Icarus 78:1-13

Poulet F, Bibring J-P, Mustard JF, Gendrin A, Mangold N, Langevin Y, Arvidson, RE, Gondet B, and Gomez C (2005) Phyllosilicates on Mars and implications for early Martian climate. Nature 438:623-627, doi: 10.1038/nature04274

Quirico E, Doute S, Schmitt B, de Bergh C, Cruikshank DP, Owen TC, Geballe TR, Roush TL (1999) Composition, physical state, and distribution of ices at the surface of Triton. Icarus 139:159-178

Quirico E, Schmitt B (1997a) Near-infrared spectroscopy of simple hydrocarbons and carbon oxides diluted in solid N_2 and as pure ices: Implications for Triton and Pluto. Icarus 127:354-378

Quirico E, Schmitt B (1997b) A spectroscopic study of CO diluted in N_2 ice: Applications for Triton and Pluto. Icarus 128:181-188

Quirico E, Montagnac G, Lees V, McMillan PF, Szopa C, Cernogora G, Rouzaud JN, Simon P, Bernard JM, Coll P, Fray N, Minard RD, Raulin F, Reynard B, Schmitt B (2008) New experimental constraints on the composition and structure of tholins. Icarus 198:218-231

Ramaprasad KR, Caldwell J, McClure DS (1978) The vibrational overtone spectrum of liquid methane in the visible and near infrared: Applications to planetary studies. Icarus 35:400-409

Rieke GH, Lebofsky LA, Lebofsky MJ (1985) A search for nitrogen on Triton. Icarus 64:153-155

EBSCOhost - printed on 2/13/2023 5:26 AM via . All use subject to https://www.ebsco.com/terms-of-use

Riner MA, Lucey PG (2012) Intense Space Weathering On Mercury: Are There Any Surface Exposures Of Immature Material?, 43rd Lunar and Planetary Science Conference, 2866. *http://www.lpi.usra.edu/meetings/lpsc2012/pdf/2866.pdf*

Rivkin AS, Emery JP (2008) Water Ice on 24 Themis? Asteroids, Comets, Meteors (abstract), *http://www.lpi.usra.edu/meetings/acm2008/pdf/8099.pdf*

Rivkin AS, Emery JP (2010) Detection of ice and organics on an asteriodal surface. Nature 464:1322-1323

Rodriguez S, Le Mouélic S, Sotin C, Clenet H, Clark R, Buratti B, Brown R, McCord T, Nicholson P, Baines K, and the VIMS Science Team (2006), Cassini/VIMS hyperspectral observations of the HUYGENS landing site on Titan. Planet Space Sci 54:1510-1523

Roush TL, Cruikshank DP, Owen TC (1995) Surface ices in the outer solar system. *In:* Volatiles in the Earth and Solar System. AIP Conference Proceedings 341. Farley KA (eds) Am Inst Phys, New York, p 143-153

Ruff SW (2004) Spectral evidence for zeolite in the dust on Mars. Icarus 168(1):1310-143

Sagan C, Thompson WR, Khare B (1992) Titan: A laboratory for pre-biological organic chemistry. Acc Chem Res 25:286-292

Sanford and Allamandola (1993) The condensation and vaporization behavior of ices containing SO_2, H_2S, and CO_2: implications for Io. Icarus 106:478-88

Schaller EL, Brown ME (2007) Volatile loss and retention on Kuiper belt objects. Astrophys J 659:L61-L64

Schenk PM, Zahnle K (2007) On the negligible surface age of Triton. Icarus 192:135-149

Schmitt B, de Bergh C, Festou M (eds) (1998a) Solar System Ices. Kluwer, Dordrecht

Schmitt B, de Bergh C, Lellouch E, Maillard JP, Barbe A, Doute S (1994) Identification of three absorption bands in the 2-mm spectrum of Io. Icarus 111:79-105

Schmitt B, Quirica E, Trotta F, Grundy WM (1998b) Optical properties of ices from the UV to infrared. *In:* Solar System Ices. Schmitt B, DeBergh C, Festou M (eds) Kluwer, Dordrecht, p 199-240

Schroder SE, Keller HU (2008) The reflectance spectrum of Titan's surface at the Huygens landing site determined by the descent imager/spectral radiometer. Planet Space Sci 56:753-769

Schubert G, Anderson JD, Spohn T, McKinnon WB (2004) Interior composition, structure, and dynamics of the Galilean satellites. *In:* Jupiter: The Atmosphere, Satellites, and Magnetosphere. Bagenal F, Dowling TE, McKinnon W (eds) Cambridge Univ. Press, Cambridge, p. 281-306

Scott (1976) Solid and liquid nitrogen. Phys Rep 27:89-157

Shapiro MM, Gush HP (1966) The collision-induced fundamental and first overtone bands of oxygen and nitrogen. Can J Phys 44:949-963

Sheng DT, Ewing GE (1971) Collision induced infrared absorption of gaseous nitrogen at low temperatures. J Chem Phys 55:5425-5430

Shirley JH, Dalton JB, Prockter LM, Kamp LW (2010) Europa's ridged plains and smooth low albedo plains: Distinctive compositions and compositional gradients at the leading side-trailing side boundary. Icarus 210:358-384

Smythe WD, Carlson RW, Ocampo A, Matson D, Johnson TV, McCord TB, Hansen GE, Soderblom LA, Clark RN, (1998) Absorption bands in the spectrum of Europa detected by the Galileo NIMS instrument. XXIX Lunar and Planetary Science Conference, Vol. CD. Lunar and Planetary Institute, Houston, Texas

Smythe WD, Nelson RM, Nash DB (1979) Spectral evidence for SO_2 frost or adsorbate on Io's surface. Nature 280:766

Soderblom LA, Barnes JW, Brown RH, Clark RN, Janssen MA, McCord TB, Niemann HB, Tomasko MG (2009) Composition of Titan's Surface. *In:* Titan from Cassini-Huygens. Brown RH, Lebreton JP, Waite JH (eds) Springer, p 141-175, doi: 10.1007/978-1-4020-9215-2

Soifer BT, Neugebauer G, Matthews K (1981) Near-infrared photometry of the satellites and rings of Uranus. Icarus 45:612-617

Sotin C, Jaumann R, Buratti BJ, Brown RH, Clark RN, Soderblom LA, Baines KH, Bellucci G, Bibring JP, Capaccioni F, Cerroni P, Combes M, Coradini A, Cruikshank DP, Drossart P, Formisano V, Langevin Y, Matson DL, McCord TB, Nelson RM, Nicholson PD, Sicardy B, LeMouelic S, Rodriguez S, Stephan K, Scholz CK (2005) Release of volatiles from a possible cryovolcano from near-infrared imaging of Titan. Nature 435:786-789, doi: 10.1038nature03596

Spencer JR, Calvin WM (2002) Condensed O_2 on Europa and Callisto. Astron J 124:3400-3403

Spencer JR, Calvin WM, Person MJ (1995) Charge-coupled-device spectra of the Galilean satellites: Molecular-oxygen on Ganymede. J Geophys Res 100:19049-19056

Spencer JR, Jessup KL, McGrath MA, Ballester GE, Yelle R (2000) Discovery of gaseous S_2 in Io's Pele plume. Science 288:1208-1210

Stansberry JA, Pisano DJ, Yelle RV (1996) The emissivity of volatile ices on Triton and Pluto. Planet Space Sci 44:945-955

Sunshine JM, A'Hearn MF, Groussin O, Li JY, Belton MJS, Delamere WA, Kissel J, Klaasen KP, McFadden LA, Meech KJ, Melosh HJ, Schultz PH, Thomas PC, Veverka J, Yeomans DK, Busko IC, Desnoyer M, Farnham TL, Feaga LM, Hampton DL, Lindler DJ, Lisse CM, Wellnitz DD (2006) Exposed water ice deposits on the surface of comet 9P/Tempel 1. Science 311:1453-1455, doi: 10.1126/science.1123632

EBSCOhost - printed on 2/13/2023 5:26 AM via . All use subject to https://www.ebsco.com/terms-of-use

Sunshine JM, Feaga L, Groussin O, Protopapa S, A'Hearn MF, Farnham TL, Besse S (2012) The distribution of water ice on comet 103P/Hartley 2. Asteroids, Comets, Meteors. Nigata, Japan

Sunshine JS, Farnham TL, Feaga LM, Groussin O, Merlin F, Milliken RE, A'Hearn MF (2009) Temporal and spatial variability of Lunar hydration as observed by the Deep Impact Spacecraft. Science 326:565-568, doi: 10.1126/science.1179788

Swayze GA, Clark RN, Goetz FH, Chrien TG, Gorelick NS, (2003) Effects of spectrometer band pass, sampling, and signal-to-noise ratio on spectral identification using the Tetracorder algorithm. J Geophys Res 108(E9):5105, doi: 10.1029/2002JE001975

Swayze, GA, Ehlmann, BL, Milliken, RE, Poulet, F, Wray, JJ, Rye, RO, Clark, RN, Desborough, GA, Crowley, JK, Gondet, B, Mustard, JF, Seelos, KD, Murchie, SL, and the MRO CRISM team (2008) Discovery of the acid-sulfate mineral alunite in Terra Sirenum, Mars, using MRO CRISM: possible evidence for acid-saline lacustrine deposits? Eos Trans. AGU 89(53), Fall Meet. Suppl. Abstract P44A-04

Swayze GA, Milliken RE, Clark RN, Bishop JL, Ehlmann BL, Pelkey SM, Mustard JF, Murchie SL, Brown AJ, and the MRO CRISM Team (2007) Spectral evidence for hydrated volcanic and/or impact glass on Mars with MRO CRISM. Seventh International Conference on Mars, July 9-13, 2007, Pasadena, California, LPI Contribution No. 1353, 3p

Swayze GA, Smith KS, Clark RN, Sutley SJ, Pearson RN, Rust GS, Vance JS, Hageman PL, Briggs PH, Meier AL, Singleton MJ, Roth S (2000) Using imaging spectroscopy to map acidic mine waste. Environ Sci Technol 34:47-54

Teanby NA, Irwin PGJ, de Kok R, Jolly A, Bezard B, Nixon CA, Calcutt SB (2009) Titan's stratospheric C_2N_2, C_3H_4, and C_4H_2 abundances from Cassini/CIRS far-infrared spectra. Icarus 202:620-631

Tegler SC, Cornelison DM, Grundy WM, Romanishin W, Abernathy MR, Bovyn MJ, Burt JA, Evans DE, Maleszewski CK, Thompson Z, Vilas F (2010) Methane and nitrogen abundances on Pluto and Eris. Astrophys J 725:1296-1305

Thollot P, Mangold N, Ansan V, Le Mouelic S, Milliken RE, Bishop JL, Weitz CM, Roach LH, Mustard JF, Murchie SL (2012) Most Mars minerals in a nutshell: Various alteration phases formed in a single environment in Noctis Labyrithus. J Geophys Res Planets 117:E11, doi: 10.1029/2011JE004028

Thomson BJ, Bridges NT, Milliken R, Baldridge A, Hook SJ, Crowley JK, Marion GM, de Souza Filho CR, Brown AJ, Weitz CM (2011) Constraints on the origin and evolution of the layered mound in Gale Crater, Mars using Mars Reconnaissance Orbiter data. Icarus 214:413-432

Titov DV, Svedhem H, Taylor FW, Barabash S, Bertaux JL, Drossart P, Formisano V, Häusler B, Korablev O, Markiewicz WJ, Nevejans D, Pätzold M, Piccioni G, Sauvaud JA, Zhang TL, Witasse O, Gerard JC, Fedorov A, Sanchez-Lavega A, Helbert J, Hoofs R (2009) Venus Express: Highlights of the Nominal Mission. Solar System Res 43:185-209

Tomasko MG, Archinal B, Becker T, Bezard B, Bushroe M, Combes M, Cook D, Coustenis A, de Bergh C, Dafoe L, Doose L, Doute S, Eibl A, Engel S, Gliem F, Grieger B, Holso K, Howington-Kraus E, Karkoschka E, Keller HU, Kirk R, Kramm R, Kuppers M, Lanagan P, Lellouch E, Lemmon M, Lunine J, McFarlane E, Moores J, Prout GM, Rizk B, Rosiek M, Rueffer P, Schroder SE, Schmitt B, See C, Smith P, Soderblom L, Thomas N, West R (2005) Rain, wind and haze during the Huygens probe's descent to Titan's surface. Nature 438:765-778

Trujillo CA, Brown ME, Barkume KM, Schaller EL, Rabinowitz DL (2007) The surface of 2003 EL61 in the near-infrared. Astrophys J 655:1172-1178

Tryka KA, Brown RH, Anicich V, Cruikshank DP, and Owen TC (1993) Spectroscopic determination of the phase composition and temperature of nitrogen ice on Triton. Science 261:751-754

Tryka KA, Brown RH, Anicich V, Cruikshank DP, and Owen TC, Geballe TR, and de Bergh C (1994) Temperature of nitrogen ice on Pluto and its implications for flux measurements. Icarus 112:513-527

Ustin SL, Gitelson AA, Jacquemoud S, Schaepman M, Asner GP, Gamon JA, Zarco-Tejada P (2009) Retrieval of foliar information about plant pigment systems from high resolution spectroscopy. Remote Sens Environ 113:S67–S77, doi: 10.1016/j.rse.2008.10.019

Vilas F, Domingue DL, Sprague AL, Izenberg NR, Klima RL, Jensen EA, Helbert J, D'Amore M, Stockstill-Cahill KR, Solomon SC (2012) Search for absorption features. *In:* Mercury's Visible Reflectance Spectra: Recent Results From Messenger. 43rd Lunar and Planetary Science Conference, 1330. *http://www.lpi.usra.edu/meetings/lpsc2012/pdf/1330.pdf*

Vilas F, Larson SM, Stockstill KR, Gaffey J (1996) Unraveling the zebra: Clues to the Iapetus dark material composition. Icarus 124:262-267

Vuitton V, Yelle RV, Cui J (2008) Formation and distribution of benzene on Titan. J Geophys Res 113:E05007, doi: 10.1029/2007JE002997

Wade LG (2005) Organic Chemistry, 5th edition. Prentice Hall, Inc., New Jersey

Waite H, Young D, Cravens T, Coates A, Crary F, Magee B, Westlake J (2007) The Process of Tholin Formation in Titan's Upper Atmosphere, Science 316:870-875

Wong MC, Johnson RE (1996) A three-dimensional azimuthally symmetric model atmosphere for Io .2. Plasma effect on the surface. J Geophys Res 101:23255-23259

EBSCOhost - printed on 2/13/2023 5:26 AM via . All use subject to https://www.ebsco.com/terms-of-use

Wray JJ, Milliken RE, Dundas CM, Swayze GA, Andrews-Hanna JC, Baldridge AM, Chojnacki M, Clark RN, Murchie SL, Ehlmann BL, Bishop JL, Seelos FP, Tornabene LL, and Squyers S (2011) Columbus crater and other possible groundwater-fed paleolakes of Terra Sirenum, Mars. J Geophys Res 116:E01001. doi: 10.1029/2010JE003694

Wyatt MB, McSween HY (2002) Spectral evidence for weathered basalt as an alternative to andesite in the northern lowlands of Mars. Nature 417:6886:263-266

Yung YL, DeMore WB (1999) Photochemistry of Planetary Atmospheres. Oxford University Press, p 201-234

Zahnle K, Schenk P, Levison H, Dones L (2003) Cratering rates in the outer solar system. Icarus 163:263-289

Zellner B (1972) On the nature of Iapetus. Astrophys J Lett 174:L107-L109

Zolotov MY, Fegley B (1998) Volcanic production of sulfur monoxide (SO) on Io. Icarus 132:431-434

Zolotov MY, Fegley B (1999) Oxidation state of volcanic gases and the interior of Io. Icarus 141:40-52

Zolotov MY, Fegley B (2000) Eruption condition of Pele volcano on Io inferred from chemistry of its volcanic plume. Geophys Res Lett 27:2789-2792

EBSCOhost - printed on 2/13/2023 5:26 AM via . All use subject to https://www.ebsco.com/terms-of-use

Reviews in Mineralogy & Geochemistry
Vol. 78 pp. 447-479, 2014
Copyright © Mineralogical Society of America

SR-FTIR Microscopy and FTIR Imaging in the Earth Sciences

Giancarlo Della Ventura[1,2], Augusto Marcelli[2], Fabio Bellatreccia[1,2]

[1]*Dipartimento Scienze*
Università di Roma Tre
Largo S. Leonardo Murialdo 1
I-00146 Roma, Italy

giancarlo.dellaventura@uniroma3.it, fabio.bellatreccia@uniroma3.it

[2]*Istituto Nazionale di Fisica Nucleare*
Laboratori Nazionali di Frascati
Via E. Fermi 40
I-00044 Frascati (Rome), Italy

marcelli@lnf.infn.it

INTRODUCTION

Infrared spectroscopy was developed at the beginning of the 20th century for analytical chemical purposes and it is remarkable that the first contribution of the first issue of Physical Review, one of the first and among the most important physical magazines, published in 1883, was devoted to "a study of the transmission spectra of certain substances in the infrared" that included also a plate of a quartz rock crystal (Nichols 1883). In 1905, William W. Coblentz released the very first database of IR spectra where the characteristic wavelength at which various materials absorbed the IR radiation were listed. For more than a century IR spectroscopy has been considered as a powerful analytical tool for phase identification and to characterize the structural features and quantify molecules or molecular arrangements in solids, and also in liquids and gases. This technique has been used extensively by organic chemists, and since the 1950s it has been recognized as a fundamental technique in mineralogical and Earth sciences in conjunction with X-ray diffraction (Keller and Pickett 1949, 1950; Launer 1952; Adler and Kerr 1965). The first "encyclopedia" of IR spectra of minerals appeared in 1974 (Farmer 1974) and is still a primary reference for those using infrared spectroscopy as a tool in material science.

In the late '60s and beginning of '70s a new IR technique, Fourier-transform infrared (FTIR) spectroscopy, was developed and later a new class of spectrometers was commercially available, based upon the combination of a FFT (Fast-Fourier-Transform) algorithm and computers. The advantage of these instruments over the previously used wavelength-dispersive spectrometers is fully described in several books, e.g., Griffiths and de Haseth (1986) and Smith (1996). Briefly, in FTIR spectrometers IR light is focused through an interferometer and then through the sample. A moving mirror inside the apparatus alters the distribution of infrared light (wavelength) that passes through the interferometer. The recorded signal, called an interferogram, represents light output as a function of mirror position, which correlates with wavelength. A FFT data-processing transforms the raw data into the sample spectrum. A major advantage of the FTIR spectrometers is that the information in the *entire* frequency range is collected simultaneously, improving both speed and signal-to-noise ratio (SNR).

1529-6466/14/0078-0011$05.00 http://dx.doi.org/10.2138/rmg.2014.78.11

EBSCOhost - printed on 2/13/2023 5:26 AM via . All use subject to https://www.ebsco.com/terms-of-use

During the last decades, several books have been devoted to the application of spectroscopic methods in mineralogy, e.g., Volume 18 of Reviews in Mineralogy (Hawthorne 1988). Several short courses (e.g., Beran and Libowitzky 2004) and meetings have addressed particular aspects of spectroscopy, such as the analysis of hydrous components in minerals and Earth materials (e.g., Keppler and Smyth 2006). In these books, a complete treatment of the infrared theory and practical aspects of instrumentation and methods, along with an exhaustive list of references, can be found.

The present chapter is intended to cover those aspects of infrared spectroscopy that have been developed in the past decade and are not included in earlier reviews such as Volume 18 of Reviews in Mineralogy. These new topics involve primarily: (1) the use of synchrotron radiation (SR), which, although not a routine method, is now rather extensively applied in infrared studies, in particular those requiring ultimate spatial and time resolution and the analysis of extremely small samples (a few tens of micrometers); (2) the development of imaging techniques also for foreseen time resolved studies of geo-mineralogical processes and environmental studies.

There are now several synchrotron beamlines around the world that are dedicated to IR spectroscopy and microscopy, hosting an ever-increasing number of multidisciplinary users. Interest in synchrotron-IR radiation (SR-IR) increased in the last 20 years because of its unique properties and effective advantages, including the possibility to perform experiments using an intense fully-linear polarized light source.

A non-thermal SR source is an intense source whose emission at long wavelengths is asymptotic and, for accumulated electrons at $E > 0.5$ GeV, does not depend on the energy. Its intensity is also proportional to the large horizontal opening angle and to the current circulating in the storage ring. The unique features of SR-IR radiation overcome limitations of conventional "benchtop" instruments and open new fields of applications, in particular those associated to extreme experimental conditions (e.g., high-pressure, cryogenic/high temperatures).

As we will discuss in more details later, the main advantage of synchrotron radiation over conventional black body sources is its brilliance, which is defined as the photon flux density normalized to the source area and to the horizontal and vertical angle of emission (photons/mm^2/mrad^2). The gain in brilliance of an infrared SR source with respect to a conventional source is from 100-1000 times going from the near-IR (NIR) to the far-IR (FIR), and increases when working at small apertures. It is worth stressing, however, that the best advantage of a SR source over a conventional source is obtained when using a confocal microscope or when performing time-resolved experiments. A microscope has a confocal geometry when the objective and the collector share the same focus at the sample location and both have a small aperture, placed at the conjugated focus, limiting the illuminated or the detected area of the sample, respectively. The use of small apertures such as pinholes allows images with a high spatial resolution to be obtained, but at the cost of a low throughput. In this latter case the signal-to-noise ratio (SNR) must ensure the recognition of small features in the image. The drawback of the use of pinholes or extremely small apertures (say < 20 μm^2) in a microscope is the dramatic degradation of the SNR and the need to increase the collection time unless using brilliant SR sources.

In addition, the recent advent of area-detectors ("focal-plane-array, FPA") has revolutionized the world of mid-IR FTIR spectroscopy. These arrays are composed of small IR detectors (pixels) a few tens of microns or less in dimension, and allow the acquisition of thousands of IR spectra simultaneously generating mid-IR (MIR) images with a high resolving power. The optical system of an IR microscope equipped with a FPA is an *apertureless* imaging system, whose ultimate spatial resolution is comparable but never better than that attainable by

EBSCOhost - printed on 2/13/2023 5:26 AM via . All use subject to https://www.ebsco.com/terms-of-use

confocal microscopes. Nevertheless, FPAs enable different imaging modes at the resolution of a few microns and, thanks to their sensitivity and read-out speed, massive and fast data collection within minutes are possible (Bhargava and Levin 2001; Petibois and Déléris 2006; Petibois et al. 2010a).

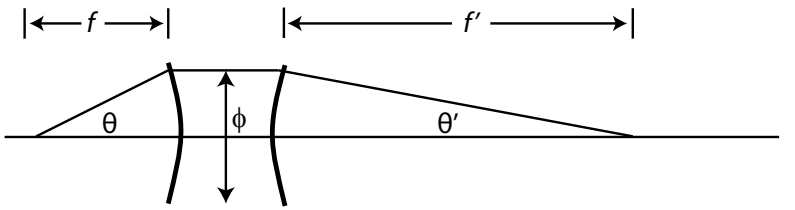
For Earth science materials, SR-IR has been applied in studies where an improved spatial resolution was needed, for example for fine-grained synthetic crystals, or when high brilliance was needed, such as in high-pressure (HP) studies using diamond-anvil cells (DAC) (Scott et al. 2007; Noguchi et al. 2012). The new imaging capabilities of FTIR detectors were used to address features such as zoning of volatile species across the sample or possible configurational changes of structurally-bound carbon molecular species (e.g., CO_2 vs. CO_3) during the crystal growth. Such features, which are barely accessible with micro-analytical techniques, may provide constraint in terms of physico-chemical parameters relating to the conditions of formation of the samples, and important information on the evolution of geological systems vs. time. Some significant recent studies that explore the use of FTIR imaging to investigate experimental systems and to monitor processes in real time will be reviewed here.

FTIR MICROSCOPY AND IMAGING TECHNIQUES

More than a century ago, Ernst Abbe showed experimentally that the resolving power of an optical instrument is subject to a physical limit, i.e., the diffraction limit, which cannot be overcome by designing better objective lenses. The diffraction limit is ~ $2\lambda/NA$ where *NA* is the numerical aperture of the microscope objective. Working with commercial objectives having *NA* ~0.6, the resolution is 3 to 4 times the wavelength (~ 1.7 μm at 4000 cm^{-1}). In a confocal microscope, where the objectives are placed both before and after the sample, the spatial resolution can be improved to ~ $\lambda/2$ (Minsky 1988).

The goal of FTIR microscopy is to achieve the best spatial resolution at the sample location, i.e., to allow imaging to the diffraction limit. However, as it has been shown recently (Levin and Bhargava 2005; Levenson et al. 2006; Bhargava and Levin 2007), the concept of spatial resolution in IR imaging is not an independent parameter: it is diffraction limited and is also affected by both the optical design (e.g., objectives and apertures) and contrast. To avoid the chromatic aberration, IR microscopes are equipped with two Schwarzschild objectives, which are based on two spherical mirrors centered on the same optical axis and allow magnifications of 15× or 36× with numerical apertures (*NA*) in the range 0.3-0.7. The magnification, the parameter that determines how much small features in the specimen can be enlarged, must be adjusted in proportion to distance (see Fig. 1). To increase the magnification, the objective of the microscope has to be positioned nearer to the specimen to be observed. The correlation between the magnification and the *NA* of the objective and the condenser of a microscope is: $M = (f'/f) = (NA/NA')$, where f and f' are the focal distance of the objective and the condenser microscope optical elements, respectively. This definition is practical and useful because it is independent of any specific characteristics of the optical system ($M \propto NA$). The concept of the lateral spatial resolution of an image, i.e., the spatial resolution in the plane perpendicular to the propagation of the light through the specimen, has to be related to a resolution criterion, i.e., how we may clearly separate two closely spaced objects inside a sample. According to the Rayleigh criterion, two points can be separated when the central maximum of the first Airy disk is placed at a distance greater than the radius of the first minimum of the Airy disk (see Fig. 2). When a point source of monochromatic radiation goes through a microscope, an Airy pattern is observed at the beam focus. The central circular area, i.e., the Airy disc, of the point spread function (PSF) in Figure 2 is characterized by a radius $r = 0.61(\lambda/NA)$, where λ is the wavelength and *NA* is the numerical aperture of the microscope. However, the Rayleigh criterion is valid only when the two points to be separated both sit on an identical and

EBSCOhost - printed on 2/13/2023 5:26 AM via . All use subject to https://www.ebsco.com/terms-of-use



Object Side:
$NA = \sin\theta = \phi/2f$
$2f \sin\theta = \phi$

Image Side:
$NA' = \sin\theta' = \phi/2f'$
$2f' \sin\theta' = \phi$

$$M = f'/f = \sin\theta/\sin' = NA/NA'$$

Figure 1. The magnification (M) can be defined as the ratio between the two numerical apertures (*NA*) of the microscope, the one on the object side (*NA*) and the one on the image side (*NA′*). Φ is the clear aperture or f-stop of the optical elements (i.e., mirrors) of the IR microscope, *f* and *f′* are the focal distances and θ and θ′ their angular apertures.

negligible background and have the same intensity, a condition that corresponds to a minimum contrast of 26.4% (Levenson et al. 2006; Pawley 2006).

If we consider a standard optical microscope illuminating a large sample region, the ultimate resolution is achieved by the "detection system" made by the objective optics and our eye. Similarly, in an IR microscope, when using an area-detector, i.e., a focal-plane array (FPA) detector, the maximum spatial resolution is determined by the magnification of the optical system, but the size of the individual pixel of the detector is also a relevant parameter (Miller and Smith 2005). FPA detectors are still not widespread because almost all IR microscopes are equipped with single-element MCT detectors.

In a microscope, reducing with a field stop the field of view (FOV) at the sample location, for example by an aperture placed at an intermediate focal point, the spatial resolution is determined by the fraction of light from each point of the specimen that reaches the detector, i.e., its sensitivity pattern. As outlined above, if we reduce the illumination region while maintaining a homogeneous illumination, then the spatial resolution is a function of the number of photons that illuminate the small selected region of the specimen. To probe this small region of a specimen, the microscope must illuminate it and simultaneously detect the light. A confocal microscope has apertures for both the illumination and detection systems. It achieves the ultimate spatial resolution by reducing to the same size both the illuminated region and the region to be detected. An image of the specimen under analysis can be then collected, although with much longer times, by rastering the sample through the focus of the confocal microscope. In this case, because of their intrinsic noise, large single-element detectors (50×50 μm or larger) are not suitable to work at high spatial resolution and the dimension of the single-element detector is the real bottleneck.

In contrast to confocal microscopes with single-element detectors, combining a SR source with a two-dimensional FPA detector is an efficient way to take advantage of a SR source for imaging and time resolved experiments. Using area-detectors we may collect FTIR spectra simultaneously on large areas (several tens of μm^2) depending on the magnification. Images containing hundreds of points are obtained within minutes compared with longer acquisitions (hours) typically required by a single-element detector mapping. Although, in principle, a

EBSCOhost - printed on 2/13/2023 5:26 AM via . All use subject to https://www.ebsco.com/terms-of-use

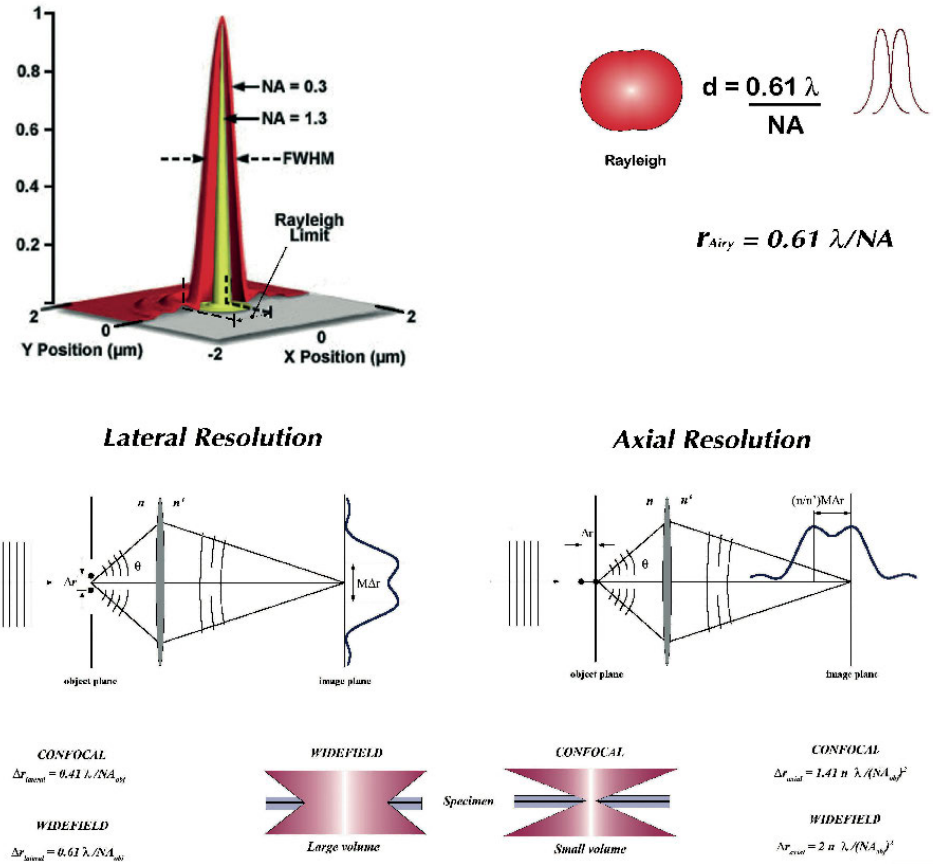


Figure 2. (*Top, left*) Comparison of the Point Spread Function (PSF) between two optical systems with different Numerical Apertures (*NA*). According to the Rayleigh criterion (*Top, right*), two source points can be separated when the central maximum of the Airy disc is placed at the position of the first dark fringe of the second diffraction pattern (0.61 λ/*NA*). Higher the *NA*, higher will be the spatial resolution of the system. However, in a real case, with this criterion a full separation can be obtained only if the background is negligible and the signal associated with the two source points has the same intensity, a condition that corresponds to a minimum contrast of 26.4% (e.g., Levenson et al. 2006). (*Bottom*) comparison of spatial lateral (*left*) and axial (*right*) resolution for confocal and widefield microscopies. Equations show that both the lateral and axial extent of the confocal PSFs are reduced by ~30% respect to a widefield illumination and that the *NA* of the objective is much more effective in the axial resolution case (~NA^2).

thermal source may achieve a sub-second resolution for a single spectrum, using the raster scan method images can be collected at a much slower time. Moreover, working with a high current synchrotron radiation facility, the intense IR beam can be shaped to illuminate only a limited number of pixels of a FPA detector increasing the SNR ratio of the image achieved with high contrast (Petibois et al. 2010a). For these reasons, FPAs are used extensively in biological studies (e.g., Petibois et al. 2009), while very few studies of Earth materials have been made so far, despite its wide potential applications.

When considering the resolution, great emphasis is given to the lateral resolution. However, to interpret an image it is also important to consider the axial resolution, i.e., the axial resolving power of the objective measured along the optical axis. As with the lateral resolution,

EBSCOhost - printed on 2/13/2023 5:26 AM via . All use subject to https://www.ebsco.com/terms-of-use

the axial resolution (Fig. 2) also depends on the numerical aperture (*NA*) of the objective (Born and Wolf 1997; Inoué 1995). Lateral and axial spatial resolution for a confocal microscope are reduced by ~ 30% if compared with a corresponding microscope working with a wide-field illumination (Fig. 2). A large *NA* improves both the lateral and axial spatial resolution of the microscope although the *NA* of the microscope objective is much more effective for the axial resolution (~ NA^2). Knowledge of the axial resolution is fundamental to performing "optical sectioning", a technique that makes possible a three-dimensional reconstruction of a sample via non-destructive depth profiling, collecting images as the focus is moved deeper into the sample. This method offers clear advantages with respect to mechanically cutting a cross-section (microtomy), avoiding in particular the need for any destructive sample preparation.

In this context, it is worth also mentioning the opportunity offered by scanning near-field optical microscopy (SNOM), a technique which allows optical imaging that can be extended to the FTIR domain with a resolution down to few tenths of nm, i.e., well beyond the Abbe diffraction limit (e.g., Cricenti et al. 2002; Vobornik et al. 2005). SNOM systems are based on optical waveguides with a nano-aperture much smaller than the light wavelength λ. The use of a nano-aperture as a local probe makes it possible to overcome the λ/2 diffraction limit that occurs if the light is detected in far field, i.e., when the detector distance is much larger than the wavelength λ of the light used in the experiment. However, to the authors' knowledge, no application of this technique to geological samples has been published so far, except some work aimed at studying diffuse nanoparticles in meteorite's metal inclusions thought to be responsible for the problem of asteroid reddening (Pompeo et al. 2010). Imaging can be obtained with an *apertureless* scanning near-field optical microscope, leading to an extreme spatial resolution at IR wavelengths. However, we need to point out that it is practically impossible to map a large sample with SNOM optics. Moreover, because optical methods measure the index of refraction of a material, the real part returns only the sample topography while the imaginary part is proportional to the sample absorption, and so when looking at extremely small areas the local absorption is weak. In other words, if the signal is too small to be detected or comparable to the noise, differential methods such as photoacoustic or photothermal detection are more efficient. A new IR spectromicroscopy technique, based on the coupling between a tunable free-electron IR laser and an Atomic Force Microscope in the IR range (AFMIR) was recently setup at the CLIO free-electron laser facility (Dazzi et al. 2005, 2007a,b; Ortega et al. 2006) allowing IR mapping at the nm scale. Detection is performed directly by an AFM tip in the contact mode, probing the local thermal expansion of the sample, irradiated at the wavelength of specific absorption bands. As the duration of expansion and relaxation of the sample is always shorter than the response time of the cantilever in contact, by recording the amplitude of the cantilever oscillations it is possible to measure the corresponding IR absorption as a function either of space or wavelength. A spatial resolution around 50 nm has been achieved in the mid-IR region at λ = 22 μm (Houel et al. 2009), although, because of the inherent near-field character, the sensitivity of this technique is reduced for objects located below the surface.

For FTIR imaging in transmission mode, the sample preparation is another crucial aspect to consider. The specimen must be prepared as a slice with parallel and doubly- polished surfaces to allow the IR beam to pass through the sample without scattering. A fragment of each material under investigation, either a rock or a single-crystal, is cut into a block and polished on both sides using different kinds of abrasives, e.g., silicon carbide or alumina powders, diamond pastes, or abrasives plastic foils. Final polishing is obtained with a 1.0 to 0.25 μm grit. During the grinding, the sample is usually mounted on a glass slide with easily removable glues, such as Crystalbond™. The final thickness depends on the type of sample and on the problem under investigation. At the end, the slice is removed from the glass and carefully washed from any residual from epoxy or binding agent. The result is a thin (typically in the range 300–15 μm) freestanding doubly polished wafer. For quantitative purposes, an additional critical point is the measurement of the slice thickness. This is usually achieved using a micrometer, and

EBSCOhost - printed on 2/13/2023 5:26 AM via . All use subject to https://www.ebsco.com/terms-of-use

checked with the IR microscope using standard slabs with known thickness as reference. When high precision is required, measurements using a scanning electron microscope (SEM) or an optical profilometer (e.g., Della Ventura et al. 2012) are preferred. Non-conventional techniques recently available for sample preparation involve the use of focused ion beam (FIB) instruments to cut extremely thin slices from target sample locations (Koch-Müller et al. 2004; see also Wirth 2004 and Marquardt and Marquardt 2012). An example of FIB machining to prepare oriented very thin crystal sections for polarized-light FTIR measurements is given in Figure 3.

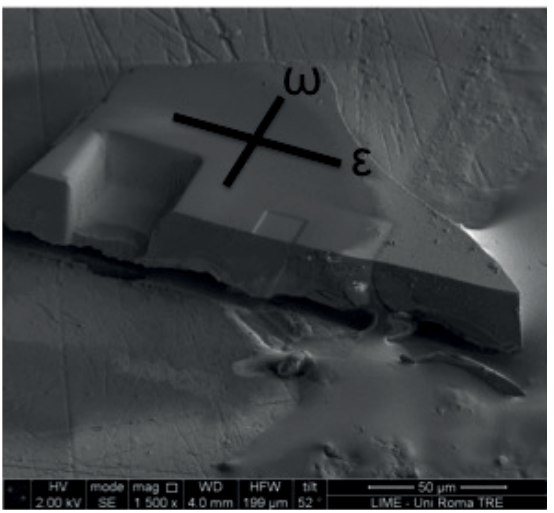


Figure 3. Oriented (hk0) doubly polished, 40 µm thick, crystal section of wardite, prepared for polarized FTIR measurements in the water stretching region (Bellatreccia and Della Ventura, unpublished). Because the transmitted IR signal is out of scale at these conditions, a hole 20×20 µm^2 was machined using a FIB (Helios Nanolab, at LIME, University Roma Tre) such as at the bottom of the cavity the thickness is reduced to 8 µm. Note that the edges of the hole have been oriented such as to be parallel to the optical directions in the crystal.

SYNCHROTRON-RADIATION FTIR SPECTROSCOPY IN MINERAL SCIENCES

Introduction

As a light source for spectroscopy, synchrotron radiation has several key properties: (1) a high brilliance, (2) a continuous distribution of the intensity over the entire spectral range, (3) a pulsed nature, (4) a high degree of polarization and (5) a high stability. Synchrotrons and storage rings use magnetic structures, i.e., dipoles, quadrupoles and sextupoles to bent and focus electrons to circulate along closed orbits. Radiation is emitted when particles travelling at relativistic velocities are deflected by a constant magnetic field as it occurs inside a bending magnet. This is the classical synchrotron radiation bending magnet emission whose spectral range is characterized by a broad spectrum extending from the microwave to the X-ray domain (Hofmann 2004). Radiation is also emitted by electron travelling through a fringing field of a dipole magnet. This emission is called "Edge Radiation" (ER). For electrons at a relativistic speed, the fringe field is like a "sharp edge transition" from a zero field to a full field value and the associated impulsive acceleration originates the emission of light. The emission spectrum of ER is limited and does not extend to the X-ray domain; however, in the low-frequency (IR, THz) range it is comparable to the standard synchrotron radiation spectrum (Geloni et al. 2009a,b).

The main advantage of synchrotron radiation is its brilliance. In spite of it, large angles are required to extract from bending magnets long wavelength radiation such as IR radiation, because the "natural" opening angle increases up to several tens milliradians in the far-IR range. On the contrary, long-wavelength radiation emitted as Edge Radiation is characterized by a significantly smaller opening angle than standard bending-magnet radiation. Long

EBSCOhost - printed on 2/13/2023 5:26 AM via . All use subject to https://www.ebsco.com/terms-of-use

wavelength SR sources may have a strong potential for IR spectroscopy or imaging techniques (Petibois et al. 2009) particularly considering that both ER and bending magnet radiation have equivalent brilliance. The history of SR utilization in the long wavelength region (from micrometer to millimeter waves) is more recent than that in the short wavelength domain (Marcelli and Cinque 2011). In fact, SR sources are some order of magnitude more brilliant than a conventional black body source in the same spectral range as shown in Figure 4. A highly brilliant source is not a priority for a spectroscopic measurement, while becomes mandatory in microscopy where a spot size down to the diffraction limit is desired. However, the SNR decreases drastically as apertures are reduced to confine the beam into a small area to increase the lateral resolution of an image, as shown in Figure 5. The use of IR microscopes coupled to SR sources may guarantee outstanding results just because the high brilliance of this source allows reducing the microscope apertures down to the *diffraction limit*, i.e., down to a few microns in the mid-IR region, still assuring a good SNR (Carr 2001).

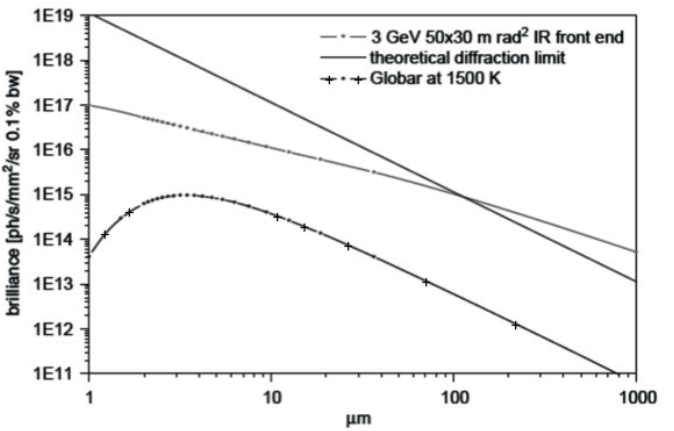
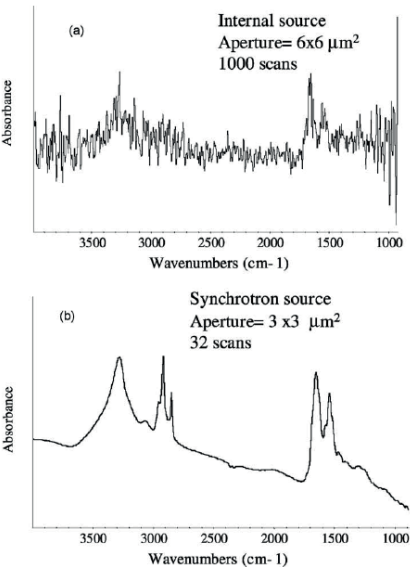


Figure 4. Calculated synchrotron radiation brilliance of a 3 GeV source in comparison to a conventional source and the ideal SR diffraction limited source (courtesy G. Cinque, from DLS, design report of the IR beamline at Diamond).



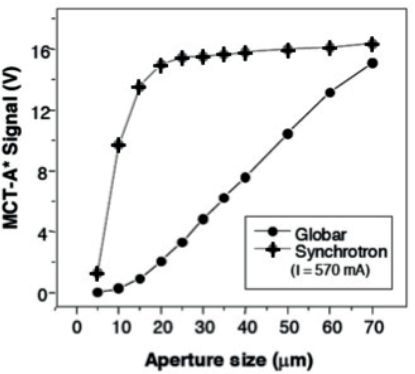


Figure 5. (*Left*) comparison between the IR spectrum taken with a conventional source, using an aperture 6×6 μm², accumulating 1000 scans, and the SR-IR spectrum taken on the same sample location using an aperture 3×3 μm², accumulating 32 scans. (*Above*) intensity of infrared light reaching the detector as a function of the aperture size for conventional vs SR beam.

EBSCOhost - printed on 2/13/2023 5:26 AM via . All use subject to https://www.ebsco.com/terms-of-use

Because the electrons in the storage ring do not form a continuous distribution around the orbit but are stored and travel as bunches in a circular accelerator, the resulting emission has a time structure. The SR is indeed emitted as light pulses characteristic of each accelerator, being another interesting feature of this source for time resolved experiments. The bunch length ranges from tens of ps to a few ns, values hardly to be obtained with conventional sources (Mills 1984; Innocenzi et al. 2009; Xu et al. 2011; Marcelli et al. 2012).

An additional important feature of synchrotron radiation is its polarization. Owing to its relativistic character, the SR emission is linearly polarized in the orbital plane. Since the early pioneering work in the visible region, studies performed both in the VUV and X-ray regions demonstrated that when observed at a particular angle over the orbit, the radiation is circularly polarized. The polarization properties of the SR at long wavelengths are very promising for many applications, in particular in the far-IR region. By placing a slit on the exit port, one can in principle select the desired degree of circular polarization and the flux of the emitted radiation. Dealing with polarization, we may define three polarization rates, of which two are more important: the linear polarization (P1) and the circular polarization (P3). Experimental observations indicate that values up 80% of circularly polarized light can be obtained using a slit that selects ~50% of the total flux available (Cestelli Guidi et al. 2005).

In SR-IR beamlines, commercial optical benches and microscopes are installed and the synchrotron beam replaces the conventional black body source. The beam is focused in the upper aperture of the microscope (Fig. 6) and is projected onto the sample plane by a Catoptric objective; the size of the aperture determines the lateral resolution that one can attain in the analysis; the problems associated with the SNR and the resolution in these conditions have been introduced before. More details can be found in Marcelli and Cinque (2011).

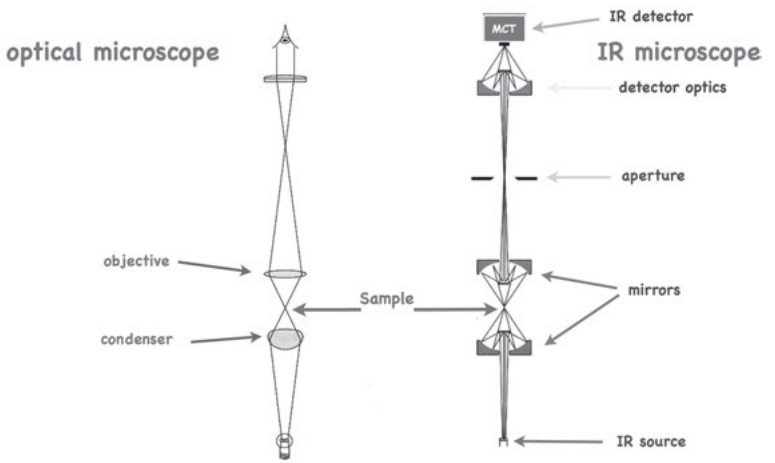


Figure 6. Schematic layout of an IR microscope compared to that of an optical microscope.

Applications in mineral sciences

For materials of interest in the Earth Sciences SR-FTIR has been mostly applied in the study of inclusions within minerals, in the analysis of H_2O/OH in nominally anhydrous minerals (NAMs), of H and C molecules of interplanetary dust particles (IDPs) and in high-pressure studies. Few applications in the field of cultural heritage have also been reported.

EBSCOhost - printed on 2/13/2023 5:26 AM via . All use subject to https://www.ebsco.com/terms-of-use

Guilhamou et al. (1998) and Bantignies et al. (1998) were among the very first to explore the potentiality of SR-FTIR microspectrometry for the study of samples of geological interest (Fig. 7). In particular, Guilhamou et al. (1998) addressed the analysis of hydrocarbon-rich fluid inclusions in siliceous diagenetic materials, aimed at constraining petroleum formation and migration. Using a beam size of 3×3 μm^2 they were able to obtain high SNR spectra for an accurate chemical identification of aliphatic components, CO_2 and water entrapped in fluorite cementing the host rock. In the same paper they also reported preliminary tests for the analysis of CO_2 and H_2O in glass inclusions within olivine from tholeitic basalts from South Vietnam and the detection of trace OH in NAMs.

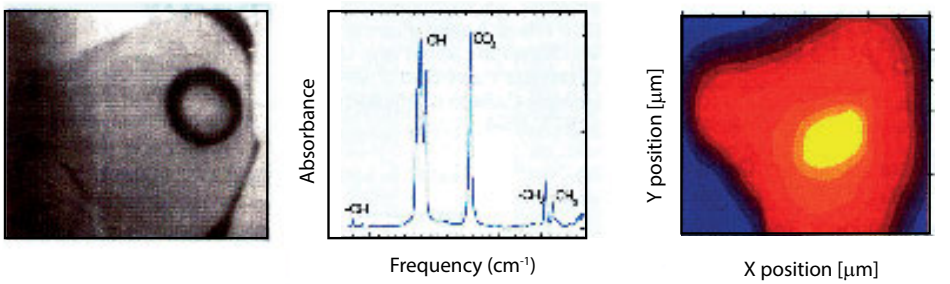


Figure 7. Infrared microspectroscopy of the CO_2 distribution within a fluid inclusion. (*left*) optical image, (*center*) selected FTIR spectrum, (*right*) resulting CO_2 map. Modified from Bantignies et al. (1998).

Guilhaumou et al. (2005) studied melt inclusions within garnets and exsolved pyroxenes from deep-seated ultramafic xenoliths uplifted in the Jagersfontein kimberlite pipe (South Africa). Petrographical and mineralogical data showed these samples to record evidence of multistage fluid-rock interactions during their ascent from the asthenosphere through the lithosphere. Primary and secondary OH-bearing melt inclusions were recognized, the first representing the result from an early partial melting of the garnet host, and the second originating from volume change of the hydrated pyroxene during ascent. The data were interpreted as evidence for unusual water contents in the primary ultradeep-seated garnets. Evidence of a carbonaceous magma rich in dissolved CO_2 was provided by the presence of secondary inclusions containing a CO_3-bearing glassy phase associated with a vapor phase rich in CO_2 and H_2O.

Koch-Müller et al. (2004) and Koch-Müller et al. (2006) studied, using SR-FTIR, the hydroxyl content of pyroxenes and olivines from high-pressure occurrences. Three groups of absorption bands in the OH-stretching region were observed in omphacites from the upper mantle and lower crust beneath the Siberian platform (Koch-Müller et al. 2004). The intensity of the peaks centered in the higher wavenumber 3600-3624 cm^{-1} range were found to be strongly correlated with inclusion-rich regions within the pyroxene crystals. TEM bright- and dark-field images obtained on crystal foils cut in different parts of the examined grains using a FIB, clearly showed that these bands could be associated with nm-sized inclusions of a sheet silicate within the omphacite matrix. It is worth noting that the spectra also showed a weak band in the high wavenumber range characteristic of omphacite and caused by vibration of intrinsic hydroxyl groups. Some of the inclusions were interpreted to have formed during the uplift of the host rock as a product of interaction with fluids. The intensities of the other peaks in the FTIR patterns could be related with $^{[4]}$Al or octahedral vacancies at M2, respectively. As an additional test for the assignment of the higher wavenumber bands to a phyllosilicate phase, high-pressure spectra were collected using a diamond anvil cell up to 12 GPa and the behavior of the OH bands with pressure was compared with those of chlorite and omphacite. The OH

EBSCOhost - printed on 2/13/2023 5:26 AM via . All use subject to https://www.ebsco.com/terms-of-use

content in the samples could be quantified using polarized radiation measurements on oriented sections, and was found to vary from 31 to 514 ppm, the lowest value from the pyroxene in the highest pressure rock, a diamond-bearing eclogite xenolith from a kimberlite pipe. Up to 20 strongly polarized bands were observed (Koch-Müller et al. 2006) in the OH-spectra of olivines from the Udachnaya kimberlite pipe (Russia). Peaks at higher energy (3730-3670 cm^{-1}) were assigned to inclusions of serpentine, talc and the 10 Å phase. OH groups were correlated to point defects associated with either Si sites or vacant M1 sites. Polarized experiments showed that H was bonded to O1 and O2 oxygens, forming O-H vectors parallel to the *a* crystallographic axis. Combination of the FTIR data with SIMS (Secondary Ion Mass Spectrometer) analyses allowed the calibration of the integrated absorption coefficient ε_i = 37,500±5,000 L mol H_2O cm^{-2}. Later Thomas et al. (2009) pointed out that this is a wave-number independent absorption coefficient, which can be used to quantify all types of OH-defects in olivine.

Koch-Müller et al. (2003) studied the solubility of hydrogen into coesite at pressure in the 4.0-9.0 GPa range and temperature in the 750-1300 °C range by using Al and B doped SiO_2 as starting materials. The OH-spectra were extremely complex with several bands, assigned to different substitutional mechanisms responsible for OH incorporation into synthetic coesite. To improve the resolution for overlapping bands, low temperature spectra were collected using a Linkam T600 freezing stage (Fig. 8). The most intense and sharp peaks were attributed to the hydrogarnet substitution $^{(T2)}Si^{4+} + 4O^{2-} = {}^{T2}$vacancy + $4OH^-$, consistent with the observation that more than 80% of the dissolved water is incorporated via this mechanism. Based on the positive correlation between the content of B determined by SIMS, some of the weaker bands were assigned to B-based point defects, while others were assigned to OH groups incorporated via the $Si^{4+} \rightarrow Al^{3+}$ + H substitution. The water solubility was quantified using the molar absorption coefficient ε_i = 190,000 Å ± 30,000 L mol H_2O cm^{-2} calibrated by Koch-Müller et al. (2001) and was found to increase with both temperature and pressure. Interestingly, the incorporation mechanism for H seemed to change for pressure in excess of 8.5 GPa, at 1200 °C. New sharp bands appeared in the spectrum at lower wavenumbers, while those observed for $P <$ 8.5 GPa and assigned to the hydrogarnet substitution disappeared. On the basis of single-crystal, Raman and polarized IR, these new bands were assigned to OH groups in coesite; however both their polarization and high-pressure behavior was significantly different from that of the higher-frequency components, suggesting a different substitutional mechanism for H in coesite at higher pressures. Koch-Müller et al. (2003) also reported the first FTIR spectrum of a natural OH-

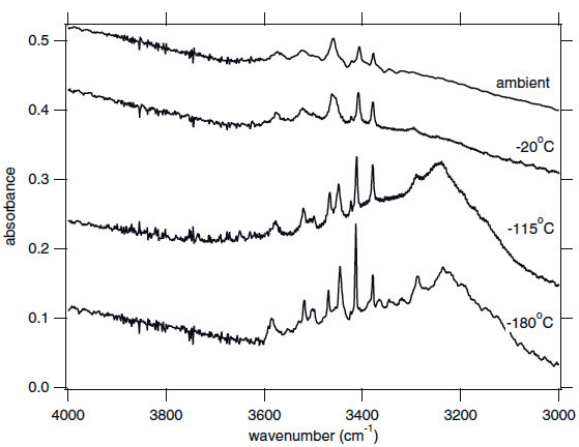


Figure 8. Unpolarized IR spectra of coesite collected at different temperatures. The broad band centered near 3200 cm^{-1} is from ice condensation in the stage. From Koch-Müller et al. (2003).

EBSCOhost - printed on 2/13/2023 5:26 AM via . All use subject to https://www.ebsco.com/terms-of-use

bearing coesite occurring as an inclusion within a diamond from Venezuela. The FTIR spectrum of the omphacitic pyroxene associated with coesite in the diamond also showed OH-bands.

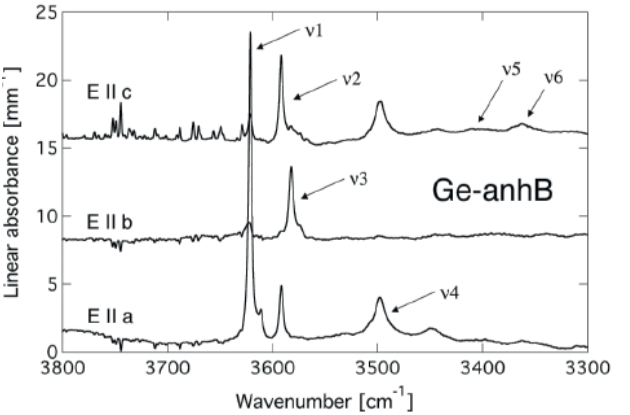


Figure 9. Polarized SR-FTIR spectra of Ge anhydrous phase B showing the strong pleochroism of the OH bands. From Thomas et al. (2008).

Thomas et al. (2008) studied the hydroxyl solubility in synthetic Ge analogues of the high-pressure silicates ringwoodite, anhydrous phase B and superhydrous phase B. Ge-ringwoodite was found to contain up to 2200 ppm H_2O, the incorporation mechanism of which was found to be different from that of Si-ringwoodite. Polarized experiments on oriented slices yielded from 2400 to 5300 ppm H_2O in Ge-anhydrous phase B. Single-crystal X-ray and polarized IR measurements (Fig. 9) on oriented crystal sections showed that two mechanisms could be responsible for the incorporation of OH into this phase, i.e., the hydrogarnet substitution and the creation of vacant Mg sites (Fig. 10). The findings of Thomas et al. (2008) however implied that the use of germanates as analogues for high-pressure silicates in experimental studies was probably not recommended for anhydrous phases, since their behavior with respect the water incorporation was probably different from the Si-counterparts.

Thomas et al. (2009) calibrated specific absorption coefficient for synthetic olivines, SiO_2 polymorphs and rutile-type GeO_2 combining FTIR, proton-proton scattering, Raman microspectroscopy and SIMS. One interesting conclusion of their work was that for SiO_2 phases the absorption coefficient is not related with the vibration frequency of the OH point defect, but with the structure type. A mean ε_i = 89,000 ±15,000 L mol H_2O cm^{-2} could be determined for a suite of quartz samples with varying OH defects, while much higher values were obtained for the denser polymorphs coesite and stishovite (Fig. 11). According to the work of Thomas et al. (2009) the negative correlation between the absorption coefficient and the OH band position (Paterson 1982; Libowitzky and Rossman 1997) does not hold for NAMs, thus for quantitative purposes specific coefficients must be independently calibrated. This point

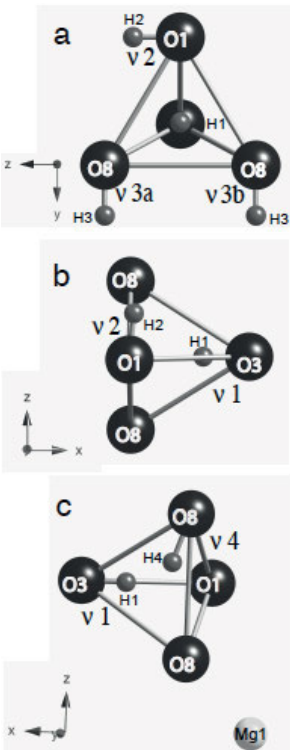


Figure 10. Orientation of the different OH groups in Ge-anhB modeled on the basis of the polarized FTIR spectra. From Thomas et al. (2008).

EBSCOhost - printed on 2/13/2023 5:26 AM via . All use subject to https://www.ebsco.com/terms-of-use

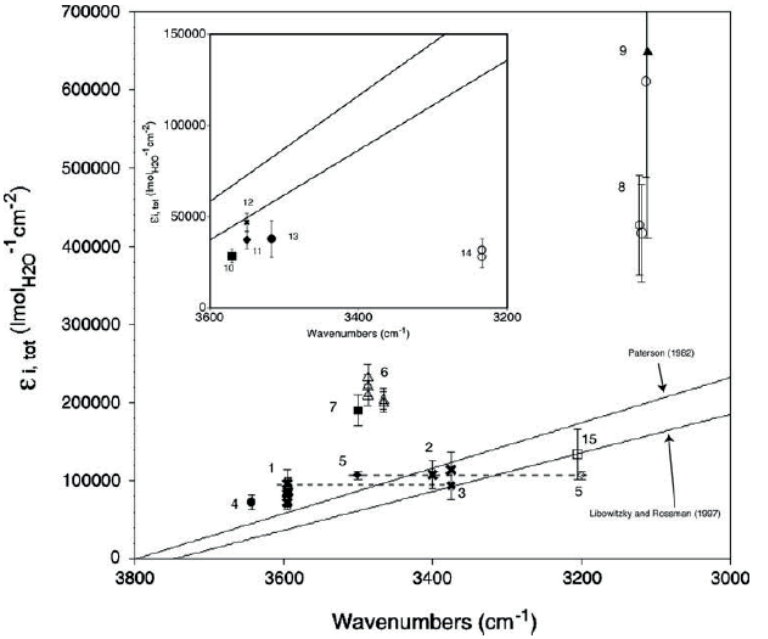


Figure 11. Absorption coefficients of doped quartz (1, 2), natural quartz (3), quartz glass (4), feldspar (5), coesite (6, 7), stishovite (8, 9) and r-GeO_2 (15) plotted onto the Paterson (1982) and Libowitzky and Rossman (1997) diagrams. The inset gives a magnified section of the 3,600-3,500 cm^{-1} region with different olivine data. [Used with kind permission of Springer Science and Business Media, from Thomas et al. (2009), *Phys Chem Miner*, Vol. 36, Fig. 11, p. 502].

is particularly crucial when the estimation of the water content of high-pressure minerals is used for geophysical modeling. Thomas et al. (2009) also present a routine to quantify water contents in NAMs based on Raman spectroscopy. An improved version of the routine with respect to the correction procedure to use in case of minerals containing heavy atoms is described in Mrosko et al. (2011).

The superior lateral resolution of SR-FTIR with respect the Globar source was exploited by Feenstra et al. (2009) to examine the zoning of hydrogen in zinc-bearing staurolite from a high-*P*, low-*T* occurrence from Samos (Greece). SIMS data showed higher hydrogen concentrations in crystal cores compared to rims, the OH content being negatively correlated with Al. The same kind of zonation was obtained using SR-FTIR on slices cut out from the crystals using a FIB. Interestingly, Feenstra et al. (2009) found that the absolute H concentration derived by FTIR were systematically lower to those derived by SIMS by about 25%. They interpreted this feature as due to a water loss at the crystal surface during FIB machining.

Piccinini et al. (2006a,b) examined the polarization behavior of the OH-stretching band of phlogopites by tilting the mica flake under the polarized SR beam. They observed a strong decrease of the absorbance intensity as a function of the angle between the (001) cleavage plane and the IR beam (Fig. 12).

SR-FTIR spectroscopy for the analysis of extraterrestrial materials, such as interplanetary dust particles (IDPs) was aimed at defining the global mineralogy of the samples, for example the presence of silicates vs. carbonates or phyllosilicates. In these studies the use of synchrotron radiation was needed because of the extremely small dimension of these samples, typically 5-10

EBSCOhost - printed on 2/13/2023 5:26 AM via . All use subject to https://www.ebsco.com/terms-of-use

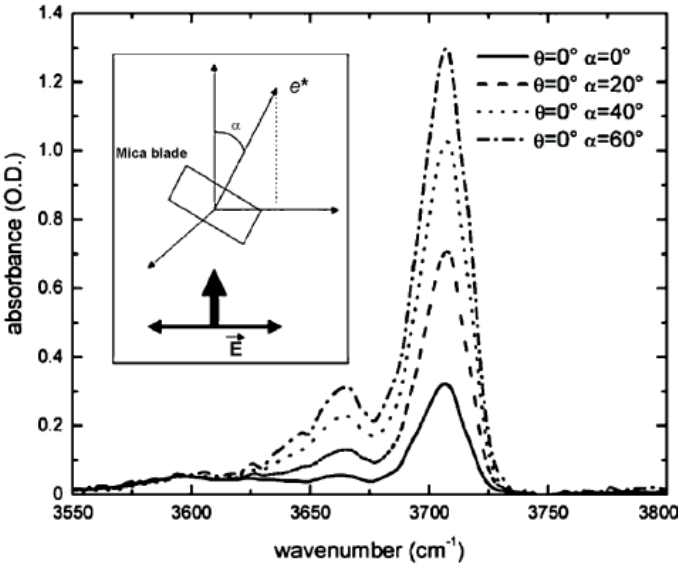


Figure 12. Polarized-light SR-IR spectra of natural phlogopite in the OH-stretching region collected by rotating the sample with respect the electric vector (see inset). [Used by permission of Elsevier, from Piccinini et al. (2006b), *Vib Spectrosc*, Vol. 42, Fig. 3, p. 60].

μm in size. Most SR-FTIR studies were however devoted to the capability of IR in detecting light-elements molecular arrangements such as OH/H_2O or C-H groups in the specimen. Flynn et al. (2002, 2004) reported for the first time the evidence for the presence of aliphatic hydrocarbons and of a ketone group in IDPs, by detecting CH_2, CH_3 and C=O functional groups in acid-etched particles, while Matrajt et al. (2005) measured the CH_2/CH_3 ratio in several IDPs and compared it to the CH_2/CH_3 ratio in diffuse interstellar medium (DISM). Flynn et al. (2004) found that IDPs may be composed by a significant fraction (up to 90%) of organic components, leading to estimate that, in the current era interplanetary dust contributes ~15 tons/year of unpyrolized organic matter to the surface of the Earth, and that during the first 0.6 billion years of Earth's history, this contribution is likely to have been much greater.

Probably the most common use of SR-FTIR in mineral sciences has been for high-*P* studies with a DAC; these studies were aimed at examining behavior and stability of important rock-forming minerals at high pressure and studying phase transitions of minerals as a function of pressure. For these researches SR is particularly useful for its brilliance in the far-IR region. Koch-Müller et al. (2005) showed that superhydrous phase B, one of the candidate minerals to occur in the Earth's mantle, exists in two polymorphic forms. The OH-spectrum of the lower-*T* phase, with space group *Pnn*2, consists of two well-defined bands, while the OH-spectrum of the higher-*T* phase, with space group *Pnnm*, consists of a single broad band. The band shifts as a function of pressure in the MIR and FIR regions indicated the HT polymorph to be more compressible than the lower symmetry, LT polymorph. The thermodynamic properties of chloritoid were derived by Koch-Müller et al. (2002) from detailed band assignment in the powder IR spectra and based on the pressure dependence of bands in the MIR and FIR spectral range. Scott et al. (2007) collected high-pressure spectra of lawsonite in the NIR region up to 25 GPa to constrain the Grüneisen parameters and the vibrational density of states under pressure. Pressure-induced FIR mode shifts were consistent with phase transitions at 4 and 8.6 GPa, respectively, in accordance with previous MIR, Raman, and X-ray studies. The 8.6 GPa

EBSCOhost - printed on 2/13/2023 5:26 AM via . All use subject to https://www.ebsco.com/terms-of-use

transition, in particular, could be clearly identified by abrupt slope changes and the appearance of a new feature in the spectrum near 368 cm^{-1}. High-pressure infrared spectra of talc were collected (Scott et al. 2007) up to 30 GPa in the whole 150 to 3800 cm^{-1} range (Fig. 13). Significant changes in relative intensities were observed in the FIR region. The pressure shift of the hydroxyl vibration of talc was non-linear with a faster rate at higher pressures, the average pressure shift being close to 2.1 cm^{-1}/GPa. The ambient pressure spectrum was fully reproduced upon decompression for both minerals, implying that all pressure-induced structural changes are reversible. This being the case, both minerals could metastably transport water to depths in the Earth corresponding to pressure well beyond the known thermodynamic decomposition conditions for these phases. HP spectra presented by Liu et al. (2003) showed that the crystal structures of both OH-chondrodite and OH-clinohumite were preserved up to 38 and 29 GPa, respectively. Broadening of the absorption bands suggested however increasing disordering of the silicate framework at high pressure (Fig. 14). For both minerals, three bands are observed in the OH-stretching region at ambient conditions. For increasing pressure all bands shift linearly to higher frequency; above 18 GPa, the slopes for the three OH bands are significantly different as a result of different degrees of hydrogen bonding.

Koch-Müller et al. (2011) performed high-pressure SR-FTIR measurements of synthetic hydrous ringwoodite $(Mg_xFe_{1-x})SiO_4$ with x = 0.00 to 0.61, using three different pressure

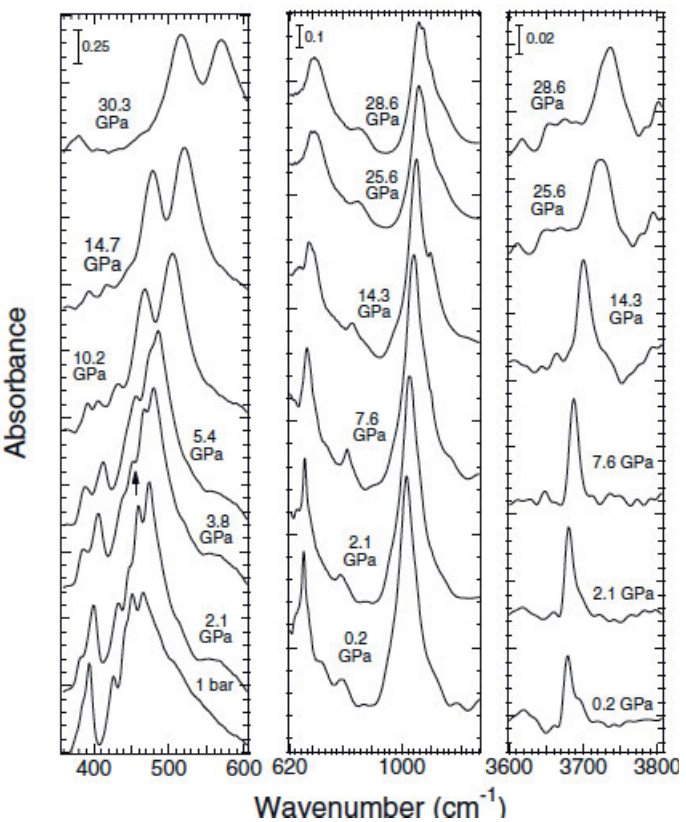


Figure 13. High-pressure SR-IR spectra of talc. Note that the ambient *P* spectrum is fully reproduced upon decompression. After Scott et al. (2007).

EBSCOhost - printed on 2/13/2023 5:26 AM via . All use subject to https://www.ebsco.com/terms-of-use

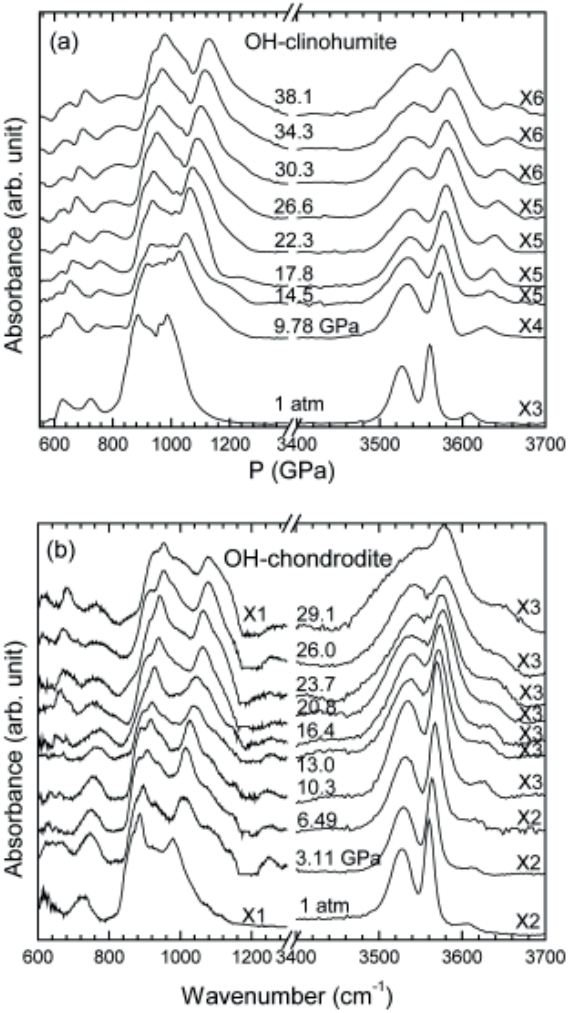


Figure 14. SR-FTIR OH-spectra of clinohumite (a) and chondrodite (b) at increasing pressure. After Liu et al. (2003).

-transmitting media. All samples loaded with CsI powder or liquid argon showed a sudden disappearance of the OH bands and discontinuities in the pressure shift of the lattice modes between 10 and 12 GPa. When using liquid argon annealed at 120 °C and 8.6 GPa as a pressure medium for the same samples, the OH bands and the lattice vibrations could be observed linearly shifting up to 30 GPa. The disappearance of the OH bands for non-hydrostatic conditions was interpreted as due to a stress-induced proton disordering in ringwoodite (Koch-Müller et al. 2011).

Iezzi et al. (2006) examined the high-pressure behavior of synthetic amphibole Na(NaMg) $Mg_5Si_8O_{22}(OH)_2$. The data showed a $P2_1/m \leftrightarrow C2/m$ phase-transition at 20-22 GPa (Fig. 15). Upon release of pressure, the room-pressure pattern is immediately recovered indicating that the pressure-induced phase-transition is reversible. By analogy with structurally related pyroxenes, Iezzi et al. (2006) suggested the existence of a new *C*2/*m* amphibole polymorph

EBSCOhost - printed on 2/13/2023 5:26 AM via . All use subject to https://www.ebsco.com/terms-of-use

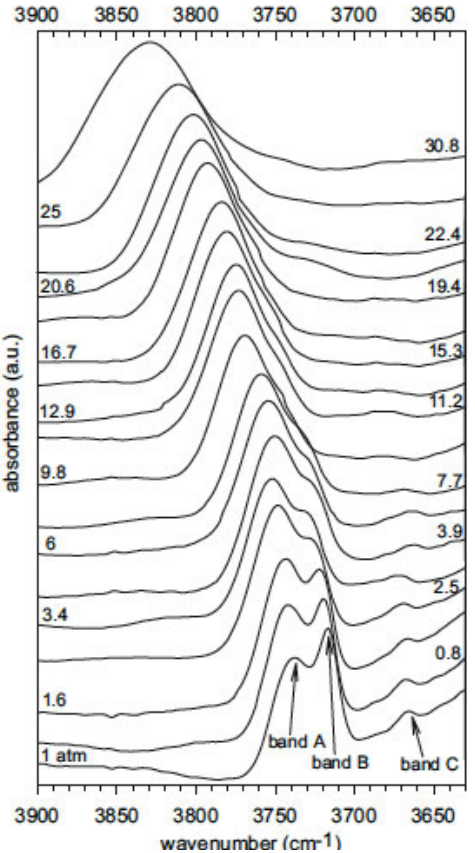


Figure 15. SR-IR high-pressure OH-spectra of synthetic amphibole $Na(NaMg)Mg_5Si_8O_{22}(OH)_2$. After Iezzi et al. (2006).

stable at high pressure and characterized by fully kinked double-chains. The high-pressure behavior of amphiboles in the same system, but with increasing Li for Na substitution at the B-sites was studied by Iezzi et al. (2009) who found that the pressure at which the $P2_1/m$ to $C2/m$ phase transition occurs was linearly correlated to the aggregate B-site dimension.

The pressure-dependent behavior of strontium feldspar and wadsleyite was studied up to 24 GPa by Mrosko et al. (2011). Polarized measurements yielded 1100 ppm and 12500 ppm of water, respectively for these two minerals. A new microscope was developed for high-P measurement in the THz/FIR range. A $I2/c$ to $P2_1/c$ phase transition was detected at 6.5 GPa for strontium feldspar, while a transition at 8.4 and 10.0 GPa was observed for hydrous and dry wadsleyite, respectively. These results highlighted that the presence of water in NAMs may have a significant effect on their transition behavior with pressure. More recently, Noguchi et al. (2012) studied the pressure-induced amorphization of antigorite. They observed an anomalous behavior of the bands due to the outer OH groups with respect to the bands due to the inner OH groups upon compression. Amorphization of the sample was observed for conditions in excess of 300 °C and 25.6 GPa; interestingly, the spectra indicated that OH groups were still retained in the amorphized material.

EBSCOhost - printed on 2/13/2023 5:26 AM via . All use subject to https://www.ebsco.com/terms-of-use

Synchrotron infrared microspectroscopy has made in the recent years considerable impact in archaeology, archeometry and in the study of cultural heritage materials because of its capability as a reliable and non-destructive analytical tool. The most important results are related to the study of ancient painting materials (Salvadó et al. 2005), which are typically multi-layered and structurally heterogeneous, consisting of various fine-grained mixtures of mineral pigments and binding media. *In situ* characterization of the various components in these materials is essential to extract information on the techniques used in their manufacture, the origin of the materials used, and to design appropriate restoration procedures. A combination of X-ray diffraction/absorption, Raman spectroscopy and SR-FTIR spectroscopy has provided considerable advancements in these studies. Notable investigations involved the analysis of frescos in the Acireale (Sicily) cathedral (Barilaro et al. 2005), Romanesque wall paintings from Spain (Salvadó et al. 2008), the characterization of prehistoric polished serpentinite artefacts (Bernardini et al. 2011) and the study of the alteration of silver foils in medieval painting from Museums in Spain (Salvadó et al. 2011).

FTIR IMAGING

Introduction

There are essentially three possible experimental set-ups in FTIR microscopy: (1) point detector analysis in a confocal layout, (2) FTIR *mapping* done by integrating the signal from successive locations of the specimen surface, (3) FTIR *imaging*, performed with bi-dimensional arrays such as focal plane array (FPA) detectors. The main advantage of observing an entire field of view at the same time allows spatially resolved spectroscopy of large and multi-phase samples (like polycrystalline rocks), or monitoring dynamic processes in real time.

The single spot analysis can be performed both in transmission and reflection mode. The beam size typically ranges from 100 μm to 30 μm using a conventional source, and, as discussed above, can be reduced down to 3-5 μm using a synchrotron radiation source. To characterize the spatial distribution of an absorber across a sample, a standard practice is to isolate a small area of interest using apertures placed before or after (or both) the sample, and then collect several spectra along traverses. Guilhaumou et al. (1998) presented the first application of this technique using SR-FTIR microscopy to monitor the evolution of the OH peak with a small aperture, and follow the OH diffusion profile across a pyroxene single crystal experimentally treated by Ingrin et al. (1995). More recent applications of the single spot analysis have been published by Castro et al. (2008) and Feenstra et al. (2009, reviewed above). Castro et al. (2008) measured water concentration profiles around spherulites in obsidian using synchrotron radiation with a spot size of 2 μm. The distribution of OH groups surrounding the spherulites was found to reflect the expulsion of water during crystallization of an anhydrous mineral assemblage replacing the spherulite glass. The concentration profiles were found to be controlled by a balance between the growth rate of the spherulites and the diffusivity of H throughout the rhyolitic melt, thus allowing determination of the kinetics of the spherulite growth.

In the FTIR mapping mode one measures the infrared spectrum at each in-plane point and then uses peak heights, peak areas, the integer performed in a defined spectral region or other criteria to visualize the distribution of the target molecule. This experimental set-up can be coupled to a confocal-like set-up (Minsky 1988) to achieve a high statistic and a high SNR. However, the method involves collecting a large number of single spectra and an accurate motion of the sample on the stage, thus resulting in extremely long acquisition time, up to several hours, to collect data from large areas, say few mm.

In the FPA imaging mode, one obtains the whole image in a single data collection thanks to a multichannel detection similar to the concept of recording images with charge-coupled

EBSCOhost - printed on 2/13/2023 5:26 AM via . All use subject to https://www.ebsco.com/terms-of-use

devices (CCDs) in optical microscopy. The number of pixels (the detectors) and their effective size will depend on the FPA type. Typical arrays, designed for conventional sources, range from the 64×64 channels, providing 4096 individual spectra, to 256×256 or 1024×1024 channels allowing imaging of large areas. These are however not optimized to match a synchrotron radiation source that, because of its brilliance, may illuminate only a limited portion of these bidimensional detectors (Petibois et al. 2010a,b). Such arrays are typically coupled with 15× or 36× objectives, so that with a single image up to few square mm, a single pixel corresponds to a physical dimension in the range 2.5 to 5 μm.

Among the most recent attempt to push forward the imaging capability using synchrotron radiation, we can cite the IRENI beamline at SRS (Madison, USA) that collects 320 hor. × 25 vert. $mrad^2$ of IR radiation from a dedicated bending magnet. The main goal of this project is to reduce the acquisition times of IR maps by using an FPA illuminated by several beams coming from multiple optical systems. The incoming radiation is separated in 12 beams and rearranged into a 3×4 beam bundle with the help of a total of 48 mirrors and is then sent into an IR microscope equipped with a 128×128 pixels FPA (Nasse et al. 2011). Due to the use of multiple brilliant synchrotron beams and image reconstruction methods based on Fourier-based deconvolutions, this optical system could provide a very high spatial resolution at the diffraction limit for all wavelengths, a very short acquisition time and a high SNR.

H-C-O functional groups are characterized by highly polar bonds and absorb infrared radiation with a high efficiency, therefore FTIR micro-spectroscopy coupled with imaging possibilities may be used to qualitatively and quantitatively measure these molecular arrangements in geological materials (both minerals and glasses) with a high-spatial resolution (Pironon et al. 2001; Della Ventura et al. 2010). Although FTIR imaging has rapidly evolving as a tool in biological and biochemical sciences (Dumas and Miller 2003; Burattini et al. 2007; Heraud et al. 2007; Petibois et al. 2009, 2010a,b), very few applications have so far been published in Earth Sciences (Della Ventura et al. 2010). We will review in the following the available data.

The distribution of H and C in minerals

High-pressure nominally anhydrous minerals contain trace hydrous species (see the paragraph above and reviews of Skogby 2006 and Beran and Libowitzky 2006). However, recent studies have shown that structural hydrous species, such as OH, H_2O and CO_2 can also be incorporated in most nominally anhydrous low-pressure minerals in the crust (Johnson 2006; Della Ventura et al. 2008a,b; Bellatreccia et al. 2009 among the others). It follows that careful analysis of trace volatile species in these minerals may provide qualitative but also quantitative information on topics such as water and CO_2 activity, oxygen fugacity and fluid composition in the mineralizing system. In particular, the analysis of volatile traces in volcanic materials, both minerals and glasses, may provide significant constraints on the genesis and evolution of magmatic systems (De Vivo et al. 2005).

The analysis of water in minerals (Libowitzky and Rossman 1996; Aubaud et al. 2007) and glasses (Ihinger et al. 1994; Di Matteo et al. 2004; Aubaud et al. 2007) using FTIR spectrometry is now a relatively routine technique. On the contrary, the spectroscopic analysis of CO_2 is common in glasses (e.g., King et al. 2002; Behrens et al. 2004; Morizet et al. 2010), while rare tests have been made for fluid inclusions within minerals (Linnen et al. 2004). Work on minerals has been so far restricted on few cases: beryl and cordierite (Wood and Nassau 1967; Armbruster and Bloss 1980; Kolesov and Geiger 2000; Khomenko and Langer 2005; Della Ventura et al. 2009, 2012), feldspathoid minerals (Della Ventura et al. 2005, 2007, 2008a; Bellatreccia et al. 2009; Balassone et al. 2012), phyllosilicate minerals (Zhang et al. 2005) and some particular forms of hydrous silica (Kolesov and Geiger 2003; Viti and Gemmi 2009).

An issue of extreme interest regarding volcanic materials is the distribution of the volatile constituent across the crystal, which can provide insight into the evolution of the crys-

EBSCOhost - printed on 2/13/2023 5:26 AM via . All use subject to https://www.ebsco.com/terms-of-use

tallizing system with time; such possibility is now offered by modern FTIR imaging systems. Della Ventura et al. (2007) studied the carbon speciation and distribution across vishnevite, a microporous mineral belonging to the cancrinite-sodalite group of feldspathoids, with ideal formula $[Na_6(SO_4)][Na_2(H_2O)_2](Si_6Al_6O_{24})$. This mineral is structurally characterized by open channels and columns of cages extending along the crystallographic *c*-axis, where a variety of extra-framework cations and anionic groups may be hosted (Bonaccorsi and Merlino 2005). Infrared spectra show that most samples, and in particular the specimens from the holotype locality at Vishnevye Mts. (Urals), contain molecular CO_2 as main carbon species in the structural pores, while few others were found to be CO_3-rich. Moreover, polarized-light measurements (Della Ventura et al. 2007) show that the linear CO_2 molecules are oriented perpendicular to the crystallographic ***c*** axis in these minerals. Several single crystals from Latium (Italy) were found to be optically zoned, from milky-white to transparent. One of these crystals, 200×100×100 μm was manually extracted from the host-rock and examined using an FTIR microscope equipped with a mapping stage and a single element MCT detector. The data were collected using a square aperture of 30×30 μm^2. Figure 16 shows a surprising change in the carbon speciation during the crystal growth: the side attached to the host rock (milky-white) is CO_3-free while being rich in CO_2, whereas the opposite is observed for the transparent rim of the crystal. The reason for the observed phenomenon is not clear at the present, however the extreme zonation of Figure 16 is clearly connected with a major change in the physical conditions during the mineral crystallization.

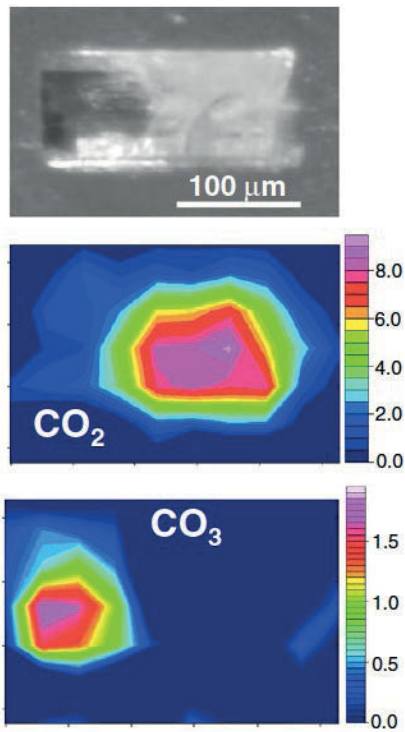


Figure 16. (*top*) optical micrograph of the vishnevite crystal studied. Note that the specimen is not a polished section, but a prismatic euhedral hexagonal single crystal manually extracted from the rock; the terminal pinacoid of the crystal is on the left side of the picture. (*middle*) and (*bottom*) FTIR mappings of the CO_2 and the CO_3 distribution across the specimen. The color intensity from blue to red is proportional to the content of the target molecule. [Used by permission of Elsevier, from Della Ventura et al. (2010), *Anal Bioanal Chem*, Vol. 397, Fig. 1, p. 2043].

Della Ventura et al (2008b) studied a set of carefully selected, transparent leucite crystals, free from any evidence of analcime alteration from the Alban Hills volcano (Rome, Italy). The purity of the specimens was checked by SEM-EDAX microanalyses across the grains, which showed Na contents systematically < 1.0 wt%. FTIR microanalyses showed for most crystals a well-defined and rather broad absorption in the H_2O stretching 3000-4000 cm^{-1} region (Fig. 17a), consisting of three components centered at 3604, 3500 and 3245 cm^{-1}, respectively. FTIR mapping under conventional light showed some crystals to be homogeneously hydrated (Fig. 17b) with H_2O contents up to 1600 ppm. Other samples showed an extremely zoned H_2O distribution (Fig. 17c) consisting of a completely anhydrous core with a hydrous rim containing significant (~1200 ppm) homogeneously distributed water. High-resolution mapping (Fig. 17d) showed a sharp rim/core transition suggesting a sudden change in the magmatic conditions during the crystal growth.

EBSCOhost - printed on 2/13/2023 5:26 AM via . All use subject to https://www.ebsco.com/terms-of-use

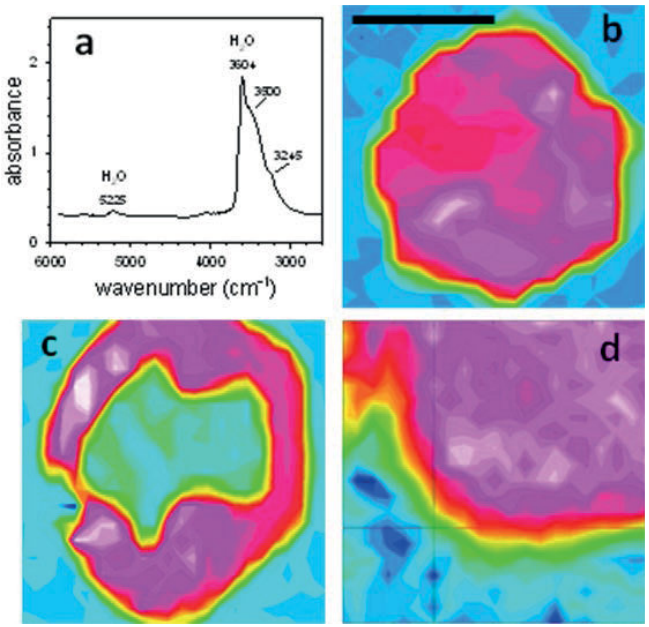


Figure 17. (a) FTIR spectrum of leucite in the NIR range. (b) homogeneous distribution of H_2O across sample L131 from Tre Fontane (Rome). (c) zoning of H_2O in sample LCQM2 from Quarto Miglio (Rome) showing a well-defined anhydrous core surrounded by an homogeneously hydrated rim. (d) high resolution mapping across the core-to-rim boundary for the same sample as in (c). The scale bar in (b) is 2 mm. The color intensity from blue to red is proportional to the content of the target molecule. [Used by permission of Elsevier, from Della Ventura et al. (2010), *Anal Bioanal Chem*, Vol. 397, Fig. 2, p. 2044].

Bellatreccia et al (2009) and Balassone et al. (2012) studied a large set of sodalite-haüyne group minerals, from a wide variety of geological occurrences. Unpolarized spectra showed intense and multi-component absorptions in the H_2O stretching (4000-3000 cm^{-1}) region and, in most cases, a very sharp and intense band at 2351 cm^{-1} indicating the presence of CO_2 molecules in the studied samples (Della Ventura et al. 2005, 2007, 2008a; Bonelli et al. 2000; Miliani et al. 2008). According with the systematic work of Bellatreccia et al (2009), sulfatic members in the group (haüyne and nosean) are typically CO_2-rich, while chlorine-rich members (sodalite) are systematically CO_2-free. FTIR maps collected by Bellatreccia et al. (2009) and Balassone et al. (2012) (Fig. 18) showed a non-homogeneous distribution correlated to micro-fractures across the crystal; interestingly, the amount of CO_2 was inversely correlated to that of H_2O (Fig. 18).

The distribution of H and C across cordierite was examined by Della Ventura et al. (2009, 2012). Figure 19b shows a strongly zoned distribution of the H_2O signal across a sample from a granulitic enclave within the dacitic lava dome of El Hoyazo (SE Spain), which contrasts with the relatively homogeneous distribution of CO_2 in the same section (Fig. 19a). FPA images (Fig. 19c-d) shows that most of the intensity in the 3700-3400 cm^{-1} region is associated with micro-fractures within the cordierite, where secondary alteration products are present. Noteworthy, the FPA images of Figure 19e-f show that acicular sillimanite crystals enclosed within the cordierite host are occasionally hydrated. The image of Figure 19e-f provides a direct proof that using an FPA detector, at these wavelengths (2-3 μm), the spatial resolution is few μm, i.e., close to the diffraction limit. Similar results were obtained by Della Ventura et al. (2012) on samples from different localities.

EBSCOhost - printed on 2/13/2023 5:26 AM via . All use subject to https://www.ebsco.com/terms-of-use

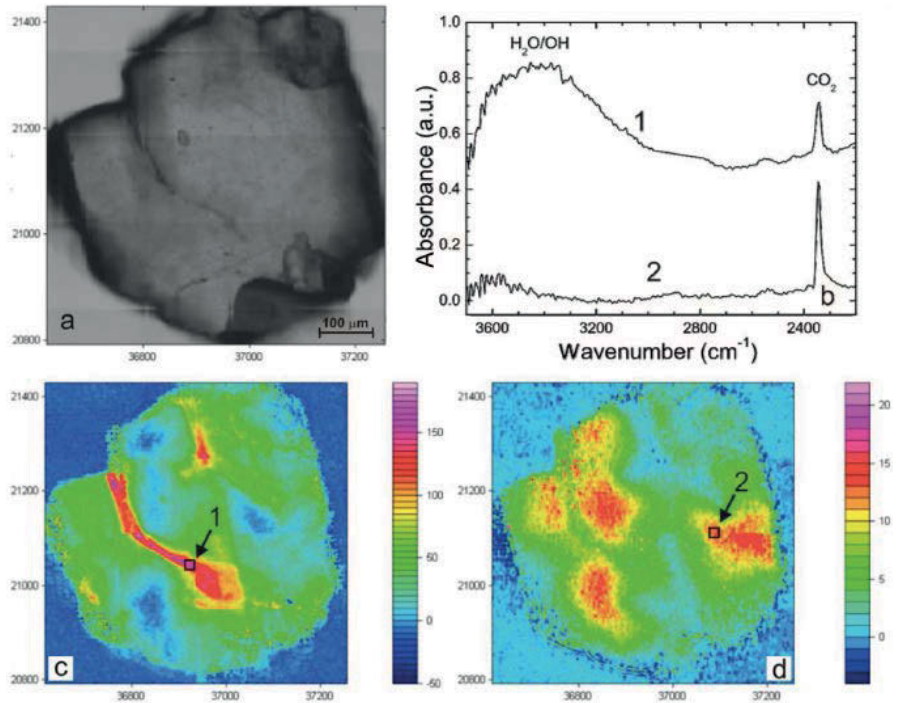


Figure 18. Distribution of H_2O and CO_2 in haüyine from Somma-Vesuvius; (a) optical image of the examined crystal, (b) selected FTIR spectra at points 1 and 2 in the (c) H_2O and (d) CO_2 images. Note that images in (c) and (d) are the result of 4×4 matrix of 170×170 μm FPA images. [Used by permission of Mineralogical Society, from Balassone et al. (2012), *Mineral Mag*, Vol. 76, Fig. 9, p. 206].

Imaging of inclusions in minerals

Crystals may contain tiny, generally micrometric-sized and variable shaped impurity parcels within their cavities or fractures. Parcels of liquid ± vapor ± solid are known as fluid inclusions (e.g., Roedder 1984); analogously melt inclusions are droplets of glass ± vesicles ± solid (e.g., Sobolev 1996; Frezzotti 2001). Fluid inclusion studies are largely applied (Andersen and Neumann 2001) in order to define the role of fluids on the genesis and deformational processes in mantle and crustal rocks. They also allow constraining models on the genesis of ore deposits and providing information for the geothermal and petroleum explorations and production industry (McLimans 1987; Guilhamou et al 1998, 2000).

Melt inclusions are considered samples of melt that were trapped within crystals as they grew from the magma (Lowenstern 1995; Sobolev 1996, Frezzotti 2001; Danyushevsky et al 2002). Depending on favorable conditions (absence of crystallization, alteration and re-melting processes), melt inclusions preserve the composition of the melt in thermodynamic equilibrium with their host minerals. Therefore, the content of dissolved H_2O-CO_2 in the inclusions provides information related to the entrapment pressure and to the volatile budget of the magma, with implication from magma genesis and crustal storage to magma rheology and to eruptive dynamics.

Due to their typically small size, inclusions in minerals are studied using Raman spectroscopy, a technique that allows analyzing areas as small as 0.5-1 μm^2. The increasing availability of synchrotron-radiation FTIR facilities and the development of FTIR imaging

EBSCOhost - printed on 2/13/2023 5:26 AM via . All use subject to https://www.ebsco.com/terms-of-use

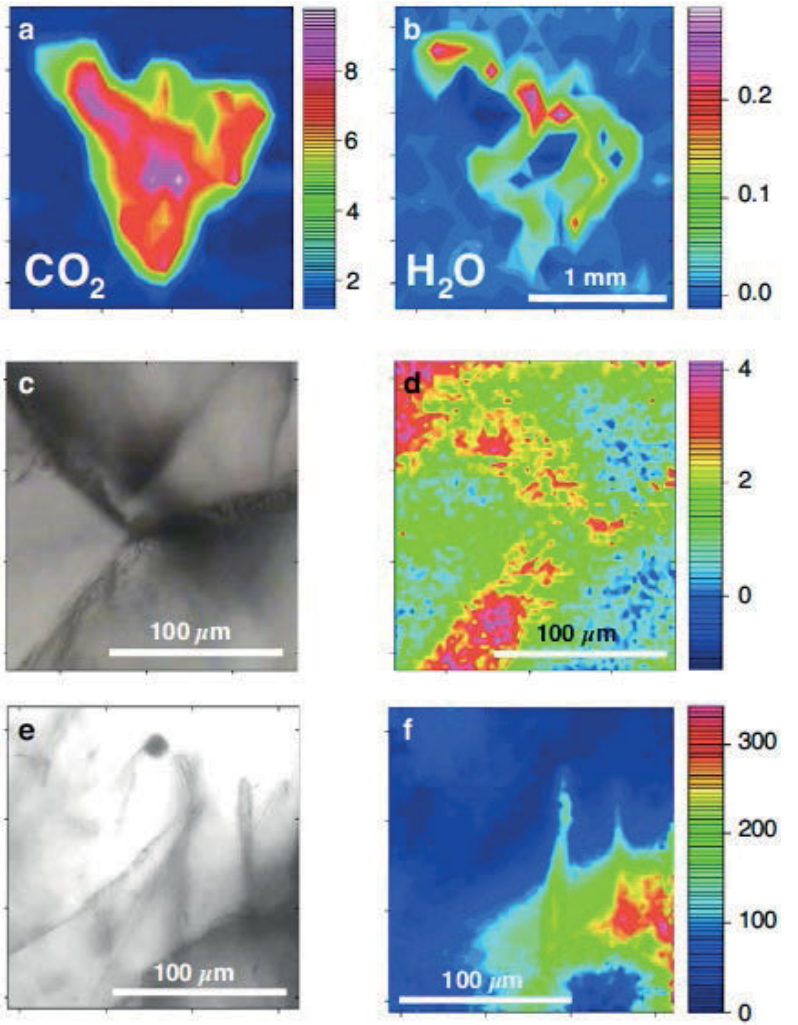


Figure 19. (a) and (b) FTIR mapping of CO_2 and H_2O on a (010) oriented crystal section of cordierite from El Hoyazo, Spain, of thickness 140 μm. (c) to (f) FTIR FPA images of the H_2O distribution in the same section; the optical image is on the left side, the corresponding FTIR image is on the right side. The image in (d) shows how the water content of this sample is associated with fractures and is probably related to alteration products, whereas the image in (f) shows that water is also associated with sillimanite needles included in the host cordierite matrix. [Used by permission of Elsevier, from Della Ventura et al. (2010), *Anal Bioanal Chem*, Vol. 397, Fig. 4, p. 2046].

techniques under both synchrotron and conventional light, now allow extending the application of infrared spectroscopy to the study of this particular type of geological samples.

As said above, probably the first FTIR images of hydrocarbon-rich fluid inclusions within geological samples were those of Guilhamou et al. (1998, 2000) showing the presence of H_2O, CO_2 and aliphatic molecules in their samples. Wysoczanski and Tani (2006) examined the water content distribution in silicic volcanic glasses and related melt inclusions from Sumisu Caldera and Torishima Volcano in the Izu Bonin Arc (Japan). They found that H_2O measurements done

EBSCOhost - printed on 2/13/2023 5:26 AM via . All use subject to https://www.ebsco.com/terms-of-use

with the FPA had a precision comparable to that obtained on the same locations with single-spot analyses. Similar water contents were analyzed in both the groundmass glasses and melt inclusions within honeycomb plagioclase, indicating that the inclusions underwent water loss by degassing and/or diffusion (Wysoczanski and Tani 2006).

Detailed SR-FTIR maps were collected in the water stretching region by Seaman et al. (2006) using 10×10 to 15×15 μm^2 aperture size and displacing the sample by steps smaller than the aperture across anorthoclase megacrysts and enclosed melt parcels. Based on polarized measurements on three orthogonal sections, a water content of 126 ppm was obtained for the anorthoclase. Absence of a band at 1630 cm^{-1} pointed to the presence of OH groups only in the inclusion's melt, in concentrations from 0.12 to 0.39 wt%, one order of magnitude higher than the crystal host. FTIR maps showed zones of elevated water concentration at the crystal-melt inclusion boundary (Fig. 20) suggesting that water probably diffused from the inclusion into the crystal (Seaman et al. 2006).

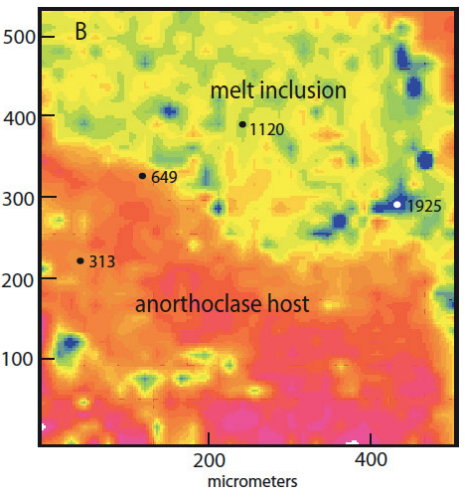


Figure 20. FTIR map in the water region across a melt inclusion/host anorthoclase crystal boundary. There is an approximately 50 μm wide zone of gradational water concentrations on the edge of the anorthoclase crystal, likely due to diffusion of water into the crystal from the melt inclusion; water concentrations shown in parts per million. After Seaman et al. (2006).

Mormone et al. (2011) used FPA-FTIR imaging to characterize the content and distribution of C-H-O species in melt inclusions within olivines from the most primitive rocks erupted at Procida island, Phlegrean Volcanic District (Naples, Italy). Optical and SEM microscopy showed the inclusion to be mostly glassy, with few being partly to almost totally crystallized. FPA images of a sample containing only molecular CO_2 revealed the inclusion core to be water- and CO_2-free (Fig. 21). SEM data showed that the apparently homogeneous core actually was partly crystallized (thus accounting for the absence of H_2O and CO_2) and contained several nanometer-sized crystals (possibly clinopyroxene) and bubbles. The resolution of the FPA (~3-5 μm in the H_2O stretching region) was unable to resolve the glass interspersed with the crystals, however some red pixels (Fig. 21) documented the presence of local enrichments in molecular CO_2, corresponding to proto-bubbles of size comparable to the FPA image resolution. The spectra showed a doubled band in the 1400-1500 cm^{-1} region, typical of CO_3 groups dissolved in the glass (Dixon and Pan 1995), and a doubled peak at 2349-2361 cm^{-1} typical of gaseous CO_2 (Stolper and Ahrens 1987). H_2O contents in the range 0.80 to 1.72 wt% in the glassy inclusions, and up to 2.69 wt% in the partly crystallized ones, could be quantified using FPA-collected spectra. These latter inclusions also showed CO_2 contents up to 890 ppm. CO_3 contents up to 2653 and 1293 ppm were also found in the glassy and crystallized inclusion, respectively. The data allowed to recalculate entrapment pressures ranging from 350 MPa to less than 50 MPa, suggesting that the magma ascent was dominated by degassing (Mormone et al. 2011).

Figure 22a from Della Ventura et al. (2010) shows the distribution of H_2O in a melt inclusion entrapped within olivine phenocrysts from a scoria erupted at Stromboli (Sicily, Italy). The inclusion is relatively large (~100 μm across) but to perform the experiment the host

EBSCOhost - printed on 2/13/2023 5:26 AM via . All use subject to https://www.ebsco.com/terms-of-use

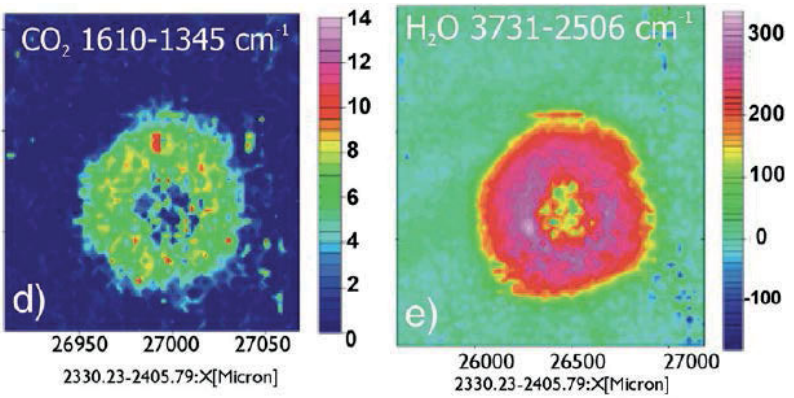


Figure 21. CO_2 (*left*) and H_2O (*right*) distribution (FTIR-FPA images) across a partially crystallized melt inclusion within a olivine host from the Phlegrean volcanic district (southern Italy). [Used by permission of Elsevier, modified from Mormone et al. (2011), *Chem Geol*, Vol. 287, Fig. 6, p. 74].

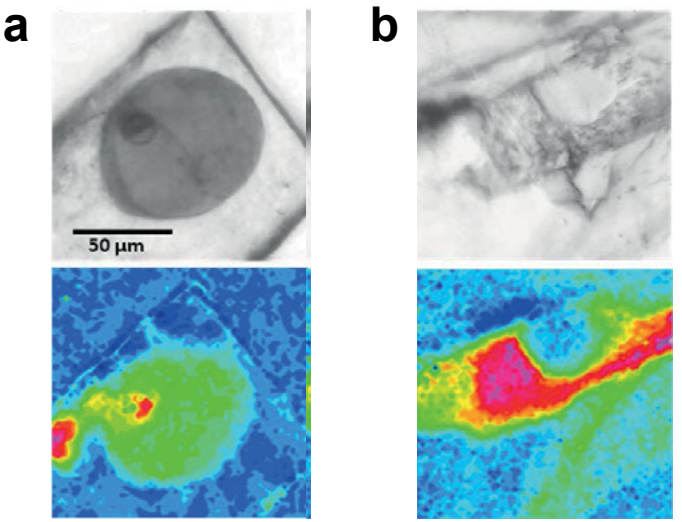


Figure 22. FTIR-FPA images (a) a melt inclusion within olivine from Stromboli (Italy) and (b) a solid inclusion within edenite from Franklin Furnace (USA). (*top*) optical images; (*bottom*) FTIR FPA images. The scale bar is 50 µm for all images. [Used by permission of Elsevier, modified from Della Ventura et al. (2010), *Anal Bioanal Chem*, Vol. 397, Fig. 5, p. 2047].

crystal has been doubly-polished to a thickness of ~30 µm, in such a way that the inclusion is completely exposed on both sides of the crystal slice, and the beam interact only with the parcel (Fig. 22, above) without contaminations from the host. The FTIR image (Fig. 22a, below) shows a roughly homogeneous distribution of water in the glass (note how the host olivine is anhydrous) and highlights the presence of a central volume with a higher water content (shrinkage bubble), probably derived from water saturation consequent to depressurization. Exsolved volatiles can generate internal overpressure that blows up the inclusion and allows gas escaping. The outer red area that appears to be linked to the inclusion in Figure 22a can represent the water outflow from the melt inclusion.

EBSCOhost - printed on 2/13/2023 5:26 AM via . All use subject to https://www.ebsco.com/terms-of-use

Figure 22b displays the case of a solid inclusion within a sample of F-rich edenite, $NaCa_2(Mg,Fe)_5(Si_7Al)O_{22}F_2$. The FTIR image shows the presence of a highly hydrated phase within the host F-edenite, which, on the basis of the IR signal in the OH-stretching region, can be identified as a layer silicate intermixed within the host double-chain silicate. The presence of such exsolutions may be common in this type of amphiboles, and reflect the narrow stability field of the amphibole with respect to the layer-silicate, which has similar chemistry and a very close local structure (Na et al. 1986). The FTIR image displayed in Figure 22b reveals a very interesting feature: while the host amphibole is F-rich, the associated layer-silicate is OH-rich, suggesting a strong preference of the hydroxyl component for the layer-silicate structure with respect to the edenite structure.

FTIR imaging of dynamic processes

As outlined above SR may open new opportunities in many research areas and in particular in time resolved imaging applications to investigate complex phenomena in real time. Actually, FTIR spectroscopy is an extremely powerful tool in high-temperature studies where exsolution of volatile species (such as dehydration) is involved (Aines and Rossman 1984; Prasad et al. 2005; Zhang et al. 2006; Bonaccorsi et al. 2007 among the others). Typically, single spot data are collected *in situ*, and the band intensity of H_2O/OH absorptions at each step during the heating experiment is plotted as a function of the varying temperature. In such a way, dehydration curves are obtained (e.g., Prasad et al. 2005; Zang et al. 2006; Bonaccorsi et al. 2007). In other cases, the absorbance is plotted as a function of time; in such a case, kinetic information on the dehydration process (Tokiwai and Nakashima 2010), or H diffusion mechanisms throughout the matrix (Ingrin et al. 1995; Stalder and Skogby 2003; Castro et al. 2008) are obtained.

Prechtel and Stalder (2010) synthesized pure enstatite at 6 GPa, 1250 °C under water-saturated conditions and variable silica activity. Polarized FTIR measurements showed a strong pleochroic behavior of the OH-bands. The intensity variation of the observed peaks as a function of the Si/Mg ratio in the system allowed assignment of the higher- and lower- energy band to tetrahedral (Si) and octahedral (Mg) defects, respectively. FPA images were used to characterize the evolution of the pyroxene chemistry during the crystal growth by monitoring (Fig. 23) the intensity evolution of the IR bands across the samples.

The possibility to collect *in situ* images of an area of the sample during high-temperature experiments provides a new way to monitor these complex processes. An example is given in Figure 24 from Della Ventura et al. (2010), where preliminary results obtained during dehydration experiments on leucite are displayed. Figure 24a shows the images collected along a continuous ramp where the crystal fragment was heated using at a constant rate of 5°/min using a Linkam T600 FTIR heating/freezing stage. FPA images were taken *in situ* during the experiment with a 64×64 array and a 15× objective at the nominal resolution of 16 cm^{-1} adding 32 scans. With this experimental set-up each image was collected in ~90 seconds. Although these conditions are still insufficient to study very fast reactions, they represent a clear advantage when compared to conventional spectroscopic data collection. Images refer to a crystal fragment of dimension of ~250×250 μm^2 and thickness 190 μm. The IR light illuminates only an edge of the fragment and the condenser of the microscope collects the light only from an area of ~170×170 μm^2, which is less than the overall size of the crystal. In this way it was possible to enhance the contrast of the water band at the edge of the section monitoring the hydration mechanism in real time. Selected images at constant temperature interval of ~100 °C (corresponding to ~20 min heating) show that the sample dehydrates smoothly, and that at ~400 °C it is almost anhydrous. In Figure 24b a second fragment of the same starting material has been heated abruptly (50°/min) up to 300 °C. Images show that when arrived at the target temperature, the sample has lost almost half of its initial water content. At constant T = 300 °C, the FPA images (taken at the same conditions as in Fig. 24a) show a continuous, although relatively slow, dehydration. After 150 minutes the

EBSCOhost - printed on 2/13/2023 5:26 AM via . All use subject to https://www.ebsco.com/terms-of-use

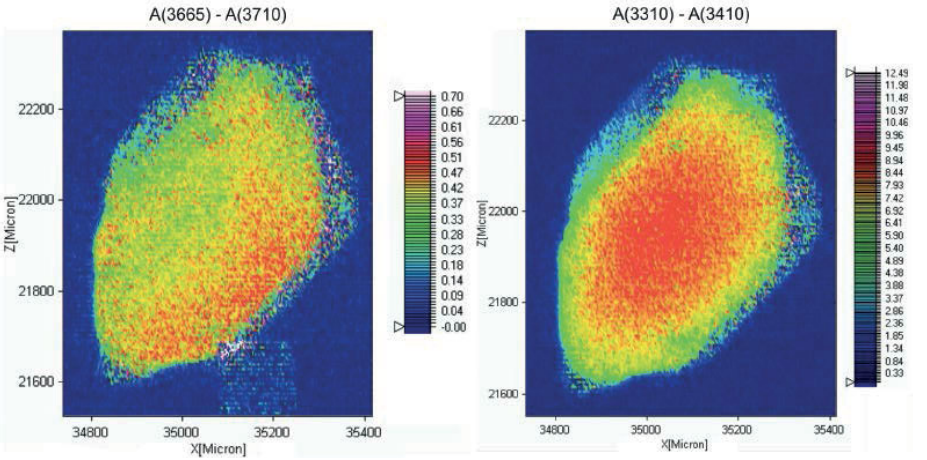


Figure 23. FTIR-FPA images of experimentally treated enstatite. OH-defects giving rise to the absorption band around 3687 cm^{-1} show increasing concentration toward the rim (*left*), and OH-defects giving rise to the absorption band around 3362 cm^{-1} show decreasing concentration toward the rim (*right*). Modified after Prechtel and Stalder (2010).

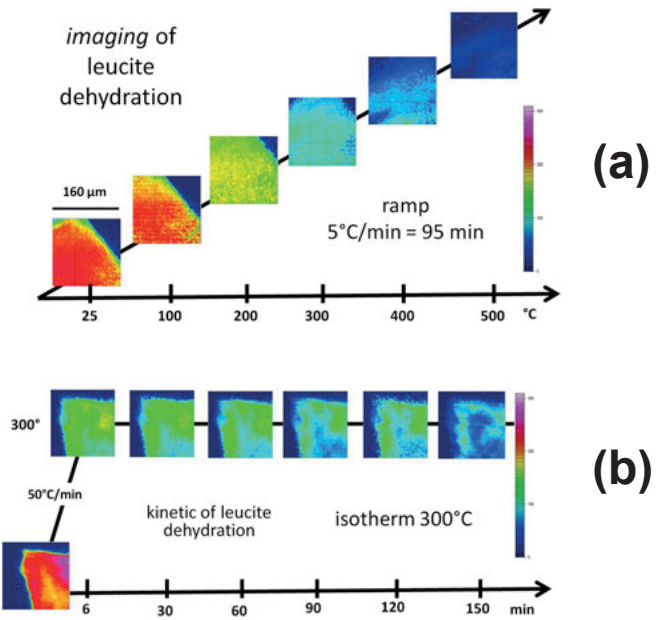


Figure 24. FTIR images obtained with a FPA detector during the *in situ* heating of a single crystal of leucite. (a) continuous ramp of 5 °C/min, showing that leucite dehydrates continuously to become almost anhydrous after 400 min. (b) kinetic study of the dehydration behavior of leucite. *T* was increased up to 300 °C at 50 °C/min and then fixed at *T* = 300 °C. The figure shows that at 300 °C after about 6 min the sample lost half of its initial water content, and then continues to dehydrate. After 150 min the sample is almost anhydrous. [Used by permission of Elsevier, from Della Ventura et al. (2010), *Anal Bioanal Chem*, Vol. 397, Fig. 6, p. 2048].

EBSCOhost - printed on 2/13/2023 5:26 AM via . All use subject to https://www.ebsco.com/terms-of-use

sample is again almost anhydrous. The results of the procedure shown in Figure 24 are still preliminary, and other tests are underway to extract a quantitative behavior from the data. In the last images of the processes shown in Figure 24 a slightly not homogeneous distribution can be recognized. Different causes may be at the origin of the observed distribution, the most probable being the occurrence of a non-perfect flat sample surface. In any case, from the discussion above it is evident that the possibility to monitor the distribution of an absorber *vs.* time across the studied material, in addition to measure it, opens new opportunities for studying and understand phenomena occurring in anisotropic materials, or performing experiments with a temperature gradient set across the sample. All these processes are "non-equilibrium" phenomena in which it is extremely difficult to identify parameters describing the system. The investigations of these complex dynamical processes with imaging techniques is probably the most suitable approach to achieve a better understanding of many phenomena of great geophysical interest.

CONCLUSIONS

Combination of SR-FTIR and imaging techniques provides new opportunities in high-pressure studies, different types of reactions, characterization of materials of interest in Earth Science, such as the presence and evolution with crystallization of light-element (notable H and C) species in geological materials. Moreover, the high-sensitivity of modern spectrometers, coupled with the high resolution offered by FPA detectors now allows imaging of features few μm in size, such as inclusions within minerals, traditionally accessed only by Raman spectroscopy. Such features, which are hardly accessible with other micro-analytical techniques, may help in constraining the genesis and evolution of the geological system. Finally, the possibility to collect high-resolution images in a very short time, from few tens of seconds to minutes using modern array detectors, provides a new opportunity to study many dynamic phenomena in non-ambient conditions *in situ*. Thermal treatments, dehydration processes, and other non-equilibrium processes have been already investigated in many geological and geophysical systems, but many others are just beyond the corner in order to understand Earth and environmental science phenomena.

ACKNOWLEDGMENTS

We like to acknowledge the several people who contributed and are still contributing to the improvement of our spectroscopic research, and in particular the technical and scientific staff of the DAΦNE-L (Frascati, Rome), Diamond (Oxford) and Bessy (Berlin) synchrotron radiation facilities. Financial support was provided by PRIN 2008 to GDV. MD Welch (London), M. Koch-Müller (Potsdam) and an anonimous referee helped in improving the clarity of the manuscript.

REFERENCES

Adler HH, Kerr PF (1965) Variation in infrared spectra, molecular symmetry and site symmetry of sulfate minerals. Am Mineral 50:132-147

Aines RD, Rossman GR (1984) The high temperature behaviour of water and carbon dioxide in cordierite and beryl. Am Mineral 69:319-327

Andersen T, Neumann ER (2001) Fluid inclusions in mantle xenoliths. Lithos 55:301-320

Armbruster T, Bloss FD (1980) Channel CO_2 in cordierite. Nature 286:140-141

Aubaud C, Withers AC, Hirschmann MM, Guan Y, Leshin LA, Mackwell SJ, Bell DR (2007) Intercalibration of FTIR and SIMS for hydrogen measurements in glasses and nominally anhydrous minerals. Am Mineral 92:811-828

EBSCOhost - printed on 2/13/2023 5:26 AM via . All use subject to https://www.ebsco.com/terms-of-use

Balassone G, Bellatreccia F, Mormone A, Biagioni C, Pasero M, Petti C, Mondillo N, Fameli G (2012) Sodalite-group minerals from the Somma-Vesuvius volcanic complex, Italy: a case study of K-feldspar-rich xenoliths. Mineral Mag 76:191-212

Bantignies JL, Carr L, Dumas P, Miller L, Williams GP (1998) Applications of infrared microspectroscopy to geology, biology and cosmetics. Synchrotron Radiation News 11:31-37

Barilaro D, Crupi V, Majolino D, Barone G, Ponterio R (2005) A detailed spectroscopic study of an Italian fresco. J Appl Phys 97:044907, doi: 10.1063/1.1849427

Behrens H, Tamic N, Holtz F (2004) Determination of the molar absorption coefficient for the infrared absorption band of CO_2 in rhyolitic glasses. Am Mineral 89:301-306

Bellatreccia F, Della Ventura G, Piccinini M, Cavallo A, Brilli M (2009) H_2O and CO_2 in minerals of the hauyine-sodalite group: an FTIR spectroscopic study. Mineral Mag 73:399-423

Beran A, Libowitzky E (eds) (2004) Spectroscopic Methods in Mineralogy. Notes in Mineralogy 6, European Mineralogica Union

Beran A, Libowitzky E (2006) Water in natural mantle minerals II: olivine, garnets and accessory minerals. Rev Mineral Geochem 62:169-192

Bernardini F, Eichert D, Lenaz D, De Min A, Tuniz C, Velušček A, Montagnari Kokelj E (2011) Synchrotron FTIR micro-spectroscopy applied to the study of polished serpentinite artefacts: a non-destructive analytical approach. Archaeometry 53:753–764

Bhargava R, Levin IW (2001) Fourier transform infrared imaging: theory and practice. Anal Chem 73:5157-5167

Bhargava R, Levin IW (2007) Fourier transform mid-infrared spectroscopic imaging. *In*: Spectrochemical Analysis Using Infrared Multichannel Detectors. Bhargava R, Levin IW (eds) Blackwell Publishing, p 1-24

Bonaccorsi E, Della Ventura G, Bellatreccia F, Merlino S (2007) The thermal behaviour and dehydration of pitiglianoite, a mineral of the cancrinite group. Microporous Mesoporous Mater 99:225-235

Bonaccorsi E, Merlino S (2005) Modular microporous minerals: cancrinite-davyne group and C-S-H pahses. Rev Mineral Geochem 57:241-290

Bonelli B, Civalleri B, Fubini B, Ugliengo P, Otero Areán C, Garrone E (2000) Experimental and quantum chemical studies on the adsorption of carbon dioxide on alkali-metal-exchanged ZSM-5 zeolites. J Phys Chem B 104:10978-10988

Born M, Wolf E (1997) Principles of Optics. Cambridge University Press, Cambridge

Burattini E, Malvezzi-Campeggi F, Chilosi M, Conti C, Ferraris P, Monti F, Sabbatini S, Tosi g, Zamò A (2007) FPA microspectral imaging of non-Hodgkin lymphomas. J Mol Struct 834-836:170-175

Carr GL (2001) Resolution limits for infrared microspectroscopy explored with synchrotron radiation. Rev Sci Instrum 72:1613, doi: 10.1063/1.1347965

Castro JM, Beck P, Tuffen H, Nichols ARL, Dingwell DB, Martin MC (2008) Timescale of spherulite crystallization in obsidian inferred from water concentration profiles. Am Mineral 93:1816-1822

Cestelli Guidi M, Piccinini M, Marcelli A, Nucara A, Calvani P, Burattini E (2005) Optical performance of SINBAD, the IR source at DAΦNE. J Opt Soc Am A 22:2810

Coblentz WW (1905) Investigations of infra-red spectra. Carnegie Institution of Washington. Washington DC

Cricenti A, Generosi R, Luce M, Perfetti P, Margaritondo G, Talley D, Sanghera JS, Aggarwal ID, Tolk NH (2002) Very high resolution near-field chemical imaging using an infrared free electron laser. Phys Chem Chem Phys 4: 2738-2741

Danyushevsky LV, McNeill AW, Sobolev AV (2002) Experimental and petrological studies of melt inclusions in phenocrysts from mantle-derived magmas: an overview of techniques, advantages and complications. Chem Geol 183:5-24

Dazzi A, Prazeres R, Glotin F, Ortega JM (2005) Local infrared microspectroscopy with subwavelength spatial resolution with an atomic force microscope tip used as a photothermal sensor. Opt Lett 30:2388-90

Dazzi A, Prazeres R, Glotin F, Ortega JM (2007a) Analysis of nano-chemical mapping performed by an AFM-based ("AFMIR") acousto-optic technique. Ultramicroscopy 107:1194–200

Dazzi A, Kjoller K, Reading M (2007b) High-frequency deflection measurement of IR absorption. U.S. patent 11/803,421

De Vivo B, Lima A, Webster JD (2005) Volatiles in magmatic-volcanic systems. Elements 1:19-24

Della Ventura G, Bellatreccia F, Bonaccorsi E (2005) CO_2 in cancrinite-sodalite group minerals: pitiglianoite. Eur J Mineral 17:847-851

Della Ventura G, Bellatreccia F, Parodi GC, Cámara F, Piccinini M (2007) Single-crystal FTIR and X-ray study of vishnevite, ideally $[Na_6(SO_4)][Na_2(H_2O)_2](Si_6Al_6O_{24})$. Am Mineral 92:713-721

Della Ventura G, Bellatreccia F, Piccinini M (2008a) Channel CO_2 in feldspathoids: a review of existing data and new perspectives. Rend Acc Lincei 19:141-159

Della Ventura G, Bellatreccia F, Piccinini M (2008b) Presence and zoning of hydrous components in leucite from the Albani Hills volcano (Rome, Italy). Am Mineral 93:1538-1544

EBSCOhost - printed on 2/13/2023 5:26 AM via . All use subject to https://www.ebsco.com/terms-of-use

Della Ventura G, Bellatreccia F, Cesare B, Harley S, Piccinini M (2009) FTIR microspectroscopy and SIMS study of water-poor cordierite from El Hoyazo, Spain: application mineral and melt devolatilization. Lithos 113:498-506

Della Ventura G, Bellatreccia F, Marcelli A, Cestelli Guidi M, Piccinini M, Cavallo A, Piochi M (2010) FTIR imaging in Earth Sciences. Anal Bioanal Chem 397:2039-2049

Della Ventura G, Radica F, Bellatreccia F, Cavallo A, Capitelli F, Harley S (2012) The quantitative analysis of H_2O and CO_2 in cordierite using single-crystal polarized-light FTIR microspectroscopy. Contrib Mineral Petrol 164:881-894

Di Matteo V, Carroll MR, Behrens H, Vetere F, Brooker RA (2004) Water solubility in trachytic melts. Chem Geol 213:187-196

Dixon JE, Pan V (1995) Determination of the molar absorptivity of dissolved carbonate in basaltic glass. Am Mineral 80:1339-1342

Dumas P, Miller L (2003) The use of synchrotron infrared microspectroscopy in biological and biomedical investigations. Vib Spectrosc 32:3-21

Farmer VC (ed) (1974) The infrared spectra of minerals. The Mineralogical Society, London

Feenstra A, Rhede D, Koch-Müller M, Wiedenbech M, Heinrich W (2009) Hydrogen zoning in zinc-bearing staurolite from a high-P, low-T diasporite (Samos, Greece): a combined EMP-SIMS-FIB-FTIR study. Am Mineral 94:737-745

Flynn J, Keller LP, Joswiak D, Brownlee DE (2002) infrared analysis of organic carbon in anhydrous and hydrated interplanetary dust particles: FTIR identification of carbonyl (C=O) in IDPs. Lunar Planet Sci 33:1320

Flynn GJ, Keller LP, Jacobsen C, Wirick S (2004) An assessment of the amount and types of organic matter contributed to the Earth by interplanetary dust. Adv Space Res 33:57–66

Frezzotti ML (2001) Silicate-melt inclusions in magmatic rocks: applications to petrology. Lithos 55:273-299

Geloni G, Kocharyan V, Saldin E, Schneidmiller E, Yurkov M (2009a) Theory of edge radiation. Part I: Foundations and basic applications. Nucl Instrum Methods Phys Res A 605:409-429

Geloni G, Kocharyan V, Saldin E, Schneidmiller E, Yurkov M (2009b) Theory of edge radiation. Part II: Advanced applications. Nucl Instrum Methods Phys Res A 605:409-429

Griffiths IP, de Haseth J (1986) Fourier Transform Infrared Spectrometry. Wiley, New York.

Guilhamou N, Dumas P, Carr GL, Williams GP (1998) Synchrotron infrared microspectroscopy applied to petrography in micrometer-scale range: fluid chemical analysis and mapping. Appl Spectrosc 52:1029-1034

Guilhaumou N, Ellouz N, Jaswall T, Mougin P (2000) Genesis and evolution of hydrocarbon entrapped in fluorite deposits of Koh-i-Maran (North Kirthar Range, Pakistan). Marine Petrol Geol 17:1151-1164

Guilhamou N, Sautter V, Dumas P (2005) Synchrotron FTIR microanalysis of volatiles in melt inclusions and exsolved particles in ultramafic deep-seated garnets. Chem Geol 223:82-92.

Hawthorne FC (ed) (1988) Spectroscopic Methods in Mineralogy and Geology. Reviews in Mineralogy, Volume 18. Mineralogical Society of America

Heraud P, Caine S, Sanson G, Gleadow R, Wood BR, McNaughton D (2007) Focal plane array infrared imaging: a new way to analyse leaf tissue. New Phytol 173:216-225

Hofmann A (2004) The Physics of Synchrotron Radiation, Cambridge University Press

Houel J, Homeyer E, Sauvage S, Boucard P, Dazzi A, Prazeres R, et al. (2009) Midinfrared absorption measured at λ/400 resolution with an atomic force microscope. Opt Express 17:10887-94

Iezzi G, Liu Z, Della Ventura G (2006) High pressure synchrotron infrared spectroscopy of synthetic Na(NaMg) $Mg_5Si_8O_{22}(OH)_2$ up 30 GPa: a possible high-pressure new amphibole polymorph. Am Mineral 91:479-482

Iezzi G, Liu Z, Della Ventura G (2009) The role of B-site on the compressional behaviour of synthetic $P2_1/m$ amphiboles in the system $^{A}Na^{B}(Na_xLi_{1-x}Mg_1)\ ^{C}Mg_5\ Si_8\ O_{22}\ (OH)_2$ (with x=1, 0.6, 0.2 and 0): an high pressure synchrotron infrared study. Phys Chem Miner 36:343-354

Ihinger PD, Hervig RL, McMillan PF (1994) Analytical methods for volatiles in glasses. Rev Mineral 30:67-121

Ingrin J, Hercule S, Charton T (1995) Diffusion of hydrogen in diopside: results of dehydration experiments. J Geophys Res 100:15489-15499

Innocenzi P, Malfatti L, Piccinini M, Grosso D, Marcelli A (2009) Stain effects studied by time-resolved infrared imaging. Anal Chem 81:551-556

Inoué S (1995) Foundations of confocal scanned imaging in light microscopy. *In*: Handbook of Biological Confocal Microscopy. Pawley JB (ed) Plenum Press, New York p 1-18

Johnson EA (2006) Water in nominally anhydrous crustal minerals: speciation, concentration and geologic significance. Rev Mineral Geochem 62:117-154

Keller WD, Pickett EE (1949) The absorption of infrared radiation by powdered silica minerals. Am Mineral 34:855-868

Keller WD, Pickett EE (1950) The absorption of infrared radiation by clay minerals. Am J Science 248:264-273

EBSCOhost - printed on 2/13/2023 5:26 AM via . All use subject to https://www.ebsco.com/terms-of-use

Keppler H, Smyth JR (eds) (2006) Water in Nominally Anhydrous Minerals. Reviews in Mineralogy and Geochemistry, Volume 62. Mineralogical Society of America.
Khomenko VM, Langer K (2005) Carbon oxides in cordierite channels: determination of CO_2 isotopic species and CO by single crystal IR spectroscopy. Am Mineral 90:1913-1917
King PL, Venneman TW, Holloway JR, Hervig RL, Lowenstern JB, Forneris JF (2002) Am Mineral 87:1077-1082
Koch-Müller M, Fei Y, Hauri E, Liu Z (2001) Location and quantitative analysis of OH in coesite. Phys Chem Min 28:693-705
Koch-Müller M, Hofmeister AM, Fei Y, Liu Z (2002) High-pressure IR-spectra and the thermodynamic properties of chloritoid. Am Mineral 87:609-622
Koch-Müller M, Dera P, Fei Y, Reno B, Sobolev N, Hauri E, Wysoczanski R (2003) OH^- in synthetic and natural coesite. Am Mineral 88:1436-1445
Koch-Müller M, Matsyuk SS, Wirth R (2004) Hydroxyl in omphacites and omphacitic clinopyroxenes of upper mantle to lower crustal origin beneath the Siberian platform. Am Mineral 89:921-931
Koch-Müller M, Dera P, Fei Y, Hellwig H, Liu Z, Van Orman J, Wirth R (2005) Polymorphic phase transition in Superhydrous Phase B. Phys Chem Miner 32:349-361
Koch-Müller M, Matsyuk SS, Rhede D, Wirth R, Khisina N (2006) Hydroxyl in mantle olivine xenocrysts from the Udachnaya kimberlite pipe. Phys Chem Miner 33:276-287
Koch-Müller M, Speziale S, Deon F, Mrosko M, Schade U (2011) Stress-induced proton disorder in hydrous ringwoodite. Phys Chem Miner 38:65-73
Kolesov BA, Geiger CA (2000) Cordierite II: the role of CO_2 and H_2O. Am Mineral 85:1265-1274
Kolesov BA, Geiger CA (2003) Molecules in the SiO_2-clathrate melanophlogite: a single crystal Raman study. Am Mineral 88:1364-1368
Launer PJ (1952) Regularities in the infrared absorption spectra of silicate minerals. Am. Mineral 37:764-784
Levenson E, Lerch P, Martin MC (2006) Infrared imaging: synchrotron vs. arrays, resolution vs. speed. Infrared Phys Tech 49:45-52
Levin IW, Bhargava R (2005) Fourier transform infrared vibrational spectroscopic imaging: integrating microscopy and molecular recognition. Ann Rev Phys Chem 56:429-74
Libowitzky E, Rossman GR (1996) Principles of quantitative absorbance measurements in anisotropic crystals. Phys Chem Miner 23:319-327
Libowitzky E, Rossman GR (1997) An IR absorption calibration for water in minerals. Am Mineral 82:1111-1115
Linnen RL, Keppler H, Sterner SM (2004) In situ measurements of the H_2O:CO_2 ratio in fluid inclusions by infrared spectroscopy. Can Mineral 42:1275-1282
Liu Z, Lager, GA, Hemley RJ, Ross NL (2003) Synchrotron infrared spectroscopy of OH-chondrodite and OH-clinohumite at high pressure. Am Mineral 88:1412-1415
Lowenstern JB (1995) Applications of silicate-melt inclusions to the study of magmatic volatiles. *In*: Magmas, Fluid and Ore Deposits. Thompson JFH (ed) Mineral Association of Canada Short Course Series 23:71-99
Marcelli A, Cinque G (2011) Infrared synchrotron radiation beamlines: high brilliance tools for IR spectromicroscopy. A practical guide to the characteristics of the broadband and brilliant non-thermal sources. *In*: Biomedical Applications of Synchrotron Infrared Microspectroscopy. Moss D (ed) Royal Society of Chemistry, p 67-104
Marcelli A, Innocenzi P, Malfatti L, Newton MA, Rau JV, Ritter E, Schade U, Xu Wei (2012) IR and X-ray time resolved simultaneous experiments: an opportunity to investigate the dynamics of complex systems and non-equilibrium phenomena using 3rd generation synchrotron radiation sources. J Synchrotron Rad 19:892-904
Marquardt H, Marquardt K (2012) Focused ion beam preparation and characterization of single-crystal samples for high-pressure experiments in the diamond-anvil cell. Am Mineral 97:299-304
Matrajt G, Muñoz Caro GM, Dartois E, d'Hendecourt L, Deboffle D, Borg J (2005) FTIR analysis of the organics in IDPs: Comparison with the IR spectra of the diffuse interstellar medium. Astron Astrophys 433:979–995
McLimans RK (1987) The application of fluid inclusions to migration of oil and diagenesis in petroleum reservoirs. Appl Geochem 2:585-603
Miliani C, Daveri A, Brunetti BG, Sgamellotti A (2008) CO_2 entrapment in natural ultramarine blue. Chem Phys Lett 466:148-151
Miller LM, Smith RJ (2005) Synchrotrons versus globars, point-detectors versus focal plane arrays: Selecting the best source and detector for specific infrared microspectroscopy and imaging applications Vib Spectr 38:237-240
Mills DM (1984) Time-resolution experiments using X-ray synchrotron radiation. Phys Today 37:22, http://dx.doi.org/10.1063/1.2916191
Minsky M (1988) Memoir on inventing the confocal scanning microscope. Scanning 10:128-138

EBSCOhost - printed on 2/13/2023 5:26 AM via . All use subject to https://www.ebsco.com/terms-of-use

Morizet Y, Paris M, Gaillard F, Scaillet B (2010) C–O–H fluid solubility in haplobasalt under reducing conditions:An experimental study. Chem Geol 279:1-16

Mormone A, Piochi M, Bellatreccia F, De Astis G, Della Ventura G, Moretti R, Cavallo A, Mangiacapra A (2011) A CO_2 –rich magma source beneath the Phlegraean Volcanic District (Southern Italy): evidence from a melt inclusion study. Chem Geol 287:66-80

Mrosko M, Koch-Müller M, Schade U (2011) In-situ mid/far micro-FTIR spectroscopy to trace pressure-induced phase transitions in strontium feldspar and wadsleyite. Am Mineral 96:1748-1759

Na KC, McCauley ML, Crisp JA, Ernst WG (1986) Phase relations to 3 kbar in the systems edenite + H_2O and edenite + excess quartz + H_2O. Lithos 19:153-163

Nasse MJ, Mattson EC, Reininger R, Kubala T, Janowski S, El-Bayyari Z, Hirschmugl CJ (2011) Multi-beam synchrotron infrared chemical imaging with high spatial resolution: Beamline realization and first reports on image restoration. Nucl Instrum Methods Phys Res A 649:172-176

Nichols EF (1883) A study of the transmission spectra of certain substances in the infra-red. Phys Rev 1:1-18

Noguchi N, Moriwaki T, Ikemoto Y, Shinoda K (2012) OH group behavior and pressure-induced amorphization of antigorite examined under high pressure and temperature using synchrotron infrared spectroscopy. Am Mineral 97:134-142

Ortega JM, Glotin F, Prazeres R (2006) Extension in far-infrared of the CLIO free-electron laser. Infrared Phys Technol 49:133-138

Paterson M (1982) The determination of hydroxyl by infrared absorption in quartz, silicate glasses and similar materials. Bull Mineral 105:20-29

Pawley JB (2006) Chapter 2: Fundamental limits in confocal microscopy. *In:* Handbook of Biological Confocal Microscopy, 3rd Edition. Pawley JB (ed) Plenum Press, New York, p 19-38

Petibois C, Déléris G (2006) Chemical mapping of tumor progression by FT-IR imaging: towards molecular histopathology. Trends Biotech 24:455-462

Petibois C, Piccinini M, Cestelli Guidi M, Déléris G, Marcelli A (2009) Infrared Synchrotron sources – a boon for biology. Nature Photonics 3:177

Petibois C, Cestelli Guidi M, Piccinini M, Moenner M, Marcelli A (2010a) Synchrotron radiation FTIR imaging in minutes: a first step towards real time cell imaging. Anal Bional Chem 397:2123-2129

Petibois C, Piccinini M, Cestelli Guidi M, Marcelli A (2010b) Facing the challenge of biosample imaging by FTIR with a synchrotron radiation source. J Synchrotron Rad 17:1-11

Piccinini M, Cibin G, Marcelli A, Mottana A, Della Ventura G, Bellatreccia F (2006a) Synchrotron radiation micro-spectroscopy on natural micas in the OH-stretching region. Infrared Phys Technol 49:64-68

Piccinini M, Cibin G, Marcelli A, Della Ventura G, Bellatreccia F, Mottana A (2006b) Synchrotron radiation micro-spectroscopy of fluor-phlogopite in the OH-stretching region. Vib Spectrosc 42:59-62

Pironon J, Thiery R, Ayt Ougougdl M, Teinturier S, Beaudoin G, Walgenwitz F (2001) FT-IR measurements of petroleum fluid inclusions: methane, *n*-alkanes and carbon dioxide quantitative analysis. Geofluids 1:2-10

Pompeo G, Longo G, Girasole M, Moretti P, Palomba E, Maras A, Somma F, Cricenti A (2010) AFM and SNOM characterization of ordinary chondrites: a contribution to solve the problem of asteroid reddening. Phys Status Solidi B 247:2061-2066

Prasad PSR, Prasad KS, Murthy SR (2005) Dehydration of natural stilbite: an in situ FTIR study. Am Mineral 90:1636-1640

Prechtel F, Stalder R (2010) FTIR spectroscopy with a focal plane array detector: a novel tool to monitor the spatial OH-defect distribution in single crystals applied to synthetic enstatite. Am Mineral 95:888-891

Roedder E (ed) (1984) Fluid Inclusions. Reviews in Mineralogy, Volume 12. Mineralogical Society of America

Salvadó N, Buti S, Tobin M, Pantos E, Pradell T (2005) Advantages of the use of SR-FTIR microspectroscopy: applications to cultural heritage. Anal Chem 77:3444-3451

Salvadó N, Buti S, Pantos E, Bahrami F, Labrador A, Pradell T (2008) The use of combined synchrotron radiation micro FT-IR and XRD for the characterization of Romanesqu wall paintings. Appl Phys A 90:67-73

Salvadó N, Butí S, Labrador A, Cinque G, Emerich H, Pradell T (2011) SR-XRD and SR-FTIR study of the alteration of silver foils in medieval paintings. Anal Bioanal Chem 399:3041-3052

Scott HP, Liu Z, Hemley RJ, Williams Q (2007) High-pressure infrared spectra of talc and lawsonite. Am Mineral 92:1814-1820

Seaman SJ, Dyar MD, Marinkovic N, Dunbar NW (2006) An FTIR study of hydrogen in anorthoclase and associated melt inclusions. Am Mineral 91:12-20

Skogby H (2006) Water in natural mantle minerals I: pyroxenes. Rev Mineral Geochem 62:155-167

Smith BC (1996) Fundamentals of Fourier Transform Infrared Spectroscopy. CRC Press, New York

Sobolev A (1996) Melt inclusions in minerals as a source of principle petrological information. Petrol 4:228-239

Stalder R, Skogby H (2003) Hydrogen diffusion in natural and synthetic orthopyroxene. Phys Chem Miner 30:12-19

Stolper EM, Ahrens TJ (1987) On the nature of pressure-induced coordination changes in silicate melts and glasses. Geophys Res Lett 14:1231-1233

EBSCOhost - printed on 2/13/2023 5:26 AM via . All use subject to https://www.ebsco.com/terms-of-use

Thomas SM, Koch-Muller M, Kahlenberg V, Thomas R, Rhede D, Wirth R, Wunder B (2008) Protonation in germanium equivalents of ringwoodite, anhydrous phase B, and superhydrous phase B. Am Mineral 93:1282-1294

Thomas SM, Koch-Muller M, Reichart P, Rhede D, Thomas R, Wirth R, Matsyuk S (2009) IR calibrations for water determination in olivine, r-GeO_2, and SiO_2 polymorphs. Phys Chem Miner 36:489-509

Tokiwai K, Nakashima S (2010) Dehydration kinetics of muscovite by in situ infrared microspectroscopy. Phys Chem Miner 37:91-101

Viti C, Gemmi M (2009) Nanostructures and microinfrared behavior of black opal from Gracias, Honduras. N Jb Miner Abh 186:11-20, doi: 10.1127/0077-7757/2009/0142

Vobornik D, Margaritondo G, Sanghera JS, Thielen P, Aggarwal ID, Ivanov B, Tolk NH, Manni V, Grimaldi S, Lisi A, Rieti S, Piston DW, Generosi R, Luce M, Perfetti P, Cricenti A (2005) Spectroscopic infrared scanning near-field optical microscopy (IR-SNOM). J Alloy Comp 401:80-85

Wirth R (2004) Focused Ion Beam (FIB): A novel technology for advanced application of micro- and nanoanalysis in geosciences and applied mineralogy. Eur J Mineral 16:863-876

Wood DL, Nassau K (1967) Infrared spectra of foreign molecules in beryl. J Chem Phys 47: 2220-2228

Wysoczanski R, Tani K (2006) Spectroscopic FTIR imaging of water species in silicic volcanic glasses and melt inclusions: an example from the Izu-Bonin Arc. J Volcan Geotherm Res 156:302-314

Xu W, Marcelli A, Hampai D, Malfatti L, Innocenzi P, Schade U Wu Z (2011) New opportunity to investigate physico-chemical phenomena: time resolved X-ray and IR concurrent analysis. Ren Acc Lincei 22:59-79

Zhang M, Wang L, Hirai S, Redfern SAT, Salje EKD (2005) Dehydroxylation and CO_2 incorporation in annealed mica (sericite): an infrared spectroscopic study. Am Mineral 87:173-180

Zhang M, Hui Q, Lou XJ, Redfern ST, Salje EKH, Tarantino SC (2006) Dehydroxylation, proton migration, and structural changes in heated talc: an infrared spectroscopic study. Am Mineral 91:816-825

EBSCOhost - printed on 2/13/2023 5:26 AM via . All use subject to https://www.ebsco.com/terms-of-use

EBSCOhost - printed on 2/13/2023 5:26 AM via . All use subject to https://www.ebsco.com/terms-of-use

Reviews in Mineralogy & Geochemistry
Vol. 78 pp. 481-508, 2014
Copyright © Mineralogical Society of America

Carryover of Sampling Errors and Other Problems in Far-Infrared to Far-Ultraviolet Spectra to Associated Applications

Anne M. Hofmeister

Department of Earth and Planetary Science
Washington University
St Louis, Missouri 63130, U.S.A.

hofmeist@wustl.edu

INTRODUCTION AND PURPOSE

The thin, smooth curves representing spectroscopic data suggest a high degree of accuracy. Yet, experimental uncertainties do exist, as in any measurement. Overlooked problems in data collection, processing, and interpretation have repercussions for applications in mineral physics, planetary science, and astronomy. Random errors (i.e., noise) are fairly obvious, and are not discussed here. The concern is subtle and overlooked errors that arise in acquisition, processing, and interpretation of spectral data. These types of errors are systematic, not random. This chapter identifies various systematic errors and problems that the author encountered in her efforts to provide absolute values of absorbance or reflectivity. Re-occurring issues in data collection include underestimating the importance of surface polish and not accounting for peak profiles depending on sample thickness relative to band strengths. Processing of emission spectra is problematic. Common instrumental problems are briefly described.

Optical spectroscopy is the name generally attached to the visible region which we probe with our eyes, which are convenient built-in spectrometers, but can also include the infrared (IR) region wherein the type of vibrational mode known as "optical" is detected. Because some applications require very high frequency (ν) data, this chapter concerns ν from ~10 to 10^6 wavenumbers, which is equivalent to wavelengths (λ) of ~10^6 to 10 nm or of ~1000 to 0.01 μm). The X-ray region is included due to the extreme breadths of metal-oxygen charge-transfer bands of minerals which peak in the ultraviolet (UV). The author points out errors in her own results as well those of others. Mistakes provide opportunity for learning! Correct methodologies are discussed along with measurements needed to improve constraints on spectral parameters and hence to make interpretations more definitive. Ideal conditions are difficult to achieve, so another goal is enable the reader to recognize what is "sufficiently accurate" and/or "representative" of the material properties for the problem being addressed.

Spectra find use in two completely different applications: (1) identification of unknowns through comparison, and (2) calculation of physical properties. Both types are discussed by example in this chapter. Identification has its origins in chemistry, as fingerprinting run products from chemical syntheses. Identification is important to geology, planetary science, and astronomy because spectra are a cost-effective means of probing distant objects or surfaces with conditions destructive to equipment or of providing surveys or reconnaissance efforts. I discuss planetary surfaces, and dust clouds in astrophysical environments. These two examples illustrate how not duly considering effects of sampling conditions on spectra have led to questionable inferences of phases present (asteroid surfaces and glass vs. crystals in astronomical environments). Regarding inference of physical properties, one example is presented

1529-6466/14/0078-0012$05.00 http://dx.doi.org/10.2138/rmg.2014.78.12

EBSCOhost - printed on 2/13/2023 5:26 AM via . All use subject to https://www.ebsco.com/terms-of-use

here: calculation of the rate of heat diffused through a material at high frequency. I discuss how difficulties in measuring absorption coefficients that are near zero have led to misrepresentation of radiative thermal conductivity values. This application was chosen because diffusive radiative thermal conductivity ($k_{rad,dif}$) is important to engineering (smokes), astronomy (stellar interiors), and possibly planetary interiors (but see Hofmeister 2010); yet $k_{rad,dif}$ cannot be measured directly, so spectroscopic calculations are the only means to establish heat transfer rates of visible light. For other examples of physical properties that can be obtained from spectra, see Hofmeister (2004).

EXPERIMENTAL METHODS

Spectral data collected at Washington U are as described in the cited papers. For IR measurements, a Bomem DA3.02 Fourier transform interferometer is equipped with beam splitters, detectors, and accessories to cover ~10 to 20,000 cm^{-1}. Unpolarized visible to ultraviolet (UV) spectra from 9090 to 52630 cm^{-1} were collected using a double-beam Shimaduzu UV-1800 with 1 nm resolution at the slowest scan speed available.

EXTRACTION OF SPECTRAL PROPERTIES FROM LABORATORY MEASUREMENTS

Ideal interactions of light with perfect, single crystals

Spectral conventions and representations. We measure the amount of light received relative to either a standard (the reference) or to the intensity of the incident beam. The purpose is to determine the physical properties of the material. Engineering definitions are used, i.e., we wish to known how much light is actually absorbed by the sample, and/or how much is actually reflected, and/or how much is actually emitted (Siegel and Howell 1972; Brewster 1992). This chapter focuses on data collected at room temperature, where emissions of the sample are low compared to incident light and can be neglected except in emission experiments, which pertain to planetary and astronomy applications. Emissivity is discussed at the end of this section. Absorptivity or absorbance or absorption coefficient (quantities are defined below) are important because these describe how light is attenuated within the sample. In the spectroscopy, chemistry and mineralogical literature, common logarithms are used to describe attenuation of light: this convention is incorporated in commercial software. However, the physics of attenuation is mathematically described by the exponential function and thus the natural logarithm pertains. Formulae provide below use natural logarithms.

Spectra can be represented in different ways. For a complete description of how light interacts with the solid, any of three pairs of functions can be used: (1) The absorption coefficient (A) and reflectivity (r) are directly and most commonly measured. (2) The complex index of refraction ($n + ik$) is essential to radiative transfer models, where n is the index of refraction, and also because direct measurements of n provide an independent constraint on r (e.g., Hofmeister et al. 2009). Several names are used for the imaginary part, k, some of which are confusing. We use "absorption index" (e.g., Brewster 1992) as opposed to "extinction coefficient" (e.g., Bell 1967) because the latter is used to describe the combined effects of physical scattering and absorption (e.g., Shankland et al. 1979). Together, n and k are referred to as optical functions, which is preferred over historic use of "optical constants," because spectral properties depend on frequency. (3) The complex dielectric function ($e_1 + ie_2$) is used in the physics literature because this links optical properties with electrical properties of a material. Although this representation is completely equivalent, the connection with light measurements is less direct, and thus dielectric functions are less frequently used to represent spectroscopic data. However, direct measurements of e_1 set independent constraints on r (e.g., Hofmeister et al. 2003).

EBSCOhost - printed on 2/13/2023 5:26 AM via . All use subject to https://www.ebsco.com/terms-of-use

Formulae for spectral functions accounting for surface reflections. If emissions are small compared to the intensity of the beam in the spectrometer, which is reasonable at room temperature, then energy conservation is described by:

$$1 = \frac{I_{tra}}{I_0} + \frac{I_{abs}}{I_0} + \frac{I_{refl}}{I_0} = \tau + \alpha + r \tag{1}$$

where I_0 is beam intensity impinging on the sample, I_{tra} is the intensity of light transmitted by the sample, I_{abs} is the intensity of light actually absorbed, and I_{refl} is the intensity of light reflected on the first bounce from the front face (Fig. 1a), τ is transmittivity, α is absorptivity, and r is reflectivity. We *cannot* directly measure how much light is absorbed, and thus values of A involve data processing and can include systematic errors. Specifically, we measure the amount of light exiting the sample (Fig. 1a), which is a combination of reflection and absorption losses. For normal incidence and parallel light rays crossing a flat sample with parallel faces of thickness d, computing the true absorption coefficient (A) requires accounting for first-order back reflections:

$$A(\nu)d = -\ln\left[\frac{I_{tra}(\nu)}{I_0(\nu)}\right] + 2\ln\left[1 - r(\nu)\right] \tag{2}$$

The closely related variable, absorbance ($a = Ad$), is frequently used because thickness is not always known (e.g., sample ground and dispersed in a pellet) and r is not always known. Commonly, a baseline is assumed which serves to remove the effect of both surface (specular) reflection and scattering from various imperfections, discussed below. Baseline subtraction is useful for applications needing peak parameters only, but this approach does not provide absolute intensities.

Equation (2) assumes a single reflective bounce (Fig. 1a). Multiple reflections are possible. We tested for their importance in the visible-UV region using highly transparent samples (e.g., MgF_2) and could find no difference, which is consistent with Figure 1, which shows that each additional reflection involves another factor of (1-r). For the transparent regions, r is ~ 0.05, providing a small, but non-negligible correction. For strongly absorbing regions r~1, so the reflectivity term can be neglected to a first approximation. Similarly, in determining reflectivity for strongly absorbing regions, if the crystal is sufficiently thick, the effect of absorption can be neglected because α~1 (Fig. 1a). Where one encounters problems is frequency regions of

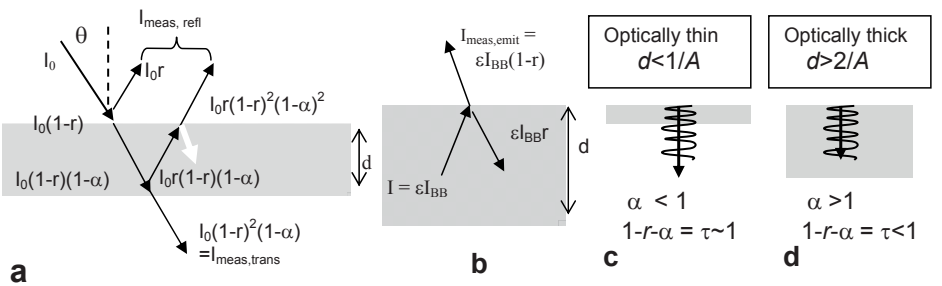


Figure 1. Schematics relevant to light received vs. spectral functions. One back reflection is shown per surface at near-normal incidence (angles are exaggerated and the white arrow is not labeled). (a) Transmission (lower face) and reflection (upper face) experiments. The light received by a detector (I_{meas}) relative to incident intensity (I_0) is a combination of reflection and absorption, depending on thickness, d. [After Fig. 1 of Hofmeister et al. (2003).] (b) Emission experiments, where I_{BB} is blackbody intensity. (c) Effect of optically thin vs. optically thick conditions on spectral functions. These divisions pertain to emission as well as transmission and reflection experiments.

EBSCOhost - printed on 2/13/2023 5:26 AM via . All use subject to https://www.ebsco.com/terms-of-use

rapid change in $A(\nu)$ and $r(\nu)$, such as immediately above the main IR bands, discussed below, because these do not meet the above criteria.

Commercial software provides raw absorbance:

$$a_{raw} = -\log\left(\frac{I_{tra}}{I_0}\right) \tag{3}$$

so $Ad = 2.3016a_{\text{raw}} - 2\ln(1-r)$. If a definition is not provided in a paper, most likely common logs were used. This report uses natural logarithms, unless stated otherwise.

It should be clear from Figure 1 and Equations (1) and (2) that A and r as a pair describe the optical properties of the solid (assuming emissions are low). Reflectivity as discussed above would be determined from direct measurements. Importantly, r is also described by Fresnel's law:

$$r = \frac{\left(n - n_{\text{medium}}\right)^2 + k^2}{\left(n + n_{\text{medium}}\right)^2 + k^2} \tag{4}$$

where the index of refraction of the medium n_{medium} is 1 for most cases (air or vacuum). The imaginary part of the optical function k is related to the absorption coefficient:

$$k(\nu) = \frac{A(\nu)}{4\pi\nu} \tag{5}$$

It is fortunate that the absorption index (k) is negligibly small for weakly colored silicates and oxides at high frequencies, which reduces Fresnel's equation to:

$$r \cong \frac{\left(n-1\right)^2}{\left(n+1\right)^2} \quad \text{if} \quad k \cong 0 \tag{6}$$

and permits computation of r in the visible region from direct measurements of n, which are well-known for minerals because n can be directly measured in the visible region with a refractometer or visual comparison to oils with known n values (see any mineralogy textbook). That determinations of n are wholly independent of spectral measurements provides an important cross-check on reflectivity measurements (e.g., Hofmeister et al. 2009).

Equations (4) to (6) show than n and k as a pair of variables are equivalent to describing spectra in terms of A and R. Optical functions are advantageous as these are both small (<10) at high frequency.

The third pair is the complex dielectric constant:

$$e_1 = n^2 - k^2 \quad \text{and} \quad e_2 = 2nk \tag{7}$$

Brewster (1992) provides equations appropriate to metals with magnetic interactions. Importantly, at frequencies below the strong absorptions in the infrared, k~0, and hence independent measurements of e_1 at low frequencies, denoted e_0 (e.g., Shannon and Subramanian 1989), provides another cross-check on reflectivity measurements (inserting $n = e_0^{1/2}$ into Eqn. 6 relates r to e_0). Due to this behavior, e_0 is commonly used as a constraint in classical dispersion analysis (the damped harmonic oscillator or Lorentz model; e.g., Spitzer and Kleinman 1961). Similarly, $n = e_\infty^{1/2}$ can be used for this purpose to constrain r in the visible region. The equations can be cast to use either, but not BOTH e_0 and e_∞: both approaches exist in spectroscopy literature, and are specified in each paper. This situation occurs because of sum rules stemming from causality (Wooten 1972). The tie of the high and low frequency dielectric constants and vibrational frequencies is evident in the Lydanne-Sachs-Teller relationship which is derived from the damped harmonic oscillator model (e.g., Burns 1990).

EBSCOhost - printed on 2/13/2023 5:26 AM via . All use subject to https://www.ebsco.com/terms-of-use

Transmission and reflection results depend on optical thickness. Regarding transmission experiments, non-negligible light must exit the sample to quantify *A* (Fig. 1). For a thick sample, if excessive intensity is lost via attenuation, then the light received is similar to the noise level of the detector, and $\tau = 0$ within uncertainty (Fig. 1c). Under such optically thick conditions, the top of the peak appears round and noisy because no difference actually exists between large absorbance (~4) and infinite absorbance. The peak profile is distorted. Distortion onsets as thickness increases (Fig. 2) because peaks have sloping sides and optical thickness depends on *d* and on $A(\nu)$. To avoid non-linear behavior (distortions), experimental conditions must fall in the category of "optically thin," wherein path length is small compared to the attenuation (Fig. 1c). Siegel and Howell (1972) consider optically thin to require $d < 2/A$, but I have found that this is insufficient. Instead, this case depicts optically thick conditions (Fig. 1d) Note that optically thick is not the same as opaque conditions, where no light is received. Opacity occurs at some greater thickness, and arises for all materials at some thickness and some frequency because reflection removes light in addition to absorption and that detectors have noise.

Optical thickness is strongly frequency dependent. At frequencies where a transition is excited, *A* is large, and thus meeting optically thin conditions varies not only with the sample and the spectral range, but more over is specific to the peak being probed. Very roughly, IR fundamentals are the strongest types of transitions, next are anion-cation charge-transfer bands in the UV, then intervalence charge transfer bands, next is overtones in the near-IR, and lastly *d-d* electronic transitions in the visible region. It is also important to recognize that conditions can change from optically thin to thick over a very narrow frequency range.

Artifacts arise in using too thick and too thin of a sample (Fig. 2). Peaks must be distinct from the background, or a different type of distortion exists, this time, it is the wings or shoulders which are affected. With thin samples, back reflections become more important (Fig. 1a). Back reflections are evident in the thinnest films of Figure 2 at 1200-1300 cm^{-1}, where stronger apparent absorbance is seen above the main peak for the thin than for the thicker films, due to interference fringes. Due to these effects, fine structure is lost and the peak profiles are altered for overly thin samples (Fig. 2), which shift the barycenter of asymmetric peaks from their true values.

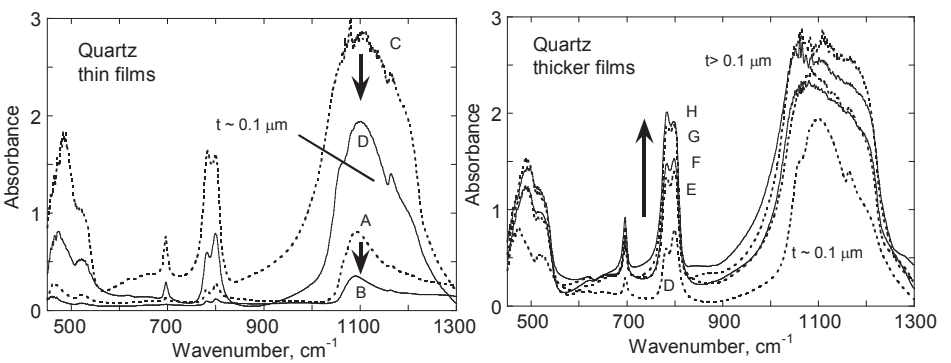


Figure 2. Absorption spectra of Lisbon quartz compressed in a diamond anvil cell. Left, effect of thinning the sample (heavy arrows). Right, effect of adding sample to produce a thicker film. Film D is ~0.1 μm thick. Films A and B are thinner. Films C, E-H are thicker than 0.1 μm, but remain in the submicron range. Film B is too thin to resolve the shoulders on the Si-O stretching peak near 1100 cm^{-1}. Film C is too thick, causing incorrect relative intensities and rounding of the most intense peak. Films D-H show that non-linear effects occur in the peaks near 800 cm^{-1} just before optically thick conditions are reached, whereas the changes in the peak near 1100 cm^{-1} shows that for optically thick conditions, spectra still change, but mostly in width and changes are artifacts due to low light levels (films are imperfect and light "leaks" through cracks. These spectra were not baseline corrected because most of the reflection is from the smooth diamond faces with high *r* values due to high *n*. [After Fig. 1 of Hofmeister et al. (2000).]

EBSCOhost - printed on 2/13/2023 5:26 AM via . All use subject to https://www.ebsco.com/terms-of-use

Accurately determining transmission profiles thus requires the proper thickness of sample for the peak of interest. Depending on the spectrum, a range of thicknesses may be needed, even for an individual peak, depend on the application. This filtering effect is very important for dispersions and remote sensing applications (discussed below).

In contrast to transmission experiments, for reflection experiments, optically thick and preferably opaque conditions are required. Otherwise, reflections from the second surface are recorded by the detector. For reflection, however, it is not A at the peak that is important, but A in the "valleys" i.e., at the transmitting frequencies. The value of r also has an effect. Figure 3 shows spectra of MgO: at 1 mm thickness, the sample is opaque in the absorbing region, but not in the near-IR.

Non-normal incidence alters path length, polarization and light loss through refraction. Refraction being important is obviated by Equations (4) to (6). For most measurements of transmission, the most important effects are increasing path length and mixing polarizations (Fig. 4). In addition, for materials which have high n (i.e., dense materials), refractive losses can exist at high angles of incidence, due to the critical angle being exceeded. This effect pertains to modern equipment wherein high power microscope optics converge light at steep angles, a cone of 60° in some cases. For applications involving the diamond anvils with $n \cong 2.5$, not only does path length change, but critical angles are exceeded (Fig. 5). Depending on location of the sample in the cell (i.e., on the specific ray path), light losses from refraction can exceed those from absorption (Hofmeister 2010); discussed further below.

For reflection experiments, Fresnel's equation is modified to account for the angle of incidence (Fahrenfort 1961). Roessler (1965) provides needed modifications for Kramers-Kronig relations. The classical dispersion relations (damped harmonic oscillator model) need only to be changed to include the angular dependence of r. The S-polarization, where electromagnetic field of the incident light, designated the y-axis, is normal to the surface (Fig. 4e), avoids polarization mixing. From Wyncke et al. (1990), with θ as the difference from the normal angle,

$$r = \frac{(\cos\theta - a)^2 + b^2}{(\cos\theta + a)^2 + b^2} \tag{8}$$

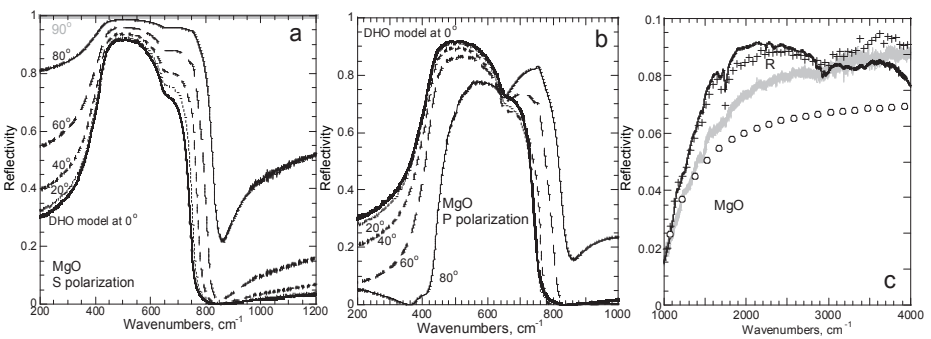


Figure 3. Calculated and measured reflection spectra of MgO. (a) The damped harmonic model at normal incidence (thick curve) is indistinguishable from the data. Calculations of R in the S-polarization at the different angles of incidence, as labeled, use n and k from the DHO model. (b) Calculations for the P-polarization. (c) Comparison of the DHO model (dots) to measurement of MgO crystals. + = singly polished 1 mm thick section. Black curve = doubly polished 1 mm section. Grey = a dry sample of similar thicknesses, showing that back reflections are present in mm sized samples. [After Fig. 4a of Hofmeister et al. (2003).]

EBSCOhost - printed on 2/13/2023 5:26 AM via . All use subject to https://www.ebsco.com/terms-of-use

where a and b are defined by n and k along the y direction:

$$a = \left\{ \left[(n_y^2 - k_y^2 - \sin^2\theta)^2 + 4n_y^2 k_y^2 \right]^{1/2} + (n_y^2 - k_y^2 - \sin^2\theta) \right\}^{1/2} \quad (9)$$

$$b = \left\{ \left[(n_y^2 - k_y^2 - \sin^2\theta)^2 + 4n_y^2 k_y^2 \right]^{1/2} - (n_y^2 - k_y^2 - \sin^2\theta) \right\}^{1/2} \quad (10)$$

Equations for the P-polarization (for which the field is perpendicular to that shown in Fig. 4e) are more complicated due to polarization mixing, involving n and k in the X and Z directions (Wyncke et al. 1990). As shown in Figure 3 for the very simple spectrum of MgO, increasing

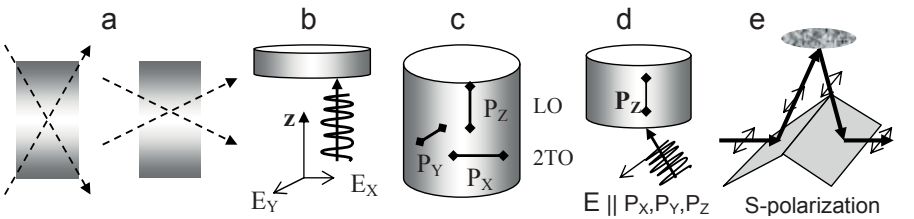


Figure 4. Effects of angle of incidence on path length and polarization on measurements. (a) Edge view. More focused beams (left) have longer path lengths. (b) An electromagnetic wave traveling along **Z** has its amplitude along X and Y. (c) Perspective view of atom pairs vibrating in three directions in the solid. Those with dipoles along X and Y are directly stimulated by light, because the electric field of the dipole is proportional to the polarization and in the same direction. These are the TO modes of the orientation shown. Indirect coupling stimulates the LO modes, which are equivalent to TO modes in the perpendicular orientations. For longer paths, more LO modes are excited. (d) During non-normal incidence, the electromagnetic wave has amplitude in the direction of all vibrating dipoles, so all are stimulated. As the angle increases from normal, more LO component is present, thus mixing polarizations. (e) Schematic of the S-polarization for reflectivity measurements.

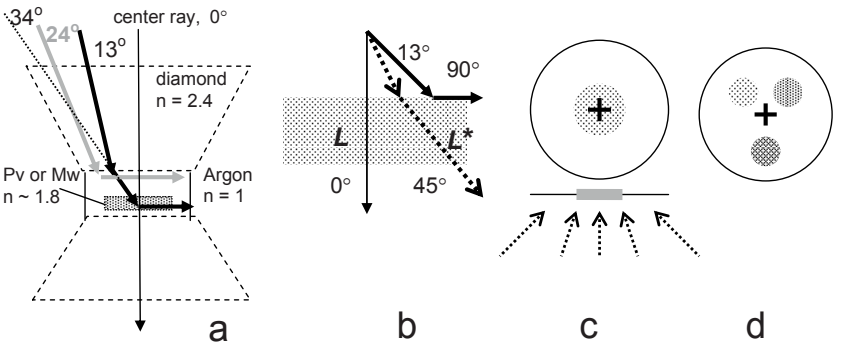


Figure 5. Schematic of refraction effects in highly converging beams in DAC measurements. (a) Critical angles in DAC spectroscopy. Thin arrow = perpendicular incidence. Grey arrows illustrate that light within a cone of 24.5° reaches the detector through gas media. Black arrows show that only light within a cone of 13.5° traversing dense minerals in the gas which have a high index of refraction reaches the detector. Thus, DAC spectroscopy is dominated by refraction, not absorption. (b) Effect of refraction on path length. Central rays experience sample thickness L. This 1-dimensional side view does not show the spatial perspective of the rays. For a sample covering most of the aperture, the average angle of incidence is ~45°, associated with path length L*. (c) Planar view of Keppler et al.'s (2008) experimental configuration, below which is a schematic of ray paths, showing that samples close to the center experience a greater proportion of central rays. (d) Planar view of Goncharov et al.'s (2008) experimental configuration, in which samples, being off-center, encounter larger angles of incidence and are thus more affected by refraction than centered samples. [Reprinted with permission of Elsevier from Hofmeister (2010) *Phys Earth Planet Interior*, Vol. 180, p 138-147.]

EBSCOhost - printed on 2/13/2023 5:26 AM via . All use subject to https://www.ebsco.com/terms-of-use

the angle of incidence in the S-polarization broadens the peak and r in the transparent regions becomes larger, whereas in the P-polarization, the peak is shifted towards the LO modes with some changes in the transparent regions.

Limitations of real measurements

Scattering. The above equations pertain to specular reflectance, i.e., the surface is polished like a mirror, and internal scattering from internal imperfections is negligibly small. Natural samples are not always gem quality. Scattering will reduce throughput, since beams are usually normal to the sample and form a fairly narrow cone of light, whereas scattering provides a large cone. Therefore scattering makes the measured reflectivity lower than intrinsic values whereas the measured absorptivity is higher than the material property.

Scattering depends on the size of the grains relative the wavelength of light (e.g., Bohren and Huffmann 1983). Elastic (Rayleigh) scattering occurs when the scattering centers are smaller than λ and has a strong affect, going as d^6/λ^4. For this reason, the quality of the surface polish is increasingly important as frequency increases, and UV measurements are particularly susceptible. For particles larger than λ, Mie scattering goes as d^2, and thus is not negligible.

Essentially, scattering contributes a baseline that depends strongly on frequency. Internal imperfections have a similar effect.

Reflection standards. For specular reflection, front surfaced mirrors are used. The National Institute of standards provides a calibrated Al mirror for high frequency. The calibration ends at 250 nm due to the above mentioned scattering problem. In the IR, gold mirrors suffice, in part because r approaches unity at low, far-IR frequencies, and in part because polishing achieves the required smoothness. For other types of reflection measurements, materials such as Teflon are used and the measurements must be considered as relative, particularly at visible wavelengths, where surface finish is important.

Errors originating in instrumentation

Several books and review articles cover errors in instrumentation, both for grating instruments used to acquire data at high frequency (e.g., Sommer 1989) and Fourier transform methods used at low frequency (e.g., Brault 1984; Griffiths and de Haseth 1986). A list of the most important and common sources of experimental uncertainty follows:

Uncertainties for all types of spectrometer. Detectors vary in their sensitivity. At low throughput, this property determines how weak a spectra feature can be resolved from the noise, and thus limits the strength of bands detectable (0% transmission has a spread) A greater number of scans can improve the noise, but this is limited by instrumental stability and statistics of averaging ($n^{1/2}$).

All detectors are less sensitive at the end of their spectral ranges. For this reason, better results are obtained in merging spectral segments when the overlap of ranges is large.

Although high detector sensitivity is needed to measure high A values, this can lead to nonlinear response. The problem is that references need to be collected at the same experimental conditions as the sample (excluding gains which can be changed and controlled independently) and that detectors saturate at high light levels. Saturation can be tested by examining the phase. Saturation is potentially a problem for synchrotron studies. It is immaterial whether a small aperture is used: if any part of the detector element is saturated, its response becomes non-linear.

Resolution is usually set to enable separation of components in a doublet. In studies involving changing (low) temperatures, higher resolution is needed to accurately determine spectral profiles. For grating instruments, resolution is determined by slit widths which can be more of a problem.

Alignment and stability are important: both cause spectral artifacts and baseline drift.

EBSCOhost - printed on 2/13/2023 5:26 AM via . All use subject to https://www.ebsco.com/terms-of-use

Uncertainties associated with grating spectrometers. High sensitivity of detectors, double beam configurations, and low expense make this type of instruments worthwhile. Many of the factors that make Fourier transform spectrometers essential for quantitative IR studies are not terribly important for visible-UV measurements. Potential problems are: source fluctuation, wavelength calibration, and stray light. With modern instruments, stray light is by far the most important.

Concerns in obtaining quantitative spectra from powders

The convenience of the powder dispersion method must be weighed against inaccuracies due to sampling effects. Problems include surface modes, scattering, fragments being opaque to partially opaque, and irreproducibility associated with highly polarizable compounds (e.g., Farmer 1974; Horak and Vitek 1978). Many of the problems arise from dispersions containing a size distribution of particles, and are thus mitigated by ball milling if the sample is sufficiently resilient or hand-grinding for long periods of time and testing for reproducibility of spectra (e.g., Boffa-Ballaran et al. 1998). Care in sample preparation can produce a fairly uniform distribution of grain-sizes that are optically thin. Complex structures with many bands and little differences among polarizations should produce good results. Glasses are somewhat problematic because these shear rather than crush. Clumping of grains may occur in any case, so it is important to recognize commonly occurring artifacts to ascertain how close powder dispersion data represent material properties, regarding both newer studies and older.

Trade-offs. If the dispersion consists of tiny and well-separated particles, some light can leak around the particles, which is similar to a film not covering the aperture (Fig. 6). Spectra in regions of high absorbance are especially affected in part because back reflections reduce throughput. Figure 6 also shows the effect of areal coverage on an ideal sample but one that is optically thick at the peak due to back reflections. Essentially, the line of "zero transmission" is defined by light leakage. This type of non-linearity is connected with detectors not being free of noise (discussed above). For this reason, commercial software often truncates raw absorbance at values of 2 to 4, which creates a spectra with the appearance of much noise at high absorbance. Optically thin conditions reduce the distortion, as implied by Figure 6 in the more transmitting regions.

If the dispersion is too dense, conditions are optically thick for frequencies near barycenters of strong peaks, which rounds peak tops. LO modes are exaggerated (e.g., Berreman 1963),

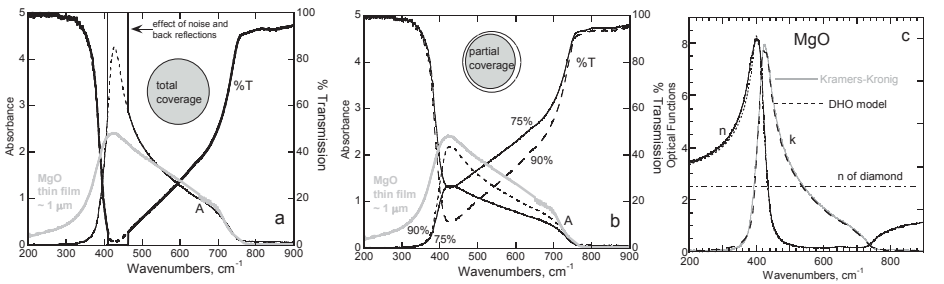


Figure 6. Illustration of how spectral artifacts are created from light leakage using optical functions for MgO obtained from reflectivity, and calculated for thickness of 1 μm. (grey curve = thin film data, thickness approximately 1 μm). (a) Broken lines = transmission and absorbance for a perfect thin film. Solid lines = functions whereby the measurement has null transmission at the peak, from back reflections or detector noise. (b) Broken lines = transmission and absorbance for a film that covers 90% of the aperture. Solid lines = functions for 75% coverage. (c) Optical functions from reflectivity datga in Fig. 2. Solid lines = n and k from Kramers-Kronig analysis. Broken lines = classical dispersion analysis. Dash-dot line = approximately constant index of refraction of diamond. [After Figs. 2c and 6a,b of Hofmeister et al. (2003).]

EBSCOhost - printed on 2/13/2023 5:26 AM via . All use subject to https://www.ebsco.com/terms-of-use

which increases the intensity on the high frequency side of each peak. These problems are easy to recognize by changing the dilution, which is analogous to thinning (Fig. 2). Once peak ratios cease to change with dilution, optically thin conditions have been met.

Clumping of the particles creates additional problems. The effect on the spectra is equivalent to a wide distribution of grain-sizes. Large particles or the thicker parts of particles are opaque, which alters the 0% transmission line at the frequencies where the sample absorbs. Some particles transmit on their edges, but not centers, which also alters the baseline. Light leakage still occurs which affects the 0% transmission line is altered as illustrated in Figure 6. The end result is that peak profiles differ from intrinsic shapes, being more rounded.

Filtering. Despite the numerous problems with dispersions, spectra so obtained from a range of particle sizes still resemble the intrinsic pattern. This occurs due to filtering: optically thin conditions dominate the spectra at any frequency, which means that at any given frequency, a certain range of thicknesses overwhelming contribute to the spectral results. Grains that are essentially transparent provide scattering, whereas grains that are essentially opaque contribute a baseline in a different way. Both lessen spectral relief. This problem in the laboratory is reduced by gathering spectra at different dilutions. When dilution has little effect, the results most closely represent the material property. Filtering to a large extent is the reason powder dispersion spectra represent mineral properties qualitatively.

Reflectance from powder. Pressed powders, even of soft materials, have a rough surface and reflectivity is reduced from that obtained from a mirror surface. Long et al. (1993) showed that optical constants obtained from pressed powders of calcite and gypsum are about ½ those obtained from specular reflectance. Similarly reflectivity of pressed clays (e.g., Glotch et al. 2007) is low, providing n that is overall too low, except at transmitting frequencies, n from powder reflection is relatively high (compared to the peaks) due to back reflections. In transmitting regions, k is appropriately low, but in absorbing regions k is about ½ that determined from thin films (Pitman et al. 2010).

Concerns regarding thin-film spectra obtained in the diamond anvil cell

In a converging (focused) beam, refraction losses can occur. This section evaluates the extent to which refraction affects infrared spectral results obtained in the diamond anvil cell (e.g., Hofmeister et al. 2003; and other papers). The worst case scenario is provided by MgO, which is a hard material and has a single, broad and strong IR band (Figs. 3 and 6). Hard materials resist deformation, so that the films produced are thicker and less uniform than those provided by soft materials and are thus more prone to yielding cracks and light leakage (c.f. MgO to brucite, $Mg(OH)_2$; Hofmeister and Bowey 2006). For substances with many IR modes, e.g., complex silicate minerals, the change of r and A from opaque to optically thick to optically thin to essentially transparent with ν is less rapid with frequency than for structures with few IR bands.

Comparisons provided by Pitman et al. (2010) between thin-film and reflectivity of single-crystals confirms that hardness of the material is key. For CaO which is soft, with a single IR band, good agreement of thin-film and reflectivity measurement from single-crystals (Galtier et al. 1972) is obtained. Better agreement is obtained for fayalite which is softer than forsterite. Comparisons of forsterite and fayalite show that two problems arise: (1) Agreement is worse for intense bands, which is consistent with the above discussions of light leakage and not meeting optically thin conditions. (2) Agreement overall is predicated on knowing the physical thickness of the films. For soft materials, which are commonly hydrous, thickness can be obtained from merging thin film spectra with appropriately scaled spectral measurements of thick films: the OH bands are on scale for both types of measurements (e.g., Hofmeister and Bowey 2006).

EBSCOhost - printed on 2/13/2023 5:26 AM via . All use subject to https://www.ebsco.com/terms-of-use

For MgO, thin film data and *A* calculated from reflectivity data do not match well at low frequency (Fig. 6). Several possible explanations exist. One is refraction because *n* is large, exceeding that of diamond, and *k* is small at low ν. Light leakage of ~15% explains the profile at higher frequency, but does not explain the profile below 300 cm^{-1}, and is consistent with MgO being hard and not forming perfect films, like soft CaO. However, CaO has similar optical functions and does not display such a discrepancy (Pitman et al. 2010), which indicates that index of refraction mismatch is not the main source of the mismatch. This finding is consistent with our beam condenser having a fairly small angle (~14°). Back reflections are unlikely, given the results on CaO and that allowing for back reflections did not explain the mismatch from 200 to 400 cm^{-1} (Hofmeister et al. 2003). Another possibility exists: namely, that MgO hydrates on the surface. Different amounts of hydration on the film and crystal would cause a material property difference and a spectral difference. For the crystal, the surface is chemically distinct, which may explain discrepancies among available reflectance spectra (Kachare et al. 1972; Hofmeister et al. 2003; Sun et al. 2008), although back-reflections and polish should also be considered. Further study is needed to resolve this problem.

Obtaining quantitative results from thin films requires accurate and independent determinations of thickness, production of uniform films without cracks that leak light, and care to ensure optically thin conditions are met. From Figure 2, multiple measurements of different thicknesses are needed.

Propagation of errors

Basic error analysis is provided by Bevington (1969). For spectra, uncertainties depend on frequency.

Errors are propagated by comparison to a reference, spectral subtraction, and averaging. Let us describe one spectral segment as X with error σ_X and another as Y with error or variance σ_Y, and the combination as Z with σ_Z. Note that all variables depend on ν. For the simple case of division or multiplication (Z = XY or Z = X/Y, the error in the result is

$$\frac{\sigma_Z^2}{Z^2} = \frac{\sigma_X^2}{X^2} + \frac{\sigma_Y^2}{Y^2} \tag{11}$$

For addition or subtraction $Z = aX + bY$

$$\sigma_Z^2 = a^2\sigma_X^2 + b^2\sigma_Z^2 \tag{12}$$

Although averaging serves as a smoothing function and reduces errors, it does not remove errors.

A robust discussion of errors in IR spectral data processing is provided by Gillette et al. (1985). Because their concern is multi-component analysis, the results pertain to determining phases from remotely sensed spectra through comparison to laboratory data.

Errors arising during data processing and extracting spectral parameters

Different approaches to extracting peak parameters from spectra each have their advantages, disadvantages and trade-offs. One practice that should be avoided is smoothing, which effectively decreases resolution.

Regarding reflectivity data, both Kramers-Kronig and classical dispersion analyses are used (e.g., Wooten 1972). Good results are predicated on good spectra, which mean that absolute *r* values are needed. Here, errors and uncertainties arise because spectra sometimes have fewer fundamental modes than expected, but sometimes have additional overtone-combination bands that are activated through resonances. One effect does not preclude the other, although in simple spectra such as that of spinels overtones are more obvious (e.g., Hofmeister and Mao 2001). Unresolved doublets cause the dielectric functions to "reverse" at the position of the

EBSCOhost - printed on 2/13/2023 5:26 AM via . All use subject to https://www.ebsco.com/terms-of-use

doublet, which is useful, but annoying because the peak parameters are then untrustworthy. In this case, using classical dispersion analysis is required (e.g., Giesting and Hofmeister 2002).

Regarding absorption-transmission spectra, which are more commonly collected, several different approaches for extracting peak parameters exist, as follows.

Fitting. Peak fitting is mostly done to absorbance spectra which have shapes similar to Gaussian, Lorentzian, or a mixture. Theoretically, these are not the correct shapes: instead peaks in e_2 are Lorentzians. This approach forces fits, but gives reasonably accurate parameters. Weak peaks ($n \sim 1$) are better fit than strong ones because $A(\nu) = 2\pi\nu e_2(\nu)/n(\nu)$, from combining Equations (5) and (7).

With currently available computational hardware and software, one can fit absorption spectra to a damped harmonic oscillator model (e.g., Pitman et al. 2010). There are tradeoffs in fitting, even with a correct form. Quantitative results require quantitative spectra, discussed above.

Fourier deconvolution. This method (Kauppinen et al. 1981a,b) is available through commercial software although infrequently used in geoscience. If the signal-to-noise ratio of a spectrum is high, overlapping bands can be resolved. This method induces spectral noise away from the peaks, but makes no assumption about peak shapes and is therefore useful for deciphering which of the strong, overlapping bands in a spectrum is a doublet. Knowing the positions of all fundamental modes in a spectrum is are needed to determine density of states (e.g., in calculating physical properties).

Auto-correlation method. This approach provides peak widths that are not intrinsic to the material but is very useful in constraining the changes across a series of samples (Salje et al. 2000). In practice, spectra segments are examined. It would be useful to test whether shifting the segment changes the trends in widths or frequencies. Another unexplored question concerns how peaks near each end of the segment respond to the analysis.

Emission spectra

These experiments are less common than transmission or reflection studies and therefore less well-understood. All experiments involve reflection to some degree. Emission spectra are similar to transmission measurements in that optical thickness controls the degree to which reflection affects the measurements. Hence, experiments record emissions, not emissivity, which cannot be directly measured. Because sample surfaces are rough, it is also necessary to discuss the effect of scattering. A detailed analysis is provided because some important misconceptions are entrenched in geology, planetary science, and astronomy.

Problems in ascertaining emissivity from emission spectra of minerals. Emission spectra of large grains in planetary science have been misinterpreted as providing emissivity due to two interwoven factors. (1) Back reflections exist for large grains or samples, providing a reduction of $1-r$ (Fig. 1b). This behavior is seen in emission spectra, but this has been misinterpreted as emissivity because Kirchhoff's law for metals and semiconductors also provides $\varepsilon = 1-r$, but for different reasons, discussed below. (2) Minerals are dielectric materials with low lattice thermal conductivity and low absorption coefficients which impede radiative transfer. As discussed by Brewster (1992), the combination of these physical properties in ceramics and glasses (which are similar to partially transparent minerals) causes the length scale of significant temperature change to be comparable to the mean free photon path, and thus the isothermal requirement of Kirchhoff's law is not satisfied, so $\varepsilon \neq 1-r$. As discussed by Bates (1978), transmittivity must be considered in Kirchhoff's law for dielectrics, as follows.

Basic equations. We begin with the fundamental form for Kirchhoff's law, which states that for a body in thermodynamic equilibrium, absorptivity equals emissivity,

$$\alpha = \varepsilon \tag{13}$$

EBSCOhost - printed on 2/13/2023 5:26 AM via . All use subject to https://www.ebsco.com/terms-of-use

where ε is defined as the light actually emitted divided by I_{bb} (e.g., Siegel and Howell 1972; Bates 1978: Brewster 1992). Kirchhoff's law is only *strictly* true when there is no net heat transfer to or from the surface. We use the fundamental form because this is less affected by grain-size than the relations of ε with spectral functions such as *r*. Planck's blackbody function is:

$$I_{bb}(\nu) = \frac{2h\nu^3}{c^2}\left[\frac{1}{\exp\left(h\nu / k_B T\right) - 1}\right] \tag{14}$$

where h is Planck' constant, k_B is Boltzmann's constant, and c is the speed of light. In one direction,

$$\varepsilon(\nu, d) = 1 - \exp[-dA(\nu)] \tag{15}$$

The total emissions, if no reflections occur (e.g., grain to grain in a homogeneous mantle, where $n_{medium} = n$ in Eqn. 4) are described by:

$$E = \varepsilon I_{bb}, \text{ inside a homogeneous medium} \tag{16}$$

The fundamental form of Kirchhoff's law (Eqn. 13) states that emissivity will be high where transitions occur, which is consistent with physical principles. If a vibrational mode is excited, it will emit energy near the transition frequency in order to return to the ground state from the excited state. However, measurements of emission spectra are complicated by the presence of back reflections (Fig. 1b). Hence, in all cases where the sample butts against air or vacuum, emitted light goes as

$$E = \varepsilon I_{bb}(1-r), \text{ for a surface against "space"} \tag{17}$$

Grain-size is crucial because this affects the amount of light reflected and that emitted, analogous to transition measurements, discussed above. Thus, the emissions will depend on optical thickness (Fig. 1).

Problems exist in the planetary science literature mainly due to use of representations other than Equation (13) for Kirchhoff's law. In this body of literature, large grains are measured, which should be optically thick, so Christensen et al. (2000) and Salisbury et al. (1991), for example, used the approximation of $\tau = 0$ (in Eqn. 1) to arrive at $\varepsilon + r \cong 1$. However, this approximation is only valid for materials that very strongly absorb, such as metals and semiconductors. The correct form for dielectrics (e.g., partially transparent minerals) is the extended form of Kirchhoff's law:

$$\varepsilon + r + \tau \cong 1 \tag{18}$$

which was derived by Bates (1978) by considering forward and backwards scattering at an interface. Detailed analyses are presented by McMahon (1950) and Gardon (1956). Equation (18) was verified using thermodynamic considerations (McMahon 1950). The exact form (Bates 1978) is

$$\varepsilon + r + \tau = 1 + \varepsilon r\tau + r\tau \tag{19}$$

although the cross-products are small. Rearranging terms in Equation (19) gives:

$$\varepsilon = 1 - r - \tau + \varepsilon r\tau + r\tau \cong 1 - r + 2r\tau \text{ (optically thick conditions)} \tag{20}$$

Although τ is small, it is non-negligible, making ε larger than $1-r$ for optically thick conditions. For optically thin conditions, rearranging terms in Equation (19) gives:

$$\varepsilon = \frac{1 - r - \tau + r\tau}{1 + r\tau} \cong \frac{1 - \tau}{1 + r} < 1 \text{ (optically thin)} \tag{21}$$

Under optically thin conditions, it is simpler and more direct to use Equation (13) ($\varepsilon = \alpha < 1$).

We now discuss various measurements from the literature.

EBSCOhost - printed on 2/13/2023 5:26 AM via . All use subject to https://www.ebsco.com/terms-of-use

Emission experiments under optically thin conditions. Thin films of molten nitrates studied by Bates and Boyd (1973) meet optically thin conditions, so $\alpha = \varepsilon < 1$ (Fig. 1c). Emitted light follows Equation (15). However, transmission dominates optically thin conditions, so the light lost due to reflection ($1-r$) equals ($\alpha+\tau$). Since α is small and $\tau \sim 1$, then $1-r$ is reasonably approximated by unity (Eqn. 21). For thin films and small grains, thermal equilibrium exists, so conditions underlying Kirchhoff's law are met. Emission peaks of the salts point up (Bates and Boyd 1973). In essence, back reflection at the interface exists, but the rapid change of absorptivity or absorption with frequency (e.g., Fig. 2) swamps out the small reflection losses. It is also relevant that emission experiments are not taken from mirror polish surfaces, but typically from grains, and thus scattering alters r through its dependence on angle (Eqns. 13-15), mainly reducing the difference in reflection at peaks vs. valleys. Importantly, as film thickness increases, the height of the most intense peak decreases (e.g., Bates and Boyd 1973) due to r being largest for the intense peak. This behavior parallels the dependence of absorptivity on thickness in transmission experiments (Fig. 2)

Another case of optically thin conditions, one in which thermal equilibrium is met, concerns dust in circumstellar environments. These dust grains are small, ~μm sizes, so optically thin conditions exist, particularly in the far-IR in which peaks are weak. High frequency starlight warms the grains at visible to UV frequencies, which then re-radiate the heat at low frequencies, due to low temperatures. Thermal equilibrium exists, due to the dust being a suspension in vacuum: no conductive mechanism exists and temperatures are governed solely by radiative transfer from the central star. Spectra from dust grains in the proto-planetary nebula NGC-6302 are thus emission spectra, which is entirely consistent with peaks pointing up (Fig. 7a). Far-IR peaks of silicates and complex oxides are narrow, leading to a multitude of lines. Obviously, many minerals constitute the nebula. One obvious phase is forsterite (Molster et al. 2001) for

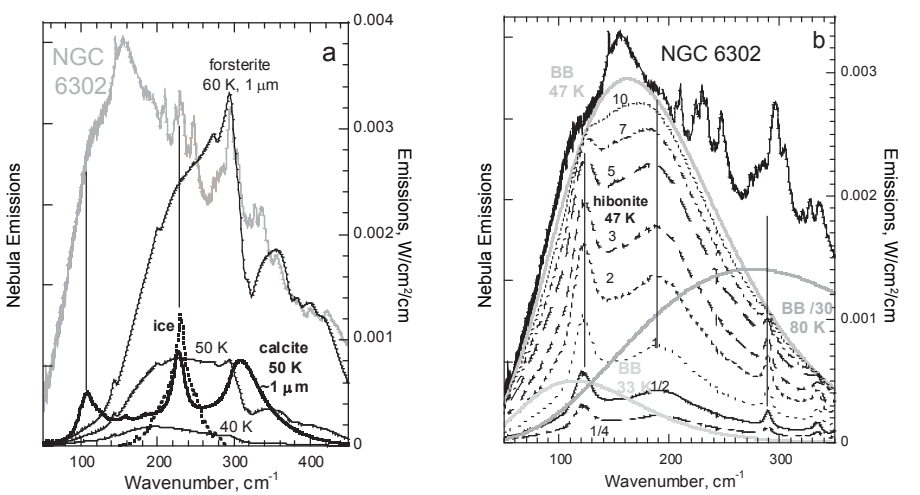


Figure 7. Emission spectra of dielectrics under optically thin conditions. (a) Emissions from small grains in the dusty nebula (grey curve) measured by the Infrared Space Observatory, provided by T. Lim and J.E. Bowey and also presented by Molster et al. (2001) and others. Emission spectra (left axis) were calculated from thin film absorption spectra for 1 μm grain size and temperatures as labeled. Ice was frozen on the window at 77 K. Vertical lines connect mineral spectra with the nebula peaks. (b) Comparison of nebula dust emissions (black curve) to blackbody curves (grey) to emissions of hibbonite grains of various sizes as labeled (patterns). These spectra were calculated from absorption spectra, assuming that back reflections are negligible. [Reprinted with permission of Elsevier from Hofmeister et al. (2004) *Geochim Cosmochim Acta* Vol. 68, p 4485-4503, Fig. 5.]

EBSCOhost - printed on 2/13/2023 5:26 AM via . All use subject to https://www.ebsco.com/terms-of-use

which the match is shown. Figure 7b shows that the nebula grains emit over ~30 to 80 K as well as the dependence of emissivity on grain size for hibonite, which may also present the nebula. The large number of peaks makes it difficult to exactly determine the mineralogy (cf. Kemper et al. 2002 who favor calcite; vs. Hofmeister et al. 2004 who favor calcium aluminates), but nonetheless it is obvious that more light is emitted at the transition frequencies, in accord with Equation (13).

Expected behavior of ε as grain size increases into optically thick conditions. Emissivity reaches its maximum of unity for hibonite grains near $d \sim 10$ μm at 47 K. At different temperatures optically thick conditions will be achieved at different grain size. Nonetheless, Fig. 7b demonstrates that the maximum emissivity of unity is reached at fairly small d. Larger grain sizes cannot have less emissivity, per the engineering definitions of optical properties (Eqn. 1 and text beneath Eqn. 13). Peak strengths vary among the bands (Fig. 2) but IR fundamental modes are not all that different from one another in a given mineral or amongst minerals (Hofmeister and Bowey 2006). Hence, sub-mm grains meet optically thick conditions (Fig. 1d) and will have $\alpha = \varepsilon = 1$ in thermal equilibrium. Inserting $\varepsilon = 1$ in Equation (15) shows that emissions from large grains will go as $I_{bb}(1-r)$, due to the reflection at the surface. Thus, for the d ~0.8 mm grains studied by Christensen et al. (2000) less light is received at frequencies where transitions occur, i.e., peaks point down as seen in their spectra (Fig. 8a). The appearance of their emission spectra is due to back reflections, and in no way constrain emissivity.

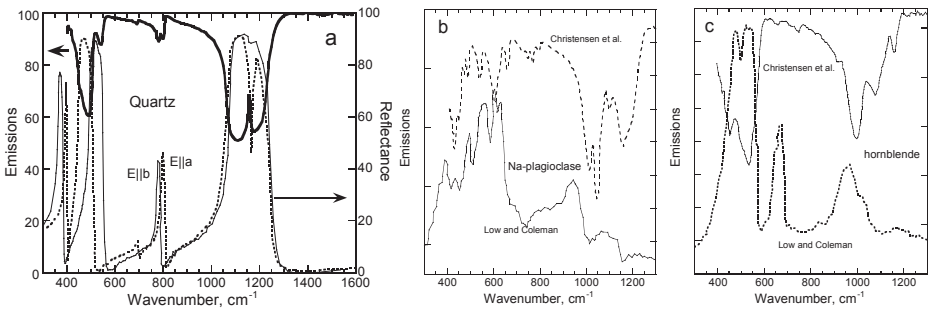


Figure 8. Emission spectra of dielectrics under optically thick conditions (~1 mm grain-size). (a) Quartz emissions (heavy line) from Christensen et al. (2000) compared to polarized specular reflectance= r/100 of Spitzer and Kleinman (1961). (b) Comparison of emissions from albitic plagioclase from Christensen et al. (2000) to that of Low and Coleman (1965). The compositions are unlikely to be exactly the same. (c) Comparison of hornblende emissions from the same sources.

Emission experiments under optically thick conditions. To understand the shape of emission spectra under optically thick conditions, one must recognize that reflection spectra (e.g., Fig. 3) are determined using plane polarized light, which distinguishes TO from LO modes (Fig. 4, see discussions in Wooten 1972; Burns 1990). At frequencies between the TO and LO modes, r determined in reflectivity measurements is large and more or less constant for strong peaks but for weak peaks, r is low and the shape is pointy (Fig. 8a). Different shapes occur for strong and weak peaks in reflection measurements because the separation of the TO and LO mode for any given peak depends on its oscillator strength (Wooten 1972). The separation also makes reflectivity high and broad for the strong modes. Strong peaks are pointy in absorption-transmission measurements (Fig. 2) because only the TO components are sampled. In contrast, blackbody radiation is not plane polarized, but is scattered, so polarizations in emission spectra are mixed (Fig. 4) and TO and LO modes are not wholly distinguished. Due to essentially negligible TO-LO splitting, r is lower for emission spectra and peak shapes aris-

EBSCOhost - printed on 2/13/2023 5:26 AM via . All use subject to https://www.ebsco.com/terms-of-use

ing from reflection are close to Lorentzian shapes, as in absorption spectra. Consequently the reflectivity loss for all peaks measured in emission measurements of large grains (optically thick conditions) involves sharp peaks that point down, and an appearance of upside down absorption spectra (cf. Fig. 8a to Fig. 2a). Much of the variation in oscillator strength is retained, but not the flat tops due to optically activity over a comparatively wide range of frequencies. In addition, scattering decreases the relief in r between the emitting and reflecting spectral regions (Fig. 3). Because of the scattering, hemispherical reflectance is a better match than biconical (e.g., Salibury et al. 1991) or specular, shown here. Brewster (1992) and Siegel and Howell (1972) discuss the various types of reflection and emission experiments.

In summary, emission spectra from large dielectric grains do not quantify emissivity beyond $\varepsilon \sim 1$, although they do provide a reflectivity spectrum compatible with scattering, which is relevant to some applications.

That $\varepsilon = 1$ for large grains has not been recognized in the remote sensing literature (e.g., Salisbury et al. 1991; Christensen et al. 2000); instead, the factor of $(1-r)$ has been considered the emissivity. Their reasoning was for $\tau = 0$ for an opaque or optically thick material, Equation (1) provides $1 = r + \alpha$ and thus $1 = r + \varepsilon$ from Kirchhoff's law. However, this form of Kirchhoff's law is only valid for metals and semi-conductors where the absorption index is large and isothermal conditions hold, but as pointed out by Brewster (1992), i.e., isothermal conditions needed for Kirchhoff's law are not met in electrical insulators (silicate and oxide minerals). Moreover, if emissivity did equal $1-r$, then the light received would be $(1-r)^2 I_{bb}$. If this truly were the case, Christensen et al.'s (2000) database would consist of spectra with peaks pointing down that are more rounded than in the reflectivity spectrum, not more pointed. These experiments involve mineral grains heated to 80ºC, which shed light to the detector. Thermal equilibrium does not exist between the detector and sample, due to each being held at their respective temperatures. However, thermal disequilibrium is not entirely the cause of failure to meet Kirchhoff's law for dielectrics. The problem is that relating Kirchhoff's law to r for partially transparent minerals also needs to account for transmissivity, even for an optically thick material (McMahon 1950; Gaudon 1956; Bates 1978), see Equations (18)-(20). This is the case because light is emitted from the surface: specifically, light is emitted from whatever skin-depth can transmit. Due to this physical behavior, ε cannot equal $1-r$ for minerals.

Emission experiments under optically thick conditions with a surface temperature gradient. Emissivity similar to absorptivity was recorded in earlier experiments by Low and Coleman (1966) for grain-sizes and mineral compositions similar to those of Christensen et al. (2000). The difference in results arises from the configuration used by Low and Coleman (1966) which involves a dry ice block separated the sample which is held at slightly lower temperature (20 °C) than the detector at 24 °C. The sample radiates its heat to the dry ice block, creating a thermal gradient at the surface, which make the conditions effectively optically thin. Data on albite and hornblende from both studies are compared in Figure 8bc. For albite, it is clear that some, but not all, emissions are lost to reflection near 1000 cm^{-1} for the strong Si-O bending modes. The hornblende spectra differ from these two studies, likely due to compositional effects.

Summary. Hopefully, it is clear that the database of Christensen et al. (2000) does not provide emissivity, as these authors assume, but reflectivity associated with back scattering. For the large grains examined, $\varepsilon = 1$. Given the above, emissivity of small to intermediate size is best computed from absorption coefficients (e.g., Hofmeister et al. 2003, 2004). The above findings pertain to asteroid surfaces, discussed below.

EBSCOhost - printed on 2/13/2023 5:26 AM via . All use subject to https://www.ebsco.com/terms-of-use

EXAMPLES OF SAMPLING PROBLEMS IN THE LABORATORY

The above descriptions of errors, uncertainties, and potential problems in spectroscopy included several examples with varying amounts of details. It should be clear that absolute values of reflectivity and transmissivity are difficult to establish because back reflections affect both types of measurements, which precludes direct measurement of absorptivity. Similar problems exist in emission measurements. Refraction affecting results is generally not considered, but this has a strong effect on high frequency measurements using strongly convergent optics coupled with diamond anvil cells. How data are affected is portrayed in the figures presented so-far. This section provides a few additional examples and describes how reflections in transmission measurements can be useful.

Overly large grains in absorbing regions

In the astronomy literature, mid-IR peak positions obtained from dispersions have been shifted by ~0.3 μm to allegedly account for effects of the KBr matrix (Dorschner et al. 1978). Different peak positions have been observed at low absorbance for very dilute fine-grained dispersions of SiC (Borghesi et al. 1985) than for standard dilutions with absorbance of 1 to 2.5 (Papoular et al. 1998). Because peak positions of SiC are relevant to circumstellar dust of carbon stars, we collected thin film spectra on similar samples. The dilute dispersion (Borghesi et al. 1985) agrees with our thin film data, showing that KBr is not the cause of the shift (Speck et al. 1999). Silicon carbide, like MgO has one strong IR band with some structure, and therefore optically thin conditions at the transition frequency require very low thickness (i.e., extreme dilutions). The origin of the so-called KBr correction is apparently use of overly large grains, which produced a large LO contribution and shifted the peaks from intrinsic values obtained from reflectivity measurements (Spitzer et al. 1959). SiC is more prone to such errors than many materials due to its single, broad, strong band and this material being very hard, making preparation of fine grain sizes difficult.

Similarly, the quantitative results of Spitzer et al. (1959) on absorption coefficients were discounted in the astronomical literature because dispersion data gave much lower values, and a better match to spectra of the dust around the star (observational data). For large grains, as discussed above, some of the particulates are opaque and do not contribute to the peaks, but to the baseline. Repeat measurements of a wide variety of SiC samples (Pitman et al. 2008) confirmed the accuracy of the Spitzer et al. (1959) absorption coefficients. The better match of dispersion spectra to observational data is connected with back reflections existing for the dust suspensions in space and the filtering mechanism discussed above, whereby particles with sizes appropriate to optically thin conditions at any given frequency dominate the recorded spectrum.

Too small of crystals for the near-IR transparent region

If a crystal is thin in a transparent spectral region, absorptions are overridden by reflections. The near-IR (to visible, if transition metals are lacking) is generally transparent. From Equation (1):

$$\tau = \frac{1-(r-1)^2 e^{-Ad}}{1+r^2 e^{-2Ad}} \tag{22}$$

If Ad is sufficiently small to be negligible, then $\tau = (1-r)/(1+r)$ and can be related to n through Equation (5) (the limiting method: Lipson 1960). Hence, very thin crystals provide information on reflection and refraction in highly transparent regions. If the polish is not sufficiently fine and internal imperfections exist, then these are recorded, and r includes intrinsic and scattering contributions.

EBSCOhost - printed on 2/13/2023 5:26 AM via . All use subject to https://www.ebsco.com/terms-of-use

In order to obtain information on attenuation (A or k), which is needed for radiative transfer models, either for deep Earth or astronomical applications, one can compare two thin crystals designated as "thin" and "thick" (the difference method: Hofmeister et al. 2009):

$$A = \frac{a_{thick} - a_{thin}}{d_{thick} - d_{thin}} \quad \text{and} \quad r = 1 - e^{(d_{thin}A - a_{thin})/2} \tag{23}$$

The difference method assumes that the two crystals are exactly the same, including degree of polish and imperfections, which is difficult to achieve.

Alternatively, very thick sections can be used in the transparent region. However, this requires gem quality samples. Because of these difficulties, the compilation by Palik (1998) omits k values in the near IR, which are $<10^{-6}$.

Making use of back reflections in transmission measurements. Measurements on SiC illustrate the difficulties in determining A in transparent regions. Raw data (Fig. 9a) show a steep rise to the UV which means fairly thin samples need to be examined. Platelets differing by a factor of 6 in thickness have the same uncorrected, raw absorbance, which compares closely to a gem quality sample that is 100 times thicker. Calculated values of A (not shown) and k (Fig. 9b) for these samples agree below 20000 cm^{-1} but are null, within uncertainty. The difference method agrees with direct measurements and Kramers-Kronig or classical dispersion analysis, on average for n over the range of our measurements. For k, agreement is good with Kramers-Kronig, but not with absorption data (Fig. 9b). Part of the disagreement with other absorption studies is likely related to impurities and also that SiC is non-stoichometric due to nearly complete miscibility of Si in C (the diamond structure) and vice versa (Kimura et al. 2005). Both types of impurity are difficult to characterize at low levels. To determine A and k in the near IR for SiC will require large, gem quality samples, measurements that extend to the UV, as well as data on trace impurities.

Optical functions of olivines in the near IR. Zeidler et al (2011) measured mm to sub-mm sized samples in the near-IR to visible (Fig. 9c). For such thicknesses, the *d-d* electronic

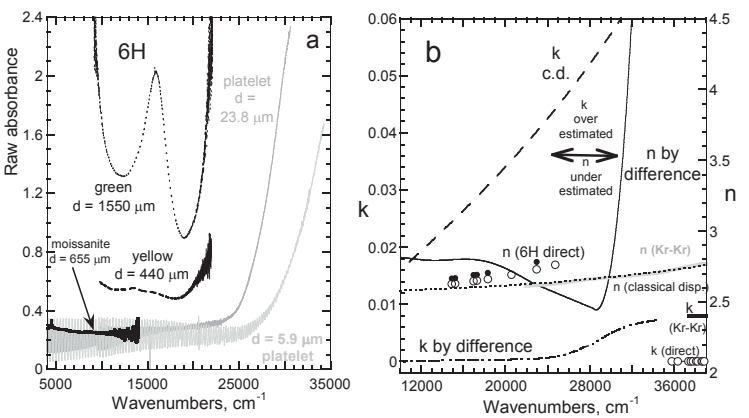


Figure 9. The transparent spectral region for SiC. (a) Raw data in common logs of various samples of SiC with thickness as labeled. Coloration is from impurities, present in all but the moissanite. (b) Processed data on the complex indices of refraction, applying the difference method to the two platelets using a high-order polynomial fit to the results. These are compared to direct measurements of n (circles: Shaffer and Naum 1969); to classical dispersion (dots and dashes) and Kramers-Kronig analyses (triangles) of UV data from Philipp and Taft (1960), as well as direct measurements of absorption (grey: Philipp 1958). [After Figs. 7 and 8b of Hofmeister et al. (2009).]

EBSCOhost - printed on 2/13/2023 5:26 AM via . All use subject to https://www.ebsco.com/terms-of-use

transitions are on-scale but as a consequence, absorptions in the near-IR are zero within experimental uncertainty. The authors corrected for reflections, using n from Palik (1998) and Equation (6). The stated source, however, does not report indices of refraction for olivine, although data on n is available in the mineralogical literature, so it is unclear what was subtracted. More importantly, at these thicknesses, imperfections, as shown in the micrographs of Zeidler et al. (2011) and degree of polish control transmission data.

Our largest sample of olivine (Fo90 from Spat, Pakistan) have some rutile needles and thus some internal scattering. Nevertheless, I collected data in the near-IR from these samples trying to avoid the rutile impurities to estimate k near 5000 cm^{-1}. Our reflectivity data (not shown) are consistent with k~0 and being independent of frequency, so Equation (6) is valid. Values from refractometry are n = 1.65 **E**||**b**, = 1.67 for **E**||**c** and =1.69 for **E**||**a** (e.g., Deer et al. 1966). From Figure 10, k obtained from the thick sections is an order of magnitude lower than that obtain from ~1 mm sections by Zeidler et al. (2011). Their San Carlos sample lacks OH and should be less absorbing. Their larger k values thus record scattering, not intrinsic values. Our best estimate is $<3\times10^{-6}$ from 4000-5500 cm^{-1}. A firmer constraint requires gem-quality samples of several mm thickness and a fine polish, and use of reflectivity vs. frequency (either measurements or classical dispersion analysis).

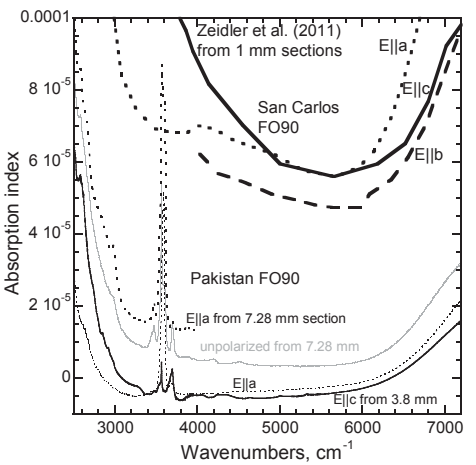


Figure 10. Comparison of k for the transparent region of Fo90 olivine obtained from thin sections (heavy lines, Zeidler et al. 2011) and thick sections (light lines, this work). Our sample has hydroxyl and rutile needles and should have higher absorbance than pure olivine. Correcting for back reflections caused k to go below zero for our 3.8 mm section, indicating that k = 0 within uncertainty.

Information on *d-d* transitions in the UV may pertain to band assignments

Orthopyroxene spectra. Significantly lower UV charge transfer is observed for colorless (En96) and green (En90) gemstones, than for yellow (En98) and orange (En89) gemstones (Fig. 11a; Hofmeister 2012). Sharp and weak peaks are similar to previous studies of orthopyroxenes: assignments are based on the summary of Rossman (1988). The upturn near 350 nm produces yellow coloration in En98. This feature is resolved at 300 nm in colorless gemstone and in thin sections of yellow and green gemstones (Fig. 11b) and is attributed to charge transfer of Fe^{3+} with O^{2-}. Protoenstatite has a small amount of Al, which we tentatively assign to the 314 nm band. A very small amount of Fe^{3+} is present in En96. Concentrations are significant in the remaining samples, increasing in the order En96 < En90 < En98 ~ En89. Green En90 has Cr^{3+} and colorless En96 has Al^{3+} both of which limits the amount of ferric iron through charge balance.

From Figure 11, absorption coefficients in the visible and UV regions differ by a factor of about ×100. Studying the *d-d* electronic transitions requires thick (>1 mm) samples for

EBSCOhost - printed on 2/13/2023 5:26 AM via . All use subject to https://www.ebsco.com/terms-of-use

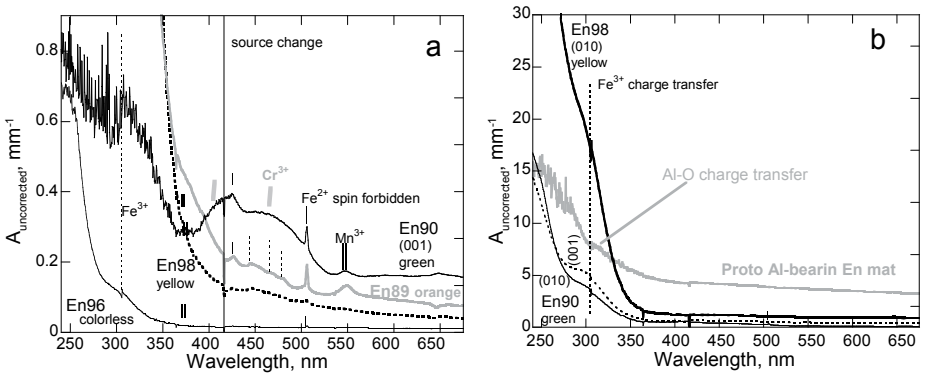


Figure 11. UV-visible unpolarized spectra of mostly electronic transition of Fe ions. Raw absorption coefficients are shown (common logs, not corrected for reflections. (a) Large gemstones. Thin line = green En90, (001) section collected from a sample with L = 2.05 mm. Sections for all other gemstones were planes containing the c-axis. Thicknesses used were 5.37 mm for En96; 1.62 mm for En 98; and 0.965 mm for En89. For large L, reflection corrections have little effect. Vertical lines indicate peak assignments (solid = spin-forbidden Fe^{2+}, double = Mn^{3+}; dotted = tetrahedral Fe^{3+}; grey = octrahedral Cr^{3+}). Peaks at 489 and 646 nm exist in several spectra and may be artifacts. Spikes at 315 and 416 nm are instrumental artifacts. Only En89 has a peak at 380 nm, see text. (b) Thinned gemstones. L = 0.055 mm for En98; 0.10 mm for En90 (010); 0.20 mm for En90 (001). The peak at 300 nm is resolved in thinner sections of the gemstones is assigned to Fe^{3+} charge transfer with oxygen. En100 has a peak at 314 nm which is assigned to Al-O charge transfer, because no Fe is present. This sample has the protoenstatite structure. [After Fig. 3 in Hofmeister (2012). For online access see *www.schweizerbart.de*.]

low concentrations of various transition metals, which is generally pursued, limiting data collection to below ~320 nm, although many available instruments reach shorter wavelengths. Our samples have bands near 300 nm that can be resolved for ~0.1 mm sections, whereas bands below 250 nm require sections with thickness of ~0.05 mm, which are difficult to prepare, or reflectivity measurements. The later approach requires a reflectivity standard, but mirrors commercially available are calibrated above 250 nm, due to the above mentioned problems with polish. Yet, a complete understanding of electronic transitions requires such types of data.

Possibly, the decades old controversy regarding band assignments of Fe-rich olivine (Wood 1981; Burns 1985) could be resolved by collecting spectra at higher frequencies.

REMOTELY SENSED SPECTRA AND OBSERVATIONAL DATA

Spectra from remote objects are obtained under uncontrolled conditions and contain a mixture of absorption, emission, and reflection features. To relate these data to laboratory measurements of minerals, we need to understand how sampling conditions affect both laboratory spectra and remote sensing measurements. The preceding sections cover laboratory derived spectra: many of these same problems exist in remotely collected spectra. Note that it is necessary to distinguish between two different cases, involving large bodies vs. small grains, because grain-size differences of objects from which spectra are remotely obtained are associated with different types of uncertainties and errors, just as in laboratory studies. The application mostly covered in the planetary science literature involves inferring the mineralogy of large bodies (e.g., asteroids) from reflectance and emission measurements over the IR to visible regions. For this case, grains are relatively large. In contrast, behavior associated with small grains are relevant to astronomy where the goal is to understand characteristics of suspended dust in environments such as a nebula, which emits, absorbs, and scatters far-IR to

EBSCOhost - printed on 2/13/2023 5:26 AM via . All use subject to https://www.ebsco.com/terms-of-use

mid-IR light to varying degrees. The data involved in these two applications are very different, because conditions are presumed to be optically thick for large bodies but optically thin for small grains. We therefore use the terms "remotely sensed spectra" from the planetary science literature when discussing large bodies and "observational" data from the astronomy literature when discussing dispersions of dust in space.

Ascertaining surface mineralogy of large bodies

The example chosen is asteroids, wherein their cold temperatures permit separation of emission from reflection regimes. Misinterpretation of laboratory emission spectra, discussed above, has led to incorrect data processing of asteroid emission spectra. Vesta is selected due to timeliness (the Dawn mission).

Effect of temperature on spectra. Within any given frequency range, temperature (T) controls whether a large object emits or reflects light. Blackbody emission curves depend strongly on T and frequency (Fig. 12a). The 1st law of thermodynamics requires that the flux from an asteroid match that received from the Sun (Fig. 12b): roughly speaking, the areas under the curves must be equal. Due to the properties of Planck curves, Vesta, which is cold ($85 < T < 255$ K; e.g., Lucey et al., 1998) outputs virtually all its light below 2200 cm^{-1}, and therefore emits in the infrared but reflects light in the near-IR to visible. This separation simplifies analysis.

Effect of grain-size on spectra. Grain-size controls whether peaks are superimposed positively or negatively on the baseline, and strengths of the features. For an opaque surface, $1 = \alpha + r$ (Eqn. 1). Although asteroids are large and opaque, in contrast, the dust grains on their surface are partially transparent. For the part of the asteroid that is preferentially sampled, $1 = \alpha + r + t$, where $t = I_{tran}/I_0$ is transmittivity of the uppermost layer.

Regarding reflected near-IR to visible light, for grain sizes of rocks, measured reflectance is reduced by back reflections (Fig. 1). As laboratory spectra of eucrites demonstrate (Fig. 13), larger grain size at the surface means deeper absorption features. Very small grains are not detected: these contribute only to scattering.

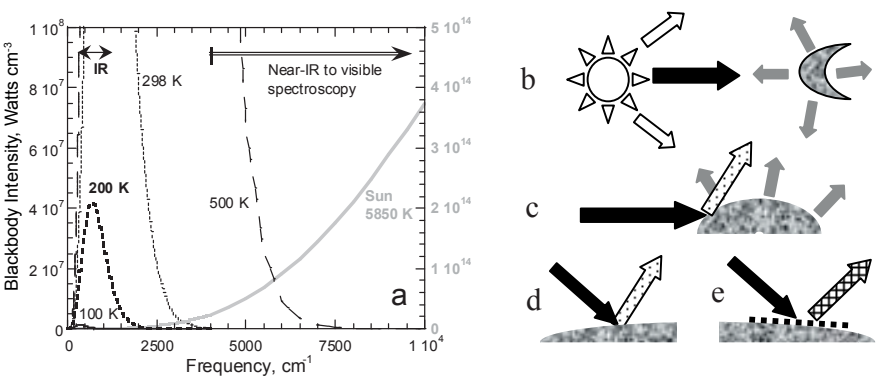


Figure 12. Factors governing whether light is emitted or reflected from a remote body. (a) Dependence of blackbody curves on temperature, as labeled. Except for the Sun at ~6000 K (grey), the left *y*-axis pertains. Arrows indicate spectral ranges. (b) Schematic of the first law of thermodynamics. Black arrow = light from Sun. Grey arrows = light emitted, which integrated over the area and frequency must equal the flux received. (c) Cold objects emit at low frequency, and reflect sunlight at high frequency (speckled arrow). Both are modified by spectral properties, which depend largely on whether the surface is bare (d) or dusty **(e)**, as sketched for the case of reflected sunlight. [After Fig. 8 of Hofmeister and Criss (2012).]

EBSCOhost - printed on 2/13/2023 5:26 AM via . All use subject to https://www.ebsco.com/terms-of-use

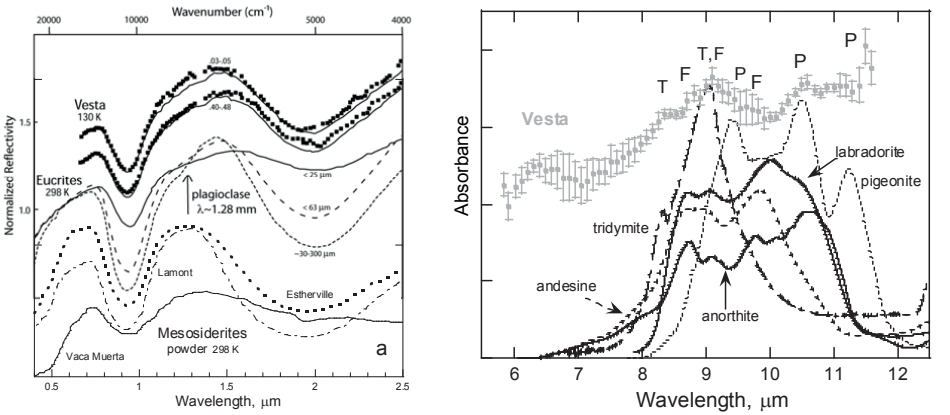


Figure 13. Spectra of Vesta and comparison to mineral data. (a) Reflection spectra in the near-IR. Comparison of orientational differences in spectra for Vesta to the grain-size dependence of reflectance-absorbance spectra from eucrites [solid = Padvarminkai (Hiroi et al. 1995); dashed = Macibini (Burbine et al. 2001); dotted = Padvarminkai (Gaffey 1976)] and powdered mesosiderites as labeled (Burbine et al. 2007). Vesta spectra (Gaffey 1997) are shown for two rotational aspects (dots), with each compared to the average (lines) of 4 to 5 rotational aspects. The uncertainties are roughly 2-3 times the symbol size, and the placement of the points near 2 μm is not exact because spectra presented at different scales were merged. Spectra offset for clarity. [After Fig. 9a of Hofmeister and Criss (2012).] (b) Emission spectra in the mid-IR. Dots = baseline subtracted mid-IR spectra of emissions from Vesta (Dotto et al. 2000). Peaks are labeled with the associated mineral phase (T = tridymite; F = feldspar; P = pigeonite). Dashed line = thin-film absorptions spectra of andesine. Light solid line = anorthite. Heavy solid line = labradorite. Dot-dashed line = tridymite. Dotted line = pigeonite. Film thicknesses are roughly 1 μm for each phase.

Regarding emitted light, for a bare, thick surface or large grains, ε = 1, so mid-IR emissions go as $I_{BB}(1-r)$. At frequencies where transitions occur less light is received due to reflection losses, i.e., peaks point down (Fig. 8a). However, if the surface is covered with dust, this layer is heated by lattice conduction from below and emitted light comes only from this layer. As discussed above, emissions from a dusty surface go as εI_{BB} and peaks point up as seen in spectra from small grains (Figs. 7, 8bc).

Effect of Fe^{2+} contents and grain-size on near-IR reflectance spectra of Vesta. High frequency reflection spectra (Fig. 13a) have the strong peaks of pigeonite (as in eucrites). Fe-bearing plagioclase may be present: the 8000 cm^{-1} band is weak for Serra de Magé eucrite (Hofmeister and Rossman 1984). Peaks for orthopyroxene (dioginites) or olivine (pallasites) are not evident Such may be extracted by peak fitting, but variations in grain-size of pigeonite suffice to explain the scant differences, as is clear from Figure 13. This inference is supported by recent inference of variation in grain-size from analysis of mid-IR light-curves (Chamberlain et al. 2011).

Mesosiderite spectra are similar to eucrites, but the presence of orthopyroxene broadens the peak at 2000 nm and shifts it to 1800 nm (Fig. 13a). The surface of Vesta was impacted. Rapid surface cooling at produces pigeonite as in terrestrial lavas. From Figure 13a, the surface of Vesta could be a mixture of pigeonite and metal. The proportion of pigeonite is high, based on peak depths, which is consistent with Vesta's density of 3.9 g cm^{-3}, which suggests about ~20% iron and ~80% silicate.

Importantly, the depths of the peaks are connected with Fe^{2+} content of the minerals. Orthopyroxene in the HEDs has Fe/(Mg+Fe) of 0.25 which is half that of pigeonites. Therefore, pigeonite will dominate if in equal proportions. Orthopyroxene is also coarse grained:

EBSCOhost - printed on 2/13/2023 5:26 AM via . All use subject to https://www.ebsco.com/terms-of-use

sufficiently large crystals will not provide back reflections. The spectra of Vesta could contain all phases of mesosiderites, but we can only prove that pigeonite is present and abundant.

Problems with interpretation of mid-IR emission spectra from Vesta. Spectra obtained of Vesta using the Infrared Satellite Observatory (ISO) record its emitted light. A broad peak near 450 cm^{-1} (Heras et al. 2000) indicates a blackbody temperature of 130 K, consistent with previous inferences (e.g., Lucey et al. 1998). ISO spectra in this range and below are noisy, obscuring features of minerals. Mid-IR features are weak, consistent with a dust covering (Dotto et al. 2000; Lim et al. 2005). Hence, these features are in emission. Unfortunately, spectral analyses by these authors assume that emissions are that of a solid body [$I_{meas,emit} = I_{BB}(1-r)$] whereas presence of a dust cover requires that $I_{meas,emit} = \varepsilon I_{BB}$ (as discussed above, see Figs. 1, 7, 8, 13). Available fits and need redoing.

Re-analysis of emission spectra from Vesta to account for surface dust. Mid-IR data (Fig. 13b) show weak, positive features superimposed on the blackbody continuum. The weakness of the emission features in the mid-IR has been independently confirmed by telescope observations (Lim et al. 2005) who concluded their weakness is related to a thick dust covering. Hence, these features are in emission and peaks point up.

We compared the data on Vesta to mid-IR data on about 50 different minerals known to occur in meteorites. Infrared absorption spectra were obtained at ambient conditions from thin films made by compression in a diamond anvil cell (e.g., Hofmeister et al. 1992, who provide tridymite spectra). Data are shown in Figure 13b for synthetic pigeonite powder ($Mg_{0.63}Fe_{0\cdot27}Ca_{0.10}SiO_3$), and various plagioclase feldspars (described by Hofmeister and Rossman 1984). Other samples (e.g., hydrosilicates and olivines) from our database (e.g., Hofmeister and Bowey 2006; Pitmann et al. 2010) were measured, but no spectral matches were found.

The positions and the pattern are consistent with a combination of three phases in significant amounts: mostly pigeonite, but also tridymite, and calcic plagioclase (~An_{75}). We could not fit the spectra with fewer minerals or with other minerals. In particular, orthopyroxenes with compositions across the binary can be ruled out, as well as significant amounts of olivine. The Fe content of the pigeonite is poorly constrained as ~30%, but the Ca content must be near 10% $CaSiO_3$, because higher Ca contents (augite or diopside) poorly fit the data.

Our analysis is consistent with detection of pigeonite in near-IR reflection (Fig. 13a), confirming that pigenite is the major, surface phase. The mineralogy deduced from the mid-IR emissions is consistent with Vesta being a basaltic eucrite, because orthopyroxene was not detected. However, iron metal cannot be discerned in mid-IR emissions, any more than it can be detected in the near-IR. Thus, our analysis is consistent with a mesosiderite composition as well. Surface impacts and melting followed by rapid cooling explain the presence of pigeonite, see Hofmeister and Criss (2012) for further discussion.

Ascertaining the mineralogy of the 10 μm feature in observational data

Infrared spectra from many astronomical environments contain a fairly broad feature near 10 μm (1000 cm^{-1}). This feature has been attributed to amorphous silicates, because laboratory measurements of crystalline silicates show multiple bands or shoulders in this area (e.g., Figs. 2, 13b). Although such a feature is nearly ubiquitous (e.g., Mann et al. 2006), variations in position, width and intensity relative to accompanying band near 18 mm (555 cm^{-1}) are large (e.g., Ossenkopf et al. 1992). Figure 14 shows the synthetic spectrum of Drain and Lee (1984) which was constructed to match the observational data. Speck et al. (2011) compared spectra from a wide range of glass compositions thought possible in space and found that none of these matched the spectral feature of the interstellar medium.

Although the breadth of the features (Fig. 14) could result from structural disorder of various types, another possibility is suggested by Figures 2 and 6: namely, that the interstellar

EBSCOhost - printed on 2/13/2023 5:26 AM via . All use subject to https://www.ebsco.com/terms-of-use

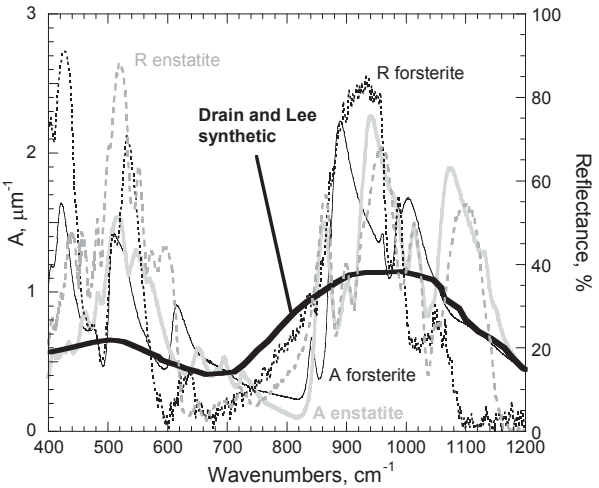


Figure 14. Comparison of laboratory and observational spectra. Absorption coefficients (left *y*-axis) of forsterite (black solid) and enstatite (grey solid) to that of Draine and Lee (1984), intended to represent average astrophysical environments (heavy black). These data are compared to reflectivity (right *y*-axis) from ceramic forsterite (black dots) and a polycrystalline mat of enstatite (grey dash).

medium consists of fairly large grains, ~1 μm, which are opaque at the transition frequency, but transmit light at the shoulders. Testing this hypothesis would require construction of spectra for different thicknesses and different dilutions (area covered), which is beyond the scope of this report. However, it is useful to compare laboratory data on the likely silicates (end-member enstatite and forsterite) to the observational data (Fig. 14). The synthetic *A*-values are about ½ that of the crystals and peaks near the strongest absorption bands. Importantly, reflectivity of the ceramics is high in a transparent region: this is due to back reflections. In a suspension, what appears to be absorbance is a combination of reflection and absorption that is filtered for thickness, which reduces the relief between the valleys and peaks. Sizes greater than ~1 μm are opaque at the Si-O stretching peak, providing a rounded profile. Greater absorbance is associated with greater reflectance losses.

DEDUCING DIFFUSIVE RADIATIVE TRANSFER FROM SPECTRA

Calculating an effective thermal conductivity from diffusive radiative transfer from spectra requires knowledge of absorption coefficients in the near-IR, where the blackbody radiation is highest at mantle temperatures (e.g., Shankland et al. 1979; Hofmeister et al. 2007). In DAC optical spectroscopy, strong refraction was misinterpreted as sample absorption and its effect on path length went unnoticed. As a consequence, baselines were (Fig. 15) interpreted as strong absorptions and inappropriate formulae were used (see discussion by Hofmeister 2010). Sample thicknesses in the diamond anvil cells are low compared to that needed to resolve peak absorbance associated with *d-d* transitions, and thus the valleys have $A = 0$, within experimental uncertainty.

Radiative transfer is a very difficult phenomenon to understand due to two factors, one being its length-scale dependence. This phenomenon depends mainly on temperature (Eqns. 13-17) and for that reason high-pressure measurements at 298 K do not represent the mantle. Determining the effective thermal conductivity requires single-crystal measurements of analogue materials. This approach is valid because the transitions in the near-IR to UV region

EBSCOhost - printed on 2/13/2023 5:26 AM via . All use subject to https://www.ebsco.com/terms-of-use

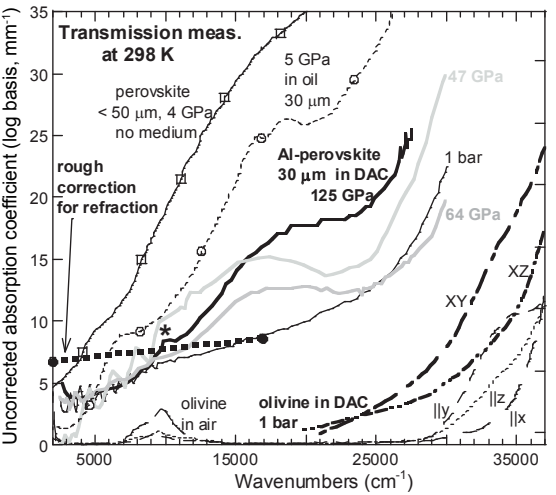


Figure 15. Uncorrected absorbance spectra (scaled to 1 mm thickness) which provides uncorrected absorption coefficients. Fine lines (dotted, short and long dashes) = the three polarizations of olivine ($Mg_{0.89}Fe_{0.11}SiO_4$) in air from 1 to 5 mm thick crystals (Runciman et al. 1973). Dot-dashed lines = diamond anvil cell data (Smith and Langer 1982) of oriented olivine ($Mg_{0.9}Fe_{0.1}SiO_4$) slabs with *d* near 30 μm. Heavy curves = spectra of $(Mg_{0.89}Fe_{0.10})(Al_{0.03}Si_{0.97})O_3$ from Keppler et al. (2008), shifted to coincide with their 1 bar spectrum at the lower ν limit of their measurements: "*" approximately marks ν for a detector change. Fine lines with symbols = $Mg_{0.9}Fe_{0.1}SiO_3$ from Goncharov et al. (2008). All perovskites have about 10% Fe as Fe^{3+}. Heavy dashed line = approximate correction for refraction losses. [Reprinted with permission of Elsevier from Hofmeister (2010) *Phys Earth Planet Interior*, Vol. 180, p 138-147.]

are specific to the sites of the chromophores, and weakly depend on the symmetry of the structure. The other factor is speed. Radiative transfer occurs at near light speed and thus is important to response of the system after transient heating events whereas slower diffusion of lattice vibrations controls slow cooling (Hofmeister 2010).

CONCLUSIONS

For the most part, spectroscopic studies are concerned with band strengths and not with absolute determinations of reflectivity or absorption coefficients and involve transmission rather than emissions measurements. Researchers tend to work with one specific technique or in one spectral range. Due to these factors, sources of experimental uncertainties are largely unimportant to early qualitative studies, and have been overlooked in more recent quantitative studies. However, applications require understanding possible and likely problems. This report discusses various spectral regions and applications, pointing to the need for reinterpretation of some spectra and to revisit problems concerning identification and calculation of radiative transfer. More data is needed in the ultraviolet region and in the far-IR, both of which are difficult to measure. More data is needed on single-crystals of relevance to geophysics and astronomy.

ACKNOWLEDGMENTS

Support was provided by AST-1008330. I thank K.M. Pitmann and A.K. Speck for helpful comments.

EBSCOhost - printed on 2/13/2023 5:26 AM via . All use subject to https://www.ebsco.com/terms-of-use

REFERENCES

Bates JB (1978) Infrared emission spectroscopy. *In:* Fourier Transform Infrared Spcctrosopy, Applications to Chemical Systems. Volume 1. Ferraro JR, Basile LJ (eds) Academic, New York, p 99-142

Bates JB, Boyd GE (1973) Infrared Emission Spectra of Molten Salts. Appl Spectrosc 27:204-208

Bell E (1967) Light and matter. *In:* Encyclopedia of Physics. Flugge S, Genzel L (eds) Springer-Verlag, Berlin, p 1-58

Berreman D (1963) Infrared absorption at longitudinal optic frequency in cubic crystal films. Phys Rev 130:2193-2198

Bevington P (1969) Data Reduction and Error Analysis for the Physical Sciences. McGraw-Hill Book Company, Saint Louis, Missouri

Boffa-Ballaran T, Carpenter M, Domeneghetti, Salje E, Tazzoli V (1998) Structural mechanisms of solid solution and cation ordering in augite-jadeite pyroxenes: II. A microscopic perspective. Am Mineral 83:434-443

Borghesi A, Bussoletti E, Colangeli L, De Blasi C (1985) Laboratory study of SiC submicron particles at IR wavelengths: a comparative analysis. Astron Astrophys 153:1-8

Bohren C, Huffman D (1998) Absorption and Scattering of Light by Small Particles. John Wiley and Sons, New York

Brewster MQ (1992) Thermal Radiative Transfer and Properties. John Wiley and Sons, Inc., New York

Brault J (1984) Fourier Transform Spectrometry. National Solar Observatory, Boulder Colorado

Burbine TH, Buchanan PC, Binzel RP, Bus SJ, Hiroi T, Hinrichs JL, Meibom A, McCoy TJ (2001) Vesta, vestoids, and the howardite, eucrite, diogenite group: Relationships and the origin of spectral differences. Meteorit Planet Sci 36:761-781

Burbine TH, Greenwood RC, Buchanan PC, Franchi IA, Smith CL (2007) Reflectance spectra of Mesosiderites: Implications for asteroid 4 Vesta. Lunar Planet Sci Conf 38: 119

Burns G (1985) Thermodynamic data from crystal field spectra. Microscopic to macroscopic – atomic environments to mineral thermodynamics. Rev Mineral 14:277-316

Burns G (1990) Solid State Physics. Academic Press Inc., San Diego

Chamberlain MA, Sykes MV, Tedesco EF (2011) Mid-infared lightcurve of Vesta. Icarus 215:57-61

Christensen PR, Bandfield JL, Hamilton VE, Howard DA, Lane MD, Piatek JL, Ruff SW, Stefanov WL (2000) A thermal emission spectral library of rock-forming minerals. J Geophys Res 105:9735-9739

Deer W, Howie R, Zussman J (1966) An Introduction to the Rock Forming Minerals. Longman, London

Dorschner J, Friedemann C, Gurtler J (1978) Laboratory spectra of phyllosilicates and the interstellar 10-micrometer absorption band. Astron Nachr 299:269-282

Dotto E, Muller TG, Barucci MA, Encrenaz TH, Knacke RF, Lellouch E, Doressoundiram A, Crovisier J, Brucato JR, Colangeli L, Mennalla V (2000) ISO results on bright Main Belt asteroids: PHT-S observations. Astron Astrophys 358:1133-1141

Draine BT, Lee HM (1984) Optical properties of interstellar graphite and silicate grains. Astrophys J 285:89-108

Fahrenfort J (1961) Attenuated total reflection: A new principal for the production of useful infra-red reflection spectra of organic compounds. Spectrochim Acta 17:698-709

Farmer V (ed) (1974) The Infrared Spectra of Minerals. Mineralogical Society, London

Gaffey M (1976) Spectral reflectance characteristics of the meteorite classes. J Geophys Res 81:905-920

Gaffey MJ (1997) Surface lithologic heterogeneity of asteroid 4 Vesta. Icarus 127:130-157

Galtier M, Montana A, Vidal G (1972) Phonons Optiques de CaO, SrO, BaO Au Centre de la Zone Brillouin a 300 et 17K. J Phys Chem Solids 33:2295-2302

Gardon R (1956) The emissivity of transparent materials. J Am Ceram Soc 39:278-287

Giesting PA, Hofmeister AM (2002) Thermal conductivity of disordered from infrared spectroscopy. Phys Rev B 65:144305.

Gillette P, Lando J, Koenig J (1985) A survey of infrared Spectral data processing techniques. *In:* Fourier Transform Infrared Spectroscopy: Applications to Chemical Systems. Ferraro J, Basile L (eds) Academic Press, Inc., New York, p 1-59

Glotch T, Rossman G, Aharonson O (2007) Mid-Infrared (5-100 μm) reflectance spectra and optical constants of phyllosilicate minerals. Icarus 192:605-622

Goncharov A, Haugen B, Struzhkin V, Beck P, Jacobsen S (2008) Radiative conductivity in the Earth's lower mantle. Nature 456:231-234

Griffiths P, de Haseth J (1986) Fourier Transform Infrared Spectrometry. John Wiley and Sons, New York

Heras AM, Morris PW, Vandenbussche B, Müller TG (2000) Asteroid 4 Vesta as seen with the ISO short wavelength spectrometer. *In:* Thermal Emission Spectroscopy and Analysis of Dust, Disks, and Regoliths. (eds) Sitko M, Sprague A, Lynch D. p. 205-212

Hiroi T, Binzel R, Shunshine J, Pieters C, Takeda H (1995) Grain sizes and mineral composition of Vesta-like asteroids. Icarus 115:374-386

EBSCOhost - printed on 2/13/2023 5:26 AM via . All use subject to https://www.ebsco.com/terms-of-use

Hofmeister AM (2004) Thermal conductivity and thermodynamic properties from infrared spectroscopy. *In*: Infrared Spectroscopy in Geochemistry, Exploration Geochemistry, and Remote Sensing. King P, Ramsey M, Swayze G (eds) Mineralogical Association of Canada, Ottawa, Ontario, p 135-154

Hofmeister AM (2010) Scale aspects of heat transport in the diamond anvil cell, in spectroscopic modeling, and in Earth's mantle. Phys Earth Planet Inter 180:138-147 doi:10.1016/j.pepi.2009.12.006

Hofmeister AM (2012) Thermal diffusivity of orthopyroxenes at elevated temperature. Eur J Mineral 24:669-681

Hofmeister AM, Bowey JE (2006) Quantitative IR spectra of hydrosilicates and related minerals. Mon Not R Astro Soc 367:577-591

Hofmeister AM, Criss R. (2012) Origin of HED meteorites from the spalling of Mercury: implications for the formation and composition of the inner planets. *In*: New Achievements in Geoscience. Lim Hwee-San (ed) InTech, Rijeka, Croatia, 153-178

Hofmeister AM, Mao HK (2001) Evaluation of shear moduli and other properties of silicates with the spinel structure form IR spectroscopy. Am Mineral 86:622-639

Hofmeister AM, Rossman G (1984) Determination of Fe^{3+} and Fe^{2+} concentrations in feldspar by optical and EPR spectroscopy. Phys Chem Minerals 11:213-224

Hofmeister AM, Rose TP, Hoering TC, Kushiro I (1992) Infrared spectroscopy of natural, synthetic, and 18O substituted α-tridymite: structural implications. J Phys Chem 96:10213-10218

Hofmeister AM, Keppel E, Bowey JE, Speck AK (2000) Causes of artifacts in the infrared spectra of powders. *In:* ISO Beyond the Peaks: The 2nd ISO workshop on analytical spectroscopy. Salama A, Kessler MF, Leech K, Schulz B, Danesy D (eds) European Space Agency, Noordwijk, p 343-346

Hofmeister AM, Keppel E, Speck AK (2003) Absorption and reflection spectra of MgO and other diatomic compounds. Mon Not R Astron Soc 345:16-38

Hofmeister AM, Wopenka B, Locock A (2004) Spectroscopy and structure of hibonite, grossite, and $CaAl_2O_4$: implications for astronomical environments. Geochim Cosmochim Acta 68:4485-4503

Hofmeister AM, Pertermann M, Branlund, J M (2007) Thermal conductivity of the Earth. *In*: Treatise in Geophysics: Vol. 2 Mineral Physics. Price GD (ed) Elsevier, The Netherlands, p 543-578

Hofmeister AM, Pitman KM, Goncharov AF, Speck AK (2009) Optical constants of silicon carbide for astrophysical applications. II. Extending optical functions from IR to UV using single-crystal absorption spectra. Astrophys J 696:1502-151

Horak M, Vitek A (1978) Interpretation and Processing of Vibrational Spectra. John Wiley, New York

Kachare A, Andermann G, Brantley L (1972) Reliability of classical dispersion analysis of LiF and MgO reflectance data. J Phys Chem Solids 33:467-475

Kauppinen J, Moffatt D, Mantsch H, Cameron D (1981a) Fourier self-deconvolution: a method for resolving intrinsically overlapping bands. Appl Spectros 35:271-276

Kauppinen J, Moffatt D, Cameron D, Mantsch H (1981b) Noise in Fourier self-deconvolution. Appl Optics 20:1866-1879

Kemper F, Jaeger C, Waters LBFM (2002) Detection of carbonates in dust shells around evolved stars. Nature 415:295-297

Keppler H, Dubrovinsky L, Narygina O, Kantor I (2008) Optical absorption and radiative thermal conductivity of silicate perovskite to 125 Gigapascals. Science 322:1529-1532

Kimura Y, Sato T, Kaito C (2005) Production of diamond and solid-solution nanoparticles in the carbon-silicon system using radio-frequency plasma. Carbon 43:1157-1583

Lim L, McConnochie T, Bell J, Hayward T (2005) Thermal infrared (8-13 μm) spectra of 29 asteroids: the Cornell Mid-Infrared Asteroid Spectroscopy (MIDAS) Survey. Icarus 173:385-408

Lipson H (1960) Infra-red transmission spectra of alpha silicon carbide. *In:* Silicon Carbide. O'Connor J, Smiltens J (eds) Permagon, New York, p 371-375

Long L, Querry M, Bell R, Alexander R (1993) Optical properties of calcite and gypsum in crystalline and powered form in the infrared and far infrared. Infrared Phys Technol 34:191-201

Low MJD, Coleman I (1966) Measurement of the spectral emission of infrared radiation of minerals and rocks using multiple-scan interferometry. Appl Opt 5:1453-1455

Lucey PG, Keil K, Whitely R (1998) The influence of temperature on the spectra of the A-asteroids and implications for their silicate chemistry. J Geophys Res 103:5865-5871

Mann I, Köhler M, Kimura H, Cechowski A, Minato T (2006) Dust in the solar system and in extra-solar planetary systems. Astron Astrophys Res 13:159-228

McMahon HO (1950) Thermal radiation from partially transparent reflecting bodies. J Opt Soc Am 40:376-380

Molster FJ, Lim TL, Sylvester RJ, Waters LBFM, Barlow MJ, Beintema DA, Cohen M, Cox P, Schmitt B (2001) The complete ISO spectrum of NGC 6302. Astron Astrophys 372:165-172

Ossenkopf V, Henning Th, Mathis J S (1992) Constraints on cosmic silicates. Astron Astrophys 261:567-578.

Palik E (1998) Handbook of Optical Constants of Solids. Academic Press, San Diego

EBSCOhost - printed on 2/13/2023 5:26 AM via . All use subject to https://www.ebsco.com/terms-of-use

Papoular R, Cauchetier M, Begin S, LeCaer G (1998) Silicon Carbide and the 11.3-μm feature. Astron Astrophys 329:1035-1044

Philipp H (1958) Intrinsic Optical Absorption in Single-Crystal Silicon Carbide. Phys Rev 111:440-441

Philipp HR, Taft EA (1960) Intrinsic optical absorption in single crystal silicon carbide. *In:* Silicon Carbide. O'Connor JR, Smiltens J (eds) Pergamon, New York, p 366-370

Pitman KM, Hofmeister AM, Corman A, Speck A (2008) Optical properties of silicon carbide for astrophysical environments I. New laboratory infrared reflectance spectra and optical constants. Astron Astrophys 483:661-672

Pitman KM, Dijkstra CR, Hofmeister AM, Speck AK (2010) Using classical dispersion analysis to extract peak parameters and optical constants from infrared laboratory absorbance spectra: Application to olivine. Mon Not R Astron Soc 406:460-481

Roessler D (1965) Kramers-Kronig analysis of non-normal incidence reflection. Brit J Appl Phys 16:1359-1366

Rossman GR (1988) Optical xpectroscopy. Rev Mineral 18:207-254

Runciman W, Sengupta D, Gourley J (1973) The polarized spectra of iron in silicates. II. Olivine. Am Mineral 58:451-456

Salisbury J, Walter L, Vergo N, D'Aria D (1991) Infrared (2.1-2.5 μm) Spectra of Minerals. Johns Hopkins Univ Press, Baltimore

Salje E, Carpenter M, Malcherek T, Ballaran T (2000) Autocorrection analysis of infrared spectra from minerals. Eur J Mineral 12:503-519

Shaffer PTB, Naum RG (1969) Refractive index and dispersion of beta silicon carbide. J Opt Soc Am 59:1498

Shankland TJ, Nitsan U, Duba AG (1979) Optical absorption and radiative heat transport in olivine at high temperature. J Geophys Res 84:1603-1610

Shannon RD, Subramianian M (1989) Dielectric constants of chrysoberyl, spinel, phenacite and forsterite and the oxide additivity rule. Phys Chem Miner 16:747-751

Siegel R, Howell JR (1972) Thermal Radiation Heat Transfer. McGraw-Hill, New York

Smith H, Langer K, (1982) Single crystal spectra of olivines in the range 40,000-5,000 cm^{-1} at pressures up to 200 kbar. Am Mineral 67:343-348

Sommer L (1989) Analytical Absorption Spectrophotometry in the Visible and Ultraviolet: The Principles. Elsevier, New York

Speck A, Hofmeister AM, Barlow M (1999) Resolution of the SiC problem: astronomical and meteoritic evidence reconciled. Astrophys J Lett 513:L87-L90

Speck A, Whittington A, Hofmeister AM (2011) Disordered silicates in space: a study of laboratory spectra of "amorphous" silicates. Astrophys J 740:93-110

Spitzer W, Kleinman D (1961) Infrared lattice bands of quartz. Phys Rev 121:1324-1335

Spitzer W, Kleinman D, Walsh D (1959) Infrared properties of hexagonal silicon carbide. Phys Rev 113:127-132

Sun T, Allen P, Stahnke D, Jacobsen S, Homes C (2008) Infrared properties of ferropericlase $Mg_{1-x}Fe_xO$: Experiment and theory. Phys Rev 77, doi 10.1103/PhysRevB.77.134303

Wood B (1981) Crystal field electronic effects on the thermodynamic properties of Fe^{+2} minerals. *In:* Thermodynamics of minerals and melts. Newton R, Navrotsky A, Wood B (eds) Springer Verlag, New York, p 63-84

Wooten F (1972) Optical Properties of Solids. Academic Press Inc., San Diego

Wyncke B, Brehat F, Kharoubi H (1990) Calculation of the reflectivity spectra dependence on the angle of incidence in anisotropic absorbing crystals, application to sodium nitrite. J Phys Condens Matter 2:8791-8800

Zeidler S, Posch T, Mutschke H, Richter H, Wehrhan O (2011) Near-infrared absorption properties of oxygen-rich stardust analogs. The influence of coloring metal ion. Astro Astrophys 526:A68-A78

EBSCOhost - printed on 2/13/2023 5:26 AM via . All use subject to https://www.ebsco.com/terms-of-use

Reviews in Mineralogy & Geochemistry
Vol. 78 pp. 509-541, 2014
Copyright © Mineralogical Society of America

Advances in Raman Spectroscopy Applied to Earth and Material Sciences

Daniel R. Neuville
IPGP-CNRS, Géochimie &Cosmochimie
Sorbonne Paris Cité
1 rue Jussieu, 75005 Paris, France
neuville@ipgp.fr

Dominique de Ligny
FAU Erlangen Nürnberg
Department Werkstoffwissenschaften
Martensstr. 5, 91058 Erlangen, Germany
dominique.de.ligny@fau.de

Grant S. Henderson
Department of Earth Sciences
University of Toronto
22 Russell St, Toronto, Ontario, M5S 3B1, Canada
henders@es.utoronto.ca

BRIEF HISTORICAL PERSPECTIVE AND SIMPLE THEORY

When monochromatic radiation ν_o, is incident on a system (gas, solid, liquid, glass, whether colored or transparent) most of the radiation is transmitted through the system without change, but some scattering of this radiation can also occur (approximately 1 in 10^7 photons). The scattered radiation corresponds to $\nu' = \nu_o \pm \nu_m$. In molecular systems, the energy of the scattered light (in wavenumbers, ν_m) is found to lie principally in the range associated with transitions between vibrational, rotational and electronic energy levels. Furthermore, the scattered radiation is generally polarized differently from that of the incident radiation with both scattered intensity and polarization dependent upon the direction of observation.

During the 1920's different physics groups worked on this subject around the world: 1) an Indian group composed of Raman and Krishnan (1928), who made the first observations of the phenomenon in liquids in 1928 (Raman won the Nobel Prize in Physics in 1930 for this work); 2) Landsberg and Mandelstam (1928) in the USSR reported the observation of light scattering with change of frequency in quartz and finally 3) Cabannes and Rocard (1928) in France confirmed the Raman and Krishnan (1928) observations while Rocard (1928) published the first theoretical explanation.

The principle of Raman spectroscopy is the illumination of a material with monochromatic light (laser) in the visible spectral range followed by the interaction of the incident photons with the molecular vibrations or crystal phonons which induces a slight shift in the wavelength of the scattered photons. Scattering can occur with a change in vibrational, rotational or electronic energy of a molecule. If the scattering is elastic and the incident photons have the same energy as the scattered photons, the process is called Rayleigh scattering and this is the dominant scattering interaction. If the scattering is inelastic (the scattered photons have a

1529-6466/14/0078-0013$05.00 http://dx.doi.org/10.2138/rmg.2013.78.13

EBSCOhost - printed on 2/13/2023 5:26 AM via . All use subject to https://www.ebsco.com/terms-of-use

different energy to the incident photons) the process is called Raman scattering and the scattered photons exhibit a shift in energy called the Raman shift. However, the Raman shift only occurs when the electron cloud, between the vibrating atoms involved in the interaction with the incident photon, is able to be deformed. This deformation is described as the polarizability of the molecule or bond. A change in the degree of polarization potential or polarizability with respect to the vibrational coordinates of the system being studied is required for a molecule or material to exhibit the Raman effect or a Raman shift. This wavelength or energy shift (remember $E = h\nu = hc/\lambda$, where h is Planks constant and c the speed of light) can then be measured by a spectrometer. The spectral shift or Raman shift (given in cm^{-1} where $\Delta\nu = (1/\lambda_0 - 1/\lambda_m)$: ν is the Raman shift expressed in wavenumber, λ_0 is the laser wavelength and λ_m the Raman spectrum wavelength) corresponds to the vibrational frequency of the vibrational source (molecule, molecular/atomic group) and is characteristic of the atoms undergoing vibration. The Raman spectrum can then be seen as a spectral signature of the material. Furthermore, the relative intensity of the Raman peaks or bands is related to the nature of the material and the type and concentration of the atoms undergoing vibration (specifically to the polarizability). From the relative intensities of the Raman bands, we can deduce the relative composition of the material and in some cases obtain quantitative or semi-quantitative analysis of the different atomic or molecular groups contributing to the Raman spectrum, by measuring the area of the Raman bands associated with that group via curve fitting.

In other words, monochromatic laser light with frequency ν_o interacts more or less with the oscillating dipoles. And the magnitude of these interactions is related to the degree of polarizability associated with those oscillations. Such oscillating dipoles cause the interacting photons to be scattered with three different frequencies (Fig. 1):

- A molecule with or without Raman-active modes (vibrations) will interact with a photon of frequency ν_o. The excited molecule returns back to the same basic vibrational state and scatters light with the same frequency ν_o as the excitation source. This type of interaction is elastic Rayleigh scattering.
- A photon with frequency ν_o interacts with a Raman-active molecule which at the time of interaction is in the basic vibrational state. Part of the photon's energy is transferred to the Raman-active vibration with frequency ν_m and the resulting frequency of

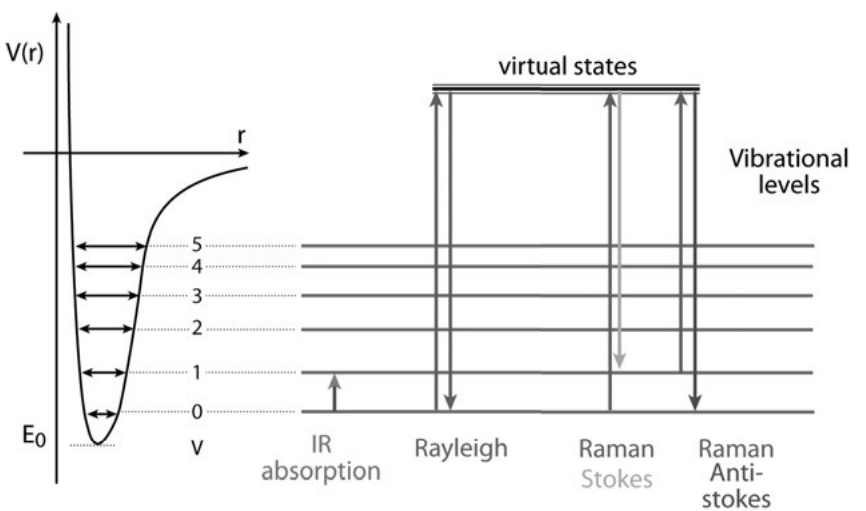


Figure 1. Virtual states versus vibrational levels.

EBSCOhost - printed on 2/13/2023 5:26 AM via . All use subject to https://www.ebsco.com/terms-of-use

scattered light is reduced to $\nu_o - \nu_m$. This Raman frequency is called Stokes frequency, or just "Stokes".

- A photon with frequency ν_o interacts with a Raman-active molecule, which, at the time of interaction, is already in the excited vibrational state. Excessive energy of the excited Raman-active mode is transferred to photon energy, the molecule returns to the basic vibrational state and the resulting frequency of scattered light goes up to $\nu_o + \nu_m$. This Raman frequency is called "Anti-Stokes."

The spectrum of the scattered light consists of a strong line (the exciting line, Fig. 2a) of the same frequency as the incident illumination together with much weaker lines on either side shifted from the strong line by frequencies ranging from a few to about 4500 cm^{-1} (Fig. 2a,b).

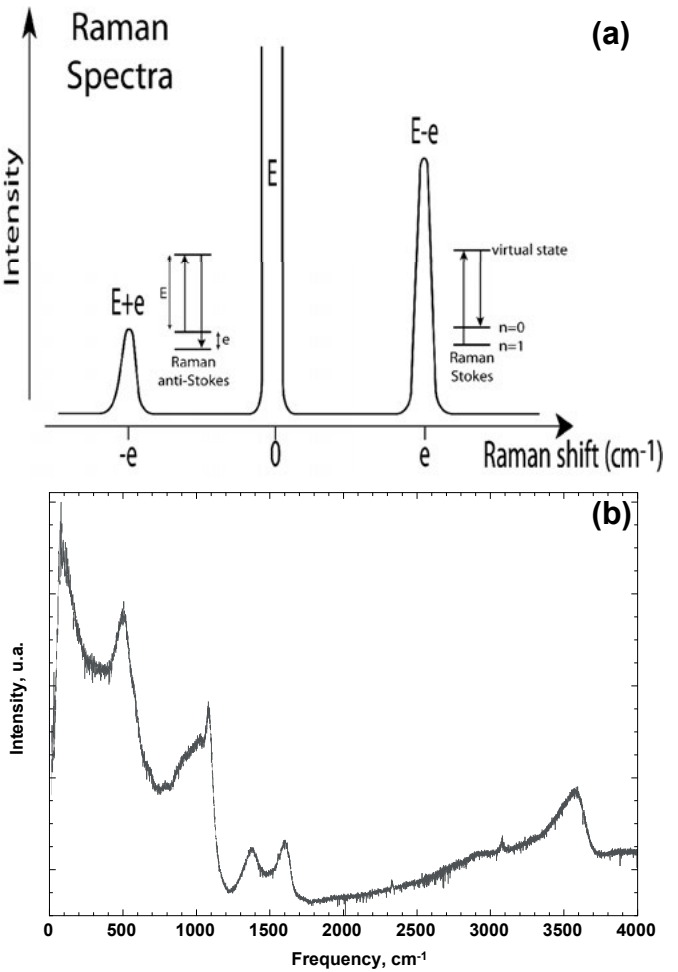


Figure 2. a) Schematic of the exciting line, at 0 cm^{-1}, and the Raman scattering on the left and right, respectively of Stokes and Anti-stokes Raman frequencies. b) Raman spectra of a hydrous aluminosilicate glass. Different regions can be observed in the spectrum that can be assigned to different types of vibrations (see below). For example, we can recognize the Boson peak (20-200 cm^{-1}), Al-O-Si-O-M bending and rocking vibrations (200-700 cm^{-1}), Si-O-Al or T-O-T stretching vibrations (700-1200 cm^{-1}), Fermi doublet due to CO_2 molecules (1300-1600 cm^{-1}) and H_2O-OH stretching vibrations (3000-4000 cm^{-1}).

EBSCOhost - printed on 2/13/2023 5:26 AM via . All use subject to https://www.ebsco.com/terms-of-use

The higher the frequency and lighter are the atoms involved in the molecular vibration: the 4500 cm^{-1} frequency corresponding to the vibrations of a H_2 molecule. Raman spectroscopy is a very important practical tool for quickly identifying molecules and minerals. For example, a Raman spectrometer was deployed on the Viking landers in 1972 and on other missions (Angel et al. 2012) and more recently in deep ocean exploration (Zhang et al. 2012). Raman spectroscopy also has important scientific applications in medical diagnostics (Tu and Chang 2012).

The *Reviews in Mineralogy* volume on spectroscopic methods (Vol. 18 *Spectroscopic Methods in Mineralogy and Geology*, Frank C. Hawthorne, ed. 1988) has an extensive chapter on symmetry, group theory and quantum mechanics (McMillan and Hess 1988) and a chapter on IR and Raman spectroscopy (McMillan and Hofmeister 1988). The reader is also referred to some general texts on molecular vibrations (Herzberg 1945a; Wilson et al. 1955), symmetry and spectroscopy (Harris and Bertolucci 1978), Raman spectroscopy (Herzberg 1945b; Sherwood 1972; Lazarev 1972; Long 1978, 2002), and applied Raman spectroscopy (Karr 1975; Dubessy et al. 2012) for a more detailed understanding of the technique. We do however briefly discuss Hyper-Raman spectroscopy (HRS) and surface enhanced Raman spectroscopy (SERS). Recent reviews of Raman spectroscopy have been made by Nasdala et al. (2004) and Das and Agrawal (2011), on HRS (Ziegler 1990), SERS (Stiles et al. 2008; Cialla et al. 2012), and coherent anti-stokes Raman spectroscopy (CARS) (Cheng 2004).

Classical theory. Raman scattering occurs when monochromatic light interacts with molecular vibrations or crystal phonons (vibrations propagating along the crystallographic axis). To a first approximation (the so-called harmonic approximation), the vibration can be modeled by a spring binding two masses (m_1 and m_2) with a force constant k. The vibrational frequency, corresponding to the Eigen mode of vibration of the spring, can be calculated as: $\nu = 1/2\pi(k/\mu)^{1/2}$ with μ, the reduced mass ($\mu = m_1m_2/(m_1 + m_2)$).

The vibrational frequency depends on several physical and chemical parameters: the chemical nature of the atoms involved in the bond, the nature of the bond (modeled by the force constant, k) and the symmetry of the molecule or molecular group undergoing the vibration. Thus, the vibrational frequency can be considered as a characteristic signature of the material being studied. Indeed, each specific molecule or crystal has its own vibrational frequencies and can be characterized and identified by using these frequencies. Raman spectroscopy enables one to measure these fundamental vibrations resulting in sharp, well-resolved bands visible in a Raman spectrum of a gas or crystalline material.

Quantum mechanical theory

A detailed quantum mechanical description of the Raman effect is complicated and beyond the scope of this paper. The reader is referred to one of the classic texts for a full description (cf. Wilson et al. 1955; Long 2002). In classical theory one is interested in the oscillating electric dipole and polarizability (see above) while from the quantum mechanical approach these are termed the transition electric dipole and polarizability and are defined by the wave functions and energy levels of the system. The two theoretical approaches are similar and are very simply described below with a number of assumptions implicitly assumed. A proper detailed discussion of these approaches is given in Chapters 2, 3 and 4 of Long (2002).

The classical total time-dependent induced electric dipole moment vector of a molecule is given by the sum of a series of time dependent induced dipole moment vectors:

$$p = p^{(1)} + p^{(2)} + p^{(3)} + \ldots \quad (1)$$

Where $p^{(1)} \gg p^{(2)} \gg p^{(3)}$ and $p^{(1)} = \alpha \cdot E$ (α is the polarizability tensor and E is the dynamic electric field). $p^{(1)}$ contains three frequency components representing the Rayleigh frequency, v_0, and Raman frequencies $\pm v_m$. The equivalent equation from a quantum mechanical approach is the total induced transition electric dipole vector:

EBSCOhost - printed on 2/13/2023 5:26 AM via . All use subject to https://www.ebsco.com/terms-of-use

$$(p)_{fi} = (p)_{fi}^{(1)} + (p)_{fi}^{(2)} + (p)_{fi}^{(3)} + \ldots \quad (2)$$

Where i and f are initial and final states and $(p)_{fi} = \left\langle \Psi'_f \middle| \hat{p} \middle| \Psi'_i \right\rangle$ with ν_f' and ν_i' the perturbed time dependent wave functions. The amplitude of the transition electric dipole for Raman scattering is then given by $(p^{(1)}(v_0 \pm v_m))_{fi} = (\alpha)_{fi} \cdot E_0(v_0)$ where v_0 is the Rayleigh scattering frequency, v_m the Raman scattering frequency, $(\alpha)_{fi}$ is the transition polarizability and E the dynamic electric field.

The main difference between them is that in the classical approach the oscillating electric dipole and polarizability are only qualitatively related to molecular properties whereas in the quantum mechanical approach the transition electric dipole and polarizability are quantitatively related to fundamental molecular properties. The latter enables much greater insight into the factors that characterize light scattering.

INSTRUMENTATION

By looking at one of the first Raman spectra of carbon tetrachloride from Raman and Krishnan (1928) (Fig. 3), it is easy to see that progress in Raman spectroscopy has been directly correlated with the development of lasers, charge coupled devices (CCD) and confocal systems.

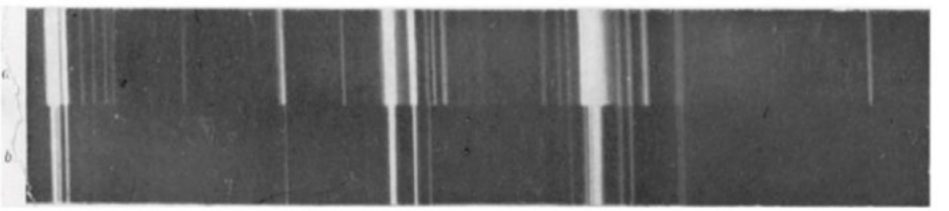


Figure 3. Raman spectra of carbon tetrachloride using a mercury arc lamp for the excitation source (Raman and Krishnan 1929).

After discovery of the Raman effect and production of the first Raman spectra between 1928 and 1935, papers on Raman spectroscopy were focused on theory (Cabannes 1928; Rocard 1928), on crystals (Landsberg and Mandelstam 1928; Cabannes 1931), liquids (Raman and Krishnan 1928; Cabannes et Rousset 1932; Hibben 1933, 1936), gases (Mulliken 1929, 1931) organic matter (Villars 1932; Hibben 1933), and on glasses (Hollaender and Williams 1929, 1931) with less than 50 papers published per year. Since then the technique has rapidly grown (Fig. 4) with applications across all scientific disciplines from physics to medicine to archeology and anthropology. In particular, the reader can note that one of the first papers on similarities between glass plates, fused quartz and quartz were made by Hollaender and Williams (1929, 1931) a few years before the well-known work of Warren (1934a,b).

Excitation line

During the first 30 years of Raman development, Raman spectra were obtained by exciting material using a mercury arc lamp. In the 1950's, Kastler and co-workers (Nobel Prize 1966) developed the laser and since the 1960's, a sample is normally illuminated with a laser in the ultraviolet (UV), visible (Vis) or near infrared (NIR) range. A laser emits light (electromagnetic radiation) through a process of optical amplification based on the stimulated

EBSCOhost - printed on 2/13/2023 5:26 AM via . All use subject to https://www.ebsco.com/terms-of-use

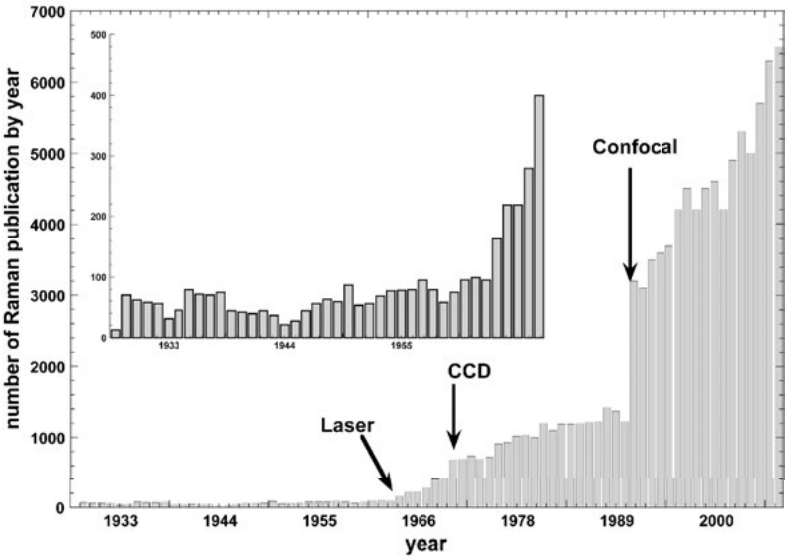


Figure 4. Number of scientific papers published per year between 1929 and 2010.

emission of photons. The term "laser" originated as an acronym for Light Amplification by Stimulated Emission of Radiation. The emitted laser light is notable for its high degree of spatial and temporal coherence. Lasers can be focused to very small spot sizes with very high irradiance. Or they can be focused into a beam with low divergence in order to concentrate their power at longer distances.

Laser light is theoretically a single wavelength but a laser actually produces radiation in several modes having slightly different frequencies, often with more than a single polarization. Consequently, in order to carry out Raman experiments one may have to tune the Laser frequency appropriate for the experiment and/or employ some sort of wavelength filter (Plasma Filter) to produce the ν_o necessary for the experiments. In addition, the laser chosen for an experiment needs to be appropriate for the type of material being studied. For example colored samples may absorb rather than scatter certain laser wavelengths and so one should choose a laser wavelength that minimizes absorption (Table 1).

Notch filters, optical spectrometer or grating

During a Raman experiment scattered light is collected with a lens and is sent through an interference filter or spectrophotometer. Since spontaneous Raman scattering is very weak

Table 1. Wavelengths absorbed by certain colored samples.

Wavelength (nm)	Sample type
244 nm	biological, catalysts (Resonance Raman)
325 nm	wide band gap semiconductors
488 & 514 nm	semiconductors, catalysts, biological, polymers, minerals & general purpose
633 nm	corrosion materials & general purpose
785 nm	polymers, biological & general purpose
830 nm	biological

EBSCOhost - printed on 2/13/2023 5:26 AM via . All use subject to https://www.ebsco.com/terms-of-use

the main difficulty of Raman spectroscopy is separating the scattered light from the intense Rayleigh scattering (ratio $1/10^9$). More precisely, the problem is not the Rayleigh scattering itself, but the fact that the intensity of stray light from the Rayleigh scattering may greatly exceed the intensity of the useful Raman signal in close proximity to the laser wavelength. In many cases the problem is resolved by simply cutting off the spectral range close to the laser line where the stray light has the most prominent effect. People use commercially available interference (Notch®) filters which cut-off a spectral range of ±80-120 cm^{-1} from the laser line. This method is efficient for stray light elimination but it does not allow detection of low-frequency Raman modes in the range below 100 cm^{-1}. Notch® filters are also very expensive and a different filter is required for each Laser excitation line. The simplest method to eliminate or reduce the Rayleigh scattering is to use a grating (100 liner/mm) in front of the laser to remove parasitic lines[1] from the laser as well as the Rayleigh scattering. Another possibility is to use a prism spectrometer to separate the Rayleigh and parasite lines. These two methods are cheaper than buying several Notch® filters and are adjustable depending on the excitation line. In all cases, whichever method is employed, Notch® filter, prism spectrometer or grating, there is a decrease in efficiency with age and/or power of the Laser.

Optics, monochromators, detectors

Stray light is generated in the spectrometer mainly from light dispersion on gratings and strongly depends on grating quality. Modern Raman spectrometers typically use holographic gratings, which normally have fewer manufacturing defects in their structure than older line gratings. The stray light produced by holographic gratings is about an order of magnitude less intense then from ruled gratings with the same groove density. Another way of stray light reduction is to use multiple dispersion stages. Double and triple spectrometers allow measurement of Raman spectra without use of notch filters. In such systems Raman-active modes with frequencies as low as 3-5 cm^{-1} can be efficiently detected.

In earlier times people primarily used single-point detectors such as photon-counting Photomultiplier Tubes (PMT). However, a single Raman spectrum obtained with a PMT detector in wavenumber scanning mode took a substantial period of time, slowing down any research or industrial activity based on the Raman analytical technique. Nowadays, more and more researchers use multi-channel detectors like Photodiode Arrays (PDA) or, more commonly, a Charge-Coupled Devices (CCD) to detect the Raman scattered light. Sensitivity and performance of modern CCD detectors are rapidly improving. Most of the times, a CCD is the detector of choice for Raman spectroscopy.

Different manufacturers and instrument types

Different companies sell Raman spectrometer with different electronic components and detectors, but the most important difference is based on the number of optical gratings used to disperse the scattered light. Spectrometers with a simple grating like Hololab from Kaiser ® (Fig. 5a) or Labram from Jobin-Yvon-Horiba produce very nice spectra, easy to obtain, with fast acquisition times, but with relatively low resolution around (~5 cm^{-1}) and it is not possible to investigate the low frequency part of the Raman spectrum close to the exciting line. Triple spectrometers (Fig. 5b) have three gratings which disperse the light and provide a resolution better than 1 cm^{-1}. However, the downside of such systems is that the Raman signal is 3× less than that obtained using a simpler system. However, an advantage is that triple monochromator

1 Gas filled lasers may contain trace impurities of other gases which also produce laser lines. For example Argon (Ar) filled lasers may contain traces of Neon (Ne) so that the laser produces a principle laser line whose frequency/wavelength is characteristic of Ar but it will also have weak lines characteristic of Ne that must be removed prior to running a Raman experiment.

EBSCOhost - printed on 2/13/2023 5:26 AM via . All use subject to https://www.ebsco.com/terms-of-use

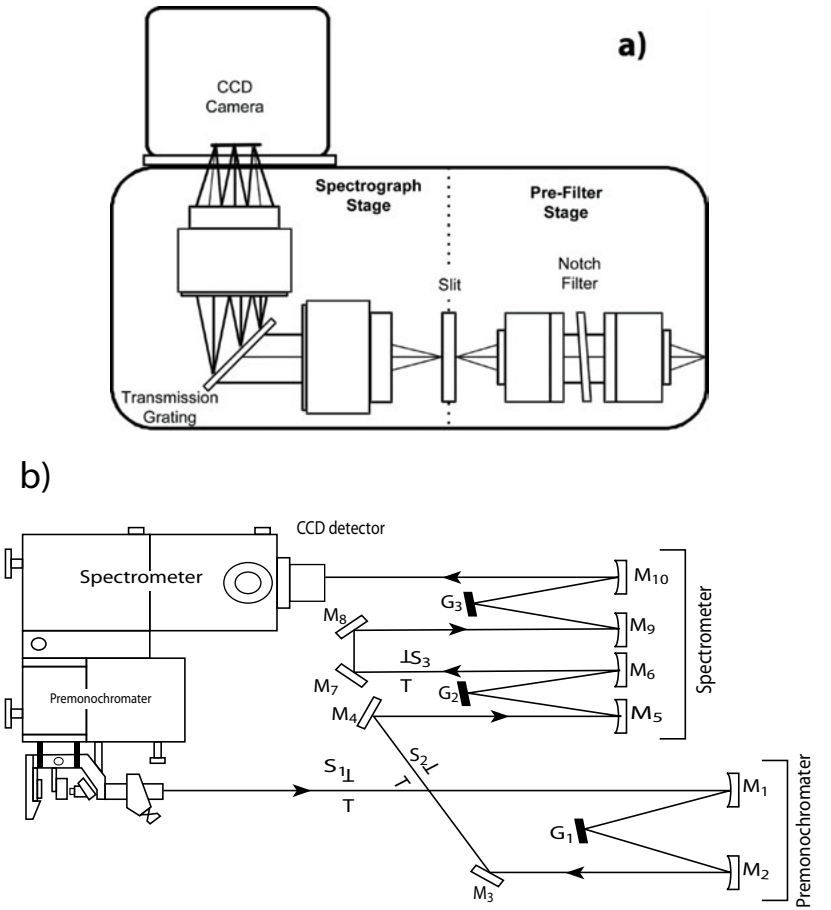


Figure 5. a) Hololab 5000, from Kaiser Optical system (© Kaiser Optical Systems, Inc. all rights reserved. Used with permission.); b) triple grating monochromator like that used in the T64000 from Horiba (after Hawthorne 1988).

systems can obtain Raman spectra at very low frequencies close to the laser line and hence can observe the Boson peak in glasses for example.

Figure 6 shows the Raman spectra on the same glass sample made with a T64000 Jobin-Yvon with one and three gratings for the same acquisition time. With only one grating, the signal is three times more intense, but it is also three times less accurate. Note the low frequency spectral cutoff is around 350 cm^{-1} for the single grating but < 50 cm^{-1} for the triple grating. The low frequency cutoff for a single grating instrument depends directly on the nature of the Notch® filter used and its age. Spectral resolution is also three times better with the triple spectrometer than with a single grating.

Confocal system

Confocal microscopy (Fig. 7) is an optical imaging technique used to increase optical resolution and contrast of an image by using a spatial pinhole to eliminate out-of-focus light in specimens that are thicker than the focal plane.

EBSCOhost - printed on 2/13/2023 5:26 AM via . All use subject to https://www.ebsco.com/terms-of-use

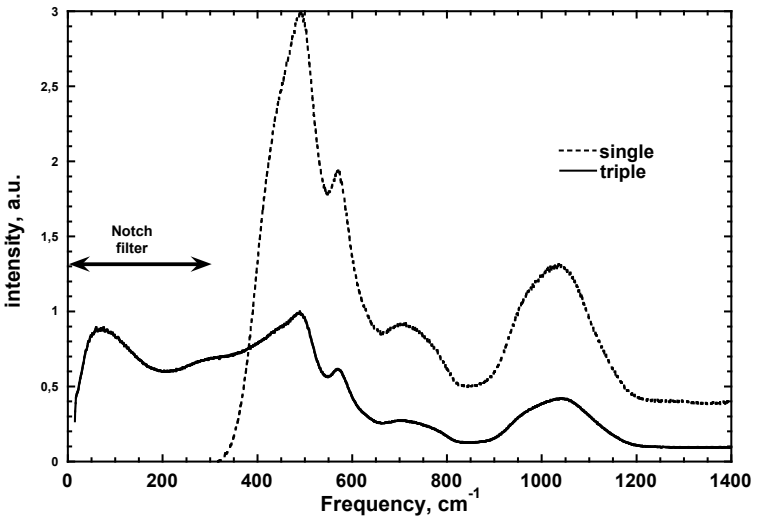


Figure 6. Raman spectra for the same sample obtained with one and three gratings using the same acquisition times. Note that with one grating it is not possible to go to low frequency and that accuracy is 3× lower compared to spectra collected with a triple grating instrument.

The original concept was developed by Minsky in 1961 (Minsky 1961) and adapted for Raman spectrometers by Dilor (now part of the Horiba-Jobin-Yvon group) in the early 1990s. This technique has gained popularity in the scientific and industrial communities and in particular in Raman spectroscopy. The laser beam illuminates the sample via the pinhole (D1), which limits the spatial resolution. The back scattered light then passes through a beamsplitter which passes the scattered light through a second pinhole (D2). The second pinhole has a diaphragm which is adjustable between 1 to >10 micron diameter with a 100 objective lens. The advantage of having the adjustable pinhole is that one can adjust the volume of the sample from which the scattered light is being collected.

Data acquisition and reduction

The quality of the Raman spectra depend on: i) the experimental parameters of the spectrometer (quality of lens, grating, detector, beamsplitter, etc.; ii) the size of confocal hole; iii) the microscope objective used; iv) the excitation line, λ_o; v) sample surface; vi) sample color λ_o; vii) sample heterogeneity; and viii) the refractive index of the sample.

Spot size, sample depth, number of acquisitions versus acquisition time. Since the 1990's, an optical microscope is generally used to focus the laser spot onto the material surface. The volume of the sample analyzed depends on several factors such as the opening of the confocal diaphragm, the nature of the sample and the excitation line. The size of the spot is defined by the objective and by the closure of the confocal hole. It must be estimated for each Raman spectrometer by using already known defined forms which are then compared at the spot size of interest. The nature of the sample will determine its refractive index and absorption characteristics. We can define two important parameters: Depth of field (d.o.f) and the diameter of the analysis spot (D):

$$\text{d.o.f.} = \frac{4\lambda}{NA^2}$$

Where *NA* represents the numerical aperture of the objective and λ the excitation wavelength.

EBSCOhost - printed on 2/13/2023 5:26 AM via . All use subject to https://www.ebsco.com/terms-of-use

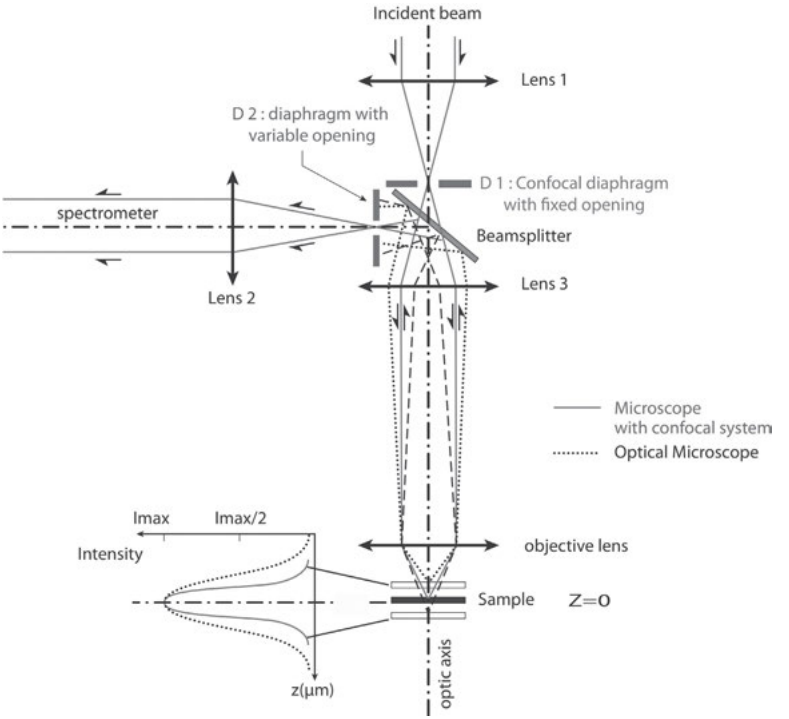


Figure 7. Confocal system developed from Minsky (1961) adapted for a Raman spectrometer (after Hawthorne 1988).

The diameter D of the spot can be estimated by using the Rayleigh criterion on the Airy function:

$$D = \frac{1.22\lambda}{NA}$$

The scattered light is collected by the same objective (backscattering configuration) and the size of the analyzed volume is determined by the confocal hole of the microscope.

Commonly, Raman spectra on crystalline phases are obtained in a few seconds with three scans usually run in order to ensure good quality spectra. Modern data collection software automatically correct spectra for non-reproducible signals (i.e., cosmic ray spikes) if more than 2 spectra are collected under the same instrumental conditions. However, for amorphous solids and liquids, the acquisition time can significantly increase (up to 600s per scan window) depending on the signal to noise required. Furthermore, for some experiments the number of repeated scans may also need to be significantly increased to >30 repeat scans. Conditions requiring such long acquisition times may be needed for example, if the experiment requires very low laser power so as not to induce damage to the sample e.g. hydrated iron-phyllosilicate, Gillet et al. (2002), or when examining low concentration elements within the sample e.g. dissolved volatiles elements (Thomas 2000).

The analyzed volume is usually adjusted to be close to the surface in the optimum region for the maximum Raman signal, i.e., within the first 10 µm of the surface (Behrens et al. 2006). Effects of focusing depth on the Raman results are only important for glasses containing iron and when very deep focusing is required (Behrens et al. 2006). For a quartz crystal, Chabiron

EBSCOhost - printed on 2/13/2023 5:26 AM via . All use subject to https://www.ebsco.com/terms-of-use

et al. (2004) noted a deviation from their calibration at 140 μm depth. They described this phenomenon as a variation in optical transmission as a function of the wavelength through the crystal. However, Behrens et al. (2006) did not recognize any change in Raman spectra due to the focusing depth for iron-free glasses, at least up to 200 μm. Focusing effects are discussed in detail in Behrens et al. (2006). For uncolored samples, focus has no effect on the Raman spectrum (see fluid inclusions section) but for colored samples Raman intensity decreases as a function of the cross section of the coloring cations.

Temperature and excitation line effects. Raman spectra can change as a function of excitation line and temperature[2]. Both effects have been described and discussed in detail in different books and papers (Shuker and Gammon 1970; Long 1977; Galeener and Sen 1978; Seifert et al. 1982; McMillan 1984; Neuville and Mysen 1996; Helhen 2010). Several authors have used the correction given below to compare Raman spectra taken at different temperatures and with different exciting lines (Mysen et al. 1982; McMillan et al. 1994; Neuville and Mysen 1996; Le Losq et al. 2012).

$$I = I_{obs} \cdot \left\{ \nu_O{}^3 \cdot \nu \frac{\left[1 - \exp(-hc\nu / kT)\right]}{(\nu_O - \nu)^4} \right\} \quad (1)$$

where h is the Planck constant, $h = 6.62607\times10^{-34}$ Js, k is the Boltzmann constant; $k = 1.38065\times10^{-23}$JK^{-1}, c is the speed of light, $c = 2.9979\times10^{10}$ cm s^{-1}, T is the absolute temperature, ν_0 is the wavenumber of the incident laser light, and ν is the measured wavenumber in cm^{-1}. This correction allows comparison of glass spectra taken with different incident excitation wavelengths, and/or comparison of spectra acquired at different temperatures, such as in the case of *in situ* measurements.

The correction stems from initial studies of glasses which exhibited an apparent temperature dependence of the low frequency bands (Hass 1969, 1970). Hass (1969) showed that for vitreous silica the region below 300 cm^{-1} was strongly affected by temperature. However, above 300 cm^{-1} the affect was essentially negligible. This temperature dependence was attributed to temperature effects on the thermal population of the initial vibrational states. The initial part of the correction given in Equation (1) [$\exp(-hc\nu/kT)$] accounts for these so called thermal effects. Prior to the mid to late 80's the low frequency Boson peak was not effectively recognized as being a real feature in the Raman spectra of glasses. The intensity attributed to "thermal effects" by Hass (1969, 1970) is in fact the Boson peak so that application of the Long correction effectively eliminates the Boson peak from the data. In addition, in nearly all papers published in the 60s and 70s on the thermal effect, the authors go to great lengths to point out that these thermal effects are limited to the low frequency region of the spectra and should not be applied beyond ~300 cm^{-1} (cf. Hass 1970; Shuker and Gammon 1970). The second part of the "Long" correction takes into account contributions to the intensity from the Rayleigh scattering. It is the ratio of the predicted intensity between the exciting and scattered photon at their effective wavenumber $[\nu\cdot\nu_O{}^3/(\nu_O-\nu)^4]$. Its effects are very small.

Black body and temperature effects. All bodies emit light, where the maximum wavelength evolves with the temperature of the body. Indeed, because of thermal excitation, atoms move and deviate from their equilibrium positions creating an electric dipole, which then emits an electromagnetic wave. To characterize the intensity of this emission, we use the luminance, which expresses the energy flow emitted in a given wavelength λ compared to the surface and to the solid angle of observation. The monochromatic luminance, L, is given by

2 Note the thermal effects influence the intensity of vibrational bands and are NOT due to structural changes in the sample as a result of heating.

EBSCOhost - printed on 2/13/2023 5:26 AM via . All use subject to https://www.ebsco.com/terms-of-use

Planck's law:

$$L = \frac{2hc^2}{\lambda^5} \cdot \frac{1}{\left(e^{\frac{hc}{\lambda k_B T}} - 1\right)}$$

where c is the speed of light, h Planck's constant and k_B Boltzmann's constant. Figure 8 shows the evolution of the luminance as a function of wavelength for different temperatures. The maximum of these curves moves towards the short wavelengths with increasing temperature and is given by Wien's law:

$$\lambda_{max} = \frac{2{,}898 \times 10^{-3}}{T}$$

Figure 8 shows that the maximum is situated at higher wavelength than the visible region used for Raman observations. As mentioned previously, the Raman signal has weak intensity

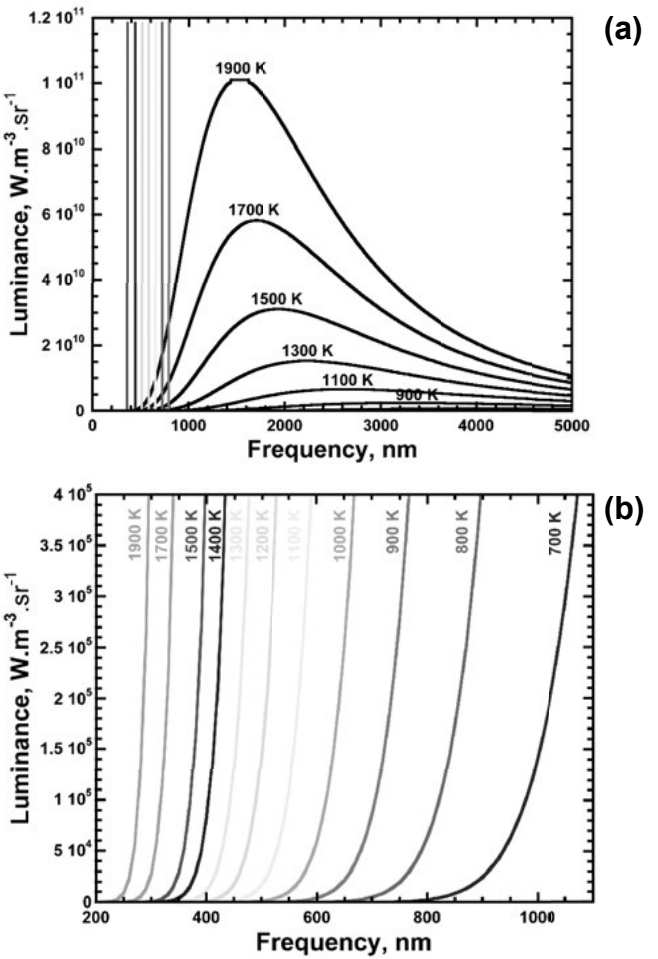


Figure 8. Evolution of the luminance as a function of wavelength for different temperatures.

EBSCOhost - printed on 2/13/2023 5:26 AM via . All use subject to https://www.ebsco.com/terms-of-use

and black body emissions are enough to mask the Raman intensity. It is therefore necessary to limit at most the number of unwanted photons which enter the objective. The luminance represented here is not the total energy flow and it is also necessary to take into account the volume of interaction, the solid angle of observation, the emissivity of the sample, the geometry of its surface and any extra reflected light coming from sample edges or the sample holder. It is then necessary when carrying out high-*T* experiments to limit these parameters by working with polished surfaces in homogeneous and transparent compounds containing as few scattering objects such as bubbles or impurities of a size equivalent or superior to the excitation wavelength, as possible. Figure 8b gives an idea of the maximum temperature reached at various wavelengths. This upper temperature limit can be improved by decreasing the size of the confocal hole, by adding an iris to mask the heating elements, by working with a small heating system like a heating wire (Neuville et al. 2014, this volume), or a pulsed laser source with the detector synchronized with the laser pulses.

Baseline correction and normalization

In order to compare several Raman spectra it is important to normalize the spectra and to use a common baseline correction. Several authors normalize Raman spectra to the maximum intensity (see Mysen and Frantz 1992, 1993, 1994a,b; McMillan 1984; McMillan et al. 1994). This is very easy to do and generally gives good results unless one wants to compare the low frequency region. In this case, it is better to divide the intensity of the Raman spectra by the power of the laser and the acquisition time to obtain a spectrum in 1 s and 1 mW (Neuville 2006). To investigate redox states or to determine the proportion of dissolve volatiles in a glass, it is preferable to normalize to the full area of the spectra after application of the temperature correction (Le Losq et al. 2012). The baseline correction to investigate volatiles in glass is developed more accurately later.

OTHER TYPES OF RAMAN SPECTROSCOPY

Hyper-Raman scattering (HRS)

HRS was developed by Denisov et al. (1987) and corresponds to a non-linear spectroscopy where two incident photons (ω_i) produce one scattered photon (ω_s) after interaction with an excitation (ω_p) in the medium. Infra-red (IR)-active modes are seen in HRS, but there are HRS-active modes that are silent both in Raman scattering and IR, while acoustic modes are HRS forbidden. As the HRS signals are usually very weak (typically $10^6\times$ smaller than Raman scattering), early work was limited in resolution, and the results did not include the low frequency region. Currently, technical advances in pulsed laser sources and charge coupled devices (CCD) allow one to reach resolutions comparable to that of Raman spectroscopy with reasonable acquisition times. HRS gives complementary information to Raman scattering, particularly on glasses where vibrational modes are IR or Raman inactive (Helhen et al. 2000, 2002; Simon et al. 2006, 2007, 2008).

Figure 9 shows: i) IR: semi-log presentation of ε''/ω derived from IR measurement where ω is wavenumbers; ii) RS: Raman spectra obtained with a T64000 Jobin-Yvon®, a triple spectrometer operating at 514.5 nm with a CCD camera and, iii) HRS, hyper-Raman spectrum of silica at low frequency after standard treatment, with frequencies in wave numbers ($\omega/2\pi c$). Figure 9 clearly shows that the HRS spectrum contains more vibrational information than the classic Raman spectrum. However HRS measurements are more difficult than classic Raman measurements and this new technique is essentially used only by physicists to investigate simple glass systems. The technique provides important information on the low frequency vibrations in amorphous states and is rapidly becoming a powerful tool to investigate amorphous materials at room temperatures but remains to be adapted for high pressure or high temperature studies.

EBSCOhost - printed on 2/13/2023 5:26 AM via . All use subject to https://www.ebsco.com/terms-of-use

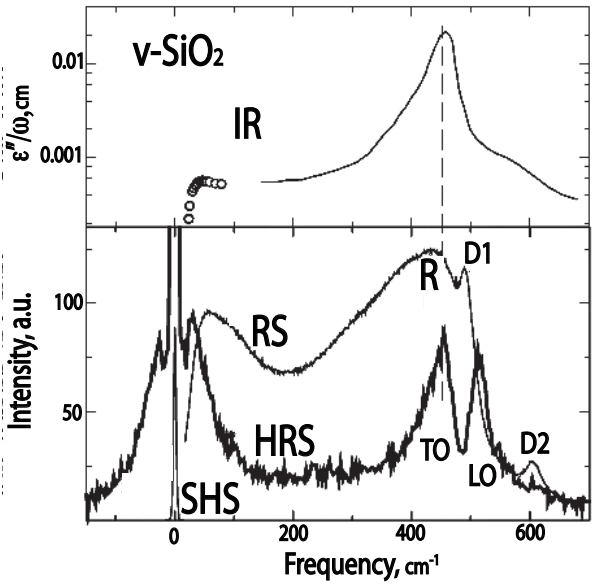


Figure 9. IR, Raman and HRS spectra of silica glass (modified from Helhen et al. 2000).

Surface Enhanced Raman Scattering (SERS)

SERS is a phenomenon in which the Raman scattering intensity from molecules close to the surface of certain finely divided metals is enhanced by a factor of about 10^6. Raman spectra arise from the vibrational frequencies of the molecules and provide molecular information that is particularly valuable in nano-chemistry. The inherently low sensitivity of conventional Raman scattering limits its applicability, but sensitivity enhancement by SERS has resulted in more widespread applications, especially in surface chemistry where the environmental sensitivity of vibrational spectra reveals how molecules interact with surfaces. The first paper reporting the phenomenon was by Fleischmann et al. (1974), who observed potential-dependent Raman signals from pyridine adsorbed on a silver electrode that had been electrochemically roughened in potassium chloride aqueous electrolyte. Two groups (Albrecht and Creighton 1977; Jeanmaire and Van Duyne 1977) clarified the degree of Raman signal enhancement in the pyridine-on-silver system and proposed enhancement mechanisms based on electromagnetic and chemical effects, respectively. Van Duyne proposed the SERS acronym and claims that his group discovered SERS. The initial paper of Fleischmann et al. (1974) has been cited more than 1200 times, and SERS is now very well used in the chemical sciences. The main contributor to the intensity enhancement is an electromagnetic effect arising from laser excitation of localized surface plasmons (collective electron oscillations) at rough metal surfaces which creates an enhanced electric field. Both the incident and scattered light are influenced by this field enhancement, resulting in a total Raman signal enhancement proportional to the energy field. A smaller contribution to SERS enhancement comes from a charge transfer mechanism for adsorbed molecules with appropriate acceptor or donor orbitals that interact with the metal substrate. The metals exhibiting the largest SERS enhancements are silver, gold and copper. More details on SERS and its applications are given by Fleischmann et al. (1974) and Jeanmaire and Van Duyne (1977).

Since 1980 SERS has been widely developed for biological interactions. However, the technique is also useful for materials and earth sciences to enhance the Raman signal obtained

EBSCOhost - printed on 2/13/2023 5:26 AM via . All use subject to https://www.ebsco.com/terms-of-use

with a portable Raman spectrometer. By using and developing SERS it's possible to perform direct *in situ* analyses when doing earth science exploration (volcanology, mineral exploration).

APPLICATIONS

Crystalline spectra

Figure 10 shows the Raman spectra of Silicon (Si), Silica polmorphs and amorphous SiO_2 (glass). The first-order Raman spectrum yields energies for the $k = 0$ optical modes of 520.2±0.5 cm^{-1} for Si. Si has a diamond structure with space group $Fd3m$ with 2 atoms in the smallest volume unit cell. It has one triply degenerated optic mode at $k = 0$ with symmetry F_{2g}. These optical vibrational modes of Si in a diamond structure are Raman active but not infrared active. A single Raman line is observed from the optic modes at $k = 0$, where k is the wave vector of the mode. Since this mode is not polar, it is not affected by transverse or longitudinal optical mode (TO and LO) splitting, and a single line, at 520 cm^{-1}, is observed. A second order transition is also visible at around 970 cm^{-1}. The ratio of the peak intensity of the second-order band to that of the first-order line is found experimentally to be ~3×10^{-3}. The intensity of these two peaks depends strongly on the crystallinity and local organization of the Si (Kravets and Kolmykova 2005).

The Raman spectrum of quartz, shows a very strong vibration at 466 cm^{-1}, lower than the 520 cm^{-1} observed for Si, which corresponds to an A_1 Raman active mode. To a first approximation, we can explain the lower frequency observed for SiO_2 compared to Si by the fact that the SiO_2 molecule is heavier than Si (heavier atoms will have corresponding vibrational bands at lower wavenumbers because of their higher mass and its effect on the vibrational frequency). Crystalline SiO_2 has been studied extensively with both the early Hg arc lamp source and more modern laser excitation. One of the first reviews of optical lattice vibrations in quartz and their assignments was made by Scott and Porto (1967), subsequently She et al. (1971) reported more accurate measurements of Raman intensities in quartz and

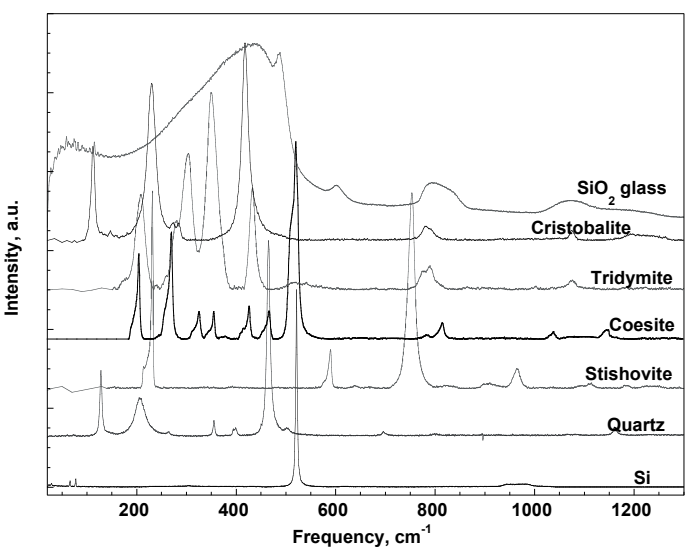


Figure 10. Raman spectra of silicon and SiO_2 crystalline polymorphs and amorphous states (New Raman spectra made with T64000 Raman spectrometer, with 488 nm excitation line).

EBSCOhost - printed on 2/13/2023 5:26 AM via . All use subject to https://www.ebsco.com/terms-of-use

Bates and Quist (1972) and Etchepare et al. (1974) obtained the polarized Raman spectra of α quartz. The lattice dynamics of quartz have also been calculated by many authors (Saskena 1940; Kleinman and Spitzer 1962; Etchepare et al. 1974). In Figure 10, we present only α-quartz but the lattice structure of α- and β- quartz are very similar; the β-phase appears at temperatures higher than 900 K (Bates and Quist 1972).

In the case of the silica polymorphs, with the exception of stishovite, molecular entities are SiO_4 tetrahedra and they are linking together by corners. Stishovite is a high pressure polymorph and is built of SiO_6 octahedra. Complete discussion of the Raman active vibrations, of the SiO_2 polymorphs can be found in Kingma et al. (1993), Hemley et al. (1986), and McMillan et al. (1994). It is clear that Raman Spectroscopy is a very good tool to discriminate between minerals and mineral polymorphs, and degree of order of minerals (Balan et al. 2001). Today, Raman spectroscopy is used to characterize materials in online industrial processes for "quality control," for identification of different mineral phases using Raman spectral databases (like RRUFF) and organic compounds in industrial processes.

Amorphous materials

Raman spectra on amorphous materials were first made by Hollaender and Williams (1929, 1931) on ordinary plate glass, which corresponds to a soda-lime silicate glass (window glass). Hollaender and Williams (1929, 1931) first observed the differences between crystals and glass a few years before Warren (1934a,b) and Zachariasen (1932). In the Raman spectrum of the plate glass, Hollaender and Williams (1929, 1931) identified 11 bands similar to those observed in the IR spectrum of fused quartz by Reinkober (1911). Their spectra clearly showed that the number, intensity and position of bands in amorphous quartz is slightly different to the bands observed in the different polymorphs of quartz. In particular a new band appears at low frequency, the boson peak, located near 80 cm^{-1}, and this band is a Raman signature of tetrahedrally connected glasses. It has been ascribed to Raman scattering involving rotational motions of almost rigid tetrahedra (Buchenau et al. 1986) although its origin remains controversial and is a continuing area of interest in condensed matter physics. In the case of silica glasses, its intensity increases and shifts to higher frequency with increasing distortion of the SiO_4 tetrahedra (Hehlen et al. 2000, 2002). This is clearly visible in Figure 11 for SiO_2 glass and soda silicate glasses (Na1, Na12, Na25, Na33).

Silicate glasses

In the Figure 11, we have plotted Raman spectra for silicate glasses between pure silica up to Mg-silicate with 38% mole of MgO. This figure summarizes the features visible in silicate glasses. We observe different regions: 20-200 cm^{-1}, 200-600 cm^{-1}, 600-800 cm^{-1}, 800-1200 cm^{-1}, which correspond to different types of vibrations resulting from differences in the organization of the glass structure. In the following, we will distinguish Q^n species as tetrahedrally coordinated cations with n Bridging Oxygens (BO) and $4–n$ Non-Bridging Oxygens (NBO).

***The boson region* (*10-250 cm^{-1}*).** Below 250 cm^{-1}, there is only a scattering continuum and the Rayleigh tail of the excitation source, except at very low frequency where there is what is termed the boson peak (Malinovsky and Sokolov 1986; Buchenau et al. 1986) noted above. In Figure 11 the Boson peak increases in frequency with decreasing silica content in the M-silicate glasses. This can be explained as proposed by Neuville (2005, 2006) and more recently by Le Losq et al. (2014) as a correlation between the frequency of the Boson peak and the glass depolymerization. Moreover, at constant silica content, and therefore constant polymerization, the Boson peak position varies linearly with the nature of the network modifier (Neuville 2005, 2006).

EBSCOhost - printed on 2/13/2023 5:26 AM via . All use subject to https://www.ebsco.com/terms-of-use

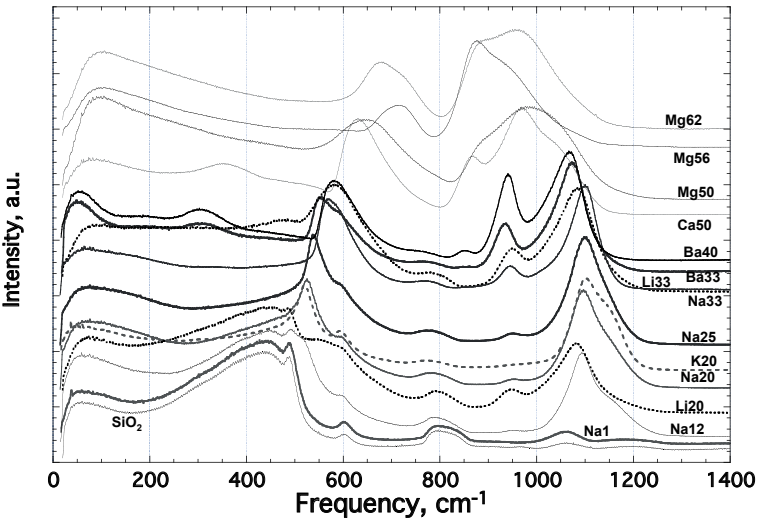


Figure 11. Raman spectra of binary silicate glasses and SiO_2 glass, Raman spectra are labeled as MX where M = Li, Na, K, Mg, Ca, Ba, and X corresponds to the molar fraction of the oxide of M. For example Na20 = NS4 = 80%SiO_2-20%Na_2O in mol% (New Raman spectra made with T64000 Jobin-Yvon Raman spectrometer, with 488nm excitation line).

The low frequency region (250-600 cm^{-1}). The room-temperature Raman spectra exhibit a strong band centered near 500 cm^{-1} for SiO_2 glass with a shoulder near 450 cm^{-1}, and another band near 600 cm^{-1} similar to other published spectra of vitreous silica (e.g., Bell et al. 1968; Bell and Dean 1972; Seifert et al. 1982; Phillips 1984; McMillan et al. 1994). Bands near 400-600 cm^{-1} in silicate networks are usually assigned to vibrations of the BO associated with three-, four-, five-, six- or higher-membered rings of tetrahedra present in silicate networks (Mysen et al. 1980a; Sharma et al. 1981, 1985; Galeener 1982a,b; McMillan and Piriou 1982; Seifert et al. 1982; Galeener et al. 1983, 1984; McMillan et al. 1994; Pasquerello and Car 1998; Pasquarello 2001; Umari and Pasquarello 2002; Umari et al. 2003; Rahmani et al. 2003). They reflect the inter-tetrahedral angle distribution and thus the ring arrangement. In pure silica, three peaks near 440 cm^{-1}, 495 cm^{-1} and 606 cm^{-1} are visible in this frequency range (e.g., see spectra in Galeener 1982a). The first peak near 440 cm^{-1} is ascribed to the predominant motions of oxygen atoms, involved in Si-O-Si bonds in five-, six or higher-membered rings (Sharma et al. 1981; McMillan et al. 1994; Kalampounias et al. 2006). The exact nature of the vibration, i.e., stretching or bending for instance, seems to be uncertain but all studies point out the motion of oxygen in Si-O-Si linkages (McMillan et al. 1994). The second band, near 485-490 cm^{-1}, is usually called the D1 band and is formed by breathing motions of oxygen atoms (i.e. movements of oxygen perpendicular to the Si-O-Si plane) in regular, but slightly puckered, four-membered rings (Sharma et al. 1981; Galeener 1982b; Pasquarello and Car 1998; Umari and Pasquarello 2002; Umari et al. 2003; Rahmani et al. 2003). The third band, located near 606 cm^{-1}, is usually called the D2 band and is ascribed to the breathing motion of oxygen atoms in planar three-membered rings (Galeener 1982a,b; Galeener et al. 1983; Pasquarello and Car 1998; Umari and Pasquarello 2002; Umari et al. 2003; Rahmani et al. 2003). With addition of alkali or alkaline earth elements these bands evolve into a peak visible at 580 and a shoulder at 600 cm^{-1}. The peak at 580 cm^{-1} has been assigned to Si-O^0 rocking motions in fully polymerized SiO_2 (Q^4) units (Bell and Dean 1972; Phillips 1984) while the maximum at 600 cm^{-1} has been assigned to Si-O-Si bending motions in depolymerized structural units (Lazarev 1972; Furukawa et al. 1981).

EBSCOhost - printed on 2/13/2023 5:26 AM via . All use subject to https://www.ebsco.com/terms-of-use

The intermediate frequency region (700-850 cm^{-1}). In the case of SiO_2, the 800 cm^{-1} band is attributed to Si-O stretching involving oxygen motions in the Si-O-Si plane (McMillan et al. 1994) or to the motion of the Si atom in its oxygen cage (Mysen et al. 1982). Another attribution arises from the central force model of Sen and Thorpe (1977), which links the 800 cm^{-1} band to the threefold –degenerate "rigid cage" vibrational mode of TO_2 units (Galeener 1979). This peak decreases in intensity with MO and shifts slowly to higher frequency. It is also asymmetric and has been assigned to two bands with TO/LO splitting (Galeener and Lucovsky 1976; Galeener et al. 1983)

The high frequency region (850-1300 cm^{-1}). Si-O stretching is responsible for the broad band observed near 1100 cm^{-1} (Bell et al. 1968; Sen and Thorpe 1977). Several studies have noted that different peaks are convoluted in this band and arise from the T-O stretching in different Q^n tetrahedral units (see McMillan (1984) and Mysen (2003) and references therein). The intensity of these bands increases with alkali or alkaline-earth content, and by curve fitting (spectral deconvolution) of this high frequency region, three Gaussian bands can be observed at 1000, 1100 and 1200 cm^{-1} in silicate glasses. Some questions remain as to assignment of these bands. Firstly, no Transverse-Optic/Longitudinal Optic (TO-LO) effect occurs in the 850-1300 cm^{-1} normal Raman spectral region (Denisov et al. 1984). Bands expressed in this frequency range arise only from the expression of particular vibrational modes of the TO_4 tetrahedra (Le Losq and Neuville 2013). For pure SiO_2 glass there are only two peaks, one near 1050 and a wider peak centered near 1200 cm^{-1}. These two peaks (cf., Fig. 11) are also visible in the Na1 Raman spectra (MX = (100–X)%SiO_2-XMO with M = Li_2, Na_2, K_2, Mg, Ca, Ba), and with increasing Na_2O content (Na12= NS7 glass), the intensity of the peak at 1050 cm^{-1} increases strongly. In the case of silica glass, the high frequency part near 1200 cm^{-1} can be split into two bands using deconvolution (Seifert et al. 1982), named $Q^{4,II}$ (1100 cm^{-1}) and $Q^{4,I}$ (1170 cm^{-1}), to account for the Q^4 signal in all spectra although these assignments remain controversial. According to the Sen and Thorpe (1977) model, the $Q^{4,II}$ band represents vibrations associated with BOs with lower T-O-T angles than the $Q^{4,I}$ band. With increasing MO content, the $Q^{4,I}$ (1170 cm^{-1}) band is lost and new bands appear at lower frequencies for NBO vibrations associated with Q^3, Q^2, Q^1 and Q^0 tetrahedra. The bands shift to lower frequency as a function of increasing M_xO and in the case of the Na25 glass spectra, the 960 cm^{-1} band is assigned to Si-O$^-$ stretching in Q^2 species (Brawer and White 1975; Mysen et al. 1982; Seifert et al. 1982; McMillan 1984; Mysen 1999). The 1100 cm^{-1} band is ascribed to Si-O$^-$ stretching occurring in Q^3 units (Brawer and White 1975; Virgo et al. 1980; McMillan 1984).

The case of the 1070 cm^{-1} band is more complicated. This band is also observed in Raman spectra of pure silica, and alkali and alkaline-earth silicate glasses (Mysen and Frantz 1992, 1993; McMillan 1984; Frantz and Mysen 1995; Neuville 2005, 2006). It has been attributed to vibrations involving bridging oxygen atoms in structural units which do not need to be fully polymerized (Mysen et al. 1982), or to vibrations of Si-O doublets associated with alkaline-earth or alkali metals (Fukumi et al. 1990; McMillan et al. 1992). However, this band is present all along the SiO_2-M_xO join (with M_x: alkaline earth ($x = 1$) or alkali ($x = 2$) elements; Mysen et al. 1982; Seifert et al. 1982; McMillan 1984; Neuville and Mysen 1996; Neuville et al. 2004, 2006, 2008). This indicates that the stretching vibrations of the Si-O pairs which cause this band are not really affected by the Q^n distribution despite frequency and intensity variations that are compositionally dependent. Therefore it probably arises from a Si-O stretching which is different from the Si-O stretching of the Q^n bands. The vibrational density of states of vitreous SiO_2 presents also a two-band splitting at high frequency: one band is located neat 1060 cm^{-1} and the other near 1200 cm^{-1}. Using a first-principle approach, Sarnthein et al. (1997) and Pasquarello et al. (1998) have ruled out the LO-TO splitting interpretation, and proposed that the two bands, observed both in the calculated vibrational density of states and in the measured neutron density of states, arise from two different vibrations of the tetrahedral subunits (i.e., the Q units). The first band, at low-frequency, can be related to a stretching

EBSCOhost - printed on 2/13/2023 5:26 AM via . All use subject to https://www.ebsco.com/terms-of-use

T_2 vibrational mode of the SiO_4 Q^4 tetrahedron (Sarnthein et al. 1997; Taraskin and Elliott 1997; Pasquarello et al. 1998). According to group theory, it corresponds to two oxygen atoms moving closer to the central Si atom while the two others oxygen atoms are moving away (Sarnthein et al. 1997; Dresselhaus et al. 2010). The second band, at higher frequency, corresponds to the A_1 vibrational mode, which is an in-phase motion of the four oxygen atoms toward the central Si atom (Sarnthein et al. 1997; Taraskin and Elliott 1997; Pasquarello et al. 1998; Dresselhaus et al. 2010). By comparing Raman spectra and the vibrational density of states (measured and calculated) of vitreous SiO_2 (see spectra in Pasquarello and Car 1998 for instance), it appears that frequencies of the two Raman bands (near 1060 and 1200 cm^{-1}) are close to those of the T_2 and A_1 bands. As the high-frequency part of the vibrational density of states and the normal Raman spectra of the SiO_2 glass are both unaffected by the LO-TO splitting (Sarnthein et al. 1997; Denisov et al. 1984), we suggest that the 1060 cm^{-1} band in Raman spectra of silica, silicate and aluminosilicate glasses can correspond to a stretching T_2 vibrational mode of TO_4 tetrahedra (Q^4). Consequently, the other bands arise from the A_1 vibrational modes of the different Q^n units.

Following the previous discussion, in the Na25 Raman spectrum we can attribute the band near 960 cm^{-1} to the A_1 vibration of Q^2 species, the band near 1100 cm^{-1} to the A_1 vibration of Q^3 species, and the band near 1050 cm^{-1} to a stretching T_2 mode of TO_4 tetrahedra (Q^4). The A_1 stretching mode of Q^4 units has a Raman signal at frequencies between 1100 and 1200 cm^{-1} (see for example Mysen et al. 1982 and references therein). In the Na25 Raman spectrum, one can account for Q^4 vibrations using one band, located near 1150 cm^{-1} (see for instance Mysen 2003, Le Losq and Neuville 2013, and Le Losq et al. 2014).

Figure 11 also shows the Raman spectra for depolymerize glasses with high MO content, in this case the intensity maximum of the T-O-T stretching bands show clearly Si in Q^0 and Q^1 species like for the Mg62 and Mg56 Raman spectra. Figure 12 shows the variation of Q species as a function of proportion of network modifier content and the average frequency for each Q species. The wavenumbers are given approximately and depend on the alkali or alkaline-earth elements.

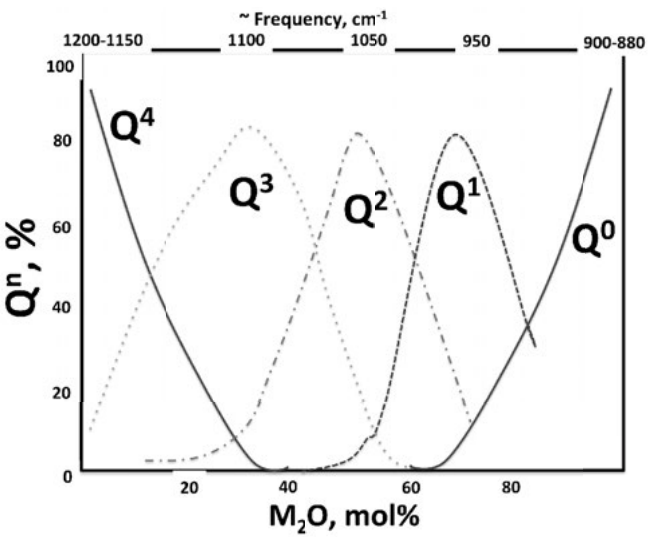


Figure 12. schematic representation Q species as a function of M_2O, M = Li, Na, K, Ca/2, Mg/2, Sr/2, Ba/2 for silicate glasses and Raman wavenumbers for each Q species.

EBSCOhost - printed on 2/13/2023 5:26 AM via . All use subject to https://www.ebsco.com/terms-of-use

Aluminosilicate glasses

In the case of aluminosilicate glasses Al substitutes for Si in tetrahedral positions (Seifert et al. 1982; Neuville and Mysen 1996; Neuville et al. 2004, 2006, 2008; Le Losq et al. 2014). Similar vibrations and combination can be observed for Al as for Si. Al can be in Q^4, Q^3 and Q^2 units (McMillan and Piriou 1983; Neuville et al. 2008, 2010; Licheron et al. 2011) and the proportion of different Q species depends on the silica content. Along the tectosilicate join, Al is only in Q^4 species whatever the charge compensator, Na, Ca, Mg (Neuville and Mysen 1996; Neuville et al. 2004, 2006, 2008); Le Losq et al. 2014. Generally, for more than 33 mol% of SiO_2 in peralkaline compositions, Al is only in Q^4. At lower content in silica, Al can be in Q^3 and Q^2 species in particular on aluminate glasses. Figure 13a,b shows the Raman spectra of calcium aluminosilicate glasses along the tectosilicate join that illustrate clearly the strong substitution between Si and Al, in particular for T-O-T stretching vibrations. The Figure 13b shows that Al substitutes for Si in the Si-O-Si vibration, to obtain finally an Al-O-Al vibration for the CA50.00 glass (calcium aluminate) (McMillan and Piriou 1983; Neuville et al. 2010; Licheron et al. 2011). We clearly observe that these wavenumber variations as a function of SiO_2 content are the same whatever the network modifier.

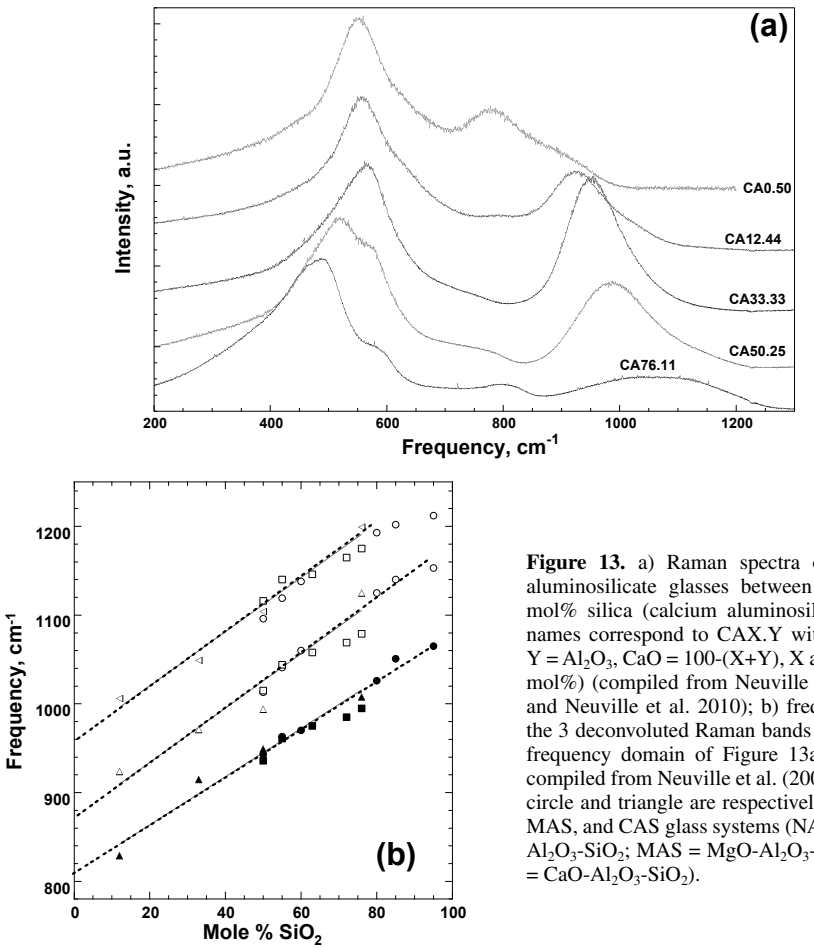


Figure 13. a) Raman spectra of calcium aluminosilicate glasses between 0 and 76 mol% silica (calcium aluminosilicate glass names correspond to CAX.Y with X=SiO_2, Y = Al_2O_3, CaO = 100-(X+Y), X and Y are in mol%) (compiled from Neuville et al. 2006 and Neuville et al. 2010); b) frequencies of the 3 deconvoluted Raman bands in the high frequency domain of Figure 13a. Data are compiled from Neuville et al. (2008), square, circle and triangle are respectively for NAS, MAS, and CAS glass systems (NAS = Na_2O-Al_2O_3-SiO_2; MAS = MgO-Al_2O_3-SiO_2; CAS = CaO-Al_2O_3-SiO_2).

EBSCOhost - printed on 2/13/2023 5:26 AM via . All use subject to https://www.ebsco.com/terms-of-use

Borosilicate glasses

Similar observations can be made for borate or borosilicate glasses (Fig. 14). Linear variations of the Q distribution can be observed as a function of the B_2O_3/SiO_2 ratio (Lenoir et al. 2008). With B_2O_3, a broad band near 1500 cm^{-1} and a narrow band slightly below 800 cm^{-1} markedly develop when the B_2O_3 content increases. Correlatively, the strong feature present near 1100 cm^{-1} in B_2O_3-free glasses becomes much less intense. Finally, below 600 cm^{-1}, the spectral changes are more subdued even though an initially sharp decrease in band intensity is observed when B_2O_3 is introduced. These observations are thus consistent with the separation of the Raman spectra of borosilicates into four different frequency ranges. Between 1600 and 1200 cm^{-1}, the bands are associated with stretching of B-O^- bonds (O^- = NBO) attached to large borate groups (Kamitsos et al. 1987; Chryssikos et al. 1990). Near 800 cm^{-1}, the narrow band observed represents breathing vibrations of the so-called boroxol rings, which are made up of three corner-sharing BO_3 triangles (Iliescu et al. 1993; Meera and Ramakrishna 1993; Manara et al. 2009a,b). In borosilicates, this peak overlaps with another peak found near 770 cm^{-1}, which has been assigned by Maniu et al. (2003) to the symmetric breathing vibrations of six-membered rings of BO_4 tetrahedra (i.e., triborate, tetraborate or pentaborate). Finally, the bands observed below 600 cm^{-1} in silicates are attributed to Si-O-Si bending modes, coupled with tetrahedral O-Si-O bending vibrations. The shoulder at 590 cm^{-1} near the main peak observed around 530 cm^{-1} has often been assigned to symmetric oxygen breathing vibrations of three-membered siloxane rings (Matson et al. 1983; Tsujimura et al. 2004).

Between 1200-1600 cm^{-1}, two Gaussian bands can be fitted to the spectra. The band centered on 1410 cm^{-1} is due to $B\emptyset_2O^-$ triangles ($\emptyset$ = bridging oxygen) linked to $B\emptyset_4^-$ units whereas the band at about 1490 cm^{-1} has been assigned to $B\emptyset_2O^-$ triangles linked to other BO_3 units (Akagi et al. 2001; Cormier et al. 2006). However, a clear band appears around 630 cm^{-1} corresponding to BO_4 tetrahedra bonding with silicate units, similar to those found in danburite (Manara et al. 2009a,b). Recently by doing a full deconvolution of borosilicate Raman spectra Cochain et al. (2012) showed that it is possible to determine the N4, $BO_4/(BO_3+BO_4)$ ratio from the Raman spectra and they found similar results to those obtained from B *K*-edge XANES or NMR spectroscopy.

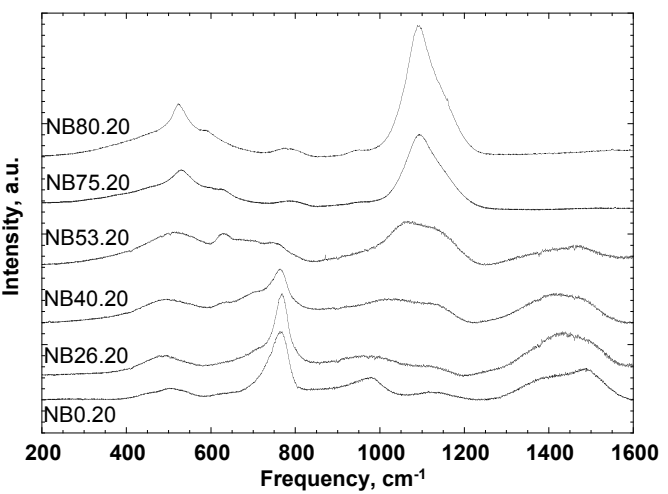


Figure 14. Raman spectra of borosilicate glasses between sodium tetrasilicate (NB80.20) and tetraborate glasses (NB0-20) data from Lenoir et al. (2008). Sodium borosilicate glass names correspond to NBX.Y with X = SiO_2, Y = Na_2O, B_2O_3 = 100-(X+Y), X and Y are in mol%.

EBSCOhost - printed on 2/13/2023 5:26 AM via . All use subject to https://www.ebsco.com/terms-of-use

Titanosilicate glasses

Several studies have been made on titanosilicate glasses by Raman spectroscopy (Henderson and Fleet 1995; Mysen and Neuville 1995; Reynard and Webb 1998). Generally a strong band appears near 880-900 cm^{-1} upon addition of TiO_2 content (Mysen and Neuville 1995; Reynard and Webb 1998). But from Raman spectroscopy it is difficult to obtain information on the coordination number of Ti in glass. However, Henderson and Fleet (1995) were able to use Raman spectroscopy to indicate the presence of five- and six-fold Ti in a series of silicate, alkali-silicate and alkaline-earth silicate glasses. They based their interpretation on comparison of the glass spectra with Ti-containing mineral standards, along with subtle changes in band shape, position and intensity as TiO_2 was added to the glass. As Henderson and Fleet (1995) point out, the band observed around 800-900 cm^{-1} is not directly attributable to Ti specifically but to the effect of added Ti on the silicate vibrations (See Henderson and Fleet 1995 for a discussion). Its presence by itself does not indicate a specific Ti coordination without a careful and detailed analysis of the compositional effects on the glass Raman spectra.

Iron silicate glasses

Iron is an important element for natural and industrial glasses, but Fe can be in different coordinations as a function of the Fe^{2+}/Fe^{3+} ratio. Fe^{2+} is essentially in six-fold coordination and acts as a charge compensator or network modifier whereas Fe^{3+} can be in four-fold coordination or six fold coordination and in four-fold coordination can act as a network former (Mysen et al. 1980c, 1985a,b; Dingwell and Virgo 1987; Magnien et al. 2006; Cochain et al. 2012). In silicate glasses with 5 mol% of FeO, a strong band is clearly visible as a function of the redox state (Magnien et al. 2006). This band at 990 cm^{-1} increases when the redox state ($Fe^{3+}/\Sigma Fe$) varies from 0.22 to 0.97. The band intensity increases with Fe^{3+} content and becomes the main band of the entire spectrum at high-Fe^{3+} content (Fig. 15). The intensity of the band clearly correlates with the Fe^{3+} abundance at constant iron content. In accordance with these trends, this band is lacking in the spectrum of the most reduced sample in the same way as it is absent in the iron-free glass (Magnien et al. 2006; Cochain et al. 2012). This band near 990 cm^{-1} clearly correlates with the abundance of Fe^{3+}, and Cochain et al. (2012) assign it to a vibration

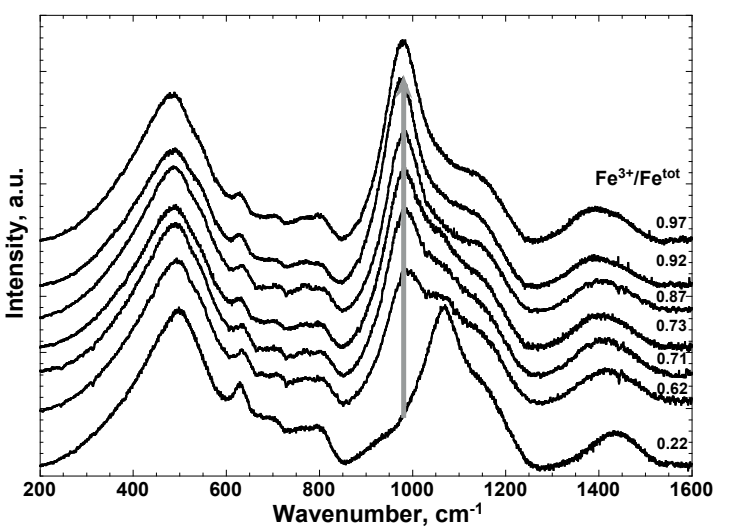


Figure 15. Raman spectra of borosilicate glasses with 5% of FeO with different ratio Fe^{3+}/Fe^{tot} (adapted from Cochain et al. 2012).

EBSCOhost - printed on 2/13/2023 5:26 AM via . All use subject to https://www.ebsco.com/terms-of-use

involving stretching of Fe^{3+}-O bonds (Magnien et al. 2006; Cochain et al. 2012). This is well correlated with previous studies (Mysen et al. 1985b; Magnien et al. 2004; Cochain et al. 2012) where in iron-rich MO-SiO_2 systems (M = Ba^{2+}, Sr^{2+}, Ca^{2+}, Mg^{2+}) the band is associated with stretching vibrations of $^{IV}Fe^{3+}$-O bonds and the decreased intensity of this band to the disappearance of tetrahedrally-coordinated ferric iron similar to that observed in the system SiO_2-CaO-MgO-Na_2O-FeO by Magnien et al. (2006), also attributed to stretching of $^{IV}Fe^{3+}$-O bonds. With the increase in the Fe^{3+} proportion, an increase in the number of bridging oxygens (n) is also observed in the Q^n species (Cochain et al. 2012).

With a low redox state, the proportion of Fe^{2+} is higher than Fe^{3+}, and Fe^{2+} can act as a charge compensator or network modifier which produces a decrease in the Q speciation (Magnien et al. 2006; Cochain et al. 2012). Raman can be an interesting tool to investigate redox state, but it is important to choose an appropriate excitation line, and to work with low laser power because at high power you can heat and locally melt the glass.

Volatiles in glasses

Gas, volatile elements and water have a strong Raman signature and are generally easy to investigate. However, it is more complicated to study dissolved gases and volatiles in glass. CO_2, H_2O, N_2, SO_4 dissolved in glass have been studied by several authors (Verweij et al. 1977; Mysen et al. 1980b; Mysen and Virgo 1980; Thomas 2000; Behrens et al. 2006; Roskosz et al. 2006; Le Losq et al. 2012, 2013; Thomas et al. 2008; Lenoir et al. 2009). Recently, Le Losq et al. (2012) have proposed a new baseline correction to quantify the water concentration and speciation in silicate glasses and melts.

To determine the water concentration, Le Losq et al. (2012) used a robust reproducible method to smooth and interpolate a baseline below the regions of interest, particularly in the silicate part of the Raman spectrum. They used *general cross validated splines* which perform an optimised smoothing and interpolation of a smooth function with known random noise (a FORTRAN code of the algorithm, references and credits can be found at *http://www.netlib.org/gcv/gcvspl*). A set of zones devoid of signal are defined, the Background Interpolation Regions (*BIR*), in order to constrain the baseline. The algorithm will smooth the data and allow interpolation within and between the chosen BIRs, taking into account the estimated standard errors and a smoothing factor. The baseline is constrained in the high frequency region (2700-4000 cm^{-1}) using 2 BIRs; defined between 2700-2800 cm^{-1} to 3100 cm^{-1}, and from 3750 cm^{-1} to the end of the spectrum as illustrated in the Figure 16. The *BIRs* are maintained constant

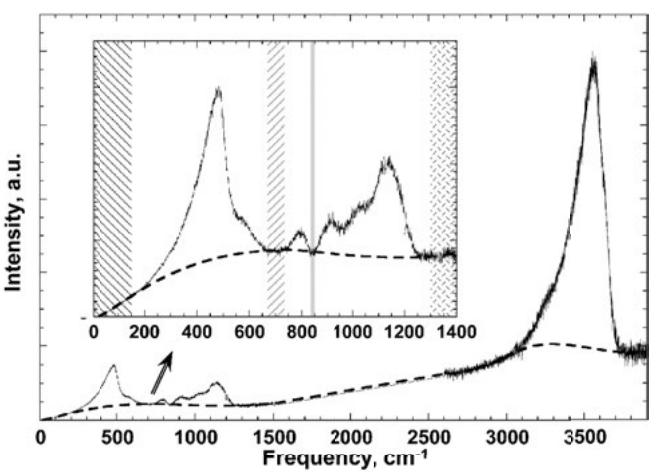


Figure 16. Raman spectra of albite glass with 3.5% of water (from Le Losq et al. 2012) the dashed zones correspond to the BIRs (adapted from Le Losq et al. 2012).

EBSCOhost - printed on 2/13/2023 5:26 AM via . All use subject to https://www.ebsco.com/terms-of-use

regardless of the composition of the sample. In this manner the high frequency region due to the presence of water can then be fitted using standard curve fitting methods. In the low frequency region, the baseline is constrained by three to four *BIRs* and then fit with the appropriate curves representative of the Si-O vibrational bands. To take into account chemistry effects, the *BIRs* are dependent on composition. For a single chemical composition, the *BIRs* are kept constant regardless of the glass water content. The first *BIR* is located at the beginning of the spectrum at 0-150 cm^{-1} and is not dependent upon composition. In the 150-1200 cm^{-1} region, two others *BIRs* are defined and their positions are dependent on silica content (Fig. 16). To place these *BIRs* and to constrain their position their slopes should tend to the horizontal. Le Losq et al. (2012) show that for similar compositions, *BIRs* values are quite similar. However, a shift to lower frequencies can be observed when silica content decreases. *BIRs* allow us to establish a unique calibration for a large chemical set of glasses.

By following the baseline correction proposed by Le Losq et al. (2012) it is possible to quantify water content in silicate glasses and melts reasonably accurately. The procedure can also be applied to investigate other volatiles such as sulfate, CO_2, and N_2, in silicate glasses. Figure 17 shows Raman spectra of a KS4 glass containing CO_2 where a strong band is visible near 1080 cm^{-1} and can be attributed to ν_1 stretching vibration of C-O in the CO_3^{2-} molecule linked to the Si-Al network following (Mysen and Virgo 1980; Guillot and Sator 2011). By doing a deconvolution of the 800-1200 cm^{-1} region for different Q species plus a Gaussian band for the ν_1 stretching C-O vibration, it is possible to quantify the CO_2 concentration in glasses or melt (Amalberti et al. 2014). Similar methods have been used for investigating SO_4^{2-} (Manara et al. 2007; Lenoir et al. 2009, 2010), N_2 (Roskosz et al. 2006) and can be made on others volatiles elements or halogens like I, Br, Cl…

Fluid inclusions

Fluid inclusions are memories of the parental liquid state trapped in a crystal during magma evolution. By investigating fluid inclusions, volcanologists can determine the history of a volcanic eruption (Nasdala et al. 2003; Metrich et al. 2011). But a fluid inclusion is a glass inside a crystal so to obtain good Raman spectra, a confocal system is needed. However, Raman spectra of fluid inclusions are often the sum of the Raman spectra of the crystal and the glass. In

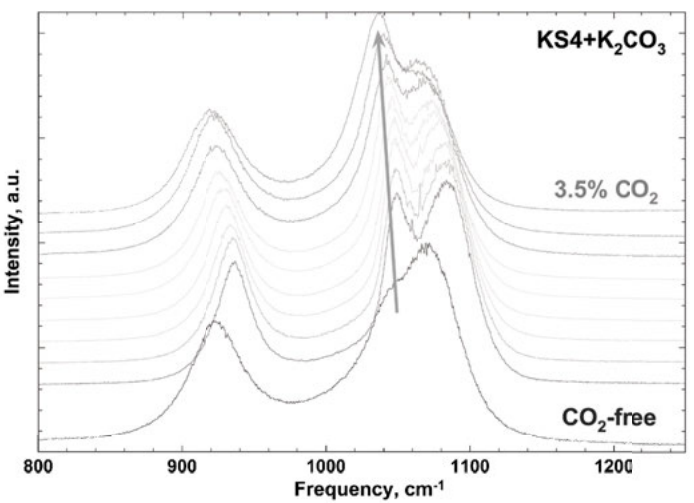


Figure 17. Raman spectra of KS4 glass with dissolved CO_2. (Raman spectra made with T64000 Jobin-Yvon Raman spectrometer, with 488 nm excitation line).

EBSCOhost - printed on 2/13/2023 5:26 AM via . All use subject to https://www.ebsco.com/terms-of-use

this case, the Raman spectrum of the inclusion can be obtained easily by subtracting the spectrum of the mineral host from the raw spectrum (Fig. 18). Finally, volatiles in fluid inclusions can be determined by Raman spectroscopy as in the previous paragraph for volatiles in glass.

In situ Raman spectroscopy

While *in situ* Raman spectroscopy can be performed at high temperature (see for example, Mysen and Frantz 1992, 1993, 1994a,b; Mysen and Neuville 1995; Neuville and Mysen 1996; Cormier et al. 2006; Magnien et al. 2006; Yano et al. 2003a,b; Le Losq and Neuville 2013; Le Losq et al. 2013), at high pressure (for example, Sharma et al. 1979; Hemley et al. 1986; Durben and Wolf 1992; Reynard et al. 1999; Kleppe et al. 2001; Champagnon et al. 2007; Deschamps et al. 2009; Kojitani et al. 2013) it is also possible to investigate dynamic processes at high temperature or high pressure, for example boron oxygen coordination changes induced by temperature or nucleation and growth process.

Change of boron oxygen coordination at high temperature. As we saw in the previous section, Raman spectra of borosilicates offer a distinct signature of boron oxygen coordination. Indeed vibrational bands around 1400-1500 cm^{-1} are assigned to BO_3 units and the narrow band at 630 cm^{-1} to BO_4 units associated with the silicate network. Consequently, these glasses appear to be good candidates for investigating the dynamic behaviour of the boron units with temperature. For example, a borosilicate glass of composition $63SiO_2$-$17B_2O_3$-$17Na_2O$-$3Cs_2O$ has been investigated with Raman spectroscopy and a Linkam© heating stage, and spectra are shown in Figure 19. Up to the glass transition at 850 K, the spectra do not exhibit any significant changes. A small shift toward lower frequency due to anharmonicity can be noticed. At higher temperature a fast drop in intensity of the BO_4 band is observed along with an increase in the area of the BO_3 band (Fig. 20a). Similar studies have been reported by *in situ* NMR or on glasses quenched from different temperatures (for example Sen et al. 2007, Wu and Stebbins 2010). An advantage of Raman spectroscopy is the ability to follow the changes in the structure of the silica-network at the same time. It can be seen in Figure 19 that above the glass transition the silicate vibrational band around 1000 cm^{-1} increases strongly in intensity and moves to lower frequency. To show more explicitly this change the Q^n bands have been

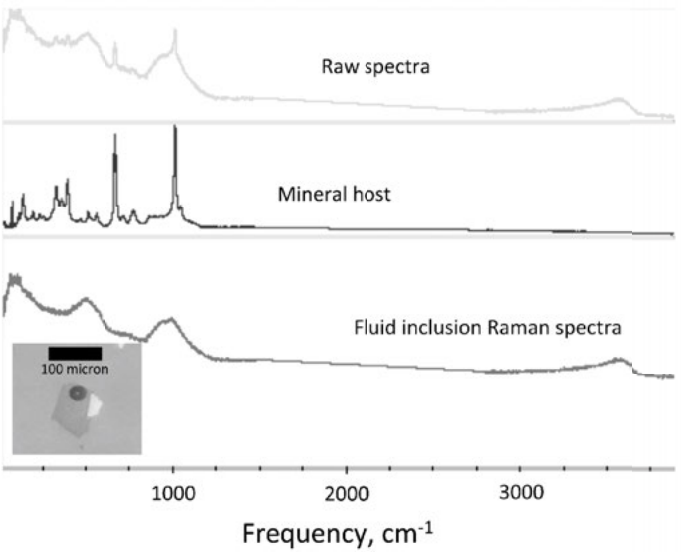


Figure 18. Example of fluid inclusion analysis by Raman spectroscopy.

EBSCOhost - printed on 2/13/2023 5:26 AM via . All use subject to https://www.ebsco.com/terms-of-use

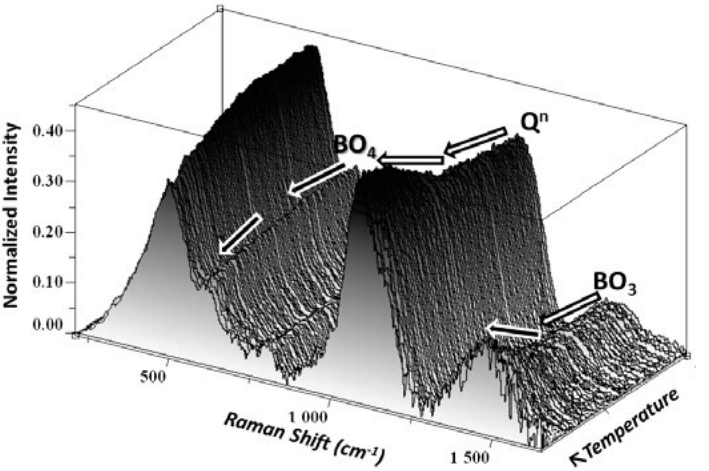


Figure 19. 3D block plot of the Raman spectra of a borosilicate glass and melt versus temperature. The spectra were collected with 532 nm laser excitation. The different boron units are shown. Distinct changes in the spectra occur at 850 K, the glass transition temperature.

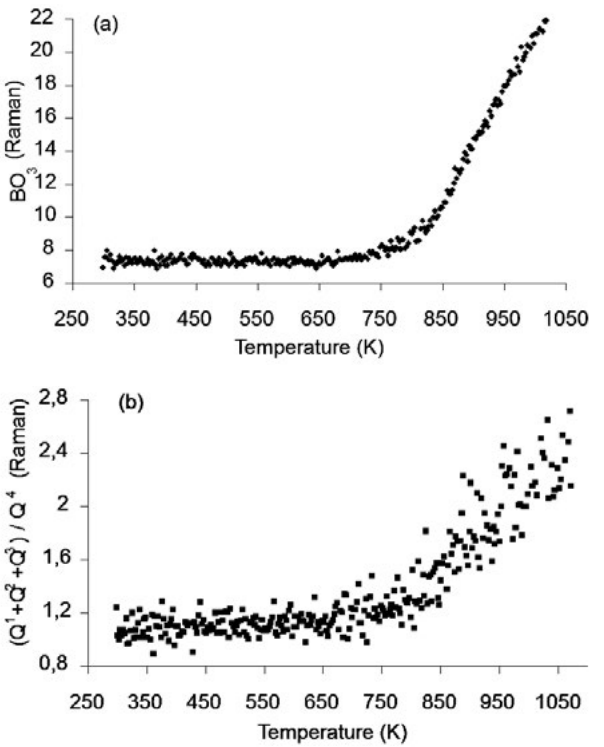


Figure 20. Evolution of Raman band area versus temperature: a) area of the total BO_3 contribution around 1400-1500 cm^{-1}; b) Area ratio between Q^n contributions after deconvolution of the 1000 cm^{-1} silicate region (Angeli et al. 2012).

EBSCOhost - printed on 2/13/2023 5:26 AM via . All use subject to https://www.ebsco.com/terms-of-use

fitted using Gaussian functions representing the different Q^n species. Figure 20b shows the area ratio of low *n* Q species and the Q^4 contribution. There is a strong correlation between the Q species behaviour and the area of the BO_3 band reported in Figure 20a. This suggests a strong relationship between the silicate network and the boron-network. This can be explained by the reaction $BO_4 + Q^n \rightarrow BO_3 + Q^{n-1}$ proposed by Sen et al. (1998).

In situ crystallization. In the nuclear waste storage context, a possible solution could be the use of a glass ceramic in which the fission products and minor actinides are concentrated in crystals within a glass matrix. This solution would take advantage of the better stability of the crystal and the easy processing of glasses. For a first step all the elements would be dissolved in the liquid state then quenched. In a second step crystals would be nucleated and grown by heat treatment. Knowledge of the optimal process parameters, time and temperature, are needed and *in situ* experiments are highly suitable for determining these parameters (Putnis 1992). For example by looking at a borosilicate glass composition with around 4 mol% of Nd_2O_3 (a good candidate to simulate nuclear waste encapsulation material) such crystallization can be observed directly by doing HT *in situ* experiments. Some silico-apatite ($Ca_2Nd_8[SiO_4]_6O_2$) crystallized within the glass during isothermal heat treatments. A Pt-Rh10% heating wire was used to quench the glass and perform the heat treatments (see Neuville et al. 2014, this volume). Its very low thermal inertia allowed very quick temperature equilibration (de Ligny and Neuville 2013; Neuville and Cormier 2013). Raman spectra were recorded every 10 minutes during two isothermal heat treatments at 1090 K and 1220 K and are shown in Figure 21. At 820 °C the first crystal peaks can be observed after 1 h 16 min. Later, crystal growth takes place and seems to reach its maximum after 3 h 16 min. At 950 °C crystals appeared as soon as 9 min from the start of the isotherm and are totally crystallized after 1 h 18 min. Therefore as temperature rises both initial crystallization and final crystallization time decreases. This is characteristic of a thermal activated process. Combined with other isotherms not presented here similar activation energies of 150±30 kJ/mol are measured for both the initial crystallization time ignition and the crystal growth. This last result is consistent with Nd self-diffusion which controls both nucleation and crystal growth.

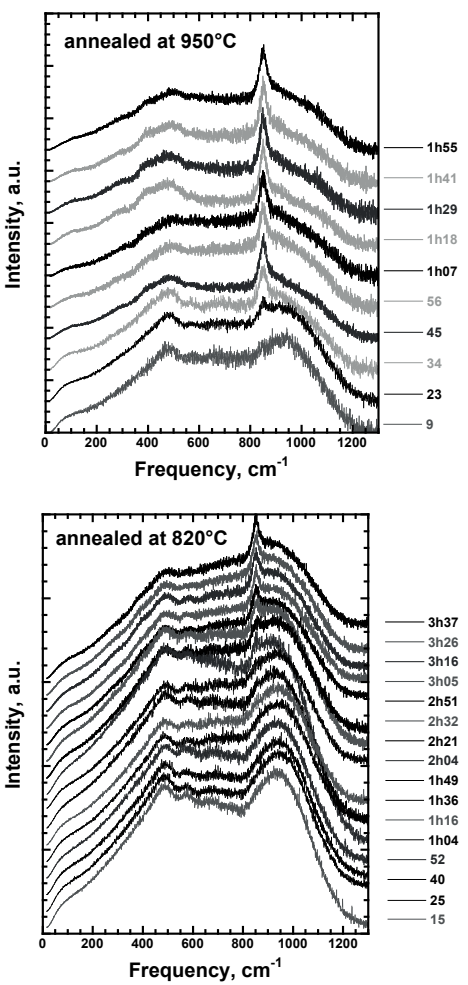


Figure 21. Raman spectra of the melt during isothermal crystallization at 820 °C and 950 °C. The spectra were collected under 514 nm excitation every 11 min with an integration time of 9 min. The spectra were corrected for baseline and temperature effects (see above).

EBSCOhost - printed on 2/13/2023 5:26 AM via . All use subject to https://www.ebsco.com/terms-of-use

CONCLUSIONS

Raman spectroscopy is a powerful tool to investigate minerals, gases, glasses, and disordered materials at room temperature. By coupling Raman spectroscopy with a high-pressure apparatus or high temperature device, it is also possible to investigate the structure of these materials *in situ* and to follow phase transformations and thermodynamic processes. For a long time Raman spectroscopy was confined to research labs. However its non-destructive properties and long working distance coupled with the lowering of laser prices have made it much more practical for everyday use. For example, Raman spectroscopy is now used to investigate quality control during industrial processes, to make pressure and temperature sensors, follow volatile speciation in exhaust fumes, and to detect pollutant organic compounds in effluent, to name a few. With the new small and compact instruments available today, it is possible to make direct Raman spectroscopic analyses on-site such as at volcanoes, polluted industrial sites, or on a picture or a sculpture in a museum. Raman spectroscopy is an excellent tool to investigate a multitude of different materials but the absence of an interactive database leads to difficulties with analysis and interpretation of the data. The RRUFF database (*http://rruff.info*) is very useful and an asset for the mineralogical community. However its use is somewhat limited because one needs to have some idea of the chemical composition of the material under investigation.

REFERENCES

Akagi R, Ohtori N, Umesaki N (2001) Raman spectra of K_2O–B_2O_3 glasses and melts. J Non-Cryst Solids 293/295:471-476

Albrecht MG, Creighton JA (1977) Anomalously intense Raman spectra of pyridine at a silver electrode. J Am Chem Soc 99:5215-5217

Amalberti J, Neuville DR, Sarda Ph, Sator N, Guillot B (2014) Quantification of CO_2 in silicates glasses and melts using Raman spectroscopy. Geochim Cosmochim Acta (submitted)

Angel SM, Gomer NR, Sharma SK, McKay C (2012) Remote Raman spectroscopy for planetary exploration: a review. App Spectrosc 66:137-150

Angeli F, Villain O, Schuller S, Charpentier T, de Ligny D, Bressel L, Wondraczek L (2012) Effect of temperature and thermal history on borosilicate glass structure. Phys Rev B 85:054110

Balan E, Neuville DR, Trocellier P, Fritsch E, Muller JP, Calas G (2001) Zircon metamictization, zircon stability and zirconium mobility. Am Mineral 86:1025-1033

Bates D, Quist A (1972) Polarized Raman spectra of β-quartz. J Chem Phys 56:1529-1533

Behrens H, Roux J, Neuville DR, Siemann M (2006) Quantification of dissolved H_2O in silicate glasses using Raman spectroscopy. Chem Geol 229:96-113

Bell RJ, Bird NF, Dean P (1968) The vibrational spectra of vitreous silica, germania and beryllium fluoride. J Phys C Solid State 1:299-303

Bell RJ, Dean P (1972) Localization of phonons in vitreous silica and related glasses. *In*: International Conference on the Physics of Non-Crystalline Solids 3rd. Douglas RW, Ellis B (eds) Wiley-Interscience, p 443-452

Brawer SA, White WB (1975) Raman spectroscopic investigation of the structure of silicate glasses. I. The binary alkali silicates. J Chem Phys 63:2421-2432

Bucheneau U, Prager M, Nucker N, Dianoux AJ, Ahmad N, Phillips WA (1986) Low-frequency modes in vitreous silica. Phys Rev B 34:5665-5673

Cabannes J (1928) Un nouveau phénomène d'optique : les battements qui se produisent lorsque des molécules anisotropes en rotation et vibration diffusent de la lumière visible ou ultraviolette. CR Acad Sci 186:1201-1202

Cabannes J (1931) Règles de polarization des raies Raman dans les cristaux. CR Acad Sci 193:2134-2136

Cabannes J, Rocard Y (1928) Les observations de Mr Raman sur le nouveau type de radiation secondaire. J Phys 10:32-34

Cabannes J, Rousset A (1932) Les règles de polarisation des raies de Raman dans les liquides. Enoncés théoriques et vérifications expérimentales. CR Acad Sci 194:79-81

Chabiron A, Pironon J, Massare D (2004) Characterization of water in synthetic rhyolitic glasses and natural melt inclusion by Raman spectroscopy. Contrib Mineral Petrol 146:485-492

Champagnon B, Martinet C, Coussa C, Deschamps T (2007) Polyamorphism: Path to new high density glasses at ambient conditions. J Non-Cryst Solids 353:4208-4211

EBSCOhost - printed on 2/13/2023 5:26 AM via . All use subject to https://www.ebsco.com/terms-of-use

Cheng J-X (2004) Coherent anti-Stokes Raman scattering microscopy: instrumentation, theory, and applications. J Phys Chem B 108:827-840

Chryssikos GD, Kamitsos EI, Patsis AP, Bitsis MS, Karakassides MA (1990) The devitrification of lithium metaborate: polymorphism and glass formation. J Non-Cryst Solids 126:42-51

Cialla D, Marz, A, Bohme R, Theil F, Weber K, Schmitt M, Popp J (2012) Surface-enhanced Raman spectroscopy (SERS):progress and trends. Anal Bioanal Chem 403:27-54

Cochain B, Neuville D R, Henderson GS, McCammon C, Pinet O, Richet P (2012) Iron content, redox state and structure of sodium borosilicate glasses:A Raman, Mössbauer and boron *K*-edge XANES spectroscopy study. J Am Ceram Soc 94:1-12

Cormier L, Majérus O, Neuville DR, Calas G (2006) Temperature-induced structural modifications between alkali borate glasses and melts. J Am Ceram Soc 89:13-19

Das RS, Agrawal YK (2011) Raman spectroscopy: recent advancements, techniques and applications. Vib Spectrosc 57:163-176

de Ligny D, Neuville DR (2013) La spectrométrie Raman: un outil de choix pour l'étude des mécanismes de nucléation et de croissance cristalline. *In:* Du verre au Cristal: Nucléation, Croissance et Démixtion, de la Recherche aux Applications. Neuville DR, Cormier L, Caurant D, Montagne L (eds) EDP-Sciences, p 285-309

Denisov VN, Mavrin BN, Podobedov VB, Sterin KE, Varshal BG (1984) Law of conservation of momentum and rule of mutual exclusion for vibrational excitations in hyper-Raman and Raman spectra of glasses. J Non-Cryst Solids 64:195-210

Denisov VN, Mavrin BN, Podobedov YB (1987) Hyper-Raman Scattering by vibrational excitations in crystals, glasses and liquids. Phys Rep 151:1-92

Deschamps T, Martinet C, Neuville DR, de Ligny D, Coussa C, Champagnon B (2009) Silica under hydrostatic pressure: a non continuous medium behavior. J Non-Cryst Solids 355:2422-2425

Dingwell DB, Virgo D (1987) The effect of oxidation state on the viscosity of melts in the system Na_2O-FeO-Fe_2O_3-SiO_2. Geochim Cosmochim Acta 51:195-205

Dresselhaus MS, Dresselhaus G, Jorio A (2010) Group Theory, Application to the Physics of Condensed Matter. Springer-Verlag, Berlin

Dubessy J, Caumon M-C, Rull F (2012) Raman spectroscopy applied to Earth Sciences and Cultural Heritage. European Mineralogical Union Volume 12. Cambrian Printers, Aberystwyth, UK

Durben DJ, Wolf GH (1992) High-temperature behavior of metastable $MgSiO_3$ perovskite: A Raman spectroscopic study. Am Mineral 77:890-893

Etchepare J, Merian M, Smetankine L (1974) Vibrational normal modes of SiO_2. I. α and β quartz. J Chem Phys 60:1873-1879

Fleischmann M, Hendra PJ, McQuillan AJ (1974) Raman spectra of pyridine adsorbed at a silver electrode. Chem Phys Lett 26:163-66

Frantz JD, Mysen BO (1995) Raman spectra and structure of BaO-SiO_2, SrO-SiO_2 and CaO-SiO_2 melts to 1600°C. Chem Geol 121:155-176

Fukumi K, Hayakawa J, Komiyama T (1990) Intensity of Raman band in silicate glasses. J Non-Cryst Solids 119:297-302

Furukawa T, Fox KE, White WB (1981) Raman spectroscopic investigation of the structure of silicate glasses. III. Raman intensities and structural units in sodium silicate glasses. J Chem Phys 75:3226-3237

Galeener FL (1979) Band limits and the vibrational spectra of tetrahedral glasses. Phys Rev B 19:4292-4397

Galeener FL (1982a) Planar rings in vitreous silica. J Non-Cryst Solids 49:53-62

Galeener FL (1982b) Planar rings in glasses. Solid State Commun 44:1037-1040

Galeener FL, Lucovsky G (1976) Longitudinal optical vibrations in glasses: GeO_2 and SiO_2. Phys Rev Lett 37:1474-1478

Galeener FL, Sen PN (1978) Theory for 1st-order vibrational-spectra of disordered solids. Phys Rev B 17:1928-1933

Galeener FL, Leadbetter AJ, Stringfellow MW (1983) Comparison of the neutron, Raman, and infrared vibrational spectra of vitreous SiO_2, GeO_2, and BeF_2. Phys Rev B 27:1052-1078

Galeener FL, Barrio RA, Martinez E, Elliott RJ (1984) Vibrational decoupling of rings in amorphous solids. Phys Rev Lett 53:2429-2432

Gillet Ph, Barrat JA, Deloule E, Wadhwa W, Jambon A, Sautter V, Devouard B Neuville DR, Benzerara K, Lesourd M (2002) Aqueous alteration in the North west Africa 817 (NWA 817) Martian meteorite. Earth Planet Sci Lett 203:431-444

Guillot B, Sator N (2011) Carbon dioxide in silicate melts: A molecular dynamics simulation study. Geochim Cosmochim Acta 75:1829-1843

Harris DC, Bertolucci MD (1978) Symmetry and Spectroscopy: An Introduction to Vibrational and Electronic Spectroscopy. Oxford University Press, New York

Hass M (1969) Temperature dependence of the Raman spectrum of vitreous silica. Solid State Commun 7:1069-1071

EBSCOhost - printed on 2/13/2023 5:26 AM via . All use subject to https://www.ebsco.com/terms-of-use

Hass M (1970) Raman spectra of vitreous silica, germania and sodium silicate glasses. J Phys Chem Solids 31:415-42

Hawthorne FC (ed) (1988) Spectroscopic Methods in Mineralogy and Geology. Volume 18 Reviews in Mineralogy. Mineralogical Society of America

Hehlen B (2010) Inter-tetrahedra bond angle of permanently densified silicas extracted from their Raman spectra. J Phys Condens Matter 22:025401-25411

Hehlen B, Courtens E, Vacher R, Yamanaka A, Kataoka M, Inoue K (2000) Hyper-Raman scattering observation of the Boson peak in vitreous silica. Phys Rev Lett 84:5355-5358

Hehlen B, Courtens E, Yamanaka A, Inoue K (2002) Nature of the Boson peak of silica glasses from hyper-Raman scattering. J Non-Cryst Solids 307-310:87-91

Hemley RJ, Mao HK, Bell PM, Mysen BO (1986) Raman spectroscopy of SiO_2 glass at high pressure. Phys Rev Lett 57:747-750

Henderson GS, Fleet ME (1995) The structure of Ti silicate glasses by micro-Raman spectroscopy. Can Mineral 33:399-408

Herzberg G (1945a) Molecular spectra and molecular structure. I. Spectra of diatomic molecule. Princeton Press

Herzberg G (1945b) Molecular spectra and molecular structure. II. Infrared and Raman spectra of polyatomic molecules. Princeton Press

Hibben JH (1933) Raman spectra in inorganic chemistry. Chem Rev 13:345-478

Hibben JH (1936) Raman spectra in organic chemistry. Chem Rev 18:1-231

Hollaender A, Williams JW (1929) The molecular scattering of light from solids. Plate glass. Phys Rev 34:380-381

Hollaender A, Williams JW (1931) The molecular scattering of light from amorphous and crystalline solids. Phys Rev 38:1739-1744

Iliescu T, Simon S, Maniu D, Ardelean I (1993) Raman spectroscopy of oxide glass system $(1-x)[yB_2O_3{\cdot}zLi_2O]{\cdot}xGd_2O_3$. J Mol Struct 294:201-203

Jeanmarie DL, Van Duyne RP (1977) Surface Raman spectroelectrochemistry. Part 1: heterocyclic, aromatic, and aliphatic amines adsorbed on the anodized silver electrode. J Electroanal Chem 84:120-127

Kalampounias AG, Yannopoulos SN, Papatheodorou GN (2006) Temperature-induced structural changes in glassy, supercooled, and molten silica from 77 to 2150 K. J Chem Phys 124:014504-014509

Kamitsos EI, Karakassides MA, Chryssikos GD (1987) Vibrational-spectra of magnesium-sodium-borate glasses. 1. Far-infrared investigation of the cation-site interactions. J Phys Chem 91:1067-1073

Karr C (1975) Infrared and Raman spectroscopy of lunar and terrestrial minerals. Academic Press

Kingma KJ, Hemley RJ, Mao H, Veblen D (1993) New high-pressure transformation in α-quartz. Phys Rev Lett 70:3927-3932

Kleinman DA, Spitzer WG (1962) Theory of the optical properties of quartz in the infrared. Phys Rev 125:16-30

Kleppe AK, Jephcoat AP, Olijnyk H, Slesinger AE, Kohn SC, Wood BJ (2001) Raman spectroscopy study of hydrous wadsleyite (β-Mg_2SiO_4) to 50 GPa. Phys Chem Mineral 28:232-241

Kojitani H, Többens DM, Akaogi M (2013) High-pressure Raman spectroscopy, vibrational mode calculation, and heat capacity calculation of calcium ferrite-type $MgAl_2O_4$ and $CaAl_2O_4$. Am Mineral 98:197-206

Kravets VG, Kolmykova VY (2005) Optics and spectroscopy, Raman scattering of light in silicon nanostructures: first and second order spectra. Opt Spectrosc 99:68-73

Landsberg G, Mandelstam L (1928) A new occurrence in the light diffusion of crystals. Naturwissenschaften 16:557-558

Lazarev AN (1972) Vibrational Spectra and Structure in Silicates. Consultant Bureau New-York, 350 pp

Le Losq Ch, Neuville DR (2013) Effect of K/Na mixing on the structure and rheology of tectosilicate silica-rich melts. Chem Geol 346:57-71

Le Losq Ch, Neuville DR, Moretti R, Roux J (2012) Water quantification and speciation in silicate melt using Raman spectroscopy. Am Mineral 97:779-791

Le Losq Ch, Moretti R, Neuville DR (2013) Speciation and amphoteric behavior of water in aluminosilicate melts and glasses: high-temperature Raman spectroscopy and reaction equilibria. European Journal of Mineralogy 25:777-790

Le Losq Ch, Neuville DR, Florian P, Henderson GS, Massiot D (2014) Role of Al^{3+} on rheology and nano-structural changes of sodium silicate and aluminosilicate glasses and melts. Geochim Cosmochim Acta 126:495-517

Lenoir M, Grandjean A, Linard Y, Cochain B, Penelon B, Neuville DR (2008) The influence of the Si, B substitution and of the nature of network modifying cations on the properties and structure of borosilicate glasses and melts. Cheml Geol 256:316-325

Lenoir M, Grandjean A, Poissonnet S, Neuville DR (2009) Quantification of sulfate solubility in borosilicate glasses using in situ Raman spectroscopy. J Non- Cryst Solids 355:1468-1473

Lenoir M, Neuville DR, Malki M, Grandjean A (2010) Volatilization kinetics of sulphur from borosilicate melts:a correlation between sulphur diffusion and melt viscosity. J Non-Cryst Solids 356:2722-2727

EBSCOhost - printed on 2/13/2023 5:26 AM via . All use subject to https://www.ebsco.com/terms-of-use

Licheron M, Montouillout V, Millot F, Neuville DR (2011) Raman and ^{27}Al NMR structure investigations of aluminate glasses:$(1-x)Al_2O_3$-xMO, with M = Ca, Sr, Ba and 0.5<x<0.75). J Non Cryst Solids 257:2796-2801

Long DA (1977) Raman Spectroscopy. McGraw-Hill

Long DA (2002) The Raman effect: A unified treatment of the theory of Raman scattering by molecules. J Wiley and Sons

Magnien V, Neuville DR, Cormier L, Mysen BO, Richet P (2004) Kinetics of iron oxidation in silicate melts:A preliminary XANES study. Chem Geol 213:253-263

Magnien V, Neuville DR, Cormier L, Roux J, Pinet O, Richet P (2006) Kinetics of iron redox reactions: A high-temperature XANES and Raman spectroscopy study. J Nucl Mater 352:190-195

Malinovsky, VK, Sokolov AP (1986) The nature of the boson peak in Raman scattering in glasses. Solid State Commun 57:757-761

Manara D, Grandjean A, Pinet O, Dussossoy JL, Neuville DR (2007) Sulphur behaviour in silicate glasses and melts:implications for sulphate incorporation in nuclear waste glasses as a function of alkali cation and V_2O_5 content. J. Non-Cryst Solids 353:12-23

Manara D, Grandjean A, Neuville DR (2009a) Advances in understanding the structure of borosilicate glasses:A Raman spectroscopy study. Am Mineral 94:777-784

Manara D, Grandjean A, Neuville DR (2009b) Structure of borosilicate glasses and melts: a revision of the Yun, Bray and Dell model. J Non-Cryst Solids 355:2528-2532

Maniu D, Iliescu T, Ardelean I, Cinta S, Tarcea N, Kiefer W (2003) Raman study on B_2O_3-CaO glasses. J Mol Struct 651-653:485-488

Matson DW, Sharma SK, Philpotts JA (1983) The structure of high-silica alkali silicate glasses: A Raman spectroscopic investigation. J Non-Cryst Solids 58:323-352

McMillan P (1984) Structural studies of silicate glasses and melts - Applications and limitations of Raman-spectroscopy. Am Mineral 69:622-644

McMillan PF (1985) Vibrational spectroscopy in the mineral sciences. Rev Mineral 4:9-63

McMillan PF, Hess AC (1988) Symmetry, group-theory and quantum-mechanics. Rev Mineral 18:11-61

McMillan PF, Hofmeister AM (1988) Infrared and Raman-spectroscopy. Rev Mineral 18:99-159

McMillan PF, Piriou B (1982) The structures and vibrational spectra of crystals and glasses in the silica-alumina system. J Non-Cryst Solids 53:279-298

McMillan PF, Piriou B (1983) Raman spectroscopy of calcium aluminate glasses and crystals. J Non-Cryst Solids 55:221-242

McMillan PF, Wolf GH, Poe BT (1992) Vibrational spectroscopy of silicate liquids and glasses. Chem Geol 96:351-366

McMillan PF, Poe BT, Gillet P, Reynard B (1994) A study of SiO_2 glass and supercooled liquid to 1950 K via high-temperature Raman spectroscopy. Geochim Cosmochim Acta 58:3653-3664

Meera BN, Ramakrishna J (1993) Raman spectral studies of borate glasses. J Non-Cryst Solids 159:1-16

Metrich N, Allard P, Aiuppa A, Bani P, Bertagnini P, Shinohara H, Parello F, Dimuro A, Garaebiti E, Belhadj O, Massare D (2011) Magma and volatile supply to post-collapse volcanism and block resurgence in Siwi Caldera (Tanna Island,Vanuatu Arc). J Petrol 52:1077-1105

Minsky M (1961) US-Patent US3013467 (A) Microscopy apparatus – 1961-12-19

Mulliken RS (1929) Band spectra and chemistry. Chem Rev 6:503-545

Mulliken RS (1931) Bonding power of electrons and theory of valence. Chem Rev 9:347-388

Mysen BO (1999) Structure and properties of magmatic liquids: from haplobasalt to haploandesite. Geochim Cosmochim Acta 63:95-112

Mysen BO (2003) Physics and chemistry of silicate glasses and melts. Eur J Mineral 15:781-802

Mysen BO, Frantz JD (1992) Raman spectroscopy of silicate melts at magmatic temperatures:Na_2O-SiO_2, K_2O-SiO_2 and Li_2O-SiO_2 binary compositions in the temperature range 25-1475 °C. Chem Geol 96:321-332

Mysen BO, Frantz JD (1993) Structure and properties of alkali silicate melts a magmatic temperatures. Eur J Mineral 5:393-413

Mysen BO, Frantz JD (1994a) Silicate melts at magmatic temperatures: *in situ* structure determination to 1651 °C and effect of temperature and bulk composition on the mixing behavior of structural units. Contrib Mineral Petrol 117:1-14

Mysen BO, Frantz JD (1994b) Structure of haplobasaltic liquids atmagmatic temperatures:in situ, high-temperature study of melts on the join $Na_2Si_2O_5$-$Na_2(NaAl)_2O_5$. Geochim Cosmochim Acta 58:1711-1733

Mysen BO, Neuville DR (1995) Effect of temperature and TiO_2 content on the structure of $Na_2Si_2O_5$-$Na_2Ti_2O_5$ melts and glasses. Geochim Cosmochim Acta 59:325-342

Mysen BO, Virgo D (1980) Solubility mechanisms of carbon dioxide in silicate melts: a Raman spectroscopic study. Am Mineral 65:885-899

Mysen BO, Virgo D, Scarfe CM (1980a) Relations between the anionic structure and viscosity of silicate melts - A Raman spectroscopic study. Am Mineral 65:690-710

EBSCOhost - printed on 2/13/2023 5:26 AM via . All use subject to https://www.ebsco.com/terms-of-use

Mysen BO, Virgo D, Wendy JH, Scarfe CM (1980b) Solubility mechanisms of H_2O in silicate melts at high pressures and temperatures: a Raman spectroscopic study. Am Mineral 65:900-914

Mysen BO, Seifert FA, Virgo D (1980c) Structure and redox equilibria of iron-bearing silicate melts. Am Mineral 65:867-884

Mysen BO, Finger LW, Virgo D, Seifert FA (1982) Curve-fitting of Raman spectra of silicate glasses. Am Mineral 67:686-695

Mysen BO, Virgo D, Neumann E-R, Seifert FA (1985a) Redox equilibria and the structural states of ferric and ferrous iron in melts in the system CaO-MgO-SiO_2-Fe-O: relationships between redox equilibria, melt structure and liquidus phase equilibria. Am. Mineral 70:317-331

Mysen BO, Carmichael ISE, Virgo D (1985b) A comparison of iron redox ratios in silicate glasses determined by wet chemical and ^{57}Fe Mossbauer resonant absorption methods. Contrib Mineral Petrol 90:101-106

Nasdala L, Brenker FE, Glinnemann J, Hofmeister W, Gasparik T, Harris JW, Stachel T, Reese I (2003) Spectroscopic 2D-tomography: Residual pressure and strain around mineral inclusions in diamonds. Eur J Mineral 15:931-935

Nasdala L, Smith DC, Kaindl R, Ziemann MA (2004) Raman spectroscopy: analytical perspectives in mineralogical research. EMU Notes in Mineralogy 6:196-259

Neuville DR (2005) Structure and properties in (Sr, Na) silicate glasses and melts. Phys Chem Glasses 46:112-119

Neuville DR (2006) Viscosity, structure and mixing in (Ca, Na) silicate melts. Chem Geol 229:28-42

Neuville DR, Mysen BO (1996) Role of aluminum in the silicate network: *in situ*, high-temperature study of glasses and melts on the join SiO_2-$NaAlO_2$. Geochim Cosmochim Acta 60:1727-1737

Neuville DR, Cormier L (2013) Grands instruments, vers des approches in situ de la cristallisation. *In:* Du verre au Cristal: Nucléation, Croissance et Démixtion, de la Recherche aux Applications. Neuville DR, Cormier L, Caurant D, Montagne L (eds) EDP-Sciences, p 311-326

Neuville DR, Cormier L, Massiot D (2004) Role of aluminium in peraluminous region in the CAS system. Geochim Cosmochim Acta 68:5071-5079

Neuville DR, Cormier L, Massiot D (2006) Al speciation in calcium aluminosilicate glasses: a NMR and Raman spectroscopy. Chem Geol 229:173-185

Neuville DR, Cormier L, Montouillout V, Florian P, Millot F, Rifflet JC, Massiot D (2008) Structure of Mg- and Mg/Ca aluminosilicate glasses: ^{27}Al NMR and Raman spectroscopy investigations. Am Mineral 83:1721-1731

Neuville DR, Henderson GS, Cormier L, Massiot D (2010) Structure of CaO-Al_2O_3 crystal, glasses and liquids, using X-ray absorption at Al *L* and *K* edges and NMR spectroscopy. Am Mineral 95:1580-1589

Neuville DR, Hennet L, Florian P, de Ligny D (2014) In situ high-temperature experiments. Rev Mineral Geochem 78:779-801

Pasquarello A (2001) First-principles simulation of vitreous systems. Curr Opin Solid State Mater Sci 5:503-508

Pasquarello A, Car R (1998) Identification of Raman defect lines as signatures of ring structures in vitreous silica. Phys Rev Lett 80:5145-5147

Pasquarello A, Sarnthein J, Car R (1998) Dynamic structure factor of vitreous silica from first principles:comparison to neutron-inelastic-scattering experiments. Phys Rev B 90:14133-14140

Phillips JC (1984) Microscopic origin of anomalously narrow Raman lines in network glasses. J Non-Cryst Solids 63:347-355

Putnis A (1992) Introduction to mineral science. Cambridge University Press

Rahmani A, Benoit M, Benoit C (2003) Signature of small rings in the Raman spectra of normal and compressed amorphous silica:A combined classical and ab initio study. Phys Rev B 68:184202

Raman CV, Krishnan KS (1928) A new type of secondary radiation. Nature 121:501-502

Reinkobes O (1911) Über Absorption und Reflexion ultraroter Strahlen durch Quarz, Turmalin und Diamant. Ann Phys-Berlin 34:343-347

Reynard B, Webb SL (1998) High-temperature Raman spectroscopy of Na_2TiSi_{207} glass and melt: coordination of Ti^{4+} and nature of the configurational changes in the liquid. Eur J Mineral 10:49-58

Reynard B, Okuno M, Shimada Y, Syono Y, Willaime C (1999) A Raman spectroscopic study of shock-wave densification of anorthite ($CaAl_2Si_2O_8$) glass. Phys Chem Miner 26:432-436

Rocard Y (1928) Les nouvelles radiations diffusées. CR Acad Sci 190:1107-1109

Roskosz M, Mysen BO, Cody GD (2006) Dual speciation of nitrogen in silicate melts at high pressure and temperature: an experimental study. Geochim Cosmochim Acta 70:2902-2918

Saksena BD (1940) Analysis of the Raman and infrared spectra of alpha-quartz. P Indian Acad Sci A 12:93-138

Sarnthein J, Pasquarello A, Car R (1997) Origin of the high-frequency doublet in the vibrational spectrum of vitreous SiO_2. Science 275:1925-1927

Scott JF, Porto SPS (1967) Longitudinal and transverse optical lattice vibrations in quartz. Phys Rev 161:903-910

Seifert F, Mysen BO, Virgo D (1982) 3-dimensional network structure of quenched melts (glass) in the systems SiO_2-$NaAlO_2$, SiO_2-$CaAl_2O_4$ and SiO_2-$MgAl_2O_4$. Am Mineral 67:696-717

EBSCOhost - printed on 2/13/2023 5:26 AM via . All use subject to https://www.ebsco.com/terms-of-use

Sen PN, Thorpe MF (1977) Phonon in AX_2 glasses: from molecular to band-like modes. Phys Rev B 15:4030-4038
Sen S, Xu Z, Stebbins JF (1998) Temperature dependent structural changes in borate borosilicate and boroaluminate liquids:high-resolution ^{11}B, ^{29}Si and ^{27}Al NMR studies. J Non-Cryst Solids 226:29-40
Sen S, Topping T, Yu P, Youngman RE (2007) Atomic-scale understanding of structural relaxation in simple and complex borosilicate glasses. Phys Rev B 75:094203-094207
Sharma SK, Virgo D, Mysen BO (1979) Raman study of the coordination of aluminum in jadeite melts as a function of pressure. Am Mineral 64:779-787
Sharma SK, Mammone JF, Nicol MF (1981) Raman investigation of ring configurations in vitreous silica. Nature 292:140-141
Sharma SK, Philpotts JA, Matson DW (1985) Ring distributions in alkali- and alkaline-earth aluminosilicate framework glasses - A Raman spectroscopic study. J Non-Cryst Solids 71:403-410
She Y, Masso JD, Edwards DF (1971) Raman scattering by polarization waves in uniaxial crystals. J Phys Chem Solids 32:1887-1900
Sherwood PMA (1972) Vibrational spectroscopy of solids. 1. Cambridge, Cambridge University Press
Shuker R, Gammon RW (1970) Raman-scattering selection-rule breaking and density of states in amorphous materials. Phys Rev Lett 25:222-225
Simon G, Hehlen B, Courtens E, Longueteau E, Vacher R (2006) Hyper-Raman scattering from vitreous boron oxide: coherent enhancement of the boson peak. Phys Rev Lett 96:105502-105506
Simon G, Hehlen B, Vacher R, Courtens E (2007) Hyper-Raman scattering analysis of the vibrations in vitreous boron oxide. Phys Rev B 76:054210-054220
Simon G, Hehlen B, Vacher R, Courtens E (2008) Nature of the hyper-Raman active vibrations of lithium borate glasses. J Phys-Condens Matter 20:155103-155110
Stiles PL, Dieringer JA, Shah NC, Van Duyne RP (2008) Surface-enhanced Raman spectroscopy. Annu Rev Anal Chem 1:601-626
Taraskin SN, Elliott SR (1997) Nature of vibrational excitations in vitreous silica. Phys Rev B 56:8605-8622
Thomas R (2000) Determination of water concentrations of granite melt inclusion by confocal laser Raman microprobe spectroscopy. Am Mineral 85:868-872
Thomas SM, Thomas R, Davidson P, Reichart P, Koch-Müller M, Dollinger G (2008) Application of Raman spectroscopy to quantify trace water concentrations in glasses and garnets. Am Mineral 93:1550-1557
Tsujimura T, Xue X, Kanzaki M, Walter MJ (2004) Sulfur speciation and network structural changes in sodium silicate glasses: constraints from NMR and Raman spectroscopy. Geochim Cosmoschim Acta 68:5081-5101
Tu Q, Chang C (2012) Diagnostic applications of Raman spectroscopy. Nanomed-Nanotech Biol Med 8:545-558
Umari P, Pasquarello A (2002) Modeling of the Raman spectrum of vitreous silica: concentration of small ring structures. Physica B 316-317:572-574
Umari P, Gonze X, Pasquarello A (2003) Concentration of small ring structures in vitreous silica from a first-principles analysis of the Raman spectrum. Phys Rev Lett 90:867-755
Verweij H, Boom Hvd, Breemer RE (1977) Raman scattering of carbonate ions dissolved in potassium silicate glasses. J Am Ceram Soc 60:529-34
Villars DS (1932) The energy levels and statistical weights of polyatomic molecules. Chem Rev 11:369-436
Virgo D, Mysen BO, Kushiro I (1980) Anionic constitution of silicate melts quenched at 1 atm from Raman spectroscopy: implications for the structure of igneous melts. Science 208:1371-1373.
Warren BE (1934a) The diffraction of X-rays in glass. Phys Rev B 45:657-661
Warren BE (1934b) X-ray determination of the structure of glass. J Am Ceram Soc 17:249-254
Wilson EB, Decius JC, Cross PC (1955) Molecular Vibrations. McGraw-Hill, New York
Wu J, Stebbins JF (2010) Quench rate and temperature effects on boron coordination in aluminoborosilicate melts. J Non-Cryst Solids 356:2097-2108
Yano T, Kunimine N, Shibata S, Yamane M (2003a) Structural investigation of sodium borate glasses and melts by Raman spectroscopy. II. Conversion between BO_4 and BO_2O^- units at high temperature. J Non-Cryst Solids 321:147-156
Yano T, Kunimine N, Shibata S, Yamane M (2003b) Structural investigation of sodium borate glasses and melts by Raman spectroscopy. III. Relation between the rearrangement of super-structures and the properties of the glass. J Non-Cryst Solids 321:157-168
Zachariasen WH (1932) The atomic arrangement in glass. J Am Chem Soc 54:3841-3851
Zhang X, Kirkwood WJ, Walz PM, Peltzer ET, Brewer PG (2012) A Review of advances in deep-ocean Raman spectroscopy. Appl Spectrosc 66:237-249
Ziegler LD (1990) Hyper-Raman spectroscopy. J Raman Spectrosc 21:769-779

EBSCOhost - printed on 2/13/2023 5:26 AM via . All use subject to https://www.ebsco.com/terms-of-use

EBSCOhost - printed on 2/13/2023 5:26 AM via . All use subject to https://www.ebsco.com/terms-of-use

Reviews in Mineralogy & Geochemistry
Vol. 78 pp. 543-603, 2014
Copyright © Mineralogical Society of America

Brillouin Scattering and its Application in Geosciences

Sergio Speziale, Hauke Marquardt
Deutsches GeoForschungsZentrum GFZ
Telegrafenberg, 14473 Potsdam, Germany
speziale@gfz-potsdam.de *hama@gfz-potsdam.de*

Thomas S. Duffy
Princeton University
Princeton, New Jersey 08544, U.S.A.
duffy@princeton.edu

INTRODUCTION

Brillouin spectroscopy is an optical technique that allows one to determine the directional dependence of acoustic velocities in minerals and materials subject to a wide range of environmental conditions. It is based on the inelastic scattering of light by spontaneous collective motions of particles in a material in the frequency range between 10^{-2} to 10 GHz.

Brillouin spectroscopy is used to determine acoustic velocities and elastic properties of a number of crystalline solids, glasses, and liquids. It is most commonly performed on transparent single crystals where the complete elastic tensor of the sample material can be derived. However, Brillouin spectra can be also measured from opaque materials, from which partial or complete information on the elastic tensor can be determined. It is a very flexible technique with many possible areas of application in research disciplines from condensed matter physics to biophysics to materials sciences to geophysics.

Brillouin scattering can be performed on very small samples and it can be easily combined with the diamond anvil cell and carried out at high pressures and temperatures (see reviews by Grimsditch and Polian 1989 and Eremets 1996). This makes this technique the method of choice to study the elastic properties of deep Earth materials, relevant to construct a mineralogical model of the interior of our planet that is consistent with the constraints from seismology.

Several of the candidate minerals of the Earth's interior are not stable at ambient conditions, and only recently has there been substantial progress in their synthesis. Unfortunately, those deep earth minerals that can be metastably preserved at ambient pressure and temperature are only available as single crystals with sizes of the order of several tens of microns at most. However, crystals of this size are large enough for Brillouin scattering to be performed. In addition, more sophisticated methods for the characterization, manipulation and preparation of such precious samples are becoming available. These developments allow one to significantly broaden the accessible pressure range of Brillouin scattering experiments.

A challenging application of Brillouin scattering in geophysics is to characterize the elastic properties of materials of the lowermost mantle that are synthesized as microcrystalline aggregates in the diamond anvil cell and cannot be quenched to ambient conditions. New results regarding the average shear velocities of Mg-silicate perovskite and post-perovskite have been recently obtained by Brillouin scattering. These results open new opportunities of developing a systematic understanding of pressure and compositional effects on the elastic properties of the rocks of the lowermost mantle based on experimental data.

1529-6466/14/0078-0014$10.00 http://dx.doi.org/10.2138/rmg.2014.78.14

EBSCOhost - printed on 2/13/2023 5:26 AM via . All use subject to https://www.ebsco.com/terms-of-use

In this chapter, we will discuss some important results obtained in geosciences by Brillouin scattering. We will focus particularly on the measurements performed at elevated pressure and/or temperature, and their implications for our understanding of the Earth's interior. As with any experimental technique Brillouin scattering has several limitations. We will also discuss some of the potential solutions to these technical limitations.

HISTORICAL BACKGROUND

The fundamental problem of light scattering attracted much interest among physicists more than a century ago. This interest was initially directed towards the intensity of the scattered light. Among the pioneering early developments were the work by Tyndall (1868) and Rayleigh (1899) regarding the scattering of light by particles suspended in a homogeneous fluid. Expressions for the intensity of molecular light scattering from fluids were initially proposed by Smoluchowski (1908) and Einstein (1910). The theory was then improved by Landau and Placzek (1934) and a formulation based on a generalized hydrodynamic theory was outlined by Mountain (1966b).

Brillouin (1922) and Mandelstam (1926) independently investigated the problem of light scattered by density fluctuations associated with acoustic waves in a homogeneous medium. The theory proposed by both Brillouin and Mandelstam was that light scattered by thermally excited acoustic waves in a medium should be shifted in frequency with respect to the incident light by an amount equal to the frequency of the scattering fluctuations. The kinematics of the scattering is described by the Bragg equation and the energy shift by the Doppler effect caused by the thermal acoustic waves propagating across the medium. This phenomenon, called Brillouin scattering (or Brillouin-Mandelstam scattering) could be detected spectroscopically in experiments in which light was scattered by acoustic waves with wavelength in the range of 100 nm. Brillouin scattering was first observed experimentally by Gross (1930b). However, with the conventional light sources available before the development of lasers, the measurement of Brillouin scattering was limited to compressed gases and fluids plus a handful of solids (see Krishnan 1971 for a review). The advent of laser sources in the 1960s made it possible to perform measurements on a wider range of solids, liquids and gases.

Since then, Brillouin scattering has been used to investigate elastic properties and high-frequency viscous behavior of crystalline and amorphous solids (Shapiro et al. 1966) liquids, molecular solids and glass-forming compounds, with a special interest in polymers (Patterson 1983; Krüger 1989). The advancement of the technology of Fabry-Perot interferometers then opened new fields of application of this technique, from the study of ferroelectric compounds and their behavior at phase transitions (Jiang and Kojima 2000; Ahart et al. 2010; Marquardt et al. 2013b), to the investigation of surface and interface vibrational and magnetic excitations of bulk materials and of thin films and multilayers (Wittkowski et al. 2002; Milano and Grimsditch 2010). Additional recent applications of Brillouin scattering range from the study of viscoelastic behavior of delicate biomaterials (Speziale et al. 2003) to the investigation of the elastic response of nanocomposites (Li Bassi et al. 2004), the characterization and design of phononic materials (Cheng et al. 2006) to the recent experimental detection of Bose-Einstein condensation of quasiparticles as an effect of external energy pumping (Demokritov et al. 2006).

The application of Brillouin scattering to the study of Earth materials dates back to the very early days of the technique. The first Brillouin measurements were performed on quartz by Gross (1930a) and on gypsum by Raman and Venkateswaran (1938). Starting in the 1970s a significant contribution to the knowledge of the anisotropic elasticity of geophysically important minerals at ambient conditions has been furnished by the groups led by D.J. Weidner at Stony Brook and J.D. Bass at the University of Illinois (e.g., Weidner et al. 1975, 1982; Weidner and Carleton 1977; Vaughan and Weidner 1978; Bass and Weidner 1984; Bass 1989; Yeganeh-Haeri

EBSCOhost - printed on 2/13/2023 5:26 AM via . All use subject to https://www.ebsco.com/terms-of-use

et al. 1992; Xia et al. 1998; Sinogeikin and Bass 2000; Sinogeikin et al. 2004b; Jackson et al. 2005; Stixrude and Jeanloz 2009). An important advance in the field of high-pressure Brillouin scattering was the study of the elastic tensor of NaCl to 3.5 GPa by Whitfield et al. (1976). In this work, the Brillouin frequency shift was measured in a symmetric scattering geometry that simplifies the determination of acoustic velocity from the measured frequency shift by making its conversion independent of the refractive index of the sample. The new experimental set-up opened the opportunity to investigate the elasticity of upper mantle and transition-zone minerals at the pressure conditions of the Earth's interior as well as to study of simple molecular solids of relevance in planetary science (Polian and Grimsditch 1984; Duffy et al. 1995; Shimizu et al. 1996; Zha et al. 1998; Sinogeikin and Bass 2000; Sinogeikin et al. 2003; Jiang et al. 2004a; Speziale and Duffy 2004; Murakami et al. 2007a,b; Mao et al. 2008b; Marquardt et al. 2009b).

PHYSICAL PRINCIPLES OF THE BRILLOUIN EFFECT

Linear or thermal Brillouin scattering is inelastic scattering of light by spontaneous thermal fluctuations/excitations (in the wavelength range between 10^{-7} and 10^{-6} m) in a material. In a quantum view, such fluctuations correspond to acoustic phonons at the Brillouin zone center (i.e., small wavevector or long wavelength). Phonons, together with other excitations (magnons, plasmons and others) contribute to fluctuations of the dielectric tensor of the material that are responsible for the scattering of light in directions different from that of the incident light propagation (Nizzoli and Sandercock 1990).

In the classical description of light scattering, the electromagnetic field acts on charged particles in the medium that, in turn, act as independent scatterers (Rayleigh 1899). The charged particles accelerated in the scattering volume radiate light. However, the theory encountered a serious difficulty in explaining the observations in dense media: the oscillating electromagnetic field polarizes the medium, but different scatterers that are closer to one another than the wavelength of light each scatter out of phase, thereby creating destructive interference in all but the forward scattering direction. The solution to this problem in explaining the experimentally observed scattering in all directions is the presence of spatially correlated heterogeneities (fluctuations) of the dielectric constant of a material at finite temperatures due to the presence of translational and rotational motion of particles (Smoluchowski 1908; Einstein 1910).

In the classical picture, if we consider a medium in thermodynamic equilibrium, thermal motions of its atoms (particles) will determine fluctuations of their number density as a function of position and time (Fleury 1970; Pecora 1972; Dil 1982):

$$N(r,t) = N + \Delta N(r,t) \tag{1}$$

Where N is the average number density, $\Delta N(r,t)$ is its fluctuating part, r is position and t is time.

Incident light interacts with the particles acting as dipoles. The interaction results in a Doppler shift of the scattered light. The wavevector and frequency of the scattered light depend on those of the incident light and on the wavevectors and frequencies that are present in the density fluctuations. We can express the density fluctuations as 3D Fourier series:

$$\Delta N(r,t) = \frac{1}{(2\pi)^4}\int_{-\infty}^{+\infty}\int_{-\infty}^{+\infty} dq^3 d\Omega \Delta N(q,\Omega)\exp\left[i(q\cdot r - \Omega t)\right] \tag{2}$$

where q is the wavevector, Ω is frequency and $\Delta N(q,\Omega)$ is the fluctuating part of the number density as a function of wavevector and frequency. The fluctuations are superpositions of phase (sinusoidal) gratings with wavelength Λ:

$$\Lambda = \frac{2\pi}{q} \tag{3}$$

EBSCOhost - printed on 2/13/2023 5:26 AM via . All use subject to https://www.ebsco.com/terms-of-use

and phase velocity v:

$$\nu = \frac{\Omega}{q} \tag{4}$$

The scattering from the phase gratings is analogous to Bragg's reflection picture of X-ray scattering, and the wavevector and frequency of the scattered light in the medium are:

$$k_s = k_i \pm q \tag{5}$$

$$\omega_s = \omega_i \pm \Omega \tag{6}$$

where k_i, k_s, ω_i and ω_s are the incident and scattered light wavevectors and frequencies respectively (Cummins and Schoen 1972).

Brillouin scattering takes place in the hypersonic frequency region (10^7 $s^{-1} < \Omega < 10^{12}$ s^{-1}) of the vibrational energy spectrum of the medium. The dispersion $q = q(\Omega)$ is determined by the (visco)elastic properties of the medium.

The frequencies of the incident and scattered light are approximately equal ($k_s \approx k_i$) and based on the scattering geometry (the angle between incident and scattered wave normals) only one Fourier component of the fluctuation is involved in the scattering. Its wavenumber is (Cummins and Schoen 1972):

$$q = 2k_i \sin\left(\frac{\theta}{2}\right) \tag{7}$$

where θ is the scattering angle (Fig. 1).

The wavelength of the scattering inhomogeneity extends over many atoms and the phase velocity corresponds to the hypersonic acoustic velocity. The spectrum of the scattered light includes a doublet at frequencies (Fig. 2):

$$\omega_s = \omega_i \pm 2\nu k_i \sin\left(\frac{\theta}{2}\right) \tag{8}$$

The analysis of Brillouin spectra allows us to access information about four features characteristic of Brillouin scattering: (a) spectral character that allows us to determine information about the acoustic velocity and (visco)elastic coefficients, (b) intensity that allows us to quantify the coupling coefficient between fluctuations and the electromagnetic field, (c) line width that is related to the lifetime of the interaction between fluctuations and light (giving information

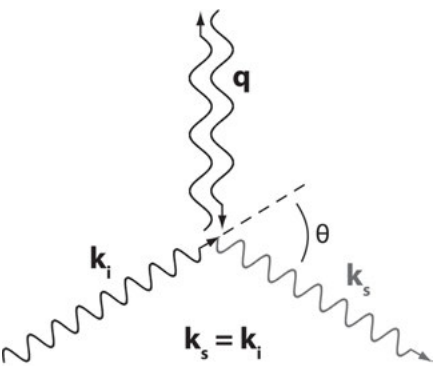


Figure 1. Schematic diagram of the geometry of Brillouin scattering. Symbols are explained in the text.

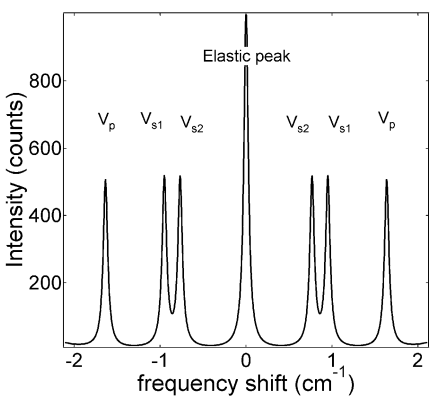


Figure 2. Idealized Brillouin scattering spectrum from an elastically anisotropic medium. The spectrum contains an unshifted line, corresponding to Rayleigh scattering, and three doublets (symmetric with respect to the unshifted line) due to Brillouin scattering from the three polarizations of the scattering wave. V_{s1} is the fast quasi-shear acoustic mode; V_{s2} is the slow quasi-shear acoustic mode and V_p is the quasi-longitudinal mode.

EBSCOhost - printed on 2/13/2023 5:26 AM via . All use subject to https://www.ebsco.com/terms-of-use

about viscous properties), and (d) polarization that is related to anisotropic properties of the medium at the microscopic level.

The coupling of light with fluctuations in a medium is given by the fluctuating part of the dielectric tensor as a function of position and time

$$\varepsilon_{ij}(r,t) = \varepsilon_{ij} + \Delta\varepsilon_{ij}(r,t) \tag{9}$$

where ε_{ij} is the average dielectric tensor and $\Delta\varepsilon_{ij}(r,t)$ is its fluctuating part. In the simple case of a monoatomic isotropic dielectric medium, the dielectric tensor is of the form $\varepsilon_{ij} = (\varepsilon + \Delta\varepsilon)\delta_{ij}$ (where δ_{ij} is the Kronecker delta) and the coupling with density fluctuations is expressed by (Fleury 1970; Dil 1982):

$$\varepsilon + \Delta\varepsilon(r,t) = \varepsilon + \frac{\partial\varepsilon}{\partial\rho}\Delta\rho(r,t) \tag{10}$$

This is related to density fluctuations $\Delta\rho$. The strength of the coupling ($\partial\varepsilon/\partial\rho$) can be expressed based on the Lorentz-Lorenz relation:

$$\frac{\partial\varepsilon}{\partial\rho} = \frac{\varepsilon_0}{\rho}\left(\frac{n^2+2}{3}\right)\left(n^2-1\right) \tag{11}$$

where ε_0 is the permittivity of free space and n is the refractive index.

The macroscopic electric polarization

$$\mathcal{P}(r,t) = N(r,t)\,p(r,t) = Np(r,t) + \Delta\mathcal{P}(r,t) \tag{12}$$

(where $p(r,t)$ is the dipole moment and $\Delta\mathcal{P}(r,t)$ is an excess polarization due to fluctuations) caused by the incident electromagnetic field is connected with the microscopic atomic dipole moment (and the density fluctuations):

$$\Delta\mathcal{P}(k_s,\omega_s) = \Delta\varepsilon(\omega_i,q,\Omega)e^i = \frac{\partial\varepsilon(\omega_i)}{\partial\rho}\Delta\rho(k_s-k_i,\omega_s-\omega_i) \tag{13}$$

where k_i is the wavevector and e^i is the polarization of the incident electromagnetic field usually represented as a monochromatic wave.

The details of the coupling and the basic theory of Brillouin scattering in fluids and solids are summarized in the next two sections. A far more detailed presentation of these topics can be found elsewhere (Fabelinskii 1968; Fleury 1970; Cummins and Schoen 1972; Dil 1982). However, it is important here to highlight that in systems that are more complex than monoatomic fluids the second rank dielectric tensor is not diagonal having non-zero off-diagonal coefficients.

Brillouin scattering in fluids

The calculation of the intensity and the spectral characteristics of Brillouin scattering in fluids is based on the determination of the appropriate value of the fluctuating part of the dielectric tensor, $\Delta\varepsilon$, and its coupling with fluctuations of pressure, density, temperature or entropy. In absence of a complete dynamical theory of fluids, the problem has been approached at three different levels of theory: (a) thermodynamic, (b) hydrodynamic and (c) microscopic. Here we will give a very brief account of each of them. More detailed information can be found by the interested reader in several reviews and in specialized studies (Rytov 1958; Benedek and Greytak 1965; Mountain 1966b; Wang 1986).

(a) The thermodynamic approach considers that the fluctuating part of the dielectric tensor can be characterized by its dependence on two parameters, pressure and entropy:

EBSCOhost - printed on 2/13/2023 5:26 AM via . All use subject to https://www.ebsco.com/terms-of-use

$$\Delta\varepsilon = \left(\frac{\partial\varepsilon}{\partial P}\right)_S \Delta P + \left(\frac{\partial\varepsilon}{\partial S}\right)_P \Delta S \tag{14}$$

Where P is pressure and S is entropy.

The total intensity of the scattered electromagnetic field derived by the fluctuation-dissipation theorem (e.g., Landau and Lifshitz 1969) is proportional to the mean square fluctuations of ε that are related to fluctuations in temperature and density (Fleury 1970; Cummins and Schoen 1972):

$$I_s \propto < \left|\Delta\varepsilon\right|^2 > \tag{15}$$

By simple thermodynamic identities we can express $< \left|\Delta\varepsilon\right|^2 >$ as

$$< \left|\Delta\varepsilon^2\right| > = \left(\frac{\partial\varepsilon}{\partial P}\right)_S^2 \frac{k_B T}{\beta_S V_0} + \left(\frac{\partial\varepsilon}{\partial T}\right)_P^2 \frac{k_B T^2}{\rho C_P V_0} \tag{16}$$

where

$$\left(\frac{\partial\varepsilon}{\partial T}\right)_P^2 \frac{k_B T^2}{\rho C_P V_0} = \left(\frac{\partial\varepsilon}{\partial S}\right)_P^2 < \left(\Delta S\right)^2 >$$

and k_B is Boltzmann's constant, β_S is the isentropic compressibility, C_P is the specific heat at constant pressure, and V_0 is the ambient-pressure volume.

The two terms on the right side of (16) represent two spectral components of the scattered light: (I) the Brillouin scattered light caused by isentropic pressure fluctuations (i.e., the acoustic vibrations) producing a doublet with frequencies $\omega_B = \omega_i \pm \Omega$ (where ω_B is the frequency of the Brillouin spectral feature, ω_i and Ω are the frequencies of incident light and scattering vibration, see also Eqn. 6 and Fig. 2) and (II) a component caused by isobaric (non-propagating) entropy fluctuations. The second component is not shifted in frequency, $\omega_C = \omega_i$, where ω_C indicates that this spectral feature is not shifted in frequency.

The ratio of the intensities of the two components has been the subject of intense theoretical investigation. One important result is the famous Landau-Placzek ratio (Landau and Placzek 1934):

$$\frac{I_C}{I_B} = \left(\frac{\partial\varepsilon}{\partial T}\right)_P^2 \left(\frac{\partial\varepsilon}{\partial P}\right)_S^{-2} \approx \frac{C_P - C_V}{C_V} = \frac{\beta_T - \beta_S}{\beta_S} \tag{17}$$

(where I_C, I_B are the intensities of the central feature and the shifted doublet, C_P, C_V are the specific heat at constant volume and at constant pressure, β_S is the isentropic compressibility, and β_T is the isothermal compressibility) based on simple thermodynamic identities and on the simplifying assumption that $(\partial\varepsilon/\partial T)_\rho \approx 0$ (where the subscript ρ indicates constant density).

Due to the fact that the Brillouin components are related to hypersonic acoustic waves while the central unshifted feature is due to slow (isothermal) fluctuations, the parameters in the Landau-Placzek ratio should take into account the possibility of dispersion in the hypersonic frequency range. A revised form of the ratio was presented by Cummins and Gammon (1965) as:

$$\frac{I_C}{I_B} \approx \frac{\left(\beta_T - \beta_S\right)_{ST}}{\left(\beta_S\right)_{HS}} \tag{18}$$

where the indices *ST* and *HS* refer to static and hypersonic.

EBSCOhost - printed on 2/13/2023 5:26 AM via . All use subject to https://www.ebsco.com/terms-of-use

(b) The hydrodynamic approximation represents a more complete description of the spectrum. It includes the dynamics of the fluctuations that affect the spectral line-shapes which cannot be captured by a thermodynamic (equilibrium) approach. In this case, the decay of the spontaneous fluctuations is described with the classical equations describing macroscopic relaxation processes. One example of this approach is the model presented by Mountain (1966a) in which the dynamics of the fluctuations is expressed by the linearized equations of hydrodynamics. The spectrum is of the form:

$$S(\omega,q) \propto \frac{C_P - C_V}{C_V}\left[\frac{2D_T q^2}{D_T + \omega^2}\right] + \frac{C_V}{C_P}\left[\frac{\Gamma q^2}{\left(\Gamma q^2\right)^2 + \left(\omega + \nu q\right)^2} + \frac{\Gamma q^2}{\left(\Gamma q^2\right)^2 - \left(\omega + \nu q\right)^2}\right] \quad (19)$$

where D_T is the thermal diffusivity, and the terms in brackets are the central and the two shifted Lorentzian peaks whose full width at half maximum is equal to Γq^2, where Γ is the acoustic absorption coefficient.

This model correctly describes the frequency content of the spectrum, the intensity ratio of the spectral features (similarly to the Landau-Placzek ratio) and their linewidth. The addition of phenomenological parameters was introduced by Mountain (1966a) to describe spectral features due to the coupling of internal (molecular) and external degrees of freedom (whole molecule translations) in real liquids.

Phenomenological models based on the hydrodynamic approximation can also tackle the problem of modeling the depolarized scattering from molecular liquids with intrinsic molecular anisotropy (scattering involving 90° change of the polarization with respect to the incident light) that cannot be accounted for by a thermodynamic theory because they are related to the presence of non-zero off-diagonal coefficients in the dielectric fluctuation tensor $\Delta\varepsilon_{ij}$. Detailed theories of Brillouin scattering of anisotropic molecular liquids have been developed (e.g., Rytov 1970; Wang 1986).

(c) Models based on microscopic theories describe the relaxation of the fluctuations of physical properties of the medium by means of stochastic differential equations with a random driving force. The microscopic foundation of the generalized relaxation equations is based on the work of Zwanzig (1961) and Mori (1965). Microscopic theories of the Brillouin spectra of fluids have been developed in several studies often in order to interpret the depolarized spectra of viscous fluids (e.g., Kivelson and Madden 1980) and of supercooled glass-forming liquids.

Brillouin scattering in solids

In the case of solids, any atomic displacement $u_{ij}(r,t)$ affects the local polarization field. The excess polarization for a non-piezoelectric solid can be expressed as (Dil 1982):

$$\Delta\mathcal{P}_i\left(k_s,\omega_s\right) = \Delta\varepsilon_{ij}\left(\omega_i,q,\Omega\right)e_j^i = -\frac{1}{2}\left[\varepsilon_0^{-1}\varepsilon_{im}\left(\omega_i\right)\varepsilon_{jn}\left(\omega_i\right)p_{mnkl}u_{kl}\left(k_s - k_i,\omega_s - \omega_i\right)\right]e_j^i \quad (20)$$

Where p_{ijkl} is the photoelastic tensor and $u_{kl}(q,\Omega)$ is the frequency and wavevector Fourier transform of the displacement gradient $u_{kl}(r,t) = \partial u_k/\partial x_l$. All the remaining quantities have already been introduced above. In case of optically isotropic solids and of static homogeneous deformations, the fourth rank tensor p_{mnkl} has the symmetry of the Laue symmetry class of the solid (e.g., Nye 1985).

Nelson and Lax (1971) have developed a microscopic theory of the photoelastic interaction that includes also coupling of rotations to the scattering process. The fluctuating part of the dielectric tensor is expressed as a function of the strain tensor S_{ij} and also of the rotation tensor R_{ij} (the anti-symmetric part of the displacement gradient). In strongly birefringent materials, the Pockels photoelastic tensor is symmetric upon interchange of m and n but it is not symmetric

EBSCOhost - printed on 2/13/2023 5:26 AM via . All use subject to https://www.ebsco.com/terms-of-use

upon exchange of the indices k and l. In this case, the dependence on strain and rotation (the symmetric and anti-symmetric parts of u_{ij}) is treated by explicitly separating the symmetric and asymmetric contributions.

$$\Delta\varepsilon_{ij}\left(\omega_i,q,\Omega\right)e^i_j = -\varepsilon_0^{-1}\varepsilon_{im}\left(\omega_i\right)\varepsilon_{jn}\left(\omega_i\right)\left[\, p_{mnkl}S_{kl}\left(q,\Omega\right)p_{mn[kl]}R_{[kl]}\left(q,\Omega\right)\right] e^i_j \tag{21}$$

where the brackets indicate antisymmetry upon interchange of indices, $S_{kl} = 1/2(\partial u_k/\partial x_l + \partial u_l/\partial x_k)$ is the strain tensor and $R_{kl} = 1/2(\partial u_k/\partial x_l - \partial u_l/\partial x_k)$ is the rotation tensor.

In a thermodynamic approach, $\Delta\varepsilon_{ij}$ for an isotropic solid can be decomposed into a density and a thermal component. The microscopic theory of the effect of temperature fluctuations on the polarizability of solids is treated by Wehner and Klein (1972). Central non-shifted spectral features (see discussion of Eqn. 16) have actually been observed in Si, diamond, TiO_2, $SrTiO_3$, ZnSe (Lyons and Fleury 1976; Hehlen et al. 1995; Stoddart and Comins 2000; Koreeda et al. 2006). Some of these spectral features have been interpreted as the effect of two-phonon difference scattering (Anderson et al. 1984; Stoddart and Comins 2000; Koreeda et al. 2006).

In the long wavelength limit, the equation of motion of the atomic displacement field can be treated as that of an elastic continuum (Cummins and Schoen 1972; Every 2001):

$$\rho\frac{\partial^2 u_i\left(r,t\right)}{\partial t^2} = c_{ijkl}\frac{\partial^2 u_k\left(r,t\right)}{\partial x_j \partial x_l} \tag{22}$$

where c_{ijkl} is the stiffness tensor. The derivation of the equation of motion for discrete atomic displacements starts from the expansion of the interatomic potential energy in a power series, which is truncated to the second order term in the case of the harmonic approximation, or to higher orders if we want to take into account damping of the elastic constants.

Equation (22) expresses the dependence of the components of the atomic displacement u_i from the equilibrium position on the spatial derivatives of the displacement field by means of the elastic constants. For plane wave solutions of the form $u_i(q,\omega) = u_i^0 \exp i\,(qr - \omega t)$ we obtain by substitution in (22):

$$\left(c_{ijkl}q_j q_l - \rho\omega^2\delta_{ik}\right)u_k^0\left(q,\omega\right) = 0 \tag{23}$$

where q_j are the components of the scattering wavevector, where δ_{ik} is the Kronecker delta, and u_k^0 is the polarization.

This equation admits non-trivial solutions that satisfy the secular equation:

$$\left|c_{ijkl}q_j q_l - \rho\omega^2\delta_{ik}\right| = 0 \tag{24}$$

The secular equation has three solutions per each direction of q, which correspond to the three phonon branches. The solutions $\Omega^\alpha(q,c_{ijkl}) = ((c_{ijkl}/\rho)^{1/2})^\alpha q = v^\alpha q$ (where the superscript $\alpha = 1, 2, 3$ identifies the three solutions and v^α is the phase velocity) for high symmetry q directions have displacement vectors parallel and perpendicular to q and correspond to one pure longitudinal and two pure shear modes. In a general direction of an anisotropic medium the displacement vectors are mixed and the vibrations are composed of one quasi-longitudinal and two quasi-shear modes (Fig. 2).

The spectral intensity, I_s, can be derived from the excess dipole moment. In thermal equilibrium it is proportional (as in the case of liquids) to the mean square of the fluctuating part of the dielectric tensor:

$$I_s \propto (e^s)^2 \cdot < \left|\Delta\varepsilon\right|^2 > \cdot (e^i)^2 \tag{25}$$

where e^s and e^i are the polarizations of the incident and scattered light.

EBSCOhost - printed on 2/13/2023 5:26 AM via . All use subject to https://www.ebsco.com/terms-of-use

The intensity of the α^{th} acoustic mode with velocity v^{α} for a direction q can be expressed as (Cummins and Schoen 1972):

$$I_s = I_i \frac{k_B T \pi^2 V}{2\lambda_s^4 \rho \left(v^{\alpha}\right)^2 r^2} \frac{n_s}{n_i} \left[e_s \cdot \mathrm{T}^{\alpha} \cdot e_i \right]^2 \tag{26}$$

where I_i is the intensity of the incident beam, V is the scattering volume, n_s and n_i are the refractive indices of the medium in the incident and scattered directions, λ_s is the wavelength (in vacuum) of the scattered light, r is the distance of observation from the scattering volume and T^{α} is a tensor that describes the distortion of the dielectric tensor associated with the acoustic mode α.

Tabulated expressions for the tensors T^{α} are given in Cummins and Schoen (1972) and Vacher and Boyer (1972) for several high symmetry directions in different crystal systems.

BRILLOUIN SPECTROSCOPY

Brillouin scattering measurements are performed in a range of experimental setups and use different scattering geometries. However, the basic features of the experiments are similar across the different setups. In the following subsections, we will introduce the basic design of Brillouin scattering experiments. We will then describe some details of the setups required for specific applications and address limitations and common problems encountered in performing measurements at extreme conditions.

Basic experimental setup

The basic design of a Brillouin scattering experiment is illustrated in Figure 3. Monochromatic light is focused with a lens L1 on the sample, thereby defining a scattering volume V and an incident external wavevector, k_i*. Scattered light in a selected direction is collected by the lens L2 that defines the external scattered wavevector, k_s*, parallel to the direction of observation, the external scattering angle, θ* (these quantities are, in general, different from k_i, k_s and θ in the scattering material as defined in the section "Physical Principles of the Brillouin Effect"), and a solid angle δΩ around the direction of observation; the collimated light from L2

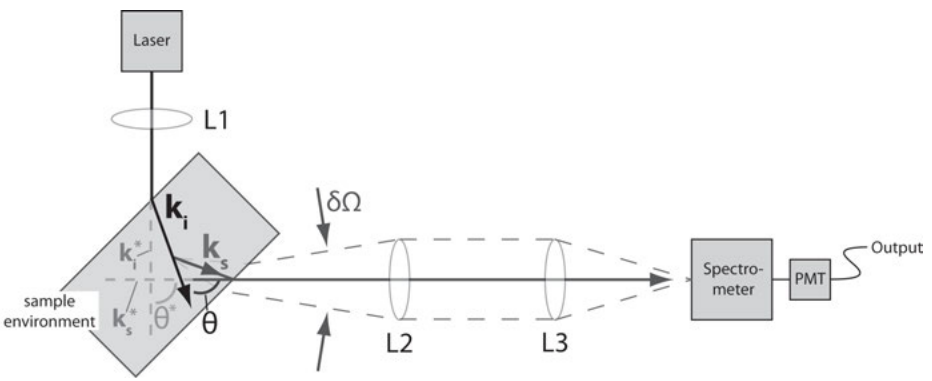


Figure 3. Schematic outline of a typical Brillouin scattering experiment. L: lens; δΩ: solid angle around the direction of observation determined by the numerical aperture of the collecting lens; k_i: incident wavevector in the sample; k_s: scattered wavevector in the sample; θ: scattering angle inside the sample; k_i*: incident wavevector outside the sample environment; k_s*: scattered wavevector outside the sample environment; θ*: external scattering angle (determined by the directions of the incident and scattered wavevectors outside the sample environment); PMT: photomultiplier tube.

EBSCOhost - printed on 2/13/2023 5:26 AM via . All use subject to https://www.ebsco.com/terms-of-use

is focused with a lens L3 on the entrance of the spectrometer. After passing through the spectrometer, the light is detected by a photomultiplier tube or a solid state detector and recorded by a multichannel analyzer.

Light source

The light source for Brillouin scattering experiments has to be strictly monochromatic (i.e., single longitudinal mode, generally by means of an etalon in the laser resonator) to prevent ambiguities in the spectrum that would make it impossible to assign the observed peaks. Gas or solid-state lasers are both commonly used in current Brillouin scattering system designs. Due to the λ^{-4} dependence of the intensity of scattered light, green and blue lasers are the most commonly adopted. However, systems designed for opaque semiconductors use near infrared laser sources (Gehrsitz et al. 1997). The power of the source radiation rarely exceeds 100 mW except for experiments performed on samples at extreme conditions (i.e., very small samples compressed in the diamond anvil cell).

Scattering geometry

In order to determine acoustic velocities from Brillouin spectra we must know the value of the scattering wavevector and the scattering angle in the medium (Eqns. 4-7). In order to define the scattering angle within the sample, we have to account for the paths of the incident and scattered light outside the sample, and we have to precisely know the characteristics of the sample (or the sample container) such that we can calculate the internal scattering angle by applying Snell's law. By constraining the external light path and by knowing the refractive index of the medium we can determine the value of the wavevector of the scattering fluctuation and, from the measurement of its frequency, also determine its phase velocity.

The geometry of the light path outside the sample can be easily set to better than 10^{-2} degrees. Similar levels of precision can be achieved by accurate machining and polishing of the external surface of the sample (or sample assemblage). The final accuracy at which the internal scattering geometry can be constrained is limited by the uncertainty in the refractive indices of sample (and container). This becomes the limiting factor especially in high-pressure experiments, where both the refractive index of highly stressed diamond windows and that of the sample under pressure are poorly known.

Different scattering geometries are used to simplify the determination of the internal scattering angle (Fig. 4). Among the most commonly used geometries is the 90° normal geometry (90N) in which the sample incidence and scattering faces are 90° from each other, and perpendicular to the incident and scattered light paths. In this geometry, the effect of refraction at the samples surfaces is removed by symmetry and the wavevector of the scattering vibration is at 45° from both the incident and scattered wavevectors (Fig. 4a). The magnitude of the scattering wavevector is $q = n(2)^{1/2}/\lambda_0$, where n is the refractive index and λ_0 is the wavelength of the incident light in vacuum. The most useful scattering geometry for high-pressure applications is the forward symmetric geometry (Fig. 4b). In this case, the incident and scattered sample interfaces are parallel to each other and perpendicular to the bisector of the external scattering angle set by the arrangement of the focusing and collecting optics. This geometry does not require knowledge of the refractive index of the sample and allows one to determine the orientation of the scattering wavevector if just one orientation on the sample face is known. By rotating the sample around an axis perpendicular to the plane of the sample, one can select any scattering orientation within the samples' surface plane. The scattering wavevector is $q = 2 \sin(\theta^*/2)/\lambda_0$ where θ^* is the external scattering angle as defined by the axes of the focusing and collecting lenses (see also Fig. 3). Two additional examples of scattering geometries are presented in Figure 4. 180° (backscattering) geometry (Fig. 4c) gives only information about the quasi-longitudinal mode (in this geometry the elasto-optic coupling with the shear modes vanishes). The magnitude of the scattering wavevector is $q = 2n/\lambda_0$.

EBSCOhost - printed on 2/13/2023 5:26 AM via . All use subject to https://www.ebsco.com/terms-of-use

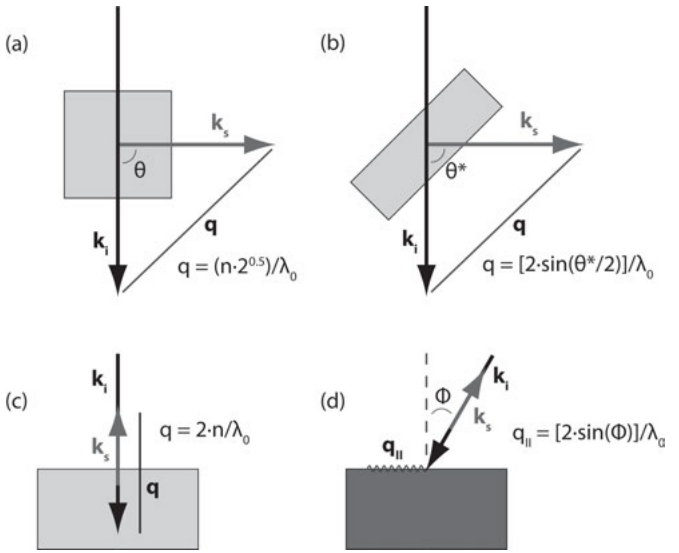


Figure 4. Schematic diagrams of different scattering geometries used in Brillouin spectroscopy. (a) 90° normal geometry; (b) forward symmetric geometry (here refraction is not taken into account and θ* is the external scattering angle (see text); (c) 180° backscattering geometry; (d) tilted backscattering geometry for surface Brillouin scattering measurements. Symbols are explained in the text.

It can be used in combination with the symmetric forward scattering geometry to determine the refractive index of an isotropic medium (such as a fluid) at the laser frequency. A tilted backscattering geometry (Fig. 4d) is used to measure surface Brillouin scattering from opaque materials. In this case, the magnitude of the scattering wavevector (of the surface vibration) is $q_{\|} = 2 \sin \phi/\lambda_0$, where ϕ is the angle between the incident (and scattered) wavevector and the surface normal. This scattering geometry will be further discussed in the section "Measurements of surface Brillouin scattering on opaque materials and thin-films."

The spectrometer

Due to the very small frequency shifts of the thermal acoustic phonons measured in Brillouin scattering, Fabry-Perot interferometers are used to separate the spectral components of the light instead of grating monochromators. Brillouin spectral lines are extremely close to the unshifted source frequency (the measured frequency shift $\Delta\omega$ is generally limited to the range $10^{-2} < \Delta\omega < 10\ \text{cm}^{-1}$) and the spectral resolution required for such measurements is of the order of $10^{-3}\ \text{cm}^{-1}$. Grating monochromators are rarely capable of reaching frequency regions closer than $10^{2}\ \text{cm}^{-1}$ to the source frequency and their resolution is in the range of $10^{-1}\ \text{cm}^{-1}$.

A Fabry-Perot interferometer consists of two flat mirror plates with faces very parallel to each other separated by a distance L. An incident beam is subject to multiple reflections at the opposing mirrors' surfaces. Light of wavelength λ is transmitted only if it satisfies the interference condition:

$$m\lambda = 2nL\cos\alpha \tag{27}$$

where m is an integer, n is the refractive index of the medium between the two mirrors of the interferometer, L is the mirror spacing and α is the incidence angle (normally 0°). The free spectral range, Δk, of the interferometer is defined as the frequency interval (expressed usually in wavenumbers) corresponding to the difference between two wavelengths that are simultaneously transmitted by adjacent interference orders: $\Delta k = 1/\Delta\lambda = 1/(2nL)$ for $\lambda << L$.

EBSCOhost - printed on 2/13/2023 5:26 AM via . All use subject to https://www.ebsco.com/terms-of-use

The instrumental function of a single Fabry-Perot interferometer is determined by the convolution of three factors that depend on (a) the non-perfect reflectivity of the mirrors, (b) their non-perfect parallelism (and surface imperfections), and (c) the finite range of angles incident on the Fabry-Perot (which causes a finite transmitted wavelength bandwidth). The ratio of transmitted to incident light (transmission function) can be expressed by the Airy function (e.g., Jacquinot 1960):

$$A(\lambda, L, \alpha) = \frac{T}{1 + 4\left(\frac{F^2}{\pi^2}\right)\sin^2\left[\left(\frac{2\pi nL}{\lambda}\right)\cos\alpha\right]} \tag{28}$$

where T is the maximum (peak) transmitted intensity and F is the effective finesse, defined as the ratio of the instrumental linewidth divided by the free spectral range. The finesse determines the maximum number of features that can be resolved within a given free spectral range. The effective finesse is strongly affected by the imperfections of the mirror surfaces. If the surfaces of the two mirrors match each other within λ/m, the effective finesse will not exceed $m/2$. For high quality mirror surfaces, the effective finesse is $F \approx 10^2$. Increasing the finesse can only be achieved at the cost of a substantial loss of throughput. The spectral contrast, $C = 1 + 4F^2/\pi^2$, defined as the ratio of maximum and minimum transmission, is always below 10^4. The throughput of the Fabry-Perot is controlled by geometric parameters of the external optical system (lenses, focal lenses, mirrors, aperture, maximum angular spread of the beam) that determine the minimum achievable free spectral range, which for a single Fabry-Perot interferometer is in the order of 0.5×10^{-2} cm^{-1}. A thorough discussion of the Fabry-Perot interometer and its applications can be found in Jacquinot (1960) and Hernandez (1988).

In the standard Brillouin scattering experiment, the Fabry-Perot interferometer is used as a variable narrow band-pass filter by scanning the selected free spectral range. This can be performed by one of two main methods: (a) by varying the refractive index, n, of the medium between the mirrors, or (b) by scanning the mirror separation, L. Method (a) is implemented by pressurizing a gas medium in which the interferometer is immersed inside a sealed vessel (Durvasula and Gammon 1978); method (b) is the most commonly used in modern designs of spectrometers for Brillouin scattering, and it is implemented using systems that drive the mirror motion by piezoelectric transducers and achieve rapid and linear scan rates. In the following we will focus only on (b).

The main limitations in the use of a single Fabry-Perot interferometer as a Brillouin scattering spectrometer is due to low spectral contrast and by overlapping of transmission from different interference orders. A single Fabry-Perot interferometer does not have a sufficient contrast to measure Brillouin scattered light in presence of very intense elastic scattering from the surface of a material (this is true especially for opaque materials). Multi-passing a single Fabry-Perot or using multiple interferometers operated in series both increase the spectral contrast as $C_n = (C)^n$ (where C_n is the overall contrast and C is the contrast of the single Fabry-Perot interferometer). However, as systems based on multiple interferometers in series suffer from imperfect synchronization of the interferometers scans, multi-passing a single interferometer is a solution that guarantees higher stability and performance. Studies on the design and performance of multi-pass Fabry-Perot systems for Brillouin scattering spectrometry show that 5-passes through the same interferometer increase the contrast C from 10^4 to 10^9-10^{10} (Sandercock 1971; Hillebrands 1999) while maintaining a finesse that is comparable with that of a single-pass system (50-100). However there is an appreciable reduction of the throughput (Fig. 5).

At a constant effective spectral finesse, the spectral resolution is increased by reducing the free spectral range. This allows one to resolve low-frequency spectral features generally related to shear acoustic modes. The disadvantage of reducing the free spectral range below twice the highest frequency Brillouin peak is that adjacent orders of interference of the Brillouin compo-

EBSCOhost - printed on 2/13/2023 5:26 AM via . All use subject to https://www.ebsco.com/terms-of-use

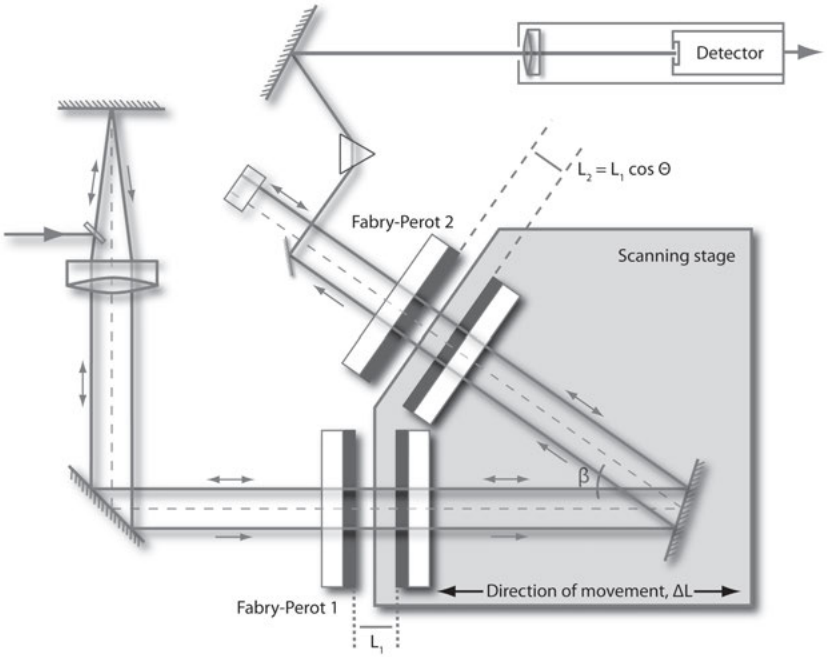


Figure 5. Multi-pass Fabry-Perot interferometer in the "tandem" implementation by Sandercock (1980), Symbols are explained in the text.

nents can partially overlap. The identification and attribution of the observed spectral features is then ambiguous.

Alternatively, the overall free spectral range can be expanded by combining (in series) interferometers of different mirror spacings L_i (where the index i refers to the ith interferometer in series). In case of a "tandem" design and incidence angle $\alpha = 0$ (see Eqn. 27), the first interferometer transmits wavelengths that satisfy $\lambda_1 = 2nL_1/m_1$, the second interferometer transmits wavelengths that satisfy $\lambda_2 = 2nL_2/m_2$. The tandem system will transmit only when both the conditions are simultaneously satisfied, that is when $\lambda_1 = \lambda_2$. This condition effectively increases the free spectral range by a factor of few tens (Fig. 6). In order to effectively use such combinations of interferometers, their scanning needs to be precisely synchronized such that the increments of the mirror distances for the first and second interferometer, δL_1 and δL_2, satisfy the condition:

$$\frac{\delta L_1}{\delta L_2} = \frac{L_1}{L_2} \tag{29}$$

Achieving both synchronization and constant increment of the mirrors' distances is technically challenging when the interferometers are scanned separately (Dil et al. 1981). One ingenious design of a tandem multi-pass interferometer has been developed by Sandercock (1978, 1980) (Fig. 5). In this system, two Fabry-Perot interferometers are scanned using a single stage actuated by a highly linear piezo-transducer. The axis of the second interferometer is oriented at an angle β with respect to the first one. A fixed mirror scanned together with the two interferometers reflects light transmitted by the first interferometer to the second one. The mirror distance of the second interferometer is such that $L_2 = L_1\cos\beta$. This condition is maintained across the whole scan, such that Equation (29) is strictly satisfied at all times

EBSCOhost - printed on 2/13/2023 5:26 AM via . All use subject to https://www.ebsco.com/terms-of-use

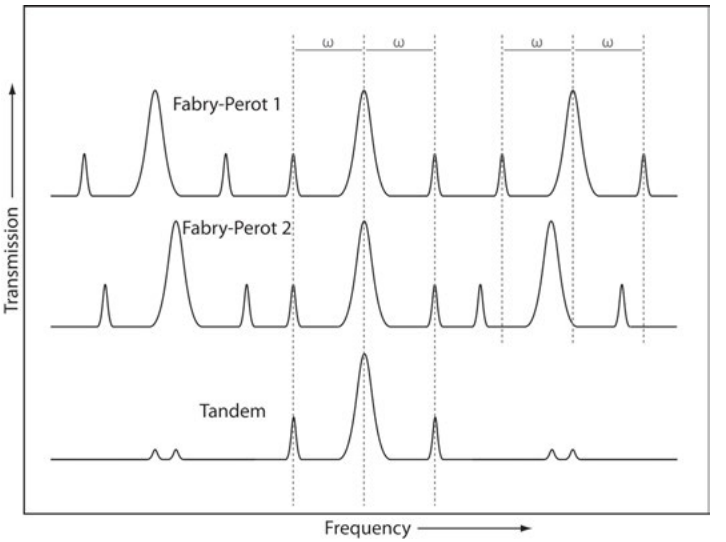


Figure 6. Transmission spectrum (as a function of frequency) of the two interferometers and the total transmission of a tandem Fabry-Perot system. The use of a second Fabry-Perot interferometer in series with the first but with offset mirror distance suppresses the signal of the first interferometer at any position when the condition $L_1/m_1 = L_2/m_2$ is not satisfied (see text for explanations). This effectively increases the free spectral range of the spectrometer. ω is the Brillouin scattering frequency shift.

during operation of the tandem interferometer. This design is by far the most widely used and it has allowed the application of Brillouin spectroscopy to various types of weakly scattering samples, such as samples in the diamond anvil cell, and systems characterized by the presence of intense elastically scattered signal that could otherwise mask Brillouin scattering features (such as opaque materials). Problems connected to the long-term alignment stability of the interferometers are reduced by controlling and stabilizing the environmental temperature within ±2 °C over a 24 h period. In addition, the implementation of feed-back alignment stabilization control (that systematically adjusts the fine mirrors' tilting to ensure their best parallelism) and of dynamic vibration controls -to filter environmental vibrations (in the frequency range between 1 and 10^2 Hz) that can affect the efficiency of the interferometer- extends the stability of the system allowing up to 48-h continuous acquisition times (Lindsay et al. 1981; Sandercock 1987; Hillebrands 1999).

Detectors

The selection of the detector for a Brillouin scattering spectrometer represents a compromise between high efficiency in the energy range of interest and good signal-to-noise ratio. In experiments performed on large samples producing intense signals, the use of photomultiplier tubes guarantees the best signal-to-noise ratio due to extremely low dark count (down to less than 5 counts/s) and large dynamic range even though the quantum efficiency is only of the order of 20%. In case of small, weakly scattering samples, such as those in the diamond anvil cell, the high quantum efficiency of avalanche photodiodes (up to 70%) and moderately low dark count (about 25 counts/s) substantially reduces collection times, and can thus mitigate problems of long-term stability of the interferometers' alignment and the natural drift of the source frequency. However, due to the lower dark current, photomultiplier tubes can still be the best choice in case of materials that produce extremely weak Brillouin signal in the presence of a comparably strong elastic scattering from surface imperfections, such as in case of opaque materials.

EBSCOhost - printed on 2/13/2023 5:26 AM via . All use subject to https://www.ebsco.com/terms-of-use

The essential components of a setup for Brillouin scattering at high pressure in the diamond anvil cell are sketched in Figure 7. This experimental configuration allows one to determine acoustic velocities with a precision of ~ 0.5% and accuracy better than 1% (measured on standard materials). The best achievable uncertainty on the recovered single crystal elastic constants is better than 1% (Speziale and Duffy 2002).

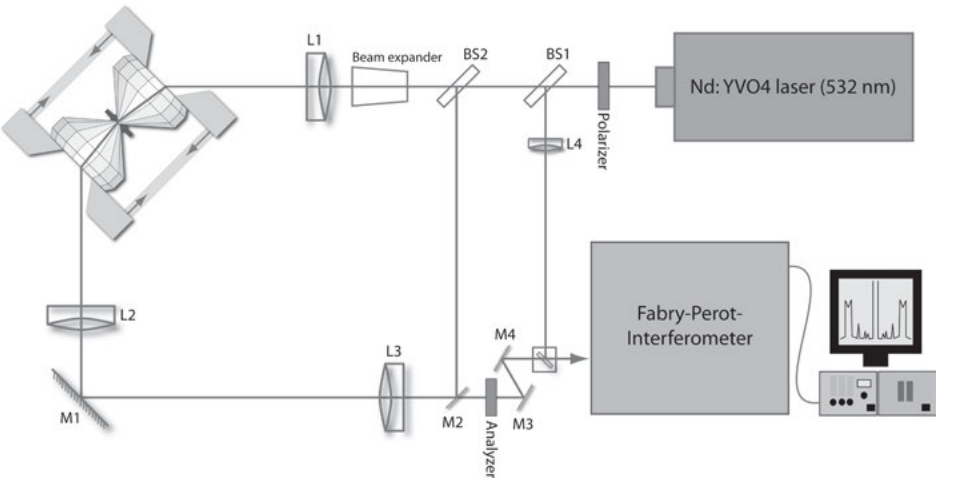


Figure 7. Schematic drawing of the setup for Brillouin scattering in the diamond anvil cell. BS: beamsplitter; L: lens; M: mirror.

Measurements on transparent materials

The most common use of Brillouin scattering is to perform measurements on optically transparent materials. In this case, the scattering geometry can be selected from nearly forward scattering to 180° back scattering. The region of the first Brillouin zone that can be accessed goes from the zone center ($q \to 0$ corresponding to $\theta \to 0$; see Eqn. 7) to $q = 2nk_0$ (where k_0 is the incident light wavenumber in vacuum and n is the refractive index), assuming an optically isotropic material. Brillouin scattering in optically anisotropic materials is described by generalizing Equation (7) (Krishnan 1971):

$$q = k_0\sqrt{\left(n_i^2 + n_s^2 - 2n_i n_s \cos\theta\right)} \tag{30}$$

where n_i, n_s are the refractive indices in the directions of the incident and scattered light. Thus, for a general (external) orientation of the incident light, there are 12 doublets in the Brillouin scattering spectrum, one for each acoustic mode for each combination of the refractive indices. The application of Equation (30) allows the correct determination of the scattering wavevector. However, for typical birefringences and with the spectral resolution of the available spectrometers, no measurements have been reported that resolved components due to birefringence effects even in materials with exceptionally strong birefringence such as calcite (Chen et al. 2001).

The orientation of the scattering phonon in experiments performed on single crystals (that is, acoustically anisotropic materials) requires a precise knowledge of the orientation of the sample with respect to the experimental reference system. In the simple case of an optically isotropic material, it is important to determine the effect of refraction at the interface between the sample and the surrounding medium. This requires that the external surface of the sample

EBSCOhost - printed on 2/13/2023 5:26 AM via . All use subject to https://www.ebsco.com/terms-of-use

(or sample assemblage) is shaped such that it has flat faces in the direction of the incident and scattered light. In case of irregularly shaped (small) samples, one solution is to immerse the sample in a fluid of matching refractive index (with a tolerance of the order of ≈ 3-5%; Weidner et al. 1975; Gleason et al. 2009) in a container with a regular shape appropriate for the scattering geometry selected in that experiment. This set-up allows one to exactly know the scattering wavevector once the coefficients of the optical indices of the sample material (at the wavelength of the light source) are known. The internal scattering angle θ is determined by applying Snell's law to the external surfaces of the container (Vaughan and Weidner 1978).

Among the different scattering geometries, the platelet geometry (Fig. 4b) has the advantage that it does not require any knowledge of the refractive index of the sample. Due to the parallelism of the interfaces, the application of Snell's law for both entrance and final exit surface allows one to determine the internal scattering wavevector by only using the "external" scattering angle θ* and the refractive index of the surrounding medium (in case of air $n_{air} \cong 1$). In case of an optically isotropic sample material, Equation (7) transforms into $q = 2k_0\sin(\theta^*/2)$, where k_0 is the incident light wavevector in vacuum.

The measurement of Brillouin scattering is facilitated when the scattering volume is free of large dislocations and fractures and the surfaces are optically clear. In fact, intense elastic scattering from flaws and inclusions can increase the spectrum background to the level of masking the weak Brillouin spectral features. Thus, optical-grade crystals are typically required. The minimum size of a single-crystal sample for Brillouin scattering measurements can be as small as the focal volume determined by the system optics. Samples smaller than 50 μm in diameter and as thin as 15 μm are sufficient for Brillouin scattering measurements in the most common experimental setups. The majority of geophysically relevant minerals of the Earth's mantle are optically transparent even when they contain amounts of iron (~10 at%) in substitution of magnesium (Keppler and Smyth 2005; Keppler et al. 2007, 2008). This makes it possible to use Brillouin scattering to study their elastic properties to the relevant conditions of the deep Earth.

Measurements of surface Brillouin scattering on opaque materials and thin films

Measurements of Brillouin scattering from opaque materials have been a subject of interest starting from the 1970s (Sandercock 1972; Comins 2001). Due to the sample's optical opacity, the scattering process is limited to a very shallow region near the surface. For this reason, the technique is generally referred as surface Brillouin scattering (e.g., Comins et al. 2000). Surface Brillouin scattering is in general not observable in transparent materials, where bulk effects dominate the scattered intensity. Brillouin scattering is a viable method to investigate acoustic wave velocities in opaque solids including metals (e.g., Mendik et al. 1992; Zhang et al. 2001; Graczykowski et al. 2011) and metallic liquids (Visser et al. 1984) and of metals at high pressures (Crowhurst et al. 1999) and it represents a potential method to study the elastic properties of candidate planetary core materials at extreme conditions.

The dominant scattering mechanism depends on the opacity of the material. In an isotropic solid with complex refractive index $n = \eta + i\kappa$ and $\kappa < \eta$ (semi-opaque material), elasto-optic coupling will be the dominant process. In case of materials with $\kappa \approx \eta$, due to its small penetration, light will be mostly scattered by surface ripples that are caused by phonons and that propagate in thermal equilibrium. This second effect does not involve coupling of light with phonon-induced modulations of the dielectric constant of the sample material. The coexistence of the two mechanisms in the same system produces additional spectral features due to degeneracies of surface excitations with bulk ones. Additional spectral features can arise from scattering by interfacial waves between a thin opaque layer and a substrate. These occur when the thickness of the layer is comparable or smaller than the wavelength of the scattering acoustic mode (Sandercock 1982; Every 2002).

EBSCOhost - printed on 2/13/2023 5:26 AM via . All use subject to https://www.ebsco.com/terms-of-use

In the simple case of an opaque solid in backscattering geometry ($\theta = 180°$) with incident (and scattered) wavevectors oriented perpendicular to the sample's surface (Fig. 4c), the scattering volume is reduced to a depth of the same order of magnitude as the wavelength of the vibrations involved in the process as a result of the strong light absorption. This relaxes the wavevector conservation requirement expressed by Equation (5). The interaction of the incident light with the phonons is not limited to the frequency Ω but extends to a finite range around the value determined by Equation (6). This causes a broadening of the Brillouin peak (Sandercock 1982).

Experimental results (e.g., Sandercock 1972) show that the Brillouin peaks from backscattering measurements performed on opaque solids show asymmetry and a shift in frequency, with respect to the calculated scattering phonon frequency Ω. These can be determined by a thorough analysis including the effect of coherent reflection of the phonon at the surface (Dervisch and Loudon 1976). The calculated Brillouin lineshape is then asymmetric because q and $-q$ contribute to both Stokes and anti-Stokes processes while this is not the case in transparent materials (each contributes only to one of the two processes). In addition to the asymmetric broadening, the maximum of the calculated lineshape is shifted in frequency from $\Omega = 2\eta k_0 \nu$ to $\Omega = 2(\eta^2 + \kappa^2)^{1/2} k_0 \nu$, where η and κ are the real and imaginary part of the complex refractive index of the scattering solid $n = \eta + i\kappa$, k_0 is the wavevector of the incident light in vacuum and ν is the acoustic velocity of the opaque solid (Sandercock 1982; Nizzoli and Sandercock 1990).

In the more general case in which Brillouin scattering experiments are performed in geometries with oblique incidence on the sample surface (Fig. 4d), the scattering process involves excitations whose wavevectors have non-zero component on the surface plane. In the simple case of backscattering at an oblique incidence angle ϕ (defined as the angle of the incident and scattered wavevectors with respect to the normal to the surface), the relationship between the wavevector of the scattering surface mode and those of the incident and scattered light will be

$$q_{\parallel} = 2k_{0i} \sin\phi \tag{30}$$

where $q_{\parallel}$ is the surface wavevector, k_{0i} is the incident wavevector (assumed equal to the scattered wavevector k_{0s}; $k_{0i} \cong k_{0s}$). The additional index 0 has been added here to specify that the wavevectors are considered outside the sample and there is not any dependence on the refractive index of the sample material (this is not the case for Eqn. (7) used for bulk phonons).

In the isotropic case, the general features of the surface modes involved in Brillouin scattering from opaque materials, thin-films and multilayered materials can be identified by comparison with the simple case of transverse resonance in an isotropic plate of thickness H (see Auld 1973 for the details). For the case of shear waves with polarization on the surface of the plate (SH), the solution that fulfils the required boundary conditions and symmetry of the plate forms a continuum with a lower cutoff at $\omega = \pi \nu_t / H$ (where ν_t is the bulk shear velocity). The SH waves in the "free" plate correspond to a limiting case of the Love waves (Love 1911), which are defined for thin plates on a semi-infinite substrate. For shear waves with a general polarization, a longitudinal (L) in addition to a shear vertical (SV) component can be produced by reflection at the plate boundaries. Four plane wave solutions satisfy the boundary conditions, and the frequency spectrum will be characterized by three regimes: (a) $\omega/q < \nu_t$ (where q is the plate normal mode wavevector and ν_t is the shear velocity of the bulk sample) in which all the transverse and longitudinal modes are dissipative (their q are imaginary) and localized at the surface and are related to the Rayleigh mode of a semi-infinite solid; (b) $\nu_t < \omega/q < \nu_l$ (where ν_l is the bulk longitudinal velocity of the plate) where the solutions are combinations of transverse and longitudinal modes and they are called Lamb waves; (c) $\omega/q > \nu_l$ where all the solutions are real and they are bulk normal modes. In the case of a semi-infinite medium (corresponding to the limit $Hq \to \infty$) the low order solutions (a) give rise to the Rayleigh surface mode and the SH and the Lamb wave solutions form continua that are indistinguishable from bulk shear modes. Only the Lamb waves have a longitudinal component localized at the surface. In case of

EBSCOhost - printed on 2/13/2023 5:26 AM via . All use subject to https://www.ebsco.com/terms-of-use

anisotropic extended opaque media, surface Brillouin scattering spectra present peaks arising from both pure surface transverse modes (surface acoustic waves, SAW) or their combinations with transverse bulk normal modes of the material (pseudo-SAW; e.g., Every 2002).

The most important features detected by surface Brillouin scattering from anisotropic thin films supported by thick substrates and multilayered composites can be summarized in two basic cases depending on the relative magnitudes of the acoustic velocity of the film and the substrate. (a) In the case of a supported thin layer of lower acoustic velocity than the semi-infinite substrate in the low frequency regime ($\omega/q < v_t^{layer}$) it is possible to observe a SAW whose velocity approaches (at large thin-film thickness) the bulk Rayleigh wave velocity; Lamb waves and Sezawa waves (localized waves supported by the film layer whose displacement field decays towards the substrate) are observed in the frequency regime $v_s^{layer} < \omega/q < v_t^{substrate}$. Finally, at frequencies such that $\omega/q > v_t^{substrate}$, combinations of Sezawa waves with bulk modes of the substrate can be observed. (b) In case of a supported thin layer with higher acoustic velocity than the substrate at very low layer thickness, the Rayleigh wave of the substrate dominates the spectrum. It transforms into a SAW reaching the bulk shear wave threshold of the substrate at increasing thickness. At still increasing thickness, the SAW of the layer becomes detectable and it merges the Rayleigh wave velocity at the limit at which the thin layer becomes effectively a semi-infinite layer. In the case of thick semi-transparent layers with appropriate matching elastic and elasto-optic properties of both layer and substrate, localized interfacial waves (Stoneley waves) can be also observed (Every 2002; Li Bassi et al. 2004). It is noteworthy to remember that Brillouin scattering from SH waves can take place only by the elasto-optic coupling mechanism because they do not contribute to surface ripples (for a theoretical analysis of the associated spectral intensity see Albuquerque et al. 1980). The detection of Brillouin scattering from SH waves is limited to semi-transparent materials (e.g., Albuquerque et al. 1980; Zhang et al. 2000). In order to detect Brillouin scattering from SH waves in metals, it is necessary to take advantage of the penetration through the interface between metal films and transparent substrates of the displacement field associated with SH waves of the substrate (Bell et al. 1987b).

A theoretical interpretation of surface Brillouin scattering spectral intensity has been the subject of several studies from different groups of researchers. Two different approaches have been used: (a) the elastodynamic Green's function approach and (b) the direct calculation of the surface scattered electromagnetic field intensity.

(a) As an example of the first approach, for a layer supported by a substrate (Every 2002), the appropriate surface elastodynamic Green's function (in the frequency domain) is $G_{3,3}(k_{\|}; x = 0; \omega)$, which describes the (surface-)normal component of displacement of the free surface ($x = 0$) of a supported layer or a semi-infinite solid in response to periodic forces acting on the same surface and having spatial frequency $k_{\|}$ and time frequency ω. The imaginary part of the function, in the limit of $\omega << k_B T/\hbar$ (where k_B is Boltzmann's constant and $\hbar = h/2\pi$ is the reduced Plank's constant), can be related to the surface displacement power spectrum that is proportional to the scattering efficiency and it gives information about the relevant surface modes that contribute to the measured Brillouin signal (Zhang et al. 1998b; Beghi et al. 2004):

$$I(\omega) = D\frac{T}{\omega}\mathrm{Im}\left\{G_{3,3}\left(k_{\|}; x = 0; \omega\right)\right\} \tag{31}$$

where $I(\omega)$ is the scattering efficiency and D is a factor depending on the properties of the sample, the scattering geometry, and the frequency and polarization of the incident light.

The Green's function appropriate for the system under study is calculated based on the density and elastic constants of the material (or materials in case of supported thin films) of interest. If the model includes the surface modified bulk fluctuations of the dielectric constant of the material (elasto-optic contribution to the scattering) the calculated scattering efficiency will include terms describing the elasto-optic coupling (Pockel's coefficients) of the scattering

EBSCOhost - printed on 2/13/2023 5:26 AM via . All use subject to https://www.ebsco.com/terms-of-use

materials (Loudon 1978). The prediction of the frequencies (and amplitudes) of the spectral features allows one to put constraints on the elastic constants and the Pockel's coefficients of the scattering medium by least-square fits of dispersion curves of the surface waves, which are obtained as a function of the momentum transfer by changing the incidence angle ϕ (see Eqn. 30) or as a function of orientation by rotating the sample around the axis normal to the scattering surface. Single-crystal elastic constants of metals and semiconductors have been successfully determined with this approach (e.g., Mendik et al. 1992; Tlali et al. 2004). The comparison of this approach with the direct inversion of closed-form expressions of the solutions of the secular equation for surface waves in special directions (Every et al. 2001) and a recent Monte Carlo method (Wittkowski et al. 2004) has produced consistent results in case of tungsten carbide films (Wittkowski et al. 2006). A thorough analysis of the stability of the solutions and of the quality of the elastic constants retrieved from surface acoustic wave velocities is presented by Sklar et al. (1995).

(b) In the second approach, the electromagnetic scattered field in the bulk system is calculated and it is specialized for the case of surface scattering. The scattering cross-section is then calculated from the Poynting vector of the scattered field. This approach allows a more direct identification of the modes that contribute to the scattering cross-section (see discussion in Marvin et al. 1980a). In this approach, as well as in the one based on the elastodynamic Green's function, the inclusion of both ripple and elasto-optic contributions allows one to interpret the experimental spectra and the dispersion curves both in terms of elastic constants and of photo-elastic coefficients of the investigated materials.

Several studies develop the theory for scattering in isotropic and anisotropic semi-infinite media and in supported or unsupported plates (Rowell and Stegeman 1978; Bortolani et al. 1983). The comparison with available experimental results confirms the prevalence of the ripple scattering mechanism in the highly opaque systems (Zhang et al. 1998a). Experimental studies performed with semiconductor layers supported by metals, have confirmed the importance of adding the elasto-optic contribution to fully interpret the observed spectral features (Sandercock 1978; Loudon and Sandercock 1980).

Finally, theoretical studies have been carried out to predict the intensity of surface Brillouin scattering in dielectric and metallic liquids (Dil and Brody 1976; Albuquerque 1983) and the results have been utilized to interpret existing experimental results on alcohols, mercury and gallium (Dil and Brody 1976; Visser et al. 1984).

The limited penetration of light in strongly opaque materials strongly limits Brillouin scattering as a technique to determine the elements of their elastic tensor. The use of surface Brillouin scattering from surface ripples involves additional experimental problems. The quality of the flatness and polishing of the sample surface is extremely strict. In addition, a critical aspect of surface Brillouin scattering experimental design is precisely determining the scattering geometry, especially in experiments performed in "tilted" backscattering geometry. This is due to the limited constraint on the scattering wavevector (see discussion above about the coherent reflection at the surface). In order to map the dispersion curve of the surface modes, the numerical aperture of the collecting optical system has to be minimized, compatibly with the need for a sufficient light throughput. The effect of a finite numerical aperture on the collected spectra is that of integrating both across wavevector and orientation space. This broadens and shifts the positions of the spectral features as a function of the experimental geometry and of the properties of the material. Decreasing the numerical aperture of the collecting lens reduces the width of the solid angle, $\delta\Omega$, about the scattering wavevector and increases the resolution of the wavevector. A careful quantitative evaluation of the effect of adding spatial filtering and slits to the basic experimental design on the accuracy of the measurements and of the recovered properties of the material is presented in Gigault and Dutcher (1998) and in Stoddart et al. (1998).

EBSCOhost - printed on 2/13/2023 5:26 AM via . All use subject to https://www.ebsco.com/terms-of-use

Brillouin scattering at ambient or near-ambient conditions

Most Brillouin scattering studies are performed at ambient conditions and used to determine the acoustic velocities and the full elastic tensors of single crystals and polycrystalline samples. Compared with other methods for elasticity determination, Brillouin spectroscopy is especially useful for small samples (even down to a few tens of microns in size) (Sinogeikin et al. 2004b). Examples include rare natural samples that do not grow to a large size, crystals synthesized at very high pressures, and technological materials with heterogeneities at very small scales (Beghi et al. 2002a). The development of the theoretical interpretation of Brillouin scattering from surfaces and interfaces as discussed in the preceeding subsection has opened a whole range of applications to the study of the behavior of thin films and nano-layered materials (Nizzoli and Sandercock 1990; Comins et al. 2000).

Brillouin spectroscopy is also useful as a non-contact method to investigate the elastic properties of delicate organic and biomaterials that cannot sustain large mechanical loads (Tao et al. 1988; Speziale et al. 2003). It is a method to investigate viscoelastic behavior of materials by analyzing the peaks' broadening associated with acoustic attenuation in the GHz frequency regime in polymers and other soft materials as a function of temperature (up to few hundred degrees K; Adshead and Lindsay 1982; Takagi et al. 2007). Finally, the analysis of the intensity of Brillouin scattering spectra is a method to obtain quantitative information on the photo-elastic tensor of materials (e.g., Nelson et al. 1972; Vacher and Boyer 1972; Grimsditch and Ramdas 1976; Wallnöfer et al. 1994; Mielcarek et al. 2008).

The potential of Brillouin scattering in Geosciences was recognized by Anderson et al. (1969), the first experimental realization was due to Weidner et al. (1975) and nowadays this technique is one of the few methods of choice to investigate the elastic properties of the minerals of the Earth mantle. In the following parts of this section, we briefly summarize the most relevant (in our opinion) results and technical advancements in the different fields of application of Brillouin scattering at ambient conditions.

Condensed matter physics. The interest in the dynamics of molecular systems such as noble gases and simple fluids and solids has driven early Brillouin scattering research about acoustic wave velocity and acoustic attenuation in the GHz frequency range as a function of temperature down to few K (Palin et al. 1971). The measurements at extremely low temperatures required cryogenic vessels optimized for Brillouin scattering (Pike et al. 1970; Grigoriantz and Clouter 1998), usually performed in 90° scattering geometry (Fig. 4a). The development of multi-pass Fabry-Perot spectrometers has improved the quality of the data especially regarding the central features in the depolarized spectra in fluids and the generally weak shear modes of soft solids (Patterson 1976; Vacher and Pelous 1976; Gammon et al. 1983).

Brillouin scattering is a well-established technique for the study of the mechanical properties of polymers as a function of composition or temperature at ambient pressure (Patterson 1983; Krüger 1989). Brillouin spectra of polymers and other viscoelastic organic materials allow researchers to obtain information about (a) acoustic velocities and elastic moduli (Krüger et al. 1986), and (b) acoustic attenuation in the GHz frequency regime from the analysis of the peak linewidths (Levelut et al. 1996). Additional bulk properties can be inferred by the analysis of the peak-shape of the central (unshifted) features of the spectrum, the Rayleigh peak (related to thermal diffusivity) and the Mountain peak, an additional broad central feature that is related to viscous relaxation strengths of intramolecular vibrational degrees of freedom (Patterson 1983; Fioretto et al. 1999).

Brillouin scattering studies of liquid-like polymers as temperature decreases across the melting temperature and the glass transition show that: (a) the Brillouin linewidth increases in the high-temperature regime in which the dissipative processes have a timescale that is shorter than the inverse Brillouin frequency, (b) the linewidth decreases in the lower temperature re-

EBSCOhost - printed on 2/13/2023 5:26 AM via . All use subject to https://www.ebsco.com/terms-of-use

gime where the relaxation timescales are longer compared to the inverse Brillouin frequency and the measured acoustic velocity increases above the zero-frequency (thermodynamic) value corresponding to the relaxed elastic modulus (e.g., Patterson 1983). The quantitative analysis of the temperature dependence of Brillouin linewidth in terms of fluctuations relaxation time and longitudinal viscosity is generally based on the hydrodynamic approximation (Mountain 1966a). Tests of different functions to describe the temperature dependent Brillouin results are presented by Brodin et al. (2002).

Important additional information on the dynamics of the molecules in fluid polymers comes from Brillouin spectra measured by selecting the incident light polarization and the scattered light polarization such that they are perpendicular to each other (depolarized spectra; e.g., Dil 1982). Depolarized spectra present an additional low-frequency doublet, not visible in the polarized spectra (i.e., incident and scattered light polarizations are parallel), that is related to coupling between rotations and translations of the molecules in viscous molecular systems (Wang 1980). With decreasing temperature, these additional features progressively narrow down and eventually collapse in an unresolved single line as a consequence of the viscoelastic behavior of the material, up to the appearance of two transverse acoustic modes (Brillouin peaks) at even lower temperature in the solid state (Patterson 1976). New macroscopic and microscopic theoretical analyses of scattering from coupling of molecular rotation-translation dynamics of anisotropic molecular fluids have been recently tested by new experimental observations (Zhang et al. 2004). Recently, Brillouin scattering has been used to monitor the time-progress of the photo-induced polymerization of binary mixtures of monomer organic compounds as a function of their composition and of temperature (Ziobrowski et al. 2011).

Brillouin spectroscopy is being traditionally applied to the study of acoustic dissipation by analyzing the peak linewidth and important information has been obtained from the central (unshifted) peaks. This type of analysis, initially restricted to fluids (O'Connor and Schlupf 1967; Lucas et al. 1970; Zhao and Vanderwal 1997), has since then become very important also in the field of glass-forming materials (Loheider et al. 1990; Monaco et al. 1998; Rat et al. 2005) and of crystalline solids near phase transitions (Mroz et al. 1989; Jiang and Kojima 2000). Indeed, Brillouin scattering at ambient conditions or at low to moderate temperatures (100-300 K) has proved to be a method of choice in the study of ferroelectric phase transitions where the transition is associated with a soft acoustic mode and with additional mode coupling with central features related to a frequency-dependent shear viscosity (e.g., Ahart et al. 2007, 2009, 2011; Ohta et al. 2011; Marquardt et al. 2013b). Detailed studies of the quasi-elastic (unshifted) components of the Brillouin scattering spectra observed in few solids including Si and $SrTiO_3$ at conditions far from phase transitions, show the presence of two different components each characterized by different linewidth dependencies on frequency, temperature and wavevector. These features are interpreted either as two-phonon difference scattering or diffusive entropy fluctuations (see for instance Koreeda et al. 2006).

The experimental and theoretical developments in the analysis of surface and interface Brillouin scattering have accompanied a specific interest in the study of the ripple scattering elasto-optic coupling in bulk strongly absorbing solids (Sandercock 1972, 1982; Sathish et al. 1991; Carlotti et al. 1992a; Every 2002). Surface Brillouin scattering has been used to investigate the elastic tensor of metallic and opaque solids from polycrystals and single crystals both as bulk samples, thin films and thin interlayered composites (superlattices), especially designed to enhance the intensity of waveguide shear and longitudinal acoustic modes (Mock and Guntherodt 1984; Bhadra et al. 1989; Chirita et al. 2001; Kotane et al. 2011). Experiments on supported thin layers and superlattices have often allowed the determination of anomalies in the elastic properties of films as a function of thickness, of reaction effects at the free surfaces and of stresses at the interface with the substrate due to large structural mismatches and microtextures induced by the thin film deposition techniques (Hillebrands et al. 1985; Pang et al. 1999; Wittkowski et al. 1999, 2002; de Bernabé et al. 2001).

EBSCOhost - printed on 2/13/2023 5:26 AM via . All use subject to https://www.ebsco.com/terms-of-use

Brillouin light scattering from bulk and surface collective fluctuations of electronic spins (magnons) has been experimentally observed together with phonon scattering since the advent of multi-pass tandem Fabry-Perot interferometers (Sandercock and Wettling 1973). Due to the non-linear dependence of frequency on wavevector, the study of the dispersion curve of the acoustic magnons near the Brillouin zone center is of interest together with their spatial dispersion (Borovik-Romanov and Kreines 1982; Wittkowski et al. 2002). Brillouin scattering has since then been used to investigate magnetic properties of dielectric and metallic ferromagnetic, antiferromagnetic and ferrimagnetic materials. Scattering from bulk acoustic magnons dominates in transparent and semi-transparent materials (Sandercock 1974; Jantz et al. 1976), while the negligible penetration depth of light in metallic materials makes the intensities of Brillouin scattering from surface and bulk magnons comparable (Grünberg and Metawe 1977; Grimsditch et al. 1980). Both spin dynamics and the elastic constants have been simultaneously determined for semitransparent materials (e.g., $FeBO_3$; Jantz et al. 1976). Surface Brillouin scattering of single crystal antiferromagnetic NiO has helped to elucidate the details of the magnetic structure that exhibits eight antiferromagnetic resonance modes which are interpreted by a model of four interpenetrating antiferromagnetic sublattices (Grimsditch et al. 1994a; Milano et al. 2004; Milano and Grimsditch 2010). These results confirm the richness of information that Brillouin spectroscopy can give about the magnetic properties of materials. Theoretical models of light scattering from magnons have explained the characteristic large difference of the intensity of the Stokes and anti-Stokes magnon peaks and the asymmetric peak lineshape of surface magnon peaks (see review by Borovik-Romanov and Kreines 1982).

Surface Brillouin scattering has become a technique of choice to study the magnetic structure and properties of magnons in magnetic films, multilayers and composites with nanoscale magnetic patterns. This research has impact in the fundamental understanding of the spin dynamics in nanoscale magnetic systems with potential applications to storage and signal processing technologies (Grimsditch et al. 1979, 2001; Hicken et al. 1995; Carlotti and Gubbiotti 2002; Crew et al. 2004, 2005; Perzlmaier et al. 2005).

Brillouin scattering from spin waves has recently found application to fundamental topics in quantum thermodynamics. Measurements of Brillouin scattering in an yttrium iron garnet (YIG) thin film subject to microwave pumping at ambient temperature has given the first experimental proof of the existence of Bose-Einstein condensation transition of quasi-equilibrium quasiparticles (magnons in this case) produced in a solid as an effect of external energy pumping (Demokritov et al. 2006).

Materials science. Brillouin scattering is an ideal method for systematic studies of the mechanical properties of technological materials as a function of chemical substitutions, for instance studies of single-crystal elasticity of yttrium aluminum garnets (YAG, $Y_3Al_5O_{12}$) as a function of Yb-Y substitution (Marquardt et al. 2009a). Beghi et al. (2000) in a study of Er-Y substitution in YAG used Brillouin scattering as a function of temperature in combination with photoluminescence spectroscopy to evaluate optimal levels of doping for optical communication applications. Brillouin scattering is also used to study bulk and surface elastic properties of materials with very high hardness such as natural and polycrystalline synthetic diamond (Grimsditch and Ramdas 1976; Jiang et al. 1991; Vogelgesang et al. 1996; Zouboulis et al. 1998; Krüger et al. 2000), diamond-like amorphous and nanocrystalline carbon (Djemia et al. 2001; Beghi et al. 2002b), carbides (Kamitani et al. 1997; Zhang et al. 1998a; Wittkowski et al. 2006; Zhuralev et al. 2013) and nitrides (Grimsditch et al. 1994b; Polian et al. 1996; Zinin et al. 2002; Tkachev et al. 2003; Manghnani et al. 2005; Zhang et al. 2011).

The study of the elastic and mechanical properties of a wide range of new single and multilayered materials is facilitated by the use of Brillouin scattering of thin films (thinner than 1 μm). Micro- and nano-multilayered composites represent a wide range of materials with important technological applications whose properties are strictly linked to their structure

EBSCOhost - printed on 2/13/2023 5:26 AM via . All use subject to https://www.ebsco.com/terms-of-use

and thickness (e.g., Alexopoulos and O'Sullivan 1990). The knowledge of the mechanical properties of such materials is necessary for their complete characterization and helps to direct the improvement of their design. Both supported and unsupported thin layers can be measured by Brillouin scattering (Bhadra et al. 1989; Pang et al. 1999; Zhang et al. 2004). The measurements performed on thin films generally combine surface and bulk Brillouin spectral features in transparent materials (Djemia et al. 2001). The measurement of Brillouin scattering has made the determination of the full elastic tensor of films possible (Carlotti et al. 1995; Wittkowski et al. 2004). In case of opaque thin films, the measurement of the spatial and wavenumber dispersion of surface and interfacial acoustic modes as a function of film thickness makes it possible to determine subsets or the full set of elastic constants of the film especially in the case in which the supporting substrate has higher elastic stiffnesses than the film material (Sumanya et al. 2007). Brillouin scattering has found successful application in the study of the effective elastic moduli of superlattices (composite multilayers with individual layers thinner than the wavelength of light) whose elastic properties are equivalent to those of a corresponding homogeneous medium (Bell et al. 1987a; Carlotti et al. 1992b).

Brillouin scattering has been extensively used to investigate the mechanical properties of nanomaterials and nanocomposites. Both acoustic velocity and acoustic attenuation have been determined by analyzing bulk Brillouin scattering and surface scattering (Li Bassi et al. 2004). Brillouin peaks broadening and central unshifted spectral features have been investigated in heterogeneous nanocomposites and represent a tool to investigate the lengthscale of the heterogeneities (Beghi et al. 2002a). The study on composite materials based on crystalline nanoparticles dispersed in oligomeric matrices has evidenced the presence of distinct enhancement of the mechanical properties even at very low nanoparticle concentrations (Eschbach et al. 2007). The systematic study of monodispersed hard nanospheres colloids in a fluid matrix of very different refractive index has also allowed the investigation of the behavior of modes propagating across both media and of localized interfacial modes as a function of increasing nanoparticle concentration. While the frequencies of the first type of excitations increase with increasing particle fraction, those of the second type soften with increasing particle fraction (Kriegs et al. 2004).

Recently, Brillouin scattering has become the tool for testing and designing phononic materials with band gaps in the hypersonic regime ($10^6 < \omega < 10^{11}$ Hz). The presence of a band gap in the hypersonic region of the phonon dispersion curve in synthetic face-centered colloidal crystals based on ordered assemblies of polystyrene nanoparticles infiltrated by fluids was observed by Cheng et al. (2006). The extension of phononic crystals to the hypersound regime and the progress in tuning the elastic impedance mismatch between their components promises to expand the potential for technological applications of these materials as acousto-optical devices (Sato et al. 2010). Brillouin scattering measurements of acoustic velocities of heterogeneous nanoscale composite materials allows testing of the different models to describe the effective elastic properties of highly heterogeneous media. In the case of nanoporous 4H-SiC, Devaty et al. (2010) verified the correctness of the effective medium model in the case of arrays of columnar 20 nm diameter pores in quasi-hexagonal arrangement.

Biomaterials. The study of the elastic properties of delicate macromolecular biomaterials supplements the structural characterization of their molecular architecture. It gives important information about the strength of the intermolecular interactions in close-packing molecular arrangements that can be compared with the arrangement of the same molecules in their natural fluid environment. Brillouin scattering is especially useful in the case of solid anisotropic biomaterials because it is a non-contact technique that allows for a systematic study of the directional dependence of the elastic properties and their sensitivity to changes of environmental conditions (such as temperature or relative humidity). The fields of application of Brillouin scattering to biomaterials range from the study of structural materials like tendon and bone

EBSCOhost - printed on 2/13/2023 5:26 AM via . All use subject to https://www.ebsco.com/terms-of-use

tissues, with implications for the stability of bone implants (Cusack and Miller 1979; Sakamoto et al. 2008; Mathieu et al. 2011) to the study of lipids, important in cell-membranes (by bulk and surface scattering measurements; LePesant et al. 1978; Chen et al. 1991; Manglkammer and Krüger 2005), eye lens (Randall and Vaughan 1982), and DNA and proteins in the form of molecular solids (Lee et al. 1987, 1993; Speziale et al. 2003). Brillouin scattering studies of the temperature effect on the elastic properties of tetragonal lysozyme have shown the presence of an unknown transition (e.g., Sakamoto et al. 2008; Svanidze et al. 2009). New time dependent measurements of dehydration of lysozyme crystals of tetragonal and monoclinic symmetry have been investigated by Hashimoto et al. (2008). Finally, Brillouin scattering has been used to probe the thermally induced denaturation of molecular lysozyme in its natural state in aqueous solutions (Svanidze et al. 2011). In the case of bone tissues and solid protein crystals, the comparison of Brillouin scattering in the GHz frequency regime with MHz ultrasonics and static bending measurements allows us to better understand the viscoelastic behavior of these materials (Speziale et al. 2003; Gautieri et al. 2012).

Determination of Pockel's coefficients

In addition to elastic and magnetic properties and attenuation, Brillouin scattering allows determination of the photoelastic constants of materials (see the section "Physical Principles of the Brillouin Effect"). When the density, elastic constants and refractive index of the sample material are known, measurements of intensity performed in selected high-symmetry crystallographic directions while varying the incident and scattered light polarization can be used to determine the photo-elastic tensor. A substantial advancement in the interpretation of Brillouin peak intensities in anisotropic materials was the theoretical work by Nelson and Lax (1971) who first postulated and demonstrated the existence of non-zero antisymmetric elements in the elasto-optic tensor due to existence of coupling of rotations (instead of strains) with the light scattering process. Nelson et al. (1972) developed a generalized formula to analyze the intensity of Brillouin scattering in terms of the photo-elastic coupling constants valid for all the crystal symmetries based on a new Green's radiation function in anisotropic media. Cummins and Schoen (1972) and Vacher and Boyer (1972) presented a large number of closed-form expressions to detetermine the values of the elements of the tensors T^{α} (see Eqn. 26) for a large number of crystallographic directions in the different symmetry classes.

While in transparent media, the photoelastic constants have been determined for many materials (crystalline and amorphous solids) from bulk phonons (Grimsditch and Ramdas 1976; Heiman et al. 1979; Schroeder 1980; Rand and Stoicheff 1982; Trzaskowska et al. 2010) constraining the full tensor in opaque materials is a much more difficult task due to the weakness of the Brillouin scattering by elasto-optic coupling and the larger relative intensity of ripple scattering (which is insensitive to the elasto-optic coupling). Subsets of the photoelastic tensor can still be constrained in semi-opaque materials by investigating the dispersion of surface waves and by fitting the spectral intensities (when the elastic constants are known) with the use of the elasto-optic constants as free parameters (Marvin et al. 1980b; Bassoli et al. 1986). This procedure is aided by the coexistence in the spectra of contributions from both the elasto-optic and the ripple scattering mechanism.

The determination of the photoelastic constants is restricted to measurements performed at ambient pressure because the measurements in the diamond anvil cell suffer from the effect of partial depolarization of light in the diamonds culets due to the large stress gradient to which they are subject when the cell is in operation.

Brillouin scattering at extreme conditions

There has been much interest in understanding the effects of pressure and temperature on the elastic properties of solids. As a non-contact probe, Brillouin scattering is ideally suited for studies at non-ambient conditions where the sample material is surrounded by a heater or con-

EBSCOhost - printed on 2/13/2023 5:26 AM via . All use subject to https://www.ebsco.com/terms-of-use

tained in a pressurizing apparatus. In addition, Brillouin scattering of single crystals determines the elastic anisotropy at extreme conditions. This makes it an invaluable source of information for interpreting seismological models of the very deep Earth and for geophysical modeling. Due to their transparency, diamond anvil cells are the optimal high-pressure device to perform Brillouin scattering at extreme conditions. The geometry of Brillouin scattering in a diamond anvil cell is drawn in Figure 8.

Brillouin scattering at high temperature. Use of Brillouin scattering at high temperatures introduces some experimental challenges. The intensity of Brillouin scattering is linearly proportional to temperature while the thermal background radiation (blackbody radiation) from the sample increases with temperature to the fourth power. As a result, at very high temperatures, the Brillouin peaks may be masked by blackbody radiation.

However, Brillouin measurements (using a green or blue light source) of both melts and solid oxides have been reported at temperatures as high as ~2300 K using resistive heating (Zouboulis and Grimsditch 1991b; Askarpour et al. 1993; Zaug et al. 1993; Vo-Thanh et al. 1996; Polian et al. 2002) and as high as ~2500 K (Sinogeikin et al. 2004a, 2005) using laser heating. However, there are only few very high-temperature Brillouin data and the (material-dependent) temperature limits for Brillouin scattering experiments in the diamond anvil cell are still to be explored.

Metal wires or foils (e.g., tungsten, platinum, rhodium) surrounding the sample are most commonly used as resistive heating element (e.g., Zouboulis and Grimsditch 1991a,b; Xu and Manghnani 1992; Askarpour et al. 1993; Krüger et al. 1998; Ko et al. 2008). Alternatively, a thin graphite foil can be employed (e.g., Bucaro and Dardy 1974). The sample is contained in an inert gas atmosphere to avoid chemical reactions. In order to minimize possible temperature gradients, the measurements are sometimes performed placing the samples in ovens with small surface windows for optic access (preferentially) in backscattering and 90° scattering geometry (Harley et al. 1978; Mjwara et al. 1991). The temperature at the sample position is usually measured with a thermocouple. Additional thermocouples whose junctions are positioned at different distance from the heating element, can detect the presence of temperature gradients.

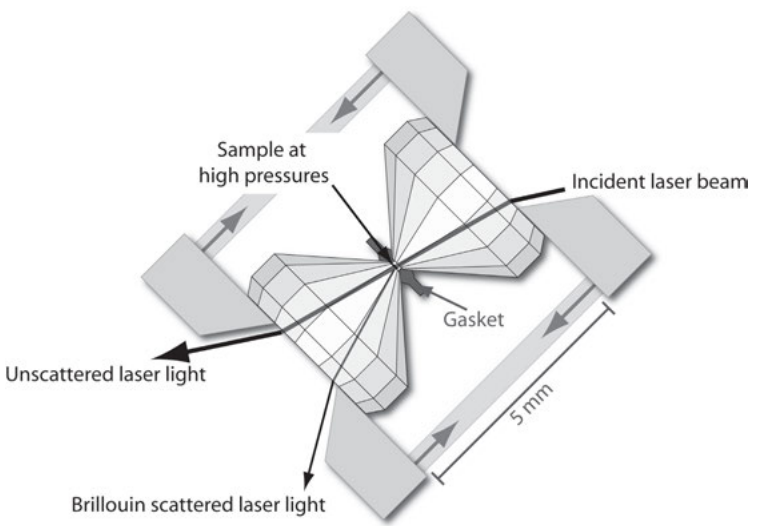


Figure 8. Schematic drawing of the geometry for Brillouin scattering experiments at high pressure in the diamond anvil cell. These experiments are performed in forward symmetric scattering geometry.

EBSCOhost - printed on 2/13/2023 5:26 AM via . All use subject to https://www.ebsco.com/terms-of-use

The advent of platelet forward symmetric scattering geometry has aggravated the issue of temperature gradients. Due to the large scattering angles used in these experiments, furnaces with large optic access are required for these experiments (Xu and Manghnani 1992; Sinogeikin et al. 2000a). In case of resistive heating at high pressure, the space constraints imposed by the diamond anvil cell are very strict, and special miniature heaters are designed to fit in the small space available in the high-pressure cell (Fig. 9).

In general, continuous wave near infrared (IR) lasers are used as energy source in laser heating techniques. A simplified sketch of the geometry of double-side laser heating in a diamond anvil cell is shown in Figure 10. The two most popular choices are CO_2 laser, with a wavelength of 10.6 μm, or solid-state lasers (e.g., YAG, YLF, fibre laser), with wavelength ~1 μm. CO_2 laser radiation is strongly absorbed by the majority of optically transparent samples. It has

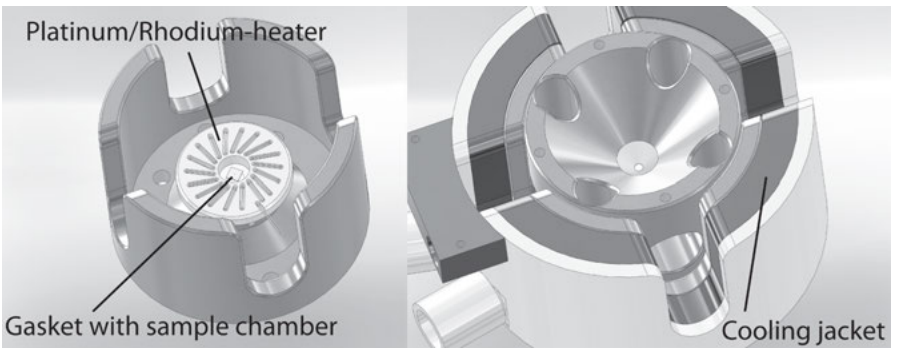


Figure 9. Schematic drawing of a high-temperature resistive-heated diamond anvil cell. On the left: the detail of the micro-heater, positioned inside the diamond cell piston, surrounding the sample chamber of a BX-90 DAC (Kantor et al. 2012). On the right: a custom designed water-cooling jacket for the BX-90 DAC. The cooling jacket has lateral windows that are optimized to combine Brillouin scattering and X-ray diffraction in radial geometry (Drawing by R. Schultz, GFZ).

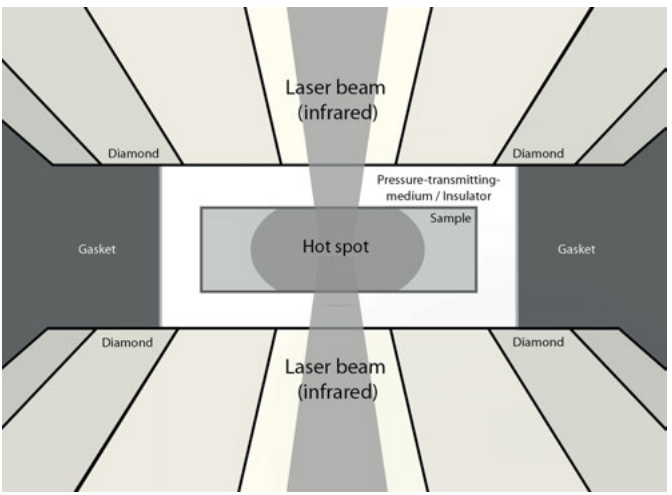


Figure 10. Schematic diagram of the geometry of laser heating of a sample in the DAC. The sample is heated from both sides. The sample has to be thermally insulated from the diamond anvils. The insulator can also act as a pressure transmitting medium.

EBSCOhost - printed on 2/13/2023 5:26 AM via . All use subject to https://www.ebsco.com/terms-of-use

been shown that by using CO_2 lasers it is possible to perform Brillouin scattering experiments of oxides to temperatures in excess of 2000 K (Sinogeikin et al. 2004a, 2005). One important limitation in the use of CO_2 laser heating is its poor laser stability compared with solid-state IR lasers. In addition, the 10.6 μm radiation is absorbed by optic glasses and the setup of the whole laser path requires the use of reflective optics.

Shorter wavelength solid-state lasers, however, are easier to handle and the recent developments in fiber lasers makes them a very versatile and a promising tool for laser heating experiments (e.g., Dubrovinsky et al. 2009; Shen et al. 2010). However, ~1 μm wavelength lasers are weakly (or not) absorbed by optically transparent materials. This represents a serious limitation for their use in Brillouin scattering measurements in forward scattering geometry, which require sample materials that are transparent to the Brillouin probing laser and is the one that offers the most complete access to the full single-crystal elastic tensor. Customized sample preparation techniques are required to overcome this challenge (e.g., Marquardt and Marquardt 2012).

In laser heating experiments, temperature is usually determined by fitting the measured thermal radiation spectrum of the sample to a greybody curve. Here, the intensity of thermal emission depends on the surface conditions of the heated material and it has been documented that well-polished transparent plates, such as single-crystal samples used for Brillouin spectroscopy, show too low emissivity (e.g., Gardon 1956) for temperature to be determined at moderate temperatures (Sinogeikin et al. 2004a, 2005). In these cases, alternative ways of measuring temperature have to be used, such as measuring the intensity ratio of Stokes and anti-Stokes Raman peaks from Raman scattering. Thermal gradients are also a serious general problem in the laser-heating approach at both ambient pressure (e.g., Rantala and Levoska 1989; Shen and Zhang 2001) and in the diamond-anvil cell (Panero and Jeanloz 2001; Kiefer and Duffy 2005; Kavner and Nugent 2008).

Brillouin scattering at high pressure. Brillouin spectroscopy at high pressure has opened new opportunities to investigate anisotropic single-crystal elastic properties of materials especially for geophysical applications. Measurements were conducted initially in 90° scattering geometry in gas pressure vessels adapted for Brillouin spectroscopy (e.g., Asenbaum et al. 1986). A major advance was the introduction of the diamond anvil cell in combination with the symmetric forward scattering geometry (see Fig. 4b) (Whitfield et al. 1976). However, the requirement of parallelism of the surfaces of a small sample makes it even more difficult to prepare ideal samples for this type of study. Deviations from parallelism of the interfaces in typical high-pressure Brillouin scattering experiments produce errors in the frequency shift measurements. The quantitative effect on the determination of acoustic velocity and elastic constants is analyzed by Zha et al. (1996), Sinogeikin and Bass (2000) and Zhuralev et al. (2013).

Starting from the 1980s, high-pressure Brillouin spectroscopy has been used both in the study of minerals (see the "Applications of Brillouin Spectroscopy in Geosciences" section) and for the study of the elastic properties of solid noble gases (Grimsditch et al. 1986; Polian and Grimsditch 1986; Shimizu et al. 2001; Zha et al. 2004), hydrogen (Zha et al. 1993; Duffy et al. 1994) and other simple molecular solids (Kiefte et al. 1985; Lee et al. 1986; Gagnon et al. 1990; Shimizu et al. 1994, 1995, 1996; Chen et al. 2010; Ahart et al. 2011). The determination of the full single-crystal tensor of high-pressure phases synthesized in the diamond anvil cell by compressing a fluid was achieved by combining Brillouin scattering measurements with X-ray diffraction that determine both density and the orientation of the plate-like single crystal (or few crystals) produced in the sample chamber (Shimizu and Sasaki 1992). In fact, for high symmetry solids (mostly cubic and hexagonal), it is possible to determine the full elastic tensor by measuring the spatial dispersion of the acoustic phonon branches in one or two single-crystal platelets (with different orientations) by forward symmetric Brillouin scattering (Shimizu and Sasaki 1992). High-pressure low-temperature Brillouin scattering measurements have been performed on H_2S (Murase et al. 2002).

EBSCOhost - printed on 2/13/2023 5:26 AM via . All use subject to https://www.ebsco.com/terms-of-use

Recently, Stevens et al. (2007) conducted a high-pressure study of different polymeric elastomers at high pressures in the diamond anvil cell. The measurement of the shear modulus at high pressure adds important new information about the properties of systems for which it is often difficult to detect the propagation of shear acoustic waves at ambient and low pressure. In addition, Brillouin scattering of polymers at high pressures under nonhydrostatic conditions can furnish new information on the effect of non-isotropic stress on the hypersonic anisotropy of polymers. Thus, the results already available from Brillouin scattering studies of anisotropy in polymer films subject to tensile stress at ambient pressure are extended to high-pressure regimes (Yoshida et al. 2001).

Over the past decades, several important contributions to aspects of geophysics, materials science and condensed matter physics have been made by high-pressure Brillouin scattering experiments (e.g., Shimizu and Sasaki 1992; Duffy et al. 1995; Marquardt et al. 2009c) and the achievable pressure limits have been subsequently pushed forward (e.g., Polian 2003). Currently, the highest pressure reported is 81 GPa for single-crystal measurements (Marquardt et al. 2009b) and 172 GPa and 207 GPa for polycrystalline materials and glasses, respectively (Murakami et al. 2007a; Murakami and Bass 2010).

The combination of Brillouin scattering and X-ray diffraction for density determination makes it possible to perform pressure-volume equation of state measurements independent of a secondary pressure scale. In fact, by the definition of the isothermal bulk modulus $K_T = (\partial P/\partial \ln\rho)_T$ (where P, T, ρ are pressure, temperature and density, respectively) it is possible to determine pressure by combining volume measurements by X-ray diffraction and simultaneous determination of $K_S = (\partial P/\partial \ln\rho)_S = K_T(1 + \alpha\gamma T)$ (where S, α and γ are entropy, volume thermal expansion coefficient and Grüneisen parameter, respectively) by Brillouin scattering measurements, if γ and α are known (Zha et al. 2000; Zhuralev et al. 2013).

The success of Brillouin scattering to determine elastic properties of materials at elevated pressure comes together with a continual improvement of this experimental technique to tackle many challenges. In order to maximize the optical throughput, sample containers with very wide optic access and collecting lenses of large numerical aperture are often used. Additional slits or apertures are added in order to reduce the amount of parasitic diffuse scattered light from parts of the sample container close to the sample. However, if not perfectly aligned, the apertures may asymmetrically "clip" the solid angle defined by the collecting part of the optical system and effectively change the orientation of the scattering wavevector, causing an artificial shift of the position of Brillouin feature for all the observed acoustic modes. The effect of this vignetting is not easily detected unless by simultaneously measuring standard materials of known acoustic velocity (Oliver et al. 1992; Sinogeikin and Bass 2000).

One of the biggest technical challenges of Brillouin scattering at high pressure is the study of phases synthesized at high pressure in the diamond anvil cell, which are unquenchable to ambient conditions. These materials are generally polycrystalline and Brillouin scattering can be used to infer the pressure dependence of aggregate (average) elastic moduli of the polycrystals (e.g., Murakami et al. 2007a,b, 2009b, 2012; Kudo et al. 2012). The interpretation of the measured high-pressure average acoustic velocity in some systems is still a subject of investigation (Speziale et al. 2013). Indeed, Brillouin scattering of polycrystalline or composite materials at ambient conditions and moderate high pressures has sometimes shown additional spectral features that have been the subject of intense research (Hernandez et al. 1996; Ahart et al. 2006; Gleason et al. 2009). The persistence of regions of finer material at the interfaces between larger grains or in the original porous spaces can give rise to additional spectral features from interfacial modes, and the "bulk modes" present evidence of dispersion both in frequency and in the volume fraction of the grains of the dispersed phase (Kriegs et al. 2004). The interpretation of similar spectral features that could be detected in high-pressure measurements in the DAC is relevant to assess the reliability of measurements on materials that cannot be analyzed as single-crystals.

EBSCOhost - printed on 2/13/2023 5:26 AM via . All use subject to https://www.ebsco.com/terms-of-use

Important results have been recently obtained from the studies of nano-sized materials by Brillouin scattering at high pressures. However, the results from some nanomaterials differ from those obtained from their equivalent bulk counterparts (Gleason et al. 2011; Marquardt et al. 2011). The interpretation of these differences is still a matter of debate, and the possibility that grain-size reduction in the DAC can produce nano-sized powders requires special attention. The goal is to determine the pressure/grain-size effect (in addition to stress heterogeneities) on the effective elastic properties of polycrystalline samples of the candidate phases of the deep Earth.

Brillouin scattering at simultaneous high pressures and temperatures. Until now few Brillouin scattering measurements have been reported at combined high *P-T*-conditions (Matsuishi et al. 2002, 2003; Li et al. 2006; Sinogeikin et al. 2006; Goncharov et al. 2007; Asahara et al. 2010; Mao et al. 2012; Murakami et al. 2012; Lu et al. 2013).

In principle, both resistive heating and laser heating can be employed in the diamond-anvil cell to heat the sample at high pressure. However, due to the limited temperature-stability of diamond, the achievable temperature range is limited to less than 1000 K for resistive heating unless the exposed diamond surfaces are flushed with a reducing gas mixture or the whole cell is immersed in a reducing atmosphere in order to prevent diamond surface oxidation (Liermann et al. 2009).

The first results have emerged from Brillouin scattering at simultaneously high pressure (up to 65 GPa) and high-temperature (up to 900 K) using a resistive-heated diamond cell (Sinogeikin et al. 2006, 2007; Mao et al. 2012; Lu et al. 2013; Marquardt et al. 2013a). The use of a graphite heater may allow one to extend the accessible temperature range (Liermann et al. 2009). Li et al. (2006) used a YLF heating laser to study "hot ice" in the diamond-anvil cell up to ~22 GPa and ~1200 K. To couple the short wavelength laser (1064 nm) to the transparent sample, a gold film was deposited inside the sample chamber. Murakami et al. (2009a) reported first Brillouin scattering results on the sound wave velocities of polycrystalline MgO compresed to 49 GPa in a DAC and simultaneously laser-heated to ~2300 K using a CO_2-laser. In a more recent study both MgO and $MgSiO_3$ perovskite have been investigated at simultaneous high pressures and temperatures to a maximum of 91 GPa and 2700 K (Murakami et al. 2012).

High-pressure/moderately high-temperature ($T \leq 800$ K) measurements of CO_2, CO_2-H_2O mixtures and of aqueous fluids relevant for metamorphic processes in the uppermost mantle have been recently performed in externally-heated diamond anvil cells paying special attention to precise pressure determination (Giordano et al. 2006; Qin et al. 2010; Mantegazzi et al. 2012; Valenti et al. 2011; Sanchez-Valle et al. 2012).

ANALYSIS OF THE BRILLOUIN SPECTRA AND RECOVERY OF THE ELASTIC TENSOR

One of the most important applications of Brillouin scattering, and the most relevant in the Earth sciences, is determining acoustic velocities in Earth materials, and from acoustic velocities and density, constraining the full elastic tensor. The objective of this section is to introduce the general problem of extracting information about the anisotropic elastic properties of the sample material (ideally a single crystal) from the velocity determined by Brillouin scattering measurements. The relationship between the Brillouin frequency shift and acoustic velocity was given in Equation (8).

In the long wavelength limit, the acoustic phonons involved in the scattering process can be considered acoustic waves propagating in an elastic continuum. The phase velocity determined by Equation (8) is a solution of the equations of motion of the form of Equation (22). In order to describe the actual approach used to reduce the data and determine the elements of the elastic

EBSCOhost - printed on 2/13/2023 5:26 AM via . All use subject to https://www.ebsco.com/terms-of-use

stiffness tensor, we will briefly introduce the basic concepts of anisotropic linear elasticity. The choice of limiting this introduction to linear elasticity is related to the fact that in crystalline Earth materials linear elastic behavior is generally a valid approximation in the frequency range of the acoustic vibrations involved in Brillouin scattering. More complete treatments of anisotropic elasticity can be found in Auld (1973), Musgrave (1970) and a concise summary is given by Every (2001).

Linear elasticity of anisotropic solids

A solid subject to a distortion (strain, ε_{ij}) deforms elastically when it instantaneously recovers its original form when the cause of the distortion (stress, σ_{ij}) is removed. Linear elasticity is restricted to the case in which the relationship between the stress and the distortion is linear. This is expressed in three dimensions by Hooke's law:

$$\varepsilon_{ij} = s_{ijkl}\sigma_{kl} \tag{33}$$

or inversely

$$\sigma_{ij} = c_{ijkl}\varepsilon_{kl} \tag{34}$$

where s_{ijkl} and c_{ijkl} are the second-order elastic compliances and stiffnesses, respectively. The indices have values 1, 2, 3, and summation is carried out for repeated indices (Einstein's summation rule). All the quantities of Equations (34) are tensors. The infinitesimal strain is defined as the symmetric part of the displacement gradient tensor. In a Cartesian reference system (x_1, x_2, x_3):

$$\varepsilon_{ij} = \frac{1}{2}\left(\frac{\partial u_i}{\partial x_j} + \frac{\partial u_j}{\partial u_i}\right) \tag{35}$$

where $u(x)$ is the displacement. The strain tensor is a symmetric second rank tensor with only six independent components. The diagonal elements represent changes in linear extension or compression; the off-diagonal coefficients represent the change of the angle between two directions (Fig. 11).

The (Cauchy) stress tensor σ_{ij} (Fig. 12) is defined as:

$$T_i(n) = \sigma_{ij} n_j \tag{36}$$

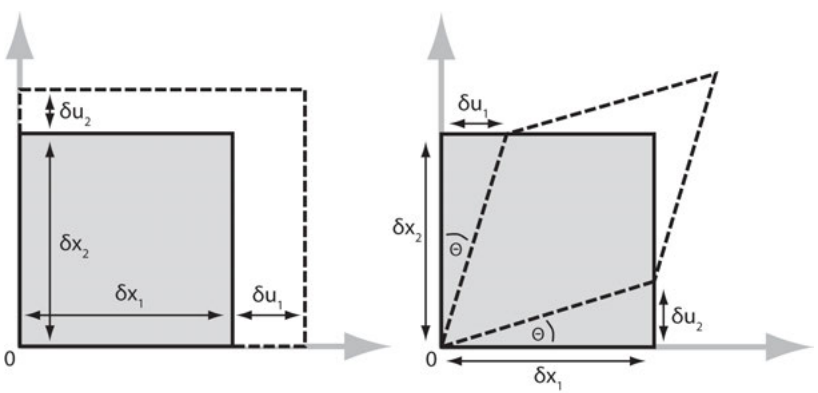


Figure 11. Graphical representation of the elements of the strain tensor in a two-dimensional representation (modified from Every 2001). (a) compressional strain; (b) shear strain. Symbols are explained in the text.

EBSCOhost - printed on 2/13/2023 5:26 AM via . All use subject to https://www.ebsco.com/terms-of-use

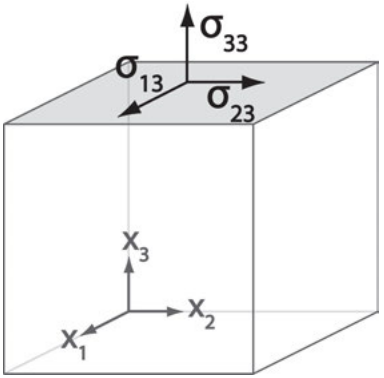


Figure 12. Sketch of the orientation and the elements of the (Cauchy) stress tensor relative to the face, whose normal is parallel to x_3, of a cubic element of a material.

where $T_i(n)$ is the traction vector relative to an infinitesimal surface δA with normal direction n (with component n_i in the direction x_i). The traction vector is defined as $T_i(n) = \lim_{\delta A \to 0}(\delta F_i/\delta A)$, where δF_i is the ith component of the force acting on δA. The definition of traction and stress tensor requires that $\sigma_{ij}n_j = -\sigma_{ij}(-n_j)$ to prevent infinite tractions at the limit for $\delta A \to 0$. Another important property of the stress tensor is that $\sigma_{ij} = \sigma_{ji}$ to prevent that the forces applied to a vanishingly small volume of a material can produce finite torques.

From Hooke's law (Eqn. 34) we see that the compliance and stiffness tensors are fourth rank tensors with 81 components. Due to the symmetries of the stress and strain tensors the number of independent components reduces to 36. Compliance and stiffness tensors are reciprocal, $c_{ijkl}s_{klmn} = \delta_{im}\delta_{in}$ (where δ_{im} and δ_{in} are Kronecker deltas). Voigt contracted notation exploits the invariance by exchange of indices i,j and k,l where the first and second pair of indices i,j (k,l) transform into α (β) following the rules: $i,j \to \alpha$:11 $\to$ 1, 22 $\to$ 2, 33 $\to$ 3, 23 = 32 $\to$ 4, 13 = 31 $\to$ 5, 12 = 21 $\to$ 6. It is applied to the stress, strain, stiffness and compliance tensors. For instance: $c_{1123} \to c_{14}$. In the case of strain (ε_{ij}) the coefficient 1/2 is necessary for $\alpha > 3$. In the case of compliance (s_{ijlk}) the coefficient 1/2 is necessary if one of the contracted indices is larger than 3, a coefficient of 1/4 is necessary if both the contracted indices are larger than 3. The contracted notation simplifies the computations in many cases. The compliance and stiffness tensors are thus reduced to 6×6 matrices.

The number of independent non-zero elements of the elastic tensor is also affected by crystal symmetry (Nye 1985). The elastic tensor of materials belonging to the same Laue symmetry classes will have the same number of independent elastic constants. Isotropic solids have only two independent constants c_{11} and c_{44} and the third non-zero constant c_{12} is defined as $c_{12} = c_{11} - 2c_{44}$. Anisotropic solids have a number of non-zero independent elastic constants that increases at the decreasing of their symmetry to a maximum of 21 in the triclinic system (Table 1).

Table 1. Number of non-zero, independent single crystal elastic constants as a function of the symmetry of a material.

Crystal System	Elastic Moduli
Isotropic	2
Cubic	3
Hexagonal	5
Trigonal	6 or 7
Tetragonal	6 or 7
Orthorhombic	9
Monoclinic	13
Triclinic	21

Determining the elastic constants

We can now rewrite the wave equation for a linear elastic anisotropic solid in a Cartesian reference system:

$$\rho \frac{\partial^2 u_i}{\partial t^2} = c_{ijkl} \frac{\partial^2 u_k}{\partial x_j \partial x_l} \tag{37}$$

Plane wave solutions of Equation (37) have the form $u_i = u_i^0 \exp i\,(qx - \omega t)$ where u_i^0 is the polarization. By substituting into (37) we obtain:

EBSCOhost - printed on 2/13/2023 5:26 AM via . All use subject to https://www.ebsco.com/terms-of-use

$$\left(c_{ijkl}q_jq_l - \rho\omega^2\delta_{ik}\right)u_k^0 = 0 \tag{38}$$

We can substitute direction cosines $n = q/|q|$ and phase velocity $\nu = \omega/q$ in Equation (38) and we can solve for acoustic velocity by solving the secular equation:

$$\left|c_{ijkl}n_jn_l - \rho\,\nu^2\delta_{ik}\right| = 0 \tag{39}$$

The quantity $c_{ijkl}n_jn_l$ is the Christoffel's tensor Γ_{ij}. Equation (39) is a cubic equation in ν^2 that admits three real solutions that can be expressed in closed form by using Cardan's method (Every 1980). The polarization vector u^0 associated with the three phase velocity solutions can be determined for each solution by substituting each solution ν in $(c_{ijkl}q_jq_l - \rho\omega^2\delta_{ik})\mu_k{}^0 = 0$ (Eqn. 38).

Starting from velocities ν (and polarizations u^0) determined by Brillouin scattering measurements performed along a series of directions (Figs. 13, 14) with direction cosines n on a single-crystal of density ρ, the elastic constants c_{ijkl} can be determined by inverting Equations (39) using a least-square method. In case of measurements performed in general directions, the polarization of the scattering acoustic wave is not easily constrained. In the case of measurements inside a diamond anvil cell, the polarization is typically unknown because of depolarization by the stressed diamond windows. In this case the inversion procedure needs additional steps to assign the correct polarizations to the velocities. In general, the fastest velocity is associated with the quasi-longitudinal mode (that with a displacement that is the closest to the phonon propagation wavevector), the assignment of the two slower solutions is often helped by symmetry considerations, but fundamental ambiguities may remain.

Additional difficulties arise when the orientation of the single crystal is not well defined. This can be the case for high-pressure experiments where crystalline phases are synthesized in the diamond-anvil cell (Shimizu and Sasaki 1992). *In situ* X-ray diffraction is always the best method to pre-determine the orientation of the sample. However, in the case of high-symmetry single crystals measured in platelet geometry it is possible to simultaneously refine both the elastic constants and sample orientation. Shimizu and Sasaki (1992) have resolved the elastic tensor of H_2S grown in the diamond anvil cell with this approach. Alternatively, Brillouin measurements can be used to refine the initial X-ray orientation of the sample, accounting for differences in optical and X-ray paths through the sample (e.g., Castagnede et al. 1992; Mao et al. 2008c). The ability to recover or refine a crystal's orientation through Brillouin measurements is a function of the degree of elastic anisotropy, and so varies from material to material.

The large redundancy of phase velocity measurements (with respect to the number of independent constants to be determined) is one of the strengths of Brillouin scattering (Fig. 14), especially when different scattering geometries are used. Except for directions with degeneracies of the acoustic phonon branches or directions with vanishingly low photoelastic efficiency, it is possible to observe all three acoustic modes for each direction. In principle, it would be possible to determine the full elastic tensor of crystals of any symmetry with a relatively small number of measurements performed in general directions. However, subsets of moduli, especially in materials with low symmetry, are strongly correlated, and in addition limited datasets can strongly decrease our ability to recover the full tensor (Castagnede et al. 1992). In reality, the determination of the full tensor of triclinic minerals is limited to a handful of cases (Brown et al. 2006). A much larger number of full tensors of monoclinic crystals have been determined by Brillouin scattering at ambient pressure. Materials with symmetries higher than monoclinic do not present serious difficulties at ambient or high pressures. Once the full elastic tensor is determined, it is possible to calculate the directional dependence of the elastic response to arbitrary applied stress fields (within the elastic limits). One of the most important properties is the volume compressibility of a crystal, defined as the volume change due to an applied pressure:

EBSCOhost - printed on 2/13/2023 5:26 AM via . All use subject to https://www.ebsco.com/terms-of-use

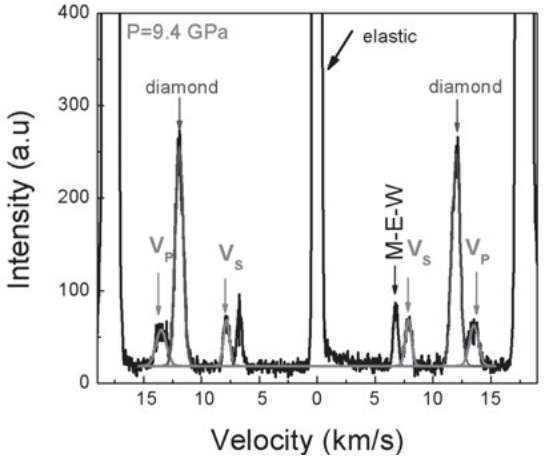


Figure 13. A typical Brillouin spectrum of stishovite at high pressure in the diamond anvil cell (modified from Jiang et al. 2009).

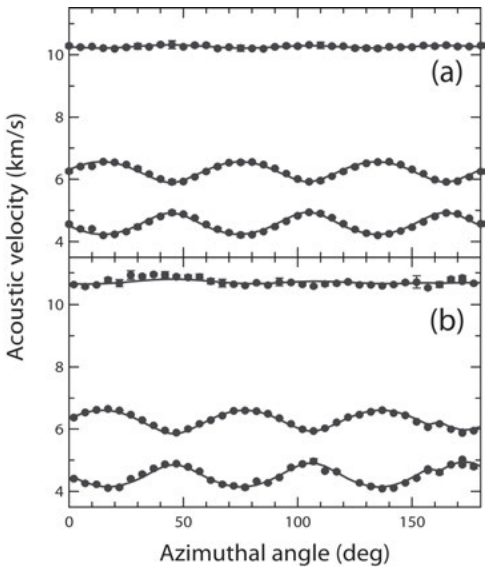


Figure 14. Experimental spatial dispersions of acoustic velocity in synthetic spinel, $MgAl_2O_4$ (Speziale, unpublished data). (a) Measurements at ambient conditions. (b) Measurements at 11 GPa of pressure. The symbols represent measured phase velocities and the curves best fit models based on the elastic tensor retrieved from the same data.

$$\beta = \frac{\varepsilon_{ii}}{P} = s_{iikk} \tag{40}$$

where ε_{ii} is the volume compression, P is pressure defined as $\sigma_{kl} = P\delta_{kl}$ (where δ_{kl} is the Kronecker delta). Compressibility is a key parameter to construct the pressure volume equation of state of a solid. The thermodynamic definition of compressibility:

$$\beta = \frac{d\ln\rho}{dP} \tag{41}$$

where ρ is density, allows one to determine the isothermal pressure—density equation of state if we measure compressibility as a function of pressure just by integrating Equation (41) (Shimizu et al. 1981). However, it is necessary to convert the compressibility determined by

EBSCOhost - printed on 2/13/2023 5:26 AM via . All use subject to https://www.ebsco.com/terms-of-use

Brillouin scattering, which is defined under isentropic conditions, to isothermal conditions. The conversion is obtained noting that the ratio of the isothermal and isentropic compressibilities is the same as that of specific heat measured at constant pressure and at constant volume:

$$\frac{\beta_T}{\beta_S} = \frac{C_P}{C_V} = 1 + \alpha\gamma T \tag{42}$$

where β_T is the isothermal compressibility, β_S is the isentropic compressibility, C_P is specific heat at constant pressure, C_V is the specific heat at constant volume, α is the thermal expansion coefficient, γ is the Grüneisen parameter, and T is temperature. The correction from isentropic to isothermal conditions does not affect the value of the room-temperature compressibility by more than a few percent in oxides and silicates of relevance for the Earth's interior except for conditions close to phase transitions. The difference is larger for soft solids and fluids, or at high temperatures.

Average elastic constants can also be calculated for aggregates of crystals once their orientation distribution is determined (e.g., Tomé 2000). This is necessary in order to determine the effective anisotropy of a "real" material. In geophysics, it is relevant to determine the change of seismic speed in different directions across a rock. Average elastic properties for orientationally isotropic aggregates of crystals of a single mineral phase or weighted mixtures of different minerals can be calculated following different approaches (Watt et al. 1976). Two moduli are of special interest in geophysics, the bulk modulus or incompressibility K, defined as the inverse of the compressibility β and the shear modulus or rigidity μ that represents the resistance to a change in shape caused by a pure shear stress. The two elastic moduli, in terms of the elastic tensor (in matrix form) of the isotropic medium are defined as:

$$K = \frac{c_{11} + 2c_{12}}{3} \qquad \mu = c_{44} = \frac{c_{11} - c_{12}}{2} \tag{43}$$

These moduli are directly related to the average compressional and shear seismic velocities (v_P and v_S, respectively) by the relationships:

$$v_P = \sqrt{\frac{K + 4/3\mu}{\rho}} \qquad v_S = \sqrt{\frac{\mu}{\rho}} \tag{44}$$

What is the information from Brillouin scattering that is relevant to Earth science?

Determining the elastic properties of the candidate materials of inner layers of the Earth is of fundamental importance in order to translate the information from seismology into a consistent model of the composition and structure of the Earth. Average bulk and shear elastic moduli of candidate materials of the deep Earth compared to the average seismic velocities from radially symmetric seismic models of the Earth, such as PREM (Dziewonski and Anderson 1981), AK135 (Kennett et al. 1995) or STW105 (Kustowski et al. 2008) are eventually converging toward a dominant unified view of the radial compositional structure of the Earth's interior, even though uncertainties are still present about the existence of a compositional layering at the transition from the upper to the lower mantle corresponding to the 660 km discontinuity or at deeper levels in the lower mantle (see review by Anderson 2005).

The increasing amount and quality of information from deep-Earth seismology has added a new dimension to our view of the structure of the Earth's interior. The presence of lateral heterogeneity is depicted at various scales by seismic tomography (Trampert and van der Hilst 2005). To determine the causes of the heterogeneity at transition zone level and in the D″ zone, the lowermost part of the mantle, we need more detailed information about the compositional dependence of the elastic properties of the single mineral phases that are present in the rocks at such great depths inside our planet. This requires improvement of our available techniques

EBSCOhost - printed on 2/13/2023 5:26 AM via . All use subject to https://www.ebsco.com/terms-of-use

to quantify the effect of pressure and temperature on single minerals, pushing their resolution to the level of detecting the fine effects of chemical exchange at a wide range of physical conditions.

Brillouin scattering is one of the few techniques that can be effectively combined with the diamond-anvil cell to be able to determine elastic properties at the pressures and temperatures of the lower mantle: from 24 GPa and ~2000 K at its top (660-km seismic discontinuity) to 135 GPa and ~2800 K at its base (the core-mantle boundary). In addition to seismic heterogeneity, deep Earth seismological studies detect down to the deepest mantle the signature of seismic anisotropy, both as azimuthal variation of seismic velocity, and as shear polarization anisotropy (see review by Nowacki et al. 2011). Observations of seismic anisotropy in the D″ layer are growing in number and they are convincingly indicating that anisotropy is not limited to the uppermost layers of the Earth, but it is present also in the lower mantle and in the solid inner core (Ishii and Dziewonski 2002; Garnero et al. 2004; Fouch and Rondenay 2006; Wookey and Kendall 2008).

The complete directional dependence of the elastic properties of minerals under conditions approaching those of the deep Earth is also very important for our understanding of the relationship between plastic deformation and seismic anisotropy in regions of the deep mantle of the Earth (or even in the solid inner core). In fact, the seismic anisotropy of aggregates can be determined only if the full elastic anisotropy of the mineral components is known. In this sense, techniques such as Brillouin scattering are the only ones that can offer experimental tests of the computational results based on density functional theory, like in the case of MgO at ultrahigh pressures (Karki et al. 1999; Murakami et al. 2009b).

APPLICATIONS OF BRILLOUIN SPECTROSCOPY IN GEOSCIENCES

The elastic properties of crustal and mantle minerals are of critical importance for interpreting radial and lateral seismic velocity variations and seismic anisotropy in the Earth's interior. To properly understand seismic observations, it is necessary to understand the variation of elastic properties as a function of composition, structure, pressure, and temperature. Brillouin spectroscopy is one of the most established and reliable techniques for the study of the single crystal elastic anisotropy of minerals of the Earth's interior, and a large number of studies have been conducted both at ambient conditions and at high pressures or temperatures.

Here, after summarizing the other main techniques that allow one to determine single crystal elasticity, we will focus particularly on the measurements performed at elevated pressure and/or temperature, and their implications for our understanding of the Earth's interior.

Experimental techniques to determine the anisotropic elasticity of Earth materials

Brillouin scattering is one of a family of methods that are used to access the full single crystal anisotropy of Earth materials (Fig. 15, Table 2). Ultrasonic interferometry (UI) techniques from MHz to GHz frequencies have been used to determine the full elastic tensor of cubic minerals up to 8 GPa and 10 GPa respectively (Chen et al. 1998; Jacobsen and Smyth 2006). Resonant ultrasound spectroscopy (RUS) is the method of choice to determine the elastic tensor at high temperatures (up to 1800 K) at ambient pressure, with a level of precision up to one order of magnitude better than Brillouin scattering (Isaak and Ohno 2003). A recent development of RUS to higher frequencies (HFRUS) has made it possible to use this method to study very small specimens from high-pressure syntheses such as stishovite (Yoneda et al. 2012). Phonon imaging is an optical technique that has been recently applied to the diamond anvil cell to investigate the single-crystal elastic constants of Si (Decremps et al. 2010). A femtosecond laser pulse focused on one face of a plate-shaped sample is absorbed setting a local thermal stress near the surface. A spatially uniform angular distribution of acoustic wavevectors will

EBSCOhost - printed on 2/13/2023 5:26 AM via . All use subject to https://www.ebsco.com/terms-of-use

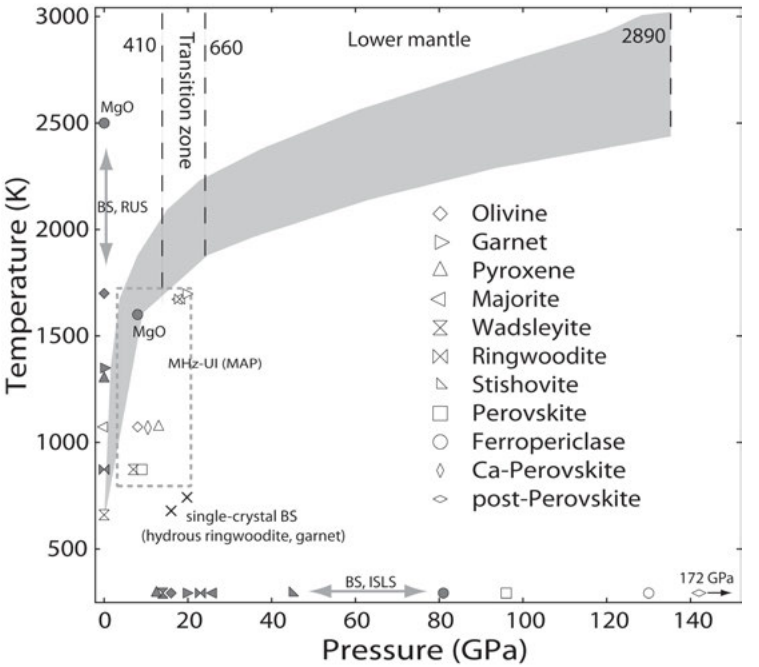


Figure 15. Available elasticity data of important mantle materials measured at high-pressures and/or high-temperatures. The shaded area illustrates the range of expected *P-T*-conditions in the Earth's transition zone and lower mantle. Open symbols: Measurements performed on polycrystalline samples; full symbols: single-crystal data. Note that many data points collected at either high-pressures or high-temperatures were measured on single-crystals (by BS, ISLS, RUS), whereas measurements at simultaneous high-pressures and high-temperatures are mostly performed on polycrystals (MHz-UI in a multi-anvil press). However, the cross denote first single-crystal data sets measured at both high-pressures and high-temperatures by Brillouin scattering (Mao et al. 2012; Liu et al. 2013).

produce at the exit surface focused patterns related to the topology of the anisotropic group velocity surface. Fast detection of the patterns as a function of time allows one to determine group velocity spatial dispersion and recover the full elastic tensor. Momentum-resolved inelastic X-ray scattering (IXS) is a synchrotron-based technique that can be considered as an extension of Brillouin scattering to the THz frequency range. It can be used to determine acoustic velocities in selected single crystals directions up to very high pressure in the DAC by measuring energy-wavevector dispersion curves (Antonangeli et al. 2011).

Finally, another optical spectroscopy technique that furnishes information about elastic anisotropy of materials is impulsive stimulated light scattering or ISLS (Nelson and Fayer 1980). This technique is related to (spontaneous) Brillouin scattering, and is also easily combined with the DAC allowing one to determine the spatial dispersion of velocities on single crystals at high pressures and temperatures (Chai et al. 1997b; Crowhurst et al. 2008). In ISLS, excitations, such as acoustic phonons, are coherently stimulated by infrared laser pulses by means of electrostriction and optical absorption producing a set of three-dimensional time-dependent standing wave gratings. A secondary light probe is then elastically (Bragg) scattered by the gratings and the diffracted intensity is analyzed in the time domain (Yan and Nelson 1987a; Brown et al. 1989). A theoretical analysis of this method in comparison with frequency domain laser scattering techniques is presented by Yan and Nelson (1987a; 1987b). In general, both stimulated scattering and spontaneous Brillouin scattering experiments yield similar

EBSCOhost - printed on 2/13/2023 5:26 AM via . All use subject to https://www.ebsco.com/terms-of-use

EBSCOhost - printed on 2/13/2023 5:26 AM via . All use subject to https://www.ebsco.com/terms-of-use

Table 2. Maximum pressure and temperature conditions of elasticity measurements of mantle minerals.

Material	max *P* [GPa] (method)	max *T* [K] (method)	max *P*/*T* [GPa, K] (method)
Ppv	172 (poly-BS) Murakami et al. (2007a)	—	—
Pv	96 (poly-BS) Murakami et al. (2007b)	—	9, 873 (MHz-UI) Li and Zhang (2005), Sinelnikov et al. (1998b)
Fp	81 (BS) Marquardt et al. (2009b), 130 (poly-BS) Murakami et al. (2009b)	2500 K (BS) Sinogeikin et al. (2004a)	8, 1600 (sc-MHz-UI) Chen et al. (1998)
Ca-Pv	—	—	10, 1073 (MHz-UI) Sinelnikov et al. (1998a)
Rw	23 (BS) Wang et al. (2006)	873 (BS) Jackson et al. (2000)	18, 1673 (MHz-UI) Higo et al. (2008)
Wad	14 (BS) Zha et al. (1997)	660 (RUS) Isaak et al. (2007)	7, 873 (MHz-UI) Li et al. (1998)
Mj	26 (BS) Murakami et al. (2008)	1073 (BS) Sinogeikin and Bass (2002b)	18, 1673 (MHz-UI) Irifune et al. (2008)
Stish	22 (BS) Jiang et al. (2009), 45 (BS) Lakshtanov et al. (2007)		
Ol	16 (BS) Duffy et al. (1995), Zha et al. (1996)	1700 (RUS) Isaak et al. (1989)	8, 1073 (MHz-UI) Liu et al. (2005)
Px	12.5 (ISLS) Chai et al. (1997b)	1073 (BS) Jackson et al. (2007), cpx 1300 (RUS) Isaak et al. (2006)	13, 1073 (MHz-UI) Kung et al. (2005)
Grt	11 (BS) Jiang et al. (2004a,b) 20 (ISLS) Chai et al. (1997a), (BS) Liu et al. (2013)	1073 (BS) Sinogeikin and Bass (2002b), 1350 (RUS) Isaak et al. (1992)	20, 1700 (MHz-UI) Zou et al. (2012) 20, 750 (BS) Liu et al. (2013)

Ppv: Mg-rich post-perovskite; Pv: Mg-rich perovskite; Fp: Mg-rich (Mg,Fe)O; Ca-pv: $CaSiO_3$ perovskite; Rw: ringwoodite; Wad: wadsleyite; Mj: majoritic garnet; Stish: stishovite; Ol: olivine; Px: pyroxene; Grt: garnet.
BS: Brillouin scattering; MHz-UI: MHz ultrasonic interferometry; GHz-UI: GHz ultrasonic interferometry; RUS: resonant ultrasound spectroscopy; ISLS: impulsively stimulated light scattering.

information, except for differences in the efficiency of the two techniques that depend on material properties and experimental constraints. The two methods are largely complementary, and there are in the literature some rare examples of coupling time- and frequency domain analysis approaches in a single combined setup (Maznev et al. 1996).

Detailed descriptions of the application of these different techniques can be found in several review articles (e.g., Bass 2007; Angel et al. 2009).

Lithosphere and upper mantle

Olivine, $(Mg,Fe)_2SiO_4$, is the dominant constituent (40-60% by volume) in upper mantle mineralogical models and its phase transformations are believed responsible for the 410- and 660-km seismic discontinuities (Ringwood and Major 1966; Duffy and Anderson 1989; Katsura and Ito 1989). Not surprisingly, the elastic properties of olivines at high pressure have received considerable attention in Brillouin scattering studies (e.g., Shimizu et al. 1982; Duffy et al. 1995; Zha et al. 1996, 1998; Speziale and Duffy 2004). At ambient conditions, there have also been studies of Ca- Ni- and Mn-olivines as well as germanate analogs (Weidner and Hamaya 1983; Bass et al. 1984; Peercy and Bass 1990; Lin and Chen 2011). Olivine single crystal elasticity has also been investigated by MHz UI (Kumazawa and Anderson 1969; Chen et al. 1996a), GHz UI (Chen et al. 1996b), RUS (Isaak et al. 1989; Isaak 1992) and ISLS (Zaug et al. 1993; Abramson et al. 1997).

Olivine (and its high-pressure polymorphs) can store significant quantities of water as hydroxyl-containing point defects (Smyth 1987; Kohlstedt et al. 1996; Smyth et al. 2006). Even if present in small quantities in the mantle, hydrogen can strongly affect phase relations, rheological and transport properties, and seismic properties of the deep Earth (Mei and Kohlstedt 2000; Karato 2006; Manthilake et al. 2009; Mao et al. 2010). Knowledge of the elastic properties of hydrous olivine polymorphs is thus necessary to interpret seismic data in potentially hydrous regions of the mantle. The elastic properties of hydrous olivine have recently been measured both at ambient conditions (Jacobsen et al. 2008) and high pressure (Mao et al. 2010). The presence of 0.9 wt% H_2O results in an increase in the pressure derivatives of the aggregate moduli. As a result, the bulk and shear moduli and hence the sound velocities of hydrous forsterite become greater than those of anhydrous forsterite at high pressures. At 14 GPa (~400 km depth), the compressional and shear velocities of hydrous forsterite are surprisingly 1-2% faster than those of anhydrous forsterite (Mao et al. 2010).

Garnets are important minerals widely found in metamorphic and igneous rocks of the Earth's crust. Garnets occur in both peridotitic and eclogitic compositions in upper mantle assemblages and are expected to be important components down to 660 km depth. As high-quality natural garnet crystals are widely available and have cubic symmetry with generally little elastic anisotropy, these minerals have been extensively studied to understand compositional effects on elastic properties. Silicate garnets in the pyralspite and ugrandite groups have also been subject of Brillouin scattering studies at ambient conditions to deep upper mantle pressures (Bass 1986, 1989; O'Neill et al. 1989, 1991, 1993; Conrad et al. 1999; Sinogeikin and Bass 2000; Jiang et al. 2004a,b). In a very recent study, Liu et al. (2013) have investigated single-crystal elastic properties of Fe-bearing pyrope to simultaneous high pressures and temperatures up to 20 GPa and 750 K.

The results of studies of olivines and garnets were used in solid-solution models of Fe-Mg substitution in olivine and Fe-Ca-Mg substitution in garnet by Speziale et al. (2005) to model the systematics of heterogeneity parameters, defined as $(\partial \ln v_{p,s}/\partial X_i)_P$ (where $v_{p,s}$ are compressional and shear velocity, X_i is the atomic fraction of the element in isomorphic substitution and P is pressure), for both minerals as a function of depth through the whole upper mantle. These parameters are of prime importance for interpreting seismic tomographic data in terms of chemical heterogeneity (Karato and Karki 2001).

EBSCOhost - printed on 2/13/2023 5:26 AM via . All use subject to https://www.ebsco.com/terms-of-use

Ortho- and clinopyroxenes are chain silicates that are present as abundant components in the crust and upper mantle rocks. Measurements on orthophyroxenes, $(Mg,Fe)SiO_3$, have focused mainly on constraining the effect of Mg-Fe substitution at ambient conditions (Weidner et al. 1978; Bass and Weidner 1984; Duffy and Vaughan 1988; Jackson et al. 1999) but other compositional and structural effects on elasticity have been studied as well by Brillouin scattering (Vaughan and Bass 1983; Perrillat et al. 2007). High temperature investigations of $MgSiO_3$ orthoenstatite show evidence for elastic softening associated with the onset of a displacive phase transition (Jackson et al. 2004a, 2007). Implications of orthopyroxene elasticity data for interpretation of seismic data in the crust and lithosphere have been discussed by Wagner et al. (2008) and Reynard et al. (2010).

Due to their monoclinic symmetry, the study of the elastic properties of clinopyroxenes is more challenging. Nevertheless, there have been extensive measurements, mostly by Brillouin scattering, of the full set of elastic constants at ambient conditions (Levien et al. 1979; Vaughan and Bass 1983; Kandelin and Weidner 1988a,b; Bhagat et al. 1992; Sang et al. 2011) and also by RUS (Isaak and Ohno 2003; and at high temperature, Isaak et al. 2006) and by ISLS (Collins and Brown 1998).

A variety of other common crustal minerals have been investigated by Brillouin scattering. These include quartz and its polymorphs (Weidner and Carleton 1977; Yeganeh-Haeri et al. 1992; Gregoryanz et al. 2000; Lakshtanov et al. 2007). A particularly notable feature is the negative bulk Poisson's ratio for the SiO_2 polymorph, cristobalite (Yeganeh-Haeri et al. 1992). Elastic constants by Brillouin scattering have also been reported for zeolites, natrolite, analcine and pollucite (Sanchez-Valle et al. 2005, 2010); cordierite (Toohill et al. 1999); glaucophane (Bezacier et al. 2010b), zoisite (Mao et al. 2007), diaspore (Jiang et al. 2008), alunite (Majzlan et al. 2006), phenacite (Yeganeh-Haeri and Weidner 1989), fluorite (Speziale and Duffy 2002), ettringite (Speziale et al. 2008a) and portlandite (Speziale et al. 2008b). Brillouin scattering of synthetic spinel (MgA_2O_4) has been measured at ambient pressure by Askarpour et al. (1993) to 1273 K. The phyllosilicates that have also been characterized by the technique are muscovite (Vaughan and Guggenheim 1986) and antigorite (Bezacier et al. 2010a, 2013).

Brillouin scattering of hydrous minerals has helped to improve our knowledge of the changes in elastic properties associated with the incorporation of hydrogen in the structure of oxides and silicates, with important impact on our understanding of deep water recycling in areas of active subduction. In addition to the nominally anhydrous olivine polymorphs, hydrous minerals studied to date include: brucite (Xia et al. 1998; Jiang et al. 2006), chondrodite (Sinogeikin and Bass 1999), clinohumite (Fritzel and Bass 1997), lawsonite (Sinogeikin et al. 2000b; Schilling et al. 2003) as well as the dense hydrous magnesian silicate phase A and phase D (Sanchez-Valle et al. 2008; Rosa et al. 2012). In addition to hydrogen, the recycling and deep budget of carbon is of interest in studying the composition of the deep Earth. Thus carbonates have been also studied by Brillouin spectroscopy in order to identify their potential contribution to the overall elastic properties of the subducting oceanic lithosphere at shallow depth (Chen et al. 2001, 2006; Sanchez-Valle et al. 2011).

Brillouin scattering of silica-rich glasses and melts has been measured as a function of pressure and temperature in order to determine compressibility and viscosity of granitic melts as a function of composition and put constraints on their density as a function of depth (Tkachev et al. 2005a,b; Hushur et al. 2013).

Transition zone

The Earth's transition zone, i.e., the region between 410 km and 660 km depth, is characterised by several major phase transitions. In particular, the structural changes that occur in $(Mg,Fe)_2SiO_4$ from olivine to wadsleyite to ringwoodite to a perovskite assemblage are of enormous interest to geophysicists. Comparison of the characteristics of the observed seismic

EBSCOhost - printed on 2/13/2023 5:26 AM via . All use subject to https://www.ebsco.com/terms-of-use

discontinuities such as depth, width and velocity contrast to laboratory data provides constraints on the bulk chemical composition, the thermal state and potentially also the water content of the transition zone (e.g., Cammarano and Romanowicz 2007; Frost 2008).

The complete set of elastic stiffness coefficients of a single crystal of Mg_2SiO_4 in the wadsleyite structure has been reported at ambient conditions (Sawamoto et al. 1984) and at high pressure (Zha et al. 1997). The effect of Fe/(Fe+Mg) ratio on the single-crystal elastic properties of wadsleyite and ringwoodite has been determined at ambient conditions (Sinogeikin et al. 1998) and for ringwoodite at high pressure (Sinogeikin et al. 2001). The other major component of the transition zone is majoritic garnet. The bulk elastic properties of single crystal and of polycrystalline majorite have been measured by Pacalo et al. (1992) and by Sinogeikin and Bass (2002a) respectively. The effect of chemical substitution has been investigated by Yeganeh-Haeri et al. (1990) and Sinogeikin and Bass (2002a) in the majorite-pyrope system, as well as by Pacalo et al. (1992) and Reichmann et al. (2002) in the majorite-jadeite system. Recently, single-crystal majorite was grown in a high-pressure/high-temperature synthesis and measured by Brillouin scattering to high pressures (Murakami et al. 2008).

As with olivine, there has been much interest in the incorporation of OH^- defects in the crystal structures of wadsleyite and ringwoodite (Smyth 1987, 1994; McMillan et al. 1991; Kohlstedt et al. 1996). The single-crystal elasticity of hydrous wadsleyite and ringwoodite has been determined at room conditions (Inoue et al. 1998; Wang et al. 2003; Mao et al. 2008c) and at high pressure (Wang et al. 2006; Mao et al. 2008b, 2010, 2011) and also by GHz UI (Jacobsen et al. 2004; Jacobsen and Smyth 2006), and the results imply that OH^- defects have a pronounced effect on the elasticity of the high-pressure olivine polymorphs. The available data raise the hope that it might be feasible to "map" hydration in the transition zone by combining mineral physics data with constraints from seismic tomography (Jacobsen and Smyth 2006; Shito et al. 2006; Li et al. 2011). Very recently, the elastic properties of hydrous ringwoodite have been measured to 16 GPa and 673 K (Mao et al. 2012).

The elastic properties of stishovite have been determined by Weidner et al. (1982) at ambient conditions. Lakshtanov et al. (2007) has investigated the stishovite to $CaCl_2$-type phase transition by measuring Brillouin scattering along the [110] crystallographic direction. This displacive transition, which takes place at pressures of the lower mantle, is characterized by a substantial shear acoustic softening along [110], and its depth is strongly influenced by aluminium (and hydrogen) content in stishovite. Jiang et al. (2009) in a study of stishovite up to 22 GPa, observed signs of the incipient elastic softening already at pressures of the transition zone.

Based on the available data on transition zone minerals, it appears that the steep velocity gradients indicated by seismology are not consistent with a homogeneous mantle of pyrolitic composition (Cammarano and Romanowicz 2007). However, to draw final conclusions about the state of the transition zone, more input data from mineral physics, ideally determined at realistic pressure and temperature conditions, is needed. This includes data on elastic properties, but also an improved understanding of anelastic effects on the propagation behaviour of seismic waves (e.g., Stixrude and Jeanloz 2009).

Lower mantle

The two major components of the pyrolitic Earth's lower mantle are Mg-rich silicate perovskite (with a simplified formula $(Mg_{1-x}Fe_x)SiO_3$) and ferropericlase $(Mg_{1-y}Fe_y)O$. Brillouin scattering of Mg-rich ferropericlase (y = 0.013) has been measured up to 9 GPa (Reichmann et al. 2008). Ferropericlase with composition $(Mg_{0.94}Fe_{0.06})O$ has been measured to a maximum pressure of 20 GPa (Jackson et al. 2006). Recently, Brillouin scattering of single-crystal $(Mg_{0.9}Fe_{0.1})O$ ferropericlase has been measured to 81 GPa corresponding to 1900 km depth (Marquardt et al. 2009b). This study showed that ferropericlase is elastically very

EBSCOhost - printed on 2/13/2023 5:26 AM via . All use subject to https://www.ebsco.com/terms-of-use

anisotropic in the Earth's lower mantle, particularly when Fe^{2+} is in low spin state (Badro et al. 2003). However, it is still debated if the spin crossover of Fe^{2+} is accompanied by a "softening" of compressional wave velocities based on measurements of other ferropericlase compositions by ISLS (Crowhurst et al. 2008) and by IXS (Antonangeli et al. 2011). Brillouin scattering is not currently able to resolve this issue, because of the overlap of the Brillouin signal from diamonds anvils in the DAC (Marquardt et al. 2009c). However, in principle, this limitation can be overcome (e.g., Zha et al. 2000) and Brillouin scattering is certainly a candidate tool to resolve this fundamental question, with all its consequences for our understanding of the state of the lower mantle (e.g., Cammarano et al. 2010).

The other major component of the lower mantle, Mg-rich perovskite, has only been measured as a single-crystal at room pressure (Yeganeh-Haeri et al. 1989; Yeganeh-Haeri 1994; Jackson et al. 2004b; Sinogeikin et al. 2004b). High-pressure measurements are restricted at present to polycrystalline iron-free perovskite (Jackson et al. 2005; Murakami et al. 2007b). Measuring single-crystal anisotropic elastic properties of iron-bearing perovskite at pressure/temperature-conditions relevant for the lower mantle is certainly among the biggest challenges in experimental mineral physics. Brillouin scattering of polycrystalline $CaSiO_3$ perovskite, which represents 5 vol% of the bulk lower mantle, has been measured throughout the whole lower mantle pressure range (Kudo et al. 2012).

In addition to the minerals of the pyrolitic bulk mantle, also the aluminum-rich phase with composition $Na_{0.4}Mg_{0.6}Al_{1.6}Si_{0.4}O_4$ and its higher pressure polymorph with Ca-ferrite phase, both relevant components of lithospheric rocks deeply subducted at lower mantle pressures, have been subject of a high-pressure study based on Brillouin scattering of polycrystalline samples up to 73 GPa (Dai et al. 2013).

In the Earth's lowermost mantle, perovskite undergoes a structural phase transition to post-perovskite (Murakami et al. 2004; Oganov and Ono 2004; Tsuchiya et al. 2004). The single-crystal elastic properties of this phase are experimentally unknown, even though they are of enormous importance for interpreting seismic anisotropy in the lowermost mantle (e.g., Miyagi et al. 2010). Brillouin scattering has, however, been performed on polycrystalline Mg-endmember post-perovskite to a pressure of 172 GPa (Murakami et al. 2007a). It should be noted here that the potential effect of the electronic spin transition of iron on the elastic properties of both perovskite and post-perovskite is still unknown (Lin et al. 2013).

Silicate glasses are model systems for understanding the behaviour of silicate melts at deep mantle conditions. Glasses with compositions of interest for geophysics have been measured to lower mantle pressures up to more than 200 GPa (Zha et al. 1994; Murakami and Bass 2010, 2011; Sanchez-Valle and Bass 2010). These studies reveal interesting changes in the pressure derivative of shear velocities that might indicate amorphous silicate densification. Furthermore, these measurements document that the experimental limits of Brillouin scattering at extreme conditions are still not mapped out (Murakami and Bass 2011).

FRONTIERS

Elasticity under deep mantle conditions

Brillouin scattering is one of the few techniques capable of providing information about single-crystal elastic anisotropy, at pressure and temperature conditions relevant to the deep Earth interior. However, the vast majority of experimental work on materials of geophysical relevance has been limited to either high pressure or high temperature, and not simultaneously at the high *P-T* conditions of the interior of our planet (Fig. 15). This poses limitations on the mineral physics interpretation of seismological observations at present.

EBSCOhost - printed on 2/13/2023 5:26 AM via . All use subject to https://www.ebsco.com/terms-of-use

Indeed, it has been shown that the *P*-*T*-cross-derivatives, which are only accessible by measurements performed at simultaneously high-*P* and -*T*, cannot be disregarded (Chen et al. 1998). In addition, only recently the first single-crystal measurements were performed (at 300 K) at pressures expected for the Earth's lower mantle (Zha et al. 2000; Marquardt et al. 2009b,c) or at 1 bar at temperatures relevant to the deep mantle (Jackson et al. 2000, 2007; Sinogeikin and Bass 2002b; Sinogeikin et al. 2004a). At present, there are no high-pressure or high-temperature Brillouin data on single crystals of $MgSiO_3$ perovskite, the most abundant mineral phase of the Earth's lower mantle. In this chapter, we provide some perspectives on future directions for Brillouin spectroscopy.

Extending the experimental pressure range for single-crystal measurements. Sample preparation for Brillouin scattering is challenging as the technique requires small, optical grade, parallel, and well-polished samples in specific crystal orientations. It has recently been demonstrated that focused ion beam (FIB) cutting and milling are well suited techniques to prepare single-crystal samples with dimensions of few tens of microns and precisely defined shapes (Marquardt and Marquardt 2012). These procedures result in little damage and thus allow for machining designed samples from materials that are brittle, metastable, or show a strong cleavage. In addition, FIB techniques allow for cutting more than one sample from a single fragment of material, for instance, platelets with different orientations from one single-crystal of less than 100 μm width.

Another serious limitation in Brillouin-scattering experiments extending to very high pressures (>30 GPa), or on materials with fast acoustic velocities, arises from the overlap of Brillouin peaks from the shear waves of the diamond anvils with those of the sample's compressional wave. As a result, the compressional waves can only be measured in certain directions or even not at all. This reduces the ability to recover the full set of elastic tensor components. In the case of cubic materials, *in situ* X-ray diffraction data can be used to supplement the Brillouin data. Using the (isothermal) bulk modulus $K_T = (c_{11} + 2c_{12})/3$ together with the results from Brillouin scattering from the shear acoustic modes, one can extract the three independent elastic constants, if appropriate corrections are made between the isothermal and adiabatic moduli (e.g., Marquardt et al. 2009c). Methods for spatial filtering and the use of cylindrical lenses can, in principle, be used to suppress the diamond signal (Zha et al. 1998, 2000) and further developments of these techniques are needed.

Extending Brillouin spectroscopy to simultaneous high pressures and high temperatures. A small number of Brillouin scattering measurements at combined high pressures and high temperatures have been performed in the diamond-anvil cell, using resistive (Goncharov et al. 2007; Jia et al. 2008; Mao et al. 2012; Lu et al. 2013) or laser heating (Li et al. 2006; Murakami et al. 2009a, 2012). The maximum temperature that has been reported in single-crystal Brillouin experiments at high pressures by using resistive heating is about 900 K (Sinogeikin et al. 2006). The temperature range that can be accessed by resistive heating might be extended using different heaters and enclosing the whole diamond-anvil cell in a sealed container with a controlled atmosphere (e.g., Liermann et al. 2009), but is limited due to graphitization of the diamonds that occurs at roughly 1200-1500 K.

Alternatively, infrared laser heating can be employed to heat the sample. Recent progresses in implementation of laser-heating techniques for single-crystal studies (Dubrovinsky et al. 2010) has applications to Brillouin spectroscopy. The solid-state lasers that are commonly employed for laser-heating in the diamond-anvil cell operate at wavelengths in the near infrared (~1 μm) where there is tradeoff between the optical transparency required for Brillouin spectroscopy and the absorption required for effective heating at these wavelengths. Silicates and oxides (including lower-mantle ferropericlase and Mg-perovskite) that contain some amount of iron (~10 at%) are perfectly suited for Brillouin spectroscopy (e.g., Marquardt et al. 2009c), while absorbing enough energy from a ~1 μm heating laser to allow for effective

EBSCOhost - printed on 2/13/2023 5:26 AM via . All use subject to https://www.ebsco.com/terms-of-use

heating to thousands of degrees (Dubrovinsky et al. 2009). The possibility of laser-heating the sample chamber by employing "internal furnaces," i.e., adding some laser absorbing material to the sample chamber, has also been discussed (Goncharov and Crowhurst 2005; Li et al. 2006). Alternatively, CO_2 lasers (wavelength ~10 μm) have been employed to heat transparent samples (Sinogeikin et al. 2004a; Murakami et al. 2009a).

Brillouin scattering combined with synchrotron X-ray diffraction. The combination of Brillouin spectroscopy and synchrotron X-ray diffraction is very useful for studies at high *P-T*, because the density of the sample can be directly determined under the same experimental conditions as the Brillouin data. X-ray diffraction data provide a precise control and knowledge of the sample orientation (in case of slight rotation of the single crystal by increasing pressure and temperature), which reduces the number of phonon directions necessary to constrain the elastic tensor and thus minimizes experimental collection time, especially when measurements are performed at extreme conditions. In addition, the X-ray data give information on crystal quality, twinning, etc. In case of experiments performed on polycrystalline samples, other useful results potentially derived from X-ray measurements include the average grain size, texture, and stress distribution (Marquardt et al. 2011; Speziale et al. 2013). The combination of Brillouin scattering and synchrotron X-ray diffraction can be realized by having the Brillouin system "on-line" at a beamline. Such systems are installed at the Advanced Light Source (APS) Sector 13 (Sinogeikin et al. 2006) and SPring 8 beamline BL10XU (Murakami et al. 2009a). They allow for a simultaneous collection of acoustic velocity measurements and X-ray diffraction data. Figure 16 shows both a Brillouin spectrum collected on a single-crystal of $(Mg_{0.9}Fe_{0.1})O$ ferropericlase at APS Sector 13 and the corresponding integrated diffraction pattern at around 10 GPa and 700 K.

One possible drawback of such systems lies in the experimental time requirements of the two techniques. While it takes only several minutes to collect X-ray diffraction datasets in the DAC, especially if only the unit cell volume is to be determined, the typical collection time for one Brillouin spectrum is several tens of minutes, sometimes even hours. Additionally, multiple crystallographic directions have to be probed in single-crystal Brillouin spectroscopy to invert for the complete elastic tensor at a given pressure, especially if the symmetry of the

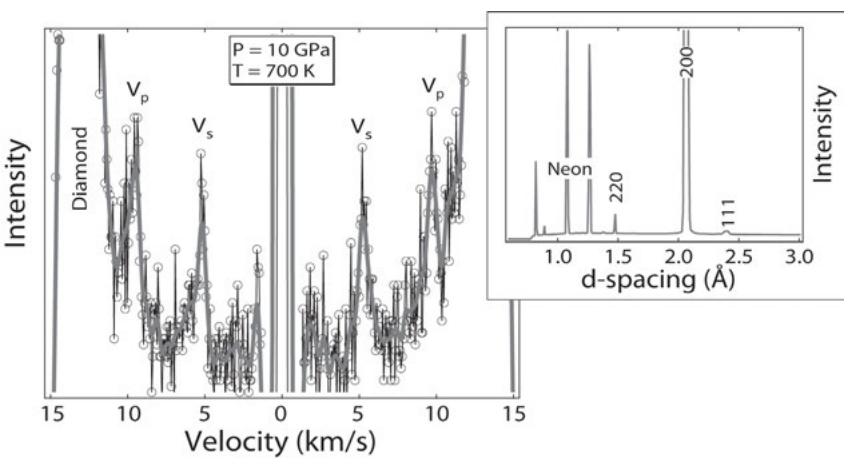


Figure 16. Brillouin scattering spectrum of a single crystal of $(Mg_{0.9}Fe_{0.1})O$ and corresponding X-ray diffraction pattern simultaneously collected at high pressure and temperature at Sector 13 of the APS (Marquardt, unpublished data).

EBSCOhost - printed on 2/13/2023 5:26 AM via . All use subject to https://www.ebsco.com/terms-of-use

material is not cubic or hexagonal. Thus, the use of "on-line" systems represents the optimal use of beamtime only when the collection of Brillouin spectra can be limited to one or a few directions as is the case for liquids, glasses, random polycrystals, and elastically isotropic or high-symmetry single crystals.

An alternative approach to combining Brillouin scattering and X-ray diffraction is the installation of a Brillouin system in close proximity to a synchrotron beamline. With this arrangement, the time-consuming acoustic velocity measurements of elastic anisotropy can be performed "off-line" and the measurements of X-ray diffraction are performed only once per *P-T* step by transferring the sample to the beamline at the same environmental conditions. Such a setup is now available at DESY-PETRA III Beamline P02.2 (Extreme Conditions Beamline ECB) (Speziale et al. 2013). This approach is most effective for high-pressure and temperature measurements of single-crystals, especially when the crystal symmetry is lower than cubic.

The combination of Brillouin scattering with synchrotron X-ray diffraction at high pressure in the DAC can supplement the velocity data with very important information that help to constrain the full elastic tensor when the Brillouin data alone are insufficient. X-ray diffraction of powders can supply cell volume (and hence density) and constrain the isothermal bulk modulus (Sinogeikin et al. 2006; Marquardt et al. 2009b; Murakami et al. 2009a). Single crystal diffraction can place tight constraints on the axial compressibilities which place independent constraints on subsets of the elastic constants. X-ray diffraction of powders in radial geometry can supply information about texture development, useful to evaluate the results of Brillouin scattering from polycrystalline samples (Marquardt et al. 2011; Speziale et al. 2013), and in the case of high-symmetry materials it can also place constraints on subsets of single crystal elastic constants (Speziale et al. 2006; Mao et al. 2008a) by applying anisotropic lattice strains theories (e.g., Funamori et al. 1994; Singh et al. 1998; Matthies et al. 2001).

Brillouin scattering of polycrystalline aggregates. Brillouin measurements on polycrystalline aggregates offer some advantages, especially for experiments at higher pressures and combined high *P-T* conditions. For isotropic samples such as glasses and random polycrystals, only one single Brillouin measurement is necessary to obtain the two elastic moduli that characterize such materials, although more measurements are typically performed in practice. Good agreement for bulk properties (shear and bulk modulus) between Brillouin scattering measurements performed on polycrystalline and single-crystal perovskite has been demonstrated at ambient conditions (Sinogeikin et al. 2004b). However, even for elastically isotropic materials, the anisotropy of the photoelastic tensor (that determines the intensity of Brillouin scattered light; see "Brillouin scattering in solids" section) could bias the experimentally determined average velocity with respect to the theoretical average from single-crystal elastic constants.

In the case of loosely packed powders, the spectra show a characteristic distribution of frequency shifts caused by the large variation in scattering geometries (Hernandez et al. 1996). Thorough investigations of Brillouin spectra from heterogeneous micro-aggregates have elucidated the details of their dispersion relation in the GHz regime, including fine details of localized eigenmodes of the particles of the dispersed components (Kriegs et al. 2004). In the case of predefined microstructure, Brillouin scattering has been successfully used to determine the effective elastic properties of the composite by applying effective medium models (e.g., Devaty et al. 2010). These promising results suggest that Brillouin scattering could be used to infer properties of unknown materials when they form microstructurally well-characterized aggregates with materials of known elastic properties at extreme conditions.

Recently, Brillouin experiments on packed powders have been performed to high pressures (Murakami et al. 2007a,b, 2009b; Gleason et al. 2011; Marquardt et al. 2011). Even though these results are promising, effort is still necessary to understand the quality and reliability of bulk

EBSCOhost - printed on 2/13/2023 5:26 AM via . All use subject to https://www.ebsco.com/terms-of-use

properties determined by Brillouin scattering from polycrystalline materials at high pressures. As the stress distribution in a diamond-anvil cell at high pressure will not be uniform, a major complication might arise from the development of a crystallographic-preferred orientation (CPO) in the polycrystalline sample. In this case, the measured aggregate velocities will be average distribution functions weighted by the grains' orientation and could strongly deviate from the isotropic average velocities. Furthermore, the anisotropic deformation behavior of the constituents leads to intergranular stresses, which may bias the measured velocities. Additional care has to be taken to precisely characterise the average crystallite size since small grain size can have an impact on the measured bulk elastic properties (Marquardt et al. 2011).

Combining Brillouin scattering with other techniques to characterize elastic anisotropy at high pressures

The combination of single-crystal Brillouin scattering at extreme pressures and temperatures with other techniques that determine elastic properties of materials can allow one to put constraints on the full elastic tensor of materials even when the individual techniques alone cannot. One example of this approach is represented by the study of the effect of the Fe^{2+} spin crossover on the elastic properties of ferropericlase $(Mg_{1-x}Fe_x)O$ (with $x < 0.3$) at lower mantle pressures. Brillouin scattering, X-ray diffraction, IXS and ISLS experiments on ferropericlase of similar compositions have furnished direct information on all the constants of the elastic tensor of this mineral, which is the second most abundant phase of the lower mantle (Lin et al. 2005; Crowhurst et al. 2008; Marquardt et al. 2009c; Antonangeli et al. 2011). This body of experimental results, generally in mutual agreement, has placed strong constraints on the behavior of the shear elastic anisotropy of ferropericlase, which shows an increase across the spin crossover. The results regarding the compressional constant c_{11} are still contradictory, but the combination of the available results along with density functional theory computations (Wentzcovitch et al. 2009; Wu et al. 2013) is progressing in the direction of an unequivocal picture. Due to inherent limitations of the different techniques, it is the combination of multiple approaches that best places quantitative constraints on the elastic anisotropy at these extreme conditions.

Surface Brillouin scattering at extreme conditions

One of the biggest challenges in mineral physics is that of directly probing the elastic properties of the materials of the Earth's core. Measurements of the elastic properties of polycrystalline hcp-Fe (the most probable stable polymorph in the inner core) have been measured to megabar pressures by IXS (Fiquet et al. 2001; Antonangeli et al. 2004, including elastic anisotropy) and by ISLS (Crowhurst et al. 2005). Measurements of Fe-Ni and Fe-Ni-Si alloy compositions have been performed at high pressures and temperatures (Kantor et al. 2007; Antonangeli et al. 2010). These experiments provide, up to now, the best constraints on shear and compressional velocities of solid Fe and Fe alloys at extreme pressures. A coherent picture requires additional experimental investigations at even higher pressures and at significantly higher temperatures.

Brillouin scattering can be one technique to determine acoustic velocities of both solid and liquid metals at extreme conditions in the DAC. Surface Brillouin scattering of liquid metals has been reported at ambient conditions (Dil and Brody 1976) and the theory has been developed to interpret the spectral features present in spectra collected from the interface between a transparent container and a metal liquid (Visser et al. 1984). In addition, surface Brillouin scattering of solid thin-film Au has been measured to a pressure of 4.8 GPa (Crowhurst et al. 1999). Advances in the design of Brillouin spectrometers (that is both the optic path and the interferometers) allow, in principle to detect the scattering from interfacial waves at the contact between liquid and solid iron as well as between diamond and a transparent pressure medium.

EBSCOhost - printed on 2/13/2023 5:26 AM via . All use subject to https://www.ebsco.com/terms-of-use

ACKNOWLEDGMENTS

We thank E. S. Zouboulis, Z. Geballe, H. J. Reichmann and an anonymous reviewer for their very useful comments, which helped us to improve the manuscript. H. M. was supported by DFG-grant SP 1216/3-1 within SPP1236.

REFERENCES

Abramson EH, Brown JM, Slutsky LJ, Zaug J (1997) The elastic constants of San Carlos olivine to 17 GPa. J Geophys Res 102:12253-12263

Adshead A, Lindsay SM (1982) Brillouin scattering from polyurethane gels. Polymer 23:1884-1888

Ahart M, Yarger JL, Lantzky KM, Nakano S, Mao H-k, Hemley RJ (2006) High-pressure Brillouin scattering of amorphous BeH_2. J Chem Phys 124:14502-14505

Ahart M, Somayazulu M, Ye Z-G, Cohen RE, Mao H-k, Hemley RJ (2009) High-pressure Brillouin scattering of $Pb(Mg_{1/3}Nb_{2/3})O_3$. Phys Rev B 79:132103

Ahart M, Asthagiri A, Ye Z-G, Dera P, Mao H-k, Cohen RE, Hemley RJ (2007) Brillouin scattering and molecular dynamics study of the elastic properties of $Pb(Mg_{1/3}Nb_{2/3})O_3$. Phys Rev B 75:144410

Ahart M, Mao H-k, Cohen RE, Hemley RJ, Samara GA, Bing Y, Ye Z-G, Kojima S (2010) Pressure effects on relaxor ferroelectricity in disordered $Pb(Sc_{1/2}Nb_{1/2})O_3$. J Appl Phys 107:074110

Ahart M, Somayazulu M, Gramsch SA, Boehler R, Mao H-k, Hemley RJ (2011) Brillouin scattering of H_2O ice to megabar pressures. J Chem Phys 134:124517-124516

Albuquerque EL (1983) Surface-ripple Brillouin scattering from a glass–metallic liquid interface. Phys Status Solidi B 118:223-227

Albuquerque EL, Loudon R, Tilley DR (1980) Theory of Brillouin scattering by Love waves. J Phys C: Solid State Physics 13:1775-1789

Alexopoulos PS, O'Sullivan TC (1990) Mechanical properties of thin films. Annu Rev Mater Sci 20:391-420

Anderson DL (2005) Self-gravity, self-consistency, and self-organization in geodynamics and geochemistry. *In*: Earth's Deep Mantle: Structure, Composition, and Evolution. (Geophysical Monograph Series, Book 160). Van der Hilst RD, Bass JD, Matas J, Trampert J (eds) AGU, Washington, DC, p 137-165

Anderson DL, Sammis C, Phinney R (1969). Brillouin scattering: A new geophysical tool. *In*: The Application of Modern Physics to Earth and Planetary Interiors. Runcorn S (ed) Wiley, New York, p 465-477

Anderson MW, Lindsay SM, Harley RT (1984) Quasielastic light scattering in silicon. J Phys C: Solid State Physics 17:6877-6882

Angel RJ, Jackson JM, Reichmann HJ, Speziale S (2009) Elasticity measurements on minerals: A review. Eur J Mineral 21:525-550

Antonangeli D, Occelli F, Requardt H, Badro J, Fiquet G, Krisch M (2004) Elastic anisotropy in textured hcp-iron to 112 GPa from sound wave propagation measurements. Earth Planet Sci Lett 225:243-251

Antonangeli D, Siebert J, Badro J, Farber DL, Fiquet G, Morard G, Ryerson FJ (2010) Composition of the Earth's inner core from high-pressure sound velocity measurements in Fe–Ni–Si alloys. Earth Planet Sci Lett 295:292-296

Antonangeli D, Siebert J, Aracne CM, Farber DL, Bosak A, Hoesch M, Krisch M, Ryerson FJ, Fiquet G, Badro J (2011) Spin crossover in ferropericlase at high pressure: A seismologically transparent transition? Science 331:64-67

Asahara Y, Murakami M, Ohishi Y, Hirao N, Hirose K (2010) Sound velocity measurement in liquid water up to 25 GPa and 900 K: Implications for densities of water at lower mantle conditions. Earth Planet Sci Lett 289:479-485

Asenbaum A, Blaschko O, Hochheimer HD (1986) Brillouin scattering on rubidium iodide under high pressure. Phys Rev B 34:1968-1971

Askarpour V, Manghnani MH, Fassbender S, Yoneda A (1993) Elasticity of single-crystal $MgAlO_4$ spinel up to 1273 K by Brillouin spectroscopy. Phys Chem Miner 19:511-519

Auld BA (1973) Acoustic Fields and Waves in Solids. Wiley, New York

Badro J, Fiquet G, Guyot F, Rueff J-P, Struzhkin VV, Vanko G, Monaco G (2003) Iron partitioning in Earth's mantle: Toward a deep lower mantle discontinuity. Science 300:789-791

Bass JD (1986) Elasticity of uvarovite and andradite garnets. J Geophys Res B 91:7505-7516

Bass JD (1989) Elasticity of grossular and spessartite garnets by Brillouin spectroscopy. J Geophys Res B, Solid Earth and Planets 94:7621-7628

Bass JD (2007) Techniques for measuring high P/T elasticity. *In*: Treatise on Geophysics - Mineral physics. Vol 2. Price GD (ed) Elsevier, Amsterdam, p 269-291

Bass JD, Weidner DJ (1984) Elasticity of single-crystal orthoferrosilite. J Geophys Res 89:4359-4371

EBSCOhost - printed on 2/13/2023 5:26 AM via . All use subject to https://www.ebsco.com/terms-of-use

Bass JD, Weidner DJ, Hamaya N, Ozima M, Akimoto S (1984) Elasticity of the olivine and spinel polymorphs of Ni_2SiO_4. Phys Chem Miner 10:261-272
Bassoli L, Nizzoli F, Sandercock JR (1986) Surface brillouin scattering in polycrystalline gold. Phys Rev B 34:1296-1299
Beghi MG, Bottani CE, Russo V (2000) Debye temperature of erbium-doped yttrium aluminum garnet from luminescence and Brillouin scattering data. J Appl Phys 87:1769-1774
Beghi MG, Casari CS, Li Bassi A, Bottani CE, Ferrari AC, Robertson J, Milani P (2002a) Acoustic phonon propagation and elastic properties of nano-sized carbon films investigated by Brillouin light scattering. Thin Solid Films 420-421:300-305
Beghi MG, Ferrari AC, Bottani CE, Libassi A, Tanner BK, Teo KBK, Robertson J (2002b) Elastic constants and structural properties of nanometre-thick diamond-like carbon films. Diamond Relat Mater 11:1062-1067
Beghi MG, Every AG, Zinin PV (2004) Brillouin scattering measurements of SAW velocities for determiningnear-surface elastic properties. *In*: Ultrasonic Nondestructive Evaluation. Kundu T (ed) CRC Press, Boca Raton, p 581-651
Bell JA, Bennett WR, Zanoni R, Stegeman GI, Falco CM, Nizzoli F (1987a) Elastic constants of Mo/Ta superlattices measured by Brillouin scattering. Phys Rev B 35:4127-4130
Bell JA, Zanoni RJ, Seaton CT, Stegeman GI, Bennett WR, Falco CM (1987b) Brillouin scattering from Love waves in Cu/Nb metallic superlattices. Appl Phys Lett 51:652-654
Benedek G, Greytak T (1965) Brillouin scattering in liquids. Proc IEEE 53:1623-1629
Bezacier L, Reynard B, Bass JD, Sanchez-Valle C, Van de Moortèle B (2010a) Elasticity of antigorite, seismic detection of serpentinites, and anisotropy in subduction zones. Earth Planet Sci Lett 289:198-208
Bezacier L, Reynard B, Bass JD, Wang J, Mainprice D (2010b) Elasticity of glaucophane, seismic velocities and anisotropy of the subducted oceanic crust. Tectonophysics 494:201-210
Bezacier L, Reynard B, Cardon H, Montagnac G, Bass JD (2013) High-pressure elasticity of serpentine and seismic properties of the hydrated mantle wedge. J Geophys Res 118:1-9
Bhadra R, Grimsditch M, Schuller IK, Nizzoli F (1989) Brillouin scattering from unsupported Al films. Phys Rev B 39:12456-12459
Bhagat SS, Bass JD, Smyth JR (1992) Single-crystal elastic properties of omphacite-C2/c by Brillouin spectroscopy. J Geophys Res 97:6843-6848
Borovik-Romanov AS, Kreines NM (1982) Brillouin-Mandelstam scattering from thermal and excited magnons. Phys Rep 81:351-408
Bortolani V, Marvin AM, Nizzoli F, Santoro G (1983) Theory of Brillouin scattering from surface acoustic phonons in supported films. J Phys C: Solid State Physics 16:1757-1776
Brillouin L (1922) Diffusion de la lumière et des rayons X par un corps transparent homogène: Influence de l'agitation thermique. Annalen der Physik (Paris) 17:88-122
Brodin A, Frank M, Wiebel S, Shen G, Wuttke J, Cummins HZ (2002) Brillouin-scattering study of propylene carbonate: An evaluation of phenomenological and mode coupling analyses. Phys Rev E 65:051503
Brown JM, Slutsky LJ, Nelson KA, Cheng LT (1989) Single-crystal elastic constants for San Carlos peridote: An application of impulsive stimulated scattering. J Geophys Res 94:9485-9492
Brown J, Abramson E, Angel R (2006) Triclinic elastic constants for low albite. Phys Chem Miner 33:256-265
Bucaro JA, Dardy HD (1974) High-temperature Brillouin scattering in fused quartz. J Appl Phys 45:5324-5329
Cammarano F, Romanowicz B (2007) Insights into the nature of the transition zone from physically constrained inversion of long-period seismic data. Proc Natl Acad Sci 104:9139-9144
Cammarano F, Marquardt H, Speziale S, Tackley PJ (2010) Role of iron-spin transition in ferropericlase on seismic interpretation: A broad thermochemical transition in the mid mantle? Geophys Res Lett 37:L03308
Carlotti G, Fioretto D, Giovannini L, Nizzoli F, Socino G, Verdini L (1992a) Brillouin scattering by pseudosurface acoustic modes on $(1\,\bar{1}\,1)$ GaAs. J Phys Condens Matt 4:257-262
Carlotti G, Fioretto D, Socino G, Rodmacq B, Pelosin V (1992b) Interface effects and elastic constants of Ag/Ni superlattices studied by Brillouin scattering. J Appl Phys 71:4897-4902
Carlotti G, Fioretto D, Socino G, Verona E (1995) Brillouin scattering determination of the whole set of elastic constants of a single transparent film of hexagonal symmetry. J Phys Condens Matt 7:9147-9153
Carlotti G, Gubbiotti G (2002) Magnetic properties of layered nanostructures studied by means of Brillouin light scattering and the surface magneto-optical Kerr effect. J Phys Condens Matter 14:8199-8233
Castagnede B, Every AG, Sachse W (1992) Numerical simulation of the instabilities associated to the recovery of elastic constants of anisotropic solids from quasi-longitudinal velocities alone. CR Acad Sci Paris 314:865-871
Chai M, Brown JM, Slutsky LJ (1997a) The elastic constants of a pyrope-grossular-almandine garnet to 20 GPa. Geophys Res Lett 24:523-526
Chai M, Brown JM, Slutsky LJ (1997b) The elastic constants of an aluminous orthopyroxene to 12.5 GPa. J Geophys Res 102:14779-14785

EBSCOhost - printed on 2/13/2023 5:26 AM via . All use subject to https://www.ebsco.com/terms-of-use

Chen YL, Helm CA, Israelachvili JN (1991) Measurements of the elastic properties of surfactant and lipid monolayers. Langmuir 7:2694-2699

Chen G, Li B, Liebermann RC (1996a) Selected elastic moduli of single-crystal olivines from ultrasonic experiments to mantle pressures. Science 272:979-980

Chen G, Yoneda A, Getting IC, Spetzler HA (1996b) Cross pressure and temperature derivatives of selected elastic moduli for olivine from gigahertz ultrasonic interferometry. J Geophys Res 101:25161-25171

Chen G, Liebermann RC, Weidner DJ (1998) Elasticity of single-crystal MgO to 8 Gigapascals and 1600 Kelvin. Science 280:1913-1916

Chen C-C, Lin C-C, Liu L-G, Sinogeikin SV, Bass JD (2001) Elasticity of single-crystal calcite and rhodochrosite by Brillouin spectroscopy. Am Mineral 86:1525-1529

Chen P-F, Chiao L-Y, Huang P-h, Yang Y-j, Liu L-g (2006) Elasticity of magnesite and dolomite from a genetic algorithm for inverting Brillouin spectroscopy measurements. Phys Earth Planet Inter 155:73-86

Chen B, Gleason AE, Yan JY, Koski KJ, Clark S, Jeanloz R (2010) Elasticity, strength, and refractive index of argon at high pressures. Phys Rev B 81:144110

Cheng W, Wang J, Jonas U, Fytas G, Stefanou N (2006) Observation and tuning of hypersonic bandgaps in colloidal crystals. Nat Mater 5:830-836

Chirita M, Sooryakumar R, Venugopal R, Wan J, Melloch MR (2001) Acoustic barriers and observation of guided elastic waves in GaN-AlN structures by Brillouin scattering. Phys Rev B 63:205302

Collins MD, Brown JM (1998) Elasticity of an upper mantle clinopyroxene. Phys Chem Miner 26:7-13

Comins JD (2001) Surface Brillouin scattering. *In*: Handbook of Elastic Properties of Solids, Liquids, and Gases, vol. 1. Dynamic Mehods for Measuring the Elastic Properties of Solids. Levy M, Bass H, Stern R and Keppens V (eds) Academic Press, New York, p 349-378

Comins JD, Every AG, Stoddart PR, Zhang X, Crowhurst JC, Hearne GR (2000) Surface Brillouin scattering of opaque solids and thin supported films. Ultrasonics 38:450-458

Conrad PG, Zha C-S, Mao H-K, Hemley RJ (1999) The high-pressure, single-crystal elasticity of pyrope, grossular, and andradite. Am Mineral 84:374-383

Crew DC, Stamps RL, Liu HY, Wang ZK, Kuok MH, Ng SC, Barmak K, Kim J, Lewis LH (2004) Spin wave excitations in exchange spring Co/CoPt thin film bilayers. J Magn Magn Mater 272-276(1):273-274

Crew DC, Stamps RL, Liu HY, Wang ZK, Kuok MH, Ng SC, Barmak K, Kim J, Lewis LH (2005) Light scattering from spin wave excitations in a Co/CoPt exchange spring. J Magn Magn Mater 2900291(1):530-532

Crowhurst JC, Hearne GR, Comins JD, Every AG, Stoddart PR (1999) Surface Brillouin scattering at high pressure: Application to a thin supported gold film. Phys Rev B 60:R14990

Crowhurst JC, Goncharov AF, Zaug JM (2005) Direct measurements of the elastic proeprties of iron and cobalt to 120 GPa - Implications for the composition of Earth's core. *In*: Advances in High-Pressure Technology for Geophysical Applications. Chen J, Wang Y, Duffy TS, Shen G and Dobrzhinetskaya LF (eds) Elsevier, Amsterdam, p 3-23

Crowhurst JC, Brown JM, Goncharov AF, Jacobsen SD (2008) Elasticity of (Mg,Fe)O through the spin transition of iron in the lower mantle. Science 319:451-453

Cummins HZ, Gammon RW (1965) Rayleigh and Brillouin scattering in benzene: Depolarization factors. Appl Phys Lett 6:171-173

Cummins HZ, Schoen PE (1972) Linear scattering from thermal fluctuations. *In*: Laser handbook. Arecchi FT and Schultz-DuBois EO (eds). North Holland Publishing Co., Amsterdam, p 1029-1075

Cusack S, Miller A (1979) Determination of the elastic constants of collagen by Brillouin light scattering. J Mol Biol 135:39-51

Dai L, Kudo Y, Hirose K, Murakami M, Asahara Y, Ozawa H, Ohishi Y, Hirao N (2013) Sound velocities of $Na_{0.4}Mg_{0.6}Al_{1.6}Si_{0.4}O_4$ NAL and CF phases to 73 GPa determined by Brillouin scattering. Phys Chem Miner 40:195-201; doi: 10.1007/s00269-012-0558-0

de Bernabé A, Prieto C, Cáceres D, Vergara I, Every AG, Fischer HE (2001) Anomalous elastic properties of Si/Ge superlattices: The role of interfaces. Phys Status Solidi A 188:1023-1040

Decremps F, Belliard L, Gauthier M, Perrin B (2010) Equation of state, stability, anisotropy and nonlinear elasticity of diamond-cubic (ZB) silicon by phonon imaging at high pressure. Phys Rev B 82:104119

Demokritov SO, Demidov VE, Dzyapko O, Melkov GA, Serga AA, Hillebrands B, Slavin AN (2006) Bose-Einstein condensation of quasi-equilibrium magnons at room temperature under pumping. Nature 443:430-433

Dervisch A, Loudon R (1976) Theory of the Brillouin scattering lineshape in an opaque material. J Phys C Solid State Physics 9:L669-L673

Devaty RP, Clouter MJ, Ke Y, Choyke WJ (2010) Elastic waves in nano-columnar porous 4H-SiC measured by Brillouin scattering. Mater Sci Forum 645-648:447-450

Dil JG (1982) Brillouin scattering in condensed matter. Rep Prog Phys 45:285-334

Dil JG, Brody EM (1976) Brillouin scattering from isotropic metals. Phys Rev B 14:5218-5227

EBSCOhost - printed on 2/13/2023 5:26 AM via . All use subject to https://www.ebsco.com/terms-of-use

Dil JG, van Hijningen NCJA, van Dorst F, Aarts RM (1981) Tandem multipass Fabry-Perot interferometer for Brillouin scattering. Appl Optics 20:1374-1381
Djemia P, Dugautier C, Chauveau T, Dogheche E, De Barros MI, Vandenbulcke L (2001) Mechanical properties of diamond films: A comparative study of polycrystalline and smooth fine-grained diamonds by Brillouin light scattering. J Appl Phys 90:3771-3779
Dubrovinsky L, Glazyrin K, McCammon C, Narygina O, Greenberg E, Ubelhack S, Chumakov AI, Pascarelli S, Prakapenka V, Bock J, Dubrovinskaia N (2009) Portable laser-heating system for diamond anvil cells. J Synchrotron Radiat 16:737-741
Dubrovinsky L, Boffa-Ballaran T, Glazyrin K, Kurnosov A, Frost D, Merlini M, Hanfland M, Prakapenka VB, Schouwink P, Pippinger T, Dubrovinskaia N (2010) Single-crystal X-ray diffraction at megabar pressures and temperatures of thousands of degrees. High Press Res 30:620-633
Duffy TS, Vaughan MT (1988) Elasticity of enstatite and its relationship to crystal structure. J Geophys Res 93:383-391
Duffy TS, Anderson DL (1989) Seismic velocities in mantle minerals and the mineralogy of the upper mantle. J Geophys Res B 94:1895-1912
Duffy TS, Vos WL, Zha C-S, Hemley RJ, Mao H-k (1994) Sound velocities in dense hydrogen and the interior of Jupiter. Science 263:1590-1593
Duffy TS, Zha C-s, Downs RT, Mao H-k, Hemley RJ (1995) Elasticity of forsterite to 16 GPa and the composition of the upper mantle. Nature 378:170-173
Durvasula LN, Gammon RW (1978) Pressure-scanned three-pass Fabry-Perot interferometer. Appl Optics 17:3298-3303
Dziewonski AM, Anderson DL (1981) Preliminary reference Earth model. Phys Earth Planet Inter 25:297-356
Einstein A (1910) Theorie der Opaleszenz von homogenen Flüssigkeiten und Flüssigkeitsgemischen in der Nähe des kritischen Zustandes. Ann Phys 33:1275-1298
Eremets M (1996) High Pressure Experimental Methods. Oxford University Press
Eschbach J, Rouxel D, Vincent B, Mugnier Y, Galez C, Le Dantec R, Bourson P, Krüger JK, Elmazria O, Alnot P (2007) Development and characterization of nanocomposite materials. Mater Sci Eng C 27:1260-1264
Every AG (1980) General closed-form expressions for acoustic waves in elastically anisotropic solids. Phys Rev B 22:1746-1760
Every AG (2001) The elastic properties of solids: Static and dynamic properties. *In*: Handbook of Elastic Properties of Solids, Liquids, and Gases. Volume 1: Dynamic Methods for Measuring the Elastic Properties of Solids. Levy M, Bass H, Stern R and Keppens V (eds) Academic Press, New York, p 3-36
Every AG (2002) Measurement of the near-surface elastic properties of solids and thin supported films. Meas Sci Technol 13:R21-R39
Fabelinskii IL (1968) Molecular Scattering of Light. Plenum, New York
Fioretto D, Comez L, Socino G, Verdini L, Corezzi S, Rolla PA (1999) Dynamics of density fluctuations of a glass-forming epoxy resin revealed by Brillouin light scattering. Phys Rev E 59:1899-1907
Fiquet G, Badro J, Guyot F, Requardt H, Krisch M (2001) Sound velocities in iron to 110 Gigapascals. Science 291:468-471
Fleury PA (1970) Light scattering as a probe of phonons and other excitations. *In*: Physical Acoustics. Mason WP, Thurston RN (eds). Academic Press, New York, p 1-64
Fouch MJ, Rondenay S (2006) Seismic anisotropy beneath stable continental interiors. Phys Earth Planet Inter 158:292-320
Fritzel TLB, Bass JD (1997) Sound velocities of clinohumite, and implications for water in Earth's upper mantle. Geophys Res Lett 24:1023-1026
Frost DJ (2008) The upper mantle and transition zone. Elements 4:171-176
Funamori N, Yagi T, Uchida T (1994) Deviatoric stress measurement under uniaxial compression by a powder X-ray diffraction method. J Appl Phys 75:4327-4331
Gagnon RE, Kiefte H, Clouter MJ, Whalley E (1990) Acoustic velocities and densities of polycrystalline ice Ih, II, III, V, and VI by Brillouin spectroscopy. J Chem Phys 92:1909-1914
Gammon PH, Kiefte H, Clouter MJ (1983) Elastic constants of ice samples by Brillouin spectroscopy. The J Phys Chem 87:4025-4029
Gardon R (1956) The emissivity of transparent materials. J Am Ceram Soc 39:278-285
Garnero EJ, Moore MM, Lay T, Fouch MJ (2004) Isotropy or weak vertical transverse isotropy in D'' beneath the Atlantic Ocean. J Geophys Res 109:B08308
Gautieri A, Vesentini S, Redaelli A, Buehler MJ (2012) Viscoelastic properties of model segments of collagen molecules. Matrix Biol 31:141-149
Gehrsitz S, Sigg H, Siegwart H, Krieger M, Heine C, Morf R, Reinhart FK, Martin W, Rudigier H (1997) Tandem triple-pass Fabry-Perot interferometer for applications in the near infrared. Appl Opt 36:5355-5361
Gigault C, Dutcher JR (1998) Analysis of a simple method for the reduction of phonon peak broadening in surface Brillouin light scattering. Appl Opt 37:3318-3323

EBSCOhost - printed on 2/13/2023 5:26 AM via . All use subject to https://www.ebsco.com/terms-of-use

Giordano VM, Datchi F, Dewaele A (2006) Melting curve and fluid equation of state of carbon dioxide at high pressure and high temperature. J Chem Phys 125:54504-54508
Gleason AE, Chen B, Jeanloz R (2009) Grain-boundary effects in Brillouin scattering at ambient and high pressure. Geophys Res Lett 36:L23309
Gleason AE, Marquardt H, Chen B, Speziale S, Wu J, Jeanloz R (2011) Anomalous sound velocities in polycrystalline MgO under non-hydrostatic compression. Geophys Res Lett 38:L03304
Goncharov AF, Crowhurst JC (2005) Raman spectroscopy under extreme conditions. J Low Temp Phys 139:727-737
Goncharov AF, Sinogeikin S, Crowhurst JC, Ahart M, Lakshtanov D, Prakapenka V, Bass J, Beck P, Tkachev SN, Zaug JM, Fei Y (2007) Cubic boron nitride as a primary calibrant for a high temperature pressure scale. High Press Res 27:409-417
Graczykowski B, Mroz B, Mielcarek S, Breczewski T, M LN, Juan JS (2011) Surface acoustic waves and elastic constants of Cu14%Al4%Ni shape memory alloys studied by Brillouin light scattering. J Phys D Appl Phys 44:455307
Gregoryanz E, Hemley RJ, Mao H-k, Gillet P (2000) High-pressure elasticity of α-quartz: Instability and ferroelastic transition. Phys Rev Lett 84:3117-3120
Grigoriantz E, Clouter MJ (1998) The elastic constants of CH_4 by Brillouin spectroscopy. J Low Temp Phys 111:717-722
Grimsditch M, Polian A (1989) Brillouin scattering at high pressures. *In*: Simple Molecular Systems at Very High Density. Polian A, Loubeyre P and Boccara N (eds) Plenum, New York, p 237-255
Grimsditch MH, Ramdas AK (1976) Elastic and elasto-optic constants of rutile from a Brillouin scattering study. Phys Rev B 14:1670-1682
Grimsditch M, Malozemoff A, Brunsch A (1979) Standing spin waves observed by Brillouin scattering in amorphous metallic $Fe_{80}B_{20}$ films. Phys Rev Lett 43:711-714
Grimsditch M, Malozemoff A, Brunsch A, Suran G (1980) Brillouin scattering from bulk and surface magnons in amorphous magnetic metals. J Magn Magn Mater 15-18(2):769-770
Grimsditch M, Loubeyre P, Polian A (1986) Brillouin scattering and three-body forces in argon at high pressures. Phys Rev B 33:7192-7200
Grimsditch M, Kumar S, Goldman RS (1994a) A Brillouin scattering investigation of NiO. J Magn Magn Mater 129:327-333
Grimsditch MH, Zouboulis ES, Polian A (1994b) Elastic constants of boron nitride. J Appl Phys 76:832-834
Grimsditch M, Guedes I, Vavassori P, Metlushko V, Ilic B, Neuzil P, Kumar R (2001) Brillouin scattering and diffracted magneto-optical Kerr effect from arrays of dots and antidots (invited). J Appl Phys 89:7096-7100
Gross E (1930a) Change of wavelength of light due to elastic heat waves at scattering of liquids. Nature 126:201-202
Gross E (1930b) Über Änderung der Wellenlänge bei Lichtzerstreuung in Kristallen. Z Phys A 63:685-587
Grünberg P, Metawe F (1977) Light scattering from bulk and surface spin waves in EuO. Phys Rev Lett 39:1561-1565
Gwanmesia GD, Zhang J, Darling K, Kung J, Li B, Wang L, Neuville D, Liebermann RC (2006) Elasticity of polycrystalline pyrope ($Mg_3Al_2Si_3O_{12}$) to 9 GPa and 1000 °C. Phys Earth Planet Inter 155:179-190
Gwanmesia GD, Wang L, Triplett R, Liebermann RC (2009) Pressure and temperature dependence of the elasticity of pyrope–majorite [Py60Mj40 and Py50Mj50] garnets solid solution measured by ultrasonic interferometry technique. Phys Earth Planet Inter 174:105-112
Harley RT, Manning DI, Ryan JF (1978) A vacuum furnace for optical spectroscopy. J Phys E Sci Instrum 11:517-520
Hashimoto E, Aoki Y, Seshimo Y, Sasanuma K, Ike Y, Kojima S (2008) Dehydration process of protein crystals by micro-Brillouin scattering. Jap J Appl Phys 47:3839-3842
Hehlen B, Pérou A-L, Courtens E, Vacher R (1995) Observation of a doublet in the quasielastic central peak of quantum-paraelectric $SrTiO_3$. Phys Rev Lett 75:2416-2419
Heiman D, Hamilton DS, Hellwarth RW (1979) Brillouin scattering measurements on optical glasses. Phys Rev B 19:6583-6592
Hernandez G (1988) Fabry-Perot Interferometers. Cambridge University Press
Hernandez J, Li G, Cummins HZ, Callender RH, Pick RM (1996) Low-frequency light-scattering spectroscopy of powders. J Opt Soc Am B 13:1130-1134
Hicken RJ, Eley DEP, Gester M, Gray SJ, Daboo C, Ives AJR, Bland JAC (1995) Brillouin light scattering studies of magnetic anisotropy in epitaxial Fe/GaAs films. J Magn Magn Mater 145:278-292
Higo Y, Inoue T, Irifune T, Funakoshi K-i, Li B (2008) Elastic wave velocities of $(Mg_{0.91}Fe_{0.09})_2SiO_4$ ringwoodite under P-T conditions of the mantle transition region. Phys Earth Planet Inter 166:167-174
Hillebrands B (1999) Progress in multipass tandem Fabry--Perot interferometry: I. A fully automated, easy to use, self-aligning spectrometer with increased stability and flexibility. Rev Sci Instrum 70:1589-1598
Hillebrands B, Baumgart P, Mock R, Guntherodt G, Bechthold PS (1985) Dispersion of localized elastic modes in thin supported gold layers measured by Brillouin scattering. J Appl Phys 58:3166-3168

EBSCOhost - printed on 2/13/2023 5:26 AM via . All use subject to https://www.ebsco.com/terms-of-use

Hushur A, Manghnani MH, Williams Q, Dingwell DB (2013) A high-temperature Brillouin scattering study of four compositions of haplogranitic glasses and melts: High-frequency elastic behavior through glass transition. Am Mineral 98:367-375

Inoue T, Weidner DJ, Northrup PA, Parise JB (1998) Elastic properties of hydrous ringwoodite (γ-phase) in Mg_2SiO_4. Earth Planet Sci Lett 160:107-113

Irifune T, Higo Y, Inoue T, Kono Y, Ohfuji H, Funakoshi K (2008) Sound velocities of majorite garnet and the composition of the mantle transition region. Nature 451:814-817, doi: 10.1038/nature06551

Isaak DG (1992) High-temperature elasticity of iron-bearing olivines. J Geophys Res 97:1871-1885

Isaak DG, Ohno I (2003) Elastic constants of chrome-diopside: Application of resonant ultrasound spectroscopy to monoclinic single-crystals. Phys Chem Miner 30:430-439

Isaak DG, Anderson OL, Goto T, Suzuki I (1989) Elasticity of single-crystal forsterite measured to 1700 K. J Geophys Res 94:5895-5906

Isaak DG, Anderson OL, Oda H (1992) High-temperature thermal expansion and elasticity of calcium-rich garnets. Phys Chem Miner 19:106-120

Isaak DG, Ohno I, Lee PC (2006) The elastic constants of monoclinic single-crystal chrome-diopside to 1,300 K. Phys Chem Miner 32:691-699

Isaak DG, Gwanmesia GD, Falde D, Davis MG, Triplett RS, Wang L (2007) The elastic properties of β-Mg_2SiO_4 from 295 to 660 K and implications on the composition of Earth's upper mantle. Phys Earth Planet Inter 162:22-31

Ishii M, Dziewonski AM (2002) The innermost inner core of the earth: Evidence for a change in anisotropic behaviorat the radius of about 300 km. Proc Natl Acad Sci USA 99:14026-14030

Jackson JM, Sinogeikin SV, Bass JD (1999) Elasticity of $MgSiO_3$ orthoenstatite. Am Mineral 84:677-680

Jackson JM, Sinogeikin SV, Bass JD (2000) Sound velocities and elastic properties of γ-Mg_2SiO_4 to 873 K by Brillouin spectroscopy. Am Mineral 85:296-303

Jackson JM, Sinogeikin SV, Carpenter MA, Bass JD (2004a) Novel phase transition in orthoenstatite. Am Mineral 89:239-244

Jackson JM, Zhang J, Bass JD (2004b) Sound velocities and elasticity of aluminous $MgSiO_3$ perovskite; implications for aluminum heterogeneity in Earth's lower mantle. Geophys Res Lett 31:L10614

Jackson JM, Zhang J, Shu J, Sinogeikin SV, Bass JD (2005) High-pressure sound velocities and elasticity of aluminous $MgSiO_3$ perovskite to 45 GPa: Implications for lateral heterogeneity in Earth's lower mantle. Geophys Res Lett 32:L21305

Jackson JM, Sinogeikin SV, Jacobsen SD, Reichmann HJ, Mackwell SJ, Bass JD (2006) Single-crystal elasticity and sound velocities of $(Mg_{0.94}Fe_{0.06})O$ ferropericlase to 20 GPa. J Geophys Res 111:B09203

Jackson JM, Sinogeikin SV, Bass JD (2007) Sound velocities and single-crystal elasticity of orthoenstatite to 1073 K at ambient pressure. Phys Earth Planet Inter 161:1-12

Jacobsen SD, Smyth JR (2006) Effect of water on the sound velocities of ringwoodite in the transition zone. *In*: Earth's Deep Water Cycle, Geophysical Monograph 168. Jacobsen SD and van der Lee S (eds) American Geophysical Union, p 131-145

Jacobsen SD, Smyth JR, Spetzler H, Holl CM, Frost DJ (2004) Sound velocities and elastic constants of iron-bearing hydrous ringwoodite. Phys Earth Planet Inter 143:47-56

Jacobsen SD, Jiang F, Mao Z, Duffy TS, Smyth JR, Holl CM, Frost DJ (2008) Effects of hydration on the elastic properties of olivine. Geophys Res Lett 35:L14303

Jacquinot P (1960) New developments in interference spectroscopy. Rep Prog Phys 23:267-312

Jantz W, Wettling W, Sandercock JR (1976) Determination of magnetic and elastic properties of $FeBO_3$ by light scattering. J Phys C Solid State Phys 9:2229-2240

Jia R, Li F, Li M, Cui Q, He Z, Wang L, Zhou Q, Cui T, Zou G, Bi Y, Hong S, Jing F (2008) Brillouin scattering studies of liquid argon at high temperatures and high pressures. J Chem Phys 129:154503-154507

Jiang FM, Kojima S (2000) Microheterogeneity and relaxation in $0.65Pb(Mg_{1/3}Nb_{2/3})O_3$-$0.35PbTiO_3$ relaxor single crystals. Appl Phys Lett 77:1271-1273

Jiang F, Speziale S, Duffy TS (2004a) Single-crystal elasticity of grossular- and almandine-rich garnets to 11 GPa by Brillouin scattering. J Geophys Res 109:B10210

Jiang F, Speziale S, Shieh SR, Duffy TS (2004b) Single-crystal elasticity of andradite garnet to 11 GPa. J Phys Condens Matter 16:S1041-1052

Jiang F, Speziale S, Duffy TS (2006) Single-crystal elasticity of brucite, $Mg(OH)_2$, to 15 GPa by Brillouin scattering. Am Mineral 91:1893-1900

Jiang F, Majzlan J, Speziale S, He D, Duffy TS (2008) Single-crystal elasticity of diaspore, AlOOH, to 12GPa by Brillouin scattering. Phys Earth Planet Inter 170:221-228

Jiang F, Gwanmesia GD, Dyuzheva TI, Duffy TS (2009) Elasticity of stishovite and acoustic mode softening under high pressure by Brillouin scattering. Phys Earth Planet Inter 172:235-240

Jiang X, Harzer JV, Hillebrands B, Wild C, Koidl P (1991) Brillouin light scattering on chemical-vapor-deposited polycrystalline diamond: Evaluation of the elastic moduli. Appl Phys Lett 59:1055-1057

EBSCOhost - printed on 2/13/2023 5:26 AM via . All use subject to https://www.ebsco.com/terms-of-use

Kamitani K, Grimsditch M, Nipko JC, Loong CK, Okada M, Kimura I (1997) The elastic constants of silicon carbide: A Brillouin-scattering study of 4H and 6H SiC single crystals. J Appl Phys 82:3152-3154

Kandelin J, Weidner DJ (1988a) Elastic properties of hedenbergite. J Geophys Res 93:1063-1072

Kandelin J, Weidner DJ (1988b) The single-crystal elastic properties of jadeite. Phys Earth Planet Inter 50:251-260

Kantor AP, Kantor IY, Kurnosov AV, Kuznetsov AY, Dubrovinskaia NA, Krisch M, Bossak AA, Dmitriev VP, Urusov VS, Dubrovinsky LS (2007) Sound wave velocities of fcc Fe-Ni alloy at high pressure and temperature by mean of inelastic X-ray scattering. Phys Earth Planet Inter 164:83-89

Kantor I, Prakapenka V, Kantor A, Dera P, Kurnosov A, Sinogeikin S, Dubrovinskaia, Dubrovinsky L (2012) BX90: A new diamond anvil cell design for X-ray diffraction and optical measurements. Rev Sci Instrum 83:125102

Karato S (2006) Influence of hydrogen-related defects on the electrical conductivity and plastic deformation of mantle minerals: A critical review. *In*: Earth's Deep Water Cycle. Geophysical Monograph Series 168. Jacobsen SD, van der Lee S (eds) AGU Washington, DC, p 113-130

Karato Si, Karki BB (2001) Origin of lateral variation of seismic wave velocities and density in the deep mantle. J Geophys Res 106:21,771-721,783

Karki BB, Wentzcovitch RM, de Gironcoli S, Baroni S (1999) First-principles determination of elastic anisotropy and wave velocities of MgO at lower mantle conditions. Science 286:1705-1707

Katsura T, Ito E (1989) The system Mg_2SiO_4-Fe_2SiO_4 at high pressures and temperatures: Precise determination of stabilities of olivine, modified spinel, and spinel. J Geophys Res 94:15663-15670

Kavner A, Nugent C (2008) Precise measurements of radial temperature gradients in the laser-heated diamond anvil cell. Rev Sci Instrum 79:024902

Kennett BLN, Engdahl ER, Buland R (1995) Constraints on seismic velocities in the Earth from traveltimes. Geophys J Int 122:108-124

Keppler H, Smyth JR (2005) Optical and near infrared spectra of ringwoodite to 21.5 GPa: Implications for radiative heat transport in the mantle. Am Mineral 90:1209-1212

Keppler H, Kantor I, Dubrovinsky L (2007) Optical absorption of ferropericlase to 84 GPa. Am Mineral 92:433-436

Keppler H, Dubrovinsky LS, Narygina O, Kantor I (2008) Optical absorption andr thermal conductivity of silicate perovskite to 125 Gigapascals. Science 322:1529-1532

Kiefer B, Duffy TS (2005) Finite element simulations of the laser-heated diamond-anvil cell. J Appl Phys 97:114902

Kiefte H, Clouter MJ, Gagnon RE (1985) Determination of acoustic velocities of clathrate hydrates by Brillouin spectroscopy. J Phys Chem 89:3103-3108

Kivelson D, Madden PA (1980) Light scattering studies of molecular liquids. Ann Rev Phys Chem 31:523-558

Ko J-H, Kim DH, Kojima S (2008) Central peaks, acoustic modes, and the dynamics of polar nanoregions in $Pb[(Zn_{1/3}Nb_{2/3})_xTi_{1-x}]O_3$ single crystals studied by Brillouin spectroscopy. Phys Rev B 77:104110

Kohlstedt DL, Keppler H, Rubie DC (1996) Solubility of water in the α, β and γ phases of $(Mg,Fe)_2SiO_4$. Contrib Mineral Petrol 123:345-357

Koreeda A, Nagano T, Ohno S, Saikan S (2006) Quasielastic light scattering in rutile, ZnSe, silicon, and $SrTiO_3$. Phys Rev B 73:024303

Kotane LM, Comins JD, Every AG, Botha JR (2011) Surface Brillouin scattering measurement of the elastic constants of single crystal $InAs_{0.91}Sb_{0.09}$. J Phys Conf Ser 278:012001

Kriegs H, Petekidis G, Fytas G, Penciu RS, Economou EN, Schofield AB (2004) Phonons in suspensions of hard sphere colloids: Volume fraction dependence. J Chem Phys 121:7849-7854

Krishnan RS (1971). Brillouin scattering. *In*: The Raman Effect. Vol 1. Anderson A (ed) Dekker, New York, p 343-404

Krüger JK (1989). Brillouin spectroscopy and its application to polymers. *In*: Optical Techniques to Characterize Polymer Systems, Volume 5. Bässler H (eds) Elsevier, Amsterdam, p 429-534

Krüger JK, Marx A, Peetz L, Roberts R, Unruh HG (1986) Simultaneous determination of elastic and optical properties of polymers by high performance Brillouin spectroscopy using different scattering geometries. Colloid Polym Sci 264:403-414

Krüger JK, Embs JP, Brierley J, Jiménez R (1998) A new Brillouin scattering technique for the investigation of acoustic and opto-acoustic properties: Application to polymers. J Phys D Appl Phys 31:1913-1917

Krüger JK, Embs JP, Lukas S, Hartmann U, Brierley CJ, Beck CM, Jimenez R, Alnot P, Durand O (2000) Spatial and angle distribution of internal stresses in nano- and microstructured chemical vapor deposited diamond as revealed by Brillouin spectroscopy. J Appl Phys 87:74-77

Kudo Y, Hirose K, Murakami M, Asahara Y, Ozawa H, Ohishi Y, Hirao N (2012) Sound velocity measurements of $CaSiO_3$ perovskite to 133 GPa and implications for lowermost mantle seismic anomalies. Earth Planet Sci Lett 349-350:1-7

Kumazawa M, Anderson OL (1969) Elastic moduli, pressure derivatives, and temperature derivatives of single-crystal olivine and single-crystal forsterite. J Geophys Res 74:5961-5972

EBSCOhost - printed on 2/13/2023 5:26 AM via . All use subject to https://www.ebsco.com/terms-of-use

Kung J, Li B, Uchida T, Wang Y (2005) In-situ elasticity measurement for the unquenchable high-pressure clinopyroxene phase: Implication for the upper mantle. Geophys Res Lett 32:L01307
Kustowski B, Ekstrom G, Dziewonski AM (2008) Anisotropic shear-wave velocity structure of the Earth's mantle: A global model. J Geophys Res 113:B06306
Lakshtanov DL, Sinogeikin SV, Litasov KD, Prakapenka VB, Hellwig H, Wang J, Sanches-Valle C, Perrillat J-P, Chen B, Somayazulu M, Li J, Ohtani E, Bass JD (2007) The post-stishovite phase transition in hydrous alumina-bearing SiO_2 in the lower mantle of the earth. Proc Natl Acad Sci 104:13588-13590
Landau LD, Lifshitz EM (1969) Statistical Physics, Course of Theoretical Physics. Pergamon Press, Oxford
Landau LD, Placzek G (1934) Structure of the undisplaced line of scattering. Phys Z Sowjetunion 5:172
Lee SA, Pinnick DA, Lindsay SM, Hanson RC (1986) Elastic and photoelastic anisotropy of solid HF at high pressure. Phys Rev B 34:2799-2806
Lee SA, Lindsay SM, Powell JW, Weidlich T, Tao NJ, Lewen GD, Rupprecht A (1987) A Brillouin scattering study of the hydration of Li- and Na-DNA films. Biopolymers 26:1637-1665
Lee SA, Flowers MR, Oliver WF, Rupprecht A, Lindsay SM (1993) Brillouin-scattering study of hyaluronic acid: Dynamic coupling with the water of hydration and phase transitions. Phys Rev E 47:677-683
LePesant J-P, Powers L, Pershan PS (1978) Brillouin light scattering measurement of the elastic properties of aligned multilamella lipid samples. Proc Natl Acad Sci 75:1792-1795
Levelut C, Scheyer Y, Boissier M, Pelous J, Durand D, Emery JR (1996) A Brillouin scattering investigation of relaxation versus crosslink density in glass- and gel-forming polymers. J Phys Condens Matter 8:941-957
Levien L, Weidner D, Prewitt C (1979) Elasticity of diopside. Phys Chem Miner 4:105-113
Li B, Zhang J (2005) Pressure and temperature dependence of elastic wave velocity of $MgSiO_3$ perovskite and the composition of the lower mantle. Phys Earth Planet Inter 151:143-154
Li B, Liebermann RC, Weidner DJ (1998) Elastic moduli of wadsleyite (β-Mg_2SiO_4) to 7 Gigapascals and 873 Kelvin. Science 281:675-677
Li Bassi A, Bottani CE, Casari C, Beghi M (2004) Inelastic light scattering: A multiscale characterization approach to vibrational, structural and thermo-mechanical properties of nanostructured materials. Appl Surf Sci 226:271-281
Li F, Cui Q, He Z, Cui T, Gao C, Zhou Q, Zou G (2006) Brillouin scattering spectroscopy for a laser heated diamond anvil cell. Appl Phys Lett 88:203507-203503
Li L, Weidner DJ, Brodholt JP, Alfè D (2011) Prospecting for water in the transition zone: d ln(Vs)/d ln(Vp). Phys Earth Planet Inter 189:117-120
Liermann H-P, Merkel S, Miyagi L, Wenk H-R, Shen G, Cynn H, Evans WJ (2009) Experimental method for *In situ* determination of material textures at simultaneous high pressure and high temperature by means of radial diffraction in the diamond anvil cell. Rev Sci Instrum 80:104501
Lin C-C, Chen C-C (2011) Elasticity of tephroite (α-Mn_2SiO_4) and a comparison of the elastic properties of silicate olivines. Eur J Mineral 23:35-43
Lin J-F, Struzhkin VV, Jacobsen SD, Hu MY, Chow P, Kung J, Liu H, Mao H-k, Hemley RJ (2005) Spin transition of iron in magnesiowüstite in the Earth's lower mantle. Nature 436:377-380
Lin J-F, Speziale S, Mao Z, Marquardt H (2013) Effects of the electronic spin transitions of iron in lower-mantle minerals: Implications for deep-mantle geophysics and geochemistry. Rev Geophys 51:244-275
Lindsay SM, Anderson MW, Sandercock JR (1981) Construction and alignment of a high performance multipass vernier tandem Fabry-Perot interferometer. Rev Sci Instrum 52:1478-1486
Liu W, Kung J, Li B (2005) Elasticity of San Carlos olivine to 8 GPa and 1073 K. Geophys Res Lett 32:L16301
Loheider S, Vogler G, Petscherizin I, Soltwisch M, Quitmann D (1990) Brillouin scattering on the glass former $GeSBr_2$. J Chem Phys 93:5436-5447
Loudon R (1978) Theory of lineshapes for oblique-incidence Brillouin scattering by acoustic phonons. J Phys C: Solid State Physics 11:2623-2637
Loudon R, Sandercock JR (1980) Analysis of the light-scattering cross section for surface ripples on solids. J Phys C: Solid State Physics 13:2609-2622
Love AEH (1911) Some Problems of Geodynamics. Cambridge University Press,
Liu C, Mao Z, Lin J-F, Zhuvarlev KK, Tkachev SN, Prakapenka VB (2013) Elasticity of iron-bearing pyrope to 20 GPa and 750 K. Earth Planet Sci Lett 361:134-142
Lucas HC, Jackson DA, Powles JG, Simic-Glavaski B (1970) Temperature variation of polarized and depolarized scattered light spectra from liquid benzene derivatives. Molec Phys 18:505-521
Lyons KB, Fleury PA (1976) Dynamic central peaks in a crystalline solid: $KTaO_3$. Phys Rev Lett 37:161-164
Majzlan J, Speziale S, Duffy T, Burns P (2006) Single-crystal elastic properties of alunite, $KAl_3(SO_4)_2(OH)_6$. Phys Chem Miner 33:567-573
Mandelstam LI (1926) On light scattering by an inhomogeneous medium (in Russian). J Russian Phys Chem Soc 58:381-
Manghnani MH, Tkachev SN, Zinin PV, Glorieoux C, Karvankova P, Veprek S (2005) Elastic properties of nc-TiN/a-Si_3N_4 and nc-TiN/a-BN nanocomposite films by surface Brillouin scattering. J Appl Phys 97:054308

EBSCOhost - printed on 2/13/2023 5:26 AM via . All use subject to https://www.ebsco.com/terms-of-use

Manglkammer W, Krüger JK (2005) Brillouin scattering of lipid membranes. J Phys IV France 129:65-67
Mantegazzi D, Sanchez-Valle C, Reusser E, Driesner T (2012) Thermodynamic properties of sodium sulfate solutions to 773 K and 3 GPa derived from acoustic velocity measurements in the diamond anvil cell. J Chem Phys 137:224501
Manthilake MAGM, Matsuzaki T, Yoshino T, Yamashita S, Ito E, Katsura T (2009) Electrical conductivity of wadsleyite as a function of temperature and water content. Phys Earth Planet Inter 174:10-18
Mao Z, Jiang F, Duffy TS (2007) Single-crystal elasticity of zoisite, $Ca_2Al_3Si_3O_{12}(OH)$, by Brillouin scattering. Am Mineral 92:570-576
Mao WL, Struzhkin VV, Baron AQR, Tsutsui S, Tommaseo CE, Wenk H-R, Hu MY, Chow P, Sturhahn W, Shu J, Hemley RJ, Heinz DL, Mao H-K (2008a) Experimental determination of the elasticity of iron at high pressure. J Geophys Res 113:B09213
Mao Z, Jacobsen SD, Jiang F, Smyth JR, Holl CM, Duffy TS (2008b) Elasticity of hydrous wadsleyite to 12 GPa: Implications for Earth's transition zone. Geophys Res Lett 35:L21305
Mao Z, Jacobsen SD, Jiang FM, Smyth JR, Holl CM, Frost DJ, Duffy TS (2008c) Single-crystal elasticity of wadsleyites, β-Mg_2SiO_4, containing 0.37-1.66 wt.% H_2O. Earth Planet Sci Lett 268:540-549
Mao Z, Jacobsen SD, Jiang F, Smyth JR, Holl CM, Frost DJ, Duffy TS (2010) Velocity crossover between hydrous and anhydrous forsterite at high pressures. Earth Planet Sci Lett 293:250-258
Mao Z, Jacobsen SD, Frost DJ, McCammon CA, Hauri EH, Duffy TS (2011) Effect of hydration on the single-crystal elasticity of Fe-bearing wadsleyite to 12 GPa. Am Mineral 96:1606-1612
Mao Z, Lin JF, Jacobsen SD, Duffy TS, Chang Y-Y, Smyth JR, Frost DJ, Hauri E, Prakapenka V (2012) Sound velocities of hydrous ringwoodite to 16 GPa and 673 K. Earth Planet Sci Lett 331-332:112-119
Marquardt H, Marquardt K (2012) Focused ion beam preparation and characterization of single-crystal samples for high-pressure experiments in the diamond-anvil cell. Am Mineral 97:299-304
Marquardt H, Speziale S, Jahn S, Ganschow S, Schilling FR (2009a) Single-crystal elastic properties of $(Y,Yb)_3Al_5O_{12}$. J Appl Phys 106:093519
Marquardt H, Speziale S, Reichmann HJ, Frost DJ, Schilling FR (2009b) Single-crystal elasticity of $(Mg_{0.9}Fe_{0.1})O$ to 81 GPa. Earth Planet Sci Lett 287:345-352
Marquardt H, Speziale S, Reichmann HJ, Frost DJ, Schilling FR, Garnero EJ (2009c) Elastic shear anisotropy of ferropericlase in Earth's lower mantle. Science 324:224-226
Marquardt H, Gleason AE, Marquardt K, Speziale S, Miyagi L, Neusser G, Wenk HR, Jeanloz R (2011) Elastic properties of MgO nano-crystals and grain boundaries to high pressures. Phys Rev B 84:064131
Marquardt H, Speziale S, Gleason AE, Singogeikin S, Kantor I, Prapapenka V (2013a) Brillouin scattering and x-ray diffraction of solid argon to 65 GPa and 700 K: Shear strength of argon at HP/HT. J Appl Phys 114:093517
Marquardt H, Waeselmann N, Wehber M, Angel RJ, Gospodinov M, Mihailova B (2013b) High-pressure Brillouin scattering of the single-crystal $PbSc_{1/2}Ta_{1/2}O_3$ relaxor ferroelectric. Phys Rev B 87:184113
Marvin AM, Bortolani V, Nizzoli F (1980a) Surface Brillouin scattering from acoustic phonons. I. General theory. J Phys C: Solid State Physics 13:299-317
Marvin AM, Bortolani V, Nizzoli F, Santoro G (1980b) Surface Brillouin scattering from acoustic phonons. II. Application to semiconductors. J Phys C: Solid State Physics 13:1607-1616
Mathieu V, Fukui K, Matsukawa M, Kawabe M, Vayron R, Soffer E, Anagnostou F, Haiat G (2011) Micro-Brillouin scattering measurements in mature and newly formed bone tissue surrounding an implant. J Biomech Eng 133:021006
Matsuishi K, Gregoryanz E, Mao HK, Hemley RJ (2002) Brillouin and Raman scattering of fluid and solid hydrogen at high pressures and temperatures. J Phys Condens Matter 14:10631-10636
Matsuishi K, Gregoryanz E, Mao H-k, Hemley RJ (2003) Equation of state and intermolecular interactions in fluid hydrogen from Brillouin scattering at high pressures and temperatures. J Chem Phys 118:10683-10695
Matthies S, Merkel S, Wenk HR, Hemley RJ, Mao H-k (2001) Effects of texture on the determination of elasticity of polycrystalline ε-iron from diffraction measurements. Earth Planet Sci Lett 194:201-212
Maznev AA, Nelson KA, Yagi T (1996) Surface phonon spectroscopy with frequency-domain impulsive stimulated light scattering. Solid State Commun 100:807-811
McMillan PF, Akaogi M, Sato RK, Poe B, Foley J (1991) Hydroxyl groups in beta-Mg_2SiO_4. Am Mineral 76:354-360
Mei S, Kohlstedt DL (2000) Influence of water on plastic deformation of olivine aggregates 2. Dislocation creep regime. J Geophys Res 105:21471-21481
Mendik M, Sathish S, Kulik A, Gremaud G, Wachter P (1992) Surface acoustic wave studies on single-crystal nickel using Brillouin scattering and scanning acoustic microscope. J Appl Phys 71:2830-2834
Mielcarek S, Trzaskowska A, Mroz B, Breczewski T (2008) Pressure dependence of the elastic properties of composite host/guest type crystals. J Phys Condens Matter 20:365216
Milano J, Grimsditch M (2010) Magnetic field effects on the NiO magnon spectra. Phys Rev B 81:094415

EBSCOhost - printed on 2/13/2023 5:26 AM via . All use subject to https://www.ebsco.com/terms-of-use

Milano J, Steren LB, Grimsditch M (2004) Effect of dipolar interaction on the antiferromagnetic resonance spectra of NiO. Phys Rev Lett 93:077601
Miyagi L, Kanitpanyacharoen W, Kaercher P, Lee KKM, Wenk H-R (2010) Slip Systems in $MgSiO_3$ Post-Perovskite: Implications for D″ Anisotropy. Science 329:1639-1641
Mjwara PM, Comins JD, Ngoepe PE, Chadwick AV (1991) Brillouin scattering in superionic compounds: NdF_3 and CaF_2 (ReF_3). Radiat Effects Defects Solids 119-121:237-242
Mock R, Guntherodt G (1984) Bulk elastic properties of metals determined by Brillouin scattering and its application to RCu_2Si_2 (R=rare earth). J Phys C: Solid State Physics 17:5635-5644
Monaco G, Ruocco G, Comez L, Fioretto D (1998) Dynamic structure factor of glassy o-terphenyl: A Brillouin light scattering study. J Non-Cryst Solids 235-237:208-211
Mori H (1965) Transport, collective motion, and brownian motion. Prog Theor Phys 33:423-455
Mountain RD (1966a) Thermal relaxation and Brillouin scattering in liquids. J Res Natl Bureau Standards 70A:207-220
Mountain RD (1966b) Spectral distribution of scattered light in a simple fluid. Rev Modern Phys 38:205-214
Mroz B, Tuszynski JA, Kiefte H, Clouter MJ (1989) On the ferroelastic phase transition of $LiNH_4SO_4$: A Brillouin scattering study and theoretical modelling. J Phys Condens Matter 1:783-796
Murakami M, Hirose K, Kawamura K, Sata N, Ohishi Y (2004) Post-perovskite phase transition in $MgSiO_3$. Science 304:855-858
Murakami M, Sinogeikin SV, Bass JD, Sata N, Ohishi Y, Hirose K (2007a) Sound velocity of $MgSiO_3$ post-perovskite phase; A constraint on the D" discontinuity. Earth Planet Sci Lett 259:18-23
Murakami M, Sinogeikin SV, Hellwig H, Bass JD, Li J (2007b) Sound velocity of $MgSiO_3$ perovskite to Mbar pressure. Earth Planet Sci Lett 256:47-54
Murakami M, Sinogeikin SV, Litasov K, Ohtani E, Bass JD (2008) Single-crystal elasticity of iron-bearing majorite to 26 GPa: Implications for seismic velocity structure of the mantle transition zone. Earth Planet Sci Lett 274:339-345
Murakami M, Asahara Y, Ohishi Y, Hirao N, Hirose K (2009a) Development of *In situ* Brillouin spectroscopy at high pressure and high temperature with synchrotron radiation and infrared laser heating system: Application to the Earth's deep interior. Phys Earth Planet Inter 174:282-291
Murakami M, Ohishi Y, Hirao N, Hirose K (2009b) Elasticity of MgO to 130 GPa: Implications for lower mantle mineralogy. Earth Planet Sci Lett 277:123-129
Murakami M, Bass JD (2010) Spectroscopic evidence for ultrahigh-pressure polymorphism in SiO_2 glass. Phys Rev Lett 104:025504
Murakami M, Bass JD (2011) Evidence of denser $MgSiO_3$ glass above 133 gigapascal (GPa) and implications for remnants of ultradense silicate melt from a deep magma ocean. Proc Natl Acad Sci 108:17286-17289
Murakami M, Ohishi Y, Hirao N, Hirose K (2012) A perovskite lower mantle inferred from high-pressure, high-temperature sound velocity data. Nature 485:90-94
Murase S, Yanagisawa M, Sasaki S, Kume T, Shimizu H (2002) Development of low-temperature and high-pressure Brillouin scattering spectroscopy and its application to the solid I form of hydrogen sulphide. J Phys Condens Matter 14:11537-11541
Musgrave MJP (1970) Crystal Acoustics. Holden Day, San Francisco
Nelson DF, Lax M (1971) Theory of the photoelastic interaction. Phys Rev B 3:2778-2794
Nelson DF, Lazay PD, Lax M (1972) Brillouin scattering in anisotropic media: Calcite. Phys Rev B 6:3109-3120
Nelson KA, Fayer MD (1980) Laser induced phonons: A probe of intermolecular interactions in molecular solids. J Chem Phys 72:5202-5218
Nizzoli F, Sandercock JR (1990). Surface Brillouin scattering from phonons. *In*: Dynamical Properties of Solids. Horton GK, Maradudin AA (eds) North-Holland, Amsterdam, p 281-335
Nowacki A, Wookey J, Kendall JM (2011) New advances in using seismic anisotropy, mineral physics and geodynamics to understand deformation in the lowermost mantle. J Geodynam 52:205-228
Nye J (1985) Physical Properties of Crystals. Clarendon Press, Oxford
O'Connor CL, Schlupf JP (1967) Brillouin scattering in water: The Landau-Placzek ratio. J Chem Phys 47:31-38
O'Neill B, Bass JD, Smyth JR, Vaughan MT (1989) Elasticity of a grossular-pyrope-almandine garnet. J Geophys Res 94:17819-17824
O'Neill B, Bass JD, Rossman GR, Geiger CA, Langer K (1991) Elastic properties of pyrope. Phys Chem Miner 17:617-621
O'Neill B, Bass JD, Rossman GR (1993) Elastic properties of hydrogrossular garnet and implications for water in the upper mantle. J Geophys Res 98:20031-20037
Oganov AR, Ono S (2004) Theoretical and experimental evidence for a post-perovskite phase of $MgSiO_3$ in Earth's D" layer. Nature 430:445-448
Ohta R, Zushi J, Ariizumi T, Kojima S (2011) Order-disorder behavior of ferroelectric phase transition of $KTa_{1-x}Nb_xO_3$ probed by Brillouin scattering. Appl Phys Lett 98:92909-92903

EBSCOhost - printed on 2/13/2023 5:26 AM via . All use subject to https://www.ebsco.com/terms-of-use

Oliver W, Herbst C, Lindsay S, Wolf G (1992) A general method for determination of Brillouin linewidths by correction for instrumental effects and aperture broadening: Application to high-pressure diamond anvil cell experiments. Rev Sci Instrum 63:1884-1895

Pacalo REG, Weidner DJ, Gasparik T (1992) Elastic properties of sodium-rich majorite garnet. Geophys Res Lett 19:1895-1898

Palin CJ, Vinen WF, Pike ER, Vaughan JM (1971) Rayleigh and Brillouin scattering from superfluid ^{3}He- ^{4}He mixtures. J Phys C: Solid State Physics 4:L225-L228

Panero WR, Jeanloz R (2001) Temperature gradients in the laser-heated diamond anvil cell. J Geophys Res 106:6493-6498

Pang W, Every AG, Comins JD, Stoddart PR, Zhang X (1999) Brillouin scattering from acoustic excitations in TiN films on high speed steel - a stiffening system. J Appl Phys 86:311-317

Patterson GD (1976) Brillouin scattering from amorphous bisphenol-A polycarbonate. J Polymer Sci: Polymer Physics Edition 14:741-747

Patterson GD (1983) Light scattering from bulk polymers. Annu Rev Mater Sci 13:219-245

Pecora R (1972) Quasi-elastic light scattering from macromolecules. Annu Rev Biophys Bioeng 1:257-276

Peercy MS, Bass JD (1990) Elasticity of monticellite. Phys Chem Miner 17:431-437

Perrillat J-P, Nestola F, Sinogeikin S, Bass JD (2007) Single-crystal elastic properties of $Ca_{0.07}Mg_{1.93}Si_2O_6$. Am Mineral 92:109-113

Perzlmaier K, Buess M, Back CH, Demidov VE, Hillebrands B, Demokritov SO (2005) Spin-wave eigenmodes of permalloy squares with a closure domain structure. Phys Rev Lett 94:057202

Pike ER, Vaughan JM, Vinen WF (1970) Brillouin scattering from superfluid ^{4}He. J Phys C: Solid State Physics 3:L40-L43

Polian A (2003) Brillouin scattering at high pressure: An overview. J Raman Spectrosc 34:633-637

Polian A, Grimsditch M (1984) New high-pressure phase of H_2O: Ice X. Phys Rev Lett 52:1312-1314

Polian A, Grimsditch M (1986) Elastic properties and density of helium up to 20 GPa. Europhys Lett 2:849-855

Polian A, Grimsditch M, Grzegory I (1996) Elastic constants of gallium nitride. J Appl Phys 79:3343-3344

Polian A, Dung V-T, Richet P (2002) Elastic properties of a-SiO_2 up to 2300 K from Brillouin scattering measurements. Europhys Lett 57:375-381

Qin J, Li M, Li J, Chen R, Duan Z, Zhou Q, Li F, Cui Q (2010) High temperatures and high pressures Brillouin scattering studies of liquid H_2O + CO_2 mixtures. J Chem Phys 133:154513-154516

Raman CV, Venkateswaran CS (1938) Optical observation of the Debye heat waves in crystals. Nature 142:250-250

Rand SC, Stoicheff BP (1982) Elastic and photo-elastic constants of CH_4 and CD_4 obtained by Brillouin scattering. Can J Phys 60:287-298

Randall J, Vaughan JM (1982) The measurement and interpretation of Brillouin scattering in the lens of the eye. Proc Royal Soc London. Series B. Biological Sci 214:449-470

Rantala TT, Levoska J (1989) A numerical simulation method for the laser-induced temperature distribution. J Appl Phys 65:4475-4479

Rat E, Foret M, Massiera G, Vialla R, Arai M, Vacher R, Courtens E (2005) Anharmonic versus relaxational sound damping in glasses. I. Brillouin scattering from densified silica. Phys Rev B 72:214204

Rayleigh L (1899) On the transmission of light through an athmosphere containing small particles in suspension, and on the origin of the blue of the sky. Philos Mag 47:375-394

Reichmann HJ, Sinogeikin SV, Bass JD, Gasparik T (2002) Elastic moduli of jadeite-enstatite majorite. Geophys Res Lett 29:1936-1239

Reichmann HJ, Sinogeikin SV, Bass JD (2008) Single-crystal elastic properties of $(Mg_{0.987}Fe_{0.013})O$ to 9 GPa Am Mineral 93:1306-1311

Reynard B, Bass JD, Brenizer J (2010) High-temperature elastic softening of orthopyroxene and seismic properties of the lithospheric upper mantle. Geophys J Int 181:557-566

Ringwood AE, Major A (1966) Synthesis of Mg_2SiO_4-Fe_2SiO_4 spinel solid solutions. Earth Planet Sci Lett 1:241-245

Rosa AD, Sanchez-Valle C, Gosh S (2012) Elasticity of phase D and implication for the degree of hydration of deep subducted slabs. Geophys Res Lett 39:L06304

Rowell NL, Stegeman GI (1978) Theory of Brillouin scattering from opaque media. Phys Rev B 18:2598-2615,

Rytov SM (1958) Correlation theory of thermal fluctuations in an isotropic medium. Soviet Physics JETP 6:130-140

Rytov SM (1970) Relaxation theory of Rayleigh scattering. Soviet Physics JETP 31:1163-1171

Sakamoto M, Kawabe M, Matsukawa M, Koizumi N, Ohtori N (2008) Measurement of wave velocity in bovine bone tissue by micro-Brillouin scattering. Japan Soc Appl Phys 47:4205-4208

Sanchez-Valle C, Bass JD (2010) Elasticity and pressure-induced structural changes in vitreous $MgSiO_3$-enstatite to lower mantle pressures. Earth Planet Sci Lett 295:523-530

EBSCOhost - printed on 2/13/2023 5:26 AM via . All use subject to https://www.ebsco.com/terms-of-use

Sanchez-Valle C, Sinogeikin SV, Lethbridge ZAD, Walton RI, Smith CW, Evans KE, Bass JD (2005) Brillouin scattering study on the single-crystal elastic properties of natrolite and analcime zeolites. J Appl Phys 98:053508

Sanchez-Valle C, Sinogeikin SV, Smyth JR, Bass JD (2008) Sound velocities and elasticity of DHMS phase A to high pressure and implications for seismic velocities and anisotropy in subducted slabs. Phys Earth Planet Inter 170:229-239

Sanchez-Valle C, Chio C-H, Gatta GD (2010) Single-crystal elastic properties of $(Cs,Na)AlSi_2O_6{\cdot}H_2O$ pollucite: A zeolite with potential use for long-term storage of Cs radioisotopes. J Appl Phys 108:093509

Sanchez-Valle C, Ghosh S, Rosa AD (2011) Sound velocities of ferromagnesian carbonates and the seismic detection of carbonates in eclogites and the mantle. Geophys Res Lett 38:L24315

Sanchez-Valle C, Mantegazzi D, Bass JD, Reusser E (2012) Equation of state, refractive index and polarizability of compressed water to 7 GPa and 673 K. J Chem Phys 138:054505

Sandercock JR (1971) Fabry-Perot interferometer for Brillouin scattering. *In*: Proceedings of the 2nd International Conference on Light Scattering in Solids. Balkanski M (ed) Flammarion, Paris, p 9

Sandercock JR (1972) Brillouin-scattering measurements on silicon and germanium. Phys Rev Lett 28: 237-240

Sandercock JR (1974) A light scattering study of the ferromagnet $CrBr_3$. Solid State Commun 15:1715-1719

Sandercock JR (1978) Light scattering from surface acoustic phonons in metals and semiconductors. Solid State Commun 26:547-551

Sandercock JR (1980) Light scattering from thermally excited surface phonons and magnons. *In*: Proceedings of the 7th international conference on Raman spectroscopy. Murphy WF (ed) North-Holland, Amsterdam, p 364

Sandercock JR (1982) Trends in Brillouin scattering: Studies of opaque materials, supported films, and central modes. *In*: Light scattering in Solids III: Recent Results, Topics in Applied Physics. Cardona M, Güntherodt G (eds) Berlin, Springer, p 173-206

Sandercock JR (1987) A dynamic antivibration system. *In*: Proceedings of the 1st International Conference on Vibration Control in Optics and Metrology. vol. 732. Society of Photo-Optical Instruments Engineers p 157-165

Sandercock JR, Wettling W (1973) Light scattering from thermal acoustic magnons in yttrium iron garnet. Solid State Commun 13:1729-1732

Sang L, Vanpeteghem CB, Sinogeikin SV, Bass JD (2011) The elastic properties of diopside, $CaMgSi_2O_6$. Am Mineral 96:224-227

Sathish S, Mendik M, Kulik A, Gremaud G, Wachter P (1991) Polish-induced surface damage in nickel: Scanning acoustic microscopy and Brillouin scattering study. Appl Phys Lett 59:167-168

Sato A, Pennec Y, Shingne N, Thurn-Albrecht T, Knoll W, Steinhart M, Djafari-Rouhani B, Fytas G (2010) Tuning and switching the hypersonic phononic properties of elastic impedance contrast nanocomposites. ACS Nano 4:3471-3481

Sawamoto H, Weidner DJ, Sasaki S, Kumazawa M (1984) Single-crystal elastic properties of the modified spinel (beta) phase of magnesium orthosilicate. Science 224:749-751

Schilling FR, Sinogeikin SV, Bass JD (2003) Single-crystal elastic properties of lawsonite and their variation with temperature. Phys Earth Planet Inter 136:107-118

Schroeder J (1980) Brillouin scattering and pockels coefficients in silicate glasses. Journal of Non-Crystalline Solids 40:549-566

Shapiro SM, Gammon RW, Cummins HZ (1966) Brillouin scattering spectra of crystalline quartz, fused quartz and glass. Appl Phys Lett 9:157-159

Shen G, Wang L, Ferry R, Mao HK, Hemley RJ (2010) A portable laser heating microscope for high pressure research. J Phys Conf Ser 215:012191

Shen Z-H, Zhang S-Y (2001) Laser heating of thin plate with time-dependent absorptance. Microwave Opt Technol Lett 28:364-367

Shimizu H, Sasaki S (1992) High-pressure Brillouin studies and elastic properties of single-crystal H_2S grown in a diamond cell. Science 257:514-516

Shimizu H, Brody EM, Mao HK, Bell PM (1981) Brillouin measurements of solid n-H_2 and n-D_2 to 200 kbar at room temperature. Phys Rev Lett 47:128-131

Shimizu H, Bassett WA, Brody EM (1982) Brillouin-scattering measurements of single-crystal forsterite to 40 kbar at room temperature. J Appl Phys 53:620-626

Shimizu H, Sakoh H, Sasaki S (1994) High-pressure Brillouin scattering and elastic properties of liquid and solid nitrous oxide and carbon dioxide. J Phys Chem 98:670-673

Shimizu H, Ohnishi M, Sasaki S, Ishibashi Y (1995) Cauchy relation in dense H_2O Ice VII. Phys Rev Lett 74:2820-2823

Shimizu H, Nakashima N, Sasaki S (1996) High-pressure Brillouin scattering and elastic properties of liquid and solid methane. Phys Rev B 53:111-115

Shimizu H, Tashiro H, Kume T, Sasaki S (2001) High-pressure elastic properties of solid argon to 70 GPa. Phys Rev Lett 86:4568-4571

EBSCOhost - printed on 2/13/2023 5:26 AM via . All use subject to https://www.ebsco.com/terms-of-use

Shito A, Karato S, Matsukage KN, Nishihara Y (2006) Towards mapping the three-dimensional distribution of water in the upper mantle from velocity and attenuation tomography. *In*: Earth's Deep Water Cycle, Geophysical Monograph 168. Jacobsen SD, Van der Lee S (eds) American Geophysical Union, p 225-236

Sinelnikov YD, Chen G, Liebermann RC (1998a) Elasticity of $CaTiO_3$–$CaSiO_3$ perovskites. Phys Chem Miner 25:515-521

Sinelnikov YD, Chen G, Neuville DR, Vaughan MT, Liebermann RC (1998b) Ultrasonic shear wave velocities of $MgSiO_3$ perovskite at 8 GPa and 800 K and lower mantle composition. Science 281:677-679

Singh AK, Balasingh C, Mao H-k, Hemley RJ, Shu J (1998) Analysis of lattice strains measured under nonhydrostatic pressure. J Appl Phys 83:7567-7575

Sinogeikin SV, Bass JD (1999) Single-crystal elastic properties of chondrodite: Implications for water in the upper mantle. Phys Chem Miner 26:297-303

Sinogeikin SV, Bass JD (2000) Single-crystal elasticity of pyrope and MgO to 20 GPa by Brillouin scattering in the diamond cell. Phys Earth Planet Inter 120:43-62

Sinogeikin SV, Bass JD (2002a) Elasticity of majorite and a majorite-pyrope solid solution to high pressure; Implications for the transition zone. Geophys Res Lett 29:1017-1020

Sinogeikin SV, Bass JD (2002b) Elasticity of pyrope and majorite-pyrope solid solutions to high temperatures. Earth Planet Sci Lett 203:549-555

Sinogeikin SV, Katsura T, Bass JD (1998) Sound velocities and elastic properties of Fe-bearing wadsleyite and ringwoodite. J Geophys Res 103:20819-20825

Sinogeikin SV, Jackson JM, O'Neill B, Palko JW, Bass JD (2000a) Compact high-temperature cell for Brillouin scattering measurements. Rev Sci Instrum 71:201-206

Sinogeikin SV, Schilling FR, Bass JD (2000b) Single crystal elasticity of lawsonite. Am Mineral 85:1834-1837

Sinogeikin SV, Bass JD, Katsura T (2001) Single-crystal elasticity of gamma-$(Mg_{0.91}Fe_{0.09})_2SiO_4$ to high pressures and to high temperatures. Geophys Res Lett 28:4335-4338

Sinogeikin SV, Bass JD, Katsura T (2003) Single-crystal elasticity of ringwoodite to high pressures and high temperatures: Implications for 520 km seismic discontinuity. Phys Earth Planet Inter 136:41-66

Sinogeikin SV, Lakshtanov DL, Nicholas JD, Bass JD (2004a) Sound velocity measurements on laser-heated MgO and Al_2O_3. Phys Earth Planet Inter 143-144:575-586

Sinogeikin SV, Zhang J, Bass JD (2004b) Elasticity of single crystal and polycrystalline $MgSiO_3$ perovskite by Brillouin spectroscopy. Geophys Res Lett 31:L06620

Sinogeikin SV, Lakshtanov DL, Nicholas JD, Jackson JM, Bass JD (2005) High temperature elasticity measurements on oxides by Brillouin spectroscopy with resistive and IR laser heating. J Eur Ceram Soc 25:1313-1324

Sinogeikin S, Bass J, Prakapenka V, Lakshtanov D, Shen G, Sanchez-Valle C, Rivers M (2006) Brillouin spectrometer interfaced with synchrotron radiation for simultaneous X-ray density and acoustic velocity measurements. Rev Sci Instrum 77:103905-103911

Sinogeikin SV, Lakshtanov DL, Prakapenka VB, Sanchez-Valle C, Wang J, Chen B, Shen G, Bass JD (2007) Toward a self-consistent pressure scale: Elastic moduli and equation of state of MgO by simultaneous X-ray density and Brillouin sound velocity measurements at high-pressure high-temperature conditions. Eos Trans AGU 88: Fall Meet. Suppl., Abstract MR53A-07

Sklar Z, Mutti P, Stoodley NC, Briggs GAD (1995). Surface Brillouin scattering—Extending surface wave measurements to 20 GHz *In*: Advances in Acoustic Microscopy. Briggs GAD (ed) Plenum, New York, p 209-247

Smoluchowski M (1908) Molekular-kinetische Theorie der Opaleszenz von Gasen im kritischen Zustande, sowie einiger verwandter Erscheinungen. Ann Phys 22:205-226

Smyth JR (1987) β-Mg_2SiO_4: A potential host for water in the mantle? Am Mineral 72:1051-1055

Smyth JR (1994) A crystallographic model for hydrous wadsleyite (beta-Mg_2SiO_4): An ocean in the Earth's interior? Am Mineral 79:1021-1024

Smyth JR, Frost DJ, Nestola F, Holl CM, Bromiley G (2006) Olivine hydration in the deep upper mantle: Effects of temperature and silica activity. Geophys Res Lett 33:L15301

Speziale S, Duffy TS (2002) Single-crystal elastic constants of fluorite (CaF_2) to 9.3 GPa. Phys Chem Miner 29:465-472

Speziale S, Duffy TS (2004) Single-crystal elasticity of fayalite to 12 GPa. J Geophys Res 109:B12202

Speziale S, Jiang F, Caylor CL, Kriminski S, Zha CS, Thorne RE, Duffy TS (2003) Sound velocity and elasticity of tetragonal lysozyme crystals by Brillouin spectroscopy. Biophys J 85:3202-3213

Speziale S, Jiang F, Duffy TS (2005) Compositional dependence of the elastic wave velocities of mantle minerals; implications for seismic properties of mantle rocks. *In*: Earth's Deep Mantle; Structure, Composition, and Evolution. Geophysical Monographs Series 160. van der Hilst RD, Bass JD, Matas J, Trampert J (eds) American Geophysical Union, Washington, DC, United States, p 301-320

Speziale S, Shieh SR, Duffy TS (2006) High-pressure elasticity of calcium oxide: A comparison between Brillouin spectroscopy and radial X-ray diffraction. J Geophys Res 111:B02203

EBSCOhost - printed on 2/13/2023 5:26 AM via . All use subject to https://www.ebsco.com/terms-of-use

Speziale S, Jiang F, Mao Z, Monteiro PJM, Wenk H-R, Duffy TS, Schilling FR (2008a) Single-crystal elastic constants of natural ettringite. Cement Concrete Res 38:885-889

Speziale S, Reichmann HJ, Schilling FR, Wenk HR, Monteiro PJM (2008b) Determination of the elastic constants of portlandite by Brillouin spectroscopy. Cement Concrete Res 38:1148-1153

Speziale, S, Marquardt H, Liermann H.-P. (2013) Approaches to constrain single-crystal elastic properties from Brillouin scattering of polycrystalline samples. High Pressure Res, doi: 10.1080/08957959.2013.806501

Stevens LL, Orler EB, Dattelbaum DM, Ahart M, Hemley RJ (2007) Brillouin-scattering determination of the acoustic properties and their pressure dependence for three polymeric elastomers. J Chem Phys 127:104906-104913

Stixrude L, Jeanloz R (2009) Constraints on seismic models from other disciplines - constraints from mineral physics on seismological models. *In*: Treatise on Geophysics - Seismology and Structure of the Earth. Vol. 1. Price GD (ed) Elsevier, Amsterdam, p 775-803

Stoddart PR, Comins JD (2000) Quasielastic light scattering in silicon. Phys Rev B 62:15383-15385

Stoddart PR, Crowhurst JC, Every AG, Comins JD (1998) Measurement precision in surface Brillouin scattering. J Opt Soc Am B 15:2481-2489

Sumanya C, Comins JD, Every AG (2007) Surface brillouin scattering in opaque thin films. J Phys Conf Series 92:012103

Svanidze AV, Huth H, Lushnikov SG, Kojima S, Schick C (2009) Phase transition in tetragonal hen egg-white lysozyme crystals. Appl Phys Lett 95:263702-263703

Svanidze A, Romanov V, Lushnikov S (2011) Anomalous behavior of Brillouin light scattering at thermal denaturation of lysozyme. J Exp Theor Phys Lett 93:409-414

Takagi Y, Hosokawa T, Hoshikawa K, Kobayashi H, Hiki Y (2007) Relaxation of polystyrene near the glass transition temperature studied by acoustic measurements. J Phys Soc Japan 76:024604

Tao NJ, Lindsay SM, Rupprecht A (1988) Dynamic coupling between DNA and its primary hydration shell studied by brillouin scattering. Biopolymers 27:1655-1671

Tkachev SN, Solozhenko VL, Zinin PV, Manghnani MH, Ming LC (2003) Elastic moduli of the superhard cubic BC_2N phase by Brillouin scattering. Phys Rev B 68:052104

Tkachev SN, Manghnani MH, Williams Q (2005a) *In situ* Brillouin spectroscopy of a pressure-induced apparent second-order transition in a silicate glass. Phys Rev Lett 95:057402

Tkachev SN, Manghnani MH, Williams Q, Ming LC (2005b) Compressibility of hydrated and anhydrous Na_2O-$2SiO_2$ liquid and also glass to 8 GPa using Brillouin scattering. J Geophys Res 110:B07201

Tlali SB, Mathe BA, Kotane LM, Schöning FRL, Comins JD, Every AG, Sithole HM, Ngoepe PE, Wright KV (2004) Brillouin scattering studies and computational simulations of the elastic properties of pyrite (FeS_2) at high temperatures. Phys Status Solidi C 1:3073-3076

Tomé CN (2000) Tensor properties of textured polycrystals. *In*: Texture and Anisotropy: Preferred Orientation in Polycrystals and Their Effect on Materials Properties. Kocks UF, Tomé CN, Wenk HR (eds) Cambridge University Press, p 282-325

Toohill K, Siegesmund S, Bass JD (1999) Sound velocities and elasticity of cordierite and implications for deep crustal seismic anisotropy. Phys Chem Miner 26:333-343

Trampert J, van der Hilst RD (2005) Towards a quantitative interpretation of global seismic tomography. *In*: Earth's Deep Mantle: Structure, Composition, and Evolution. Van der Hilst RD, Bass JD, Matas J and Trampert J (eds) AGU Geophysical Monograph Series (Book 160), Washington, DC, p 47-62

Trzaskowska A, Mielcarek S, Mroz B, Trybula Z (2010) Elastic and elasto-optical properties of $Rb_{1-x}(NH_4)_xH_2AsO_4$ mixed crystals studied by Brillouin spectroscopy. Cryst Res Technol 45:48-52

Tsuchiya T, Tsuchiya J, Umemoto K, Wentzcovitch RM (2004) Phase transition in $MgSiO_3$ perovskite in the earth's lower mantle. Earth Planet Sci Lett 224:241-248

Tyndall J (1868) On the blue colour of the sky, the polarization of skylight, and on the polarization of light by cloudy matter generally. Proc Royal Soc London 17:223-233

Vacher R, Boyer L (1972) Brillouin scattering: A tool for the measurement of elastic and photoelastic constants. Phys Rev B 6:639-673

Vacher R, Pelous J (1976) Measurement of the intensity of the Brillouin lines in amorphous media at very low temperature. Phys Status Solidi B 75:K101-K103

Valenti P, Reichmann HJ, Schmidt C, Speziale S (2011) A new setup for combined Brillouin and Raman scattering to measure P-V-T-x properties of fluids in the system H_2O-NaCl at high P and T in the diamond-anvil cell. Abstract MR43-2128 presented at 2011 Fall Meeting, AGU, San Francisco

Vaughan MT, Weidner DJ (1978) The relationship of elasticity and crystal structure in andalusite and sillimanite. Phys Chem Miner 3:133-144

Vaughan MT, Bass JD (1983) Single crystal elastic properties of protoenstatite: A comparison with orthoenstatite. Phys Chem Miner 10:62-68

Vaughan MT, Guggenheim S (1986) Elasticity of muscovite and its relationship to crystal structure. J Geophys Res 91:4657-4664

EBSCOhost - printed on 2/13/2023 5:26 AM via . All use subject to https://www.ebsco.com/terms-of-use

Visser D, Van Hijningen NCJA, Dil JG (1984) Brillouin scattering near rigid interfaces. J Phys 45:C5-83-C85-91
Vogelgesang R, Ramdas AK, Rodriguez S, Grimsditch M, Anthony TR (1996) Brillouin and Raman scattering in natural and isotopically controlled diamond. Phys Rev B 54:3989-3999
Vo-Thanh D, Polian A, Richet P (1996) Elastic properties of silicate melts up to 2350 K from Brillouin scattering. Geophys Res Lett 23:423-426
Wagner LS, Anderson ML, Jackson JM, Beck SL, Zandt G (2008) Seismic evidence for orthopyroxene enrichment in the continental lithosphere. Geology 36:935-938
Wallnöfer W, Krempl PW, Asenbaum A (1994) Determination of the elastic and photoelastic constants of quartz-type $GaPO_4$ by Brillouin scattering. Phys Rev B 49:10075-10080
Wang CH (1980) Depolarized Rayleigh-Brillouin scattering of shear waves and molecular reorientation in a viscoelastic liquid. Molec Phys 41:541-565
Wang CH (1986) A continuum mechanics theory of depolarized and polarized Rayleigh-Brillouin light scattering spectra of supercooled liquids. Molec Phys 58:497-508
Wang J, Sinogeikin S, Inoue T, Bass JD (2003) Elastic properties of hydrous ringwoodite. Am Mineral 88:1608-1611
Wang J, Sinogeikin S, Inoue T, Bass JD (2006) Elastic properties of hydrous ringwoodite at high-pressure conditions. Geophys Res Lett 33:L14308
Watt JP, Davies GF, O'Connell RJ (1976) The elastic properties of composite materials. Rev Geophys 14:541-563
Wehner RK, Klein R (1972) Scattering of light by entropy fluctuations in dielectric crystals. Physica 62:161-197
Weidner DJ, Carleton HR (1977) Elasticity of coesite. J Geophys Res 82:1334-1346
Weidner DJ, Hamaya N (1983) Elastic properties of the olivine and spinel polymorphs of Mg_2GeO_4, and evaluation of elastic analogues. Phys Earth Planet Inter 33:275-283
Weidner DJ, Swyler K, Carleton HR (1975) Elasticity of micrcrystals. Geophys Res Lett 2:189-192
Weidner DJ, Wang H, Ito J (1978) Elasticity of orthoenstatite. Phys Earth Planet Inter 17:P7-P13
Weidner DJ, Bass JD, Ringwood AE, Sinclair W (1982) The single-crystal elastic moduli of stishovite. J Geophys Res 87:4740-4746
Wentzcovitch RM, Justo JF, Wu Z, da Silva CRS, Yuen DA, Kohlstedt D (2009) Anomalous compressibility of ferropericlase throughout the iron spin cross-over. Proc Natl Acad Sci 106:8447-8452
Whitfield CH, Brody EM, Bassett WA (1976) Elastic moduli of NaCl by Brillouin scattering at high pressure in a diamond anvil cell. Rev Sci Instrum 47:942-947
Wittkowski T, Jorzick J, Jung K, Hillebrands B (1999) Elastic properties of thin h-BN films investigated by Brillouin light scattering. Thin Solid Films 353:137-143
Wittkowski T, Jorzick J, Jung K, Hillebrands B, Keunecke M, Bewilogua K (2002) Brillouin light scattering study on the elastic properties of thick sputtered c-BN films. J Appl Phys 91:2729-2736
Wittkowski T, Distler G, Jung K, Hillebrands B, Comins JD (2004) General methods for the determination of the stiffness tensor and mass density of thin films using Brillouin light scattering: Study of tungsten carbide films. Phys Rev B 69:205401
Wittkowski T, Jung K, Hillebrands B, Comins JD (2006) Structural and chemical phase transitions in tungsten carbide films evidenced by the analysis of their stiffness tensors. J Appl Phys 100:073513
Wookey J, Kendall JM (2008) Constraints on lowermost mantle mineralogy and fabric beneath Siberia from seismic anisotropy. Earth Planet Sci Lett 275:32-42
Wu Z, Justo JF, Wentzcovitch RM (2013) Elastic anomalies in a spin-crossover system: Ferropericlase at lower mantle conditions. Phys Rev Lett 110:228501
Xia X, Weidner DJ, Zhao H (1998) Equation of state of brucite: Single-crystal Brillouin spectroscopy study and polycrystalline pressure-volume-temperature measurement. Am Mineral 83:68-74
Xu J-a, Manghnani MH (1992) Brillouin-scattering studies of a sodium silicate glass in solid and melt conditions at temperatures up to 1000°C. Phys Rev B 45:640-645
Yan Y-X, Nelson KA (1987a) Impulsive stimulated light scattering. I. General theory. J Chem Phys 87:6240-6256
Yan Y-X, Nelson KA (1987b) Impulsive stimulated light scattering. II. Comparison to frequency-domain light-scattering spectroscopy. J Chem Phys 87:6257-6265
Yeganeh-Haeri A (1994) Synthesis and re-investigation of the elastic properties of single-crystal magnesium silicate perovskite. Phys Earth Planet Inter 87:111-121
Yeganeh-Haeri A, Weidner DJ (1989) Elasticity of a beryllium silicate (phenacite: Be_2SiO_4). Phys Chem Miner 16:360-364
Yeganeh-Haeri A, Weidner DJ, Ito E (1989) Elasticity of $MgSiO_3$ in the perovskite structure. Science 243:787-789
Yeganeh-Haeri A, Haeri A, Weidner DJ, Ito E (1990) Elastic properties of the pyrope-majorite solid solution series. Geophys Res Lett 17:2453-2456

EBSCOhost - printed on 2/13/2023 5:26 AM via . All use subject to https://www.ebsco.com/terms-of-use

Yeganeh-Haeri A, Weidner DJ, Parise JB (1992) Elasticity of α-cristobalite: A silicon dioxide with a negative Poisson's ratio. Science 257:650-652

Yoneda A, Cooray T, Shatskiy A (2012) Single-crystal elasticity of stishovite: New experimental data obtained using high-frequency resonant ultrasound spectroscopy and a Gingham check structure model. Phys Earth Planet Inter 190-191:80-86

Yoshida M, Hisa K, Matsukawa M, Otani T, Ohtori N (2001) Effects of tensile stress on the hypersonic wave velocities in polymer films. Acoust Sci Technol 22:375-377

Zaug JM, Abramson EH, Brown JM, Slutsky LJ (1993) Sound velocities in olivine at Earth mantle pressures. Science 260:1487-1489

Zha C-S, Duffy TS, Mao H-K, Hemley RJ (1993) Elasticity of hydrogen to 24 GPa from single-crystal Brillouin scattering and synchrotron X-ray diffraction. Phys Rev B 48:9246-9255

Zha C-S, Hemley RJ, Mao H-K, Duffy TS, Meade C (1994) Acoustic velocities and refractive index of SiO_2 glass to 57.5 GPa by Brillouin scattering. Phys Rev B 50:13105-13112

Zha C-S, Duffy TS, Downs RT, Mao H-K, Hemley RJ (1996) Sound velocity and elasticity of single-crystal forsterite to 16 GPa. J Geophys Res 101:17535-17545

Zha C-S, Duffy TS, Mao H-K, Downs RT, Hemley RJ, Weidner DJ (1997) Single-crystal elasticity of β-Mg_2SiO_4 to the pressure of the 410 km seismic discontinuity in the Earth's mantle. Earth Planet Sci Lett 147:E9-E15

Zha C-S, Duffy TS, Downs RT, Mao H-K, Hemley RJ (1998) Brillouin scattering and X-ray diffraction of San Carlos olivine: Direct pressure determination to 32 GPa. Earth Planet Sci Lett 159:25-33

Zha C-S, Mao H-K, Hemley RJ (2000) Elasticity of MgO and a primary pressure scale to 55 GPa. Proc Natl Acad Sci 97:13494-13499

Zha C-S, Mao H-K, Hemley RJ (2004) Elasticity of dense helium. Phys Rev B 70:174107

Zhang X, Comins JD, Every AG, Stoddart PR (1998a) Surface Brillouin scattering studies on vanadium carbide. Int J Refractory Metals Hard Mater 16:303-308

Zhang X, Comins JD, Every AG, Stoddart PR, Pang W, Derry TE (1998b) Surface Brillouin scattering study of the surface excitations in amorphous silicon layers produced by ion bombardment. Phys Rev B 58:13677-13685

Zhang X, Manghnani MH, Every AG (2000) Evidence for a shear horizontal resonance in supported thin films. Phys Rev B 62:R2271-R2274

Zhang X, Stoddart PR, Comins JD, Every AG (2001) High-temperature elastic properties of a nickel-based superalloy studied by surface Brillouin scattering. J Phys Condens Matter 13:2281-2294

Zhang HP, Brodin A, Barshilia HC, Shen GQ, Cummins HZ, Pick RM (2004) Brillouin scattering study of salol: Exploring the effects of rotation-translation coupling. Phys Rev E 70:011502

Zhang JS, Bass JD, Taniguchi T, Goncharov AF, Chang Y-Y, Jacobsen SD (2011) Elasticity of cubic boron nitride under ambient conditions. J Appl Phys 109:063521

Zhao P, Vanderwal JJ (1997) Brillouin scattering study of gelatin gel. Polymer Gels Networks 5:23-36

Zhuralev, KK, Gonchariov AF, Tkachev SN, Dera P, Prakapenka VB (2013) Vibrational, elastic and structural properties of cubic silicon carbide under pressure up to 75 GPa: Implication for a primary pressure scale. J Appl Phys 113:113503

Zinin P, Manghnani MH, Zhang X, Feldermann H, Ronning C, Hofsass H (2002) Surface Brillouin scattering of cubic boron nitride films. J Appl Phys 91:4196-4204

Ziobrowski P, Nowicka A, Andrzejewska E, Marcinkowska A, Drozdowski M (2011) Brillouin study of photopolymerization process of two-monomer systems. Spectrochim Acta Part A: Molec Biomolec Spectrosc 79:815-818

Zou YT, Irifune T, Greaux S, Whitaker ML, Shinmei T, Ohfuji H, Negishi R, Higo Y (2012) Elasticity and sound velocities of polycrystalline $Mg_3Al_2(SiO_4)_3$ garnet up to 20 GPa and 1700 K. J Appl Phys 112:014910

Zouboulis ES, Grimsditch M (1991a) Refractive index and elastic properties of MgO up to 1900 K. J Geophys Res 96:4167-4170

Zouboulis ES, Grimsditch M (1991b) Refractive index and elastic properties of single-crystal corundum (α-Al_2O_3) up to 2100 K. J Appl Phys 70:772-776

Zouboulis ES, Grimsditch M, Ramdas AK, Rodriguez S (1998) Temperature dependence of the elastic moduli of diamond: A Brillouin-scattering study. Phys Rev B 57:2889-2896

Zwanzig R (1961) Statistical mechanics of irreversibility. *In*: Boulder Lectures in Theoretical Physics. Vol 3. Brittin WE, Downs BW, Downs J (eds) Interscience, New York, p 106-141

EBSCOhost - printed on 2/13/2023 5:26 AM via . All use subject to https://www.ebsco.com/terms-of-use

EBSCOhost - printed on 2/13/2023 5:26 AM via . All use subject to https://www.ebsco.com/terms-of-use

Reviews in Mineralogy & Geochemistry
Vol. 78 pp. 605-653, 2014
Copyright © Mineralogical Society of America

NMR Spectroscopy of Inorganic Earth Materials

Jonathan F. Stebbins
Dept. of Geological and Environmental Sciences
Stanford University
Stanford, California, 94305, U.S.A.
stebbins@stanford.edu

Xianyu Xue
Institute for Study of the Earth's Interior
Okayama University
Yamada 827, Misasa
Tottori 682-0193, Japan
xianyu@misasa.okayama-u.ac.jp

INTRODUCTION

Nuclear Magnetic Resonance (NMR) methods are now widely used for studying the structure and dynamics of solid, inorganic materials, including those central to the Earth sciences, as well as silicate melts and aqueous solutions. Spectra of minerals (as conveniently large single crystals) were collected soon after NMR was developed in the late 1940's, and were instrumental in early refinements of the theory of NMR interactions in solids (Pound 1950; Petch et al. 1953). NMR on single crystals also provided important insights into issues such as symmetry distortion and phase transitions in minerals (Brun and Hafner 1962; Ghose 1964; Ghose and Tsang 1973). The critical, resolution-enhancing method of "magic-angle sample spinning" (MAS) was invented in the late 1950's and demonstrated on NaCl (Andrew et al. 1959). However, it was not until the development of relatively high-field (e.g., 4.7 Tesla and above) superconducting magnets, and pulsed, Fourier-transform methods (requiring fast micro-computers) in the late 1970's and early 1980's that high-resolution NMR spectroscopy on nuclides such as ^{29}Si and ^{27}Al routinely started providing new structural information on minerals and glasses (Lippmaa et al. 1980; Smith et al. 1983; Mägi et al. 1984). Technological advances continue to push the development of new applications of high resolution, solid-state NMR, for example magnets with fields of 21 T and even higher, MAS probes with spinning rates above 100 kHz (6 million revolutions per minute), and capabilities to observe high-quality spectra of ever-smaller samples (e.g., <1 mg).

Probably more than any other commonly-applied spectroscopic methodology, NMR includes a wide array of techniques that allow the complex, and time-dependent, manipulation of the system under observation, in this case the nuclear spins of isotopes of many different elements. A rich variety of information about short-range (first and second atom neighbor distributions) and intermediate-range structure (molecular connections out to third-, fourth-neighbor or even more, distances to the nm scale) can thus be obtained that often includes data on interactions among different types of atoms, and on dynamics at timescales from about 0.1 second to 1 nanosecond. Many books on the basics of NMR (Abragam 1961; Fukushima and Roedder 1981; Harris 1983; Derome 1987; Ernst et al. 1987; Keeler 2010) and on its theory and applications to solids (Fyfe 1983; Duer 2002, 2004; Apperley et al. 2012; Wasylishen et al. 2012) are available. Applications of high-resolution solid-state NMR to inorganic materials of wide vari-

1529-6466/14/0078-0015$05.00 http://dx.doi.org/10.2138/rmg.2014.78.15

EBSCOhost - printed on 2/13/2023 5:26 AM via . All use subject to https://www.ebsco.com/terms-of-use

ety (including minerals) have been thoroughly and clearly reviewed early on (Engelhardt and Michel 1987) and more recently (Mackenzie and Smith 2002). The latter book is an especially good summary not only of commonly studied nuclides, but of many others that could be of interest for inorganic Earth materials. These and a few other sources (Sherriff et al. 1991; Stebbins 1995b) include detailed tabulations of NMR data on minerals as well as tables of properties of NMR-accessible nuclides that are more complete than the selected list included here (Table 1). Some other nuclides have potential applications, but have not been widely applied in these materials. In some cases, other isotopes of listed elements are observable, but are generally less useful. Many useful articles appear in the hardcopy and online versions of the Encyclopedia of Magnetic Resonance (Wiley). Introductions and reviews of the basics and of applications to minerals, glasses, and melts, focusing on the Earth sciences, particularly the NMR chapters in the 1988 MSA RIM volume (Kirkpatrick 1988; Stebbins 1988), and the 2004 EMU volume (Fechtelkord 2004) on spectroscopic methods in mineralogy will be the starting points for this chapter, which is intended to complement, not duplicate, these earlier introductions. Our goal here of course cannot be to cover the field in its entirety, or to give a complete foundation in the basic theory and methods, but is to provide the most important basic concepts to mineralogists and geochemists to allow informed and critical reading of the literature beyond the "black box" level. Further, we provide examples of applications of NMR to inorganic Earth materials (and their simplified synthetic equivalents) to inspire and facilitate future work.

The basics provided here do apply to NMR applications in general, but we have restricted the scope of applications to solid and molten inorganic materials (mostly silicates and oxides), with a few examples for aqueous solutions. With that said, we will note in passing that solid-state NMR has been widely applied to *organic* Earth materials as well, where it plays a unique role in constraining the distribution of molecular species in the extremely complex, often insoluble (and thus non-analyzable) carbonaceous material of coals, soils, and even, recently, of meteorites. Low-resolution ^{1}H NMR methods are widely used in the laboratory and in oil field borehole tools to evaluate the distributions of liquid hydrocarbons and aqueous fluids, and magnetic resonance imaging (MRI) is used in the laboratory to observe multi-phase fluid flow in rock cores.

In this chapter, we emphasize applications of NMR to the types of problems most commonly encountered in the Earth sciences, where information on atomic-scale structure and dynamics is needed to progress in the understanding and prediction of large-scale processes. These problems are, of course, by no means unique to the Earth sciences, and the distinctions among mineralogy, geochemistry, materials science, and solid-state chemistry, have long been blurred. It is important to keep in mind, as well, that natural minerals and their pure synthetic equivalents, having structures known from diffraction studies, have often been used in fundamental solid-state NMR studies, from the earliest days to the present. Review of this work is beyond the scope of this chapter, but such studies range from the development of the basic physics of nuclear spin interactions, the testing of sophisticated new pulse sequences, the validation of theoretical methods of predicting spectra, and to the all-important discovery of empirical correlations between structure and observable NMR parameters such as chemical shift and quadrupolar coupling constants (Engelhardt and Michel 1987; Kirkpatrick 1988; Stebbins and Farnan 1989; Farnan 1991; Kirkpatrick and Phillips 1993; Stebbins 1995b; Mackenzie and Smith 2002; Fechtelkord 2004). All of these contribute to the background that allows NMR to be applied to unknown aspects of the structure and dynamics of more complex solids and melts.

THE BASICS

Nuclear spins, NMR frequencies and signal intensities

Neutrons, protons and electrons all have spin quantum numbers of 1/2, meaning that they each have magnetic moments that can interact with magnetic fields, both from other nearby

EBSCOhost - printed on 2/13/2023 5:26 AM via . All use subject to https://www.ebsco.com/terms-of-use

Table 1. Selected NMR nuclides for studies of solid silicate and oxide materials. Data from Mackenzie and Smith (2002) and Kirkpatrick (1988).

Isotope	Spin	Natural Abundance, %	Frequency, MHz at 11.7 T	Quadrupolar Moment, mb	Notes
spin=1/2					
^{1}H	1/2	99.99	500.00	—	1, 2
^{13}C	1/2	1.11	125.73	—	3
^{15}N	1/2	0.37	50.68	—	3
^{19}F	1/2	100	470.47	—	1, 2
^{29}Si	1/2	4.70	99.33	—	2
^{31}P	1/2	100	202.40	—	1, 2
^{89}Y	1/2	100	24.59	—	4
^{109}Ag	1/2	48.18	22.3	—	4
^{113}Cd	1/2	12.26	110.97	—	
^{119}Sn	1/2	8.58	186.45	—	
^{207}Pb	1/2	22.6	104.60	—	
quadrupolar nuclides					
^{2}H	1	0.015	76.75	2.8	3
^{6}Li	1	7.42	73.58	−0.81	
^{7}Li	3/2	92.5	194.33	−40.1	1, 2
^{11}B	3/2	80.1	160.53	40.6	1, 2
^{14}N	1	99.63	36.1	20.4	4
^{17}O	5/2	0.037	67.85	−25.6	2, 3
^{23}Na	3/2	100	132.40	104	1, 2
^{25}Mg	5/2	10.0	30.65	199.4	2, 4
^{27}Al	5/2	100	130.45	146.6	1, 2
^{33}S	3/2	0.75	38.43	−67.8	3, 4
^{35}Cl	3/2	75.77	49.07	−81.7	
^{39}K	3/2	93.26	23.37	58.5	4
^{43}Ca	7/2	0.135	33.72	−49.0	3, 4
^{45}Sc	7/2	100	121.72	−220	1
^{47}Ti	5/2	7.28	28.25	302	4
^{49}Ti	7/2	5.51	28.25	247	4
^{51}V	7/2	99.75	131.75	−52	1
^{67}Zn	5/2	4.11	31.37	150	4
^{79}Br	3/2	50.69	125.78	313	
^{87}Sr	9/2	7.00	21.77	335	4
^{91}Zr	5/2	11.22	46.70	−176	
^{93}Nb	9/2	100	122.7	−320	
^{127}I	5/2	100	100.78	−616	
^{133}Cs	7/2	100	66.07	−3.4	2

1. especially high sensitivity (may be detectable as a minor component)
2. applied to inorganic materials relatively frequently
3. isotopic enrichment sometimes or often necessary
4. particularly low frequency, may require special equipment

particles and that imposed externally. In the nucleus of an isotope with a given mass number, the number of protons and neutrons, and the way in which they are paired, determines the net nuclear spin number (I). Nuclides with equal, even numbers of protons and neutrons, especially in multiples of four, are particularly stable during stellar nucleosynthesis and comprise the most common elements in the solar system (and the Earth) beyond ^{1}H, e.g., ^{12}C, ^{16}O, ^{24}Mg, ^{28}Si. Because these have $I = 0$, they cannot be observed by NMR, which must therefore rely

EBSCOhost - printed on 2/13/2023 5:26 AM via . All use subject to https://www.ebsco.com/terms-of-use

on less common odd-numbered isotopes of these elements, such as ^{13}C, ^{17}O, ^{25}Mg, and ^{29}Si. These have spin numbers that are odd multiples of 1/2 ("half-integer spins," 1/2, 5/2, 5/2, 1/2 respectively for these examples). In a few such cases, natural abundances are low enough such that most NMR is done on (often expensive!) isotopically-enriched synthetic samples, most notably for ^{17}O and ^{33}S. A few nuclides have equal but odd numbers of protons and neutrons (e.g., ^{2}H, ^{6}Li, ^{10}B, ^{14}N) and spin numbers that are even multiples of 1/2 (1, 1, 3, 1 respectively). In contrast, the most common isotopes of elements with odd atomic numbers usually have unequal numbers of protons and neutrons and thus must also have $I > 0$ with half-integer spins. Favorable NMR nuclides in this large group sometimes comprise 100% (or nearly so) of such atoms, often making spectra much more readily obtainable, e.g., ^{1}H (I = 1/2), ^{31}P (I = 1/2), ^{23}Na (I = 3/2), and ^{27}Al (I = 5/2). The abundance of the NMR-active nuclide(s) is thus one starting point for determining the utility of the method for a given problem (Table 1).

A nucleus has $2I + 1$ nuclear spin states. The energy difference ΔE between each adjacent level ($2I$ such transitions), resulting from interaction with an external magnetic field of magnitude B_0, scales linearly with the field and with a nuclide-specific parameter called the gyromagnetic ratio (γ). Ignoring chemical shift and quadropolar effects (see below),

$$\Delta E = \left| \frac{\gamma h B_0}{2\pi} \right| \quad (1)$$

where h is Planck's constant. In modern spectrometers with commonly-used magnetic fields, these energies are equivalent to "Larmor" frequencies ($\nu_L = \gamma B_0/2\pi$) in the radiofrequency (RF) range, typically 10's to 100's of MHz but sometimes ranging to >1 GHz for ^{1}H in ultra-high field magnets. In modern spectrometers, NMR signals come from energy released from such transitions after excitation by a short, but carefully controlled, pulse of radiofrequency energy at ν_L for the nuclide being observed at the magnetic field of the spectrometer, which is usually fixed. (In early "continuous wave" spectrometers, the radiofrequency was fixed and the magnetic field was scanned to record spectra: this led to the still-used convention of plotting spectra with higher frequency to the left, corresponding to lower external magnetic field.) Compared to the radiation utilized in most other types of spectroscopies such as EPR, IR, visible, X-ray and Mössbauer, RF frequencies and thus energies are very low and $\Delta E << kT$ (Boltzman constant times temperature). Because ratios of populations of atoms in higher energy spin states to those in lower energy states are proportional to $e^{(-\Delta E/kT)}$, and thus close to 1 for NMR, relatively low signal intensities and correspondingly low sensitivity often result. In challenging cases spectra can be slow to acquire as signals from many pulses are added together, requiring hours or even days. Nonetheless, for favorable nuclides (e.g., ^{1}H, ^{11}B, ^{23}Na, ^{27}Al, ^{31}P), useful data can be obtained for minor components in minerals at concentrations <1% in samples a few mg in weight, for example the distribution of boron on three- and four-coordinated sites in biogenic calcite (Fig. 1). Recent sensitivity enhancements from higher magnetic fields and smaller-diameter MAS rotors have been especially important in studying small (1 to 10 mg) samples synthesized in multi-anvil high pressure apparatus, such as Al-doped $MgSiO_3$ perovskite (Fig. 2) (Stebbins et al. 2006; Ashbrook et al. 2007a).

Equation (1) also indicates that the NMR transition energy (and ν_L), and thus the ratio of lower energy state to higher energy state populations and the signal intensity, increases with external field and with γ. This enhanced sensitivity with higher field is one of the drivers for the development of stronger magnets. On the other hand, the lower sensitivity for lower γ's can be a significant limitation for many interesting nuclides where, nonetheless, some useful and interesting NMR studies have been made in silicates and oxides, e.g., ^{25}Mg, ^{43}Ca and ^{89}Y (Mackenzie and Smith 2002). As discussed below, for quadrupolar nuclides (I > 1/2) in non-cubic sites, even "high-resolution" MAS NMR spectra are often broadened significantly, to an extent depending on the local gradient in the electric field and the nuclide-specific

EBSCOhost - printed on 2/13/2023 5:26 AM via . All use subject to https://www.ebsco.com/terms-of-use

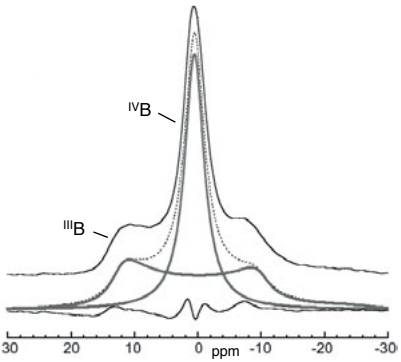


Figure 1. ^{11}B MAS NMR spectrum (7.1 T) and line shape simulation for a trace amount of boron in calcite foraminifera shells (Klochko et al. 2009).

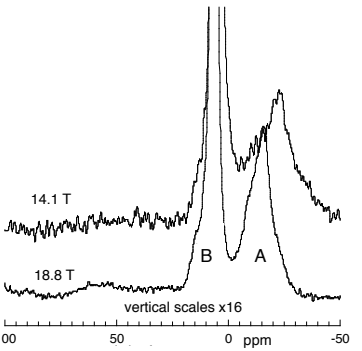


Figure 2. ^{27}Al MAS NMR spectra (14.1 and 18.8 T) of a 4 mg sample of $MgSi_{0.95}Al_{0.05}O_{2.975}$ perovskite, showing peaks for Al in octahedral "B" site and in larger "A" site (Stebbins et al. 2006).

quadrupole moment eQ (Table 1). This broadening spreads the NMR signal out, reduces resolution and reduces the signal-to-noise ratio. These effects increase with eQ and decrease strongly with increasing ν_L. Quadrupolar "low-γ" nuclides can thus be especially challenging to observe, and studies of such systems can be greatly facilitated by higher magnetic fields. Other broadening mechanisms, particularly the electron-nuclear magnetic dipolar interactions caused by unpaired electron spins (e.g., those in many transition metal cations, see section below on dipolar interactions) can also reduce resolution and sensitivity to the point where NMR spectra may no longer be useful: this has been a major limitation on applying NMR to most natural minerals with iron oxide contents of more than a few per cent.

This seemingly esoteric physics of nuclear spin transitions becomes interesting for studies of chemical structure because the spin energies are affected by interactions with electrons and other nuclei in the sample, all of which are dependent on the structure and dynamics. The most commonly exploited effect is that the magnetic field at the nucleus, and hence the NMR frequency, is slightly perturbed ("shielded") by the distribution of the electrons of the atom being observed and its neighbors. This in turn is affected by the local chemical environment: electrostatic and bonding interactions, orbital hybridization, numbers and types of first, second, and higher-shell neighbors, bond distances and angles, etc. Together, these effects determine the "chemical shift" of the NMR signal for an atom in a particular coordination environment in a molecule, crystal, glass, or liquid. In frequency units, the chemical shift increases linearly with increasing field, giving greater separation at higher fields for signals from different sites: another motivation for using bigger magnets. However, when normalized by the external field, the chemical shift for a given site is a *constant* that characterizes the structure. For this reason, and for convenience in both data acquisition and comparison of data from different instruments, NMR frequencies are most commonly reported relative to a standard and normalized by the excitation frequency (as measured by the frequency for the standard), on a parts per million (ppm) scale:

$$\delta = 10^6 \left(\frac{\nu_{\text{sample}} - \nu_{\text{standard}}}{\nu_{\text{standard}}} \right) \tag{2}$$

Chemical shift differences of 0.01 to 0.1 ppm are routinely measured. The total variation in chemical shift with structure within a group of compounds varies widely depending on the element observed. It can be just a few ppm, for example ^{6}Li in three- to six-coordination in

EBSCOhost - printed on 2/13/2023 5:26 AM via . All use subject to https://www.ebsco.com/terms-of-use

silicates (Xu and Stebbins 1995), or thousands of ppm for electron-rich heavy isotopes such as ^{207}Pb (Fayon et al. 1998). The extreme sensitivity to structure in the latter case can be "too much of a good thing:" in a disordered material such as a glass, the spectrum may be so broad as to become difficult to observe, requiring special two-dimensional methods.

An unusual feature and real advantage of NMR relative to other spectroscopies is that in an ideal experiment, the relative intensities of different components of an NMR spectrum depend only on the number of atoms of a given nuclide in different "sites," meaning distinct local electronic environments, not the strict crystallographic sense. Thus, integration of observed peak areas can readily give accurate relative populations of different sites, without the need for matrix-dependent intensity corrections, structure-dependent absorption cross sections, etc. Furthermore, the high instrumental stability common to modern spectrometers means that intensities can easily be compared from sample to sample. Of course, an "ideal experiment" is not always feasible, and, as in any method, improperly-collected spectra can be misleading.

How NMR experiments are done

A full, quantitative understanding of modern NMR experiments generally requires a rather lengthy description based on quantum mechanics, and is beyond the scope of this chapter. However, as also described in more detail elsewhere (Harris 1983; Kirkpatrick 1988; Apperley et al. 2012), a simplified classical description can serve well to introduce the basic approach taken.

In most modern NMR experiments, nuclear spin states are manipulated by one or more short pulses (typically a few μs long) of radiofrequency (RF) energy at the Larmor frequency of the nuclide being observed, which are emitted from a tuned antenna coil surrounding the sample volume. In more complex experiments, e.g., "double resonance," pulses for two or more different nuclides may be applied simultaneously or sequentially. An RF pulse contains frequency components that extend for a significant range below and above the center frequency, roughly the inverse of the pulse length. As a result, NMR transitions are excited over this "bandwidth" (typically 100's of kHz to 1 MHz or more) all at the same time. After the pulse sequence and a short instrumental "dead time," the signals given off by the spins in the sample over this range of frequencies induce a voltage in a receiver coil (usually the same as that used for the excitation pulses), which is amplified and digitized for the time period until it decays to undetectability, typically ms to s. This intensity vs. time record is called the "free induction decay," or FID. FID's from many sequential pulses are usually added together to enhance the signal to noise ratio, then are processed and Fourier transformed to give a frequency domain spectrum. The pulses generally need to be separated by a long enough "pulse delay" or "recycle delay," to allow at least partial relaxation of the spin system back to its initial state (see section below on nuclear spin relaxation).

In the classical view of a simple, "one pulse" NMR experiment, the nuclear magnetization vector is initially along the external field B_0. When described in a reference frame that rotates at the Larmor frequency, the magnetic field of the excitation pulse (B_1, applied perpendicular to the external field) effectively rotates the magnetization about an axis along the applied field as long as the pulse is turned on. The applied power of the RF pulse controls the rate of this rotation, which is typically in the range of 50 to 100 kHz but can be much lower or considerably higher. At the latter value, for example, a complete 360° rotation occurs in 1/100,000 s or 10 μs. The maximum NMR signal will be observed when the largest vector component of the magnetization is perpendicular to the external field, after a rotation of 90° ("π/2-pulse" in radians), or 2.5 μs in this example. "RF tip angles" of less than 90° are often used for a number of technical reasons, however. A single 180° pulse will produce a null NMR signal, but may be used as part of a pulse sequence to induce one or more "spin echoes," which can be very useful for exploring spin interactions and dynamics or for observing very broad signals

EBSCOhost - printed on 2/13/2023 5:26 AM via . All use subject to https://www.ebsco.com/terms-of-use

that decay too rapidly compared to instrumental deadtime. NMR spectrometers are capable of generating long pulse sequences on several simultaneous frequency channels for which powers, shapes and phases are rapidly changed to manipulate spins in complex fashions; NMR spectroscopists who develop such methods are often capable of creating suitably complex acronyms to describe such sequences, as hinted at in descriptions below.

Anisotropy, motional averaging, and magic-angle spinning

Magnetic interactions are by nature directional. Therefore, the energies of nuclear spin transitions in a molecule or a solid material, and the frequencies of their NMR signals, generally depend on the orientation with respect to the vector defined by the external magnetic field. This dependence is commonly described by a tensor (3×3 matrix) with three principal components and the angles that orient it relative to the local coordinates in the molecule or crystal: analogous to an optical indicatrix that describes the variation of refractive index with direction in a crystal. Thus, for a spin-1/2 nuclide (e.g., ^{13}C or ^{29}Si) in a non-cubic site in an ordered single crystal in which magnetic dipole couplings are also small, a narrow NMR peak will be observed, whose chemical shift may vary over 100's of ppm as the crystal is rotated about an axis different from the external field vector. The complete "chemical shift anisotropy" (CSA) tensor can be mapped out by collecting data over two appropriate rotations, although such experiments are time-consuming and are rarely done for silicates (Spearing and Stebbins 1989). Much more commonly, the CSA parameters (without crystallographic orientation) are derived from patterns of spinning sidebands in magic-angle spinning experiments on powdered samples (see below) (Smith et al. 1983). For nuclides with $I > 1/2$, the anisotropy of the quadrupolar interaction can produce even larger effects, which have been measured in many early single crystal studies of nuclides such as ^{27}Al (Brun and Hafner 1962; Ghose and Tsang 1973). In the now much-more-commonly studied case of a random, polycrystalline powder or a non-crystalline glass, all of the frequencies for all of the orientations would be observed together, resulting in what is often a very broad "powder pattern" with a resulting low signal-to-noise and low resolution among signals for different sites.

In a liquid, random re-orientation of molecules or ionic groupings, if rapid with respect to the frequency width of the NMR spectrum, averages all such anisotropic interactions to zero, generally resulting in narrow lines, high signal-to-noise, and high spectral resolution. The spectra thus yield "isotropic" average chemical shifts δ_{iso}. This single effect means that liquid-state spectra, most commonly collected for the high-γ, high abundance nuclide ^{1}H in organic molecular liquids, can often be very rapidly collected, and are informative enough to have long been an "every day" tool for much of organic chemistry. Remarkably, an analogous "motional averaging" effect has become a key method for high-resolution NMR of solids. For spin = 1/2 nuclides, the most important anisotropic interactions are usually the chemical shift anisotropy and magnetic dipolar interactions (see section below). Theory shows that these are averaged to zero if the entire sample is rotated about an axis at the "magic angle" θ of 54.74° relative to the external field, for which $1 - 3\cos^2\theta$ goes to 0 (Duer 2002; Mackenzie and Smith 2002). To accomplish this, the sample is enclosed in a small (typically 1 to 10 mm diameter) cylindrical rotor, usually made of high-strength ceramic, and spun on an air bearing at rates at which the gas velocity over the rotor surface may approach the speed of sound. To be effective, the spinning rate (frequency) must be a significant fraction of the total "static" (non-spinning) peak width. In some cases, these widths can be 50 kHz or more, motivating the development of very rapid spinning systems. For spinning rates less than the static peak width, the spectrum breaks up into a central band at the isotropic chemical shift and "spinning sidebands" spaced at the spinning frequency, which map out the static line shape. Total signal intensity is constant, so lowering the spinning rate reduces the signal-to-noise ratio, but sidebands can provide information on the CSA and other interactions. In spectra with sidebands, if the CSA (or other interactions) are different for different sites, site populations derived from intensity ratios of the

EBSCOhost - printed on 2/13/2023 5:26 AM via . All use subject to https://www.ebsco.com/terms-of-use

central peaks may be incorrect if the sidebands intensities are not included in the integrations. Simulated ^{29}Si spectra of the mineral clinoenstatite ($Mg_2Si_2O_6$, with two slightly different Si sites), calculated based on published experimental data (Smith et al. 1983), illustrate the effects of magic angle spinning (Fig. 3). These are shown at the same absolute scale to illustrate the enormous enhancement in peak height as well as resolution from MAS: in fact, the static spectra would be very difficult to directly observe with natural isotopic abundance, and the presence of two distinct Si sites would probably not be detected. This figure also shows the equivalent scales for *relative* frequency in ppm and in kHz (as referenced to a standard sample of tetramethylsilane), as well as *absolute* frequency in MHz.

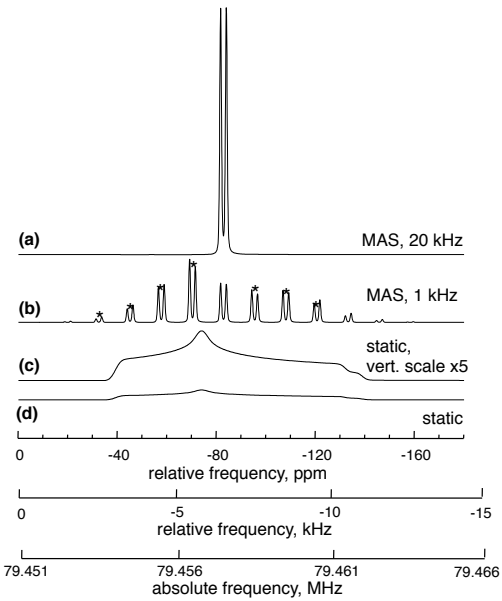


Figure 3. Simulated ^{29}Si static and MAS NMR spectra for clinoenstatite (9.4 T), illustrating effects of spinning speed. All except (c) are plotted with the same absolute vertical scale. Spinning sidebands are marked by *. The three frequency scales are equivalent.

CHEMICAL SHIFT VS. STRUCTURE

To use NMR to constrain structures, the starting point now usually involves knowledge of how structure affects chemical shift. In detail, the physics of the chemical shift is complex, as it involves the distribution of electrons in bonding and non-bonding orbitals of the atom being observed and those of the first, second, and sometimes more distant neighbors. Rapid progress is being made in theoretical, *ab initio* calculations of chemical shifts and other NMR parameters, especially for lighter elements, as computational power increases (Tossell 2001; Xue and Kanzaki 2001; Ashbrook et al. 2007a; Charpentier 2011). Many structure-shift correlations, originally revealed by experimental data for crystals and molecules of known structures, are now being complemented and clarified by first principles calculations (Engelhardt and Michel 1987; Mackenzie and Smith 2002) (see the section below on first-principles calculations of NMR parameters).

Because most nuclides that are commonly observed in NMR of silicates and other oxides are in cations (M) coordinated by oxide ions, the variety of chemical shift effects is somewhat reduced. For most of these, the largest and most obvious effect is that of the first-shell coordination number, i.e., the number of first-neighbor oxygen neighbors. This is generally strongly correlated with the mean cation-oxygen distance. Increasing the coordination number (and accompanying large increase in the mean M-O distance) generally decreases the chemical shift,

EBSCOhost - printed on 2/13/2023 5:26 AM via . All use subject to https://www.ebsco.com/terms-of-use

as has been well-documented for ^{6}Li, ^{11}B, ^{23}Na, ^{25}Mg, ^{27}Al, ^{29}Si, ^{31}P, ^{39}K, ^{43}Ca, ^{45}Sc, ^{89}Y and other less-commonly studied nuclides. For at least the high field-strength cations, e.g., B^{3+}, Al^{3+}, Si^{4+}, chemical shift ranges for their well-defined coordination polyhedra have limited or no overlap. Thus, for cations that have significant variations in coordination number, such first-order NMR peak assignments are generally straightforward. Examples include four-and six-coordinated Si (^{IV}Si and ^{VI}Si) in high-pressure garnets (Fig. 4), Al in the A and B sites of $MgSiO_3$ perovskite (Fig. 2), and ^{VI}Ca in calcite vs. ^{IX}Ca in aragonite (Fig. 5). The latter two examples also show effects of quadrupolar coupling on line shapes (see below on quadrupolar interactions); the ^{43}Ca data are for an especially difficult experiment on a low-abundance (0.14%), low-γ nuclide.

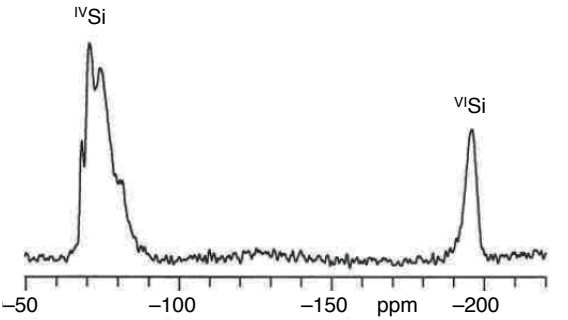


Figure 4. ^{29}Si MAS NMR spectrum of a high pressure garnet on the majorite ($MgSiO_3$)-pyrope ($Mg_3Al_2Si_3O_{12}$) join (Phillips et al. 1992a). The complex line shape for the ^{IV}Si was modeled to describe cation disorder.

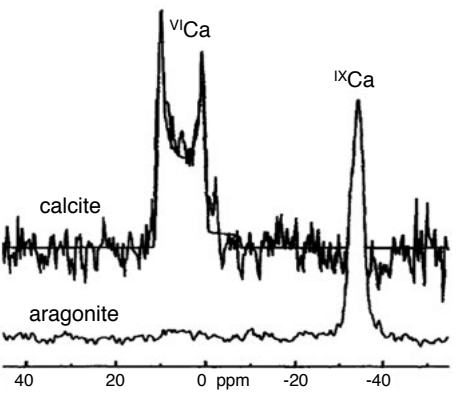


Figure 5. ^{43}Ca MAS NMR spectra (natural, 0.14% isotopic abundance, 8.5 T, 14 mm NMR rotor) and line shape simulations for calcite and aragonite. [Used by permission of Elsevier, from Dupree et al. (1997) *Chemical Physics Letters*, Vol. 276, Fig. 2, p. 401].

Of course, in many cases, such as ^{29}Si in almost all low-pressure silicates, cations *don't* have important changes in coordination number, and more subtle effects come into play. The effects of the identity and numbers of first-neighbor cations are often the first correlations sought, as these can change the length, covalency, and degree of orbital hybridization in first-shell M-O bonds. The most often-applied examples are the partially-overlapping ranges of ^{29}Si chemical shifts for SiO_4 groups with varying numbers of oxygens (n) that are "bridging" to other network cations such as Si or Al, as denoted by Q^n where "Q" derives from the chemical term "quaternary" (Smith et al. 1983; Kirkpatrick 1988). Each decrease by 1 in n from 4 to 0 (tecto- to orthosilicates) raises the chemical shift by about 10 ppm, in this case to less negative values. For related reasons, ^{29}Si chemical shifts for tectosilicate groups (Q^4) have increments of about +5 ppm for each first cation Si neighbor that is replaced by Al. This latter correlation has been especially important in the widespread application of ^{29}Si MAS NMR to determining Si/Al site occupancies in framework aluminosilicates, such as analcimes with varying Si/Al ratios (Fig. 6). Within a group of closely-related structures, such as zeolites and feldspars, or silica polymorphs, more detailed correlations with local structural variables such as mean Si-O-Si bond angle or Si-O distance have been established (Engelhardt and Michel 1987). More recent ^{29}Si NMR study on a double-layered aluminosilicate (K-cymrite) has shown that different permutations of a given

EBSCOhost - printed on 2/13/2023 5:26 AM via . All use subject to https://www.ebsco.com/terms-of-use

set of nSi and $(4 - n)$Al over neighboring tetrahedral sites of markedly unequal Si-O-T angles give distinct peaks, suggesting differences in the dependencies of ^{29}Si chemical shift on Si-O-Si and Si-O-Al angles (Xue and Kanzaki 2012). For SiO_6 groups that are common in high-pressure mantle minerals (Stebbins and Kanzaki 1990), there are more varieties in local structures because of the larger number of neighboring cations and the greater variety of polyhedral connectivity (both corner- and edge-sharing). SiO_6 octahedra with edge-shared neighbors tend to give less negative chemical shifts than those with only corner-shared neighbors, and also show similar dependency on the Si/Al distribution as those displayed by SiO_4 tetrahedra (Xue et al. 2006, 2010).

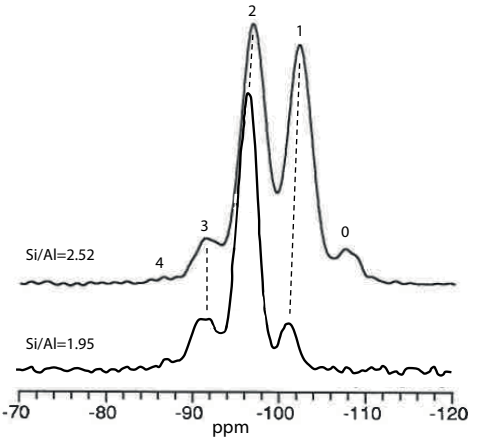


Figure 6. ^{29}Si MAS spectra for analcime samples with Si/Al as labeled (Phillips and Kirkpatrick 1994). Signals from Si sites with varying numbers of Al neighbors are marked. Peak areas were analyzed to estimate the configurational entropy due to Si-Al disorder.

Among commonly-studied cations in inorganic materials, ^{1}H is a special case as it can generally be considered to be strongly bonded to only one oxygen, in an OH^- group, H_2O molecule, or less commonly an H_3O^+ group, and is often hydrogen-bonded to one or more other oxygens or other anions, whose strength is an important structural factor affecting the stability and properties of hydrous minerals (see section below). The chemical shift range for ^{1}H is relatively small (around 20 ppm). However, the ^{1}H shift is well-correlated with the hydrogen-bond (O-H···O and H···O) distances for various types of OH and H_2O groups, generally increasing with increasing hydrogen bonding strength, rendering it a valuable tool for inferring such information (Xue and Kanzaki 2009). This correlation may at first sight seem to be discouraging for differentiating second neighbors. However, because the hydrogen-bonding strength itself reflects, to a large extent, the number and type of cations to which the OH is bonded, different OH groups often show characteristic ^{1}H chemical shift and hydrogen-bonding distance ranges. Examples include moderate to large chemical shifts for more acidic SiOH and POH groups, especially those hydrogen-bonded to nonbridging oxygens, and relatively small chemical shifts for more basic CaOH and MgOH groups (Xue and Kanzaki 2004; Xue and Kanzaki 2009). This factor has been important for resolving OH groups in different environments, such as SiOH vs. [Ca,Mg]OH in hydrous silicate glasses and minerals by ^{1}H MAS NMR (Fig. 7). In the absence of significant hydrogen bonding, the ^{1}H chemical shift shows more subtle dependence on the number and types of cations to which the OH is bonded, for example 3Mg vs. 2Mg1Al in phyllosilicates and amphiboles, rendering it useful for probing cation distributions (Welch et al. 1994; Fechtelkord et al. 2003).

For *anions* studied by NMR in inorganic materials, both the number and identities of *first-shell* cations may vary, and thus there are more variables that can have large effects on the chemical shift. The best-studied case, even though isotopic enrichment is usually needed, is ^{17}O (Mackenzie and Smith 2002). In series of structurally-similar compounds, there are large and consistent effects of increasing cation-oxygen distance and hence ionicity. For example, the chemical shift increases by 100's of ppm from SiO_2 (as stishovite) to TiO_2 (as rutile), and from MgO to CaO to SrO to BaO. Analogous effects are known for the non-bridging oxygens (NBO) in $MgSiO_3$, $CaSiO_3$, and $BaSiO_3$ and comparable glasses. However, even the first-order correlations of chemical shift with coordination number that are well-known for

EBSCOhost - printed on 2/13/2023 5:26 AM via . All use subject to https://www.ebsco.com/terms-of-use

cations are complicated for ^{17}O by its wide range of bonding environments: increasing oxygen coordination from 2 to 3 in SiO_2 or GeO_2 polymorphs *increases* the ^{17}O chemical shift, but higher oxygen coordination numbers in more ionic oxides such as HfO_2, ZrO_2 and Ta_2O_5 generally seem to *decrease* the chemical shift. Here, improving ab initio calculations are becoming especially important in analyzing spectra. As noted below, the quadrupolar character of ^{17}O (I = 5/2), although broadening peaks, often provides other NMR observables that can be correlated with local structure. Other nuclides that commonly occur in anions, notably ^{19}F, ^{33}S, and ^{35}Cl, have also been studied in minerals and have shown systematic chemical shift/structure correlations somewhat analogous to those of ^{17}O. These have been used to constrain the chemical environments of these anions in silicate glasses (see section on glasses, below).

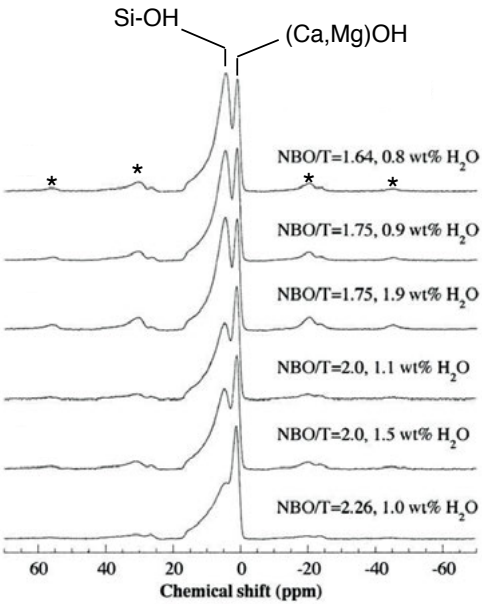


Figure 7. ^{1}H MAS NMR spectra for hydrous Ca,Mg silicate glasses along the SiO_2-$CaMgSiO_4$ join with ratios of non-bridging oxygen to Si (NBO/T) increasing from top to bottom. Spinning sidebands are marked by *. [Used by permission of Elsevier, from Xue and Kanzaki (2004) *Geochimica et Cosmochimica Acta*, Vol. 68, Fig. 2, p. 5032].

In disordered crystalline solids and glasses, NMR peaks (especially for I = 1/2) are often much broader than in ordered crystals, reducing resolution among different sites and making quantification more difficult. However, if chemical shift is well-correlated with a particular structural variable, then the extent of broadening can be mapped into the extent of disorder, which can be a fundamental characteristic of the material. A good example is the distribution of Si-O-Si angles in silica glass (Mackenzie and Smith 2002; Clark et al. 2004).

QUADRUPOLAR INTERACTIONS AND STRUCTURE

The majority of NMR-observable nuclides have $I > 1/2$, most commonly an odd multiple of 1/2 such as 3/2 (e.g., ^{11}B, ^{23}Na) or 5/2 (e.g., ^{17}O, ^{27}Al). Such nuclides have electric quadrupolar moments, $2I + 1$ energy levels, and $2I$ transitions between adjacent levels. These are affected not only by the magnetic field but by the electric field gradient (EFG) at the nucleus: for non-cubic sites, this changes the transition energies systematically so that, in principle, separate signals from each of the transitions can be observed. These interactions are again described most completely by second-rank tensors, but are commonly summarized by the "quadrupolar coupling constant" $C_Q = e^2qQ/h$, where e is the charge of the electron, eq is the largest principle value of the electric field gradient tensor (greater values for more distorted sites) and eQ is the nuclide-specific nuclear quadrupole moment. The second key variable is the quadrupolar asymmetry parameter, η_Q, which varies from 0 to 1 and measures the deviation of the EFG tensor from uniaxial symmetry. Early single-crystal work on nuclides such as ^{27}Al in minerals often measured all of the transitions as function of orientation and derived the full quadrupolar tensor. From such data, rough correlations of C_Q and/or η_Q with crystallographic site distortion were noted

EBSCOhost - printed on 2/13/2023 5:26 AM via . All use subject to https://www.ebsco.com/terms-of-use

(Ghose and Tsang 1973) and symmetry changes during phase transitions in minerals such as anorthite were observed (Staehli and Brinkmann 1974). In some cases, large differences in symmetry between sites allowed measurements of site occupancies and therefore structural disorder, as for $MgAl_2O_4$ spinel, even at low magnetic fields where chemical shift differences were unresolvable (Fig. 8) (Brun and Hafner 1962).

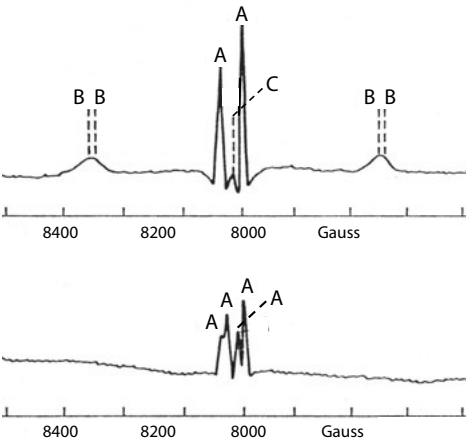


Figure 8. ^{27}Al NMR spectrum (about 0.8 T) of a single crystal of a natural spinel ($MgAl_2O_4$ with minor Fe, Cr, etc.). The upper spectrum is with the external magnetic field parallel to the four-fold axis; the lower is for an oblique orientation. A and B mark the central and satellite transitions for ^{VI}Al; C marks ^{IV}Al. [Used by permission of Oldenbourg Wissenschaftsverlag GmbH, from Brun and Hafner (1962) *Zeitschrift für Kristallographie*, Vol. 117, Fig. 1, p. 44].

The electric quadrupolar interactions are in general much larger than dipolar coupling or chemical shielding, so that their effect on the spin energies often need to be considered to second order. For half-integer quadrupolar nuclei, such as ^{27}Al (I = 5/2), the "central" transition (–1/2 to +1/2) is not affected by quadrupolar coupling to first order, whereas the "satellite" transition (e.g., +1/2 to +3/2, –1/2 to –3/2) frequencies show large orientation-dependent shifts, often on the order of MHz. In modern, high-resolution MAS NMR, often only the "central" transition is analyzed. The satellite transitions, which can have much larger static peak widths, can contribute wide manifolds of spinning sidebands whose intensity pattern may also be simulated to obtain the chemical shift and quadrupolar parameters and where resolution among signals for different sites can sometimes be enhanced. Although the orientation dependence of the first order quadrupolar effect can be averaged out by magic angle spinning, the second-order quadrupolar effect is more complicated and is only partially averaged by normal magic-angle spinning. The central transition is broadened and shifted to lower frequency by factors proportional to C_Q^2, with a complex, often "split" peak shape that can readily be calculated from C_Q and η_Q, or, conversely, fitted to yield those variables. (See Figs. 5, 9, and 10 and (Kirkpatrick 1988; Mackenzie and Smith 2002) for illustrations of how peak shapes change with these parameters.) These effects, in frequency units, increase linearly with decreasing ν_L. They can thus be particularly severe for "low-γ" quadrupolar nuclides, in some cases making useful spectra difficult to obtain because of severe broadening. On the other hand, because chemical shifts increase linearly with ν_L, for a given nuclide the size of the quadrupolar broadening and shift *relative* to the chemical shift *decrease* as the square of the external magnetic field. For this reason, higher and higher fields have progressively improved the chemical shift resolution of spectra for quadrupolar nuclides, and have made more and more of the periodic table accessible to high-resolution NMR. Analysis of spectra from two or more fields can often be very helpful in separating quadrupolar effects from chemical shifts in complex spectra, especially for disordered materials. *Ab initio* methods (see section below) have become increasingly important for predicting and analyzing quadrupolar parameters, and are often computationally more straightforward than chemical shift calculations. This has been especially useful in predicting correlations between local structural variables (e.g., Si-O-Si angles) and C_Q and η_Q, which have been helpful in analyzing spectra, for example for ^{17}O in silicate glasses (Charpentier et al. 2004; Clark et al. 2004; Clark and Grandinetti 2005; Pedone et al. 2010; Angeli et al. 2011).

EBSCOhost - printed on 2/13/2023 5:26 AM via . All use subject to https://www.ebsco.com/terms-of-use

A number of important practical issues resulting from quadrupolar interactions are illustrated in Figure 9, which shows simulated spectra for a hypothetical case of ^{27}Al in two tetrahedral sites with slightly different chemical shifts but very different C_Q's, calculated to illustrate results for high-silica "Libyan Desert" glass containing <1% dissolved Al_2O_3 (Stebbins et al. 2005). 5% of the total Al is in sites with δ_{iso} = 60 ppm and C_Q = 2 MHz, 95% has δ_{iso} = 50 ppm and C_Q = 15 MHz. η_Q for both is 1. These C_Q values are near the low and high ends of the range commonly seen for this nuclide in minerals, but are not unrealistic. Figure 9a shows a currently rarely obtainable case of an MAS speed of 100 kHz but illustrates the true peak shapes at 9.4 T, although the quadrupolar distortion for the low-C_Q site (A) is not visible at the scale plotted. The peak maximum for the high-C_Q site (B) is shifted down by over 150 ppm; δ_{iso} lies at its high-frequency (left) end. Its width is 360 ppm or 38 kHz. If the spectrum is now calculated at 9.4 T and a more realistic, but now insufficient, spinning speed of 10 kHz, the orientational effects on the signal from the high-C_Q site are only partially averaged and the peak is spread out to the point of near invisibility (Fig. 9b). If we now add in bit of spectrometer deadtime (which discriminates further against broad signals) and some noise, only the low-C_Q site would be visible, representing only 5% of the total Al in the sample (Fig. 9c). Much lower spinning speeds of 3-5 kHz were common in early generations of MAS NMR probes, compounding such difficulties. If the total signal were integrated and compared

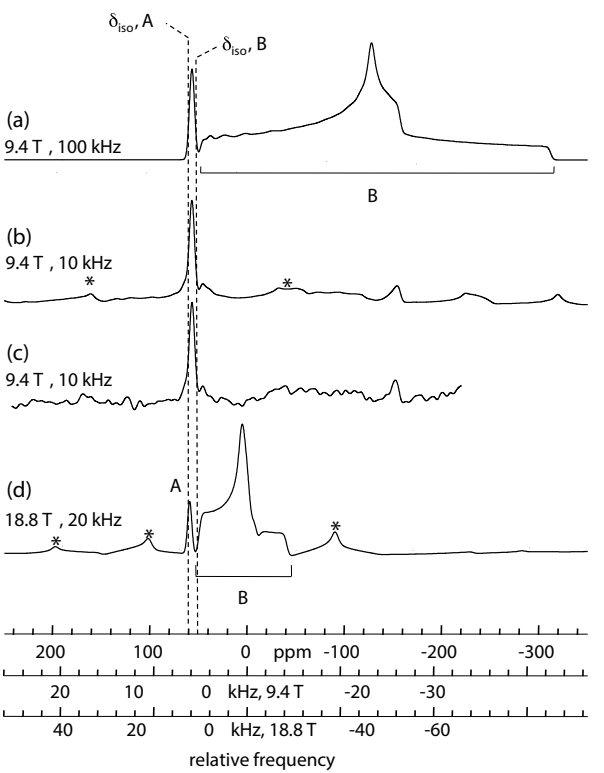


Figure 9. Simulated ^{27}Al MAS NMR spectra for a hypothetical material with Al in two sites, showing only the central transitions. 5% of the Al is in site A, with δ_{iso} = 60 ppm, C_Q = 2 MHz, and η_Q = 1; 95% is in site B with δ_{iso} = 50 ppm, C_Q = 15 MHz, and η_Q = 1. The fields and spinning speeds for the calculations are shown; (c) differs from (b) only by increased spectrometer deadtime and noise. Spinning sidebands are marked by *. See text for details.

EBSCOhost - printed on 2/13/2023 5:26 AM via . All use subject to https://www.ebsco.com/terms-of-use

to that of a suitable standard, this discrepancy would readily be detected. Such calibrations are often not made, but the issue of "invisible aluminum" has been noted in a number of careful early studies at relatively low fields (Mackenzie and Smith 2002). Finally, and reassuringly, Figure 9d shows the spectrum at the increasingly common high field of 18.8 T, with a readily attainable spinning speed of 20 kHz. Here, the full spectrum would be readily and accurately observed, as the width of the signal from the high-C_Q is reduced by a factor of four on a chemical shift scale. Systematic effects of increasing fields on experimental spectra of crystals and glasses are illustrated in a number of studies (Mackenzie and Smith 2002).

Several NMR methods have been developed, which, unlike MAS, completely average the anisotropy of quadrupolar interactions for half-integer spins (Duer 2002; Mackenzie and Smith 2002). These can often greatly enhance resolution, and hence the content of structural information, that can be obtained. The average frequency shift induced for the central transition by the second-order quadrupolar coupling, with sample rapidly spinning about an axis at angle θ with respect to the external magnetic field, can be described by three terms. These are an isotropic part that contributes to an overall shift in peak position from that of the isotropic chemical shift, an orientation-dependent term scaled by $P_2(\cos\theta)$ (second-order Legendre polynomial as shown in Eqn. 3) that is eliminated by MAS, and another orientation-dependent term scaled by $P_4(\cos\theta)$ (fourth-order Legendre polynomial shown in Eqn 4) that is not averaged to zero by MAS, but may be averaged out by spinning at two other angles of its root (30.6° and 70.1°).

$$P_2(\cos\theta) = \frac{1}{2}(3\cos^2\theta - 1) \tag{3}$$

$$P_4(\cos\theta) = \frac{1}{8}(35\cos^4\theta - 30\cos^2\theta + 3) \tag{4}$$

In "Double Rotation" (DOR) NMR, the sample is rotated simultaneously about two angles (54.7 and 30.6° or 70.1°) to average out both $P_2(\cos\theta)$ and $P_4(\cos\theta)$; in "Dynamic Angle Spinning" (DAS) NMR, the sample spinning angle is flipped sequentially between two different angles that together lead to the cancellation of these terms over time. Both can give highly quantitative spectra. However, both are mechanically challenging to implement because they require special probes and have not been widely applied to Earth materials. Much more readily implemented is "Multiple Quantum" MAS (MQMAS, most commonly "triple quantum" or 3QMAS) NMR, which can be done with most normal MAS NMR probes and eliminates the anisotropic broadening via manipulation of the nuclear spins by RF pulses. Like the central (–1/2 to +1/2) transition, all symmetric (–m to +m, where m = 3/2, 5/2, etc.) multiple ($2m$) quantum transitions are unaffected by quadrupolar coupling to first order, and their average second-order quadrupolar frequency shifts all include three terms as above, differing only in the respective coefficients describing their relative contributions. In a MQMAS experiment, the $P_2(\cos\theta)$ term is averaged out by magic angle spinning, and the $P_4(\cos\theta)$ term is averaged out by allowing the nuclear spins to first evolve in a $2m$ (e.g., 3 or 5) multiple quantum coherence state (after excitation by a strong pulse) for a time duration t_1, and then converting it to single-quantum central transition coherence for detection (t_2). The MQMAS (and DAS) experiments are two-dimensional (2D) experiments for which a series of spectra are acquired with incremented t_1. These are then Fourier transformed with respect to both time variables, followed by a shearing transformation to project the isotropic spectrum in the first (indirect) dimension, F_1. This results in a two-dimensional spectrum correlating the usual MAS dimension (F_2) with the isotropic dimension (F_1). Projection to the MAS dimension yields a spectrum that resembles the central transition of the normal, one-dimensional (1D) MAS spectrum; projection to the isotropic dimension yields a high-resolution isotropic spectrum that is free from anisotropic broadening, although the peak position is shifted from the isotropic chemical shift because of the isotropic term of the second-order quadrupolar coupling. For

EBSCOhost - printed on 2/13/2023 5:26 AM via . All use subject to https://www.ebsco.com/terms-of-use

a spectrum containing multiple peaks, MAS cross sections (traces) taken at each isotropic peak position give a series of MAS spectra as if each site is taken out and measured by MAS separately, greatly enhancing the resolution (Fig. 10) (Xue and Kanzaki 2007b).

A limiting factor for MQMAS experiments is sensitivity, because multiple-quantum excitation and its conversion to single quantum coherence are relatively inefficient. Efforts have been made to increase the sensitivity through the design of more efficient pulse sequences. Another complication is that the experiment is intrinsically not quantitative because the efficiencies of multiple quantum excitation and reconversion to single-quantum coherence depend on C_Q and experimental conditions (e.g., RF field strength), and in particular, are known to deteriorate for very large (or very small) values of C_Q. Intensity corrections based on data for reference compounds and/or numerical simulations may be made. Alternatively and more straightforwardly, for samples with well-ordered structures, the MQMAS data may be used to first extract the chemical shift and quadrupolar coupling parameters, which are then used to further simulate the more quantitative normal 1D MAS spectrum to obtain relative abundances.

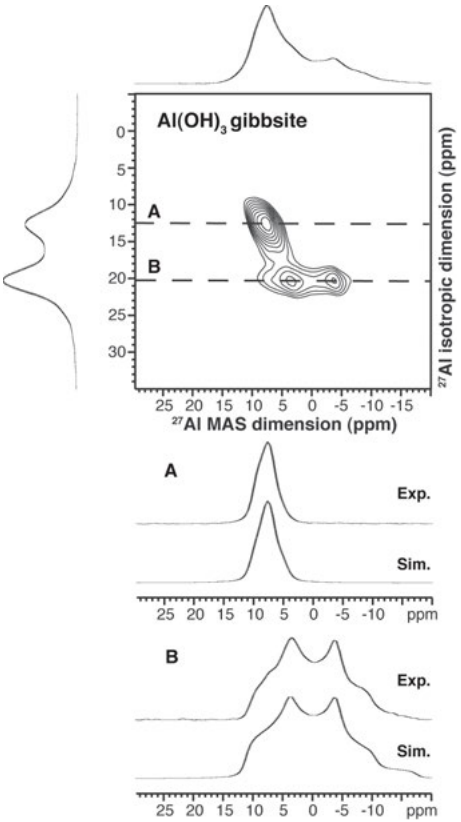


Figure 10. ^{27}Al 3QMAS spectrum for gibbsite ($Al[OH]_3$). Projections in the MAS (F2) and isotropic (F1) dimensions are shown, illustrating enhanced resolution in the latter. A and B are the two crystallographically distinct Al sites, with C_Q values of 2.2 and 4.7 MHz, respectively. Note the quadrupolar splitting of the latter in the MAS dimension only. MAS dimension cross sections ("traces"), with experimental and simulated line shapes, are shown below. [Used by permission of the American Chemical Society, from Xue and Kanzaki (2007b) *Journal of Physical Chemistry B*, Vol. 111, Fig. 11, p. 13164].

Another related high-resolution technique for half-integer quadrupolar nuclei is satellite transition (ST) MAS, which similarly achieves high resolution by manipulating the nuclear spins to correlate the satellite transitions with the central transition in a 2D MAS experiment. It in general yields higher sensitivity than MQMAS because only single-quantum transitions are involved, but has more stringent requirements on the experimental conditions such as magic angle setting and spinning rate stability. STMAS could be the method of choice when sensitivity is a limiting factor (Ashbrook and Wimperis 2004).

MAGNETIC DIPOLAR INTERACTIONS AND INDIRECT SPIN-SPIN COUPLINGS

The spins of nuclei with $I > 0$, as well as those of unpaired electrons, act as magnetic dipoles and can significantly perturb the energy of an NMR transition being observed, in a

EBSCOhost - printed on 2/13/2023 5:26 AM via . All use subject to https://www.ebsco.com/terms-of-use

complex, structure-, orientation- and time-dependent fashion. The size of these effects scale with the product of the gyromagnetic ratios for the spin being observed (γ_I) and that causing the perturbation (γ_S). Such "dipole-dipole" couplings thus can be particularly important for NMR on ^{1}H or ^{19}F or on other nuclides in materials that contain abundant H or F, as the γ's for these nuclides are unusually high and they have ca. 100% isotopic abundances. Since γ for the electron is much greater than for nuclear spins, dipolar interactions from unpaired electron spins, as in many transition metal and rare earth ions, can also be very important. The energies of dipole-dipole couplings scale inversely with the cube of the separation of the spins, meaning that they are extremely sensitive to distance and thus, potentially, to structural details.

Dipole-dipole interactions can cause significant broadening of spectra. In many cases, especially for dilute spins such as ^{29}Si, these are small enough (<10's of kHz) to be averaged to zero by MAS. In other cases, for example when observing ^{13}C in an H-rich organic compound, special "decoupling" methods remove the influence of the ^{1}H spins. Observation of ^{1}H spectra in H-rich materials is a particular challenge, as couplings can reach 70 kHz and the ^{1}H-^{1}H homonuclear dipolar couplings are only partially averaged out at moderate spinning rates, resulting in broadened peak widths that scale inversely with the spinning rate. This has been one impetus for the development of faster spinning probes, necessitating smaller rotors and samples. With currently available spinning rates (typically about 25 to 40 kHz, but up to about 100 kHz with very small rotor diameters), the resolution in 1D ^{1}H MAS NMR spectra for H-rich materials such as hydroxides are often still not satisfactory. Multiple pulse excitation combined with rotation ("CRAMPS") often provides better resolution. The more traditional CRAMPS techniques (e.g., "WAHUHA") were performed in the quasi-static limit (typically a few kHz MAS) to avoid interference between the multi-pulse and sample rotation. Newer-generation (1D or 2D) CRAMPS experiments (e.g., "FSLG," "PMLG," "DUMBO") are applicable at faster spinning rates (> 10 kHz) and often yield better resolution (Lesage 2009; Xue and Kanzaki 2009).

In many materials with abundant unpaired electrons, dipolar broadening (and other effects) can be large enough to make acquisition of a spectrum nearly impossible, but this is not always the case as shown by recent work on Fe-containing garnets (Palke and Stebbins 2011b), on rare-earth containing monazites and xenotimes (Palke and Stebbins 2011a) and on ions sorbed to iron oxyhydroxides (Nielsen et al. 2005; Kim et al. 2008, 2011). These applications are described in the section below on minerals containing unpaired electron spins.

In addition to dipolar coupling, which is a through-space interaction, nuclear spins also interact with one another indirectly through bonding electrons. This through-bond interaction is known as indirect spin-spin, scalar or J coupling. Its magnitude is determined by the J coupling constant, which is much smaller than dipolar coupling, and also in general decreases with increasing number of intervening bonds, for example < 20 Hz between the ^{29}Si pair in the ^{29}Si-O-^{29}Si bonds, and much smaller for pairs separated by more bonds. In solution-state NMR, J coupling often results in peak splitting, and has been widely explored in various multiple dimensional experiments to provide direct connectivity information about the molecular structure. For solid-state NMR, peak splittings resulting from J couplings are often not resolved in 1D MAS NMR spectra. Nevertheless, especially in recent years, various NMR techniques utilizing J coupling have been applied to solids, allowing the connectivity of nuclei of the same or different types to be probed, and the magnitude of J coupling constants to be measured. The latter, like chemical shift and quadrupolar coupling parameters, are useful for gaining insight about local structural parameters. For example, the $^{2}J_{TT'}$ coupling constants (where 2 stands for the number of bonds that separate the two nuclei, T,T′ stand for tetrahedral cations, such as Si, P, Al,…) for T-O-T′ bonds have been shown to be correlated with the T-O-T′ angles (Massiot et al. 2010; Kanzaki and Xue 2012; Xue and Kanzaki 2012).

EBSCOhost - printed on 2/13/2023 5:26 AM via . All use subject to https://www.ebsco.com/terms-of-use

MORE ADVANCED NMR METHODS

The truly powerful, as well as simply fascinating, aspect of NMR spectroscopy that provides unique advantages lies in its ability to gain direct atomic connectivity or proximity information via various multiple-resonance NMR techniques, which involve the excitation of more than one nuclide in a single experiment (Duer 2002; Mackenzie and Smith 2002). These are often combined with two-dimensional methods, which correlate two frequencies via experiments containing more than one time variables. These experiments utilize either through-space dipolar coupling or through-bond spin-spin (J) coupling among spins and manipulate the spin system by RF pulses and/or sample rotation, "to such an extent that some experiments border on sorcery" (Ernst et al. 1987).

The most basic and widely used double-resonance experiment is cross-polarization (CP), usually combined with magic angle spinning (CPMAS). For an I→S CP experiment, the I spin is first excited by a 90° pulse, and the polarization is then transferred to S spin via dipolar interaction by applying simultaneous "contact" pulses on both frequency channels, before detection of the NMR signal from the S spin. ^{1}H→X (e.g., ^{13}C, ^{29}Si) CPMAS NMR is a well-established method for organic and inorganic solid materials, and may lead to significant sensitivity enhancement for phases with abundant protons, such as most organic materials and hydrous minerals, because the maximum intensity is proportional to the ratio of the gyromagnetic ratios of the two spins. Also, the proton relaxation times T_1 (see below on relaxation), and thus the delay times between pulses, are often much shorter than those of dilute spins such as ^{29}Si. The CP experiment is generally not a quantitative measurement because signal intensities depend in a complex way on the CP dynamics as well as the distributions of both spins involved. This could nevertheless be used to advantage: the I→S CP experiment can provide insight into relative I-S proximities because the signal intensity at relatively short contact times is a function of the distance between the two spins, and thus it is a valuable tool for assisting peak assignment. For example, the combination of ^{29}Si MAS and ^{1}H-^{29}Si CPMAS NMR experiments allows easy distinction of peaks of hydrous phases from those of anhydrous phases in mixed samples, and can also differentiate local structures with different H-Si proximities in a homogenous phase (e.g., Si Q^4 and Q^3-OH in hydrous silicate glasses). CPMAS NMR experiments can also be applied to other spin pairs, including the reversed X-^{1}H pair (detecting ^{1}H) and X-Y pairs other than ^{1}H (e.g., ^{27}Al-^{29}Si) to obtain analogous information. For example, as described below, combining quantitative ^{1}H MAS NMR with (^{1}H-)^{29}Si-^{1}H and ^{27}Al-^{1}H CPMAS NMR was indispensable in resolving and quantifying the distribution of different OH species (SiOH, AlOH, [Ca,Mg]OH) in hydrous aluminosilicate glasses (Fig. 11) (Xue 2009; Malfait and Xue 2010). It should be noted that for CPMAS experiments involving one or two quadrupolar nuclei, the optimal experimental condition depends complexly on the spinning rate, C_Q and RF field strength for the CP contact pulses (Duer 2002).

There are a number of other dipolar-based double-resonance experiments that are similarly sensitive to inter-nuclear distances, including "Rotational Echo DOuble Resonance" (REDOR), "Transferred Echo DOuble Resonance" (TEDOR), "TRAnsfer of Populations by DOuble Resonance" (TRAPDOR) and "Rotational-Echo Adiabatic Passage DOuble Resonance" (REAPDOR) experiments, with the latter two designed for quadrupolar nuclei (Duer 2002; Mackenzie and Smith 2002). These experiments all rely on the reintroduction of the dipolar interactions, otherwise averaged by magic-angle spinning, by applying either 180° pulses or continuous irradiation to the non-observe nuclei during a rotor period. Among them, the TEDOR experiment, like CPMAS, is a dipolar-based polarization transfer MAS experiment, with the polarization of the initially excited spin transferred to the detected spin, and is thus amenable to 2D correlation experiments described below.

The 1D CP and TEDOR experiments can be extended into a two-dimensional (2D) "HETeronuclear CORrelation" (HETCOR) experiment by introducing an evolution time period (t_1)

EBSCOhost - printed on 2/13/2023 5:26 AM via . All use subject to https://www.ebsco.com/terms-of-use

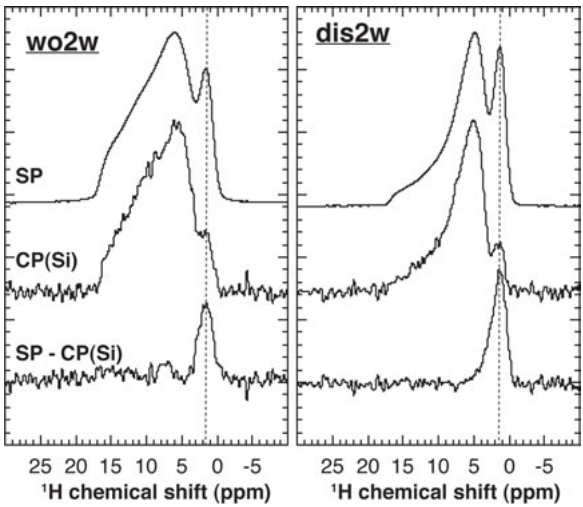


Figure 11. ^{1}H MAS (single pulse, "SP," top) and ^{1}H to ^{29}Si to ^{1}H CPMAS (middle) NMR spectra (9.4 T) of hydrous $CaSiO_3$ (left) and Ca,Mg silicate (right) glasses with 2 wt% H_2O, showing less enhancement by CP of the signal from (Ca,Mg)OH (narrow peak marked by dotted lines) relative to SiOH groups (broader, higher-frequency peak). The lowermost curves are difference spectra (Xue 2009).

after the excitation pulse of the first spin. This again involves acquiring a series of spectra with incremented t_1 values and performing a 2D Fourier transform with respect to both time variables (the final acquisition time, t_2, and the evolution time t_1) to obtain a 2D spectrum. For quadrupolar nuclei, the HETCOR experiment can be combined with the MQ experiment to achieve higher resolution (MQ-D-HETCOR). As HETCOR experiments directly provide correlation of spectra for two different nuclides, and often offer higher resolution than the corresponding 1D experiment, the method is a powerful and direct way to distinguish peaks belonging to the same or different phases, and their relative proximities, alleviating the ambiguities of peak assignment based solely on peak positions. An example is the resolution of AlOH species in a hydrous aluminosilicate glass from 2D ^{27}Al-^{1}H HETCOR and 3Q-HETCOR spectra (Fig. 12). This species was unresolved in the single-resonance ^{27}Al 3QMAS NMR spectrum (Xue and Kanzaki 2006).

Analogous J coupling-based double resonance experiments have also been increasingly applied to inorganic and organic solids, including ^{29}Si-^{27}Al, ^{27}Al-^{31}P, and ^{17}O-^{27}Al (Massiot et al. 2010). Examples include 1D "INsensitive Nuclei Enhanced by Polarization Transfer" (INEPT) and 2D HETCOR experiments utilizing methods such as "INEPT," "J-HMQC" and "J-HSQC." Such experiments are analogous to those used in solution-state NMR, for which dipolar interactions are averaged out by rapid isotropic motion (Keeler 2010). These generally involve multiple 90° and 180° pulses separated by spin echo delay times with polarization transfer achieved by simultaneous 90° pulses on both spins. Despite the fact that J couplings are much smaller in comparison with dipolar interactions, and generally do not lead to resolved peaks in 1D NMR spectra, it has been demonstrated that comparable sensitivity to dipolar-based HETCOR experiments can often be achieved, especially for those involving quadrupolar nuclei (Wiench and Pruski 2004). These can again be combined with multiple quantum methods to achieve high resolution for half-integer quadrupolar nuclei. As the two types of HETCOR experiments give respectively through-space and through-bond connectivity information, and the dipolar and J couplings have different dependencies on structural parameters (e.g., bond angles) they are complementary to each other (Kanzaki and Xue 2012).

EBSCOhost - printed on 2/13/2023 5:26 AM via . All use subject to https://www.ebsco.com/terms-of-use

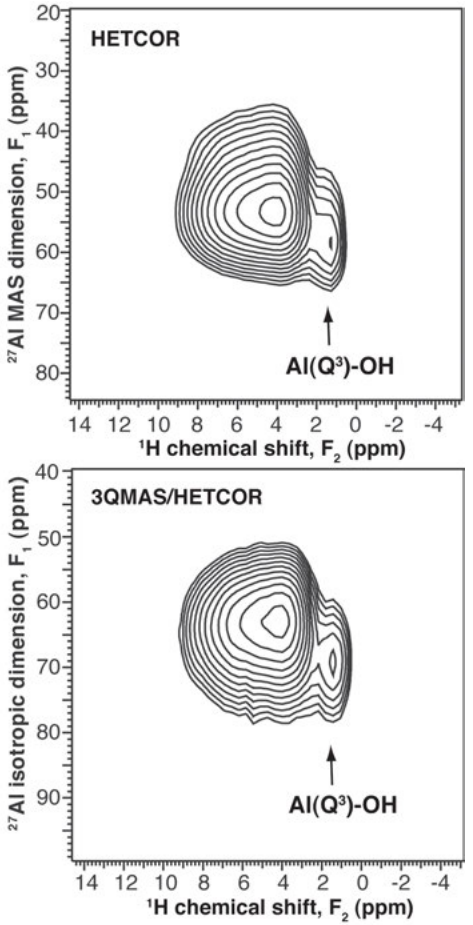


Figure 12. ^{27}Al to ^{1}H HETCOR (top) and 3QMAS/HETCOR (bottom) spectra (9.4 T) of a $KAlSi_3O_8$ glass with 2.3 wt% H_2O (Xue and Kanzaki 2006).

2D dipolar and J-coupling based correlation experiments can also be performed on nuclei of the same type, providing direct information about homonuclear connectivity or proximity. One typical such experiment is based on the "NOESY" (Nuclear Overhauser Effect SpectroscopY) sequence, or its variants, that include a mixing time between the evolution time (t_1) and the final detection time (t_2), during which the signal is modulated by spin diffusion (dipolar coupling mediated spin exchange) and/or spin dynamics (motions). Also important are variants of double-quantum (DQ) experiments (e.g., "C7," "BABA") that all utilize multiple pulses to re-introduce homonuclear dipolar couplings that are otherwise averaged out by MAS (Mackenzie and Smith 2002). Applications utilizing J-coupling based homonuclear correlation experiments have also recently increased (Massiot et al. 2010). Among them, the DQ experiment, "INADEQUATE" ("Incredible Natural Abundance Double-QUAntum Transfer spectroscopy"), analogous to a well-known liquid-state experiment (Keeler 2010), has been increasingly applied to both natural abundance and isotopically enriched ^{29}Si and to ^{31}P in both crystalline and glassy silicates, phosphates and other inorganic materials. This has provided direct information about the site-specific connectivities. The magnitude of the isotropic J coupling constant and the numbers of such couplings can be directly obtained from 2D J-resolved MAS experiments, which include a series of rotor-synchronized spin echoes with incremented echo delay time, t_1. Such J-resolved experiments can (under favorable conditions) resolve the peak splittings from J couplings in the indirect (F_1) dimension, which are hidden in the broader normal 1D MAS spectra. This can provide a direct means of evaluating the Q^n speciation for tetrahedral (T) cations such as P and Si, the latter with isotopic enrichment (Massiot et al. 2010; Xue and Kanzaki 2012) and can thus alleviate ambiguities of peak assignment based on chemical shift alone. For example, this method has demonstrated for a double-layered K-cymrite ($KAlSi_3O_8.H_2O$) phase (with Si/Al distributed in a single crystallographically unique Q^4 tetrahedral site) that there are two sets of ^{29}Si MAS NMR peaks for Si with mixed Si/Al neighbors and a total of eight peaks for all Si (with 0 to 4 Si/Al neighbors), which correspond to different permutations of Si/Al on neighboring tetrahedral sites with two distinct Si-O-T angles (Xue and Kanzaki 2012). The assignment would be in error (and two distinct tetrahedral sites would be required) if the conventional view of a maximum of five ^{29}Si MAS NMR peaks each corresponding to Si with n (= 0 to 4) neighboring Si (Al) were simply assumed.

EBSCOhost - printed on 2/13/2023 5:26 AM via . All use subject to https://www.ebsco.com/terms-of-use

FIRST-PRINCIPLES CALCULATIONS OF NMR PARAMETERS

There are two quantum chemical approaches to calculating NMR parameters such as chemical shift, electric field gradient and J coupling tensors. One involves *ab initio* molecular orbital (MO) calculations on small clusters of atoms that mimic the local structure of interest, often with dangling bonds at the periphery terminated by H atoms. Such an approach has been applied to many inorganic structures and has provided insight into various NMR parameter vs. structure correlations, complementing empirical findings (Tossell 2001). Examples include ^{29}Si chemical shift as a function of Si coordination (Kanzaki 1996), Q^n speciation and Si-O-Si angle (Xue and Kanzaki 1998), ^{17}O C_Q as a function of Si-O-Si angle (Xue and Kanzaki 1998; Clark and Grandinetti 2005), and ^{17}O C_Q and ^{1}H chemical shift as a function of hydrogen bonding distance in OH groups (Xue and Kanzaki 2001). However, the small-cluster approach is limited because it is difficult to faithfully model local structures containing cations with relatively large coordination numbers (e.g., Na, Ca and even Si and Al with coordination numbers larger than 4), and longer-range effects and site symmetry often cannot be well-represented. A more powerful approach that is becoming increasingly routine and widely used is first-principles calculation on periodic systems, which efficiently exploits the translational symmetry of crystals using plane wave basis sets and density functional theory (DFT). This method has been widely applied to calculate EFG tensors in periodic systems since its first introduction in 1985 (Blaha et al. 1985). The more challenging chemical shift or shielding tensor calculation was made feasible with the introduction of the efficient gauge-including projector augmented wave (GIPAW) method in 2001(Pickard and Mauri 2001). Such calculations yield reliable predictions of NMR spectra for a given crystal structure, which may be either that measured by diffraction techniques or optimized with first-principles calculations. This method has been applied to a wide range of nuclides in silicates, including ^{29}Si, ^{27}Al, ^{17}O, ^{23}Na, ^{43}Ca and ^{25}Mg (Profeta et al. 2003, 2004; Charpentier et al. 2004; Ashbrook et al. 2007b).

More recently, calculations of J coupling tensors have also been reported (Yates 2010). Such results are very useful for assisting NMR peak assignments, especially when there are no simple empirical correlations between structure and NMR parameters, and have sometimes led to corrections of errors in peak assignment based on such inferences (Ashbrook et al. 2007b). Periodic first-principles calculations are applicable not only to fully-ordered crystalline systems, but also to crystal structures with disorder and other defects by using supercells. This approach has also been successfully applied to disordered structures derived from first-principles molecular dynamics simulations of glasses (Pedone et al. 2010; Angeli et al. 2011). As such calculations can now often be performed on PC-type computers with generally available (either commercial or free) software, this approach is rapidly becoming a routine tool for experimentalists to strengthen and guide data interpretations (Charpentier 2011).

NUCLEAR SPIN RELAXATION

The *rates* of energy transfer into, out of, and among nuclear spin systems are often complex, but potentially information-rich components of NMR spectroscopy. "Spin-spin relaxation," characterized by inverse rates (time constants) T_2, involves transfer of energy among similar spins and is often important in understanding line widths. More commonly discussed is "spin-lattice" relaxation, usually described by inverse rates labeled as "T_1." This involves the loss of energy from the spin system into random thermal motions of the host structure (the "lattice"). T_1's vary widely and are of crucial pragmatic importance. Most NMR experiments are done by repeated excitation pulses followed by recording of time-domain signals: if pulsing is too rapid with respect to T_1, the signal will saturate and less-and-less signal per pulse will be observed. Relaxation can be especially slow for spin-1/2 nuclides (e.g., ^{13}C, ^{29}Si, ^{31}P) in materials lacking magnetic impurities, for example T_1 measured to be hours in pure silica glass (Gladden et al.

EBSCOhost - printed on 2/13/2023 5:26 AM via . All use subject to https://www.ebsco.com/terms-of-use

1986). This problem can place major limitations on the quality of spectra that can be obtained in a practical amount of spectrometer time; in synthetic materials this can often be mitigated by doping with magnetic impurities such as 100's to 1000's of ppm of transition metal or rare earth cations. Different phases in a mixed material (e.g., mixes of different minerals, or phase-separated glasses) may relax at different rates, complicating quantitation if spectra are not fully relaxed, but in some cases allowing measurement of phase proportions. In contrast, relaxation can be very rapid in some systems, such as those containing abundant unpaired electron spins or for quadrupolar nuclides with mobile cations (T_1's of seconds, milli- or even microseconds). This may make obtaining spectra more rapid, but in extreme cases will result in severe peak broadening even to the point of non-observability.

Spin-lattice relaxation is especially sensitive to dynamics such as molecular rotation, ionic site hopping, and fluctuations during phase transitions. Detailed studies of mobile systems (both solids and liquids) have often yielded data on mechanisms and rates of dynamical processes (Stebbins 1988, 1991b; Borsa and Rigmonti 1990). In less mobile solids, detailed relaxation time studies are uncommon, as they are time-consuming and can be difficult to interpret. However, it is useful to note that bulk relaxation can generally be described by the equation

$$\frac{M}{M_\infty} = A\left\{1 - \exp\left[-\left(\frac{\tau}{T'}\right)^{\beta}\right]\right\} \tag{5}$$

Here, the ratio of the observed intensity (or "magnetization" M) to that at full relaxation (M_∞) is described as a function of time τ with a scaling constant A and a time constant T'**.** In cases with strong coupling among spins, relaxation rates are the same for all of the observed nuclei in the sample, the exponent β equals 1, and there is a single T_1 (= T') value. However, when relaxation is dominated by dipolar coupling to magnetic impurities, relaxation can be heterogeneous. In this case, as is common for ^{29}Si in silicates, a "stretched" exponential ($\beta = 0.5$) generally is a much better description (Hartman et al. 2007; Stebbins et al. 2009d).

APPLICATIONS TO CRYSTALLINE SILICATES, OXIDES AND OTHER INORGANIC MATERIALS

Structural order/disorder in minerals

Most of the minerals that make up the terrestrial planets are complex, multicomponent solid solutions. Details of short-range structure such as cation and anion site occupancies, "ideal" random mixing vs. ordering, and local distortion of sites from long-range average symmetry, can often be best determined by spectroscopic methods such as NMR, which complement the long-range average structure observed by diffraction methods. Such information is important to make accurate models of bulk properties. For example, the extent of disorder among Al and Si cations on tetrahedral sites in aluminosilicate minerals can affect the configurational entropy, and hence the free energy, enough to cause changes of 100's of degrees or many kilobars in predicted phase equilibria (Putnis 1992).

Framework aluminosilicates, in the form of feldspar and zeolite minerals, are of course very common in the Earth's crust. The latter group also has particular importance in technology, e.g., catalytic refinement of petroleum and water purification. Because of the now well-known systematic effects of SiO_4 vs. AlO_4 neighbors on ^{29}Si chemical shifts described above, together with its quantitative peak intensities, MAS NMR has been widely applied for determining Si-Al site occupancies and the extent of structural disorder in such minerals (Engelhardt and Michel 1987; Mackenzie and Smith 2002). Especially in complex structures, this information is often not obtainable by other methods. This approach has resolved details of site occupancy in alkali feldspars and plagioclases (Sherriff and Hartman 1985; Kirkpatrick

EBSCOhost - printed on 2/13/2023 5:26 AM via . All use subject to https://www.ebsco.com/terms-of-use

et al. 1987; Phillips et al. 1988; Xiao et al. 1995) and changes in symmetry and Si-Al ordering with composition and temperature in anorthite (Phillips and Kirkpatrick 1995; Phillips et al. 1997c), the latter involving challenging *in situ* high temperature MAS NMR. Extensive studies of Si-Al distribution in feldspathoids such as analcime, leucite and nepheline have also been made by this approach (Fig. 6) (Murdoch et al. 1988; Hovis et al. 1992; Phillips and Kirkpatrick 1994; Teertstra et al. 1994; Kohn et al. 1995). Any violations in "aluminum avoidance" (i.e., ^{IV}Al-O-^{IV}Al linkages) can often be readily detected by assessment of peak areas for Q^4 groups with varying numbers of Al neighbors and are usually found to be minimal, especially for low temperature phases such as zeolites. Notable exceptions to this "rule" have been demonstrated by NMR of highly disordered aluminosilicates that can crystallize metastably from supercooled melts, including anorthite ($CaAl_2Si_2O_8$) (Phillips et al. 1992b), β-eucryptite ($LiAlSiO_4$) (Phillips et al. 2000), and cordierite ($Mg_2Al_4Si_5O_{18}$) (Putnis and Angel 1985; Putnis et al. 1985; Vinograd 1996). When coupled with rate and calorimetric studies and calculations of configurational entropy these have provided unique and important information on the energetics and kinetics of reactions among various tetrahedral linkages, such as 2Si-O-Al = Al-O-Al + Si-O-Si. The latter is especially important in models of aluminosilicate glasses and melts (see section on glasses below).

The literature on NMR of natural and synthetic zeolites is vast, with many studies of framework order/disorder but also of ions and molecules in the cage sites (Engelhardt and Michel 1987; Mackenzie and Smith 2002). Ordering beyond that of aluminum avoidance has often been noted, apparently increasing stability by distributing partially charged Si-O-Al oxygen bridges more uniformly than predicted by random models ("Dempsey's rule," minimizing the number of Al-O-Si-O-Al groupings). In some cases, results on Si-Al distributions have been analyzed to constrain models of configurational entropy and component activities that place important constraints on phase equilibria in natural systems (Neuhoff et al. 2002, 2003).

Complementing information from ^{29}Si MAS NMR with high-resolution ^{27}Al NMR is an obvious goal (Phillips et al. 1988). In ordered framework aluminosilicates, measurements of isotropic ^{27}Al chemical shifts demonstrated that local structural effects are similar to those for ^{29}Si (Phillips and Kirkpatrick 1994). However, second-order quadrupolar broadening, and the fact that Al tetrahedra in such minerals usually have four Si first neighbors, often lowers information content. Nonetheless, partially resolved peaks can sometimes be observed in high-field ^{27}Al MAS spectra for Al in different tetrahedral sites; resolution may be better in the spinning sidebands for the inner satellite transitions (Phillips and Kirkpatrick 1994) or in 3QMAS spectra (Baltisberger et al. 1996; Larsen and Farnan 2004). The application of 2D ^{27}Al-^{29}Si HETCOR further improved resolution, resolving otherwise (partially) overlapping ^{29}Si peaks for zeolites with Si-Al distributed in more than one T sites (e.g., ZSM-4) (Kennedy et al. 2008). Advanced double resonance methods have clarified the tetrahedral Si/Al disorder in gehlenite ($Ca_2Al_2SiO_7$) as well (Florian et al. 2012).

A few aluminosilicate minerals (e.g., natural cymrite, $BaAl_2Si_2O_8.H_2O$, and synthetic high-pressure K-cymrite, $KAlSi_3O_8{\cdot}H_2O$) have double-layered structures, for which the local environments around Si/Al (Q^4) resemble those of tectosilicates. ^{29}Si MAS NMR in combination with two-dimensional J-coupling-based experiments has confirmed that the Si-Al distribution in K-cymrite obeys the "aluminum avoidance" rule (Xue and Kanzaki 2012).

Disorder among tetrahedral Si and Al in sheet silicates (micas and especially clay minerals) has also been widely characterized by ^{29}Si NMR, usually relying on empirical structure-shift correlations analogous to those in framework aluminosilicates, particularly the number of Al neighbors in the tetrahedral layers (Sanz and Robert 1992; Mackenzie and Smith 2002; Sanz et al. 2006). Again, issues of cation ordering and "aluminum avoidance" are explored, together with the complex effects of non-tetrahedral (interlayer) cations and mixing of different layer structures (Barron et al. 1985; Herrero et al. 1987; Weiss et al. 1990b; Herrero and Sanz 1991;

EBSCOhost - printed on 2/13/2023 5:26 AM via . All use subject to https://www.ebsco.com/terms-of-use

Jakobsen et al. 1995; Lausen et al. 1999; Sanz et al. 2003). Complementary calorimetric studies or theoretical analyses have revealed the energetic consequences of observed ordering (Circone et al. 1991; Circone and Navrotsky 1992; Vinograd 1995). In mixed-layer clays, preferential exchange with magnetic cations such as Mn^{2+} in one phase can produce marked differential spin-lattice relaxation that can be used to quantify phase proportions (Altaner et al. 1988).

Other aspects of the structures of sheet silicates have been explored by less common NMR methods. Single-crystal ^{1}H and ^{19}F NMR has proven useful even in Fe-rich micas, and, taking advantage of strong dipolar line broadening, showed clear evidence of ordering of H and F with respect to Fe^{2+} and Mg^{2+} in octahedral sites (Sanz and Stone 1979). High-resolution NMR studies of other nuclides (e.g., ^{1}H, ^{2}H, ^{13}C, ^{23}Na, ^{39}K, ^{87}Sr, ^{133}Cs, etc.) as interlayer cations or sorbed species have taken advantage of the high surface areas of clays, to give important data on reactions, interfacial phenomena, and dynamics (Weiss et al. 1990a; Kim and Kirkpatrick 1997, 2006; Bowers et al. 2006, 2008, 2011; Morrow et al. 2013). The use of probe molecules that give intense NMR signals, for example for ^{19}F, can be very helpful in detecting reactive sites and measuring reactive surface areas (Sanders et al. 2010).

In a number of important groups of minerals, Al can occupy sites with different coordination numbers, usually tetrahedra (^{IV}Al) and octahedra (^{VI}Al). Here, ^{27}Al NMR has played a more important role, especially for micas and clays. Particularly for the latter group, ^{27}Al NMR has proven quite helpful in determining site occupancies and the distribution of Al in mixed-layer phases (Fig. 13) (Kinsey et al. 1985; Engelhardt and Michel 1987; Woessner 1989; Schroeder 1993). More complex, two-dimensional multiple quantum and double-resonance NMR experiments such as HETCOR have recently improved resolution and given details of H^+, Na^+ and F^- distributions and their effects on the structures of sheet silicates (Delevoye et al. 2003; Fechtelkord et al. 2003; Alba et al. 2005; Takahashi et al. 2008).

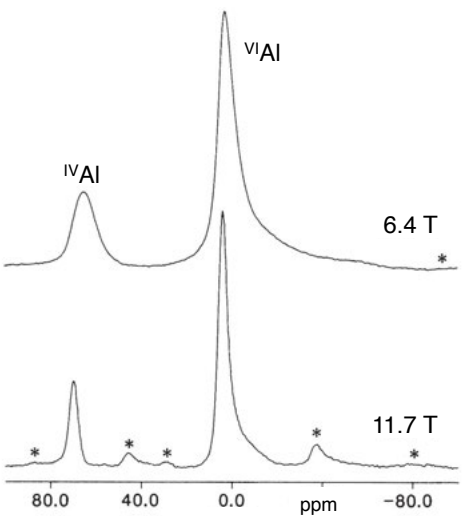


Figure 13. ^{27}Al MAS NMR spectra (6.3 vs. 11.7 T) of a beidelite clay (Woessner 1989). * marks spinning sidebands.

For aluminous pyroxenes (Flemming and Luth 2002), amphiboles (Raudsepp et al. 1987; Jenkins et al. 1997; Welch et al. 1998; Hawthorne et al. 2000), and biopyriboles (Welch et al. 1992; Maresch et al. 2009), both ^{29}Si and ^{27}Al NMR have helped to determine cation distributions on chains, tetrahedral and octahedral disorder, and other structural details. These groups of minerals also often contain both ^{IV}Al and ^{VI}Al. Determining their relative proportions is important for defining charge-balancing mechanisms such as the Tschermak's substitution, $^{IV}Si + {}^{VI}Mg = {}^{IV}Al + {}^{VI}Al$. For accurate quantitation for any quadrupolar nuclide, careful experimental procedure and data analysis is required, for example in a recent study of hydrous, aluminous orthopyroxenes (Kohn et al. 2005). ^{1}H and ^{19}F NMR have also proven useful for anion distributions in hydrous chain silicates (Welch et al. 1994).

Spinel group minerals are widely used in geothermometry of igneous and metamorphic rocks. The distribution of Mg and Al on octahedral and tetrahedral sites in the $MgAl_2O_4$

EBSCOhost - printed on 2/13/2023 5:26 AM via . All use subject to https://www.ebsco.com/terms-of-use

end-member has become an important test of models of energetics in such structures (Putnis 1992). Even in early single-crystal studies, C_Q differences permitted the detection of temperature effects on the degree of Mg/Al disorder (Fig. 8) (Brun and Hafner 1962). High-resolution ^{27}Al MAS NMR has relied on the large chemical shift difference between $^{[4]}$Al and $^{[6]}$Al to improve such measurements (Fig. 14) (Wood et al. 1986; Millard et al. 1992), and further *in situ*, high-temperature NMR has been done on single crystals (Maekawa et al. 1997). One important finding from such studies is the rapid re-ordering that can occur on cooling from temperatures above about 900 °C. Some evidence has suggested that the silicate spinel ringwoodite (Mg_2SiO_4, important in the transition zone of the mantle) could also have a small degree of cation disorder leading to the formation of ^{VI}Si. However, ^{29}Si spectra on isotopically enriched samples detected none of the high-coordinated species, again suggesting the possibility of re-ordering during quench (Stebbins et al. 2009c).

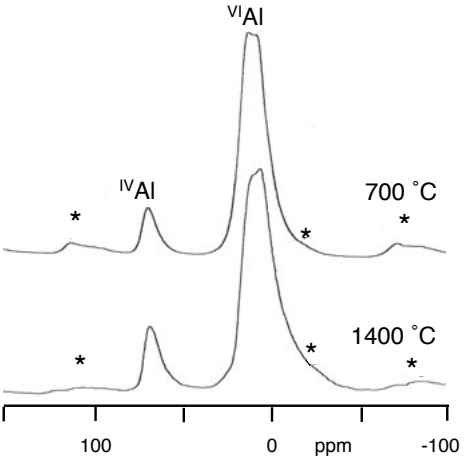


Figure 14. ^{27}Al MAS NMR spectra (9.4 T) of synthetic spinel annealed at the temperatures shown (Millard et al. 1992). Note increase in ^{IV}Al, and hence in disorder, with higher temperature. Spinning sidebands are marked by *.

Although Al is much less abundant in the mantle than in the crust, Al-rich high-pressure phases could be important in subducted slabs, and substitution of minor amounts of this element into the predominant Mg silicates in the bulk mantle can affect properties needed to constrain geophysical data. ^{27}Al NMR studies of synthetic high-pressure minerals such as aluminous stishovite and $MgSiO_3$ perovskite are thus important in determining mechanisms of solid solution (Fig. 2) (Stebbins et al. 2006). ^{27}Al and ^{29}Si NMR has also been important in helping to determine crystal structures of new, high pressure phases such as that of a disordered polymorph of topaz-OH (II) ($Al_2SiO_4[OH]_2$) (Xue et al. 2010), and in resolving the Si-Al coordination distribution in the high-pressure CAS phase ($CaAl_4Si_2O_{11}$), which has a unique crystal structure containing trigonal bipyramidal Si/Al sites (Xue et al. 2009).

Cation order/disorder has also been evaluated by ^{29}Si and ^{27}Al NMR in high-pressure garnet solid solutions. In the pyrope-grossular binary ($[Mg,Ca]_3\ ^{VI}Al_2\ ^{IV}Si_3O_{12}$), complex and well-resolved ^{29}Si spectra were modeled to suggest some non-randomness in Mg-Ca distributions (Bosenick et al. 1999). In several studies of both nuclides along the pyrope-majorite ($Mg_3\ ^{VI}[Mg,Si]\ ^{IV}Si_3O_{12}$) join, all Al was determined to be octahedral, and tetrahedral sites with varying numbers of cation neighbors supported a nearly random distribution of octahedral-site cations (Fig. 4) (McMillan et al. 1989; Phillips et al. 1992a). Many high-pressure minerals, believed to be stable in the lower mantle and/or in deep subduction zones, contain Si exclusively in octahedral coordination. Si-Al-Mg distributions in octahedral sites are thus important for their stabilities and physical properties. ^{29}Si MAS, as well as ^{27}Al MAS and 3QMAS NMR have provided constraints on the order/disorder of octahedral Si-Al distributions in phase egg ($AlSiO_5OH$) (Xue et al. 2006) and octahedral Si-Mg distribution in the dense hydrous magnesium silicate phase D (Xue et al. 2008).

The higher sensitivity and resolution obtainable at higher magnetic fields has also begun to allow detection of cations in sites with different coordination numbers even when present

EBSCOhost - printed on 2/13/2023 5:26 AM via . All use subject to https://www.ebsco.com/terms-of-use

in relatively low concentrations, such as ^{45}Sc in high-pressure garnet solid solutions (Kim et al. 2007). Given that minor and trace elements in minerals are widely-used records of diverse geochemical processes, but that substitution mechanisms are often poorly constrained, such spectroscopic studies of short-range structure should be of increasing importance. For "sensitive" nuclides such as ^{11}B and ^{31}P, NMR can measure cation coordination numbers even at concentrations well below 1%. Examples include biominerals such as calcium carbonate with <100 ppm B (Fig. 1) (Sen et al. 1994; Klochko et al. 2009), phosphorus in corals and speleothems (Mason et al. 2007, 2011), B-doped diopside (Halenius et al. 2010), and octahedral PO_6 groups in aluminous stishovite (Stebbins et al. 2009b). ^{31}P MAS and double-resonance NMR has very recently been used to observe phosphate sorption and crystallization on even low surface area oxides (Li et al. 2012, 2013).

^{17}O NMR can provide local structural information that is useful for a wide range of problems involving oxides and silicates. Because isotopic enrichment is usually required, such studies have generally been done on synthetic materials (Stebbins 1995b; Mackenzie and Smith 2002). Empirical and theoretical results on known, ordered structures have led to correlations among parameters such as C_Q and δ_{iso} and structural variables such as bond distances and angles, that have been used to constrain the structures of disordered materials, especially silicate glasses (see section on glasses below) (Stebbins et al. 2001). Recently, ^{17}O NMR has been extended to include 2D, satellite transition MAS (STMAS) and 3QMAS NMR on small samples of synthetic high pressure minerals such as pyroxenes, garnets, and Mg silicates (Fig. 15) (Ashbrook et al. 2005a, 2007a,b; Kelsey et al. 2007). In an exceptionally thorough study of hydrous wadsleyite (Mg_2SiO_4), which included advanced theoretical calculations and ^{17}O, ^{29}Si, ^{25}Mg, ^{1}H and ^{2}H NMR, new details about the hydroxylated sites in this important mantle mineral have been obtained (Griffin et al. 2013). Relatively few ^{17}O NMR studies have been done on oxide or silicate minerals that are disordered by solid solution or temperature, and hence where there are significant unknowns in the structure. Both 1-D MAS and static spectra are useful, as in disordered spinels (Millard et al. 1992, 1995) and zeolites (Timken et al. 1986; Amoureux et al. 1998; Xu and Stebbins 1998; Stebbins et al. 1999). In pyrope-grossular garnets, ^{17}O 3QMAS spectra added new constraints to thermodynamic mixing models (Kelsey et al. 2008).

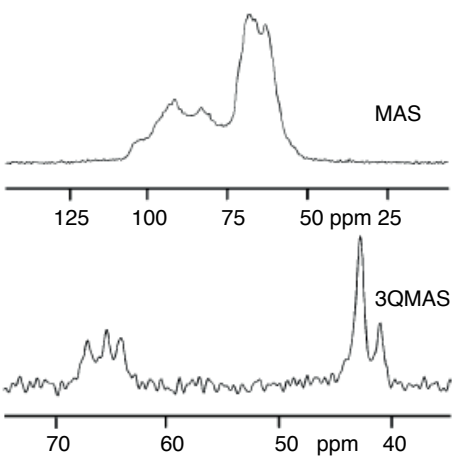


Figure 15. ^{17}O MAS and isotropic dimension projection of 3QMAS spectra (14.1 T) for majorite garnet ($MgSiO_3$, 16 mg sample) grown at 19.5 GPa. [Used by permission of the American Chemical Society, from Ashbrook et al. (2007a) *Journal of the American Chemical Society*, Vol. 129, Fig. 5, p. 13219.]

^{1}H NMR in minerals

^{1}H NMR studies of hydrous minerals and nominally anhydrous minerals are another major application of NMR spectroscopy, because ^{1}H is the most sensitive nuclide for NMR study, whereas X-ray diffraction is insensitive to hydrogen because of its low scattering factor. Strong ^{1}H-^{1}H homonuclear dipolar coupling often leads to relatively broad peaks for hydrous phases with large water contents, such as hydroxides and high-water content silicates. Nevertheless, with the development of fast MAS and new-generations of CRAMPS experiments, high-resolution ^{1}H NMR spectra can now be readily obtained for most samples.

EBSCOhost - printed on 2/13/2023 5:26 AM via . All use subject to https://www.ebsco.com/terms-of-use

^{1}H NMR is now routinely used to help resolve and evaluate the hydrogen-bonding distances for water in hydrous silicate and (oxy)hydroxide minerals, especially those with strong hydrogen bonding, including pectolite, ussignite and δ-AlOOH. Compared with the other often-used parameter for studying hydrogen bond distances, the OH stretching frequency from vibrational spectroscopy, ^{1}H NMR is more straightforward because of its more quantitative nature and one-to-one correspondence to local structures. In contrast, the OH stretching bands have composition-dependent absorption coefficients, and can be complicated by vibrational coupling, especially for strong hydrogen bonds for which the bands tend to become very broad. Disorder in hydrogen distribution has been detected by 2D high-resolution CRAMPS-MAS correlation experiments on high-pressure minerals with Si-Al or Si-Mg disorder, such as phase egg, topaz-OH (II) and phase D (Xue et al. 2008, 2009, 2010). ^{1}H NMR in combination with the ^{1}H-^{27}Al double-resonance experiment has been applied to Al-rich phlogopite (Fechtelkord et al. 2003) and layered Al-Mg double hydroxides (Sideris et al. 2008) to distinguish OH groups linked to 3Mg and 2Mg1Al in the octahedral sheets, providing constraints on the Mg-Al distribution. Similarly, ^{1}H MAS NMR was used to resolve OH groups linked to 3Mg and 2Mg1Al in pargasite (Welch et al. 1994). Molecular H_2O groups have strong dipolar coupling between their two protons, and when relatively immobile and not in isolation (as in many inorganic materials) they tend to give broad peaks at moderate MAS spinning rates. Thus, the two distinct H_2O molecules in brushite ($CaHPO_4{\cdot}2H_2O$) could not be distinguished by ^{1}H MAS at an 8 kHz spinning rate (Yesinowski and Eckert 1987), but could be resolved at 40 kHz (Xue et al. 2009). New-generation CRAMPS methods gave even better resolution (Xue and Kanzaki 2009). Here, the two protons within each water molecule, in spite of unequal hydrogen-bonding distances, give a single NMR peak, possibly because of rapid flipping motion. This phenomenon is well known for H_2O molecules in many minerals.

Trace amounts of water in nominally anhydrous minerals, as well as hydrogen in defect sites of hydrous minerals, can be readily detected by ^{1}H NMR, if probe background signals are reduced sufficiently. ^{1}H MAS NMR has detected trace amounts (down to a few tens of ppm) of structural water as molecular H_2O and/or OH groups, as well as fluid inclusions in natural feldspars (Yesinowski et al. 1988; Johnson and Rossman 2003). Rigid, isolated molecular H_2O was distinguished from isolated OH groups by more extensive spinning sidebands arising from greater H-H dipolar coupling within the former. Water in fluid inclusions in contrast showed very narrow, liquid-like ^{1}H MAS peaks. The concentration and speciation of water in nominally anhydrous high-pressure minerals is an issue important for understanding the physical properties of the earth's mantle, and have been the subject of a number of NMR studies. ^{1}H MAS NMR can detect water in nominally anhydrous forsterite, enstatite and wadsleyite synthesized at high pressure, often revealing several distinct peaks for each sample (Kohn 2006; Griffin et al. 2013). One complication of such studies is the possibility of contributions from grain boundaries and coexisting impurity (hydrous) phases, as a small amount of the latter could readily dominate the total water content. This type of problem can be addressed by including double-resonance (e.g., ^{1}H-^{29}Si) and two dimensional correlation (homo- or heteronuclear) experiments and/or measurements with different recycle delays. For example, a sharp ^{1}H MAS peak at 9.4 ppm attributable to a trace amount of water in aluminous stishovite can be identified (Xue et al. 2006), which is in good agreement with that expected from the observed OH stretching frequency. The ^{1}H T_1 for aluminous stishovite has been noted to be much longer than that of the coexisting hydrous phase (topaz-OH). Such slow ^{1}H relaxation is a common feature for trace amounts of isolated OH groups in nominally anhydrous minerals lacking paramagnetic impurities, and sufficient relaxation delay should thus be allowed for their detection. Vacancies in Si sites compensated by protonation of adjacent oxygens in the high-pressure 10 Å phase (a hydrous Mg sheet silicate) were identified in a combined ^{1}H and ^{29}Si NMR study (Phillips et al. 2007). ^{1}H-^{29}Si HETCOR spectra provided particularly useful constraints for the association of silanol protons with defect Si.

EBSCOhost - printed on 2/13/2023 5:26 AM via . All use subject to https://www.ebsco.com/terms-of-use

Static (non-MAS) ^{1}H NMR has been utilized to estimate the H-H distance (and dynamics) and clustering via homonuclear dipolar interactions. This method has been applied since early days to estimate the H-H distance within isolated H_2O molecules in hydrate minerals such as gypsum. More recently, static ^{1}H NMR has been used to estimate the H-H distances in high-pressure dense hydrous magnesium silicate phases A and B and superhydrous B from simulation of the peak shape for powdered samples (Phillips et al. 1997a; Kagi et al. 2000). The peak shapes for these phases all deviate from symmetric "Pake doublets" due to contributions from CSA. More mobile H_2O molecules (e.g., those in some zeolites) tend to give narrower ^{1}H static NMR peaks than expected for rigid molecules; ^{1}H static peak shape analysis in this case has led to the estimation of their dynamics. ^{1}H static NMR and multiple-quantum experiments on natural grossular samples containing low levels of OH, as well as a synthetic hydrogrossular ($Ca_3Al_2(O_4H_4)_3$, revealed clusters of two H atoms (+ four H) in the former and four H in the latter (Cho and Rossman 1993). The latter is consistent with the "hydrogarnet substitution" mechanism of four H substituting for one Si in the tetrahedral site.

NMR crystallography

NMR has traditionally been looked at as a tool for providing fine details of local structures. However, it is increasingly being used in combination with diffraction techniques and first principles calculations to help determine and refine the complete crystal structure, resulting in the field "NMR crystallography." Information concerning the number of sites and their proximities provided by 1D or 2D NMR can help distinguish structure candidates otherwise unsettled by diffraction techniques. An example is the clarification of the space group for a high-pressure dense hydrous magnesium silicate, superhydrous B, from constraints on the proton distributions provided by 2D ^{1}H double-quantum NMR (Xue et al. 2008). The local structural information (e.g., number of sites and coordination) from NMR (or other spectroscopic techniques) can also be incorporated into computer protocols as constraints to facilitate the crystal structural determination from powder diffraction data. For example, this approach has led to the determination of crystal structures for three newly-discovered high-pressure forms of $AlPO_4$, one with a SiO_2 moganite-type structure and two containing five- and six- coordinated Al (Kanzaki et al. 2011; Kanzaki and Xue 2012). This material is also well-known to have phases with structures similar to SiO_2 polymorphs such as quartz and cristobalite at ambient pressure. Similar methods have been applied to a new high-pressure polymorph of topaz-OH (II) with extensive cation disorder (Kanzaki 2010). Crystal structural determination and refinement based solely on NMR criteria (e.g., the ^{29}Si dipolar coupling based double quantum evolution curve, or chemical shift tensors), either with unit cell parameters and space group from powder diffraction, or in combination with first-principles calculation without diffraction data input, has also been done for zeolites (Brouwer et al. 2005; Brouwer 2008). This method holds promise as a new approach for crystal structure studies of fine-grained samples, such as zeolites and other materials synthesized at low temperatures. It may be expected that the importance of NMR in crystal structure studies will continue to grow as its capacity becomes increasingly explored.

APPLICATIONS TO GLASSES, MELTS AND OTHER AMORPHOUS MATERIALS

Volatile-free silicate glasses

NMR has had a major impact on our knowledge of the structure of oxide glasses (Kirkpatrick et al. 1986; Dupree et al. 1992; Eckert 1994; Stebbins 1995a, 2002; Kohn 2004). As for crystalline minerals, there is close overlap between questions posed, and the types of information gained, for geological and technological materials. Again, the emphasis here will be on questions particularly relevant to the geosciences, focusing on silicate and aluminosilicate glasses.

EBSCOhost - printed on 2/13/2023 5:26 AM via . All use subject to https://www.ebsco.com/terms-of-use

Aluminosilicate glasses, as amorphous solids, are widespread at the Earth's surface, mostly in the form of volcanic ash deposits. The properties of these materials, for example their mechanisms of reaction with water during hydrothermal alteration or weathering, depend on the glass structure. As in studies of the corrosion of man-made glasses (in particular those for radioactive waste storage), these processes have led to a number of NMR studies. Amorphous silicates, most obviously opaline silica, can also form by low temperature, aqueous processes; or by the highly energetic process of radiation damage as in metamict zircons.

However, most studies of glass structure in the Earth sciences have been motivated by the clues that they provide about the structure of the high-temperature molten silicates that occur as magmas in nature. A glass formed on cooling of a melt records the structure when the system falls out of equilibrium through the glass transition region. This is often a good starting point for determining the types of structural species present in the melt, their concentrations, the extent of their order/disorder, and how these change with composition. However, magmatic temperatures are often many 100's of degrees above glass transitions, and most silicate melts have important "configurational" components to their heat capacities and thermal expansivities, and thus to their free energies and molar volumes (Richet 1984; Mysen and Richet 2005). Significant increases in structural disorder must therefore take place with higher temperature. Measuring such changes has thus become a goal in a number of spectroscopic studies. These have involved both NMR done *in situ* at high temperature, and studies of glasses quenched at different rates, which record the melt structure at different "fictive" temperatures (T_f) (Stebbins 1995a, 2008; Stebbins et al. 2008).

Early work on crystalline silicates demonstrated different (if partially overlapping) ranges of ^{29}Si chemical shifts for SiO_4 groups with varying numbers (n) of bridging oxygens, denoted as Q^n, with $4-n$ non-bridging oxygens (Smith et al. 1983; Engelhardt and Michel 1987). Soon after this discovery, NMR studies of alkali silicate glasses showed that two, three, or sometimes even four, overlapping peaks could often be observed and quantified by fitting (Dupree et al. 1984; Murdoch et al. 1985; Maekawa et al. 1991; Malfait et al. 2007), with peak assignments made on the basis of chemical shift ranges defined by known crystalline silicates. Because of incomplete resolution, some constraints on fitting have often been applied, such as peak widths and positions that are constant or vary in a systematic way across a series of compositions, or ratios of peak areas that are fixed to match nominal or (better!) analyzed compositions. A detailed analysis of these issues (common to most spectroscopies of disordered materials) has been recently made (Malfait et al. 2007). While nearly all of these studies have used MAS, a few more time-consuming results from static (non-spinning) samples provided unequivocal measurements of species with distinctively small chemical shift anisotropy (CSA), notably Q^4 sites (Stebbins 1987; Dupree et al. 1990). These experiments, including a few that varied the fictive temperature of the glass by changing the cooling rate, have been crucial in defining the extent and even the thermodynamics of speciation reactions that can be important contributors to the configurational disorder, such as $2Q^3 = Q^2 + Q^4$ (Brandriss and Stebbins 1988). NMR studies of Q^n species have also served as important calibrations for other spectroscopic measurements, notably Raman, that can more readily be applied in situ at high temperature and even at high pressure (Mysen and Richet 2005). When signals from different Q^n species show different spin-lattice relaxation rates, liquid-liquid phase separation is indicated, as magnetic impurity ions typically partition out of the silica-rich phase (Sen and Stebbins 1994; Stebbins et al. 2009a).

Because alkaline earth silicate glasses are generally more disordered than alkali silicates, with all component peak shapes being broader, ^{29}Si NMR usually cannot resolve signals for different Q^n species, although two-dimensional "magic-angle flipping" methods that separate out components with differing CSA can provide more information and have been crucial in confirming the systematic dependence of Q^n speciation reactions on modifier cation field strength (Zhang et al. 1996; Davis et al. 2011). For the special case of Mg,Ca silicate glasses

EBSCOhost - printed on 2/13/2023 5:26 AM via . All use subject to https://www.ebsco.com/terms-of-use

close to the orthosilicate composition (made by levitation- or hyper-quenching), the shapes of both MAS and static ^{29}Si NMR peaks have shown the presence of significant fractions of Q^1 groups as well as the predominant Q^0 species, which in turn must be balanced by "free" oxide ions not bonded to any Si (Sen and Tangeman 2008; Sen et al. 2009). NMR-derived Q^n species in lead silicate glasses also suggest significant quantities of "free" Pb-O-Pb oxygens at even higher silica contents (Fayon et al. 1998), as expected for this highly electronegative cation.

In aluminosilicate glasses that begin to approach the complexity of natural rhyolitic compositions, extracting structural data from ^{29}Si NMR is even more difficult, but spectra can be very helpful in testing and constraining models (Merzbacher et al. 1990). A useful approach involves collecting data in a compositional series, and simultaneously fitting all spectra with a small set of component peaks of constant width and position, such as for Q^4 groups with varying number of Al neighbors. For example, in the SiO_2-$NaAlSiO_4$ and corresponding Ca systems, this method yielded robust thermodynamic models for the degree of ordering related to aluminum avoidance, i.e., the extent of the reaction 2Si-O-Al = Al-O-Al + Si-O-Si (Lee and Stebbins 1999), which were consistent with calorimetry and later directly confirmed by ^{17}O NMR (see below).

Simple, one-dimensional ^{17}O NMR spectra of glasses can sometimes resolve and quantify different oxygen anionic species, when ranges of chemical shifts are large. For example, in comparing such spectra for crystalline and glassy $CaTiSiO_5$ (titanite) (Kroeker et al. 2002), oxygen sites in the glass that are similar to those in the crystal, i.e., Ti-O-Ti and Si-O-Ti, can be assigned, although they are much broader in the amorphous phase, perhaps in part because of a distribution in Ti coordination numbers (Fig. 16). At the same time, major additional peaks seen for the glass correspond to none in the crystal. These can be assigned to Si-O-Ca and Si-O-Si based on data from calcium silicates, and their presence presumably contributes to the high degree of structural disorder in the glass and melt. More routinely, in compositions with relatively large network modifier cations (e.g., K^+, Ca^{2+}, Ba^{2+}, etc.), the NMR peak for nonbridging oxygens (NBO) can be resolved, even in compositions where this species is absent from conventional structural models, such as the metaluminous SiO_2-$CaAl_2O_4$ binary (Stebbins and Xu 1997; Thompson and Stebbins 2011). This method also directly confirmed the common assumption that NBO in aluminosilicate glasses are preferentially located on Si instead of Al (Allwardt et al. 2003). A significant NMR peak from "free" oxide ions (not bonded to any network cations) has been directly detected by ^{17}O NMR in Ca-Mg silicate glasses with "sub-orthosilicate" compositions (<33.3% silica) (Nasikas et al. 2012) as predicted by ^{29}Si results noted above. However, this species was not detected at about the 0.1 to 1% level in a Ca-silicate glass with 44% silica (Thompson et

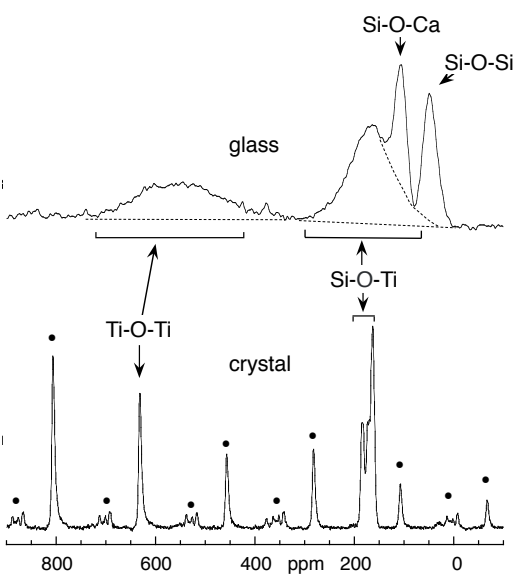


Figure 16. ^{17}O MAS NMR spectra for $CaTiSiO_5$ (titanite) glass (14.1 T) and crystal (18.8 T) (Kroeker et al. 2002). Dots mark spinning sidebands.

EBSCOhost - printed on 2/13/2023 5:26 AM via . All use subject to https://www.ebsco.com/terms-of-use

al. 2012) or in a K-silicate glass with 60% silica (Stebbins and Sen 2013). Two-dimensional methods, including ^{17}O DAS and especially 3QMAS NMR, provide more resolution and have been especially useful at measuring the extent of mixing of different modifier cations around NBO. In some cases (e.g., Na^+ vs. K^+ and Mg^{2+} vs. Ca^{2+}) (Florian et al. 1996; Allwardt and Stebbins 2004), these results give accurate confirmation of conventional random mixing assumptions; in others (e.g., Mg^{2+} vs. K^+) considerable non-randomness is present that have important implications for thermodynamic models (Allwardt and Stebbins 2004; Lee et al. 2005). In aluminosilicate compositions in which nearly all oxygens are bridging, ^{17}O 3QMAS NMR first definitively measured the extent of the Si-Al disorder reaction noted above by allowing the counting of Si-O-Si, Si-O-Al, and Al-O-Al species (Dirken et al. 1997; Lee and Stebbins 2000a,b). Glasses prepared with higher fictive temperatures show increased disorder, giving estimates of the contribution of these species to the bulk entropy and enthalpy (Fig. 17) (Dubinsky and Stebbins 2006). Recent advances in theoretical calculation of such spectra give great promise to extracting even more information from experimental data (Pedone et al. 2010; Angeli et al. 2011).

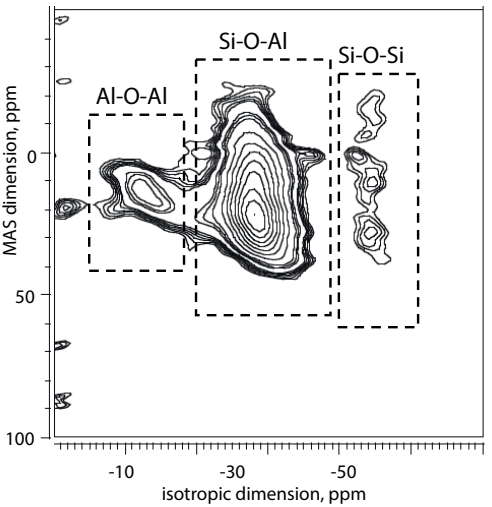


Figure 17. ^{17}O 3QMAS spectrum (9.4 T) for a $NaAlSiO_4$ glass, showing three types of bridging oxygens (Dubinsky and Stebbins 2006). Note that axis orientation is different from that of Figure 10.

A surprising finding from ^{27}Al NMR on aluminosilicate glasses has been the quantitation of five-coordinated Al (^{V}Al) in ambient-pressure alkaline earth aluminosilicate glasses, commonly at the 2-8% level; even small amounts of ^{VI}Al have been seen in aluminous compositions (McMillan and Kirkpatrick 1992; Toplis et al. 2000; Neuville et al. 2006; Stebbins et al. 2008; Xue and Kanzaki 2008). Here, 3QMAS and very high field (17.6 to 21 T) MAS NMR have been especially important. These and other minor species can be important in models of melt properties, but went undetected through decades of structural studies by other spectroscopic and diffraction methods. Tiny amounts (<1%) of ^{V}Si has been found in ^{29}Si-enriched samples of some ambient-pressure alkali silicate glasses by ^{29}Si NMR (Stebbins 1991a), perhaps giving credence to the observation of such species in molecular dynamics simulations.

As for minerals, effects of pressure on silicate melt structure are of particular importance in the Earth sciences. At this time, NMR studies must be done on quenched, decompressed glasses, which may retain only part of the high pressure/temperature effects, but which nonetheless provide unique information on compositional effects and mechanisms of structural change. Increases in the concentration of ^{V}Al and ^{VI}Al with pressure, and with modifier cation field strength (e.g., K^+ to Na^+ to Ca^{2+} to Mg^{2+}) are particularly dramatic, in samples quenched from melts at pressures up to about 12 GPa (Fig. 18) (Yarger et al. 1995; Allwardt et al. 2005; Lee et al. 2006; Kelsey et al. 2009). ^{29}Si NMR, again on isotopically-enriched glasses, showed the development of up to about 6-8% ^{V}Si and ^{VI}Si in alkali and alkaline earth binary silicates up to about 12 GPa (Stebbins and McMillan 1989; Xue et al. 1991; Stebbins and Poe 1999; Allwardt et al. 2004; Gaudio et al. 2008). Figure 19 illustrates how comparison of the ^{29}Si spectrum for triclinic crystalline $CaSi_2O_5$, which is unique in containing ^{IV}Si, ^{V}Si and ^{VI}Si, to a high pressure

EBSCOhost - printed on 2/13/2023 5:26 AM via . All use subject to https://www.ebsco.com/terms-of-use

glass can confirm the peak assignments. In aluminosilicate glasses, Al changes coordination much more readily than Si, as expected from pressure effects on phase changes in minerals: only recently have high-coordinated forms of both cations been directly seen in the same glass, in compositions with high Si/Al ratios (Kelsey et al. 2009).

^{17}O 3QMAS NMR has also revealed dramatic changes in the network linkages as Si and Al coordination numbers increase in high-pressure, densified glasses (Fig. 20) (Allwardt et al. 2004; Lee et al. 2004, 2006), and has been especially important in defining structural mechanisms of these transformations, particularly the loss of NBO to form high-coordinate network species. The implications for transport and thermodynamic properties are dramatic and have been modeled in some detail (Lee 2005). The interplay among network cation coordination and oxygen species, as affected by temperature, pressure composition effects in silicates, germanates, and borate, has been emphasized in a recent synthesis (Stebbins et al. 2013).

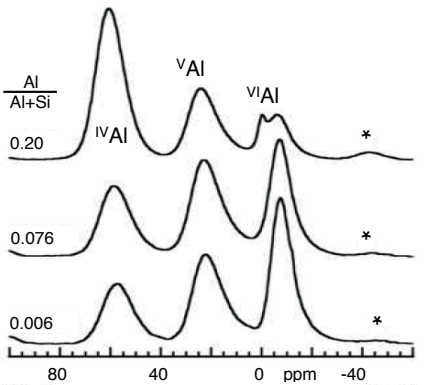


Figure 18. ^{27}Al MAS NMR spectra (18.8 T) for Na silicate glasses containing small concentrations of Al, quenched from melts at 6 GPa (Kelsey et al. 2009).

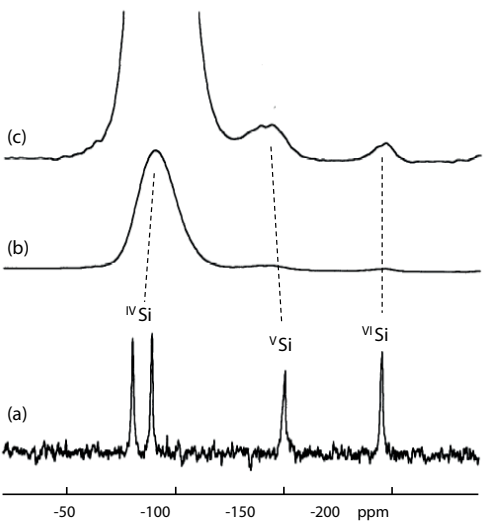


Figure 19. ^{29}Si MAS NMR spectra for high-pressure phases of $CaSi_2O_5$ (Stebbins and Poe 1999). (a) Crystalline, triclinic phase with natural (4.7%) ^{29}Si abundance; (b) glass quenched from melt at 10 GPa (95% enriched ^{29}Si); (c) same as (b), vertical scale ×8.

Volatile-containing glasses

Silicate melts can dissolve considerable quantities of water and other volatiles at high pressure, which can have large effects on properties and phase equilibria. NMR has thus been widely applied to the complex issues of the structural roles of OH and H_2O in aluminosilicate glasses. Low-temperature static ^{1}H NMR measurements successfully distinguished and quantified molecular H_2O and OH groups in hydrous glasses of various compositions (Riemer et al. 2000). The method can be more straightforward than vibrational spectroscopy, especially for systems with strong hydrogen bonding (e.g., alkali silicates), because it does not suffer from complications with band assignment and quantification as the latter. For the differentiation of different types of OH groups, high-resolution ^{1}H, ^{17}O, ^{23}Na, ^{27}Al and ^{29}Si MAS (and 3QMAS for quadrupolar nuclei) spectra have all provided clues, although interpretations for more complicated aluminosilicate systems can be ambiguous (Xu et al. 1998; Zeng et al. 1999; Schmidt et al. 2000). More recent studies have demonstrated that combining quantitative ^{1}H MAS (which includes contributions from all water species) with double resonance methods such as ^{27}Al→^{1}H and (^{1}H→)^{29}Si→^{1}H CP (which provide information about the

EBSCOhost - printed on 2/13/2023 5:26 AM via . All use subject to https://www.ebsco.com/terms-of-use

relative Al-H and Si-H proximities) render it possible to distinguish and quantify the different types of OH species. It was shown that OH may be present in silicate glasses/melts in the form of SiOH, AlOH and free OH (e.g., MgOH), whose relative proportions depend on the melt composition (Fig. 7, 11) (Xue and Kanzaki 2004, 2009; Xue 2009; Malfait and Xue 2010). 2D $^{27}Al \rightarrow {}^{1}H$ HETCOR and 3Q-HETCOR further revealed the ^{27}Al NMR characteristics of the Al(Q^3)-OH species (Fig. 12) (Xue and Kanzaki 2006, 2007a, 2008).

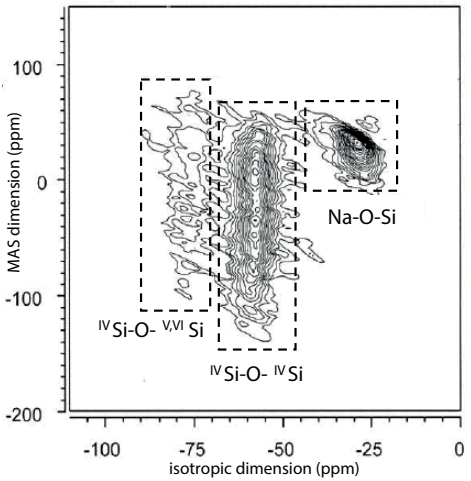


Figure 20. ^{17}O 3QMAS spectrum (7.1 T) of $Na_2Si_3O_7$ glass quenched from 8 GPa, showing different oxygen sites. Note that axis orientation is different from that of Figure 10. [Used by permission of Elsevier, from Lee et al. (2004) *Geochimica et Cosmochimica Acta*, Vol. 68, Fig. 1, p. 4190].

NMR has proven useful for other volatile species in silicate glasses of interest in Earth sciences. ^{13}C MAS NMR can readily quantify molecular CO_2 and carbonate groups (Kohn et al. 1991a). ^{19}F NMR has confirmed the strong interaction of F^- with Al in aluminosilicates and has revealed small amounts of Si-F bonding (Kohn et al. 1991b; Zeng and Stebbins 2000). The "difficult" nuclide ^{35}Cl (low resonance frequency, large quadrupolar moment) can give surprisingly useful structural data for Cl^- ions in glasses, indicating that most Cl is coordinated by the network modifiers (Sandland et al. 2004). Even more technically challenging is ^{33}S NMR, requiring isotopic enrichment and sophisticated NMR methods, which has been applied to sulfide- and sulfate-bearing silicate glasses, and compared in detail to other methods such as Raman and XANES (O'Dell et al. 2008; Klimm et al. 2012).

Other amorphous materials

Amorphous silicates important in geochemical and technological processes can form in ways other than by quenching a melt. Hydrous amorphous silica (e.g., opal and siliceous sinter) forms in a number of low-temperature environments, from soils and geothermal systems to the products of leaching by acidic volcanic gasses. Si with one or more OH groups (Q^3, Q^2, etc.) can most readily be observed by ^{29}Si CPMAS NMR (Adams et al. 1991; Graetsch et al. 1994; Brown et al. 2003) and are the key structural variation in these compositionally simple materials. However, accurate quantitation requires experiments without CP, which can be very time-consuming because of long spin-lattice relaxation times. Nonetheless, it is now clear that large differences in structural OH content can occur from one environment to another (Chemtob et al. 2012). In contrast, the amorphization caused by radiation damage in silicates (e.g., metamict zircons in nature and minerals that may serve to sequester nuclear waste) involves very high-energy, disequilibrium processes that have recently been studied in detail by ^{29}Si NMR in both natural and in highly radioactive synthetic materials (Farnan and Salje 2001; Farnan et al. 2004). Allophanes (amorphous aluminosilicates) formed during weathering have also been characterized by NMR (see section below on dynamics). Hydrated, amorphous calcium carbonate, a common precursor to both inorganic and biogenic calcite, has recently been explored by ^{43}Ca NMR on isotopically enriched aqueous precipitates, collected at the very high field of 20 T to enhance sensitivity and limit quadrupolar broadening (Singer et al. 2012).

EBSCOhost - printed on 2/13/2023 5:26 AM via . All use subject to https://www.ebsco.com/terms-of-use

Silicate and oxide melts

Even at the fastest obtainable cooling rates, beyond about 200 °C above standard glass transition temperatures (T_g, typically about 600 to 800 °C for aluminosilicates), short-range structural changes occur too rapidly to be quenched and then studied at room temperature. *In situ* NMR and other methods such as Raman and X-ray spectroscopy (Mysen and Richet 2005) on silicate and oxide melts at higher temperatures can thus be informative. More uniquely for NMR, the dynamics of short-range processes such as bond-breaking and cation site hopping at time scales from seconds to nanoseconds can often be observed (Stebbins 1995a). Remarkably, ^{27}Al NMR has been done on a number of oxide melt systems, primarily aluminates, on gas-levitated droplets of liquid to temperatures above 2500 °C (Coutures et al. 1990; Massiot et al. 1995). At the very low viscosities in such systems, bond-breaking and re-orientation of structural units is very rapid, and only single, narrow peaks at the mean chemical shift of all components are observed, reflecting, for example, varying proportions of ^{IV}Al, ^{V}Al, ^{VI}Al. Modeling of these spectra can give important data on variations in structure with composition and temperature. At somewhat lower temperatures (to about 1500 °C), *in situ* NMR on melts in non-metallic capsules has been done on nuclides such as ^{23}Na, ^{25}Mg, ^{27}Al, and ^{29}Si and has again indicated changes with structure (Stebbins et al. 1985; Stebbins and Farnan 1992; Fiske and Stebbins 1994; Maekawa and Yokokawa 1997; Kanehashi and Stebbins 2007). Spin-lattice relaxation in liquids can be complex, but systematic measurements in melts, sometimes requiring only simple linewidth measurements, have provided new insights into diffusional dynamics, emphasizing processes that take place at time scales near the inverse of the Larmor frequency, i.e., typically 10's of ns (George and Stebbins 1996; Sen and Stebbins 1997).

At temperatures up to about 200 °C above T_g, silicate melt viscosities are often high enough that network bond breaking, exchange among structural groups such as Q^n species, different cation coordination, or bridging and non-bridging oxygen, occur at much longer time scales. These vary from seconds just above T_g to milliseconds to microseconds with increasing temperature. When these rates become similar to inverses of observable NMR peak widths (Hz to 100's of kHz), line shapes are affected as motional averaging and "chemical exchange" begins, as can be seen for the bridging (BO) and non-bridging (NBO) sites in $K_2Si_4O_9$ melt (Fig. 21) (Stebbins et al. 1992). The resulting *in situ* spectra, if signals from multiple species are resolvable, can often be simulated to give quantitative measures of at least average exchange rates. Data collection on stationary ("static") samples is most feasible, but MAS NMR to about 700 °C can reach well above T_g in some compositions and gives more resolution and thus access to longer time scales, as can 2D experiments in which a "mixing time" is varied to explore the exchange time scale (Farnan and Stebbins 1994). In some cases, such as Q^n species in alkali sili-

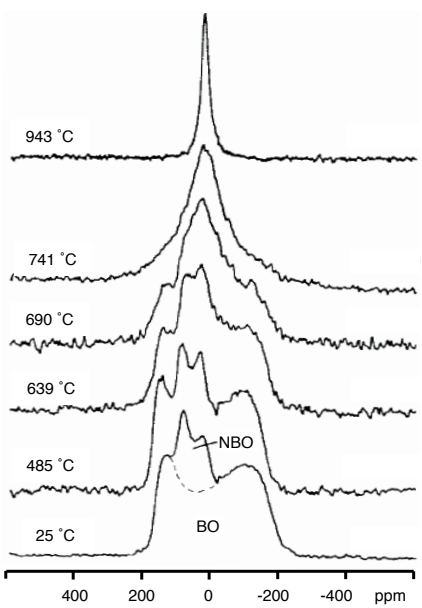


Figure 21. ^{17}O static (non-MAS) spectra for $K_2Si_4O_9$ glass (25 °C) and supercooled liquid, collected at the temperatures shown, showing motional averaging caused by exchange among non-bridging (NBO) and bridging (BO) oxygens. The lower temperature spectra have quadrupolar line shapes for both species. [Used by permission of Elsevier, from Stebbins et al. (1992) *Chemical Geology*, Vol. 96, Fig. 4, p. 377].

EBSCOhost - printed on 2/13/2023 5:26 AM via . All use subject to https://www.ebsco.com/terms-of-use

cates, these rates have been shown to be closely related to shear relaxation rates derived from viscosity data, demonstrating close links between this atomic-scale process and macroscopic flow (Farnan and Stebbins 1990a,b, 1994). In other cases, for example recent high-*T* MAS ^{17}O NMR on a K-silicate melt with very high silica content, some network bond switching can occur at a more rapid time scale, pointing to more heterogeneous dynamics (Sen 2008).

DYNAMICS, KINETICS AND TRANSITIONS

Understanding of the dynamics, kinetics, and mechanisms of transitions and reactions in minerals, melts, and fluids is especially important in the Earth sciences (Putnis 1988, 1992; Stebbins 1991b). Not only are natural processes generally multi-phase and inherently complex, but their time scales are often so long that empirical measurements fall short by many orders of magnitude. Models must thus be based on knowledge of fundamental, atomic-scale processes to permit accurate extrapolation to natural conditions. NMR studies of dynamics in silicate melts, for example, are mentioned in the previous section; sorption processes in minerals such as clays are touched upon in section on disordered crystals.

Phase transitions

Many phase transitions in minerals are unquenchable, requiring *in situ* studies to elucidate dynamics and short-range structure and thus complement data from diffraction studies of long-range symmetry. A large literature exists on spin-lattice relaxation studies of such transitions in silicates and oxides, generally in low-resolution NMR work of abundant, high-γ nuclides such as ^{1}H, ^{7}Li, ^{23}Na, ^{27}Al, and ^{93}Nb (Borsa and Rigmonti 1990). Single crystal NMR studies can more directly constrain symmetry changes, as in early studies of anorthite ($CaAl_2Si_2O_8$) (Staehli and Brinkmann 1974) and later work on quartz (Spearing et al. 1992). The high resolution and chemical shift information obtainable in high-field, MAS NMR spectra has been utilized for *in situ*, high-temperature ^{29}Si studies of transitions in minerals such as tridymite (Kitchin et al. 1996), cristobalite (Spearing et al. 1992), and anorthite (Phillips and Kirkpatrick 1995). High-resolution NMR work has also emphasized the characterization of diffusion processes by the motional averaging of distinct resonances for ions in different structural sites, for example with high temperature MAS NMR of ^{23}Na in sodalites (Fechtelkord 2000), in cryolite (Na_3AlF_6) (Spearing et al. 1994) and in nepheline ([Na,K]$AlSiO_4$) (Fig. 22) (Stebbins et al. 1989), and in ^{25}Mg NMR study of a single crystal of forsterite (Mg_2SiO_4) to 1400 °C (Stebbins 1997). Changes with increasing temperature in the static lineshape can be caused by either static changes in site symmetry or dynamic exchange among different polyhedral orientations, observable without the need for high-T MAS. Examples include ^{23}Na in albite ($NaAlSi_3O_8$) (George and Stebbins 1995) and ^{27}Al and ^{133}Cs in pollucite ($CsAlSi_2O_6$) (Ashbrook et al. 2005b). Detailed analysis of lineshapes in cases of such exchange, especially for quadrupolar nuclides, can be a complex problem, where recent progress has been made (Kristensen and Farnan 2001; Griffin et al. 2009).

Interactions of water with minerals and glasses

Interactions of minerals and glasses with water are geochemically and technologically important, and have often been studied by NMR. For example, early high-resolution NMR studies of the acidic corrosion of $NaAlSi_3O_8$ and rhyolite glasses demonstrated the sensitivity of ^{27}Al NMR to the formation of secondary phases containing $^{[6]}Al$, and of ^{23}Na NMR to the hydration of the Na^+ cations from the glass (Yang and Kirkpatrick 1989, 1990). These and later studies have often used double and triple resonance CPMAS NMR, and more complex experiments involving probe molecules, to enhance signals from sites near to protons and thus emphasize hydrated surface layers (Carroll et al. 2002; Tsomaia et al. 2003; Washton et al. 2008; Davis et al. 2009). Reactions between minerals and water can sometimes be shown to be site

EBSCOhost - printed on 2/13/2023 5:26 AM via . All use subject to https://www.ebsco.com/terms-of-use

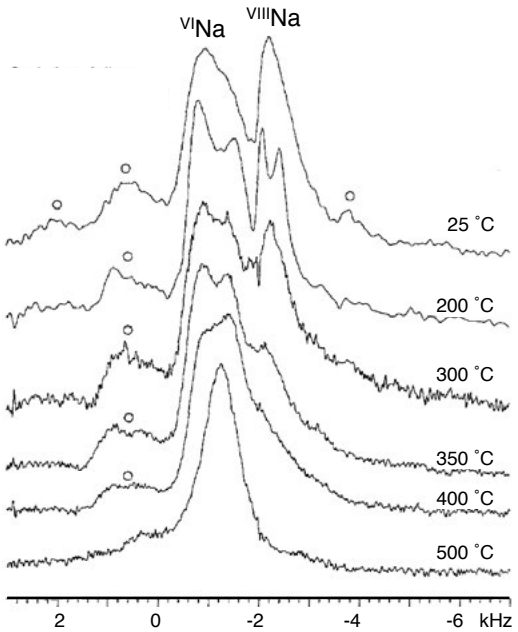


Figure 22. ^{23}Na MAS NMR spectra (9.4 T), collected *in situ* at the temperatures shown, for $Na_{0.75}(Na_{0.20}K_{0.05})AlSiO_4$ nepheline, showing motional averaging caused by exchange of Na^+ between the two sites above 300 °C. Circles mark spinning sidebands. [Used by permission of Springer, from Stebbins et al. (1989) *Physics and Chemistry of Minerals*, Vol. 16, Fig. 2, p. 764].

specific: for example, the rate of exchange of ^{17}O between $H_2{}^{17}O$ vapor and Si-O-Si (slowest), Si-O-Al, and Al-O-Al (fastest) sites in the zeolite stilbite (Xu and Stebbins 1998; Stebbins et al. 1999). Transformations of minerals in low-temperature hydrothermal environments often involve poorly crystalline or disordered phases and can be elucidated by NMR, for example in studies of clay mineral transitions (Alba et al. 2010; Hidalgo et al. 2010). In poorly-crystalline, naturally-occurring, weathering products such as allophane, ^{29}Si and ^{27}Al NMR have been particularly useful, the latter allowing quantitation of ^{IV}Al, ^{VI}Al, and, in some samples, ^{V}Al, in these complex materials (Ildefonse et al. 1994; Childs et al. 1999; Hiradate and Wada 2005).

Aqueous solutions: ambient to elevated pressures

Structural and dynamical information about aqueous solutions themselves are of course critical complements to understanding their interactions with minerals. NMR has played an important role in the modern understanding of aqueous ions, and has great potential for furthering such work. Space permits only a few examples here.

In many cases (barring too rapid relaxation and line broadening), solution NMR peaks are very narrow and provide much more sensitivity than in solids. For small inorganic ions in aqueous solutions, ligand exchange and bond-breaking are usually rapid enough so that only single, motionally averaged peaks are observed (as in silicate melts described above), which nonetheless can be very informative about cation coordination and complexing (Mason 1987). More details can be obtained in some cases, such as the complex, long-lived silicate anionic molecules that occur in concentrated (high pH) alkali silicate solutions, whose structures and exchange rates can be determined by ^{29}Si NMR (Harris and Knight 1983; Knight et al. 1988). For rapidly-exchanging ions, more commonly studied are the dynamics of the exchange process

EBSCOhost - printed on 2/13/2023 5:26 AM via . All use subject to https://www.ebsco.com/terms-of-use

itself, between anions or H_2O molecules and cations. Data for and modeling of the temperature dependence of relaxation times can reveal activation energies for exchange and much about the mechanisms of such processes. For example, much early work was done on ^{17}O relaxation in transition metal salt solutions (Swift and Connick 1962), and later, further studies using $^{35,37}Cl$ (Sharps et al. 1993) and other nuclides (Mason 1987). Extensive studies using ^{17}O NMR, complemented recently by sophisticated computational modeling, have revealed much about exchange processes involving complex aqueous aluminum ions, which are potentially interesting in understanding dynamics at mineral-water interfaces (Phillips et al. 1997b; Casey and Rustad 2007; Harley et al. 2011). Examples of findings include evidence for a five-coordinated aqueous Al species (Swaddle et al. 2005) and *in situ*, high pressure NMR that yields activation volumes for exchange reactions and thus further constrains mechanisms (Loring et al. 2004).

NMR has been done for decades on molecular and ionic liquids and even on static (non-spinning) solids in gas-pressurized vessels in the 100's to 1000's of bars range, usually at sub-ambient or modest elevated temperatures (Jonas 1991). Recent interest in CO_2 sequestration in deep geological reservoirs has stimulated renewed geochemical applications of these approaches. Chemical exchange is often slow enough so that ^{13}C NMR peaks for aqueous HCO_3^- and aqueous CO_2 remain separate, and several groups have developed probes that allow direct, in situ quantitation of these species during fluid reactions with solid carbonate, hydroxide, or silicate phases (Diefenbacher et al. 2011; Hoyt et al. 2011; Surface et al. 2013). In some cases, sensitivity is sufficient to observe solid carbonate phases as well (Surface et al. 2013); remarkably, MAS rotors have been built that can spin samples pressurized with CO_2 up to at least 150 bar to yield higher resolution spectra of reacting solids (Hoyt et al. 2011). The long-proven application of ^1H NMR to H-rich liquids and even to solids in large-volume diamond anvil pressure cells (Lee et al. 1992) holds great promise for future work on speciation of aqueous solutions at higher pressures and temperatures.

MINERALS CONTAINING ABUNDANT UNPAIRED ELECTRON SPINS

Applications of high-resolution NMR to naturally-occurring minerals have often been limited by the severe line broadening, and even loss of signal, that can be caused by the unpaired electron spins in most transition metal and rare earth element cations. Given that iron is among the most abundant elements in the Earth, this has meant that NMR work on many major groups of minerals (e.g., olivines, garnets, pyroxenes, amphiboles, spinels) has generally been limited to rare, low-Fe end members, or to synthetic, Fe-free compositions. There are a few early exceptions, such as pioneering single-crystal ^{27}Al NMR studies of iron-rich silicates such as pyrope-almandine garnet ($[Mg,Fe]_3Al_2Si_3O_{12}$), in which large shifts in NMR frequencies caused by electron-nuclear dipolar couplings were noted (Ghose 1964).

Effects of such paramagnetic impurities are complex, and can include increases in spin-lattice relaxation rates to the point of severe peak broadening, and the shifting of resonances via either the through-bond perturbations of electron spin density (Fermi contact shifts) or via classical through-space dipolar interactions ("pseudocontact" shifts) (Mackenzie and Smith 2002; Grey and Dupré 2004). In cases where peak broadening is not overwhelming, as in rare-earth doped stannate pyrochlore phases, and manganese oxides (birnessite) with interlayer Na, both of these effects can produce resolvable peaks, that may be shifted by 10's to many 100's of ppm—often far outside of normal chemical shift ranges (Grey et al. 1989, 1990; Aldi et al. 2012). Such measurements have the potential to yield unique information on cation site distributions. Contact-shifted peaks, which show characteristically large effects of temperature on their frequencies, have now been detected in a few natural and synthetic silicate minerals, including V^{4+}-doped zircon (Dajda et al. 2003), synthetic forsterite and wadsleyite (Stebbins et al. 2009c), naturally-occurring low-Fe pyropes (Palke and Stebbins 2011b), as well as in rare-

EBSCOhost - printed on 2/13/2023 5:26 AM via . All use subject to https://www.ebsco.com/terms-of-use

earth doped phosphates xenotime and monazite (Fig. 23) (Palke and Stebbins 2011a). Improved understanding of such interactions should provide renewed prospects for using NMR to learn about short-range order/disorder in minerals containing significant concentrations of paramagnetic cations, at least at the few per cent level. For example, in recent work on ferric iron phosphates of major interest as Li-ion battery cathodes, real progress in the theoretical calculation of such "hyperfine" interactions was demonstrated (Kim et al. 2010).

Even more complex are the often poorly-crystalline iron oxyhydroxides that are common products of weathering and of the mining of Fe-sulfide containing ore deposits, and which thus can play important roles in the sorption and release of toxic metals. Recent NMR studies have produced informative spectra from cations sorbed onto such "NMR-impossible" Fe-rich minerals, such as ^{31}P, ^{6}Li, ^{7}Li and ^{1}H and ^{2}H on goethite and lepidocrocite (FeOOH). Here, in addition to large effects on relaxation and peak widths, well-defined contact shifts can sometimes be noted, especially if the sample is above its Néel (or Curie) temperature and thus lacks magnetic ordering (Fig. 24) (Nielsen et al. 2005; Kim et al. 2008, 2011). In some cases, the loss of signal intensity sometimes caused by nearby magnetic ions such as Fe^{3+} can be exploited to estimate such proximities and the extent of mixing or local ordering, such as in Al-substituted ferrihydrite (Cismasu et al. 2012) and $MgSiO_3$ perovskite co-substituted with Fe^{3+} and Al^{3+} (Palke et al. 2012).

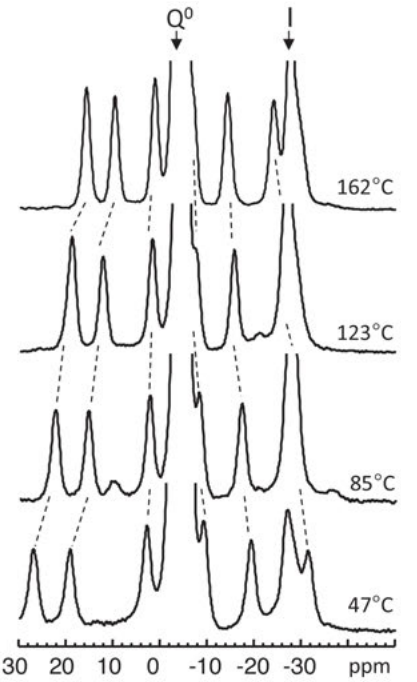


Figure 23. ^{31}P MAS NMR spectra for monazite ($LaPO_4$) doped with 1% Nd, collected at the temperatures shown (Palke and Stebbins 2011a). "Q^0" marks the unshifted peak for P cations in the monazite that are distant from Nd^{3+} ions; "I" marks a minor impurity phase. All other peaks are for P cations in the monazite that have close Nd^{3+} neighbors and thus have significant contact shifts: note the large effects of temperature on their positions. Each of these peaks represents only a fraction of a percent of the total signal; their intensity is greatly exaggerated by the short pulse delay used (0.05 s) and by enlargement of the vertical scale.

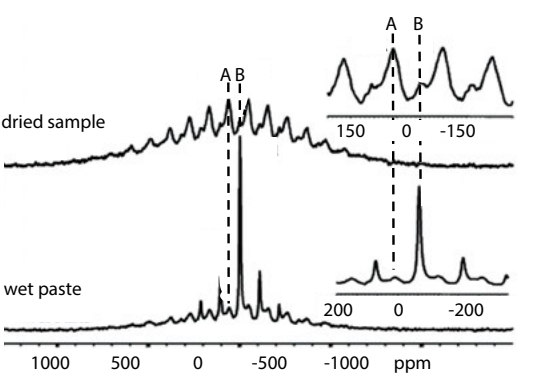


Figure 24. ^{7}Li MAS spectra (8.5 T) for Li ions sorbed onto lepidocrocite (γ-FeOOH). "A" marks the central peak for an inner-sphere complex with Fe^{3+} in the first cation shell of Li^+ and has a large contact shift. "B" marks that of an outer-sphere complex with all H_2O first neighbors, which is more abundant in the wet sample, and is not strongly shifted. All other peaks are spinning sidebands, which are greatly increased by magnetic interactions from the unpaired electron spins in the iron mineral. [Used by permission of the American Chemical Society, from Kim et al. (2008) *Journal of the American Chemical Society*, Vol. 130, Fig. 13, p. 1291].

EBSCOhost - printed on 2/13/2023 5:26 AM via . All use subject to https://www.ebsco.com/terms-of-use

ACKNOWLEDGMENTS

This work was supported by NSF grant EAR 1019596 to JS and Grants-in-Aid for Scientific Research from MEXT to XX. We thank the anonymous reviewers for very helpful comments and corrections on the original manuscript and the volume editors, Grant Henderson and Daniel Neuville, for their great efforts at bringing this volume together.

REFERENCES

Abragam A (1961) Principles of Nuclear Magnetism. Clarendon Press, Oxford

Adams SJ, Hawkes GE, Curzon EH (1991) A solid state ^{29}Si nuclear magnetic resonance study of opal and other hydrous silicas. Am Mineral 76:1863-1871

Alba MD, Castro MA, Chain P, Naranjo M, Perdigon AC (2005) Structural studies of synthetic mica-montmorillonite by means of 2D MAS NMR experiments. Phys Chem Miner 32:248-254

Alba MA, Castro MA, Chain P, Orta MM, Pazos MC, Pavón E (2010) Hydrothermal stability of layered silicates in neutral and acidic media: effect on engineered-barrier safety. Clays Clay Miner 58:501-514

Aldi KA, Cabana J, Sideris PJ, Grey CP (2012) Investigation of cation ordering in triclinic sodium birnessite via ^{23}Na MAS NMR spectroscopy. Am Mineral 97:883-889

Allwardt JR, Stebbins JF (2004) Ca-Mg and K-Mg mixing around non-bridging oxygens in silicate glasses: An investigation using oxygen-17 MAS and 3QMAS NMR. Am Mineral 89:777-784

Allwardt JR, Lee SK, Stebbins JF (2003) Bonding preferences of non-bridging oxygens in calcium aluminosilicate glass: evidence from ^{17}O MAS and 3QMAS NMR on calcium aluminate and low-silica Ca-aluminosilicate glasses. Am Mineral 88:949-954

Allwardt JR, Schmidt BC, Stebbins JF (2004) Structural mechanisms of compression and decompression in high pressure $K_2Si_4O_9$ glasses: An investigation utilizing Raman and NMR spectroscopy of high-pressure glasses and crystals. Chem Geol 213:137-151

Allwardt JR, Stebbins JF, Schmidt BC, Frost DJ, Withers AC, Hirschmann MM (2005) Aluminum coordination and the densification of high-pressure aluminosilicate glasses. Am Mineral 90:1218-1222

Altaner SP, Weiss CA, Kirkpatrick RJ (1988) Evidence from ^{29}Si NMR for the structure of mixed-layer illite/smectite clay minerals. Nature 331:699-702

Amoureux JP, Bauer F, Ernst H, Fernandez C, Freude D, Michel D, Pingel UT (1998) O^{17} multiple-quantum and H^{1} MAS NMR studies of zeolite ZSM-5. Chem Phys Lett 285:10-14

Andrew ER, Bradbury A, Eades RG (1959) Removal of dipolar broadening of nuclear magnetic resonance spectra of solids by specimen rotation. Nature 183:1802-1803

Angeli F, Villain O, Schuller S, Ispas S, Charpentier T (2011) Insight into sodium silicate glass structural organization by multinuclear NMR combined with first-principles calculations. Geochim Cosmochim Acta 75:2453-2469

Apperley DC, Harris RK, Hodgkinson P (2012) Solid-State NMR: Basic Principles & Practice. Momentum Press, LLC, New York

Ashbrook SE, Wimperis S (2004) High-resolution NMR of quadrupolar nuclei in solids: the satellite-transition magic angle spinning (STMAS) experiment. Prog Nucl Magn Reson Spectrosc 45:53-108

Ashbrook SE, Berry AJ, Hibberson WO, Steuernagel S, Wimperis S (2005a) High-resolution ^{17}O MAS NMR spectroscopy of forsterite (α-Mg_2SiO_4), wadsleyite (β-Mg_2SiO_4) and ringwoodite (γ-Mg_2SiO_4). Am Mineral 90:1861-1870

Ashbrook SE, Whittle KR, Le Polles L, Farnan I (2005b) Disorder and dynamics in pollucite from ^{133}Cs and ^{27}Al NMR. J Am Ceram Soc 88:1575-1583

Ashbrook SE, Le Polles L, Pickard CJ, Berry AJ, Wimperis S, Farnan I (2007b) First-principles calculations of solid-state ^{17}O and ^{29}Si NMR spectra of Mg_2SiO_4 polymorphs. Phys Chem Chem Phys 9:1587-1598

Ashbrook SE, Berry AJ, Frost DJ, Gregorovic A, Pickard CJ, Readman JE, Wimperis S (2007a) ^{17}O and ^{29}Si NMR parameters of $MgSiO_3$ phases from high-resolution solid-state NMR spectroscopy and first-principles calculations. J Am Chem Soc 129:13213-13224

Baltisberger JH, Xu Z, Stebbins JF, Wang S, Pines A (1996) Triple-quantum two-dimensional ^{27}Al magic-angle spinning nuclear magnetic resonance spectroscopic study of aluminosilicate and aluminate crystals and glasses. J Am Chem Soc 118:7209-7214

Barron PF, Slade P, Frost RL (1985) Ordering of aluminum in tetrahedral sites in mixed-layer 2:1 phyllosilicates by solid-state high-resolution NMR. J Phys Chem 89:3880-3885

Blaha P, Schwarz K, Herzig P (1985) 1st-principles calculation of the electric field gradient of Li_3N. Phys Rev Lett 54:1192-1195

Borsa F, Rigmonti A (1990) Comparison of NMR and NQR studies of phase transitions in disordered and ordered crystals. *In*: Structural Phase Transitions-II. Muller KA, Thomas H (eds) Springer-Verlag, New York, p 83-175

EBSCOhost - printed on 2/13/2023 5:26 AM via . All use subject to https://www.ebsco.com/terms-of-use

Bosenick A, Geiger CA, Phillips BL (1999) Local Ca-Mg distribution of Mg-rich pyrope-grossular garnets synthesized at different temperatures revealed by ^{29}Si MAS NMR spectroscopy. Am Mineral 84:1422-1432

Bowers GM, Ravella R, Komarneni S, Mueller KT (2006) NMR study of strontium binding by a micaceous mineral. J Phys Chem B 110:7159-7164

Bowers GM, Bish DL, Kirkpatrick RJ (2008) H_2O and cation structure and dynamics in expandable clays: ^{2}H and ^{39}K NMR investigations of hectorite. J Phys Chem C 112:6430-6438

Bowers GM, Singer JW, Bish DL, Kirkpatrick RJ (2011) Alkali metal and H_2O dynamics at the smectite/water interface. J Phys Chem C 115:23395-23407

Brandriss ME, Stebbins JF (1988) Effects of temperature on the structures of silicate liquids: ^{29}Si NMR results. Geochim Cosmochim Acta 52:2659-2670

Brouwer DH (2008) A structure refinement strategy for NMR crystallography: An improved crystal structure of silica-ZSM-12 zeolite from ^{29}Si chemical shift tensors. J Magn Reson 194:136-146

Brouwer DH, Darton RJ, Morris RE, Levitt MH (2005) A solid-state NMR method for solution of zeolite crystal structures. J Am Chem Soc 127:10365-10370

Brown LD, Ray AS, Thomas PS (2003) ^{29}Si and ^{27}Al NMR study of amorphous and paracrystalline opals from Australia. J Non-Cryst Solids 332:242-248

Brun E, Hafner S (1962) Die elektrische Quadrupolaufspaltung von Al^{27} in Spinell $MgAl_2O_4$ und Korund Al_2O_3. Z Kristallogr 117:37-62

Carroll SA, Maxwell RS, Bourcier W, Martin S, Hulzey S (2002) Evaluation of silica-water surface chemistry using NMR spectroscopy. Geochim Cosmochim Acta 66:913-926

Casey WH, Rustad JR (2007) Reaction dynamics, molecular clusters, and aqueous geochemistry. Annu Rev Earth Planet Sci 35:21-46

Charpentier T (2011) The PAW/GIPAW approach for computing NMR parameters: A new dimension added to NMR study of solids. Solid State Nucl Magn Reson 40:1-20

Charpentier T, Ispas S, Profeta M, Mauri F, Pickard CJ (2004) First-principles calculation of O^{17}, Si^{29}, and Na^{23} NMR spectra of sodium silicate crystals and glasses. J Phys Chem B 108:4147-4161

Chemtob SM, Rossman GR, Stebbins JF (2012) Natural hydrous amorphous silica: quantitation of network speciation and hydroxyl content by ^{29}Si NMR and vibrational spectroscopy. Am Mineral 97:203-211

Childs CW, Hayashi S, Newman RH (1999) Five-coordinate aluminum in allophane. Clays Clay Miner 47:64-69

Cho H, Rossman GR (1993) Single-crystal NMR studies of low-concentration hydrous species in minerals-grossular garnet. Am Mineral 78:1149-1164

Circone S, Navrotsky A (1992) Substitution of $^{[6,4]}$Al in phlogopite: high-temperature solution calorimetry, heat capacities, and thermodynamic properties of the phlogopite-eastonite join. Am Mineral 77:1191-1205

Circone S, Navrotsky A, Kirkpatrick RJ, Graham CM (1991) Substitution of $^{[6,4]}$Al in phlogopite: mica characterization, unit-cell variation, ^{27}Al and ^{29}Si MAS-NMR spectroscopy, and Al-Si distribution in the tetrahedral sheet. Am Mineral 76:1485-1501

Cismasu AC, Michel FM, Stebbins JF, Levard CM, Brown GE Jr (2012) Properties of impurity-bearing ferrihydrite I. Effects of Al content and precipitation rate on the structure of 2-line ferrihydrite. Geochim Cosmochim Acta 92:275-291

Clark TM, Grandinetti PJ (2005) Calculation of bridging oxygen ^{17}O quadrupolar coupling parameters in alkali silicates: A combined *ab initio* investigation. Solid State Nucl Magn Reson 27:233-241

Clark TM, Grandinetti PJ, Florian P, Stebbins JF (2004) Correlated structural distributions in silica glass. Phys Rev B 70:064202-064201-064208

Coutures JP, Massiot D, Bessada C, Echegut P, Rifflet JC, Taulelle F (1990) Etude par RMN ^{27}Al d'aluminates liquides dans le domaine 1600-2100 °C. C R Acad Sci Paris II 310:1041-1045

Dajda N, Dixon JM, Smith ME (2003) Atomic site preferences and structural evolution in vanadium-doped $ZrSiO_4$ from multinuclear solid-state NMR. Phys Rev B 67:024201-024201-024201-024209

Davis MC, Brouwer WJ, Wesolowski DJ, Anovitz LM, Lipton AS, Mueller KT (2009) Magnesium silicate dissolution investigated by ^{29}Si MAS, ^{1}H-^{29}Si CPMAS, ^{25}Mg QCPMG, and ^{1}H-^{25}Mg CP QCPMG NMR. Phys Chem Chem Phys 11:7013-7021

Davis MC, Sanders KJ, Grandinetti PJ, Gaudio SJ, Sen S (2011) Structural investigations of magnesium silicate glasses by ^{29}Si 2D magic-angle flipping NMR. J Non-Cryst Solids 357:2787-2795

Delevoye L, Robert J-L, Grandjean J (2003) ^{23}Na 2D 3QMAS NMR and ^{29}Si, ^{27}Al MAS NMR investigation of laponite and synthetic saponites of variable layer charge. Clay Miner 38:63-69

Derome AE (1987) Modern NMR Techniques for Chemistry Research. Pergamon Press, New York

Diefenbacher J, Piwowarczyk J, Marzke RF (2011) Note: solution NMR probe for the study of CO_2 sequestration at elevated pressure and temperature. Rev Sci Instrum 82:076107-1-3

Dirken PJ, Kohn SC, Smith ME, van Eck ERH (1997) Complete resolution of Si-O-Si and Si-O-Al fragments in an aluminosilicate glass by ^{17}O multiple quantum magic angle spinning NMR spectroscopy. Chem Phys Let 266:568-574

EBSCOhost - printed on 2/13/2023 5:26 AM via . All use subject to https://www.ebsco.com/terms-of-use

Dubinsky EV, Stebbins JF (2006) Quench rate and temperature effects on framework ordering in aluminosilicate melts. Am Mineral 91:753-761

Duer MJ (2002) Solid-State NMR Spectroscopy: Principles and Applications. Blackwell, Oxford, U.K.

Duer MJ (2004) Introduction to solid-state NMR spectroscopy. Blackwell, Oxford, U.K.

Dupree R, Holland D, McMillan PW, Pettifer RF (1984) The structure of soda-silica glasses: a MAS NMR study. J Non-Cryst Solids 68:399-410

Dupree R, Holland D, Mortuza MG (1990) A MAS-NMR investigation of lithium silicate glasses and glass ceramics. J Non-Cryst Solids 116:148-160

Dupree R, Howes AP, Kohn SC (1997) Natural abundance solid state ^{43}Ca NMR. Chem Phys Let 276:399-404

Dupree R, Kohn SC, Mortuza MG, Holland D (1992) NMR studies of glass structure. *In*: Physics of Non-Crystalline Solids. Pye LD, La Course WC, Stevens HJ (eds) Taylor and Francis, London, p 718-723

Eckert H (1994) Structural studies of non-crystalline solids using solid state NMR. New experimental approaches and results. *In*: Solid-State NMR IV Methods and Applications of Solid-State NMR. Blümich B (ed) Springer-Verlag, Berlin, p 127-198

Engelhardt G, Michel D (1987) High-Resolution Solid-State NMR of Silicates and Zeolites. Wiley, New York

Ernst RR, Bodenhausen G, Wokaun A (1987) Principles of Nuclear Magnetic Resonance in One and Two Dimensions. Oxford Science Publications, Oxford

Farnan I (1991) NMR spectroscopy in the Earth sciences. *In*: Encyclopedia of Earth System Science. Nierenberg W A (ed) Academic Press, San Diego, CA, p 750

Farnan I, Cho H, Weber WJ, Scheele RD, Johnson NR, Kozelisky AE (2004) High-resolution solid-state nuclear magnetic resonance experiments on highly radioactive ceramics. Rev Sci Instrum 75:5232-5236

Farnan I, Salje EKH (2001) The degree and nature of radiation damage in zircon observed by ^{29}Si nuclear magnetic resonance. J Appl Phys 89:2084-2090

Farnan I, Stebbins JF (1990a) A high temperature ^{29}Si NMR investigation of solid and molten silicates. J Am Chem Soc 112:32-39

Farnan I, Stebbins JF (1990b) Observation of slow atomic motions close to the glass transition using 2-D ^{29}Si NMR. J Non-Cryst Solids 124:207-215

Farnan I, Stebbins JF (1994) The nature of the glass transition in a silica-rich oxide melt. Science 265:1206-1209

Fayon F, Bessada C, Massiot D, Farnan I, Coutures JP (1998) ^{29}Si and ^{207}Pb NMR study of local order in lead silicate glasses. J Non-Cryst Solids 232-234:403-408

Fechtelkord M (2000) Influence of sodium ion dynamics on the ^{23}Na quadrupolar interaction in sodalite: A high-temperature ^{23}Na MAS NMR study. Solid State Nucl Magn Reson 18:70-88

Fechtelkord M (2004) Solid state NMR spectroscopy as supporting method in Rietveld structure refinements of rock-forming minerals: New developments and examples. *In*: Spectroscopic Methods in Mineralogy. Beran A, Libowitsky E (eds) Eotvos University Press, Budapest, p 421-464

Fechtelkord M, Behrens H, Holtz F, Bretherton JL, Fyfe CA, Groat LA, Raudsepp M (2003) Influence of F content on the composition of Al-rich synthetic phlogopite: Part II. Probing the structural arrangement of aluminum in tetrahedral and octahedral layers by ^{27}Al MQMAS and ^{1}H/^{19}F-^{27}Al HETCOR and REDOR experiments. Am Mineral 88:1046-1054

Fiske P, Stebbins JF (1994) The structural role of Mg in silicate liquids: a high-temperature ^{25}Mg, ^{23}Na, and ^{29}Si NMR study. Am Mineral 79:848-861

Flemming RL, Luth RW (2002) ^{29}Si MAS NMR study of diopside-Ca-Tschermak clinopyroxenes: Detecting both tetrahedral and octahedral Al substitution. Am Mineral 87:25-36

Florian P, Vermillion KE, Grandinetti PJ, Farnan I, Stebbins JF (1996) Cation distribution in mixed alkali disilicate glasses. J Am Chem Soc 118:3493-3497

Florian P, Veron E, Green TFG, Yates JR, Massiot DR (2012) Elucidation of the Al/Si ordering in gehlenite $Ca_2Al_2SiO_7$ by combined ^{29}Si and ^{27}Al NMR/quantum chemical calculations. Chem Mater 24:4068-4079

Fukushima E, Roedder SBW (1981) Experimental Pulse NMR. Addison-Wesley, Reading, MA

Fyfe CA (1983) Solid State NMR for Chemists. CFC Press, Guelph

Gaudio SJ, Sen S, Lesher CE (2008) Pressure-induced structural changes and densification of vitreous $MgSiO_3$. Geochim Cosmochim Acta 72:1222-1230

George AM, Stebbins JF (1995) High temperature ^{23}Na NMR data for albite: comparison to chemical shift models. Am Mineral 80:878-884

George AM, Stebbins JF (1996) Dynamics of Na in sodium aluminosilicate glasses and liquids. Phys Chem Miner 23:526-534

Ghose S (1964) Nuclear magnetic resonance spectrum of ^{27}Al in a natural almandine garnet, $(Fe'',Mg)_3Al_2(SiO_4)_3$. Solid State Commun 2:361-362

Ghose S, Tsang T (1973) Structural dependence of quadrupole coupling constant e^2qQ/h for ^{27}Al and crystal field parameter D for Fe^{3+} in aluminosilicates. Am Mineral 58:748-755

Gladden LF, Carpenter TA, Elliot SR (1986) ^{29}Si MAS NMR studies of the spin-lattice relaxation time and bond-angle distribution in vitreous silica. Philos Mag B 53:L81-L87

EBSCOhost - printed on 2/13/2023 5:26 AM via . All use subject to https://www.ebsco.com/terms-of-use

Graetsch H, Gies H, Topalovic I (1994) NMR, XRD and IR study on microcrystalline opals. Phys Chem Miner 21:166-175

Grey CP, Dupré N (2004) NMR studies of cathode materials for lithium-ion rechargeable batteries. Chem Rev 104:4493-4512

Grey CP, Dobson CM, Cheetham AK, Jakeman RJB (1989) Studies of rare-earth stannates by ^{119}Sn MAS NMR. The use of parmagnetic shift probes in the solid state. J Am Chem Soc 111:505-511

Grey CP, Smith ME, Cheetham AK, Dobson R, Dupree R (1990) ^{89}Y MAS NMR study of rare-earth pyrochlores-paramagnetic shifts in the solid state. J Am Chem Soc 112:4670-4680

Griffin JM, Wimperis S, Berry AJ, Pickard CJ, Ashbrook SE (2009) Solid-state ^{17}O NMR spectroscopy of hydrous magnesium silicates: Evidence for proton dyanmics. J Phys Chem C 113:465-471

Griffin JM, Berry AJ, Frost DJ, Wimperis S, Ashbrook SE (2013) Water in the Earth's mantle: a solid-state NMR study of hydrous wadsleyite. Chem Sci 4:1523-1538

Halenius U, Skogby H, Edén M, Nazzareni S, Kristiansson P, Resmark J (2010) Coordination of boron in nominally boron-free rock-forming silicates; Evidence for incorporation of BO_3 groups in clinopyroxene. Geochim Cosmochim Acta 74:5672-5679

Harley SJ, Ohlin CA, Casey WH (2011) Geochemical kinetics via the Swift-Connick equations and solution NMR. Geochim Cosmochim Acta 75:3711-3725

Harris RK (1983) Nuclear Magnetic Resonance Spectroscopy. Pitman, London

Harris RK, Knight CTG (1983) Silicon-29 nuclear magnetic resonance studies of aqueous silicate solutions. V. First-order patterns in potassium silicate solutions enriched with silicon-29. J Chem Soc Farad Trans 79:1524-1538

Hartman JS, Narayanan A, Rigby SS, Sliwinski DR, Halden NM, Bain AD (2007) Heterogeneities in sol-gel-derived paramagnetics-doped forsterites and willemites. Electron microprobe analysis and stretched-exponential ^{29}Si NMR spin-lattice relaxation studies. Can J Chem 85:56-65

Hawthorne FC, Welch MD, Della Ventura G, Liu S, Robert J-L, Jenkins DM (2000) Short-range order in synthetic aluminous tremolites: An infrared and triple-quantum MAS NMR study. Am Mineral 85:1716-1724

Herrero CP, Sanz J (1991) Short-range order of the Si, Al distribution in layer silicates. J Phys Chem Solids 52:1129-1135

Herrero CP, Gregorkiewitz M, Sanz J, Serratosa JM (1987) ^{29}Si MAS-NMR spectroscopy of mica-type silicates: observed and predicted distribution of tetrahedral Al-Si. Phys Chem Mineral 15:84-90

Hidalgo C, Etchevers JD, Martinez-Richa A, Yee-Madeira H, Calderon HA, Vera-Graziano R, Matus F (2010) Mineralogical characterization of the fine fraction (<2 μm) of degraded volcanic soils and tepetes in Mexico. Appl Clay Sci 49:348-358

Hiradate S, Wada SI (2005) Weathering process of volcanic glass to allophane determined by ^{27}Al and ^{29}Si solid-state NMR. Clays Clay Miner 53:401-408

Hovis GL, Spearing DR, Stebbins JF, Roux J, Clare A (1992) X-ray powder diffraction and ^{23}Na - ^{27}Al - ^{29}Si MAS-NMR investigation of nepheline-kalsilite crystalline solutions. Am Mineral 77:19-29

Hoyt DW, Turcu RVF, Sears JA, Rosso KM, Burton SD, Felmy AR, Hu JZ (2011) High-pressure magic angle spinning nuclear magnetic resonance. J Magn Reson 212:378-385

Ildefonse P, Kirkpatrick RJ, Montez B, Calas G, Flank AM, Lagarde P (1994) ^{27}Al MAS NMR and aluminum x-ray absorption near-edge structure study of imogolite and allophanes. Clays Clay Miner 42:276-287

Jakobsen HJ, Nielsen NC, Lindgreen H (1995) Sequences of charged sheets in rectorite. Am Mineral 80:247-252

Jenkins DM, Sherriff BL, Cramer J, Xu Z (1997) Al, Si, and Mg occupancies in tetrahedrally and octahedrally coordinated sites in synthetic aluminous tremolite. Am Mineral 82:280-290

Johnson EA, Rossman GR (2003) The concentration and speciation of hydrogen in feldspars using FTIR and ^{1}H MAS NMR. Am Mineral 88:901-911

Jonas J (ed) (1991) High Pressure NMR. Springer-Verlag, Berlin

Kagi H, Parise JB, Cho H, Rossman GR (2000) Hydrogen bonding interactions in phase A [$Mg_7Si_2O_8(OH)_6$] at ambient and high pressure. Phys Chem Miner 27:225-233

Kanehashi K, Stebbins JF (2007) *In situ* high temperature ^{27}Al NMR study on dynamics of calcium aluminosilicate glass and melt. J Non-Cryst Solids 353:4001-4010

Kanzaki M (1996) Ab initio calculation of ^{29}Si NMR chemical shifts for the clusters of $Si(OH)_4$, $Si(OH)_5^-$ and $Si(OH)_6^{-2}$. Mineral J 18:1-8

Kanzaki M (2010) Crystal structure of a new high-pressure polymorph of topaz-OH. Am Mineral 95:1349-1352

Kanzaki M, Xue XY (2012) Structural characterization of moganite-type $AlPO_4$ by NMR and powder X-ray diffraction. Inorg Chem 51:6164-6172

Kanzaki M, Xue X, Reibstein S, Berryman E, Namgung S (2011) Structures of two new high-pressure forms of $AlPO_4$ by X-ray powder diffraction and NMR spectroscopy. Acta Crystallogr B 67:30-40

Keeler J (2010) Understanding NMR Spectroscopy. John Wiley & Sons Ltd., Chichester

EBSCOhost - printed on 2/13/2023 5:26 AM via . All use subject to https://www.ebsco.com/terms-of-use

Kelsey KE, Stebbins JF, Du L-S, Hankins B (2007) Constraining ^{17}O and ^{27}Al NMR spectra of high pressure crystals and glasses: new data for jadeite, pyrope, grossular, and mullite. Am Mineral 92:210-216

Kelsey KE, Stebbins JF, Du L-S, Mosenfelder JL, Asimow PD, Geiger CA (2008) Cation order/disorder behavior and crystal chemistry of pyrope-grossular garnets: An ^{17}O 3QMAS and ^{27}Al MAS NMR spectroscopic study. Am Mineral 93:134-143

Kelsey KE, Stebbins JF, Mosenfelder JL, Asimow PD (2009) Simultaneous aluminum, silicon, and sodium coordination changes in 6 GPa sodium aluminosilicate glasses. Am Mineral 94:1205-1215

Kennedy GJ, Wiench JW, Pruski M (2008) Determination of ^{27}Al-^{29}Si connectivities in zeolites with 2D ^{27}Al-^{29}Si RAPT-CPMG-HETCOR NMR. Solid State Nucl Magn Reson 33:76-81

Kim Y, Kirkpatrick RJ (1997) ^{23}Na and ^{133}Cs NMR study of cation adsorption on mineral surfaces: Local environments, dynamics, and effects of mixed cations. Geochim Cosmochim Acta 61:5199-5208

Kim Y, Kirkpatrick RJ (2006) ^{11}B NMR investigation of boron interaction with mineral surfaces: Results for boehmite, silica gel and illite. Geochim Cosmochim Acta 70:3231-3238

Kim N, Stebbins JF, Quartieri S, Oberti R (2007) Scandium-45 NMR of pyrope-grossular garnets: resolution of multiple scandium sites and comparison with x-ray diffraction and x-ray spectroscopy. Am Mineral 92:1875-1880

Kim J, Nielsen UG, Grey CP (2008) Local environments and lithium adsorption on the iron oxyhydroxides lepidocrocite (γ-FeOOH) and goethite (α-FeOOH): A ^{2}H and ^{7}Li solid-state MAS NMR study. J Am Chem Soc 130:1285-1295

Kim J, Middlemass DS, Chernova NA, Zhu BXY, Masquelier C, Grey CP (2010) Linking local environments and hyperfine shifts: A combined experimental and theoretical ^{31}P and ^{7}Li solid-state NMR study of paramagnetic Fe(III) phosphates. J Am Chem Soc 132:16825-16840

Kim J, Li W, Phillips BL, Grey CP (2011) Phosphate adsorption on the iron oxyhydroxides goethite (β-FeOOH), akaganite (β-FeOOH), and lepidocrocite (γ-FeOOH): a ^{31}P NMR study. Energy Environ Sci 4:4298-4305

Kinsey RA, Kirkpatrick RJ, Hower J, Smith KA, Oldfield E (1985) High resolution aluminum-27 and silicon-29 nuclear magnetic resonance studies of layer silicates, including clay minerals. Am Mineral 70:537-548

Kirkpatrick RJ (1988) MAS NMR spectroscopy of minerals and glasses. *In*: Spectroscopic Methods in Mineralogy and Geology. Hawthorne FC (ed) Mineralogical Society of America, Washington D.C., p 341-403

Kirkpatrick RJ, Phillips BL (1993) ^{27}Al NMR spectroscopy of minerals and related materials. Appl Magn Reson 4:213-236

Kirkpatrick RJ, Dunn T, Schramm S, Smith KA, Oestrike R, Turner G (1986) Magic-angle sample-spinning nuclear magnetic resonance spectroscopy of silicate glasses: a review. *In*: Structure and Bonding in Noncrystalline Solids. Walrafen G E, Revesz A G (eds) Plenum Press, New York, p 302-327

Kirkpatrick RJ, Carpenter MA, Yang WH, Montez B (1987) ^{29}Si magic-angle NMR spectroscopy of low-temperature ordered plagioclase feldspars. Nature 325:236-238

Kitchin SJ, Kohn SC, Dupree R, Henderson CMB, Kihara K (1996) *In situ* ^{29}Si MAS NMR studies of structural phase transitions of tridymite. Am Mineral 96:550-560

Klimm K, Kohn SC, O'Dell LA, Botcharnikov RE, Smith ME (2012) The dissolution mechanism of sulfur in hydrous silicate glasses. I: Assessment of analytical techniques in determining the sulfur speciation in iron-free and iron-poor glasses. Chem Geol 322:237-249

Klochko K, Cody GD, Tossell JA, Dera P, Kaufman AJ (2009) Re-evaluating boron speciation in biogenic calcite and aragonite using ^{11}B MAS NMR. Am Mineral 73:1890-1900

Knight CTG, Kirkpatrick RJ, Oldfield E (1988) Two-dimensional ^{29}Si nuclear magnetic resonance spectroscopic study of chemical exchange pathways in potassium silicate solutions. J Magn Reson 78:31-40

Kohn SC (2004) NMR studies of silicate glasses. EMU Notes Mineral 6:399-419

Kohn SC (2006) Structural studies of OH in nominally anhydrous minerals using NMR. Rev Mineral Geochem 62:53-62

Kohn SC, Brooker RA, Dupree R (1991a) ^{13}C NMR-a method for studying CO_2 speciation in glasses. Geochim Cosmochim Acta 55:3879-3884

Kohn SC, Dupree R, Mortuza MG, Henderson CMB (1991b) Evidence for five- and six-coordinated aluminum fluoride complexes in F-bearing aluminosilicate glasses. Am Mineral 76:309-312

Kohn SC, Henderson CMB, Dupree R (1995) Si-Al order in leucite revisited; new information from an analcite-derived analogue. Am Mineral 80:705-714

Kohn SC, Roome BM, Smith ME, Howes AP (2005) Testing a potential mantle geohygrometer; the effect of dissolved water on the intracrystalline partitioning of Al in orthopyroxene. Earth Planet Sci Lett 238:342-350

Kristensen JH, Farnan I (2001) Measurement of molecular motion in solids by nuclear magnetic resonance spectroscopy of half-integer quadrupolar nuclei. J Chem Phys 114:9608-9624

Kroeker SK, Rice D, Stebbins JF (2002) Disordering during melting: and oxygen-17 NMR study of crystalline and glassy $CaTiSiO_5$ (titanite). Am Mineral 87:572-579

EBSCOhost - printed on 2/13/2023 5:26 AM via . All use subject to https://www.ebsco.com/terms-of-use

Larsen FH, Farnan I (2004) Site populations and short range order in aluminosilicates investigated by ^{27}Al solid-state NMR. J Phys Chem B 108:9764-9771

Lausen SK, Lindgreen H, Jakobsen HJ, Neilsen NC (1999) Solid-state ^{29}Si MAS NMR studies of illite and illite-smectite from shale. Am Mineral 84:1433-1438

Lee SK (2005) Microscopic origins of macroscopic properties of silicate melts and glasses at ambient and high pressure: implications for melt generation and dynamics. Geochim Cosmochim Acta 69:3695-3710

Lee SK, Stebbins JF (1999) The degree of aluminum avoidance in aluminosilicate glasses. Am Mineral 84:937-945

Lee SK, Stebbins JF (2000a) Al-O-Al and Si-O-Si sites in framework aluminosilicate glasses with Si/Al=1: quantification of framework disorder. J Non-Cryst Solids 270:260-264

Lee SK, Stebbins JF (2000b) The structure of aluminosilicate glasses: high-resolution ^{17}O and ^{27}Al MAS and 3QMAS NMR study. J Phys Chem B 104:4091-4100

Lee SH, Conradi MS, Norberg RE (1992) Improved NMR resonator for diamond anvil cells. Rev Sci Instrum 63:36743676

Lee SK, Cody GD, Fei Y, Mysen BO (2004) Nature of polymerization and properties of silicate melts and glasses at high pressure. Geochim Cosmochim Acta 68:4189-4200

Lee SK, Cody GD, Mysen BO (2005) Structure and extent of disorder in quaternary (Ca-Mg and Ca-Na) aluminosilicate glasses and melts. Am Mineral 90:1393-1401

Lee SK, Cody GD, Fei Y, Mysen BO (2006) The effect of Na/Si ratio on the structure of sodium silicate and aluminosilicate glasses quenched from melts at high pressure: A multi-nuclear (^{27}Al, ^{23}Na, ^{17}O) 1D and 2D solid-state NMR study. Chem Geol 229:162-172

Lesage A (2009) Recent advances in solid-state NMR spectroscopy of spin I=1/2 nuclei. Phys Chem Chem Phys 11:6876-6891

Li W, Xu W, Parise JB, Phillips BL (2012) Formation of hydroxylapatite from co-sorption of phosphate and calcium by boehmite. Geochim Cosmochim Acta 85:289-301

Li W, Pierre-Louis AM, Kwon KD, Kubicki JD, Strongin DR, Phillips BL (2013) Molecular level investigations of phosphate sorption on corundum (α-Al_2O_3) by ^{31}P solid-state NMR, ATR-FTIR and quantum chemical calculation. Geochim Cosmochim Acta 107:252-266

Lippmaa E, Mägi M, Samoson A, Engelhardt G, Grimmer AR (1980) Structural studies of silicates by solid-state high-resolution ^{29}Si NMR spectroscopy. J Am Chem Soc 102:4889-4893

Loring J, Yu P, Phillips BL, Casey WH (2004) Activation volume for oxygen exchange between the $GaO_4Al_{12}(OH)_{24}(H_2O)_{12}^{7+}$(aq) ($GaAl_{12}$) polyoxocation and aqueous solution from variable pressure ^{17}O NMR spectroscopy Geochim Cosmochim Acta 68:2791-2798

MacKenzie KJD, Smith ME (2002) Multinuclear Solid-State NMR of Inorganic Materials. Pergamon, New York

Maekawa H, Yokokawa T (1997) Effects of temperature on melt structure: A high-temperature ^{29}Si NMR study of $Na_2Si_2O_5$. Geochim Cosmochim Acta 61:2569-2576

Maekawa H, Maekawa T, Kawamura K, Yokokawa T (1991) The structural groups of alkali silicate glasses determined from ^{29}Si MAS-NMR. J Non-Cryst Solids 127:53-64

Maekawa H, Kato S, Kawamura K, Yokokawa T (1997) Cation mixing in natural $MgAl_2O_4$ spinel: A high-temperature ^{27}Al NMR study. Am Mineral 82:1125-1132

Mägi M, Lippmaa E, Samoson A, Engelhardt G, Grimmer AR (1984) Solid-state high-resolution silicon-29 chemical shifts in silicates. J Phys Chem 88:1518-1522

Malfait WJ, Xue X (2010) The nature of hydroxyl groups in aluminosilicate glasses: quantifying Si-OH and Al-OH abundances along the SiO_2-$NaAlSiO_4$ join by ^{1}H, ^{27}Al-^{1}H and ^{29}Si-^{1}H NMR spectroscopy. Geochim Cosmochim Acta 74:719-737

Malfait WJ, Halter WE, Morizet Y, Meier BH, Verel R (2007) Structural control on bulk melt properties: Single and double quantum ^{29}Si NMR spectroscopy on alkali-silicate glasses. Geochim Cosmochim Acta 71:6002-6018

Maresch WV, Welch MD, Gottschalk M, Ruthmann W, Czank M, Ashbrook SE (2009) Synthetic amphiboles and triple-chain silicates in the system Na_2O-MgO-SiO_2-H_2O: phase characterization, compositional relations, and excess H. Mineral Mag 73:957-996

Mason HE, Frisia S, Tang Y, Reeder RJ, Phillips BL (2007) Phosphorus speciation in calcite speleothems determined from solid-state NMR spectroscopy. Earth Planet Sci Lett 254:313-322

Mason HE, Montagna P, Kubista L, Taviani M, McCulloch M, Phillips BL (2011) Phosphate defects and apatite inclusions in coral skeletal aragonite revealed by solid-state NMR spectroscopy. Geochim Cosmochim Acta 75:7446-7457

Mason J (ed) (1987) Multinuclear NMR. Plenum Press, New York

Massiot D, Trumeau D, Touzo B, Farnan I, Rifflet JC, Douy A, Coutures JP (1995) Structure and dynamics of $CaAl_2O_4$ from liquid to glass: A high-temperature ^{27}Al NMR time-resolved study. J Phys Chem 99:16455-16459

EBSCOhost - printed on 2/13/2023 5:26 AM via . All use subject to https://www.ebsco.com/terms-of-use

Massiot D, Fayon F, Deschamps M, Cadars S, Florian P, Montouillout V, Pellerin N, Hiet J, Rakhmatullin A, Bessada C (2010) Detection and use of small J couplings in solid state NMR experiments. C R Acad Sci Paris 13:117-129

McMillan PF, Kirkpatrick RJ (1992) Al coordination in magnesium aluminosilicate glasses. Am Mineral 77:898-900

McMillan P, Akaogi M, Ohtani E, Williams Q, Nieman R, Sato R (1989) Cation disorder in garnets along the $Mg_3Al_2Si_3O_{12}$-$Mg_4Si_4O_{12}$ join: an infrared, Raman, and NMR study. Phys Chem Miner 16:428-435

Merzbacher CI, Sherriff BL, Hartman JS, White WB (1990) A high resolution ^{29}Si and ^{27}Al NMR study of alkaline earth aluminosilicate glasses. J Non-Cryst Solids 124:194-206

Millard RL, Peterson RC, Hunter BK (1992) Temperature dependence of cation disorder in $MgAl_2O_4$ spinel using ^{27}Al and ^{17}O magic-angle spinning NMR. Am Mineral 77:44-52

Millard RL, Peterson RC, Hunter BK (1995) Study of the cubic to tetragonal transition in Mg_2TiO_4 and Zn_2TiO_4 spinels by ^{17}O MAS NMR and Rietveld refinement of X-ray diffraction data. Am Mineral 80:885-896

Morrow CP, Yazaydin AO, Krishnan M, Bowers GM, Kalinichev AG, Kirkpatrick RJ (2013) Structure, energetics, and dynamics of smectite clay interlayer hydration: molecular dynamics and metadynamics investigation of Na-hectorite. J Phys Chem C 117:5172-5187

Murdoch JB, Stebbins JF, Carmichael ISE (1985) High-resolution ^{29}Si NMR study of silicate and aluminosilicate glasses: the effect of network-modifying cations. Am Mineral 70:332-343

Murdoch JB, Stebbins JF, Carmichael ISE, Pines A (1988) A silicon-29 nuclear magnetic resonance study of silicon-aluminum ordering in leucite and analcite. Phys Chem Miner 15:370-382

Mysen BO, Richet P (2005) Silicate Glasses and Melts, Properties and Structure. Elsevier, Amsterdam

Nasikas NK, Edwards TG, Sen S, Papatheodorou GN (2012) Structural characteristics of novel Ca-Mg orthosilicate and suborthosilicate glasses: results from ^{29}Si and ^{17}O NMR spectroscopy. J Phys Chem B 116:2696-2702

Neuhoff PS, Kroeker S, Du L-S, Fridriksson T, Stebbins JF (2002) Order/disorder in natrolite group zeolites: A ^{29}Si and ^{27}Al MAS NMR study. Am Mineral 87:1307-1320

Neuhoff PS, Stebbins JF, Bird DK (2003) Si-Al disorder and solid solutions in analcime, chabazite, and wairikite. Am Mineral 88:410-423

Neuville DR, Cormier L, Massiot D (2006) Al coordination and speciation in calcium aluminosilicate glasses: effects of composition determined by ^{27}Al MQ-MAS NMR and Raman spectroscopy. Chem Geol 229:173-185

Nielsen UG, Paik Y, Julmis K, Schoonen MAA, Reeder RJ, Grey CP (2005) Investigating sorption on iron-oxyhydroxide soil minerals by solid-state NMR spectroscopy: A ^{6}Li MAS NMR study of adsorption and absorption on goethite. J Phys Chem B 109:18310-18315

O'Dell LA, Klimm K, Freitas JCC, Kohn SC, Smith ME (2008) ^{33}S MAS NMR of a disordered sulfur-doped silicate: signal enhancement via RAPT, QCPMG and adiabatic pulses. Appl Magn Reson 35:247-259

Palke AC, Stebbins JF (2011a) Paramagnetic interactions in the ^{31}P NMR spectroscopy of rare earth element orthophosphate ($REPO_4$, monazite/xenotime) solid solutions. Am Mineral 96:1343-1353

Palke AC, Stebbins JF (2011b) Variable temperature ^{27}Al and ^{29}Si NMR studies of synthetic forsterite and Fe-bearing Dora Maira pyrope garnet: temperature dependence and mechanisms of contact-shifted peaks. Am Mineral 96:1090-1099

Palke AC, Stebbins JF, Frost DJ, McCammon CA (2012) Incorporation of Fe and Al in $MgSiO_3$ perovskite: An investigation by ^{27}Al and ^{29}Si NMR spectroscopy. Am Mineral 97:1955-1964

Pedone A, Charpentier T, Menziani MC (2010) Multinuclear NMR of $CaSiO_3$ glass: simulation from first-principles. Phys Chem Chem Phys 12:6054-6066

Petch HE, Cranna NG, Volkoff GM (1953) Second order nuclear quadrupolar effects in single crystals, part II. Experimental results for spodumene. Can J Phys 31:837-858

Phillips BL, Kirkpatrick RJ (1994) Short-range Si-Al order in leucite and analcime: Determination of the configurational entropy from ^{27}Al and variable-temperature ^{29}Si NMR spectroscopy of leucite, its Cs- and Rb-exchanged derivatives, and analcime. Am Mineral 79:1025-1036

Phillips BL, Kirkpatrick RJ (1995) High-temperature ^{29}Si MAS NMR spectroscopy of anorthite ($CaAl_2Si_2O_8$) and its P1-I1 structural phase transition. Phys Chem Miner 22:268-276

Phillips BL, Kirkpatrick RJ, Hovis GL (1988) ^{27}Al, ^{29}Si, and ^{23}Na MAS NMR study of an Al,Si ordered alkali feldspar solid solution series. Phys Chem Miner 16:262-275

Phillips BL, Howell DA, Kirkpatrick RJ, Gasparik T (1992a) Investigation of cation order in $MgSiO_3$-rich garnet using ^{29}Si and ^{27}Al MAS NMR spectroscopy. Am Mineral 77:704-712

Phillips BL, Kirkpatrick RJ, Carpenter MA (1992b) Investigation of short-range Al,Si order in synthetic anorthite by ^{29}Si MAS NMR spectroscopy. Am Mineral 77:484-495

Phillips BL, Burnley PC, Worminghaus K, Navrotsky A (1997a) ^{29}Si and ^{1}H NMR spectroscopy of high-pressure hydrous magnesium silicates. Phys Chem Mineral 24:179-190

EBSCOhost - printed on 2/13/2023 5:26 AM via . All use subject to https://www.ebsco.com/terms-of-use

Phillips BL, Casey WH, Crawford SN (1997b) Solvent exchange in $AlF_x(H_2O)_{6-x}^{3-x}$(aq) complexes: ligand-directed labilization of water as an analog for ligand-induced dissolution of oxide minerals. Geochim Cosmochim Acta 61:3041-3049

Phillips BL, McGuin MD, Redfern SAT (1997c) Si-Al order and the I1-I2/c phase transition in synthetic $CaAl_2Si_2O_8$-$SrAl_2Si_2O_8$ feldspar: a ^{29}Si MAS-NMR spectroscopic study. Am Mineral 82:1-7

Phillips BL, Xu HW, Heaney PJ, Navrotsky A (2000) ^{29}Si and ^{27}Al MAS-NMR spectroscopy of beta-eucryptite ($LiAlSiO_4$): The enthalpy of Si,Al ordering. Am Mineral 85:181-188

Phillips BL, Mason HE, Guggenheim S (2007) Hydrogen bonded silanols in the 10 Å phase: Evidence from NMR spectroscopy. Am Mineral 92:1474-1485

Pickard CJ, Mauri FPRB (2001) All-electron magnetic response with pseudopotentials: NMR chemical shifts. Phys Rev B 63:245101

Pound RV (1950) Nuclear quadrupolar interactions in crystals. Phys Rev 79:685-702

Profeta M, Mauri F, Pickard CJ (2003) Accurate first principles prediction of ^{17}O NMR parameters in SiO_2: Assignment of the zeolite ferrierite spectrum. J Am Chem Soc 125:541-548

Profeta M, Benoit M, Mauri F, Pickard CJ (2004) First-principles calculation of the ^{17}O NMR parameters in Ca oxide and Ca aluminosilicates: the partially covalent nature of the Ca-O bond, a challenge for density functional theory. J Am Chem Soc 126:12628-12635

Putnis A (1988) Solid state NMR spectroscopy and phase transitions in minerals. *In*: Physical Properties and Thermodynamic Behaviour of Minerals. Salje E K H (ed) Reidel, Dordrecht, p 325-358

Putnis A (1992) Introduction to Mineral Sciences. Cambridge University Press, Cambridge

Putnis A, Angel RJ (1985) Al, Si ordering in cordierite using magic angle spinning NMR. 2. Models of Al, Si order from NMR data. Phys Chem Miner 12:217-222

Putnis A, Fyfe CA, Gobbi GC (1985) Al,Si ordering in cordierite using "magic angle spinning" NMR. Phys Chem Miner 12:211-216

Raudsepp M, Turnock AC, Hawthorne FC, Sherriff BL, Hartman JS (1987) Characterization of synthetic pargasitic amphiboles ($NaCa_2Mg_4M^{3+}Si_6Al_2O_{22}(OH,F)_2$; M^{3+} = Al, Cr, Ga, Sc, In) by infrared spectroscopy, Rietveld structure refinement and ^{27}Al, ^{29}Si and ^{19}F MAS NMR spectroscopy. Am Mineral 72:580-593

Richet P (1984) Viscosity and configurational entropy of silicate melts. Geochim Cosmochim Acta 48:471-483

Riemer T, Schmidt B, Behrens H, Dupree R (2000) H_2O/OH ratio determination in hydrous aluminosilicate glasses by static proton NMR and the effect of chemical shift anisotropy. Solid State Nucl Magn Reson 15:201-207

Sanders RL, Washton NM, Mueller KT (2010) Measurement of the reactive surface area of clay minerals using solid-state NMR studies of a probe molecule. J Phys Chem C 114:5491-5498

Sandland TO, Du L-S, Stebbins JF, Webster JD (2004) Structure of Cl-containing silicate and aluminosilicate glasses; a ^{35}Cl MAS-NMR study. Geochim Cosmochim Acta 68:5059-5069

Sanz J, Robert JL (1992) Influence of structural factors on ^{29}Si and ^{27}Al NMR chemical shifts of 2:1 phyllosilicates. Phys Chem Miner 19:39-45

Sanz J, Stone WEE (1979) NMR study of micas, II. Distribution of Fe^{2+}, F^- and OH^- in the octahedral sheet of phlogopites. Am Mineral 64:119-126

Sanz J, Herrero CP, Robert J-L (2003) Distribution of Si and Al in clintonites: a combined NMR and Monte-Carlo study. J Phys Chem B 107

Sanz J, Robert J-L, Diaz M, Sobrados I (2006) Influence of charge location on ^{29}Si NMR chemical shift of 2:1 phyllosilicates. Am Mineral 91:544-550

Schmidt BC, Riemer T, Kohn SC, Behrens H, Dupree R (2000) Different water solubility mechanisms in hydrous glasses along the Qz-Ab join: evidence from NMR spectroscopy. Geochim Cosmochim Acta 64:513-526

Schroeder PA (1993) A chemical, XRD, and ^{27}Al MAS NMR investigation of Miocene Gulf Coast shales with application to understanding illite/smectite crystal-chemistry. Clays Clay Miner 41:668-679

Sen S (2008) Differential mobility and spatially heterogeneous dynamics of oxygen atoms in a supercooled glass-forming network liquid. Phys Rev B 78:100201

Sen S, Stebbins JF (1994) Phase separation, clustering and intermediate range order in $Li_2Si_4O_9$ glass: a ^{29}Si MAS NMR spin-lattice relaxation study. Phys Rev 50:822-830

Sen S, Stebbins JF (1997) Na ion transport in borate and germanate glasses and liquids: a ^{23}Na and ^{11}B NMR spin-lattice relaxation study. Phys Rev B 55:3512-3519

Sen S, Tangeman J (2008) Evidence for anomalously large degree of polymerization in Mg_2SiO_4 glass and melt. Am Mineral 93:946-949

Sen S, Stebbins JF, Hemming NG, Ghosh B (1994) Coordination environments of B impurities in calcite and aragonite polymorphs: A ^{11}B MAS NMR study. Am Mineral 79:819-825

Sen S, Maekawa H, Papatheodorou GN (2009) Short-range structure of invert glasses along the pseudo-binary join $MgSiO_3$-Mg_2SiO_4: results from ^{29}Si and ^{25}Mg MAS NMR spectroscopy. J Phys Chem B 113:152434-115248

EBSCOhost - printed on 2/13/2023 5:26 AM via . All use subject to https://www.ebsco.com/terms-of-use

Sharps JA, Brown GE, Jr., Stebbins JF (1993) Kinetics and mechanism of ligand exchange of Au(III), Zn(II), and Cd(II) chlorides in aqueous solution: An NMR study from 28-98 °C. Geochim Cosmochim Acta 57:721-731

Sherriff BL, Hartman JS (1985) Solid-state high-resolution ^{29}Si NMR of feldspars: Al-Si disorder and the effects of paramagnetic centres. Can Mineral 23:205-212

Sherriff BL, Grundy HD, Hartman JS (1991) The relationship between ^{29}Si MAS NMR chemical shift and silicate mineral structure. Eur J Mineral 3:751-768

Sideris PJ, Nielsen UG, Gan ZH, Grey CP (2008) Mg/Al ordering in layered double hydroxides revealed by multinuclear NMR spectroscopy. Science 5885:113-117

Singer JW, Yazaydin AO, Kirkpatrick RJ, Bowers GM (2012) Structure and transformation of amorphous calcium carbonate: A solid-state ^{43}Ca NMR and computational molecular dynamics investigation. Chem Mater 24:1828-1836

Smith KA, Kirkpatrick RJ, Oldfield E, Henderson DM (1983) High-resolution silicon-29 nuclear magnetic resonance spectroscopic study of rock-forming silicates. Am Mineral 68:1206-1215

Spearing DR, Stebbins JF (1989) The ^{29}Si NMR shielding tensor in low quartz. Am Mineral 74:956-959

Spearing DR, Farnan I, Stebbins JF (1992) Dynamics of the α-β phase transitions in quartz and cristobalite as observed by *in situ* high temperature ^{29}Si and ^{17}O NMR. Phys Chem Miner 19:307-321

Spearing DR, Stebbins JF, Farnan I (1994) Diffusion and the dynamics of displacive phase transitions in cryolite (Na_3AlF_6) and chiolite ($Na_5Al_3F_{14}$): multi-nuclear NMR studies. Phys Chem Miner 21:373-386

Staehli JL, Brinkmann D (1974) A nuclear magnetic resonance study of the phase transition in anorthite, $CaAl_2Si_2O_8$. Zeit Kristallogr 140:360-373

Stebbins JF (1987) Identification of multiple structural species in silicate glasses by ^{29}Si NMR. Nature 330:465-467

Stebbins JF (1988) NMR spectroscopy and dynamic processes in mineralogy and geochemistry. Rev Mineral 18:405-430

Stebbins JF (1991a) Experimental confirmation of five-coordinated silicon in a silicate glass at 1 atmosphere pressure. Nature 351:638-639

Stebbins JF (1991b) Nuclear magnetic resonance at high temperature. Chem Rev 91:1353-1373

Stebbins JF (1995a) Dynamics and structure of silicate and oxide melts: nuclear magnetic resonance studies. *In*: Structure, Dynamics, and Properties of Silicate Melts. Stebbins JF, McMillan PF, Dingwell DB (eds) Mineralogical Society of America, Washington, D.C., p 191-246

Stebbins JF (1995b) Nuclear magnetic resonance spectroscopy of silicates and oxides in geochemistry and geophysics. *In*: Handbook of Physical Constants. Ahrens TJ (ed) American Geophysical Union, Washington D.C., p 303-332

Stebbins JF (1997) Magnesium site exchange in forsterite: a direct measurement by high temperature ^{25}Mg nuclear magnetic resonance spectroscopy. Am Mineral 81:1315-1320

Stebbins JF (2002) NMR studies of oxide glass structure. *In*: Solid State NMR: Theory and Applications. Duer M (ed) Blackwell Scientific, Oxford, p 391-436

Stebbins JF (2008) Temperature effects on the network structure of oxide melts and their consequences for configurational heat capacity. Chem Geol 256:80-91

Stebbins JF, Farnan I (1989) NMR spectroscopy in the earth sciences: structure and dynamics. Science 245:257-262

Stebbins JF, Farnan I (1992) The effects of temperature on silicate liquid structure: a multi-nuclear, high temperature NMR study. Science 255:586-589

Stebbins JF, Kanzaki M (1990) Local structure and chemical shifts for six-coordinated silicon in high pressure mantle phases. Science 251:294-298

Stebbins JF, McMillan P (1989) Five- and six- coordinated Si in $K_2Si_4O_9$ glass quenched from 1.9 GPa and 1200°C. Am Mineral 74:965-968

Stebbins JF, Poe BT (1999) Pentacoordinate silicon in high-pressure crystalline and glassy phases of calcium disilicate ($CaSi_2O_5$). Geophys Res Lett 26:2521-2523

Stebbins JF, Sen S (2013) Oxide ion speciation in potassium silicate glasses: new limits from ^{17}O NMR. J Non-Cryst Solids 368:17-22

Stebbins JF, Xu Z (1997) NMR evidence for excess non-bridging oxygens in an aluminosilicate glass. Nature 390:60-62

Stebbins JF, Murdoch JB, Schneider E, Carmichael ISE, Pines A (1985) A high temperature nuclear magnetic resonance study of ^{27}Al, ^{23}Na, and ^{29}Si in molten silicates. Nature 314:250-252

Stebbins JF, Farnan I, Williams EH, Roux J (1989) Magic angle spinning NMR observation of sodium site exchange in nepheline at 500°C. Phys Chem Minerals 16:763-766

Stebbins JF, Farnan I, Xue X (1992) The structure and dynamics of alkali silicate liquids: one view from NMR spectroscopy. Chem Geol 96:371-386

Stebbins JF, Zhao P, Lee SK, Cheng X (1999) Reactive Al–O–Al sites in a natural zeolite: triple-quantum oxygen-17 nuclear magnetic resonance. Am Mineral 84:1680-1684

EBSCOhost - printed on 2/13/2023 5:26 AM via . All use subject to https://www.ebsco.com/terms-of-use

Stebbins JF, Oglesby JV, Lee SK (2001) Oxygen sites in silicate glasses: a new view from oxygen-17 NMR. Chem Geol 174:63-75

Stebbins JF, Du L-S, Pratesi G (2005) Aluminum coordination in natural silica glasses from the Libyan Desert (Egypt): high field NMR results. Phys Chem Glasses 46:340-344

Stebbins JF, Du L-S, Kelsey K, Kojitani H, Akaogi M, Ono S (2006) Aluminum substitution in stishovite and $MgSiO_3$ perovskite: High-resolution ^{27}Al NMR. Am Mineral 91:337-343

Stebbins JF, Dubinsky EV, Kanehashi K, Kelsey KE (2008) Temperature effects on non-bridging oxygen and aluminum coordination number in calcium aluminosilicate glasses and melts. Geochim Cosmochim Acta 72:910-925

Stebbins JF, Kim N, Andrejcak MJ, Boymel PM, Zoitos BK (2009a) Characterization of phase separation and thermal history effects in magnesium silicate glass fibers by NMR spectroscopy. J Am Ceram Soc 92:68-74

Stebbins JF, Kim N, Brunet F, Irifune T (2009b) Confirmation of octahedrally-coordinated phosphorus in $AlPO_4$-containing stishovite by ^{31}P NMR. Eur J Mineral 21:667-671

Stebbins JF, Panero WR, Smyth JR, Frost DJ (2009c) Forsterite, wadsleyite, and ringwoodite (Mg_2SiO_4): ^{29}Si NMR constraints on structural disorder and effects of paramagnetic impurity ions. Am Mineral 94:626-629

Stebbins JF, Smyth JR, Panero WR, Frost DJ (2009d) Forsterite, hydrous and anhydrous wadsleyite and ringwoodite (Mg_2SiO_4): ^{29}Si NMR results for chemical shift anisotropy, spin-lattice relaxation, and mechanism of hydration. Am Mineral 94:905-915

Stebbins JF, Wu J, Thompson LM (2013) Interactions between network cation coordination and non-bridging oxygen abundance in oxide melts and glasses: insights from NMR spectroscopy. Chem Geol 346:34-46

Surface JA, Skemer P, Hayes SE, Conradi MS (2013) *In situ* measurements of magnesium carbonate formation from CO_2 using static high-pressure and -temperature ^{13}C NMR. Environ Sci Technol 47:119-125

Swaddle TW, Rosenqvist J, Yu P, Bylaska E, Phillips BL, Casey WL (2005) Kinetic evidence for five-coordination in $AlOH(aq)^{2+}$ ion. Science 308:1450-1453

Swift TJ, Connick RE (1962) NMR-relaxation mechanism of O^{17} in aqueous solutions of paramagnetic cations and the lifetime of water molecules in the first coordination sphere. J Chem Phys 37:307-320

Takahashi T, Kanehashi K, Saito K (2008) First evidence of multiple Al sites in Na-montmorillonite by ^{27}Al multiple quantum MAS NMR. Clays Clay Miner 56:520-525

Teertstra DK, Sherriff BL, Xu Z, Cerny P (1994) MAS and DOR NMR study of Al-Si order in the analcime-pollucite series. Can Mineral 32:69-80

Thompson LM, Stebbins JF (2011) Non-bridging oxygen and high-coordinated aluminum in metaluminous and peraluminous calcium and potassium aluminosilicate glasses: High-resolution ^{17}O and ^{27}Al MAS NMR results. Am Mineral 96:841-853

Thompson LM, McCarty RJ, Stebbins JF (2012) Estimating accuracy of ^{17}O NMR measurements in oxide glasses: Constraints and evidence from crystalline and glassy calcium and barium silicates. J Non-Cryst Solids 358:2999-3006

Timken HKC, Janes N, Turner GL, Lambert SL, Welsh LB, Oldfield E (1986) Solid-state oxygen-17 nuclear magnetic resonance spectroscopic studies of zeolites and related systems. 2. J Am Chem Soc 108:7236-7241

Toplis MJ, Kohn SC, Smith ME, Poplett IJF (2000) Five coordinate aluminum in tectosilicate glasses observed by triple quantum MAS NMR. Am Mineral 85:1556-1560

Tossell JA (2001) Calculating the NMR properties of minerals, glasses, and aqueous species. Rev Mineral Geochem 43:437-458

Tsomaia N, Brantley SL, Hamilton JP, Pantano CG, Mueller KT (2003) NMR evidence for formation of octahedral and tetrahedral Al and repolymerization of the Si network during dissolution of aluminosilicate glass and crystal. Am Mineral 88:54-67

Vinograd VL (1995) Substitution of $^{[4]}$Al in layer silicates: calculation of the Al-Si configurational entropy according to ^{29}Si NMR spectra. Phys Chem Mineral 22:87-98

Vinograd VL (1996) Computer simulations of the Al-Si disorder in synthetic cordierites: configurational entropy constrained by ^{29}Si NMR data. Phys Chem Minerals 23:391-401

Washton NM, Brantley SL, Mueller KT (2008) Probing the molecular-level control on aluminosilicate dissolution: A sensitive solid-state NMR proxy for reactive surface area. Geochim Cosmochim Acta 72:5949-5961

Wasylishen RE, Ashbrook SE, Wimperis S (eds) (2012) NMR of Quadrupolar Nuclei in Solid Materials. John Wiley & Sons Ltd., Chichester, UK

Weiss CA Jr, Kirkpatrick RJ, Altaner SP (1990a) The structural environments of cations adsorbed onto clays; ^{133}Cs variable-temperature MAS NMR spectroscopic study of hectorite. Geochim Cosmochim Acta 54:1655-1669

Weiss CA Jr, Kirkpatrick RJ, Altaner SP (1990b) Variations in interlayer cation sites of clay minerals as studied by ^{133}Cs MAS nuclear magnetic resonance spectroscopy. Am Mineral 75:970-982

Welch MD, Rocha J, Klinowski J (1992) Characterization of polysomatism in biopyriboles: double-/triple-chain lamellar intergrowths. Phys Chem Mineral 18:460-468

EBSCOhost - printed on 2/13/2023 5:26 AM via . All use subject to https://www.ebsco.com/terms-of-use

Welch MD, Kolodziejski W, Klinowski J (1994) A multinuclear NMR study of synthetic pargasite. Am Mineral 79:261-268

Welch MD, Liu S, Klinowski J (1998) ^{29}Si MAS NMR systematics of calcic and sodic-calcic amphiboles. Am Mineral 83:85-96

Wiench JW, Pruski M (2004) Probing through bond connectivities with MQMAS NMR. Solid State Nucl Magn Reson 26:51-55

Woessner DE (1989) Characterization of clay minerals by ^{27}Al nuclear magnetic resonance spectroscopy. Am Mineral 74:203-215

Wood BJ, Kirkpatrick RJ, Montez B (1986) Order-disorder phenomena in $MgAl_2O_4$ spinel. Am Mineral 71:999-1006

Xiao YH, Kirkpatrick RJ, Hay RL, Kim YJ, Phillips BL (1995) Investigation of Al,Si order in K-feldspars using ^{27}Al and ^{29}Si MAS NMR. Mineral Mag 59:46-61

Xu Z, Maekawa H, Oglesby JV, Stebbins JF (1998) Oxygen speciation in hydrous silicate glasses - An oxygen-17 NMR study. J Am Chem Soc 120:9894-9901

Xu Z, Stebbins JF (1995) ^{6}Li nuclear magnetic resonance chemical shifts, coordination number and relaxation in crystalline and glassy silicates. Solid State Nucl Magn Reson 5:103-112

Xu Z, Stebbins JF (1998) Oxygen site exchange kinetics observed with solid state NMR in a natural zeolite. Geochim Cosmochim Acta 62:1803-1809

Xue X (2009) Water speciation in hydrous silicate and aluminosilicate glasses: Direct evidence from ^{29}Si-^{1}H and ^{27}Al-^{1}H double-resonance NMR. Am Mineral 94:395-398

Xue X, Kanzaki M (1998) Correlations between ^{29}Si, ^{17}O and ^{1}H NMR properties and local structures in silicates: an ab initio calculation. Phys Chem Mineral 26:14-30

Xue X, Kanzaki M (2001) An *ab initio* calculation of the ^{17}O and ^{1}H NMR parameters for various OH groups: Implications to the speciation and dynamics of dissolved water in silicate glasses. J Phys Chem B 105: 3422–3434

Xue X, Kanzaki M (2004) Dissolution mechanisms of water in depolymerized silicate melts: constraints from ^{1}H and ^{29}Si NMR spectroscopy and *ab initio* calculations. Geochim Cosmochim Acta 68:5027-5057

Xue X, Kanzaki M (2006) Depolymerization effect of water in aluminosilicate glasses: direct evidence from ^{1}H-^{27}Al heteronuclear correlation NMR. Am Mineral 91:1922-1926

Xue X, Kanzaki M (2007a) Al coordination and water speciation in hydrous aluminosilicate glasses: Direct evidence from high-resolution ^{1}H-^{27}Al correlation NMR. Solid State Nucl Magn Reson 31:10-27

Xue X, Kanzaki M (2007b) High-pressure δ-$Al(OH)_3$ and δ-AlOOH phases and isostructural hydroxides/oxyhydroxides: new structural insights from high-resolution ^{1}H and ^{27}Al NMR. J Phys Chem B 111:13156-13166

Xue X, Kanzaki M (2008) Structure of hydrous alumniosilicate glasses along the diopside-anorthite join: A comprehensive one- and two-dimensional ^{1}H and ^{27}Al NMR study. Geochim Cosmochim Acta 72:2331-2348

Xue X, Kanzaki M (2009) Proton distributions and hydrogen bonding in crystalline and glassy hydrous silicates and related inorganic materials: insights from high-resolution solid-state NMR spectroscopy. J Am Ceram Soc 92:2803-2830

Xue X, Kanzaki M (2012) Distinct ^{29}Si MAS NMR peaks from Si-Al permutation on neighboring T sites of unequal Si-O-T angles: Direct evidence from J-resolved experiment on K-Cymrite ($KAlSi_3O_8.H_2O$). J Phys Chem C 116:10714-10722

Xue X, Stebbins JF, Kanzaki M, McMillan PF, Poe B (1991) Pressure-induced silicon coordination and tetrahedral structural changes in alkali silicate melts up to 12 GPa: NMR, Raman, and infrared spectroscopy. Am Mineral 76:8-26

Xue X, Kanzaki M, Fukui H, Ito E, Hashimoto T (2006) Cation order and hydrogen bonding of high-pressure phases in the Al_2O_3-SiO_2-H_2O system: An NMR and Raman study. Am Mineral 91:850-861

Xue X, Kanzaki M, Shatskiy A (2008) Dense hydrous magnesium silicates, phase D, and superhydrous B: New structural constraints from one- and two-dimensional ^{29}Si and ^{1}H NMR. Am Mineral 93:1099-1111

Xue X, Zhai S, Kanzaki M (2009) Si-Al distribution in high-pressure $CaAl_4Si_2O_{11}$ phase: a ^{29}Si and ^{27}Al NMR study. Am Mineral 94:1739-1742

Xue X, Kanzaki M, Fukui H (2010) Unique crystal chemistry of two polymorphs of topaz-OH: A multi-nuclear NMR and Raman study. Am Mineral 95:1276-1293

Yang W-H, Kirkpatrick RJ (1989) Hydrothermal reaction of albite and a sodium aluminosilicate glass: A solid-state NMR study. Geochim Cosmochim Acta 53:805-819

Yang W-H, Kirkpatrick RJ (1990) Hydrothermal reaction of a rhyolitic-composition glass: a solid-state NMR study. Am Mineral 75:1009-1019

Yarger JL, Smith KH, Nieman RA, Diefenbacher J, Wolf GH, Poe BT, McMillan PF (1995) Al coordination changes in high-pressure aluminosilicate liquids. Science 270:1964-1967

Yates JR (2010) Prediction of NMR J-coupling in solids with the planewave pseudopotential approach. Magn Reson Chem 48:S23-S31

EBSCOhost - printed on 2/13/2023 5:26 AM via . All use subject to https://www.ebsco.com/terms-of-use

Yesinowski JP, Eckert H (1987) Hydrogen environments in calcium phosphate-^{1}H MAS NMR at high spinning speeds. J Am Chem Soc 109:6274-6282

Yesinowski JP, Eckert H, Rossman GR (1988) Characterization of hydrous species in minerals by high-speed ^{1}H MAS NMR. J Am Chem Soc 110:1367-1375

Zeng Q, Stebbins JF (2000) Fluoride sites in aluminosilicate glasses: high-resolution ^{19}F NMR results. Am Mineral 85:863-867

Zeng Q, Nekvasil H, Grey CP (1999) Proton environments in hydrous aluminosilcate glasses: a ^{1}H MAS, ^{1}H/^{27}Al, and ^{1}H/^{23}Na TRAPDOOR NMR study. J Phys Chem B 103:7406-7415

Zhang P, Dunlap C, Florian P, Grandinetti PJ, Farnan I, Stebbins JF (1996) Silicon site distribution in an alkali silicate glass derived by two-dimensional ^{29}Si nuclear magnetic resonance. J Non-Cryst Solids 204:294-300

EBSCOhost - printed on 2/13/2023 5:26 AM via . All use subject to https://www.ebsco.com/terms-of-use

EBSCOhost - printed on 2/13/2023 5:26 AM via . All use subject to https://www.ebsco.com/terms-of-use

Reviews in Mineralogy & Geochemistry
Vol. 78 pp. 655-690, 2014
Copyright © Mineralogical Society of America

Electron Paramagnetic Resonance Spectroscopy: Basic Principles, Experimental Techniques and Applications to Earth and Planetary Sciences

Yuanming Pan

Department of Geological Sciences
University of Saskatchewan
Saskatoon, SK S7N 5E2, Canada

yuanming.pan@usask.ca

Mark J. Nilges

Illinois EPR Research Center
University of Illinois at Urbana-Champaign
Urbana, Illinois 61801, U.S.A.

mjnilges@illinois.edu

INTRODUCTION

Electron paramagnetic resonance (EPR) spectroscopy, also known as electron spin resonance (ESR) spectroscopy, is a group of techniques used to study paramagnetic species that contain one or more unpaired electrons. The basic principles of EPR are analogous to those of nuclear magnetic resonance (NMR) spectroscopy, because they both deal with interactions between electromagnetic radiation and magnetic moments. However, the former is based on the excitation of electron spins, whereas nuclear spins are excited in the latter. EPR as a structural probe provides a wealth of information about the local structures and dynamic processes of the paramagnetic species studied, and is known for its unique sensitivity (~10^{12} spins/cm^3 or parts per billion; Pan et al. 2002a; Weil and Bolton 2007), unmatched by any other structural techniques. In addition, quantitative EPR, provided that sufficient calibration and standardization are carried out, is possible and is useful for chemical analysis, dosimetry and geochronology, with applications to not only rocks and minerals but also other Earth and planetary materials such as coals, crude oils and meteorites (Ikeya 1993; Dyrek et al. 1996, 2003; Eaton et al. 2009).

The basic principles of EPR spectroscopy can be found in various textbooks and monographs (Abragam and Bleaney 1970; Poole and Farah 1999; Schweiger and Jeschke 2001; Weil and Bolton 2007; Brustolon and Giamello 2009; Eaton et al. 2009; Misra 2011). Excellent reviews with emphasis on applications of EPR spectroscopy to minerals can be found in Marfunin (1979), Calas (1988), Vassilikou-Dova (1993), and Goodman and Hall (1994). However, most previous reviews on applications to minerals focused almost exclusively on conventional continuous-wave (CW) techniques, whereas more advanced techniques such as pulse electron nuclear double resonance (ENDOR) and electron spin echo envelope modulation (ESEEM) spectroscopy were generally not included. Therefore, the present chapter starts with a brief outline of the basic principles based upon the treatise of Weil and Bolton (2007) and is followed by two main sections on practical guides to CW and pulse EPR experiments and their applications to Earth and planetary sciences.

1529-6466/14/0078-0016$05.00 http://dx.doi.org/10.2138/rmg.2014.78.16

EBSCOhost - printed on 2/13/2023 5:26 AM via . All use subject to https://www.ebsco.com/terms-of-use

BASIC PRINCIPLES AND SPIN HAMILTONIAN

Electron resonance condition and EPR spectra

Electrons are charged particles that possess intrinsic, quantized angular momentum (i.e., spin) and behave like tiny bar magnets. However, the electron spin magnetism cancels if electrons are all paired. The phenomenon of EPR arises only when unpaired electrons are present, and those atoms, ions, molecules and radicals possessing at least one unpaired electron are commonly referred to as "paramagnetic centers."

In the simplest case, the spin magnetic moment of a single free electron (spin quantum number S = 1/2) in the presence of an external magnetic field **B** can assume only two (2S + 1 = 2) orientations (i.e., $M_S = +1/2$ and $-1/2$). The energies of these two directions are proportional to the strength of the external magnetic field B by

$$E = g_e \beta_e B M_S \tag{1}$$

Where g_e (= 2.0023193) is the *g* factor of a free electron and β_e is the electronic Bohr magneton. Therefore, electrons in the lower energy state, $M_S = -1/2$, can be excited to the upper level ($M_S = +1/2$), by electromagnetic radiation of appropriate frequency to satisfy the resonance condition (Fig. 1):

$$\Delta E = \frac{1}{2} g_e \beta_e B - \left(-\frac{1}{2} g_e \beta_e B \right) = g_e \beta_e B = h\nu \tag{2}$$

where *h* is Planck's constant and ν is the frequency of the applied radiation.

When this condition of resonance is met, absorption occurs and is measured in EPR experiments. Obviously, the EPR spectrum of a free electron consists of a single absorption line, which is usually shown in the first-derivative of the energy absorbed in the magnetic field B (Fig. 1). Fortunately, the spectrum of most paramagnetic centers in solids such as minerals and other Earth and planetary materials is usually more complicated and informative for a number of reasons: 1) effects of the local electric field, 2) interactions with nuclear magnetic moments, 3) interactions between electron magnetic moments (i.e., species with more than one unpaired electrons), and 4) presence of multiple paramagnetic centers in the sample investigated.

The absorption intensity of EPR spectra is proportional to the population difference of spins between the ground and excited spin states (Fig. 1). At thermal equilibrium there is

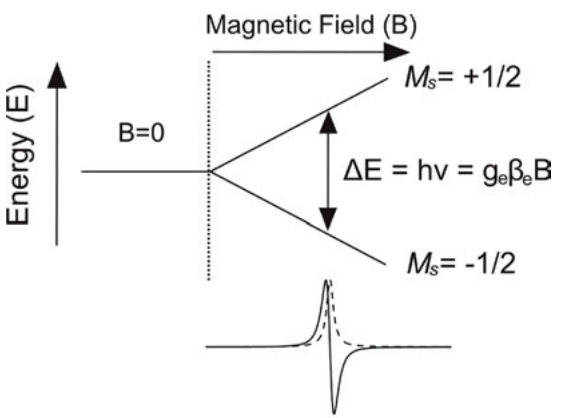


Figure 1. The energy levels of free electron S = 1/2 in a magnetic field **B**. Also shown are the resulting EPR spectrum in both the absorption (dashed line) and first-derivative (solid line) form.

EBSCOhost - printed on 2/13/2023 5:26 AM via . All use subject to https://www.ebsco.com/terms-of-use

a slight excess of spins in the ground state over the excited state, and the population ratio between the two states follows Boltzmann's distribution law:

$$\frac{n_e}{n_g} = \exp\left(-\frac{\Delta E}{k_B T}\right) = \exp\left(-\frac{h\nu}{k_B T}\right) \tag{3}$$

where n_e and n_g are the number of spins at the excited and ground states, respectively, and k_B is the Boltzmann constant. Equation (3) predicts that decreasing temperature and increasing the applied field would both increase the population difference of spins between the two states and, hence, are commonly used in EPR experiments to enhance sensitivity.

The lineshape and linewidth of EPR spectra are affected by a large number of mechanisms, including relaxation processes (i.e., spin-lattice relaxation time t_1 and spin-spin relaxation time t_2). Spin-lattice relaxation determined by the dissipation of energy via the thermal vibration of the lattice is temperature-dependent and is reduced at low temperatures. Spin-spin relaxation related to dipolar and exchange interactions of neighboring spins is temperature-independent and is lowered by measuring dilute samples. Quantitative analysis of the lineshape and linewidth of EPR spectra is an integral part of EPR studies and can provide valuable information about not only the structures of paramagnetic centers but also their dynamic behaviors (e.g., Abragam and Bleaney 1970).

Spin Hamiltonian

An experimental EPR spectrum measures the energy absorbed by the unpaired spins in a sample under an applied magnetic field and can be described by an appropriate spin Hamiltonian with spin operators (Abragam and Bleaney 1970; Weil and Bolton 2007; McGavin and Tennent 2009). Because of complex interactions of the unpaired spins with the external magnetic field, the crystal field, nuclear dipoles and electric quadrupole moments of the central ion and neighboring nuclei, the general spin Hamiltonian required to describe an experimental EPR spectrum contains a large number of terms (McGavin and Tennant 2009). These terms, including the Zeeman interaction of the unpaired electrons with the external magnetic field, zero-level splitting due to spin-spin and indirect effects of the crystal field (i.e., giving rise to fine structures), hyperfine (and superhyperfine) structures due to the presence of nuclear magnetic dipoles and electric quadrupole moments belonging to the central ion or surrounding ions, and the Zeeman interaction of the nuclear moment with the external magnetic field, are briefly discussed below. Additional high-spin terms may also be required, when the paramagnetic centers contain multiple unpaired electrons or involve interactions among multiple magnetic nuclei with nuclear spin numbers I > 1/2 (McGavin and Tennant 2009).

Electronic Zeeman interaction and the g matrix. In crystals the g factor deviates from g_e and takes on values depending upon the crystal orientation relative to the magnetic field. This g anisotropy is due to the spin orbit interaction and reflects the local crystal field. The deviations of g (Δg) are produced by a mixing of the electronic ground and excited states, and the magnitude of Δg is inversely proportional to the energy separation between those states.

The electronic Zeeman interaction between the magnetic moments associated with the unpaired electron **S** and the magnetic field **B** is given by

$$\mathcal{H} = \beta_e \mathbf{B}^{\mathbf{T}} \cdot \mathbf{g} \cdot \mathbf{S} \tag{4}$$

Where the superscript T indicates transpose; and **g** is a symmetric 3×3 matrix and contains six parameters, with three diagonal values (g_{xx}, g_{yy} and g_{zz}) on the axes of the experimental coordinate system. Often, the g matrix is transformed to a diagonal form by selection of an appropriate coordination system (McGavin 1987), and only three g factor values (g_x, g_y and g_z or g_1, g_2 and g_3) along the three principal axes are reported. Of course, paramagnetic centers of isotropic and uniaxial local symmetries require only one ($g_x = g_y = g_z$) and two ($g_x = g_y = g_\perp$ and $g_z = g_{//}$) prin-

EBSCOhost - printed on 2/13/2023 5:26 AM via . All use subject to https://www.ebsco.com/terms-of-use

cipal g factor values, respectively. Readers are cautioned that the order of the principal g factor values differs among EPR researchers in the literature, because a unified system has not been recommended by the International Union of Pure and Applied Chemistry (IUPAC).

Nuclear hyperfine and superhyperfine structures. Many nuclei have a nonzero nuclear spin (I) and, therefore, are magnetic as well (Table 1). The nuclear Zeeman levels are analogous to the electron-spin energy levels and are given by:

$$E = -g_n \beta_n B M_I \tag{5}$$

where g_n is the nuclear g factor, β_n is the nuclear magneton, and M_I is the nuclear spin operator. Note that the nuclear magnetic moment is much weaker than the electronic counterpart, because β_n is 1836 times smaller than β_e. Similar to the electron spin, the nuclear spin states in the presence of an external magnetic field are quantized and are labeled on the basis of the (2I + 1) values: I, (I – 1), (I – 2)…, –I.

Therefore, for a paramagnetic center containing one or more magnetic nuclei the unpaired electron will experience not only interaction with the external magnetic field, but also that from the magnetic nuclei. The latter interaction is usually weak but produces a further splitting of the spin energy levels, giving rise to (2I + 1) components of the EPR spectrum (i.e., the hyperfine structure; Fig. 2). In addition, a paramagnetic center may interact with one or more neighboring atoms with nonzero nuclear spins, and this interaction gives rise to the so-called superhyperfine structure.

For example, a nucleus with the spin number I = 1/2 is aligned both along and opposite to the direction of the external magnetic field (M_I = +1/2 and −1/2). Interaction of an unpaired electron with such a nucleus results in an EPR spectrum having two lines of equal intensity (Fig. 2) and a separation between them related to the isotropic hyperfine constant. By extension, the EPR spectrum for a nucleus with spin I consists of (2I + 1) lines of equal distance and equal intensity. However, this extension is not strictly true when the hyperfine interaction relative to the electronic Zeeman energy is large or the nuclear quadrupole effect is considerable (see below).

When the unpaired electron interacts with more than one magnetic nucleus, the resulting EPR spectrum reflects interactions with all magnetic nuclei present. A special situation of this

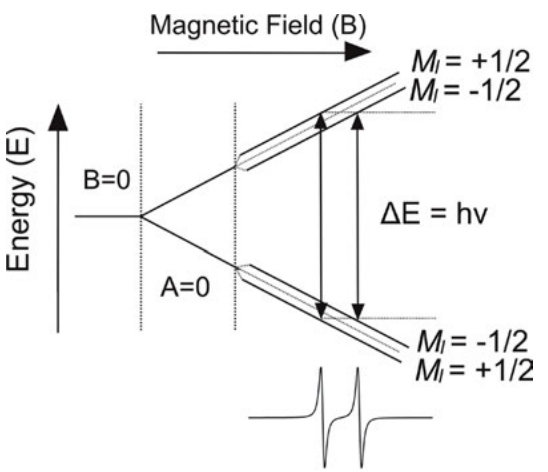


Figure 2. The energy levels of a spin system with S = I = 1/2 at a hyperfine coupling constant $A = 0$ and A. Also shown is the EPR spectrum arising from the allowed transitions ($\Delta M_s = 1$ and $\Delta M_I = 0$).

EBSCOhost - printed on 2/13/2023 5:26 AM via . All use subject to https://www.ebsco.com/terms-of-use

Table 1. Magnetic properties of selected nuclei.

Isotope	Spin (I)	Abundance (%)	g_n	a_0 (mT)	b_0 (mT)
^{1}H	1/2	99.9850	5.5856948	50.6850	
^{6}Li	1	7.5	0.8220575	5.43	
^{7}Li	3/2	92.5	2.170977	14.34	
^{10}B	3	19.8	0.600220	30.43	0.760
^{11}B	3/2	80.2	1.792437	90.88	2.271
^{13}C	1/2	1.11	1.40483	134.77	3.832
^{14}N	1	99.63	0.4037637	64.62	1.981
^{17}O	5/2	0.038	−0.757522	−187.80	−6.009
^{19}F	1/2	100	5.257771	1886.53	62.80
^{23}Na	3/2	100	1.478402	31.61	
^{25}Mg	5/2	10.00	−0.34218	17.338	
^{27}Al	5/2	100	1.456612	139.55	2.965
^{29}Si	1/2	4.67	−1.1106	−163.93	−4.075
^{31}P	1/2	100	2.26322	474.79	13.088
^{33}S	3/2	0.75	0.42911	123.57	3.587
^{35}Cl	3/2	75.77	0.5479198	204.21	6.266
^{37}Cl	3/2	24.23	0.4560854	169.98	5.216
^{39}K	3/2	93.26	0.2609928	8.238	
^{45}Sc	7/2	100	1.35962	100.73	3.430
^{47}Ti	5/2	7.4	−0.31539	−27.904	−1.051
^{49}Ti	7/2	5.4	−0.315468	−27.910	−1.051
^{51}V	7/2	99.750	0.556597	56.335	2.368
^{53}Cr	3/2	9.50	−0.3147	−26.698	−1.470
^{55}Mn	5/2	100	1.3819	179.70	−8.879
^{57}Fe	1/2	2.15	0.1806	26.662	1.395
^{59}Co	7/2	100	1.318	212.20	12.065
^{63}Cu	3/2	69.2	1.484	213.92	17.085
^{65}Cu	3/2	30.8	1.588	228.92	18.283
^{69}Ga	3/2	60.1	1.34440	435.68	7.274
^{71}Ga	3/2	39.9	1.70819	553.58	9.242
^{73}Ge	9/2	7.8	−0.1954371	−84.32	−1.716
^{75}As	3/2	100	0.959654	523.11	11.905
^{77}Se	1/2	7.6	1.0693	717.93	17.542
^{89}Y	1/2	100	0.2748381	−44.60	−0.888
^{93}Nb	9/2	100	1.3712	235.15	6.527
^{111}Cd	1/2	12.8	−1.19044	−487.07	−18.41
^{127}I	5/2	100	1.12531	1484.40	28.989
^{155}Gd	3/2	14.8	−0.1723	−69.48	−0.940
^{157}Gd	3/2	15.7	−0.2253	−90.85	−1.229
^{183}W	1/2	22.1	0.2355711	206.14	2.605
^{207}Pb	1/2	22.1	1.1748	2908.49	23.208

Modified from Weil and Bolton (2007): a_0 and b_0 are isotropic and uniaxial hyperfine constants, respectively.

EBSCOhost - printed on 2/13/2023 5:26 AM via . All use subject to https://www.ebsco.com/terms-of-use

type is that all the nuclei are magnetically equivalent and a symmetrical multiplet with the intensity ratio according to the binomial law is obtained. For example, an unpaired electron interacts with two magnetically equivalent ^{1}H (I = 1/2) nuclei, yielding a triplet with the intensity ratio of 1:2:1.

Another special situation is the presence of a single element having several isotopes with nonzero nuclear spins (e.g., ^{10}B, I = 3 and isotope abundance = 19.8%; and ^{11}B, I = 3/2 and 80.2%). The resulting EPR spectrum is the superposition of individual hyperfine structures from all isotopes, with distances approximately proportional to their nuclear g_n factors and intensities according to their relative isotope abundances (Fig. 3). Hyperfine structures of this type provide unambiguous identification of the paramagnetic centers (and of the neighboring atoms in the case of superhyperfine structures).

The hyperfine and nuclear Zeeman interactions between the unpaired electron and a magnetic nucleus, as an addition to the electronic Zeeman term (Eqn. 4), are given by:

$$\mathcal{H} = \left(\beta_e \mathbf{B}^{\mathbf{T}} \cdot \mathbf{g} \cdot \mathbf{S}\right) + \left(\mathbf{I}^{\mathbf{T}} \cdot \mathbf{A} \cdot \mathbf{S}\right) - \left(\beta_n \mathbf{B}^{\mathbf{T}} \cdot \mathbf{g}_{\mathbf{n}} \cdot \mathbf{I}\right) \tag{6}$$

when more than one magnetic nucleus interacts with the unpaired spin, the summation over all magnetic nuclei (1 to *i*) yields:

$$\mathcal{H} = \left(\beta_e \mathbf{B}^{\mathbf{T}} \cdot \mathbf{g} \cdot \mathbf{S}\right) + \sum_{i=1}^{i} \left[\left(\mathbf{I}_i^{\mathbf{T}} \cdot \mathbf{A}_i \cdot \mathbf{S}\right) - \left(\beta_n \mathbf{B}^{\mathbf{T}} \cdot \mathbf{g}_{\mathbf{n}i} \cdot \mathbf{I}_i\right)\right] \tag{6a}$$

There are two main mechanisms by which electrons and magnetic nuclei interact: 1) Fermi contact interaction and 2) dipolar interaction. The former applies largely to the case of isotropic interactions (i.e., independent of the crystal orientation in a magnetic field), whereas the latter represents anisotropic interactions (i.e., spectra dependent on the sample orientation in a magnetic field).

When a nucleus has a spin number I > 1/2, an electric field gradient on that nucleus can orient its charge ellipsoid and hence its spin direction. Such a gradient is caused by the distribution of the unpaired electrons in the *p*, *d* or *f* orbitals. The energy of such nuclear alignment, called the nuclear quadrupole energy, for a nucleus with I > 1/2 adds to those from its hyperfine and nuclear Zeeman terms:

$$\mathcal{H} = \left(\beta_e \mathbf{B}^{\mathbf{T}} \cdot \mathbf{g} \cdot \mathbf{S}\right) + \left(\mathbf{I}^{\mathbf{T}} \cdot \mathbf{A} \cdot \mathbf{S}\right) - \left(\beta_n \mathbf{B}^{\mathbf{T}} \cdot \mathbf{g}_{\mathbf{n}} \cdot \mathbf{I}\right) + \left(\mathbf{I}^{\mathbf{T}} \cdot \mathbf{P} \cdot \mathbf{I}\right) \tag{6b}$$

For multiple nuclei with I > 1/2, we have:

$$\mathcal{H} = \left(\beta_e \mathbf{B}^{\mathbf{T}} \cdot \mathbf{g} \cdot \mathbf{S}\right) + \sum_{i=1}^{i} \left[\left(\mathbf{I}_i{}^{\mathbf{T}} \cdot \mathbf{A}_{\mathbf{i}} \cdot \mathbf{S}\right) - \left(\beta_n \mathbf{B}^{\mathbf{T}} \cdot \mathbf{g}_{\mathbf{ni}} \cdot \mathbf{I}_{\mathbf{i}}\right) + \left(\mathbf{I}^{\mathbf{T}} \cdot \mathbf{P}_i \cdot \mathbf{I}_{\mathbf{i}}\right)\right] \tag{6c}$$

Here **P** is the nuclear quadrupole tensor and is traceless (i.e., $P_{xx} + P_{yy} = -P_{zz}$). The nuclear quadrupole effect on the hyperfine structure of some nuclei (e.g., ^{75}As) can be considerable, resulting in the presence of "forbidden" nuclear transitions (Fig. 4).

Fine structures (S > 1/2). Many paramagnetic centers contain more than one unpaired electron. For example, transition metal ions Cr^{3+} and Fe^{3+} in their high spin states have 3 and 5 unpaired electrons, respectively. These electrons interact through spin-orbit and spin-dipolar magnetic coupling, resulting in the so-called fine structure. These interactions introduce a new term $\mathbf{S^T \bullet D \bullet S}$ (where **D** is the electronic quadrupole matrix and is traceless) to the spin Hamiltonian:

$$\mathcal{H} = \left(\beta_e \mathbf{B}^{\mathbf{T}} \cdot \mathbf{g} \cdot \mathbf{S}\right) + \left(\mathbf{S}^{\mathbf{T}} \cdot \mathbf{D} \cdot \mathbf{S}\right) \tag{7}$$

EBSCOhost - printed on 2/13/2023 5:26 AM via . All use subject to https://www.ebsco.com/terms-of-use

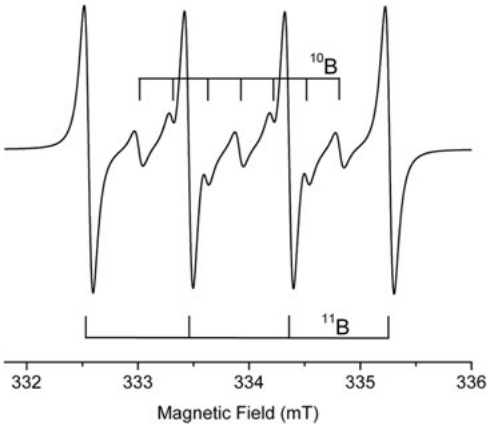


Figure 3. Simulated spectrum of the $[BO_4]^0$ center in zircon at **B**||*c* (data from Walsby et al. 2000), showing the ^{10}B and ^{11}B hyperfine structures at their natural abundances of 19.8% and 80.2%, respectively. Spectral simulation used a microwave frequency ν = 9.4 GHz, Lorentzian line shape, and linewidth = 0.08 mT.

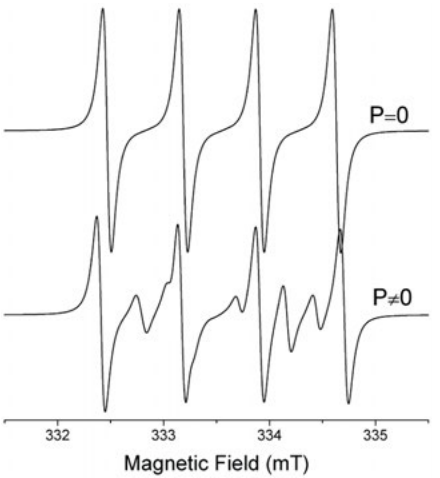


Figure 4. Simulated spectra of the $[AsO_4]^{2-}$ center in hemimorphite at **B**||*c* showing the presence of weak "forbidden" transition arising from the nuclear quadrupole effect (data from Mao et al. 2010a).

where D is commonly referred to as the zero-field splitting (ZFS) parameter, which is named for the splitting of spin energy levels in the absence of an applied magnetic field. Figure 5 shows the energy levels of the high-spin Fe^{3+} ion containing 5 unpaired electrons in an octahedral environment with and without an applied magnetic field.

Other species such as biradicals and triplet-state centers also contain two or more unpaired electrons and, therefore, involve electron-electron interactions (Weil and Bolton 2007; Mashkovtshev et al. 2007; Mao et al. 2010c; Mashkovtsev and Pan 2011, 2012b).

The general spin Hamiltonian is the summation of all energy terms discussed above. For example, the spin Hamiltonian for the high-spin $^{55}Mn^{2+}$ center (S = I = 5/2) is of the form (Pan et al. 2002a):

$$\mathcal{H} = \left(\beta_e \mathbf{B}^{\mathbf{T}} \cdot \mathbf{g} \cdot \mathbf{S}\right) + \left(\mathbf{S}^{\mathbf{T}} \cdot \mathbf{D} \cdot \mathbf{S}\right) + \left(\mathbf{I}^{\mathbf{T}} \cdot \mathbf{A} \cdot \mathbf{S}\right) + \left(\mathbf{I}^{\mathbf{T}} \cdot \mathbf{P} \cdot \mathbf{I}\right) - \left(\beta_n \mathbf{B}^{\mathbf{T}} \cdot \mathbf{g_n} \cdot \mathbf{I}\right) \quad (8)$$
$$+ \text{ high-spin terms } (S^4,\ BS^3,\ BS^5)$$

It is important to note, however, that some of the energy terms may not be required for specific paramagnetic centers, and selection of an appropriate spin Hamiltonian is central to successful analysis of EPR spectra.

EBSCOhost - printed on 2/13/2023 5:26 AM via . All use subject to https://www.ebsco.com/terms-of-use

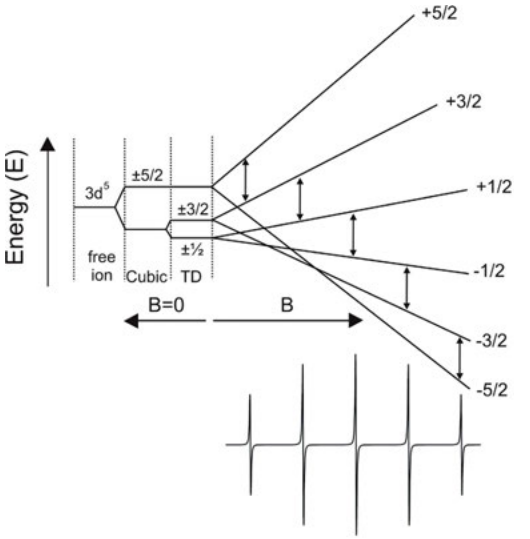


Figure 5. Energy levels of high-spin Fe^{3+} ($3d^5$) as a free ion, in a cubic environment and a cubic environment with a small tetragonal distortion with and without an applied magnetic field B. Also shown is an EPR spectrum of high-spin Fe^{3+} in a cubic site with a small tetragonal distortion with B parallel to the tetrad axis.

GUIDES TO EPR EXPERIMENTS AND SPECTRAL ANALYSES

An EPR study typically involves 1) selection and preparation, where necessary, of appropriate samples, 2) measurement of EPR spectra, and 3) analysis of the spectral features (i.e., intensity, lineshape, linewidth, line position, etc.) and simulation of spectra to extract spin Hamiltonian parameters, identify paramagnetic species, and determine dynamic properties.

Samples and techniques for generating paramagnetic species

The quality of the sample selected for EPR measurements directly affects the quality of the resulting spectra. Of course, all samples selected for EPR studies must contain paramagnetic species, preferably at dilute concentrations in diamagnetic hosts, because spin-spin interactions at elevated concentrations result in line broadening and thus poor spectral resolution. Nevertheless, EPR studies of concentrated samples are possible and are commonly made. It should be noted that for some fully concentrated systems, the exchange interaction can cause significant narrowing of the signal but also the loss of spectral information such as hyperfine structures (e.g., 2,2-diphenyl-1-picrylhydrazyl or DPPH; and chalcanthite $CuSO_4{\cdot}5H_2O$, SivaRamaiah et al. 2011).

Paramagnetic samples used for EPR studies can vary widely in form from fluids to frozen fluids, powdered solids, and single crystals. For Earth and planetary materials, powder EPR experiments are by far the most common and are usually made by use of pulverized samples contained in tubes with minimal or no background paramagnetic signals. For powder EPR measurements of crystalline solids it is important to grind the sample sufficiently to avoid any preferred orientation of the crystallites, which can be evaluated by re-measuring a spectrum after rotating the sample tube. On the other hand, powder EPR measurements using the oriented film technique (Clozel et al. 1995) are often used for clay minerals and have provided information about the orientations of paramagnetic centers in crystal lattices, which is not available from conventional powder EPR spectra.

EBSCOhost - printed on 2/13/2023 5:26 AM via . All use subject to https://www.ebsco.com/terms-of-use

Single-crystal EPR measurements are far more desirable than their powder counterparts, because the former allow quantitative determination of the orientations of various spin Hamiltonian parameters in selected coordinate systems. The orientations of these spin Hamiltonian parameters can be compared with specific symmetry or bond directions in the host crystal lattice and thereby provide information about the site occupancies and the local structural environments of the paramagnetic species (Pan et al. 2002b; Mao et al. 2010a). However, the challenges of selecting appropriate samples for single-crystal EPR are many, not least of which is the requirement of millimeter-sized crystals for experiments at X-band frequencies of ~9 GHz. Other potential complications of samples for single-crystal EPR experiments include: 1) poorly developed morphology that makes crystal alignment difficult, 2) twinning and composite crystals that give rise to multiple (and often overlapping) sets of EPR lines, and 3) other imperfections (e.g., strain, micro-domains and compositional heterogeneities) that lead to line broadening.

Some transition-metal ions (e.g., Fe^{3+}, Mn^{2+}, Gd^{3+}) are intrinsically paramagnetic and, therefore, are directly amenable to EPR experiments. Also, virtually all diamagnetic species can be converted into a paramagnetic state through various chemical and physical methods. Two of the most commonly used methods to produce paramagnetic centers from diamagnetic precursors are photolysis and radiolysis. The former usually involves irradiation of samples in the UV region. Radiolysis involves high-energy radiation (e.g., X-ray, γ-ray, electron beams from accelerators, and neutrons from nuclear reactors). For example, γ- and X-ray radiations can excite electrons to higher energy levels, and even to orbitals of other atoms or molecules to form hole or electron centers. Similarly, electron beams can influence the electrons in minerals and other materials to form paramagnetic centers. Neutrons only have kinetic energies and also can produce paramagnetic defects, although nuclear reactions usually occur at the same time. The desired amount of paramagnetic species in these experiments can usually be controlled by managing the radiation doses.

Continuous-wave (CW) EPR

Conventional EPR spectra are measured by using a constant microwave frequency (ν) and sweeping the external magnetic field (**B**). A basic magnetic field-swept EPR spectrometer consists of a microwave source, a magnetic field, a resonant cavity, a solid-state diode detector, and a computer for data acquisition and display (Fig. 6). Commercial EPR spectrometers commonly operate at X-band, K-band (~24 GHz), Q-band (~34 GHz), and W-band (~94 GHz) frequencies. However, home-built spectrometers at lower and higher frequencies (~1.1 GHz ≤ ν ≥ 3 THz) have been developed to take advantages of multi-frequency EPR studies (Lebedev 1990; Nokhrin et al. 2005; Reijerse 2010). The microwave power in standard instruments is incident on the sample continuously, hence commonly known as continuous-wave (CW) EPR. Similarly, the original electron nuclear double resonance (ENDOR) spectra were of the CW type (Feher 1959).

The fact that the various spin Hamiltonian parameters of EPR spectra respond to microwave frequencies differently makes multi-frequency experiments useful to simplify and improve their determinations. For example, increasing the microwave frequency enhances the *g*-factor features while minimizing the hyperfine features. Conversely, lowering the microwave frequency leads to a hyperfine dominated EPR spectrum. Also, higher microwave frequency results in improved absolute sensitivity, although the cavity volume is scaled down, and allows observation of transitions involving large zero-field splitting parameters.

Multi-frequency measurements also serve as an independent test for the best-fit spin Hamiltonian parameters. Spectral simulations using one set of parameters obtained from spectra measured at a given microwave frequency reproduce those measured at different frequencies, providing support for these parameters. When this is not the case, the spin Hamiltonian parameters are questionable and require reanalysis. For example, Priem et al. (2001) measured powder

EBSCOhost - printed on 2/13/2023 5:26 AM via . All use subject to https://www.ebsco.com/terms-of-use

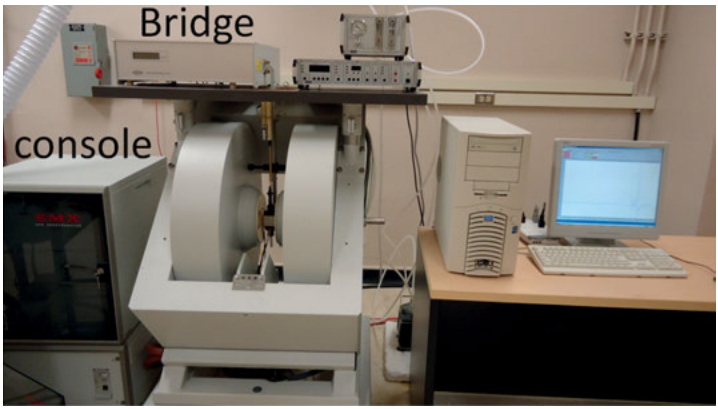


Figure 6. Photograph illustrating the principal components of a CW-EPR spectrometer (Bruker EMX), including the radiation source and the detector in the microwave bridge, the resonance cavity between the magnets, a console containing signal processing and control electronics, and a computer.

EPR spectra for Fe^{3+} in α-alumina (i.e., corundum) from 4 GHz to 130 GHz and noted that the spin Hamiltonain parameters from the 130 GHz spectra do not fully reproduce those measured at 9 GHz and 35 GHz. They emphasized that a careful step-by-step analysis and spectral simulation of powder spectra from all frequencies are necessary to obtain the relative sign and magnitude of the zero-field splitting parameters (D, B_4^0 and B_4^3). Similarly, our multi-frequency single-crystal EPR studies on natural and artificially irradiated quartz (Nilges et al. 2008, 2009; Pan et al. 2008, 2009b) removed a number of discrepancies among previous X-band studies, which are attributable to small asymmetries undetectable at low microwave frequencies, and produced improved spin Hamiltonian parameters to establish a series of superoxide radicals.

Interpretation of an experimental EPR spectrum often starts with an evaluation whether the resonance signals arise from a single or several paramagnetic centers and is followed by identification of the individual species present. This is often difficult on the basis of the lineshapes and linewidths alone, unless where diagnostic hyperfine structures are present for unambiguous identification. Often, multiple measurements with different experimental conditions (e.g., temperatures and microwave powers) and sample treatments (e.g., thermal annealing, variable radiation doses, and doping of artificially enriched isotopes) are required to distinguish different paramagnetic species. Also, multi-frequency measurements are often useful in discriminating multiple paramagnetic centers present in a sample as well.

In single-crystal EPR studies, detailed measurements for one, two or three rotational planes are commonly made, dependent on both the site symmetry of the paramagnetic center and the crystal symmetry of its host. Then, the line positions of all absorption signals, when well resolved, can be followed according to the crystal orientation. These angular dependences of line positions (i.e., roadmaps) offer further tests to the interpreted center(s), when considered with the knowledge of the Laue symmetry of the crystal and the site symmetry of the paramagnetic species (Rae 1969), These line-position data along with the experimental microwave frequencies are then used for fitting with appropriate spin Hamiltonian (McGavin and Tennent 2009). One additional consideration required for the fitting of spin Hamiltonian parameters is the selection of an experimental coordination system (McGavin 1987), which may or may not coincide with the crystallographic axes. Often, selection of an appropriate experimental coordination system could prevent misinterpretation of the spectra and reduce the number of parameters to be determined (and avoid the possibility of the best-fit parameters without physical meanings, McGavin 1987).

EBSCOhost - printed on 2/13/2023 5:26 AM via . All use subject to https://www.ebsco.com/terms-of-use

Our study on synthetic stishovite ($P4_2/mnm$) before and after electron and/or gamma-ray irradiation offers an example for the acquisition and analysis of single-crystal CW EPR spectra (Pan et al. 2011). Synchrotron micro-X-ray fluorescence analysis of synthetic stishovite revealed ~70 ppm Cr, which probably arises from contamination in the experimental assembly. These stishovite crystals have well-developed (110) and (001) faces that allow detailed single-crystal EPR measurements in those planes at both 85 K and 294 K, at a constant angle interval of 5°.

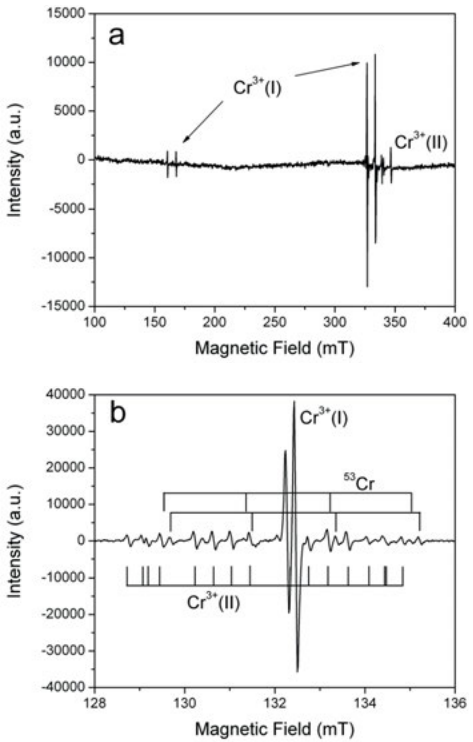


Figure 7. Representative single-crystal EPR spectra of stishovite (without gamma-ray irradiation) at 294 K and microwave frequencies of ~9.390 GHz: (a) a wide-scan spectrum measured at 1° away from an a axis, illustrating that the two transitions within ±1/2 and ±3/2 Kramers doublets of the Cr^{3+}(I) center are split into two lines each from two magnetically nonequivalent sites; additional weak lines at ~350 mT belong to Cr^{3+}(II); and (b) a narrow-scan spectrum at $\mathbf{B} \wedge c = 12°$, illustrating the two $M_s = -1/2 \leftrightarrow +1/2$ transition lines and their accompanied ^{53}Cr hyperfine lines (marked) of the Cr^{3+}(I) center; also marked are the 16 main lines of the Cr^{3+}(II) center (modified from Pan et al. 2011).

The single-crystal EPR spectra of stishovite without artificial irradiation contain two high-spin (S = 3/2) Cr^{3+} centers: Cr^{3+}(I) and Cr^{3+}(II) (Fig. 7). Center Cr^{3+}(I) is confirmed by its diagnostic ^{53}Cr hyperfine structure (I = 3/2 and isotope abundance = 9.5%) that accompanies the main absorption line(s) from the three even isotopes ^{50,52,54}Cr (I = 0 and 90.5%). The main absorption line(s) represent the two Kramers doublets arising from the Zeeman levels $M_s = \pm 1/2$ and $M_s = \pm 3/2$. These doublets are resolved into two lines away from the crystallographic *a* and *c* axes, indicating that the Cr^{3+}(I) center has a D_{2h} site symmetry in the tetragonal stishovite. The observed angular dependences of both the main absorptions lines from ^{50,52,54}Cr and the ^{53}Cr hyperfine lines suggest that this center has principal axes along the crystal [001], $[\bar{1}\,\bar{1}0]$ and $[1\,\bar{1}0]$ directions, which are then taken as the *x*, *y* and *z* axes of the experimental coordinate system (Fig. 8). The two datasets from the main lines and the ^{53}Cr hyperfine lines of the Cr^{3+}(I) center have been fitted, using the EPR-NMR software package of Mombourquette et al. (1996), to the following two spin Hamiltonians:

$$\mathcal{H} = \left(\beta_e \mathbf{B}^{\mathbf{T}} \cdot \mathbf{g} \cdot \mathbf{S}\right) + \left(\mathbf{S}^{\mathbf{T}} \cdot \mathbf{D} \cdot \mathbf{S}\right) + \mathrm{BS}^3 \tag{9}$$

$$\mathcal{H} = \left(\beta_e \mathbf{B}^{\mathbf{T}} \cdot \mathbf{g} \cdot \mathbf{S}\right) + \left(\mathbf{S}^{\mathbf{T}} \cdot \mathbf{D} \cdot \mathbf{S}\right) + \mathrm{BS}^3 + \left(\mathbf{I}^{\mathbf{T}} \cdot \mathbf{A} \cdot \mathbf{S}\right) + \left(\mathbf{I}^{\mathbf{T}} \cdot \mathbf{P} \cdot \mathbf{I}\right) - \left(\beta_n \mathbf{B}^{\mathbf{T}} \cdot \mathbf{g_n} \cdot \mathbf{I}\right) \tag{10}$$

Figure 7b shows that the two $M_s = \pm 1/2$ lines of the Cr^{3+}(I) center are accompanied by sixteen lines of the Cr^{3+}(II) center, which have been shown by spectral simulations to arise from both a low site symmetry and superhyperfine interaction with a ^{1}H nucleus. The similarities in the angular dependence of line positions between the Cr^{3+}(I) and Cr^{3+}(II) centers suggest that the experimental coordination system for the former is also appropriate for the latter.

EBSCOhost - printed on 2/13/2023 5:26 AM via . All use subject to https://www.ebsco.com/terms-of-use

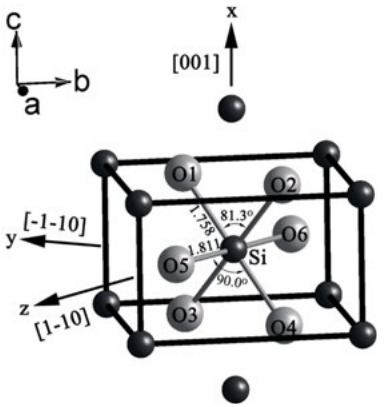


Figure 8. Crystal structure of stishovite illustrating the central SiO_6 octahedron and its neighboring Si atoms, including the two nearest Si atoms along the [001] direction and eight next-nearest Si atoms at the corners (data from Yamanaka et al. 2002). Also shown are the experimental axes *x*, *y* and *z* along the [001], [$\bar{1}\,\bar{1}$0] and [1 $\bar{1}$ 0] directions, respectively (modified from Pan et al. 2011).

The dataset for the Cr^{3+}(II) center with a ^{1}H superhyperfine structure but no detectable ^{53}Cr hyperfine structure has been fitted to the spin Hamiltonian of the form:

$$\mathcal{H} = \left(\beta_e \mathbf{B}^{\mathbf{T}} \cdot \mathbf{g} \cdot \mathbf{S}\right) + \left(\mathbf{S}^{\mathbf{T}} \cdot \mathbf{D} \cdot \mathbf{S}\right) + BS^3 + \left(\mathbf{I}^{\mathbf{T}} \cdot \mathbf{A} \cdot \mathbf{S}\right) - \left(\beta_n \mathbf{B}^{\mathbf{T}} \cdot \mathbf{g_n} \cdot \mathbf{I}\right) \quad (11)$$

The D_{2h} site symmetry and the best-fit spin Hamiltonian parameters from the EPR spectra show that the Cr^{3+}(I) center represents a substitutional Cr^{3+} ion at the octahedral Si site without an immediate charge compensator (Fig. 8). The Cr^{3+}(II) center also arises from a substitutional Cr^{3+} ion at the octahedral Si site but has as a neighboring H^+ ion as the charge compensator, which explains the reduced site symmetry and the observed ^{1}H superhyperfine structure. The best-fit orientation and magnitude of the principal A(^{1}H) parameter also allow a determination for the position of the H atom at (0.42, 0.12, 0), which is consistent with results from available DFT calculations (Gibbs et al. 2003, 2004; Pan et al. 2011).

The single-crystal CW-EPR spectra of electron-irradiated stishovite do not show any Cr^{3+} centers but contain two S = 1/2 species: an Al-O_2^{3-} radical and a Cr^{5+} center (Fig. 9). The former is characterized by its well-resolved ^{27}Al (I = 5/2 and 100%) hyperfine structure (Ogoh et al. 1996; Botis and Pan 2010; Pan et al. 2012). The Cr^{5+} center is identified again by its diagnostic ^{53}Cr hyperfine structure. The main absorption line from the even Cr isotopes, observed along crystallographic axes, is split into two at general crystal orientations, also indicative of a D_{2h} site symmetry. In addition, two sets of doublets are present as satellites symmetrically distributed about both the main absorption line and the four ^{53}Cr hyperfine lines (Fig. 9). One set of the doublets with a separation of ~1 mT has an integrated intensity of ~10% of the main absorption line, whereas the other set with a narrower separation of ~0.2 mT has an integrated intensity of ~30% of the main absorption line. These two sets of doublets evidently correspond to two distinct ^{29}Si (4.79% and I = 1/2) superhyperfine structures arising from interactions with two nearest-neighbor and eight next-nearest-neighbor Si atoms, respectively (Fig. 8).

The four sets of line-position data for the main absorption lines, the ^{53}Cr hyperfine structure, and the two ^{29}Si superhyperfine structures from the Cr^{5+} center have be fitted into the spin Hamiltonians found in Equations (4), (6), and (6b):

$$\mathcal{H} = \beta_e \mathbf{B}^{\mathbf{T}} \cdot \mathbf{g} \cdot \mathbf{S} \quad (4)$$

$$\mathcal{H} = \left(\beta_e \mathbf{B}^{\mathbf{T}} \cdot \mathbf{g} \cdot \mathbf{S}\right) + \left(\mathbf{I}^{\mathbf{T}} \cdot \mathbf{A} \cdot \mathbf{S}\right) - \left(\beta_n \mathbf{B}^{\mathbf{T}} \cdot \mathbf{g_n} \cdot \mathbf{I}\right) + \left(\mathbf{I}^{\mathbf{T}} \cdot \mathbf{P} \cdot \mathbf{I}\right) \quad (6b)$$

$$\mathcal{H} = \left(\beta_e \mathbf{B}^{\mathbf{T}} \cdot \mathbf{g} \cdot \mathbf{S}\right) + \left(\mathbf{I}^{\mathbf{T}} \cdot \mathbf{A} \cdot \mathbf{S}\right) - \left(\beta_n \mathbf{B}^{\mathbf{T}} \cdot \mathbf{g_n} \cdot \mathbf{I}\right) \quad (6)$$

EBSCOhost - printed on 2/13/2023 5:26 AM via . All use subject to https://www.ebsco.com/terms-of-use

The angular dependence of the Cr^{5+} center is also closely comparable to those of the two Cr^{3+} centers. It is convenient, therefore, to adopt the experimental *x*, *y* and *z* axes along the [001], [$\bar{1}\,\bar{1}$0] and [1 $\bar{1}$0] directions, respectively. The observed site symmetry and the best-fit spin Hamiltonian parameters (including ^{29}Si superhyperfine coupling constants from the two nearest- and eight next-nearest-neighbor Si nuclei) of the Cr^{5+} center provide unambiguous evidence for its location at the octahedral Si site (Fig. 8). Evidently, this Cr^{5+} center formed from trapping of two electrons on the two Cr^{3+} centers (and removal of the H^+ ion for Cr^{3+}(II)) during artificial irradiation (Pan et al. 2011).

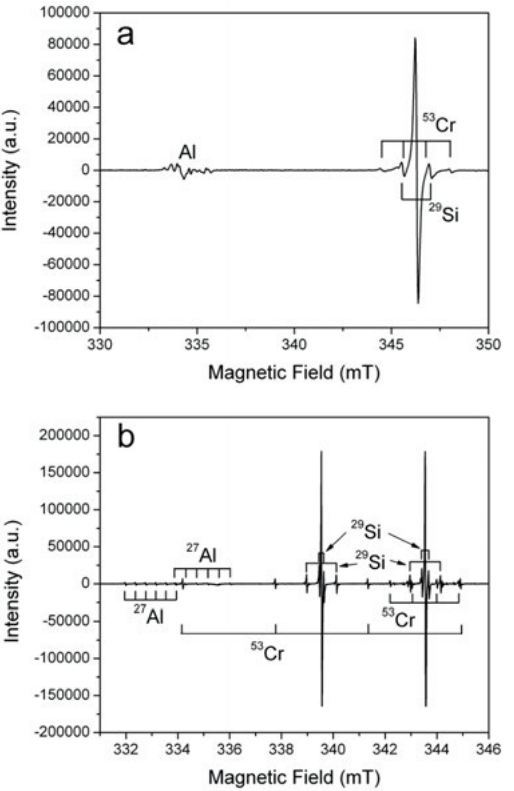


Figure 9. Single-crystal EPR spectra of the Cr^{5+} center in: a) an electron-irradiated stishovite measured at ν = 9.390 GHz, **B**||*c*, and 294 K, and b) an electron- and gamma-ray-irradiated stishovite with ν = 9.394 GHz, **B**∧*c* = 90°, and 85 K. The irregular multiplet at ~335 mT in a) spectrum belongs to the Al–O_2^{3-} center (Pan et al. 2012), as indicated by the characteristic ^{27}Al hyperfine structure at 85 K (modified from Pan et al. 2011).

Pulse ESEEM and ENDOR

Two notable limitations of the CW EPR techniques are: 1) a significant portion of the measurement time is spent on recording the baseline rather than the signals, and 2) the EPR spectrum is the result of all the interactions and relaxation processes in the sample, often making spectral interpretation difficult. An alternative to the CW techniques is the excitation of electron spins by the use of various sequences of microwave pulses (Schweiger and Jeschke 2001). The pulse EPR techniques represent an area of rapid developments in recent years, and modern ESEEM and ENDOR spectra that measure interactions between the unpaired electrons and neighboring nuclei are commonly carried out with the pulse techniques (Schweiger and Jeschke 2001).

The basic ESEEM pulsed scheme is a two-pulse ($\pi/2 - \tau - \pi -$ echo) sequence where τ is the time between pulses. The second refocusing pulse gives rise to a Hahn echo that decays exponentially with τ/t_{2e} (where t_{2e} is the spin-spin relaxation time for the electron). The decay is modulated by the interference between nuclear transitions and the Fourier transform after correcting for the exponential decay gives rise to a frequency spectrum akin to ENDOR. The intensity of the ESEEM spectra is dependent upon the presence of forbidden transitions. Thus, anisotropic interactions (anisotropic hyperfine and/or nuclear quadrupole coupling) are necessary to observing an ESEEM spectrum. For example, for an axial S = I = 1/2 system the ESEEM intensity will go to zero along and perpendicular to the major (*z*) axis of the hyperfine. Because the modulation of the echo is an interference effect, one also can observe combination and harmonics of the fundamental frequencies. In addition, the resolution of two-pulse ESEEM is limited by the value of $1/t_{2e}$.

EBSCOhost - printed on 2/13/2023 5:26 AM via . All use subject to https://www.ebsco.com/terms-of-use

For three-pulse ESEEM ($\pi/2 - \tau - \pi/2 - t - \pi/2$ – echo), primarily t_{1e} (the spin-lattice relaxation time for the electron) determines the resolution and combination peaks due to a single spin system are eliminated. In a three-pulse ESEEM, the second separation time, t, is varied instead of τ. However, because ESEEM involves interference between EPR transitions, there will be blind spots that depend on the value of τ. For an S = I = 1/2 system, the blind spots for the ν_α peak will occur at multiples of $\nu_\beta\tau$, and *vice versa*. To eliminate such blind spots, one can either choose a value of τ so the suppression of peaks of interest is small or averaged over a range of τ values, as for Mims ENDOR (see below).

For the case of S = I = 1/2 there are two ENDOR transitions:

$$\nu_\alpha = \left| \frac{A}{2} + \nu_n \right| \tag{12a}$$

$$\nu_\beta = \left| \frac{A}{2} - \nu_n \right| \tag{12b}$$

where A is the hyperfine coupling constant, ν_α and ν_β are transition frequencies, and ν_n the nuclear Larmor frequency. The transitions result in two $\Delta M_I = 1$ transitions either centered at ν_n and split by A ($2\nu_n > A$) or centered at $A/2$ and split by $2\nu_n$ ($A > 2\nu_n$) (Fig. 10). For I > 1/2 there will be further splitting by nuclear quadrupole interaction, in addition to peaks with $\Delta M_I > 1$.

Pulsed ENDOR spectra are usually performed using either a Davies or Mims pulse sequence. Davies ENDOR (Gemperle and Schweiger 1991) is somewhat preferred, because it gives a spectrum that is free of blind spots and is the easiest to quantify intensities. Davies ENDOR uses a preparatory inversion pulse followed by a Hahn two-pulse detection sequence that gives rise to an inverted spin echo (π – RF – $\pi/2 - \tau - \pi$ – echo). The height of this echo depends on the relaxation time of the electron spin (T_{1e}) and the time between the preparatory pulse and the Hahn two-pulse sequence. If a RF pulse is given during this time period (typically 10 to 20 μs) and is at resonance with an ENDOR transition, the intensity of the echo will increase. By sweeping the RF frequency an ENDOR spectrum is obtained.

In order to observe an ENDOR effect, the first π pulse must be selective: i.e., it must excite only one of the hyperfine transitions. For Davies ENDOR, if the pulse width is too small it will invert (excite) all hyperfine transitions and the ENDOR effect disappears. This suppression effects is given by (Fan et al. 1992):

$$I \propto \frac{A^2}{A^2 + \left(\frac{(1/\tau_\pi)^2}{2} \right)} \tag{13}$$

where A is the hyperfine coupling constant and τ_π is the length of the initial inverting pulse. This suppression can serve two useful purposes: 1) strong matrix peaks, i.e., peaks from distant nuclei, are almost nearly suppressed; and 2) one can use this suppression effect to assess whether the condition $\nu_n > A$ or $A > \nu_n$ is valid for an observed ENDOR peak. If the peak is suppressed when τ_π is decreased, the condition $\nu_n > A$ should be valid. For example, this can be used to distinguish between overlapping proton and ^{14}N peaks (Doan et al. 1991). Because of this suppression effect the Davies technique is mostly used for detecting larger hyperfine couplings (> 10 MHz). Smaller couplings can be observed by using longer (softer and more selective) π pulses, although the length of the π pulse is limited by the value of t_{2e}. Therefore, it is difficult to observe hyperfine splittings smaller than a few MHz.

The Mims ENDOR technique (Gemperle and Schweiger 1991) is basically a 3-pulse stimulated echo sequence in which the RF mixing or soak pulse is placed between the second and third pulses ($\pi/2 - \tau - \pi/2$ – RF – $\pi/2$ – echo). When the RF frequency is at resonance with

EBSCOhost - printed on 2/13/2023 5:26 AM via . All use subject to https://www.ebsco.com/terms-of-use

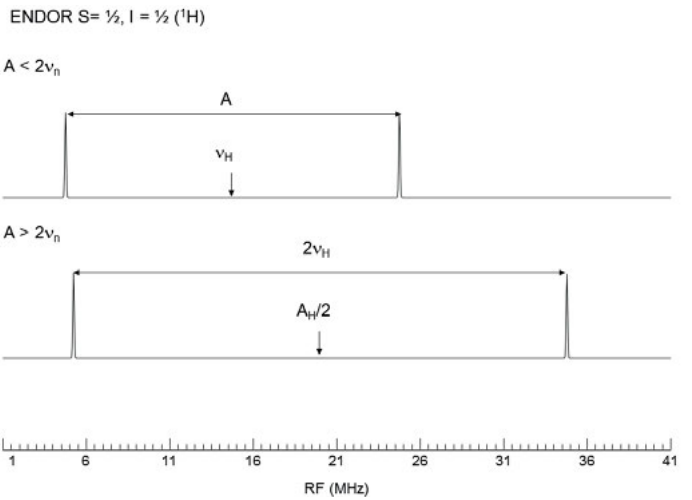


Figure 10. Simulated ENDOR spectra for an S = I = 1/2 (^{1}H) system with $A < 2\nu_n$ (upper trace) and $A > 2\nu_n$ (lower trace).

an ENDOR transition a frequency shift causes a defocusing of the spin packet resulting in a decrease in echo and an amplitude-inverted ENDOR spectrum. Because interferences between the transitions cause the ENDOR effect, non-selective, hard, short pulses are used and there is no suppression of small couplings as in Davies ENDOR. Thus, Mims ENDOR is best used to observe small hyperfine couplings. Mims ENDOR (as does 3-pulse ESEEM, see below) results in τ-dependent blind spots (Schweiger and Jeschke 1991):

$$I \propto \left\{1 - \cos(2\pi A\tau)\right\} \tag{14}$$

where A is the hyperfine coupling constant and τ is the time between the first and second pulse. To eliminate such blind spots, one can either choose a value of τ so the suppression of peaks of interest is small or average over a range of τ values.

Because both Mims and Davies ENDOR require a radiofrequency mixing time on the order of 10 μs the temperature must be low enough that t_{1e} is significantly longer than 10 μs. For ESEEM there is no radiofrequency mixing pulse and the t_{1e} requirement is not as stringent. Pulse ENDOR and ESEEM are best suited for systems with inhomogeneously broadened lines that may contain underlying hyperfine structure(s) unresolved in CW EPR.

The study of the O^- center in hydroxylapophyllite (Mao et al. 2010b) is taken here as an example for the measurement and analysis of pulse ENDOR and ESEEM spectra. Single-crystal CW EPR spectra of a natural hydroxylapophyllite measured at 294 K and 90 K revealed an O^- center, corresponding to trapping of an unpaired electron in the $2p_z$ orbital of the hydroxyl oxygen atom (after removal of the proton) in the interlayer. The CW spectra measured at 90 K also contain four sets of well-resolved satellite peaks that have been successfully fitted as pairs of the O^- center (i.e., biradicals). The results of these biradicals provide further confirmation for the structural model of the O^- center in hydroxylapophyllite (Mao et al. 2010b). However, CW EPR spectra of the O^- center do not disclose any superhyperfine interactions with neighboring nuclei in the lattice.

Three-pulse ESEEM spectra at 25 K were collected on a Bruker E580-10 Elexsys spectrometer. The time domain ESEEM spectra were baseline corrected, zero-filled, apodized, and Fourier transformed to give frequency domain spectra. To reduce the effect of blind-spots that

EBSCOhost - printed on 2/13/2023 5:26 AM via . All use subject to https://www.ebsco.com/terms-of-use

arise from an oscillating τ dependence, ESEEM spectra were also recorded as a function of τ and later summed. ESEEM spectra at a rotation angle of every 10° were collected on a crystal mounted with the rotation axis in the (001) face. As CW EPR spectra do not show any site splitting, all eight symmetry related sites are excited simultaneously by the microwave pulse. As such, angle corrections (accurate to ~0.5°) had to be calculated directly from the fitting of the well-resolved ^{29}Si ESEEM spectra. Angle corrections indicated that the rotation axis was ~4.5° from the [110] direction. ESEEM spectra were then simulated using SIMEND (Nilges et al. 2009), with the addition of a routine to simulate dead-time effects using FFT (Keijzers et al. 1987) and a routine to simulate the additional effects of cross-term averaging. Because the observed modulations were very weak, the contributions from the various nuclei could be considered independently.

ESEEM spectra show very weak modulation at frequencies very close to those of ^{29}Si and ^{1}H at 2.9 MHz and 14.6 MHz. respectively. The ^{29}Si "matrix" peak is actually split into three to eight pairs depending on orientation (Fig. 11). Spectral fittings show that these spectra can be readily accounted for by one ^{29}Si with a hyperfine splitting on the order of 0.5 MHz. The anisotropic component of the ^{29}Si hyperfine is equal to −0.62 MHz, which corresponds to a distance (r) of 3.71 Å on the basis of the point-dipole model:

$$A_z = \left(\frac{2\mu_0}{4\pi}\right)\left(\frac{g\beta_e g_n \beta_n}{r^3}\right) \tag{15}$$

where A_z is a component of the traceless dipolar hyperfine interaction ($A_x = A_y = -A_z/2$) and g_n is equal to −1.1097 for ^{29}Si. This value is the same as that between the hydroxyl oxygen atom and the nearest neighbor Si, while the orientation of the unique hyperfine axis is only 3.4° from this O–Si direction. Simulations could be improved somewhat if the next-nearest-neighbor Si is also included. The hyperfine constants obtained for this second Si are close to those predicted for the next-nearest-neighbor Si. This second Si, however, gives rise to much weaker (the ESEEM intensity decreases roughly as r^{-3}) spectra with narrower width, hence larger uncertainty in the fitted values.

Similarly, the ESEEM spectra allow an analysis of eight neighboring ^{1}H nuclei (Fig. 12), although the hyperfine matrices of the outer-most H6, H7 and H8 were taken directly from

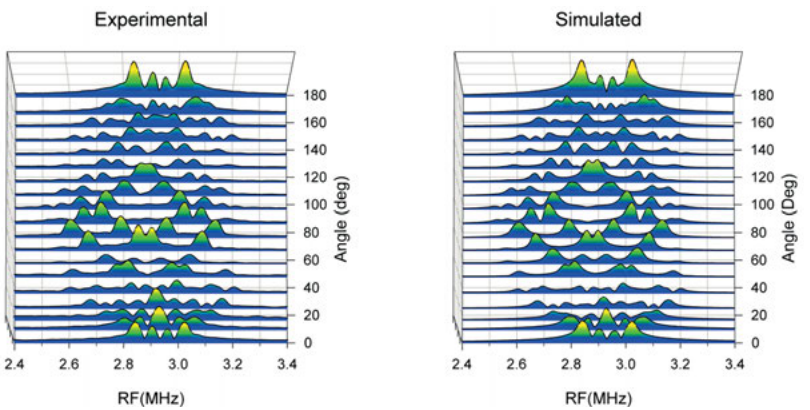


Figure 11. Stacked plots of the ^{29}Si portion of the experimental and simulated three-pulse, Fourier-transform ESEEM spectra of the O^- center in hydroxylapophyllite as a function of rotation angles. Spectral simulations included 2 Si nuclei. Intensity in the vertical axis unlabeled (arbitrary unit; modified from Mao et al. 2010b).

EBSCOhost - printed on 2/13/2023 5:26 AM via . All use subject to https://www.ebsco.com/terms-of-use

point-dipole-model calculations with the ideal hydroxylapophyllite structure. For the best fitted H1 to H5, the distances of 4.35 Å and 4.41 Å for H1a and H1b are only ~0.2 Å smaller than those from room-temperature X-ray and neutron diffraction experiments (Prince 1971; Rouse et al. 1978). The values of 4.84 Å and 4.94 Å for H2a and H2b are within experimental uncertainty of those from X-ray and neutron diffraction. Also, the calculated orientations of the unique hyperfine axes for H1 and H2 are close to those reported for X-ray and neutron diffraction experiments. The distances obtained by fitting H3, H4, and H5 are close to those determined from X-ray and neutron diffraction experiments as well, despite larger uncertainties in fitting the hyperfine matrices for these more distant protons as well as a number of assumptions made.

In addition, a number of peaks centered between 0.4 and 1.0 MHz in the ESEEM spectra allow identification and analysis of four neighboring ^{39}K nuclei (K1 to K4; Fig. 13), with K4 located at 14.2 Å away. For the best determined K1, its O–K1 distance of 6.32 Å calculated from the point-dipole model agrees well with the experimental value of 6.35 Å determined from

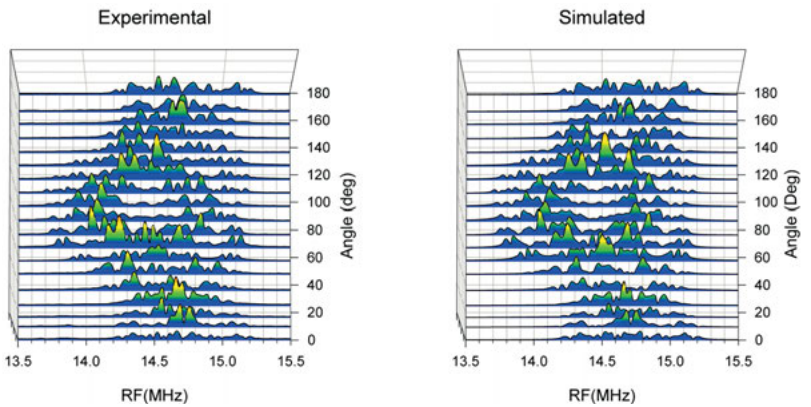


Figure 12. Stacked plots of the ^{1}H portion of the experimental and simulated three-pulse, Fourier-transform ESEEM spectra as a function of rotation angles. Spectral simulations included eight H nuclei. Intensity in the vertical axis unlabeled (arbitrary unit; modified from Mao et al. 2010b).

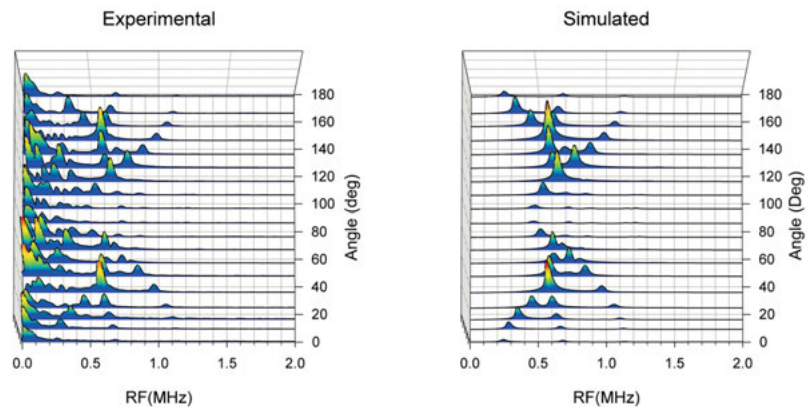


Figure 13. Stacked plots of the ^{39}K portion of the experimental and simulated three-pulse, Fourier-transform ESEEM spectra as a function of rotation angles. Note that intensity in the vertical axis (unlabeled, arbitrary units) has been reduced five times (relative to those in Figs. 11 and 12) to show the strong ^{39}K spectra. Spectral simulations included four ^{39}K nuclei (modified from Mao et al. 2010b).

EBSCOhost - printed on 2/13/2023 5:26 AM via . All use subject to https://www.ebsco.com/terms-of-use

X-ray diffraction data. The unique axis of the hyperfine matrix is found to be only 1.4° away from the O–K1 direction as well. Figure 13a also shows the presence of a number of peaks below 0.4 MHz. They may be attributable to other quadrupolar nuclei with small magnetic moments (e.g., ^{41}K) and/or can arise as artifacts due to the imperfect subtraction of the decay of the spin echo.

Ab initio calculations of EPR parameters

The combination of complex natural materials like minerals, common presence of magnetically similar defects, and general lack of complementary structural techniques with similar sensitivities, makes experimental EPR data often difficult to interpret unambiguously. In this context, first-principles theoretical modeling represents an excellent approach for predicting the identity, geometry, electronic structure and properties of paramagnetic species, complementing the EPR techniques. Over the last decade, tremendous progresses have been made in *ab initio* calculations of EPR parameters of paramagnetic species in both molecules and complex crystalline solids (e.g., van Lenthe et al. 1998; Patchkovskii and Ziegler 2001; Mallia et al. 2001; Pichard and Mauri 2002; Kaupp et al. 2004; Pietrucci et al. 2006; Asher and Kaupp 2007; Li and Pan 2011, 2012). Often, calculated energies of different structural models are too close to allow a unique identification. Calculated EPR parameters such as the magnitude and orientations of nuclear hyperfine and quadrupole parameters, on the other hand, provide unambiguous identification of paramagnetic centers (Botis et al. 2009; Nilges et al. 2009; Botis and Pan 2010; Li and Pan 2011; Li et al. 2012; Mashkovtsev et al. 2013).

For example, boron oxygen hole centers (BOHC) are fundamental radiation-induced defects in borates and borosilicates as well as their glass counterparts. These defects, which exert profound influences on the applications of these materials from fiber optics to long-term disposal of high-level nuclear wastes, have attracted intense research since 1950s but remain controversial about their structures. In particular, interpretation of experimental EPR spectra of borates and borosilicates is often difficult, because they commonly contain several BOHC with similar EPR parameters (Li et al. 2011). Li and Pan (2011) investigated the geometries and electronic structures of BOHC in calcite and calculated their EPR parameters such as ^{11}B hyperfine and quadrupole parameters by use of *ab initio* Hartree-Fock (HF) and various density functional theory (DFT) methods based on the supercell approach with all-electron basis sets. These theoretical results combined with literature EPR data (Eachus and Symons 1968; Bacquet et al. 1975) established three distinct $[BO_3]^{2-}$ centers corresponding to: (I) the classic $[BO_3]^{2-}$ radical with the D_{3h} symmetry and the unpaired spin equally distributed among the three equivalent oxygen atoms (i.e., BO_3^{5-}), (II) the previously proposed $[BO_2]^{2-}$ center with the unpaired electron equally distributed on two of the three oxygen atoms (OBO_2^{3-}), and 3) a new center with ~90% of the unpaired spin localized on one of the three oxygen atoms (O_2BO^-) (Fig. 14). Calculated EPR parameters confirm that the first two $[BO_3]^{2-}$ centers share similar ^{11}B hyperfine coupling constants to the $[BO_4]^0$ center, making their identification on the basis of experimental EPR spectra alone difficult (Li and Pan 2011; Li et al. 2011). These atomistic and electronic structures of BOHC in minerals from theoretical calculations (Li and Pan 2011; Li et al. 2011) provide important insights into their precursors and analogues in glasses and other amorphous materials.

In addition, theoretical calculations of EPR parameters are important even when experimental EPR spectra provide an unambiguous identification of the paramagnetic species. In this case, the calculated EPR parameters can be taken as an independent test for the experimental values and may provide additional (and quantitative) information about the geometry and electronic structure of the paramagnetic species (e.g., Mallia et al. 2001; Nilges et al. 2009; Botis and Pan 2009, 2011; Botis et al. 2009; Li et al. 2011, 2012).

EBSCOhost - printed on 2/13/2023 5:26 AM via . All use subject to https://www.ebsco.com/terms-of-use

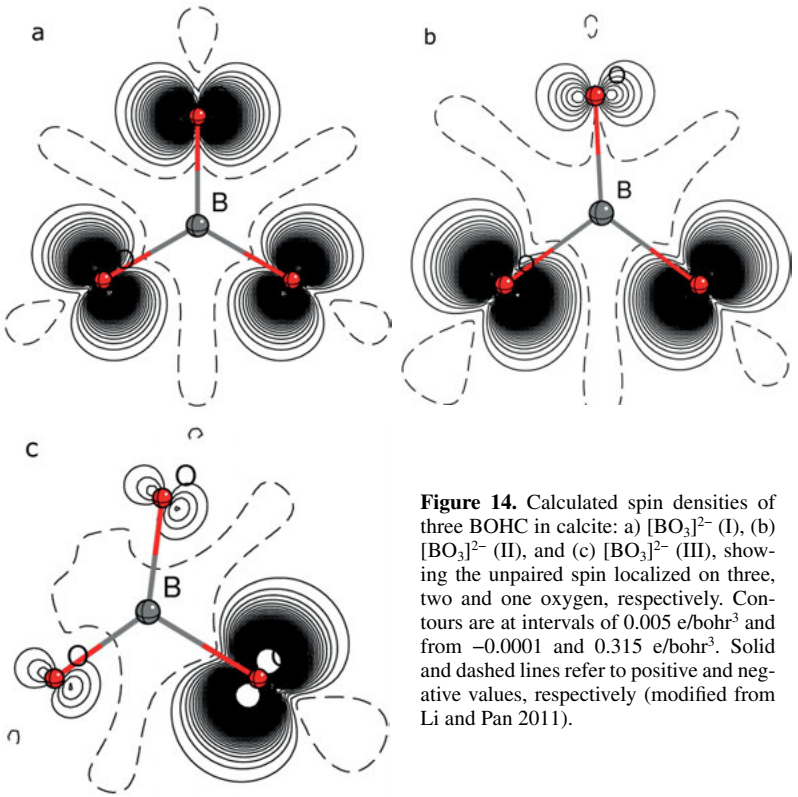


Figure 14. Calculated spin densities of three BOHC in calcite: a) $[BO_3]^{2-}$ (I), (b) $[BO_3]^{2-}$ (II), and (c) $[BO_3]^{2-}$ (III), showing the unpaired spin localized on three, two and one oxygen, respectively. Contours are at intervals of 0.005 e/bohr^3 and from −0.0001 and 0.315 e/bohr^3. Solid and dashed lines refer to positive and negative values, respectively (modified from Li and Pan 2011).

APPLICATIONS TO EARTH AND PLANETARY SCIENCES

EPR as a structural probe of point defects in minerals

EPR studies to probe the local structures of impurity ions and other point defects have been carried in almost all major groups of minerals from native elements to oxides, hydroxides, halides, sulfides, sulfates, arsenates, vanadates, tungstates, phosphates and silicates (Marfunin 1979; Calas 1988; Vassilikova-Dova 1993; Goodman and Hall 1994; Nadolinny et al. 2005, 2009a,b). This section is not intended to provide a comprehensive survey of EPR studies on minerals but takes representative examples to demonstrate the capabilities of the EPR techniques.

In addition to the two EPR studies on Cr in stishovite and the radiation-induced O^- center in hydroxylapophyllite in the "*Guides to EPR experiments and Spectral Analyses*" section, we take the investigations of Fe^{3+} in quartz (Weil 1994) as another example to further illustrate the capacities of EPR as a structural probe. The common presence of iron as a trace element in quartz and its apparent association with the amethyst color have attracted numerous studies by use of diverse techniques from optical spectroscopy to magnetic susceptibility, Mössbaur spectroscopy and synchrotron X-ray absorption spectroscopy (Cohen and Hassan 1974; Cressey et al. 1993; Schofield et al. 1995; Dedushenko et al. 2004; Hebert and Rossman 2008; Di Benedetto et al. 2010; SivaRamaiah et al. 2011; SivaRamaiah and Pan 2012). However, it is EPR that has contributed greatly to our knowledge about Fe^{3+} in quartz (Weil 1994), because ferric iron with the ground-state valence-electron configuration of $3d^5$ adopts either the low-spin state with 1 unpaired electron or the high-spin state with 5 unpaired electrons, both of which are amenable

EBSCOhost - printed on 2/13/2023 5:26 AM via . All use subject to https://www.ebsco.com/terms-of-use

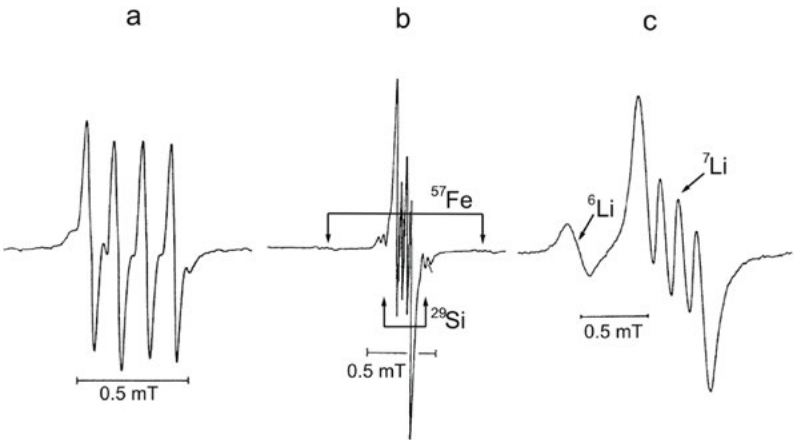


Figure 15. Single-crystal EPR spectra of the $[FeO_4/Li]^0_\alpha$ (aka S_1) center in synthetic, iron-doped α-quartz at 9.52 GHz and 50K showing: a) the ±3/2 transition with the ^{7}Li superhyperfine structure and weak satellites arising from an ^{57}Fe hyperfine structure and a ^{29}Si superhyperfine structure at **B**||*b*; and b) the ±5/2 transition with both the well-resolved ^{7}Li and incompletely-resolved ^{6}Li superhyperfine structures at **B**||*a* (reproduced with permission from Stegger and Lehmann 1989).

to EPR studies. Single-crystal EPR studies have established a series of high-spin Fe^{3+} species in quartz, which are confirmed by characteristic ^{57}Fe hyperfine structure (I = 1/2 and 2.19%; Fig. 15; Stegger and Lehmann 1989). Quantitative determinations of spin Hamiltonian parameters (including their orientations relative to the crystal axes and the coordination-polyhedron symmetry axes) and detailed analyses of the fourth-order high-spin parameters by use of the pseudosymmetry approach (Michoulier and Gaite 1972) demonstrated that these Fe^{3+} species all occur as substitutional ions at the tetrahedral Si site and vary from the $[FeO_4]^-$ type without an immediate charge compensator (Mombourquette et al. 1986) to the $[FeO_4/M^+]^0$ species with a monovalent charge compensating ion such as H^+, Li^+ and Na^+ (Weil 1994). These monovalent charge compensators were identified by ^{1}H, ^{7}Li and ^{23}Na superhyperfine structures (Fig. 15). Quantitative determinations of these superhyperfine structures, including those by the ENDOR technique, allow the location of the monovalent charge compensators in the *c*-axis channel. For example, two varieties of $[FeO_4/H^+]^0_{\alpha,\beta}$ have the proton located at the opposite sites of the $[FeO_4]$ tetrahedron but both possess the C_1 site symmetry, which is reduced from the C_2 symmetry of the Si site and is caused by perturbation from the proton location off the two-fold axis in the channel (Halliburton et al. 1989; Minge et al. 1989). Similarly, the $[FeO_4/Li^+]^0_\beta$ center has the C_1 site symmetry at 20 K but transforms to the C_2 symmetry at ~80 K (Minge et al. 1989). Two $[FeO_4/Li^+]^0_\alpha$ centers, on the other hand, maintain the C_2 site symmetry down to 4 K and have been interpreted to have the Li^+ ion along the two-fold axis (Halliburton et al. 1989). These examples demonstrate the power of EPR techniques for providing unambiguous information about the oxidation state, spin state, site occupancy, and substitution mechanisms of impurity ions in minerals (Weil 1994; Pan et al. 2009, 2011).

Furthermore, the capacity of EPR techniques for determination of transition-metal speciation in solids (as well as liquid and gaseous hosts) makes them useful in studies of heavy-metal contaminations, including those associated with mining and milling activities. For example, Cu^{2+} ($3d^9$) is intrinsically paramagnetic and is amenable to EPR studies (Abragam and Bleaney 1970). Similarly, native or radiation-induced Pb^+, Pb^{3+}, Cr^{5+}, Cd^+, Se^-, and Zn^+ ions contain an unpaired electron(s) and are accessible to EPR investigations (Fig. 16; Popescu 1973; Petrov et al. 1993; Nistor et al. 1994; Morin et al. 2002; Pan and Fleet 2002; Di Benedetto

EBSCOhost - printed on 2/13/2023 5:26 AM via . All use subject to https://www.ebsco.com/terms-of-use

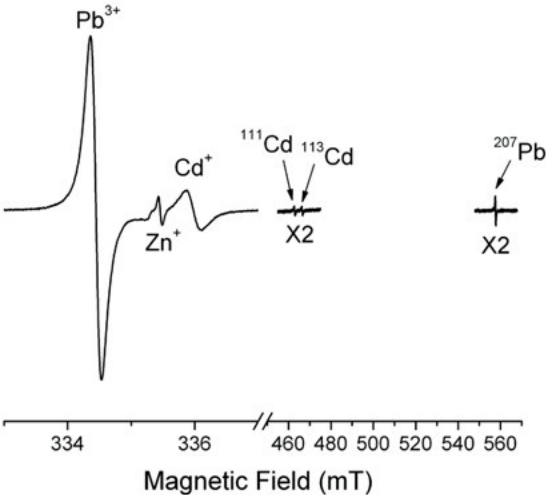


Figure 16. Single-crystal EPR spectra of gamma-ray-irradiated calcite at 9.38 GHz and 110 K showing the Pb^{3+}, Cd^{+} and Zn^{+} centers. Diagnostic ^{207}Pb (I = 1/2 and 22.1%), ^{111}Cd (I = 1/2 and 12.8%) and ^{113}Cd (I = 1/2 and 12.2%) hyperfine lines are marked. Observation of the ^{67}Zn (I = 5/2 and 4.1%) hyperfine structure requires different experimental conditions (not shown).

et al. 2006; Mao and Pan 2012). Likewise, the diamagnetic $[AsO_4]^{3-}$ and $[AsO_3]^{3-}$ groups that commonly occur only as trace constituents in rock-forming minerals can be transformed by ionization irradiation to paramagnetic $[AsO_2]^{2-}$, $[AsO_2]^{0}$, $[AsO_3]^{2-}$, $[AsO_4]^{2-}$, and $[AsO_4]^{4-}$ centers for detection and detailed characterization by EPR (Fig. 17; Knight et al. 1995; Mao et al. 2010a; Lin et al. 2011, 2013; Pan 2013). In addition, EPR studies of 4*f* lanthanides and 5*f* actinides in various minerals (e.g., apatites, monazite, pyrochlore, titanite, and zircon; Fig. 18) are directly relevant to the storage of high-level nuclear wastes (Bray 1978; Ursu and Lupei 1984; Poirot et al. 1988; Kot et al. 1993; Boatner 2002; Pan et al. 2002).

In situ high-temperature and high-pressure EPR experiments

While most EPR experiments have been performed under ambient conditions or at cryogenic temperatures, *in situ* high-temperature and high-pressure EPR experiments would be most relevant to study geological processes occurring in the Earth's interior. Attempts at *in situ* high-temperature and high-pressure EPR experiments can both be traced back to as early as 1950s and have been continued today (Vallauri and Forsbergh 1957; Walsh 1959, 1961; Wait 1963; Müller et al. 1968; Yager and Kingery 1979; Barnett et al. 1985; Bielecki 1988; Bromberg and Chan 1992; Kambe et al. 2003; Sienkiewicz et al. 2005; Náfrádi et al. 2008; Sakurai et al. 2010). We emphasize that *in situ* high-temperature and high-pressure EPR experiments are not restricted to the CW techniques but have been conducted with other techniques such as ENDOR and ESEEM as well (Doyle et al. 1969; Chan and Chung 1989; Baber and Chan 1992; van Wyk et al. 1992; Nokhrin et al. 2005, 2006; Hoffmann et al. 2010).

Poole (1996) classified *in situ* high-temperature EPR experiments into two broad groups: 1) inserting the resonant cavity containing the sample into an oven and 2) heating applied directly to the sample inside the resonant cavity. The former group heats the sample and the resonant cavity simultaneously and, therefore, steps have to be taken to prevent oxidation of the walls of the resonant cavity and to protect the magnetic pole pieces (Poole 1996). The latter group heats the sample only, while the resonant cavity is kept to the room temperature (e.g., Singer et al. 1961; Poole 1996). For example, the classic design of Singer et al. (1961) uses a platinum-coated silica tube resistively heated inside a water-cooled cavity. Experiments with temperatures up to 1675 K have been reported (Poole1996).

One example of *in situ* high-temperature EPR studies is that of Müller et al. (1968), who measured single-crystal EPR spectra for the Fe^{3+} center at the octahedral Al site in $LaAlO_3$

EBSCOhost - printed on 2/13/2023 5:26 AM via . All use subject to https://www.ebsco.com/terms-of-use

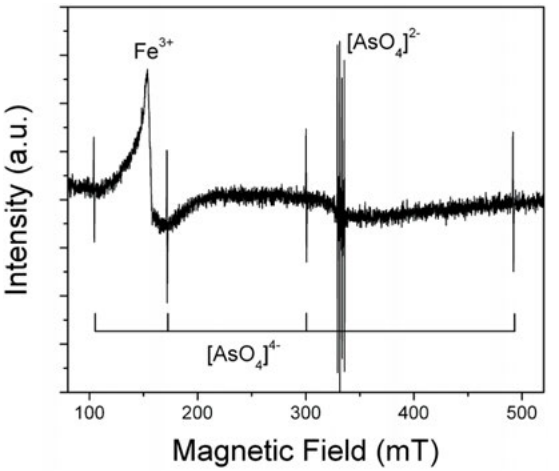


Figure 17. A single-crystal EPR spectrum of gamma-ray-irradiated hemimorphite (Durango, Mexico) at **B**||*c*, 9.38 GHz and 294 K illustrating the $[AsO_4]^{4-}$ and $[AsO_4]^{2-}$ centers arising from the $[AsO_4]^{3-}$ precursors by trapping an electron and hole, respectively (modified from Mao et al. 2010a).

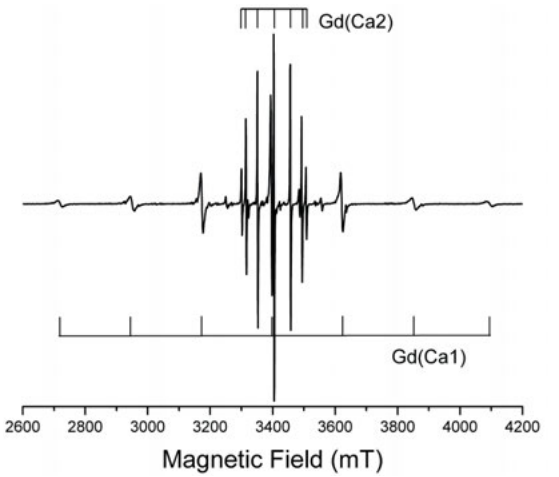


Figure 18. Single-crystal W-band spectrum of two Gd^{3+} ($4f^7$) centers at the Ca1 and Ca2 sites in synthetic fluorapatite, measured at T = 287 K, ν = 94.3767 GHz and magnetic field along the crystallographic *c* axis [AP30-1 containing 1.2(2) wt% Gd_2O_3; modified from Pan et al. 2002b].

from 4.2 to 900 K. These spectra showed that the trigonal-to-cubic phase transition in this perovskite-type compound is of the second order and occurs at 800±10 K, as monitored by the temperature dependence of the zero-field splitting parameter D and the fourth-order parameter B_4^0 of the Fe^{3+} center (Fig. 19).

Another interesting *in situ* high-temperature EPR study on phase transition is that of Lang et al. (1977), who measured Q-band EPR spectra of the substitutional Fe^{3+} center $[FeO_4]^0$ in quartz and isostructural berlinite ($AlPO_4$) from 4.2 K to 860 K (Fig. 20). They showed that spectra of this Fe^{3+} center in berlinite change with temperature and provide direct evidence for the α–β phase transition at 854 K, whereas the signals of the $[FeO_4]^0$ center in quartz was greatly reduced above 670 K and hence did not allow a direct observation of the phase transition at 847 K. However, the changes of the zero-field splitting parameter D and the rhombic angle below 670 K are similar in both minerals. In particular, the temperature dependence, but not the magnitude, of these EPR parameters (Fig. 20a) is similar to that predicted by using a point-dipole model and the Blume-Orbach mechanism with available crystallographic data for quartz. Also, Lang et al. (1977) observed a notable increase in linewidth near the phase transition (Fig. 20b) and interpreted it to represent fluctuations at the phase transition (see also Mao et al. 2013).

EBSCOhost - printed on 2/13/2023 5:26 AM via . All use subject to https://www.ebsco.com/terms-of-use

Shinar and Jaccarino (1983) measured X- and K-band EPR spectra of the substitutional Mn^{2+} center in fluorite and isostructural compounds SrF_2, BaF_2 and PbF_2 to 1500 K and observed systematic temperature dependence of the linewidth. Specifically, the ^{19}F superhyperfine structure superimposed on each ^{55}Mn hyperfine component is found to collapse when the F hopping rate exceeds the ^{19}F hyperfine coupling constant. The integrated intensity and frequency dependence of the line profiles reveal three distinct line-broadening mechanisms: 1) a quasi-static, nonlocal distortion of the cubic crystal field that arises from the growth of ion disorder with increasing T, 2) a local, dynamic broadening related to enhanced anharmonic phonon effects, and 3) a combined Mn-concentration and T-dependent collision broadening that proceeds via dipolar encounters between diffusing Mn^{2+} ions and is proportional to their hopping rate. The last mechanism is closely related to the effects of magnetic tagging on the ^{19}F NMR relaxation in Mn-doped PbF_2 (Shinar and Jaccarino 1983).

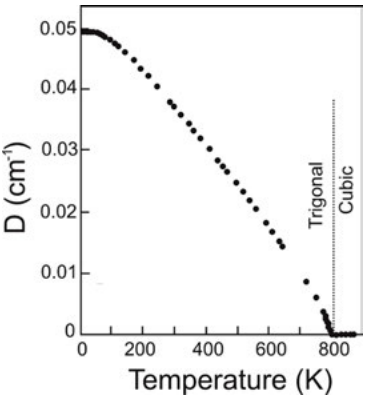


Figure 19. Temperature dependence of the zero-field splitting parameter (D) of the Fe^{3+} center at the octahedral Al site in $LaAlO_3$ across the trigonal-to-cubic phase transition (reproduced with permission from Müller et al. 1968).

Egerton et al. (2000, 2001) investigated the diffusion of Cr^{3+} and Fe^{3+} into rutile by measuring the growth of the substitutional Cr^{3+} and Fe^{3+} signals in a high-temperature cavity up to 1000 K. They showed that the EPR signals at g = 5.04 (Cr^{3+}) and 8.1 (Fe^{3+}) have a parabolic dependence of intensity with time, typical of diffusion processes (Fig. 21). The fitted activation energies for the diffusion of Cr^{3+} and Fe^{3+} into rutile are closely comparable to those obtained from the radio-tracer method (Egerton et al. 2000, 2001).

Designs for *in situ* high-pressure EPR experiments are diverse (Sakai and Pifer 1985; Bromberg and Chan 1992; Hoffman et al. 1993; Poole 1996; Kambe et al. 2003; Sienkiewicz et al. 2005; Náfrádi et al. 2008; Sakurai et al. 2010). Of particular interests are those combined with diamond anvil cells (DAC), for which ultra-high hydrostatic pressures up to ~500 GPa can be made (Ruoff et al. 1992). Sakai and Pifer (1985) first incorporated a regular DAC into a

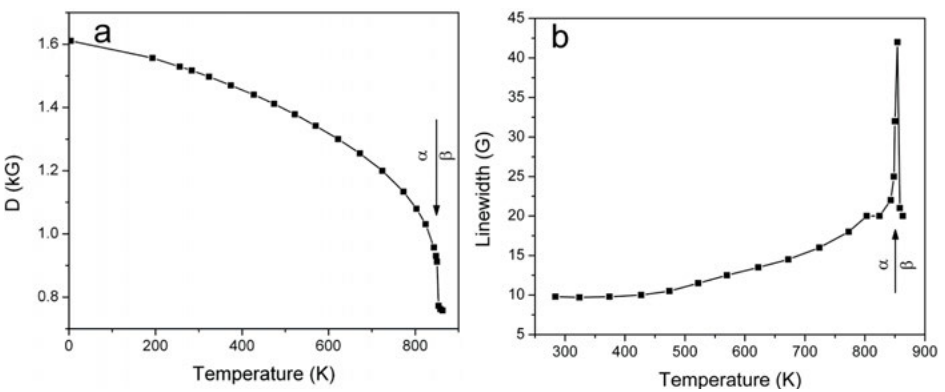


Figure 20. Temperature dependence of (a) the zero-field splitting parameter (D) and (b) the linewidth of the $[FeO_4]^0$ center in berlinite $AlPO_4$ (modified with permission from Lang et al. 1977).

EBSCOhost - printed on 2/13/2023 5:26 AM via . All use subject to https://www.ebsco.com/terms-of-use

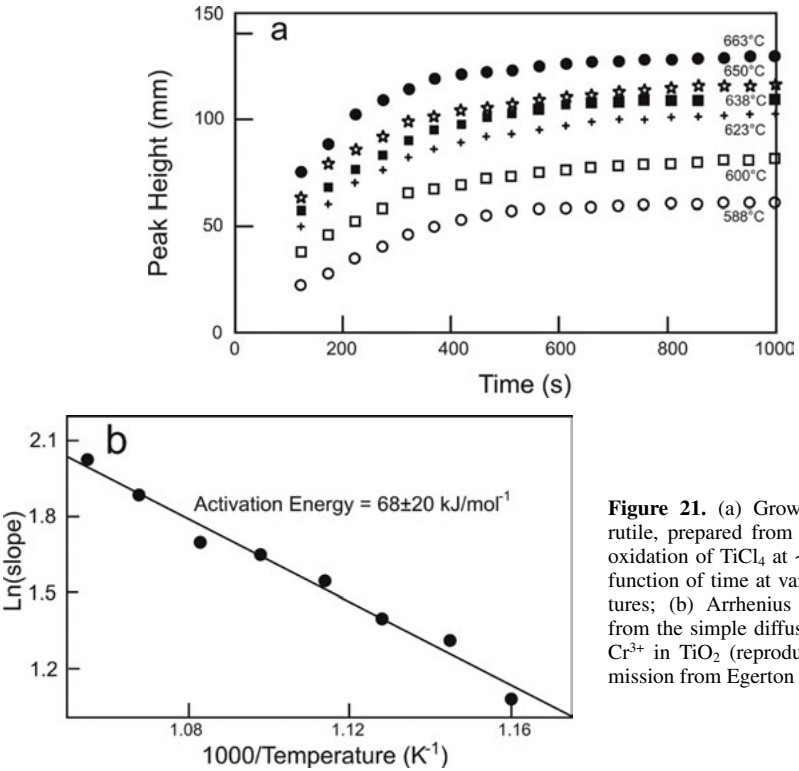


Figure 21. (a) Growth of Cr^{3+} in rutile, prepared from the gas phase oxidation of $TiCl_4$ at ~1500 ºC, as a function of time at various temperatures; (b) Arrhenius plots derived from the simple diffusion model for Cr^{3+} in TiO_2 (reproduced with permission from Egerton et al. 2000).

tunable-shorted X-band waveguide and performed EPR measurements at hydrostatic pressures up to 10 GPa. Their design included a Be-Cu-based gasket, which is an integral part of the DAC and also serves as a linear microwave resonator. One major drawback of this design was its relatively low sensitivity with a resonator quality factor (Q) of only ~300. Bromberg and Chan (1992) improved on this design by using two mutually coupled TiO_2 dielectric resonators with a large spacing of 4.5 mm to accommodate the standard Merrill-Bassett DAC. This configuration produces a tangential microwave magnetic field at the brass gasket for EPR experiments. This design was shown to yield a much improved Q value of ~1200 at room temperature and ~5000 at 2 K, with a single-scan sensitivity of 2.1×10^{15} spins. Sienkiewicz et al. (2005) modified the design of Bromberg and Chan (1992) by using plastic materials, which are transparent to the magnetic field modulation frequency of 100 kHz and thus further improving on the overall sensitivity of the system. This modified double-stacked configuration resonates in the fundamental quasi TE_{011} mode at ~9.2 GHz and has been successfully coupled with the much cheaper sapphire anvil cells (SAC) for hydrostatic pressures up to 2 GPa. The overall sensitivity of this modified system was shown to be only ~3 times less than that yielded by a commercial TE_{102} cavity operating at room pressure (Sienkiewicz et al. 2005).

An example of *in situ* high-pressure EPR experiments applied to minerals is that of Wait (1963), who measured the hydrostatic pressure dependence of the Mn^{2+} center in calcite at room temperature. His results showed that neither the g factor nor the linewidth of this center has any pressure dependence and that the fractional change in the magnitude of the ^{55}Mn hyperfine coupling constant is only one-tenth of the volume change. The zero-field splitting parameter D and the fourth-order parameters (e.g., B_4^0), on the other hand, have marked and linear dependences of pressure (Fig. 22). Wait (1963) noted that the pressure dependence of the zero-field splitting

EBSCOhost - printed on 2/13/2023 5:26 AM via . All use subject to https://www.ebsco.com/terms-of-use

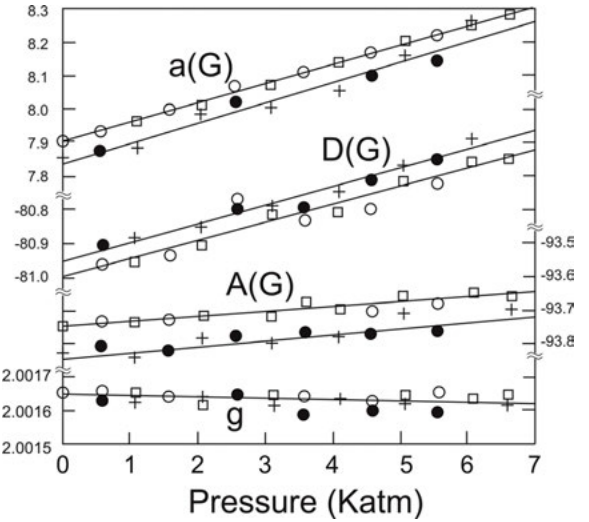


Figure 22. Pressure dependence of spin Hamiltonian parameters (g factor, zero-field splitting parameter D, hyperfine coupling constant *A*, and the fourth-order cubic parameter $a = 24B_4^0$) of the $^{55}Mn^{2+}$ center in calcite. Symbols denote data from different transitions (reproduced with permission from Wait 1963).

parameter can be explained by the point-dipole model. He assumed that D is linearly dependent on the axial crystal field and deduced a local compressibility of ~30% for Mn^{2+} relative to the pure host lattice. Wait (1963) also noted that the fourth-order parameters depend approximately on a second power of the axial crystal field. Subsequently, Barnett et al. (1985) measured single-crystal EPR spectra of this Mn^{2+} center across the calcite-$CaCO_3$(II) displacive phase transition near 1.6 GPa. The substitutional Mn^{2+} ion at the Ca site in $CaCO_3$(II) of space group $P2_1/c$ has a site symmetry of 1. This reduction in site symmetry gives rise to a large anisotropic zero-field splitting parameter E that allows the definition of new principal axes not along any crystallographic directions. These new principal axes are shown to be rotated by Euler angle (30°, +17°, 30°) from the crystallographic *c*-axis of the original calcite. Barnett et al. (1985) also showed that both the zero-field splitting parameters D and E and the Euler angle of the Mn^{2+} center in $CaCO_3$(II) vary significantly with pressure as well.

Nelson et al. (1967), on the basis of single-crystal EPR measurements of the well-known Cr^{3+} center in ruby with the magnetic field parallel to the c-axis from 26 to 76 kbar, noted that the zero-field splitting parameter along this direction (D_c) increases linearly with pressure (Fig. 23). This pressure dependence of the zero-field splitting parameter of the Cr^{3+} center in ruby is particularly interesting, because it is potentially useful for independent pressure calibration in future *in situ* high-pressure EPR experiments.

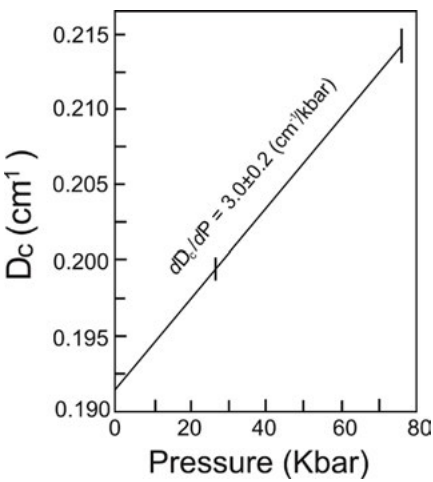


Figure 23. Pressure dependence of the zero-field splitting parameter D_c of the Cr^{3+} center in ruby (reproduced with permission from Nelson et al. 1967).

EBSCOhost - printed on 2/13/2023 5:26 AM via . All use subject to https://www.ebsco.com/terms-of-use

These examples demonstrate that *in situ* high-temperature and high-pressure EPR studies are capable of providing large amounts of structural and dynamic information, from phase transition to spin dynamics, diffusion and many more. However, there have been only a few reports of *in situ* EPR studies at combined high temperatures and high pressures. Berlinger (1982) described a K-band system for applying an uniaxial stress up to 35 kp and temperatures up to 1300 K. Ibraham and Seehra (1992) described an apparatus for *in situ* X-band EPR studies of coal conversion processes from ambient temperature to 500 °C for gaseous pressures up to 800 psi.

Optically detected magnetic resonance (ODMR) and mineral coloration

Optically detected magnetic resonance (ODMR) measures the resonant absorption of microwave radiation through changes induced by optical means (Geschwind 1972; Davies 1973; Janssen et al. 2001). Major advantages of ODMR over conventional EPR techniques include superior sensitivities resulting from detection in the optical region and investigation in the excited states rather than the ground states. Moreover, resonance signals investigated by ODMR are specific to individual species by selection of the corresponding luminescence/absorption bands (Janssen et al. 2001), making this technique particularly powerful in the study of mineral coloration (Meyer et al. 1984; Hayes et al. 1984; Gruber et al. 1997; Janssen et al. 2001; Krambrock et al. 2004). For example, the origin of smoky color in quartz has been the subject of long debates (Nassau and Prescott 1975, Schirmer 1976). An ODMR study of the $[AlO_4]^0$ center in smoky quartz at 1.4 K provided direct evidence for linkage between the 1.96(5) and 2.85(5) eV bands and this center. Similarly, Hayes et al. (1984) performed ODMR measurements on the 2.8 eV blue luminescence in quartz and showed it to arise from a triplet state with a very large zero-field splitting with D = 22.6±0.05 GHz and E = 1.60±0.05 GHz. They also determined the principal axes of the triplet and proposed a structural model involving a transient oxygen-vacancy-interstitial pair, which has been supported by a subsequent theoretical calculation (Fisher et al. 1989).

In particular, the ODMR techniques (e.g., van Oort et al. 1988; Hiromitsu et al. 1992; Westra et al. 1992; Gruber et al. 1997) have been widely applied to investigate the color centers in diamond, including the well-known nitrogen-vacancy (N-V) center that has potential applications for spintronics, quantum cryptography and quantum computing (Gruber et al. 1997; Jelezko et al. 2004; Hanson et al. 2006; Dutt et al. 2007; Mizuochi et al. 2012). The N-V center consists of a substitutional nitrogen atom adjacent to a carbon vacancy containing an electron and has a C_{3v} symmetry, with the three-fold symmetry axis along the [111] direction of the host crystal (Davies and Hamer 1976, Loubser and van Wyk 1978; Redman et al. 1991). Gruber et al. (1997) noted that individual N-V centers can be detected at room temperature by confocal fluorescence microscopy and used ODMR to demonstrate that magnetic resonance on single centers at room temperature is feasible as well.

Another ODMR study by Westra et al. (1992) showed that the long-lived luminescence with a zero-phonon line at 441 nm (2.818 eV) in brown diamond crystals originates from a photo-excited phosphorescent triplet state (Fig. 24). Westra et al. (1992) measured the magnetic-field dependence and the angular variation of the ODMR peak positions, and fitted these experimental data to the triplet-state (S = 1) spin Hamiltonian, yielding $g = 2.00$, $D = 924 \pm 2$ MHz and $E = 198 \pm 2$ MHz. The principal axes of the zero-field fine-structure tensor were found to be along the [100], [011] and [01 $\bar{1}$] directions of the diamond crystal, indicative of a rhombic site symmetry for this defect. These data led Westra et al. (1992) to interpret this center to represent impurity oxygen atoms at the carbon sites [i.e., the O–C–O defect in the (110) plane].

EPR as structural probe for other Earth and planetary materials

Numerous EPR studies of natural and synthetic glasses, including those relevant to magmatic melts, have been made and provide a wide range of information from the coordination

EBSCOhost - printed on 2/13/2023 5:26 AM via . All use subject to https://www.ebsco.com/terms-of-use

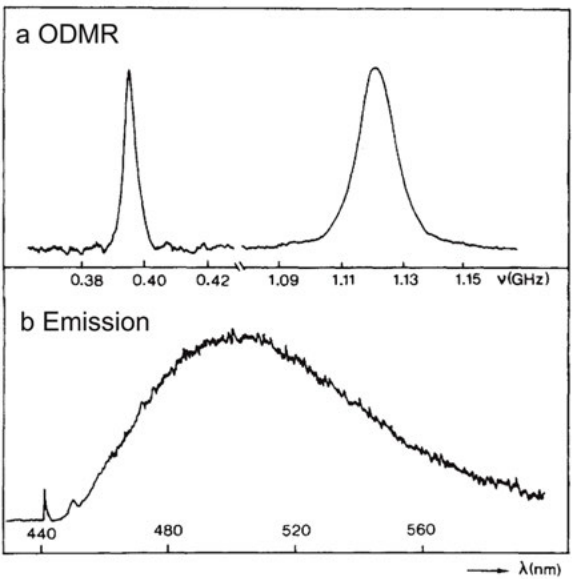


Figure 24. (a) Zero-field ODMR and spectrum of the 2.818-eV center in brown diamond and (b) ODMR intensity as a function of the detection wavelength (reproduced with permission from Westra et al. 1992).

environments and polymerizations of the network formers to the structures and roles of network modifiers and the effects of composition, temperature, pressure, and redox equilibrium (e.g., Morris and Haskin 1974; Morris et al. 1974; Lauer and Morris 1977; Iwamoto et al. 1983; Calas 1988; Petrini et al. 1999; Griscom 2011). For example, Petrini et al. (1999) measured EPR spectra to identify different Fe^{3+} sites in volcanic glasses from the Neapolitan Yellow Tuff and showed that the relative abundances of these species vary among the samples investigated. Griscom (2011) reviewed half a century of research on radiation-induced defects in pure and doped silica glasses and pointed out that EPR provides the best means of identifying specific defects responsible for the otherwise difficult-to-attribute optical signals. For example, EPR identifications of the classic E′ center and its B and Al counterparts show the presence of three-coordinated Si, B and Al in silica glasses (Griscom et al. 1976; Brower 1979; Weeks et al. 2008; Griscom 2011; Mashkovtsev et al. 2013).

Similarly, extensive EPR studies have been carried out to investigate structures and applications of various paramagnetic transition metals (e.g., V^{4+}, Mn^{2+}, Fe^{3+}, Cu^{2+}) and free radicals in coals, bitumen, tar sands, asphaltenes, and crude oils from wide geographic locations and diverse geological settings (Petrakis and Grandy 1983; Malhotra and Buckmaster 1984; Bresgunov et al. 1990; Calemma et al. 1995; Galtsev et al. 1995; Guedes et al. 2006; Piccinato et al. 2009; Pilawa et al. 2009; Augustyniak-Jabłokow et al. 2010). For example, a comprehensive X- and Q-band EPR study by Zhang et al. (1994) showed that the Mn^{2+} signal in Argonne and Alberta coals arises from this ion in the calcite impurity. Malhotra and Buckmaster (1984) conducted a Q-band EPR study on a variety of petroleum asphaltenes and divided them into two groups: one with vanadyl square-planar complexes in the form of porphyrins and the other with oxovanadium(IV) etio-porphyrins. The presence of porphyrins in asphaltenes was subsequently confirmed by the ^{14}N and ^{1}H ENDOR spectra of Atherton et al. (1987). Wong and Yen (2000) used the oxovanadium complexes detected by EPR to investigate the petroleum asphaltene macrostructures under different temperatures and microwave powers. Guedes et al. (2006) used the EPR signals of VO^{2+} and organic free radicals to evaluate the degradation

EBSCOhost - printed on 2/13/2023 5:26 AM via . All use subject to https://www.ebsco.com/terms-of-use

of Arabian and Colombian crude oils that were subjected to photochemical weathering under tropical conditions.

Skrzypczak-Bonduelle et al. (2008) reported π-radicals stabilized by the aromatic structure in carbonaceous matter of primitive siliceous rocks and noted that the linewidths and line shapes vary systematically with time, from Gaussian-Lorentzian (recent) to Lorentzian (~2000 Ma) and supra-Lorentzian (~3500 Ma). These authors suggested that the supra-Lorentzian line shape arises from low-dimensional spatial distribution of electron spins and proposed a relationship between the line shape and the age of the organic matter in the range from 600 Ma to 3500 Ma (Fig. 25).

In addition, extensive EPR studies have been made on paramagnetic transition-metal ions, ferromagnetic centers, and free radicals in lunar and Martian samples and meteorites (e.g., Weeks 1973; Tsay 1988; Yamanaka et al. 1993; Sasaki et al. 2003; Delpoux et al. 2008). For example, Tsay (1988) proposed a miniaturized spectrometer for NASA's Mars-Rover-Sample mission to perform *in situ* EPR analyses of Martian samples: 1) detection of active oxygen species and characterization of Martian surface chemistry and photocatalytical oxidation processes, 2) detection of paramagnetic transition-metal ions and ferromagnetic centers in Martian minerals, and 3) detection of diagnostic organic free radicals to search for ancient organic compounds in Martian soils and sedimentary deposits. Sasaki et al. (2003) used EPR to confirm the presence of nanophase metallic iron as evidence for space weathering of S-type asteroids.

Quantitative EPR analysis

The fact that the absorption intensity of EPR spectra is proportional to the concentration of unpaired spins makes EPR useful for quantitative analysis, with wide applications to Earth and planetary sciences from chemical analysis to dosimetry and EPR dating (Ikeya 1993; Dyrek et al. 1996, 2003; Blakley et al. 2001; Weil and Bolton 2007; Eaton et al. 2009). All previous studies emphasized that quantitative EPR analysis requires fulfillment of several conditions.

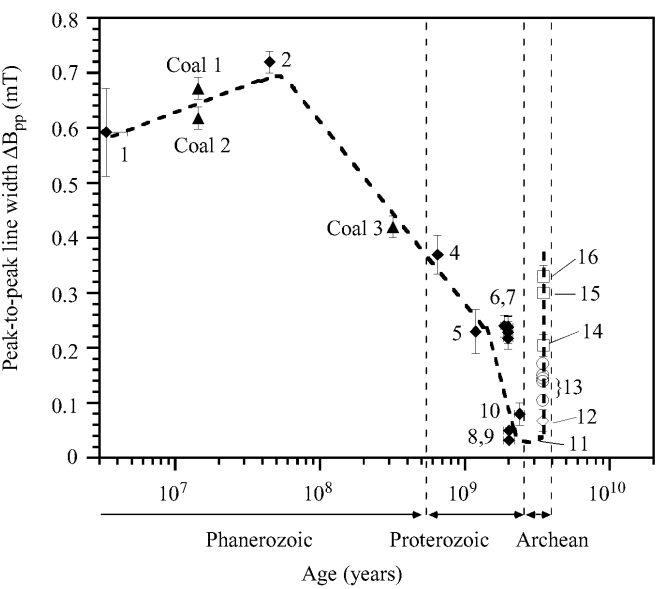


Figure 25. Variation of the peak-to-peak linewidth of the insoluble-organic-matter (IOM) radicals as a function of the age of the host cherts (1-16) and coals (reproduced with permission from Skrypczak-Bonduelle et al. 2008).

EBSCOhost - printed on 2/13/2023 5:26 AM via . All use subject to https://www.ebsco.com/terms-of-use

For example, Dyrek et al. (1996) noted the importance of homogenous standards, in addition to optimal experimental setting to eliminate instrumental interferences. Blakley et al. (2001) discussed the need of matching the resonator Q for standard and sample. Eaton et al. (2009) provided the most comprehensive review about the state-of-the-art quantitative EPR analysis and discussed a large number of topics from samples to instruments, standards and software.

One remarkable example of early quantitative EPR analyses applied to Earth materials is that Saraceno et al. (1961), who first established that almost all vanadium in crude oils exists in the +4 oxidation state and then demonstrate that EPR can be utilized to quantitatively determine the vanadium concentration in petroleum down to the sub-ppm level. Morris and Haskin (1974) measured the concentrations of Eu^{2+} and Gd^{3+} (an analog for diamagnetic Eu^{3+}) in quenched silicate glasses to investigate the Eu^{2+}/Eu^{3+} redox equilibrium, with applications to the common Eu anomalies in igneous rocks and other geological environments (see also Morris et al. 1974; Lauer and Morris 1977).

Natural radiation such as alpha particles, electrons and gamma rays emitted from radioactive elements in the material or its environment bombards the material and produces paramagnetic defects or radicals. These radiation-induced paramagnetic defects or radicals, if sufficiently stable, will accumulate with time and can be analyzed by quantitative EPR and thereby correlated to the total dose of natural radiation: i.e., the basis of EPR dosimetry and dating (Ikeya 1993, 2004). Therefore, one major aspect of EPR dosimetry and dating is the accurate determination of the spin concentration in the sample studied, for which all instrumental calibrations and standard characterizations required for quantitative EPR are important here as well. Indeed, significant uncertainties and errors in early attempts of EPR dating were largely attributed to either insufficient instrumental calibrations or poor signal-to-noise ratios in the experimental spectra (Ikeya 1993, 2004; Grün 2008).

Applications of EPR radiation dosimetry to Earth and planetary sciences are many and include monitoring the migration and pathway of radioactive nuclei in the environment (Ikeya 1993, 2004; Allard et al. 2007; Sun et al. 2007) and as a tool for the exploration of uranium deposits in sedimentary basins (Pan et al. 2006, 2012; Hu et al. 2008; Morichon et al. 2010). For example, EPR studies of natural and artificially irradiated quartz (Botis et al. 2005, 2008; Nilges et al. 2008, 2009; Pan et al. 2008, 2009b) have established a series of superoxide radicals and linked them to bombardments of alpha particles emitted from uranium and thorium. Also, these alpha-particle-induced defects in quartz from mineralized areas in the uranium-rich Athabasca basin (Canada) are one to two orders of magnitude higher in intensity than those in samples from barren areas. Moreover, quantitative EPR analysis of these alpha-particle-induced defects in quartz can be used to define and trace pathways of uranium-bearing fluids and thus useful as an exploration tool for uranium deposits in sedimentary basins (Pan et al. 2006, 2013; Hu et al. 2008).

The total radiation dose of a radiation-induced paramagnetic center in a sample is the product of the radiation dose rate and the time elapsed after its formation or an event that zeroed its spin concentration (Ikeya 1993, 2004). Therefore, application of EPR dating, in addition to accurate determination of the total radiation dose, requires knowledge about the radiation dose rate. This is accomplished by either the additive or regenerative dose method measuring the dependence of the intensity (or amplitude) of selected EPR lines on artificial radiation doses (Ikeya 1993; Skinner 2000; Grün 2008; Tissoux et al. 2008). The time period covered by the EPR technique spans from a few thousand years to several million years, far beyond the capability of the ^{14}C method. The most commonly used materials for EPR dating are carbonates (calcite and aragonite in stalagmite, travertine, coral, shell, foraminifera, etc.), sulfates (gypsum and anhydrite from fault gouge, desert deposit, cave, lake, etc.), phosphates (hydroxylapatite in fossil bones and teeth), silicates (quartz, feldspar and zircon in volcanic rocks, sand, sandstone, fault gouge, etc.) and carbonaceous matter (Ikeya 1993).

EBSCOhost - printed on 2/13/2023 5:26 AM via . All use subject to https://www.ebsco.com/terms-of-use

For example, Koshchug et al. (2005) used the well-established $[AlO_4]^0$ center in quartz (Nuttall and Weil 1981; Walsby et al. 2003) to reconstruct the evolution of the Elbrus volcano in the Main Caucasus Range, Russia, which is one of the highest volcanoes in Europe and formed from multiple cycles of eruption. Comparison of their EPR results with data from geomorphological, ^{14}C, K-Ar and SHRIMP U-Th methods shows agreements for the Late Neo-Pleistocene and Holocene activities but that the EPR ages (250-340 ka) for the oldest rocks are only about half of those (670-720 ka) from the K-Ar and SHRIMP U-Th techniques. These authors attributed the underestimation of the EPR ages for the oldest rocks to mainly uncertainties with the paleodose measurements and the recombination of defect centers during geological time. Skinner (2000) also pointed out that the biggest challenge of the EPR dating technique is the determination of the sample's radiation history. Another complication is the presence of multiple magnetically similar radiation-induced defects in minerals that are commonly utilized in EPR dating (Ikeya 1993; Toyoda and Schwarcz 1997; Nokhrin et al. 2005, 2006; Lin et al. 2006; Nilges et al. 2008, 2009; Pan et al. 2008, 2009b; Mashkovtsev and Pan 2012a). Alternative methods of EPR dating with applications to Earth and planetary sciences are also available. For example, Binet et al. (2007) reported that the EPR lineshapes of the radicals correlate with the maturity of carbonaceous matter and thus can be used an age marker for old (>1 b.y.) carbonaceous matter (Delpoux et al. 2008).

ACKNOWLEDGMENTS

We wish to thank Grant Henderson for invitation, Franco Di Benedetto, Grant Henderson and Rudolf I. Mashkovtsev for reviews, and the Natural Science and Engineering Research Council (NSERC) of Canada for financial support.

REFERENCES

Abragam Am Bleaney B (1970) Electron Paramagnetic Resonance of Transition Ions. Clarendon Press, Oxford.

Allard T, Calas G, Ildefonse P (2007) Reconstruction of past U migration in a sedimentary deposit (Coutras, France): Implications for a radiowaste repository: Chem Geol 239:50–63

Asher JR, Kaupp M (2007) Hyperfine coupling tensors of benzosemiquinone radical anion from Car-Parrinello molecular dynamics. ChemPhysChem 8:69-79

Atherton NM, Fairhurst SA, Hewson GJ (1987) ENDOR spectra of vanadyl complexes in asphaltenes. Magn Reson Chem 25:829-830

Augustyniak-Jabłokow MA, Yablokov YV, Andrzejewski B, Kempiński W, Łoś Sz, Tadyszak K, Yablokov MY, Zhikharev VA (2010) EPR and magnetism of the nanostructured natural carbonaceous material shungite. Phys Chem Miner 37:237-247

Bacquet G, Dugas J, Belin C (1975) RPE de BO_2 dans la calcite synthetique irradiee. Magn Reson Relat Phenom Proc No Congr AMPERE, 18th, Nottingham 1:161-162

Barber JL, Chan IY (1992) Pressure dependence of zero-field splitting in organic triplets. III. Vibronic systems. J Chem Phys 96:5591-5599

Barnett JD, Nelson HM, Tyagi SD (1985) High-pressure EPR study of the calcite-$CaCO_3$(II) displacive phase transformation near 1.6 GPa. Phys Rev 31:1248-1257

Berlinger W (1982) High-temperature EPR cavity for application of uniaxial stress. Rev Sci Instrum 53:338-341

Bielecki K (1988) A high pressure EPR study of Cr^{3+} doped deuterated potassium aluminium alum. Phys Stat Solid B 148:K53-K56

Binet L, Gourier D, Skrzypczak-Bonduelle A, Delpoux O, Derenne S (2007) EPR and primitive life: dating and visualizing the organic matter in the oldest rocks. Lunar Planet Sci XXXVIII:1533

Blakley RL, Henry DD, Morgan WT, Clapp WL, Smith CJ, Barr D (2001) Quantitative electron paramagnetic resonance: the importance of matching the Q-factor of standards and samples. Appl Spectrosc 55:1375-1381

Boatner LA (2002) Synthesis, structure, and properties of monazite, pretulite, and xenotime. Rev Mineral Geochem 48:87-121

Botis SM, Pan Y (2009) First-principles calculations on the $[AlO_4/M^+]_0$ (M=H,Li,Na,K) defects in quartz and crystal-chemical controls on the uptake of Al. Mineral Mag 73:537-550

EBSCOhost - printed on 2/13/2023 5:26 AM via . All use subject to https://www.ebsco.com/terms-of-use

Botis SM, Pan Y (2010) Theoretical modeling of the Al paramagnetic center and its precursors in stishovite. Phys Chem Miner 37:119-127
Botis SM, Pan Y (2011) Modeling of $[AlO_4/Li^+]^+$ paramagnetic defects in α-quartz. Can J Phys 89:809-816
Botis SM, Nokhrin S, Pan Y, Xu Y, Bonli T, Sopuck V (2005) Natural radiation-induced damage in quartz. I. Correlations between cathodoluminescence colors and paramagnetic defects. Can Mineral 43:1565-1580
Botis SM, Pan Y, Nokhrin S, Nilges MJ (2008) Natural radiation-induced damage in quartz. III. A single-crystal EPR study of drusy quartz from the Athabasca basin, Saskatchewan. Can Mineral 46:122-135
Botis SM, Adriaens D, Pan Y (2009) Ab initio calculations of the (O_2^{3-}–Y^{3+}) center in CaF_2 and SrF_2: its electronic structure and hyperfine constants. Phys Chem Miner 36:1-7
Bray JE (1978) Paramagnetic resonance of tetravalent neptunium-237 in Cs_2ZrCl_6. Phys Rev B 18:2973-2977
Bresgunov AYu, Dubinsky AA, Poluektov OG, Vorob'eva GA, Lebedev YaS (1990) Electron paramagnetic resonance of coals: New approaches to an old problem with multifrequency electron paramagnetic resonance and spin echo. J Chem Soc Faraday Trans 86:3185-3189
Bromberg SE, Chan IY (1992) Enhanced sensitivity for high-pressure EPR using dielectric resonators. Rev Sci Instrum 63:3670-3673
Brower KL (1979) Electron paramagnetic resonance of Al E'_1 centers in vitreous silica. Phys Rev B 20:1799-1811
Brustolon M, Giamello E (2009) Electron Paramagnetic Resonance: A Practitioner's Toolkit. John Wiley & Sons
Calas G (1988) Electron paramagnetic resonance. Rev Mineral 18:513-571
Calemma V, Iwanski P, Nali R (1995) Structural characterization of asphaltenes of different origins. Energy & Fuel 9:225-230
Chan IY, Chung WM (1989) Electronic spin-echo experiments under high pressure. J. Chem Phys 91:5852-5853
Clozel B, Gaite J-M, Muller J-P (1995) Al-O-Al paramagnetic defects in kaolinite. Phys Chem Miner 22:351-356
Cohen AJ, Hassan F (1974) Ferrous and ferric ions in synthetic α-quartz and natural amethyst. Am Mineral 59:719–728
Cressey G, Henderson CMB, van der Laan G (1993) Use of L-edge X-ray absorption spectroscopy to characterize multiple valence states of 3d transition metals; a new probe for mineralogical and geochemical research. Phys Chem Miner 20:111
Davies G, Hamer MF (1976) Optical studies of the 1.945 eV vibronic band in diamond. Proc Royal Soc London, Series A 348:285
Davies JJ (1973) Optically-detected magnetic resonance and its applications. Contemp Phys 17:275-294
Dedushenko SK, Makhina IB, Mar'in AA, Mukhanov VA, Perfiliev YD (2004) What oxidation state of iron determines the amethyst colour. Hyperf Interact 156/157:417-422
Delpoux O, Gourier D, Binet L, Vezin H, Derenne S, Robert F (2008) CW- and pulsed-EPR of carbonaceous matter in primitive meteorites: Solving a lineshape paradox. Spectrochim Acta Part A 69:1301-1310
Di Benedetto F, Costagliola P, Benvenuti M, Lattanzi P, Romanelli M, Tanelli G (2006) Arsenic incorporation in natural calcite lattice: Evidence from electron spin echo spectroscopy. Earth Planet Sci Lett 246:458-465
Di Benedetto F, D'Acapito F, Fornaciai G, Innocenti M, Montegrossi G, Pardi LA, Tesi S, Romanelli M (2010) A Fe K-edge XAS study of amethyst. Phys Chem Miner 37:283-289
Doan PE, Fan C, Davoust CE, Hoffman BM (1991) A simple method for hyperfine-selective heteronuclear pulsed ENDOR via proton suppression. J Magn Reson 95:196-200
Doyle WT, Dutton TF, Liu HP (1969) High pressure ENDOR cavity. Rev Sci Instrum 40:171-172
Dutt MVG, Childress L, Jiang L, Togan E, Maze J, Jelezko F, Zibrov AS, Hemmer PR (2007) Quantum register based on individual electronic and nuclear spin qubits in diamond. Science 316:1312–1316
Dyrek K, Rokosz A, Madej A, Bidzinska E (1996) Quantitative EPR studies of transition metal ions in oxide, aluminosilicate and polymer matrices. Appl Magn Reson 10:319-338
Dyrek K, Bidzinska E, Adamski A (2003) Quantitative EPR – a versatile tool in fundamental and applied studies. Mol Phys Rep 37:9–23
Eachus RS, Symons MCR (1968) oxides and oxyions of the non-metals. Part X. The BO_3^{2-} impurity centre in irradiated calcium carbonate. J Chem Soc (A) 2438-2441
Eaton GR, Eaton SE, Barr DP, Weber RT (2009) Quantitative EPR. Springer, New York
Egerton TA, Harris E, Lawson EJ, Mile B, Rowlands CC (2000) An EPR study of diffusion of chromium in rutile. Phys Chem Chem Phys 2:3275-3281
Egerton TA, Harris E, Lawson EJ, Mile B, Rowlands CC (2001) An EPR study of diffusion of iron in rutile. Phys Chem Chem Phys 3:497-504
Fan C, Doan PC, Davoust CE, Hoffman BM (1992) Quantitative studies of davies pulsed ENDOR. J Magn Res 98:62-72
Feher G (1959) Electron spin resonance experiments on donors in silicon. I. Electronic structure of donors by the electron nuclear double resonance technique. Phys Rev 114:1219-1244
Fisher AJ, Hayes W, Stoneham AM (1989) Theoretical studies of the blue luminescence in α-quartz. J Chem Soc Faraday Trans 85:467-469

EBSCOhost - printed on 2/13/2023 5:26 AM via . All use subject to https://www.ebsco.com/terms-of-use

Galtsev VE, Armetov IM, Grinberg OYa (1995) Asphaltene association in crude oil as studied by ENDOR. Fuel 74:670-673

Gemperle C, Schweiger A (1991) Pulsed electron-nuclear double resonance methodology. Chem Rev 91:1481–1505

Geschwind S (1972) Optical techniques in EPR in Solids. *In*: Electron Paramagnetic Resonance. Geschwind S (ed), Plum, New York, p 121-216

Gibbs GV, Cox DF, Boisen MB, Downs RT, Ross NL (2003) The electron localization function: a tool for locating favorable proton docking sites in the silica polymorphs. Phys Chem Miner 30:305–316

Gibbs GV, Cox DF, Ross NL (2004) A modeling of the structure and favourable H-docking sites and defects for the high-pressure silica polymorph stishovite. Phys Chem Miner 31:232-239

Goodman BA, Hall PL (1994) Electron paramagnetic resonance spectroscopy. *In*: Clay Mineralogy: Spectroscopic and Chemical Determinative Methods. Wilson MJ (ed) Springer, p 173-221

Griscom DL (2011) Trapped-electron centers in pure and doped glassy silica: A review and synthesis. J Non-Cryst Solids 357:1945-1962

Griscom DL, Sigel GHJr, Ginther RJ (1976) Defect centers in a pure-silica-core borosilicate-clad optical fiber: ESR studies. J Appl Phys 47:960–967

Gruber A, Dräbenstedt A, Tietz C, Fleury L, Wrachtrup J, von Borczykowski C (1997) Scanning confocal optical microscopy and magnetic resonance on single defect centers. Science 276:2012-2014

Grün R (2008) Electron spin resonance (ESR) dating. *In*: Encyclopedia of Archeology, Pearsall D (ed), Elsevier, Oxford, p 429-433

Guedes CL, Di Mauro E, De Campos A, Mazzochin LF, Bragagnolo GM, De Melo FA, Piccinato MT (2006) EPR and fluorescence spectroscopy in the photodegradation study of Arabian and Colombian crude oils. Int J Photoenergy 2006:48462(1-6)

Halliburton LE, Hantehzadeh MR, Minge J, Mombourquette MJ, Weil JA (1989) EPR study of Fe^{3+} in alpha quartz: a reexamination of the lithium-compensated center. Phys Rev B40:2076-2081

Hanson R, Gywat O, Awschalom DD (2006) Room-temperature manipulation and decoherence of a single spin in diamond. Phys Rev B 74:161203

Hayes W, Kane MJ, Salminen O, Wood RL, Doherty SP (1984) ODMR of recombination centres in crystalline quartz. J Phys C: Solid State Phys 17:2943-2951

Hebert LB, Rossman GR (2008) Greenish quartz from the Thunder Bay amethyst mine Panorama, Thunder Bay, Ontario, Canada. Can Mineral 46:61-74

Hiromitsu II, Westra J, Glasbeek M (1992) Cross-relaxation dynamics of the N-V center in diamond as studied via optically detected microwave recovery transients. Phys Rev B 46:10600-10612

Hoffman SK, Krupski M, Hilszer W (1993) High-pressure EPR studies of intermolecular interactions in solids. Appl Magn Reson 5:407-424

Hoffmann SK, Goslar J, Lijewski S, Jankowska A, Kowalak S (2010) Electron spin resonance (ESR) and electron spin echo envelope modulation (ESEEM) studies on the ultramarine analogs obtained from zeolite A with various alkaline cations at different temperatures. Micropor Mesopor Materials 127:205-212

Hu B, Pan Y, Botis SM, Rogers B, Kotzer T & Yeo G (2008) Radiation-induced defects in drusy quartz, Athabasca basin: A new aid to exploration for U deposits. Econ Geol 103:1571-1580

Ibrahim MM, Seehra MS (1992) An apparatus for in situ high temperature/high pressure ESR spectroscopy and its applications in coal conversion studies. ACS Division Fuel Chem Preprints 37:1131-1140

Ikeya M (1993) New Applications of Electron Paramagnetic Resonance: ESR Dating, Dosimetry, and Spectroscopy. World Scientific, Singapore

Ikeya M (2004) ESR dating, dosimetry and microscopy for terrestrial and planetary materials. Electron Paramagn Reson 19:1-32.

Iwamoto N, Hikada H, Makino Y (1983) State of Ti^{3+} ions and Ti^{3+}–Ti^{4+} redox reaction in reduced silicate glasses. J Non-Crystal Solids 58:131-141

Janssen G, Bouwen A, Casteels P, Goovaerts E (2001) Implementation of optically detected magnetic resonance spectroscopy in a commercial W-band cylindrical cavity. Rev Sci Instrum 72:4295-4296

Jelezko F, Gaebel T, Popa I, Gruber A, Wrachtrup J (2004) Observation of coherent oscillations in a single electron spin. Phys Rev Lett 92:076401

Kambe T, Fujiwara M, Oshima K, Garaj S, Sienkiewisz A, Forró L (2003) High pressure ESR system with double-stacked dielectric resonators – its application to the polymerization of the TDAE-C60 organic ferromagnet. J Phys Soc Japan 72:151-155

Kaupp M, Bühl M, Malkin VG (2004) Calculation of NMR and EPR Parameters. Wiley-VCH, Weinheim

Keijzers CP, Reijerse EJ, Stam P, Dumont MF, Gribnau MCM (1987) MAGRES: A general program for electron spin resonance, ENDOR and ESEEM. J Chem Soc Faraday Trans 83:3493–3503

Knight LB, Jones GC, King GM, Babb RM (1995) Electron spin resonance and theoretical studies of the PO_2 and AsO_2 radicals in neon matrices at 4 K: laser vaporization and x-irradiation radical generation techniques. J Chem Phys 103:497-505

EBSCOhost - printed on 2/13/2023 5:26 AM via . All use subject to https://www.ebsco.com/terms-of-use

Koshchug DG, Gazeev VM, Gurbanov AG, Shabalin RV, Vyatkin SV (2005) ESR dating and evolution of the Elbrus volcano. Appl Magn Res 28:331-342

Kot WK, Edelstein NM, Abraham MM, Boatner LA (1993) Zero-field splitting of Cm^{3+} in $LuPO_4$ single crystals. Phys Rev B 48:12704-12712

Krambrock K, Pinheiro MVB, Guedes KJ, Medeiros SM, Schweizer S, Spaeth J-M (2004) Correlation of irradiation-induced yellow color with the O^- hole center in tourmaline. Phys Chem Miner 31:168-175

Lang R, Calvo C, Datars WR (1977) Phase transformation in $AlPO_4$ and quartz studied by electron paramagnetic resonance of Fe^{3+}. Can J Phys 55:1613-1620

Lauer HV, Morris RV (1976) Redox equilibria of multivalent ions in silicate glasses. J Am Ceram Soc 60:443-451

Lebedev YS (1990) High-frequency continuous-wave electron spin resonance. In Kevan L, Bowman MK (eds), Modern Pulsed and Continuous-wave Electron Spin Resonance, 365-404

Li Z, Pan Y (2011) First-principles study of boron oxygen hole centers in crystals: Electronic structures and nuclear hyperfine and quadrupole parameters. Phys Rev B 84:115112.

Li Z, Pan Y (2012) First-principles calculations of the E'_1 center in quartz: Structural models, ^{29}Si hyperfine parameters and association with Al impurity. In: Quartz, Deposits, Mineralogy and Analytics. Götze J, Möckel R (eds) Springer, Berlin, p 161-175

Li R, Li Z, Mao M, Pan Y (2011) Single-crystal EPR and DFT studies of a $[BO_4]^0$ center in datolite: Electronic structure, formation mechanism and implications. Phys Chem Miner 38:33-43

Li R, Li Z, Pan Y (2012) Single-crystal EPR and DFT study of a ^{VI}Al-O-^{VI}Al center in jeremejevite: Electronic structure and ^{27}Al hyperfine constants. Phys Chem Miner 39: 491-501

Lin M, Yin G, Ding Y, Cui Y, Chen K, Wu C, Xu L (2006) Reliability study on ESR dating of the aluminum center in quartz. Radiat Measur 41:1045-1049

Lin J, Pan Y, Chen N, Mao M, Li R, Feng R (2011) Arsenic incorporation in colemanite from borate deposits: Data from ICP-MS, μ-SXRF, XAFS and EPR analyses. Can Mineral 49:809-822

Lin J, Chen N, Nilges MJ, Pan Y (2013) Arsenic speciation in synthetic gypsum ($CaSO_4{\cdot}2H_2O$): A synchrotron XAS, single-crystal EPR and pulsed ENDOR study. Geochim Cosmochim Acta106: 524-540

Loubser JHN, van Wyk JA (1978) Electron spin resonance in the study of diamond. Reports Progress Phys 41:1201-1246

Malhotra VM, Buckmaster HA (1984) 34 GHz e.p.r. study of vanadyl complexes in various asphaltenes: statistical correlative model of the coordination ligands. Fuel 64:335-341

Mallia G, Orlando R, Roetti P, Ugliengo P, Dovesi R (2001) F center in LiF: a quantum mechanical ab initio investigation of the hyperfine interaction between the unpaired electron and the vacancy and its first seven neighbors. Phys Rev B 63:235102

Mao M, Pan Y (2012) Nature of heavy metals in hemimorphite: A cation-exchange and single-crystal EPR study. Can Mineral 50:319-331

Mao M, Lin J, Pan Y (2010a) Hemimorphite as a natural sink for arsenic in zinc deposits and related mine tailings: Evidence from single-crystal EPR spectroscopy and hydrothermal synthesis. Geochim Cosmochim Acta 74:2943-2956

Mao M, Nilges MJ, Pan Y (2010b) Radiation-induced defects in apophyllites. II. An O^- center and related O^-–O^- pairs in hydroxylapophyllite. Eur J Mineral 22:89-102

Mao M, Nilges MJ, Pan Y (2010c) Single-crystal EPR and ENDOR study of an Al–O^- center in prehnite: Implications for Al-associated oxyradicals in layer silicates. Eur J Mineral 22:381-392

Mao M, Li Z., Pan Y (2013) Phase transitions and proton ordering in hemimorphite: New insights from single-crystal EPR experiments and DFT calculations. Phys Chem Miner 40:133-143

Marfunin AS (1979) Spectroscopy, Luminescence and Radiation Centers in Minerals. Springer Verlag, Berlin

Mashkovtsev RI, Pan Y (2011) Biradical states of oxygen-vacancy defects in α quartz: Centers E''2 and E''4. Phys Chem Miner 38:647-654

Mashkovtsev RI, Pan Y (2012a) Five new E' type centers and their ^{29}Si hyperfine structures in electron-irradiated α-quartz. Phys Chem Miner 39:79-85

Mashkovtsev RI, Pan Y (2012b) Stable states of E'' centers in α-quartz. EPL (Europhys Lett) 98:56005

Mashkovtsev RI, Howarth DF, Weil JA (2007) Biradical states of oxygen-vacancy defects in α-quartz. Phys Rev B 76:214114

Mashkovtsev RI, Li Z, Mao M, Pan Y (2013) ^{73}Ge, ^{17}O and ^{29}Si hyperfine interactions of the Ge E'_1 center in crystalline SiO_2. J Magnet Reson 233:7-16

McGavin DG (1987) Symmetry constraints on EPR spin-Hamiltonian parameters. J Magn Reson 74:19-55

McGavin DG, Tennant WC (2009) Higher-order Zeeman and spin terms in the electron paramagnetic resonance spin Hamiltonian; their description in irreducible form using Cartesian, tesseral spherical tensor and Stevens' operator expressions. J Phys Conden Matter 21:245501

Meyer BK, Lohse F, Spaeth J-M, Weil JA (1984) Optically detected magnetic resonance of the $(AlO_4)^0$ centre in crystalline quartz. J Phys C: Solid State Phys 17:L31.

EBSCOhost - printed on 2/13/2023 5:26 AM via . All use subject to https://www.ebsco.com/terms-of-use

Michoulier J, Gaite JM (1972) Site assignment of Fe^{3+} in low symmetry crystals. Application to $NaAlSi_3O_8$. J Chem Phys 56:5205-5213

Minge J, Weil JA, McGavin DG (1989) EPR study of Fe^{3+} in α-quartz: Characterization of a new type of cation-compensated center. Phys Rev B 40:6490-6498

Misra SK (2011) Multifrequency Electron Paramagnetic Resonance: Theory and Applications. Wiley-VCH Verlag

Mizuochi N, Makino T, Kato H, Takeuchi D, Ogura M, Okushi H, Nothaft M, Neumann P, Gali A, Jelezko F, Wrachtrup J, Yamasaki S (2012) Electrically driven single-photo source at room temperature in diamond. Nature Photonics 6:299-303

Mombourquette MJ, Tennant WC, Weil JA (1986) EPR study of Fe^{3+} in α-quartz: A reexamination of the so-called I center. J Chem Phys 86:68-79

Mombourquette MJ, Weil JA, McGavin DG (1996) EPR-NMR (Users' Manual). Department of Chemistry, University of Saskatchewan, Saskatoon, SK., Canada

Morichon E, Beauford D, Allard T, Quirt D (2010) Tracing past migrations of uranium in Paleoproterozoic basins: New insights from radiation-induced defects in clay minerals. Geology 38:983-986

Morin G, Allard T, Balan E, Ildefonse P, Calas G (2002) Native Cd^{+} in sedimentary fluorapatite. Eur J Mineral 14:1087-1094

Morris RV, Haskin LA (1974) EPR measurement of the effect of glass composition on the oxidation of europium. Geochim Cosmochim Acta 38:1435-1445

Morris RV, Biggar GM, O'Hara MJ (1974): Measurement of the effects of temperature and partial pressure of oxygen on the oxidation states of europium. Geochim Cosmochim Acta 38:1447-1459

Müller KA, Berlinger W, Waldner F (1968) Characteristic structural phase transition in perovskite-type compounds. Phys Rev Lett 21:814-817

Nadolinny VA, Baker JM, Yuryeva OP, Newton ME, Twitchen DJ, Palyanov YN (2005) EPR study of the peculiarities of incorporating transition metal ions into the diamond structure. Appl Magn Res 28:365-381

Nadolinny VA, Yuryeva OP, Shatsky VS (2009a) New data on the nature of the EPR OK1 and N3 centers in diamond. Appl. Magn. Res 36:97-108

Nadolinny VA, Yuryeva OP, Chepurov AI, Shatsky VS (2009b) Titanium ions in the diamond structure: Model and experimental evidence. Appl Magn Res 36:109-113

Náfrádi B, Gaál R, Sienkiewicz A, Fehér T, Forró L (2008) Continuous-wave far-infrared ESR spectrometer for high-pressure measurements. J Magn Reson 195:206-210

Nassau K, Prescott BE (1975) A reinterpretation of smoky quartz. Phys Status Solidi (a) 29**:**659-663

Nelson HM, Larson DB, Gardner JH (1967) Very high pressure effects upon the EPR spectrum of ruby. J Chem Phys 47:1994-1998

Nilges MJ, Pan Y, Mashkovtsev R (2008) Radiation-damage-induced defects in quartz. I. Single-crystal W-band EPR study of hole centers in quartz. Phys Chem Miner 35:221-235.

Nilges MJ, Pan Y, Mashkovtsev RI (2009) Radiation-induced defects in quartz. III. W-band EPR, ENDOR and ESEEM study of a peroxy radical. Phys Chem Miner 36:61-73

Nistor SV, Schoemaker D, Ursu I (1994) Spectroscopy of the ns^1-centers in ionic crystals. Phys. Stat. Sol. (b) 185:9-75

Nokhrin S, Pan Y, Weil JA, Nilges MJ (2005) Multifrequency EPR study of radiation- induced defects in chlorapatite. Can Mineral 43:1581-1588

Nokhrin S, Pan Y, Nilges MJ (2006) Electron paramagnetic resonance spectroscopic study of carbonate-bearing fluorapatite: New defect centers and constraints on the incorporation of carbonate ions in apatites. Am Mineral 91:1425-1431

Nuttall RHD, Weil JA (1981) The magnetic properties of the oxygen-hole aluminum centers in crystalline SiO_2. I. $[AlO_4]^0$. Can J Phys 59:1696-1708

Pan Y (2013) Arsenic speciation in rock-forming minerals determined by EPR spectroscopy. *In*: Arsenic: Sources, Environmental Impact, Toxicity and Human Health: A Medical Geology Perspective. Massotti A (ed) Nova Publishers Inc. p 39-52

Pan Y, Botis SM, Nokhrin S (2006) Applications of natural radiation-induced defects in quartz to exploration in sedimentary basins. J China Univ Geosci 17:258-271

Pan Y, Fleet ME (2002) Compositions of the apatite-group minerals: substitution mechanisms and controlling factors. Rev Mineral Geochem 48:13-49

Pan Y, Chen N, Weil JA, Nilges MJ (2002a) Electron paramagnetic resonance spectroscopic study of synthetic fluorapatite. Part III. Structural characterization of sub-ppm-level Gd and Mn in minerals at W-band frequency. Am Mineral 87:1333-1341

Pan Y, Fleet ME, Chen N, Weil JA, Nilges MJ (2002b) Site preference of Gd in synthetic fluorapatite by single-crystal W-band EPR and X-ray refinement of the structure: A comparative study. Can Mineral 40:1103-1112

Pan Y, Nilges MJ, Mashkovtsev RI (2008) Radiation-induced defects in quartz. II. Single-crystal W-band EPR study of a natural citrine quartz. Phys Chem Miner 35:387-397

EBSCOhost - printed on 2/13/2023 5:26 AM via . All use subject to https://www.ebsco.com/terms-of-use

Pan Y, Mao M, Lin J (2009a) Single-crystal EPR study of Fe^{3+} and VO^{2+} in prehnite from the Jeffrey mine, Asbestos, Quebec. Can Mineral 47:933-945

Pan Y, Nilges MJ, Mashkovtsev RI (2009b) Radiation-induced defects in quartz: Multifrequency EPR study and DFT modeling of new peroxy radicals. Mineral Mag 73:517-535

Pan Y, Mashkovtsev RI, Huang D, Mao M, Shatskiy A (2011) Mechanisms of Cr and H incorporation in stishovite determined by single-crystal EPR spectroscopy and DFT calculations. Am Mineral 96:1333-1342

Pan Y, Mao M, Li Z, Botis SM, Mashkovtsev RI, Shatskiy A (2012) Single-crystal EPR study of three radiation-induced defects ($Al–O_2^{3-}$, Ti^{3+} and W^{5+}) in stishovite. Phys Chem Miner 39: 627-637

Pan Y, Yeo G, Rogers B, Austman C, Hu B (2013) Application of natural radiation-induced defects in quartz to uranium exploration: A case study on the Maw Zone, Athabasca Basin. J Expl Mining Geol (in press)

Patchkovskii S, Ziegler T (2001) Calculation of the EPR g-tensors of high-spin radicals with density function theory. J Phys Chem 105:5490-5497

Petrakis L, Grandy DW (1983) Free Radicals in Coals and Synthetic Fuels. Elsevier, Amsterdam

Petrini R, Forte C, Contin G, Pinzino G, Orsi G (1999) Structure of volcanic glasses from the NMR-EPR perspective: a preliminary application to the Neapolitan yellow tuff. Bull Volcanol 60:425-431

Petrov I, Mineeva RM, Bershov LV, Agel A (1993) EPR of $[Pb–Pb]^{3+}$ mixed valence pairs in amazonite-type microcline. Am Mineral 78:500-510

Piccinato MT, Guedes CLB, Di Mauro E (2009) EPR characterization of organic free radicals in marine diesel. Appl Magn Reson 35:379-388

Pichard CJ, Mauri F (2002) First-principles theory of the EPR g tensor in solids: Defects in quartz. Phys Rev Lett 88:086403

Pietrucci F, Bernasconi M, Di Valentin C, Mauri F, Pichard CJ (2006) EPR g-tensor of paramaganteic centers in yttria-stablizied zirconia from first-principles calculations. Phys Rev B 73:134112.

Pilawa B, Pusz S, Krzesińska M, Koszorek A, Kwiecińska B (2009) Application of electron paramagnetic resonance spectroscopy to examination of carbonized coal blends. Int J Coal Geol 77:372-376

Poirot I, Kot W, Shalimoff G, Edelstein N, Abraham MM, Finch CB, Boatner LA (1988) Optical and EPR investigation of Np^{4+} in single crystals of $ZrSiO_4$. Phys Rev B 37: 3255-3264

Poole CP Jr (1996) Electron Spin Resonance: A comprehensive Treatise on Experimental Techniques, 2nd ed., Interscience, New York

Poole CP Jr, Farah HA (1999) Handbook of Electron Spin Resonance. Springer-Verlag, New York

Popescu F (1973) EPR study of Zn^+ in calcite. Solid State Commun 13:749-751

Priem A, van Bentum PJ, Hagen WR, Reijerse EJ (2001) Estimation of higher-order magnetic spin interactions of Fe(III) and Gd(III) ions doped in α-alumina powder with multifrequency EPR. Appl Magn Reson 21: 535-548

Prince E (1971) Refinement of the crystal structure of apophyllite. III. Determination of the hydrogen positions by neutron diffraction. Am Mineral 56:1241-1251

Rae AD (1969) Relationship between the experimental Hamiltonian and the point symmetry of a paramagnetic species in a crystal. J Chem Phys 50:2672-2685

Redman D, Brown S, Sands R, Rand S (1991) Spin dynamics and electronic states of N-V centers in diamond by EPR and four-wave-mixing spectroscopy. Phys Rev Lett 67:3420-3423

Reijerse EJ (2010) High-frequency EPR instrumentation. Appl Magn Reson 37:795-818

Rouse RC, Peacor RD, Dunn PJ (1978) Hydroxyapophyllite, a new mineral, and a redefinition of the apophyllites group. II. Crystal structure. Am Mineral 63:199-202

Ruoff AL, Xia H, Xia Q (1992) The effect of a tapered aperture on x-ray diffraction from a sample with a pressure gradient: studies on three samples with a maximum pressure of 560 GPa, Rev Sci Instrum 63:4342-4348

Sakai N, Pifer JH (1985) Electron paramagnetic resonance at high pressure using a diamond anvil cell. Rev Sci Instrum 56:726–732

Sakurai T, Hoire T, Tomoo M, Kondo K, Matsumi N, Okubo S, Ohta H, Uwatoko Y, Kudo K, Koike Y, Tanaka H (2010) Development of high-pressure, high-field and multi-frequency ESR apparatus and its application to quantum spin system. J Phys Conf Ser 215:012184

Saraceno AJ, Fanale DT, Coggeshall ND (1961) An electron paramagnetic resonance investigation of vanadium in petroleum oils. Anal Chem 33:500–505

Sasaki S, Kurahashi E, Yamanaka C, Nakamura K (2003) Laboratory simulation of space weathering: Changes of optical properties and TEM/ESR confirmation of nanophase metallic iron. Adv Space Res 31:2537-2542

Schirmer OF (1976) Smoky coloration of quartz caused by bound small hole polaron optical absorption. Solid State Commun 18:1349-1351

Schofield PF, Henderson CMB, Cressey G, van der Laan G (1995) 2p X-ray absorption spectroscopy in the earth sciences. J Synchrotron Radiat 2:93-98

Schweiger A, Jeschke G (2001) Principles of Pulse Electron Paramagnetic Resonance. Oxford University Press, New York

Shinar J, Jaccarino V (1983) High-temperature EPR in superionic fluorites. Phys Rev B 27:4034-4051

Sienkiewicz A, Vileno B, Garaj S, Jaworski M, Ferró L (2005) Dielectric resonator-based resonant structure for sensitive ESR measurements at high-hydrostatic pressures. J Magn Reson 177:278-290

EBSCOhost - printed on 2/13/2023 5:26 AM via . All use subject to https://www.ebsco.com/terms-of-use

Singer LS, Smith WH, Wagoner G (1961) Microwave cavity for high temperature electron spin resonance measurements. Rev Sci Instrum 32:213-214

SivaRamaiah G, Pan Y (2012) Thermodynamic and magnetic properties of surface Fe^{3+} species on quartz: Effects of gamma ray irradiation and implications for aerosol-radiation interaction. Phys Chem Miner 39:515-523

SivaRamaiah G, Lin J, Pan Y (2011) Electron paramagnetic resonance spectroscopy of Fe^{3+} ions in amethyst: Thermodynamic potentials and magnetic susceptibility. Phys Chem Miner 38:159-167

Skinner AR (2000) ESR dating: is it still an "experimental" technique? Appl Rad Isotop 52:1311-1316

Skrzypczak-Bonduelle A, Binet L, Delpoux O, Vezin H, Derenne S, Robert F, Gourier D (2008) EPR of radicals in primitive organic matter: A tool for the search of biosignatures of the most ancient traces of life. Appl Magn Reson 33:371-397

Stegger P, Lehmann G (1989) The structures of three centers of trivalent iron in α-quartz. Phys Chem Miner 16:401-407

Sun Y, Tada R, Chen J, Chen H, Toyoda S, Tani A, Isozaki Y, Nagashima K, Hasegawa H, Ji J (2007) Distinguishing the sources of Asian dust based on electron spin resonance signal intensity and crystallinity of quartz. Atmospheric Environ 41:8537-8548

Tissoux H, Toyoda S, Falguréres C, Voinchet P, Takada M, Bahain J-J, Despriée J (2008) ESR dating of sedimentary quartz from Pleistocene deposits using Al and Ti-centers. Geochron 30:23-31

Toyoda S, Schwarcz HP (1997) The hazard of the counterfeit E'_1 signal in quartz to the ESR dating of fault movements. Quantern Sci Rev 16:483-486

Tsay F-D (1988) Sample selection and preservation techniques for the Mars sample return mission. Lunar Planet Inst Workshop on Mars Sample Return Science, 173-174

Ursu I, Lupei V (1984) EPR of uranium ions. Bull Magnet Reson 6:162-224

Vallauri MG, Forsbergh PW (1957) Wide-band high-pressure dielectric cell. Rev Sci Instrum 28:198-199

van Lenthe E, van der Avoird A, Wormer PES (1998) Density functional calculations of molecular hyperfine interactions in the zero order regular approximation for relativistic effects. J Chem Phys 108:4783-4796

van Oort E, Manson NB, Glasbeek M (1988) Optically detected spin coherence of the diamond N-V centre in its triplet ground state. J Phys C: Solid State Phys 21:4385-4391

van Wyk JA, Loubser JHN, Newton ME, Baker JM (1992) ENDOR and high temperature EPR of the N3 centre in natural type Ib diamonds. J Phys Condens Matter 4:2651-2656

Vassilikou-Dova AB (1993) EPR-determined site distributions of low concentrations of transition-metal ions in minerals: Review and predictions. Am Mineral 78:49-66

Wait DF (1963) Hydrostatic pressure dependence of the paramagnetic resonance of an S-state ion in a noncubic lattice: Mn^{2+} in calcite. Phys Rev 132:601-607

Walsby CJ, Lees NS, Claridge RFC, Weil JA (2003) The magnetic properties of oxygen-hole aluminum centres in crystalline SiO_2. VI: A stable AlO_4/Li centre. Can J Phys 81:583-598

Walsh WM Jr (1959) Pressure dependence of the paramagnetic resonance spectra of two dilute chromium salts. Phys Rev 114:1485-1490

Walsh WM Jr (1961) Effects of hydrostatic pressure on the paramagnetic resonance spectra of several iron group ions in cubic crystals. Phys Rev 122:762-771

Weeks RA (1973) Paramagnetic resonance spectra of Ti^{3+}, Fe^{3+} and Mn^{2+} in lunar plagioclase. J Geophys Res 78:2393-2401

Weeks RA, Magruder RH, Stesmans A (2008) Review of some experiments in the 50 year saga of the *E'* center and suggestions for future research. J Non-Cryst Solids 354:208-216

Weil JA (1994) EPR of iron centres in silicon dioxide. Appl Magn Reson 6:1-16

Weil JA, Bolton JR (2007) Electron Paramagnetic Resonance: Elementary Theory and Practical Applications. John Wiley & Sons, New York.

Westra J, Sitters R, Glasbeek M (1992) Optical detection of magnetic resonance in the photoexcited triplet state of a deep center in diamond. Phys Rev B 45:5699-5702

Wong GK, Yen TF (2000) An electron spin resonance probe method for the understanding of petroleum asphaltene macrostructure. J Petrol Sci Eng 28:55-64

Yager TA, Kingery WD (1979) Laser-heated high-temperature EPR spectroscopy. Rev Sci Instrum 51:464-466

Yamanaka C, Toyoda S, Ikeya M (1993) ESR applications to meteorite samples. Proc NIPR Symposium Antarctic Meteorites 6: 417-422

Yamanaka T, Fukuda T, Komatsu Y, Sumiya H (2002) Charge density analysis of SiO_2 under pressure over 50 GPa using new diamond anvil cell for single crystal structure analysis. J Phys Condens Matter 14: 10545-10551

Zhang YP, Buckmaster HA, Kudynska J (1994) E.p.r. HFS spectral characteristics of Mn^{2+} impurity in Argonne and Alberta coals. Fuel 74:1307-1312

Zheng S, Feng J-W, Maciel GE (2005) In situ high-temperature EPR investigation of the charring of tabacco and the O_2-induced and H_2O-induced behavior of the char. Energy & Fuels 19:2247-2253

EBSCOhost - printed on 2/13/2023 5:26 AM via . All use subject to https://www.ebsco.com/terms-of-use

Reviews in Mineralogy & Geochemistry
Vol. 78 pp. 691-743, 2014
Copyright © Mineralogical Society of America

Theoretical Approaches to Structure and Spectroscopy of Earth Materials

Sandro Jahn[1] and Piotr M. Kowalski[1,2]

[1]*GFZ German Research Centre for Geosciences*
Telegrafenberg, 14473 Potsdam, Germany

[2]*IEK-6 Institute of Energy and Climate Research*
Forschungszentrum Jülich, 52425 Jülich, Germany

sandro.jahn@gfz-potsdam.de *p.kowalski@fz-juelich.de*

INTRODUCTION

The characterization of complex materials in terms of their structure, electronic, magnetic, vibrational, thermodynamic or other physical and chemical properties is often a challenging task that requires the combination of a number of complementary techniques. Experimental approaches such as diffraction or spectroscopic methods usually provide fingerprint information about the material under investigation. The interpretation of measured data is either done by reference to analogue materials or by constructing a theoretical (e.g., structural) model that fits the experimental data. For the latter, computational methods have become very powerful in recent years. For example, Rietveld refinement of powder diffraction data or curve fitting of various spectra is now done on a routine basis.

The continuous improvement in hardware performance resulting in a huge and progressive increase of computing power by a factor of ~1000 per decade, as well as advanced algorithms and codes provide the basis for predictive modeling of material properties *ab initio*, i.e., from *first principles* using quantum chemical methods such as density functional theory (DFT). DFT enthalpy predictions for the major lower mantle minerals, $MgSiO_3$ perovskite and post-perovskite, periclase (MgO) and $CaSiO_3$ perovskite at zero temperature, over the relevant pressure range from the transition zone to the core-mantle boundary can be made in a few hours on an office PC. Free energy calculations for these phases at finite temperatures using lattice vibrational modes in the (quasi-)harmonic approximation require at most a couple of days. More realistic compositions of these mantle minerals with Fe substituting some of the Mg atoms in a solid solution are computationally more demanding but have also become accessible. The same is true for structural investigations of disordered phases, such as glasses, melts and fluids. Both first-principles and classical molecular dynamics simulations are useful methods for a statistically significant sampling of disordered structures. While the former can accurately account for complex chemical processes, e.g., hydrolysis reactions, simulations with classical interaction potentials are computationally less expensive, which allows to study systems with thousands to millions of atoms over time periods up to the nano- or microsecond range.

Regarding physical and chemical properties that can be measured by spectroscopic techniques, substantial advances have been made in the last decade to predict, e.g., Raman and infrared (IR) frequencies, nuclear magnetic resonance (NMR) chemical shifts or X-ray absorption spectra. With such quantitative predictions, problems related to the interpretation of spectroscopic data, e.g., band assignments can be solved with much less ambiguity than by using traditional empirical methods alone. Furthermore, if the computational models are accurate enough to represent real materials, the simulations can be used as a guideline to

1529-6466/14/0078-0017$10.00 http://dx.doi.org/10.2138/rmg.2014.78.17

EBSCOhost - printed on 2/13/2023 5:26 AM via . All use subject to https://www.ebsco.com/terms-of-use

design future experimental work and theoretical predictions can be made for conditions that are difficult to access experimentally (for instance investigations of complex melts and fluids at high temperatures and pressures). The new computational functionalities have the potential to make atomic scale simulation methods a strong every-day companion of spectroscopists and to intensify interdisciplinary research in the field of geomaterials research.

The intention of this chapter is to provide some theoretical background and practical advice concerning atomic scale simulations to complement the more experimentally oriented chapters of this volume. For sampling the structure and the vibrational dynamics, two different computational approaches are outlined. While for crystals at not too high temperature the computations are usually based on numerical or analytic derivatives from the perfect lattice, the structure and dynamics of melts, fluids or strongly anharmonic crystals are preferentially sampled by molecular dynamics simulations. In the latter case, related properties are described through correlation functions in time and space, such as structure factors or velocity autocorrelation functions. Throughout this chapter, we will make use of the Born-Oppenheimer approximation, which assumes that electronic properties and electronic excitations are time or frequency separated from the dynamics of the nuclei, i.e., for the atomic dynamics the electronic structure is assumed to be in its ground state and for electronic excitations the nuclei are considered to be at rest.

In the following section, we will give an introduction to electronic structure methods, classical interaction potentials and the molecular dynamics method. Then, the computational approaches to specific characterization methods are described and illustrated with examples. This includes structure determination by diffraction, vibrational spectroscopy, electronic excitation spectroscopy and spectroscopy related to nuclear excitations. While the focus of this chapter is on structure and spectroscopy, extensive reviews of other aspects of molecular modeling with particular focus on Earth sciences are provided in two dedicated issues of Reviews in Mineralogy and Geochemistry, volumes 42 and 71 (Cygan and Kubicki 2001; Wentzcovitch and Stixrude 2010).

THEORETICAL FRAMEWORK

The first and foremost task in molecular modeling is the calculation of the total energy of a system (e.g., a molecule, crystal or fluid), which is a sum of kinetic energy and potential energy. Treatment of the latter is more demanding as it involves the interactions between all atomic nuclei and electrons of the system. Particle interactions can be modeled in a simplified manner by classical force fields that describe interactions between atoms, ions and/or molecules by potential energy surfaces that are parameterized either by reference to experimental data or to a more basic theory. However, such an approach does not consider the electronic structure of the studied system explicitly and can therefore not be used to model electronic excitation spectra. In addition, the applicability of a classical potential is often restricted to a narrow range of chemical compositions and thermodynamic conditions. Alternatively, the interactions between electrons and nuclei can be computed explicitly using *ab initio* methods that are based on quantum theory. First-principles calculations are predictive, transferable between different chemical environments and are derived from basic laws of Physics, i.e., they do not require any empirical input e.g., from experiments. On the downside, such calculations are computationally much more demanding.

The use of a reliable interaction model is a prerequisite to characterize the thermodynamic state of the system of interest accurately. Computed Gibbs free energy differences, e.g., between crystal polymorphs at various pressure and temperature conditions, may then be used to construct phase diagrams. The energetics of hydrated ions or molecules in aqueous solution determines, e.g., the solubility of minerals. Thus, molecular models are able to link structure and

EBSCOhost - printed on 2/13/2023 5:26 AM via . All use subject to https://www.ebsco.com/terms-of-use

thermodynamics or, in other words, to predict the lowest energy structure of a system of atoms. In practice, accurate energies for a given interaction model are obtained if the calculations are converged with respect to a number of model-specific parameters (e.g., number of basis set functions, sampling grid of the electronic structure, statistical fluctuations for dynamic simulations). It is the responsibility of the user that such basic convergence criteria are met. In addition, there are systematic errors that arise from the approximations necessary to make the computations feasible, which will be explained in more detail below. Consequently, there are systematic differences between predicted and experimental properties that are inherent to the specific model used. Typically, quantum-chemical methods on the DFT level provide lattice constants within at most a few percent and elastic constants within 10% of the experimental values. For phase diagrams, transition pressures may differ up to a few tens of gigapascals from the experimental values, especially if the difference in free energies between the two phase assemblies on both sides of the phase boundary is small over a wide range of pressures. This seems unacceptable from an experimentalist's point of view. However, relative energy changes are usually much better described and the calculations yield realistic slopes of phase boundaries. Nevertheless, one should keep in mind the relatively large uncertainties related to prediction of (free) energies on the absolute scale.

Spectroscopy is used to characterize a material in terms of its vibrational, electronic and nuclear properties. From a molecular modeling perspective, vibrational properties are accessible by both classical and quantum mechanical approaches subject to an accurate representation of the interatomic forces. Spectra that involve electronic excitations require an explicit treatment of the electronic structure and hence the use of quantum mechanical methods. Usually, the quantum mechanical methods are computationally expensive and therefore a compromise between accuracy and efficiency has to be found. In this section, most emphasis will be put on the description of density-functional theory in conjunction with more accurate correction schemes as currently this is the most promising approach to modeling electronic excitation spectra of complex Earth materials. Because the ab initio molecular modeling methods are currently limited to systems containing no more than a few hundred atoms, classical simulations using force fields are useful complements to provide structural models of larger systems, especially for disordered phases or for extended defects in crystals.

Because a correct description of particle interactions and of the electronic structure of materials are essential for performing meaningful molecular simulations we start our review with a more formal introduction into the computational methodology that is widely applied in modeling the structure and spectroscopic characteristics of Earth materials.

Quantum-chemical methods

The fundamental equation describing the quantum state of any many-particle system, such as a crystal, a fluid, a molecule or just a single atom, is the Schrödinger equation, which in time-independent form has a simple form (Davydov 1965; Koch and Holthausen 2000; Martin 2004)

$$\hat{H}\Psi = E\Psi \tag{1}$$

$\Psi = \Psi(\mathbf{r}_i, \sigma_i, ...)$ is the many-body wavefunction that represents a space ($\mathbf{r}$) and spin (σ) dependent solution of the Schrödinger equation for a given Hamilton operator $\hat{H}$ and E is the total energy of the system. The Hamiltonian can be decomposed into

$$\hat{H} = \hat{K} + \hat{U} = \hat{K} + \hat{U}_{ne} + \hat{U}_{ee} + E_{nn} \tag{2}$$

or more explicitly

$$\hat{H} = -\frac{1}{2}\sum_i \nabla_i^2 - \sum_i \sum_k \frac{Z_k}{\left|\mathbf{r}_i - \mathbf{d}_k\right|} + \frac{1}{2}\sum_i \sum_{i \neq j} \frac{1}{\left|\mathbf{r}_i - \mathbf{r}_j\right|} + \frac{1}{2}\sum_k \sum_{l \neq k} \frac{Z_k Z_l}{\left|\mathbf{d}_k - \mathbf{d}_l\right|} \tag{3}$$

EBSCOhost - printed on 2/13/2023 5:26 AM via . All use subject to https://www.ebsco.com/terms-of-use

$\hat{K}$ and $\hat{U}$ are the electronic kinetic energy and the potential energy operators, $\hat{U}_{ne}$ and $\hat{U}_{ee}$ describe the electron-nucleus and the electron-electron interactions, and E_{nn} represents the interaction energy between nuclei. The equations are written in atomic units, i.e., the electronic mass, Planck's constant and the electronic charge are set to unity, $\Sigma_i \nabla_i^2 = \Sigma_i \partial^2/\partial \mathbf{r}_i^2$ is the Laplace operator, Z_k is the charge of nucleus k (in units of the elementary charge) at position $\mathbf{d}_k$, and $\mathbf{r}_i$ is the position vector of electron i.

The solution of the Schrödinger equation requires integrations of the wavefunctions containing $3N$ variables in a $3N$-dimensional space, where N is the number of electrons, through the integration of the Hamiltonian for the total energy,

$$E = \frac{\left\langle \Psi \middle| \hat{H} \middle| \Psi \right\rangle}{\left\langle \Psi \mid \Psi \right\rangle} = \left\langle \hat{K} \right\rangle + \left\langle \hat{U}_{ne} \right\rangle + \left\langle \hat{U}_{ee} \right\rangle + E_{nn} \tag{4}$$

Angular brackets indicate quantum mechanical expectation values. The allowed energy values are given by the stationary points of the above expression for the energy. The ground state of a many-particle system is the state with the lowest energy. Most of the computational methods determine this energy by application of the variational method, i.e., by minimizing the energy with respect to all the parameters in the many-electron wavefunction $\Psi(\mathbf{r}_1, \sigma_1, \ldots, \mathbf{r}_n, \sigma_n)$. Because the mass of the electron is much smaller than the mass of the nuclei, the Born-Oppenheimer approximation is usually used, i.e., the nuclei remain at fixed positions during electronic structure calculations. Thus, the E_{nn} term is constant and usually omitted in the formulation of electronic structure methods. Nuclei only contribute as an external potential to the electronic interactions via the $\hat{U}_{ne}$ term. However, for the calculation of the total energy and for interatomic forces nucleus-nucleus interactions have to be included again.

Even with modern supercomputer technology, the Schrödinger equation cannot be solved exactly for a many-electron system within a reasonable time. Consequently, one can either search for an approximate solution of the Schrödinger equation or for an exact solution of an approximation to the Schrödinger equation. One important approach to solve the Schrödinger equation approximately is the independent-electron approximation. In this case, the individual inter-electron interactions are replaced by an effective interaction potential, which represents an average force acting on an electron moving in an average potential produced by all other electrons and by the nuclei. Most of the current computational methods of quantum chemistry are based on this methodology. One successful realization of such a simplification to the solution of the Schrödinger equation is by Hartree and Fock (Fock 1930). In this approach a set of one-electron wave equations is solved

$$\hat{H}_{eff}\psi_i(\mathbf{r},\sigma_i) = \left(-\frac{1}{2}\nabla^2 + \hat{U}_{eff}(\mathbf{r}) \right)\psi_i(\mathbf{r},\sigma_i) = \varepsilon_i \psi_i(\mathbf{r},\sigma_i) \tag{5}$$

where $\hat{U}_{eff}(\mathbf{r})$ is the effective potential operator acting on electron i at position $\mathbf{r}$ and ε_i is the respective energy eigenvalue. Because of the Pauli Exclusion Principle, the many-electron wavefunction has to be antisymmetric in its arguments and is usually expressed as a Slater determinant of the single particle orbitals $\psi_i(\mathbf{r},\sigma_i)$(Davydov 1965).

$$\Psi = \frac{1}{\sqrt{N!}} \begin{vmatrix} \psi_1(\mathbf{r}_1,\sigma_1) & \psi_1(\mathbf{r}_2,\sigma_2) & \cdots & \psi_1(\mathbf{r}_N,\sigma_N) \\ \psi_2(\mathbf{r}_1,\sigma_1) & \psi_2(\mathbf{r}_2,\sigma_2) & \cdots & \psi_2(\mathbf{r}_N,\sigma_N) \\ \vdots & \vdots & \ddots & \vdots \\ \psi_N(\mathbf{r}_1,\sigma_1) & \psi_N(\mathbf{r}_2,\sigma_2) & \cdots & \psi_N(\mathbf{r}_N,\sigma_N) \end{vmatrix} \tag{6}$$

The effective potential $\hat{U}_{eff}$ is a sum of Coulomb and exchange interactions, the latter arising

EBSCOhost - printed on 2/13/2023 5:26 AM via . All use subject to https://www.ebsco.com/terms-of-use

from the Pauli Exclusion Principle (Davydov 1965). Then, the full Hartree-Fock equations are given by

$$\varepsilon_i \psi_i(\mathbf{r},\sigma_i) = \left(-\frac{1}{2}\nabla^2 - \sum_k \frac{Z_k}{|\mathbf{r}-\mathbf{d}_k|} + \sum_j \int d\mathbf{r}' \frac{|\psi_j(\mathbf{r}',\sigma_j)|^2}{|\mathbf{r}-\mathbf{r}'|} \right) \psi_i(\mathbf{r},\sigma_i) \tag{7}$$

$$-\sum_j \delta_{\sigma_i\sigma_j} \int d\mathbf{r}' \frac{\psi_j^*(\mathbf{r}',\sigma_j)\psi_i(\mathbf{r}',\sigma_j)}{|\mathbf{r}-\mathbf{r}'|} \psi_j(\mathbf{r},\sigma_i)$$

In the above equations the exchange term acts only between electrons of the same spin state σ ($\delta_{\sigma_i\sigma_j} = 1$ if $\sigma_i = \sigma_j$ and zero otherwise).

In general, the individual orbitals are expanded in a basis set $\{\zeta_k\}$ and expressed as a linear combination of basis functions ($\psi_i = \Sigma_k c_{ik} \zeta_k$). The energy is then expressed in terms of the orbital expansion coefficients c_{ik}, which are obtained by applying the variational method, and of the integrals involving the basis functions (Davydov 1965; Martin 2004). In principle this method requires the computation of M^4 integrals and therefore it scales as M^4, where M is the number of basis functions. Through the solution of the Hartree-Fock equation one gets the eigenvalue spectrum, which is important in the context of electronic spectroscopy. According to Koopmans' theorem (Koopmans 1934), the eigenvalue of an orbital is equal to the change in the total energy upon subtraction or addition of an electron to the system, assuming that all other orbitals do not change. The shortcoming of the Hartree-Fock approach is that by describing an electron moving in an average field produced by the all other electrons it omits all quantum-mechanical effects related to the electron-electron interaction, except the ones introduced by the Pauli exclusion principle and therefore gives only an approximation to the real eigenvalues. As a result, it usually overestimates the excitation energies, including a large overestimation of the energy gaps for semiconductors (e.g., Svane 1987).

All improvements of the wavefunction to include electronic interactions unaccounted for by the Hartree-Fock method lower the energy of the system. Such a lowering of the energy is called the "correlation energy" (MacDonald 1933). There are several methods aimed at the inclusion of this energy term into the all-electron calculations and all these approaches are called "post-Hartree-Fock" methods. The Møller-Plesset perturbation theory (Møller and Plesset 1934) adds the correlations by means of perturbation theory to second (MP2) (scales as M^5), third (MP3) and fourth orders (MP4) (scales as M^6). It uses the solution of the Hartree-Fock equation as a zero-order term and derives the higher order corrections to the energies by lower order wavefunctions. For instance, Hartree-Fock wave functions are used to derive the MP2 correlation energy. Another widely used method is the configuration interaction (CI) method, in which for a desired N-electron wavefunction a linear combination of excited Slater determinants (i.e., Slater determinants that include one or more higher energy single particle orbitals representing an excited electronic state) is used and the weighting factors C_I, which describe the contribution of each Slater determinant, are optimized using variational methods (Davydov 1965). Another similar method is the coupled cluster method proposed by Cizek (1966, 1969). Both methods scale as $M^6 - M^7$. With current computational resources the Hartree-Fock method is limited to systems containing no more than about 50 atoms. Because of power law scaling of the post-Hartree-Fock methods they are extremely expensive and applicable to systems containing no more than a few atoms. Post-Hartree-Fock methods predict excitation energies very accurately and have been used widely in calculations of electronic excitation spectra of simple molecules such as H_2, H_2O and N_2 among others (Hättig 2006; Bartlett and Musial 2007). However, because of the huge computing demand these methods are not yet applicable to the simulation of complex materials important for geosciences.

Another group of methods for solving the Schrödinger equation proceeds via the explicit integration of the Schrödinger equation by an approximate evaluation of many electron

EBSCOhost - printed on 2/13/2023 5:26 AM via . All use subject to https://www.ebsco.com/terms-of-use

wavefunctions using Monte-Carlo techniques. These methods, however, are of limited use for the computation of electronic excitations as they derive the ground-state wavefunction only. More information on these methods can be found in Ceperley (2010).

Density Functional Theory (DFT)

As was outlined above, for a full description of an *N*-electron system using wavefunction-based methods we have to solve the Schrödinger equation for the *N*-particle wavefunction, which is usually a very complicated problem and for calculations going beyond the Hartree-Fock scheme it quickly reaches an unmanageable size. On the other hand, because the Hamilton operator $\hat{H}$ (Eqn. 3) contains only summations of pair interactions it acts only on one or two particles at a time. In addition, it is possible to write a Schrödinger-like equation that depends on fewer than 4*N* variables (three spatial + one spin variable for each of the *N* electrons). A very successful approach of this kind is the Density Functional Theory (DFT, see e.g., Perdew and Ruzsinszky 2010, for a recent review), where one uses the charge density produced by the electrons, $\rho(\mathbf{r})$, that depends only on the three spatial variables, for a full quantum mechanical description of the *N*-electron system, thus reducing the dimensionality of the problem to three spatial and one spin variables only. Because such a lowering of dimensionality allows to introduce efficient approximations that result in a significant reduction of required computing time, DFT methods are used extensively in quantum chemistry and condensed matter physics to compute the electronic structure and properties of crystals, complex molecules and structurally disordered phases such as fluids or melts. In the last decade the increasing performance of supercomputers allowed for direct DFT-based *ab initio* simulations of multi-particle systems containing up to a few hundred nuclei and a few thousand electrons.

The idea of using the electron density in quantum calculations was realized for the first time in the Thomas-Fermi model (TF, Thomas 1927; Fermi 1927), which was developed to calculate energies of a single many-electron atom. In this model the energy of the *N* electrons moving around the nucleus of charge *Z* positioned at $\mathbf{d} = 0$ is given by

$$E_{\mathrm{TF}} = \frac{3}{10}(3\pi^2)^{2/3}\int \rho^{5/3}(\mathbf{r})d\mathbf{r} - Z\int \frac{\rho(\mathbf{r})}{r}d\mathbf{r} + \frac{1}{2}\int\int \frac{\rho(\mathbf{r})\rho(\mathbf{r}')}{|\mathbf{r}-\mathbf{r}'|}d\mathbf{r}d\mathbf{r}' \tag{8}$$

where the first term represents the kinetic energy approximated by that of the free electron gas, which is known exactly. The following two terms are the Coulomb electron-nucleus and electron-electron interactions. The electron density $\rho(\mathbf{r})$ representing the lowest energy of the system is found by applying the variational method. The significant deficiencies of the TF model are that the kinetic energy term (derived from free electron gas properties) does not represent well the kinetic energy of a system of interacting electrons and that the inter-electronic exchange and correlation quantum effects (Koch and Holthausen 2000) are completely neglected. As a result the TF model fails to reproduce the shell structure of atoms and bonding of atoms in molecules.

The formal justification for expressing the electronic energy in terms of the electron charge density was provided half a century ago by Hohenberg and Kohn (1964). They showed that the ground state electron density, $\rho(\mathbf{r})$, uniquely determines the Hamilton operator and all properties of the system (the first Hohenberg-Kohn theorem) and that there is only one such electron density for a given Hamilton operator (the second Hohenberg-Kohn theorem). Having the electron density, the electronic energy can be represented as a sum of two terms

$$E_e[\rho(\mathbf{r})] = \int \rho(\mathbf{r})\sum_k \frac{Z_k}{|\mathbf{r}-\mathbf{d}_k|}d\mathbf{r} + F_{\mathrm{HK}}[\rho(\mathbf{r})] \tag{9}$$

The first term represents the electron-nucleus interaction energy and the second term F_{HK} is the Hohenberg-Kohn functional. The latter accounts for the electron-electron interaction terms

EBSCOhost - printed on 2/13/2023 5:26 AM via . All use subject to https://www.ebsco.com/terms-of-use

only and is represented by a sum of the kinetic energy of the electrons K and the electron-electron interactions E_{ee}, i.e.,

$$F_{\mathrm{HK}}[\rho(\mathbf{r})] = K[\rho(\mathbf{r})] + E_{ee}[\rho(\mathbf{r})] \tag{10}$$

This functional is system independent so that for a given $\rho(\mathbf{r})$ it does not depend on the positions of the nuclei. If we knew exactly how the F_{HK} functional depends on the electron density, Equation (9) would give us the exact ground state energy for any ground state electron charge density, which could be found by the variational method. Furthermore, the first Hohenberg-Kohn theorem states that the ground state electron density determines the Hamiltonian, which characterizes also all the electronic excited states of the system. Hence, knowing the ground state electron density is equivalent to the exact solution of the Schrödinger equation. Unfortunately, the exact analytical form of the functional F_{HK} is not known and various approximations have been proposed to estimate the kinetic energy of the electrons and the electron-electron interaction energy from the electron charge density. One of these approximations is the already discussed TF model, which however fails for most systems, mainly because the kinetic energy is approximated by that of a free electron gas, which is not adequate to describe electrons strongly bonded in atoms. Further developments of the kinetic energy functionals have not resulted in satisfying removal of the limitations observed by applying the TF model. To overcome this difficulty, Kohn and Sham (1965) proposed a different approach to the electronic kinetic energy. As this method is applied in most of the currently used DFT codes we will discuss it in more detail.

The Kohn-Sham Approach. Similar to the Hartree-Fock approximation, Kohn and Sham (1965) mapped the problem of the N interacting electrons to an equivalent system of N non-interacting electrons. Such a reference system of non-interacting electrons is represented by a Kohn-Sham Hamiltonian

$$\hat{H}_s = -\frac{1}{2}\sum_i \nabla_i^2 + \sum_i U_s(\mathbf{r}_i) \tag{11}$$

where $U_s(\mathbf{r}_i)$ is an effective local potential. The electronic density is determined by the solution of a one-electron Kohn-Sham (KS) equation

$$\hat{f}^{\mathrm{KS}}\phi_i(\mathbf{r},\sigma) = \left(-\frac{1}{2}\nabla^2 + U_s(\mathbf{r})\right)\phi_i(\mathbf{r},\sigma) = \varepsilon_i\phi_i(\mathbf{r},\sigma) \tag{12}$$

where $\hat{f}^{\mathrm{KS}}$ is the one-electron KS operator and $\phi_i(\mathbf{r},\sigma)$ are the Kohn-Sham orbitals. The electron density is then derived as

$$\rho(\mathbf{r}) = \sum_i \sum_s \left|\phi_i(\mathbf{r},\sigma_s)\right|^2 \tag{13}$$

The reference system of non-interacting electrons is related to the real system by the $\rho(\mathbf{r})$-dependent effective potential $U_s(\mathbf{r})$ generated by all the electrons and in which the single electrons move. This potential is given by

$$U_s(\mathbf{r}) = \int \frac{\rho(\mathbf{r}')}{|\mathbf{r}-\mathbf{r}'|} d\mathbf{r}' + U_{xc}(\mathbf{r}) - \sum_k \frac{Z_k}{|\mathbf{r}-\mathbf{d}_k|} \tag{14}$$

where $U_{xc}(\mathbf{r})$ is the exchange-correlation potential, which is defined in terms of the exchange-correlation energy E_{xc},

$$U_{xc} = \frac{\delta E_{xc}[\rho(\mathbf{r})]}{\delta\rho(\mathbf{r})} \tag{15}$$

EBSCOhost - printed on 2/13/2023 5:26 AM via . All use subject to https://www.ebsco.com/terms-of-use

Because the effective potential $U_s(\mathbf{r})$ depends on the electron density, which in turn depends on the KS orbitals, Equations (12) and (14) are to be solved self-consistently. However, as $U_s(\mathbf{r})$ is local, i.e., it depends only on values at $\mathbf{r}$, the KS equation has a much less complicated structure than the single electron equation in the Hartree-Fock approximation, where the exchange operator acting on the orbital i depends on the value of one-electron orbitals everywhere in the coordinate space (see Eqn. 7), and therefore its solution requires substantially less computational effort. With the knowledge of the KS orbitals, the total energy is given by

$$E_e = -\frac{1}{2}\sum_i \sum_s \phi_i^*(\mathbf{r},\sigma_s)\nabla^2\phi_i(\mathbf{r},\sigma_s)d\mathbf{r} + \frac{1}{2}\int\int \frac{\rho(\mathbf{r})\rho(\mathbf{r}')}{|\mathbf{r}-\mathbf{r}'|}d\mathbf{r}d\mathbf{r}' \qquad (16)$$
$$+E_{xc}[\rho(\mathbf{r})] - \int \sum_k \frac{Z_k\rho(\mathbf{r})}{|\mathbf{r}-\mathbf{d}_k|}d\mathbf{r}$$

Unlike in the Hartree-Fock model, where the form of the wavefunction is assumed to be a Slater determinant, the KS approach is, in principle, exact. The only approximation has to be made for the unknown functional of the exchange-correlation energy E_{xc}. Its exact knowledge would be equivalent to an exact solution of the Schrödinger equation. Some of the common approximations for E_{xc} are given in the next section.

Approximations for the exchange-correlation energy. One of the simplest approximations to the exchange-correlation energy is the *local density approximation* (LDA). It uses the exchange-correlation functional of the uniform electron gas, which is known exactly, and is given by

$$E_{xc}^{\mathrm{LDA}} = \int \rho(\mathbf{r})\varepsilon_{xc}(\rho(\mathbf{r}))d\mathbf{r} \qquad (17)$$

where ε_{xc} is the exchange-correlation energy per particle of a uniform electron gas of density $\rho(\mathbf{r})$. The exchange part of this functional can be calculated analytically (Becke 1988), whereas the correlation part is derived from accurate quantum Monte-Carlo simulations of the homogeneous electron gas (Ceperley and Alder 1980). Even if in most real systems the electron densities are not even close to that of the uniform electron gas, LDA has been successfully used in many cases.

A more realistic description of the electronic structure may be obtained by accounting explicitly for the spatial variations of $\rho(\mathbf{r})$ in the exchange-correlation functional. The most widely used approach is the *generalized gradient approximation* (GGA), in which the density gradient ($\nabla\rho$) is used in the construction of the exchange-correlation functional. Several approximations exist for the exchange and correlation parts of E_{xc}^{GGA}. They are constructed to recover the properties of selected sets of atoms, molecules or simple solids or from the knowledge of the behavior of the exchange-correlation functional at certain electronic density limits (e.g., at slowly varying densities). The most common approximations are the so-called PBE (Perdew et al. 1996a), PW91 (Perdew and Wang 1992) and BLYP (Becke 1988; Lee et al. 1988) functionals.

Figure 1 shows the electron charge density of an isolated helium atom (for which an exact result is known; Hart and Herzberg 1957) calculated with the DFT formalisms in the LDA and the GGA-PBE approximations for the exchange-correlation functional. Both DFT methods reproduce qualitatively the exact charge density. However, in this case the GGA-PBE functional gives a much better agreement with the exact result. Although GGA methods are currently the most commonly used in density functional-based simulations of complex systems, GGA functionals do not always perform in the same way and they are not always better than LDA. Moreover, both LDA and GGA may also fail on qualitative level. For instance, they predict metallic behavior for some materials (e.g., transition metal oxides) that are known to be semiconductors. Thus, for practical applications the exchange-correlation functional should be chosen carefully and its reliability tested for the specific system of interest.

EBSCOhost - printed on 2/13/2023 5:26 AM via . All use subject to https://www.ebsco.com/terms-of-use

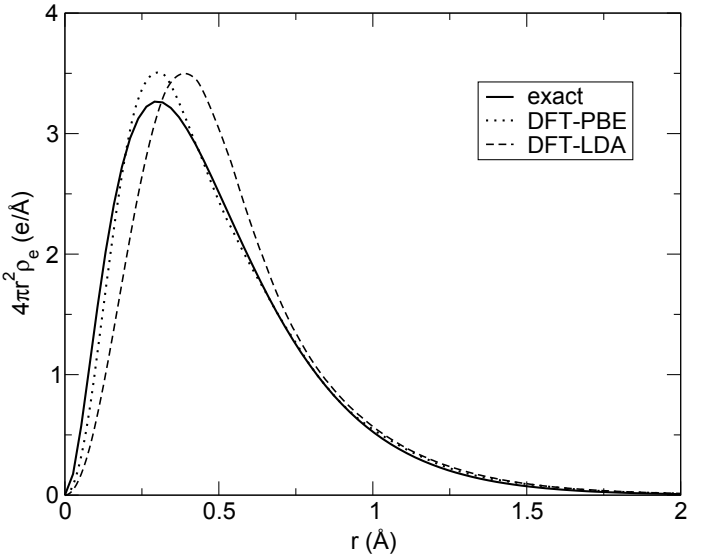


Figure 1. Radially averaged charge density of single helium atom using different approximations for the exchange-correlation functional: exact (Hart and Herzberg 1957, solid line), DFT-LDA (dashed line), and DFT-PBE (dotted line).

Some hints for practical DFT calculations. This section summarizes a number of points that need to be considered in practical DFT calculations. More details are provided e.g., in the book by Martin (2004). The first issue is concerned with the representation of the Kohn-Sham orbitals $\phi_i(\mathbf{r})$. They are usually expressed as a superposition of basis functions, which may be atomic orbitals centered on the atoms, planewaves or basis functions discretized on a real space grid. For instance, in the case of planewaves the Kohn-Sham orbitals are expanded as

$$\phi_j(\mathbf{r}) = \sum_{\mathbf{k}} c_{j,\mathbf{k}} \exp(i\mathbf{k} \cdot \mathbf{r}) \tag{18}$$

where $\mathbf{k}$ is the momentum of the electron. The coefficients $c_{j,\mathbf{k}}$ are varied to search for the ground state electronic structure. While localized atomic basis sets (mostly Gaussian-type orbitals) are dominantly used for molecules or atomic clusters, planewave basis sets are especially suited for condensed phases (e.g., crystals, liquids, glasses), i.e., for calculations that employ periodic boundary conditions. Special localized basis sets are also employed for periodic systems to improve scaling of DFT calculations from about N^3 to N (N being the number of particles), which allows to access system sizes of tens of thousands up to millions of atoms. Linear scaling DFT codes such as SIESTA (Artacho et al. 2008) or ONETEP (Skylaris et al. 2005) are actively being developed and they could have a great potential if they could reach the accuracy and general applicability needed, e.g., to model complex Earth materials.

In many cases, especially for periodic systems in planewave DFT calculations, the computational efficiency can be greatly improved by replacing the all-electron potential by an effective *pseudopotential*. Such effective potentials are constructed in a way that core electrons (which do not significantly contribute to the chemical bonding) are eliminated from the electronic structure calculation and treated together with the nuclei as an effective ionic potential. The valence electrons are described by simplified pseudo-wavefunctions that resemble the all-electron valence states outside a chosen cutoff radius r_c from the position of the nucleus. Different types of pseudopotentials vary in the constraints they have to fulfill outside

EBSCOhost - printed on 2/13/2023 5:26 AM via . All use subject to https://www.ebsco.com/terms-of-use

the cutoff radius compared to the all-electron orbitals. Norm-conserving pseudopotentials require that the pseudo- and the all-electron valence states for an atomic reference state have the same energies and charge densities outside r_c. Ultrasoft pseudopotentials (Vanderbilt 1990) relax on this condition and are considerably more efficient. Another important pseudopotential method that reconstructs all-electron behavior is the projector augmented wave (PAW) method (Blöchl 1994). As the core electrons are strongly localized and their orbitals vary rapidly on very short length scales, localized basis sets are usually employed to describe the core region. Some of the all-electron approaches for periodic systems treat core electrons explicitly by an atomic-like description which is coupled to a planewave approach for the region outside r_c. Such methods, e.g., the full potential linearized augmented planewave (LAPW) or the Korringa-Kohn-Rostoker (KKR) methods (Martin 2004) are computationally more expensive than pseudopotential techniques but considered the most precise electronic structure methods for solid state calculations.

Which of the described methods is the most appropriate depends on the specific system and the property of interest. Generally, the choice of pseudopotentials or an all-electron method, of the exchange-correlation functional, the type of basis set and the number of basis functions (for planewave calculations usually defined by the maximum planewave energy) and sampling grid in reciprocal space (the so-called Brillouin zone or *k*-point sampling) should be tested in each case to ensure convergence of the DFT calculation.

Strengths and shortcomings of standard DFT. Because the Kohn-Sham approach is one of the computationally least demanding methods for a quantum mechanical solution of many-particle systems it has been successfully applied for a few decades in many research fields to compute structural and dynamic properties of molecules or periodic systems, which includes bond-lengths and angles, vibrational frequencies and elastic constants. The deviation from the experimental data is usually no more than a few percent in these aspects (Haas et al. 2009). DFT methods also predict relatively well total energies of many electron systems and inter-particle interactions, which is important for an accurate simulation of complex real materials.

However, there are also some limitations. For instance, LDA calculations often result in electronic charge densities that are more homogeneous (delocalized) than the exact ones, which is even evident in Figure 1. The agreement is improved significantly when the density gradient-corrected GGA methods are used. DFT usually overestimates the binding energies of molecules and solids. Another important difficulty of DFT is that the DFT ground state is usually a bonding state, which leads to pairs of electrons even in well-separated atoms (Cohen et al. 2008). Weak inter-molecular interactions such as hydrogen bonding or van der Waals attraction are not well described in standard DFT but correction schemes have been proposed recently (e.g., Klimeš and Michaelides 2012; Tkatchenko et al. 2012). Of major importance for accurate predictions of electronic excitation spectra is the large underestimation of the electronic energy band gaps in semiconductors, which can be as large as ~40% for wide-gap semiconductors or even lead to the prediction of metallic behavior for materials that exhibit small band gaps of not more than a few eV (Friedrich and Schindlmayr 2006; Marsman et al. 2008; Xiao et al. 2011). Although in many cases GGA functionals improve the description of binding and atomic energies as well as bond-lengths and angles compared to LDA, the description of semiconductors is only marginally better. The underlying problem is that in principle the eigenvalue spectra obtained using standard DFT approach have no direct physical meaning (however, these eigenvalues have a well defined mathematical meaning, see next section) and their usage for the derivation of the electronic transition energies is questionable. Strongly correlated materials containing elements with incompletely filled *d*- or *f*-electron shells are also badly described. For instance, the electronic ground state of transition metal and actinide oxides is often predicted to be metallic whereas in reality these materials are insulators (Wen et al. 2013). Furthermore, the enthalpies of reactions involving actinide-bearing molecules are

EBSCOhost - printed on 2/13/2023 5:26 AM via . All use subject to https://www.ebsco.com/terms-of-use

highly overestimated, for instance by as much as 30% or about 100 kJ/mol in case of uranium (Shamov et al. 2007). Below, we will present methods to overcome some of these difficulties.

Hybrid functionals. Hybrid functionals are constructed by combining standard DFT functionals with Hartree-Fock exact exchange. The relative weights of the two ingredients are fitted to reproduce selected properties of a test set of molecules or chosen from theoretical considerations. The leading idea behind this approach is that the exchange energy, which can be exactly computed using the Hartree-Fock method, is usually much larger than the correlation effects. However, a simple combination of exact exchange as computed by the Hartree-Fock method and the correlation energy functional used in standard DFT leads to a worse performance than using standard DFT (Koch and Holthausen 2000). Instead of using full exact exchange, Becke (1993) proposed the weighted combination of the different descriptions of the exchange-correlation energy. The contribution of each term is fitted to best reproduce the atomization and ionization energies as well as the proton affinities. The most commonly and successfully used functionals of this type are B3LYP (Stephens et al. 1994) and PBE0 (Perdew et al. 1996b; Burke et al. 1997). The latter functional was constructed from theoretical considerations that suggest an admixture of 25% exact exchange to the DFT exchange-correlation functional. Hybrid functionals often provide an improved description of the total energies and the band gaps (e.g., Xiao et al. 2011). They also have been proven to provide the correct physical behavior of Mott-insulators, such as the band gap state of the reduced TiO_2 (110) surface (Di Valentin et al. 2006). However, the performance of these methods for an accurate determination of the electronic excitation energies is not guaranteed and the result often depends on the functional used in the investigation. For instance, in the case of bulk TiO_2, although the overall electronic structure is better described than by standard DFT functionals, the experimental band gap of about 3 eV is overestimated by 1.1 eV by PBE0 (Ammal and Heyden 2010) and 0.4 eV by B3LYP (Di Valentin et al. 2006). On the other hand the standard DFT underestimates the band gap by about 1.1 eV (Di Valentin et al. 2006). The underlying reason for such a behavior of hybrid functionals is that for bulk TiO_2 the amount of exact exchange needed to reproduce the experimental band gap is smaller than the 25% and 20% included in PBE0 and B3LYP functionals respectively (~13% according to Zhang et al. 2005a). Similar overcorrection of the band gap by hybrid functionals is also observed in case of bulk silicon, for which band gaps obtained with both PBE0 and B3LYP functionals are also overestimated (Jain et al. 2011; see also Table 1). These examples illustrate that hybrid functionals do not necessarily provide accurate excitation energies and resulting absorption coefficients, although they were successfully applied to compute the excitation energies and band gaps of variety of materials, which we will discuss later.

Table 1. Band gap energy for bulk Si computed using different electronic excitation methods. The values are taken from Table 1 of Jain et al. (2011).

Method	**Energy (eV)**
Hartree-Fock	6.63
PBE (DFT)	0.55
PBE0 (hybrid DFT)	1.71
B3LYP (hybrid DFT)	1.83
GW	1.23
GW-BSE	1.23
experiment	1.16

DFT+$\mathcal{U}$ approach. The quantitative difference between the measured electronic structure and that predicted by DFT is especially large for materials in which electrons tend to localize and strongly interact between themselves. These include the transition metal oxides and *f*-elements such as rare earth or actinide elements and compounds. One of the methods used to correct the band structure is DFT+$\mathcal{U}$, in which an additional orbital-dependent interaction is added to the Kohn-Sham Hamiltonian (Eqn. 11) to improve the description of strongly

EBSCOhost - printed on 2/13/2023 5:26 AM via . All use subject to https://www.ebsco.com/terms-of-use

correlated electrons, by application of a Hubbard-like model (see Cococcioni 2010), i.e.,

$$E_{\mathcal{U}} = \sum_{l,\sigma} \frac{\mathcal{U}^l}{2} \mathrm{Tr}\left[\mathbf{n}^{l\sigma}(1-\mathbf{n}^{l\sigma})\right] \tag{19}$$

with $\mathcal{U}^l$ being the interaction parameter and Tr[...] the trace of the matrix [...]. In the above equation $\mathbf{n}^{l\sigma}$ is the occupation matrix of the considered orbitals of given angular momentum l (l = 2 for d and 3 for f electrons) and spin σ. The effect of adding the Hubbard term is the shift of the energy of localized orbitals relative to the other orbitals. The shift equals $\mathcal{U}/2$ and is negative for fully occupied orbitals and positive for empty orbitals. It usually leads to the increase of the band gap in semiconductors. Because of its simplicity this method has an important advantage over the other corrections to standard DFT such as the hybrid functionals introduced above, as it does not require substantial computational effort in addition to standard DFT. The $\mathcal{U}$ parameter can be found on empirical basis, i.e., it can be adjusted to reproduce given properties such as band gap or bulk modulus, but it can also be computed using linear-response theory e.g., by the method of Cococcioni and de Gironcoli (2005). The full method and its applicability have been described in a recent review by Cococcioni (2010). It has been successfully applied for the computation of various properties of materials involving transition-metal compounds (Calzado et al. 2008; Morgan and Watson 2009). This method has been used together with quantum molecular dynamics to simulate the distribution and dynamic behavior of electric charge in reduced metal-oxide (Kowalski et al. 2010). However, DFT+$\mathcal{U}$ is applicable to particular orbitals only and it is known that it can only partially correct the band gaps of transition-metals (Morgan and Watson 2009). Therefore, compared to the methods described below it has a limited applicability for electronic excitation spectroscopy.

Excitation methods

Standard DFT only provides information about the ground state properties of the considered system. Spectroscopic techniques are usually based on the interaction of a probe (e.g., photon, electron, and neutron) with the sample, which involves the creation or annihilation of collective excitations such as lattice vibrations (phonons) or of electronic excited states. In the following we provide a short overview about some popular or emerging approaches to make reliable predictions of such excited states, which is a prerequisite to compute e.g., theoretical spectra.

Density functional perturbation theory. Many properties of materials that are measured using spectroscopic methods can be formally described by derivatives of the total energy with respect to some perturbations, which may be atomic displacements or external electromagnetic fields. These derivatives can be computed by direct methods, e.g., by applying small finite displacements to the nuclear positions to compute the force constant matrix, from which the vibrational spectra of a crystal can be derived. An alternative approach that avoids the use of supercells and extends beyond the capabilities of the finite difference methods uses the electron-density linear response following density-functional perturbation theory (Baroni et al. 1987, 2001, 2010; Gonze 1997; Gonze and Lee 1997). The computational cost for the computation of the response of the electron-density to a single perturbation is of the same order as the cost for the solution of standard Kohn-Sham equation for the electron-charge density. Applications of density-functional perturbation theory include the computation of phonon spectra (Baroni et al. 2001), Raman scattering cross-sections (Veithen et al. 2005) or nuclear magnetic resonance spectra (Putrino et al. 2000), which will be dealt with in more detail later.

Electronic excitation methods. In order to compute the electron excitation properties of a given system the excited states have to be derived. For the Hartree-Fock method, in line with Koopmans' theorem, the eigenvalue of an orbital is equal to the change in the total energy of the N-electron system upon subtraction or addition of an electron, assuming that all other orbitals do not change during this process. This implies that the Hartree-Fock eigenvalue

EBSCOhost - printed on 2/13/2023 5:26 AM via . All use subject to https://www.ebsco.com/terms-of-use

spectrum can be directly used for the analysis of the electronic excitations of a given system. Despite its similarity to Hartree-Fock approach, in case of DFT methods there is a conceptual problem of using them for analysis of electronic excitations, as DFT is a ground state theory by principle. The KS eigenvalues are not the true energies for adding or subtracting electrons or for excitations. In principle these do not have a physical meaning. However, the KS orbitals have a definitive mathematical meaning, which is related to the Slater-Janak theorem. According to Janak (1978) the KS eigenvalue ε_i is the derivative of the total energy with respect to the occupation of a state n_i

$$\varepsilon_i = \frac{dE_{total}}{dn_i} \tag{20}$$

The key issue for DFT-based electronic spectroscopy is to obtain a correct description of energy differences between the highest occupied and lowest unoccupied molecular orbitals, so called HOMO-LUMO gaps (or band gaps in case of solids), that are significantly below the experimental values for most materials, and the failure is most pronounced for wide gap semiconductors (Marsman et al. 2008). Unfortunately, even knowledge of the exact exchange-correlation functional is not expected to provide the correct band-gaps (Perdew and Levy 1983). At first glance this disqualifies DFT as a tool for the investigation of electronic excitation spectra of materials. However, Hohenberg and Kohn (1964) have shown that the ground state electron density determines the external potential. This implies that DFT methods could be used in principle to calculate excitation energies—which are also determined by the external potential! However, the approach to extract such information does not have to be simple. Below we present a short overview of DFT-based methods that allow for the calculation of electron excitation energies and associated absorption spectra. Details about the theory and performance of different electronic excitation methods are provided, e.g., in a review by Onida et al. (2002).

D*SCF methods.* The simplest way to derive excitation energies is to compute the energies of a system with removed or added electrons. These methods are called ΔSCF methods, as such an energy difference approach can be used in any self-consistent field (SCF) method, including Hartree-Fock. The electron removal energy can be computed as

$$E_{removal} = E(N) - E(N-1) \tag{21}$$

where $E(N)$ and $E(N-1)$ are the energies of the system with N and $N-1$ electrons, respectively. This energy can be also estimated from the Slater transition state as the eigenvalue of the system containing half an electron in the considered orbital i

$$E_{removal} = \varepsilon_i(n_i = 0.5) \tag{22}$$

In similar fashion one can compute the electron addition energy and therefore the excitations. This method gives a good estimation of the ionization energies and the transition energies (McMahan et al. 1988; Massobrio et al. 1995, 1996). It can also be applied to studies of excited molecules on surfaces (Gavnholt et al. 2008) and in dense fluids (Kowalski 2010). However, as DFT is derived assuming ground state properties, such a method has a theoretical justification only for the states with the lowest energy for a given symmetry, such as 1*s* to 2*p* transitions. The lack of a solid theoretical background is an important limitation of the ΔSCF methods and its applicability to the higher excitation states could be questionable.

GW approximation and BSE equation. Failure of DFT to describe correctly electron excitation energies is also due to the fact that it is based on a single electron description. If an electron is added to or removed from a many-electron system, complicated many-body interactions occur that need to be considered. For instance, an additional electron moving in a semiconductor interacts with all the other electrons and nuclei of the system and as a consequence behaves like a much heavier particle compared to an electron in free space. In

EBSCOhost - printed on 2/13/2023 5:26 AM via . All use subject to https://www.ebsco.com/terms-of-use

order to obtain the physically correct excitation energies of a given system one has to derive the so-called *quasiparticle* (QP) energies, which are the energies required to remove or add an electron. Formally, one has to solve the quasiparticle equation (Friedrich and Schindlmayr 2006; Deslippe et al. 2012),

$$-\frac{\nabla^2}{2} + v_s(\mathbf{r})\psi_i^{\mathrm{QP}}(\mathbf{r},\sigma) + \int d\mathbf{r}'\Sigma(\mathbf{r},\mathbf{r}',\varepsilon_i^{\mathrm{QP}})\psi_i^{\mathrm{QP}}(\mathbf{r}',\sigma) = \varepsilon_i^{\mathrm{QP}}\psi_i^{\mathrm{QP}}(\mathbf{r},\sigma) \tag{23}$$

which is similar to the KS Equation (12) except that the exchange-correlation potential is replaced by the non-local self-energy $\Sigma(\mathbf{r},\mathbf{r}',\varepsilon_i^{\mathrm{QP}})$ that accounts for all the many-body interaction effects among the electrons, i.e.:

$$U_{xc}(\mathbf{r}) \rightarrow \int d\mathbf{r}'\Sigma(\mathbf{r},\mathbf{r}') \tag{24}$$

The self-energy Σ can be expanded in terms of the single particle Green's function G and the screened Coulomb interaction W. $G(\mathbf{r},\mathbf{r}',t)$ represents the conditional probability of finding an electron at $\mathbf{r}$ and time t when there was an electron at $\mathbf{r}'$ and time $t = 0$. W is a product of the dielectric matrix and the electron Coulomb potential, and can be derived within the so-called random phase approximation. Truncating the expansion of Σ after the first term leads to $\Sigma = iGW$, thus the name GW approximation (Hedin 1965). After computing Σ and a ground state DFT calculation, the first order approximation to quasiparticle energies can be derived from 0^{th} order perturbation theory

$$\varepsilon_i^{\mathrm{QP}} = \varepsilon_i^{\mathrm{DFT}} + \left\langle \phi^{\mathrm{DFT}} \middle| \Sigma(\mathbf{r},\mathbf{r}',\varepsilon_i^{\mathrm{QP}}) - U_{xc} \middle| \phi^{\mathrm{DFT}} \right\rangle \tag{25}$$

The *GW* approximation from principle works for a charged excitation, i.e., removal or addition of an electron. However, an optical absorption can be viewed as the addition of an electron and the formation of the hole left behind, and both structures, i.e., the electron and the hole, can interact with one another. Inclusion of electron-hole interaction can be performed by solving the two-particle Bethe-Salpeter equation (BSE) (Salpeter and Bethe 1951). The BSE equation is the last step, after DFT and *GW* methods, in determining the optical properties of materials. By considering the electron-hole interactions, good agreement between theory and experiment can be achieved, which is important for insulators and semiconductors. The Bethe-Salpeter equation has been successfully applied to the calculation of absorption spectra of various systems, which we will discuss later. A full theoretical background of these advanced electronic structure methods is described, e.g., in Kohanoff (2006).

Time-dependent DFT. Another method used for the derivation of electronic excitation energies is the time-dependent density functional theory (TDDFT). In TDDFT, one looks for the time-dependent charge density $\rho(t)$, which is the result of the solution of the time-dependent Schrödinger equation. TDDFT can be formulated in an equivalent way through an analog of the Hohenberg-Kohn theory, which is the backbone of conventional DFT. Runge and Gross (1984) have shown that for any many-particle system that is subject to a time-dependent potential (e.g., due to interaction with a photon) all physical observables are uniquely determined by the knowledge of the time-dependent electronic density $\rho(\mathbf{r},t)$ and the state of the system at any moment of time. The single particle time dependent KS equation reads

$$\hat{f}^{\mathrm{KS}}(t)\phi_i(\mathbf{r},\sigma,t) = i\frac{\partial}{\partial t}\phi_i(\mathbf{r},\sigma,t) \tag{26}$$

where $\hat{f}^{KS}(t)$ is the time dependent single particle operator (analog to Eqn. 12)

$$\hat{f}^{\mathrm{KS}}(t) = -\frac{1}{2}\nabla^2 + U_s(\mathbf{r},t) \tag{27}$$

and $U_s(\mathbf{r},t)$ is the time-dependent single particle potential.

EBSCOhost - printed on 2/13/2023 5:26 AM via . All use subject to https://www.ebsco.com/terms-of-use

If the time-dependent external perturbation is small, the dynamics of the electronic system can be described by linear-response theory. The respective linear density-response function $\chi(\mathbf{r},\mathbf{r}',t-t')$ describes the coupling between the external potential $U_{ext}(\mathbf{r}',t')$ and the electron density of the system $\rho(\mathbf{r},t)$. The poles of its time Fourier transform $\chi(\mathbf{r},\mathbf{r}',\omega)$ (with ω being the angular frequency) correspond to the exact excitation energies. Furthermore, the linear response function is a functional of the ground-state density $\rho(\boldsymbol{r})$, which is accessible by standard DFT (see e.g., Botti et al. 2007). In addition to the static DFT exchange-correlation functional, TDDFT calculations require the knowledge of the functional derivative of the time-dependent exchange-correlation potential with respect to the time-dependent density, the so called exchange-correlation kernel. A major task in TDDFT is to find an approximation for this kernel. The difficulty arises from the fact that such an effective potential at any given instant depends on the value of the density at all previous times. This is the reason, why the development of the TDDFT is still behind that of DFT itself. In most of the TDDFT implementations the so-called *adiabatic approximation* is used in which the exchange-correlation kernel is approximated by the functional derivative of the time-independent exchange-correlation energy with respect to the charge density at a given time. A persisting problem for many applications is the fact that TDDFT often ignores the non-locality of the core-hole interaction. Despite some fundamental challenges, TDDFT has been extensively used in the computation of the energies of excited states, mainly of isolated systems (Dreuw and Head-Gordon 2005). Its application to condensed phases is more recent (Botti et al. 2007). TDDFT functionality has been implemented in a number of codes that compute e.g., optical or X-ray absorption spectra, which will be discussed in more detail below.

So far, we have introduced basic ideas about quantum-chemical methods and their application to excitation spectroscopy. For a more comprehensive description of these methods we refer the reader to the many existing books on electronic structure calculations and applied quantum mechanics (e.g., Koch and Holthausen 2000; Martin 2004). In the remainder of this section we summarize approaches to describe particle interactions or the atomic dynamics by classical laws of Physics.

Classical force field methods

The electronic structure methods described above are computationally expensive and sometimes more efficient representations of atomic interactions are needed, e.g., to model the structure of complex silicate melts, extended defects in crystals, or thermal and ionic diffusion processes in minerals and melts. For that purpose, interatomic potentials are constructed that approximate the electronic subsystem by a set of analytical functions. Usually, such potentials are pairwise additive and the functional form of the individual terms of the potential are chosen based on the classical theory of intermolecular forces (Stone 1996). For oxides and silicates, these classical potentials are dominated by electrostatic Coulomb interactions between anions and cations, and by short-range repulsion that mimics the overlap of the charge densities of neighboring ions. In addition, an attractive potential term is added that represents van der Waals interactions that arise, e.g., from instantaneous dipole fluctuations (London dispersion forces). Using such a simple ionic interaction model (also called rigid ion model), the potential energy U of a system of N ions is calculated using the following formula

$$U = \sum_{i=1}^{N} \sum_{j>i}^{N} \left(\frac{q_i q_j}{r_{ij}} + A_{ij} \exp(-\alpha_{ij} r_{ij}) - \frac{C_{ij}}{r_{ij}^6} \right) \tag{28}$$

where $r_{ij} = |\mathbf{r}_i - \mathbf{r}_j|$ is the distance between the two ions i and j, q_i and q_j are their charges. A_{ij}, σ_{ij} and C_{ij} are parameters characteristic for each pair of ions (e.g., O-O, Si-O and Si-Si in the case of SiO_2). Although rigid ion models have been used to study the structure and some physical properties of silicate crystals and melts (e.g., Matsui 1988; van Beest et al. 1990; Matsui 1996; Horbach et al. 2001; Guillot and Sator 2007; Lacks et al. 2007), they are often

EBSCOhost - printed on 2/13/2023 5:26 AM via . All use subject to https://www.ebsco.com/terms-of-use

not appropriate to reproduce vibrational properties. One of their apparent deficiencies is the neglect of polarization effects. For example, Wilson et al. (1996) showed that the explicit inclusion of dipole polarizability into a classical potential was needed to obtain the correct number of infrared absorption peaks for amorphous SiO_2.

A simple extension of the rigid ion model to include polarization is the shell model by Dick and Overhauser (1958). In this model, the polarizable ions (e.g., the oxygen anion) are described by a positively charged ionic core and a flexible negatively charged shell that are connected by springs. The force constant of the springs is related to the polarizability. Shell models with empirically fitted parameters were, for instance, used to reproduce the phonon dispersion curves of SiO_2 quartz (Schober et al. 1993b) and Al_2O_3 corundum (Schober et al. 1993a). An alternative formulation of a polarizable ion model using ionic polarizabilities was successfully explored by Madden and Wilson (2000). A second extension of the rigid ion model is related to the ionic radii, which depend on the atomic environment. This effect is related to the compressibility of the electronic charge density, which is substantial for anions, but also for the larger cations. Such breathing shell models were parameterized to reproduce experimental lattice volumes and elastic constants of individual mantle silicates in a range of pressures and temperatures (Matsui 2000; Matsui et al. 2000; Zhang et al. 2005b).

The appeal to use the shell model and its extensions has been their simplicity expressed in a small number of adjustable parameters. For many potentials, the latter were optimized to reproduce experimental data. This approach becomes less evident for more complicated crystal structures or even for melts where only a relatively small number of experimental data is available. Furthermore, a potential that reproduces, e.g., experimental densities does not necessarily produce the correct structure. However, this is a prerequisite for an accurate prediction, e.g., of vibrational properties. A more systematic approach of constructing reliable potentials was introduced by Laio et al. (2000), who optimized the parameters of their classical model for Fe by fitting classical interatomic forces to forces obtained from reference DFT calculations. Using the same idea, a successful polarizable force field for SiO_2 was parameterized by fitting to *ab initio* forces, stress tensors and total energies (Tangney and Scandolo 2002). However, the extension of the latter potential to silicates appeared to be difficult since the potential uses (constant) partial charges, which limits its transferability.

Recent advances in electronic structure calculations have enabled the explicit optimization of the polarization terms of an ionic potential through the *ab initio* calculation of ionic dipoles and quadrupoles from maximally localized Wannier functions (MLWF) (Marzari and Vanderbilt 1997; Aguado et al. 2003) and of ionic polarizabilities from the linear response of the MLWFs to an electric field perturbation (Heaton et al. 2006). The "aspherical ion model" (Aguado et al. 2003; Madden et al. 2006) combines ideas of the breathing shell model and an explicit parameterization of individual contributions to the ionic interactions up to the quadrupolar level in both ion polarization and shape deformations. It necessarily contains a larger number of parameters than the other classical potentials described above. However, this choice is justified by a systematic fitting of subsets of parameters to different DFT-related properties. In addition to forces and stress tensors, these potentials are also optimized by fitting to *ab initio* dipoles and quadrupoles. An optimized set of potentials for the CaO-MgO-Al_2O_3-SiO_2 system has been shown to be transferable in a wide range of pressures and temperatures and in a wide compositional range (Jahn and Madden 2007a). Some aspects of future developments of force fitting for ionic systems are discussed in a review by Salanne et al. (2012).

A purely ionic approach to represent atomic interactions fails for molecular systems. In this case, strong covalent bonds have to be accounted for by adding additional terms to the potential function. For carbonates, rigid ion (Dove et al. 1992) or shell models (Rohl et al. 2003) were complemented by an intramolecular spring-like C-O interaction as well as three- and four-body geometric terms. For aqueous solutions, a number of polarizable and

EBSCOhost - printed on 2/13/2023 5:26 AM via . All use subject to https://www.ebsco.com/terms-of-use

non-polarizable water potentials exist (e.g., Berendsen et al. 1981; Jorgensen et al. 1983; Berendsen et al. 1987; Mahoney and Jorgensen 2000; Abascal and Vega 2005; Tazi et al. 2012). The performance of some water models in terms of structure and vibrational properties was reviewed by Kalinichev (2001). Generally, they provide a more or less reasonable structure of liquid water. The TIP4P/2005 model (Abascal and Vega 2005) was specifically optimized to reproduce the phase diagram of H_2O up to pressures of 4 GPa. Recently, dissociative water potentials were parameterized (e.g., Mahadevan and Garofalini 2007; Pinilla et al. 2012).

Molecular dynamics

Descriptions of the particle interactions discussed in previous sections allow us to simulate dynamic properties of an atomic or ionic system. One of the most commonly used techniques to perform such simulations is molecular dynamics (MD). MD is a finite difference method to evolve a set of particles through time and space by a numerical solution of Newton's equations of motion. It is a very useful technique for sampling the structure of disordered systems (fluids, melts, glasses) but also for the investigation of crystal properties, especially at high temperatures where anharmonic effects are significant.

For a system of classical particles in thermodynamic equilibrium, potential and kinetic energies are distributed according to the equipartition theorem. A system that is out of equilibrium would tend to reach equilibrium in the course of a MD simulation. The total energy of the system, E, is defined as the sum of the total potential energy and the total kinetic energy:

$$E = U + K = U + \sum_{i=1}^{N} \frac{m_i}{2} v_i^2 \tag{29}$$

where m_i and v_i are the mass and the velocity of particle i. In practice, the starting point of MD is a set of N atoms that is distributed in a simulation box, e.g., close to a feasible crystal structure but for a melt simulation one may also use a random atomic configuration. In addition, it is necessary to define atomic masses and provide an interaction model, which may be a classical potential or based on an electronic structure method such as DFT. Forces $\mathbf{F}_i$ acting on the individual particles i are calculated from the gradient of the respective potential $U(\mathbf{r})$. These forces accelerate the atoms according to Newton's second law, which leads to a set of differential equations

$$\mathbf{F}_i = -\frac{\partial}{\partial \mathbf{r}_i} U(\mathbf{r}) = m_i \frac{\partial^2}{\partial t^2} \mathbf{r}_i \tag{30}$$

In addition to the initial atomic positions, a starting velocity is assigned to each atom. In order to integrate the equations of motion numerically, the infinitesimal time interval ∂t is replaced by a (small) time step Δt, typically of the order of 10^{-15} s. Knowing the positions, velocities and forces of all atoms at some instant of time, t, the system can evolve to the next time step. In an isolated system, the total energy and the simulation cell volume are constant and the system equilibrates at a specific temperature, which is related to the average kinetic energy, which is given by statistical mechanics

$$\left\langle \frac{m_i}{2} v_i^2 \right\rangle = \frac{3}{2} k_B T \tag{31}$$

with k_B being the Boltzmann constant. The corresponding thermodynamic ensemble is called *NVE*, which reflects the constant number of particles, N, volume, V, and total energy, E. MD simulations can also be run at constant volume and temperature (*NVT*) or, similar to experiments, at constant pressure and temperature (*NPT*). In the latter case, which constitutes a closed system, temperature and pressure are controlled by a thermostat and a barostat that can exchange heat and work with the system (see e.g., Martyna et al. 1994).

EBSCOhost - printed on 2/13/2023 5:26 AM via . All use subject to https://www.ebsco.com/terms-of-use

For a more comprehensive introduction to the molecular dynamics method in general and to technical aspects of classical MD, the reader is referred to textbooks by Allen and Tildesley (1987) or Frenkel and Smit (2002). *Ab initio* molecular dynamics (Marx and Hutter 2000), which is based on a quantum mechanical evaluation of the forces, has become feasible with the availability of high performance computers. After the computation of forces, the nuclei are moved according to classical mechanics. There are two types of *ab initio* MD: In Born-Oppenheimer MD the electronic energy of the system is minimized in each time step whereas in Car-Parrinello MD (Car and Parrinello 1985) the electrons are represented as quasi-particles with a ficticious mass and temperature. In well behaved systems, the Car-Parrinello electron dynamics oscillates around the true Born-Oppenheimer energy surface and energy transfer between the electronic and the nuclei dynamics is avoided by choosing characteristic frequencies of the two subsystems that do not overlap. Although the time steps in Car-Parrinello MD are typically a factor of ten smaller than those in Born-Oppenheimer MD, Car-Parrinello MD is usually more efficient. On the other hand, Born-Oppenheimer MD is considered more robust and more generally applicable. For investigations of some properties of light particles (H, He) or hydrogen-bonded systems such as water, the dynamics of the nuclei may also have to be treated quantum mechanically, e.g., by using path integral molecular dynamics simulations (Marx and Parrinello 1996).

In the course of a molecular dynamics simulation, a number of properties are frequently recorded. This includes, among others, the atomic positions and velocities as well as instantaneous values of the total energy, volume, pressure and temperature of the system, the simulation cell parameters and the stress tensor. One quick way to characterize the thermodynamic state of the system is to compute average values of T, P, V or E. Structural, transport and vibrational properties are usually derived from the recorded simulation data via spatial and/or time correlation functions. A comparison to experimental data that are often recorded in Fourier space requires a Fourier transformation of the correlation function f from real (position vector $\mathbf{r}$) to reciprocal (wavevector $\mathbf{Q}$) space or from the time (t) to the frequency ($\omega = 2\pi\nu$) domain, which for a periodic system can schematically be written as

$$g(\mathbf{Q}) = \frac{1}{2\pi}\int_{-\infty}^{\infty} d\mathbf{Q}\left\langle f(\mathbf{r}-\mathbf{r}')f(\mathbf{r}')^{*}\right\rangle \exp(-i\mathbf{Q}\cdot\mathbf{r}) \tag{32}$$

$$g(\omega) = \frac{1}{2\pi}\int_{-\infty}^{\infty} dt\left\langle f(t-t')f(t')^{*}\right\rangle \exp(-i\omega t) \tag{33}$$

STRUCTURE DETERMINATION AND OPTIMIZATION

Crystals are characterized by a three-dimensional periodic arrangement of atoms. The crystal structure consists of a basis (e.g., group of atoms) located on points of a lattice with a certain symmetry, which may be represented by a unit cell, i.e., a small (or the smallest) periodic spatial unit of the crystal (see text books such as Putnis 1992). At the limit of zero temperature (T = 0 K), entropy vanishes and a perfect defect-free crystal becomes thermodynamically stable. In this situation, the Gibbs free energy can be replaced by the enthalpy $H = E + PV$, where V is the unit cell volume. Often, this approximation is used to study the relative phase stability of different crystal structures. To obtain the lattice energy at T = 0 K, E_0, the atoms of the crystal structure should not experience any force, i.e., they should be positioned in the minimum of their potential energy function. Likewise, the lattice parameters should be chosen such that the computed pressure tensor corresponds to the desired (e.g., hydrostatic) pressure conditions. The search for such an optimized crystal structure is a standard tool of most of the relevant molecular modeling codes. Note that a proper quantum mechanical treatment requires the evaluation of the zero-point energy, which arises due to the fact that atomic vibrations do not vanish even

EBSCOhost - printed on 2/13/2023 5:26 AM via . All use subject to https://www.ebsco.com/terms-of-use

at the lowest possible temperatures. However, the relative effect of a zero point energy correction to free energy differences between two crystal structures is often small compared to the systematic errors arising e.g., from choice of the specific DFT exchange-correlation functional.

The possibility to predict crystal structure parameters and crystal lattice energies or enthalpies accurately motivated the development of new computational methods of crystal structure prediction, such as random structure search (Pickard and Needs 2011), metadynamics (Martoňák et al. 2003) and evolutionary algorithms (Oganov and Glass 2006, 2008). Phase transitions may be observed directly in MD simulations if they are displacive (see e.g., Mendelssohn and Price 1997; Shimobayashi et al. 2001; Jahn 2008b, for $MgSiO_3$ enstatites). The mechanisms of martensitic or other reconstructive phase transitions have been explored by metadynamics, e.g., for SiO_2 (Martoňák et al. 2006, 2007) and $MgSiO_3$ (Oganov et al. 2005; Jahn and Martoňák 2008; Jahn 2010), or by transition path sampling MD (Zahn 2013).

The periodically repeated structure of a crystal results in well-defined peaks in the neutron or X-ray diffraction patterns, which are used to solve a crystal structure or to refine structural parameters. A new crystal structure can be solved using single crystal diffraction provided that a sufficiently large single crystal is available. However, experiments often yield fine-grained polycrystalline samples, which are characterized by powder diffraction. The refinement of such diffraction patterns requires a structural model, which in the case of an unknown crystal structure is not easy to obtain and may be provided from molecular simulations. For example, the structure of the so-called 3.65 Å phase, which is a dense hydrous phase of $MgSi(OH)_6$, has recently been solved by combination of educated guess, DFT calculations and Rietveld refinement (Wunder et al. 2012). In a first step, Wunder et al. (2011) suggested that the structure of this phase could be similar to one of the $Al(OH)_3$ polymorphs assuming a substitution mechanism $2\ Al^{3+} \rightarrow Mg^{2+} + Si^{4+}$. Assuming a random distribution of Si and Mg on the octahedral sites, Rietveld refinement of the powder diffraction pattern using a structure model similar to δ-$Al(OH)_3$ with space group *Pnam* yielded satisfactory results. However, two small diffraction peaks around $2\theta = 21°$ were not resolved (see Fig. 2a). A more ordered structure with alternating Mg and Si between neighboring octahedra (shown in Fig. 2b), which is plausible due to electrostatic considerations, reduces the space group to $P2_1$. A full DFT structure optimization, which includes atomic positions and lattice parameters, provided a new structure model. Furthermore, the resulting total energies for different initial atomic configurations put some constraints on the positions of the H atoms in the structure that are not resolvable by powder diffraction. Using the DFT-optimized structure, Rietveld refinement was repeated and resulted in an excellent fit of the experimental diffraction pattern, now including the two previously unresolved peaks (Fig. 2b). Additional evidence that the new structure model is correct came from comparison of IR spectra with computed vibrational spectra (Wunder et al. 2012), which will be discussed in more detail below.

At high temperatures, diffraction peaks broaden due to the increased thermal atomic motion and they shift due to the thermal expansion of the lattice. Both effects can be studied in molecular dynamics simulations. Diffraction experiments also provide a unique fingerprint of the structure of non-crystalline materials, such as melts and glasses. Due to the lack of long-range order, however, there are no sharp diffraction peaks and there is no directional dependence, which does not allow a unique structural solution by direct inversion. The oscillatory behavior of the diffraction pattern of a melt or glass (see e.g., Fig. 3) arises from the short-range (nearest atomic neighbor) and intermediate-range (up to a few next nearest neighbors) chemical or topological order.

Formally, a diffraction pattern of a powder sample or of a liquid is proportional to the static structure factor, $S(Q)$, which is defined as

$$S(Q) = \sum_{\alpha}\sum_{\beta}(c_\alpha c_\beta)^{1/2}\frac{b_\alpha b_\beta}{\langle b^2\rangle}S_{\alpha\beta}(Q) \tag{34}$$

EBSCOhost - printed on 2/13/2023 5:26 AM via . All use subject to https://www.ebsco.com/terms-of-use

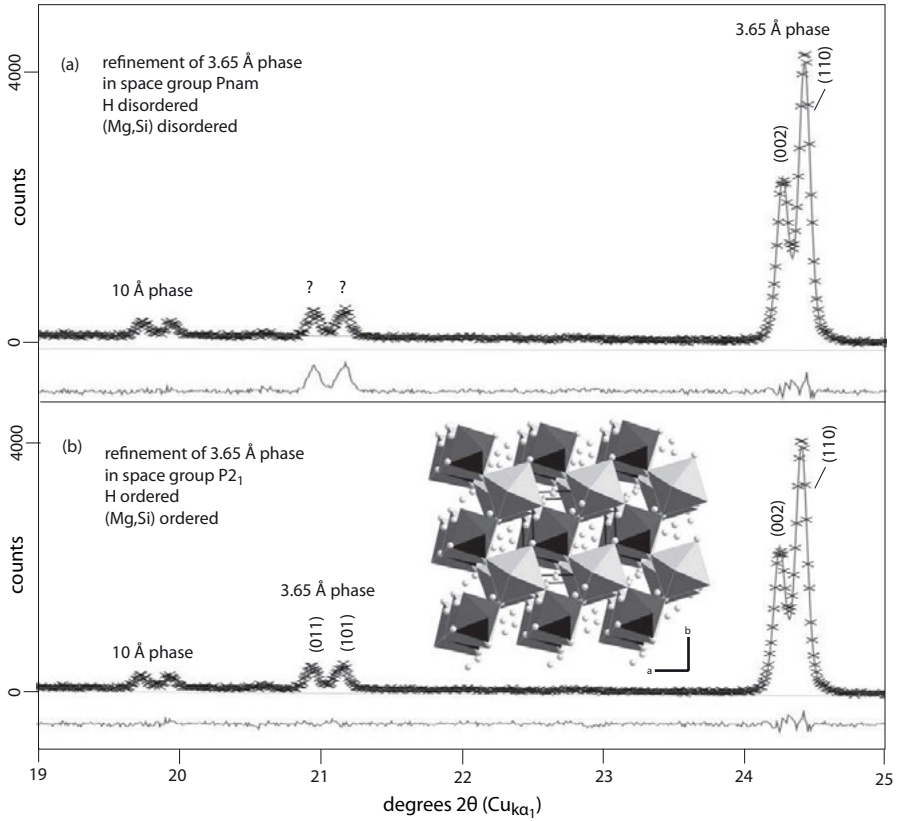


Figure 2. Part of the X-ray powder diffraction pattern of the 3.65 Å phase ($MgSi(OH)_6$) using a Cu K_{a1} source (Wunder et al. 2011, 2012). Initially, refinement was made using a structure with space group *Pnam* (a). DFT structure optimization lead to a new crystal structure model with reduced symmetry (space group $P2_1$) (b). Also shown is a snapshot of this structure viewed along *c* (modified after Wunder et al. 2012).

where the double sums run over the number of different elements in the system, $\langle b^2 \rangle = \Sigma_\alpha(c_a b_a^2)$, c_α and b_α are the respective concentrations and scattering lengths (e.g., for X-rays or neutrons). Q is the momentum transfer, i.e., the difference between the incoming and the diffracted wavevector of the probe. Assuming elastic scattering, $Q = 4\pi\sin(\theta)/\lambda$, where θ and λ are the Bragg angle (i.e., half of the angle between the incident and the diffracted wavevector) and the wavelength of the diffracted beam. For X-rays, the scattering lengths b_i depend on Q. The partial structure factors $S_{a\beta}(Q)$ are related to the atomic positions $\mathbf{r}_j$ by the relation

$$S_{\alpha\beta}(Q) = \frac{1}{\sqrt{N_\alpha N_\beta}} \left\langle \sum_{j=1}^{N_\alpha} \sum_{k=1}^{N_\beta} \exp(-i\mathbf{Q} \cdot (\mathbf{r}_j - \mathbf{r}_k)) \right\rangle \tag{35}$$

with N_α being the number of atoms of element α. Angular brackets indicate an ensemble average, i.e., an average over many atomic configurations that can be obtained from long MD simulations.

While a theoretical diffraction pattern for a crystal can be calculated by considering the lattice parameters and idealized atomic positions in the unit cell, the structural description of a disordered phase (fluid, melt or glass) requires some statistical sampling. This is achieved by

EBSCOhost - printed on 2/13/2023 5:26 AM via . All use subject to https://www.ebsco.com/terms-of-use

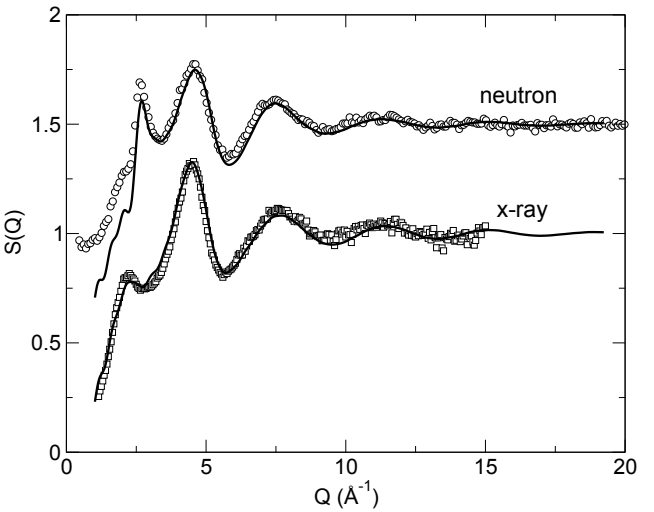


Figure 3. Structure factors of $MgAl_2O_4$ melt from neutron and X-ray diffraction (symbols) and classical molecular dynamics simulations (solid lines) (modified after Jahn 2008a).

using a large cell containing many atoms and/or by averaging over many structural configurations. The latter can be generated, e.g., in a molecular dynamics or a Monte-Carlo simulation (Allen and Tildesley 1987; Frenkel and Smit 2002). Figure 3 shows an example where the structure factors of a spinel, $MgAl_2O_4$, melt computed from classical MD simulations using an advanced ionic potential (Jahn and Madden 2007a) are in excellent agreement with measurements from X-ray and neutron diffraction (Hennet et al. 2007; Jahn 2008a).

The structure factor depends on the wavevector transfer, Q, i.e., it is a function in the so-called reciprocal space (Ashcroft and Mermin 1976). A related function in real space that describes the distribution of interatomic distances is the radial distribution function, $g(r)$. It is defined as the ratio between the actual atomic density at a radial distance r from a reference point (e.g., the position of a specific atom) to the average atomic density of the system, i.e., $g(r) = \rho(r)/\rho_0$. For a multicomponent system, partial radial distribution functions can be defined for each pair of elements (see Fig. 4)

$$g_{\alpha\beta}(r) = \frac{1}{c_\alpha c_\beta \rho_0 N} \left\langle \sum_{j=1}^{N_\alpha} \sum_{k=1}^{N_\beta} \delta\left(\mathbf{r} - (\mathbf{r}_j - \mathbf{r}_k)\right) \right\rangle \tag{36}$$

with N being the total number of atoms in the system. $\delta(\mathbf{x})$ is the Dirac delta function, which is zero except at $\mathbf{x} = \mathbf{0}$ with an integral value of one. Partial structure factors and radial distribution functions are related by Fourier transformation (formula given here is for radial symmetry)

$$S_{\alpha\beta}(Q) = \delta_{\alpha\beta} + \sqrt{c_\alpha c_\beta}\,\rho_0 \int_0^\infty 4\pi r^2 (g_{\alpha\beta}(r) - 1) \frac{\sin(Qr)}{Qr} dr \tag{37}$$

A similar equation can also be derived for the reverse transformation.

From the integration over the first peak of $g_{\alpha\beta}(r)$ up to the first minimum at r_{min} (Fig. 4) the average coordination number n_α^β of atom α by atoms β is obtained using the relation

$$n_\alpha^\beta = 4\pi\rho_0 c_\beta \int_0^{r_{\min}} g_{\alpha\beta}(r) r^2 dr \tag{38}$$

EBSCOhost - printed on 2/13/2023 5:26 AM via . All use subject to https://www.ebsco.com/terms-of-use

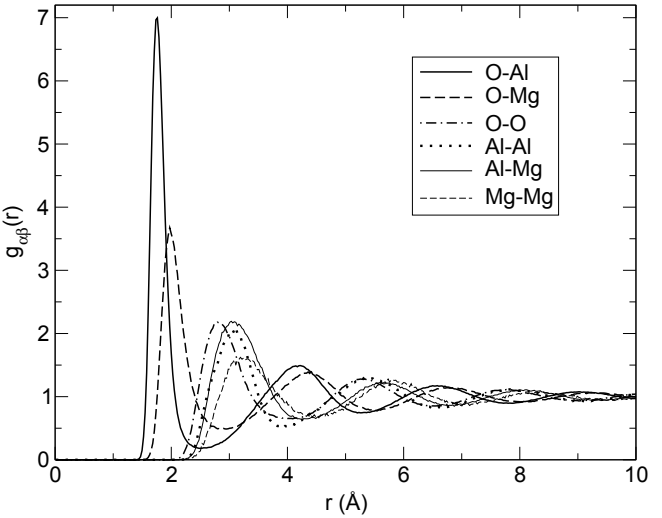


Figure 4. Partial radial distribution functions of $MgAl_2O_4$ melt from classical molecular dynamics simulations (modified after Jahn 2008a).

The peak positions of $g_{a\beta}(r)$ represent the most probable interatomic distances of the different coordination shells. The width and asymmetry of these peaks provide information about the distribution of distances. Furthermore, the configurations obtained from the simulation are frequently used to analyze topological and chemical ordering, bond angle distributions and other structural properties of disordered phases.

Experimentally, it is extremely difficult to obtain partial structure factors or radial distribution functions because in a single diffraction experiment a weighted superposition of these functions is measured. Due to the overlap of different $g_{a\beta}(r)$ (see Fig. 4), the determination of coordination numbers from the integration described above becomes increasingly uncertain with an increasing number of different elements. There are already 6 partials for a phase with three elements. Recently, a number of diffraction experiments were made to obtain more detailed information about the structure of such three-component refractory melts and glasses by making use of the different scattering lengths b_α for neutrons and X-rays (e.g., Drewitt et al. 2011) or between different isotopes for neutrons (e.g., Drewitt et al. 2012). These studies were accompanied by molecular dynamics simulations that greatly supported the interpretation of the experimental data. Currently, there is no experimental method that can provide a full three-dimensional structure model for non-crystalline phases, which puts molecular modeling in a unique position. On the other hand, the quality of the structure predictions can only be assessed by comparison to experimental data, which includes diffraction patterns discussed in this section and vibrational or electronic excitation spectra that will be dealt with in the following.

VIBRATIONAL SPECTRA

Vibrational spectroscopy probes the normal modes of an oscillating system of atoms. This includes characteristic vibrational frequencies of isolated molecules or molecules in solution as well as normal modes of crystals (phonons), glasses and melts. The sensitivity of a specific spectroscopy towards a specific normal mode vibration depends on the interaction of the probe (neutron, electron, and photon) with the sample. The first part of this section is dedicated to the calculation of the normal mode spectra for periodic systems using harmonic lattice dynamics.

EBSCOhost - printed on 2/13/2023 5:26 AM via . All use subject to https://www.ebsco.com/terms-of-use

Then, the calculation of vibrational spectra from molecular dynamics trajectories using time correlation functions is reviewed. Finally, the general methodology to compute IR and Raman spectra using density-functional perturbation theory is outlined.

Lattice dynamics in the harmonic approximation

In a crystal with N atoms in the primitive unit cell, there are $3N$ normal modes ν with a frequency $\omega_\nu(\mathbf{q})$ that depends on the wavevector $\mathbf{q}$. Three of these modes, the *acoustic* modes, are strongly dispersive at low $\mathbf{q}$ with a linear relation between ω and $\mathbf{q}$ and a vanishing frequency at $\mathbf{q} = (000)$, the Γ point of the Brillouin zone (Ashcroft and Mermin 1976; Dove 2003). The proportionality constants are related to the longitudinal (P) and the two transverse (S) wave velocities of the crystal in a specific crystallographic direction. The remaining N–3 *optical* modes are less dispersive close to Γ and reach a finite frequency at Γ. A quantum mechanical description leads to the quantization of lattice vibrations and to the introduction of *phonons* as the fundamental quanta (Ashcroft and Mermin 1976; Dove 2003).

The distribution of vibrational frequencies in a crystal structure at reasonably low temperatures (this may well be a few hundred Kelvin) is well described using the (quasi-) harmonic approximation (Wentzcovitch et al. 2010). The harmonic theory of lattice dynamics assumes that all atoms vibrate in a harmonic potential with small displacements $\mathbf{u}$ around their equilibrium positions. In order to account for the thermal expansion of a crystal, the quasiharmonic approximation may be used, by which harmonic frequencies are computed using the lattice parameters corresponding to the pressure and temperature conditions of interest. Within the harmonic approximation, the total energy E can be expanded around the ground state total energy E_0

$$E = E_0 + \sum_{i,\alpha} \left.\frac{\partial E}{\partial u_{i,\alpha}}\right|_0 u_{i,\alpha} + \frac{1}{2}\sum_{i,j,\alpha,\beta} \left.\frac{\partial^2 E}{\partial u_{i,\alpha}\partial u_{j,\beta}}\right|_0 u_{i,\alpha}u_{j,\beta} + \ldots \tag{39}$$

and the expansion is terminated after the quadratic term in energy. The indices i and j refer to the atoms, α and β to the three Cartesian directions. For the ideal structure with $E = E_0$, the forces on the individual atoms and consequently the second term of the above equation vanishes. The second derivative of the energy with respect to atomic displacements constitutes the interatomic force constant matrix, which is the central quantity to calculate the vibrational mode spectrum. The Fourier transform of the force constant matrix weighted by the masses of the atoms i and j yields the dynamical matrix

$$D_{i\alpha,j\beta}(\mathbf{q}) = \frac{1}{\sqrt{m_i m_j}} \sum_{\mathbf{R}_i - \mathbf{R}_j} \frac{\partial^2 E}{\partial u_{i,\alpha}(\mathbf{R}_i)\partial u_{j,\beta}(\mathbf{R}_j)} \exp(-i\mathbf{q}\cdot(\mathbf{R}_i - \mathbf{R}_j)) \tag{40}$$

The eigenvalues of the dynamical matrix yield the squares of the phonon frequencies $\omega_\upsilon^2(\mathbf{q})$. For calculations of the vibrational frequencies at Γ, the dynamical matrix of polar insulators has to be modified by a "non-analytic" correction term that arises because the eigenvectors of $D_{i\alpha,j\beta}(\mathbf{q} = 0)$ are not equal to those of $D_{i\alpha,j\beta}(\mathbf{q} \to \mathbf{0})$, which leads to the splitting of longitudinal and transverse optic modes (LO-TO splitting) (Gonze and Lee 1997; Baroni et al. 2001)

$$D^{na}_{i\alpha,j\beta}(\mathbf{q} \to \mathbf{0}) = \frac{1}{\sqrt{m_i m_j}} \frac{4\pi}{\Omega} \frac{\left(\sum_k q_k Z^*_{\alpha,ki}\right)\left(\sum_{k'} q_{k'} Z^*_{\beta,k'j}\right)}{\sum_{kk'} q_k \varepsilon^\infty_{kk'} q_{k'}} \tag{41}$$

where Ω, Z^* and ε^∞ are the volume of the primitive cell, the Born effective charge and the high-frequency dielectric tensor. The latter is computed as the second energy derivative with respect to the electric field $\mathbf{E}$ (with Cartesian components E_i)

EBSCOhost - printed on 2/13/2023 5:26 AM via . All use subject to https://www.ebsco.com/terms-of-use

$$\varepsilon_{ij}^{\infty} = \delta_{ij} + 4\pi \frac{\partial^2 E}{\partial E_i \partial E_j} \tag{42}$$

The Born effective charge is the mixed second derivative of the energy with respect to atomic displacements and a macroscopic electric field, which can also be expressed as the relation between the force acting on atom i, $\mathbf{F}_i$, and the macroscopic electric field or between the polarization of the unit cell $\mathbf{P}$ and a displacement of atom i (Gonze and Lee 1997)

$$Z_{i,\beta\alpha}^{*} = \frac{\partial F_{i,\alpha}}{\partial E_\beta} = \Omega \frac{\partial P_\beta}{\partial u_{i,\alpha}(\mathbf{q}=0)} \tag{43}$$

A direct computation of the interatomic force constant matrix may be done by finite displacement of atoms in a supercell. Alternatively, density functional perturbation theory allows the evaluation of the dynamical matrix in Fourier space (Gonze and Lee 1997; Baroni et al. 2001; Refson et al. 2006). The latter approach appears to be more popular and convenient in the DFT community. As an example, the phonon dispersion curve of MgO is shown in Figure 5. It was calculated with the planewave code ABINIT (Gonze et al. 2002, 2009) using the LDA exchange-correlation functional, the DFT-optimized lattice constant at $P = 0$ GPa, a planewave set with a maximum planewave energy of 1000 eV and a Brillouin zone sampling with a 4×4×4 k-point set. Practical aspects for lattice dynamics calculations using classical force fields and density functional perturbation theory as well as applications were reviewed recently by Gale and Wright (2010), Baroni et al. (2010) and Wentzcovitch et al. (2010).

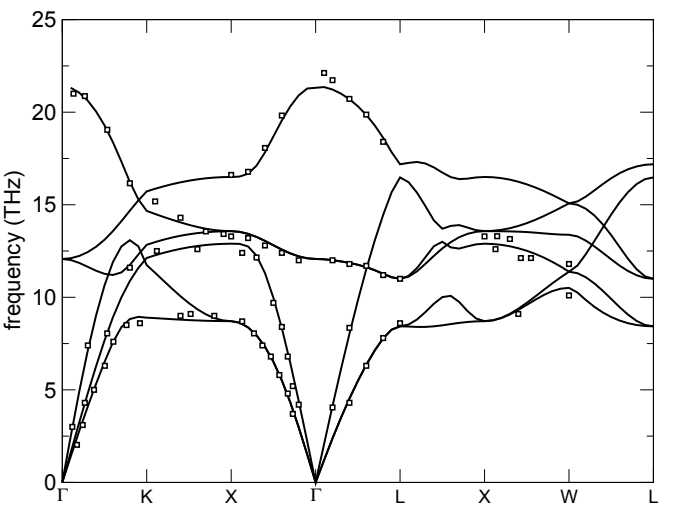


Figure 5. Phonon dispersion curve of MgO from a density-functional perturbation theory calculation using the planewave code ABINIT (Gonze et al. 2009) and the LDA exchange-correlation functional (solid lines). Symbols refer to experimental data by Sangster et al. (1970).

Atomic dynamics via time correlation functions

For disordered phases, such as melts and glasses, the concept of lattice dynamics is not applicable. However, sound waves also propagate through liquids and collective "phonon-like" motions still exist down to length scales of interatomic distances (Boon and Yip 1980; Balucani and Zoppi 1994). Crystalline solids at high temperatures (close to the melting point) may be very anharmonic and therefore the quasiharmonic approximation is no longer valid for the esti-

EBSCOhost - printed on 2/13/2023 5:26 AM via . All use subject to https://www.ebsco.com/terms-of-use

mation of the thermal expansion of a crystal. Hence, the investigation of the atomic dynamics of such systems requires a different approach that includes explicitly effects of high temperature. For the determination of the structure, the method of choice is molecular dynamics, here in conjunction with time correlation functions. By using this approach one has to be aware of the fact that MD does not provide the correct quantum mechanical occupation of phonon modes, which is governed by the Bose-Einstein relation (see e.g., Dove 2003). Hence, the relative intensities of phonon modes obtained from MD (which represents their occupation) have to be modified by a quantum correction term, at least at temperatures below the Debye temperature of the material. In addition, MD simulations should be long enough to obtain a reasonable statistical sampling even of the classical distribution. The simulation time needed increases with decreasing temperature.

The dynamic structure factor $S(Q,\omega)$ is directly proportional to the inelastic scattering cross-section for neutrons or X-rays

$$\frac{d^2\sigma}{d\Omega dE_f} = \frac{k_f}{k_i}\frac{\sigma_B}{4\pi}S(Q,\omega) \tag{44}$$

where the term on left side is the double differential cross-section, which gives the probability of inelastic scattering of a neutron or X-ray from the initial state $|\mathrm{i}\rangle$ to a final state $|f\rangle$ into a solid angle increment $d\Omega$. σ_B is the total scattering cross-section of the sample and k_i and k_f are the magnitudes of the initial and final wavevectors of the probe (see e.g., Loong 2006). As in the case of elastic scattering (Eqn. 34), the total $S(Q,\omega)$ is composed of a weighted sum of partial dynamic structure factors

$$S(Q,\omega) = \sum_{\alpha}\sum_{\beta}(c_\alpha c_\beta)^{1/2}\frac{b_\alpha b_\beta}{\langle b^2\rangle}S_{\alpha\beta}(Q,\omega) \tag{45}$$

The latter are defined as a space and time Fourier transform of the time correlation function of density fluctuations (van Hove 1954)

$$S_{\alpha\beta}(Q,\omega) = \frac{1}{2\pi\sqrt{N_\alpha N_\beta}}\int_{-\infty}^{\infty} dt\exp(-i\omega t)\sum_{j=1}^{N_\alpha}\sum_{k=1}^{N_\beta}\left\langle\exp\left(i\mathbf{Q}\cdot\left(\mathbf{r}_j(t)-\mathbf{r}_k(0)\right)\right)\right\rangle \tag{46}$$

As an example, Figure 6 shows the total X-ray $S(Q,\omega)$ of alumina melt from inelastic X-ray scattering experiments on levitated samples (Sinn et al. 2003) and the respective results of classical molecular dynamics simulations (Jahn and Madden 2007b, 2008) using an advanced ionic interaction model that accounts for anion polarization and shape deformations (Jahn et al. 2006).

The analysis of such spectra is not straight forward as the theory of the atomic dynamics of liquids at finite Q is rather complicated (Boon and Yip 1980; Balucani and Zoppi 1994). However, at small Q, generalized hydrodynamics may be applied, which adds a Q-dependence to known hydrodynamic properties (viscosity, sound velocity, thermal conductivity, ...). A plausible explanation for this behavior is that the macroscopic response of a melt to a long-wavelength compressional wave is viscoelastic whereas it becomes increasingly elastic when the wavelength approaches interatomic distances. In analogy to crystals, melts exhibit distinct inelastic peaks that are representative of propagating acoustic-like modes (see Fig. 6). These modes are strongly damped with increasing Q and increasing frequency ω. The mode frequencies may be extracted by inspection of the maxima of $S(Q,\omega)$ or of the related longitudinal current correlation function $J_l(Q,\omega) = (\omega/Q)^2 S(Q,\omega)$. Alternatively, a model function, such as a Lorentzian or a damped harmonic oscillator model, may be fit to the measured or calculated $S(Q,\omega)$ (Sinn et al. 2003; Jahn and Madden 2008). The result is a dispersion relation as shown in Figure 7. From the linear initial slope of the dispersion curve a high-frequency longitudinal

EBSCOhost - printed on 2/13/2023 5:26 AM via . All use subject to https://www.ebsco.com/terms-of-use

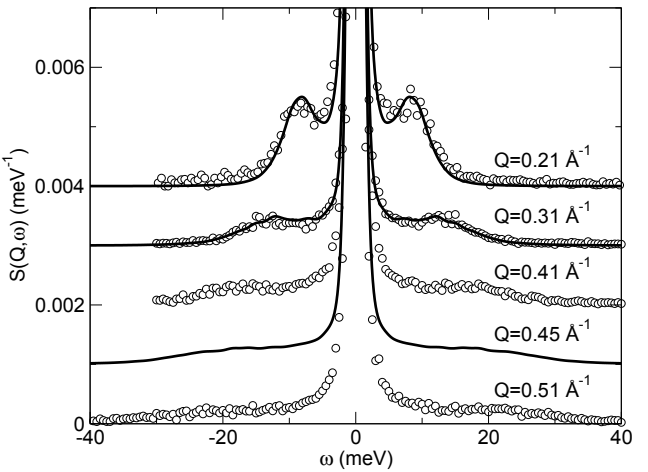


Figure 6. Total X-ray dynamic structure factor $S(Q,\omega)$ of alumina melt. The symbols are experimental data from inelastic X-ray scattering (Sinn et al. 2003) and the lines refer to classical MD simulations (Jahn and Madden 2007b, 2008).

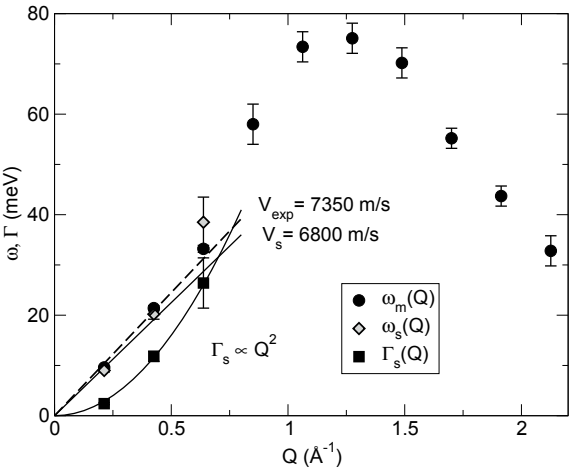


Figure 7. Dispersion relations of Al_2O_3 melt obtained from the maxima of the longitudinal current correlations, ω_m(Q), and from the fit of a damped harmonic oscillator (DHO) model to the total $S(Q,\omega)$, ω_s(Q). The line width Γ_s of the DHO increases approximately with Q^2, as predicted by generalized hydrodynamic theory. The initial slope of the dispersion curve (solid line) yield the high frequency longitudinal wave velocity v_s which is consistent within the error with the experimentally derived dispersion from Sinn et al. (2003) shown by the dashed line (modified after Jahn and Madden 2008).

mode velocity can be obtained. This velocity is often somewhat larger than the sound velocity of the melt since at high frequencies the relaxation times are short and thus the solid-like elastic response of the melt is sampled rather than the viscous response.

The correlation function approach is also applicable to crystals and to the computation of phonon dispersion curves. For example, it was used in combination with classical molecular dynamics to test the performance of interatomic potentials for α-Al_2O_3 (Jahn et al. 2006), MgO (Aguado et al. 2002; Aguado and Madden 2004) or Li_2O (Wilson et al. 2004).

EBSCOhost - printed on 2/13/2023 5:26 AM via . All use subject to https://www.ebsco.com/terms-of-use

Infrared absorption spectroscopy

The low frequency dielectric permittivity tensor relates the macroscopic displacement field to the macroscopic electric field. For a frequency ω it can be written as (Gonze and Lee 1997)

$$\varepsilon_{ij}(\omega) = \varepsilon_{ij}^{\infty} + \frac{4\pi}{\Omega}\sum_{\upsilon}\frac{\left(\sum_{i'\alpha} Z^{*}_{\alpha,ii'}u^{\upsilon}_{\alpha i'}\right)\left(\sum_{j'\beta} Z^{*}_{\beta,jj'}u^{\upsilon}_{\beta j'}\right)}{\left(\omega_{\upsilon}\right)^{2} - \omega^{2}} \tag{47}$$

where $Z^{*}_{\alpha,ii'}$ and $u^{\upsilon}_{\alpha i'}$ are the Born effective charges and the displacement of atom α in direction *i* for mode ν. These properties are usually computed in the framework of density-functional perturbation theory, which was already introduced (see "Excitation methods" section). In a first-order approximation, the polarized IR absorption spectra are proportional to the diagonal elements of the imaginary part of $\varepsilon_{ij}(\omega)$. Isotropic spectra are computed by averaging over these three diagonal elements. This approach has been used, e.g., to test different hydrogen incorporation mechanisms in nominally anhydrous minerals by comparing experimental and theoretical IR absorption spectra (Blanchard et al. 2009; Balan et al. 2011b, 2013; Jahn et al. 2013). Other theoretical studies of IR spectra using B3LYP hybrid exchange-correlation functionals were performed, e.g., for calcite (Prencipe et al. 2004), forsterite (Noel et al. 2006) or garnet solid solutions (De La Pierre et al. 2013). Predicted infrared absorption coefficients of OH in minerals (Balan et al. 2008b, 2011b) show trends similar to experimental calibrations (Libowitzky and Rossman 1997; Koch-Müller and Rhede 2010) but are systematically too large. Giacomazzi et al. (2009) derived IR spectra for vitreous SiO_2 and found only a poor sensitivity of this spectroscopy to the medium range order of the network structure.

To illustrate the power of DFT calculations to support the interpretation of experimental IR spectra, we return to the example of the 3.65 Å phase (Wunder et al. 2012) that was already introduced in the section about X-ray diffraction. Due to the very low scattering cross-section for X-rays, the hydrogen positions in the crystal structure cannot be constrained from the X-ray diffraction experiment, not even from single-crystal refinements (Welch and Wunder 2012). However, the experimental IR spectrum of the 3.65 Å phase shows a number of bands in the frequency range of the OH stretching vibrations (see Fig. 8). Due to the low symmetry of the crystal structure ($P2_1$), six crystallographically inequivalent hydrogen positions need to be derived. DFT structure optimization followed by the calculation of the low frequency dielectric permittivity tensor $\varepsilon_{ij}(\omega)$ was performed to test different models for the distribution of hydrogen atoms. Initial hydrogen positions were chosen by reference to published structure models of the related δ-$Al(OH)_3$ phase. All optimized structures would be virtually indistinguishable by X-ray diffraction. However, the vibrational spectrum computed from the lowest energy structure also resembles best the measured IR spectrum (see Fig. 8). All main bands are reproduced, including the two split peaks above 3350 cm^{-1}. Also, the relative band positions and intensities fit the experiment much better than the example spectrum of one of the higher energy (metastable) structures shown by a dashed line in Figure 8. Another example demonstrating the predictive power of DFT calculations was published by Churakov and Wunder (2004). They studied the hydrogen positions in topaz-OH, $Al_2SiO_4(OH)_2$, and found four different H positions, which later was verified experimentally by IR spectroscopy (Watenphul and Wunder 2010).

Measured and computed band positions may vary by up to a few tens of cm^{-1}, which can have several reasons. Besides systematic errors of the electronic structure calculations, e.g., due to the approximations used for constructing the exchange-correlation functional, one has to keep in mind that the calculations are usually performed at zero Kelvin. Some bands show a stronger temperature-dependence than others. For instance, the lowest frequency band of the experimental spectrum at about 3137 cm^{-1} shown in Figure 8 shifts to higher frequencies by about 50 cm^{-1} when heating the sample from −190 °C to room temperature while the position

EBSCOhost - printed on 2/13/2023 5:26 AM via . All use subject to https://www.ebsco.com/terms-of-use

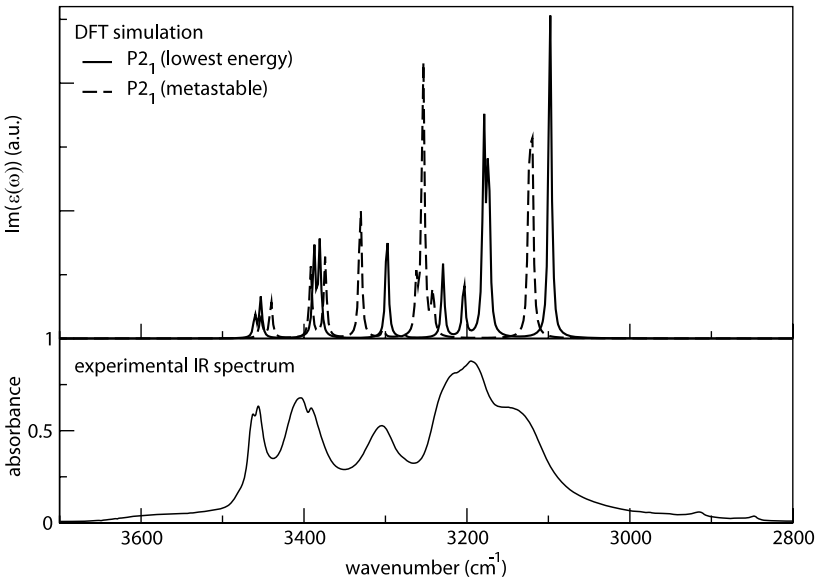


Figure 8. (*top*) Computed isotropic average of the imaginary part of $\varepsilon_{ij}(\omega)$ of two different structure models and (*bottom*) IR absorption spectra of the 3.65 Å phase, $MgSi(OH)_6$, measured at a temperature of −190 °C, in the frequency range of OH stretching vibrations (modified after Wunder et al. 2012).

of other bands is almost unaffected (Wunder et al. 2012). Another important issue is concerned with the shape and the size of the sample. For powder samples with particle sizes smaller than the wavelength of the IR radiation (e.g., 2.8 μm for 3600 cm^{-1} or 40 μm for 250 cm^{-1}), IR absorption bands may be shifted significantly compared to the bulk dielectric response or even split into several bands depending on the particle shape. This effect arises from a depolarization field induced in a particle by the surface polarization charges when the particle is subjected to an external electric field. Respective powder spectra have been computed for a number of minerals, including kaolinite (Balan et al. 2001; Fourdrin et al. 2009), lizardite (Balan et al. 2002), gibbsite (Balan et al. 2006), bayerite (Balan et al. 2008a), hematite (Blanchard et al. 2008), apatite (Balan et al. 2011a) and diaspore (Delattre et al. 2012). A distribution of particle size and shape in a powder or anharmonic interactions between phonons are possible reasons for a broadening of the IR absorption bands. Some of these effects are discussed in the case of apatite (Balan et al. 2011a and references therein).

Going beyond the harmonic approximation, IR spectra may be derived again through a time correlation function approach from molecular dynamics trajectories. The frequency-dependent Beer-Lambert absorptivity coefficient, $\alpha(\omega)$, is proportional to the time Fourier transform of the total polarization autocorrelation function (McQuarrie 2000). For a classical system, this may be written as (Iftimie and Tuckerman 2005)

$$\alpha(\omega) = \frac{\pi\omega^2}{3cV\varepsilon_0 k_B T n(\omega)} \frac{1}{2\pi} \int_{-\infty}^{\infty} dt \exp(-i\omega t) \left\langle \mathbf{P}(t) \cdot \mathbf{P}(0) \right\rangle \tag{48}$$

where V, ε_0 and c are the sample volume, the vacuum permittivity and the speed of light. $n(\omega)$ is the index of refraction and $\mathbf{P}(t)$ is the total polarization vector of the simulation cell at time t. The IR spectra obtained from classical MD simulations of SiO_2 (Wilson et al. 1996; Liang et al. 2006) and MgO (Sun et al. 2008; Adebayo et al. 2009) show qualitative agreement with experimental data. In the case of vitreous SiO_2 (Wilson et al. 1996) it was shown that a simple

EBSCOhost - printed on 2/13/2023 5:26 AM via . All use subject to https://www.ebsco.com/terms-of-use

Born-Mayer type potential was not sufficient to produce the correct number of peaks in the IR spectra and anion polarization effects have to be accounted for. Car-Parrinello MD simulations of liquid water (Iftimie and Tuckerman 2005) predicted IR intensities in very good agreement with experiment. However, the ficticious electron mass of this method seemed to have an effect on the frequencies. IR spectra of water from *ab initio* MD were also computed by Habershon et al. (2008) and Lee et al. (2008). Anharmonic IR spectra of naphtalene were studied by Pagliai et al. (2008).

Raman spectra

Raman spectroscopy is based on inelastic scattering of visible light, which arises from the emission or absorption of quantized vibrational modes of the system. This effect leads to a frequency shift of the scattered photon. As the momentum of a photon in the visible part of the electromagnetic spectrum is very small, the maximum scattering vector Q is also small, i.e., for crystals it is close to the Γ point of the Brillouin zone (Ashcroft and Mermin 1976). Since the dispersion of the optical modes sampled by Raman scattering is small, it is reasonable to neglect any Q-dependence by setting $Q = 0$. Raman scattering is caused by fluctuations of the polarizability of the sample due to the atomic vibrations. Traditionally, Raman frequencies and intensities were computed for molecules or small clusters using quantum-chemical models (Kubicki 2001). Examples of this approach include studies of aluminosilicate (Kubicki and Sykes 1993; Tossell 2005b), $MgSO_4$ (Pye and Rudolph 1998, 2001), arsenite and arsenate (Tossell and Zimmermann 2008) molecules.

One approach to compute Raman susceptibilities for extended systems involves the evaluation of mixed third order energy derivatives twice with respect to electric field and once with respect to atomic displacements. Technically, this can be done by using density functional perturbation theory (Lazzari and Mauri 2003; Veithen et al. 2005; Miwa 2011) or by applying finite electric fields to a periodic system (Umari and Pasquarello 2002). For crystals, most studies of Raman frequencies and intensities relied on the density functional perturbation scheme (Lazzari and Mauri 2003; Veithen et al. 2005). The intensity of the mode at ω_υ in non-resonant Stokes mode is given by

$$I^\upsilon \propto \left|\mathbf{e}_i \cdot \boldsymbol{\alpha}^\upsilon \cdot \mathbf{e}_s\right|^2 \frac{1}{\omega_\upsilon}(n_\upsilon + 1) \tag{49}$$

where $\mathbf{e}_i$ and $\mathbf{e}_s$ are the polarization of the incoming and scattered photon, and $n_\upsilon = (\exp(\hbar\omega_\upsilon / k_B T) - 1)^{-1}$. ω_υ and $\hbar$ are the frequency of the optical phonon at the Γ point and Planck's constant divided by 2π, and

$$\alpha_{kl}^\upsilon = \sum_{ij} \frac{\partial^3 E}{\partial E_k \partial E_l \partial u_{ij}} \frac{w_{ij}^\upsilon}{\sqrt{m_j}} = \sum_{ij} \frac{\partial \Pi_{kl}}{\partial u_{ij}} \frac{w_{ij}^\upsilon}{\sqrt{m_j}} \tag{50}$$

Here, w_{ij}^υ is the n^{th} eigenmode and u_{ij} is the displacement of the j^{th} atom in direction i. This method has been implemented into a number of DFT codes. Raman spectra of minerals have been calculated for SiO_2 polymorphs (Lazzari and Mauri 2003), $MgSiO_3$ perovskite and post-perovskite (Caracas and Cohen 2006), $MgAl_2O_4$ spinel (Caracas and Banigan 2009), δ-AlOOH (Tsuchiya et al. 2008), α-AlOOH (San Juan-Farfan et al. 2011), Mg_2SiO_4 forsterite (McKeown et al. 2010) and cordierite (Kaindl et al. 2011). The WURM project (Caracas and Bobocioiu 2011) provides a database of computed physical properties of minerals, which includes Raman spectra obtained from density-functional perturbation theory. The finite electric field method has been used to study disordered systems and to relate the Raman spectra to the network structure in SiO_2, GeO_2 and B_2O_3 glasses (Umari and Pasquarello 2005; Giacomazzi and Pasquarello 2007; Giacomazzi et al. 2009). Umari et al. (2001) used a finite difference scheme for the displacement derivative of the polarizability tensor of α-quartz. The latter was calculated by a density-functional linear response approach.

EBSCOhost - printed on 2/13/2023 5:26 AM via . All use subject to https://www.ebsco.com/terms-of-use

In a direct but computationally much more expensive way, the Raman cross-section can be obtained from the dynamic autocorrelation functions of the polarizability tensor $\mathbf{\Pi}(t)$ (Berne and Pecora 1976)

$$I_{kl}(\omega) \propto \mathrm{Re} \int_{-\infty}^{\infty} dt \left\langle \Pi_{kl}^{*}(0)\Pi_{kl}(t) \right\rangle \exp(-i\omega t) \tag{51}$$

with

$$\Pi_{kl}(t) = -\frac{\partial P_k}{\partial E_l} = \frac{\partial^2 E}{\partial E_k \partial E_l} \tag{52}$$

where P_k and E_l are the Cartesian components of the simulation cell dipole moment and electric field vectors, and E is the energy. The correlation function approach requires the evaluation of $\mathbf{\Pi}(t)$ along a molecular dynamics trajectory, as e.g., implemented in the CPMD package (Putrino et al. 2000). The advantages of this direct method are that it is (at least in principle) equally applicable to crystals and disordered phases, that it includes anharmonic effects and that it can be applied *in situ* at high pressure and high temperature. However, to obtain a reasonably smooth correlation function, the polarizability tensor has to be computed for many time steps, which requires substantial computational resources. The feasibility of this *ab initio* approach has been demonstrated in a number of studies, including high pressure ice (Putrino and Parrinello 2002) and a naphthalene crystal (Pagliai et al. 2008). In those studies, Raman intensities were predicted for different polarization scattering geometries (ISO, VV, and VH) after computing separately the isotropic and the anisotropic part of the Raman tensor.

One difficulty in interpreting experimental Raman spectra is the assignment of observed bands to individual species. Regarding the Raman frequencies, partial vibrational spectra of individual molecules in an aqueous solution or in a melt may be extracted from MD trajectories by the projection of particle velocities on (quasi-)normal modes that are considered Raman active. The Fourier transformation of the autocorrelation function of these projected velocities yields a power spectrum that represents the frequency content of these modes. This approach has been used, e.g., in conjunction with classical MD simulations of supercritical water (Kalinichev and Heinzinger 1995) and halide melts (Pavlatou et al. 1997) and with *ab initio* MD simulations for SiO_2 species in aqueous solutions (Spiekermann et al. 2012a,b) and in silicate glasses (Spiekermann et al. 2013). Normal mode projection techniques were also used to resolve a long-standing controversy about the origin of a doublet in the neutron scattering spectra of amorphous SiO_2 (Sarnthein et al. 1997).

A more quantitative assessment of these modes in terms of Raman activity requires an estimation of Raman intensities. One approach that avoids the computationally expensive direct approach mentioned above is the parameterization of a polarizability model that is combined with MD simulation. Bond polarizability models were used in various studies, e.g., of silicate glass (Zotov et al. 1999), silica species in aqueous solution (Zotov and Keppler 2000), Mg speciation in aqueous fluids (Kapitán et al. 2010), molten salts (Ribeiro et al. 1999; Madden et al. 2004; Akdeniz and Madden 2006; Heaton and Madden 2008) or SiO_2 polymorphs (Liang et al. 2006). The concept of using a bond polarizability model to compute Raman spectra was investigated in an *ab initio* study of vitreous SiO_2 (Giacomazzi et al. 2009). Using the same structural configurations, very good agreement was achieved between the predictions of an optimized bond polarizability model and the spectrum obtained directly from first principles calculations. A recent review of parametric models for the calculation of Raman spectra was published by Bougeard and Smirnov (2009).

EBSCOhost - printed on 2/13/2023 5:26 AM via . All use subject to https://www.ebsco.com/terms-of-use

ELECTRONIC EXCITATION SPECTRA

When computing theoretical spectra representing electronic transitions one is faced with two problems. First, an accurate description of the initial and final (excited) electronic states is needed to predict the band positions or excitation energies. Second, the band intensities and line shapes are related to the probability of electronic transitions, which is usually expressed in terms of the transition matrix. The level of electronic structure theory required to make reasonable predictions of electronic excitation spectra crucially depends on the relevant transitions that are e.g., governed by selection rules. Hartree-Fock or DFT approaches are often insufficient to reproduce the experimental electronic excitation energies of minerals and therefore more advanced methods have to be applied. In the following, we present a short overview on the performance of different methods for modeling various types of electronic excitation spectra including optical spectroscopy (UV-vis), X-ray absorption fine structure and X-ray Raman spectroscopy (XAFS and XRS), electron energy loss spectroscopy (EELS) and X-ray photoelectron spectroscopy (XPS).

UV-vis

Optical spectroscopy is mainly concerned with excitations of valence electrons into the lowest unoccupied electronic states. The relevant excitation energies are in the near infrared to near ultraviolet frequency range, which also contains the range of visible light. A number of processes may contribute to a measured optical absorption spectrum including ligand-metal and metal-metal charge transfer, crystal field *d-d* transitions, color centers or other transitions across the band gap of a crystal. In addition, vibrational modes or their overtones may still be present in the lower energy part of the spectra. Of special interest in mineralogy are optical spectra of transition metal cations, which contain fingerprint information about the cation valence and the local cation site symmetry in the crystal structure.

A first approach to compute such spectra is based on a single-atom multi-electron description within the framework of ligand or crystal field theory (Sugano et al. 1970; Cowan 1981). To compute the multiplet spectra (see e.g., Rossano et al. 2000, for optical spectra of Ni^{2+}-bearing compounds), a number of empirical parameters, such as the Racah parameter or the crystal-field splitting parameters, need to be supplied. Non-empirical first-principles analysis of the electronic excitation spectra is usually based on DFT often coupled with the more advanced quantum chemical methods to account for multielectronic effects. DFT alone relies on the one-electron approximation, which makes it difficult to estimate the energies and intensities of multiplet spectra. Therefore, hybrid methods e.g., based on DFT and the configuration interaction (CI) method have been developed and tested (e.g., Watanabe et al. 2009; Novita and Ogasawara 2012). For example, Watanabe et al. (2009) studied the optical properties of Cr^{3+} in ruby, Cr^{3+}:Al_2O_3, and alexandrite, Cr^{3+}:$BeAl_2O_4$. They first optimized the crystal structure around the defect site using planewave DFT and then used the DFT-CI hybrid method to compute the multiplet structure and optical absorption spectra using clusters of about 60 atoms.

When the electronic band structure of minerals is investigated, a crucial point for any first-principles calculation is an accurate description of the electronic band gap. The performance of Hartree-Fock or DFT approaches is often unsatisfactory in this respect. While the Hartree-Fock approach significantly overestimates the band gaps of semiconductors (e.g., von Oertzen et al. 2005), the Kohn-Sham band gap is often underestimated or even closed, which results in predicting metallic character for some semiconducting materials including transition metal oxides and silicates (see e.g., Cococcioni and de Gironcoli 2005; Hsu et al. 2011). Generally, hybrid functionals improve the band gaps and other properties such as lattice parameters, bulk moduli, and heats of formation, which was demonstrated for variety of materials such as Si and C, oxides and sulfides (Muscat et al. 2001; Paier et al. 2006a,b). However, a good

EBSCOhost - printed on 2/13/2023 5:26 AM via . All use subject to https://www.ebsco.com/terms-of-use

performance of these hybrid functionals is not guaranteed and there are counter examples where standard DFT functionals are to be preferred. For instance, a computational study of sulfates showed that while for sphalerite, ZnS, the hybrid functional B3LYP performed better than LDA or GGA functionals, the reverse was true for galena, PbS, and pyrite, FeS_2 (von Oertzen et al. 2005). Paier et al. (2006a,b) have shown that hybrid functionals may provide a substantially worse description of the atomization energies compared to standard DFT. They also overestimate the band gap of TiO_2(110) and bulk Si by as much as ~30% (Ammal and Heyden 2010; Jain et al. 2011).

As already described above, an alternative approach to at least partially correct for the DFT band gap problem especially for transition metal oxides and silicates is to use DFT+*U* (Cococcioni and de Gironcoli 2005; Cococcioni 2010; Hsu et al. 2011). This method is attractive because it only causes a moderate increase in computational cost and it is possible to derive the $\mathcal{U}$ parameter from first principles (Cococcioni and de Gironcoli 2005; Cococcioni 2010). Using a realistic value of $\mathcal{U}$=4.5 eV in GGA+*U* calculations for fayalite, Fe_2SiO_4, Jiang and Guo (2004) computed an indirect band gap of about 1.5 eV, whereas GGA without *U* predicts fayalite to be a metal. However, the GGA+*U* band gap is still considerably lower than the experimental one (about 4.2 eV). Even if the absolute excitation energies may not be reproduced in a fully satisfactory way for such transition metal oxides, the computed band structures strongly support the assignment of observed optical absorption bands to specific electronic transitions. Optical absorption spectra can be calculated from the electronic band structure via the computation of the complex dielectric tensor $\varepsilon_{ij}(\omega)$ (see e.g., Jiang and Guo 2004, for fayalite).

More advanced methods such as TDDFT or the Bethe-Salpeter equation (BSE) approach have been used to date mainly for applications in Physics or Chemistry but they are potentially very useful for understanding e.g., the optical properties of minerals as they are becoming increasingly accessible. Therefore we reference a few recent examples. For instance, the improvement in performance of TDDFT in combination with hybrid functionals with respect to standard DFT functionals has been shown for many materials, including polyoxometalates (Ravelli et al. 2011), Si nanocrystallites (Ramos et al. 2008), Si, GaAs, SiC, C, LiF (Paier et al. 2008) and low energy silica clusters (Zwijnenburg et al. 2008). TDDFT itself leads to good description of the absorption spectra for many systems. However, it also underperforms when compared with the BSE method or even fails on some occasions. Because of the reduced electron-hole attraction it underperforms comparing with BSE for Si nanocrystallites (Ramos et al. 2008) and although it performs well in describing the localized excitations in silica clusters, bulk silicon and solid argon (Sottile et al. 2007; Zwijnenburg et al. 2008), it fails for charge-transfer excitations (Zwijnenburg et al. 2008).

The currently most accurate and reliable method to calculate the UV and optical absorption spectra is the Bethe-Salpeter equation (BSE). This method represents the final stage of a chain of three computational steps: (1) Kohn-Sham calculations of ground state charge density, (2) *GW* calculation of electron self-energy and removal energies and (3) BSE calculations of electron-hole interaction. The perfect agreement of computed absorption spectra with the experiment has been shown for many materials including TiO_2 (Kang and Hybertsen 2010), solid Ne and Ar (Galamic-Mulaomerovic and Patterson 2005; Sottile et al. 2007), silicon nanocrystallites passivated with hydrogen (Ramos et al. 2008), and solid silicon (Sottile et al. 2007). A set of promising calculations of simple H and Si bearing molecules and 1 nm Si cluster are presented in Rocca et al. (2010). It has been shown that the GW correction itself reproduces the results of photoemission and inverse photoemission experiments on copper (Marini et al. 2002b) and that the *GW* quasiparticle corrections result in good agreement of the computed optical spectrum, electron energy loss spectrum and reflectivity of silver with experimental spectra (Marini et al. 2002a). An extensive review on performance of *GW*, BSE and TDDFT methods is given by Onida et al. (2002).

EBSCOhost - printed on 2/13/2023 5:26 AM via . All use subject to https://www.ebsco.com/terms-of-use

We illustrate the performance of the outlined methods for prediction of the optical spectra for the case of bulk silicon. In Table 1, we present the values for the band gap computed by Jain et al. (2011) using Hartree-Fock, DFT, hybrid functionals, *GW* and *GW*-BSE approximations. One can immediately see the improvements of all of the methods over Hartree-Fock, which highly overestimates the band gap, and over DFT, which predicts a band gap that is too narrow. Although hybrid functionals give larger band gaps than standard DFT, they overestimate the experimental value by the same amount standard DFT underestimates it. The *GW* and *GW*-BSE methods predict band gaps consistent with the experimental value. In Figure 9 we present the optical absorption spectra computed for bulk silicon using DFT, TDDFT, *GW* and *GW*-BSE methods. DFT underestimates the absorption energies and the absorption bands are shifted to lower energies by about 0.5 eV. The TDDFT method in the adiabatic LDA (ALDA) approximation gives a result that is very similar to DFT, although Sharma et al. (2011) have shown that a good match to the experiment could be achieved with a modified exchange-correlation kernel. The *GW* method reproduces the peak positions reasonably well, but the absorption strengths are inconsistent with experiment. The best agreement with experiment, both regarding band position and intensities, are obtained with the BSE method.

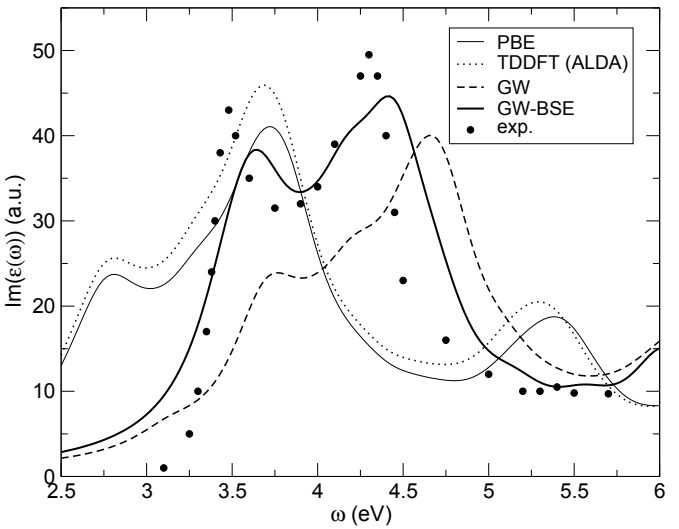


Figure 9. Silicon absorption spectrum, Im(ε(ω)), computed using standard DFT-PBE (thin solid line), TDDFT-ALDA (dotted line), *GW* (dashed line), and *GW*-BSE (thick solid line). The synthetic spectra were computed with Yambo code (www.yambo-code.org, Marini et al. (2009)). The points represent the experimental data of Lautenschlager et al. (1987).

XAFS and XRS

X-ray absorption fine structure (XAFS) spectroscopy measures the fine structure close to an X-ray absorption edge. The principal process at the edge is the excitation of a core electron to an unoccupied higher energy state by a photon. The fine structure of the absorption spectrum close to an edge provides site-specific information about the atomic and electronic structure close to the absorbing atom. The X-ray absorption near edge structure (XANES, up to about 50 eV above the edge) is most sensitive to the valence state and the chemical bonding whereas the extended X-ray absorption spectroscopy (EXAFS, above 50 eV from the edge) provides mainly information about the local atomic environment, which includes the mean distance to and the number of neighboring atoms. X-ray Raman scattering (XRS) spectroscopy is a related

EBSCOhost - printed on 2/13/2023 5:26 AM via . All use subject to https://www.ebsco.com/terms-of-use

method that samples the same type of electronic excitation based on non-resonant inelastic scattering of X-rays. As XRS can always be performed with hard X-rays it is especially suited for measuring low-energy core electron absorption edges of light elements for samples that cannot be studied in ultrahigh vacuum.

A quantitative interpretation of XAFS or XRS spectra, especially close to the absorption edge, often requires advanced theoretical modeling. The best suited method in a specific case depends on the type of absorption edge, the absorbing atom and the excitation energy relative to the edge. One crucial point is whether the final state after excitation of a core electron is localized or not. If the final state is non-localized, e.g., at the *K*-edge after a transition from a 1*s* to a non-occupied *p*-state, the X-ray absorption process is well described by a single-electron multi-atomic approach since the photoelectron spatially extends far from the absorbing atom and multielectronic interactions can be considered to be small. In these cases, DFT-based methods may be applied. On the contrary, the absorption spectra involving strongly localized final states, e.g., at the $L_{2,3}$-edges of transition metal materials, are dominated by multi-electronic processes and theories going beyond the independent-particle approximation are required.

Among the available single-electron codes, a first group is based on real space multiple scattering theory (e.g., FEFF; Rehr and Albers 2000), which is computationally efficient through the use of the "muffin-tin" approximation for representing the scattering potential (Ashcroft and Mermin 1976). Real space calculations are made for atomic clusters centered around the absorbing atom. The muffin-tin potential is composed of a spherical scattering potential centered at each atom and a constant potential in the interstitial region. This method works well especially in the EXAFS region where due to the large kinetic energy of the photoelectron scattering occurs mainly close to the nuclei and the spherical potential is a good approximation. The applicability of the muffin-tin approach to compute XANES spectra depends on the specific material. Such calculations have been successfully used in a number of studies to investigate the effect of different coordination environments on the expected XANES at the *K*-edges of, e.g., Cr in model compounds with different valence state (Farges 2009), Ti in zircon (Tailby et al. 2011) or Zr in aqueous fluids (Wilke et al. 2012). The FDMNES code (Joly 2001) can go beyond the muffin-tin approximation. In this case, the Schrödinger equation is solved by the finite difference method within the local density approximation.

Other DFT-based real space codes employ Gaussian-type orbitals. As an example, the experimental and computed XRS spectra of the oxygen *K*-edge of water from ambient to supercritical conditions are shown in Figure 10 (Sahle et al. 2013). The calculations were performed using the ERKALE code (Lehtola et al. 2012), which computes XAFS and XRS spectra based on the Slater transition state approximation (see paragraph on ΔSCF methods). The input structures were produced by *ab initio* MD simulations using a GGA exchange-correlation functional. While the agreement between experiment and simulation is rather good at elevated pressure and temperature, the computed spectrum at ambient conditions is somewhat less featured than the experimental one. This reflects the known difficulties of DFT-GGA to predict the properties of liquid water accurately (Jonchiere et al. 2011). Another reason for the observed difference in the spectra may be related to the single-electron approximation in the calculation of the XRS spectra. Nevertheless, the relative spectral changes with pressure and temperature are well reproduced in the calculations, which provide confidence that the relevant structural changes between ambient and supercritical water are captured by the simulations. The direct access to the atomic structure sampled during the MD simulations allows a detailed structural analysis and to draw conclusions on the behavior of water under extreme conditions (Sahle et al. 2013), which would not be possible using the spectral information alone.

Another single-electron approach to compute XAFS or XRS spectra of periodic systems relies on a band structure description in reciprocal space. Usually, such calculations are based on DFT using planewave-related or Gaussian-type basis sets and either an all electron method

EBSCOhost - printed on 2/13/2023 5:26 AM via . All use subject to https://www.ebsco.com/terms-of-use

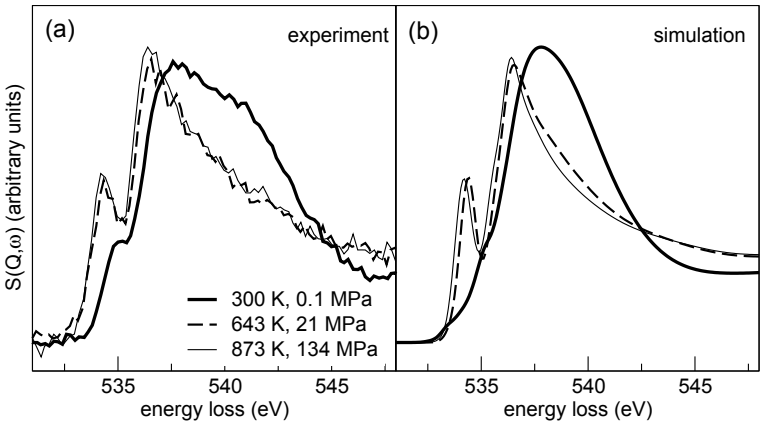


Figure 10. Spectra of the oxygen *K*-edge of water at room temperature and pressure, close to the critical point and at *P-T* conditions beyond the critical point. (a) Experimental and (b) calculated spectra (modified after Sahle et al. 2013).

(Schwarz et al. 2002) or pseudopotentials (Taillefumier et al. 2002; Cabaret et al. 2005; Gao et al. 2009; Gougoussis et al. 2009). The interaction between the core hole and the excited electron is approximated by removing an electron from the core level of interest and adding it to the conduction band. Interactions between periodic "core-holes" are minimized by using a supercell approach, i.e., by treating the excited atom as a defect. In the case of pseudopotential calculations, the all electron wavefunctions of the final state may be reconstructed using the PAW method (Blöchl 1994). Periodic DFT calculations have been performed to predict the *K*-edge spectra of various elements in minerals or glasses. The agreement of the computed spectra compared to experiment is found to be excellent in some cases and only fair in others. For instance, the O and Si *K*-edges of quartz are very well reproduced while the C *K*-edge of diamond is significantly different, especially at low energies (Taillefumier et al. 2002). Calculations of the Mg *K*-edge spectra of minerals and silicate glasses, the structure of the latter sampled by MD simulations, helped to constrain the atomic environment of Mg in the glasses (Trcera et al. 2009, 2011). Thermal effects on the *K*-edge spectra of Al and Ti in minerals were studied by Brouder et al. (2010) and Manuel et al. (2012).

In a number of other studies, measured *K*-edge XANES spectra representing the structural environment of defect sites in minerals were complemented by first-principles calculations, e.g., for Ti, Cr and Fe in corundum, α-Al_2O_3 (Gaudry et al. 2005), Cr in emerald, $Be_3Si_6Al_2O_{16}$ (Gaudry et al. 2007), Cr in spinel, $MgAl_2O_4$ (Juhin et al. 2007), and Cr in pyrope garnet, $Mg_3Al_2(SiO_4)_3$ (Juhin et al. 2008b). Juhin et al. (2008a) and Cabaret et al. (2010) focused on the *K* pre-edge structure of transition metal ions. From these investigations it was concluded that DFT-based single-electron calculations generally capture the essential features of the *K*-edges and pre-edges of 3*d* elements, which allows the interpretation of such spectra in terms of monoelectronic transitions. However, the observed differences point to some of the limitations of the DFT-approach. According to Cabaret et al. (2010) the main drawbacks are the insufficient account for the core-hole interaction and for the 3*d* electron-electron repulsion. For illustration, experimental and computed vanadium *K*-edge spectra of V^{3+}-bearing grossular garnet, $Ca_3Al_2(SiO_4)_3$, by Bordage et al. (2010) are shown in Figure 11. Analysis of the computed spectra allowed an assignment of the pre-edge features shown in Figure 11b to electric quadrupole transitions only. Further, the magnitude of the 3*d* crystal field splitting derived from the DFT calculations was found to be in good agreement with values from optical spectroscopy (Bordage et al. 2010).

EBSCOhost - printed on 2/13/2023 5:26 AM via . All use subject to https://www.ebsco.com/terms-of-use

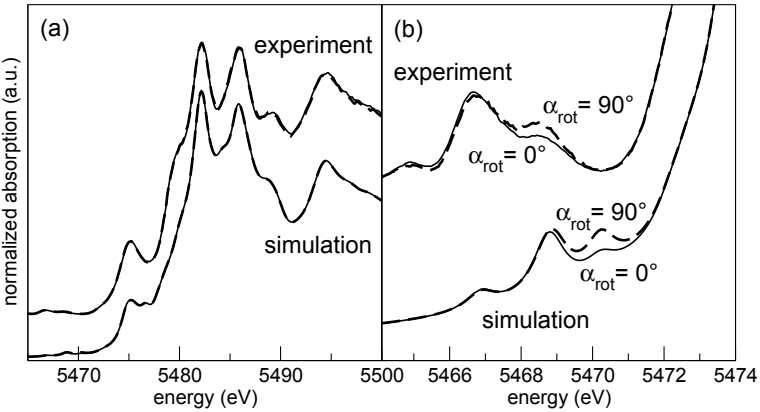


Figure 11. (a) Comparison of experimental and computed vanadium *K*-edge spectra of a V^{3+}-bearing grossular garnet single crystal. (b) Zoom into the pre-edge region of the same spectra. Full and dashed lines refer to different orientations α_{rot} of the crystal with respect to the polarization and the direction of the incident X-ray beam (modified after Bordage et al. 2010).

Single-atom multi-electron approaches such as multiplet calculations (de Groot 2005) usually lead to a better description of the pre-edge region. Crystal field effects are considered on a semi-empirical basis or, more recently, using an *ab initio* configuration-interaction method (Ikeda et al. 2009). For instance in the case of Cr-doped spinel the angular dependence of the Cr *K* pre-edge showed much better agreement with experiment when multiplets were used instead of single-particle DFT (Juhin et al. 2008a). Multiplet calculations of the $L_{2,3}$-edges of 3*d* transition metals and of zirconium oxide were performed by Ikeno et al. (2011, 2013). However, non-local transitions cannot be accounted for in a single-atom approach, which restricts these calculations to the pre-edge region. Hence, single-electron multi-atomic and multi-electron single-atom techniques are complementary but each of them has some limitations. More advanced methods that are multi-atomic and multi-electronic are computationally much more expensive but they are increasingly becoming feasible. Experimental $L_{2,3}$-edge spectra of transition metals have been successfully reproduced using the Bethe-Salpeter equation (BSE) (Laskowski and Blaha 2010; Vinson and Rehr 2012). TDDFT implementations (e.g., Ankudinov et al. 2003; Bunau and Joly 2012a,b) are computationally more efficient and cure some of the problems of DFT but for a number of $L_{2,3}$-edges of transition metals the BSE approach performed much better (Vinson and Rehr 2012). Another method that combines multiple scattering and multiplet approaches is the multi-channel multiple scattering theory, that was used, e.g., to calculate the $L_{2,3}$-edge spectra of Ca in CaO and CaF_2 (Krüger and Natoli 2004).

EELS and ELNES

Formally, electron energy loss spectroscopy (EELS) and specifically the measurement of the electron energy loss near edge structure (ELNES) samples a physical process similar to the XAFS or XRS methods described in the previous section, i.e., the excitation of an inner-shell electron and the interaction of the excited electron with surrounding nuclei and other electrons. The apparent difference is that electrons instead of X-rays are used to excite the inner shell electron. While the different interaction cross-sections lead to different constraints for the applicability of these types of spectroscopy, the theoretical treatment is very similar between these different methods. In both cases the excited electron probes the same unoccupied electronic states. As for XAFS/XRS, a number of computational studies have been performed to interpret experimental measurements. Dadsetani et al. (2010) computed the ELNES spectra of carbon allotropes, including graphite and diamond. They used the ΔSCF method for the

EBSCOhost - printed on 2/13/2023 5:26 AM via . All use subject to https://www.ebsco.com/terms-of-use

description of the core-hole interaction and achieved good agreement with the experimental spectra. A similar method was used by Tanaka et al. (2002) and Mizoguchi et al. (2004) to compute ELNES spectra of selected wide-gaps materials by using the linear combination of atomic orbitals (LCAO) method. Pippel et al. (2000) used DFT calculations of ELNES to interpret the measured ELNES features of Si-C-O glasses. They found that O-Si-C bonds are formed in the glass in addition to SiO_2 and SiC species. The Si *K*- and $L_{2,3}$-edge and O *K*-edge features of quartz were interpreted in terms of projected densities of states from band structure calculations (Garvie et al. 2000). The comparison of computed ELNES of ZnO nanocrystals with different vacancy concentration with the experimental spectra provided information of the structure of the surface (Dileep et al. 2011). Comparing computed and measured EELS spectra of TiO_2, Vast et al. (2002) characterized excitations from the Ti 3*p* core levels to 3*d* states. The DFT-based and measured EELS spectra were used to determine the dielectric function of the skutterudite-related thermoelectric materials CoP_3, $CoAs_3$ and $CoSb_3$ (Prytz et al. 2006), and to interpreted the measured EELS spectra of ZrO_2 (Dash et al. 2004). An application of the all-electron *GW* approximation to derive the EELS of silicon can be found in Arnaud et al. (2005). The authors show that a good description of the electron-hole coupling is essential to obtain the correct EELS line shape of this small gap semiconductor. Suenaga and Koshino (2010) successfully applied the DFT and transition state methods for estimating the threshold energy of the carbon *K*-edge in graphene. EELS and XAFS spectra can be computed using the multiplet CTM4XAS code (Stavitski and de Groot 2010). Theoretical ELNES calculations using one-particle and multi-particle methods were reviewed recently by Mizoguchi et al. (2010).

XPS

X-ray photoelectron spectroscopy (XPS) measures the kinetic energy and the number of electrons escaping a material after exposing it to a beam of X-rays. The method is used to quantify the chemical composition, electronic states or the character of chemical bonding of elements in a material. It is especially sensitive to surfaces as the electrons measured by XPS originate from 1 to 10 nm depth inside the material. Therefore, the method is mainly used in surface science, e.g., to analyze the surface structure of adsorbed species, but it also provides information about the local atomic environment in minerals and glasses. From the experimental spectra, the electron binding energy can be extracted using the following relation

$$E_{binding} = E_{ph} - (E_{kin} + \phi) \tag{53}$$

where E_{ph} and E_{kin} are the energy of the photon and the kinetic energy of the photoelectron measured with a detector. ϕ is the work function that depends on the Fermi levels of the sample and on the detector. In a series of investigations, Zakaznova-Herzog et al. (2005, 2006, 2008) studied experimental and theoretical valence-band XPS spectra of silicates. The calculations were performed using DFT pseudopotential calculations and a GGA exchange-correlation functional using the SIESTA code (Artacho et al. 2008). The XPS spectra were calculated from the theoretical projected density of states of the individual atoms weighted by the corresponding theoretical atomic cross-sections. Generally, the agreement between experimental and theoretical spectra was found to be rather good with some deviations for the Fe-bearing silicates. Differences in the XPS spectra of the studied minerals were related to the different degree of SiO_4 polymerization. The existence of H-bearing surface complexes during leaching of olivine and pyroxenes suggested from experimental results was supported by calculations of XPS spectra for forsterite with an Mg atom substituted by two H atoms (Zakaznova-Herzog et al. 2008). Recently, the effect of thermal vibrations on the line width of XPS spectra of silicates was investigated by combining electronic excitation methods with *ab initio* molecular dynamics simulations (Bancroft et al. 2009). An investigation of the O 1*s* core level shifts between an H_2O molecule, Zn oxo compounds, ZnO surfaces and ZnO bulk using wavefunction based methods and the ΔSCF approach lead to excellent agreement with

EBSCOhost - printed on 2/13/2023 5:26 AM via . All use subject to https://www.ebsco.com/terms-of-use

experimental data. The results indicate that hydroxylation stabilizes the polar O-terminated ZnO $(000\bar{1})$ surface (Kotsis and Staemmler 2006). Takahashi et al. (2008) computed the 3*s* and 1*s* spin-resolved XPS spectra of ferromagnetic iron by using a core-hole potential and obtained good agreement with the experimental spectra. Lizárraga et al. (2011) studied changes in the XPS spectra of crystalline and amorphous Al_2O_3 using DFT methods and concluded that the Al 2*p* spectra do not resolve well the differences in the chemical environment of Al^{3+} due to the strong ionicity of the Al-O bond. In another study, Guittet et al. (2001) derived ionic charges on Si, Zr and O in zircon, $ZrSiO_4$, from a Voronoi analysis of the DFT-derived charge density and compared to the respective ionic charges in the oxides SiO_2 and ZrO_2. The analysis showed that Zr becomes more ionic and Si more covalent in the mixed oxide, which was related to the observed changes in the experimental XPS spectra.

SPECTROSCOPY RELATED TO NUCLEAR EXCITATIONS

NMR

Nuclear magnetic resonance (NMR) spectroscopy is a powerful technique to sample the structure and dynamics of matter on the atomic scale. It probes the energy differences between allowed spin states of the atomic nuclei in the presence of an external magnetic field. The exact resonance frequency for the transition between spin states depends on the local electronic environment of the nucleus, which partially shields the external magnetic field.

The fundamental property to derive chemical shifts from a theoretical point of view is the magnetic shielding tensor $\boldsymbol{\sigma}$ which is formally computed as the second energy derivate with respect to the external magnetic field $\mathbf{B}$ and the magnetic moment of the nucleus $\boldsymbol{\mu}_I$

$$\sigma_{I,\alpha\beta} = \frac{\partial^2 E}{\partial \mu_{I,\alpha} \partial B_\beta} \tag{54}$$

The chemical shift tensor is then simply given by the difference between the shielding tensors of the sample and a reference compound. Instead of presenting the full chemical shift tensor $\boldsymbol{\delta}$, the contributions of individual nuclei to the full NMR signal is expressed in terms of the isotropic chemical shift

$$\delta_{iso} = \frac{1}{3} Tr[\delta] = \sigma_{iso,reference} - \sigma_{iso} \tag{55}$$

and two other parameters, e.g., the chemical shift anisotropy $\Delta_{CSA} = \sigma_{zz} - \sigma_{iso}$ and the asymmetry parameter $\eta_{CSA} = (\sigma_{yy} - \sigma_{xx}) / \Delta_{CSA}$. This definition uses the Haeberlen convention (Haeberlen 1976) $|\sigma_{zz} - \sigma_{iso}| \geq |\sigma_{xx} - \sigma_{iso}| \geq |\sigma_{yy} - \sigma_{iso}|$.

For quadrupolar nuclei (with spin >1/2) the NMR signal is influenced by nuclear quadrupole coupling, whose parameters can be expressed in terms of the principle components V_{xx}, V_{yy} and V_{zz} of the electric field gradient (EFG) tensor. With the convention $|V_{zz}| > |V_{yy}| > |V_{xx}|$, the quadrupolar coupling constant and the asymmetry parameter are defined as

$$C_Q = \frac{eQV_{zz}}{h} \tag{56}$$

and

$$\eta_Q = \frac{V_{xx} - V_{yy}}{V_{zz}} \tag{57}$$

where *e* is the electron charge, *h* is Planck's constant and *Q* is the nuclear electric quadrupole moment. Finally, the quadrupolar product is defined as

EBSCOhost - printed on 2/13/2023 5:26 AM via . All use subject to https://www.ebsco.com/terms-of-use

$$P_Q = C_Q \left(\frac{1 + \eta_Q^2}{3} \right)^{1/2} \tag{58}$$

Another parameter that is important for the understanding and assignment of NMR spectra is the indirect nuclear spin-spin coupling constant J_{AB}. It is defined as the mixed second derivative of the energy with respect to the involved nuclear spins $\mathbf{I}_A$ and $\mathbf{I}_B$ (Gauss 2000)

$$J_{AB} = \frac{1}{3h} \sum_i \frac{\partial^2 E}{\partial I_{A,i} \partial I_{B,i}} \tag{59}$$

Different methods to calculate these coupling constants are assessed and discussed in a recent review by Krivdin and Contreras (2007).

Since the most important contributions to the shielding originate from the nearest and next nearest neighbor atoms and for reasons of accuracy and computational efficiency, the theoretical prediction of NMR parameters had traditionally been based on molecules or atomic clusters representing the solid state. Technically, one has to deal with the gauge-dependence problem, which is related to the choice of origin for the vector potential of the external magnetic field. For molecular systems, several schemes of distributed sets of gauge origins have been proposed. The "individual gauge for localized orbitals" (IGLO) and the "localized orbital/localized origin" (LORG) methods are based on molecular orbitals, while the popular "gauge including atomic orbitals" (GIAO) method is based on atomic orbitals (for more details, see e.g., Gauss 2000; Tossell 2001). For heavy elements, relativistic effects have to be considered (Autschbach and Zheng 2009). Quantum-chemical computations of important NMR parameters, such as chemical shifts, spin-spin coupling constants or electric field gradients, are now widely used (see e.g., recent reviews and text books by Tossell 2001; Kaupp et al. 2004; Casabianca and de Dios 2008; Bühl and van Mourik 2011).

Computations of NMR parameters of molecules or clusters were reviewed in an earlier volume of this journal (Tossell 2001). More recent studies in the field of geomaterials include calculations of ^{17}O NMR shielding of clusters representing alkaline earth oxides and silicates (Tossell 2004), aluminosilicate glasses (Kubicki and Toplis 2002; Kubicki and Sykes 2004; Tossell and Horbach 2005; Lee and Stebbins 2006), aluminosilicates during dissolution (Criscenti et al. 2005) as well as ^{11}B and ^{13}C chemical shifts of boric, carbonic and silicic acid molecules (Tossell 2005a,b). Most of these studies were performed using the program GAUSSIAN (Frisch et al. 2004) but there are also a number of other quantum chemistry codes that are able to compute NMR parameters.

As mentioned above, periodic systems such as crystals or glasses have been approximated by molecular clusters to allow the application of gas phase methods to approximate NMR parameters. However, convergence with respect to basis sets and cluster size is not easy to achieve and computationally expensive. The problem of calculating NMR parameters for a periodic system with periodic boundary conditions was first solved by Mauri et al. (1996) by introducing a modulated magnetic field. The response to a uniform magnetic field, which represents the experimental situation, is obtained as the long wavelength limit of the periodic field. An alternative approach was suggested by Sebastiani and Parrinello (2001), which is based on localized Wannier orbitals. Conceptually, this method is similar to the IGLO method for molecules described above. It uses norm-conserving pseudopotentials and was implemented into the DFT planewave code CPMD (Marx and Hutter 2000).

The currently most popular technique for periodic NMR calculations is the gauge-included projector augmented wave (GIPAW) method that was introduced by Pickard and Mauri (2001). It is an adoption of the PAW method (Blöchl 1994) considering the translational invariance of the magnetic field and allows the computation of NMR parameters within a

EBSCOhost - printed on 2/13/2023 5:26 AM via . All use subject to https://www.ebsco.com/terms-of-use

planewave pseudopotential approach with the accuracy of an all-electron method. The latter is important since the NMR parameters are also very sensitive to core electrons. While the original GIPAW method was developed for the use of norm-conserving pseudopotentials, an extension to computationally cheaper ultrasoft pseudopotentials was suggested recently by Yates et al. (2007). The GIPAW method is now implemented in the CASTEP (Clark et al. 2005) and Quantum ESPRESSO (Giannozzi et al. 2009) codes. A method to calculate NMR *J*-coupling constants for periodic systems using PAW and density-functional perturbation theory was presented by Joyce et al. (2007). Recent advances in the computation of NMR parameters of solids using the PAW/GIPAW approach were reviewed by Charpentier (2011) and Bonhomme et al. (2012). The performance of different DFT functionals for the calculation of NMR chemical shifts using the all-electron augmented planewave method was discussed recently by Laskowski et al. (2013).

Since the introduction of periodic NMR calculations, a number of studies were concerned with the computation of NMR parameters for oxide and silicate crystals and glasses. Computed ^{29}Si NMR spectra of solid, liquid and glassy $ZrSiO_4$ provided new insights into the local structure of metamict zircons (Balan et al. 2003; Farnan et al. 2003). ^{17}O, ^{29}Si and ^{27}Al isotropic chemical shifts as well as ^{17}O and ^{27}Al quadrupolar coupling constant and asymmetry parameters of the three $SiAl_2O_5$ polymorphs were computed by Gervais et al. (2004). The predicted NMR parameters were found to be in good agreement with available experimental and previous computational data from cluster and all electron calculations. NMR parameters of sodium silicate crystals and glasses were computed by Charpentier et al. (2004). In that study, the glass structure was sampled by snapshots from Car-Parrinello molecular dynamics simulations. A similar approach was used to study the ^{11}B chemical shifts in vitreous B_2O_3 and correlate them to B-O-B bond angles (Umari and Pasquarello 2005).

A DFT-PBE study of ^{17}O NMR parameters of Mg and Ca oxides and Ca aluminosilicates showed that the partially covalent Ca-O bond has a large impact on the O chemical shifts (Profeta et al. 2004). The authors also showed that the PBE functional overestimates the Ca-O covalence and introduced a simple and transferable modification of the Ca pseudopotential to correct for this deficiency. This modified Ca pseudopotential was used in subsequent studies with very good results (Benoit et al. 2005; Pedone et al. 2010). Having computed the different NMR parameters defined at the beginning of this section it is possible to construct 2D-NMR spectra (e.g., the ^{17}O NMR 3QMAS spectra) and to support the interpretation of respective experimental spectra (Charpentier et al. 2004; Gervais et al. 2004; Benoit et al. 2005). Multinuclear NMR spectra of $CaSiO_3$ glass were derived by combining GIPAW calculations of the electric field gradients and the chemical shift tensors by Pedone et al. (2010), who also introduced an analysis code called fpNMR.

The effect of temperature on the NMR chemical shifts of MgO crystals was studied by Rossano et al. (2005) who used lattice dynamics in the quasiharmonic approximation and a quantum statistical averaging of normal mode populations. A different approach to treat dynamical effects including anharmonicity was chosen by Robinson and Haynes (2010) who calculated and averaged chemical shifts of an L-alanine molecular crystal for a number of configurations from classical and *ab initio* MD simulations. In a combined experimental and computational study, all oxygen species of different $MgSiO_3$ enstatite polymorphs could be assigned in ^{17}O high resolution triple-quantum magic angle spinning NMR spectra (Ashbrook et al. 2007). The quantitative predictions from the GIPAW calculations suggested somewhat different assignments than previous ones based on empirical experimental correlations. The ^{43}Ca quadrupolar and chemical shift tensors for different $CaCO_3$ polymorphs were measured and computed by Bryce et al. (2008). The surface structure of hydroxyapatite was investigated by NMR spectroscopy and first principles calculations of ^{31}P, ^{1}H and ^{17}O shielding tensors by Chappell et al. (2008). Using NMR spectroscopy and the full potential linear augmented plane

EBSCOhost - printed on 2/13/2023 5:26 AM via . All use subject to https://www.ebsco.com/terms-of-use

wave (FP-LAPW) method, Zhou et al. (2009) attempted to resolve two different Al sites in kaolinite. Sadoc et al. (2011) measured ^{17}F isotropic chemical shifts of fluorides and computed the respective isotropic chemical shielding using the GIPAW approach. From the correlation of the experimental and computed NMR parameters, predictions of ^{19}F NMR spectra of crystalline compounds could be made.

Finally, it should be mentioned that the computation of electron paramagnetic resonance (EPR) *g* tensors follows a similar route. A theory to predict EPR tensors of spin 1/2 centers in the framework of the GIPAW method is outlined in Pickard and Mauri (2002).

Mössbauer spectroscopy

Mössbauer spectroscopy is based on the Mössbauer effect, which describes the recoil-free absorption and emission of γ-rays by an atomic nucleus bound in a solid (Bancroft 1973). The chemical environment of the nucleus causes a very small shift in the nuclear transition energy and this shift is measured experimentally by using the Doppler effect. Three types of energy shifts are observed: (1) isomer shift, (2) quadrupole splitting and (3) hyperfine splitting.

A molecular orbital approach to compute Mössbauer parameters for molecules and clusters, the spin-polarized self-consistent-charge Xα method, was proposed by Grodzicki (1980) and Grodzicki et al. (1987). It has been applied to minerals by representing the crystal by a cluster of about 100 to 150 atoms around the Mössbauer nucleus. Electric field gradient tensors and isomer shifts were computed, e.g., for chlorites (Lougear et al. 2000), fayalite (Lottermoser et al. 2002), crysoberyl and sinhalite (Lottermoser et al. 2011). For solids treated in periodic boundary conditions, the full potential linearized augmented plane wave (LAPW) approach is considered the most accurate. Using this method as implemented in the Wien2k code (Schwarz et al. 2002), the effect of the electronic spin state of iron on the Mössbauer quadrupole splitting in $(Mg,Fe)SiO_3$ perovskite was investigated by Bengtson et al. (2009).

More efficiently and yet with sufficient accuracy, quadrupole couplings and isomer shifts may be computed using a scheme based on DFT and the PAW formalism (Zwanziger 2009). The quadrupole splitting is derived from the calculation of the electric field gradient, which couples to the nuclear electric quadrupole moment. The isomer shift is related to the electronic wavefunction density at the nuclear site of the absorber and the source. For benchmarking the DFT-PAW approach, Zwanziger (2009) computed ^{119}Sn, ^{73}Ge and ^{67}Zn valence electron densities and showed a linear correlation to measured isomer shifts for different structures. In the case of ^{67}Zn, the isomer shifts were corrected for the second-order Doppler shifts and in addition Lamb-Mössbauer factors were derived. For ZnO at ambient pressure, the relative difference between the experimental and the computed electric field gradient is in the order of 15 %. The pressure dependence of the Mössbauer parameters showed much larger differences, which was explained by an extreme sensitivity of the bonding to local structural changes in this compound.

CONCLUDING REMARKS

Theoretical and computational spectroscopy is expanding quickly and therefore it is impossible to even make an attempt to include all new developments in this field in such a review. Neither were we able to make an exhaustive list of references that includes all case studies in the field of geomaterials. We hope to have transported some ideas on how to approach spectroscopic and other characterization methods from a computational point of view. It is important to keep in mind the possibility to use different methods for computing theoretical spectra of crystals, melts or fluids, at low or high pressures and temperatures, with different computational efficiency. There may also be different implementations for computing a particular material property in different codes but eventually calculations on the same level of theory (e.g., DFT with the same

EBSCOhost - printed on 2/13/2023 5:26 AM via . All use subject to https://www.ebsco.com/terms-of-use

exchange-correlation functional) should be consistent with each other. Many codes come with a useful manual or a tutorial that can facilitate to start the first calculations (see e.g., *www.abinit.org*; *www.quantum-espresso.org*). A list of available molecular modeling codes can be found, e.g., on *electronicstructure.org* or *www.psi-k.org/codes.shtml*. As many of these codes can be executed even on a single desktop PC, the simulation methods introduced in this chapter may soon become an everyday tool for experimentalists. We hope that this review will encourage experimental groups to use state-of-the-art molecular modeling as a complementary technique to shed light on their measured data.

ACKNOWLEDGMENTS

The authors thank the volume editor Grant Henderson, Max Wilke, Sergio Speziale, Volker Haigis, Johannes Wagner and two anonymous reviewers for useful discussion and comments. Financial support by DFG under grant no. JA1469/4-1 is gratefully acknowledged.

REFERENCES

Abascal JLF, Vega C (2005) A general purpose model for the condensed phases of water: TIP4P/2005. J Chem Phys 123:234505

Adebayo GA, Liang Y, Miranda CR, Scandolo S (2009) Infrared absorption of MgO at high pressures and temperatures: A molecular dynamic study. J Chem Phys 131:014506

Aguado A, Madden PA (2004) Fully transferable interatomic potentials for large-scale computer simulations of simple metal oxides: Application to MgO. Phys Rev B 70:245103

Aguado A, Bernasconi L, Madden PA (2002) A transferable interatomic potential for MgO from ab initio molecular dynamics. Chem Phys Lett 356:437-444

Aguado A, Bernasconi L, Jahn S, Madden PA (2003) Multipoles and interaction potentials in ionic materials from planewave-DFT calculations. Faraday Discuss 124:171-184

Akdeniz Z, Madden PA (2006) Raman spectra of ionic liquids: A simulation study of AlF_3 and its mixtures with NaF. J Phys Chem B 110:6683-6691

Allen MP, Tildesley DJ (1987) Computer Simulations of Liquids. Oxford University Press

Ammal SC, Heyden A (2010) Modeling the noble metal/TiO_2 (110) interface with hybrid DFT functionals: A periodic electrostatic embedded cluster model study. J Chem Phys 133:164703

Ankudinov AL, Nesvizhskii AI, Rehr JJ (2003) Dynamic screening effects in X-ray absorption spectra. Phys Rev B 67:115120

Arnaud B, Lebegue S, Alouani M (2005) Excitonic and quasiparticle lifetime effects on silicon electron energy loss spectra from first principles. Phys Rev B 71:035308

Artacho E, Anglada E, Dieguez O, Gale JD, Garcia A, Junquera J, Martin RM, Ordejon P, Pruneda JM, Sanchez-Portal D, Soler JM (2008) The SIESTA method; developments and applicability. J Phys: Condens Matter 20:064208

Ashbrook SE, Berry AJ, Frost DJ, Gregorovic A, Pickard CJ, Readman JE, Wimperis S (2007) ^{17}O and ^{29}Si NMR parameters of $MgSiO_3$ phases from high-resolution solid-state NMR spectroscopy and first-principles calculations. J Am Chem Soc 129:13213-13224

Ashcroft NW, Mermin ND (1976) Solid State Physics. Saunders College Publishing.

Autschbach J, Zheng S (2009) Relativistic computations of NMR parameters from first principles: Theory and applications. Annu Rep NMR Spectrosc 67:1-95

Balan E, Saitta AM, Mauri F, Calas G (2001) First-principles modeling of the infrared spectrum of kaolinite. Am Mineral 86:1321-1330

Balan E, Saitta AM, Mauri F, Lemaire C, Guyot F (2002) First-principles calculation of the infrared spectrum of lizardite. Am Mineral 87:1286-1290

Balan E, Mauri F, Pickard CJ, Farnan I, Calas G (2003) The aperiodic states of zircon: an ab initio molecular dynamics study. Am Mineral 88:1769-1777

Balan E, Lazzeri M, Morin G, Mauri F (2006) First-principles study of the OH-stretching modes of gibbsite. Am Mineral 91:115-119

Balan E, Blanchard M, Hochepied JF, Lazzeri M (2008a) Surface modes in the infrared spectrum of hydrous minerals: the OH stretching modes of bayerite. Phys Chem Miner 35:279-285

Balan E, Refson K, Blanchard M, Delattre S, Lazzeri M, Ingrin J, Mauri F, Wright K, Winkler B (2008b) Theoretical infrared absorption coefficient of OH groups in minerals. Am Mineral 93:950-953

EBSCOhost - printed on 2/13/2023 5:26 AM via . All use subject to https://www.ebsco.com/terms-of-use

Balan E, Delattre S, Roche D, Segalen L, Morin G, Guillaumet M, Blanchard M, Lazzeri M, Brouder C, Salje EKH (2011a) Line-broadening effects in the powder infrared spectrum of apatite. Phys Chem Miner 38:111-122

Balan E, Ingrin J, Kovacs I, Blanchard M (2011b) Theoretical infrared spectrum of OH-defects in forsterite. Eur J Mineral 23:285-292

Balan E, Blanchard M, Yi H, Ingrin J (2013) Theoretical study of OH-defects in pure enstatite. Phys Chem Miner 40:41-50

Balucani U, Zoppi M (1994) Dynamics of the liquid state. Oxford University Press, New York.

Bancroft GM (1973) Mössbauer spectroscopy. An introduction for inorganic chemists and geochemists. McGraw-Hill, New York.

Bancroft GM, Nesbitt HW, Ho R, Shaw DM, Tse JS, Biesinger MC (2009) Toward a comprehensive understanding of solid-state core-level XPS linewidths: Experimental and theoretical studies on the Si 2p and O 1s linewidths in silicates. Phys Rev B 80:075405

Baroni S, Giannozzi P, Testa A (1987) Green's-function approach to linear response in solids. Phys Rev Lett 58:1861-1864

Baroni S, de Gironcoli S, Dal Corso A, Giannozzi P (2001) Phonons and related crystal properties from density-functional perturbation theory. Rev Mod Phys 73:515-562

Baroni S, Giannozzi P, Isaev E (2010) Density-functional perturbation theory for quasi-harmonic calculations. Rev Mineral Geochem 71:39-57

Bartlett RJ, Musial M (2007) Coupled-cluster theory in quantum chemistry. Rev Mod Phys 79:291-352

Becke AD (1988) Density-functional exchange-energy approximation with correct asymptotic behavior. Phys Rev A 38:3098-3100

Becke AD (1993) Density-functional thermochemistry. III. The role of exact exchange. J Chem Phys 98:5648-5652

Bengtson A, Li J, Morgan D (2009) Mössbauer modeling to interpret the spin state of iron in (Mg,Fe)SiO_3 perovskite. Geophys Res Lett 36:L15301

Benoit M, Profeta M, Mauri F, Pickard CJ, Tuckerman ME (2005) First-principles calculation of the ^{17}O NMR parameters of a calcium aluminosilicate glass. J Phys Chem B 109:6052-6060

Berendsen HJC, Postma JPM, van Gunsteren WF, Hermans J (1981) Interaction models for water in relation to protein hydration. *In*: Intermolecular forces. Reidel, Dordrecht, p 331-342

Berendsen HJC, Grigera JR, Straatsma TP (1987) The missing term in effective pair potentials. J Phys Chem 91:6269-6271

Berne BJ, Pecora R (1976) Dynamic light scattering. John Wiley & Sons, New York

Blanchard M, Lazzeri M, Mauri F, Balan E (2008) First-principles calculation of the infrared spectrum of hematite. Am Mineral 93:1019-1027

Blanchard M, Balan E, Wright K (2009) Incorporation of water in iron-free ringwoodite: A first-principles study. Am Mineral 94:83-89

Blöchl PE (1994) Projector augmented-wave method. Phys Rev B 50:17953-17979

Boon JP, Yip S (1980) Molecular Hydrodynamics. McGraw-Hill, New York

Bonhomme C, Gervais C, Babonneau F, Coelho C, Pourpoint F, Azais T, Ashbrook SE, Griffin JM, Yates JR, Mauri F, Pickard CJ (2012) First-principles calculation of NMR parameters using the gauge including projector augmented wave method: A Chemist's point of view. Chem Rev 112:5733-5779

Bordage A, Brouder C, Balan E, Cabaret D, Juhin A, Arrio MA, Sainctavit P, Calas G, Glatzel P (2010) Electronic structure and local environment of substitutional V^{3+} in grossular garnet $Ca_3Al_2(SiO_4)_3$: K-edge X-ray absorption spectroscopy and first-principles modeling. Am Mineral 95:1161-1171

Botti S, Schindlmayr A, del Sole R, Reining L (2007) Time-dependent density-functional theory for extended systems. Rep Prog Phys 70:357-407

Bougeard D, Smirnov KS (2009) Calculation of off-resonance Raman scattering intensities with parametric models. J Raman Spectrosc 40:1704-1719

Brouder C, Cabaret D, Juhin A, Sainctavit P (2010) Effect of atomic vibrations on the X-ray absorption spectra at the K edge of Al in α-Al_2O_3 and Ti in TiO_2 rutile. Phys Rev B 81:115125

Bryce DL, Bultz EB, Aebi D (2008) Calcium-43 chemical shift tensors as probes of calcium binding environments. Insight into the structure of the vaterite $CaCO_3$ polymorph by ^{43}Ca solid-state NMR spectroscopy. J Am Chem Soc 130:9282-9292

Bühl M, van Mourik T (2011) NMR spectroscopy: quantum-chemical calculations. WIREs Comput Mol Sci 1:634-647

Bunau O, Joly Y (2012a) Full potential X-ray absorption calculations using time dependent density functional theory. J Phys: Condens Matter 24:215502

Bunau O, Joly Y (2012b) Time-dependent density functional theory applied to X-ray absorption spectroscopy. Phys Rev B 85:155121

Burke K, Ernzerhof M, Perdew JP (1997) The adiabatic connection method: A non-empirical hybrid. Chem Phys Lett 265:115-120

EBSCOhost - printed on 2/13/2023 5:26 AM via . All use subject to https://www.ebsco.com/terms-of-use

Cabaret D, Gaudry E, Taillefumier M, Sainctavit P, Mauri F (2005) XANES calculation with an efficient 'non muffin-tin' approach: Application to the angular dependence of the Al K-edge in corundum. Physica Scripta T115:131-133

Cabaret D, Bordage A, Juhin A, Afaoui M, Gaudry E (2010) First-principles calculations of X-ray absorption spectra at the K-edge of 3d transition metals: an electronic strcuture analysis of the pre-edge. Phys Chem Chem Phys 12:5619-5633

Calzado CJ, Hernandez NC, Sanz JF (2008) Effect of on-site coulomb repulsion term U on the band-gap states of the reduced rutile (110) TiO_2 surface. Phys Rev B 77:045118

Car R, Parrinello M (1985) Unified approach for molecular dynamics and density functional theory. Phys Rev Lett 55:2471-2474

Caracas R, Banigan EJ (2009) Elasticity and Raman and infrared spectra of $MgAl_2O_4$ spinel from density functional perturbation theory. Phys Earth Planet Int 174:113-121

Caracas R, Bobocioiu E (2011) The WURM project - a freely available web-based repository of computed physical data for minerals. Am Mineral 96:437-443

Caracas R, Cohen RE (2006) Theoretical determination of the Raman spectra of $MgSiO_3$ perovskite and post-perovskite at high pressure. Geophys Res Lett 33:L12S05

Casabianca LB, de Dios AC (2008) Ab initio calculations of NMR chemical shifts. J Chem Phys 128:052201

Ceperley DM (2010) An overview of quantum Monte Carlo methods. Rev Mineral Geochem 71:129-135

Ceperley DM, Alder BJ (1980) Ground state of the electron gas by a stochastic method. Phys Rev Lett 45:566-569

Chappell H, Duer M, Groom N, Pickard C, Bristowe P (2008) Probing the surface structure of hydroxyapatite using NMR spectroscopy and first principles calculations. Phys Chem Chem Phys 10:600-606

Charpentier T (2011) The PAW/GIPAW approach for computing NMR parameters: A new dimension added to NMR study of solids. Solid State Nucl Mag Reson 40:1-20

Charpentier T, Ispas S, Profeta M, Mauri F, Pickard CJ (2004) First-principles calculation of ^{17}O, ^{29}Si, and ^{23}Na NMR spectra of sodium silicate crystals and glasses. J Phys Chem B 108:4147-4161

Churakov SV, Wunder B (2004) Ab-initio calculations of the proton location in topaz-OH, $Al_2SiO_4(OH)_2$. Phys Chem Miner 31:131-141

Cizek J (1966) On the correlation problem in atomic and molecular systems. Calculation of wavefunction components in Ursell-type expansion using quantum-field theoretical methods. J Chem Phys 45:4256-4266

Cizek J (1969) On the use of the cluster expansion and the technique of diagrams in calculations of correlation effects in atoms and molecules. Adv Chem Phys 14:35-89

Clark SJ, Segall MD, Pickard CJ, Hasnip PJ, Probert MIJ, Refson K, Payne MC (2005) First principles methods using CASTEP. Z Krist 220:567-570

Cococcioni M (2010) Accurate and efficient calculations on strongly correlated minerals with the LDA+U method: Review and perspectives. Rev Mineral Geochem 71:147-167

Cococcioni M, de Gironcoli S (2005) Linear response approach to the calculation of the effective interaction parameters in the LDA+U method. Phys Rev B 71:035105

Cohen AJ, Mori-Sanchez P, Yang W (2008) Insights into current limitations of density functional theory. Science 321:792-794

Cowan RD (1981) The theory of atomic structure and spectra. University of California Press.

Criscenti LJ, Brantley S, Mueller KT, Tsomaia N, Kubicki JD (2005) Theoretical and ^{27}Al CPMAS NMR investigation of aluminum coordination changes during aluminosilicate dissolution. Geochim Cosmochim Acta 69:2205-2220

Cygan RT, Kubicki JD (eds) (2001) Molecular modeling theory: Applications in the Geosciences. Reviews in Mineralogy and Geochemistry, Volume 42. Mineralogical Society of America

Dadsetani M, Titantah JT, Lamoen D (2010) Ab initio calculation of the energy-loss near-edge structure of some carbon allotropes: Comparison with n-diamond. Diam Relat Mater 19:73-77

Dash LK, Vast N, Baranek P, Cheynet MC, Reining L (2004) Electronic structure and electron energy-loss spectroscopy of ZrO_2 zirconia. Phys Rev B 70:245116

Davydov AS (1965) Quantum Mechanics. Addison-Wesley, Oxford.

de Groot F (2005) Multiplet effects in X-ray spectroscopy. Coord Chem Rev 249:31-63

De La Pierre M, Noël Y, Mustapha S, Meyer A, D'Arco P, Dovesi R (2013) The infrared vibrational spectrum of andradite-grossular solid solutions: A quantum mechanical simulation. Am Mineral 98:966-976

Delattre S, Balan E, Lazzeri M, Blanchard M, Guillaumet M, Beyssac O, Haussühl E, Winkler B, Salje EKH, Calas G (2012) Experimental and theoretical study of the vibrational properties of diaspore (α-AlOOH). Phys Chem Miner 39:93-102

Deslippe J, Samsonidze G, Strubbe DA, Jain M, Cohen ML, Louie SG (2012) BerkeleyGW: A massively parallel computer package for the calculation of the quasiparticle and optical properties of materials and nanostructures. Comp Phys Commun 183:1269-1289

EBSCOhost - printed on 2/13/2023 5:26 AM via . All use subject to https://www.ebsco.com/terms-of-use

Di Valentin C, Pacchioni G, Selloni A (2006) Electronic structure of defect states in hydroxylated and reduced rutile TiO_2 (110) surfaces. Phys Rev Lett 97:166803

Dick BG, Overhauser AW (1958) Theory of the dielectric constants of alkali halide crystals. Phys Rev 112:90-103

Dileep K, Panchakarla LS, Balasubramanian K, Waghmare UV, Datta R (2011) Electron energy loss spectroscopy of ZnO nanocrystals with different oxygen vacancy concentrations. J Appl Phys 109:063523

Dove MT (2003) Structure and dynamics: An atomic view of materials. Oxford University Press.

Dove MT, Winkler B, Leslie M, Harris MJ, Salje EKH (1992) A new interatomic potential model for calcite: Applications to lattice dynamics studies, phase transition, and isotope fractionation. Am Mineral 77:244-250

Dreuw A, Head-Gordon M (2005) Single-reference ab initio methods for the calculation of excited states of large molecules. Chem Rev 105:4009-4037

Drewitt JWE, Jahn S, Cristiglio V, Bytchkov A, Leydier M, Brassamin S, Fischer HE, Hennet L (2011) The structure of liquid calcium aluminates as investigated by neutron and high-energy X-ray diffraction in combination with molecular dynamics simulation methods. J Phys: Condens Matter 23:155101

Drewitt JWE, Hennet L, Zeidler A, Jahn S, Salmon PS, Neuville DR, Fischer HE (2012) Structural transformations on vitrification in the fragile glass forming system $CaAl_2O_4$. Phys Rev Lett 109:235501

Farges F (2009) Chromium speciation in oxide-type compounds: application to minerals, gems, aqueous solutions and silicate glasses. Phys Chem Miner 36:463-481

Farnan I, Balan E, Pickard CJ, Mauri F (2003) The effect of radiation damage on local structure in the crystalline fraction of $ZrSiO_4$: Investigating the ^{29}Si NMR response in zircon and reidite. Am Mineral 88:1663-1667

Fermi E (1927) Un metodo statistico per la determinazione di alcune prioprieta dell'atomo. Rend Accad Naz Lincei 6:602-607

Fock V (1930) Näherungsmethode zur Lösung des quantenmechanischen Mehrkörperproblems. Z Phys 61:126-148

Fourdrin C, Balan E, Allard T, Boukari C, Calas G (2009) Induced modifications of kaolinite under ionizing radiation: an infrared spectroscopic study. Phys Chem Miner 36:291-299

Frenkel D, Smit BJ (2002) Understanding Molecular Simulation: From Algorithms to Applications. Academic Press, San Diego.

Friedrich C, Schindlmayr A (2006) Many-body perturbation theory: The GW approximation. *In*: Computational Nanoscience: Do It Yourself! Grotendorst J, Blügel S, Marx D (eds) Forschungszentrum Jülich, NIC Series, Vol 31, p 335-355

Frisch MJ, Trucks GW, Schlegel HB, Scuseria GE, Robb MA, Cheeseman JR, Montgomery Jr JA, Vreven T, Kudin KN, Burant JC, Millam JM, Iyengar SS, Tomasi J, Barone V, Mennucci B, Cossi M, Scalmani G, Rega N, Petersson GA, Nakatsuji H, Hada M, Ehara M, Toyota K, Fukuda R, Hasegawa J, Ishida M, Nakajima T, Honda Y, Kitao O, Nakai H, Klene M, Li X, Knox JE, Hratchian HP, Cross JB, Bakken V, Adamo C, Jaramillo J, Gomperts R, Stratmann RE, Yazyev O, Austin AJ, Cammi R, Pomelli C, Ochterski JW, Ayala PY, Morokuma K, Voth GA, Salvador P, Dannenberg JJ, Zakrzewski VG, Dapprich S, Daniels AD, Strain MC, Farkas O, Malick DK, Rabuck AD, Raghavachari K, Foresman JB, Ortiz JV, Cui Q, Baboul AG, Clifford S, Cioslowski J, Stefanov BB, Liu G, Liashenko A, Piskorz P, Komaromi I, Martin RL, Fox DJ, Keith T, Al-Laham MA, Peng CY, Nanayakkara A, Challacombe M, Gill PMW, Johnson B, Chen W, Wong MW, Gonzalez C, Pople JA (2004) Gaussian 03. Gaussian, Inc., Wallingford CT.

Galamic-Mulaomerovic S, Patterson CH (2005) Ab initio many-body calculation of excitons in solid Ne and Ar. Phys Rev B 72:035127

Gale JD, Wright K (2010) Lattice dynamics from force-fields as a technique for mineral physics. Rev Mineral Geochem 71:391-411

Gao SP, Pickard CJ, Perlov A, Milman V (2009) Core-level spectroscopy calculation and the plane wave pseudopotential method. J Phys: Condens Matter 21:104203

Garvie LAJ, Rez P, Alvarez JR, Buseck PR, Craven AJ, Brydson R (2000) Bonding in alpha-quartz (SiO_2): A view of the unoccupied states. Am Mineral 85:732-738

Gaudry E, Cabaret D, Sainctavit P, Brouder C, Mauri F, Goulon J, Rogalev A (2005) Structural relaxations around Ti, Cr and Fe impurities in α-Al_2O_3 probed by X-ray absorption near-edge structure combined with first-principles calculations. J Phys: Condens Matter 17:5467-5480

Gaudry E, Cabaret D, Brouder C, Letard I, Rogalev A, Wilhlem F, Jaouen N, Sainctavit P (2007) Relaxations around the substitutional chromium site in emerald: X-ray absorption experiments and density-functional theory. Phys Rev B 76:094110

Gauss J (2000) Molecular properties. *In*: Modern Methods and Algorithms of Quantum Chemistry. Grotendorst J (ed) Forschungszentrum Jülich, NIC Series, Vol 1, p 509-560

Gavnholt J, Olsen T, Engelund M, Schiøtz J (2008) Δ self-consistent field method to obtain potential energy surfaces of excited molecules on surfaces. Phys Rev B 78:075441

Gervais C, Profeta M, Babonneau F, Pickard CJ, Mauri F (2004) Ab initio calculations of NMR parameters of highly coordinated oxygen sites in aluminosilicates. J Phys Chem B 108:13249-13253

EBSCOhost - printed on 2/13/2023 5:26 AM via . All use subject to https://www.ebsco.com/terms-of-use

Giacomazzi L, Pasquarello A (2007) Vibrational spectra of vitreous SiO_2 and vitreous GeO_2 from first principles. J Phys: Condens Matter 19:415112

Giacomazzi L, Umari P, Pasquarello A (2009) Medium-range structure of vitreous SiO_2 obtained through first-principles investigation of vibrational spectra. Phys Rev B 79:064202

Giannozzi P, Baroni S, Bonini N, Calandra M, Car R, Cavazzoni C, Ceresoli D, Chiarotti GL, Cococcioni M, Dabo I, Dal Corso A, de Gironcoli S, Fabris S, Fratesi G, Gebauer R, Gerstmann U, Gougoussis C, Kokalj A, Lazzeri M, Martin-Samos L, Marzari N, Mauri F, Mazzarello R, Paolini S, Pasquarello A, Paulatto L, Sbraccia C, Scandolo S, Sclauzero G, Seitsonen AP, Smogunov A, Umari P, Wentzcovitch RM (2009) Quantum Espresso: a modular and open-source software project for quantum simulations of materials. J Phys: Condens Matter 21:395502

Gonze X (1997) First-principles responses of solids to atomic displacements and homogeneous electric fields: implementation of a conjugate-gradient algorithm. Phys Rev B 55:10337-10354

Gonze X, Lee C (1997) Dynamical matrices, born effective charges, dielectric permittivity tensors, and interatomic force constants from density-functional perturbation theory. Phys Rev B 55:10355-10368

Gonze X, Beuken JM, Caracas R, Detraux F, Fuchs M, Rignanese GM, Sindic L, Verstraete M, Zerah G, Jollet F, Torrent M, Roy A, Mikami M, Ghosez P, Raty JL, Allan DC (2002) First-principles computation of material properties: the ABINIT software project. Comput Mater Sci 25:478-492

Gonze X, Amadon B, Anglade PM, Beuken JM, Bottin F, Boulanger P, Bruneval F, Caliste D, Caracas R, Cote M, Deutsch T, Genovese L, Ghosez P, Giantomassi M, Goedecker S, Hamann DR, Hermet P, Jollet F, Jomard G, Leroux S, Mancini M, Mazevet S, Oliveira MJT, Onida G, Pouillon Y, Rangel T, Rignanese GM, Sangalli D, Shaltaf R, Torrent M, Verstraete MJ, Zerah G, Zwanziger JW (2009) ABINIT: First-principles approach of materials and nanosystem properties. Comput Phys Comm 180:2582-2615

Gougoussis C, Calendra M, Seitsonen AP, Mauri F (2009) First-principles calculations of X-ray absorption in a scheme based on ultrasoft pseudopotentials: From α-quartz to high-T_c compounds. Phys Rev B 80:075102

Grodzicki M (1980) A self-consistent charge Xα method. I. Theory. J Phys B 13:2683-2691

Grodzicki M, Männing V, Trautwein AX, Friedt JM (1987) Calibration of isomer shift and quadrupole coupling for ^{119}Sn, ^{127}I and ^{129}I as derived from self-consistent charge Xα calculations and Mössbauer measurements. J Phys B 20:5595-5625

Guillot B, Sator N (2007) A computer simulation study of natural silicate melts. Part I: Low pressure properties. Geochim Cosmochim Acta 71:1249-1265

Guittet MJ, Crocombette JP, Gautier-Soyer M (2001) Bonding and XPS chemical shifts in $ZrSiO_4$ versus SiO_2 and ZrO_2: Charge transfer and electrostatic effects. Phys Rev B 63:125117

Haas P, Tran F, Blaha P (2009) Calculation of the lattice constant of solids with semilocal functionals. Phys Rev B 79:085104

Habershon S, Fanourgakis GS, Manolopoulos DE (2008) Comparison of path integral molecular dynamics methods for the infrared absorption spectrum of liquid water. J Chem Phys 129:074501

Haeberlen U (1976) High resolution NMR in solids selective averaging. Vol. suppl. 1 of Advances in Magnetic Resonance. Academic Press, New York.

Hart JF, Herzberg G (1957) Twenty-parameter eigenfunctions and energy values of the ground states of He and He-like ions. Phys Rev 106:79-82

Hättig C (2006) Beyond Hartree-Fock: MP2 and coupled-cluster methods for large systems. *In*: Computational Nanoscience: Do It Yourself! Grotendorst J, Blügel S, Marx D (eds) Forschungszentrum Jülich, NIC Series, Vol 31, p 245-278

Heaton RJ, Madden PA (2008) Fluctuating ionic polarizabilities in the condensed phase: first-principles calculations of the Raman spectra of ionic melts. Mol Phys 106:1703-1719

Heaton RJ, Madden PA, Clark SJ, Jahn S (2006) Condensed phase ionic polarizabilities from plane wave density functional theory calculations. J Chem Phys 125:144104

Hedin L (1965) New method for calculating the one-particle Green's function with application to the electron-gas problem. Phys Rev 139:A796-A823

Hennet L, Pozdnyakova I, Cristiglio V, Cuello GJ, Jahn S, Krishnan S, Saboungi ML, Price DL (2007) Short- and intermediate-range order in levitated liquid aluminates. J Phys: Condens Matter 19:455210

Hohenberg P, Kohn W (1964) Inhomogeneous electron gas. Phys Rev 136:B864-B871

Horbach J, Kob W, Binder K (2001) Structural and dynamical properties of sodium silicate melts: an investigation by molecular dynamics computer simulation. Chem Geol 174:87-101

Hsu H, Umemoto K, Cococcioni M, Wentzcovitch RM (2011) The Hubbard U correction for iron-bearing minerals: A discussion based on $(Mg,Fe)SiO_3$ perovskite. Phys Earth Planet Int 185:13-19

Iftimie R, Tuckerman ME (2005) Decomposing total IR spectra of aqueous systems into solute and solvent contributions: A computational approach using maximally localized Wannier orbitals. J Chem Phys 122:214508

Ikeda H, de Groot FMF, Stavitski E, Tanaka I (2009) Multiplet calculations of $L_{2,3}$ X-ray absorption near-edge structures for 3d transition-metal compounds. J Phys: Condens Matter 21:104208

EBSCOhost - printed on 2/13/2023 5:26 AM via . All use subject to https://www.ebsco.com/terms-of-use

Ikeno H, Krause M, Höche T, Patzig C, Hu Y, Gawronski A, Tanaka I, Rüssel C (2013) Variation of Zr-$L_{2,3}$ XANES in tetravalent zirconium oxides. J Phys: Condens Matter 25:165505
Ikeno H, Mizoguchi T, Tanaka I (2011) Ab initio charge transfer multiplet calculations on the $L_{2,3}$ XANES and ELNES of 3d transition metal oxides. Phys Rev B 83:155107
Jahn S (2008a) Atomic structure and transport properties of MgO-Al_2O_3 melts: A molecular dynamics simulation study. Am Mineral 93:1486-1492
Jahn S (2008b) High-pressure phase transitions in $MgSiO_3$ orthoenstatite studied by atomistic computer simulation. Am Mineral 93:528-532
Jahn S (2010) Integral modeling approach to study the phase behavior of complex solids: Application to phase transitions in $MgSiO_3$ pyroxenes. Acta Cryst A66:535-541
Jahn S, Madden PA (2007a) Modeling Earth materials from crustal to lower mantle conditions: A transferable set of interaction potentials for the CMAS system. Phys Earth Planet Int 162:129-139
Jahn S, Madden PA (2007b) Structure and dynamics in liquid alumina: simulations with an ab initio interaction potential. J Non-Cryst Solids 353:3500-3504
Jahn S, Madden PA (2008) Atomic dynamics of alumina melt: A molecular dynamics simulation study. Condens Matter Phys 11:169-178
Jahn S, Martoňák R (2008) Plastic deformation of orthoenstatite and the ortho- to high-pressure clinoenstatite transition: A metadynamics simulation study. Phys Chem Miner 35:17-23
Jahn S, Madden PA, Wilson M (2006) Transferable interaction model for Al_2O_3. Phys Rev B 74:024112
Jahn S, Rahner R, Dachs E, Mrosko M, Koch-Müller M (2013) Thermodynamic properties of anhydrous and hydrous wadsleyite, β-Mg_2SiO_4. High Press Res in press, doi: 10.1080/08957959.2013.806498
Jain M, Chelikowsky JR, Louie SG (2011) Reliability of hybrid functionals in predicting band gaps. Phys Rev Lett 107:216806
Janak JF (1978) Proof that $dE/dn_i=\varepsilon$ in density functional theory. Phys Rev B 18:7165-7168
Jiang X, Guo GY (2004) Electronic structure, magnetism, and optical properties of Fe_2SiO_4 fayalite at ambient and high pressures: A GGA+U study. Phys Rev B 69:155108
Joly Y (2001) X-ray absorption near-edge structure calculations beyond the muffin-tin approximation. Phys Rev B 63:125120
Jonchiere R, Seitsonen AP, Ferlat G, Saitta AM, Vuilleumier R (2011) Van der Waals effects in ab initio water at ambient and supercritical conditions. J Chem Phys 135:154503
Jorgensen WL, Chandrasekhar J, Madura JD, Impey RW, Klein ML (1983) Comparison of simple potential functions for simulating liquid water. J Chem Phys 79:926-935
Joyce SA, Yates JR, Pickard CJ, Mauri F (2007) A first principles theory of nuclear magnetic resonance J-coupling in solid-state systems. J Chem Phys 127:204107
Juhin A, Calas G, Cabaret D, Galoisy L (2007) Structural relaxation around substitutional Cr^{3+} in $MgAl_2O_4$. Phys Rev B 76:054105
Juhin A, Brouder C, Arrio MA, Cabaret D, Sainctavit P, Balan E, Bordage A, Seitsonen AP, Calas G, Eeckhout SG, Glatzel P (2008a) X-ray linear dichroism in cubic compounds: The case of Cr^{3+} in $MgAl_2O_4$. Phys Rev B 78:195103
Juhin A, Calas G, Cabaret D, Galoisy L, Hazemann JL (2008b) Structural relaxation around substitutional Cr^{3+} in pyrope garnet. Am Mineral 93:800-805
Kaindl R, Többens DM, Haefeker U (2011) Quantum-mechanical calculations of the Raman spectra of Mg- and Fe-cordierite. Am Mineral 96:1568-1574
Kalinichev AG (2001) Molecular simulations of liquid and supercritical water: Thermodynamics, structure, and hydrogen bonding. Rev Mineral Geochem 42:83-129
Kalinichev AG, Heinzinger K (1995) Molecular dynamics of supercritical water: A computer simulation of vibrational spectra with the flexible BJH potential. Geochim Cosmochim Acta 59:641-650
Kang W, Hybertsen MS (2010) Quasiparticle and optical properties of rutile and anatase TiO_2. Phys Rev B 82:085203
Kapitán J, Drahínský M, Kaminský J, Benda L, Bouň P (2010) Theoretical modeling of magnesium ion imprints in the Raman scattering of water. J Phys Chem. B 114:3574-3582
Kaupp M, Bühl M, Malkin VG (eds.) (2004) Calculation of NMR and EPR Parameters: Theory and Applications. Wiley-VCH, Weinheim.
Klimeš J, Michaelides A (2012) Perspective: Advances and challenges in treating van der Waals dispersion forces in density functional theory. J Chem Phys 137:120901
Koch W, Holthausen MC (2000) A chemist's guide to density functional theory. Wiley-VCH, Weinheim.
Koch-Müller M, Rhede D (2010) IR absorption coefficients for water in nominally anhydrous high-pressure minerals. Am Mineral 95:770-775
Kohanoff J (2006) Electronic Structure Calculations for Solids and Molecules: Theory and Computational Methods. Cambridge University Press, Cambridge.
Kohn W, Sham LJ (1965) Self-consistent equations including exchange and correlation effects. Phys Rev 140:A1133-A1138

EBSCOhost - printed on 2/13/2023 5:26 AM via . All use subject to https://www.ebsco.com/terms-of-use

Koopmans T (1934) Über die Zuordnung von Wellenfunktionen und Eigenwerten zu den einzelnen Elektronen eines Atoms. Physica 1:104-113

Kotsis K, Staemmler V (2006) Ab initio calculations of the O1s XPS spectra of ZnO and Zn oxo compounds. Phys Chem Chem Phys 8:1490-1498

Kowalski PM (2010) The origin of peculiar molecular bands in cool DQ white dwarfs. Astron Astrophys 519:L8

Kowalski P, Farnesi Camellone M, Nair NN, Meyer B, Marx D (2010) Charge localization dynamics induced by oxygen vacancies on the TiO_2(110) surface. Phys Rev Lett 105:146405

Krivdin LB, Contreras RH (2007) Recent advances in theoretical calculations of indirect spin-spin coupling constants. Ann Rep NMR Spectrosc 61:133-245

Krüger P, Natoli CR (2004) X-ray absorption spectra at the Ca $L_{2,3}$ edge calculated within the multichannel multiple scattering theory. Phys Rev B 70:245120

Kubicki JD (2001) Interpretation of vibrational spectra using molecular orbital theory calculations. Rev Mineral Geochem 42:459-483

Kubicki JD, Sykes D (1993) Molecular orbital calculations of vibrations in three-membered aluminosilicate rings. Phys Chem Miner 19:381-391

Kubicki JD, Sykes DG (2004) Ab initio calculation of ^{1}H, ^{17}O, ^{27}Al and ^{29}Si NMR parameters, vibrational frequencies and bonding energetics in hydrous silica and Na-aluminosilicate glasses. Geochim Cosmochim Acta 68:3909-3918

Kubicki JD, Toplis MJ (2002) Molecular orbital calculations on aluminosilicate tricluster molecules: Implications for the structure of aluminosilicate glasses. Am Mineral 87:668-678

Lacks DJ, Rear DB, van Orman JA (2007) Molecular dynamics investigation of viscosity, chemical diffusivities and partial molar volumes of liquids along the MgO-SiO_2 join as functions of pressure. Geochim Cosmochim Acta 71:1312-1323

Laio A, Bernard S, Chiarotti GL, Scandolo S, Tosatti E (2000) Physics of iron at Earth's core conditions. Science 287:1027-1030

Laskowski R, Blaha P (2010) Understanding the $L_{2,3}$ X-ray absorption spectra of early 3d transition elements. Phys Rev B 82:205104

Laskowski R, Blaha P, Tran F (2013) Assessment of DFT functionals with NMR chemical shifts. Phys Rev B 87:195130

Lautenschlager P, Garriga M, Cardona M (1987) Temperature dependence of the dielectric function and interband critical points in silicon. Phys Rev B 36:4821-4830

Lazzari M, Mauri F (2003) First-principles calculation of vibrational Raman spectra in large systems: Signature of small rings in crystalline SiO_2. Phys Rev Lett 90:036401

Lee SK, Stebbins JF (2006) Disorder and the extent of polymerization in calcium silicate and aluminosilicate glasses: O-17 NMR results and quantum chemical molecular orbital calculations. Geochim Cosmochim Acta 70:4275-4286

Lee C, Yang W, Parr RC (1988) Development of the Colle-Salvetti correlation-energy formula into a functional of the electron density. Phys Rev B 37:785-789

Lee MS, Baletto F, Kanhere DG, Scandolo S (2008) Far-infrared absorption of water clusters by first-principles molecular dynamics. J Chem Phys 128:214506

Lehtola J, Hakala M, Sakko A, Hämäläinen K (2012) Erkale - a flexible program package for X-ray properties of atoms and molecules. J Comput Chem 33:1572-1585

Liang Y, Miranda CR, Scandolo S (2006) Infrared and Raman spectra of silica polymorphs from an ab initio parametrized polarizable force field. J Chem Phys 125:194524

Libowitzky E, Rossman GR (1997) An IR absorption calibration for water in minerals. Am Mineral 82:1111-1115

Lizárraga R, Holmström E, Parker SC, Arrouvel C (2011) Structural characterization of amorphous alumina and its polymorphs from first-principles XPS and NMR calculations. Phys Rev B 83:094201

Loong CK (2006) Inelastic scattering and applications. Rev Mineral Geochem 63:233-254

Lottermoser W, Steiner K, Grodzicki M, Jiang K, Scharfetter G, Bats JW, Redhammer G, Treutmann W, Hosoya S, Amthauer G (2002) The electric field gradient in synthetic fayalite α-Fe_2SiO_4 at moderate temperatures. Phys Chem Miner 29:112-121

Lottermoser W, Redhammer GJ, Weber SU, Litterst FJ, Tippelt G, Dlugosz S, Bank H, Amthauer G, Grodzicki M (2011) The electric field gradient in natural iron-doped chrysoberyl Al_2BeO_4 and sinhalite $MgAlBO_4$ single crystals. Phys Chem Miner 38:787-799

Lougear A, Grodzicki M, Bertoldi C, Trautwein AX, Steiner K, Amthauer G (2000) Mössbauer and molecular orbital study of chlorites. Phys Chem Miner 27:258-269

MacDonald JKL (1933) Successive approximations by the Rayleigh-Ritz variation method. Phys Rev 43:830-833

Madden PA, Wilson M (2000) "Covalent" effects in "ionic" liquids. J Phys: Condens Matter 12:A95-A108

Madden PA, Wilson M, Hutchinson F (2004) Raman spectra of ionic liquids: Interpretation via computer simulation. J Chem Phys 120:6609-6619

EBSCOhost - printed on 2/13/2023 5:26 AM via . All use subject to https://www.ebsco.com/terms-of-use

Madden PA, Heaton R, Aguado A, Jahn S (2006) From first-principles to material properties. J Mol Struc (Theochem) 771:9-18

Mahadevan TS, Garofalini SH (2007) Dissociative water potential for molecular dynamics simulations. J Phys Chem B 111:8919-8927

Mahoney MW, Jorgensen WL (2000) A five-site model liquid water and the reproduction of the density anomaly by rigid, non-polarizable models. J Chem Phys 112:8910-8922

Manuel D, Cabaret D, Brouder C, Sainctavit P, Bordage A, Trcera N (2012) Experimental evidence of thermal fluctuations on the X-ray absorption near-edge structure at the aluminum K edge. Phys Rev B 85:224108

Marini A, Del Sole R, Onida G (2002a) First-principles calculation of the plasmon resonance and of the reflectance spectrum of silver in the GW approximation. Phys Rev B 66:115101

Marini A, Hogan C, Grüning M, Varsano D (2009) Yambo: an ab initio tool for excited state calculations. Comp Phys Comm 180:1392-1403

Marini A, Onida G, Del Sole R (2002b) Quasiparticle electronic structure of copper in the GW approximation. Phys Rev Lett 88:016403

Marsman M, Paier J, Stroppa A, Kresse G (2008) Hybrid functionals applied to extended systems. J Phys: Condens Matter 20:064201

Martin RM (2004) Electronic Structure: Basic Theory and Practical Methods. Cambridge University Press

Martoňák R, Laio A, Parrinello M (2003) Predicting crystal structures: The Parrinello-Rahman method revisited. Phys Rev Lett 90:075503

Martoňák R, Donadio D, Oganov AR, Parrinello M (2006) Crystal structure transformations in SiO_2 from classical and ab initio metadynamics. Nat Mater 5:623-626

Martoňák R, Donadio D, Oganov AR, Parrinello M (2007) From four- to six-coordinated silica: transformation pathways from metadynamics. Phys Rev B 76:014120

Martyna GJ, Tobias DJ, Klein ML (1994) Constant pressure molecular dynamics algorithms. J Chem Phys 101:4177-4189

Marx D, Hutter J (2000) Ab initio molecular dynamics: Theory and implementation. *In*: Modern Methods and Algorithms of Quantum Chemistry. Grotendorst J (ed.) Forschungszentrum Jülich, NIC Series, Vol. 1, p 301-449

Marx D, Parrinello M (1996) Ab initio path integral molecular dynamics: Basic ideas. J Chem Phys 104:4077-4082

Marzari N, Vanderbilt D (1997) Maximally localized generalized Wannier functions for composite energy bands. Phys Rev B 56:12847

Massobrio C, Pasquarello A, Car R (1995) First principles study of photoelectron spectra of Cu^-_n clusters. Phys Rev Lett 75:2104-2107

Massobrio C, Pasquarello A, Car R (1996) Interpretation of photoelectron spectra in Cu^-_n clusters including thermal and final-state effects: The case of Cu^-_7. Phys Rev B 54:8913-8918

Matsui M (1988) Molecular dynamics study of $MgSiO_3$ perovskite. Phys Chem Miner 16:234-238

Matsui M (1996) Molecular dynamics simulation of structures, bulk moduli, and volume thermal expansivities of silicate liquids in the system CaO-MgO-Al_2O_3-SiO_2. Geophys Res Lett 23:395-398

Matsui M (2000) Molecular dynamics simulation of $MgSiO_3$ perovskite and the 660-km seismic discontinuity. Phys Earth Planet Int 121:77-84

Matsui M, Parker SC, Leslie M (2000) The MD simulation of the equation of state of MgO: Application as a pressure calibration standard at high temperature and high pressure. Am Mineral 85:312-316

Mauri F, Pfrommer BG, Louie SG (1996) Ab initio theory of NMR chemical shufts in solids and liquids. Phys Rev Lett 77:5300-5303

McKeown DA, Bell MI, Caracas R (2010) Theoretical determination of the Raman spectra of single-crystal forsterite (Mg_2SiO_4). Am Mineral 95:980-986

McMahan AK, Martin RM, Satpathy S (1988) Calculated effective Hamiltonian for La_2CuO_4 and solution in the impurity Anderson approximation. Phys Rev B 38:6650-6666

McQuarrie DA (2000) Statistical mechanics. University Science Books, Sausalito.

Mendelssohn MJ, Price GD (1997) Computer modelling of a pressure induced phase change in clinoenstatite pyroxenes. Phys Chem Miner 25:55-62

Miwa K (2011) Prediction of Raman spectra with ultrasoft pseudopotentials. Phys Rev B 84:094304

Mizoguchi T, Tanaka I, Yoshioka S, Kunisu M, Yamamoto T, Ching WY (2004) First-principles calculations of ELNES and XANES of selected wide-gap materials: Dependence on crystal structure and orientation. Phys Rev B 70:045103

Mizoguchi T, Olovsson W, Ikeno H, Tanaka I (2010) Theoretical ELNES using one-particle and multi-particle calculations. Micron 41:695-709

Møller C, Plesset MS (1934) Note on an approximation treatment for many-electron systems. Phys Rev 46:618-622

Morgan BJ, Watson GW (2009) A density functional theory + U study of oxygen vacancy formation at the (110), (100), (101), and (001) surfaces of rutile TiO_2. J Phys Chem C 113:7322-7328

EBSCOhost - printed on 2/13/2023 5:26 AM via . All use subject to https://www.ebsco.com/terms-of-use

Muscat J, Wander A, Harrison NM (2001) On the prediction of band gaps from hybrid functional theory. Chem Phys Lett 342:397-401

Noel Y, Catti M, d'Arco P, Dovesi R (2006) The vibrational frequencies of forsterite Mg_2SiO_4: an all-electron ab initio study with the crystal code. Phys Chem Miner 33:383-393

Novita, M, Ogasawara K (2012) Comparative study of absorption spectra of V^{2+}, Cr^{3+}, and Mn^{2+} in α-Al_2O_3 based on first-principles configuration-interaction calculations. J Phys Soc Jpn 81:104709

Oganov AR, Glass CW (2006) Crystal structure prediction using ab initio evolutionary techniques: Principles and applications. J Chem Phys 124:244704

Oganov AR, Glass CW (2008) Evolutionary crystal structure prediction as a tool in materials design. J Phys: Condens Matter 20:064210

Oganov AR, Martoňák R, Laio A, Raiteri P, Parrinello M (2005) Anisotropy of Earth's D" layer and stacking faults in the $MgSiO_3$ post-perovskite phase. Nature 438:1142-1144

Onida G, Reining L, Rubio A (2002) Electronic excitations: density-functional versus many-body Green's-function approaches. Rev Mod Phys 74:601-659

Pagliai M, Cavazzoni C, Cardini G, Erbacci G, Parrinello M, Schettino V (2008) Anharmonic infrared and Raman spectra in Car-Parrinello molecular dynamics simulations. J Chem Phys 128:224514

Paier J, Marsman M, Hummer K, Kresse G, Gerber IC, Angyan JG (2006a) Erratum: Screened hybrid density functionals applied to solids. J Chem Phys 125:249901

Paier J, Marsman M, Hummer K, Kresse G, Gerber IC, Angyan JG (2006b) Screened hybrid density functionals applied to solids. J Chem Phys 124:154709

Paier J, Marsman M, Kresse G (2008) Dielectric properties and excitons for extended systems from hybrid functionals. Phys Rev B 78:121201R

Pavlatou EA, Madden PA, Wilson M (1997) The interpretation of vibrational spectra of ionic melts. J Chem Phys 107:10446-10457

Pedone A, Charpentier T, Menziani MC (2010) Multinuclear NMR of $CaSiO_3$ glass: simulation from first-principles. Phys Chem Chem Phys 12:6054-6066

Perdew JP, Burke K, Ernzerhof M (1996a) Generalized gradient approximation made simple. Phys Rev Lett 77:3865-3868

Perdew JP, Ernzerhof M, Burke K (1996b) Rationale for mixing exact exchange with density functional approximations. J Chem Phys 105:9982-9985

Perdew JP, Levy M (1983) Physical content of the exact Kohn-Sham orbital energies: Band gaps and derivative discontinuities. Phys Rev Lett 51:1884-1887

Perdew JP, Ruzsinszky A (2010) Density functional theory of electronic structure: A short course for mineralogists and geophysicists. Rev Mineral Geochem 71:1-18

Perdew JP, Wang Y (1992) Accurate and simple analytic representation of the electron-gas correlation energy. Phys Rev B 45:13244-13249

Pickard CJ, Mauri F (2001) All-electron magnetic response with pseudopotentials: NMR chemical shifts. Phys Rev B 63:245101

Pickard CJ, Mauri F (2002) First-principles theory of the EPR g tensor in solids: Defects in quartz. Phys. Rev. Lett. 88:086403

Pickard CJ, Needs RJ (2011) Ab initio random structure searching. J Phys: Condens Matter 23:053201

Pinilla C, Irani AH, Seriani N, Scandolo S (2012) Ab initio parameterization of an all-atom polarizable and dissociable force field for water. J Chem Phys 136:114511

Pippel E, Lichtenberger O, Woltersdorf J (2000) Identification of silicon oxycarbide bonding in Si-C-O-glasses by EELS. J Mater Sci Lett 19:2059-2060

Prencipe M, Pascale F, Zicovich-Wilson CM, Saunders VR, Orlando R, Dovesi R (2004) The vibrational spectrum of calcite ($CaCO_3$): An ab initio quantum-mechanical calculation. Phys Chem Miner 31:559-564

Profeta M, Benoit M, Mauri F, Pickard CJ (2004) First-principles calculation of the ^{17}O NMR parameters in Ca oxide and Ca aluminosilicates: the partially covalent nature of the Ca-O bond, a challenge for density functional theory. J Am Chem Soc 126:12628-12635

Prytz O, Lovvik OM, Tafto J (2006) Comparison of theoretical and experimental dielectric functions: Electron energy-loss spectroscopy and density-functional calculations on skutterudites. Phys Rev B 24:245109

Putnis A (1992) Introduction to mineral sciences. Cambridge University Press.

Putrino A, Parrinello M (2002) Anharmonic Raman spectra in high-pressure ice from ab initio simulations. Phys Rev Lett 88:176401

Putrino A, Sebastiani D, Parrinello M (2000) Generalized variational density functional perturbation theory. J Chem Phys 113:7102-7109

Pye CC, Rudolph WW (1998) An ab initio and Raman investigation of magnesium(II) hydration. J Phys Chem A 102:9933-9943

Pye CC, Rudolph WW (2001) An ab initio and Raman investigation of sulfate ion hydration. J Phys Chem A 105:905-912

EBSCOhost - printed on 2/13/2023 5:26 AM via . All use subject to https://www.ebsco.com/terms-of-use

Ramos LE, Paier J, Kresse G, Bechstedt F (2008) Optical spectra of Si nanocrystallites: Bethe-Salpeter approach versus time-dependent density-functional theory. Phys Rev B 78:195423
Ravelli D, Dondi D, Fagnoni M, Albini A, Bagno A (2011) Predicting the UV spectrum of polyoxometalates by TD-DFT. J Comput Chem 32:2983-2987
Refson K, Tulip PR, Clark SJ (2006) Variational density-functional perturbation theory for dielectrics and lattice dynamics. Phys Rev B 73:155114
Rehr JJ, Albers RC (2000) Theoretical approaches to X-ray absorption fine structure. Rev Mod Phys 72:621-654
Ribeiro MCC, Wilson M, Madden PA (1999) Raman scattering in the network liquid $ZnCl_2$ relationship to the vibrational density of states. J Chem Phys 110:4803-4811
Robinson M, Haynes P (2010) Dynamical effects in ab initio NMR calculations: Classical force fields fitted to quantum forces. J Chem Phys 133:084109
Rocca D, Lu D, Galli G (2010) Ab initio calculations of optical absorption spectra: Solution of the Bethe-Salpeter equation within density matrix perturbation theory. J Chem Phys 133:164109
Rohl AL, Wright K, Gale JD (2003) Evidence from surface phonons for the (2x1) reconstruction of the (10-14) surface of calcite from computer simulation. Am Mineral 88:921-925
Rossano S, Brouder C, Alouani M, Arrio MA (2000) Calculated optical absorption spectra of Ni^{2+}-bearing compounds. Phys Chem Miner 27:170-178
Rossano S, Mauri F, Pickard CJ, Farnan I (2005) First-principles calculation of ^{17}O and ^{25}Mg NMR shieldings in MgO at finite temperature: Rovibrational effect in solids. J Phys Chem B 109:7245-7250
Runge E, Gross EKU (1984) Density-functional theory for time-dependent systems. Phys Rev Lett 52:997-1000
Sadoc A, Body M, Legein C, Biswal M, Fayon F, Rocquefelte X, Boucher F (2011) NMR parameters in alkali, alkaline earth and rare Earth fluorides from first principle calculations. Phys Chem Chem Phys 13:18539-18550
Sahle CJ, Sternemann C, Schmidt C, Lehtola S, Jahn S, Simonelli L, Huotari S, Hakala M, Pylkkänen T, Nyrow A, Mende K, Tolan M, Hämäläinen K, Wilke M (2013) Microscopic structure of water at elevated pressures and temperatures. PNAS 110:6301-6306
Salanne M, Rotenberg B, Jahn S, Vuilleumier R, Madden PA (2012) Including many-body effects in models for ionic liquids. Theor Chem Acc 131:1143
Salpeter EE, Bethe HA (1951) A relativistic equation for bound-state problems. Phys Rev 84:1232-1242
San Juan-Farfan RE, Bayarjargal L, Winkler B, Haussühl E, Avalos-Borja M, Refson K, Milman V (2011) Pressure dependence of the lattice dynamics of diaspore, α-AlO(OH), from Raman spectroscopy and density functional perturbation theory. Phys Chem Miner 38:693-700
Sangster MJL, Peckham G, Saunderson DH (1970) Lattice dynamics of magnesium oxide. J Phys C 3:1026-1036
Sarnthein J, Pasquarello A, Car R (1997) Origin of the high-frequency doublet in the vibrational spectrum of vitreous SiO_2. Science 275:1925-1927
Schober H, Strauch D, Dorner B (1993a) Lattice dynamics of sapphire (Al_2O_3). Z Phys B 92:273-283
Schober H, Strauch D, Nutzel K, Dorner B (1993b) Lattice dynamics of alpha-quartz. II. theory. J Phys: Condens Matter 5:6155-6164
Schwarz K, Blaha P, Madsen GKH (2002) Electronic structure calculations of solids using the Wien2k package for material sciences. Comput Phys Comm 147:71-76
Sebastiani D, Parrinello M (2001) A new ab-initio approach for NMR chemical shifts in periodic systems. J Phys Chem A 105:1951-1958
Shamov GA, Schreckenbach G, Vo TN (2007) A comparative relativistic DFT and ab initio study on the structure and thermodynamics of the oxofluorides of uranium(IV), (V) and (VI). Chem Eur J 13:4932-4947
Sharma S, Dewhurst JK, Sanna A, Gross EKU (2011) Bootstrap approximation for the exchange-correlation kernel of time-dependent density-functional theory. Phys Rev Lett 107:186401
Shimobayashi N, Miyake A, Kitamura M, Miura E (2001) Molecular dynamics simulations of the phase transition between low-temperature and high-temperature clinoenstatites. Phys Chem Miner 28:591-599
Sinn H, Glorieux B, Hennet L, Alatas A, Hu M, Alp EE, Bermejo FJ, Price DL, Saboungi ML (2003) Microscopic dynamics of liquid aluminium oxide. Science 299:2047-2049
Skylaris CK, Haynes PD, Mostofi AA, Payne MC (2005) Introducing ONETEP: Linear-scaling density functional simulations on parallel computers. J Chem Phys 122:084119
Sottile F, Marsili M, Olevano V, Reining L (2007) Efficient ab initio calculations of bound and continuum excitons in the absorption spectra of semiconductors and insulators. Phys Rev B 76:161103
Spiekermann G, Steele-MacInnis M, Kowalski PM, Schmidt C, Jahn S (2012a) Vibrational mode frequencies of H_4SiO_4, D_4SiO_4, $H_6Si_2O_7$ and $H_6Si_3O_9$ in aqueous environment, obtained from ab initio molecular dynamics. J Chem Phys 137:164506
Spiekermann G, Steele-MacInnis M, Schmidt C, Jahn S (2012b) Vibrational mode frequencies of silica species in SiO_2-H_2O liquids and glasses from ab initio molecular dynamics. J Chem Phys 136:154501
Spiekermann G, Steele-MacInnis M, Kowalski PM, Schmidt C, Jahn S (2013) Vibrational properties of silica species in MgO-SiO_2 glasses using ab initio molecular dynamics. Chem Geol 346:22-33

EBSCOhost - printed on 2/13/2023 5:26 AM via . All use subject to https://www.ebsco.com/terms-of-use

Stavitski E, de Groot FMF (2010) The CTM4XAS program for EELS and XAS spectral shape analysis of transition metal l edges. Micron 41:687-694

Stephens PJ, Devlin FJ, Chabalowski CF, Frisch MJ (1994) Ab initio calculation of vibrational absorption and circular dichroism spectra using density functional force fields. J Phys Chem 98:11623-11627

Stone AJ (1996) The Theory of Intermolecular Forces. Oxford University Press, Oxford

Suenaga K, Koshino M (2010) Atom-by-atom spectroscopy at graphene edge. Nature 468:1088-1090

Sugano S, Tanabe Y, Kamimura H (1970) Multiplets of transition-metal ions in crystals. Academic Press, New York.

Sun T, Allen PB, Stahnke DG, Jacobsen SD, Homes CC (2008) Infrared properties of ferropericlase $Mg_{1-x}Fe_xO$: Experiment and theory. Phys Rev B 77:134303

Svane A (1987) Hartree-fock band-structure calculations with the linear muffin-tin-orbital method: Application to C, Si, Ge, and α-Sn. Phys Rev B 35:5496-5502

Tailby ND, Walker AM, Berry AJ, Hermann J, Evans KA, Mavrogenes JA, O'Neill HSC, Rodina IS, Soldatov AV, Rubatto D, Sutton SR (2011) Ti site occupancy in zircon. Geochim Cosmochim Acta 75:905-921

Taillefumier M, Cabaret D, Flank AM, Mauri F (2002) X-ray absorption near-edge structure calculations with the pseudopotentials: Application to the K edge in diamond and α-quartz. Phys Rev B 66:195107

Takahashi M, Igarashi JI, Hamada N (2008) Ab initio calculation of the 3s and 1s core-level X-ray photoemission spectra of iron. Phys Rev B 78:155108

Tanaka I, Mizoguchi T, Yoshiya M, Ogasawara K, Adachi H, Mo SD, Ching WY (2002) First principles calculation of ELNES by LCAO methods. J Electron Microsc 51:S107-S112

Tangney P, Scandolo S (2002) An ab initio parametrized interatomic force field for silica. J Chem Phys 117:8898-8904

Tazi S, Molina JJ, Rotenberg B, Turq P, Vuilleumier R, Salanne M (2012) A transferable ab initio based force field for aqueous ions. J Chem Phys 136:114507

Thomas LH (1927) The calculation of atomic fields. Proc Cambridge Phil Soc 23:542-548

Tkatchenko A, DiStasio Jr RA, Car R, Scheffler M (2012) Accurate and efficient method for many-body van der Waals interactions. Phys Rev Lett 108:236402

Tossell JD (2001) Calculating the NMR properties of minerals, glasses, and aqueous species. Rev Mineral Geochem 42:437-458

Tossell JA (2004) Calculation of ^{17}O NMR shieldings in molecular models for crystalline MO, M=Mg, Ca, Sr, and in models for alkaline earth silicates. Phys Chem Miner 31:41-44

Tossell JA (2005a) Boric acid, 'carbonic' acid, and n-containing oxyacids in aqueous solution: Ab initio studies of structure, pK_a, NMR shifts, and isotopic fractionations. Geochmim Cosmochim Acta 69:5647-5658

Tossell JA (2005b) Theoretical study on the dimerization of $Si(OH)_4$ in aqueous solution and its dependence on temperature and dielectric constant. Geochim Cosmochim Acta 69:283-291

Tossell JA, Horbach J (2005) O triclusters revisited: classical md and quantum cluster results for glasses of composition $(Al_2O_3)2(SiO_2)$. J Phys Chem B 109:1794-1797

Tossell JA, Zimmermann MD (2008) Calculation of the structures, stabilities, and vibrational spectra of arsenites, thioarsenites and thioarsenates in aqueous solution. Geochim Cosmochim Acta 72:5232-5242

Trcera N, Cabaret D, Rossano S, Farges F, Flank AM, Lagarde P (2009) Experimental and theoretical study of the structural environment of magnesium in minerals and silicate glasses using X-ray absorption near-edge structure. Phys Chem Miner 36:241-257

Trcera N, Rossano S, Madjer K, Cabaret D (2011) Contribution of molecular dynamics simulations and ab initio calculations to the interpretation of Mg K-edge experimental XANES in K_2O-MgO-3SiO_2 glass. J Phys: Condens Matter 23:255401

Tsuchiya J, Tsuchiya T, Wentzcovitch RM (2008) Vibrational properties of α-AlOOH under pressure. Am Mineral 93:477-482

Umari P, Pasquarello A (2002) Ab initio molecular dynamics in a finite homogeneous electric field. Phys Rev Lett 89:157602

Umari P, Pasquarello A (2005) Fraction of boroxol rings in vitreous boron oxide from first-principles analysis of Raman and NMR spectra. Phys Rev Lett 95:137401

Umari P, Pasquarello A, Dal Corso A (2001) Raman scattering intensities in α-quartz: A first-principles investigation. Phys Rev B 63:094305

van Beest BWH, Kramer GJ, van Santen RA (1990) Force fields of silicas and aluminophosphates based on ab initio calculations. Phys Rev Lett 64:1955-1958

van Hove L (1954) Correlations in space and time and Born approximation scattering in systems of interacting particles. Phys Rev 95:249-258

Vanderbilt D (1990) Soft self-consistent pseudopotentials in a generalized eigenvalue formalism. Phys Rev B 41:7892-7895

Vast N, Reining L, Olevano V, Schattschneider P, Jouffrey B (2002) Local field effects in the electron energy loss spectra of rutile TiO_2. Phys Rev Lett 88:037601

EBSCOhost - printed on 2/13/2023 5:26 AM via . All use subject to https://www.ebsco.com/terms-of-use

Veithen M, Gonze X, Ghosez P (2005) Nonlinear optical susceptibilities, Raman efficiencies, and electro-optic tensors from first-principles density functional perturbation theory. Phys Rev B 71:125107

Vinson J, Rehr JJ (2012) Ab initio Bethe-Salpeter calculations of the X-ray absorption spectra of transition metals at the l-shell edges. Phys Rev B 86:195135

von Oertzen GU, Jones RT, Gerson AR (2005) Electronic and optical properties of Fe, Zn and Pb sulfides. Phys Chem Miner 32:255-268

Watanabe S, Sasaki T, Taniguchi R, Ishii T, Ogasawara K (2009) First-principles calculation of ground and excited-state absorption spectra of ruby and alexandrite considering lattice conduction. Phys Rev B 79:075109

Watenphul A, Wunder B (2010) Temperature dependence of the OH-stretching frequencies in topaz-OH. Phys Chem Miner 37:65-72

Welch MD, Wunder B (2012) A single-crystal X-ray diffraction study of the 3.65 Å-phase $MgSi(OH)_6$, a high-pressure hydroxide perovskite. Phys Chem Miner 39:693-697

Wen XD, Martin RL, Henderson TM, Scuseria GE (2013) Density functional theory studies of the electronic structure of solid state actinide oxides. Chem Rev 113:1063-1096

Wentzcovitch R, Stixrude L (eds) (2010) Theoretical and Computational Methods in Mineral Physics: Geophysical Applications. Reviews in Mineralogy and Geochemistry, Volume 71. Mineralogical Society of America

Wentzcovitch R, Yu YG, Wu Z (2010) Thermodynamic properties and phase relations in mantle minerals investigated by first principles quasiharmonic theory. Rev Mineral Geochem 71:59-98

Wilke M, Schmidt C, Dubrail J, Appel K, Borchert M, Kvashnina K, Manning CE (2012) Zircon solubility and zirconium complexation in $H_2O + Na_2O + SiO_2 \pm Al_2O_3$ fluids at high pressure and temperature. Earth Planet Sci Lett 349-350:15-25

Wilson M, Madden PA, Hemmati M, Angell CA (1996) Polarization effects, network dynamics, and the infrared spectrum of amorphous SiO_2. Phys Rev Lett 77:4023-4026

Wilson M, Jahn S, Madden PA (2004) The construction and application of a fully flexible computer simulation model for lithium oxide. J Phys: Condens Matter 16:S2795-S2810

Wunder B, Wirth R, Koch-Müller M (2011) The 3.65 Å phase in the system $MgO\text{-}SiO_2\text{-}H_2O$: Synthesis, composition, and structure. Am Mineral 96:1207-1214

Wunder B, Jahn S, Koch-Müller M, Speziale S (2012) The 3.65 Å phase, $MgSi(OH)_6$: Structural insights from DFT-calculations and T-dependent IR spectroscopy. Am Mineral 97:1043-1048

Xiao H, Tahir-Kheli J, Goddard WA (2011) Accurate band gaps for semiconductors from density functional theory. J Phys Chem Lett 2:212-217

Yates JR, Pickard CJ, Mauri F (2007) Calculation of NMR chemical shifts for extended systems using ultrasoft pseudopotentials. Phys Rev B 76:024401

Zahn D (2013) Nucleation mechanism and kinetics of the perovskite to post-perovskite transition of $MgSiO_3$ under extreme conditions. Chem Phys Lett 573:5-7

Zakaznova-Herzog VP, Nesbitt HW, Bancroft GM, Tse JS, Gao X, Skinner W (2005) High-resolution valence-band XPS spectra of the nonconductors quartz and olivine. Phys Rev B 72:205113

Zakaznova-Herzog VP, Nesbitt HW, Bancroft GM, Tse JS (2006) High resolution core and valence band XPS spectra of non-conductor pyroxenes. Surf Sci 600:3175-3186

Zakaznova-Herzog VP, Nesbitt HW, Bancroft GM, Tse JS (2008) Characterization of leached layers on olivine and pyroxenes using high-resolution XPS and density functional calculations. Geochim Cosmochim Acta 72:69-86

Zhang Y, Lin W, Li Y, Ding K, Li J (2005a) A theoretical study on the electronic structures of TiO_2: Effect of Hartree-Fock exchange. J Phys Chem B 109:19270-19277

Zhang Y, Zhao D, Matsui M (2005b) Anisotropy of akimotoite: A molecular dynamics study. Phys Earth Planet Int 151:309-319

Zhou B, Sherriff BL, Wang T (2009) ^{27}Al NMR spectroscopy at multiple magnetic fields and ab initio quantum modeling for kaolinite. Am Mineral 94:865-871

Zotov N, Keppler H (2000) In-situ Raman spectra of dissolved silica species in aqueous fluids to 900 °C and 14 kbar. Am Mineral 85:600-604

Zotov N, Ebbsjö I, Timpel D, Keppler H (1999) Calculation of Raman spectra and vibrational properties of silicate glasses: Comparison between $Na_2Si_4O_9$ and SiO_2 glass. Phys Rev B 60:6383-6397

Zwanziger JW (2009) Computation of Mössbauer isomer shifts from first principles. J Phys: Condens Matter 21:195501

Zwijnenburg MA, Sousa C, Sokol AA, Bromley ST (2008) Optical excitations of defects in realistic nanoscale silica clusters: Comparing the performance of density functional theory using hybrid functionals with correlated wavefunction methods. J Chem Phys 129:014706

EBSCOhost - printed on 2/13/2023 5:26 AM via . All use subject to https://www.ebsco.com/terms-of-use

EBSCOhost - printed on 2/13/2023 5:26 AM via . All use subject to https://www.ebsco.com/terms-of-use

Reviews in Mineralogy & Geochemistry
Vol. 78 pp. 745-777, 2014
Copyright © Mineralogical Society of America

High-pressure Apparatus Integrated with Synchrotron Radiation

Guoyin Shen
HPCAT, Geophysical Laboratory
Carnegie Institution of Washington
Argonne, Illinois 60439, U.S.A.
gshen@ciw.edu

Yanbin Wang
Center of Advanced Radiation Sources
University of Chicago
Chicago, Illinois 60637, U.S.A.
wang@cars.uchicago.edu

INTRODUCTION

Synchrotron sources provide X-radiation with high energy and high brilliance that are well suited for high-pressure (HP) research. Powerful micron-sized sampling probes of high energy radiation have been widely used to interact with minute samples through the walls of pressure vessels, to investigate material properties *in situ* under HP. Since the late 1970s, HP synchrotron research has become a fast growing field. Of mineralogical interests are the abilities for studying structure, elasticity, phase stability/transition, and transport properties of minerals and melts at pressure-temperature conditions corresponding to the deep Earth.

The most commonly used HP apparatus are the diamond anvil cell (DAC), the large volume press (LVP), and the shock wave devices. The DAC is capable of generating pressures beyond 4 megabar (1 megabar = 100 GPa) but is limited to small samples, typically less than 10 microns in linear dimensions at the highest pressures. The pressure-temperature (*P-T*) range accessible in the DAC exceeds conditions corresponding the center of the Earth. The LVP is capable of modest pressures (currently less than 100 GPa), but the large sample volume permits a wider variety of bulk physical properties to be measured. The *P-T* range accessible in the LVP corresponds to those in the Earth's lower mantle. In shock wave experiments, the sample is subjected to high pressures and temperatures by dynamic processes. Multi-megabar to terapascal (TPa) pressures may be generated but for short durations from nano- to femto-seconds (10^{-9}-10^{-15} s).

In this chapter, we begin with synchrotron techniques that are important for HP research, followed by a review of high pressure apparatus and their integration with synchrotron X-ray techniques. We refer readers to the following review articles related to HP synchrotron techniques (Chen et al. 2005; Duffy 2005; Hemley et al. 2005; Wang et al. 2002b).

1529-6466/14/0078-0018$05.00 http://dx.doi.org/10.2138/rmg.2014.78.18

EBSCOhost - printed on 2/13/2023 5:26 AM via . All use subject to https://www.ebsco.com/terms-of-use

SYNCHROTRON TECHNIQUES APPLICABLE TO HIGH-PRESSURE RESEARCH

Synchrotron radiation

Synchrotron radiation is produced by free relativistic electrons moving along curved trajectories in a magnetic field. Research using synchrotron radiation began at storage rings designed and operated for high energy physics. At these so-called first generation synchrotron sources, the use of synchrotron radiation was of secondary importance and X-ray stations were operated parasitically. Starting in the mid-1970s, second-generation synchrotron facilities were designed and built to serve as dedicated X-radiation sources (e.g., Hartman 1982). In the late-1980s, insertion device based sources (the third generation) were built and began their operation in the early 1990s (Mills 2002). Great efforts have been made to take advantages of the unique characteristics of synchrotron radiation for HP research, including: 1) high intensity in a broad energy spectral range, 2) high brilliance (small angular divergence), 3) tunable energy with the use of monochromators, 4) pulsed time structure, 5) coherence, and 6) high polarization of the radiation. A number of HP beam-lines have been or are being built in synchrotron facilities in the US [the Advanced Light Source (ALS), Stanford Synchrotron Radiation Lightsource (SSRL), National Synchrotron Light Source (NSLS), Cornell High Energy Synchrotron Source (CHESS), the Advanced Photon Source (APS)], in Europe [European Synchrotron Research Facility (ESRF), Soleil, Diamond, Petra-III, MAX-IV], and in the Asia-Pacific [Photon Factory, Spring-8, Beijing Synchrotron Research Facility (BSRF), Shanghai Synchrotron Research Facility (SSRF), Taiwan Photon Source (TPS), Puhong Light Source (PLS), and the Australia Synchrotron (AS)]. The webpage (http://www.lightsources.org) has a comprehensive list of synchrotron sites in the world with relevant links for more information.

Synchrotron radiation provides the necessary penetration power to go through the walls of pressure vessels. Figure 1 shows transmission of commonly-used wall materials as a function of X-ray energy. The high brilliance of synchrotron radiation has made it possible for the developments of various HP synchrotron techniques. Continuously tunable wavelength opens up new capabilities, in particular in HP X-ray spectroscopy and HP inelastic X-ray scattering (Mao et al. 1997; Fiquet et al. 2001; Rueff 2010). The pulsed timing structure, together with the high brilliance, allows the study of time dependent phenomena such as phase transition

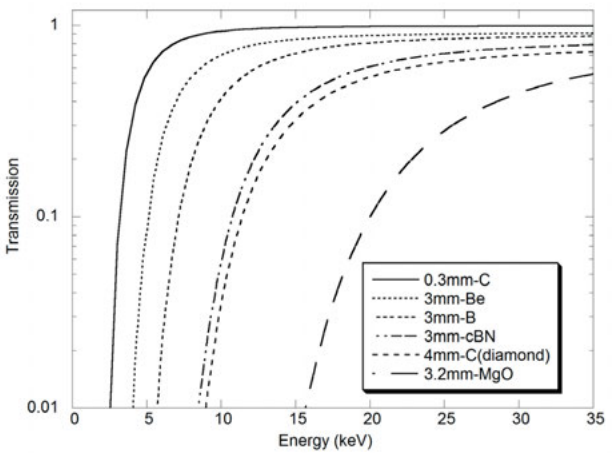


Figure 1. X-ray transmission curves of commonly used materials in high pressure devices. Curves from left to right correspond to materials in the legend from top to bottom.

EBSCOhost - printed on 2/13/2023 5:26 AM via . All use subject to https://www.ebsco.com/terms-of-use

kinetics, chemical reaction processes, transport processes, and meta-stable phases at high pressures and high/low temperatures (Jensen et al. 2012; Luo et al. 2012). The polarization of synchrotron radiation has been extensively utilized for investigations of magnetic systems at high pressure (Haskel et al. 2011; Souza-Neto et al. 2012). While coherence has been used for mapping structure and strain in nanometer-scale grains (Pfeifer et al. 2006), HP applications are still in its infancy (Le Bolloch et al. 2009; Yang et al. 2013). It should be noted that recently constructed synchrotron facilities have achieved a high degree of orbit stability, providing highly stable X-ray beams in terms of intensity and position, critical for HP experiments.

Worldwide there are growing activities in the development of free-electron lasers (FELs) (Galayda et al. 2010), such as the Linac Coherent Light Source (LCLS) in the US, the SPring-8 Compact SACE Source (SCSS) in Japan, and the European X-ray Free-Electron Laser (XFEL). These so-called fourth generation sources offer spatially highly coherent, ultra-short (~100 fs) pulses with peak brilliance of ~10^{28}-10^{33} photons/s/mm^2/mrad^2/0.1%BW. Figure 2 shows the FEL brilliance compared with those of earlier synchrotrons. In the storage rings of synchrotron radiation facilities, the radiated intensity is linearly proportional to the number of electrons in the beam, because of the lack of multi-particle coherence. In FELs, however, the electron beam is bunched together on the scale of the radiation wavelength, resulting in a high degree of multi-particle coherence, significantly enhancing the emission brilliance. The spatially coherent high intensity, short pulsed X-ray beams open up many new areas, including time-resolved studies of dynamics on sub-ps time scales, structural studies by imaging of nano-periodic systems, and probing warm dense matter—a state too dense to be described by weakly coupled plasma physics and too hot to be described by condensed matter physics. Warm dense matter is expected in the cores of some large planets. Important to HP research, significant effort has been made to produce harder X-rays with energies at 16 keV or higher in the FEL facilities. For example, an experimental station at LCLS for Matters in Extreme

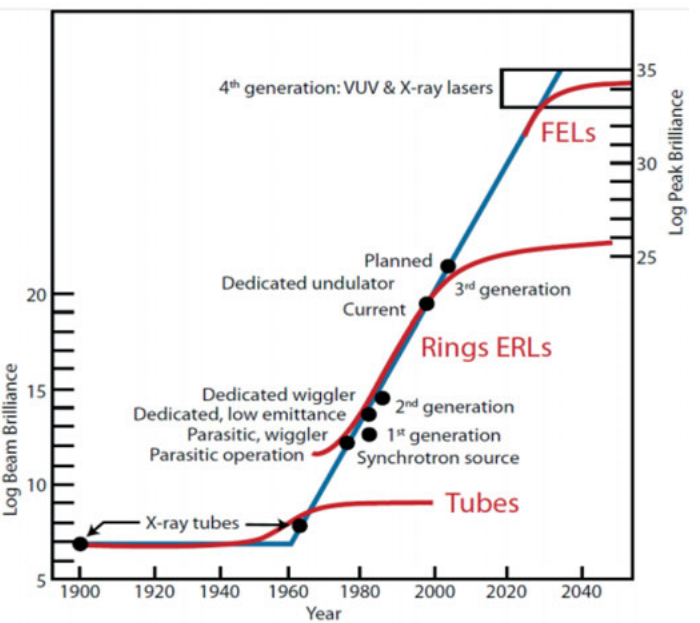


Figure 2. X-ray brilliance with orders of magnitude increase with time. Tubes represent X-tubes generally used in laboratory, "Rings": storage rings of synchrotron facilities, "ERLs": energy recovery LINACS, FELs: free electron lasers (Courtesy of M. Rivers).

EBSCOhost - printed on 2/13/2023 5:26 AM via . All use subject to https://www.ebsco.com/terms-of-use

Condition has recently become operational since 2012 for warm condensed physics, high pressure studies, shock physics, and high energy dense physics.

High-pressure synchrotron techniques

High-pressure research has become an important application area for synchrotron sources. Many previous technical limitations in capability, precision, and accuracy have been removed through optimization of source radiation, optics, sample environment, experimental configuration, motion control, automation software, and detectors and analyzers. Among the wide array of HP X-ray techniques, structure determination using X-ray diffraction (XRD) remains the dominant one, while significant progress has been made in integrating other X-ray techniques for HP research, such as X-ray radiography and tomography (Shen et al. 2002; Wang et al. 2005a; Wang et al. 2012), X-ray spectroscopy (absorption, emission) (Mao et al. 1997; Mayanovic et al. 2007b), inelastic X-ray scattering (IXS) (Rueff 2010), and nuclear resonant scattering (Cainrs et al. 1976; Lübbers et al. 2000; Sturhahn 2004). New HP synchrotron techniques are emerging rapidly, for example in HP nano-imaging techniques (full field, scanning, and coherent diffraction) (Le Bolloch et al. 2009; Wang et al. 2012) and time resolved HP X-ray techniques (Goncharov 2010; Yoo et al. 2011; Luo et al. 2012). A few firsts of HP experiments integrated with synchrotron techniques are listed in Table 1.

Table 1. Firsts of high-pressure experiments integrated with synchrotron techniques.

Technique	Abbr.	Reference
HP X-ray diffraction	XRD	(Buras et al. 1976)
HP X-ray absorption spectroscopy	XAS	(Ingalls et al. 1978)
HP X-ray emission spectroscopy	XES	(Rueff et al. 1999)
HP inelastic X-ray scattering (eV)	IXS	(Schell et al. 1995)
HP inelastic X-ray scattering (meV)	IXS	(Fiquet et al. 2001)
HP nuclear resonant inelastic X-ray scattering	NRIXS	(Lübbers et al. 2000)
HP nuclear forward X-ray scattering	NFXS	(Nasu 1996)
HP X-ray fluorescence spectroscopy	XFS	(Schmidt and Rickers 2003)
HP X-ray computed micro-tomography	CMT	(Wang et al. 2005a)

HP X-ray diffraction. X-ray diffraction (XRD) has long been the dominant application of synchrotron radiation for HP research. Samples in various forms (single crystal, polycrystalline, nano-crystals, amorphous/liquid) have been studied in HP XRD for structure and/or radial distribution functions, phase transitions (including melting), *P-V-T* equations of state, elasticity, and lattice strain.

Angular dispersive XRD (ADXRD) using monochromatic radiation and two dimensional (2D) detectors has been the primary technique in DAC experiments. Resolution in ADXRD is typically at $\Delta d/d \sim 3\times10^{-3}$ (e.g., Shen et al. 2008). The resolution in d-spacing can be improved by reducing incident beam divergence, lowering X-ray energy, and improving angular resolution in detecting systems by, for example, increasing sample-detector distance, reducing slit size or effective pixel size, or using an analyzer. High resolution is achieved at the cost of throughput; proper approaches need to be planned in advance. Intensity information in ADXRD is often used for structure refinement via Rietveld method (Rietveld 1966). However, background subtraction for removing intensity contributions from the surrounding materials (anvils, gaskets) is not trivial and precautions need to be taken when using Rietveld

EBSCOhost - printed on 2/13/2023 5:26 AM via . All use subject to https://www.ebsco.com/terms-of-use

refinement and interpreting the results from those analyses. Recently, there has been a growing effort in measuring pair distribution functions (PDF) of amorphous/liquid materials at HP where background subtraction has been critically tested (Eggert et al. 2002; Shen et al. 2003; Chapman et al. 2010; Soignard et al. 2010). The developed methods for background subtraction can be also applied to Rietveld refinement on crystalline samples. In HP ADXRD, typical X-ray energy is around 15-45 keV in DAC experiments, based on factors such as the coverage in reciprocal space, accessing angular range of the high pressure device, penetrating power, and detector efficiency. Nevertheless, a wide range from 10 keV to over 100 keV has been used for various applications. The energy tunability of synchrotron sources should allow for HP anomalous diffraction studies for solving the phase problem, partial structure factor, and element specific crystallography. To our knowledge, however, there is no report of HP anomalous XRD yet.

The primary technique in LVP experiments has been energy-dispersive XRD (EDXRD). This is mainly due to two factors: 1) in most multi-anvil devices X-ray access is limited because of the opaque anvil materials used and 2) the sample is often contained by solid pressure media which may generate overpowering scattering background if the incident beam and scattering signals are not properly collimated. EDXRD is ideal for phase identification and equation of state studies in the LVP. Data collection is fast (from seconds to minutes), and clean diffraction signals can be obtained, despite pressure media surrounding the sample. Metal capsules are often used to control the sample environment (oxygen fugacity, water content, etc). However, EDXRD provides limited sampling of crystallites in the sample because of the fixed 2θ angle, and is not suitable for probing samples near melting or with rapid crystal growth, in which case ADXRD with an area detector is desired and light scattering materials are used as "windows" (e.g., Kubo et al. 2008).

Another limitation is that EDXRD does not provide reliable intensity measurements, making it difficult to obtain crystal structure information such as bonding characteristics and atomic positions. Various efforts have been made to extract quantitative crystallographic information from EDXRD data, with limited success (e.g., Ballirano and Caminiti 2001; Skelton et al. 1982; Yamanaka and Ogata 1991). Wang et al. (2004) developed a technique which employs both ADXRD and EDXRD concepts. By scanning an energy-calibrated multichannel solid state detector (SSD), a large number of EDXRD patterns are obtained at pre-determined angular step-size. The entire dataset can be re-arranged as ADXRD patterns by plotting intensities of each channel (corresponding to a given photon energy or wavelength). Subsets of the data covering narrow energy bands may be binned to give ADXRD patterns at a single wavelength with improved counting statistics; these may be combined in a multi-pattern Rietveld analysis to efficiently utilize the entire data set: while high photon-energy data provide coverage at the low *d*-spacing range, low photon-energy data cover the high d-spacing range. An example is shown in Figure 3, for the identification on non-cubic structure of $CaSiO_3$ perovskite (Uchida et al. 2009).

When a sample is subjected to a boundary condition with a differential stress component, diffraction in a radial geometry may be applied with the loading axis perpendicular to the primary X-ray direction, a DAC diffraction technique called radial X-ray diffraction (R-XRD). In specially designed multianvil devices such as the deformation DIA (Wang et al. 2000, 2003) or rotational Drickamer apparatus (Yamazaki and Karato 2001), R-XRD is used to measure stresses in a sample under controlled differential stress field during deformation. Strains can be easily measured using radiography, hence permitting measurements of stress-strain curves of bulk samples at high *P* and *T* (e.g., Hilairet et al. 2007; Nishiyama et al. 2007). HP R-XRD provides useful information on sample stress, strain, deformation, and slip mechanism (Wenk et al. 2000, 2005; Merkel et al. 2006; Hilairet et al. 2012), by measuring diffraction as a function of the angle between the loading axis and the vector of diffraction plane. The

EBSCOhost - printed on 2/13/2023 5:26 AM via . All use subject to https://www.ebsco.com/terms-of-use

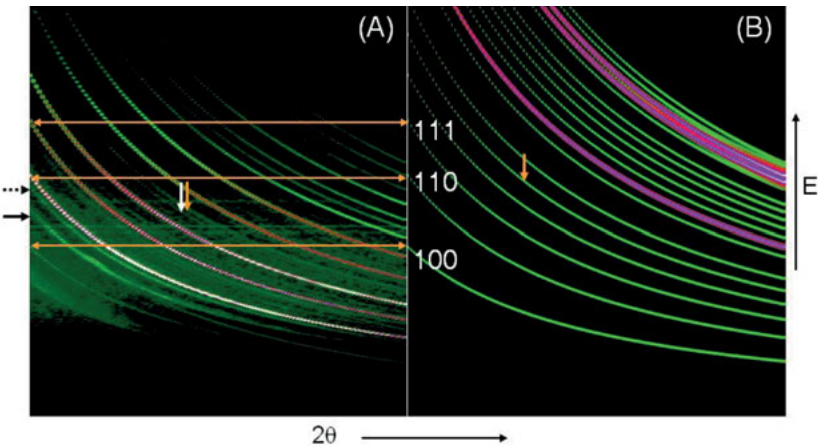


Figure 3. An example of multi-angle EDXD diffraction for $CaSiO_3$ perovskite. Horizontal axes are two-theta angle from 3° to 13°, at s step size of 0.05°, vertical axes are X-ray energy from ~0 to 150 keV. (A) Experimental data collected at 13 GPa and 1200 K. Intensities are plotted in logarithmic scale. (B) Simulated $CaSiO_3$ perovskite pattern assuming cubic (P*m3m*) symmetry. Experimental data in (A) show clear superlattice reflections (indicated by horizontal arrows), indicating non-cubic symmetry. The vertical arrows in (A) and (B) indicate the cubic (200) diffraction line. Figure modified after Uchida et al. (2009).

dependence of *d*-spacings as a function of the angle provides information on strains under deviatoric stress conditions. The relative intensity at different angles reveals the preferred orientation of a polycrystalline sample. The inverse pole figure from such data can be used to determine sample deformation and slip mechanism (e.g., Miyagi et al. 2010).

Compared to the most frequently used HP powder XRD techniques at synchrotron HP beamlines, HP single crystal XRD is relatively under-utilized, but it is a fast developing field (Lavina et al. 2014, this volume). In single crystal XRD, orientations and intensities of diffracted beams are measured. The high flux and small beam at synchrotron HP beamlines allow for studies with 1-10 micron crystal size efficiently. Detailed crystallographic information, such as structure model (atomic position, occupancies, thermal displacement parameters) and electron density distribution can be obtained (Fig. 4). With single crystal data, space groups and Miller indices can be unambiguously determined. Because the diffraction is measured at different orientations, the single crystal XRD technique has also advantages in dealing with materials of low crystallographic symmetries. HP single crystal XRD was first applied to the EDXRD method (Mao et al. 1988; Loubeyre et al. 1996). Recently, synchrotron monochromatic beam has been widely used in HP single crystal XRD by rotating samples coupled with either a point detector (Friedrich et al. 2007) or an area detector (Lavina et al. 2010; Zhang et al. 2013). Many HP beamlines in the world have established routine procedures for conducting HP single crystal XRD experiments.

When there are constraints in rotating the sample, HP single crystal XRD experiments may be conducted by scanning monochromatic energies with an area detector (Ice et al. 2005). The use of polychromatic beam (the Laue approach) is a useful alternative. The HP Laue approach does not require rotating of the sample and could provide information on deformation, mosaicity, and strains (Ice and Pang 2009) through fast measurements (less than a second).

HP XRD has been widely used to determine structure factors of amorphous/liquid materials at HP (Tsuji et al. 1989; Shen et al. 2003; Wilding et al. 2006). Interesting phenomena have been observed, including coordination number change, polyamorphysm (Katayama

EBSCOhost - printed on 2/13/2023 5:26 AM via . All use subject to https://www.ebsco.com/terms-of-use

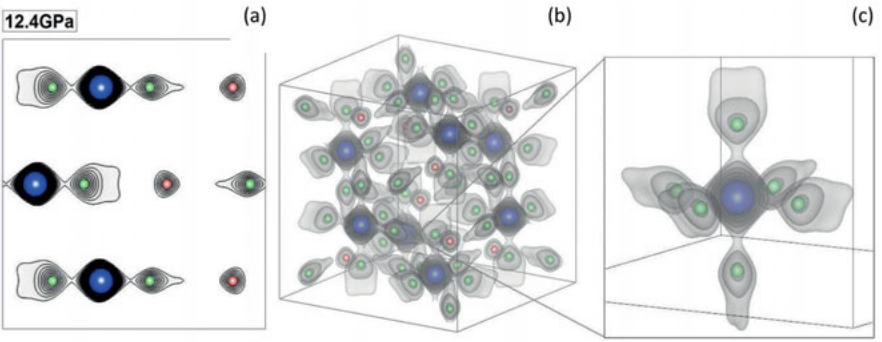


Figure 4. Electron density distributions in silicon at high pressures. (a) and (b) are the electron density data at 12.4 GPa where the two active groups are clearly observed; (a) a slide image along the [110] plane. The host lattice of the α-phase is represented by the symbols in blue. The void group is shown in red, while the vicinity group in green. The local distribution of the vicinity group has the point-group symmetry of S_4 as shown in (c). Modified from Shen et al. (2012).

et al. 2000; Deb et al. 2001), and long-range topological order (Zeng et al. 2011). In DAC experiments, the ADXRD method is often utilized with high energy monochromatic beam in order to have a large Q coverage (Chapman et al. 2010; Mei et al. 2010; Soignard et al. 2010). The EDXRD method with polychromatic radiation is often used in LVP experiments. EDXRD data are collected at multiple 2θ angles, to increase coverage in the reciprocal space for accurate determination of the radial distribution function (e.g., Tsuji et al. 1989). The synchrotron incident beam spectrum is simulated using a Monte Carlo approach and Compton scattering effects are typically dealt with based on theoretical predictions (Funakoshi 1995). The advantage of this method is the excellent collimation, through which background scattering from surrounding materials can be almost completely eliminated (Yamada et al. 2011; Sakamaki et al. 2012). This is a particularly useful technique for liquids with low scattering power (e.g., oxides and silicates). With the use of a Soller slit system, diffraction from surrounding materials can be effectively minimized and ADXRD has been successfully applied for studying liquid structures at HP and HT with LVPs such as the Paris-Edinburgh (PE) presses (Mezouar et al. 2002).

HP X-ray spectroscopy. The last decade saw rapid development for HP X-ray spectroscopy (XRS). Many new HP XRS capabilities have been enabled and established at several HP beamlines around the globe. With emerging new synchrotron sources and upgrades of many existing third generation sources, together with developments and optimization efforts of HP devices designed for HP XRS, we are entering a harvesting period for HP research using XRS.

X-ray absorption spectroscopy (XAS) is a classic technique that measures energy dependence of X-ray absorption coefficient for a core-level electron of an element of interest. Near edge X-ray absorption spectroscopy (XANES) provides information on valence state, orbital-occupancy, hybridization, charge transfer, and electronic ordering. Extended X-ray absorption fine structure (EXAFS) provides element specific local structural information. XAS is one of the first XRS technique applied for HP research (Ingalls et al. 1978). However, earlier applications of HP XAS were limited to a small energy range due to anvil absorption and Laue diffraction from single crystal anvils. Recently, perforated and partially-perforated diamond anvils have been used to successfully reduce the amount of diamond scattering in the beam path. High quality HP XANES (Zeng et al. 2010) and HP XAFS (Mayanovic et al. 2007a) data have been collected for transition metals in DAC experiments with energies between 5 and15 keV. In studying absorption edges over 30 keV, XAS data from a DAC are

EBSCOhost - printed on 2/13/2023 5:26 AM via . All use subject to https://www.ebsco.com/terms-of-use

contaminated by diffraction from single-crystal diamond anvils. Using nano-diamond as anvil material, the contamination from single crystal diffraction can be avoided (Ishimatsu et al. 2012). Morard et al. (2007a) reported results on the Ba K-edges (>37 keV) in silicon clathrate (Ba_8Si_{46}), tracking the evolution of local structure around Ba with pressure. These authors also examined iodine K-edges in iodine-intercalated single-wall carbon nanotubes, to understand the local structure of iodine in this material at high *P* and *T*.

At ESRF, an energy dispersive XRS (EDXRS) technique has been developed (Pascarelli and Mathon 2010), in which a focused polychromatic beam (~5 μm) of extremely high flux passes a sample, and is collected by an energy dispersive detector capable of fast capturing the HP XAS signals at micro-second level (Boehler et al. 2009; Andrault et al. 2010). The fast measurement and small beam size in EDXRS allow for mapping XAS images by scanning the sample position (Aquilanti et al. 2009).

When the HP environment is coupled with circularly (or linearly) polarized X-ray radiation and magnetic fields, the related X-ray magnetic circular (or linear) dichroism (XMCD or XMLD) techniques can be used to yield information on spin-polarized electronic structure, magnetic ordering, and magnetization (Iota et al. 2007; Gorria et al. 2009; Haskel et al. 2011; Souza-Neto et al. 2012).

XAS in the LVP is currently limited to photon energies above ~10 keV due to the solid pressure media used in cell assemblies that attenuate the signal. The advantage of using an LVP for XAS, on the other hand, is uniform and stable heating over a large sample volume. Both the DIA and PE press have been used for XAS studies. Yoshiasa et al. (1999) studied *P* and *T* dependence of EXAFS Debye-Waller factors in diamond-type and white-tin-type Ge to 11 GPa and 700 K; Arima et al. (2007) collected EXAFS spectra for liquid AgI up to 1200 K, to investigate pressure-induced local structural change. Both studies were conducted in the DIA apparatus at Spring-8. Coppari et al. (2008) studied local structure of liquid Cu to 4 GPa and 1350 °C using XAS in the PE cell at ESRF.

While XAS provides information on valence electrons and unoccupied density of states, X-ray emission spectroscopy (Feás et al. 2009) characterizes core electrons and occupied density of states through processes of excitation of the core electron as well as its decay to fill the core-level vacancy. This process is characteristic of an atom with weak influence of nearest neighbor species. For example, side-bands of the K_β emission line for several 3d transition metals provide signatures of spin, valence, and bonding information. In HP XES experiments, emission X-rays are collected by a θ-2θ scan of the analyzer and the detector in a Rowland circle (~1-meter in diameter) (Rueff et al. 1999). The spherically-bent, sub-eV analyzers are about 100 mm in diameter. Because emission signals can be collected at any direction, multiple analyzers may be used to increase solid angle coverage in data collection and thus the signal level. Recently, a short-distance spectrometer of large solid angle coverage has been developed, with which data collection time in HP XES is reduced from hours to only several minutes (Pacold et al. 2012) (Fig. 5). XES has been widely used to study pressure induced spin transitions of earth materials (Rueff et al. 1999; Badro et al. 2003; Lin et al. 2004). The band width change as a function of pressure was probed by HP XES for a semiconducting material (Ge) (Struzhkin et al. 2006).

Resonant XES (RXES), or partial fluorescence yield (PFY), has also been successfully utilized in HP research. HP RXES may be viewed as a combination of XES and XAS. Instead of collecting transmitted X-rays as in XAS, emission spectra are measured at each step as the incident beam energy is changed or scanned across an absorption edge. This resonant method significantly enhances footprints of electron states, and has a remarkable sharpening effect in projected spectra (RXES or PFY) (Rueff 2010; Wang et al. 2010a). RXES spectra have allowed for resolving crystal-field splitting of Fe^{3+} in Fe_2O_3 at HP (Wang et al. 2010a) and intermediate spin state of Fe_3O_4 at 15-16 GPa (Ding et al. 2008).

EBSCOhost - printed on 2/13/2023 5:26 AM via . All use subject to https://www.ebsco.com/terms-of-use

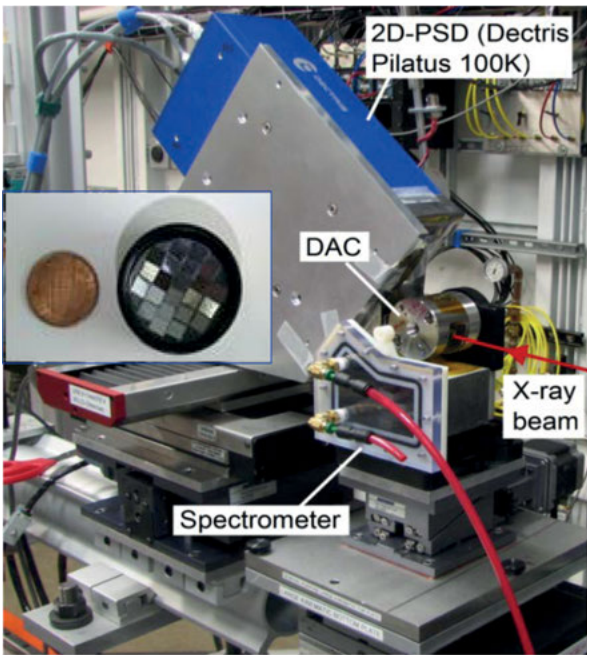


Figure 5. Setup of a short distance XES spectrometer (miniXES) at HPCAT, APS. The collection solid angle is ~50 msr (inset), about six times more than the traditional spherically-bent crystal analyzer.

HP X-ray fluorescence spectroscopy (HP XFS) permits determination of solubility of minerals in fluids at HP (Schmidt and Rickers 2003; Tanis et al. 2012). The method can be used for multi-element analytical probes and for studies of dissolution kinetics (Schmidt et al. 2007). In XFS experiments the fluorescence signals (e.g., K_α, K_β, or both) are collected by a solid-state energy dispersive detector. Currently, the detection limit for HP XFS is at a few ppm level for elements down to atomic number 22 (Ti) to a pressure of 10 GPa at high temperatures to at least 1273 K (Petitgirard et al. 2009). A confocal geometry has been developed for minimizing unwanted background signals (Wilke et al. 2010), further improving the efficiency and consequently detection limit.

HP Inelastic X-ray scattering. Inelastic X-ray scattering (IXS) has been successfully employed at the third generation synchrotron sources to study electronic and vibrational excitations in materials. HP research can now be conducted using non-resonant IXS, resonant IXS (RIXS), and nuclear resonant IXS (NRIXS). IXS may be performed with energy resolutions of 20 meV to 1 eV for electronic excitations and from sub-eV down to 0.5 meV for vibrational properties. Unlike chemical doping which introduces disorder and charge carriers, pressure provides a clean tuning mechanism that directly modifies electronic and phonon structures. Through HP IXS, fundamental properties of electron gas, strongly correlated systems such as superconducting materials, high-energy electronic excitations, and phonons in energy and momentum space can be obtained, providing critical data for code validation and tests of fundamental theories.

HP non-resonant IXS with ~1 eV energy resolution (often called X-ray Raman spectroscopy) is emerging as a powerful spectroscopic probe. HP soft X-ray spectra may be acquired with high energy X-rays which provide penetrating power through walls of a HP device. Combined with micro-focusing techniques, HP IXS can be applied to minute samples at HP (Shukla

EBSCOhost - printed on 2/13/2023 5:26 AM via . All use subject to https://www.ebsco.com/terms-of-use

et al. 2003; Lee et al. 2008; Mao et al. 2010). For example, K edges of light elements (Be, B, C, N, O, …) under HP conditions can be measured by HP IXS. Figure 6 shows the HP IXS data for graphite. Pressure-induced bonding change can be monitored through the carbon K edge. The narrow π* features at low energy are related to the 2π antibonding orbital, while the broad humps at high energy side corresponds to σ* in-plane bonds. Under pressure, partial suppressions of π bonding have been observed (Mao et al. 2003; Lin et al. 2011).

High energy resolution to meV level allows for studying lattice dynamics. Dynamical properties of materials under HP have been studied by using high energy resolution IXS (HERIXS, at ~1 meV energy resolution). Sound velocities of materials at HP to over 1 Mbar have been measured (Fiquet et al. 2001; Antonangeli et al. 2010, 2011) using this technique. With single crystal samples, complete phonon dispersions in the Brillouin zone may be mapped by HERIXS at HP (Farber et al. 2006). However, lattice dynamical data at HP are still limited, largely due to constraints by the strict requirements of sample quality, hydrostaticity, and, to some extent, beam time availability.

When the incident X-ray energy is chosen such that it coincides with one of the atomic X-ray absorption edges, resonance can greatly enhance the inelastic scattering cross section and create an excited immediate state. In resonant IXS (RIXS), the absence of a high energy core-hole in final state leads to intrinsically sharp spectra with energy and momentum. By tuning to different X-ray edges, RIXS provides element and orbital specific information. HP RIXS has been applied to various strongly correlated *d*-electron compounds (Shukla et al. 2003; Rueff 2010) and Kondo-like *f*-electron delocalization (Maddox 2006; Bradley et al. 2012).

In nuclear resonant IXS (NRIXS), incident X-rays of meV resolution is tuned near the exceedingly narrow nuclear resonant line (at neV level). By using time discrimination electron-

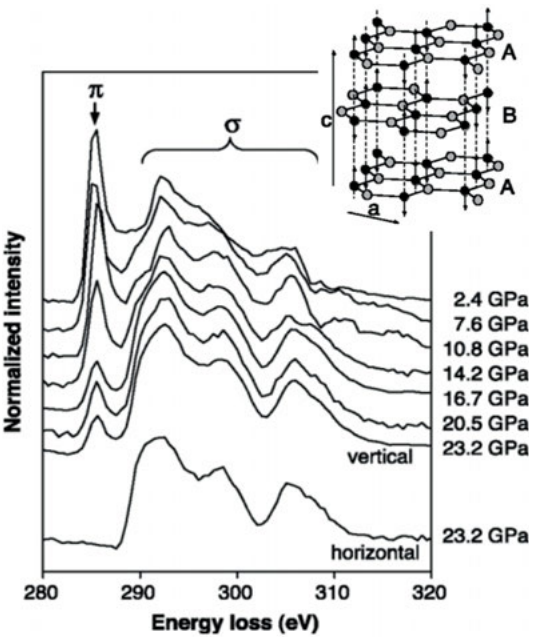


Figure 6. HP IXS spectra for graphite in two different experimental directions. The spectra in the vertical direction probe the inter-plane bonding, while those in the horizontal direction probe in-plane bonding. Insert: Graphite structure showing bridging carbon atoms (black spheres), which pair with an atom in an adjacent layer to form a σ-bond. Modified after Mao et al. (2003).

EBSCOhost - printed on 2/13/2023 5:26 AM via . All use subject to https://www.ebsco.com/terms-of-use

ics, the delayed signals caused by the narrow nuclear absorption provide NRIXS data (Sturhahn 2004). Of interest in mineral physics are measurements of phonon density of states and subsequent derivation of the Debye sound velocity (Wicks et al. 2010; Murphy et al. 2011b), which distinguishes compression and shear wave velocities as well as their temperature and pressure dependence. This technique also allows determination of anisotropy of sound velocities, and mode Grüneisen constants (Murphy et al. 2011a). HP NRIXS has been combined with laser heated diamond anvil cell to measure Debye sound velocities at HP and HT (Zhao et al. 2004; Lin et al. 2005b).

Nuclear forward scattering (NFS) using synchrotron radiation has been applied to studying Mössbauer effects at HP. Because of the high brilliance and highly focused beam, NFS is well suited for, and has been extensively used in, HP research. The NFS hyperfine signals are very sensitive to internal magnetic fields, electric field gradients, and isomer shifts, and are widely used in years to study magnetic collapse (Li et al. 2004b; Lin et al. 2005a), site occupancy (Catalli et al. 2011; Lin et al. 2012), and valence and spin state (Jackson et al. 2005; Speziale et al. 2005; Shim et al. 2009; Chen et al. 2012). Readers may refer to the reference by Sturhahn (2004) for a comprehensive description of the principle and experimental methods of the NFS technique. Compared to other nuclear resonant techniques, NFS measures the transmission signals which are relatively strong and may be collected in a fast manner. For example, fast NFS experiments have been performed to determine HP melting temperatures of iron by measuring the Lamb-Mössbauer factor which describes the probability of recoilless absorption (Jackson et al. 2013).

HP X-ray imaging. From the beginning of HP synchrotron experiments, HP X-ray imaging techniques have been used for locating HP sample position and defining sample shape. Now, a variety of HP X-ray imaging techniques have been developed for different imaging purposes, such as HP radiography, HP tomography, using the full-field imaging method or the position scanning method. Recently, HP coherent X-ray diffraction is being developed for nano-size materials (Le Bolloch et al. 2009; Yang et al. 2013).

HP radiography provides density contrast information through which the sample configuration inside the pressure device may be visible. Often times, because of the small beam in HP synchrotron experiments, radiography images are obtained by scanning sample positions. The position scanning radiography is essential in almost all HP synchrotron experiments and provides information on sample allocation, sample configuration, anvil deformation (Hemley et al. 1997), etc. By selecting proper monochromatic beams, absorption intensity contrast may be used for density determination for amorphous and liquid materials (Katayama et al. 1996; Shen et al. 2002; Hong et al. 2007).

It should be noted that the position scanning imaging method can be applied in any X-ray measurements. For example, by fast XAS measurements, images in chemical compositions and valence states may be obtained (Aquilanti et al. 2009). With increased brilliance and detection efficiency, many other measurements, such as XRD, XES, NFS (Mössbauer), may be used for mapping samples, providing images based on information of structure, valence state, spin, site occupancy etc. HP scanning imaging has great potential for detailed information not only from a single spot but from the entire sample. The image resolution in the position scanning method is limited by the beam size. Currently, all top DAC beamlines in the world have a typical beamsize of ~3-5 μm. Further reducing beam size to sub-μm is an important step in improving resolution in the scanning imaging techniques.

HP radiography can also be obtained by the full-field method, in which the incident beam is large relative to the sample size. Intensities of the transmitted X-rays are monitored by a phosphor screen which converts X-ray contrast into visible light, and recorded by a camera. The full-field radiography is fast, allowing for efficient recording the dynamic processes

EBSCOhost - printed on 2/13/2023 5:26 AM via . All use subject to https://www.ebsco.com/terms-of-use

in HP experiments. For example, a probing sphere can be *in situ* monitored for viscosity measurements of liquids at HP (Kanzaki et al. 1987; Rutter et al. 2002; Kono et al. 2013). High pressure melting processes can be recorded and the onset of melting may be defined (Dewaele et al. 2010). Phase contrast imaging measurements for bulk scale shock dynamic experiments have been demonstrated recently (Jensen et al. 2012; Luo et al. 2012). The full-field method may be also of high resolution (at sub-μm level), permitting precise determinations of sample dimensions. For example, full-field radiography is often used in HP ultrasonic measurements for sample dimensions. X-ray focusing optics (e.g., zone-plate) may be used as an "objective" similar to an optical microscope. With this, the resolution in full-field imaging can be increased significantly at the cost of the field-of-view. Such an X-ray microscope has a typical resolution of ~20-30 nm with a field-of-view of about 15 μm in diameter. Even higher resolution will enable quantifications of microstructure and grain-to-grain interactions under pressure, density determinations of amorphous/liquid materials, and phase transition. Recently, high resolution imaging microscopy has been applied to study the equations of state and phase transition of tin at HP (Wang et al. 2012).

Full-field imaging method has been applied for X-ray microtomography based on X-ray absorption. By rotating an opposed anvil device under load, radiographic images of a sample projected in a plane parallel to the loading/rotating axis can be collected at small angular intervals at HP and HT in the same way as conventional absorption-based micro-tomography (Wang et al. 2005b). The setup at 13-BM-D of the APS allows both Drickamer and torroidal anvil cells to be used in a 250 ton press, with a Si(111) monochromator tunable between 5 and 65 keV. This technique has been used for measuring volume of amorphous material for equation of state determination (Lesher et al. 2009) and 3D microstructure of composite materials under shear deformation (Wang et al. 2011). Similar apparatus have since been developed at Spring-8 (Urakawa et al. 2010) and ESRF (Alvarez-Murga 2012).

Other HP X-ray imaging techniques are being developed. There are growing activities in HP coherent diffraction imaging (HP CDI) experiments. HP CDI provides information on shapes of a nano-crystal and its internal 3D strain distributions (Pfeifer et al. 2006; Le Bolloch et al. 2009; Yang et al. 2013). X-ray topography provides information of internal strain and defects of crystals. There is no HP topography work reported so far. However, X-ray topography images are used for selecting diamond anvils (Dewaele et al. 2006) and improving the synthetic procedures in diamond crystal growth in the CVD process at Carnegie Institution of Washington.

Time resolved X-ray techniques at HP. Time resolved HP studies can provide important information on structural dynamics, phase transition kinetics, chemical reactions under HP, and materials metastability and local minimum energy configurations. Because of small samples under HP, typical time resolution is still limited to a few seconds to minutes, numerous examples can be found in studies of CO_2 sequestration rate at HP with different initial conditions (Mckelvy et al. 2004), rheology of minerals under stress at mantle pressures (Wenk et al. 2004), the post-spinel transition in Mg_2SiO_4 (Kubo et al. 2002), and HP melting temperature determination. Recently with the use of Pilatus detectors, a time resolution of 30 μs has been reached in a HP XRD study of phase transition in a Ni-Fe alloy (Yoo et al. 2011). With an intensified CCD, single crystal diffraction spots have been collected with a single pulse of beam at the APS (70 ps width with 153 ns between pulses) in dynamic shockwave experiments (Turneaure et al. 2009; Luo et al. 2012).

Because synchrotron radiation is a pulsed source with a well-defined timing structure, pump/probe experiments can be also applied besides single-shot experiments. For example, pulsed laser heating can be synchronized with X-ray beam pulses for thermal equations of state measurements (Goncharov 2010; Yoo et al. 2011). Pulsed internally-heated DAC may also be applied for more spatially uniform heating. Dynamic diamond anvil cell (dDAC) (Evans et al. 2007) may be coupled with synchrotron pulses for studying phase transition kinetics

EBSCOhost - printed on 2/13/2023 5:26 AM via . All use subject to https://www.ebsco.com/terms-of-use

and behaviors of metastable phases. Pulsed magnetic field may be integrated with HP X-ray techniques for studying strongly correlated systems.

While XRD will still remain the primary technique for developing time resolved measurements, other HP X-ray techniques (SAXS, XAS, XES, NFS, radiography, etc.) may be applied for time-resolved measurements at HP. Energy dispersive XAS (Pascarelli and Mathon 2010), for example, has been applied in time-resolved HP XAS measurements at a spatial resolution at ~20 μm level. X-ray radiography and Laue diffraction have been applied for imaging the shock front in dynamic compression experiments (Jensen et al. 2012; Luo et al. 2012).

New FEL sources will provide coherent X-ray beams of extremely high flux in a pulse-duration of sub-ps. The high flux in a single pulse (~10^{12} photons) will be sufficient for single pulse XRD experiment, and will enable HP spectroscopy measurements in time-resolved manner. Besides FELs, short pulse X-rays are generated by high power laser facilities (such as OMEGA and NIF). Such short pulsed X-rays have been used for radiography and XRD measurements in dynamic shock experiments (Lee et al. 2006; Brygoo et al. 2007).

HIGH PRESSURE TECHNIQUES INTEGRATED WITH SYNCHROTRON RADIATION

The large volume press (LVP)

Several review articles have described the LVP techniques at synchrotrons (e.g., Vaughan 1993; Wang et al. 2002a; Wang 2010). Recent technical developments and science highlights at various beamlines are reviewed by several papers (e.g., Utsumi et al. 1998; Wang et al. 2009; Mezouar 2010). Here we only provide a brief summary.

Types of LVP used at synchrotron sources. The first is the well-known cubic-anvil, or DIA apparatus (Osugi et al. 1964), which consists of upper and lower pyramidal guide blocks, four trapezoid thrust blocks, and six square-tipped anvils, as illustrated in Figure 7. A ram force applied along the vertical axis is decomposed, by the 45° sliding surfaces, into three pairs acting along orthogonal directions, forcing the six anvils to advance (retract) synchronously towards (away from) the center of the cubic cavity, where the sample assembly is located. X-ray access is through vertical gaps between the side anvils. The diffraction vector is vertical, with possible 2θ angles up to about 25°.

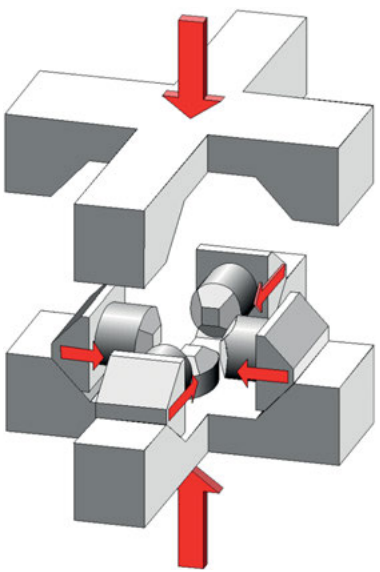


Figure 7. Conceptual diagram illustrating the principles of the DIA cubic anvil apparatus.

The second is the Kawai-type apparatus, which consists of a first-stage hardened steel cylinder cut into six parts, each having the inner tip truncated into a square surface, enclosing a cubic cavity, with the [111] axis of the cube along the ram load direction. Inside the cubic cavity is a second-stage assembly (referred to as the Kawai cell), which consists of eight WC cubes separated by spacers. Each cube has one corner truncated into a triangular face, so the eight truncated cubic anvils form an octahedral cavity in which the pressure medium is compressed. At beamline 13-ID-D of the APS (GSECARS), a Kawai-type module is used to compress 25 mm edge-length WC cubic

EBSCOhost - printed on 2/13/2023 5:26 AM via . All use subject to https://www.ebsco.com/terms-of-use

anvils. Diffracted X-rays pass through the gaps between the second-stage cubic anvils in a plane inclined at an angle of 35.264° from the loading direction. Conical access notches are made in the first-stage wedges, to allow a range of 2θ angles up to ~10° (Fig. 8).

The third is a hybrid system using a set of large DIA anvils to compress the Kawai cell (Anderson 1973). For convenience, we will refer this as the 6-8 Kawai type. The first such configuration was developed at the Photon Factory (Ohtani et al. 1989; Shimomura et al. 1992). Subsequently larger systems were adopted at SPring-8 (Utsumi et al. 1998). Figure 9 shows the apparatus at the insertion device beamline 13-ID-D at the APS (GSECARS). In this configuration hydraulic load is parallel to the [100] direction of the Kawai cell, and X-ray access is through

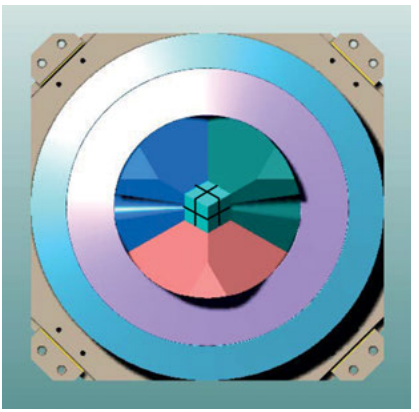


Figure 8. Top view of the T-25 module at GSECARS. The geometry is identical to Kawai-type systems used in most high-pressure laboratories, with the [111] axis of the eight-cube assembly along the loading axis. X-ray diffraction is through the gaps between WC anvils, inclined from the loading axis at 35.26°.

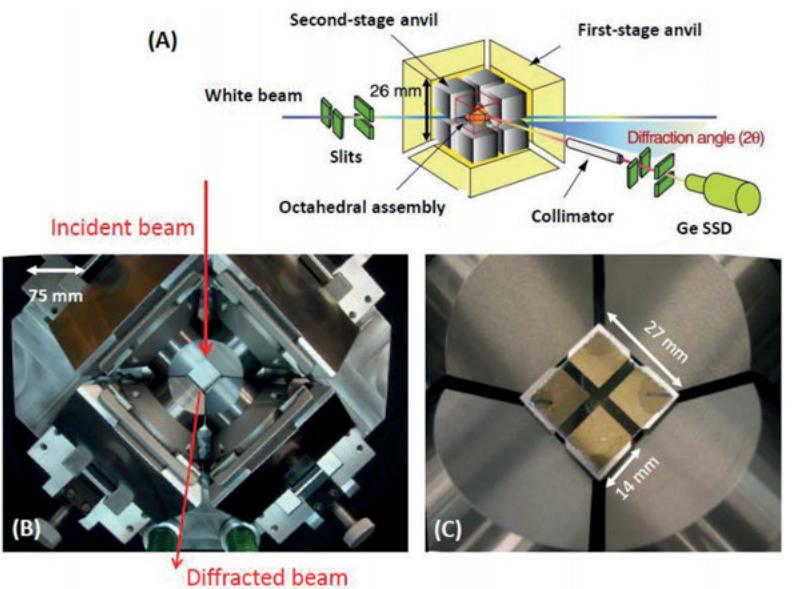


Figure 9. DDIA-30, a dual-purpose LVP for 1000 ton press at 13-ID-D of the APS. (A) Isometric view of the key components and setup (modified after SPring-8 website). (B) top view of the lower guide block showing first stage anvils and beam path. This configuration can be used as a DIA apparatus and a D-DIA for controlled deformation experiments. (C) Close-up of the second-stage cubic anvil arrangement (top view). This configuration allows HP of 50 GPa and 2000 K to be reached routinely.

EBSCOhost - printed on 2/13/2023 5:26 AM via . All use subject to https://www.ebsco.com/terms-of-use

horizontal anvil gaps when WC cubes are used as second-stage anvils. Notches are made in the first-stage DIA anvils to allow X-ray access. This apparatus is the most successful in generating "ultrahigh" pressures towards megabar using sintered diamond anvils, (e.g., Tange et al. 2008; Ito et al. 2010).

A new type of multi-anvil device was developed at the Institute for Study of Earth's Interior, Okayama University, Japan. This apparatus has a DIA-like geometry, but with each of the six anvils independently controlled by a hydraulic system (Ito et al. 2009). This configuration may add greater flexibility to the system by imposing desired hydrostatic or non-hydrostatic conditions. It is argued that the alignment of the six outer–stage anvils will also improve significantly, thus making it possible to compress the Kawai-cell with greater degree of accuracy, generating higher pressures with advanced anvil materials such as sintered diamond. A second 6-axis apparatus has been installed at Bayreuth Institute of Geosciences (Manthilake et al. 2012). Although no such systems have been used at synchrotron beamlines yet, a similar apparatus has been installed at the neutron PLANET beamline at Japan Photon Accelerator Research Complex (J-PARC; J-PARC Newsletter, No. 49, July 2012).

Not all LVPs are multi-anvil devices. The toroid anvil cell, first developed in the former Soviet Union (Khvostantsev 1977), operates on the principles of opposed anvils, similar to the DAC. Instead of flat anvil tips as in the DAC, toroid anvils have a half-spherical depression so that the two anvils enclose a semi-spherical cavity. One or several toroidal depressions are made concentric with the central sample cavity for preformed gaskets that are used to minimize extrusion (Fig. 10). Besson et al. (1992) integrated this device with a compact hydraulic system, allowing portability and great flexibility. The Paris-Edinburgh (PE) cells, as they are known now, are currently in use at many synchrotron and neutron sources. Sample size is typically in the millimeter range. X-ray access is through the gaps between the two anvils for synchrotron diffraction, where the largest diffraction angle is in the plane perpendicular to the loading axis. Hirth and Kohlstedt (2003) reviewed the HP activity at ESRF using a PE cell.

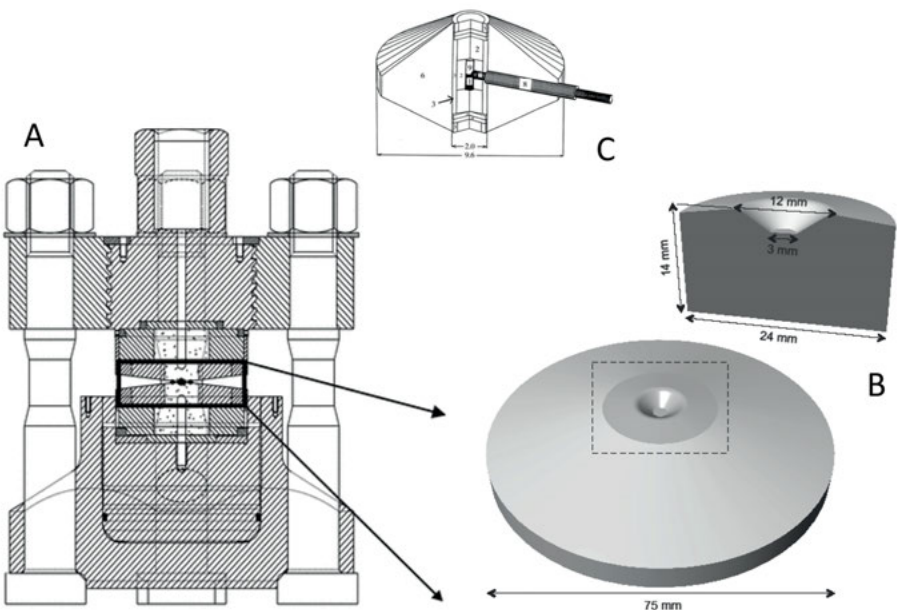


Figure 10. The Paris-Edinburgh cell. (A) Cross-section of the overall apparatus. (B) WC PE anvil, along with a cross section showing typical dimensions. (C) Schematic of a PE assembly.

EBSCOhost - printed on 2/13/2023 5:26 AM via . All use subject to https://www.ebsco.com/terms-of-use

The Drickamer cell is another widely used opposed anvil device (Balchan 1961) in which two large anvils (diameters 10 mm or above) with an optimal tapered angle are compressed inside a containment ring, typically made of WC or hardened steel, with X-ray access holes for diffraction (Fig. 11). Such devices have been used in Japan at synchrotrons (Yoshiasa et al. 1999; Gotou et al. 2006) for some time and are now used for a number of new applications, described below. Nishiyama et al. (2009) developed a modified Drickamer cell for HP deformation at HT using ADXRD. Another modified Drickamer anvil apparatus was developed by Gotou et al. (2011), where small depressions are introduced into the anvil tops, similar to the toroid anvils. This increases the height of the sample, allowing more uniform heating with slight decrease in pressure efficiency.

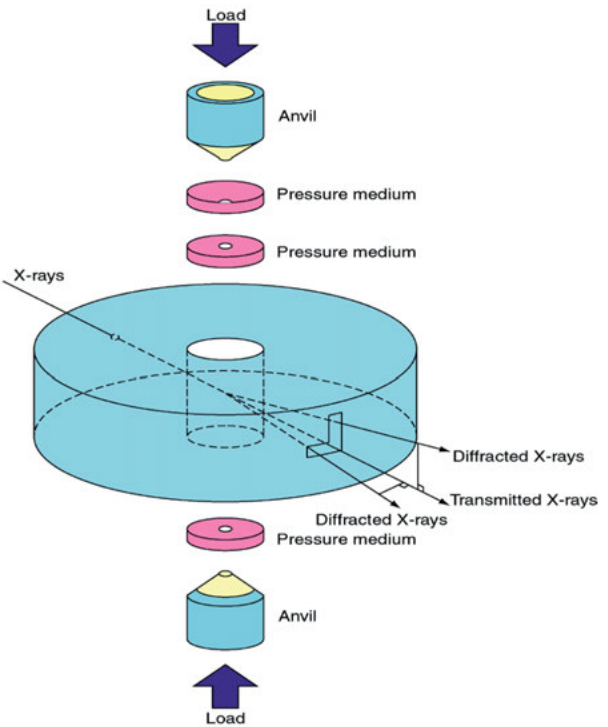


Figure 11. The Drickamer cell. With sintered diamond as anvil material, it can generate up to 30 GPa pressure, with a sample about 0.2-0.3 mm in linear dimensions.

Diffraction optics. When EDXRD is used in LVPs, it is essential to maintain fine beam collimation in order to minimize background scattering from the surrounding pressure media. This is achieved by using slits and collimators which are pairs of blades made of heavy metals (e.g., tungsten or tantalum alloys). Typical slit openings are on the order of 50 to 100 μm, defining a diffracting volume with the maximum linear dimensions about 1 mm. Cooling may be necessary especially for incident slits to minimize thermal drift caused by intense synchrotron radiation.

For ADXRD, collimation on the diffraction side is sometimes omitted. Instead, amorphous (e.g., B) and/or low scattering materials are inserted in the beam path serving as "windows". This technique works well with area detectors (CCD or image plates) when the sample has

EBSCOhost - printed on 2/13/2023 5:26 AM via . All use subject to https://www.ebsco.com/terms-of-use

sufficient scattering power so that contributions from the window materials are negligible. For weak scattering samples especially non-crystalline materials, Soller slits are necessary and have been used on the diffraction side (Yaoita 1997; Mezouar 2002; Morard 2011). These slits are multichannel collimators with two arrays of slits prefabricated to cover a given two-theta range, forming two concentric arches centered at the sample. By oscillating the two rows of slits slightly around the center of the sample, background scatter is eliminated, allowing clean diffraction signals from the sample to be recorded. This technique has been successfully applied to studying melt structures of Fe-(S, Si) alloys (Morard et al. 2007b, 2008).

Pressure temperature controls. Pressure is controlled by varying the hydraulic ram load, typically through proportional-integral-derivative (PID) feedback control logic, and measured based on the *P-V-T* equations of state of standard materials that are placed in close proximity of the sample. A comprehensive review on various pressure scales is provided by Decker et al. (1972). With positive displacement pumps (also known as syringe pumps) as load generators, extremely fine control can be achieved. Modern systems are automated for increasing and decreasing ram load, often with multiple cycles. However, ram load and sample pressure do not have a simple relation. The loading-unloading pressure "hysteresis loop" is primarily due to plastic deformation in the pressure media and gaskets. Fortunately, the hysteresis behavior is predictable for a given cell assembly. Pressure gradients in the sample are generally small when experiments are conducted properly (on the order of 0.1 GPa/mm or below), and ultimately controlled by the yield strengths of the sample and the surrounding pressure media. With increasing temperature (decreasing yield strength), pressure gradients diminish.

Temperature is generally generated by resistive heating and measured by a thermocouple. Many materials have been used as heaters, the most commonly used being graphite, noble metals, and certain ceramics (e.g. $LaCrO_3$) (Ohtani 1979). All of these materials have certain limitations. Graphite has limited pressure applicability due to its transition to diamond. Metals and $LaCrO_3$ attenuate X-rays thereby affecting diffraction signal, if used in the beam path. Recently, TiB_2 has been employed which is capable of generating temperatures in excess to 2500 K and to very high pressures (at least 50-60 GPa) (Arima et al. 2007). AC power supplies are preferred as DC supplies might generate a DC bias in the thermocouple signal, thereby causing erroneous temperature reading. PID control is commonly used for controlling heating rate and maintaining a constant temperature during data collection. Despite some attempts, the effect of pressure on thermocouple emf remains unclear. It appears that W/Re based thermocouples are the least affected by pressure effect (Ohtani 1979) and therefore the most commonly used.

Stress/strain control. Yamazaki and Karato (2001) constructed a rotational Drickamer apparatus (RDA). The pressure generation mechanism is based on the Drickamer cell, but with one of the anvils rotated under high *P* and *T*, generating large shear strains in the sample. Although stress and strain fields are heterogeneous throughout the sample, the large strain capability makes this a unique apparatus for studying plastic deformation and deformation-induced preferred orientation under high *P* and *T*.

The concept of deformation DIA (D-DIA) was first described by Wang et al. (1998). It is a modification of the DIA apparatus, with additional independent control of the displacement of one pair of anvils, provided by two additional hydraulic actuators, called differential rams (Wang et al. 2003). The differential rams are located within the guide blocks of the D-DIA module (Fig. 12) and react against the platens driven by the main hydraulic ram, which provides quasi-hydrostatic pressurization. The guide blocks not only support the forces confining the side wedges, they now have also become thick-walled pressure containers for the hydraulic fluid driving the differential rams.

When the differential rams are driven symmetrically, strain rates of 10^{-3} to 10^{-7} s^{-1} can be imposed on a sample several mm in length. The D-DIA is capable of shortening as well

EBSCOhost - printed on 2/13/2023 5:26 AM via . All use subject to https://www.ebsco.com/terms-of-use

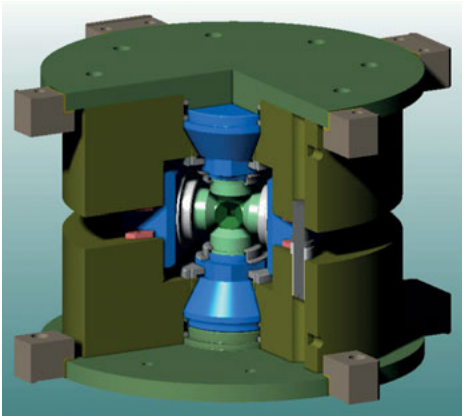


Figure 12. Cutaway view of the D-DIA with differential rams in the upper and lower guide blocks. Note locations of the differential rams. Modified after Wang et al. (2003).

lengthening the sample, making it possible to conduct stress-strain loops, a widely used method in conventional deformation studies. Deformation in simple shear, using 45°-cut pistons, is also used for much higher strains, at the cost of reducing sample volume (Ohuchi et al. 2010). By driving the differential rams cyclically, one creates a dynamic, sinusoidal stress boundary condition, which can be used to study a number of interesting phenomena at high *P* and *T* such as bulk attenuation in minerals (Li and Weidner 2008) and twin domain switching in ferroelastic materials (Li and Weidner 2010).

The D-DIA also has advantages in quasi-hydrostatic pressure generation. The differential rams make it possible to compensate elastic deformation in the high pressure apparatus at various loads. By adjusting the differential ram positions one can generate conditions closer to hydrostatic than a regular DIA. These advantages have inspired a new generation of multi-anvil systems. Large DDIA modules have been installed at LVP beamlines at SPring-8 (Kawazoe et al. 2011), ESRF, and the APS (Fig. 9) (Wang et al. 2010b).

Sample imaging. Synchrotron radiography has been used since the 1980's for measuring melt viscosity using the falling sphere technique (Kanzaki et al. 1987). Starting from the late 1990's the radiography technique was integrated into APS beamlines and used as an efficient way to visualize samples during LVP experiments (Wang et al. 2000). The technique has been adopted by virtually all LVP beamlines since then. Sample length measurements are routinely conducted in deformation studies and ultrasonic velocity measurements. Recently, this simple technique has been extended for measuring bulk attenuation (Li and Weidner 2008) with cyclic loading in the D-DIA, and for studying thermal diffusivity of minerals at high pressures (Dobson et al. 2010) with controlled sinusoidal temperature cycling.

Wang et al. (2005b) developed a high-pressure X-ray tomography imaging system. By using thrust bearings to support ram loads and high-torque gears, opposed anvil cells such as Drickamer or toroid anvil devices can have unlimited rotation with respect to the loading axis. X-rays that pass through such a rotation anvil apparatus (RAA) are converted into visible light using a scintillating screen. Absorption contrast through the sample and pressure media are recorded at various angles as radiographs, which are then processed to reconstruct three-dimensional tomographic images. With parallel beam imaging, spatial resolutions of 2-3 microns are achievable, making this device a powerful tool for observing 3D microstructure under high *P* and *T*. This technique has been used to measure density of molten material under high *P* and *T* (Lesher et al. 2009), investigate liquid-liquid surface tension (Terasaki et al. 2008), examine shear-induced fabric transition in multiphase composites (Wang et al. 2011), and study segregation process of molten Fe from silicate matrix for a better understanding

EBSCOhost - printed on 2/13/2023 5:26 AM via . All use subject to https://www.ebsco.com/terms-of-use

of the core formation processes in the Earth's early history (Chen et al. 2011). Other HP tomography techniques have since been developed at SPring-8 (Urakawa et al. 2010) and ESRF (Alvarez-Murga 2012).

Ultrasonic measurements. The large sample volume in the LVP allows one to measure acoustic wave velocities on polycrystalline and single crystals at high *P* and *T*. Synchrotron radiation with ultrasonic travel time determination offers a unique combination as sample length (which is needed to convert travel times to velocities) and density can be determined by radiography and diffraction, respectively. The reader is referred to other reviews for technical details (e.g., Li et al. 2004a; Li and Liebermann 2007). With the advanced instruments travel times of a 0.5 mm long sample can be determined accurately. This means that the technique can be applied to quite high pressures (in excess to 50 GPa). The simultaneously measured *P-V-T* (through X-ray diffraction), sample length (X-ray imaging), and acoustic travel times (ultrasonic interferometry) informative has allowed establishment of redundant equations of state, making it possible to examine closely precision and accuracy of diffraction-based pressure standards (e.g., Kono et al. 2009).

Acoustic emission (AE) techniques have been integrated with deformation in the D-DIA after successful development in the DIA apparatus at DESY (Gasc et al. 2011). By mounting acoustic transducers on the back side of all six anvils, AE events can be monitored throughout deformation process. Thanks to the development of advanced electronics and software, continuous recording of AE events allows microseismology to be performed in the laboratory. Effects of phase transformation from olivine to spinel on faulting in polycrystalline Mg_2GeO_4 samples have been investigated (Schubnel et al. 2013).

Diamond anvil cell techniques

The extreme hardness and strength of diamond allows generation of very high pressures reaching conditions corresponding to the center of the Earth (Mao et al. 1990; Akahama and Kawamura 2007; Dubrovinsky et al. 2012). Because of its transparency to much of the electromagnetic spectrum, including high energy X-rays above 10 keV and low energy ultraviolet-visible-infrared radiation below 5 eV, numerous diffraction, scattering, and absorption probes can be employed for determination of electronic, dynamic, and structural properties of samples under pressure. This transparency also allows for utilizing laser beams that can heat samples up to temperatures over 4000 K while at extreme pressures (Ming and Bassett 1974; Boehler et al. 1990; Shen et al. 2001).

Pressure generation. The DAC design is based on Bridgman's original idea in which the sample is placed between the polished culets of two diamonds and is contained by a gasket (Fig. 13). Since pressure is force divided by area, extreme pressures can be generated by opposing anvils with small culet sizes.

A number of different cell designs have been developed for various applications. To ensure precise alignment for small culets in ultra-high pressure generation, a long piston cylinder design (such as the Mao-Bell type) is often used. Symmetrical design is suitable for double sided laser heating experiments (Shen et al. 1996; Mao et al. 1998a). Special DACs have been designed for externally resistive heating techniques (Fei and Mao 1994; Bassett et al. 2000; Dubrovinsky et al. 2000). For magnetic measurements, non-magnetic alloys (such as Cu-Be alloy) are used for the cell body. The panoramic cell has been developed (Mao et al. 2001), which provides wide opening in the radial direction and is widely used in HP spectroscopy experiments. The recently developed plate cell (Boehler 2006) removed the need of guiding alignment, making the cell even more compact, with wide opening in both radial and axial directions (Fig. 14).

Many new developments have been made on the designs of diamond anvils to meet the needs of various measurements. The Boehler-Almax anvil design (Boehler 2006) (Fig.

EBSCOhost - printed on 2/13/2023 5:26 AM via . All use subject to https://www.ebsco.com/terms-of-use

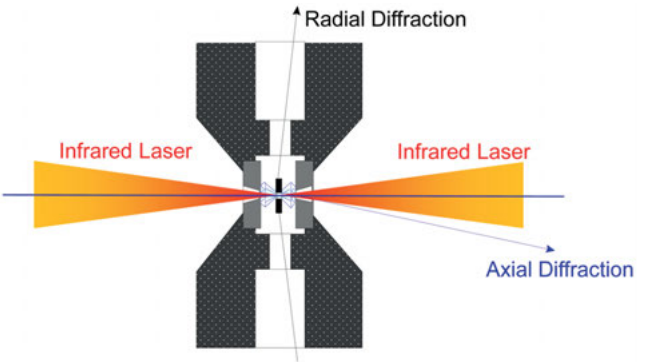


Figure 13. Schematic of a symmetrical diamond anvil cell. X-ray access may be applied in both axial and radial directions. Pressure is generated by pressing two diamond anvils with small culets.

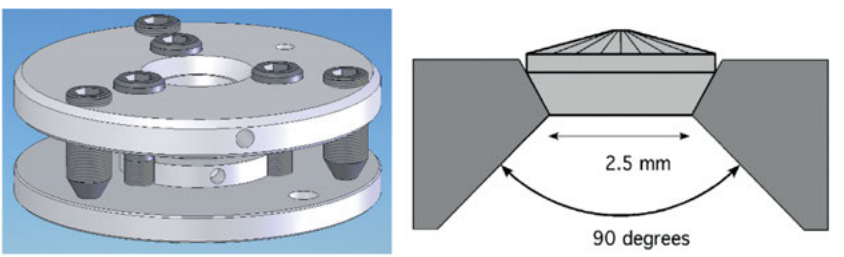


Figure 14. (a) The plate cell design; (b) large aperture diamond anvil with tungsten carbide support from the side, making the X-ray opening of more than 80 degrees. Modified after Boehler (2006).

14) provides large opening access (> 90°) along the loading axis, and is widely used in HP XRD, in particular in HP single crystal XRD. Fully or partially perforated anvils have been used to gain penetration power for low energy X-rays in HP XAS, HP XMCD, and HP PYF spectroscopy experiments. Use of partially perforated anvils can significantly reduce scattering from anvil materials, effectively minimizing Compton scattering from anvils in experiments of amorphous or liquid materials with high X-ray energy. With focused ion beam (FIB) and other micro-engineering techniques, small holes and/or grooves may be made for containing samples or to reduce the X-ray path length. For example, the so-called "holy" and "groovy" anvils are used in HP XAS experiments with hydrothermal DAC (Bassett et al. 2000; Mayanovic et al. 2007b). Electrical leads and magnetic coils may be implemented at the tip of anvils (Jackson et al. 2003), and when combined with HP synchrotron measurements, complementary information may be obtained (Uhoya et al. 2012).

The maximum pressure with the single stage type DAC is in the vicinity of 400 GPa (Akahama and Kawamura 2010). For generating pressures of 500 GPa and above, new anvil designs together with smaller probing beams (< 1 μm) are needed. Efforts are being made to optimize the anvil shape using the fine-element calculations. Recently, pressures as high as 600 GPa have been reached by a double stage mechanism, i.e., inserting a small pairs of anvils inside the sample chamber between diamond anvils (Dubrovinsky et al. 2012). Higher pressures may be reached when the double stage DAC is combined with fast ramping loading and time-resolved measurements.

EBSCOhost - printed on 2/13/2023 5:26 AM via . All use subject to https://www.ebsco.com/terms-of-use

Hard metals, such as stainless steels and rhenium, are often used as gasket materials. These metals are of high ductility and easy to machine and handle. For X-ray access in the radial direction, low-Z materials (Be, B, cBN, diamond powder) are used as gasket or insert materials in the sample chamber. Hydrostatic pressure can be generated in the DAC when a proper medium is used. Methanol-ethanol mixture, silicone oil, and noble gases such as helium and neon are few commonly used examples. However, above 11 GPa at room temperature, all known fluids solidify and develop nonhydrostatic stresses proportional to their strength. Above 20 GPa, even the weak noble gas solids, argon and neon, show non-hydrostaticity. Helium, solidified at 11 GPa at room temperature (Pinceaux et al. 1979), is considered to be the best pressure medium, which provides hydrostatic pressure up to 11 GPa, and good quasi-hydrostatic pressure condition up to 50 GPa due to its low shear strength (Takemura 2001). Quantifying the deviatoric stress under uniaxial compression has been made by HP XRD (Meng et al. 1993) and by monitoring the 3-dimensional lattice strains with radial XRD (Mao et al. 1998b).

Temperature techniques. HP DAC experiments can be combined with temperature techniques from a few degrees to thousands of degrees in Kelvin. DACs can be inserted in cryostats and cooled down to below 4 K. Various cryostats have been developed for accommodating different cells and different measurement geometry (Fig. 15).

There are two major resistive heating methods—external and internal. External furnaces provide accurate and well-controlled temperature conditions. There is an intrinsic temperature limit, however, due to rapid graphitization of diamond above 1900 K, even in an inert environment and vacuum (Seal 1963). The entire DAC may be heated by a resistively heated furnace up to 700 K. For higher temperatures, a small heater around diamond anvils may be used for temperatures up to 1200K (Fei and Mao 1994). With a graphite heater around diamond culets, temperatures as high as 1700 K have been reported with resistive heating methods (Dubrovinsky et al. 2000). Due to softening of the stress-bearing components, including the sample gasket, the diamond seat, and the diamond anvil itself, maximum attainable pressure is limited. The internally heated method, on the other hand, locally heats the sample in the chamber. Often, the sample itself is used as a conductive object and heating is applied electrically (Boehler 1986). Zha and Bassett (2003) used rhenium ribbon as a heating object and the sample was placed in a hole in the ribbon. Temperatures may be reached as high



Figure 15. Examples of cryostats at sector 16 (HPCAT) at APS.

EBSCOhost - printed on 2/13/2023 5:26 AM via . All use subject to https://www.ebsco.com/terms-of-use

as the melting temperatures of the conductors. By the chemical vapor deposition method, a resistively heated wire circuit may be built in the diamond anvil culet, this may increase the maximum pressure attainable.

The transparency of diamond allows application of near- and mid-infrared lasers (CO_2, Nd:YAG, Nd:YLF) to heat samples between two diamond anvils at high pressures (Ming and Bassett 1974). Regarding the temperature range, there is no high temperature limit with this technique in principle. The challenging part is to control and measure them accurately and to characterize the sample at defined conditions. The temperature measurement is based on spectral pyrometry. By measuring the thermal radiation from the hot sample over a wavelength range, temperatures can be calculated by fitting the radiation to Planck's equation (Boehler 1986; Heinz and Jeanloz 1987). A double sided laser heating system (Shen et al. 1996) was introduced for the minimization of temperature gradients radially and axially in a laser heated sample. Thanks to the micro X-ray beam size which improved the spatial resolution and ensured that the X-ray beam size is significantly smaller than the laser heated spot. Many synchrotron facilities have equipped with double sided laser heating systems. The laser heated DAC experiments become a routine capability in HP XRD and HP spectroscopy. Recently, portable laser heating systems have been developed (Boehler et al. 2009; Dubrovinsky et al. 2009; Shen et al. 2010), which will lead to more use of the laser heating technique in specialized beamlines with various X-ray probes.

Pressure controls and measurements. The compact design of DAC allows for pressure control by just turning screws manually. This makes the DAC device portable and applicable in many probing techniques. To gain precision in pressure control and to access remotely when contained in other equipment such as cryostats, furnaces, and magnets, the diaphragm design (sometimes referred to membrane control) using compressed gas has been developed (Daniels and Ryschkewitsch 1983), and now widely used in synchrotron facilities. By regulating the compressed gas (e.g., He-gas) pressure, the force applied to the anvils may be controlled precisely and fine pressure change can be made. Recently, motor driven gear boxes have been developed for controlling the screw turns, providing remote precise pressure controls. With these remote control devices, either by mechanical gear box or by diaphragm, X-ray measurements with small pressure increment become possible, revealing subtle changes in compression and unusual phenomena close to phase transitions.

Using the pressure-volume equations of state data of well-studied materials (e.g., MgO, NaCl, Au, W), pressures can be determined by measuring the volumes of these standard materials by HP XRD. Pressure can also be determined by optical methods, e.g., using the ruby fluorescence (Mao et al. 1986) and Raman peaks of diamond (Akahama and Kawamura 2010). Pressure determination at HT is challenging because of the lack of accurate data of pressure-volume-temperature equations of state. Nevertheless, attempts have been made to construct internally-consistent data set with available X-ray and optical techniques (Sinogeikin et al. 2006; Fei et al. 2007; Komabayashi and Fei 2010). In addition, weakly temperature dependent sensors, e.g., YAG:Sm (Zhao et al. 1998), have been developed for pressure determination at HT. It should be mentioned that establishing a reliable pressure scale remains as one of the most important goals in high pressure mineral physics.

Dynamic shockwave techniques

In shock wave experiments, the sample is subjected to HP and HT by dynamic processes. A shock wave is driven through the sample by means of an explosive charge, by the collision of a flying object, or by high power lasers. Compared to the projectile technique, the laser shock technique can yield very high amplitude pressure loadings (as high as 50 TPa) with very short durations (in fs). The DAC may be integrated with the laser-driven shock (Celliers et al. 2010; Loubeyre et al. 2004). By controlling the ramp rate, these experiments (Smith et

EBSCOhost - printed on 2/13/2023 5:26 AM via . All use subject to https://www.ebsco.com/terms-of-use

al. 2007) can provide single shot equation-of-state data close to the isentrope, information on the kinetics of phase transformations, and material strength at high pressures. A number of techniques have been developed to measure the velocity of shock wave and the velocity to which the sample material has been accelerated. These measurements allow us to derive the density and pressure of the sample under loading (Brown and McQueen 1982).

Recently, X-ray techniques have been applied in shockwave experiments at synchrotron facilities and other high power laser facilities (OMEGA, NIF). Single crystal XRD has been used for studying the deformation of materials under shock (Turneaure et al. 2009). The shock front can be monitored by X-ray radiography (Ping et al. 2011). Dynamic response of materials under shock has been measured by using the phase contrast imaging technique (Jensen et al. 2012). Using the X-ray white Laue technique, the shock wave propagation can be recorded by using the timing structure of synchrotron pulses (Suggit et al. 2010; Luo et al. 2012).

A BRIEF OUTLOOK

Expanding *P-T* range

The accessible pressure range ultimately defines the scope of HP research. In the past two decades, the number of publications from the HP synchrotron research has increased exponentially, thanks to the micro-sized (2-5 μm) synchrotron probes and new high pressure techniques. However, the highest pressure has reached a plateau at ~400 GPa (Akahama and Kawamura 2010) with the single stage type DAC. Recently, with a double stage DAC configuration, pressures up to 600 GPa have been reached in a much smaller sample volume (Dubrovinsky et al. 2012). Nano-XRD probes at synchrotron facilities therefore provide spatial resolution required for studying materials at extreme conditions with very small volume. Together with the developments in X-ray optics, ultra-stable sample stages, and advanced detectors, even higher pressures reaching 1 TPa and beyond may be feasible in the near future in the static DAC experiments. The nano-probes may be combined with dynamic DAC (d-DAC) (Evans et al. 2007), which may enable time resolved experiments at increasingly broader pressures and even more extreme temperature conditions before the anvil's failure. The nano-probes can also be applied in less homogeneous samples, or in precise single-crystal studies of individual crystallites within a powder sample.

Pressure and temperature ranges are also constantly expanding for the LVP. Using sintered diamond as second-stage anvils, the 6-8 type Kawai apparatus are approaching the megabar mark (Ito et al. 2010). With a pair of advanced nano-polycrystalline diamond as third-stage anvils (Irifune et al. 2003) in the octahedral pressure medium in the 6-8 Kawai apparatus (the so-called 6-8-2 configuration), Kunimoto and Irifune (2010) reported a pressure of 125 GPa up to 1100 K. Under these conditions the sample dimensions are about 100-200 microns in linear dimensions.

New HP synchrotron techniques

Various new types of DACs are being developed for ultra-high pressure, large opening, or compactness to fit in the varieties of X-ray measurements. Portable systems, including laser heating systems, optical Raman and ruby fluorescence systems, and microfocusing mirrors, have been developed and are being integrated at many beamlines. Rather than concentrating on HP beamlines, this approach takes advantages of specialized beamlines with well-developed X-ray techniques. Many new HP synchrotron techniques are being developed in XRD, XRS, and IXS, in particular in the areas of imaging techniques and time-resolved measurements.

Imaging capabilities (coherent diffraction imaging, mass density tomography, full field imaging) are being actively integrated with DAC for HP studies with resolutions from 1 μm down to 30 nm, which will open a new era of imaging HP phases, for studying the plasticity,

EBSCOhost - printed on 2/13/2023 5:26 AM via . All use subject to https://www.ebsco.com/terms-of-use

elasticity, and precise equations of state of amorphous/liquid materials. Imaging in the LVP has received much attention recently. Both radiography and tomography techniques will be used more intelligently. Attenuation and thermal conductivity are just recent examples of new applications for radiography. With advanced tomography techniques, high pressure tomography will see much improved mechanical and optical components, to allow 3D microstructure imaging to the sub-micron level in spatial resolution. Diffraction tomography may be applied, allowing grain-to-grain examination of a bulk sample under high *P* and *T*.

A beamline dedicated to dynamics compression science is under construction at APS for time-resolved studies in dynamic processes and would be the first of its kind at a third-generation high-energy synchrotron facility. Dynamic compression capabilities (utilizing high-velocity impacts, high-intensity lasers, and pulsed power generators), coupled with ultra-fast measurements at the APS, represent the most versatile approach for achieving the widest range of thermo-mechanical conditions in a controlled manner.

Because HP samples are always embedded in surrounding materials (anvils, gaskets, pressure media), excellent collimation is required to remove signals from surrounding materials. Developments for precise collimation down to micron size for various HP spectroscopy techniques are important and will effectively increase the signal-to-noise ratios. Spectroscopy in the LVP is an area that may see huge advances in the future. With more brilliant synchrotron radiation, a wider range of photon energies will be measureable through pressure media, allowing many techniques that currently can only be used in the DAC to be applied to the LVP. Since LVP is capable of stable and uniform *P* and *T* conditions, HT spectroscopy may be applied to minerals under conditions more representative to the Earth and planetary interiors.

ACKNOWLEDGMENTS

Thanks are due to Ligang Bai, Daijo Ikuta, and Yuming Xiao for their help in preparation of this manuscript. Mark Rivers is thanked for Figure 2. HPCAT is supported by DOE-NNSA under Award No. DE-NA0001974 and DOE-BES under Award No. DE-FG02-99ER45775, with partial instrumentation funding by NSF. GeoSoilEnviroCARS (GSECARS) is supported by the National Science Foundation - Earth Sciences (EAR-0622171) and Department of Energy - Geosciences (DE-FG02-94ER14466). APS is supported by DOE-BES, under Contract No. DE-AC02-06CH11357. YW thanks continuing NSF support for LVP developments at GSECARS (EAR-0001088, 0652574, 0711057, 0968456, and 1214376).

REFERENCES

Akahama Y, Kawamura H (2007) Diamond anvil Raman gauge in multimegabar pressure range. High Pressure Res 27(4):473-482, doi: 10.1080/08957950701659544

Akahama Y, Kawamura H (2010) Pressure calibration of diamond anvil Raman gauge to 410 GPa. J Phys 215: 012195

Alvarez-Murga M (2012) In situ microdiffraction and microtomography of heterogeneous high-pressure high-temperature forms of C_{60}. Ph.D. thesis, ESRF, Grenoble

Anderson OL (1973) Comments on the power law representation of Birch's Law. J Geophys Res 78(23):4901-4914, doi: 10.1029/JB078i023p04901

Andrault D, Munoz M, Bolfan-Casanova N, Guignot N, Perrillat J-P, Aquilanti G, Pascarelli S (2010) Experimental evidence for perovskite and post-perovskite coexistence throughout the whole D˝ region. Earth Planet Sci Lett 293:90-96

Antonangeli D, Siebert J, Badro J, Farber DL, Fiquet G, Morard G, Ryerson FJ (2010) Composition of the Earth's inner core from high-pressure sound velocity measurements in Fe–Ni–Si alloys. Earth Planet Sci Lett 295(1-2):292-296, doi: 10.1016/j.epsl.2010.04.018

Antonangeli D, Siebert J, Aracne CM, Farber DL, Bosak A, Hoesch M, Krisch M, Ryerson FJ, Fiquet G, Badro J (2011) Spin crossover in ferropericlase at high pressure: a seismologically transparent transition? Science 331(6013):64-67, doi: 10.1126/science.1198429

EBSCOhost - printed on 2/13/2023 5:26 AM via . All use subject to https://www.ebsco.com/terms-of-use

Aquilanti G, Pascarelli S, Mathon O, Munoz M, Narygina O, Dubrovinsky L (2009) Development of micro-XANES mapping in the diamond anvil cell. J Synchrotron Radiat 16:376-379, doi: 10.1107/s0909049509007134

Arima H, Ohtaka O, Hattori T, Katayama Y, Utsumi W, Yoshiasa A (2007) In situ XAFS and XRD studies of pressure-induced local structural change in liquid AgI. J Phys Condens Matter 19(7):076104

Badro J, Fiquet G, Guyot F, Rueff J-P, Struzhkin VV, Vanko G, Monaco G (2003) Iron partitioning in Earth's mantle: toward a deep lower mantle discontinuity. Science 300(5620):789-791

Balchan AS, Drickamer HG (1961) High pressure electrical resistance cell, and calibration points above 100 kbars. Rev Scic Instrum 32:309-313

Ballirano P, Caminiti R (2001) Reitveld refinements on laboratory energy dispersive X-ray diffraction (EDXD) data. J Appl Crystallogr 34:757-762

Bassett WA, Reichmann H-J, Angel RJ, Spetzler H, Smyth JR (2000) New diamond anvil cells for gigahertz ultrasonic interferometry and X-ray diffraction. Am Mineral 85:283-287

Besson JM, Nelmes RJ, Hamel G, Loveday JS, Weill G, Hull S (1992) Neutron powder diffraction above 10 GPa. Physica B 180-181(Part 2):907-910

Boehler R (1986) The phase diagram of iron to 430 kbar. Geophy Res Lett 13: 1153-1156

Boehler R (2006) New diamond cell for single-crystal X-ray diffraction. Rev Sci Instrum 77(11):115103, doi: 10.1063/1.2372734

Boehler R, Von Bargen N, Chopelas A (1990) Melting, thermal expansion, and phase transitions of iron at high pressures. J Geophys Res 95:21,731-21,736

Boehler R, Musshoff HG, Ditz R, Aquilanti G, Trapananti A (2009) Portable laser-heating stand for synchrotron applications. Rev Sci Instrum 80(4):045103

Bradley JA, Moore KT, Lipp MJ, Mattern BA, Pacold JI, Seidler GT, Chow P, Rod E, Xiao Y, Evans WJ (2012) 4f electron delocalization and volume collapse in praseodymium metal. Phys Rev B 85(10):00102

Brygoo S, Henry E, Loubeyre P, Eggert J, Koenig M, Loupias B, Benuzzi-Mounaix A, Rabec Le Gloahec M (2007) Laser-shock compression of diamond and evidence of a negative-slope melting curve. Nat Mater 6(4): 274-277, doi: 10.1038/nmat1863

Buras B, Olsen JS, Gerward L (1976) X-ray energy-dispersive powder diffractometry using synchrotron radiation. Nucl Instrum Methods 135(1):193-195, doi: 10.1016/0029-554x(76)90845-4

Cainrs RJR, Ottewill RH, Osmond DWJ, Wagstraff I (1976) Studies on the preparation and properties of latices in nonpolar media. J Colloid Interface Sci 54(1):45-51

Catalli K, Shim S-H, Prakapenka VB, Zhao J, Sturhahn W (2011) X-ray diffraction and Mössbauer spectroscopy of Fe^{3+}-bearing Mg-silicate post-perovskite at 128–138 GPa. Am Mineral 95(2-3):418-421, doi: 10.2138/am.2010.3352

Celliers PM, Loubeyre P, Eggert JH, Brygoo S, Mcwilliams RS, Hicks DG, Boehly TR, Jeanloz R, Collins GW (2010) Insulator-to-conducting transition in dense fluid helium. Phys Rev Lett 104(18), doi: 10.1103/PhysRevLett.104.184503

Chapman KW, Chupas PJ, Halder GJ, Hriljac JA, Kurtz C, Greve BK, Ruschman CJ, and Wilkinson AP (2010) Optimizing high-pressure pair distribution function measurements in diamond anvil cells. J Appl Crystallogr 43: 297-307, doi: 10.1107/s0021889810002050

Chen B, Zhang D, Leng W, Jackson JM, Wang Y, Yu T, Liu J, Li J (2011) Rapid terrestrial core formation from in situ X-ray computed microtomography. American Geophysical Union, Fall Meeting 2011, abstract #MR42A-02}

Chen B, Jackson JM, Zhao J, Wicks JK, Murphy CA (2012) Spin crossover equation of state and sound velocities of $(Mg_{0.65}Fe_{0.35})O$ ferropericlase to 140 GPa. J Geophys Res 117: B08208

Chen J, Wang Y, Duffy TS, Shen G, Dobrzhinetskaya LF (2005) Advances in High-pressure Technology for Geophysical Applications. Elsevier

Coppari F, Di Ciacco A, Filipponi A, Trapananti A, Agquilanti G, De Panfilis S (2008) Local structure of liquid and undercooled liquid Cu probed by X-ray absorption spectroscopy. J Physics Conference Series 121:042009, doi: 10.1088/1742-6596/121/4/042009

Daniels WB, Ryschkewitsch MG (1983) Simple double diaphragm press for diamond anvil cells at low-temperatures. Rev Sci Instrum 54(1):115-116, doi: 10.1063/1.1137223

Deb SK, Wilding M, Somayazulu M, Mcmillan PF (2001) Pressure-induced amorphization and an amorphous-amorphous transition in densified porous silicon. Nature 414:528-530

Decker DL, Bassett WA, Merrill L, Hall HT, Barnett JD (1972) High pressure calibration: a critical review. J Phys Chem Ref Data 1:1-79

Dewaele A, Loubeyre P, Andre R, Hartwig J (2006) An X-ray topographic study of diamond anvils: Correlation between defects and helium diffusion. J Appl Phys 99(10):104906, doi: 10.1063/1.2197265

Dewaele A, Mezouar M, Guignot N, Loubeyre P (2010) High melting points of tantalum in a laser-heated diamond anvil cell. Phys Rev Lett 104(25):255701, doi: 10.1103/PhysRevLett.104.255701

Ding Y, Haskel D, Ovchinnikov SG, Tseng Y-C, Orlov YS, Lang JC, Mao HK (2008) Novel pressure-induced magnetic transition in magnetite (Fe_3O_4). Phys Rev Lett 100:045508

EBSCOhost - printed on 2/13/2023 5:26 AM via . All use subject to https://www.ebsco.com/terms-of-use

Dobson DP, Hunt SA, Mccormack R, Lord OT, Weidner DJ, Li L, Walker AM (2010) Thermal diffusivity of MORB-composition rocks to 15 GPa: implications for triggering of deep seismicity. High Pressure Res 30(3):406-414

Dubrovinsky L, Saxena SK, Tutti F, Rekhi S, and Lebehan T (2000) In situ X-Ray study of thermal expansion and phase transition of iron at multimegabar pressure. Phys Rev Lett 84(8):1720-1723

Dubrovinsky L, Glazyrin K, McCammon C, Narygina O, Greenberg E, Ubelhack S, Chumakov AI, Pascarelli S, Prakapenka V, Bock J, Dubrovinskaia N (2009) Portable laser-heating system for diamond anvil cells. J Synchrotron Radiat 16:737-741, doi: 10.1107/s0909049509039065

Dubrovinsky L, Dubrovinskaia N, Prakapenka VB, Abakumov AM (2012) Implementation of micro-ball nanodiamond anvils for high-pressure studies above 6 Mbar. Nat Commun 3:1163, doi: 10.1038/ncomms2160

Duffy TS (2005) Synchrotron facilities and the study of the Earth's deep interior. Rep Prog Phys 68:1811-1859, doi: 10.1088/0034-4885/68/8/R03

Eggert JH, Weck G, Loubeyre P, Mezouar M (2002) Quantitative structure factor and density measurements of high-pressure fluids in diamond anvil cells by X-ray diffraction: Argon and water. Phys Rev B 65:174105

Evans WJ, Yoo C-S, Lee GW, Cynn H, Lipp MJ, Visbeck K (2007) Dynamic diamond anvil cell (dDAC): A novel device for studying the dynamic-pressure properties of materials. Rev Sci Instrum 78:073904

Farber DL, Krisch M, Antonangeli D, Beraud A, Badro J, Occelli F, Orlikowski D (2006) Lattice dynamics of molybdenum at high pressure. Physl Rev Lett 96(11):115502, doi: 10.1103/PhysRevLett.96.115502

Feás X, Fente CA, Hosseini SV, Seijas JA, Vázquez BI, Franco CM, Cepeda A (2009) Use of acrylic acid in the synthesis of molecularly imprinted polymers for the analysis of cyproheptadine. Mater Sci Eng C 29:398-404, doi: 10.1016/j.msec.2008.08.011

Fei Y, Mao HK (1994) In situ determination of the NiAs phase of FeO at high pressure and high temperature. Science 266:1678-1680

Fei YW, Ricolleau A, Frank M, Mibe K, Shen GY, Prakapenka V (2007) Toward an internally consistent pressure scale. Proc Natl Acad Sci 104(22):9182-9186, doi: 10.1073/pnas.0609013104

Fiquet G, Badro J, Guyot F, Requardt H, Krisch M (2001) Sound velocities in iron to 110 gigapascals. Science 291(5503):468-471

Friedrich A, Haussuhl E, Boehler R, Morgenroth W, Juarez-Arellano EA, Winkler B (2007) Single-crystal structure refinement of diaspore at 50 GPa. Am Mineral 92(10):1640-1644, doi: 10.2138/am.2007.2549

Funakoshi K (1995) Energy-dispersive X-ray diffraction study for alkali silicate melts using synchrotron radiation under high pressure and temperature. Ph.D. Dissertation. Tokyo Institute of Technology, 117 p

Galayda JN, Arthur J, Ratner DF, White WE (2010) X-ray free-electron lasers: present and future capabilities. J Opt Soc Am B 27(11):B106-B118

Gasc J, Schubnel A, Brunet F, Guillon S, Mueller H-J, Lathe C (2011) Simultaneous acoustic emissions monitoring and synchrotron X-ray diffraction at high pressure and temperature: Calibration and application to serpentinite dehydration. Phys Earth Planet Inter 189(3–4):121-133, doi: 10.1016/j.pepi.2011.08.003

Goncharov AF (2010) X-ray diffraction in the pulsed laser heated diamond anvil cell. Rev Sci Instrum 81(11):113902

Gorria P, Martínez-Blanco D, Pérez MJ, Blanco JA, Hernando A, Laguna-Marco MA, Haskel D, Souza-Neto N, Smith RI, Marshall WG, Garbarino G, Mezouar M, Fernández-Martínez A, Chaboy J, Fernandez Barquín L, Rodriguez Castrillón JA, Moldovan M, García Alonso JI, Zhang J, Llobet A, Jiang JS (2009) Stress-induced large Curie temperature enhancement in $Fe_{64}Ni_{36}$ Invar alloy. Phys Rev B 80(6): 064421, doi: 10.1103/PhysRevB.80.064421

Gotou H, Yagi T, Frost DJ, Rubie DC (2006) Opposed-anvil-type high-pressure and high-temperature apparatus using sintered diamond. Rev Sci Instrum 77(3):035113-035116

Gotou H, Yagi T, Okada T, Iizuka R, Kikegawa T (2011) A simple opposed-anvil apparatus for high pressure and temperature experiments above 10 GPa. High Pressure Res 31(4):592-602, doi: 10.1080/08957959.2011.618130

Hartman PL (1982) Introductory remarks. Nucl Instrum Methods Phys Res 195(1–2):1-6, doi: http://dx.doi.org/10.1016/0029-554X(82)90749-2

Haskel D, Fabbris G, Souza-Neto NM, Van Veenendaal M, Shen G, Smith AE, Subramanian MA (2011) Stability of the ferromagnetic ground state of La_2MnNiO_6 against large compressive stress. Phys Rev B 84(10):100403

Heinz DL, Jeanloz R (1987) Temperature measurements in the laser heated diamond cell. *In:* High Pressure Researches in Mineral Physics. Manghnani HM, Syono Y (eds) AGU, Washington DC, p 113-127

Hemley RJ, Mao HK, Shen G, Badro J, Gillet P, Hanfland M, Häusermann D (1997) X-ray imaging of stress and strain of diamond, iron, and tungsten at megabar pressures. Science 276:1242

Hemley RJ, Mao HK, Struzhkin VV (2005) Synchrotron radiation and high pressure: new light on materials under extreme conditions. J Synchrotron Radiat 12:135-154

EBSCOhost - printed on 2/13/2023 5:26 AM via . All use subject to https://www.ebsco.com/terms-of-use

Hilairet N, Reynard B, Wang Y, Daniel I, Merkel S, Nishiyama N, Petitgirard S (2007) High-pressure creep of serpentine, interseismic deformation, and initiation of subduction. Science 318(5858):1910-1913, doi: 10.1126/science.1148494

Hilairet N, Wang Y, Sanehira T, Merkel S, Mei S (2012) Deformation of olivine under mantle conditions: An *in situ* high-pressure, high-temperature study using monochromatic synchrotron radiation. J Geophys Res B 117(1):B01203, doi: 10.1029/2011jb008498

Hirth G, Kohlstedt D (2003) Rheology of the upper mantle and the mantle wedge: A view from the experimentalists. *In:* Inside the Subduction Factory. Eiler J (ed) AGU, Washington DC, p 83-105, doi: 10.1029/138gm06

Hong X, Shen G, Prakapenka VB, Rivers ML, Sutton SR (2007) Density measurements of noncrystalline materials at high pressure with diamond anvil cell. Rev Sci Instrum 78(10):103905

Ice GE, Dera P, Liu WJ, Mao HK (2005) Adapting polychromatic X-ray microdiffraction techniques to high-pressure research: energy scan approach. J Synchrotron Radiat 12:608-617, doi: 10.1107/s0909049505024684

Ice GE, Pang JWL (2009) Tutorial on X-ray microLaue diffraction. Mater Charact 60(11):1191-1201, doi: 10.1016/j.matchar.2009.07.006

Ingalls R, Garcia GA, Stern EA (1978) X-ray absorption at high-pressure. Phys Rev Lett 40(5):334-336, doi: 10.1103/PhysRevLett.40.334

Iota V, Klepeis JHP, Yoo CS, Lang J, Haskel D, Srajer G (2007) Electronic structure and magnetism in compressed 3d transition metals. Appl Phys Lett 90(4):042505, doi: 10.1063/1.2434184

Irifune T, Kurio A, Sakamoto S, Inoue T, Sumiya H (2003) Ultrahard polycrystalline diamond from graphite. Nature 421: 599-600

Ishimatsu N, Matsumoto K, Maruyama H, Kawamura N, Mizumaki M, Sumiya H, Irifune T (2012) Glitch-free X-ray absorption spectrum under high pressure obtained using nano-polycrystalline diamond anvils. J Synchrotron Radiat 19(5):768-772, doi: doi: 10.1107/S0909049512026088

Ito E, Katsura T, Yamazaki D, Yoneda A, Tado M, Ochi T, Nishibara E, Nakamura A (2009) A new 6-axis apparatus to squeeze the Kawai-cell of sintered diamond cubes. Phys Earth Planet Inter 174(1-4):264-269, doi: 10.1016/j.pepi.2008.11.007

Ito E, Yamazaki D, Yoshino T, Fukui H, Zhai S, Shatzkiy A, Katsura T, Tange Y, Funakoshi K-I (2010) Pressure generation and investigation of the post-perovskite transformation in $MgGeO_3$ by squeezing the Kawai-cell equipped with sintered diamond anvils. Earth Planet Science Lett 293(1-2):84-89, doi: 10.1016/j.epsl.2010.02.023

Jackson DD, Aracne-Ruddle C, Malba V, Weir ST, Catledge SA, Vohra YK (2003) Magnetic susceptibility measurements at high pressure using designer diamond anvils. Rev Sci Instrum 74:2467-2471

Jackson JM, Sturhahn W, Lerche M, Zhao J, Toellner TS, Alp EE, Sinogeikin S, Bass JD, Murphy CA, Wicks JK (2013) Melting of compressed iron by monitoring atomic dynamics. Earth Planet Sci Lett 362:143-150

Jackson JM, Sturhahn W, Shen GY, Zhao JY, Hu MY, Errandonea D, Bass JD, Fei YW (2005) A synchrotron Mossbauer spectroscopy study of (Mg,Fe)SiO_3 perovskite up to 120 GPa. Am Mineral 90(1): 199-205, doi: 10.2138/am.2005.1633

Jensen BJ, Luo SN, Hooks DE, Fezzaa K, Ramos KJ, Yeager JD, Kwiatkowski K, Shimada T, Dattelbaum DM (2012) Ultrafast, high resolution, phase contrast imaging of impact response with synchrotron radiation. AIP Advances 2(1):012170

Kanzaki M, Kurita K, Fujii T, Kato T, Shimomura O, Akimoto S (1987) A new technique to measure the viscosity and density of silicate melts at high pressure. *In:* High-pressure Research in Mineral Physics. Manghnani MH, Syono Y (eds) Terrapub/AGU, Tokyo, p 195-200

Katayama Y, Mizutani T, Utsumi W, Shimomura O, Yamakata M, Funakoshi K-I (2000) A first order liquid-liquid phase transition in phosphorus. Nature 403:170-173

Katayama Y, Tsuji K, Nosaka H, Yaoita K, Kikegawa T, Shimomura O (1996) Density of liquid tellurium under pressure. J Non-Cryst Solids 205:451-454

Kawazoe T, Nishihara Y, Ohuchi T, Nishiyama N, Higo Y, Funakoshi K-I, Irifune T (2011) In situ stress-strain measurements in a deformation-DIA apparatus at P-T conditions of the upper part of the mantle transition zone. Am Mineral 96(11-12):1665-1672, doi: 10.2138/am.2011.3818

Khvostantsev LG, Vereshchagin LF, Novikov AP (1977) Device of toroid type for high pressure generation. High Temp High Pressure 9:637-639

Komabayashi T, Fei YW (2010) Internally consistent thermodynamic database for iron to the Earth's core conditions. J Geophys Res-Solid Earth 115:B03202, doi: 10.1029/2009jb006442

Kono Y, Irifune T, Higo Y, Inoue T, Barnhoorn A (2009) P-V-T relation of MgO derived by simultaneous elastic wave velocity and *in situ* X-ray measurements: A new pressure scale for the mantle transition region. Phys Earth Planet Inter 183:196-211

Kono Y, Kenney-Benson C, Park C, Shen G, Wang Y (2013) Anomaly in the viscosity of liquid KCl at high pressures. Phys Rev B 87(2):024302

EBSCOhost - printed on 2/13/2023 5:26 AM via . All use subject to https://www.ebsco.com/terms-of-use

Kubo A, Wang Y, Runge CE, Uchida T, Kiefer B, Nishiyama N, Duffy TS (2008) Melting curve of silicon to 15 GPa determined by two-dimensional angle-dispersive diffraction using a Kawai-type apparatus with X-ray transparent sintered diamond anvils. J Phys Chem Solids 69(9):2255-2260

Kubo T, Ohtani E, Kato T, Urakawa S, Suzuki A, Kanbe Y, Funakoshi K, Utsumi W, Kikegawa T, Fujino K (2002) Mechanisms and kinetics of the post-spinel transformation in Mg_2SiO_4. Phys Earth Planet Inter 129:153-171

Kunimoto T, Irifune T (2010) Pressure generation to 125 GPa using a 6-8-2 type multianvil apparatus with nano-polycrystalline diamond anvils. J Phys Conf Series 215(1):012190

Lavina B, Dera P, Downs RT (2014) Modern X-ray diffraction methods in mineralogy and geosciences. Rev Mineral Geochem 78:1-31

Lavina B, Dera P, Downs RT, Yang WG, Sinogeikin S, Meng Y, Shen GY, Schiferl D (2010) Structure of siderite $FeCO_3$ to 56 GPa and hysteresis of its spin-pairing transition. Phys Rev B 82(6):064110, doi: 10.1103/PhysRevB.82.064110

Le Bolloch D, Itie JP, Polian A, Ravy S (2009) Combining high pressure and coherent diffraction: a first feasibility test. High Pressure Res 29:635-638

Lee KKM, Benedetti LR, Jeanloz R, Celliers PM, Eggert JH, Hicks DG, Moon SJ, Mackinnon A, Da Silva LB, Bradley DK, Unites W, Collins GW, Henry E, Koenig M, Benuzzi-Mounaix A, Pasley J, Neely D (2006) Laser-driven shock experiments on precompressed water: Implications for "icy" giant planets. J Chem Phys 125(1):014701, doi: 10.1063/1.2207618

Lee SK, Eng PJ, Mao HK, Shu JF (2008) Probing and modeling of pressure-induced coordination transformation in borate glasses: Inelastic X-ray scattering study at high pressure. Phys Rev B 78(21):214203, doi: 10.1103/PhysRevB.78.214203

Lesher CE, Wang Y, Gaudio S, Clark A, Nishiyama N, Rivers M (2009) Volumetric properties of magnesium silicate glasses and supercooled liquid at high pressure by X-ray microtomography, Phys Earth Planet Inter 174(1-4):292-301

Li B, Liebermann RC (2007) Indoor seismology by probing the Earth's interior by using sound velocity measurements at high pressures and temperatures. Proc Natl Acad Sciences 104(22):9145-9150, doi: 10.1073/pnas.0608609104

Li L, Weidner DJ (2008) Effect of phase transitions on bulk dispersion and attenuation: implications for the Earth. Nature 454:984-986

Li L, Weidner DJ (2010) Synchronized stress-strain measurements in dynamic loading at high pressure using D-DIA. Rev Sci Instrum 81:473-477

Li B, Kung J, Liebermann RC (2004a) Modern techniques in measuring elasticity of Earth materials at high pressure and high temperature using ultrasonic interferometry in conjunction with synchrotron X-radiation in multi-anvil apparatus. Phys Earth Planet Inter 143-144:559-574

Li J, Struzhkin VV, Mao H-K, Shu J, Hemley RJ, Fei Y, Mysen B, Dera P, Prakapenka V, Shen G (2004b) Electronic spin state of iron in lower mantle perovskite. Proc Natl Acad Sci 101(39):14027-14030, doi: 10.1073/pnas.0405804101

Lin J-F, Fei Y, Sturhahn W, Zhao J, Mao H-K, Hemley RJ (2004) Magnetic transition and sound velocities of Fe3S at high pressure: implications for Earth and planetary cores. Earth Planet Sci Lett 226(1-2):33-40

Lin J-F, Struzhkin VV, Jacobsen SD, Hu MY, Chow P, Kung J, Liu H, Mao H-K, Hemley RJ (2005a) Spin transition of iron in magnesiowüstite in the Earth's lower mantle. Nature 436(7049):377-380

Lin J-F, Sturhahn W, Zhao J, Shen G, Mao HK, Hemley RJ (2005b) Sound velocities of hot dense iron: Birch's law revisited. Science 308:1892-1894

Lin Y, Zhang L, Mao H-K, Chow P, Xiao Y, Baldini M, Shu J, and Mao WL (2011) Amorphous diamond: a high-pressure superhard carbon allotrope. Phys Rev Lett 107(17):175504

Lin J-F, Alp EE, Mao Z, Inoue T, Mccammon C, Xiao Y, Chow P, Zhao J (2012) Electronic spin states of ferric and ferrous iron in the lower-mantle silicate perovskite. Am Mineral 97(4):592-597, doi: 10.2138/am.2012.4000

Loubeyre P, Celliers PM, Hicks DG, Henry E, Dewaele A, Pasley J, Eggert J, Koenig M, Occelli F, Lee KM, Jeanloz R, Neely D, Benuzzi-Mounaix A, Bradley D, Bastea M, Moon S, Collins GW (2004) Coupling static and dynamic compressions: First measurements in dense hydrogen. High Pressure Res 24(1):25-31, doi: 10.1080/08957950310001635792

Loubeyre P, Letoullec R, Hausermann D, Hanfland M, Hemley RJ, Mao HK, Finger LW (1996) X-ray diffraction and equation of state of hydrogen at megabar pressures. Nature 383(6602):702-704

Lübbers R, Grünsteudel HF, Chumakov AI, Wortmann G (2000) Density of phonon states in iron at high pressure. Science 287(5456):1250-1253, doi: 10.1126/science.287.5456.1250

Luo SN, Jensen BJ, Hooks DE, Fezzaa K, Ramos KJ, Yeager JD, Kwiatkowski K, Shimada T (2012) Gas gun shock experiments with single-pulse X-ray phase contrast imaging and diffraction at the Advanced Photon Source. Rev Sci Instrum 83(7):073903

EBSCOhost - printed on 2/13/2023 5:26 AM via . All use subject to https://www.ebsco.com/terms-of-use

Maddox BR (2006) Pressure-Induced Electronic Phase Transitions in Transition Metal Oxides and Rare Earth Metals. Ph.D. Dissertation. University of California at Davis, Davis, CA, 165 p

Manthilake MaGM, Walte N, Frost DJ (2012) A new multi-anvil press employing six independently acting 8 MN hydraulic rams. High Pressure Res 32(2):195-207, doi: 10.1080/08957959.2012.680450

Mao HK, Xu J, Bell PM (1986) Calibration of the ruby pressure gauge to 800 kbar under quasi-hydrostatic conditions. J Geophys Res 91:4673-4676

Mao HK, Jephcoat AP, Hemley RJ, Finger LW, Zha C-S, Hazen RM, Cox DE (1988) Synchrotron X-ray diffraction measurements of single-crystal hydrogen to 26.5 Gigapascals. Science 239:1131-1134

Mao HK, Wu Y, Chen LC, Shu JF, Jephcoat AP (1990) Static compression of iron to 300 GPa and Fe0.8Ni0.2 alloy to 260 GPa: implications for composition of the core. J Geophys Res 95:21737-21742

Mao HK, Struzhkin VV, Hemley RJ, Kao CC (1997) Synchrotron X-ray spectroscopy at ultrahigh pressures. EOS, Trans Am Geophys Union 78:F774

Mao HK, Shen G, Hemley RJ, Duffy TS (1998a) X-ray diffraction with a double hot plate laser heated diamond cell. *In*: Properties of Earth and Planetary Materials. Manghnani MH, Yagi T (eds) AGU, Washington DC, p 27-34

Mao HK, Shu J, Shen G, Hemley RJ, Li B, Singh AK (1998b) Elasticity and rheology of iron above 200 GPa and the nature of the Earth's inner core. Nature 396:741-743

Mao HK, Xu J, Struzhkin VV, Shu J, Hemley RJ, Sturhahn W, Hu MY, Alp EE, Vocadlo L, Alfè D, Price GD, Gillan MJ, Schwoerer-Böhning M, Häusermann D, Eng P, Shen G, Giefers H, Lübbers R, Wortmann D (2001) Phonon density of states of iron up to 153 Gigapascals. Science 292:914-916

Mao WL, Mao HK, Eng PJ, Trainor TP, Newville M, Kao CC, Heinz DJ, Shu JF, Meng Y, Hemley RJ (2003) Bonding changes in compressed superhard graphite. Science 302:425-427

Mao HK, Shirley EL, Ding Y, Eng P, Cai YQ, Chow P, Xiao Y, Shu J, Hemley RJ, Kao C, Mao WL (2010) Electronic structure of crystalline ^{4}He at high pressures. Phys Rev Lett 105(18):186404, doi: 10.1103/PhysRevLett.105.186404

Mayanovic RA, Anderson AJ, Bassett WA, Chou IM (2007a) Synchrotron X-ray spectroscopy of Eu/HNO_3 aqueous solutions at high temperatures and pressures and Nb-bearing silicate melt phases coexisting with hydrothermal fluids using a modified hydrothermal diamond anvil cell and rail assembly. Rev Sci Instrum 78(5) doi:10.1063/1.2737748

Mayanovic RA, Anderson AJ, Bassett WA, Chou IM (2007b) Synchrotron X-ray spectroscopy of Eu/HNO_3 aqueous solutions at high temperatures and pressures and Nb-bearing silicate melt phases coexisting with hydrothermal fluids using a modified hydrothermal diamond anvil cell and rail assembly. Rev Sci Instrum 78(5):053904

Mckelvy MJ, Chizmeshya AVG, Diefenbacher J, Béarat H, Wolf G (2004) Exploration of the role of heat activation in enhancing serpentine carbon sequestration reactions. Environ Sci Technol 38:6897-6903

Mei Q, Sinogeikin S, Shen G, Amin S, Benmore CJ, Ding K (2010) High-pressure X-ray diffraction measurements on vitreous GeO_2 under hydrostatic conditions. Phys Rev B 81(17):174113, doi: 10.1103/PhysRevB.81.174113

Meng Y, Weidner DJ, Fei Y (1993) Deviatoric stress in a quasi-hydrostatic diamond anvil cell: effect on the volume based pressure calibration. Geophys Res Lett 20:1147-1149

Merkel S, Kubo A, Miyagi L, Speziale S, Duffy TS, Mao H-K, Wenk H-R (2006) Plastic deformation of $MgGeO_3$ post-perovskite at lower mantle pressures. Science 311(5761):644-646, doi: 10.1126/science.1121808

Mezouar M (2002) Multichannel collimator for structural investigation of liquids and amorphous materials at high pressures and temperatures. Rev Sci Instrum 73(10):3570

Mezouar M (2010) Synchrotron high-pressure high-temperature techniques. *In:* High-Pressure Crystallography. Boldyreva E, Dera P (eds) Springer Netherlands, p 23-33, doi: 10.1007/978-90-481-9258-8_3

Mezouar M, Faure P, Crichton W, Rambert N, Sitaud B, Bauchau S, Blattmann G (2002) Multichannel collimator for structural investigation of liquids and amorphous materials at high pressures and temperatures. Rev Sci Instrum 73:3570-3574

Mills DM (2002) Third-Generation Hard X-ray Synchotron Radiation Sources. John Wiley & Sons, Inc., New York

Ming LC, Bassett WA (1974) Laser heating in the diamond anvil press up to 2000 °C sustained and 3000 °C pulsed at pressures up to 260 kilobars. Rev Sci Instrum 9:1115-1118

Miyagi L, Kanitpanyacharoen W, Kaercher P, Lee KKM, Wenk HR (2010) Slip systems in $MgSiO_3$ post-perovskite: implications for D'' anisotropy. Science 329(5999):1639-1641, doi: 10.1126/science.1192465

Morard G (2011) High efficiency multichannel collimator for structural studies of liquids and low-Z materials at high pressures and temperatures. Rev Sci Instrum 82(2):023904

Morard G, Mezouar M, Rey N, Poloni R, Merlen A, Le Floch S, Toulemonde P, Pascarelli S, San-Miguel A, Sanloup C, Fiquet G (2007a) Optimization of Paris–Edinburgh press cell assemblies for *in situ* monochromatic X-ray diffraction and X-ray absorption. High Pressure Res 27(2):223-233

Morard G, Sanloup C, Fiquet G, Mezouar M, Rey N, Poloni R, Beck P (2007b) Structure of eutectic Fe-FeS melts to pressures up to 17 GPa: Implications for planetary cores. Earth Planet Sci Lett 263(1-2):128-139

EBSCOhost - printed on 2/13/2023 5:26 AM via . All use subject to https://www.ebsco.com/terms-of-use

Morard G, Sanloup C, Guillot B, Fiquet G, Mezouar M, Perrillat JP, Garbarino G, Mibe K, Komabayashi T, Funakoshi K (2008) In situ structural investigation of Fe-S-Si immiscible liquid system and evolution of Fe-S bond properties with pressure. J Geophys Res 113, doi: 10.1029/2008jb005663

Murphy CA, Jackson JM, Sturhahn W, Chen B (2011a) Grüneisen parameter of hcp-Fe to 171 GPa. Geophys Res Lett 38(24):L24306, doi: 10.1029/2011gl049531

Murphy CA, Jackson JM, Sturhahn W, Chen B (2011b) Melting and thermal pressure of hcp-Fe from the phonon density of states. Phys Earth Planet Inter 188(1–2):114-120, doi: 10.1016/j.pepi.2011.07.001

Nasu S (1996) High pressure Mossbauer spectroscopy with nuclear forward scattering of synchrotron radiation. High Pressure Res 14:405-412

Nishiyama N, Wang Y, Irifune T, Sanehira T, Rivers ML, Sutton SR, Cookson D (2009) A combination of a Drickamer anvil apparatus and monochromatic X-rays for stress and strain measurements under high pressure. J Synchrotron Radiat 16(6):742-747, doi: 10.1107/S0909049509033342

Nishiyama N, Wang Y, Rivers ML, Sutton SR, Cookson D (2007) Rheology of ε-iron up to 19 GPa and 600 K in the D-DIA. Geophys Res Lett 34, doi: 10.1029/2007gl031431

Ohtani E (1979) Melting relation of Fe_2SiO_4 up to about 200 kbar. J Phys Earth 27:189-208

Ohtani E, Kagawa N, Shimomura O, Togaya M, Suito K, Onodera A, Sawamoto H, Yoneda M, Tanaka S, Utsumi W, Ito E, Matsumuro A, Kikegawa T (1989) High pressure generation by a multiple anvil system with sintered diamond anvils. Rev Sci Instrum 60:922-925

Ohuchi T, Kawazoe T, Nishiyama N, Nishihara Y, Irifune T (2010) Technical development of simple shear deformation experiments using a deformation-DIA aparatus. J Earth Sci 21:523-531, doi: 10.1007/s12583-010-0110-4

Osugi J, Shimizu K, Inoue K, Yasunami K (1964) A compact cubic anvil high pressure apparatus. Rev Phys Chem Jpn 34:1-6

Pacold JI, Bradley JA, Mattern BA, Lipp MJ, Seidler GT, Chow P, Xiao X, Rusthoven B, Quintana J (2012) A miniature X-ray emission spectrometer (miniXES) for high pressure studies in a diamond anvil cell. J Synchroton Radiat 19:245-251

Pascarelli S, Mathon O (2010) Advances in high brilliance energy dispersive X-ray absorption spectroscopy. Phys Chem Chem Phys 12(21):5535-5546, doi: 10.1039/b926509k

Petitgirard S, Daniel I, Dabin Y, Cardon H, Tucoulou R, Susini J (2009) A diamond anvil cell for X-ray fluorescence measurements of trace elements in fluids at high pressure and high temperature. Rev Sci Instrum 80(3):033906

Pfeifer MA, Williams GJ, Vartanyants IA, Harder R, Robinson IK (2006) Three-dimensional mapping of a deformation field inside a nanocrystal. Nature 442(7098):63-66

Pinceaux J-P, Maury J-P, Besson J-M (1979) Solidification of helium, at room temperature under high pressure. J Phys Lett 40(13):307-308

Ping Y, Landen OL, Hicks DG, Koch JA, Wallace R, Sorce C, Hammel BA, Collins GW (2011) Refraction-enhanced X-ray radiography for density profile measurements at CH/Be interface. J Instrum 6:P09004, doi: 10.1088/1748-0221/6/09/p09004

Rietveld HM (1966) A method for including line profiles of neutron powder diffraction peaks in determination of crystal structures. Acta Crystallogr S 21:A228

Rueff J-P (2010) An introduction to inelastic X-ray scattering. *In:* Magnetism and Synchrotron Radiation. Springer Proceedings in Physics, Volume 133. Beaurepaire E, Bulou H, Scheurer F, Jean-Paul K (eds) Springer-Verlag, Berlin, Heidelberg, p 263-277

Rueff J-P, Kao CC, Struzhkin VV, Badro J, Shu J, Hemley RJ, Mao HK (1999) Pressure-induced high-spin to low-spin transition in FeS evidenced by X-ray emission spectroscopy. Phys Rev Lett 82:3284-3287

Rutter MD, Secco RA, Uchida T, Liu HJ, Rivers ML, Sutton SR, Wang Y (2002) Viscosity of liquid Fe at high pressure. Phys Rev B 66:060102

Sakamaki T, Wang Y, Park C, Yu T, Shen G (2012) Structure of jadeite melt at high pressures up to 4.9 GPa. J Appl Phys 111(11):112623

Schell N, Simmons RO, Kaprolat A, Schulke W, Burkel E (1995) Electronic excitations in hcp He at 61.5 MPa and 4.3 K studied by inelastic X-ray-scattering spectroscopy. Phys Rev Lett 74(13):2535-2538, doi: 10.1103/PhysRevLett.74.2535

Schmidt C, Rickers K (2003) In-situ determination of mineral solubilities in fluids using a hydrothermal diamond-anvil cell and SR-XRF: Solubility of AgCl in water. Am Mineral 88(2-3):288-292

Schmidt C, Rickers K, Bilderback DH, Huang R (2007) In situ synchrotron-radiation XRF study of REE phosphate dissolution in aqueous fluids to 800 degrees C. Lithos 95(1-2):87-102, doi: 10.1016/j.lithos.2006.07.017

Schubnel A, Brunet F, Hilairet N, Gasc J, Wang Y, Green Ii HW (2013) Deep focus earthquake analogs recorded at high pressure and temperature in the laboratory. Science 341:1377-1380, doi: 10.1126/science.1240206

Seal M (1963) The effect of surface orientation on the graphitization of diamond. Phys Status Solidi B 3(4):658-664, doi: 10.1002/pssb.19630030408

EBSCOhost - printed on 2/13/2023 5:26 AM via . All use subject to https://www.ebsco.com/terms-of-use

Shen G, Mao HK, Hemley RJ (1996) Laser-heating diamnd-anvil cell technique: Double-sided heating with multimode Nd:YAG laser. Presented at Advanced Materials '96 - New Trends in High Pressure Research, NIRIM, NIRIM, Tsukuba, Japan. *http://www.hpcat.aps.anl.gov/shen/publication/shen-Japan96.pdf* (accessed August 1, 2013)

Shen G, Rivers ML, Wang Y, Sutton SJ (2001) A laser heated diamond cell system at the Advanced Photon Source for *in situ* X-ray measurements at high pressure and temperature. Rev Sci Instrum 72:1273-1282

Shen G, Sata N, Newville M, Rivers ML, Sutton SR (2002) Molar volumes of molten indium at high pressures measured in a diamond anvil cell. Appl Phys Lett 81(8):1411-1413

Shen G, Prakapenka VB, Rivers ML, Sutton SR (2003) Structural investigation of amorphous materials at high pressures using the diamond anvil cell. Rev Sci Instrum 74:3021-3026

Shen G, Chowa P, Xiaoa Y, Sinogeikina S, Menga Y, Yanga W, Liermanna H-P, Shebanovaa O, Roda E, Bommannavara A, Maoa H-K (2008) HPCAT: an integrated high-pressure synchrotron facility at the Advanced Photon Source. High Pressure Res 28:145-162

Shen G, Wang L, Ferry R, Mao HK, Hemley RJ (2010) A portable laser heating microscope for high pressure research. J Phys 215:012191

Shim S-H, Bengtson A, Morgan D, Sturhahn W, Catalli K, Zhao J, Lerche M, Prakapenka V (2009) Electronic and magnetic structures of the postperovskite-type Fe_2O_3 and implications for planetary magnetic records and deep interiors. Proc Natl Acad Sci 106(14):5508-5512, doi: 10.1073/pnas.0808549106

Shimomura O, Utsumi W, Taniguchi T, Kikegawa T, Nagashima T (1992) A new high pressure and high temperature apparatus with sintered diamond anvils for synchrotron radiation use. *In:* High-Pressure Research: Application to Earth and Planetary Sciences. Syono Y, Manghnani MH (eds) Terra Scientific Co., Tokyo, p 3-11

Shukla A, Rueff JP, Badro J, Vanko G, Mattila A, De Groot FMF, Sette F (2003) Charge transfer at very high pressure in NiO. Phys Rev B 67(8), doi: 10.1103/PhysRevB.67.081101

Sinogeikin S, Bass J, Prakapenka V, Lakshtanov D, Shen GY, Sanchez-Valle C, Rivers M (2006) Brillouin spectrometer interfaced with synchrotron radiation for simultaneous X-ray density and acoustic velocity measurements. Rev Sci Instrum 77(10):103905, doi: 10.1063/1.2360884

Skelton EF, Kirkland J, Qadri SB (1982) Energy-dispersive measurements of diffracted synchrotron radiation as a function of pressure: applications to phase transitions in KCl and KI. J Appl Crystallogr 15(1):82-88, doi: 10.1107/S002188988201139X

Smith RF, Pollaine SM, Moon SJ, Lorenz KT, Celliers PM, Eggert JH, Park HS, Collins GW (2007) High planarity X-ray drive for ultrafast shockless-compression experiments. Phys Plasmas 14(5):057105, doi: 10.1063/1.2712450

Soignard E, Benmore CJ, Yarger JL (2010) A perforated diamond anvil cell for high-energy X-ray diffraction of liquids and amorphous solids at high pressure. Rev Sci Instrum 81(3):035110, doi: 10.1063/1.3356977

Souza-Neto NM, Zhao J, Alp EE, Shen G, Sinogeikin SV, Lapertot G, Haskel D (2012) Reentrant valence transition in EuO at high pressures: beyond the bond-valence model. Phys Rev Lett 109(2):026403

Speziale S, Milner A, Lee VE, Clark SM, Pasternak MP, Jeanloz R (2005) Iron spin transition in Earth's mantle. Proc Natl Acad Sci USA 102(50):17918-17922, doi: 10.1073/pnas.0508919102

Struzhkin VV, Mao HK, Lin J-F, Hemley RJ, Tse JS, Ma Y, Hu MY, Chow P, Kao C-C (2006) Valence band X-ray emission spectra of compressed germanium. Phys Rev Lett 96:137402

Sturhahn W (2004) Nuclear resonant scattering. J Phys Condens Matter 16:S497-S530

Suggit M, Kimminau G, Hawreliak J, Remington B, Park N, Wark J (2010) Nanosecond X-ray Laue diffraction apparatus suitable for laser shock compression experiments. Rev Sci Instrum 81(8):083902, doi: 10.1063/1.3455211

Takemura K (2001) Evaluation of the hydrostaticity of a helium pressure medium with powder X-ray diffraction techniques. J Appl Phys 89:662-668

Tange Y, Irifune T, Funakoshi K-I (2008) Pressure generation to 80 GPa using multianvil apparatus with sintered diamond anvils. High Pressure Res 28(3):245-254

Tanis EA, Simon A, Tschauner O, Chow P, Xiao Y, Shen G, Hanchar JM, Frank M (2012) Solubility of xenotime in a 2 M HCl aqueous fluid from 1.2 to 2.6 GPa and 300 to 500 °C. Am Mineral 97(10):1708-1713, doi: 10.2138/am.2012.4009

Terasaki H, Urakawa S, Funakoshi K-I, Wang Y, Shibazaki Y, Sanehira T, Ueda Y, Ohtani E (2008) Interfacial tension measurement of Ni-S liquid using high-pressure X-ray micro-tomography. High Pressure Res 28(3):327-334

Tsuji K, Yaoita K, Imai M, Shimomura O, Kikegawa T (1989) Measurements of X-ray diffraction for liquid metals under high pressure. Rev Sci Instrum 60(7):2425-2428

Turneaure SJ, Gupta YM, Zimmerman K, Perkins K, Yoo CS, Shen G (2009) Real-time microstructure of shocked LiF crystals: Use of synchrotron X-rays. J Appl Phys 105(5):053520

Uchida T, Wang Y, Nishiyama N, Funakoshi K-I, Kaneko H, Nozawa A, Von Dreele RB, Rivers ML, Sutton SR, Yamada A, Kunimoto T, Irifune T, Inoue T, Li B (2009) Non-cubic crystal symmetry of $CaSiO_3$ perovskite up to 18 GPa and 1600 K. Earth Planet Sci Lett 282(1-4):268-274

EBSCOhost - printed on 2/13/2023 5:26 AM via . All use subject to https://www.ebsco.com/terms-of-use

Uhoya W, Tsoi G, Vohra Y, Wolanyk N, Rao SM, Wu M-K, Weir S (2012) Simultaneous measurement of pressure evolution of crystal structure and superconductivity in FeSe 0.92 using designer diamonds. Europhys Lett 99(2):26002

Urakawa S, Terasaki H, Funakoshi K, Uesugi K, Yamamoto S (2010) Development of high pressure apparatus for X-ray microtomography at SPring-8. J Phys Conf Ser 215(1):012026

Utsumi W, Funakoshi K, Urakawa S, Yamakata M, Tsuji K, Konishi H, Shimomura O (1998) SPring-8 beamlines for high pressure science with multi-anvil apparatus. Rev High Pressure Sci Technol 7:1484-1490

Vaughan MT (1993) In situ X-ray diffraction using synchrotron radiation at high P and T in a multi-anvil device. *In:* Experiments at High Pressure and Applications to the Earth's Mantle, Short Course Handbook. Luth RW (ed) Mineralogical Association of Canada, Edmonton, Canada, p 95-130

Wang Y (2010) Large volume presses for high-pressure studies using synchrotron radiation. *In:* High-Pressure Crystallography. Boldyreva E, Dera P (eds) Springer Netherlands, p 81-96, doi: 10.1007/978-90-481-9258-8_8

Wang Y, Shen G, Rivers M, Sutton S (1998) A multi-anvil high pressure system with synchrotron X-ray probe: New opportunities for in-situ materials research at simultaneously high pressure and temperature. MRS Proceedings 499, http://dx.doi.org/10.1557/PROC-499-289

Wang Y, Rivers M, Uchida T, Murray P, Shen G, Sutton S, Chen J, Xu Y, Weidner D (2000) High pressure research using large-volume presses at GeoSoilEnviroCARS, Advanced Photon Source. AIRAPT-17:1047-1052

Wang Y, Shen G, Rivers M (2002a) High pressure research in third generation synchrotron sources. *In:* Third Generation Synchrotron Sources. Mills D (ed) Wiley and Son, New York, p 203-235

Wang Y, Shen G, Rivers ML (2002b) High pressure research techniques at third generation synchrotron radiation sources. *In:* Third-generation Hard X-ray Synchrotron Radiation Sources. Mills DM (ed) John Wiley & Sons, New York, p 203-236

Wang Y, Durham WB, Getting IC, Weidner DJ (2003) The deformation-DIA: A new apparatus for high temperature triaxial deformation to pressures up to 15 GPa. Rev Sci Instrum 74:3002-3011

Wang Y, Uchida T, Von Dreele RB, Rivers ML, Nishiyama N, Funakoshi K, Nozawa A, Kaneko H (2004) A new technique for angle-dispersive powder diffraction using an energy-dispersive setup and synchrotron radiation. J Appl Crystallogr 37(6):947-956, doi: 10.1107/S0021889804022502

Wang Y, Uchida T, Westferro F, Rivers ML, Nishiyama N, Gebhardt J, Lesher CE, Sutton SR (2005a) High-pressure X-ray tomography microscope: Synchrotron computed microtomography at high pressure and temperature. Rev Sci Instrum 76(7):073709

Wang Y, Uchida T, Westferro F, Rivers ML, Nishiyama N, Gebhardt J, Lesher CE, Sutton SR (2005b) High-pressure x-ray tomography microscope: synchrotron computed microtomography at high pressure and temperature. Rev Sci Instrum 40(21):5763-5766, doi: 10.1007/s10853-005-2476-8

Wang Y, Rivers M, Sutton S, Nishiyama N, Uchida T, Sanehira T (2009) The large-volume high-pressure facility at GSECARS: A "Swiss-army-knife" approach to synchrotron-based experimental studies. Phys Earth Planet Inter 174(1-4): 270-281

Wang S, Mao WL, Sorini AP, Chen C-C, Devereaux TP, Ding Y, Xiao Y, Chow P, Hiraoka N, Ishii H, Cai YQ, Kao C-C (2010a) High-pressure evolution of Fe_2O_3 electronic structure revealed by X-ray absorption. Phys Rev B 82(14):144428

Wang Y, Jing Z, Hilairet N, Yu T, Nishiyama N, Tange Y, Sakammaki T, Rivers M, Sutton S (2010b) DDIA-30: a versatile megabar mutlianvil device for in-situ high pressure studies with white and monochromatic synchrotron radiation. Eos Trans AGU: MR13A-1908

Wang Y, Lesher C, Fiquet G, Rivers ML, Nishiyama N, Siebert J, Roberts J, Morard G, Gaudio S, Clark A, Watson H, Menguy N, Guyot F (2011) In situ high-pressure and high-temperature X-ray microtomographic imaging during large deformation: A new technique for studying mechanical behavior of multiphase composites. Geosphere 7(1):40-53, doi: 10.1130/ges00560.1

Wang J, Yang W, Wang S, Xiao X, De Carlo F, Liu Y, Mao WL (2012) High pressure nano-tomography using an iterative method. J Appl Phys 111(11):112626-112625

Wenk HR, Ischia G, Nishiyama N, Wang Y, Uchida T (2005) Texture development and deformation mechanisms in ringwoodite. Phys Earth Planet Inter 152(3):191-199

Wenk HR, Lonardelli I, Pehl J, Devine J, Prakapenka V, Shen G, Mao HK (2004) In situ observation of texture development in olivine, ringwoodite, magnesiowustite and silicate perovskite at high pressure. Earth Planet Sci Lett 226(3-4):507-519, doi: 10.1016/j.epsl.2004.07.033

Wenk HR, Matthies S, Hemley RJ, Mao HK, Shu JF (2000) The plastic deformation of iron at pressures of the Earth's inner core. Nature 405:1044-1047

Wicks JK, Jackson JM, Sturhahn W (2010) Very low sound velocities in iron-rich (Mg,Fe)O: Implications for the core-mantle boundary region. Geophys Res Lett 37(15):L15304, doi: 10.1029/2010gl043689

Wilding MC, Wilson M, Mcmillan PF (2006) Structural studies and polymorphism in amorphous solids and liquids at high pressure. Chem Soc Rev 35(10):964-986

EBSCOhost - printed on 2/13/2023 5:26 AM via . All use subject to https://www.ebsco.com/terms-of-use

Wilke M, Appel K, Vincze L, Schmidt C, Borchert M, Pascarelli S (2010) A confocal set-up for micro-XRF and XAFS experiments using diamond-anvil cells. J Synchrotron Radiat 17:669-675, doi: 10.1107/s0909049510023654

Yamada A, Wang YB, Inoue T, Yang WG, Park C, Yu T, Shen GY (2011) High-pressure X-ray diffraction studies on the structure of liquid silicate using a Paris-Edinburgh type large volume press. Rev Sci Instrum 82(1):015103, doi: 10.1063/1.3514087

Yamanaka T, Ogata K (1991) Structure refinement of GeO_2 polymorphs at high pressures and temperatures by energy-dispersive spectra of powder diffraction. J Appl Crystallogr 24:111-118

Yamazaki D, Karato S (2001) High pressure rotational deformation apparatus to 15 GPa. Rev Sci Instrum 72:4207-4211

Yang W, Huang X, Harder R, Clark JN, Robinson IK, Mao H-K (2013) Coherent diffraction imaging of nanoscale strain evolution in a single crystal under high pressure. Nat Commun 4:1680, doi: 10.1038/ncomms2661

Yaoita K (1997) Angle-dispersive diffraction measurement system for high-pressure experiments using a multichannel collimator. Rev Sci Instrum 68(5):2106-2110

Yoo CS, Wei H, Chen JY, Shen G, Chow P, Xiao X (2011) Time- and angle-resolved X-ray diffraction to probe structural and chemical evolution during Al-Ni intermetallic reactions. Rev Sci Instrum 82:113901-113906

Yoshiasa A, Nagai T, Ohtaka O, Kamishima O, Shimomura O (1999) Pressure and temperature dependence of EXAFS Debye-Waller factors in diamond-type and white-tin-type germanium. J Synchrotron Radiat 6(1):43-49, doi: doi: 10.1107/S0909049598011947

Zeng Q, Ding Y, Mao WL, Yang W, Sinogeikin SV, Shu J, Mao H-K, Jiang JZ (2010) Origin of pressure-induced polyamorphism in $Ce_{75}Al_{25}$ metallic glass. Phys Rev Lett 104(10):105702

Zeng Q, Sheng HW, Ding Y, Wang L, Yang W, Jiang JZ, Mao WL, Mao H-K (2011) Long-range topological order in metallic glass. Science 332(6036):1404-1406, doi: 10.1126/science.1200324

Zha CS, Bassett WA (2003) Internal resistive heating in diamond anvil cell for *in situ* X-ray diffraction and Raman scattering. Rev Sci Instrum 74:1225-1262

Zhang L, Meng Y, Dera P, Yang W, Mao WL, Mao H-K (2013) Single-crystal structure determination of (Mg,Fe)SiO_3 postperovskite. Proc Natl Acad Sci 110(16):6292-6295, doi: 10.1073/pnas.1304402110

Zhao J, Sturhahn W, Lin JF, Shen G, Alp EE, Mao HK (2004) Nuclear resonant scattering at high pressure and high temperature. High Pressure Res 24:447-457

Zhao YC, Barvosa-Carter W, Theiss SD, Mitha S, Aziz MJ, Schiferl D (1998) Pressure measurement at high temperature using ten Sm : YAG fluorescence peaks. J Appl Phys 84(8):4049-4059, doi: 10.1063/1.368693

EBSCOhost - printed on 2/13/2023 5:26 AM via . All use subject to https://www.ebsco.com/terms-of-use

EBSCOhost - printed on 2/13/2023 5:26 AM via . All use subject to https://www.ebsco.com/terms-of-use

Reviews in Mineralogy & Geochemistry
Vol. 78 pp. 779-800, 2014
Copyright © Mineralogical Society of America

In situ High-Temperature Experiments

Daniel R. Neuville
IPGP-CNRS
1 rue Jussieu, 75005 Paris, France
neuville@ipgp.fr

Louis Hennet, Pierre Florian
CEMHTI-CNRS, 1D Avenue de la Recherche Scientifique
45071 Orléans cedex 2, France
louis.hennet@cnrs-orleans.fr, pierre.florian@cnrs-orleans.fr

Dominique de Ligny
FAU Erlangen Nürnberg
Department Werkstoffwissenschaften, Martensstr. 5
91058 Erlangen, Germany
dominique.de.ligny@fau.de

PREFACE

When Frank Hawthorne (1988) edited the *Reviews in Mineralogy* volume on "Spectroscopic Methods in Mineralogy and Geology," all the experiments presented had been performed at room pressure and room temperature because, at that time, vibrational and X-ray techniques were already quite difficult at ambient conditions so more sophisticated sample environments were not a priority. However, it has now become somewhat easier to perform experiments *in situ* at high temperatures (HT), high pressures (HP) or under combined high temperature and pressure (HP-HT). These types of experiments are becoming routine on crystals, glasses and liquids (see Shen and Wang 2014, this volume).

High-temperature experiments are important because most of the physical properties of high-temperature liquids, such as magmas and melts, are related to their atomic structure. Consequently, it is important to probe the local environment of the atoms in the sample under the conditions noted above (e.g., HT). However, at very high temperatures (~≥ 1200 °C) it is difficult to use conventional furnaces because of a number of experimental difficulties associated with their use: temperature regulation, thermal inertia and spatial obstruction of the sample. Due to the progress made in the development of lasers and X-ray, neutron and magnetic sources it is now possible to perform experiments *in situ* at HT, HP and HT-HP on samples of millimeter or micron size.

INTRODUCTION

In this chapter, we discuss some of these noncommercial methods used in performing experiments at HT, and outline the best choices for heating systems with regard to the experimental requirements. Different commercial heating systems are available such as the systems available from Linkam® (*http://www.linkam.co.uk/*) or Leica® (*http://www.leica-microsystems.com/*) for example. These two systems are well adapted to performing experiments at HT including

1529-6466/14/0078-0019$05.00 http://dx.doi.org/10.2138/rmg.2013.78.19

EBSCOhost - printed on 2/13/2023 5:26 AM via . All use subject to https://www.ebsco.com/terms-of-use

Raman (Neuville et al. 2014, this volume) and IR spectroscopy (Della Ventura et al. 2014, this volume) and X-ray absorption near-edge structure (XANES) spectroscopy (Henderson et al. 2014, this volume) in fluorescence mode. Commercial cells are capable of working at high and low temperatures, with controlled atmospheres and are relatively easy to use. But they need relatively large samples (typically 3-4 mm diameter and 1-2 mm height) and it is not possible to use them for EXAFS experiments in transmission mode or to perform HT Brillouin spectroscopy. Furthermore, it is not possible to investigate very high temperature >1800 K. There has also been a number of HT apparatus developed for use under specialized experimental conditions. For example, Berry et al. (2003) developed a controlled atmosphere furnace for X-ray absorption spectroscopy experiments under imposed oxygen fugacities at temperatures up to 1773 K. This furnace is well adapted for XANES experiments under controlled atmospheres but not suitable for investigating light elements. Eeckhout et al. (2008) have also developed a similar furnace.

Here we focus this chapter on two main heating methods: (i) levitation coupled with laser heating (Coutures et al. 1986) and (ii) heating using the wire system originally developed by Mysen and Frantz (1992). Both systems have been used with X-ray absorption and diffraction on several synchrotron beamlines, with neutron diffraction, and with Raman, IR and Brillouin spectroscopies.

LEVITATION TECHNIQUES

Introduction

The principle of levitation is to apply a force that counteracts gravity so that the sample is essentially suspended in air without a container. There are basically three main techniques widely used today: electromagnetic levitation, EML, (Jacobs et al. 1996), electrostatic levitation, ESL, (Paradis et al. 2001) and aerodynamic levitation. Some other techniques exist such as gas film levitation, GFL, (Haumesser et al. 2002), or combinations of the techniques above. In addition, we should also mention acoustic levitation (Trinh 1985), which is mostly used with liquids at lower temperatures.

EML is restricted to conducting samples (generally metals) that can be relatively large (up to 1-2 cm in diameter). ESL has the advantage of working both under vacuum preventing contamination by a surrounding gas and also under a few atmospheres gas pressure. However it requires a complex setup that complicates its use with many spectroscopies. In principle, all types of materials can be levitated using GFL technique and it is possible to use large quantities of sample (up to 200 g for oxide glasses). Up to now, these techniques have been used to study thermophysical properties such as viscosity, mass densities and surface tension in oxide melts (Grishchenko and Piluso 2011). A recent review of these techniques and their applications can be found in Price (2010). Among all containerless techniques, the CEMHTI "Conditions Extrêmes et Matériaux: Haute Température et Irradiation" laboratory in Orléans, France, has chosen to work with aerodynamic levitation in which the sample is levitated using a gas stream that flows through a convergent-divergent nozzle. In this chapter, we will mainly focus on this method, which is well adapted for studying liquid oxide melts.

The most widely used technique of this kind employed today is conical nozzle levitation, CNL, in which the levitator has a convergent-divergent nozzle. It was first used in combination with electromagnetic heating by Winborne et al. (1976). Coutures et al. (1986) introduced a CO_2 laser heating and adapted the technique for Nuclear Magnetic Resonance (NMR) experiments on HT liquids (Winborne et al. 1976; Coutures et al. 1986). The advantages of CNL are the simplicity and compactness of the levitation devices, making it easy to integrate them into different experimental setups and it has subsequently been installed in various experiments

EBSCOhost - printed on 2/13/2023 5:26 AM via . All use subject to https://www.ebsco.com/terms-of-use

at large scale facilities (synchrotron and neutron sources). A recent review of applications of aerodynamic levitation at synchrotron and neutron sources can be found in Hennet et al. (2011). Besides gas flow, sound waves, electrostatic or magnetic fields can also be used to levitate sample.

Acoustic levitation

Acoustic levitation can suspend small objects via the acoustic radiation force that results from an impedance difference between the suspension medium, normally a gas, and a solid or liquid sample. A single-axis acoustic levitator, SAL, consists mainly of two parts: a vibrating source (or transducer) generating frequencies of a few tens of kHz (i.e. ultrasound) and a reflector with a concave surface to improve the efficiency. The vibrating source-reflector axis is parallel to the direction of gravity and an acoustic wave is generated along this direction in order to counteract gravity. SAL can be used to study low melting point alloys and non-conducting materials as well as room temperature liquids. Trinth (1985) developed a device enabling work up to 700 °C. Resistive heating coils were used to heat the sample. The accessible temperature range is thus limited and this technique is not suitable for very HT studies.

Electromagnetic levitation

Electromagnetic levitation (Fig. 1) is mainly suitable for electrically conductive materials. It will be discussed here only briefly since a detailed description of EML can be found elsewhere (Eckler 1992; Jacobs et al. 1996; Holland-Moritz et al. 2005). With EML, a radiofrequency electromagnetic field is generated by a coil and Foucault currents are induced in the sample. This leads to inductive heating of the sample, and at the same time, the interaction of the Foucault currents with the magnetic field of the coil leads to a force that counteracts the gravitational force and makes it possible to levitate the sample. The electromagnetic force applied on the levitated sample depends on the power absorbed by the latter. It is essentially a function of the square of the magnetic field strength and the electrical conductivity of the sample material. So by varying the heating power, one can control the temperature of the sample. The levitation coil is situated in a vacuum chamber, which is first evacuated and then filled with a very high purity gas, usually helium (He) or a mixture of He plus a few percent of hydrogen (H_2).



Figure 1. A typical electromagnetic levitation setup developed at the German Space Center (DLR) within the "Institut für Materialphysik im Weltraum" (Institut for Materials Physics in Space). It is used for neutron diffraction on the D20 instrument at the ILL (Holland-Moritz et al. 2005).

Electrostatic levitation

With ESL (Paradis et al. 2001), the sample is electrically charged and levitated in a vertical electro-static field between two electrodes (Fig. 2). Two pairs of smaller side electrodes are used to position the sample horizontally. When it levitates, the sample is melted using lasers. With this method, it is possible to study all samples that can be electrically charged. This method has various advantages. First, it works under vacuum, preventing contamination, and allows the study of poor electrical conductors or materials with low melting points. One

EBSCOhost - printed on 2/13/2023 5:26 AM via . All use subject to https://www.ebsco.com/terms-of-use

drawback is the complexity of the setup that limits its combination with various spectroscopies. While some insulating oxides can be studied with this technique, it is used mostly with metals.

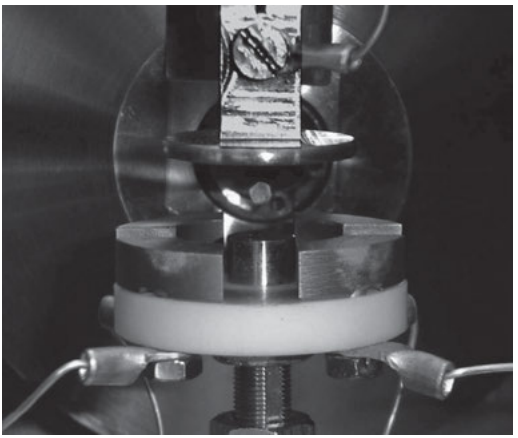


Figure 2. Levitated sample between the electrodes of an electrostatic levitator at DLR. Redrafted from Kozaily (2012).

Aerodynamics levitation

Aerodynamic levitation was first developed in the USA by D. A. Winborne and P. C. Nordine (Winborne et al. 1976) then later adopted at the CEMHTI by J.-P. Coutures (Coutures et al. 1990) for NMR studies. It has proven to be a powerful and versatile technique for studying highly reactive liquids in the equilibrium melt and the supercooled liquid state several hundred Kelvin below the melting point (Hennet et al. 2007a). In particular, it is now widely used with neutron and X-ray diffraction techniques to investigate the structural properties of liquids (Hennet et al. 2006, 2007a,b). The working principle of aerodynamic levitation is well known and is described in detail elsewhere (Landron et al. 2000). Figure 3 shows a standard aerodynamic levitation setup. The basic idea is to circulate a levitation gas (usually argon) through a nozzle onto the sample from below in order to counteract gravity and lift it above the nozzle. The sample is then heated to the desired temperature by means of one or two focused CO_2 lasers. The levitation gas flow is accurately regulated and monitored by a mass flow controller to enable the sample to be maintained in a sufficiently stable aerodynamic state for long counting times. Lasers (CO_2 or YAG) provide a natural choice of heating system for aerodynamic levitation and are also used with ESL. CO_2 infrared lasers are particularly suitable for studying oxide materials and to some extent, can also be used for melting metals in conjunction with an oxygen free environment. Heating with a single laser leads to significant temperature gradients especially with insulating samples and generally, two lasers are used to heat and melt the samples. The lasers are focused onto the sample using eithers mirrors or ZnSe lenses from the top (vertically or not) and from below through the hole (gas path) in the conical nozzle. In both systems, the gas flow is precisely regulated using mass flow controllers and video cameras are used to monitor the sample during the levitation process.

With metals, it is also possible to use electromagnetic heating as used with ELM levitation. In particular, the Deutsches zentrum für Luft-und Raumfahrt, DLR, in Cologne and CEMHTI developed a hybrid system combining a RF heating coil with the conical nozzle (Mathiak et al. 2005). With the ESL technique, metals are melted using YAG lasers or CO_2 lasers with wavelength of ~1 μm. With levitation techniques, optical pyrometry is the ideal method for temperature measurements. This technique is very easy to use but requires emissivity corrections to derive the true temperature, T, from the apparent temperature T_a measured by the pyrometer:

$$\frac{1}{T}-\frac{1}{T_a}=\frac{\lambda}{C_2}\ln(\varepsilon_\lambda)$$

where C_2 is the second radiation constant of Planck, C_2 = 1.4388 cm K and ε_λ is the material emissivity at the working wavelength λ of the pyrometer.

EBSCOhost - printed on 2/13/2023 5:26 AM via . All use subject to https://www.ebsco.com/terms-of-use

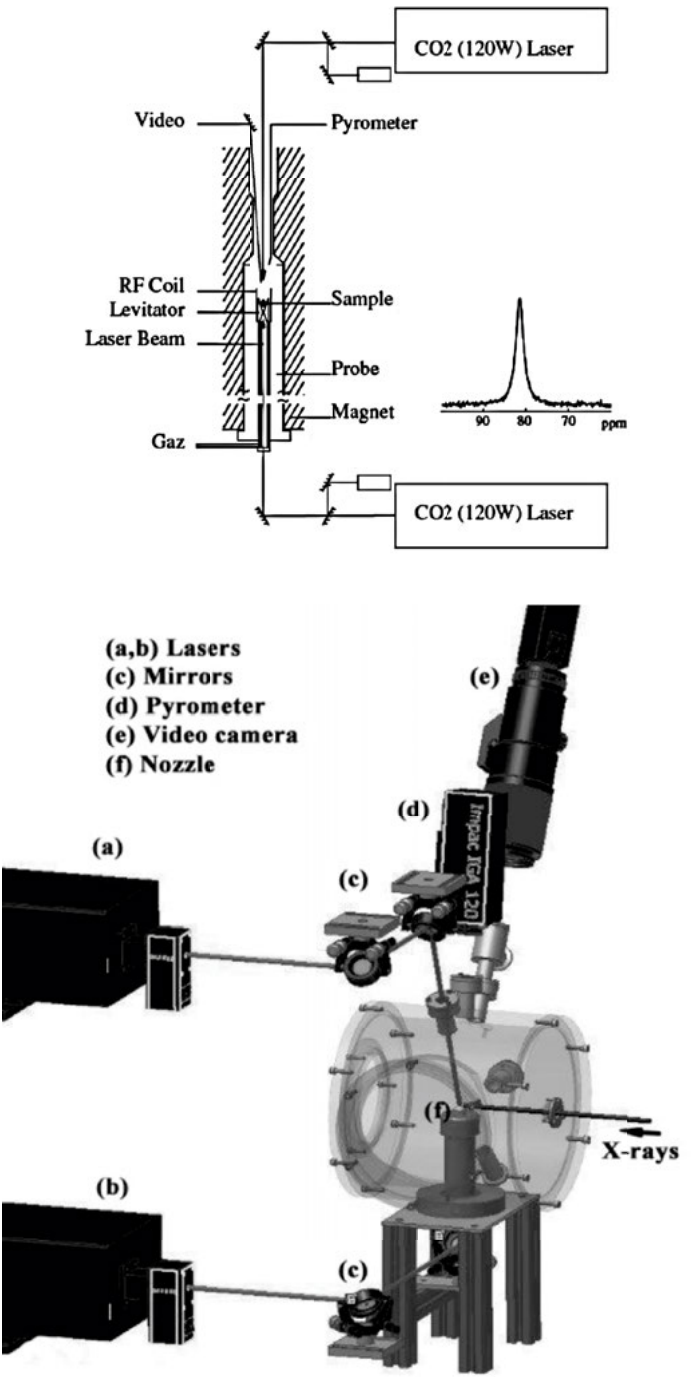


Figure 3. CNL environments developed at the CEMHTI for high-temperature experiments with NMR (*top*) and high energy X-ray diffraction at ID11 (ESRF) (*bottom*).

EBSCOhost - printed on 2/13/2023 5:26 AM via . All use subject to https://www.ebsco.com/terms-of-use

Experimental techniques

In this part, we mainly focus on selected experimental techniques that employ levitation methods to probe the structure of materials. All these applications are well described in Price (2010). However, we should point out that other properties can also be measured while using levitation techniques. For example, electrical and magnetic properties can be obtained by placing the levitating sample inside a RF coil and observing changes in the impedance and quality factors of the coil. Various systems have been developed to be used with the CNL and EML techniques (Enderby et al. 1997; Lohöfer 2005; Skinner et al. 2006). Some thermophysical properties can be also determined with levitated samples. This includes density, surface tension and viscosity using video observations (Egry et al. 1995; Millot et al. 2002; Paradis and Ishikawa 2005). With more difficulty, it is also possible to determine the specific heat (Paradis et al. 2001) and the thermal conductivity (Kobatake et al. 2007).

Finally, we can also point out that liquid dynamics can be studied using NMR experiments with the determination of relaxation times (Massiot et al. 1995; Gruener et al. 2001; Florian et al. 2007) and atomic diffusion coefficients (Rollet et al. 2009) in conjunction with inelastic X-ray and neutron techniques (Pozdnyakova et al. 2007; Meyer et al. 2008; Hennet et al. 2011). Figure 4 shows a comparison of the correlation time of liquid $CaAl_2O_4$ derived from viscosity measurements (Urbain 1983) and from NMR measurements (Massiot et al. 1995) and Quasi Elastic Neutron Scattering (QENS) (Kozaily et al. 2011).

APPLICATIONS OF AERODYNAMICS LEVITATION

NMR experiments

NMR at high temperature can be performed with a CO_2 laser heating system using boron nitride, BN, containers or without containers by using a levitation system.

With containers, the samples are packed in pyrolitic BN crucibles. The sample container is sustained inside the radiofrequency coil of an axially symmetric multi-nuclear NMR probe with a ceramic support which also acts as a thermal shield, preventing the coil from being overheated. The samples are heated with two computer-controlled high-power CO_2 lasers heating the top and bottom of the crucible to minimize thermal gradients. Temperatures up to, typically, 1400 °C can be obtained with these settings, sample temperatures being calibrated as a function of laser power using a thermocouple and the exact same experimental conditions (no NMR measurements are possible during calibration), leading to a temperature uncertainty of approximately ±10 °C. Different results can be obtained using this technique (Sen 1999; Le Losq et al. 2014; see also Stebbins and Xue 2014, this volume for a complete review of NMR at HT). More recently, using new NMR high field developments, it is now possible to measure at the same time and on the same sample two NMR signals, such as ^{23}Na and ^{27}Al (Fig. 5). For example, see in Figure 5, with this method ^{23}Na and ^{27}Al NMR spectra have been obtained on a $NaAlSi_3O_8$ composition in different states (crystalline, glass and liquid) with a high field NMR spectrometer (Brucker 750MHz, 17.6T). For these experiments, heating was provided by a CO_2-laser irradiating the sample from the bottom in a UHT Brucker probe modified at the CEMHTI laboratory to handle crucibles. Samples (approx. 100 mg) were filled in tight-closed BN crucibles and heated by steps of approximately 100 °C under dried argon. A small and large ^{27}Al background signal was also recorded at each temperature using an empty crucible and further subtracted from the actual spectra. One can also point out that this design is very well suited to the study of corrosive or air-sensitive melts such as fluorides. Using more conventional magnetic fields (i.e., 9.0 T), double CO_2 irradiation conditions and temperature calibration recording the melting point of external standards, it has led to successful investigations of fluoride molten salts (see e.g., Lacassagne et al. 2002).

EBSCOhost - printed on 2/13/2023 5:26 AM via . All use subject to https://www.ebsco.com/terms-of-use

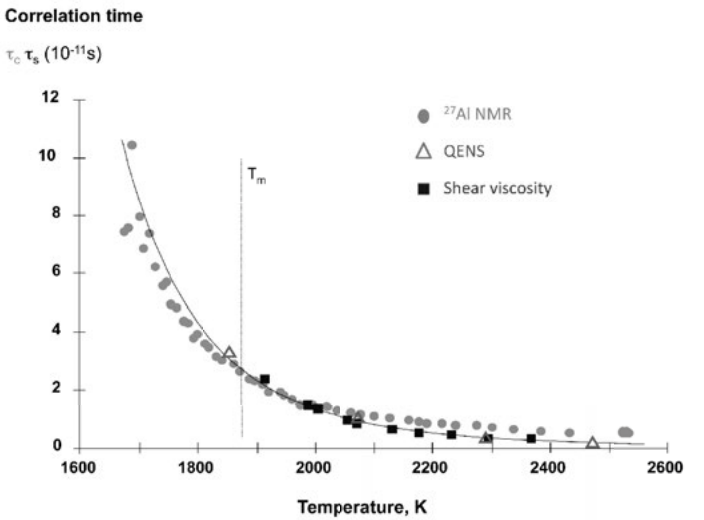


Figure 4. Correlation times of the aluminum movements obtained by NMR (Massiot et al. 1995) and Quasi Elastic Neutron Scattering, QENS (Kozaily et al. 2011) reported together with those derived from macroscopic shear viscosity (Urbain 1983).

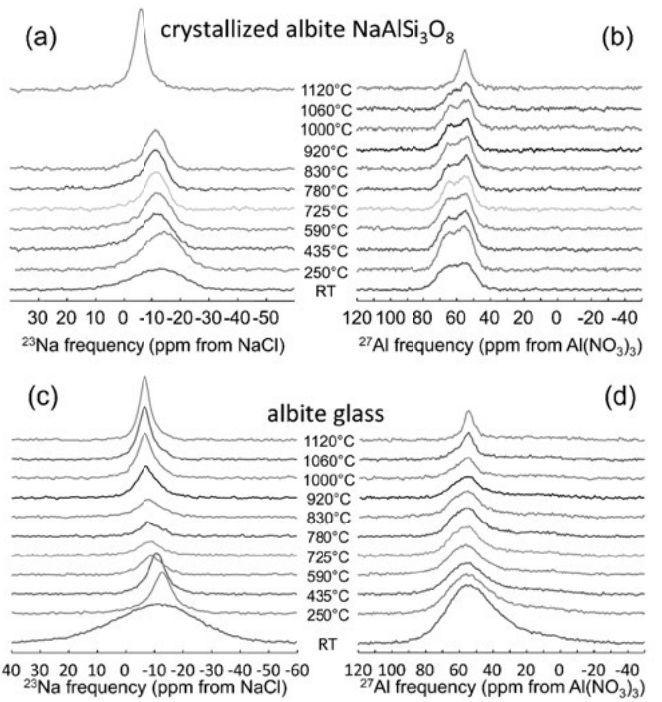


Figure 5. *In situ* high-temperature NMR measurements of (a) ^{23}Na and (b) ^{27}Al nuclei in crystallized albite $NaAlSi_3O_8$, and (c) ^{23}Na and (d) ^{27}Al nuclei in a glass of albite composition. All experiments were performed using a crucible design.

EBSCOhost - printed on 2/13/2023 5:26 AM via . All use subject to https://www.ebsco.com/terms-of-use

Without containers, the sample is first melted in an external levitation system to shape it as a sphere. It is then inserted in a convergent-divergent nozzle located inside the radio-frequency coil of a multi-nuclear probe (identical to the one used with the crucible design). Levitated samples are heated and melted in the NMR experiment using two focused CO_2 lasers irradiating the top and bottom part of the sample, (i.e., Cote et al. 1992; Poe et al. 1992; Florian et al. 1995, 2007; Le Losq et al. 2014). Temperatures up to 2500 °C can be obtained with this design. The diameter of sample sizes varies but is commonly between 3 to 5 mm, and total NMR acquisition times of less than 50 ms are sufficient to produce spectra with excellent signal to noise ratios. This allows observation of sample cooling obtained by shutting off the laser and repeatedly acquiring NMR spectra every 25 ms. This has been used to determine the time-resolved evolution of the structure and dynamics of aluminate and aluminosilicate liquids (Massiot et al. 1995; Florian et al. 1995, 2007; Gruener et al. 2001). In this cooling approach, the sample first equilibrates its temperature within 0.3 ms, leading then to the observation of a liquid without significant thermal gradients during the course of its cooling. It also allows, in most cases, exploration of the super-cooled region (i.e., the liquid below the melting point T_m) since no heterogeneous nucleation can take place under this containerless melting.

Figure 6 shows a typical ^{27}Al NMR spectra of liquid alumina made in 1990 at CEMHTI in Orléans, and the chemical shift of 50 ppm can be interpreted as a mixing of Al in four and six fold coordination. This is in good agreement with NMR experiments by Florian et al. (1995) and also with finite difference method near-edge structure (FDMNES) simulations and XANES spectroscopy at the Al *K*-edge by Neuville et al. (2009). However, some influence of the temperature and levitation gas has been noted using this NMR set-up leading to non-stoichiometric Al_2O_3 melts (Coutures et al. 1994).

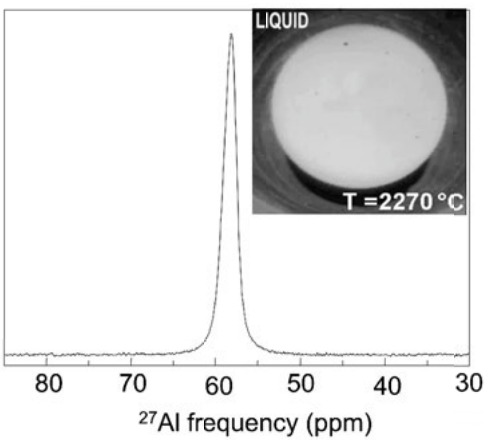


Figure 6. ^{27}Al NMR spectrum of a 66 mg levitated alumina melt at 2320 °C along with the image retrieved from the camera at a temperature of 2270 °C.

X-ray absorption spectroscopy (XAS)

X-ray absorption spectroscopy, XAS, is an element-specific method used to investigate the local structural order in materials (see Newville 2014, this volume; Henderson et al. 2014, this volume). As for solids, various types of information can be obtained with this technique. When a pre-edge peak exists, its intensity and position can give information on the Coordination Number, CN, and the oxidation state of the studied element. The detailed energy dependence of the XANES spectrum gives information about the electronic structure and from the EXAFS region it is possible to determine structural parameters such as bond lengths and CN. Compared to XRD measurements, XAS has the advantage that the determined structural information is element-specific and related to the absorbing atoms. A disadvantage is that in liquids and glasses, it is difficult to get structural information beyond the nearest neighbors of the absorbing atoms. With levitation techniques, the sample is too thick (mm range) for XAS measurements in transmission mode, and so experiments are performed by measuring the fluorescence produced by the absorption. Jacobs et al. (1996) demonstrated that it was possible to combine XAS measurements with EML techniques and to obtain information

EBSCOhost - printed on 2/13/2023 5:26 AM via . All use subject to https://www.ebsco.com/terms-of-use

about the structure of liquid and supercooled metallic melts. XAS was then combined with the CNL technique by Landron et al. (1998) to study liquid oxides with the possibility of combining XAS and XRD experiments on the same sample. XAS experiments have also been combined with the hybrid aerodynamic electromagnetic levitator mentioned previously (Egry et al. 2008).

SAXS and SANS

Only a few experiments have used X-ray or neutron small angle scattering techniques with the CNL technique. Greaves et al. (2008) combined CNL with SAXS/XRD experiments to study polyamorphism in supercooled yttrium aluminates. Aerodynamic levitation and CO_2 laser heating was also coupled with SANS experiments. This technique can be used to study phase separation in the sample, for instance. Taking advantage of the sensitivity of neutrons to magnetic moments, Fischer et al. (2007) measured the magnetic critical scattering from solid $Co_{80}Pd_{20}$ in the vicinity of the ferromagnetic transition temperature T_c.

X-ray and neutron diffraction

The first XRD experiments on levitated liquids were performed by Ansell et al. (1997) on liquid Al_2O_3 using the CNL setup developed by Krishnan et al. (1997). Following this work, the EML method was combined with energy-dispersive XRD (Notthoff et al. 2000; Kimura et al. 2001). The first XRD experiments using ESL were performed by Kelton et al. (2003) and a similar apparatus was further developed by other groups (Masaki et al. 2007). Since the first XRD experiments, CNL environments at synchrotron sources have been improved with the use of better detectors. In particular, several setups are installed at the APS (Mei 2008) and Spring 8 (Matsumura et al. 2007). The first XRD experiments with CNL using the CEMHTI levitation setup were conducted at the H10 beamline at LURE (Orsay, France) (Price 2010), and additional CNL setups have been installed at the Diffabs beamline at SOLEIL (Gif-sur-Yvette) and at the ID11 beamline at the ESRF (Bytchkov et al. 2010). The first neutron diffraction, ND, measurements on aerodynamically levitated liquids were performed by Landron et al. (2001) on liquid alumina at the SANDALS instrument at ISIS (Rutherford Appleton Laboratory, UK). A detailed description of the setup can be found in Landron et al. (2001). A similar CNL environment was developed by Weber et al. at the Intense Pulsed Neutron Source, (IPNS, Argonne, USA) (Weber et al. 2003). During the same period, Holland-Moritz team developed an EML environment for neutron investigation of metallic melts at the Institut Laue-Langevin, ILL, in Grenoble, France (Schenk et al. 2002). The ESL technique was further combined with neutron experiments by Paradis et al. (2002).

High-intensity synchrotron radiation sources have enabled the development of more selective methods such as anomalous X-ray scattering, AXS, which is not often used with levitation techniques. The first experiment combining AXS with CNL to study the liquid structure of Y_2O_3 were performed by Hennet et al. (2007b). For a polyatomic system, neutron diffraction with isotopic substitution, NDIS, is a powerful element-specific method to experimentally determine the partial structure factors. The pioneering NDIS experiment was performed by Enderby et al. (1997) who determined the partial structure factors of liquid Cu_6Sn_5. The NDIS technique consists of measuring the diffraction intensity for several samples of identical structure and chemical composition but having different isotopic compositions for one or more of the species. The use of NDIS is then dependent on the availability of the isotopes. Holland-Moritz et al. (2009) recently combined NDIS with EML to determine the partial structure factors and pair distribution functions of liquid and supercooled $Ni_{36}Zr_{64}$ alloy. The NDIS technique requires good counting statistics and EML is well adapted since it is possible to levitate relatively large samples. In spite of the small sample size currently used with the CNL method, it has also been combined with NDIS by Gruner et al. (2009) to study the structure of liquid Ni-Si alloys above the melting temperature.

EBSCOhost - printed on 2/13/2023 5:26 AM via . All use subject to https://www.ebsco.com/terms-of-use

Figures 7 and 8 show S(Q) and $g(r)$ determined from X-ray and neutron diffraction at the liquidus temperature for calcium aluminosilicate melts (Kozaily et al. 2011; Kozaily 2012). These structural data are in good agreement with those expected from knowledge of the glass structure at room temperature (Cormier et al. 2000, 2005) and also from XANES experiments at the Al and Ca *K*-edges for $CaAl_2O_4$ (Neuville et al. 2008).

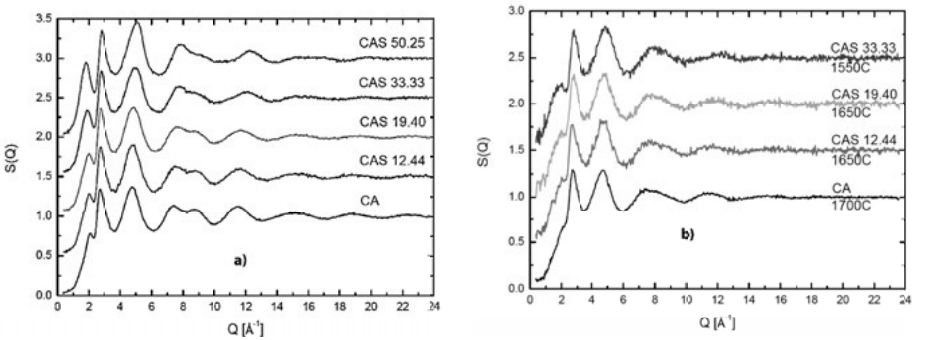


Figure 7. Typical average structure factors S(Q) measured on liquid calcium aluminosilicates using X-ray (*left*) and neutron scattering (*right*) (data from Kozaily 2012). Note that X-ray experiments are faster (typically minutes) than neutron ones (>3 hours), and chemical compositions richer in silica can be investigated without SiO_2 loss during the experiments.

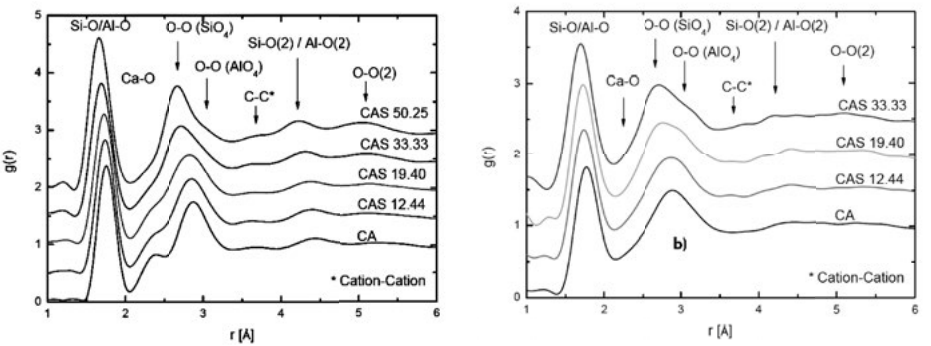


Figure 8. Average pair correlation functions $g(r)$ calculated for liquid calcium aluminosilicates using X-ray (*left*) and (*right*) neutron scattering (data from Kozaily 2012).

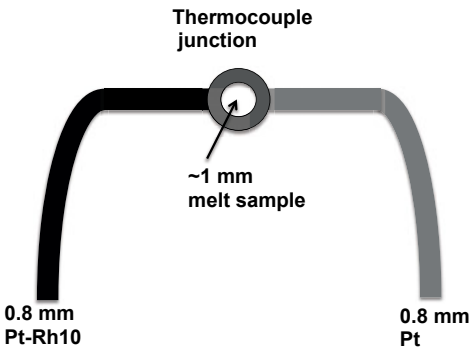
WIRE OR PLATE HEATING SYSTEM

Description, temperature and atmosphere control

The heating-wire technique was first developed by Ohashi and Hadidiacos (1976) to develop a HT microscope at the Geophysical Laboratory, Carnegie Institution of Washington. Mysen and Frantz (1992) popularized this idea, using it for high temperature Raman spectroscopy. The heating-wire, HW, was a welded junction of 1-mm-diameter thermocouple junction in Pt and Pt-Rh 10%. It serves as both a heating element and a thermocouple. The output of the thermocouple is used to regulate a 50 Hz pulse input-power supply. The thermocouple e.m.f, is measured by the same home-made apparatus between the pulses. The sample is placed within a 1 mm hole drilled mechanically at the flattened junction. This hole corresponds to the hot spot. This heating system has low thermal inertia and it is possible to change the

EBSCOhost - printed on 2/13/2023 5:26 AM via . All use subject to https://www.ebsco.com/terms-of-use

temperature between room temperature up to temperatures >1600 °C in few seconds. At temperature the heating system is relatively stable and can stay at the selected temperature as long as needed during the experiments. This device is remarkably simple and efficient. In the original design of Mysen and Frantz (1992) the wire was in a U-shape, and the position of the hole could slowly move vertically and laterally due to thermal expansion. This induced deformation of the wire and movement of the sample. To eliminate this it is possible to work with a stiffer wire. However, the principal problem of the first design of the heating device was the non-commercial power supply developed by Hadidiacos at the Geophysical Lab. A first modification of this heating system was made by using a wire in Pt-Rh10% heated by a direct current produced by a commercial power supply (Neuville and Mysen 1996). Furthermore, to avoid the movement of the sample due to dilatation, a new linear heating wire was made with a large variety of different alloys PtRh10%, PtIr10%, Ir and W (Richet et al. 1993). Platinum and its alloys are good wires to heat systems in air but to work at very high temperature, it is necessary to use Ir, W, Re or Ta which require vacuum or controlled atmospheres. Figure 9 shows drawings of the original device and a recent modified system made to work under air or controlled atmosphere conditions (Gonçalves Ferreira et al. 2013). The latest version (Fig. 9) has a double confinement box to safely heat radioactive materials like UO_2, PuO_2 and others radioactive actinides elements. This new set-up was developed with the French Atomic Energy Commission, CEA. Figure 10 shows the electric power needed to heat different wires at high temperature under different atmospheres. Ta is a good candidate to work at very high temperature without oxygen, and Ta is easily workable compared with Ir, Re or W, which cannot be flattened and need to be drilled using electro-erosion or a laser apparatus. The



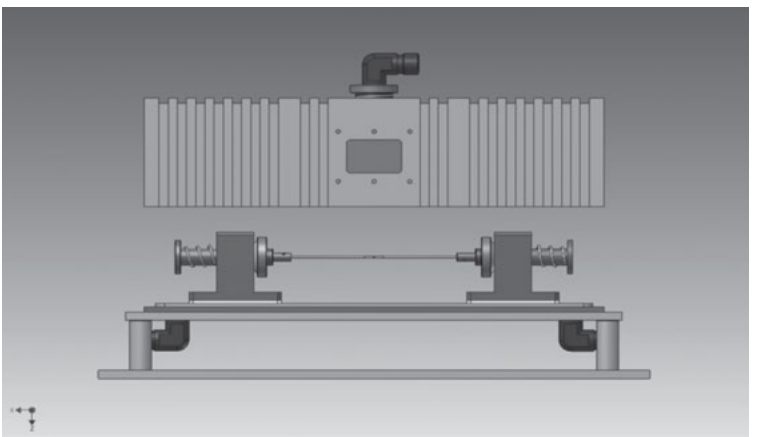


Figure 9. (*left*) The original HW setup proposed by Mysen and Frantz (1992). (*below*) New HW configuration developed with Saint-Gobain Recherche, this furnace works with controlled atmospheres (Air, N_2, O_2, Ar, ArH_2).

EBSCOhost - printed on 2/13/2023 5:26 AM via . All use subject to https://www.ebsco.com/terms-of-use

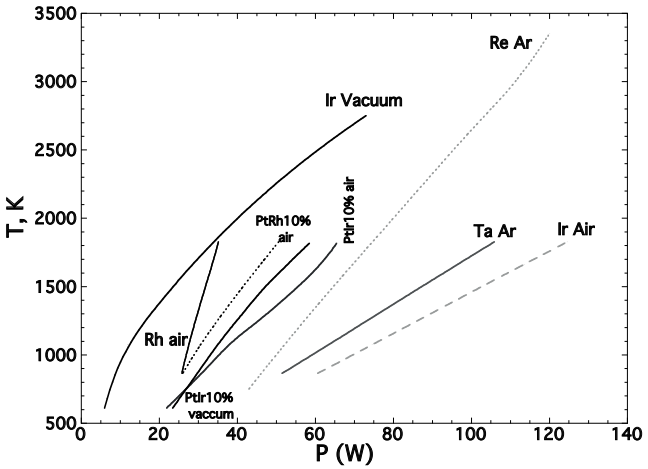


Figure 10. Electric power versus temperature for different wires and atmosphere.

maximum size of the hole varies between 100 μm in Ir or W wire up to 2 mm in Pt or Pt-Ir10%, Pt-Rh10%.

Temperature accuracy is ±5 K at high temperature (Neuville and Mysen 1996) and reproducibility is better than 10 K if the wire does not change due to volatilization of its constituent alloys at high temperature, for instance Ir. Most important is to use the appropriate wire alloy for the experimental temperature and atmosphere conditions (Table 1).

Table 1. Liquidus temperature for some metals.

Metal	Liquidus, K
Platinum, Pt	2041
Rhodium, Rh	2236
Iridium, Ir	2720
Tantalum, Ta	3293
Rhenium, Re	3455
Tungsten, W	3695

Each wire is different:

- PtIr10% or PtRh10% are very useful, easy to make, can be used in air or with many different atmospheres, and can be put in HF to be cleaned.
- Pt with higher Ir or Rh content can increase the maximum temperature used but the wires become harder and more difficult to drill.
- Rh wire has a very high melting point, is easy to drill but very expensive.
- Ir, Re or W wire are perfect to work at very high temperature up to 3000 K and more but need controlled atmospheres with very low oxygen content. These metals are very hard and very difficult to drill a hole in; Re has better mechanical properties than Ir and a higher melting point.
- Ta wire is easy to drill, very good at high temperature, needs controlled atmospheres without oxygen, and need a very high power supply due to its low electrical resistivity.

Raman spectroscopy

Several Raman spectroscopy studies at high temperature have used this technique on silicate melts (Mysen and Frantz 1992, 1993, 1994a; McMillan et al. 1994; Frantz and Mysen 1995), on aluminosilicate melts (Mysen and Frantz 1994b; Neuville and Mysen 1996; Daniel et al. 1995) on titanosilicate melts (Mysen and Neuville 1995; Reynard and Webb 1998); germanosilicate melts (Henderson et al. 2009), borate melts (Cormier et al. 2006); borosilicate melts (Manara

EBSCOhost - printed on 2/13/2023 5:26 AM via . All use subject to https://www.ebsco.com/terms-of-use

et al. 2007; Lenoir et al. 2010) and also on crystal melting (Richet et al. 1998). Raman spectra of potassium silicate melts collected using a heating wire device (Mysen and Frantz 1992) are similar to those obtained on glass using a Leitz® furnace (McMillan et al. 1992). The only precaution to be taken every time consists to verify that the chemical composition of the sample does not change during the thermal cycle. This verification can be easily made by comparison of Raman spectra at the beginning and at the end of experiment as shown by Neuville and Mysen (1996). The results obtained by HT Raman spectrometry correspond to the changes which takes place during melting, phase transitions, the glass transition, or to structural changes with changing temperature. These are developed in more detail in the Raman chapter (Neuville et al. 2014, this volume). The heating wire can also be used for Brillouin measurements at high temperature (Vo-Thanh et al. 2005).

X-ray diffraction

Crystalline materials. The heating system has been used at different light sources to investigate the structure of crystals, glasses and melts. One of the first investigations was made at the LURE light source to investigate the structure of simple compounds such as MgO, CaO, Al_2O_3, and $MgAl_2O_4$, by X-ray diffraction (Fig. 11) (Fiquet et al. 1999). In Figure 11, the lattice parameters, *a* and *c* of the four components, MgO, CaO, Al_2O_3 and $MgAl_2O_4$, are plotted and compared (Fiquet et al. 1999). For this kind of experiment, it is easy to determine the thermal expansion coefficients as a function of temperature and chemical composition.

Glasses and liquids. X-ray diffraction on glasses provides important knowledge about their structures (see Taylor and Brown 1979a,b) but we have had to wait for progress on light sources to conduct similar experiments on melts that require HT conditions and short data acquisition times. Recently, with developments at beamlines such as those at SOLEIL (DIFFABS) and ESRF (ID11) it is possible to investigate directly the structure of melts at high temperature. The wire heating device has been adapted for the DIFFABS beamline (Fig. 12) to investigate the structure of melts and glasses at the glass transition temperature (X-ray Absorption Spectroscopy was recorded in the same time, see below). The scattering measurements are carried out in transmission. In Figure 13 is shown an example of the X-ray scattering experiments recorded at 17.5 keV on a glass composition (33%SiO_2-

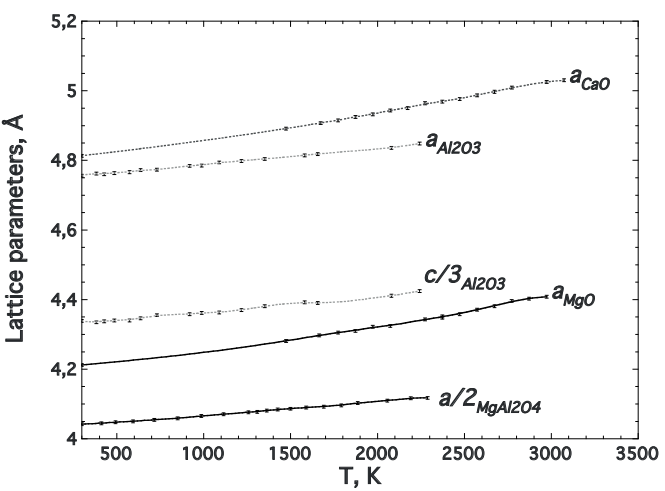


Figure 11. Lattice parameters *a* and *c* for MgO, CaO, Al_2O_3 and $MgAl_2O_3$ from Fiquet et al. (1999). The *c* parameter of Al_2O_3 has been divided by 3 and *a* of $MgAl_2O_3$ by 2.

EBSCOhost - printed on 2/13/2023 5:26 AM via . All use subject to https://www.ebsco.com/terms-of-use

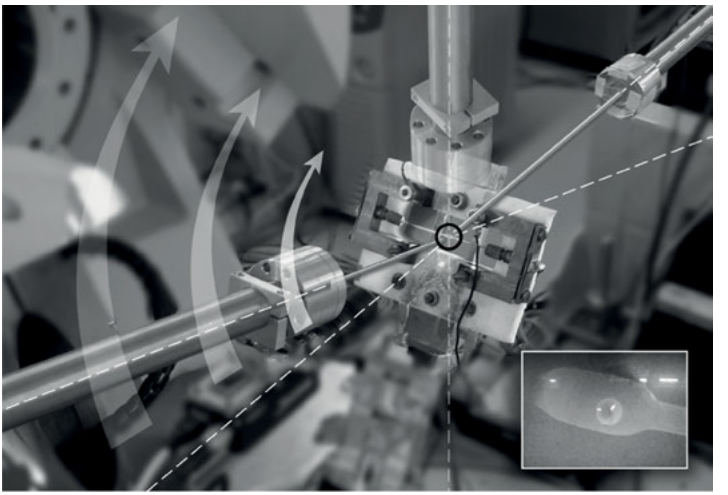


Figure 12. Heating wire assembly on the X-ray scattering set-up at the DIFFABS beamline.

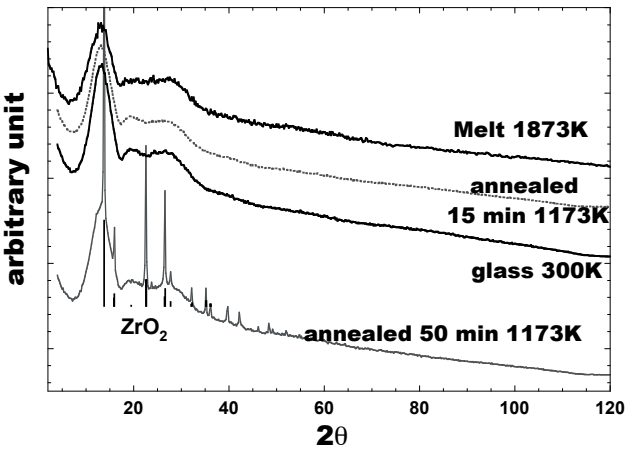


Figure 13. X-ray scattering diagram at 17.5 keV for the glass at 300 K, the stable liquid at 1873 K, and the partially annealed glass at 1173 K. The Bragg peaks visible in the annealed liquid diagram at 1173 K correspond to ZrO_2 crystals.

33%Al_2O_3-33%CaO, with a 0.1 of ZrO_2 in mol%). Several temperatures were studied from room temperature to the glass transition and to the liquid state at 1873 K (Fig. 13). The unusual geometry of the heater makes it rather complicated to acquire these spectra. Some adjustments are required in order to eliminate all of the wire diffraction peaks. Its takes two hours to acquire a X-ray diffraction pattern, which means that the apparatus must have excellent thermal stability for HT experiments, in this case at 1873 K. The spectra of the samples annealed for 15 and 50 minutes at 1173 K were obtained at ambient temperature after quenching. The spectra at different temperatures show a major peak at 15° followed by two more diffuse peaks at 20° and 30° before the intensity gradually decreases. The spectrum of the liquid at 1873 K is again similar to that of the glass at ambient temperature, in agreement with the homogeneous amorphous nature of the two samples. The spectrum of the undercooled liquid annealed for 15 minutes at

EBSCOhost - printed on 2/13/2023 5:26 AM via . All use subject to https://www.ebsco.com/terms-of-use

1173 K does not display any significant change with respect to those of glass and liquid. On the other hand, the product obtained after annealing for 50 minutes at 1173 K shows Bragg peaks, which are characteristic of the ZrO_2 phase which crystallizes at this temperature. The pair correlation functions $g(r)$ are determined from the diffraction diagrams of the glass and the liquid. These diagrams provide some insight into the structural changes occurring in the liquid in the neighborhood of the glass transition temperature and in the nucleation domain. Figure 14 shows these correlation functions $g(r)$ for the glass, the undercooled liquid annealed for 15 minutes at 1173 K and, for the first time a stable liquid at 1873 K. Although it is not easy to interpret all the $g(r)$ functions, in Figure 14 we provide a suggested assignment for the various peaks. Some significant changes are observed between the glass and the liquid. The 2.38 Å peak, which represents the Ca-O distances, is visible in the $g(r)$ for the glass, but disappears at higher temperatures. The shoulder at 2.09 Å, which represents the Zr-O distance, is more visible in the liquid than the glass, even when it overlaps the 1.74 Å peak assigned to Si-O and Al-O. The annealed liquid at 1173 K also displays significant changes, especially with the Ca-O and Zr-O distances. These changes are the result of a reorganization of the liquid before the nucleation/crystallization phenomena shown in Figure 13 for the liquid annealed at 1173 K for 50 minutes.

To understand the results on the glass and melt, we need to consider three points:

- Glass is disordered, but each atom has a stable local environment, which can be characterized by pair distances such as Si-O, Al-O, Zr-O, Ca-O, O-O (arrows in Fig. 14).
- The liquid is disordered but the atoms can move, and by performing X-ray diffraction, a statistic average is taken (red curve, Fig. 14) where T-O pair can be observed (T = Si,Al).The second peak corresponds to cation-cation pairs. But the detailed pairs are lost in the anharmonic distribution of the liquid state.
- By cooling the liquid slowly down to the glass transition temperature, atomic motion decreases and each atom reaches a minimum configurational state. At 1173 K, which is higher than the glass transition temperature (1100 K), the X-ray diffraction pattern (Fig. 13) looks similar to those of the liquid state, but by computing the pair correlation function we observe the presence of the Ca-O peak in a fixed configuration. This implies that the calcium atoms are the first to equilibrate into their crystalline positions, followed later by Al and Si.

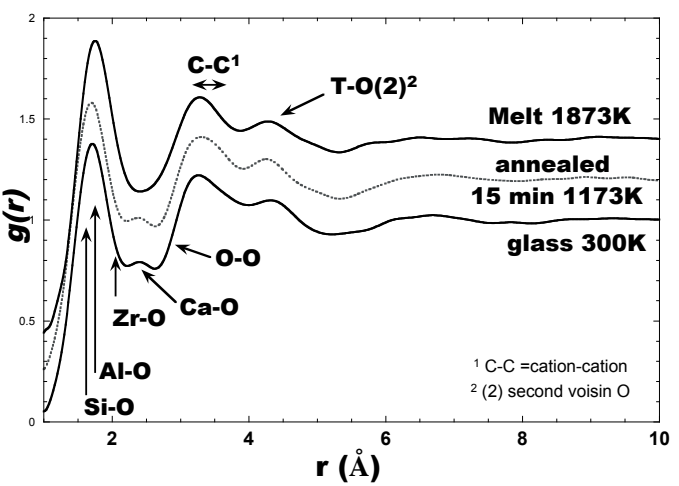


Figure 14. $g(r)$ at different temperatures for glass, liquid, and liquid annealed for 15 minutes at 1173 K, the peaks are assigned to the different atomic pair distances.

EBSCOhost - printed on 2/13/2023 5:26 AM via . All use subject to https://www.ebsco.com/terms-of-use

X-ray absorption

By using different types of heating wire, it is possible to measure X-ray absorption on heavy and light elements. Some examples on different *K*-edge or *L*-edge (Magnien et al. 2008; Neuville et al. 2008, 2009; Cochain et al. 2009; de Ligny et al. 2009) are discussed below. From X-ray absorption at the Fe *K*-edge, Magnien et al. (2008) obtain the redox state of Fe at high temperature as a function of time. This was measured by looking at the pre-edge following Wilke et al. (2001) and it was possible to demonstrate that different redox processes take place depending on the temperature. By looking at the XANES of light elements at high temperature, Neuville et al. (2008) linked changes in the Al *K*-edge in calcium aluminate compositions to viscosity, and proposed a model to understand atomic dynamics in depolymerize melt compositions.

On the same composition investigated by X-ray diffraction on the DIFFABS beamline X-ray absorption spectra at the Zr *K*-edge were recorded in transmission or fluorescence modes. Figure 15 shows the different spectra obtained on the glass or melt at different temperatures.

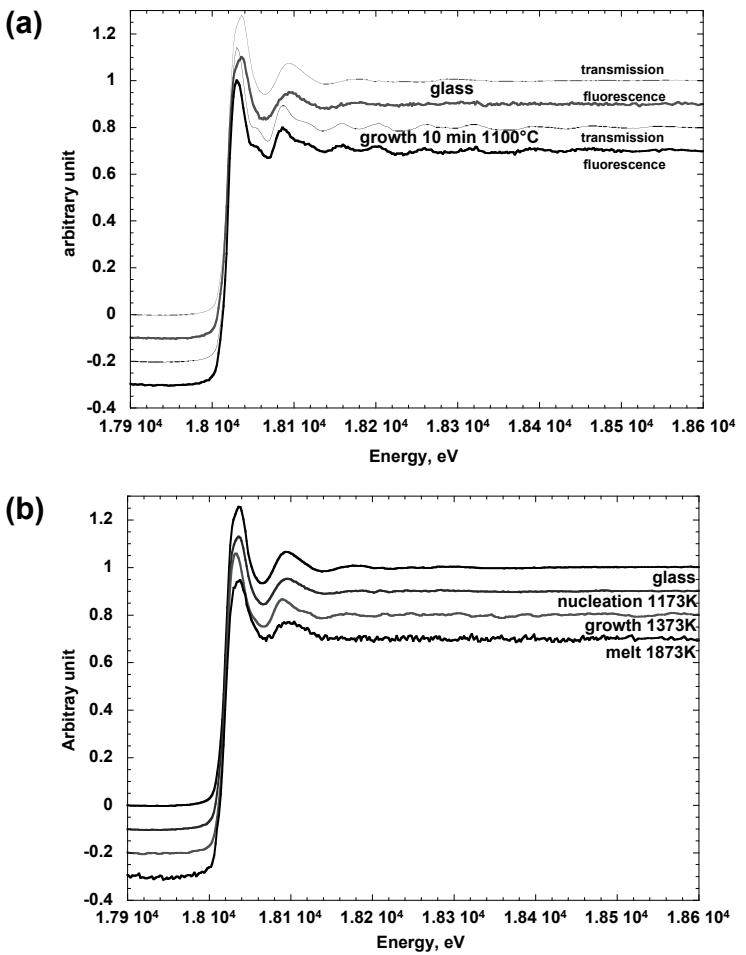


Figure 15. Absorption spectra at the *K*-edge of Zr for the glass and for the annealed liquid at 1373 K in transmission and fluorescence (a), and at different temperatures up to the liquidus (b).

EBSCOhost - printed on 2/13/2023 5:26 AM via . All use subject to https://www.ebsco.com/terms-of-use

The XANES spectrum at the *K*-edge of Zr in the glass has a significant white line and few EXAFS oscillations, which characterizes a lack of long-range order. At 1373 K, the spectra contain the same white line, but it is followed by a series of very distinct oscillations, which imply a change of order in the distribution of Zr in the liquid, due to partial crystallization of the sample or structural reorganization around Zr. The spectral differences visible in Figure 15b, between transmission and fluorescence is explained by the fact that the whole sample is analyzed in transmission, while in fluorescence only the near surface is probed over approximately ten microns. The fact that the oscillations observed in transmission mode were more distinct than those in fluorescence means that the sample is more crystallized at its core than near the surface.

The white line varies little with temperature, while the oscillations increase after the glass transition because of partial crystallization of the sample. The spectrum of the liquid beyond the liquidus is similar to that of glass, and is therefore characteristic of a homogeneous phase in which long-range order is absent.

ADVANTAGES, DIFFERENCES AND CONCLUSIONS

Levitation techniques and heating wire devices are complementary tools, which can be used with a variety of diffraction and spectroscopic techniques to investigate materials at high temperatures for heating samples. Figure 16 shows X-ray diffraction patterns obtained using both systems. It clearly demonstrates that both heating methods give similar results within experimental error. However experimentally there are some differences between the two heating techniques which one should be aware of before deciding upon the most suitable method for specific experiments.

The conical nozzle levitation, CNL, laser heating, is easy to implement at very high temperatures, (>2000 K) and for samples from 10 mg up to 100 mg (1 mm to 5 mm diameter), allows very fast quench and a glass sample can be obtained with ease. CNL works with different atmospheres, pO_2 can be controlled and it does not use containers, which avoids any contacts with the heating system and potential surface effects on crystallization. The technique can be adapted to perform experiments using a wide variety of spectroscopic techniques at high temperature e.g., neutron and X-ray diffraction, X-ray absorption, small angle scattering, Raman spectroscopy, etc. Disadvantages are that CNL can induce vaporization of light elements and the chemical composition of the sample can change during the experiment because of the gas used as levitator.

The Wire Heating, WH, device, is easy to use at low temperature with Pt-Ir10% alloy, but can go to higher temperatures with appropriate heating wires (like W, Ir, Re, Ta…). However they are more difficult to mill and need to be used with controlled atmospheres. WH can work with less than 10 mg although the heating wire is in contact with the sample. This method is however ideal for working at lower temperatures with high thermal stability and enables studies of nucleation processes around the glass transition temperature for example. It can be placed in a vacuum chamber to investigate light elements using X-ray absorption spectroscopy but is not suitable for use in with neutron techniques, which require large sample volumes. WH is ideal for working on volatile elements, because the vaporization of the elements is very small, and the sample is contained within the hole in the wire. New developments now allow work with controlled atmosphere and radioactive elements such as U, Pu, and other radioactive actinides to investigate their structure with X-ray diffraction or absorption.

EBSCOhost - printed on 2/13/2023 5:26 AM via . All use subject to https://www.ebsco.com/terms-of-use

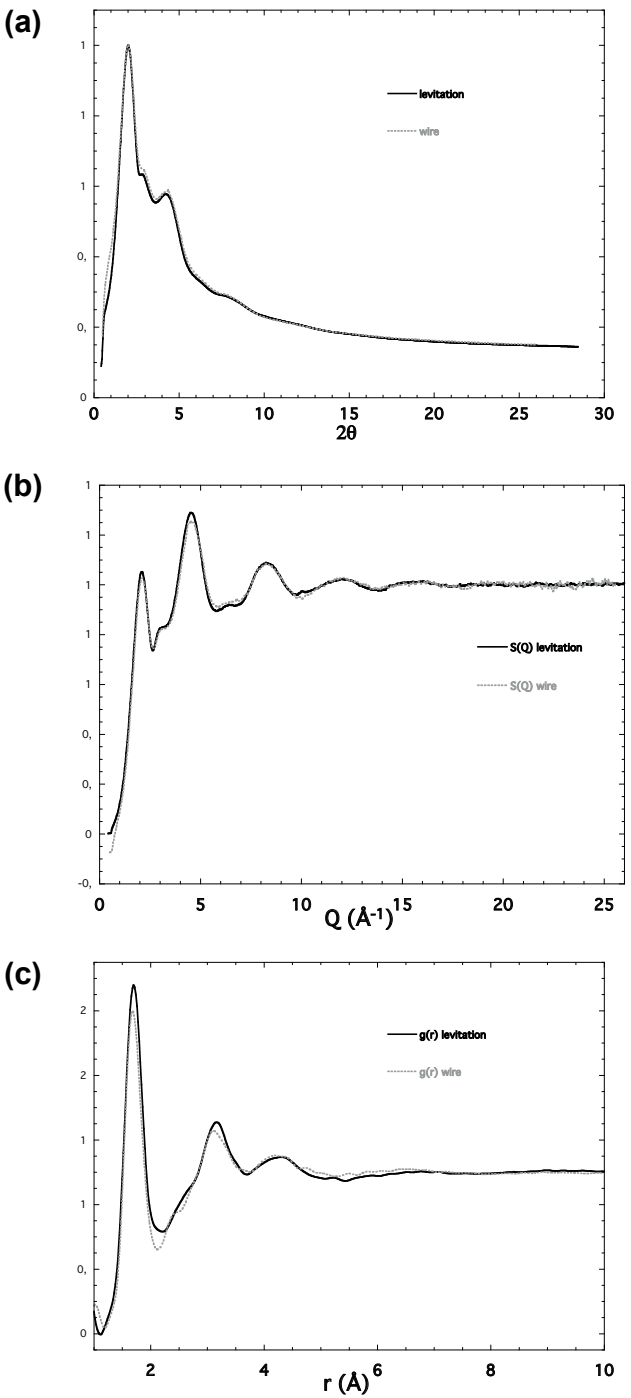


Figure 16. (a) X-ray diffraction measurements on calcium aluminosilicate (33% SiO_2-33% Al_2O_3-33% CaO in mol%), (b) S(Q) and (c) $g(r)$ obtained using levitation or a heating wire.

EBSCOhost - printed on 2/13/2023 5:26 AM via . All use subject to https://www.ebsco.com/terms-of-use

ACKNOWLEDGMENTS

Thanks to Eozen Strukelj and Mathieu Roskosz for help during measurement on DIFFABS beamline at SOLEIL. Paula Gonçalves Ferreira (Saint-Gobain Recherche), Philippe Martin (CEA-Cadarache), Florent Lebreton (CEA-Marcoule), Thibaud Delahaye (CEA-Marcoule), Dominique Thiaudière (SOLEIL) and Grant Henderson for constructive reviews.

REFERENCES

Ansell S, Krishnan S, Weber JKR, Felten JJ, Nordine PC, Beno MA, Price D, Saboungi ML (1997) Structure of liquid aluminum oxide. Phys Rev Lett 78:464-466

Berry AJ, MG Shelley, Garry J, Foran J, O'Neill H, Scott DR (2003) A furnace design for XANES spectroscopy of silicate melts under controlled oxygen fugacities and temperatures to 1773 K. J Synchrotron Radiat 10:332-336

Bytchkov A, Hennet L, Pozdnyakova I, Wright J, Vaughan G, Rossano S, Madjer K, Price DL (2010) Filming vitrification with time resolution. AIP Conf Proc 1234:219-222

Cochain B, Neuville DR, de Ligny D, Roux J, Baudelet F, Strukelj E, Richet P (2009) Kinetics of iron redox reaction in silicate melts: A high-temperature XANES study on an alkali basalt. J Physics IV 190:12182-12186

Cormier L, Neuville DR, Calas G (2000) Structure and properties of low-silica calcium aluminosilicate glasses. J Non-Cryst Solids 274:110-114

Cormier L, Neuville DR, Calas G (2005) Relationship between structure and glass transition temperature in low-silica calcium aluminosilicate glasses: the origin of the anomaly at low silica content. J Am Ceram Soc 88:2292-2299

Cormier L, Majérus O, Neuville DR, Calas G (2006) Temperature-induced structural modifications between alkali borate glasses and melts. J Am Ceram Soc 89:13-19

Cote B, Massiot D, Taulelle F, Coutures JP (1992) ^{27}Al NMR spectroscopy of aluminosilicate melts and glasses. Chem Geol 96:367-370

Coutures JP, Rifflet JC, Billard D, Coutures P (1986) Contactless treatments of liquids in a large temperature range by an aerodynamic levitation device and laser heating. *In:* Proc. 6th European Symposium on Materials Sciences Under Microgravity Conditions 5:427-430

Coutures JP, Massiot D, Bessada C, Echegut P, Rifflet JC, Taulelle F (1990) Etude par RMN ^{27}Al d'aluminates liquides dans le domaine 1600-2100 °C. C R Academie Sci Paris 310:1041-1045

Coutures JP, Rifflet JC, Florian P, Massiot D (1994) Etude par analyse thermique et par RMN très haute temperature de ^{27}Al de la solidification de Al_2O_3 en l'absence de nucleation hétérogène: effets de la temperature du liquide et de la pression partielle d'oxygène. Rev Int Hautes Temp Refract Fr 29:123-142

Daniel I, Gillet P, Ghose F (1995) An *in situ* high-temperature structural study of stable and metastable $CaAl_2Si_2O_8$ polymorphs. Mineral Mag 59:25-33

de Ligny D, Neuville D R, Cormier L, Roux J, Henderson GS. Panczer G, Shoval S, Flank A-M, Lagarde P (2009) Silica polymorphs, glass and melt: an *in situ* high temperature XAS study at the Si *K*-edge. J Non Cryst Solids 355:1099-1102

Della Ventura G, Marcelli A, Bellatreccia F (2014) SR-FTIR Microscopy and FTIR imaging in the earth sciences. Rev Mineral Geochem 78:447-479

Eckler K (1992) Dendritisches Wachstum in unterkuehlten Metallschmelzen. PhD Dissertation. Fakultät für Physik und Astronomie der Ruhr- Universität Bochum

Eeckhout SG, Gorges B, Barthe L, Pelos O, Safonova O, Giuli G (2008) A high-temperature furnace for *in situ* synchrotron X-ray spectroscopy under controlled atmospheric conditions. J Synchrotron Radiat 15:489-494

Egry I, Lohöfer G, Jacobs G (1995) Surface tension of liquid metals: results from measurements on ground and in space. Phys Rev Lett 75:4043-4046

Egry I, Hennet L, Kehr M, Mathiak G, De Panfilis S, Pozdnyakova I, Zanghi D (2008) Chemical short-range order in liquid aluminium-nickel alloys. J Chem Phys 129:064508

Enderby JE, Ansell S, Krishnan S, Price DL, Saboungi ML (1997) The electrical conductivity of levitated liquids. Appl Phys Lett 71:116-118

Fiquet G, Montagnac G, Richet P (1999) High-temperature thermal expansion of lime, periclase, corundum and spinel. Phys Chem Miner 27:103-111

Fischer HE, Hennet L, Cristiglio V, Zanghi D, Pozdnyakova I, May RP, Price DL, Wood S (2007) Magnetic critical scattering in solid $Co_{80}Pd_{20}$. J Phys Condens Matter 19: 415106-1-5

Florian P, Massiot D, Poe B, Farnan I, Coutures JP (1995) A time resolved ^{27}Al NMR study of the cooling process of liquid alumina from 2450 °C to crystallization. Solid State Nucl Magn Reson 5:233-238

EBSCOhost - printed on 2/13/2023 5:26 AM via . All use subject to https://www.ebsco.com/terms-of-use

Florian P, Sadiki N, Massiot D, Coutures JP (2007) ^{27}Al NMR study of the structure of lanthanum- and yttrium-based aluminosilicate glasses and melts. J Phys Chem B111: 9747-9757

Frantz JD, Mysen BO (1995) Raman spectra and structure of $BaO–SiO_2$, $SrO–SiO_2$ and $CaO–SiO_2$ melts to 1600 °C. Chem Geol 121:155-176

Gonçalves Ferreira P, de Ligny D, Lazzari O, Jean A, Cintora Gonzalez O, Neuville DR (2013) X-ray effect on the equilibrium redox state of iron-bearing earth alkali silicate glasses. Chem Geol 346:106-112

Greaves GN, Wilding MC, Fearn S, Langstaff D, Kargl F, Vu Van Q, Hennet L, Pozdnyakova I, Majérus O, Cernik RJ, Martin C (2008) *In situ* structural studies of alumina during melting and freezing. Adv Synchrotron Radiat 1(2):135-149

Grishchenko D, Piluso P (2011) Recent progress in the gas-film levitation as a method for thermophysical properties measurements: application to ZrO_2-Al_2O_3 system. High Temp High Press 40:127-149

Gruener G, Odier P, Meneses D, Florian P (2001) Bulk and local dynamics in glass-forming liquids: A viscosity, electrical conductivity and NMR study of aluminosilicate melts. Phys Rev B 64:024201

Gruner S, Marczinke J, Hennet L, Hoyer W, Cuello GJ (2009) On the atomic structure of liquid Ni-Si alloys: A neutron diffraction study. J Phys Condens Matter 21:385403:1-7

Haumesser PH, Garandet JP, Bancillon J, Daniel M (2002) High temperature viscosity measurements by the gas film levitation technique: application to various types of materials. Int J Thermophys 23:1217-1228

Hawthorne FC (ed) (1988) Spectroscopic Methods in Mineralogy and Geology. Reviews in Mineralogy, Volume 18. Mineralogical Society of America

Henderson GS, Neuville DR, Cochain B, Cormier L (2009) The structure of GeO_2-SiO_2 glasses and melts: A Raman spectroscopy study. J Non-Cryst Solids 355:468-474

Henderson GS, de Groot FMF, Moulton BJA (2014) X-ray absorption near-edge structure (XANES) spectroscopy. Rev Mineral Geochem 78:75-138

Hennet L, Pozdnyakova I, Bytchkov A, Cristiglio V, Palleau P, Fischer HE, Cuello GJ, Johnson M, Melin P, Zanghi D, Brassamin S, Brun J-F, Price DL, Saboungi ML (2006) Levitation apparatus for neutron diffraction investigations on high temperature liquids. Rev Sci Instrum 77:053903

Hennet L, Pozdnyakova I, Bytchkov A, Price DL, Greaves GN, Wilding M, Fearn S, Martin CM, Thiaudière D, Bérar JF, Boudet N, Saboungi ML (2007b) Development of structural order during supercooling of a fragile oxide melt. J Chem Phys 126: 074906-1-4

Hennet L, Pozdnyakova I, Cristiglio V, Cuello GJ, Jahn S, Krishnan S, Saboungi M-L, Price DL (2007a) Short- and intermediate-range order in levitated liquid aluminates J Phys-Condens Matter 19:4552101-11

Hennet L, Cristiglio V, Kozaily J, Pozdnyakova I, Fischer H.E, Bytchkov A, Drewitt J W E, Leydier M, Thiaudière D, Gruner S, Brassamin S, Zanghi D, Cuello GJ, Koza M, Magazu S, Greaves GN, Price DL (2011) Aerodynamic levitation and laser heating. Eur Phys J Special Topics 196:151-165

Holland-Moritz D, Schenk T, Convert P, Hansen T, Herlach DM (2005) Electromagnetic levitation apparatus for diffraction investigations on the short-range order of undercooled metallic melts. Meas Sci Technol 16:372-380

Holland-Moritz D, Stuber S, Hartmann H, Unruh T, Hansen T, Meyer A (2009) Structure and dynamics of liquid $Ni_{36}Zr_{64}$ studied by neutron scattering. Phys Rev B 79:064204

Jacobs G, Egry I, Maier K, Platzek D, Reske J, Frahm R (1996) Extended X-ray-absorption fine structure studies of levitated undercooled metallic melts. Rev Sci Instrum 67: 683-3687

Kelton KF, Lee GE, Gangopadhyay AK, Hyers RW, Rathz TJ, Rogers JR, Robinson DS, Robinson MB (2003) First X-ray scattering studies on electrostatically levitated metallic liquids: demonstrated influence of local icosahedral order on the nucleation barrier. Phys Rev Lett 90:195504-1-4

Kimura H, Watanabe M, Izumi K, Hibiya T, Holland-Moritz D, Schenk T, Bauchspiess KR, Schneider S, Egry I, Funakoshi K, Hanfland M (2001) X-ray diffraction study of undercooled molten silicon. Appl Phys Lett 78:604-606

Kobatake H, Fukuyama H, Minato I, Tsukada T, Awaji S (2007) Noncontact measurement of thermal conductivity of liquid silicon in a static magnetic field. Appl Phys Lett 90: 094102

Kozaily J (2012) Structure et Dynamique d'aluminosilicates de calcium fondus. PhD Dissertation. Orléans University. 165 pp

Kozaily J, Hennet L, Fischer HE, Koza M, Brassamin S, Magazu S, Kargl F (2011) Time-of-flight neutron spectroscopy: a new application of aerodynamic sample levitation. Phys Status Solidi C 8:3155-3158

Krishnan S, Felten JJ, Rix JE, Weber JKR, Nordine PC, Beno MA, Ansell S, Price DL (1997) Levitation apparatus for structural studies of high temperature liquids using synchrotron radiation. Rev Sci Instrum 68:3512-3518

Lacassagne V, Bessada C, Florian P, Bouvet S, Ollivier B, Coutures JP and Massiot D (2002) Structure of high-temperature NaF-AlF_3-Al_2O_3 melts: A multinuclear NMR study. J Phys Chem B 106:1862-1868

Landron C, Hennet L, Coutures JP, Gailhanou M, Gramond M, Bérar JF (1998) Contactless investigation on laser-heated oxides by synchrotron radiation. Europhys Lett 44:429-435

EBSCOhost - printed on 2/13/2023 5:26 AM via . All use subject to https://www.ebsco.com/terms-of-use

Landron C, Hennet L, Coutures JP, Jenkins T, Aletru C, Greaves NG, Soper AK, Derbyshire G (2000) Aerodynamic laser-heated contactless furnace for neutron scattering experiments at elevated temperatures. Rev Sci Instrum 71:1745-1751

Landron C, Hennet L, Jenkins T, Greaves GN, Coutures JP, Soper A (2001) Liquid alumina: detailed atomic coordination determined from neutron diffraction data using empirical potential structure refinement. Phys Rev Lett 86:4839-4842

Le Losq C, Neuville DR, Florian P, Henderson GS, Massiot D (2014) The role of Al^{3+} on rheology and structural changes in sodium silicate and aluminosilicate glasses and melts. Geochim Cosmochim Acta. 126:495-517

Lenoir M, Neuville DR, Malki M, Grandjean A (2010) Volatilization kinetics of sulphur from borosilicate melts: a correlation between sulphur diffusion and melt viscosity. J Non-Cryst Solids 356:2722-2727

Lohöfer G (2005) Electrical resistivity measurement of liquid metals. Meas Sci Technol 16:417-425

Magnien V, Neuville DR, Cormier L, Roux J, Hazemann JL, de Ligny D, Pascarelli S, Vickridge I, Pinet O. and Richet P (2008) Kinetics and mechanisms of iron redox reactions in silicate melts: The effects of temperature and alkali cations. Geochim Cosmochim Acta 72: 2157-2168

Manara D, Grandjean A, Pinet O, Dussossoy JL, Neuville DR (2007) Sulphur behaviour in silicate glasses and melts: implications for sulphate incorporation in nuclear waste glasses as a function of alkali cation and V_2O_5 content. J Non Cryst Solids 353:12-23

Masaki T, Ishikawa T, Paradis PF, Yoda S, Okada JT, Watanabe Y, Nanao S, Ishikukra A, Higuchi K, Mizuno A, Watanabe M, Kohara S (2007) Compact electrostatic levitator for diffraction measurements with a two axis diffractometer and a laboratory X-ray source. Compact electrostatic levitator for diffraction measurements with a two axis diffractometer and a laboratory X-ray source. Rev Sci Instrum 78:026102

Massiot D, Trumeau D, Touzo B, Farnan I, Rifflet J C, Douy A, Coutures JP (1995) Structure and dynamics of $CaAl_2O_4$ from liquid to glass - a high-temperature Al-27 NMR time-resolved study. J Phys Chem 99:16455-16459

Mathiak G, Egry I, Hennet L, Thiaudière D, Pozdnyakova I, Price DL (2005) Aerodynamic levitation and inductive heating – a new concept for structural investigations of undercooled melts. Int J Thermophys 26:1151-1166

Matsumura S, Watanabe M, Mizuno A, Kohara S (2007) Supercooled barium boric oxide melts: X-ray diffraction measurements and glass formation. J Am Ceram Soc 90:742-745

McMillan PF, Wolf GH, Poe BT (1992) Vibrational spectroscopy of silicate liquids and glasses. Chem Geol 96:351-366

McMillan PF, Poe BT, Gillet P, Reynard B (1994) A study of SiO_2 glass and supercooled liquid to 1950 K via high-temperature Raman spectroscopy. Geochim Cosmochim Acta 58:3653-3664

Mei Q, Benmore CJ, Weber JKR, Wilding M, Kim J, Rix J (2008) Diffraction study of calcium aluminate glasses and melts: II. High energy X-ray diffraction on melts. J Phys Condens Matter 20:245107-1-7

Meyer A, Stüber S, Holland-Moritz D, Heinen O, Unru T (2008) Determination of self-diffusion coefficients by quasielastic neutron scattering measurements of levitated Ni droplets. Phys Rev B 77:092201

Millot F, Rifflet JC, Wille G, Sarou-Kanian V, Glorieux B (2002) Analysis of surface tension from aerodynamic levitation of liquids. J Am Ceram Soc 85:187-192

Mysen BO, Frantz JD (1992) Raman spectroscopy of silicate melts at magmatic temperatures: Na_2O-SiO_2, K_2O-SiO_2, and Li_2O-SiO_2 binary compositions in the temperature range 25°-1783°C. Chem Geol 96:321-332

Mysen BO, Frantz JD (1993) Structure and properties of alkali silicate melts at magmatic temperatures. Eur J Mineral 5:393-407

Mysen BO, Frantz JD (1994a) Alkali silicate glass and melts structure in the temperature range 25-1651°C at atmospheric pressure and implications for mixing behavior of structural units. Contrib Mineral Petrol 117:1-14

Mysen BO, Frantz JD (1994b) Structure of haplobasaltic liquids at magmatic temperatures: *in situ*, high-temperature study of melts on the join $Na_2Si_2O_5$-$Na_2(NaAl)_2O_5$. Geochim Cosmochim Acta 58:1711-1733

Mysen BO, Neuville DR (1995) Effect of temperature and TiO_2 content on the structure of $Na_2Si_2O_5$-$Na_2Ti_2O_5$ and glasses. Geochim Cosmochim Acta 59:325-342

Neuville DR, Mysen BO (1996) Role of aluminiun in the silicate network: *in situ*, high-temperature study of glasses and melts on the join SiO_2-$NaAlO_2$. Geochim Cosmochim Acta 60:1727-1737

Neuville DR, Cormier L, Flank AM, de Ligny D, Roux J, Lagarde P (2008) Environment around Al, Si and Ca in aluminate and aluminosilicate melts by X-ray absorption spectroscopy at high temperature. Am Mineral 93:228-234

Neuville DR, de Ligny D, Cormier L, Henderson G.S, Roux J, Flank AM, Lagarde P (2009) The crystal and melt structure of spinel and alumina at high temperature: an *in situ* XANES study at the Al and Mg *K*-edge. Geochim Cosmochim Acta 73:3410-3422

EBSCOhost - printed on 2/13/2023 5:26 AM via . All use subject to https://www.ebsco.com/terms-of-use

Neuville DR, de Ligny D, Henderson GS (2014) Advances in Raman spectroscopy applied to earth and material sciences. Rev Mineral Geochem 78:509-541

Newville M (2014) Fundamentals of XAFS. Rev Mineral Geochem 78:33-74

Notthoff C, Franz H, Hanfland M, Herlach DM, Holland-Moritz D, Petry W (2000) Electromagnetic levitation apparatus for investigations of the phase selection in undercooled melts by energy-dispersive X-ray diffraction. Rev Sci Instrum 71:3791-3796

Ohashi Y, Hadidiacos CG (1976) A controllable thermocouple microheater for high-temperature microscopy. Carnegie Inst Washington Ann Rep 75:828-833

Paradis PF, Ishikawa T (2005) Surface tension and viscosity measurements of liquid and undercooled alumina by containerless techniques. Jpn J Appl Phys 44:5082–5085

Paradis PF, Ishikawa T, Yu J, Yoda S (2001) Hybrid electrostatic–aerodynamic levitation furnace for the high-temperature processing of oxide materials on the ground. Rev Sci Instrum 72:2811-2815

Paradis PF, Ishikawa T, Yoda S (2002) Electrostatic levitation furnace for structural studies of high temperature liquid metals by neutron scattering experiments. J Non-Cryst Solids 312-314: 309-313

Poe BT, McMillan PF, Coté B, Massiot D, Couture JP (1992) SiO_2-Al_2O_3 liquids: *in situ* study by high-temperature, ^{27}Al NMR spectroscopy and molecular dynamics simulation. J Phys Chem 96:8220-8224

Pozdnyakova I, Hennet L, Brun J F, Zanghi D, Brassamin S, Cristiglio V, Price DL, Albergamo F, Bytchkov A, Jahn S, Saboungi ML (2007) Longitudinal excitations in Mg–Al–O refractory oxide melts studied by inelastic X-ray scattering. J Chem Phys 126:114505

Price DL (2010) High-temperature Levitated Materials. Cambridge University Press

Reynard B, Webb SL (1998) High-temperature Raman spectroscopy of Na_2TiSi_{207} glass and melt: coordination of Ti + and nature of the configurational changes in the liquid. Eur J Mineral 10:49-58

Richet P, Gillet P, Pierre A, Bouhifd A, Daniel I, Fiquet G (1993) Raman spectroscopy, X-ray diffraction, and phase relationship determinations with a versatile heating cell for measurements up to 3600 K (or 2700 K in air). J Appl Phys 74:5451-5456

Richet P, Mysen BO, Ingrin J (1998) High-temperature X-ray diffraction and Raman spectroscopy of diopside and pseudowollastonite. Phys Chem Mineral 25:401-414

Rollet AL, Sarou-Kanian V, Bessada C (2009) Measuring self-diffusion coefficients up to 1500 K: a powerful tool to investigate the dynamics and the local structure of inorganic melts. Inorg Chem 48:10972-10975

Schenk T, Holland-Moritz D, Simonet V, Bellissent R, Herlach DM (2002) Icosahedral short-range order in deeply undercooled metallic melts. Phys Rev Lett 89: 075507

Sen S (1999) Temperature induced structural changes and transport mechanisms in borate, borosilicate and boroaluminate liquids: high-resolution and high-temperature NMR results. J Non-Cryst Solids 253:84-94

Shen G, Wang Y (2014) High-pressure apparatus integrated with synchrotron radiation. Rev Mineral Geochem 78:745-777

Skinner L, Barnes AC (2006) An oscillating coil system for contactless electrical conductivity measurements of aerodynamically levitated melts. Rev Sci Instrum 77:123904

Stebbins JF, Xue X (2014) NMR Spectroscopy of inorganic earth materials. Rev Mineral Geochem 78:605-653

Taylor M, Brown GE Jr (1979a) Structure of mineral glasses. I. The feldspar glasses $NaAlSi_3O_8$, $KAlSi_3O_8$, $CaAl_2Si_2O_8$. Geochim Cosmochim Acta 43:61-75

Taylor M, Brown GE Jr (1979b) Structure of mineral glasses. II. The SiO_2-$NaAlSiO_4$ join. Geochim Cosmochim Acta 43:1467-1473

Trinh EH (1985) Compact acoustic levitation device for studies in fluid dynamics and material science in the laboratory and microgravity. Rev Sci Instrum 56:2059-2065

Urbain G (1983) Viscosités de liquide du système CaO-Al_2O_3. Revue Internationale des Hautes Températures et des Réfractaires 20:135-139

Vo-Thanh D, Bottinga Y, Polian A, Richet P (2005) Sound velocity in alumino-silicate liquids determined up to 2550K from Brillouin spectroscopy: glass transition and crossover temperatures. J Non-Cryst Solids 351:61-68

Weber JKR, Benmore CJ, Tangeman JA, Siewenie J, Hiera KJ (2003) Structure of binary CaO–Al_2O_3 and SrO–Al_2O_3 liquids by combined levitation-neutron diffraction. J Neutron Res 11:113-121

Wilke M, Farges F, Petit PE, Brown GE Jr, Martin F (2001) Oxidation state and coordination of Fe in minerals: an Fe K-XANES spectroscopic study. Am Mineral 86:714-730

Winborne DA, Nordine PC, Rosner DE, Marley NF (1976) Aerodynamic levitation technique for containerless high temperature studies on liquid and solid samples. Metall Trans B 7:711-713

EBSCOhost - printed on 2/13/2023 5:26 AM via . All use subject to https://www.ebsco.com/terms-of-use

EBSCOhost - printed on 2/13/2023 5:26 AM via . All use subject to https://www.ebsco.com/terms-of-use

EBSCOhost - printed on 2/13/2023 5:26 AM via . All use subject to https://www.ebsco.com/terms-of-use